

**NASA Technical Memorandum 4041**

NASA-TM-4041 19880017749

**Reports of Planetary Geology  
and Geophysics Program—1987**

**JUNE 1988**

**LIBRARY COPY**

1988

LANGLEY RESEARCH CENTER  
LIBRARY, NASA  
HAMPTON, VIRGINIA

**NASA**

NASA Technical Memorandum 4041

# Reports of Planetary Geology and Geophysics Program—1987

*NASA Office of Space Science and Applications  
Washington, D.C.*



National Aeronautics  
and Space Administration

Scientific and Technical  
Information Division

1988

## FOREWORD

This is a compilation of abstracts of reports from Principal Investigators of NASA's Office of Space Science and Applications, Solar System Exploration Division, Planetary Geology and Geophysics Program.

The purpose of this publication is to document in summary form research work conducted in this program over the past year (1986). Each report reflects significant accomplishments within the area of the author's funded grant or contract.

No attempt has been made to introduce editorial or stylistic uniformity; on the contrary, the style of each report is that of the Principal Investigator and may best portray his research.

Joseph Boyce  
Discipline Scientist  
Planetary Geoscience Program





## CONTENTS

Foreword .....	iii
CHAPTER 1 - OUTER PLANET SATELLITES AND RINGS	
Dynamics of Outer Planet Rings .....	3
L.W. Esposito, G.R. Stewart, T.G. Brophy, J.E. Colwell, and P.A. Yanamandra-Fisher	
A Re-examination of Radial Diffusion in Planetary Rings .....	5
G.R. Stewart	
Dynamics and Structure of Planetary Rings .....	6
R.G. French	
Optical Depths and Equivalent Widths of the Uranian Epsilon Ring from the Voyager 2 Photopolarimeter .....	7
A.L. Graps, J.J. Lissauer, and M.R. Showalter	
Dynamical Studies of Planetary Rings .....	8
P.D. Nicholson	
Observational Studies of Saturn's Rings .....	11
C.C. Porco	
Physical Processes in Planetary Rings .....	14
J.A. Burns	
Speculative Histories of the Uranian Satellite System .....	17
S.J. Peale	
Dynamics of Satellites, Asteroids, and Rings .....	18
S.F. Dermott	
Thermal and Dynamical Processes in the Evolution of Outer Planet Satellites .....	21
G. Schubert	
Small Satellites of Uranus .....	23
P.C. Thomas and J. Veverka	
Satellites of Uranus: Shapes and Topography from Limb Coordinates .....	25
P.C. Thomas	
Shapes of Small Satellites from Limb Coordinates .....	28
P.C. Thomas	

Volatile Processes on Large Satellites of the Giant Planets .....	31
J.I. Lunine	
Cratering History of Umbriel, Titania, and Oberon .....	34
J.B. Plescia	
Vertical Relief of Martian Wrinkle Ridges: Implications for Internal Structure .....	36
J.B. Plescia	
Bombardment History of the Saturn System I: Spatial and Size- Frequency Distributions of Craters .....	38
S.W. Squyres, J.J. Lissauer, and W.K. Hartmann	
Bombardment History of the Saturn System II: Catastrophic Fragmentation of Moons .....	39
J.J. Lissauer and S.W. Squyres	
CHAPTER 2 - COMETS AND ASTEROIDS	
Comet Research .....	43
F.L. Whipple	
The Rotation of Halley's Comet .....	46
S.J. Peale and J. Lissauer	
Cometary Physics and Dynamics .....	47
P.R. Weissman	
Clathrates and Porosity in Cometary Nuclei .....	50
R. Smoluchowski and J. Green	
The Palomar Asteroid and Comet Survey (PACS), 1982-1987 .....	52
C.S. Shoemaker and E.M. Shoemaker	
Meteoroid Environment Near the Earth-Moon System .....	55
Y. Nakamura and J. Oberst	
The Size Distribution of Asteroids from IRAS and the Martian Cratering Record .....	57
R.G. Strom	
Convex-Profile Inversion of Asteroid Lightcurves .....	60
S.J. Ostro	
Meteorite Spectroscopy and Characterization of Asteroid Surface Materials .....	63
M.J. Gaffey	
The Stratigraphy of the Asteroid Belt: An Outline Model .....	66
J.F. Bell	

## CHAPTER 3 - COSMOGONY AND DYNAMICS

Solar System Dynamics .....	71
J. Wisdom	
Orbital Acceleration of Io .....	73
R. Greenberg	
Tidal Evolution of Jupiter's Satellites .....	76
J.H. Lieske	
Composition of Uranus and Neptune: Nonsolar Ice to Rock Ratios? .....	79
R.T. Reynolds and M. Podolak	
Carbon in the Outer Solar System .....	82
D.P. Simonelli, J.B. Pollack, and C.P. McKay	
Collisional and Gas Dynamics of Accretion .....	84
S.J. Weidenschilling	
Analysis of Planetary Evolution with Emphasis on Differentiation and Dynamics .....	87
W.M. Kaula, W.I. Newman, E. Myhill, and W. Weibel	
Accumulation of the Planets .....	90
G.W. Wetherill	
Protoplanet Accretion Rates .....	92
J.J. Lissauer and Y. Greenzweig	
Protoplanet Accretion Rates in a Disk of Planetesimals with Low Random Velocities .....	93
J.J. Lissauer and Y. Greenzweig	
Protoplanet Accretion Rates in a Uniform Disk of Planetesimals Neglecting Gravitational Focusing .....	94
Y. Greenzweig and J.J. Lissauer	
Gravitational Focusing During Planetary Encounters .....	95
R. Greenberg, G.B. Valsecchi, and A. Carusi	
Collisional Dynamics of Particulate Flows: Computational Studies .....	98
W.W. Roberts, Jr.	
N-Body Simulations of the Cloudy Interstellar Medium in Density Wave-Dominated Galaxies: Orbit Trapping, Sloshing, Self Gravity, and Spiral Structure .....	99
W.W. Roberts, Jr., D.S. Adler, and G.R. Stewart	
The Cloudy Interstellar Medium: Aggregation of Giant Molecular Clouds in Spiral Structures .....	102
W.W. Roberts, Jr. and D.S. Adler	
Gaseous Self Gravitational Effects in the Aggregation of Giant Molecular Clouds and the Stability of Global Spiral Structures .....	105
W.W. Roberts, Jr. and D.S. Adler	

## CHAPTER 4 - PLANETARY INTERIORS, PETROLOGY, AND GEOCHEMISTRY

Properties of Planetary Materials at High Pressures and Temperatures .....	109
W.J. Nellis, D.C. Hamilton, N.C. Holmes, H.B. Radousky, and F.H. Ree	
Melting Studies at High Pressure .....	112
W.A. Bassett, M.S. Weathers, and E. Huang	
High Pressure Cosmochemistry of Major Planetary Interiors: Laboratory Studies of the Water-Rich Region of the System Ammonia-Water .....	114
M. Nicol, S. Boone, H. Cynn, and A. Koumvakalis	
Implications of Convection in the Moon and the Terrestrial Planets .....	117
D.L. Turcotte	
Atmospheric-Lithospheric Interactions on Venus: Experimental Investigations .....	119
D.W. Tucker, J.R. Marshall, R. Greeley, C. Moore, and J. Pollack	
Iron Oxidation State in Antarctic Shergottite EETA 79001 .....	121
R.G. Burns and T.C. Solberg	
Martian (?) Volatile Compounds in SNC Meteorites .....	124
J.L. Gooding, K. Aggrey, and D.W. Muenow	
Sulfide Mineralization: Its Role in Chemical Weathering of Mars .....	127
R.G. Burns	
Climate, Atmosphere, and Volatile Inventory Evolution: Polar Processes, Climate Records, Volatile Inventories .....	130
J.B. Pollack	
The Effects of Insolation Penetration into Icy Regoliths: Application to Europa .....	131
F.P. Fanale and J.R. Salvail	
Experimental Studies of Sublimation in Ice and Ice/Particulate Mixtures: Applications to Mars .....	133
J.M. Moore and M.C. Malin	
Clathrate and Ammonia Hydrates: Physical Chemistry and Applications to the Solar System .....	135
J.I. Lunine, S.K. Croft, and J. Kargel	
Low Temperature Mineral Phases on Phobos? .....	138
K.K. Pierce and B. Murray	

## CHAPTER 5 - SPECTROSCOPY AND REMOTE SENSING

Automated Analysis of Reflectance Spectra .....	143
R.N. Clark	
Mid-Infrared (2.1-25.0 $\mu\text{m}$ ) Spectroscopic Studies .....	146
J.W. Salisbury and L.S. Walter	

Abundance Estimates Derived from Reflectance Spectra of Tricomponent Mixtures .....	149
J.F. Mustard and C.M. Pieters	
Effects of Small-Scale Surface Roughness on the Bidirectional Reflectance Spectra of Nickel-Iron Meteorites .....	150
D.T. Britt and C.M. Pieters	
Specular Reflections and the Nature of Particle Surface Interactions .....	152
S.A. Yon and C.M. Pieters	
Reflectance Properties of Planetary Surface Materials .....	154
W.D. Smythe, B.J. Buratti, R.M. Nelson, L. Horn, V. Gharakhani, and B.W. Hapke	
The Optical Effects of Surface Processes on Small Bodies .....	157
D.T. Britt and C.M. Pieters	
The Global Distribution, Abundance, and Stability of SO <sub>2</sub> on Io .....	159
A.S. McEwen, T.V. Johnson, D.L. Matson, and L.A. Soderblom	
Io Sulfur Processes .....	160
R.M. Nelson and W.D. Smythe	
Experiments on Vacuum Weathering of Sulfur and Applications to Io .....	162
D. Nash and J. Moses	
The Surface of Io: A New Model .....	165
B. Hapke	
Spectral Properties of Disulfur Monoxide, Polysulfur Oxide and Irradiated Sulfur .....	166
B. Hapke and F. Graham	
Io: A Comparison of Old and New Hapke Parameters from Voyager Disk-Integrated Photometry .....	167
P. Helfenstein, J. Veverka, and D.P. Simonelli	
Reassessment of the Reflectance Spectra of Callisto and Ganymede .....	170
T.L. Roush, J.B. Pollack, and F.C. Witteborn	
Charged Particle Modification of Surfaces in the Outer Solar System .....	171
R.E. Johnson	
Albedo Patterns of the Saturnian Satellites .....	173
B.J. Buratti, J.A. Mosher, and R.J. Terrile	
Color and Albedo Maps of Miranda .....	176
J. Hillier, P. Helfenstein, and J. Veverka	
Rhea: Analysis of Photometry Using Hapke's Equation .....	179
A. Verbiscer and J. Veverka	

Absolute Photometry of the Martian Surface and Atmosphere .....	182
K.E. Herkenhoff and B.C. Murray	
Remote Sensing of Mars .....	185
B.M. Jakosky	
Viking Landers and Remote Sensing .....	188
H.J. Moore, B.M. Jakosky, and P.R. Christensen	
Surface Composition of Mars: A Viking Multispectral View .....	191
J.B. Adams, M.O. Smith, R.E. Arvidson, M. Dale-Bannister, E.A. Guinness, and R. Singer	
Nature and Distribution of Surficial Deposits in Chryse Planitia and Vicinity, Mars .....	194
R. Arvidson, E. Guinness, M. Dale-Bannister, J. Adams, P. Christensen, and R. Singer	
Nature and Origin of Materials Exposed in the Oxia Palus-Western Arabia-Sinus Meridiani Region, Mars .....	197
M. Presley and R. Arvidson	
Thermal Emission from Planetary Regoliths .....	200
B. Hapke	
Thermal Emission Spectroscopy of Minerals and Mixtures .....	201
P.R. Christensen	
High Resolution Thermal Imaging of Volcanic Terrains on Mars .....	204
P.R. Christensen and M.C. Malin	
A Search for Subsurface Ice on Mars Using Viking Thermal Mapper Observations .....	207
D.A. Paige	
Martian Polar Frost and Atmosphere/Soil Water Exchange .....	210
T. Svitek and B.C. Murray	
Detecting the Possible Presence of Lunar Ice by Means of Coupled Neutron-Gamma Ray Spectroscopy .....	213
A.E. Metzger and E.L. Haines	
Rima Hyginus and Vicinity: Preliminary Remote Sensing Studies .....	216
B.R. Hawke and C.R. Coombs	
Stratigraphy and Evolution of the Lunar Highland Crust: A Sampling of Vertical and Regional Heterogeneities .....	219
C.M. Pieters	

## CHAPTER 6 - RADAR APPLICATIONS

Goldstone Radar Observations of Mars: 1986 Results .....	223
T.W. Thompson	
Ultra-High Resolution Radar Mapping of the Moon at 70 cm Wavelength .....	225
T.W. Thompson	

Radar Altimetry of the Martian Cratered Highlands .....	227
L.E. Roth	
Development of a Technique to Simulate the Ability of Magellan's SAR to Discriminate Volcanic Units .....	229
S.D. Wall, E. Theilig, and R.S. Saunders	
Investigations of the Relationship Between Radar Backscatter and Aeolian Roughness Characteristics of Desert Surfaces .....	232
R. Greeley, N. Lancaster, R. Sullivan, R.S. Saunders, E. Theilig, S. Wall, A Dobrovolskis, B.R. White, and J.D. Iversen	
Analysis of Simulated Venera and Magellan Images Over Terrestrial Regions and Implications for Characterizing Surficial Processes on Venus .....	235
R. Arvidson, M Schulte, R. Kwok, J. Curlander, C. Elachi, J. Ford, and R. Saunders	
Venus Gravity .....	237
W.L. Sjogren	
Improvement in Precision of Measurements Made by the Synthetic Aperture Radar Compilation System for the Magellan Mission .....	240
S.S.C. Wu, F.J. Schafer, and A. Howington-Kraus	
Lunar Radar Investigations .....	242
P.J. Mougini-Mark and B.C. Campbell	
Numerical Modeling of Radiowave Scattering .....	245
R.A. Simpson and G.L. Tyler	
Progress in Two-Dimensional Radarclinometry .....	248
R.L. Wildey	
Complex Dielectric Constants of Cyrogenic Liquid Alkanes at 1.26Hz .	251
V.G. Anicich and T. Arakelian	

## CHAPTER 7 - AEOLIAN PROCESSES

The Effect of Particle Speed and Concentration on Aeolian Gradation: Earth, Mars, and Venus .....	257
S.H. Williams and R. Greeley	
Aeolian Sorting of Heavy Minerals on Venus .....	260
R. Greeley, J.R. Marshall, D. Clemens, A Dobrovolskis, and J. Pollack	
Mechanical Aeolian Weathering of Venusian Surface Materials .....	262
J.R. Marshall, D.W. Tucker, and R. Greeley	
Comparison of Aeolian Surface Roughness Measured in a Field Experiment and a Wind Tunnel Simulation .....	264
R. Sullivan and R. Greeley	
Wind Tunnel Simulation of Planetary Eolian Phenomena .....	267
J.D. Iversen	

Semi-Quantitative Remote Sensing of Aeolian Terrains Using a Linear Mixing Model .....	273
G. Blount, R. Greeley, P.R. Christensen, and N. Lancaster	
Variations in Surface Shear Stress Over a Small Aeolian Dune .....	275
N. Lancaster	
A Possible Volatile-Rich Air-Fall Deposit in the Electris Region of Mars .....	278
J.A. Grant and P.H. Schultz	
Distribution and Timing of Thick Transient Air-Fall Deposits in Electris: Implications for the Nature of the Upland Plains .....	280
J.A. Grant and P.H. Schultz	
Erosional and Depositional Processes in the Martian Heavily- Cratered Terrain .....	283
J.M. Moore and M.C. Malin	
Mars: Dune Sand Sources in North Polar Layered Deposits .....	286
P.C. Thomas	
Accumulation of Sedimentary Debris in the South Polar Region of Mars and Implications for Climate History .....	289
J. Plaut, R. Kahn, E. Guinness, and R. Arvidson	
CHAPTER 8 - FLUVIAL PROCESSES	
Power of Martian Floods .....	293
V.R. Baker	
Peak Flows for Cataclysmic Floods .....	299
V.R. Baker and J.E. O'Connor	
The Inventory of Water on Mars .....	302
M.H. Carr	
Characteristics of Martian Channel Materials .....	305
R.A. Craddock, R. Greeley, P.R. Christensen, and F.T. Aldrich	
Morphologic Contrasts Between Nirgal and Auqakuh Valles, Mars: Evidence of Different Crustal Properties .....	308
D.J. MacKinnon, K.L. Tanaka, and P.J. Winchell	
Eastern Lunae Planum Outflow Complex: Analogy to Overbank Flooding .	311
R.A. De Hon	
Flow-Competence Evaluations of the Hydraulic Parameters of Floods: An Assessment of the Technique .....	313
P.D. Komar	
Three-Dimensional Digital Simulation of Drainage Basin Development: Modeling the Martian Valley Networks .....	316
A.D. Kelley and M.C. Malin	
Laboratory Simulation of Outflow Channel Formation on Mars .....	318
K.A. McGeehan and S.A. Schumm	



Preliminary Investigation of Geological Controls on Valleys Influenced by Groundwater Sapping .....	320
R.C. Kochel and M.A. Phillips	

## CHAPTER 9 - VOLCANIC PROCESSES AND LANDFORMS

Volcano Studies on Mars .....	325
P. Mougini-Mark, L. Wilson, and A. Mathews	
Possible Effects of Epochal/Episodic Release of SO <sub>2</sub> on Early Martian Climate .....	328
S.E. Postawko, F.P. Fanale, and A.P. Zent	
Rheologic Modeling of the Olympus Mons Aureole .....	330
J. Fink	
Physical and Chemical Conditions Implied by Volcanic Calderas .....	332
D.F. Sailer and D. Pieri	
Geomorphology of Valleys, Alcoves, and Etched Terranes at Alba Patera .....	334
D. Pieri and D. Schneeberger	
Some New Designations for Lava Flows at Alba Patera .....	337
D. Pieri and D. Schneeberger	
A New Model for Leveed Flows on Mars .....	340
S.M. Baloga and J.A. Crisp	
Constraints on Mars Sampling Based on Models of Basaltic Flow Surfaces and Interiors .....	343
J.C. Aubele and L.S. Crumpler	
Sampling and Models of Basaltic Flows .....	344
J.C. Aubele and L.S. Crumpler	
Small Martian Volcanoes .....	345
P.A. Davis and K.L. Tanaka	
Progress in Determining the Thickness and Distribution of Volcanic Materials on Mars .....	347
R.A. De Hon	
IRTM Analysis of Possible Explosive Volcanic Deposits on Mars .....	349
D.A. Crown, L.A. Leshin, and R. Greeley	
Ocean-Floor Volcanism as a Venus Analog .....	352
P.J. Mougini-Mark, P. Fryer, and L. Wilson	
Classification and Distribution of Possible Volcanic Structures in the Equatorial Region of Venus .....	356
D.A. Senske and J.W. Head	
Rheologic Properties of Industrial Sulfur Flows .....	359
D.A. Crown	
Relationships Between Morphology and Rheology of Lava Flows .....	362
J. Fink and J. Zimbelman	

Morphology of the Bishop Tuff .....	365
M.F. Sheridan	
Lateral Migration and Eruption of Magma in Volcanic Edifice	
Rift Zones .....	367
J.W. Head and L. Wilson	
Explosive Volcanism in the Mohon Mountain Volcanic Field,	
Arizona and Possible Martian Analogs .....	370
A.M. Simmons and J.S. King	
Pecacho Butte Volcanics .....	373
A.P. Kisiel and J.S. King	
Basaltic Plains Volcanism on the Eastern Snake River Plain,	
Idaho: A Geologic and Petrologic Study of Pine and Crater	
Buttes .....	376
P.F. Mazierski and J.S. King	
CHAPTER 10 - CRATERING PROCESSES AND CHRONOLOGIES	
Impact and Collisional Processes in the Solar System .....	381
T.J. Ahrens	
Impact Cratering Calculations .....	385
T.J. Ahrens and J.D. O'Keefe	
Experimental Impact Cratering Mechanics .....	389
R.M. Schmidt	
Impact Velocity and Changes in Crater Shape, Morphology, and	
Statistics .....	392
P.H. Schultz	
Transition Diameters for Crater Shape in Laboratory Experiments	
and on Planets .....	394
P.H. Schultz and D.E. Gault	
Impact Vaporization by Low-Angle Impacts .....	396
P.H. Schultz and D. Crawford	
Experimental Studies on the Impact Properties of Water Ice .....	398
F.G. Bridges, D.N.C. Lin, A.P. Hatzes, and J.S.B. McDonald	
Crater Studies on the Icy Satellites and Mercury .....	401
P.M. Schenk, A.C. Leith, and W.B. McKinnon	
Icy Satellites: Cratering and Volcanism .....	404
S.K. Croft	
Dark Ray and Dark Floor Craters on Ganymede .....	407
P.M. Schenk and W.B. McKinnon	
Spatial Distribution of Impact Craters on Venus .....	410
J.J. Plaut and R.E. Arvidson	
Viscous Relaxation of Impact Crater Relief on Venus .....	413
R.E. Grimm and S.C. Solomon	

Limits on Modes of Lithospheric Heat Transport on Venus from Impact Crater Density .....	416
R.E. Grimm and S.C. Solomon	
The Terrestrial Planet Cratering Record .....	419
R.G. Strom	
Early Intense Cratering: Effects on Growth of Earth's Crust .....	422
W.K. Hartmann	
Impact Structures of Australia (1987) .....	425
E.M. Shoemaker and C.S. Shoemaker	
Progress on the Impact Origin of the Moon and Other Topics .....	428
H.J. Melosh and A.M. Vickery	
The Use of Basin Ejecta to Determine Lunar Crustal Structure and Composition .....	431
P.D. Spudis and B.R. Hawke	
A Model for the Formation of Magnetic Anomalies Antipodal to Lunar Impact Basins .....	434
L.L. Hood	
Large Impact Basins and the Origin of the Crustal Dichotomy on Mars .....	436
H. Frey and R.A. Schultz	
Early Cratering Rates and the Nature of the Martian Cratered Uplands .....	439
P.H. Schultz	
Martian Impact Crater Ejecta and Interior Morphologies .....	442
N.G. Barlow	
Ejecta Cover on Martian Terrains as a Function of Increasing Crater Density .....	445
A. Woronow	
Ensemble Histories of Martian Samples Subjected to Meteorite Impacts .....	447
A. Woronow	
Crater Counts in West Deuteronilus Mensae, Mars .....	449
I. Nester, T.J. Parker, and R.S. Saunders	
Resurfacing History of the Lunae Planum-Xanthe Terra Region on Mars .....	452
T.D. Grant and H. Frey	
Evidence for Multiple Resurfacing Events in the Elysium-Amazonis Knobby Terrain on Mars .....	455
H. Frey, J. Semeniuk, and S. Tokarcik	

## CHAPTER 11 - STRUCTURE, TECTONICS, AND STRATIGRAPHY

Documenting Volcano-Tectonic Episodes in Mars' Stratigraphic Record .....	461
D.H. Scott and K.L. Tanaka	
Volcanic and Tectonic Evolution of Martian Impact Basins .....	463
R. Wichman and P.H. Schultz	
Longevity of Impact-Induced Faults as Preferred Sites for Later Tectonic Activity .....	465
S.C. Solomon and L. Meinke	
Ages of Fracturing and Resurfacing Along the Martian Dichotomy Boundary Between Nepenthes and Nilosyrtis Mensae .....	467
T.A. Maxwell and G.E. McGill	
Arches, Anticlinal Ridges, Crenulate and Sub-Crenulate Ridges .....	470
T.R. Watters	
The Periodic Nature and Possible Origin of Anticlinal Ridge Spacings on the Tharsis and Columbia Plateaus .....	473
T.R. Watters	
Relative Importance of Faulting and Folding in Lunar Wrinkle Ridges .....	476
M. Golombek and B. Franklin	
Ridged Plains and Gullied Terrain in the Martian Uplands .....	479
D.E. Wilhelms, R.J. Baldwin, and D.R. Harden	
Constraints on the Origin of Fractured Terrane, Northern Martian Plains .....	482
G.E. McGill	
Constraining Martian Northern Plains Surface-Forming Processes Through Analysis of Boundary Morphology .....	485
T.J. Parker and R.S. Saunders	
Striped Plains of Acidalia Planitia, Mars .....	488
R.A. De Hon	
Intercrater Plains Deposits and the Origin of Martian Valleys .....	490
G.R. Brakenridge	
Surface Units on Mars: The Assemblage in the Valles Marineris .....	493
B.K. Lucchitta	
Stability of Chasma Walls in the Valles Marineris, Mars .....	496
H.J. Moore and G.D. Clow	
A Comparative Planetology Study of Large Martian and Terrestrial Landslides .....	499
P.J. Shaller and B.C. Murray	
Rock Populations as Indicators of Geologic Processes .....	502
M.C. Malin	

Studies of Venusian Geology and Tectonics .....	505
R.C. Kozak and G.G. Schaber	
Venus: Geophysical and Tectonic Investigations .....	507
R.J. Phillips	
Dynamic Stress Modelling of Venus' Lithosphere .....	510
W.B. Banerdt	
Definition and Characterization of Morphologic Subtypes of the Venus Tesserae .....	512
D.L. Bindshadler and J.W. Head	
Evolution of the Lunar Crust: An LGO Perspective .....	515
C.M. Pieters	
Geology and Formation of Rima Mozart .....	516
C.R. Coombs, B.R. Hawke, and L. Wilson	
The Formation of Hadley Rille and Implications for the Geology of the Apollo 15 Region .....	519
P.D. Spudis, G.A. Swann, and R. Greeley	
Constraints on the Subsurface Structure of Europa .....	520
M. Golombek and B. Banerdt	
Early Thermal Profiles of Ganymede and Callisto .....	523
M.P. Golombek and W.B. Banerdt	
Tectonic and Volcanic Evolution of Dark Terrain on Ganymede and Its Implications for Internal Structure and Evolution .....	526
S.L. Murchie, J.W. Head, and J.B. Plescia	
CHAPTER 12 - GEOLOGIC MAPPING, CARTOGRAPHY, AND GEODESY	
Geology of Six Possible Martian Landing Sites .....	531
H. Masursky, A.L. Dial, Jr., M.E. Strobell, and D.J. Applebee	
Mars Sample Return: Recommended Sites .....	534
D.H. Scott	
Martian Sample Sites: Examples Based on a Global Geologic Perspective .....	537
D.H. Scott and K.L. Tanaka	
Valles Marineris, Mars: An Optimum Science-Sample Site .....	539
B.K. Lucchitta	
Preliminary Geologic Mapping in the Memnonia Region of Mars .....	541
J.R. Zimbelman	
Geologic Mapping of Io .....	544
R. Greeley, R.A. Craddock, D.A. Crown, L.A. Leshin, and G.G. Schaber	
Paleogeologic Maps of Mercury's Surface .....	545
P.D. Spudis and J.E. Guest	

Digital Cartography of the Planets .....	548
R.M. Batson	
Geometric Processing of Digital Images of the Planets .....	549
K. Edwards	
Digital Mapping of Irregular Satellites and Asteroids .....	550
R.M. Batson and K. Edwards	
Digital Elevation Model of Mars .....	551
S.S.C. Wu and A. Howington-Kraus	
Progress in Compilation of the 1:2,000,000 Scale Topographic Map Series of Mars .....	553
S.S.C. Wu, R. Jordan, and F.J. Schafer	
Geodetic Control Network of Phobos .....	554
S.S.C. Wu and F.J. Schafer	
The Control Network of Mars: November 1987 .....	555
M.E. Davies	
The Control Networks of the Satellites of Jupiter .....	557
M.E. Davies	
Large Scale Topography of Io .....	558
R.W. Gaskell and S.P. Synnott	
A Unified Lunar Control Network .....	561
M.E. Davies, T.R. Colvin, and D.L. Meyer	
CHAPTER 13 - SPECIAL PROGRAMS	
NASA Field Workshop on Ignimbrites and Domes .....	567
M.F. Sheridan and J.H. Fink	
Preliminary Analysis of Desiccation as a Planetary Geomorphic Process .	568
L.A. Rossbacher	
The Galilean Satellite Geological Mapping Program, 1987 .....	570
B.K. Lucchitta	
Planetary Nomenclature .....	571
M.E. Strobell and H. Masursky	
The IRPS Database .....	573
B. Weiss, E. Guinness, S. Slavney, and R. Arvidson	
IRPS: A Workstation for Planetary Image Databases and Image Processing	575
S. Slavney, E. Guinness, R. Arvidson, and B. Weiss	
AUTHOR INDEX .....	581

## CHAPTER 1

### OUTER PLANET SATELLITES AND RINGS





## Dynamics of Outer Planet Rings

L.W. Esposito, G.R. Stewart, T.G. Brophy, J.E. Colwell, P.A. Yanamandra-Fisher, Laboratory for Atmospheric and Space Physics, University of Colorado, Boulder, CO 80309-0392

Research efforts have concentrated on development of new numerical methods to calculate ring dynamics which are applicable to ring stability and formation of sharp edges. Inter-comparison of Voyager data sets provides new constraints on particle sizes in Saturn's rings, transport of dust in the Uranus ring system, and the age, origin and evolution of planetary rings.

The combination of Voyager (RSS, PPS, ISS, UVS) measurements provide strong constraints on the age and evolution of the Uranian rings. The rings must be younger than 1/10 the solar system age. For sharp edges to form, we must have substantial deviation from the momentum flow predicted for an unperturbed fluid ring. Possibilities include "flux reversal" proposed by Borderies, Goldreich and Tremaine (1984) or "surface tension" as proposed by Brophy and Esposito (1987). The extreme sharpness of the  $\epsilon$  ring outer edge ( $<40\text{m}$ ; Lane et al. 1986) favors the surface tension model. The Voyager observations provide only lower limits to the  $\epsilon$  ring mass. A simple scenario for the evolution of the Uranian rings involves about 100 unseen "ringmoons" whose destruction gives rise to the observed rings. The short lifetime of these rings against micrometeorite grinding (Northrop and Connerney 1987) provides a source of dust which is then swept up by the ringmoons. The similarity of this model to that proposed by Cuzzi and Burns (1987) for Saturn's F ring, the generally similar time problems for Saturn's A ring (Esposito 1986), and the exotic ring arcs of Neptune argue that youthful rings are the most common feature of planetary rings.

A common feature of planetary rings is discrete ringlets with sharp edges. Such structures are not easily explained by and apparently contrary to the commonly accepted theories of viscous spreading (e.g. Ward, 1982; Lin and Bodenheimer 1982; Borderies, Goldreich and Tremaine 1984). We have investigated radial mass transport caused by inter-particle collisions in planetary rings in terms of a kinetic theory which allows for non-local effects. The resulting momentum transport predicts radically different ring evolution than do calculations based on fluid models which do not allow for non-local effects. The momentum transport has been shown to cause rings to evolve toward an intermediate critical optical depth ( $\tau_c \approx 0.4$ ). This explains some of the C ring structure and the high frequency of occurrence of  $\tau_c$  observed at the Saturnian and Uranian ring systems. The analytical results are supported by numerical simulations which employ a Markov process method for simulating particle distributions in velocity space.

The Voyager RSS occultation data show that the particles in Saturn's rings follow a size distribution described by a power law with exponent about -3. The Voyager 1 radio occultation data indicate an upper size cutoff ranging from about 4m to 10m at several locations in the rings. The smallest particle size inferred depends upon the wavelength of observation; hence, the PPS data ( $\lambda = 0.25\mu\text{m}$ ) contains information about particles from about  $0.01\mu\text{m}$  in radius and larger, whereas the RSS data ( $\lambda = 3.6\text{cm}$  and  $13\text{cm}$ ) is sensitive to particles from about  $0.1\text{cm}$  and larger. This explains, qualitatively, why there exists a difference in the observed optical depth in the two data sets. The photopolarimeter (PPS) occultation data, onboard Voyager 2, were analysed at the same locations as those selected for the radio occultation. For example, at the location  $2.10R_S$ , we checked the Zebker et al. (1985) model for the size distribution for consistency with the PPS data. We find that a minimum size of particles is about  $1\mu\text{m}$ , and the radio optical depths predicted by this model are within 10% of the values calculated by the "finite-order-of-scattering" model of Zebker et al. (1985); the predicted uv ( $\lambda = 0.13\mu$ ) and imaging ( $\lambda = 0.5\mu\text{m}$ ) optical depths are in agreement with the observed values. The mass density,  $\sigma$ , is about  $33\text{ (g/cm}^2\text{)}$ , which is in fairly good agreement with other estimates and in close agreement with the Zebker et al. (1985) value, within the uncertainty prescribed.

The Voyager 2 high phase angle image of the Uranian rings revealed a highly structured system of dust rings (Smith et al. 1986). The short lifetime of micron sized particles due to gas drag implies that these rings are young and evolving. We model the evolution of the rings as a Markov process. In this model, transitions between states of the system are governed by a matrix of transition probabilities. The numerical value of these probabilities are determined by the physical processes included in the model. We examine the evolution of micron sized ring particles under the influence of drag from Uranus' extended neutral Hydrogen atmosphere and from Poynting-Robertson light drag. Particles may be absorbed by the planet or by macroscopic ring particles and ringmoons. Meteoroid impacts onto these latter bodies act as sources of dust particles which are continuously removed from the system. States of the system are organized by particle size and orbital radius. As a first application of this model, we have examined how the particle size distribution evolves due to drag forces. The dust band lying between the delta ring and 1986U7 has a measured power law index of  $2.5 \pm 0.5$  (Ockert et al. 1987). Dust debris generated in the region of 1986U7 with a power law index of 3.4 will, under the influence of gas drag, arrive at a particle size distribution of index 2.5, or the equivalent gamma law distribution, in  $\sim 250$  years. Smaller particles are removed more quickly causing a power law distribution to turn over at small particle sizes. The particle size distribution thus evolves away from a simple power law toward a gamma function distribution.

## A Re-examination of Radial Diffusion in Planetary Rings

Glen R. Stewart  
Department of Applied Mathematics  
University of Virginia

According to the kinetic theory of transport processes in planetary rings, the rate of radial mass transport is governed by an effective shear viscosity that is deduced from the off-diagonal component of the velocity dispersion tensor. For rings of low optical depth the dispersion tensor may be calculated from either the Boltzmann or Krook kinetic equations, suitably modified to model the inelasticity of collisions among ring particles (Goldreich and Tremaine 1978, Shu and Stewart 1985). The theory predicts that planetary rings of low optical depth spread radially so as to decrease the average surface density of ring particles. The accuracy of this prediction has been called into question by recent numerical solutions of the Boltzmann equation that seem to indicate a tendency toward radial clumping rather than spreading at low optical depths (Brophy and Esposito 1986). The possibility of a diffusional instability at low optical depth is exciting because it would provide a much needed mechanism for forming the unexplained structure of Saturn's C ring and the surprisingly sharp density gradients at the inner edges of the A and B rings.

We have begun a re-examination of the kinetic theory of planetary rings in order to identify a possible flaw in the published theory and to formulate a new theoretical derivation of the radial mass transport rate which avoids such flaws. It has been pointed out by Greenberg (1986) that when two ring particles with different semi-major axes collide inelastically, their center-of-mass velocity is often greater than the circular orbit velocity at the smaller semi-major axis or less than the circular orbit velocity at the larger semi-major axis. The net result of such collisions is often more closely spaced semi-major axes rather than radial spreading. This peculiar reversal of the velocity gradient is a consequence of the non-local character of eccentric orbits that oscillate about the radial positions of their semi-major axes. Such non-local effects may not be adequately modeled by the published kinetic theory because it is formulated in terms of the local density of particles in phase space. In particular, the standard Boltzmann collision operator does not account for the difference in semi-major axes of the colliding particles.

To avoid this difficulty, we have begun a direct calculation of the radial flux of semi-major axes due to particle collisions that does not require the determination of an effective shear viscosity from the off-diagonal component of the dispersion tensor. The basic set-up of the calculation is similar to the one described by Hameen-Anttila (1978) where one must find the first and second moments of the collisional rate of change of the semi-major axes. By relating these quantities to the collisional rate of change of the velocity dispersion tensor, one can recover the standard result of Goldreich and Tremaine. However, there is an additional contribution to the radial mass flux (neglected by Hameen-Anttila) that is non-zero when there is a radial gradient in the surface density of particles. This extra term is of the same order as the standard terms and is directly related to the non-local nature of momentum transfer between eccentric orbits. Efforts are underway to evaluate this new term numerically. Preliminary estimates suggest that radial clumping may occur for a limited range of optical depths and density gradients. This work was supported in part by the National Aeronautics and Space Administration through Grant: NASA-NAGW-929.

- Brophy, T.G., and Esposito, L.W. (1986) *Bulletin Amer. Astron. Soc.* 18, 1017.  
Goldreich, P., and Tremaine, S. (1978) *Icarus* 34, 227.  
Greenberg, R. (1986) preprint.  
Hameen-Anttila, K.A. (1978) *Astrophys. Space Sci.* 58, 477.  
Shu, F.H., and Stewart, G.R. (1985) *Icarus* 62, 360.

## Dynamics and Structure of Planetary Rings

Richard G. French

Department of Astronomy, Wellesley College

Department of Earth, Atmospheric, and Planetary Sciences, MIT

A new kinematical model for the Uranian rings has been determined by combining earth-based stellar occultation observations and Voyager 2 occultation results. The estimated accuracy of the orbit solution is  $\pm 1$  km in the semimajor axes of the rings and  $\pm 0.01^\circ$  in the direction of Uranus' pole. Formal errors of the fit are substantially smaller, but they do not take account of possible systematic errors in the Voyager trajectory, satellite masses, and positions of the Voyager occultation stars. The  $\delta$  and  $\gamma$  rings have excited normal modes: the  $\delta$  ring has an  $m=2$  mode with a pattern speed of  $23.43821 \text{ deg hr}^{-1}$ , and the  $\gamma$  ring is a combination of an  $m=1$  (precessing elliptical) mode and an  $m=0$  mode: the entire ring is undergoing radial oscillations with an amplitude of  $5.15 \pm 0.33$  km and a frequency of  $47.73198 \text{ deg hr}^{-1}$ .

A comparison of satellite resonance locations and fitted ring radii supports the suggestion of Porco and Goldreich (1987, *Astron. J.* 93, 724) that 1986U7 is shepherding the outer edge of the  $\delta$  ring and 1986U8 is shepherding the inner edge of the  $\gamma$  ring, and their identification of the 24:25 outer eccentric resonance of 1986U7 with the inner edge of the  $\epsilon$  ring and the 14:13 inner eccentric resonance of 1986U8 with the outer edge of the  $\epsilon$  ring.

The  $\epsilon$  ring shows perturbations in width and in orbital radius that are larger than the other elliptical Uranian rings. These might be signatures of edge waves associated with the resonances with 1986U7 and 1986U8. We have searched the entire set of available  $\epsilon$  ring data for evidence of multi-lobed distortions in the inner and outer edges, with the wavenumbers and pattern speeds appropriate for the resonances in question. The results have been negative. We conclude that the  $\epsilon$  ring radial and width perturbations are not primarily due to edge waves driven by the known shepherd satellites.

The  $\gamma$  ring has a mean orbital radius very near to an  $m=6$  resonance with 1986U8. We have examined the post-fit residuals of the  $\gamma$  ring occultation points for evidence of a six-lobed perturbation associated with this resonance, with negative results. The rms orbit residuals of the  $\gamma$  ring remain larger than for the other Uranian rings, implying that there are measurable dynamical effects that have not yet been identified.

Work in progress includes: 1) search for edge waves in the  $\gamma$  and  $\delta$  rings; 2) comprehensive search for excited normal modes in all of the rings, including the possibility that several modes may be present simultaneously; 3) investigation of width-longitude relations for the  $\gamma$  and  $\delta$  rings, based on the identification of their normal modes; 4) analysis of observations of the 26 February 1987 stellar occultation by Uranus; and 5) inclusion of additional weak dynamical effects in the ring orbit model.

Optical Depths and Equivalent Widths of the Uranian Epsilon Ring from the  
Voyager 2 Photopolarimeter

A.L. Graps (SUNY Stony Brook, NASA/Ames) J.J. Lissauer (SUNY Stony Brook)<sup>1</sup> M.R. Showalter (NASA/Ames)<sup>2</sup>

<sup>1</sup> Alfred P. Sloan Research Fellow <sup>2</sup> NRC Associate

Four cuts from the Voyager 2 Photopolarimeter (PPS) exist of the Uranian  $\epsilon$  ring. We wish to understand streamline shapes (e.g. azimuthal variations) of the ring because that knowledge can be used to test physical theories of the origin of features seen in individual scans (density waves, multi-lobed patterns etc.). For any particular streamline, the equivalent width,  $\int \tau(r)dr$ , interior to it is expected to be conserved. Hence we need the optical depth profile  $\tau(r)$  to the greatest possible accuracy, along with a realistic estimate of its uncertainty.

The statistical uncertainties in single PPS counts are too large to determine  $\tau$  reliably via the equation:  $k_i = k_s e^{-\tau/\mu} + k_b$  where  $k_i$  = the  $i$ th integer count from the PPS,  $k_s$  = the number of PPS counts for the star,  $\mu$  = cosine of the ring intercept angle, and  $k_b$  = the number of PPS counts for the background scattered light. Averaging over many points places undue emphasis on small regions of low  $\tau$  and may obscure real ring structure. We have developed a method to overcome these difficulties. For short sections of the scan the optical depths are modeled by fitting a polynomial to the observations in  $\tau_r = \sum_{j=0}^{n-1} a_j (r - r_0)^j$  where  $r$  = the distance from the center of Uranus and  $r_0$  = the midpoint of the segment of the ring in question. A minimum value of  $n$  can be calculated by requiring the fit to show uncorrelated consecutive residuals. Since our best estimate of  $\tau$  is a nonlinear function of the observed number of counts, we perform a nonlinear least squares fit (NLSQ) to the data. The weights used in the NLSQ are based on the PPS noise model of Showalter and Nicholson (BAAS 18, 767, 1986). The equivalent width is calculated by the straightforward method of  $\int \tau(r)dr$ . We will present the results of this analysis.

This work was supported in part by NASA contract NAGW-1107.

## Dynamical Studies of Planetary Rings

Philip D. Nicholson, Cornell University

Together with collaborators Carolyn Porco and Jay Holberg (Univ. of Arizona), Mark Showalter (Ames Research Center), Keith Matthews (Caltech), and Maren Cooke (Cornell), the P.I. is pursuing several independent investigations of the dynamics and particle properties of the Saturnian and Uranian ring systems. Highlights of these studies are summarized briefly below.

1) Photometric studies of Saturn's C Ring. By combining scans of ring brightness vs. radius obtained from Voyager images with the optical depth profile measured in the PPS stellar occultation experiment, it is possible to infer the light-scattering behaviour of individual ring particles at a variety of phase angles. Such studies can reveal variations, if they exist, in the nature (size distribution, composition) of the particles comprising different regions of the rings. To date, we have examined ~ 30 high-resolution images, at phase angles  $23^\circ \leq \alpha \leq 153^\circ$ . Fig. 1 shows several rather interesting results of this study. Each set of 3 panels presents the radial profile of  $\tilde{\omega}_0 P(\alpha)$ , the product of particle single scattering albedo and phase function, obtained from (top) a mosaic of narrow-angle images, and (middle) a wide-angle image of the same ansa taken at the same time, together with (bottom) the PPS optical depth profile. Note that (a) the light-scattering properties of the higher optical depth "plateau" features are indistinguishable from those of the low optical depth regions; and (b) there is a substantial increase in particle albedo with increasing radius. This increase is more pronounced at smaller phase angles.

Preliminary fits to the phase curve indicate a Callisto-like phase function, but an albedo which increases from  $\tilde{\omega}_0 \approx 0.15$  in the innermost C ring to  $\sim 0.35$  in the outermost C ring (Cooke, 1987). Our results indicate local homogeneity in particle properties, but larger scale variations which might be due either to radius-dependent darkening processes or to a collisional admixture of particles from different source regions.

2) Particle size distributions in Saturn's Rings. Based on a statistical analysis of the photon counts in the PPS occultation data, Showalter and Nicholson (1986) have shown that there exist distinctive variations in the distribution of particles in the 1-10 meter size range in Saturn's rings. The C ring and Cassini Division show very few particles in this range, while the A ring and outer B ring show significant populations. Local variations are also revealed by this analysis, as shown in Fig. 2. Plotted here is the dimensionless parameter  $Q$ , proportional to the effective mean particle cross-section, vs. radius through the outer Cassini Division and into the A ring. There appears to be a smooth transition between  $Q \approx 0.0$  in the Cassini Division and the value  $Q \approx 0.20$  characteristic of the entire A ring. Again, particle inter-mixing is suggested, although alternative interpretations involving gravitational clumping of smaller particles are also under investigation.

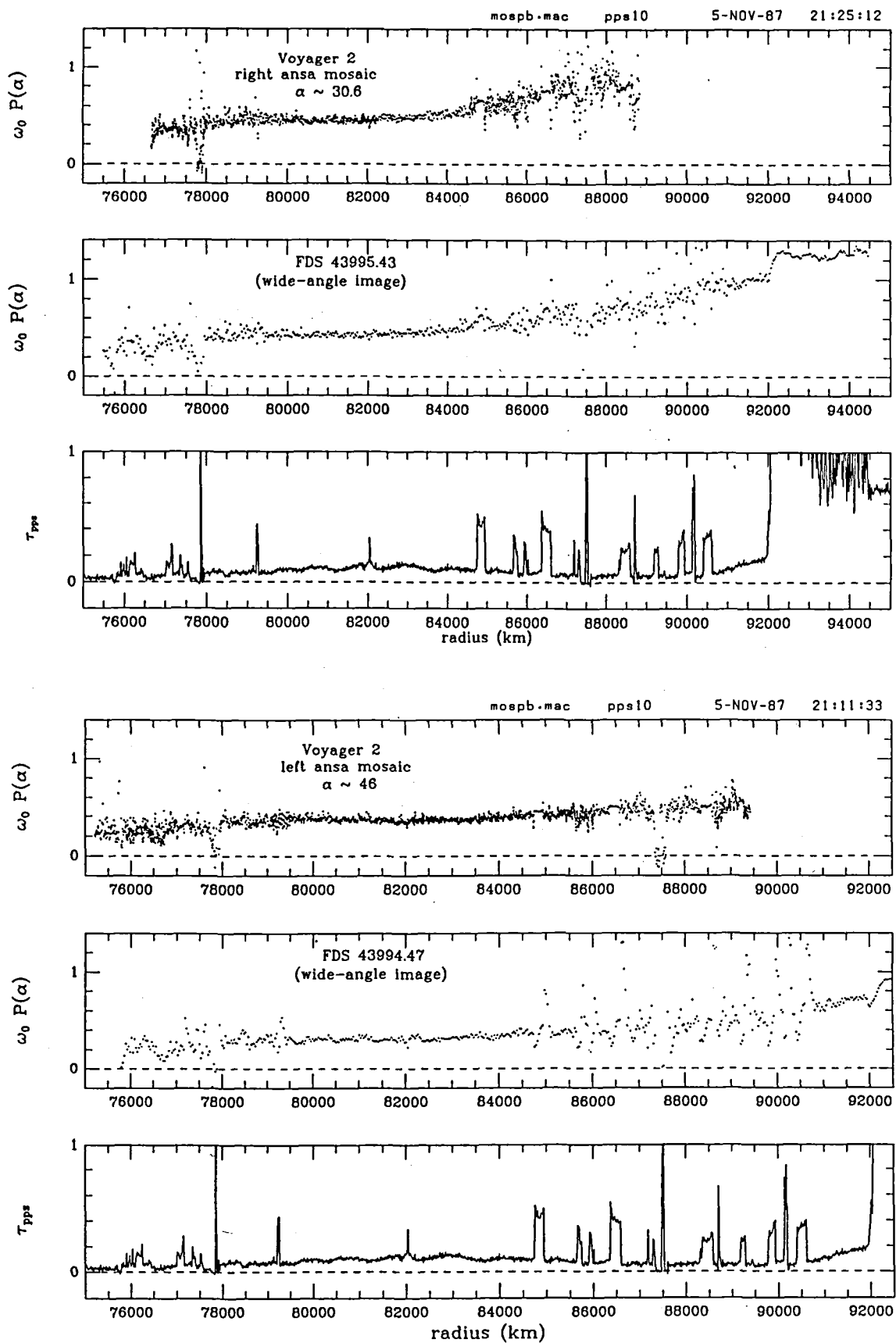
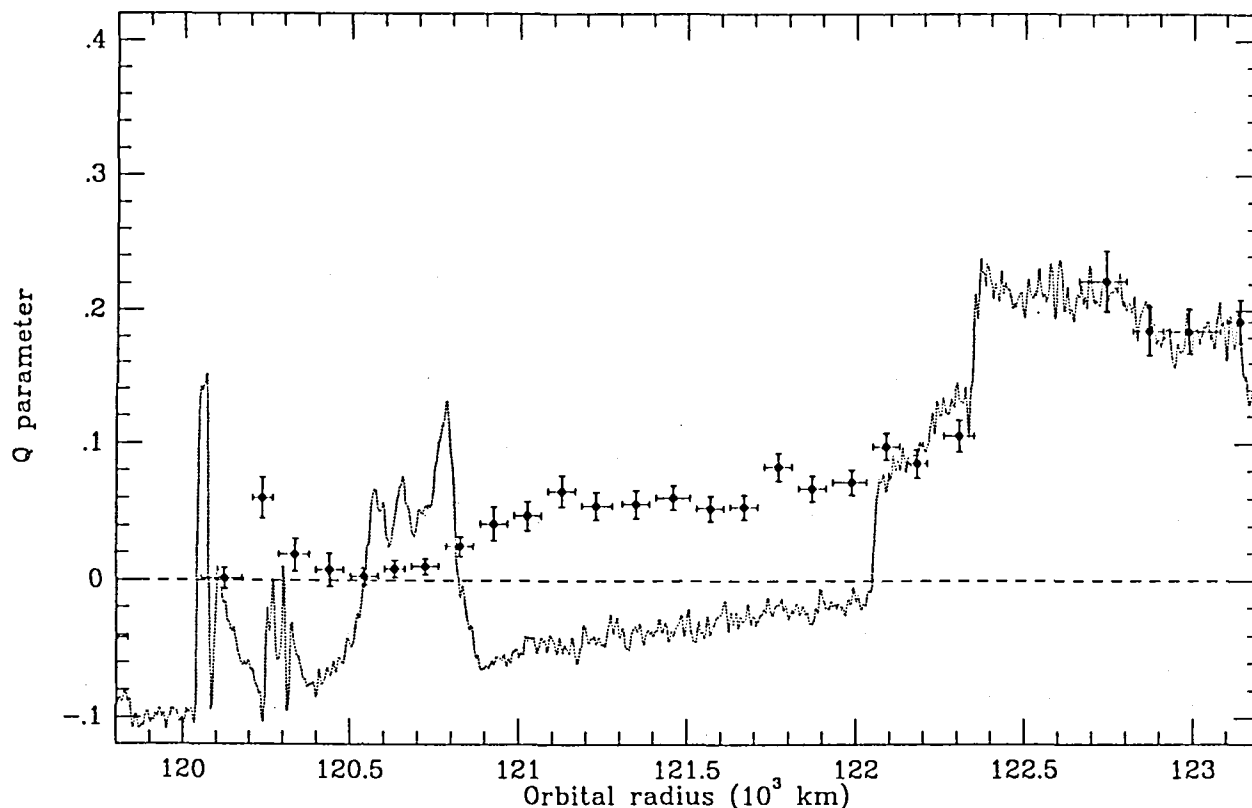


FIG. 1

FIG. 2



3) Comparison of Voyager and ground-based observations of the Uranian rings. The advent of Voyager occultation data for the narrow Uranian rings has permitted extension of previous ground-based studies at near infrared wavelengths to the ultraviolet and microwave regions of the spectrum, as well as providing data at sub-kilometer resolution. Holberg, Nicholson, French and Elliot (1987) have studied the azimuthal and spectral variations of the optical depths of the  $\delta$  and  $\epsilon$  rings, concluding that (a) the mean particle size is  $> 1$  cm, (b) the particles which dominate the rings' optical cross section are distributed in a many-particle-thick layer, and (c) the self-gravity model for eccentric rings proposed by Goldreich and Tremaine (1978) appears to be inconsistent with the observations.

#### References

- Cooke, M.L. (1987) BAAS 19, 882.
- Goldreich, P. and Tremaine, S. (1978). Astron. J. 84, 1638.
- Holberg, J.B., Nicholson, P.D., French, R.G., and Elliot, J.L. (1987). Astron. J. 94, 178.
- Showalter, M.R. and Nicholson, P.D. (1986). BAAS 18, 767.



## OBSERVATIONAL STUDIES OF SATURN'S RINGS

Carolyn C. Porco

Lunar and Planetary Lab/Department of Planetary Science  
University of Arizona, Tucson, Az. 85721

In the last year, much of the research I have been doing has focussed on the results from the Voyager encounter with Uranus (Smith *et al.* 1986): in particular, understanding the origin and maintenance of eccentric rings in that system (Porco and Goldreich 1987; Goldreich and Porco 1987), and how the particle properties compare to those of Saturn's rings (Porco *et al.* 1987; Ockert *et al.* 1987). I have discovered, along with Dr. Peter Goldreich of Caltech, that the newly discovered small satellites which straddle the  $\epsilon$  ring are undoubtedly responsible for maintaining the sharp inner and outer edges of this ring, as well as the outer edge of the  $\delta$  ring. Not only has our work revealed that this system of satellites and rings is an outstanding and classic example of the shepherding theory proposed in 1978, but it has also suggested that narrow rings exhibiting azimuthal wavenumbers of  $m \neq 1$  (the Uranian  $\delta$  ring is an example of this) may be interpreted as normal modes or standing waves excited either by internal processes or by shepherding satellites. These results have proven of great importance in understanding the processes that are likely to be working in creating and maintaining Saturn's eccentric features, and have given us another viable hypothesis to test in studying these features.

Though not related to studies of ring kinematics and dynamics, the remainder of my work on the Uranus data has shown that the Uranian rings are indeed very dark and visually colorless, making them distinctly different than their Jovian or Saturnian counterparts. Whether or not they are of sufficiently different composition to make the detailed dynamics of particle collisions, and therefore overall ring properties, also different from Saturn's rings remains to be demonstrated.

In addition to the research on the Uranian rings, I have recently completed a search for previously unidentified eccentric features in Saturn's outer C ring (Porco and Nicholson 1987). The C ring was chosen for its structural regularity (compared with, say, the B ring), for the high quality PPS and RSS occultation data existing for this region, and for the comparatively large number of images which show this region at high resolution. Two new eccentric ringlets have been discovered in the outer C ring as a result of our work. We have found that although one ringlet has only a marginally-modellable distortion, and although both ringlets lie coincident with several Lindblad resonances, both ringlets are apparently not resonantly forced as was expected but are better described by an  $m = 1$  freely-precessing Keplerian ellipse, the same model which describes most of the narrow eccentric ringlets in the Saturnian and Uranian ring systems. The addition of two new ringlets to the family of narrow eccentric rings of the Jovian, Saturnian, and Uranian systems is allowing us to draw firmer conclusions regarding the origin and behavior of these exotic features. We have also used the kinematical results found for the eccentric ringlet at  $1.29R_S$  to derive the first experimental determination of  $J_6$ , the third spherical harmonic in the expansion of Saturn's gravity field, as well as a more precise linear combination of  $J_4$  and  $J_6$  which will prove useful in constraining models of Saturn's interior (Nicholson and Porco 1987).

Recently, I have re-analyzed the time series of imaging observations of spokes in Saturn's B ring using an algorithm which compensates for the unequal precision of the data, as well as the fact that the data points are discrete, of finite length, and unevenly spaced in time (Ferraz-Mello 1981). The latter circumstance can result in unreliable power estimates at frequencies whose

phases are not covered uniformly over the entire sampling interval. In my previous work, a simple uncompensated discrete Fourier transform was used and no significance was attached to the absolute value of the spectral intensity; only the period was considered of value. The current power spectrum of the combination of Voyager 1 and Voyager 2 spoke observations using Ferraz-Mello's date-compensated discrete Fourier transform shows two prominent peaks at 641 and 611 minutes, both of which can be shown to be statistically significant. Harmonic filtering of the spectrum has proven, also, that these two features are clearly independent. The interpretation of this result is that there are indeed two distinct periods modulating the appearance of spokes in Saturn's B ring and that these periods correspond to that of the magnetic field rotation and the period of the SED's. The actual mechanisms of modulation have yet to be discovered.

Recently, I have begun a collaboration with graduate student Mark Marley and Dr. Bill Hubbard, both of LPL, in investigating the possibility that nonradial oscillations of Saturn's equilibrium density structure, in particular the pressure (or 'p') modes, may resonate with ring particles and create observable features within the rings of Saturn (Marley, Hubbard, and Porco 1987). Initial work, based on eigenfrequencies calculated by Vorontsov *et al.* (1981), has shown that one should expect ring features associated with such resonances only in ring C and that the required amplitudes of the oscillations at the planet's surface are only 200 meters. We shall continue this project by calculating new eigenfrequencies using the latest Voyager results on Saturn's helium abundance and mass, as well as the latest constraint provided by Nicholson and Porco (1987) on the gravity coefficients, and searching the C ring for associated ring features.

In the last year, I have also made substantial progress in bringing on line a complete image processing package, based on software imported from the USGS in Flagstaff, Arizona, that will allow absolute radiometric calibration of raw Voyager imaging data and correction for geometric distortion in the Voyager camera system. This software is being brought up on the Voyager Image Processing System (VIPS) at LPL, a system which I oversee and which consists of a Microvax II computer, a Peritek 512x512 color graphics image display, a color monitor, and assorted peripherals. We have incorporated into the software package a navigation program which allows absolute radial and longitudinal measurements to be made on any solar system body imaged by the Voyager cameras, including the rings of either Saturn or Uranus. This program was developed by Gary Yagi of JPL, Andrew Ingersoll of Caltech, and myself, and was used during the Uranus encounter to measure the location of the two newly discovered rings, 1986U1R and 1986U2R, as well as to identify ring features in the high phase image of the Uranian rings (Smith *et al.* 1986). It is fully operational on the VIPS and will soon be used to support my own research as well as the research of interested graduate students and visiting colleagues.

## References

- Ferraz-Mello, S. (1981). Estimation of periods from unequally spaced observations. *Astron. J.* **86**, 619-624.
- Goldreich, P. and Porco, C. C. (1987). Shepherding of the Uranian rings. II. Dynamics. *Astron. J.* **93**, 724-729.
- Marley, M. S., Hubbard, W. B., and Porco, C. C. (1987). Saturnian nonradial p-mode oscilla-

- tions and C ring structure. *Bull. Amer. Astron. Soc.* **19**, 892.
- Nicholson, P. D. and Porco, C. C. (1987). A new constraint on Saturn's zonal gravity harmonics from Voyager observations of an eccentric ringlet. *J. Geophys. Res.* , Submitted.
- Ockert, M. E., Cuzzi, J. N., Porco, C. C., and Johnson, T. V. (1987). Uranian ring photometry: results from Voyager 2. *J. Geophys. Res.* , In press.
- Porco, C. C., Cuzzi, J. N., Ockert, M. E., and Terrile, R. J. (1987). The color of the Uranian rings. *Icarus* **72**, 69-78.
- Porco, C. C. and Goldreich, P. (1987). Shepherding of the Uranian rings. I. Kinematics. *Astron. J.* **93**, 730-737.
- Porco, C. C. and Nicholson, P. D. (1987). The eccentric features in Saturn's outer C ring. *Icarus* , In press.
- Smith, B.A., et al. (1986). Encounter with Saturn: Voyager 1 imaging science results. *Science* **233**, 43-64.
- Vorontsov, et al. (1981). *Sov. Astron.* , **25** , 627.

## PHYSICAL PROCESSES IN PLANETARY RINGS

Joseph A. Burns, Cornell University

As described below, in the past year i.) we studied the structure of Jupiter's ring and the dynamics of the charged dust, ii.) we precisely placed the MeV absorption signatures measured near Saturn's F ring and then developed a model to explain these depletions, iii.) we dynamically simulated the F ring as perturbed by shepherd and embedded satellites, and iv.) we investigated the origin and fate of Uranian dust.

Jovian Ring Studies, Showalter et al. (Ref. 3) comprehensively described the properties of Jupiter's ring and of the particles that comprise it; their conclusions were summarized in last year's report for this grant. In collaboration with J.N. Cuzzi, J.B. Pollack and M.R. Showalter at NASA Ames we are now applying our techniques to material about Saturn; this will indicate the nature of the F ring's environs and may be important in deciding the hazards faced by Cassini as it repeatedly passes close to the outer edge of the ring system.

Dynamical studies of charged Jovian dust have been considered by Schaffer and Burns (4, 5, 6, 7). Weakly charged dust grains orbiting near the equatorial plane of a planet with a complex magnetic field experience small and variable in- and out-of-plane Lorentz forces. We (4) show that the linearized equations of motion are those of forced harmonic oscillators, and that large horizontal and vertical motions ensue wherever the temporal periodicities of the forces match the epicyclic (roughly the orbital) frequencies. Several of these Lorentz resonances are located tantalizingly close to major ring features. Plasma drag will cause dust orbits to evolve slowly away from synchronous position and across the resonance zones. Numerical integrations (5,6) show that, as orbits drift across resonances, jumps occur in inclination, eccentricity and semimajor axis and that they persist after resonance passage.

Electromagnetic forces depend on  $N$ , the number of electrical charges residing on the individual grains. Considering a thermal plasma containing heavy ions ( $S^+$  or  $O^+$ ), we find  $N \sim 10^2 - 10^4$  for a  $1\mu m$  grain in the Jovian ring system, depending on plasma characteristics. We also compute the stochastic variations in charge state by considering the quantized charging (5, 6). From the distribution functions governing  $N$ , we find that the typical variation in  $N$  is  $\sim \sqrt{N}/2$ . Since the charge on an individual dust grain fluctuates in time about the equilibrium value, we use a Monte Carlo routine to show that the spectrum of the perturbing Lorentz force includes a noisy component in addition to the contribution from periodic terms. However, since the variation in the charge number is typically small compared to the expected number of charges [ $\sim 1/2(\sqrt{N})$ ], numerical integrations illustrate that the resonances that we have previously described are not disrupted by stochastic charge variations even for the extreme case of small charge number ( $N \sim 10$ ). This can be understood from the convolution theorem.

We (7) have identified another orbital evolution mechanism for dust that derives from the charge variations that accompany the orbital excursions of a grain; these variations are always resonant with the grain's orbital period. Since there is a time delay in the ability of a

grain to adopt the local equilibrium charge, energy and angular momentum can be drained from, or given to, the orbit. Time scales can be short.

Saturn's F Ring In order to understand more completely the kinks, clumps, and braids that comprise the complicated structure of narrow rings, Kolvoord and Burns (2) have modelled a discrete particle system including the perturbations of both shepherding and less massive embedded satellites, using Lagrange's planetary equations to compute the distortions to strands of ring particles. Particles moving on horseshoe trajectories have been suggested as a possible way to form braids. Our integrations illustrate that the radial epicyclic motion is greater than the width of the horseshoe, whenever the particles are on eccentric trajectories with eccentricities of  $10^{-4}$  or greater, with an embedded satellite of 5 km in radius. The result of this radial excursion is an enhanced probability of particle collisions that could disrupt the organization of the braid. We consider a system of 2400 particles, placed in three concentric ringlets, being perturbed by both shepherds and an embedded satellite. The results from this simulation show a strong dependence on the initial configuration and the relative positions of the perturbers. They also indicate that the horseshoe encounters happen so slowly (due to the extremely long synodic period of the ring particles with the embedded satellite) as to be of little consequence in the overall evolution of the ring. An animation of the simulation using MacMovie has allowed us to follow clearly the development of ring structure (2). We are now extending these calculations to three dimensions.

Cuzzi and Burns (9) have studied five depletions noted in MeV charged particles by Pioneer 11 near the F ring. We have shown that two of these depletions are caused by particles absorbed by the F ring itself; none of the other three depletions is likely to be due to the ring nor to absorbers in the orbits of its shepherd satellites. Instead we hypothesize that unobserved faint (optical depth of  $\sim 10^{-4}$  to  $\sim 10^{-3}$ ), localized ( $\sim 10^2$  km x  $\sim 10^4$  km size) clouds are responsible and that the clouds are formed from the ejecta thrown off during mutual collisions among moonlets (radius 0.1-10 km) that populate the entire annulus between the orbits of the shepherds. A self-consistent scenario has been developed in which mutual collisions of parent moonlets generate debris clouds, which then spread apart due to Kepler shear and ultimately become part of an overall patchy background of faint material: the particles composing the background are continually being re-accreted onto the parents, only to be thrown off in some later collision. About one hundred clouds of various sizes and states of degradation will be present at any typical moment. If the parents have a steep size distribution, even the F ring itself could be the outcome of a collision between two of the largest moonlets, in which case the F ring is a temporary feature of the Saturnian retinue. Incomplete arcs like those detected about Neptune and perhaps about Uranus may be produced by a variant of this scheme. Our most recent effort in this area has been a further examination of the full suite of anomalous Saturnian absorption signatures: this study reveals inconsistencies in previous interpretations and several potential extensions of our "clouds" model.

We computed the nature of the global absorption signature of a faint narrow band of material in the vicinity of Saturn's F ring. We also

reviewed the existing data sets and concluded that past interpretations of the energies of the species involved may have been in error. This merits future work especially in view of Cassini's many crossings through these regions, and since such signatures may help constrain the properties of the E ring.

Uranian Dust We (8) helped the Voyager PWS team interpret the origin and fate of the dust that struck their instrument's antennae near the time of passage through the Uranian equatorial plane. We argue that the particles, which are believed to be microns in size, have brief sputtering lifetimes ( $\sim 10^6$  years) and originate in collisions with nearby small moons and other local debris. We suggest several explanations for the apparent non-equatorial position of the dust symmetry plane.

Burns published reviews on planetary rings (1) and dust motion (10).

1. J.A. Burns (1987). Rings around planets. In The Evolution of the Small Bodies of the Solar System, 301-307.
2. R.A. Kolvoord and J.A. Burns (1987). The effect of embedded and shepherding satellites on a narrow ring: Animation of a numerical simulation. BAAS 19, 891.
3. M.R. Showalter, J.A. Burns, J.N. Cuzzi, and J. B. Pollack (1987). Jupiter's ring system: New results on structure and particle properties. Icarus 69, 458-498.
4. L. Schaffer and J.A. Burns (1987). The dynamics of weakly-charged dust: Motion through Jupiter's gravitational and magnetic fields. JGR. 92, 2264-2280.
5. L.E. Schaffer and J.A. Burns (1987). Weakly charged dust grains passing through Lorentz resonances: Analytical results and stochastic charge effects. BAAS 19, 891.
6. L.E. Schaffer and J.A. Burns (1987). Stochastic Lorentz forces on dust grains with fluctuating charges. BAAS 19, 913.
7. L.E. Schaffer and J.A. Burns (1987). Resonant charge variations: Another cause for orbital evolution for dust, BAAS 20, 1987, (DPS).
8. D.A. Gurnett, W.S. Kurth, F.L. Scarf, J.A. Burns, J.N. Cuzzi, and E. Grun (1987). Micron-sized particle impacts detected near Uranus by Voyager 2 plasma wave instrument. JGR. 92, in press.
9. J.N. Cuzzi and J.A. Burns (1987). Charged particle depletion surrounding Saturn's F Ring: Evidence for a moonlet belt? Icarus 73, in press.
10. J.A. Burns (1987). The motion of interplanetary dust. In The Evolution of the Small Bodies of the Solar System, 252-275.

# Speculative Histories of the Uranian Satellite System

S. J. Peale

*Department of Physics  
University of California  
Santa Barbara CA 93106*

## ABSTRACT:

A long term occupancy of Ariel and Umbriel in a 2/1 orbital resonance could lead to sufficient tidal dissipation in Ariel to account for the observed series of resurfacing events. The dissipation in Umbriel is always negligibly small in this history, which is consistent with its primordial cratered surface. The eventual disruption of this resonance might have been effected by the growing perturbations by Titania. We consider several possible histories of the satellite system which are very sensitive on the assumed masses of the satellites within the errors of their determinations and on the  $Q$  of Uranus. The resonances which could have been encountered in these histories and constraints on the orbital eccentricities for certain capture are determined. If Miranda's mass were the upper extreme value, it, too, could have been locked in a long term 2/1 orbital resonance with Ariel forming a Laplace-like 3 body resonance including Umbriel. However, the tidal dissipation in Miranda is probably too small even in this history to have softened the interior, and much more violent events seem necessary to account for its exotic surface. Titania could have been a member only of rather high order orbital resonances with the inner satellites, so tidal heating during resonance occupancy cannot be invoked for its resurfacing.

**Dynamics of Satellites, Asteroids, and Rings**  
Stanley F. Dermott, CRSR, Cornell University

Work is in progress on: (a) determining the shapes and internal structures of satellites (with Peter Thomas of Cornell University); (b) investigating the dynamical evolution of the satellites of Saturn and Uranus (with Renu Malhotra, a graduate student at Cornell University, and Carl Murray of Queen Mary College London); (c) determining the structure of the zodiacal cloud as revealed by IRAS (with Philip Nicholson of Cornell University). Significant progress has been made in (a) the determination of the shape, mean density and internal structure of Enceladus and (b) understanding the changes in the orbital elements of satellites and dust particles on passage through resonances, particularly in those circumstances in which the motion is likely to be chaotic.

**(a) The Shape, Mean Density and Internal Structure of Enceladus**

The methods that we used to determine the shape and internal structure of Mimas (Dermott and Thomas, 1988) have now been applied to Enceladus. Limb profiles from the four best Voyager images have been used to determine the shape of the satellite. Correction of image distortions allows coordinates on the limbs to be located with an accuracy of approximately one-half picture element, about 0.5 km. Ellipses fit to the limbs show that the shape of Enceladus is well-represented by a triaxial ellipsoid. In fact, the fit is slightly better than in the case of Mimas, probably a consequence of the smoother topography on Enceladus. The ratio of the differences of the axes,  $(b - c)/(a - c)$  indicates that the satellite is close to hydrostatic equilibrium. Using a second-order theory for the ellipsoidal figure of equilibrium, we deduce that the satellite has a mean radius  $\langle R \rangle$  of  $249.5 \pm 0.2$  km and that the difference in the long and short axes,  $a - c$ , is  $11.6 \pm 0.5$  km.

The mass of Enceladus has yet to be determined (the present uncertainties are far too large to be useful for this type of analysis). However, if we assume that the satellite is differentiated and has a mantle of water-ice, then from the observed shape we are able to determine the mass, mean density, moment of inertia and rock/ice ratio of the satellite. This work represents the first indirect determination of the mass of a satellite in the solar system and it is likely that this mass estimate will remain the best that we have for Enceladus for several decades. Using these methods we have determined that the mean density of Enceladus is  $1.02 \pm 0.02$  g/cm<sup>3</sup>. We have previously determined that the mean densities of Mimas and Tethys are  $1.14 \pm 0.02$  and  $1.03 \pm 0.03$  g/cm<sup>3</sup>, respectively. Through this work, it has now become clear that the mean densities of the Saturnian satellites increase with increasing distance from the planet (Iapetus is the only exception) and that the inner satellites are probably markedly deficient in rock. The cosmogonical significance of this density trend, which is the opposite to that observed in the Jovian system, requires investigation. One possibility is that the rock in the Saturnian protosatellite nebula condensed out before the ice. In that case, drag forces due to the remaining gas could have swept part of the rock into the planet.



### **(b) Dynamics of the Uranian and Saturnian Satellites**

We have argued (Dermott et al., 1987) that the anomalously large inclination of Miranda, the post-accretional resurfacing of both Miranda and Ariel, and the anomalously large eccentricities of the inner Uranian satellites indicate that resonant configurations once existed in the Uranian satellite system that have since been disrupted. Similar anomalies that cannot be accounted for by the present resonant configurations (that is, the resonance between Mimas and Tethys and that between Enceladus and Dione) also exist in the Saturnian satellite system. We have pointed out that the values of  $J_2(R/a)^2$  for the inner Uranian satellites are small while their mass ratios,  $m/M$ , are large. It follows that resonances in the Uranian system are not well separated and that it is not always possible to analyse the dynamics of resonance in the traditional manner, that is, by using a disturbing function that is truncated to the extent that it contains only a single resonant argument. We have made some progress with this problem using the Cornell National Supercomputer to simulate the dynamics numerically. We find that second or higher order resonances can produce large increases in the eccentricities and inclinations on comparatively short timescales and that capture into resonance can result in chaotic motion. Such resonances may not be stable over the lifetime of the solar system. We consider that the temporary trapping of Miranda in a second or higher order resonance may account for the thermal event that resulted in its partial resurfacing.

### **(c) Structure of the Zodiacal Cloud as Revealed by IRAS**

The IRAS Zodiacal History File, which contains the all-sky survey data, is now to hand at Cornell. Software has been written to Fourier analyse the data and thereby separate the smooth large-scale zodiacal background from the narrower dust bands. Our preliminary results were described in a paper read at the Uppsala Asteroid, Comets and Meteors meeting (Dermott, Nicholson, and Wolven, 1986). Some of our more recent results were described at the 3rd International IRAS Conference (Dermott et al., 1988).

We have previously shown that the dust bands may be debris associated with the Hirayama asteroid families, in particular, the Eos and Themis families, and we have predicted (a) that the ecliptic latitudes of the dust bands should vary with ecliptic longitude and (b) that the central dust band should be split (Dermott et al., 1984, 1985). We now have evidence supporting both of these predictions. In particular, we have evidence showing that the central dust band is indeed split and that the separation in latitude of the two components is consistent with that expected for debris derived from the Themis family.

Our previous work concentrated on determining the structure of the background zodiacal cloud. The questions that we discussed included:

1. What is the inclination and orientation of the plane of symmetry of the zodiacal cloud? Is the plane warped? Is the sun at the center of axial symmetry of the cloud?

2. What are the distances of the solar system dust bands? What are the orbital elements of the particles in the bands? Do the particles originate in the Hirayama asteroidal families?

The importance of this work is that it may lead to a determination of the origin of the particles in the zodiacal cloud.

At present we are pursuing problems associated with the Hirayama family dustband model. We have realised that once particles are produced in the asteroid belt by collisions they must spiral in towards the sun as a result of Poynting-Robertson light drag. This motion must result in their passage through numerous resonances with Jupiter (the Kirkwood gaps) and these passages probably change the structure of the bands. Thus, the Hirayama family hypothesis cannot be fully tested until these changes have been determined. We are determining these changes using the Cornell National Supercomputer. This work is a direct extension of our work on the dynamics of satellites.

#### References

1. Dermott, S. F., and Thomas, P. C. (1988). The Shape and Internal Structure of Mimas. Icarus (in press).
2. Dermott, S. F., Malhotra, R., and Murray, C. D. (1987). Dynamics of the Uranian and Saturnian Satellites: A Chaotic Route to Melting Miranda? Icarus (submitted).
3. Dermott, S. F., Nicholson, P. D., Kim, Y., Wolven, B., and Tedesco, E. F. (1988). The Impact of IRAS on Asteroidal Science. In "Comets to Cosmology" (ed. A. Lawrence), Springer-Verlag, (in press).
4. Dermott, S. F., Nicholson, P. D., Burns, J. A., and Houck, J. R. (1984). Origin of the Solar System Dust Bands discovered by IRAS, Nature, 312, 505-509.
5. Dermott, S. F., Nicholson, P. D., Burns, J. A., and Houck, J. R. (1985). An Analysis of IRAS' Solar System Dust Bands. IAU Colloquium No. 85, "Properties and Interaction of Interplanetary Dust" (ed. Giese R.H. and P. Lamy), D. Reidel Pub. Co., 395-409.
6. Dermott, S. F., Nicholson, P. D., and Wolven, B. (1986). Preliminary Analysis of the IRAS Dust Data. In "Asteroids, Comets and Meteor II" (eds. C-I. Lagerkvist and H. Rickman) Uppsala, 583-594.

Thermal and Dynamical Processes in the Evolution of Outer Planet Satellites  
Gerald Schubert, University of California, Los Angeles

In the past year we have refined multilayered viscoelastic satellite models and applied them to the geodynamics of outer planet satellites. We have shown the utility of these models by studying the secular shape of Mimas and tidal heating in Io and Enceladus. We have made significant contributions to the tidal heating problem by finding the surface distribution of tidally generated heat flow for Io and by showing that previous calculations of tidal heating in Enceladus have been too low by a factor up to 2000.

We calculated spatial distributions of tidal dissipation for Io using multilayer Maxwell rheology models and the correspondence principle (Segatz et al., 1987). The models are required to satisfy the observed infrared heat loss and have density profiles consistent with the observed shape. Two different models were examined. A three-layer model having a silicate Maxwell mantle between an elastic lithosphere and an inviscid Fe-FeS core. A four-layer model includes a thin layer of molten silicates in a magmasphere between an elastic lithosphere and solid mantle. A successful three-layer model has shear modulus  $10^{10}$  Pa and viscosity  $2 \times 10^{16}$  Pa s. It is not possible to tightly constrain the four-layer model; typically the molten layer has viscosity  $10^4$  Pa s and thickness about 20 km. The two models predict different surface expressions of the tidally generated heat; the equator should be thermally more active than the polar regions in the four-layer model while the three-layer model should have most thermal activity at the poles.

Dissipation in a homogeneous Maxwell Enceladus model at the current eccentricity has been shown to be up to a factor 2000 greater than previously calculated (Ross and Schubert, 1987a). Multilayered models were shown to be thermally stable at the current eccentricity with 0(10 km) thick lithosphere and surface heat flow about  $5 \text{ mW m}^{-2}$ ; the models require some enhancement of near surface temperatures above the solar equilibrium values for stability. Models with and without a magma ocean of ammonia-water eutectic melt beneath the lithosphere are shown to be stable. Typically, mantle temperatures are shown to be about 210 K. Turbulent dissipation in a eutectic ocean may contribute significantly to the total tidal heating. The results suggest that the current eccentricity could have been maintained since the 2:1 resonance with Dione was established with recurring surface activity due to a thermally active interior.

The multilayered viscoelastic model can be used to study the secular shape of a satellite by letting the forcing frequency approach zero. In the case of Mimas, we have shown that a wide variety of internal structure models are consistent with the observed secular tidal distortion (Ross and Schubert, 1987b). Two-layered models may include a silicate inner core (0.43 Mimas' radius) beneath an ice mantle or a silicate-ice mixture throughout with a highly porous (about 50-60%) outer layer about 20 km thick. Density may increase smoothly with depth from pure ice at the surface to pure silicate at the satellite's center. Finally, we showed that the lithosphere may have possessed nonzero shear modulus since synchronous rotation establishment; shear modulus about  $10^7$  Pa in a 20 km thick lithosphere in a homogeneous (in density) Mimas is consistent with the shape of the satellite.

#### REFERENCES

- Ross, M. and G. Schubert (1987a). Viscoelastic models of tidal heating in Enceladus. *Icarus*, submitted.
- Ross, M. and G. Schubert (1987b). Internal structure and shape of Mimas. *Icarus*, submitted.
- Segatz, M., T. Spohn, M.N. Ross, and G. Schubert (1987). Tidal dissipation, surface heat flow, and figure of viscoelastic models of Io. *Icarus*, submitted.

# SMALL SATELLITES OF URANUS

P. C. Thomas and J. Veverka, Cornell University

Photometry of the small, inner satellites of Uranus is important in establishing the complete range of materials composing the Uranian system. Voyager 2 observed at least ten small satellites in orbits ranging in distance from Uranus from 49,700 km (1986U7, just inside  $\epsilon$  ring, to 1985U1 at 86,000 km, about halfway between the  $\epsilon$  ring and Miranda (Smith et al., 1986). Only 1985U1 is well resolved. It is irregular in shape, is about 77 km in average radius, and has a normal reflectance in clear filter ( $\lambda_{\text{eff}} \approx 0.48 \mu\text{m}$ ) estimated to be  $0.08 \pm 0.01$  (Thomas et al., 1987).

We have made photometric measurements of the best images of five of the remaining satellites unambiguously identified in clear filter images. Uncertainties of identification, and/or low signal/noise have hampered color measurements of these satellites so far.

Disk-integrated photometry has been done for clear filter images. For 1985U1 (Puck) we have two images, at  $\alpha = 33^\circ$  and 4.5 km/pxl, and one at  $14.7^\circ$  and 73.2 km/pxl. Disk-averaged reflectances are 0.028 and 0.046 respectively, yielding a disk-integrated phase coefficient of 0.029 mag/deg.

The other small satellites are imaged at 10-160 km/pxl, usually with significant smearing. 1986U7 ( $a \approx 49,700$  km, just inside  $\epsilon$  ring) was imaged at 10-33 km/pxl, and is marginally resolved though smeared by several pixels. The best measure of its diameter is  $3.3 \pm 5$  pixels (based on spread function inferred from low resolution image of 1985U1). The resulting radius is  $R = 17 \pm 2.6$  km; average reflectance is  $0.024 \pm .008$  at  $\alpha = 20.7^\circ$ . Nearly identical results obtain at  $\alpha = 19.7^\circ$  and  $13.6^\circ$  km/pixel. At  $\alpha = 15.5^\circ$ , average I/F =  $0.0264 \pm 0.008$ , which gives a disk-integrated phase coefficient of 0.025 mag/deg. (This phase coefficient is more accurate than reflectance values because of the uncertain radius.) The reflectance of 1986U7 at  $\alpha = 15.5^\circ$  of  $0.0264 \pm 0.008$  appears lower than that of Puck,  $0.045 \pm 0.005$  at  $\alpha = 14.7^\circ$ .

The radii of the other satellites are listed below; all are based on at least two images yielding consistent determinations. Typical uncertainties, relative to 1986U7, are 10-15%.

Satellite	Radius (km)*
1986U1	77
1986U4	36
1986U6	38
1986U7	17
1986U8	22

\*Assumes 17 km radius of 1987U7 is correct.

One color sequence of the  $\epsilon$  ring has been measured for eventual comparison with color data on small satellites. Relative to the Green filter, Violet is  $1.16 \pm 0.15$ , Clear is  $1.36 \pm 0.18$ .

Supported by NASA Grant NSG 7156.

#### References:

- Smith, B. A., L. A. Soderblom, R. Beebe, D. Bliss, J. M. Boyce, A. Brahic, G. A. Briggs, R. H. Brown, S. A. Collins, A. F. Cook II, S. K. Croft, J. N. Cuzzi, G. E. Danielson, M. E. Davies, T. E. Dowling, D. Godfrey, C. J. Hansen, C. Harris, G. E. Hunt, A. P. Ingersoll, T. V. Johnson, R. J. Krauss, H. Masursky, D. Morrison, T. Owen, J. B. Plescia, J. B. Pollack, C. C. Porco, K. Rages, C. Sagan, E. M. Shoemaker, L. A. Sromovsky, C. Stoker, R. G. Strom, V. E. Suomi, S. P. Synnott, R. J. Terrile, P. Thomas, W. R. Thompson, J. Veverka (1986). Voyager 2 in the Uranian System: Imaging Science Results. Science 233, 43-64.
- Thomas, P., J. Veverka, T. Johnson, R. H. Brown. 1985U1, Voyager Imaging Results. Icarus 72, 79-83, 1987.

## SATELLITES OF URANUS: SHAPES AND TOPOGRAPHY FROM LIMB COORDINATES

P. C. Thomas, Cornell University

Limb coordinates provide accurate measures of satellite sizes and shapes that are complementary to, and expand the utility of analytic triangulation techniques. Voyager 2 images allow the radii to be measured with uncertainties less than 3 km (Davies et al., 1987; Thomas, 1987). Miranda and Ariel have been shown to be ellipsoids; the solutions are triaxial, but the formal error bars (Table 1) allow equal b and c axes. The differences of long and short axes, a-c, are consistent with equilibrium figures with the published mean densities. The important finding here is that Miranda is an ellipsoidal satellite, apparently relaxed to an equilibrium shape; its considerable topography is not due to reaccretional differences or other exotic mechanisms. The more slowly rotating outer satellites are best fit by spheres; the largest expected bulge is 2 km on Umbriel.

The limb topography that is visible, measured as the radial residuals to the best-fit ellipse of the limb coordinates in a particular image, are useful in measuring or illustrating specific topographic forms. The precision of the technique is about 0.3 pixels and reveals substantial differences in the topography of the five satellites. Umbriel has a 500 km basin 6 km deep (Fig. 1), and another depression as deep and of unknown extent. If the five-hundred-km basin is impact-related, it is the largest such basin in the Uranian satellite system. The limb topography of Miranda is shown in Fig. 2. The greatest relief on Miranda is 10 km in depression-uplift combinations at the margins of coronae. The troughs reach 7 km depth and have slopes that reach 35-40° in places, at or above angle of repose. Arden corona has been deformed by a 2 km depression.

Supported by NASA grant NAGW-111.

### References:

- Davies, M., T. R. Colvin, F. Y. Katayama, and P. C. Thomas, 1987. The control networks of the satellites of Uranus. Icarus 71, 137-147.
- Dermott, S. F., and P. C. Thomas, 1988. Shape and internal structure of Mimas. Icarus, in press.
- Thomas, P. C., 1987. Radii, shapes, and topography of the satellites of Uranus from limb coordinates. Icarus, in press.
- Thomas, P., J. Veverka, T. V. Johnson, and R. Hamilton Brown, 1987. Voyager observations of 1985U1. Icarus, in press.

TABLE 1: Shapes and Mean Radii (km)

	a	b	c	a-c	Mean radius
Miranda	$240.4 \pm 0.6$	$234.2 \pm 0.9$	$232.9 \pm 1.1,$ $- 1.3$	$7.5 \pm 1.8$	$235.8 \pm 0.7$
Ariel	$581.1 \pm 0.9$	$577.9 \pm 0.6$	$577.7 \pm 1.0$	$3.4 \pm 1.5$ $- 0.8$	$578.9 \pm 0.6$
Umbriel		(spherical)			$584.7 \pm 2.8$
Titania		(spherical)			$788.9 \pm 1.8$
Oberon		(spherical)			$761.4 \pm 2.6$

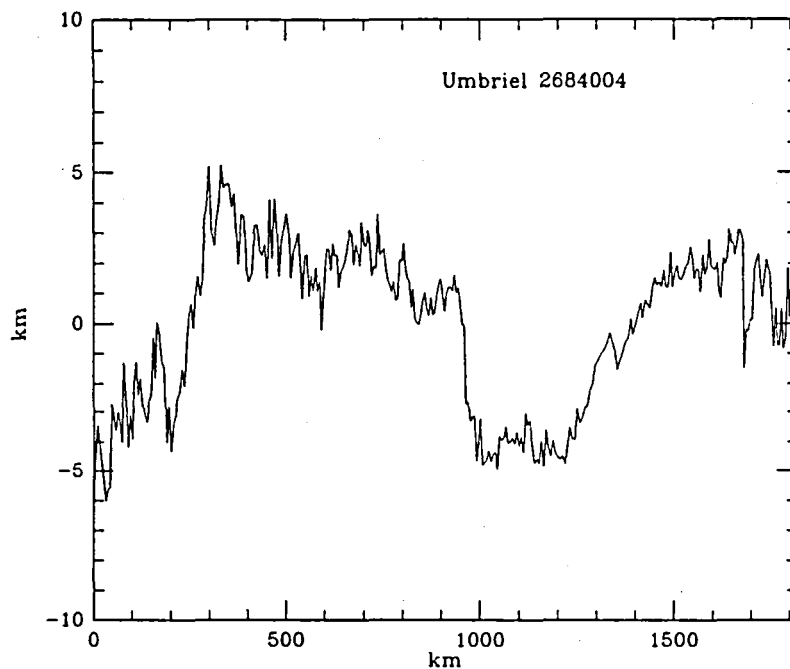
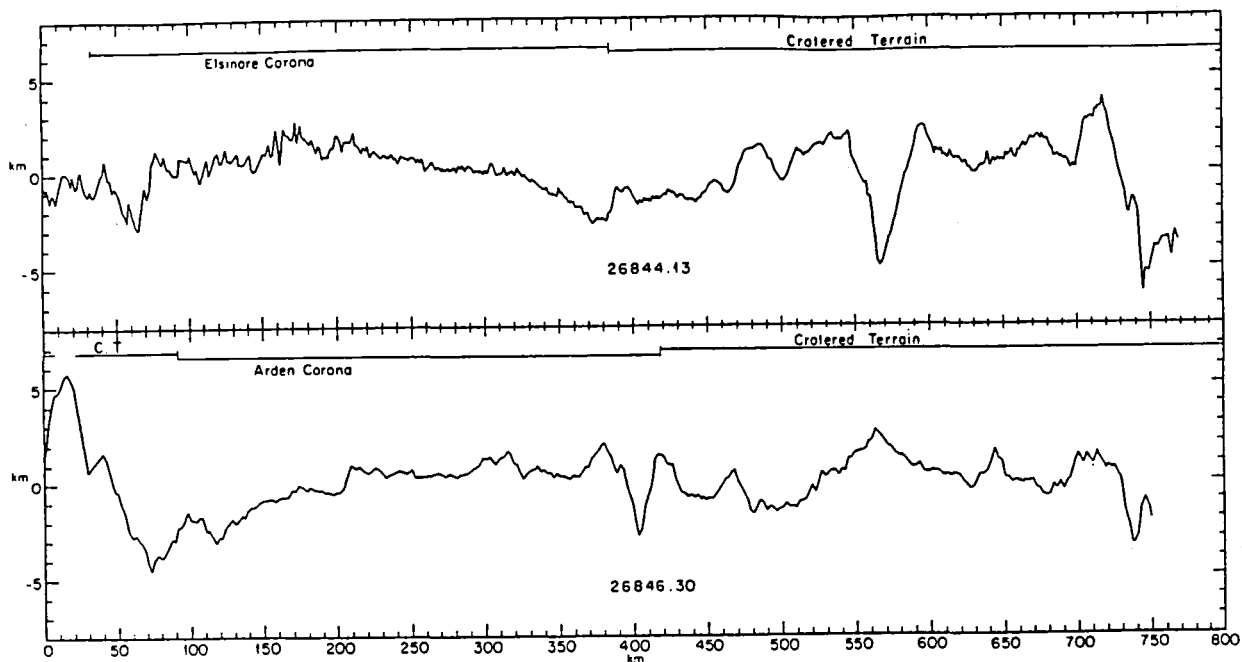


Figure 1. Limb topography of Umbriel; Image 2684004; 5.1 km/pixel. Two large basins are shown; depths reach 6 km. The precision is about 1.5 km.





**Figure 2. Limb topography of Miranda.**

Image numbers are given on plots.

Main features are the troughs

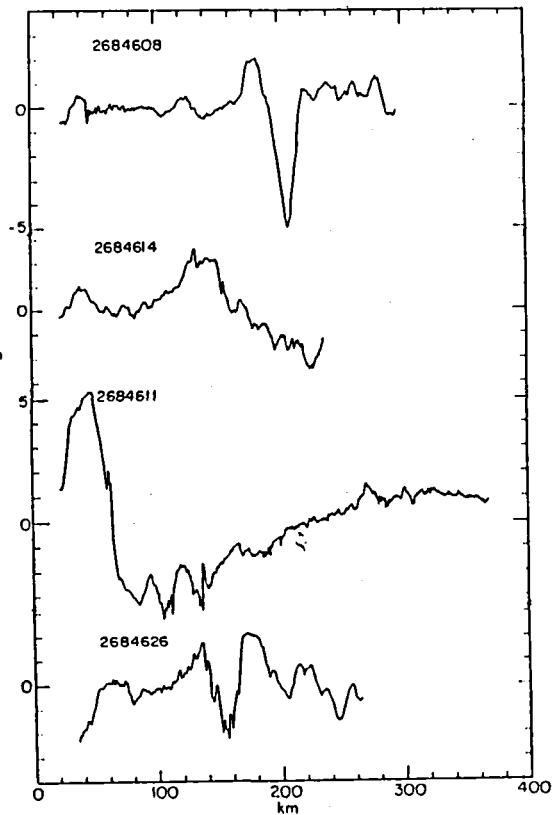
that bound coronae, and the uplifts

that are usually paired with the

troughs. Maximum relief on the

visible hemisphere of Miranda is

about 10 km.



SHAPES OF SMALL SATELLITES FROM LIMB COORDINATES  
P. C. Thomas, Cornell University

Limb coordinates have been found useful for describing the shapes of irregularly shaped small satellites, and ellipsoidal fits found useful for geometric description of small satellites, provided the physical interpretation is properly qualified.

Limb coordinates for images of Phobos and Deimos have been fit with ellipses, and the resulting axes combined for ellipsoidal solutions in the manner described by Dermott and Thomas (1988). The fit axes can be compared to those derived by Duxbury and Callahan (1982) completely independently by analytic triangulation (Table 1). The comparison is very impressive, and the solution for mean radius is very close to the triangulation fit. The ellipsoidal fit from limb profiles is thus a useful measure of volume of a satellite if good stereo is lacking.

The method has been applied to several other satellites with multiple views, and the results are listed in Table 2. Among the results is the finding that the Saturn coorbitals, Janus and Epimetheus, sharing the same orbit, have very different shapes. Janus is oblate; Epimetheus is prolate. This difference in shapes adds to the considerable evidence that shapes of small satellites cannot be used to infer mean densities. The volumes calculated for Janus and Epimetheus are probably good to 15%, a considerable improvement over early estimates (Thomas et al., 1986).

The residuals to the fit ellipses also measure its roughness, and this is plotted in Fig. 1. These data show the sharp transition in shape of icy satellites from small, irregular ones (less than 200 km in radius) to smooth, ellipsoidal objects the size of Mimas and larger.

Supported by NASA grant NAGW 111.

References:

- Dermott, S. F., and P. C. Thomas, 1988. Shape and internal structure of Mimas. Icarus, in press.
- Duxbury, T. C., and J. Callahan, 1982. Phobos and Deimos Cartography. Lunar Planet. Sci. 13, p. 190.
- Thomas, P., J. Veverka, and S. Dermott, 1986. Small Satellites. In Satellites (J. Burns and M. Matthews, eds.).

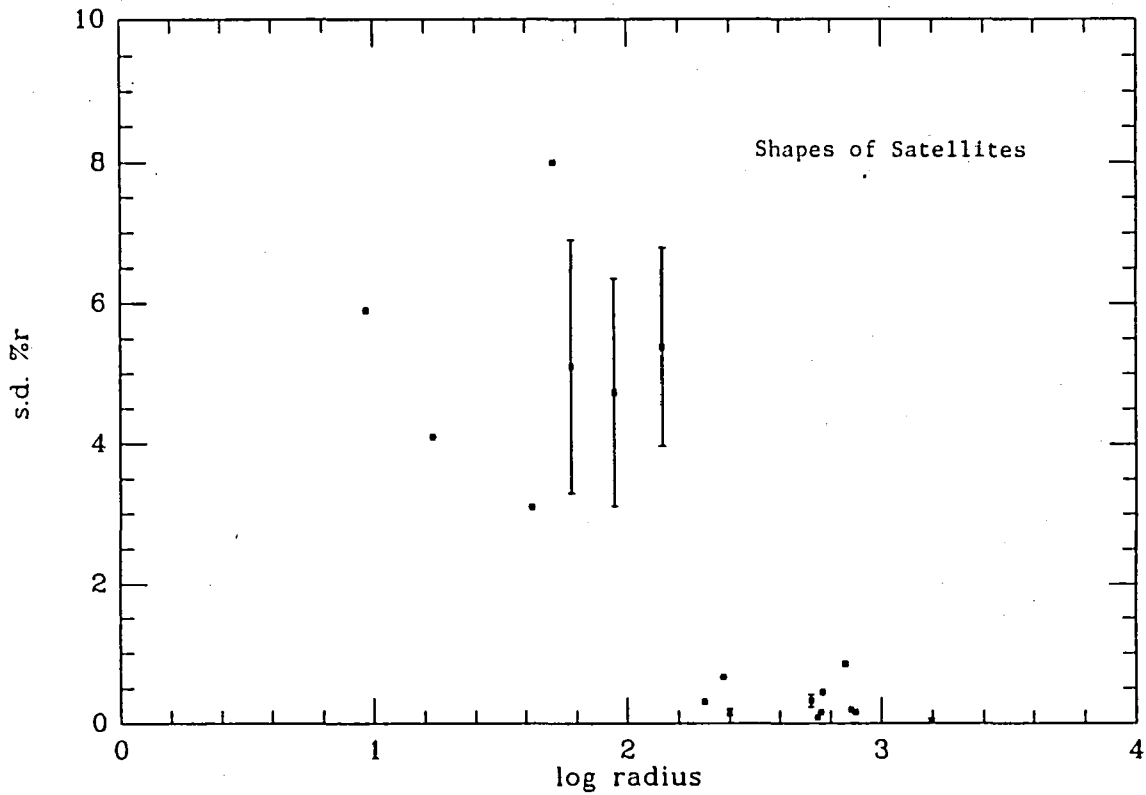


Figure 1. Roughness of icy satellites, measured by standard deviation of residuals to best-fit ellipses as a fraction of satellite radius. Mimas is the smallest of the "smooth" satellites. Data are from small icy satellites, Europa, and large satellites of Saturn and Uranus. "Error bars" show S.D. of values from different views of satellites.

TABLE 1: Comparison of Ellipsoid Fits of Phobos and Deimos by Independent Methods: Limb Coordinates and Triangulation

Control Points (Duxbury and Callahan, 1982)		Limb Coordinates
Phobos:		
a	13.3 km	13.4 km
b	11.1	11.2
c	9.3	9.2
Calc. Vol. (km <sup>3</sup> ) = 5751		5784
Mean Radius (km) = 11.11		11.13
-----		
Deimos:		
a	7.5	7.5
b	6.2	6.1
c	5.4	5.2
Calc. Vol. (km <sup>3</sup> ) = 1051		997
Mean Radius (km) = 6.31		6.19

TABLE 2: Summary of Shapes and Sizes of Small Satellites (km)

Satellite	a	b	c	Mean Radius
Phobos	13.4	11.1	9.2	11.2 ± 0.15
Deimos	7.5	6.1	5.2	6.2 ± 0.18
Amalthea	131.0	79.0	67.0	88.3 ± 3
Prometheus	74.0	50.0	34.0	50.1 ± 2
Pandora	55.0	44.0	31.0	41.9 ± 2
Janus	97.0	95.0	77.0	88.8 ± 4
Epimetheus	69.0	55.0	55.0	59.5 ± 3
Calypso	15.0	8.0	8.0	9.5 ± 1

## Volatile Processes on Large Satellites of the Giant Planets

J.I. Lunine (Lunar & Planetary Laboratory, University of Arizona, Tucson, AZ)

The large moons Io, Titan and Triton are distinguished by the importance of volatiles in surface and atmospheric processes. (Here volatile refers to a material with significantly higher vapor pressure than the bulk constituents of the object). A program is underway to apply thermodynamic modelling and existing laboratory data to interpret spacecraft and ground-based data on these moons, and place their formation and evolution in the context of the rest of the solar system. This year, work has focussed on the following areas:

Io: An outstanding issue in understanding how Io handles its prodigious heat budget is the composition and morphology of the hot spots. The largest such region observed by Voyager, Loki plumes and Loki Patera, has been modelled previously in terms of large-area silicate flows (1), and as one or several molten sulfur lakes (2). The 1985 occultations of Io by Callisto and Ganymede afforded an opportunity to test these models (3), which had originally been constructed to fit the Voyager IRIS data.

A series of models were therefore constructed to simulate the brightness temperature and size of the Loki hot spot, at several infrared wavelengths, using physical temperature distributions for molten sulfur lakes and silicate flows. The results show that ground-based observations capable of resolving area and brightness temperature at two wavelengths are diagnostic of the physical mechanisms and materials radiating energy away from the Loki region. The mutual events data obtained in 1985 yield a brightness temperature and area for the Loki hot spot at one wavelength, 3.8 microns (4). For the hot spot area derived from the observations, the brightness temperature agrees with the silicate flow model of (1) or a sulfur lake model with the lake temperature elevated by 20 K since the Voyager flybys. The spot area itself is underestimated by both models, although more closely fit by the sulfur lake, and is smaller than that predicted by a simple three-temperature fit to the Voyager IRIS data (5). The results are summarized in figure 1, taken from (6). The effect on the infrared spectrum of changes in thermal output of Loki was explored in the context of the sulfur lake model. Implications of various hot spot morphologies is considered in (7).

Titan: The presence or absence of a hydrocarbon ocean at the surface of Titan has important implications for the stability of the present atmospheric composition and thermal structure as well as the evolution of the entire surface-atmosphere system with time. In collaboration with B. Rizk, simple grey numerical and analytical models were constructed of

the evolution of the thermal structure of Titan's atmosphere, assumed to be in contact with a hydrocarbon ocean changing slowly in composition with time. The goal is to understand the response of Titan's climate as methane is progressively destroyed by photolysis in the stratosphere. We employed recent laboratory data and models for absorption coefficients of pressure-induced gas opacity of nitrogen and methane kindly provided by R. Courtin, as well as literature data on mixing properties of liquid nitrogen, methane and ethane. The grey atmosphere models are sensitive to the present-day abundance of methane in the surface ocean, and the presence of clouds. Non-grey models are required to fully incorporate the effect of the gaseous absorption coefficients. The study confirmed the very strong control an ethane-methane ocean has on the atmosphere, and reinforced the need for accurate atmospheric net flux measurements and determination of the physical state and composition of the surface. Such data can be obtained on the proposed Cassini mission.

Triton: Planning for the 1989 Voyager-Neptune encounter requires consideration of possible models of the atmosphere of Neptune's large satellite Triton. A suite of models of the surface of Triton (8,9) were used to construct surface temperature and vertical profiles of pressure for optically thin atmospheres. The profiles were used to determine the altitude range over which useful data can be collected during the ultraviolet spectrometer solar occultation and radio science earth occultation observations by Voyager. The atmospheric pressure is primarily determined by whether methane or nitrogen is the dominant surface volatile, and in a secondary sense by whether the volatiles are restricted to the poles or uniformly distributed.

The possibility of an optically thick atmosphere was assessed using opacities derived from pressure-induced absorption data for methane and nitrogen provided by R. Courtin. If Triton's surface contains substantial quantities of nitrogen, an optically thick, massive atmosphere can be sustained.

#### References

- (1) Carr, M.H., J. Geophys. Res. **91**, 3521, 1986.
- (2) Lunine, J.I. and D.J. Stevenson, Icarus **64**, 345, 1985.
- (3) McEwen, et al., Geophys. Res. Ltrrs **13**, 201, 1985.
- (4) Goguen, J.D., et al., Icarus, submitted.
- (5) Pearl, J.S. and W.M. Sinton, in Satellites of Jupiter, D. Morrison, ed., p. 724, U. of Arizona Press, 1982.
- (6) Lunine, J.I., in Time-Variable Phenomena in the Jovian System, NASA SP- , in press.
- (7) McEwen, A.S., J.I. Lunine and M.H. Carr, *ibid.*
- (8) Lunine, J.I. and D.J. Stevenson, Nature **317**, 238, 1985.
- (9) Trafton, L., Icarus **58**, 312, 1984.

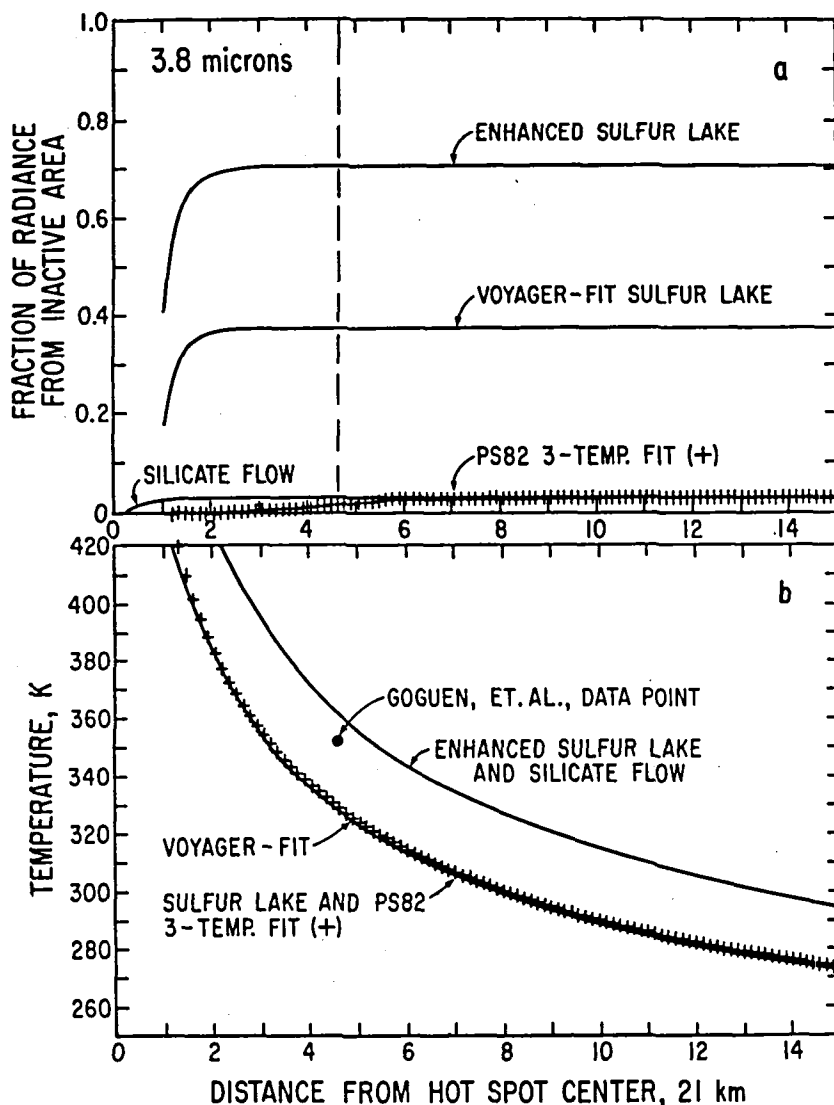


Figure 1. (a) Fraction of 3.8 micron thermal emission contributed from inactive areas adjacent to the active center of the Loki hot spot. "Inactive" is defined as follows: for the PS82 model (5), the 245 K component; for the LS85 model (2), the sulfur vapor condensation zone, and for the C86 model (1), the inactive silicate flow. The predicted observable hot spot size is given by the distance at which the curve becomes horizontal. The hot spot size from data in (4) is shown as the vertical dashed line. (b) The brightness temperature of Loki at 3.8 microns as a function of the area observed (expressed as distance from hot spot center). Reading off the hot spot size from (a), one can find the predicted brightness temperature from (b) for the various models. The data point of (4) is shown. All distances are normalized to 21 km, the size of the "hot component" in the three-temperature fit to Voyager IRIS data (5).

**CRATERING HISTORY OF UMBRIEL, TITANIA, AND OBERON.** J.B. Plescia, Jet Propulsion Laboratory, Calif. Institute of Technology, Pasadena, CA 91109

Crater frequencies have been compiled for Umbriel, Titania, and Oberon, the three outermost satellites of Uranus (Table 1).

Umbriel exhibits craters having diameters that range from 210 km down to the limit of resolution (5.2 km/pixel) in a relatively uniform distribution of sizes. Most craters are degraded, although a few remain fresh. The surface of Umbriel probably dates to a period of intense bombardment early in its history and apparently has not experienced the significant endogenic resurfacing that has occurred on Miranda and Ariel (3).

The cumulative size-frequency distribution for Umbriel has two interesting aspects: (1) distinct breaks in slope at diameters of about 30 and 50 km, the slope being about -2.2 at diameters <30 and >50 km and about -4.0 between those diameters; and (2) at diameters <50 km it lies well above the distribution for surfaces elsewhere in the solar system considered by some to be in an "equilibrium condition". Surfaces considered to be in an equilibrium condition include those of the lunar highlands (1) and many of the heavily cratered surfaces on the satellites of the outer planets (2).

Titania's surface is fairly uniformly cratered and, with the exception of the bright, smooth material around the crater Ursula, cannot be divided into different terrains. Recognizable craters range in diameter from about 140 km to the limit of resolution (3.4 km/pixel), but most have diameters <70 km. In addition, there are a well-defined impact basin (Gertrude) 315 km in diameter, a degraded basin about 330 km in diameter, and a feature that may have been a 245-km-diameter basin upon which Gertrude was superposed. The relatively high image resolution allowed the surface to be divided into several counting areas within which meaningful statistics could be compiled (Table 1). No significant differences in crater frequency were observed within the cratered terrain, so the data were combined into a single distribution. Only the degraded basin and the smooth plains around Ursula have significantly different crater frequencies. Titania has been almost completely resurfaced by endogenic processes since the presumed early intense bombardment. Apparently, only the areas around Gertrude and the degraded basin escaped this resurfacing. Endogenic resurfacing also produced the bright, smooth plains around Ursula and the smooth material found locally along some of the grabens. Whether different areas were resurfaced during distinctly different episodes of resurfacing or during a continuous process whose intensity and areal extent waned with time is uncertain. Graben formation occurred in part after the smooth material around Ursula was deposited, but the stratigraphic relations necessary to constrain the ages of most of the grabens cannot be observed at this resolution.

The cumulative size-frequency distribution for the cratered terrain, which includes most of the observed surface of Titania, has well-defined breaks in slope at diameters of 20 and 35 km, the slope being about -4 between these diameters and -2 outside that range. The distribution exceeds equilibrium values at diameters <25 km.

Oberon appears to be an ancient, relatively uniformly cratered body whose surface is not divisible into different types of terrain. Craters range in diameter from about 210 km to the limit of resolution (6 km/pixel); most diameters are <100 km. Oberon's surface dates to a period of intense bombardment early in its history and has not been subjected to satellite-



wide crustal replacement since then. Endogenic resurfacing appears to have been limited to small deposits of low-albedo material that partly fill the floors of some of the large craters.

The cumulative size-frequency distribution for Oberon has distinct breaks in slope at about 45 and 70 km; the slope is about -3 between those diameters and -2 outside that range, and at diameters <70 km the crater frequencies are significantly higher than for an equilibrium distribution.

The cumulative size-frequency distributions for these three satellites (except the distribution for the bright material around Ursula on Titania) exceed that of an equilibrium distribution at a specific diameter, indicating that these surfaces are not in the type of equilibrium as other planetary surfaces may be. Each satellite exhibits an overabundance of craters in a specific size range (45 to 70 km on Oberon; 30 to 50 km on Umbriel; 20 to 35 km on Titania) relative to what is expected at diameters outside that range. The nonequilibrium conditions apparently have developed because the number of smaller impacts is insufficient to keep the number of larger craters in equilibrium and/or because the largest basins which can destroy large numbers of craters are absent.

**REFERENCES:** (1) Shoemaker, E.M., et al., 1966, JPL Tech. Rept. 32-800, 249-337; (2) Hartmann, W.K., 1984, *Icarus*, 60, 56-74; (3) Smith, B.A., et al., 1986, *Science*, 233, 43-64.

**TABLE 1. CRATER FREQUENCIES**

	CUMULATIVE NUMBER OF CRATERS $\geq D/10^6$ KM <sup>2</sup>					COUNTING AREA (KM <sup>2</sup> )
	DIAMETER KM					
	10	20	30	40	50	
Umbriel	(1,957 <u>±</u> 67)	522 <u>±</u> 35	228 <u>±</u> 23	104 <u>±</u> 15	41 <u>±</u> 10	436,449
Oberon	(1,377 <u>±</u> 39)	(464 <u>±</u> 22)	197 <u>±</u> 14	107 <u>±</u> 11	60 <u>±</u> 8	919,812
Titania:						
Cratered terrain	(1,515 <u>±</u> 46)	355 <u>±</u> 22	70 <u>±</u> 10	25 <u>±</u> 6	16 <u>±</u> 5	722,016
Gertrude	(2,695 <u>±</u> 202)	325 <u>±</u> 70	86 <u>±</u> 36	53 <u>±</u> 28	39 <u>±</u> 24	66,146
Degraded basin	(1,668 <u>±</u> 152)	520 <u>±</u> 85	232 <u>±</u> 57	81 <u>±</u> 34	22 <u>±</u> 17	72,088
Plains	(1,066 <u>±</u> 96)	120 <u>±</u> 32	9 <u>±</u> 9	<1	<1	115,747

Data in parentheses indicate extrapolations.

VERICAL RELIEF OF MARTIAN WRINKLE RIDGES: IMPLICATIONS FOR  
INTERNAL STRUCTURE. J.B. Plescia, Jet Propulsion Laboratory,  
Pasadena, CA 91109

Wrinkle ridges are common geomorphic features on the surfaces of the Moon, Mercury, and Mars. Several structural models have been suggested to explain their origin (1,2,3). Recently, Plescia and Golombek (4) have suggested that a wrinkle ridge is formed by the anticlinal folding of surface layers over a low-angle reverse (thrust) fault. Alternatively, Watters (5) has argued that wrinkle ridges are formed simply by anticlinal folding and that faulting is of only minor importance. Regional elevation data can shed light on which model (faulting and folding versus folding) is the more appropriate.

Golombek and Franklin (6) have made an extensive analysis of the dimensional aspects of lunar wrinkle ridges using the Lunar Topographic Orthophoto Maps. They note that lunar wrinkle ridges typically had about 80 to 500 m of relief. More importantly, they observed that a regional elevation discontinuity occurs across the ridges. That is, the average elevation of the mare on one side of the ridge is different than that on the opposite side. This regional discontinuity typically was on the order of 5 to 280 m. Golombek and Franklin interpret the regional elevation discontinuity to indicate the presence of a fault associated with the ridge. Lucchitta (7) found similar results in an earlier, more limited, study.

To investigate the regional topographic aspects of martian wrinkle ridges, photogrammetric topography was derived for a part of northwest Lunae Planum (approximate center at 20 degrees N, 71 degrees W). Only a limited area is covered by overlapping images having sufficient stereo for such an analysis, hence only two models were obtained (519A06/555A04 and 519A04/555A02). Using these two models, data were collected for several ridges. Measurements were made for individual points along profiles across the ridge. Each measurement was repeated seven to ten times for the purpose of assessing the statistical uncertainty in the elevation determination of an individual point along the profile. Typically, there were 20 points in the profile across the ridge and the adjacent plains. Using such a measurement strategy, only the large-scale topographic variations can be observed; detailed topographic profiles, as obtained by Golombek and Franklin are not obtainable with this technique.

In the northwest part of Lunae Planum, the ridges are composed of a broad ridge with a narrow "wrinkled" ridge occurring either along one side of the structure or meandering across the ridge. The overall ridge structure is about 5 to 15 km wide; the narrow wrinkles are less than 2 km wide. The photogrammetric data indicate that the relief of the ridge relative to the surrounding plains is on the order of 200 to 1,100 meters. These heights are similar to those observed for

the Moon (6,7).

In many of the cases a regional elevation discontinuity is measured across the Lunar Planum ridges. That is, like the Moon, the elevation of the plains on one side of the ridge is distinctly different from that on the other side. Observed regional elevation discontinuities are as large as 1,000 m, although most are in the 100-500 m range. The minimum elevation difference that could be detected using these stereo pairs is probably on the order of 100 m, hence those ridges for which elevation discontinuities were not observed, may have elevation differences less than 100 m. Elevation differences on the Moon are as small as 5 m (6).

The presence of regional elevation discontinuities across wrinkle ridges is not consistent with an origin by folding alone. The implication of the elevation difference across the ridge is that a fault must be present at depth to accommodate the regional offset. Similarities between wrinkle ridges and terrestrial analogs (5) suggest that this fault is a thrust fault. In the case of the wrinkle ridges, the thrust would dip beneath the side having the higher elevation. The difference in elevation across the ridge would be proportional (the constant being a function of the fault dip) to the slip on the fault. Using a model whereby the regional elevation difference indicates the amount of slip along the thrust fault and the surface length over the ridge indicates the amount of folding, the net compression across the structure can be estimated.

REFERENCES: (1) Bryan, 1973, Proc. Lunar Science Conf. 4th, 93. (2) Howard and Muehlberger, 1973, Apollo 17 Prelim. Science Report, NASA SP-330, 31/22. (3) Colton et al., 1972, Apollo 16 Prelim. Science Report, NASA SP-315, 29/90. (4) Watters, T., 1987, Geol. Soc. Amer. Abst. Prog., v. ,883. (5) Plescia, J., and Golombek, M., 1986, Geol. Soc. Amer. Bull., v. 97, 1289. (6) Golombek, M., and Franklin, B., 1987, Abst. 18th Lunar Planet. Science Conf., 339. (7) Lucchitta, B., 1977, Proc. Lunar Science Conf. 8th, 2961.

## Bombardment History of the Saturn System I: Spatial and Size-Frequency Distributions of Craters

S.W. Squyres (Cornell), J.J. Lissauer<sup>(1)</sup> (SUNY Stony Brook), and W.K. Hartmann (PSI)

We have analyzed Voyager images of Saturn's satellites and developed dynamical models of relative cratering rates on these bodies in order to construct a history of satellite bombardment, disruption, and resurfacing in the Saturn system. Our observations concentrate most heavily on Rhea, the largest and best-imaged of Saturn's airless satellites. We have divided the surface of Rhea into 44 latitude-longitude quadrats for counting purposes. Detailed statistical analysis of the spatial distribution of craters shows that there is no significant evidence for local endogenic resurfacing on Rhea. There is an apparent spatial variability in the distribution of small craters, but it is strongly correlated with lighting geometry and hence unlikely to have resulted from geologic processes. More interestingly, we find that the spatial distribution of craters on Rhea with diameters  $D \geq 32$  km is unambiguously *more* uniform than a random distribution, which we interpret as indicating an approach to saturation equilibrium. (Impacts on a heavily cratered surface will tend to preferentially obliterate craters in areas of random crater clustering, leading to an increase in spatial uniformity). Craters with  $D \geq 64$  km on Rhea are more scarce and are clearly not saturated; therefore they probably represent a production function. The size-frequency relationship of these large craters on Rhea is well fit by the curve  $\log_{10} N_L = -2.73 \log_{10} D - 0.064$ , where  $N_L$  is the number of craters larger than  $D$  km per km<sup>2</sup>. A relationship with a very similar slope and a somewhat higher intercept holds for large craters on Iapetus. Iapetus is also clearly not saturated at large crater diameters. On Mimas, as on Rhea, the spatial distribution of craters shows no evidence for statistically significant spatial variability, and large craters appear to be present at densities below those expected for saturation equilibrium. We conclude that (a) there is no evidence for local geologic resurfacing on Rhea or Mimas; (b) Rhea, Mimas, and Iapetus are not saturated with craters at large crater diameters, so that observed crater densities may be used to evaluate satellite disruption probabilities; and (c) the degree of spatial uniformity of craters on a planetary surface may be a useful quantitative indicator of an approach to crater saturation equilibrium. This work was supported by the NASA Planetary Geology and Geophysics Program.

<sup>(1)</sup> Alfred P. Sloan Research Fellow

## Bombardment History of the Saturn System II: Catastrophic Fragmentation of Moons

J.J. Lissauer<sup>(1)</sup> (SUNY Stony Brook) and S.W. Squyres (Cornell)

We compute relative cratering rates and collision energies for heliocentric projectiles impacting Saturn's moons, taking into account gravitational focussing by the planet. Using crater scaling laws, we can project the large (unsaturated) crater distribution seen on one moon to that expected on others. We combine these calculations with our observations of Rhea and Iapetus to determine disruption probabilities of Saturn's inner moons. Our results vary by a factor of  $\sim 2$  depending on what crater scaling law we use and whether the impactors are predominantly Saturn family comets or long period comets. Computed disruption probabilities are 3-8 times higher when scaled to Iapetus' cratering record than to Rhea's. This could be due to Iapetus' surface being older than Rhea's, in which case the Iapetus scaling is correct; alternatively, Iapetus may have been cratered by a long-lived population of Saturn-orbiting debris which did not penetrate inside the orbit of Titan, in which case Rhea's record should be used. These uncertainties notwithstanding, we calculate disruption probabilities significantly smaller than those of Smith *et al.* (*Science* 215, 504). Our results are consistent with Mimas and larger moons being original aggregates and the smaller irregularly-shaped bodies being collisional fragments. Our results also place constraints on theories advocating recent formation of Saturn's rings from satellite disruption. This work was supported by the NASA Planetary Geology and Geophysics Program.

<sup>(1)</sup> Alfred P. Sloan Research Fellow



CHAPTER 2  
COMETS AND ASTEROIDS





## COMET RESEARCH

Fred L. Whipple, Smithsonian Astrophysical Observatory

The images obtained by the camera of ESA's Giotto mission to Halley's comet in March 1986 is a continuing source of material for study. At the International Symposium on the Diversity and Similarity of Comets, held in Brussels, Belgium in April, 1987, Whipple presented further results of this effect in a paper with co-authors Alan Delamere and Harold Reitsema. This paper centers on three major points. The first concerns the fact that whereas the major jets or rays near the nucleus were directed nearly at the Sun in the Giotto images, the early Giotto images and ground-based images, covering thousands instead of tens of kilometers at the comet, were directed some  $30^\circ$  or more south of the solar direction. This direction was more nearly perpendicular to the elongated apparent axis of the nucleus. The conclusion, supported by other evidence, was to place the major rotation axis roughly in this projected direction and account for the major activity as being the result of great continuing insolation from the current circumpolar region. This activity represented the major gas ejection whereas the dust ejection seen near the nucleus was greater from subpolar areas. Various observations indicate variable ratios of observable dust to gas emission from different areas of the nucleus and also similar variations in the composition of the gas measured by their spectra.

A second part of the paper is based on photometry around the nucleus, falling off nearly as the inverse distance from the major jet regions, indicating that the nucleus was imbedded in a large (out-going) cloud of dust of low opacity with nearly (80 to 90 percent) as much scattered sunlight between the spacecraft and the nucleus as beyond the nucleus. With the Sun some  $17^\circ$  beyond the plane of the sky and the morning side of the nucleus turned towards the spacecraft, the near symmetry in the fine-dust ejection indicates no large lag angle in sublimation. Thus the evidence is generally negative with regard to possible sublimation or activity on the night side of the nucleus, although some very weak rays might possibly be ascribed to such activities.

A measure of the very low albedo near the terminator suggests the scattering properties of the surface of the nucleus are similar to those of the moon at optical wavelengths. Continuing research on the Giotto images involves photometric and albedo studies, dust ejection and a definitive determination of the nucleus profile at the orientation observed at the encounter. The Sun is to the left in the accompanying tentative drawing of the profile of the nucleus.

Whipple's major effort in measuring the rotation periods of the nuclei of comets by the halo method (In *Comets: Gases, Ices, Grains and Plasma*, 1982, Proc. I.A.U. Coll. No. 61, ed.: L.L. Wilkening, Univ. Chicago Press) has not met with unqualified approval. Three or four of the periods that have since been measured (such as that of Halley's comet) by precise photometry are in disagreement. In fact, the study suffered

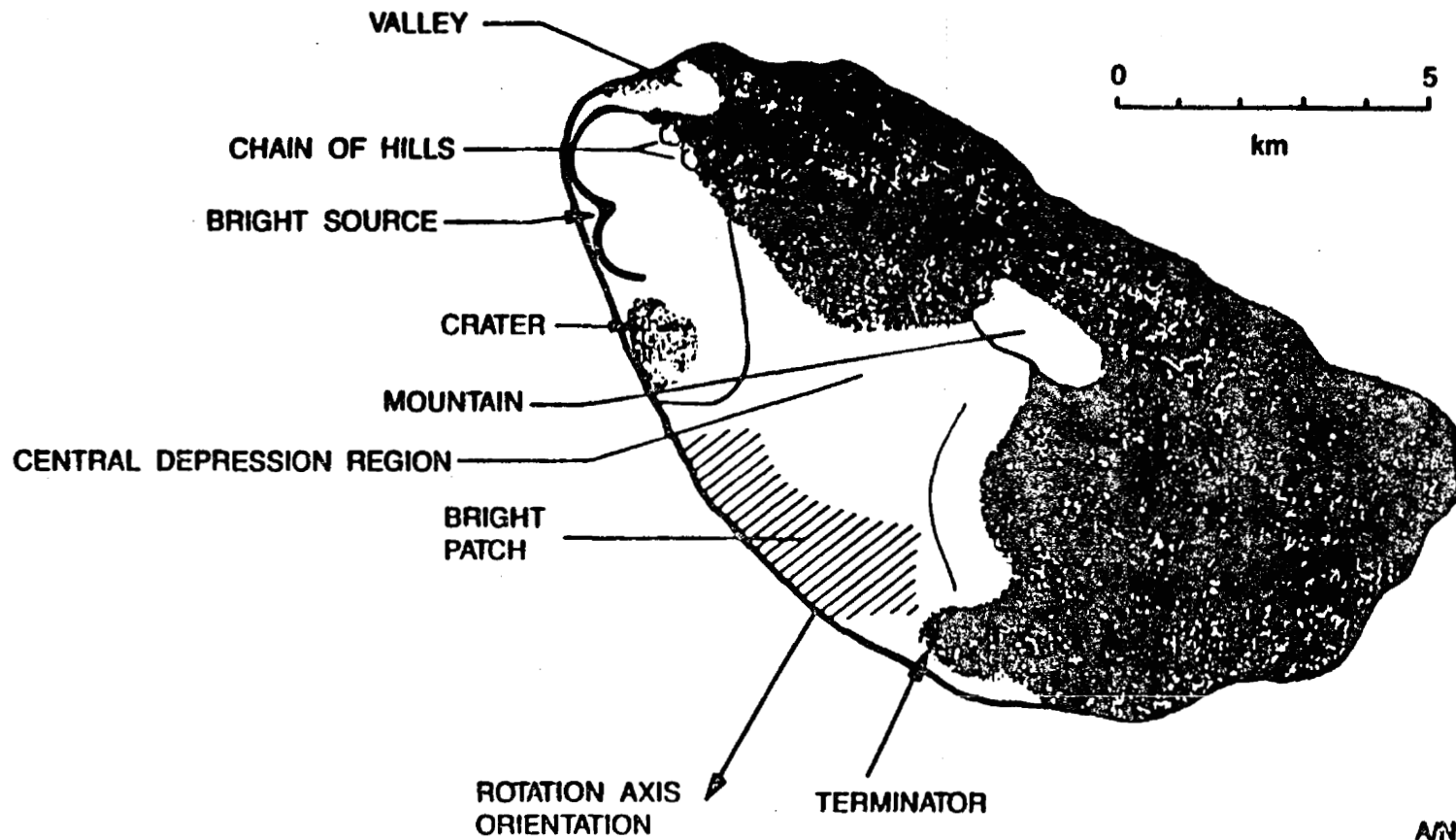
for several reasons: a) There were then no reliable photometric determinations of comet spin rates to provide calibration, b) The lack of experience with the method led to an over optimistic application to comets with multiple active areas, c) The method (quasi power function) used in search of the period was optimum for the task in the case of a single active area on the cometary nucleus but not when two or more active areas are present. It led to a minimum residual in a least-squares solution for the period from a series of calculated "zero dates" or times of halo initiation. When two or more active areas are present another type of power function has been devised to serve better. d) As pointed out by Armand Delsemme, the gas (halo) velocity ( $\nu$ ) of expansion from the nucleus is better represented by

$$\nu = 0.58r^{-1/2} km \ sec^{-1},$$

where  $r$  is the solar distance of the comet measured in AU, than by the expression  $0.535r^{-0.6} km \ sec^{-1}$  derived by Whipple empirically.

A major effort by Whipple is to reanalyze the observations of some 70 brighter comets and to recalculate the data with the above revised velocity law and a new independent search for spin periods for these and other comets using also the improved power function. The preliminary result has been satisfying in that the discrepancies with the few photometrically observed periods have been removed and many of the published spin periods have been verified with changes of only a few percent.

# HALLEY PROFILE



A/N 7230<sub>n</sub>

### The Rotation of Halley's Comet

S. J. Peale and J. Lissauer\* (U. Calif. at Santa Barbara)

The variation of the rotation state of the nucleus of Halley's comet due to a single jet, which can be located at an arbitrary point on, and inclined at an arbitrary angle with respect to the surface of a representative triaxial ellipsoid, is investigated by numerically integrating Euler's inhomogeneous equations. The magnitude of the mass flux is modulated by the cosine of the local zenith angle of the sun—being zero when the cosine is non-positive, and it is normalized to a value at perihelion with sun zenith =  $0^\circ$  such that the total effect on the orbit during one apparition is less than  $1/4$  to  $1/3$  that observed. The mass flux is further modified by a function of heliocentric distance which mimics the response of water ice or snow to solar illumination (Marsden, *et al.*, 1973). For a triaxial body with an initial 2.2 day rotation about the axis of maximum moment of inertia, the single jet can change the angular momentum of the nucleus by a substantial amount during one apparition depending on its location and orientation on the nucleus, but a substantial excitement of a wobble only occurs if the nucleus is nearly axially symmetric about the axis of minimum moment of inertia. A significant wobble could simultaneously accommodate the 2.2 day and 7.4 day periods observed in the light curve of Halley's comet. However, if Halley is significantly triaxial, such a large wobble would have to accumulate from the action of the jets over many apparitions or be the result of a major disruption of the nucleus. (The damping time for a wobble is  $O(10^6 Q)$  years), which rules out a primordial origin but allows a relatively gradual excitation.) For ellipsoid axes of 16, 8 and 7 km, two sets of initial conditions lead to a 7.4 day precession of a 2.2 day period spin (Julian, 1986). The corresponding precession about the axis of maximum moment of inertia is reasonably stable under the perturbations of the jet during one apparition, but a precession about the axis of minimum moment of inertia (*E.g.*, Sekanina, 1986) easily changes to a precession with altered period about the axis of maximum moment. This implies that the latter type of precession may not be stable under the action of the jets unless Halley is dynamically nearly axially symmetric. (If the rotation is only slightly slower or if the short axis is increased by less than 0.1 km, the period for precession about the axis of maximum moment must exceed 7.4 days.) The apparent ease with which the rotation state can be altered during a single apparition by a single jet places constraints on distribution of jets if the rotation state is to remain relatively unchanged over the historical observations of Halley's comet. The latter stability is indicated by the the apparent constancy of the non-gravitational forces modifying Halley's orbital period over more than 25 apparitions (Yeomans, 1981). With two active jets, light curves simulated by weighted integrations of the mass flux over a time window for a 7.4 day precession can exhibit a 7.4 day variation for both sets of initial conditions, but the variation is more subdued for precession about the axis of maximum moment of inertia and the shape of the light curve can vary from one 7.4 day fluxuation to the next.

\*Alfred P. Sloan Foundation Research Fellow

## COMETARY PHYSICS AND DYNAMICS

Paul R. Weissman, Earth and Space Sciences Division, Jet Propulsion Laboratory, Pasadena, CA 91109.

Work during the past year has continued to focus on analyses of observations of periodic Comet Halley in 1985-86, and explanations for the comet's gas production rates and post-perihelion brightening. At the same time, a study of Comet Halley's possible dynamical history and how it was captured to its present orbit was undertaken. In addition, revised cometary mass estimates derived from Halley results were used to estimate the total cratering flux for the Earth over the history of the solar system, including the contribution from random cometary showers from the inner Oort cloud.

During its 1985-86 appearance, Comet Halley displayed its usual pattern of being brighter following perihelion, as compared to before perihelion. This was seen in the comet's apparent magnitude and in measured gas production rates, as shown in Figure 1. Past explanations of this phenomenon, such as heat storage in the surface layers of the nucleus or energy release from amorphous ice phase transitions, were shown to be impractical through computer modeling of the thermal balance of the cometary nucleus. In addition, the suggested mechanisms can only explain post-perihelion brightening. Post-perihelion brightening is common, though not universal, among short-period (SP) comets. On the other hand, post-perihelion fading is generally the rule among long-period (LP) comets.

A solution to the problem involving "seasonal" changes on an obliquely rotating nucleus is suggested. Because of the high eccentricity of cometary orbits, very large changes in true anomaly occur as the comet moves through perihelion. As a result, the declination of the sun on the inclined nucleus can change rapidly, resulting in rapid seasonal changes. The declination of the sun on the nucleus of Comet Halley versus time from perihelion is shown in Figure 2 for three suggested rotation pole solutions. In each case, the sun moves rapidly northward as the comet rounds perihelion. As a result, the northern hemisphere goes from winter to summer in the space of less than 100 days, as compared with the 76 year period of the comet's orbit. In addition, this occurs when the comet is closest to the sun, resulting in severe heating of the northern hemisphere.

It has been shown (Green, 1986) that the thermal stresses expected in cometary surfaces will exceed the strength of the surface materials, causing cracking and flaking of the pre-existing surface crust on the nucleus. The crust will be blown off, exposing large areas of fresh ice, and increasing the gas production rate of the comet. As the sun continues to move northward after perihelion, the effect will grow, particularly if one of the active regions is located in a continuously illuminated circum-polar region. As the comet moves away from the sun the crust will reform, to repeat the process on the next perihelion passage. The advantage of this mechanism is that it can explain both pre- and post-perihelion brightening, given a random distribution of cometary rotation axes.

An analysis of Comet Halley's orbital motion was undertaken in an attempt to learn something of the comet's possible dynamical history. The comet's current orbit allows it to only make close approaches to the Earth, Venus, and Mars, planets too small to gravitationally capture it into the inner solar system. Regression of the nodes and the precession of perihelion would bring Halley's orbit close to Jupiter about  $9 \times 10^3$  years ago, about 120 returns in the past. However, it has been shown (Kozai, 1979) that Halley's orbit is currently librating, and that the motion of the nodes and the perihelion would reverse prior to the comet becoming Jupiter crossing. Observational support for the libration is afforded by detailed studies of the meteor streams associated with Comet Halley.

However, the libration amplitude is predicted to be decreasing, and thus was greater in the past. The comet could have made close Jupiter approaches about six to eight libration cycles ago, corresponding to 1.3 to  $1.5 \times 10^5$  years in the past. The comet's motion prior to that time is completely unknown, and only a matter of speculative probabilities.

An interesting implication of these results is the fact that Comet Halley has been in the inner solar system for quite a long time. Previous estimates of the lifetimes of SP comets were relatively low, typically a few hundred returns. However, the fact that as large and bright a comet as Halley could have survived 1,800 to 2,500 returns, implies that the fainter SP comets may be considerably older. This has possible implications for the contribution of SP comets to the cratering rate on the planets.

One of the major findings of the Comet Halley spacecraft flybys was the fact that the comet nucleus was darker and larger than previously thought. This fact was used last year to estimate a revised mass distribution for cometary nuclei. This year, that study was extended to determine the contribution of comets to the total cratering rate at the Earth. In addition, studies of the frequency and intensity of random cometary showers were incorporated into the study. It was found that LP comets contribute 16% of the observed cratering flux, while SP comets contribute 7%, and cometary showers (including both LP comets and SP comets derived from them) contribute 34% of the flux. Added to an expected contribution of 50% from Earth-crossing asteroids, yields a total cratering rate only 7% greater than what is observed. This result tends to rule out the possibility of additional cratering from alleged periodic cometary showers, which would result in about a 600% increase over the observed cratering rate.

#### Relevant Publications:

- Weissman, P. R., How pristine are cometary nuclei? In, The Comet Nucleus Sample Return Mission, ESA SP-249, pp. 15-25, 1986.
- Weissman, P. R., Post-perihelion brightening of Halley's comet: A case of nuclear summer. In, 20th ESLAB Symposium on the Exploration of Halley's Comet, ESA SP-250, 3, 517-522, 1986.
- Weissman, P. R., Post-perihelion brightening of Halley's comet: Spring time for Halley, Astronomy & Astrophysics, in press.
- Weissman, P. R., How typical is Halley's Comet? In, Proceedings of the ESA Symposium on the Similarity and Diversity of Comets, Brussels, in press.

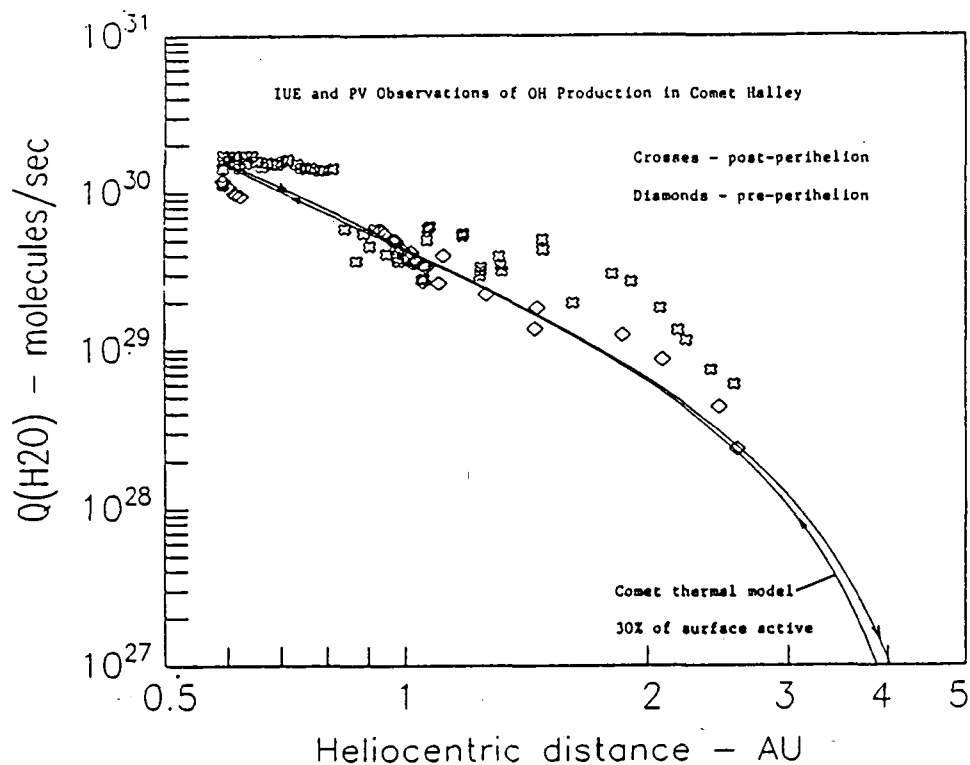


Figure 1. Observed and modeled water production rates for Comet Halley in 1985-86, showing higher production rates following perihelion.

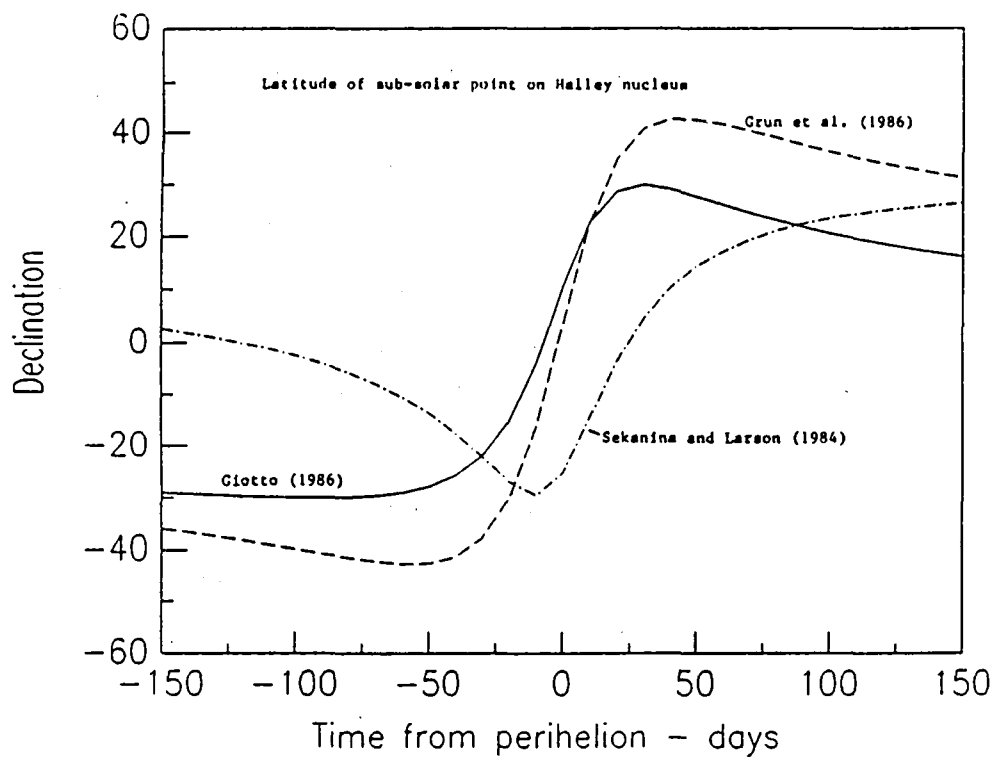


Figure 2. Latitude of the sub-solar point on the Halley nucleus for three different pole orientation solutions. The rapid motion of the sun northward as the comet rounded perihelion is readily seen.

## CLATHRATES AND POROSITY IN COMETARY NUCLEI

R. Smoluchowski and J. Green, University of Texas at Austin

### A. CLATHRATES

The idea that nuclei of new comets which are presumably condensed at very low temperatures contain, besides dust, H<sub>2</sub>O-ice in amorphous rather than crystalline form has been proposed some time ago (1). When upon approach to the Sun these nuclei heat up to nearly 150K, the ice becomes cubic in an exothermal surface reaction which accelerates the crystallization. The role of other gases has so far not been considered. Recent experimental results obtained by E. Mayer (2) indicates that a suitably slow initial condensation process of water vapor leads to the formation of ice with innumerable pores of various sizes on the surface and in the bulk. An ambient gas such as CO<sub>2</sub>, CH<sub>4</sub>, or CO will tend to be absorbed on such a surface, and, in particular, in micropores of molecular size, that is, not larger than 10-20Å. It follows that these deeply trapped impurities will become embedded in the bulk of the growing amorphous structure which can be described as amorphous non-stoichiometric clathrate. The thermal instability of such a structure has not been as yet investigated in detail, but one can surmise that upon heating, it too will gradually transform at a temperature near 150K into a crystalline, but highly imperfect form. Our calculations (3) of the energy associated with interstitial diffusion of CO<sub>2</sub> molecules in hexagonal ice suggest that, except near the melting point, only surface reactions are energetically possible. It follows that above 120K, when the CO<sub>2</sub> clathrate begins to be stable, it will be formed initially as an amorphous solid, and the evaporation of CO<sub>2</sub> with increasing temperature will be limited to surfaces of large open pores. The micropores, on the other hand, will retain the volatile impurities until higher temperatures at which H<sub>2</sub>O-ice itself begins to evaporate significantly. Besides having a major role in absorption and evaporation of volatile impurities as described above micropores have a profound influence on mechanical properties of cometary nuclei because they provide the starting points and the mechanism of cracking and of mechanical fracture. Apart from micropores produced during condensation of ice, there will be below 120K in CO<sub>2</sub> clathrates containing nuclei also microcracks resulting from differences in volume occupied by CO<sub>2</sub>-clathrate and volume occupied by the corresponding amount of H<sub>2</sub>O-ice and of solid CO<sub>2</sub>. If this CO<sub>2</sub> is not solid, but already in gaseous form, the micropores will be even larger and be more likely to start a crack in the presence of stresses.

### B. ROLE OF POROSITY

As part of on-going research into the structure and behavior of cometary nuclei, a study is being made of the influence of porosity on the heat flow, on development of stresses, and on fracture. Porosity affects material properties such as Young's modulus, Poisson's ratio, thermal conductivity, specific heat, and coefficient of expansion, which dictate how the material responds to a heat flux, the development of stress, and its subsequent fracture. The cometary nucleus is described from two conceptual points of view. The first view is microscopic in which the comet material is approximated as a loosely packed granular agglomerate held together by bonds along grain boundaries. The material is modeled analytically and effective material properties, as functions of porosity and temperature, are derived. The material properties are constrained by laboratory measurements on polycrystalline or amorphous water ice. The second point of view is macroscopic in which the entire cometary body is modeled numerically. The effective material properties are employed in the calculation of the thermal and stress gradients. The stress becomes the input for determining the fracture characteristics.



When irregular grains, such as the fractal grains suggested by B. Donn (4), form an icy matrix, irregular pore shapes and a wide distribution of pore sizes would be expected. However, it is not unreasonable to assume spheroidal pores because of sintering which will gradually fill in the crevices between the grains. Currently, the influence of the pore size distribution on the material properties is being investigated. The material properties of a porous matrix are derived using a three-phase model that had its origins in the work of inclusion physics and sintering. In this model it is assumed that: 1. Pores are distributed randomly. 2. The material is homogeneous and isotropic. 3. The total volume contains a large number of pores. A typical volume element of the solid contains a pore of radius,  $a$ ; this is surrounded by a shell of non-porous material out to a radius,  $r_0$ . This combination is then surrounded by a shell of equivalent porous homogeneous material out to a radius,  $R$ . The consistency relations are satisfied and equations for the effective material properties as functions of porosity and the non-porous material properties are derived. This result indicates that:

- a) The net thermal conductivity, even including radiation across pores, decreases as the porosity is increased.
- b) The specific heat decreases linearly with increasing porosity.
- c) The coefficient of expansion is essentially unaffected by porosity.
- d) Young's modulus and Poisson's ratio decrease with increasing porosity. Overall, the material becomes weaker and more compressible.

These effective material properties are used in a two-dimensional axi-symmetric finite element structural model to calculate the heat conduction and thermal stress field. A surface flux simulating the insolation of the cometary nucleus is employed, and a black-body radiation boundary condition is applied. Other conditions, including sublimation, will be included in the next generations of the model. Since we are interested in the effects of the porosity on the temperature and stress gradients, the simple boundary conditions are reasonable.

- (1) R. Smoluchowski, in *Asteroids, Comets, and Meteors*, Uppsala, p. 305, 1986.
- (2) E. Mayer, *Nature* **319**, 298, 1986.
- (3) R. Smoluchowski, *BAAS* **18**, 813, 1986.
- (4) B. Donn, *BAAS* **17**, 689, 1985

THE PALOMAR ASTEROID AND COMET SURVEY (PACS), 1982-1987; Carolyn S. Shoemaker and Eugene M. Shoemaker, U.S. Geological Survey, Flagstaff, Arizona 86001

In 1982, we began a new survey of special classes of asteroids and comets using the 46-cm Schmidt telescope at Palomar Observatory. This survey utilizes a stereoscopic technique that we developed to search large areas of the sky for moving objects. The immediate goal of the survey is to calculate accurately the population or flux of various classes of asteroids and comets by discovering, under well-defined conditions, a sufficient number of Earth-approaching and other planet-crossing asteroids, various classes of high-inclination asteroids, Trojan asteroids, and distant comets. The long-range purpose of this work is to understand the history of planet-crossing bodies and their interaction with planets and satellites. Our focus has been both on bodies that are presently on planet-crossing orbits and on asteroids that are thought to have been captured from swarms of planet-crossing bodies in the past.

The stereoscopic technique has allowed us to make major gains in the use of the 46-cm Schmidt telescope. Objects of interest are detected on pairs of films, each usually exposed for 4 or 6 minutes. The exposures of a given pair generally are separated by about 40 minutes. In a typical observing run, about 100 partly overlapping fields are photographed. Each field covers about 60 square degrees and, in the course of 8 observing runs a year, we have covered up to 40,000 square degrees of sky. Early in the survey we used Kodak 11a-D film; in the past year we switched to the newly available Kodak 4415 film. When hypersensitized, the 4415 film enables us to reach a threshold of 8 magnitude 18.5. The combination of much greater sky coverage and improvement in the threshold of detection, both of which are achieved with the use of short exposures and stereoscopy, has led to an order of magnitude increase in the discovery rate of asteroids and comets with the 46-cm Schmidt.

From the inception of PACS, we have obtained observations that permitted calculation of satisfactory preliminary orbits for more than 140 new asteroids, of which 20 are now numbered. Although we usually detect several hundred unnumbered asteroids on each observing run, limitations of manpower have precluded our measuring and reporting most of them. We have discovered 14 Earth-approaching asteroids (Table 1) and about 60 high-inclination asteroids, which include 31 asteroids in the Phocaea region of orbital element phase space, 13 in the Hungaria region, high-inclination Trojans, and 14 other asteroids that are either close to or have inclinations above the  $\nu_6$  secular resonance. Of the high inclination asteroids, 17 are Mars crossers; most of the others can approach Mars and probably have been derived from former Mars-crossing bodies. We interpret a few high-inclination asteroids to be extinct comets (Uranus-Neptune planetesimals) captured in stable orbits in the main asteroid belt.

In the fall of 1985, we searched the core of the L4 libration region to determine if we could discriminate Trojan asteroids with the stereoscopic technique. We discovered four new L4 Trojans, 3709 (1985 TL3), 1985 TE3, 1985 TF3, and 1985 TG3 (Table 1), and we obtained observations leading to the numbering of three previously discovered Trojans. On the basis of this test, we are planning a search with 4415 film that will cover the entire L4 and L5 libration regions. Our search, which will require several years, will utilize the standard fields of the PACS survey and should yield observations adequate for numbering about 100 new Trojans and a significant batch of new Hildas. We find it plausible that most Trojans and perhaps most Hildas may be derived from captured Jupiter-crossing, Uranus-Neptune planetesimals. We plan to test this hypothesis by examining in detail the dynamical structure and other properties of the Trojan swarms.

Comet discovery is another major objective of PACS; 11 new comets have been found to date (Table 2). In contrast to most comets discovered in the past, the majority of comets discovered in PACS have fairly large perihelion distances; two are beyond the orbit of Jupiter. The goals of our comet search are to determine the perihelion distribution of long period comets to about 5 AU, to refine the population estimate of the Oort cloud, to determine the flux of both periodic and long period comets in the neighborhood of Jupiter, and to test whether capture of Oort cloud comets to short period can fully account for the Jupiter-family.

Table 1. Asteroids of special interest discovered in the Palomar Asteroid and Comet Survey

	H	Diam. km	Epoch	M	Peri.	Node	i	e	a	Arc days	Obs.	Orbit
<u>Atens</u>												
3554 Amun	16.2	2.0	870724	316.22403	359.30903	358.04473	23.36000	0.2803628	0.9736503	---	--	MPC11618
<u>Apollos</u>												
3671 Dionysius	16.5	~2	870724	337.04433	203.60137	81.82150	13.61060	0.5404753	2.1976590	---	--	MPC12138
1984 KB	16.4	1.4	841027	61.62574	334.87816	170.56242	4.63662	0.7622750	2.2210346	37	12	MPC 9030
1986 JK	19.0	~0.5	860619	357.29785	232.40866	62.23835	2.13951	0.6797186	2.8017387	103	43	MPC11147
1987 KF	16.0	~2	870529	29.54461	15.48073	107.56433	11.87129	0.0678835	1.8375868	26	16	MPC11998
1987 SY	17.5	~1	870922	46.01117	291.15157	311.72270	5.50806	0.5851108	1.4392358	20	10	MPC12440
1959 LM =1987 MB*	14.5	~3	870724	51.87088	235.14152	295.26840	6.76649	0.6373704	1.9802024	28 yr	19	MPC12139
*rediscovery												
<u>Amors</u>												
3199 Nefertiti	15.03	3	851201	194.85382	53.24906	339.45577	32.97512	0.2837208	1.5746595	---	--	MPC 9427
3553 Mera	16.8	~2	870724	53.88744	288.87369	231.97692	36.76271	0.3206869	1.6445847	---	--	MPC11617
1983 RB	16.0	~3	841027	141.71192	114.80819	168.88445	19.42719	0.5070001	2.2233403	55	18	MPC 8394
1985 TB	15.5	~3	860619	40.03800	66.96791	23.39052	26.81942	0.5674674	2.5751109	141	23	MPC10531
1985 WA	19.0	~0.5	860619	47.23757	350.87990	43.17465	9.74509	0.6016134	2.8456763	64	31	MPC10767
1987 SF3	19.0	~0.5	870922	10.13469	133.65604	187.12220	3.31417	0.5340295	2.2484648	25	5	MPC12440
1987 UA	17.5	~1	870922	353.39147	173.61357	197.59106	16.40445	0.2967418	1.7303153	27	6	MPC12440
<u>Hildas</u>												
3694 (1984 SH5)	10.4	~60	870724	121.39364	82.43510	311.18859	4.94870	0.1975307	3.9515148	---	--	MPC12312
<u>Trojans</u>												
3317 Paris	8.35	127	851201	348.27609	147.42493	135.32679	27.89639	0.1259800	5.1924388	---	--	MPC10036
3709 (1985 TL3)	9.5	~90	880827	38.21363	246.96651	186.48226	19.60912	0.0635566	5.2647810	---	--	MPC12438
1985 TE3	9.5	~90	851002	275.13	272.02	199.75	21.60	0.0905	5.1332	52	6	MPC11417
1985 TF3	10.0	~70	870724	60.95329	34.00108	342.60943	6.06954	0.1453284	5.1863506	36 yr	8	MPC11435
1985 TG3	10.0	~70	850912	358.02	64.49	307.72	11.68	0.0622	5.3024	29	8	MPC11417

Table 2. Orbits of comets discovered in the Palomar Asteroid and Comet Survey

Comet		T	q	e	P	Perl.	Node	Incl.	Epoch	Obs.	Arc	Ref.
1983 XV	(3p)	83 Nov. 23.8034	3.344848	1.000038	----	176.0391	163.9842	137.6036	83 Dec. 12	76	83 Sept. 7 - 84 June 26	Catalogue
1984 XV	(4r)	84 Sept. 3.56034	5.4891387	0.9951794	----	183.25435	238.02591	179.21532	84 Sept. 17	44	84 Oct. 23 - 86 Oct. 30	MPC 12307
1984 XVI	(4q)	84 Sept. 16.64489	1.9768690	0.4714748	7.23	18.68402	339.31037	26.27125	84 Sept. 17	66	84 Sept. 22 - 85 Feb. 19	MPC 11623
1984 XVIII	(4u)	84 Sept. 26.69042	1.3196982	0.6656674	7.84	317.56923	54.81887	21.56444	84 Sept. 17	8	84 Nov. 18 - 84 Dec. 20	MPC 11623
1985 II	(4s)	85 Jan. 3.88788	1.2145104	0.9709050	----	229.23401	222.75689	13.88557	85 Jan. 15	65	84 Oct. 25 - 85 Apr. 11	MPC 11624
1985 XII	(4f)	85 Sept. 4.59240	2.6965104	1.0007157	----	235.46184	48.98515	116.66115	85 Sept. 12	95	84 May 27 - 87 Feb. 28	MPC 12124
1986a	(6a)	85 Dec. 18.57752	1.7940224	0.7277002	16.91	14.82070	96.63426	6.40830	85 Dec. 1	61	86 Jan. 10 - 86 May 14	MPC 10817
1986b	(6b)	86 Mar. 11.29390	3.5938642	0.9467797	----	123.58702	294.15920	159.80585	86 Mar. 31	30	86 Mar. 4 - 86 Dec. 27	MPC 12307
1987o	(7o)	86 Nov. 17.15711	5.4568461	1.0	----	17.01285	267.62412	132.46836	-----	36	87 Apr. 25 - 87 June 26	MPC 12008
1987z	(7z)	88 May 12.98244	3.0402581	0.3256751	9.57	208.95588	214.02384	4.28949	-----	15	87 Sept. 24 - 87 Oct. 26	MPC 12446
1987g1	(7g1)	88 Jan. 17.512	3.33416	1.0	----	194.427	197.650	76.731	-----	4	87 Oct. 25 - 87 Nov. 27	IAUC 4505

## Meteoroid Environment Near the Earth-Moon System

Yosio Nakamura and Jürgen Oberst, Institute for Geophysics, The University of Texas at Austin

We are conducting an in-depth analysis and interpretation of a rather unusual and unique data set to study the meteoroid environment near the earth-moon system, namely the impact data as detected by the Apollo lunar seismic network, which was in operation from 1969 through 1977. Major findings to date, which will be expanded further below, include (1) contrary to previous presumptions, those impacts detected by the lunar seismic network consist of not one but several distinct families, each with different properties and quite possibly of different origin; (2) in addition to sporadic impacts, there are several identifiable clusters of impacts, indicating existence of relatively young, coherent groups of meteoroids of common origin; (3) in contrast to previous attempts to estimate the meteoroid flux assuming that all meteoroids are of one class, we are now able to make estimates of meteoroid flux approaching from different directions separately, and this approach appears to reconcile the previously reported difference between the flux as estimated from the lunar impact data and that estimated from terrestrial observations.

Of more than 12,500 seismic events recorded on the long-period seismograms of the four-station Apollo seismic network during its operation, nearly 2000 events were identified as originating from impacts of meteoroids on the lunar surface [Nakamura *et al.*, 1982]. When we examined the temporal distribution of these impacts during each lunar day, a clear difference emerged between the distribution of low-energy impacts (those detected at only one station), and that of high-energy impacts (those detected at all stations of the network). A comparison of these results with the expected detection frequency of various classes of meteoroids known from earth-based observations allowed us to differentiate various families of impacts detected by the lunar network [Oberst and Nakamura, 1987a]. Two major families of impacts thus identified are those believed to be of cometary origin, which show a concentration of low-energy impacts in the lunar morning hours, and those which are relatively massive, possibly of high density (stony meteoroids?), which are mostly in prograde orbits.

Further distinction among various types of impacting meteoroids can be made when we plot the times of their impacts in a two-dimensional space of the time of the year, representing the location where each impacting object crosses the earth-moon orbit, and the time of the month (lunar day), representing its pre-impact direction of approach (e.g., Fig. 2 of Oberst and Nakamura, 1987a). On such plots, many impacts are seen to be clustered around common centers standing out from the background of sporadic impacts (Fig. 1). This suggests that a sizable percentage (estimated to be about 20% [Nakamura *et al.*, 1982]) of the observed objects had been travelling as coherent streams of meteoroids before impacts. Using statistical tests, we identified several clusters [Oberst and Nakamura, 1987b]. Many of the detected clusters of small impacts are found to be correlated with the fall times and radiants of meteor showers known from terrestrial observations. In addition, a few clusters of large impacts are also identified, notably in June 1975 and in January 1977. Their estimated pre-impact orbits and the observed signal strength suggest that these are from non-cometary streams of relatively massive and/or possibly dense objects. We speculate that some members of these streams may survive the terrestrial atmospheric entry and thus may be found as meteorites.

In order to estimate the overall flux of meteoroids near the earth-moon system from the impact seismic data, we need to know how the mass, velocity, density and possibly the shape of the impacting objects affect the seismic response. Once these effects are determined, then we can use the observed responses of the artificial impacts as calibrations to estimate the mass flux of meteoroids provided we have some way of estimating or assigning the expected

encounter velocities for groups of meteoroids. Based on our finding above that many of the terrestrially known objects can also be identified in the lunar impact data, we approached this problem by statistically comparing the theoretical diurnal variation of detection frequency of various classes of meteoroids with the observed distributions. Since the theoretical distributions are strongly dependent upon the assumed mass and velocity scaling (effect of mass and velocity on seismic efficiency), such comparisons can lead to acceptable scaling laws. A preliminary result indicates that the seismic efficiency (the ratio of the seismic energy to the pre-impact kinetic energy of the object) may be dependent upon the impact velocity. The density of the impacting objects appears to have little effect on the efficiency. These findings are being used to refine the flux estimates for various classes of meteoroids [Oberst and Nakamura, 1987c].

*References:* Nakamura Y., G. V. Latham and H. J. Dorman, Apollo lunar seismic experiment—Final summary, *Proc. Lunar Planet. Sci. Conf., 13th, Pt. 1, J. Geophys. Res. 87 Suppl.*, A117-A123, 1982. Oberst, J. and Y. Nakamura, Distinct meteoroid families identified on the lunar seismograms, *Proc. Lunar Planet. Sci., Conf., 17th, Pt. 1, J. Geophys. Res. 92*, E769-E773, 1987a. Oberst J. and Y. Nakamura, Lunar seismic impact clusters - Evidence for the presence of "meteorite streams," *Lunar Planet. Sci.*, 18, 736-737, 1987b. Oberst, J. and Y. Nakamura, Updated lunar seismic meteoroid flux, *EOS Trans. Am. Geophys. Union*, 68, 344, 1987c.

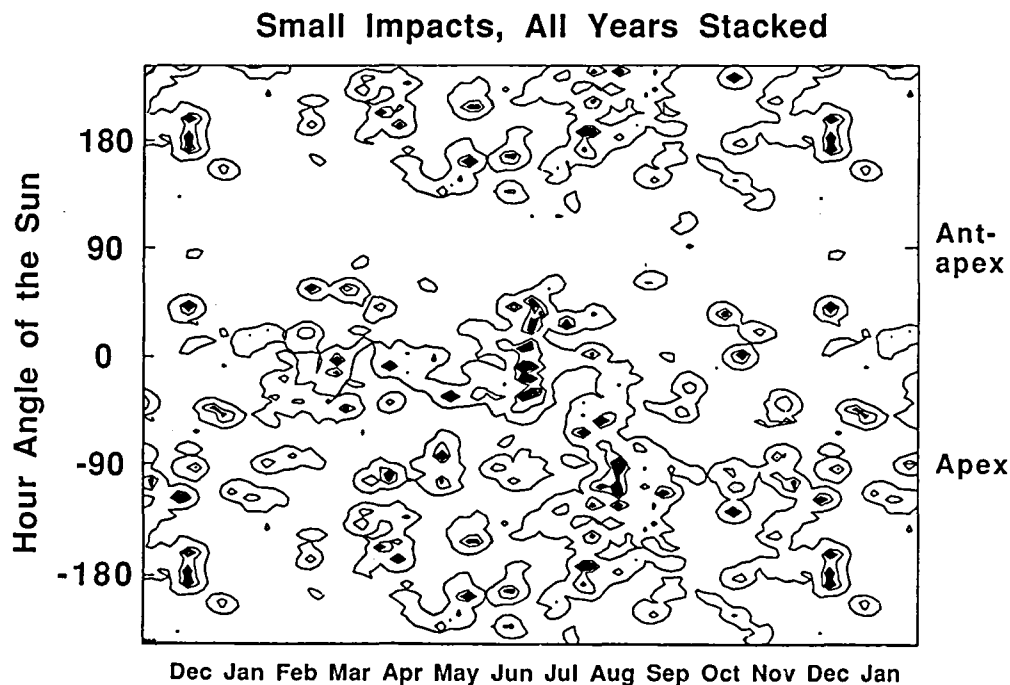


Fig. 1. Frequency of observed impacts on the lunar surface in the two-dimensional space of time-of-the-year and time-of-the-month (lunar day). The contours indicate the closeness of each impact to its nearest neighbor. The contour intervals are arbitrary.

## The Size Distribution of Asteroids from IRAS and the Martian Cratering Record

R.G. Strom, Department of Planetary Sciences, University of Arizona, Tucson, Arizona 85721

The size/frequency distribution of asteroids can be determined from IRAS observations down to a diameter of about 30 km with a fair degree of confidence. Below that diameter the size distribution is considerably more uncertain. However, the younger post-plains martian crater population can be used to derive the asteroid size/frequency distribution from about 15 km down to about 1.5 km diameter.

The younger martian plains have a crater size/frequency distribution that is characterized by a single-slope differential population index of about -3 over the diameter range of about 8 to 100 km. This crater population differs significantly from that in the heavily cratered highlands of the terrestrial planets which resulted from the period of late heavy bombardment. The younger martian crater population must represent the accumulation of asteroid and comet impacts over about the past 2 or 3 billion years. Presently, the impact rate of asteroids at Mars is at least 8 times greater than that of comets (Basaltic Volcanism Study Project, 1981) and, therefore, the young crater population should be primarily the result of asteroid impacts. A Monte Carlo computer simulation using a modified Holsapple-Schmidt crater scaling law and martian impact velocities derived from the orbital elements of present-day Mars-crossing asteroids has been used to derive the size distribution of asteroids from about 1.5 to 20 km diameters (Fig. 1). This asteroid size distribution is similar to the crater size distribution with a slope index of about -3.

The size distribution of asteroids from IRAS observations was compiled at .25 AU intervals from 1.5 AU to 3.5 AU. At diameters larger than about 40 km the curve is bell-shaped on the R plot with slope indices varying from about -2 to -4 (Fig. 2). At diameters from about 10 to 30 km the sizes were derived from both IRAS and Earth-based observations in the distance interval of 1.5 to 2.5 AU. The curve from about 10 to 30 km is very uncertain but the data suggest that the size distribution flattens out on an R plot to about a -3 slope index (Fig. 2) which is similar to that derived from the martian cratering record. The combined data (IRAS and derived from the martian cratering record) show a slope index of about -3 from 1.5 to about 40 km diameter, a slope index of about -2 from 40 to about 150 km diameter, and about a -4 from 150 to 600 km diameter (Fig. 3). This size distribution is almost identical to that derived from an asteroid collisional evolution model by Davis, *et al.* (1985) and shown in Fig. 3. The close correspondence between the "observed" asteroid distribution and the Davis model strongly suggests that the model is correct and can be applied to other aspects of a collisionally evolving planetesimal population.

The crater size/frequency distribution in the heavily cratered terrains of terrestrial planets closely mimics that of the asteroids at diameters greater than about 40 km. A Monte Carlo computer simulation similar to that employed for the martian craters was used to recover the projectile size distribution for the cratering record representing the period

of late heavy bombardment on the Moon. The shape of this projectile size distribution is similar to the asteroids but displaced to smaller diameters by over one order of magnitude (Fig. 4). This projectile size distribution may represent a collisionally evolved planetesimal population with very different collisional properties, e.g. collision velocities or planetesimal strengths, or it may represent close to the original size distribution of the planetesimals. Collisional evolution models are currently being tested based on the Davis model in order to decide between the two alternatives and to derive the original size distribution of the objects responsible for the period of late heavy bombardment in the inner Solar System.

Basaltic Volcanism Study Project, 1981. Basaltic Volcanism on the Terrestrial Planets, pp. 1049—1127. Pergamon, New York.

Davis, D.R., *et al.*, 1985. Collisional history of asteroids: evidence from Vesta and the Hirayama families. *Icarus* 62, 30—53.

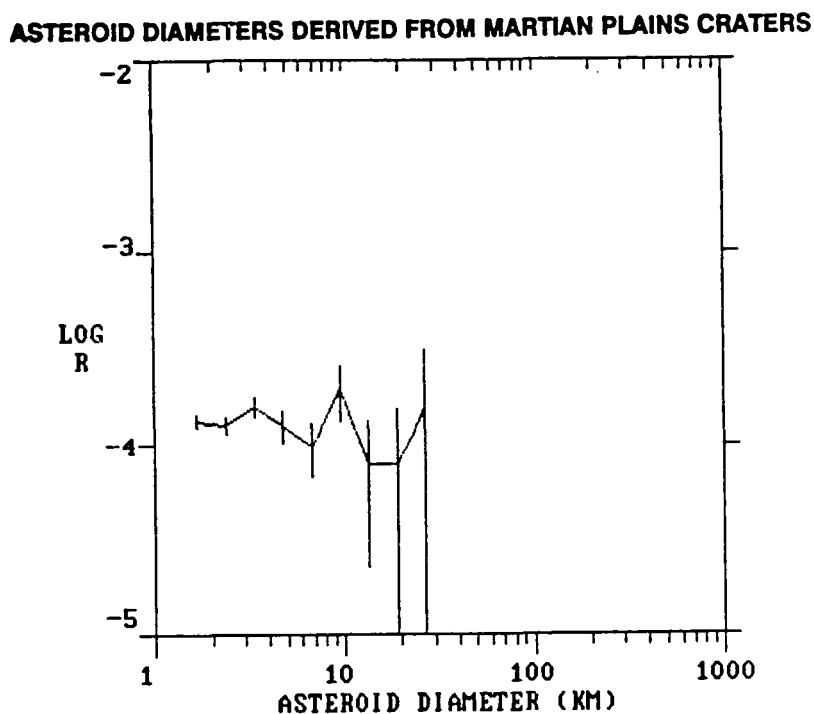


Figure 1. Asteroid size/frequency distribution derived from the young martian post-plains crater population.



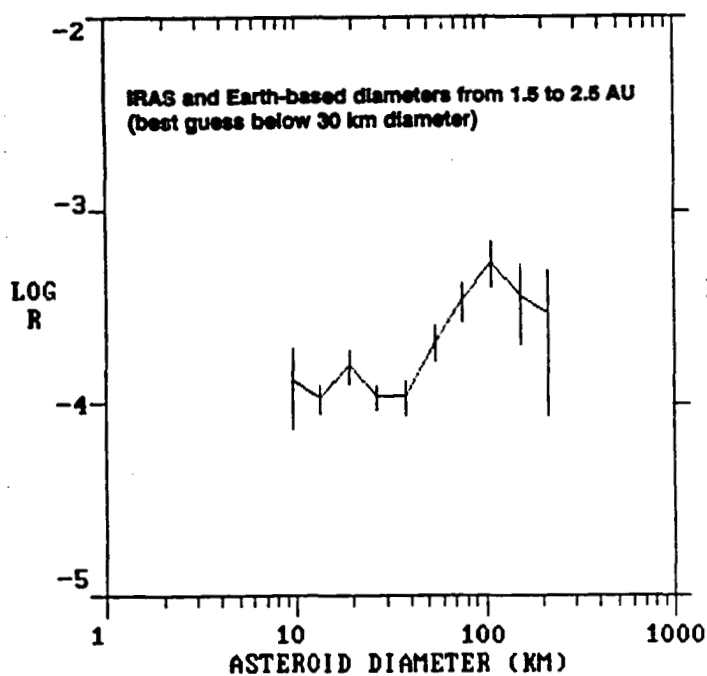


Figure 2. Asteroid size/frequency distribution from IRAS data.

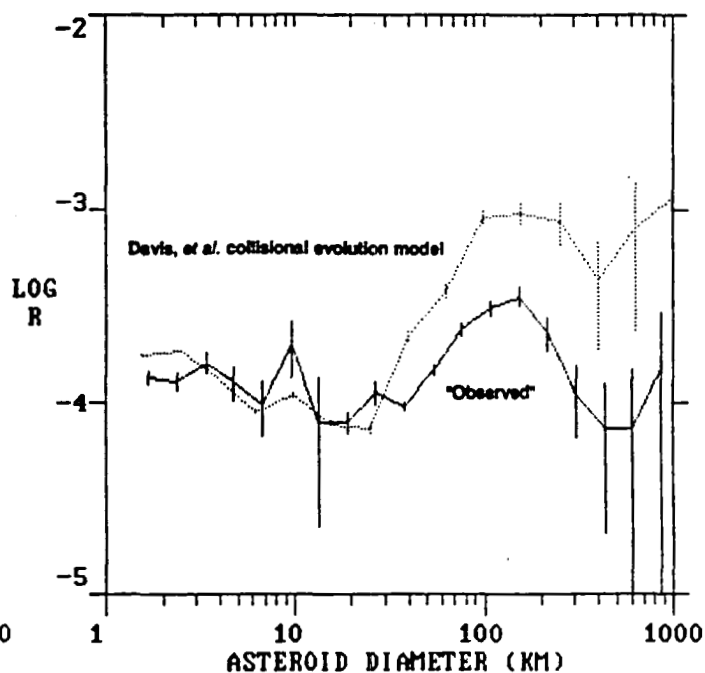


Figure 3. Combined IRAS and martian-derived asteroid size/frequency distribution ("observed") compared to that of the asteroid collisional evolution model of Davis, et al.

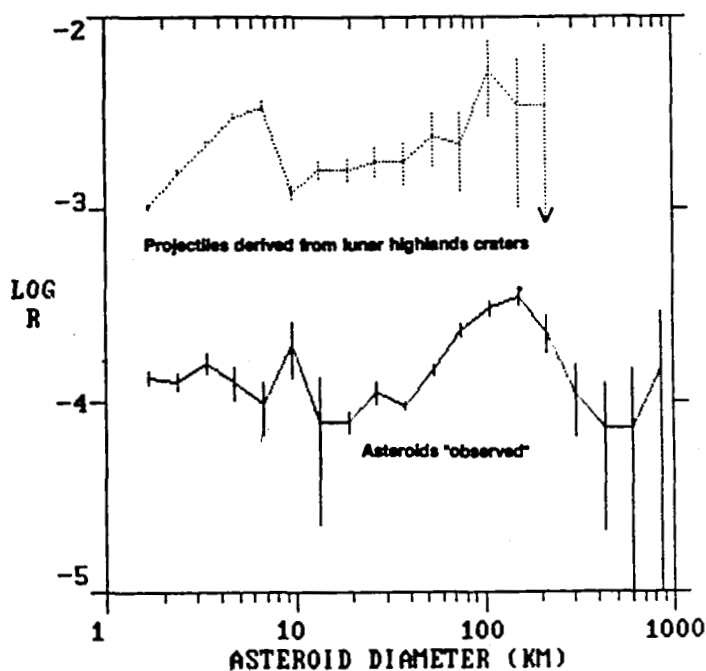


Figure 4. Asteroid size/frequency distribution compared to the projectile size/frequency distribution derived from the lunar highlands cratering record.

## CONVEX-PROFILE INVERSION OF ASTEROID LIGHTCURVES

Steven J. Ostro, Jet Propulsion Laboratory  
California Institute of Technology, Pasadena, CA 91109

This research focuses on a new approach, called "convex-profile inversion," to the interpretation of asteroid lightcurves. Originally developed by Ostro and Connelly (1984, *Icarus* 57, 443-463), this approach constitutes a promising solution to problems, first posed by Russell (1906, *Astroph. J.* 24, 1-18), encountered in extracting information about an asteroid's shape from its optical lightcurve. This endeavor is important because (i) shape is a fundamental attribute of any planetary object, (ii) asteroid shapes, which range from nearly spherical to grossly irregular, can be diagnostic of the object's history of exogenic and endogenic modification; and (iii) except for the relative handful of objects observable with radar or during stellar occultations, lightcurves provide the only clues to an asteroid's shape. Unfortunately, the form of a lightcurve is determined by the viewing/illumination geometry and by the surface's light-scattering properties as well as by body shape. Even if we had lightcurves for an asteroid for all possible Sun-Earth-asteroid configurations, it would still be impossible to determine the three-dimensional shape from those disk-integrated measurements. The best we can hope to do is to obtain useful constraints on shape that exploit all the available information.

Ostro and Connelly (1984) showed that any lightcurve can be inverted to yield a convex profile, and that under certain ideal conditions that profile represents an average of the asteroid's shape. The ideal conditions, which include equatorial viewing/illumination geometry and geometric scattering, rarely are satisfied for actual lightcurves, so the derived averages generally contain systematic error. Hence, one goal of this research during the past two years has been to calibrate the sensitivity of CPI to departures from ideal conditions; another has been to apply the inversion technique to real asteroid lightcurves. It has become increasingly clear that the power of CPI lies not just in the calculation of profiles from lightcurves, but also in the precise definition of what shape information is extractable from a lightcurve and of the circumstances that let us access that information in an optimal manner. Shape constraints derived from a lightcurve are intrinsically less informative than, say, a stellar-occultation profile, which is a two-dimensional projection of the three-dimensional shape. Given a lightcurve, the best constraint we can obtain is a two-dimensional average of the three-dimensional shape. That average is called the mean cross section,  $\bar{C}$ , and is defined as the convex set equal to the average of the convex envelopes on all surface contours parallel to the asteroid's equatorial plane. A convex profile can be represented by a radius-of-curvature function or by that function's Fourier series. Deletion of a profile's odd harmonics "symmetrizes" the profile. For example, an asteroid's symmetrized mean cross section  $\bar{C}_s$  has the same even harmonics as  $\bar{C}$  but no odd harmonics.

The following ideal conditions pertain to estimation of  $\bar{C}$  from a lightcurve:

Condition GEO: The scattering is uniform and geometric.

Condition EVIG: The viewing/illumination geometry is equatorial, i.e., the Sun and the Earth are in the asteroid's equatorial plane.

Condition CONVEX: All surface contours parallel to the equatorial plane are convex.

Condition PHASE: The solar phase angle  $\phi$  is known and does not equal  $0^\circ$  or  $180^\circ$ .

We cannot estimate  $\mathcal{Q}$ 's odd harmonics from an opposition lightcurve, but we can estimate its even harmonics and hence its symmetrization,  $\mathcal{Q}_s$ . Estimation of  $\mathcal{Q}_s$  from an opposition lightcurve is less "burdened" by ideal conditions than is estimation of  $\mathcal{Q}$  from a non-opposition lightcurve, for many reasons. For example, Condition CONVEX is irrelevant at opposition.

Much effort has been devoted to calibrating the distortion in an estimate of  $\mathcal{Q}$  caused by violation of Condition GEO. The basic strategy has been to (i) assume that the other ideal conditions are satisfied, (ii) generate lightcurves for an asteroid with a known shape and a realistic scattering law, (iii) use convex-profile inversion to obtain an estimate,  $\hat{\mathcal{Q}}$ , of the asteroid's mean cross section  $\mathcal{Q}$ , and (iv) compare  $\hat{\mathcal{Q}}$  to  $\mathcal{Q}$ . For example, suppose that the asteroid is a convex cylinder, all of whose constant-latitude contours are congruent. Also suppose that the surface's light-scattering properties are adequately described by the equations formulated by Hapke (1986, *Icarus* 67, 264-280; 1984, *Icarus* 59, 41-59; and 1981, *J. Geophys. Res.* 86, 3039-3054), with the free parameters assigned values estimated for average lunar terrain by Helfenstein and Veverka (1987, *Lunar Planet. Sci. Conf. Abstracts* 18, 415-416). Then Fig. 1 compares the asteroid's actual  $\mathcal{Q}$  and  $\mathcal{Q}_s$  to the estimates one would obtain from lightcurves at various solar phase angles  $\phi$ .

In describing or comparing profiles such as those in Fig. 1, it is useful to define a measure of the distance between any two profiles  $P_1$  and  $P_2$  as

$$\Omega = 10 \min_{\theta} | \mathbf{d}_1/d_{10} - \Theta \mathbf{d}_2/d_{20} |$$

where  $\mathbf{d}_j$  is the vector of complex Fourier coefficients in the expansion of  $P_j$ 's radius-of-curvature function;  $d_{j0}$  is the constant, or zero-harmonic term, in that expansion; and the diagonal matrix  $\Theta$  rotates  $\mathbf{d}_{2n}$  by  $e^{in\theta}$ . This distance measure is rotation-invariant and scale-invariant. We also define a profile's noncircularity  $\Omega_c$  as its distance from a circle, and a profile's breadth ratio  $\beta^*$  as the ratio of the profile's extreme breadths.

In Fig. 1,  $\Omega_E$  is the distance of  $\hat{\mathcal{Q}}$  from  $\mathcal{Q}$  (or, at  $\phi = 0^\circ$ , of  $\hat{\mathcal{Q}}_s$  from  $\mathcal{Q}_s$ ). This figure shows that the distortion in a cross section estimate depends on  $\phi$ . At opposition, the scattering is sufficiently close to geometric that  $\mathcal{Q}$  is tiny and  $\mathcal{Q}_s$  is very accurately determined. However, for estimation of  $\mathcal{Q}$ ,  $\Omega_E$  drops from more than 6 at a few degrees to 4 or less at a few tens of degrees. Our simulations have shown that whereas violation of Condition GEO does introduce systematic distortion in the estimated mean cross section, it is not necessarily severe. A particularly

significant result is that the salient characteristics of  $\hat{\mathcal{C}}$  (i.e.,  $\Omega_{\mathcal{C}}$  and  $\beta^*$ ) generally resemble those of  $\mathcal{C}$  rather closely for  $\phi$  between  $10^\circ$  and  $20^\circ$ .

Figure 2 illustrates some of the capabilities of convex-profile inversion when applied to two lightcurves obtained for asteroid 19 Fortuna. The two independent estimates of Fortuna's mean cross section have been combined in a weighted average; the weighting, which was based on goodness-of-fit statistics for the individual inversions, is reflected in the fact that the weighted average profile is not exactly midway between the parent profiles. Note that the values of  $\Omega_{\mathcal{C}}$  and  $\beta^*$  estimated for Fortuna's  $\mathcal{C}$  are comparable to those for the model in the Fig. 1 simulation.

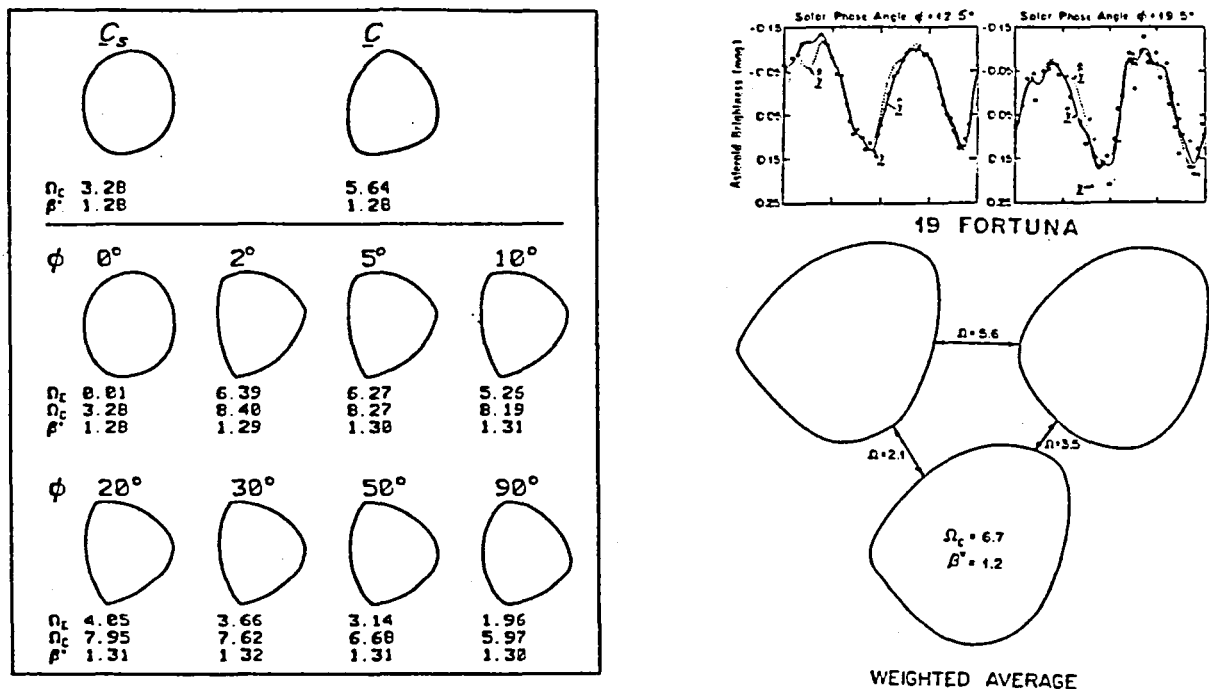


**Figure 1 (left):** Effects of non-geometric scattering on estimation of  $\mathcal{C}$  and  $\mathcal{C}_s$  for a particular model "asteroid." The model's mean cross section and symmetrized mean cross section are shown above the horizontal bar. Below the bar are estimates of those quantities from inversion of lightcurves generated at various solar phase angles  $\phi$  and employing the Hapke photometric function. ( $\hat{\mathcal{C}}_s$  is estimated at opposition and  $\hat{\mathcal{C}}$  is estimated at the seven nonzero values of  $\phi$ .) Each profile's noncircularity  $\Omega_{\mathcal{C}}$  and breadth ratio  $\beta^*$  are given.  $\Omega_{\mathcal{C}}$  is the distance between  $\hat{\mathcal{C}}$  and  $\mathcal{C}$ , or between  $\hat{\mathcal{C}}_s$  and  $\mathcal{C}_s$ . **Figure 2 (right):** Weighted average of two estimates of Fortuna's mean cross section calculated from two lightcurves measured by Weidenschilling et al. (1987, *Icarus* 70, 191).

# METEORITE SPECTROSCOPY AND CHARACTERIZATION OF ASTEROID SURFACE MATERIALS

Michael J. Gaffey, Geology Department, Rensselaer Polytechnic Institute,  
Troy, New York 12181

The asteroids are the surviving primordial remnants for the inner solar system, samples of the population of objects which accreted to form the terrestrial planets. These bodies preserve a record of the earliest conditions and processes present in the inner solar system and in the transition region between the inner and outer solar system. The asteroids and their natural samples, the meteorites, represent our sole source of physical data on the accretionary epoch of the terrestrial planets. It is unlikely that any significant fraction of the diverse asteroidal population will be visited by spacecraft missions within the professional lifetimes of most current investigators. Therefore, earth-based telescopic studies will remain the our only source of information on most of these minor planets for at least the next few decades.

The history of a rock unit is written in its mineralogy and petrology. Asteroid surface material characterizations thus provide the data base for defining the nature and evolutionary history of individual objects. Data on individual members of the population provides insight into the broader inter-relations between the asteroids and the meteorites and between different asteroid groups. The goals of the present research program are: 1) to define the nature and evolutionary history of the minor planets, 2) to elucidate their relationships to the meteorites and to establish or constrain a spatial context for the meteorite data, and 3) to constrain nebular compositional gradients, to define the pattern of post-accretionary thermal events, and to better understand early inner solar system history.

Sophisticated asteroid surface material characterizations are derived by applying advanced interpretive calibrations to high precision visible and near infrared (VNIR) reflectance spectra of selected asteroids. The quality of solar system models developed from this data base is directly related to the appropriateness of the surface material characterizations. VNIR reflectance spectroscopy is potentially an extremely powerful tool for probing the nature and history of the asteroids. But like any tool, it only performs up to its potential when properly employed. The central thrust of this research effort is to push the level of attainable interpretive sophistication to the limits of the technique, while simultaneously extending the capability of the technique.

This work involves four elements including: 1) development of improved spectral interpretive calibrations for meteorite-type assemblages, 2) analysis of high photometric precision VNIR spectra of selected asteroids to derive a detailed characterization of their surface assemblage, and to identify the type and scale of lithologic units across the surface of the body, 3) definition of the implications of these asteroid compositions for the history of each asteroid, for the asteroid population and for their possible meteoritic affinities, and 4) utilization of these results to refine theoretical models (nebular processes, collisional evolution, post-accretionary heating mechanisms) and to evaluate the completeness and bias in the meteorite flux in order to better understand the early inner solar system and the processes which produced the terrestrial planets and planetesimals. Among the ongoing work, the results of two recent asteroid spectral analyses and one meteorite spectral calibration study are outlined below. For additional recent results, see: Cloutis *et al.* (1986), Gaffey (1986a), and Holden and Gaffey (1987). Rotational Spectral Variations of (8) Flora and (15) Eunomia - It has been generally concluded that most of the asteroid types found exclusively or primarily in the inner belt (e.g. types E, A, M, R, V) result from melting and magmatic differentiation in their parent bodies. The S-type asteroids,

which dominate the inner belt, are the critical exception and considerable controversy has surrounded their interpretation. On one hand they have been interpreted as undifferentiated assemblages analogous to the ordinary chondrites, and on the other as differentiated assemblages analogous to stony-iron meteorites. The proportion of the S-type asteroids which are differentiated [none, some, many, or all] has profound significance for the source of the most common meteorite type (ordinary chondrites), for planetary models based upon data derived from these meteorites, for the thermal processes in the early planetesimal population, and for the thermal state of the bodies accreting to form the terrestrial planets.

The purpose of this detailed investigation of selected S-type asteroids is: (a) to test the interpretation - based on the available spectral survey data - that most of the large S-type asteroids underwent strong early heating, melting, and magmatic differentiation, (b) to constrain the nature of the heating events and magmatic processes, and (c) to detect or to place an upper limit on the abundance of chondritic or undifferentiated members within the S-group. The first two objects to be studied in this effort have been asteroids (8) Flora [Gaffey, 1984] and (15) Eunomia [Gaffey and Ostro, 1987]. Previous workers had suggested that Flora is among the most ordinary chondrite-like of the S-type asteroids. Eunomia is the largest member of the S-class of asteroids. It exhibits a large amplitude lightcurve suggesting that it may be an irregular fragment of a larger parent body.

For both Flora and Eunomia, the rotational variations in relative mineral composition and phase abundance between olivine and pyroxene indicate a differentiated surface assemblage. The 2 $\mu$ m (Band II) positions [a function of the iron content of the pyroxene] relative to the Band I/Band II area ratio [a function of phase abundance] at different rotational aspects for Eunomia (fig. 1) and for Flora (Gaffey, 1984) do not fall within - or even parallel - the trend for chondritic assemblages (stippled band) and, in both cases, and the slope of the observed variation has the wrong sign to be chondritic. The Band I positions [a function of the phase abundance and the calcium content of the pyroxene] versus band area ratio for Flora (Gaffey, 1984) falls outside but parallel to the chondritic trend. The Eunomia Band I positions versus band area ratio (fig. 2) intersects the chondritic trend but exhibits a different slope.

These patterns suggest that the silicate assemblage present on the surface of Flora was derived from a region in the parent planetesimal which underwent moderate partial melting and extraction of a basaltic liquid with addition of a metallic melt. The Eunomia silicates appear to sample a larger radius interval (near surface to the core mantle boundary) within a parent body which underwent more complete melting. These results indicate substantial differences in the intensity of post-accretionary heating within the S-asteroid parent bodies. These results are consistent with the proposed model that the compositional variation within the S-type population is due to post-accretionary thermal modification of an initial nebular radial compositional gradient [Gaffey, 1986b].

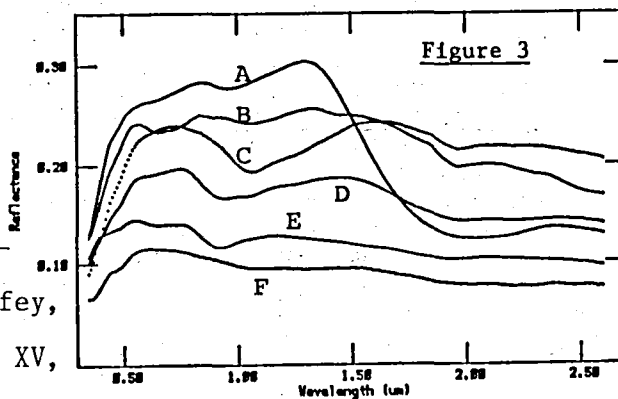
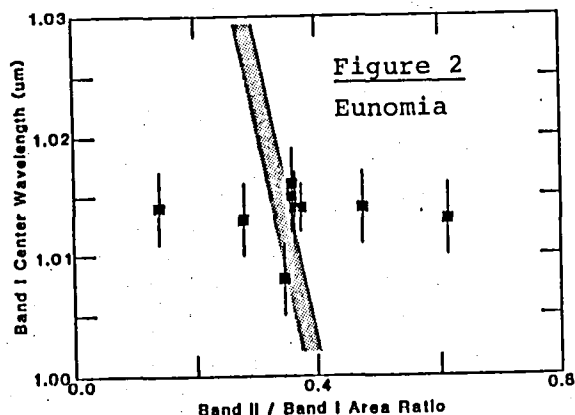
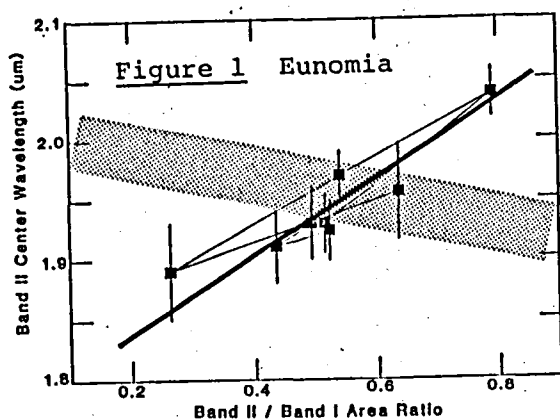
Spectral Signatures of CAI Inclusions - A preliminary study (Rajan and Gaffey, 1984) showed that some of the white inclusions in the type 3 carbonaceous chondrites, Allende, exhibited strong absorption features in the 1.5-2.5 $\mu$ m spectral region which were attributed to a spinel phase. However, due to a persistent instrumental problem with the spectrometer used in the original measurements, all of the intermediate or weak spectral features ( $\leq 10\%$  absorbance relative to the continuum) were suspect. These inclusions were re-measured using the RELAB facility at Brown University.

Six spectrally distinct components within the Allende specimen are shown on Figure 3. Curve "A" is a typical spinel-rich inclusion with the strong spinel absorption feature longwards of 1.5 $\mu$ m. There are two spectrally distinct subtypes, a cpx-bearing type with a strong spinel

feature, and an olivine-bearing type with a weaker spinel feature. Curve "B" is an inclusion dominated by a phyllosilicate phase, probably a chlorite or serpentine(antigorite). Curve "C" is the spectrum of the fine-grained olivine inclusions, with a pronounced lum olivine feature. Curves "D" and "E" are olivine-rich and pyroxene-rich chondrules, respectively, with the appropriate absorption features. Curve "F" is the dark matrix of Allende, and exhibits a broad shallow olivine absorption feature near  $1.9\mu\text{m}$ .

The fine-grained olivine inclusions all exhibit a water feature near  $1.9\mu\text{m}$ , similar to that in the phyllosilicate inclusion, indicating some degree of alteration and hydration. Such water features are not seen in the spectra of the spinel-bearing inclusions of either subtype, in the chondrules, and in the matrix. These relationships suggest that either the fine-grained olivine inclusions were exposed to a different alteration environment than the other Allende components, or the fine-grained olivine component was especially susceptible to alteration in a common environment.

The low abundance of the spinel-bearing CAI component would make a distinct spinel feature difficult to detect in asteroidal spectra. However, because of their high visible albedos (30-40%), large spectral contrast, and fine-grained nature, the spinel-bearing CAI's will contribute disproportionately to the total reflected flux. Hemispheric differences in CAI abundances of 0.5% would produce variations in the reflectance curve which are well within the detection limit of available instrumentation used in a high-precision observing program.



References: Cloutis et. al, 1986, J. Geophys. Res. 91, 11641-11653; Gaffey, 1984, Icarus 60, 83-114; Gaffey, 1986a, Icarus 66, 468-486; Gaffey, 1986b, Meteoritics 21, 365-366; Gaffey and Ostro, 1987, LPS XVIII, 310-311; Holden and Gaffey, 1987 Meteoritics 22, abstract in press; Rajan and Gaffey, 1984, LPS XV, pp. 659-660.

## THE STRATIGRAPHY OF THE ASTEROID BELT: AN OUTLINE MODEL

Jeffrey F. Bell (Planetary Geosciences Division, Hawaii Institute of Geophysics, 2525 Correa Road, Honolulu, HI 96822)

**INTRODUCTION:** During the past 15 years remote sensing data has been obtained for the asteroids with optical, infrared, and radar telescopes. Simultaneously a vast body of petrologic, chemical, and isotopic data has been acquired for meteorites, which are actual samples of asteroids. Recent work suggests that asteroids vary widely in composition and thermal history in a systematic way with orbital position and size. These variations can be explained to first order by three mechanisms: A.) condensation temperatures which decreased outward in the solar nebula; B.) intense metamorphic heating after accretion which declined rapidly with increasing solar distance and smaller planetesimal size; C.) incomplete differentiation in many inner belt objects followed by collisional fragmentation controlled by large internal strength gradients.

**BASIC DATA:** The largest homogenous body of asteroid spectra is the Arizona 8-color survey (1) of 589 objects. D.J. Tholen has used a cluster analysis of this data to divide the asteroids into 14 "taxonomic types" or "spectral classes" (2). The distribution of these classes with respect to orbital parameters is highly nonuniform, with each class clustering around a characteristic distance from the sun (3). Figure 1 is a radial profile through the main asteroid belt, showing the relative abundances of each spectral class as a function of solar distance. Recent near-IR observing programs have resolved the characteristic spectral features of olivine, pyroxene, plagioclase, and bound/adsorbed water in at least a few asteroids of most of these classes (4,5). These new spectral databases, when combined with recent laboratory studies of simulated asteroidal regoliths give us a much improved ability to assign meteorites to their parent asteroid classes. Table 1 summarizes the author's current belief system, which is similar to those of most other workers in the field.

**CONDENSATION LOCATIONS:** From Table 1 and Figure 1 it is apparent that carbonaceous chondrites (Class C) are concentrated near 3.0 AU, but are replaced at greater distances by types spectrally inconsistent with known meteorites (Classes P and D). These appear to be lower-temperature materials rich in complex organic compounds. Such compounds are a minor component in many carbonaceous chondrites, but are spectrally masked by pure carbon. The dark material on the Saturn satellite Iapetus may be of similar "ultracarbonaceous" composition (6). Basaltic achondrites, petrologically derivable from ordinary chondrites, are at 2.3 AU (Class V object Vesta). Aubrites (Class E) at 1.9 AU suggest an identical location for the closely related enstatite chondrites. This apparent sequence is strikingly similar to the sequence of radial distance in the solar nebula inferred from condensation temperatures of meteorites; but the distances involved are much smaller than those preferred by most meteorite researchers. Possibly a) the asteroids are not in their original condensation positions but were moved outward by some dynamical process which preserved their relative positions; b) the terrestrial planets accreted large numbers of planetesimals scattered in from the asteroid belt; c) the temperature and oxidation trends in chondrites represent a local perturbation in the nebula.

**METAMORPHIC HEATING:** In Table 1 Tholen's 14 spectral classes (plus the new "Eos" class (7)) are grouped into three larger associations according to the degree of metamorphic heating they have undergone. These three "superclasses" are the primitive objects which have undergone little or no heating, the metamorphosed objects which have been heated sufficiently to exhibit spectral changes, and the igneous objects whose current surfaces were formed from a melt. Figure 2 shows that the igneous types dominate the belt sunward of 2.7 AU, the metamorphosed types lie in a narrow zone around 3.2 AU, and the primitive types are dominant outside 3.4 AU. It appears that the heating mechanism which affected the asteroids was one which rapidly declined in efficiency with solar distance. The most popular heat source in the recent literature is decay of the short-lived isotope Al-26, whose daughter Mg-26 is found enhanced in Al-rich meteorite inclusions. This mechanism can explain the striking pattern of melting in the asteroid belt only if planetesimal formation began close to the sun, and slowly spread outward to reach the region of Jupiter over many half-lives of Al-26. Most models of planetesimal formation do in fact predict such a pattern, but the time required seems excessive. Alternatively, magnetic induction heating by a strong solar wind during the Sun's T-Tauri phase would produce the



pattern seen. Whatever the cause, it is clear that the asteroid belt preserves a transition between unaltered nebular condensate and highly evolved igneous materials.

**DIFFERENTIAL FRAGMENTATION:** The heating episode as described above cannot explain the rarity of metal-free achondritic rocky asteroids (classes V,R,A,E) relative to metal-rich objects (classes S and M) in the inner belt. An answer is suggested by the fact that the meteorites associated with the S-class are composed of discrete regions of silicates in a continuous metal matrix ("stony-irons" instead of "irony-stones") and presumably are much stronger than stony meteorites. A differentiated or semi-differentiated parent body will be rapidly stripped of its weak outer silicate layers by collisions with other asteroids; once a metal-dominated layer is reached, fragmentation will proceed more slowly. Only a lucky few inner-belt objects have retained their basalt crusts and dunite mantles. This "armour-deck" model is supported by the large difference in cosmic-ray exposure ages between stone meteorites and iron meteorites. However, it creates a problem in explaining the survival of several large C-type asteroids slightly farther out.

**REFERENCES:** (1) B. Zellner *et al.*, *Icarus*, 61, 355-416. (2) D.J. Tholen, thesis, Univ. of Arizona, 1984. (3) J.C. Gradie and E. Tedesco, *Science*, 216, 1405-1407. (4) J.F. Bell *et al.*, *BAAS* 17, 729. (5) M.A. Feierberg *et al.*, *BAAS* 17, 730. (6) J.F. Bell *et al.*, *Icarus* 61, 192-207. (7) J.F. Bell *et al.*, *BAAS* 19, 841.

TABLE 1: RELATIONSHIP OF ASTEROID AND METEORITE CLASSIFICATION SYSTEMS

Bell Superclass	Tholen Class	Inferred Minerals	Meteorites
PRIMITIVE	D	Clays, Organics	(None)
	P	Clays, Organics	(None)
	C	Clays, C, Organics	CI and CM chondrites
	(Eos)	Ol, Pyx, Carbon	CV and CO chondrites
METAMORPHIC	T	?	?
	B+G+F	Clays, Opaques	Altered C. C.s
	Q	Pyx, Ol, Grey NiFe	H, L, LL Chondrites
IGNEOUS	V	Plag, Pyx, Ol	Basaltic Achondrites
	R	Ol, Pyx	Ol-rich achondrites?
	S	Pyx, Ol, Red NiFe	Pallasites, Lodranites, Irons
	A	Ol	Brachinites
	M	NiFe	Irons
	E	Fe-free Pyx	Aubrites

Figure 1: DISTRIBUTION IN SPACE OF ASTEROID CLASSES

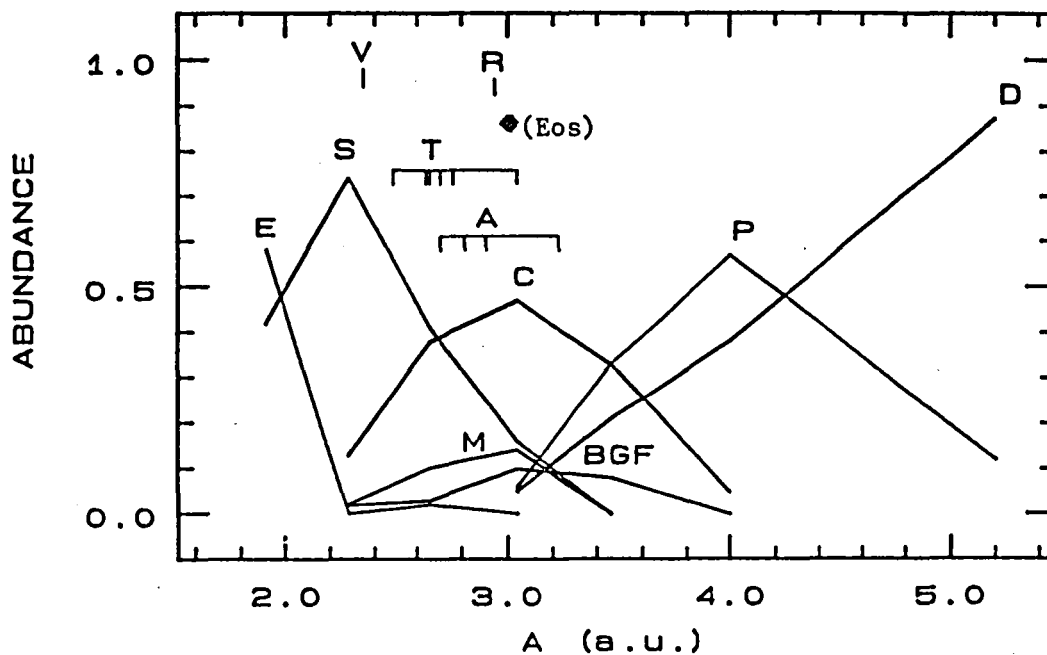
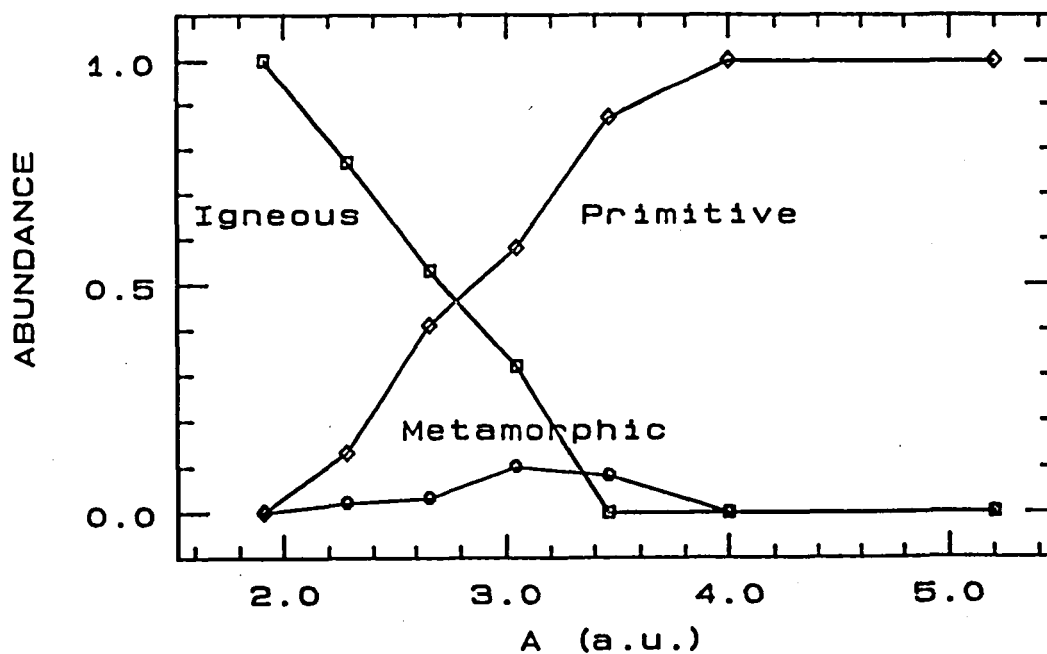


Figure 2: DISTRIBUTION IN SPACE OF ASTEROID SUPERCLASSES



CHAPTER 3  
COSMOGONY AND DYNAMICS



## SOLAR SYSTEM DYNAMICS

Jack Wisdom, Department of Earth, Atmospheric and Planetary Sciences, Massachusetts Institute of Technology, Cambridge, Massachusetts 02139

### I. Rotational Dynamics of Irregularly Shaped Satellites

In the standard picture of the tidal evolution of the rotations of the natural satellites the wobble, obliquity, and spin are damped by tidal friction. If capture does not occur in any non-synchronous spin-orbit resonance, the rotation is smoothly captured into the synchronous spin-orbit resonance where the satellite always points the same face to the planet. The standard picture must now be substantially revised for the irregularly shaped satellites. For these satellites there is a significant chaotic zone surrounding the synchronous spin-orbit resonance. In itself this is not surprising, since resonances are generically surrounded by chaotic zones in systems with more than one degree of freedom. The really surprising result is that in every case investigated, this chaotic zone is attitude unstable to chaotic tumbling. Thus all irregularly shaped satellites tumble chaotically just at the point of entry into synchronous rotation, as tidal friction brings them into the chaotic zone surrounding the synchronous resonance. The time spent in this chaotic tumbling state is not yet calculable, but is probably on the order of the tidal-despinning timescale. Thus Phobos probably spent on the order of 10 million years tumbling chaotically, while Deimos probably spent on the order of 100 millions year in this chaotic tumbling state. This episode of chaotic tumbling can have a significant effect on the orbital evolution due to the enhanced dissipation of energy as the body tumbles. The possibility of chaotic tumbling must certainly be kept in mind as the orbital histories of irregular shaped satellited as calculated. This highlights of this work are included in the Urey Lecture which is in press in *Icarus*; the complete work is in press in the *Astronomical Journal*. This work includes a detailed investigation into the effects of the episode of chaotic tumbling on the orbital evolution.

### II. Tidal Evolution of the Uranian Satellites (with William Tittlemore)

This work marks the first part of a series of investigations of the passage of the Uranian satellites through mean-motion resonances. Because of the small  $J_2$  of Uranus orbital resonances between the satellites are associated with significant chaotic zones. The most recently encountered of the first and second order resonances is the 5:3 resonance between Ariel and Umbriel. This resonance will be encountered if the  $Q$  of Uranus is less than about 100,000. We have begun our investigation with a study of the dynamics of passage through the 5:3 commensurability in the planar approximation. There is a significant chaotic zone associated with this resonance as revealed by numerically generated surfaces of section, and the presence of this chaotic zone makes the standard theory of passage through resonance inapplicable. As the resonance is encountered there are chaotic variations in the eccentricities of both Ariel and Umbriel. As tidal evolution proceeds, the peak eccentricities tend to gradually increase as long as the trajectory remains chaotic. The mechanism of capture is significantly different from the standard picture. Capture primarily occurs through the division of the energy surface as the parameters of the system evolve. Thus at the point of capture into resonant libration the trajectory may still be chaotic. Subsequent evolution brings the trajectory into a quasiperiodic libration. Capture may also occur directly onto a quasiperiodic libration island. The largest eccentricities observed for Ariel in our numerical studies was 0.023, which is probably insufficient to have a significant effect on the thermal history of Ariel. Perhaps when the inclinations are included higher eccentricities will be obtained. Studies of the passage through the other principal commensurabilities are underway. This work has been submitted for publication in *Icarus*.

### III. Chaotic Dynamics in the Solar System

The Urey Prize was awarded on the basis of work accomplished under this grant. I took the opportunity provided by the Urey Prize lecture to write a review for non-specialists of my applications of modern non-linear dynamics to the dynamics of the solar system, but also included new work on the rotational dynamics of irregularly shaped satellites and results of the systematic numerical surveys of the dynamics of the Kirkwood gaps with the Digital Orrery. The work on the irregular satellites was described above. The Digital Orrery was used to explore the dynamics of the 2/1 and 3/2 Jovian mean-motion resonances. It was found that there is a significant chaotic zone at the 2/1 resonance where there is a gap in the distribution of asteroids, while there was no evidence of chaotic behavior at the 3/2 resonance where the Hilda group of asteroids is located. There is thus a qualitative difference in the dynamics of these two resonances which corresponds to the observed differences in the distributions of asteroids. However, detailed comparison does not give perfect agreement. Most likely this is a result of the use of the planar elliptic approximation in the systematic surveys. This point will be investigated further. Integrations of chaotic trajectories including the major planets showed that very high eccentricities were reached by a path that temporarily took them to moderate inclination. Thus the three-dimensional aspect of the problem is important. The Urey lecture also summarized our integrations of the outer solar system with the Digital Orrery, emphasizing the very long-period variations in the orbit of Pluto. This paper is in press in *Icarus*.

## ORBITAL ACCELERATION OF IO

Richard Greenberg, Lunar and Planetary Lab, Univ. Arizona

The rapid heat loss from Io due to tidal heating would have quickly damped Io's orbital eccentricity, were it not for the Laplace resonance with Europa and Ganymede, which continually pumps the eccentricity. Energy for the on-going heat loss must come from Io's orbit, tending to reduce the semi-major axis and accelerate the mean motion  $n_1$ . That orbital evolution is modified by (a) interchange of energy among the resonant satellites and (b) the unknown rate of energy and angular momentum transported from Jovian rotation to Io's orbit due to tidal processes in Jupiter.

Most physical models of Jupiter, with the exception of the model by Stevenson (1983), suggest (b) would be negligible. In that case the Io dissipation rate of  $7 \times 10^{13}$  W (McEwen et al. 1985) would correspond to rapid shrinking of Io's orbit at rate  $dn_1/dt \approx 3 \times 10^{-10} n_1 \text{ yr}^{-1}$ ; Moreover the system would be evolving outward from deep resonance, with much greater tidal heating only  $10^7$  yr ago (Greenberg 1987). In contrast, a model with (b) sufficient that the system is at an equilibrium depth in resonance (Yoder 1979) gives orbital expansion at rate  $dn_1/dt \approx -10^{-10} n_1 \text{ yr}^{-1}$ . Either value would shift Io-eclipse times by several minutes over the 300 yr of observations.

From historical data, Goldstein and Jacobs (1986) found  $dn_1/dt = 4.6 \times 10^{-10} n_1 \text{ yr}^{-1} \pm 20\%$ , which seemed to support the disequilibrium model. However, Lieske (1987) finds the value  $dn_1/dt = (-7.4 \pm 8.7) \times 10^{-12} n_1 \text{ yr}^{-1}$ , consistent with the negative sign predicted by the equilibrium hypothesis, but too slow by more than an order of magnitude. Lieske's value thus implies that dissipation in Jupiter is too slow to maintain Yoder's proposed equilibrium model. Thus, either determination of  $dn_1/dt$  (Goldstein and Jacobs' or Lieske's) combined with the measured Io heat flux indicates disequilibrium, with evolution outward from deep resonance.

In order to resolve the different determinations by Lieske and by Goldstein and Jacobs I have investigated the data bases and analytical methods of these researchers. Lieske's results were based on a much more extensive data set, on a more complete theoretical model, and on a more conventional method for estimating the clock correction  $\Delta T = ET - UT$ . Goldstein and Jacobs used a rather unconventional clock correction (Goldstein 1985). However, the difference in clock corrections could only explain a small fraction of the difference between the two determinations of  $dn_1/dt$ .

Nevertheless I find there is a real flaw in Goldstein and Jacobs' determination of the acceleration. It strongly depends on Goldstein's (1975) 17th century value of the mean motion. Careful examination of Goldstein's (1975) solution shows two significant errors.

The first comes from Goldstein's evaluation of the "Great Inequality" in Io's motion. The amplitude of this oscillation, determined by the mass of Europa and the value of  $\nu = n_1 - 2n_2$ , is  $0.47^\circ$ ; its frequency is simply

$n_1 - \nu$ , approximately the same as  $n_1$ ; and its phase is well defined by the longitudes of Io and Europa. Rather than use the known amplitude and phase of the great inequality, Goldstein chose to adjust these along with the unknown parameters (mean motion and longitude at epoch) in his least squares fit to the 17th century data. His fit gave an amplitude of  $0^{\circ}4936$  and a phase  $3^{\circ}$  off the correct known values. This error introduces an artificial oscillation of  $\sim 0^{\circ}02$  in Io's longitude. Such an error might be expected to have negligible effect on the mean-motion determinations, because it has such a short period compared with the ten year interval of observations (1668-1678). However, an aliasing effect due to the frequency of observations gives a significant error. When a correction is made, it introduces an increase in the 17th century  $n_1$  of about  $3 \times 10^{-6}$  deg/day.

An even more serious error in Goldstein's (1975) determination of  $n_1$  from the 17th century data is that he used an equatorial radius for Jupiter of 70,650 km, instead of the known, correct value of 71,400 km. Apparently the smaller size was chosen to minimize the residuals of the orbital fit to the eclipse data. The error in planetary radius should not have been a serious problem if the data set included both immersion and emersion eclipse events distributed well over time. These data would have canceled any systematic errors in longitude due to the radius error. However, inspection of the data set shows that most of the data in the first half of the decade of observations (1668-1673) were immersion events, while most in the second half were emersions. Correction for this bias increases  $n_1$  by  $10^{-5}$  deg/day.

I conclude that the acceleration determined by Goldstein and Jacobs is spurious. As shown by Lieske, the acceleration of Io is probably slow and probably negative, i.e. Io is spiraling outward from Jupiter. However, Lieske's value still indicates a system out of equilibrium. On the other hand, Lieske has also determined limits on the acceleration of Europa, which, when combined with that for Io, show that  $d\nu/dt$  is in fact very small, less than  $0.5 \times 10^{-11} n_1/\text{yr}$  in absolute value, which means that the system has been in equilibrium over the 300 yr time-scale.

The only way to reconcile these results would be to conclude that over the past 300 yr, while the relevant eclipse data were being collected, the average dissipation rate on Io was  $< 10^{13} \text{ W}$ . This dissipation rate is an order of magnitude less than the heat flux from Io.

Thus the implication of Lieske's acceleration values is that for the past 10 or 15 yr heat has been coming out of Io at a rate ten times faster than the average over the past 300 yr. This increase might be due either to an actual increase in the dissipation rate or short-lived release of pent up heat. Either case speaks of very great geophysical and/or geological changes in Io on time-scales of years.



#### REFERENCES:

- Goldstein, S.J. (1975) Astron. J. 80, 532-539.
- Goldstein, S.J. (1985) Astron. J. 90, 1900-1905.
- Goldstein, S.J., and Jacobs, K.C. (1986) Astron. J. 92, 199-202.
- Greenberg, R. (1987) Icarus 70, 334-337.
- Lieske, J.H. (1987) Astron. Astrophys. 176, 146-158.
- McEwen, A.S., Matson, D.L., Johnson, T.V., and Soderblom, L.A. (1985) J. Geophys. Res. 90, 12345-12379.
- Stevenson, D.J. (1983) J. Geophys. Res. 88, 2445-2455.
- Yoder, C.F. (1979) Nature 279, 767-769.

## Tidal Evolution of Jupiter's Satellites

Jay H. Lieske, Jet Propulsion Laboratory, California Institute of Technology,  
Pasadena, California 91109

In discussions of the evolution of Jupiter's Galilean satellite system it is important to know, or to have realistic bounds upon, the possible secular changes in mean motion of the satellites. Denoting by subscripts 1 through 4 respectively the satellites Io, Europa, Ganymede and Callisto, then the sign of  $\dot{n}_1$  indicates whether Io is moving in towards Jupiter ( $\dot{n}_1 > 0$ ) or if it is moving away from Jupiter ( $\dot{n}_1 < 0$ ). The former case would result when tidal action by Jupiter on Io dominates the evolution, while the latter case would be the result if tides raised by Io on Jupiter dominate the evolution.

In addition, the relative evolution of the Io-Europa commensurability  $\dot{v} = \dot{n}_1 - 2\dot{n}_2$  is of interest to planetary scientists in order to determine whether the system is evolving into resonance ( $\dot{v} < 0$ ) or out of resonance ( $\dot{v} > 0$ ).

Previous determinations by deSitter (1928, 1931) by Goldstein (1975), and by Goldstein and Jacobs (1986) which were obtained from analyses of eclipse timings of Io suggest that  $\dot{n}_1$  is positive, although both works are somewhat in doubt because of some underlying hypotheses. In the case of deSitter, the work was done before the adoption of a uniform time scale (so-called Ephemeris Time), although deSitter did attempt to put his results on a system of "Newtonian time." Goldstein's results are somewhat suspect because of the table of  $\Delta T$  (Ephemeris Time minus Universal Time) which was used and because of an anomalous value for the radius of Jupiter which Goldstein employed.

deSitter's values could be interpreted as being in the interval of  $10^{11} \dot{n}_1 / n_1 = +3$  to  $+33 \text{ yr}^{-1}$ , while Goldstein's would be in the range  $+11$  to  $58$ , both indicating that Io is evolving in towards Jupiter. The question of  $\Delta T$  is important because it gives the relationship between a "Universal Time" clock (viz., connected with the Earth's rotation and upon which the Io eclipse timings are based) and a "uniform" clock (the Ephemeris Time system upon which one calculates the dynamics and the predicted event times). Prior to the era of atomic clocks one had to infer ET by adopting some ephemeris as being "perfect" except that its time tags had an unknown relationship to Universal Time (which can be observed via sidereal time). In practice one had to use a fast-moving object and so the Moon was often used. In this situation the resolution of  $\Delta T$  is further complicated by the fact that the Moon experiences a tidal deceleration due to interactions with the Earth and hence whatever one investigator would ascribe to lunar tidal acceleration another author might ascribe to real changes in  $\Delta T$ .

Fortunately, over the past 15 years determinations of the lunar tidal acceleration have become stabilized and are in the order of  $\dot{n}_{\text{moon}} = -25$

arcsec/cy<sup>2</sup> so that what formerly constituted a very large error source in the determinations of  $\Delta T$  now has become more manageable. Goldstein's (1985) development of a  $\Delta T$  function, however, is equivalent to a value of  $\dot{n}_{\text{moon}} = -39$  arcsec/cy<sup>2</sup>.

In the case of the Galilean satellites it is important because each unit of uncertainty in  $\dot{n}_{\text{moon}}$  of 1 arcsec per century<sup>2</sup> translates into about one second of time per century<sup>2</sup> uncertainty in the the predicted times of Io eclipses, and hence affects the derived value of  $\dot{n}_1$ .

We have adopted the Stephenson and Morrison tabular values of  $\Delta T$  and have reduced them to the classical value due to Spencer Jones (1939) of  $\dot{n}_{\text{moon}} = -22.44$  arcsec/cy<sup>2</sup> for the initial comparison, although we have the ability to estimate the value of  $\dot{n}_{\text{moon}}$  or freeze it to another value at will. We have analyzed over 16000 eclipse observations of the Galilean satellites from 1652 to 1983, as well as approximately 3000 earth-based photographic observations, mutual events (eclipses and occultations) in 1973 and 1979, and the Voyager optical navigation pictures. If the Goldstein value of  $\Delta T$  is correct (or if his estimate of  $\dot{n}_1$  is correct) then we should see a drift of about 400 seconds over the past 300 years in terms of the observed versus predicted eclipse timings. Hence the old eclipse data are of great use and the modern data serve as "anchor points" to tie down the orbital parameters.

Our preliminary results (reduced to the lunar laser derived value (Dickey et al, 1984) of  $\dot{n}_{\text{moon}} = -25.3$  arcsec/cy<sup>2</sup> are as follows:

$$10^{11} \dot{n}_1/n_1 = -0.74 \pm 0.87 \text{ yr}^{-1}$$

$$10^{11} \dot{v}/n_1 = 10^{11} (n_1 - 2n_2)/n_1 = +0.08 \pm 0.42 \text{ yr}^{-1}$$

which formally suggests that the system is evolving out from Jupiter (since  $\dot{n}_1 < 0$ ) and that the Io-Europa coupling is evolving out of resonance (since  $\dot{v} > 0$ ). However, it should also be noted that the results are consistent with no change in  $\dot{n}_1$  and with  $\dot{v} = 0$ . These results are of the opposite sign and about a factor of 60 smaller than the recent result reported by Goldstein.

Future efforts will iterate the solution by generating new ephemerides based upon the Morrison and Stephenson values of  $\Delta T$  and will evaluate solar eclipse timings to give an independent indication of whether the solar eclipse data are more consistent with Morrison and Stephenson's  $\Delta T$  or with Goldstein's values of  $\Delta T$ .

## References:

- de Sitter, W.: 1928, *Ann. Sterrew. Leiden* 16, Part 2  
de Sitter, W.: 1931, *Monthly Notices Roy. Astron. Soc.* 91, 706  
Dickey, J.O., Williams, J.G., Newhall, XX, Yoder, C.F.: 1984, *Proc. IAG/IUGG Hamburg* 2, 509  
Goldstein, S.J.: 1985, *Astron J.* 90, 1900  
Lieske, J.H.: 1987, *Astron. Astrophys.* 176, 146  
Goldstein, S.J., Jacobs, K.C.: 1986, *Astron J.* 92, 199  
Spencer Jones, H.: 1939, *Monthly Notices Roy. Astron. Soc.* 99, 541  
Stephenson, F.R., Morrison, L.V.: 1984, *Phil. Trans. Roy. Soc. London* A313,

## COMPOSITION OF URANUS AND NEPTUNE: NONSOLAR ICE TO ROCK RATIOS?

Reynolds, R.T. and M. Podolak\*, Theoretical Studies Branch, NASA Ames Research Center, Moffett Field, CA 94035

Since the composition of Uranus and Neptune is not only of considerable intrinsic interest but is also important to theories of the origin of the solar system (Podolak and Reynolds, 1984), this subject has intermittently attracted the attention of a number of researchers for many years (see Podolak and Reynolds, 1985). Most studies have taken the form of the construction of mathematical models of Uranus and Neptune according to certain ground rules. These models result from the integration of the equation of hydrostatic equilibrium; with the incorporation of high-pressure equations of state, selected cosmogonical assumptions and observationally determined values of planetary physical parameters. As advances in knowledge have been made in these areas, new and presumably improved models have been constructed. Although we are still far from a comprehensive understanding of this subject, recent work has added some significant new information. The Voyager flyby of Uranus, in particular, has accurately determined the rotation period of that planet. It was found that earlier models (e.g. Podolak and Reynolds, 1981) which were computed using a "solar" Ice/Rock ratio were not compatible with the observed rotation period. One possible implication is that the Ice/Rock ratio in Uranus and Neptune is higher than the solar value. While lower Ice/Rock ratios (at least in warmer parts of the solar system) can be explained simply by the different condensation temperatures of the two materials, it is a non-trivial problem to develop a rationale which can explain an increase in the Ice/Rock ratio. Podolak and Reynolds (1987) discussed this problem and suggested an accretion mechanism involving differential accretion of icy and rocky planetesimals in the extended atmosphere surrounding a growing planetary body.

The idea that a slowly accreting protoplanetary core of a giant planet would capture gas very rapidly after reaching a certain critical value of the mass was proposed by Mizuno (1980). Bodenheimer and Pollack (1986) have developed this idea and calculated the properties of high temperature gaseous envelopes with grain produced opacities. Alternate scenarios are available (see e.g. Stevenson, 1985 and personal communication) but this line of approach warrants further investigation.

Pollack et. al., 1986 addressed the compositional question by assessing the influence of the protoplanetary envelope on planetesimals traversing the envelope to reach the core by using simple path-independent approximations for gas drag on planetesimals, radiative and ablative heating, mass loss, and fragmentation. It was determined that the depth of deposition of the incoming material does indeed depend strongly on the composition of the material.

More detailed calculations were carried out by Podolak et. al. (in press) which treat, in a more exact manner, the physics of the interaction of planetesimals with the protoatmosphere by computing the two-body trajectory of these planetesimals through the atmosphere and calculating such effects as gas drag, ablation, etc. explicitly along the trajectory. In addition non-zero angular momentum trajectories were

also considered in this study. The more detailed treatment allows determination of the depth of distribution of the planetesimal mass for different materials and reveals some interesting features of the planetesimal - envelope interactions (Fig. 1).

Because Ice is more volatile than rock and therefore an ice planetesimal loses mass more easily, it is more easily captured. Figure 2 shows the ratio of capture cross sections for the Ice and Rock planetesimals (for various core masses) as a function of planetesimal size. For encounter velocities of  $2 \text{ km sec}^{-1}$  there is little difference for the two materials and the ratio stays near one. However, for an encounter velocity of  $5 \text{ km sec}^{-1}$ , where ablation plays an important role in mass loss for ice particles, large differences in the capture cross section can result.

This scenario thus proposes a mechanism which could describe the formation of a higher than solar Ice to Rock ratio for Uranus and Neptune. Further evaluation of this possibility is in progress.

Bodenheimer, P., and J.B. Pollack (1986). Calculations of the accretion and evolution of giant planets: The effect of solid cores, Icarus, 67, 391-408.

Mizuno, H. (1980). Formation of the giant planets. Prog. Theor. Phys., 64, 544-557.

Podolak, M and R.T. Reynolds (1981). On the structure and composition of Uranus and Neptune. Icarus, 46, 40-50.

Podolak, M. and R.T. Reynolds (1984). Consistency tests of theories from models of Uranus and Neptune. Icarus, 54, 102-111.

Podolak, M. and R.T. Reynolds (1985). What have we learned from modeling giant planet interiors? In Protostrs and Planets II (D. Black and M.S. Matthews, eds.) Univ. of Arizona Press, pp. 847-872.

Podolak, M. and R.T. Reynolds (1987). The rotation rate of Uranus, its internal structure, and the process of planetary accretion, Icarus, 70, 31-36.

Podolak, M., J.B. Pollack and R.T. Reynolds (in press). Interactions of planetesimals with protoplanetary atmospheres. Icarus.

Pollack, J.B., M. Podolak, P. Bodenheimer, and B. Christofferson (1986). Planetesimal dissolution in the envelopes of the forming, giant planets. Icarus, 67 409-443.

Stevenson, D. (1985). Cosmochemistry and structure of the giant planets and their satellites. Icarus, 62, 4-15.

\* Permanent address: Dept. of Geophysics and Planetary Sciences, Tel Aviv University, Israel.

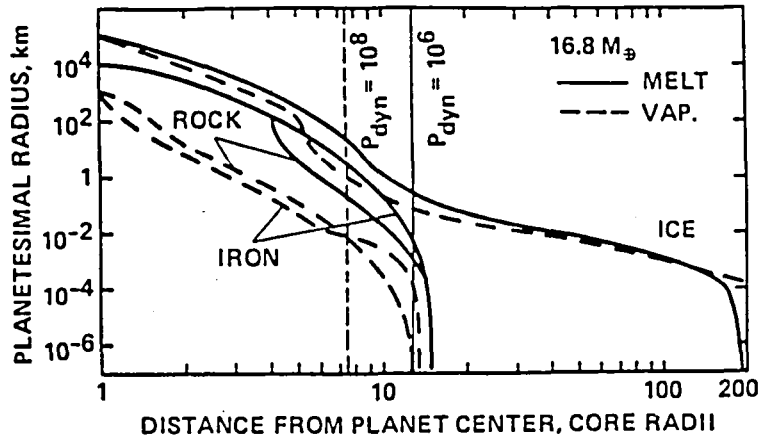


Fig. 1 Penetration curves for the melting (solid) and vaporization (dashed) of ice, rock, and iron planetesimals for a  $16.8 M_{\text{earth}}$  core: The dashed curve at the lower left is the vaporization curve for both rock and iron (see text). The solid vertical line shows the region where the dynamical pressure can reach  $10^6 \text{ dynes cm}^{-2}$ .

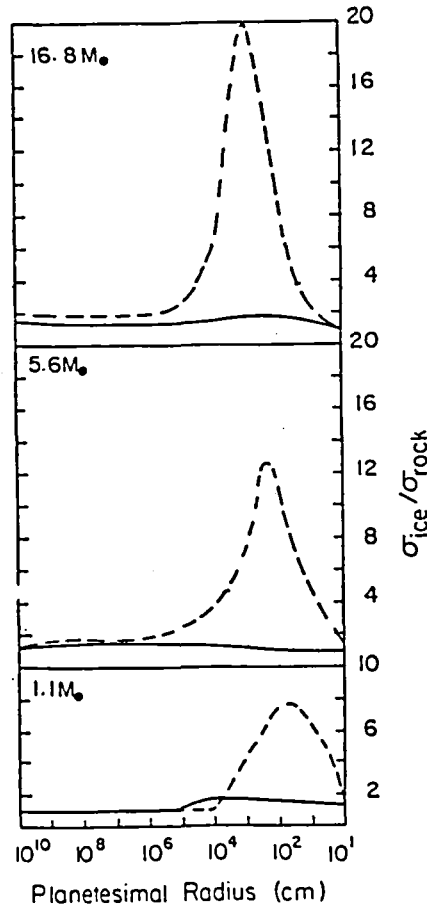


Fig. 2 Ratio of capture cross section for ice planetesimals to rock planetesimals as a function of planetesimal size for 1.1, 5.6, and  $16.8 M_{\text{earth}}$  core masses. The curves are for encounter velocities of  $2 \text{ km s}^{-1}$  (solid), and  $5 \text{ km s}^{-1}$  (dashed):

CARBON IN THE OUTER SOLAR SYSTEM  
D.P. Simonelli, J.B. Pollack, and C.P. McKay  
NASA Ames Research Center, Moffett Field, California 94035

The satellites of Uranus, with densities between  $1.3$  and  $1.7 \text{ g cm}^{-3}$  (from Voyager 2 observations), and the Pluto-Charon system, with a mean density of just above  $1.8 \text{ g cm}^{-3}$  (from terrestrial observations of mutual eclipse events), are too dense to have a significant amount of methane ice in their interiors. However, the observed densities do not preclude contributions from such organic materials as the acid-insoluble residue in carbonaceous chondrites and laboratory-produced tholins, which have densities on the order of  $\approx 1.5 \text{ g cm}^{-3}$ . These and other considerations have led us to investigate the carbon mass budget in the outer solar system, with an emphasis on understanding the contribution of organic materials.

Modeling of the interiors of Pluto and Charon (being carried out by R. Reynolds and A. Summers of NASA/Ames), assuming rock and water ice as the only constituents, suggests a silicate mass fraction for this system on the order of  $0.65$ - $0.70$ . Such a composition has two implications: (1) The silicate fraction for Pluto/Charon is larger than the typical silicate fraction of  $\approx 0.55$  found for satellites of the giant planets (Johnson et al., 1987). This compositional difference may be a result of different formation mechanisms: while Pluto and Charon formed directly from the solar nebula, and retain its rock and ice fractions, the satellites may have formed from the outer portions of the envelopes of the forming giant planets-in which case the satellites would have a lower silicate fraction than the nebula because as planetesimals bombard the forming planet, icy planetesimals dissolve in the envelope more readily than rocky planetesimals (Pollack et al., 1986). (2) The silicate fraction of objects formed directly from the solar nebula depends strongly on the fraction of nebular carbon that is in the form of CO: a greater CO abundance means that there is less oxygen available to form water ice, and implies that condensed material in the nebula will have a greater rock/ice ratio (Pollack and Bodenheimer, 1987). Simple calculations based on solar abundances suggest that in order for the Pluto-Charon system to have a silicate fraction as high as  $0.65$ - $0.70$ , the majority of the carbon in the outer solar nebula-on the order of  $70$ - $85\%$ -must have been in the form of carbon monoxide gas.

After constraining the amount of carbon in gaseous CO, we next put limits on the fraction of the remaining carbon that is in condensed materials by modeling the enhancement in C/H (over and above the solar C/H ratio) that is observed in the atmospheres of the giant planets. We use an approach first developed by Pollack et al. (1986) that emphasizes planetesimal dissolution in the envelopes of the forming giant planets; this approach assumes that the C/H enhancement depends on both the fraction of nebular C in condensed material and the fraction of carbon-bearing planetesimals bombarding a planet that dissolved in the envelope-and assumes that if all such planetesimals do dissolve, the C/H enhancement in the atmosphere would mimic the observed enhancement in their high  $z$ /low  $z$  mass ratio of the planet as a whole (where "high  $z$ " means condensed materials, "low  $z$ " refers to  $\text{H}_2$  and He gas, and enhancement is relative to predictions from solar abundances). The present work includes the most



recent estimates of the C/H enhancements and high z/low z ratios of the giant planets (Pollack and Bodenheimer, 1987), and involves a more careful estimation of the high z/low z mass ratio expected from solar abundances than was used in Pollack et al. (1986), including the influence of the fraction of C in CO on the amount of condensed water ice. These calculations indicate that for a particular fraction of C in CO and a given fraction of C-bearing planetesimals that dissolve in the envelope (most likely in the range 0.50-0.75), (1) Jupiter and Saturn require a larger fraction of C in condensed materials than Uranus and Neptune, but (2) the Jupiter and Saturn results are much less strongly constrained by the error bars on the observed C/H enhancements and high z/low z ratios than is the case for Uranus and Neptune. The clearest result is that in the region of the solar nebula near Uranus and Neptune, the minority of carbon that is not in gaseous CO (1) **must** include a nonzero amount of condensed material, but (2) is most likely **not** condensed material alone, i.e., there must be a third carbon-bearing component besides condensed material and gaseous CO. Given the implied dearth of methane ice, the condensed carbon is likely dominated by organic material, and the third component present in addition to CO and organics is assumed to be CH<sub>4</sub> gas.

#### References

- Johnson, T.V., Brown, R.H., and Pollack, J.B.: 1987, submitted to J. Geophys. Res.
- Pollack, J.B., and Bodenheimer, P.: 1987, review chapter in upcoming book "Origin and Evolution of Planetary and Satellite Atmospheres".
- Pollack, J.B., Podolak, M., Bodenheimer, P., and Christofferson, B.: 1986, Icarus 67, 409.

# COLLISIONAL AND GAS DYNAMICS OF ACCRETION

S.J. Weidenschilling, Planetary Science Institute, Tucson, AZ 85719

In conjunction with the conference and book, "Meteorites and the Early Solar System", Weidenschilling (1) has prepared a review of accretion of meteorite parent bodies (planetesimals). This is the only unified treatment of the dynamical processes involved in coagulation of solid objects ranging from submicron grains to asteroid-sized bodies, for which the influence of gas drag on their relative motions is significant. The dominant processes in various size regimes are identified by comparison of their timescales. This work includes substantial new material, particularly in the examination of consequences of turbulence. The following results are based on a combination of analytic calculations and new numerical simulations using an improved version of the program described in Ref. (2).

Gas in the solar nebula dominated the evolution of solid particles in the size range  $\sim \mu\text{m}$  to km. Its effects were strongly size-dependent, and controlled such processes as radial transport and mixing of condensates, settling to the central plane of the disk with local enhancement of the dust/gas ratio, possibility of planetesimal formation by gravitational instability of a dust layer, and collisions producing coagulation or erosion/disruption.

The disk was probably turbulent during the formation (infall) stage. The magnitude and duration of later turbulence is uncertain; existing models include disks with no turbulence (3), and those with turbulence Mach numbers,  $M$ , from a few % (4) to  $\approx 1/3$  (5). Turbulence may have been localized or intermittent. Whether turbulent or laminar, the nebula had a radial pressure gradient ( $\partial P/\partial r < 0$ ) partly supporting the gas (6), causing rotation at slightly less than the Kepler velocity.

Plausible models have fractional deviation,  $\Delta V/V_k$ , of a few  $\times 10^{-3}$ .

Small particles strongly coupled to the gas share its angular velocity, with solar gravity causing inward radial drift with velocity proportional to size. Large bodies move in Kepler orbits; the "headwind" of magnitude  $\Delta V$  causes orbital decay at a rate inversely proportional to size. Transition between these regimes occurs at  $\approx$  meter size, with  $|dr/dt|(\text{max}) = \Delta V$ , typically  $\sim 10^3 - 10^4$  cm/sec.

Turbulence and Settling. The  $z$ -component of solar gravity causes small particles to settle toward the central plane at a rate  $dz/dt = s \rho_s \Omega^2 z / \rho c$  (Epstein drag;  $s$  = particle radius,  $\rho_s$  = particle density;  $\rho$  = gas density,  $c$  = thermal velocity). If global turbulence is present, small particles ( $s \lesssim 10$  cm) are coupled to the largest eddies, which have rms velocity  $V_t = Mc$ . Equating settling and eddy velocities yields the

equilibrium half-thickness of a particle layer,  $z' \sim M \rho c^2 / \rho_s \Omega^2 s$ . For plausible nebular parameters, settling to form a layer with dust/gas  $\sim 1$  requires  $M \sim 10^{-5} \times (s/1 \text{ cm})$ ; i.e., large ( $\gtrsim$  cm-sized) particles and turbulent velocities  $\lesssim$  a few cm/sec. If the dust layer is to become

thin enough for "Goldreich-Ward" gravitational instability (7).

$M \lesssim 10^{-6} \times (s/1 \text{ cm})$ , or  $V_t \sim 0.1 \text{ cm/sec}$  for  $s=1 \text{ cm}$  ( $V_t \sim 10^{-5} \text{ cm/sec}$  for  $s=1 \mu\text{m}$ ). Published values (2,7)  $\sim 10 \text{ cm/sec}$  for random particle velocities in a marginally unstable layer implicitly assume that their motions are not controlled by gas, which is the case only for  $s \gtrsim 100 \text{ cm}$ .

If a dust layer has space density of dust  $\lambda$  that of the gas and is optically thick, the dust controls the motion of the gas in the layer. Such a layer will acquire Keplerian rotation (8). Even if the nebula is perfectly laminar, shear between the dust layer and the surrounding gas would cause localized turbulence in a boundary layer (7). Neither density stratification nor viscous dissipation can prevent this turbulence from stirring the dust layer to velocities  $\gg 1 \text{ cm/sec}$ . The probable result is that the dust layer would thicken to an equilibrium state with dust/gas  $\sim 1$  until collisional coagulation produces bodies large enough to decouple from the gas ( $s \gtrsim 100 \text{ cm}$ ). Thus, Weidenschilling (1) argues that formation of planetesimals by gravitational instability of a dust layer is extremely implausible. The alternative formation mechanism is collisional coagulation.

Coagulation and Settling. At submicron sizes, particle relative velocities are dominated by thermal Brownian motion; coagulation will produce aggregates up to  $\sim 10 \mu\text{m}$  in size on timescales  $\sim 10^2 - 10^3 \text{ y}$ . Larger aggregates have relative velocities dominated by turbulent motions and/or differences in systematic radial and vertical drift rates. Vigorous turbulence ( $M \approx 1/3$ ) promotes collisions with rapid coagulation. However, relative velocities increase with size as particles can cross eddies and their motions become uncorrelated. Aggregates with sizes  $\gtrsim 1 \text{ cm}$  collide with velocities of magnitude  $\sim V_t$ . Disruption occurs at size  $s \sim 10^{-7} E / \rho_s M^2$ , where  $E$  is impact strength. For plausible  $E = 10^5 \text{ erg/cm}^3$ , aggregate growth stops at  $s \sim 0.1 \text{ cm}$  for  $M = 1/3$ . The result is a steady state between coagulation and disruption (9). In order for aggregates to grow large enough for appreciable settling,  $M$  must be  $\lesssim 0.01$ . For such low turbulent velocities, differential settling dominates relative velocities.

The rates of vertical and radial drift are proportional to particle size. If coagulation occurs, then large aggregates grow by sweeping up smaller ones and individual grains. Self-similar fractal structures (10) probably will not be produced on scales  $\gtrsim 10 \mu\text{m}$ , where differential settling dominates over thermal motion. Minimum growth timescale (e-folding for mass) is  $\tau \sim 1/f\Omega$  ( $f = \text{solids/gas mass ratio}$ ), typically a few hundred years. Numerical simulations (2,11) show non-homologous settling with a small fraction (0.01-0.1) of the total surface density of solids incorporated into  $m$ -sized bodies in a thin layer near the central plane, with solids/gas  $\sim 1$  after  $\approx 10\tau$ . Radial drift during this stage is  $\sim 0.1r$ . Further growth to km-sized planetesimals depends on the degree of turbulence in the gas and on the size distribution during accretion; the latter depends on the former, and must be calculated numerically. Thus far, Weidenschilling (1) has examined limiting cases that are subject to analytic approximation.

Bodies larger than  $\sim m$ -size have mainly transverse motion relative to the gas. If the size distribution is broad, so that a few larger bodies can form while much of the mass remains in small particles that are strongly coupled to the gas, then the large bodies grow by sweeping up the small ones as they spiral inward. Growth must be rapid compared with orbital decay in order to avoid loss into the Sun. Planetesimals spiral inward at a decreasing rate as they grow, approaching an asymptotic limit for the final orbital radius. If the dust/gas space density is  $\sim 1$  near the central plane, this limit is  $\approx 2/3$  the initial orbital radius, and is reached in  $\sim 10^4$  y. However, this limit depends exponentially on the dust/gas ratio, and a modest decrease in this quantity below unity leads to complete loss of planetesimals. This mode of growth is possible only in a nebula that is essentially laminar.

An alternative end-member case is a narrow size distribution, with the bulk of the mass in roughly equal-sized bodies. There are two dynamical regimes, in which relative velocities are dominated by systematic differences in rates of orbital decay, or by random motions induced by turbulence. The former falls off more rapidly with increasing size, so the system may pass through both regimes during growth from  $m$ - to  $km$ -sized bodies (gravitational perturbations become dominant at larger sizes). The amount of orbital decay in this case is less sensitive to the degree of turbulence, and for plausible nebular parameters is a few tens of percent of the initial orbital radius.

More realistic cases probably lie between these. Moderate turbulence does not appear to be excluded, but further numerical simulations are needed. Previous work has concentrated on laminar (2,11) or highly turbulent (9) disk models. The effects of slight ( $M \lesssim 0.01$ ) turbulence during the  $\mu m$ - to  $m$ -size stage need to be examined to determine whether the resulting particle size distributions are compatible with further collisional growth.

This research is supported by the NASA Planetary Geology and Geophysics Program, Contract NASW-3214.

References: (1) S. Weidenschilling, in "Meteorites and the Early Solar System," J. Kerridge and M. Matthews, eds., U. of Arizona Press, 1987; (2) S. Weidenschilling, *Icarus* 44, 172 (1980); (3) C. Hayashi et al., in *Protostars and Planets II*, 1985. (4) W. Cabot et al., *Icarus* 69, 423 (1987); (5) D. Lin, *Ap. J.* 246, 972, 1981. (6) S. Weidenschilling, *MNRAS* 180, 57 (1977); (7) P. Goldreich, W. Ward, *Ap. J.* 183, 1051 (1973); (8) Y. Nakagawa et al., *Icarus* 67, 365 (1986); (9) S. Weidenschilling, *Icarus* 60, 553 (1984); (10) B. Donn, *Lunar Planet Sci. XVIII*, 243 (1987); (11) Y. Nakagawa et al., *Icarus* 45, 517 (1981).

## ANALYSIS OF PLANETARY EVOLUTION WITH EMPHASIS ON DIFFERENTIATION AND DYNAMICS

William M. Kaula, William I. Newman,  
Elizabeth Myhill, and William Weibel  
University of California, Los Angeles

### Collapse of the Proto Solar System Cloud

A three-dimensional numerical code is being developed to estimate the conditions for formation, or suppression, of a smaller companion to a solar-sized star. This work was initially undertaken to elucidate the formation of Jupiter necessarily earlier than the other planets. It is also motivated by the recent observational evidence of Jupiter-sized companions around a minority of nearby stars, but the absence of larger companions ("brown dwarfs"). The equations integrated include continuity, momentum, Poisson's law, the ideal gas law, and radiative transfer. The technique being employed is a hybrid spectral/fourth order finite difference scheme in Cartesian coordinates. The high order of this scheme should minimize spurious numerical diffusion and provide high resolution. Fast Fourier transforms and vectorization techniques are being applied.

Currently, isothermal tests are being carried out: i.e., the radiative transfer is omitted. Two procedures for the spatial gradients and derivatives in the continuity and momentum equations are being tried: (1) Fourier methods; and (2) fourth-order finite differencing. Comparisons are being made with the results obtained by Boss [1980, 1985] using a donor cell method in spherical coordinates.

A technical problem is that a Fourier representation implies a mass distribution repeating ad infinitum in all directions. This affects the potential gradients in the momentum equations. To correct for this effect, the boundary charge technique of James [1977] is being employed.

### Formation of the Post-Jovian Planets

An N-body integrator based on that of Aarseth [1972] is being applied. Effects added to a typical N-body scheme include collisions and the presence of a time-varying gaseous nebula. A significant advance over previous models [Weidenschilling & Davis, 1985; Patterson, 1987] is to allow evolution of Jupiter's orbit (and, in some simulations, those of other major planets) under the influence of the

planetesimal swarm and the gaseous nebula. Hence comparisons of the resulting semi-major axes, inclinations, and eccentricities with those observed become constraints on the models.

In the past year, efforts were directed mainly at understanding the effects of resonant interactions in problems of the small N. The 19,000-year interaction between Neptune and Pluto and the 54,000-year interaction between Jupiter and Saturn have been obtained in integrations of the motions of the five outer planets for 200,000 years. Other tests against the orrery [Applegate et al, 1987] are planned, but there is no intention to pursue such a long-term integration; rather, we seek assurance that resonances and other long-periodic effects are correctly calculated in integrations of much larger N for shorter durations.

Currently, the integrator is being applied to the stability of orbits between Jupiter and Saturn. Typically 100 test particles are used, with randomized starting values for their orbital elements. In particular, distributions of initial eccentricity with maxima ranging from  $10^{-6}$  to  $10^{-2}$  have been tried, with consistent results. Wide bands of instability develop within ten Jovian periods; orbits in the vicinity of a 5:6 commensurability with Jupiter are especially unstable. The main stable zone is at mean motions 0.5 to 0.7 of Jupiter's; some particles acquire eccentricities of 0.1, insufficient to cross Saturn's orbit.

The principal current effort in program development is in subroutines to identify and calculate collisions. At present, 100 percent dissipation is assumed, so that all collisions lead to accretion. It is planned to introduce a velocity-dependent elasticity, similar to that described by Wetherill [1980].

#### References

Aarseth, S. J. 1972, Direct integration methods of the N-body problem, Gravitational N-Body Problem, D. Reidel, Dordrecht, 373.

Applegate, J. H., Douglas, M.R., Gursel, Y., Sussman, G. J., & Wisdom, J. 1987, The outer solar system for 200 million years, Astron. J. 92, 176.

Boss, A. P. 1980, Protostellar formation in rotating interstellar clouds: III nonaxisymmetric collapse, Ap. J. 237, 866.

Boss, A. P. 1985, Three dimensional calculations of the formation of the presolar nebula from a slowly rotating cloud, Icarus 61, 3.

James, R. A. 1977, The solution of Poisson's equation for isolated source distributions, J. Comp. Phys., 25, 71.

Patterson, C. W. 1987, Resonance capture and the evolution of the planets, Icarus 70, 319.

Weidenschilling, S. J. & Davis, D. R. 1985, Orbital resonances in the solar nebula: implications for planetary accretion, Icarus 62, 16.

Wetherill, G. W. 1980, Formation of the terrestrial planets, Ann. Rev. Astron. Astrophys. 18, 77.

## Accumulation of the Planets

G. W. Wetherill, DTM, Carnegie Institution of Washington,  
Washington, D.C. 20015

### A. Early stages of planetary growth.

The growth of the terrestrial planets from  $\sim 1 - 10$  km diameter planetesimals can most conveniently be modelled in two stages:

(1) The formation of bodies up to  $\sim$  lunar mass, using the methods of gas dynamics.

(2) The accumulation of these larger bodies into objects the size of the present terrestrial planets using Monte Carlo methods of orbital dynamics.

During the past year work carried out in cooperation with G. R. Stewart of the University of Virginia on the first stage of accumulation has been extended in two ways:

(1) More accurate inclusion of the effects of stochastic collisions between bodies of comparable mass in causing dispersion of the swarm.

(2) Improvements in the fundamental expressions of Stewart for calculating velocity changes.

As a result of this work it is now clear that the orderly growth of planetesimals into ever larger planetesimals described by the Safronov and Hayashi groups is a result of their use of positive-definite expressions for the mutual gravitational perturbations of the planetesimals. The more complete expressions developed by Stewart include terms that tend to equipartition energy between the largest and smallest bodies of the swarm. As a result of this effect, together with collisional and gas drag, and other physically plausible phenomena, runaway growth of bodies up to  $\sim 10^{26}$  g in mass appears more likely than orderly growth. These runaways are in general similar to those found by Greenberg and his coworkers, in spite of the fact that their results now seem to have been at least in part a computational artifact. As a result of these runaways it seems likely that the final stages of accumulation would begin with a smaller (e.g. 30) number of  $\sim 2 \times 10^{26}$  g bodies, accompanied by a retinue of smaller bodies. It may still be expected that this will lead to a final stage of accumulation accompanied by giant impacts that may be responsible for the ejection of the moon from the Earth, and the loss of silicate material from Mercury.

### B. Final Stages of planetary growth.

These newer results on the early stage of growth have been included in more recent calculations of the growth of the terrestrial planets, that also include in a very approximate way the fragmentation of the growing planets. As mentioned above, these results are at least qualitatively similar to those found earlier. One interesting result of inclusion of fragmentation is the possible isolation of a population of moderate-size fragments ("vulcanoids") that could cause the cratering history of Mercury to differ from that of the other terrestrial planets.

### C. Evolution of the asteroid belt.

Understanding asteroidal evolution is essential to the incorporation of the wealth of laboratory data obtained by laboratory studies of meteorites into the more general context of solar system formation. Work has begun on extending the methods used for investigating the early stages of terrestrial planet growth to the asteroidal



belt. Preliminary results suggest that the longer accumulation time scale associated with the greater heliocentric distance of the asteroid belt, together with long range planetary perturbations may allow fragmentation to abort runaway in this region of the solar system, and lead to the present mass and orbital distribution of the asteroid belt. The record of these early events should be identifiable in meteorites. The relationship of these events to the growth of Jupiter and the other giant planets is also under consideration, and this work is being related to that of other investigators who are also presently concerned with this problem.

#### **D. Dynamics of small bodies in the solar system.**

My earlier work on the role of resonances in the asteroid belt on the delivery of meteorites and Apollo-Amor objects into Earth-approaching orbits has been extended to include planetary cratering. It is found that the same asteroidal fragmentation model that explains the observed meteorite data leads to a cratering rate on Mars several times larger than that on Earth. When combined with the expected contribution from extinct (Apollo-Amor) comets and active comets, however, the present-day cratering rates (per unit area) become quite similar. It is hoped to combine this work with that on the early asteroid belt to obtain some understanding of the ancient relative cratering rate on these terrestrial planets, and the geochemical "veneer" acquired by impact of small bodies early in solar system history.

# PROTOPLANET ACCRETION RATES

J.J. Lissauer and Y. Greenzweig

protoplanet, and complete at least one full orbit of the Sun before encountering the protoplanet. The encounter is followed until the test particle has receded to a considerable distance from the protoplanet, in order to be certain that the closest approach distance is found. In this abstract, we restrict our attention to orbits with no initial eccentricity.

For planar orbits, our results reproduce those of Nishida (1983) and Henon and Petit (1986); the capture cross-section of a protoplanet is  $\propto R^{\frac{1}{2}}$  (assuming  $R \ll R_H$ , see Fig. 1). This is the same functional dependence on protoplanet radius as in the 2-D two-body (constant eccentricity) approximation, even though the colliding particles come from a different region of the disk.

In the case of circular orbits with  $a \sin i = R_H$ , the capture cross-section is  $\propto R$  (Fig. 2). This functional dependence mimics that of the 3-D two-body approximation. Note that the normalized accretion rate is smaller for any given radius than in the  $i = 0$  case. Intermediate power law dependencies result when  $a \sin i \sim 0.1 R_H$ , because at such low inclinations the vertical component of the separation between planetesimal and protoplanet upon approach is significantly smaller than the horizontal component.

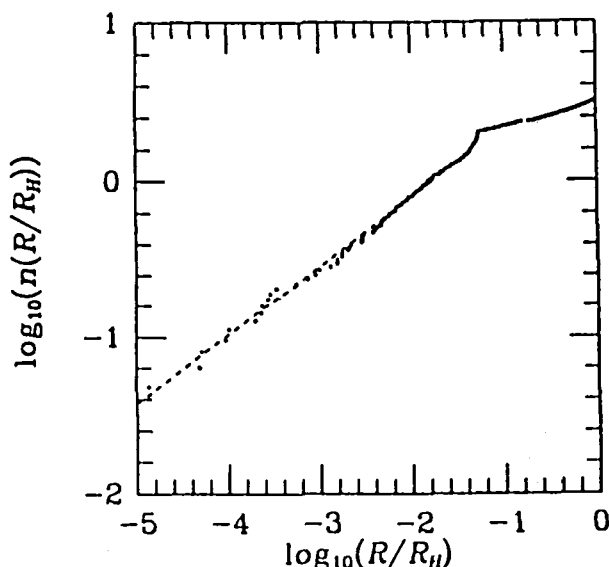


Fig. 1:  $i = 0$

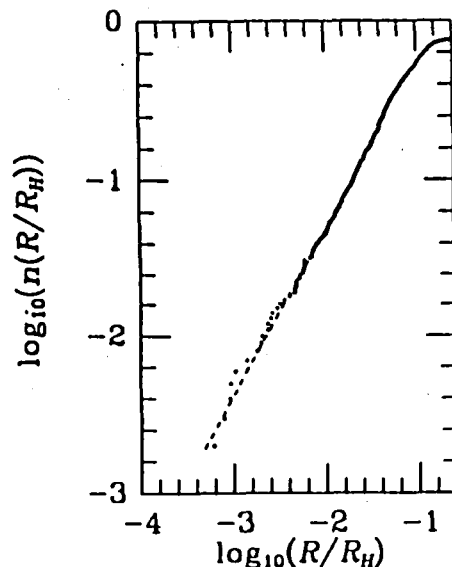


Fig. 2:  $a \sin(i) = R_H$

Bodenheimer, P. and Pollack, J. B. (1986). *Icarus* **67**, 391-408.

Greenberg, R., Wacker, J. F., Hartmann, W. L. and Chapman, C. R. (1978). *Icarus* **35**, 1-26.

Hill, G. W. (1878). *American J. Math.* **1**, 5-26, 129-147, 245-260.

Henon, M. and Petit, J.-M. (1986). *Celestial Mech.* **38**, 67.

Nishida, S. (1983). *Prog. Theor. Phys.* **70**, 93-105.

Safronov, V. S. (1969). *Evolution of the Protoplanetary Cloud and Formation of the Earth and Planets*. Moscow, Nauka Press, also NASA TTF-677, 1972.

Walter, F. M. (1986). *Astrophys. J.* **306**, 573-586.

Wetherill, G. W. and Cox, L. P. (1985). *Icarus* **63**, 290-303.

PROTOPLANET ACCRETION RATES IN A DISK OF PLANETESIMALS WITH LOW RANDOM VELOCITIES; J. J. Lissauer and Y. Greenzweig, Physics Department, University of California, Santa Barbara, CA 93106

Safronov's (1969) theory of accretion of planets from small solid planetesimals states that the cores of the gas giant planets required  $\gtrsim 10^8$  years to grow large enough to trap substantial amounts of gas from the solar nebula (Bodenheimer and Pollack 1986). However, observations of regions of current star formation suggest removal of gases from the protoplanetary disk on a  $10^6$  year timescale (Walter 1986). The cores of the giant planets could have accreted much faster via "runaway accretion" of solid particles, in which one protoplanet grows much more rapidly than other bodies in its accretion zone. Random velocities are kept low by collisions between small planetesimals, which contain most of the mass. The gravitational focusing cross-section of the protoplanet thus greatly exceeds its physical cross-section, and the accretion rate increases as the fourth power of the protoplanet's radius (Greenberg et al. 1978). Eventually, the protoplanet's accretion zone becomes so large that the two-body planetesimal-protoplanet encounter is modified by the Sun, and a full three-body treatment is required. Nishida (1983) has performed numerical integrations of the planar three-body accretion problem. Wetherill and Cox (1985) have studied the full three dimensional problem for the special case of protoplanets with the density of an uncompressed Earth and located 1AU from the Sun. We have extended these 3-D studies to the more general case of arbitrary protoplanet size and location using a combination of analytic scaling and numerical simulations.

A completely general analysis of collision cross-sections in the 3-body problem requires coverage of a parameter space of eleven dimensions. For the problem of planetary accretion, the dominance of the Sun's mass allows the use of certain approximations developed in Hill's (1878) lunar theory. Any encounter can be scaled to an equivalent encounter of a massless point planetesimal on a trajectory determined by 5 orbital elements with a protoplanet of equivalent mass  $M$  and equivalent radius  $R$  on a circular orbit. The mass, radius and semi-major axis of the protoplanet can be reduced to one parameter,  $R/R_H$ , where  $R_H$  is the radius of its Hill sphere (Henon and Petit 1986). Accretion rates can then be calculated by numerically computing the trajectories of planetesimals with a given distribution in orbital elements and comparing the closest approach distances with the protoplanet's normalized radius. Even these simplifications leave a five dimensional parameter space of planetesimal orbits to be explored; thus the results presented herein are limited to a few special cases of planetesimal velocity dispersions.

Our numerical procedure is as follows. Newton's equations of motion are integrated for test particles, with gravity of the Sun and that of the protoplanet being the only forces present. The protoplanet's mass is  $10^{-6}M_\odot$ , so errors induced by Hill's approximation are  $\leq 1\%$ . The integrator uses the extrapolation algorithm of Bulirsch and Stoer (1966). The variables of the integration are cartesian in the rotating frame, but initial and final conditions are given in heliocentric orbital elements. Initial conditions of the orbits are chosen to span the available phase space with good uniformity in order to enhance the statistical significance per orbit. This is achieved by choosing the uniformly distributed variables' initial conditions as multiples of irrational numbers (like the Golden Mean), folded back on the appropriate interval. For the runs with constant inclination and eccentricity, for example, the semimajor axis is incremented by a constant amount per orbit, while the longitude of the apse and the longitude of the ascending node are generated at each step by two distinct irrationals as explained above. Individual trajectories are computed beginning at least  $20 R_H$  away from the

Protoplanet Accretion Rates in a Uniform Disk of Planetesimals  
Neglecting Gravitational Focusing

Y. Greenzweig and J. J. Lissauer (U.C. Santa Barbara)

We calculate analytically the rate at which a protoplanet on a circular orbit collides with planetesimals on unperturbed heliocentric trajectories. The effects of gravitational focusing by the protoplanet can be accounted for to first order by multiplying the protoplanet's accretion cross section by  $(1 + (V_e/V)^2)$ , where  $V_e$  is the protoplanet's escape velocity, and  $V$  is the relative velocity of the protoplanet and planetesimal prior to encounter (Safronov, NASA TTF-677, 1972). Öpik (1951, *Proc. R. Ir. Acad. A* 54, 165), Wetherill (1967, *J.G.R.* 72, 2429), and Greenberg (1982, *A.J.* 87, 184) have computed (non-gravitational) collision probabilities in the rectilinear-orbit approximation, i.e., approximating the orbits by straight line segments at the point of intersection. We integrate collision probabilities over a disk of planetesimals of unique eccentricity,  $e$ , and inclination,  $i$ , and with a uniform distribution of apse and node longitudes and uniform surface density,  $\sigma$ , in order to determine the accretion rate. We begin by using the rectilinear approximation, and then derive the order of the correction term due to the curvature of the orbits, all this in the epicyclic approximation. To treat the curvature we use an expansion parameter  $R/(ae)$ , where  $R$  is the radius of the protoplanet, and  $a$  its semimajor axis. For the 3-dimensional problem, the mass accretion rate is

$$A_{3D} = \frac{\sigma R^2}{T} \left\{ \frac{4\sqrt{1+I^2}}{I} E\left(\sqrt{\frac{3}{4(1+I^2)}}\right) + O\left(\frac{R}{ae}, e^2\right) \right\},$$

where  $I \equiv i/e$ ,  $T$  is the planet's orbit period, and  $E(k)$  is the Complete Elliptic Integral of the Second Kind. Note that the fractional correction due to curvature is of order  $R/(ae)$ . We also derive the order of the corrections due to multiple hits (by any particular planetesimal within one synodic period) and other effects, demonstrating that they are of yet higher order in  $R/(ae)$ . The results may be applicable to low density (fluffy) accretors, in the moderate random velocity regime. As a second application, they can be used to normalize the gravitational enhancement factor,  $F_g$ , defined by Wetherill and Cox (1985, *Icarus* 63, 290). This research was supported in part by the NASA Planetary Geology and Geophysics Program.

## GRAVITATIONAL FOCUSSING DURING PLANETARY ENCOUNTERS

Richard Greenberg<sup>1</sup>, Giovanni B. Valsecchi<sup>2</sup>, and Andrea Carusi<sup>2</sup>

1. Lunar and Planetary Lab, Univ. of Arizona

2. IAS Reparto Planetologia, Roma

Our recent work on gravitational encounters between planetary bodies (Greenberg et al., Icarus 1988, in press) shows that apparent failure of the two-body approximation, although it may appear to be related to low encounter velocities, is often simply the result of distant perturbations long before encounter. Such perturbations can modify the geometry of an encounter so that the outcome is quite different from the predictions of the Opik two-body formulation, even though the actual encounter follows two-body behavior quite well. The importance of our result is that statistical mechanical treatments of collisional, keplerian swarms may still be able to invoke two-body (Rutherford scattering) formulae even given the very low relative velocities that may pertain, for example in planet formation.

That conclusion appears to contrast with the results of Wetherill and Cox (Icarus 60, 40, 1984; Icarus 63, 290, 1985; here called W&CI and W&CII, respectively) that the key criterion for success of the two-body approximation is that the encounter velocity  $V$  must be sufficiently large compared with the escape velocity  $V_e$ . Based on Monte Carlo numerical experiments, Wetherill and Cox found that the two-body approximation generally fails if  $V/V_e$  is less than about 0.35.

Reinterpretation of the results of W & C shows they are, after all, consistent with the results of our own numerical studies of motion at encounter. For example, W&CI compare "gravitational focussing" as computed in three-body numerical integration of encounter motion with the focussing predicted by the two-body formula:

$$d/b = (1 + (V_{e@d}/V)^2)^{-1/2}$$

where  $b$  is the impact parameter,  $d$  is the actual encounter distance, and  $V_{e@d}$  is the escape velocity at distance  $d$ .

W&CI show results in which the agreement between three-body numerical integration (including the two bodies involved in the close encounter, plus the sun) and the two-body formula is excellent for  $V/V_e > 0.35$ , but grossly inconsistent for  $V/V_e < 0.35$ . However, we note that in those experiments the cases with larger  $V/V_e$  also had integration starting at much greater separation distances, so that W&CI's experiments could equally well be interpreted as supporting our findings that distant perturbations can sometimes be more critical than encounter speed.

Here we show that distant perturbations are the dominant factor, rather than encounter speed. When starting distances are great enough to allow significant distant perturbations, the higher  $V/V_e$  case can give the same apparent breakdown of the two-body method as W&CI found in the low  $V/V_e$  case; Conversely, at very low values of  $V/V_e$ , where W&CI's criterion would predict failure, the two-body method works reasonably well.

Consider W&CI's Figs. 9 and 11 shown here as Figs. (a) and (b) respectively. Both figures show results of Monte Carlo experiments on

encounters of small particles with a hypothetical planet on a circular orbit at 1 AU. Particles have orbital eccentricities  $e = 0.00447$  and inclinations  $i = 10^{-5}$  in both cases, but the planetary mass is  $6 \times 10^{22}$  gm in (a) and  $6 \times 10^{25}$  gm in (b). (Note the typographical error in the mass in W&CI's caption for (a).) Thus the parameter  $V/V_e$  is 0.67 in (a) and only 0.067 in (b).

We see that in Fig. (a) with the larger value of  $V/V_e$ , the  $b$  vs.  $d$  relation agrees perfectly with the prediction of the two-body formula above. W&CI show the line  $b = d$ , but even the drop below that line for smaller values of  $b$  is in good agreement with the two-body formula. In Fig. (b) with the small  $V/V_e$ , there is little agreement.

However these results do not demonstrate the role of the parameter  $V/V_e$  because of systematic differences in the initial separation distance. In both cases the initial separation distance was 55 times the radius of the Tisserand sphere of influence of the planet. But because the planet's mass was very different in the two cases, the actual initial separation was much greater for (b) than for (a): 0.054 AU and 0.0034 AU respectively. This difference in initial separation distance is such that for Fig. (b) the test particles were exposed to strong pre-encounter perturbations, which tend to occur during critical intervals that appear as loops in the rotating, planetocentric reference frame. The much closer starting distances of Fig. (a) prevented such effects.

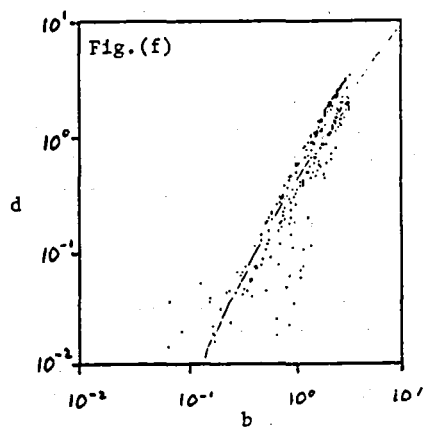
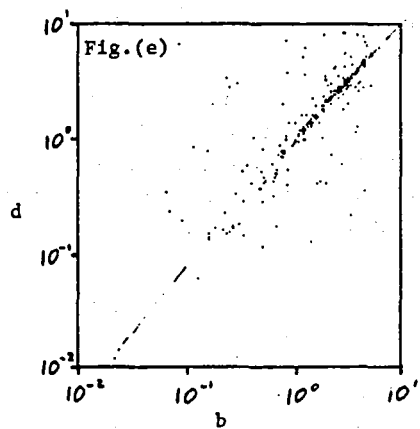
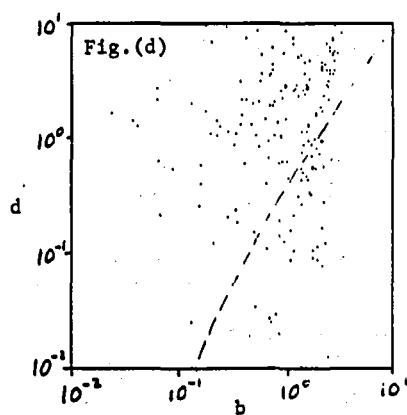
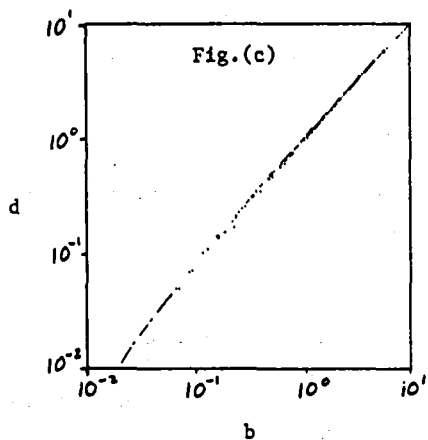
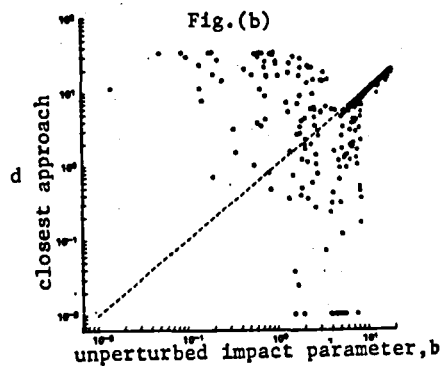
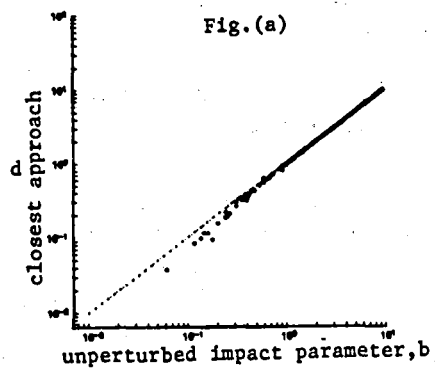
In order to confirm our suspicions, we repeated these experiments with different initial separation distances than W&CI used. First, we reproduced their results with our set of Monte Carlo experiments. Figs. (c) and (d) show our results equivalent to Figs. (a) and (b), respectively. We have reproduced their results quite well. Note that the dashed curve shows the two-body relation for  $b$  vs.  $d$ .

Next we repeated the case with the smaller planetary mass (as in Figs. (a) and (c)), but with the greater initial separation (as in Figs. (b) and (d)). According to the interpretation of W&CI, this new case should also give good agreement with the two-body formula, because  $V/V_e$  is still large. Our prediction was that the agreement would fail due to the enhanced pre-encounter distant perturbations. As shown in Fig. (e), our prediction was borne out.

Finally, we examined the converse case, with the same mass and  $V/V_e$  as Figs. (b) and (d), but with the smaller initial separation. The W&CI interpretation would predict poor agreement with the two-body formula, while we expected reasonably good agreement because pre-encounter perturbations would be minimal. Again our interpretation was borne out as shown in Fig. (f).

These numerical experiments thus serve to support our thesis that the two-body approximation can be useful even for very low values of  $V/V_e$ . Thus it may be possible to use two-body dynamics in the problem of planetary accretion, even in the intermediate stage of planet growth when values of  $V/V_e$  were very small for encounters of planetesimals with planetary embryos. Of course, the two-body approximation must be used with care under these conditions, but at least we do have the prospect of making the

simulation of intermediate stage growth a tractable problem by this approach.



## COLLISIONAL DYNAMICS OF PARTICULATE FLOWS: COMPUTATIONAL STUDIES

William W. Roberts, Jr.  
Department of Applied Mathematics  
University of Virginia

### ABSTRACT

Computational studies are carried out on the collisional dynamics of particulate flows in two areas of current focus: (1) the cloudy interstellar medium in disk-shaped galaxies, and (2) the terrestrial, hypersonic flow of rarefied, strongly-stratified gas past an obstacle.

An "N-body," cloud-particle computational code is developed for the studies in area (1) and utilized to focus on the different roles played by orbital dynamics and dissipative cloud-cloud collisions in the formation of giant molecular clouds in the global spiral structures of disk-shaped galaxies (Roberts and Stewart, 1987). The interstellar medium is simulated by a system of particles, representing clouds, which orbit in a spiral-perturbed, galactic gravitational field. Detailed comparisons are made between (i) the results of cloud-particle simulations in which the cloud-particles collide inelastically with one another and give birth to and subsequently interact with young star associations and (ii) the results of stripped-down simulations in which cloud-cloud collisions and star formation processes are omitted.

The computational studies in area (2) are focused on the three dimensional, hypersonic flow of rarefied, strongly-stratified gas past an obstacle, the incident gas stratified in a direction transverse to the mean flow (Roberts and Hausman, 1987). An "N-body" computational code based on Monte Carlo techniques is developed for these purposes. Our primary interest is centered on the three-dimensional effects induced in the gas flow by a solid obstacle comparable in size to the gas scale height and collisional mean free path. The computed results show that the obstacle induces large systematic motions in the gas, with strong radially-inward driven flow in the (radial) direction of the gradient of density stratification, and correspondingly-large density perturbations in these regions. The radial inflow of gas is prominent not only in the neighborhood of the obstacle and downstream from it but also at considerable distances radially inward from it and at z-heights well above and below. The radially-driven gas inflow is a striking three-dimensional effect induced when strongly-stratified gas impinges upon an obstacle; it constitutes a major characteristic common to all the hypersonic, stratified flows studied despite differences in Mach number, gas scale height, and shapes of obstructing objects.

The physical problems in areas (1) and (2) span far different physical scales; yet the computational techniques developed for each area, if properly utilized to complement one another, may have application to problems on other (intermediate) physical scales such as the collisional dynamics of particulate disks in the Solar System and planetary rings.

This work was supported in part by the Department of Energy under Grant DE-AC05-82OR20900, the National Science Foundation under Grants AST-82-04256 and MCS-83-04459, and the National Aeronautics and Space Administration under Grant NASA-NAGW-929.

Roberts, W. W., Jr. and Hausman, M. A. 1987, *J. Comput. Phys.* (subm. for publ.).  
Roberts, W. W., Jr. and Stewart, G. R. 1987, *Astrophysical J.*, Vol. 314, pp. 10-32.



N-BODY SIMULATIONS OF THE CLOUDY INTERSTELLAR  
MEDIUM IN DENSITY WAVE-DOMINATED GALAXIES:  
ORBIT TRAPPING, SLOSHING, SELF GRAVITY,  
AND SPIRAL STRUCTURE

William W. Roberts, Jr., David S. Adler, and Glen R. Stewart  
University of Virginia

Fluid dynamical problems in galaxies have been of considerable interest to C.C. Lin and a focus of his own research for more than two decades, dating from the early 1960s. The structure and dynamics of galaxies, the grand design spiral structures often observed, and the behavior of density wave modes constitute but a few of C.C. Lin's own research interests and those which he has helped cultivate and stimulate in his students and colleagues over the years. It was C.C. Lin's influence on this graduate student (WWR) in applied mathematics here some twenty years ago which strongly motivated initial research on galaxies and on fluid dynamical phenomena evident in galactic systems.

An N-body, cloud-particle computational code is developed for the purpose of isolating and studying various physical mechanisms and dynamical processes underlying the "cloudy" gaseous interstellar medium in density wave dominated galaxies.<sup>1,2,3,4</sup> The gaseous interstellar medium is simulated by a system of particles, representing clouds, which orbit in a spiral-perturbed galactic gravitational field. Self gravitational effects of the clouds are included via Fourier Transform techniques.<sup>5,6,7</sup> The cloud-particles undergo dissipative collisions with other clouds and experience velocity-boosting interactions with expanding supernova remnants. Associations of protostars form in clouds following such collisions and supernova interactions but take finite times before becoming active themselves and undergoing their own supernovae events.

Figure 7 shows the results when the self-gravitational effects of the gas are put back into the model (10% gas mass fraction). In the preceding case without gaseous self-gravity, the gas response along the global spiral wave arms was only moderately ragged with modest clumping into large complexes, entirely due to the presence of energy dissipating cloud-cloud collisions. Here with gaseous self-gravity, the gas cloud system exhibits a much more ragged global spiral structure. Massive aggregations and large complexes of clouds are much more evident. Of prime importance are the gravitational effects driving the low velocity dispersion gas, including its own self gravity. Gravitationally driven crowding and temporary trapping of cloud orbits in spiral arms, along with dissipative cloud-cloud collisions, underlie the aggregation of the clouds into the giant cloud complexes as well as the organization of the complexes along the ragged global spiral structures. The loosely-associated aggregations and giant complexes of clouds are found to continually disassemble and reassemble rather naturally over time under the influence of the various physical mechanisms and dynamical processes underlying the cloudy ISMs in these model spiral galaxies.

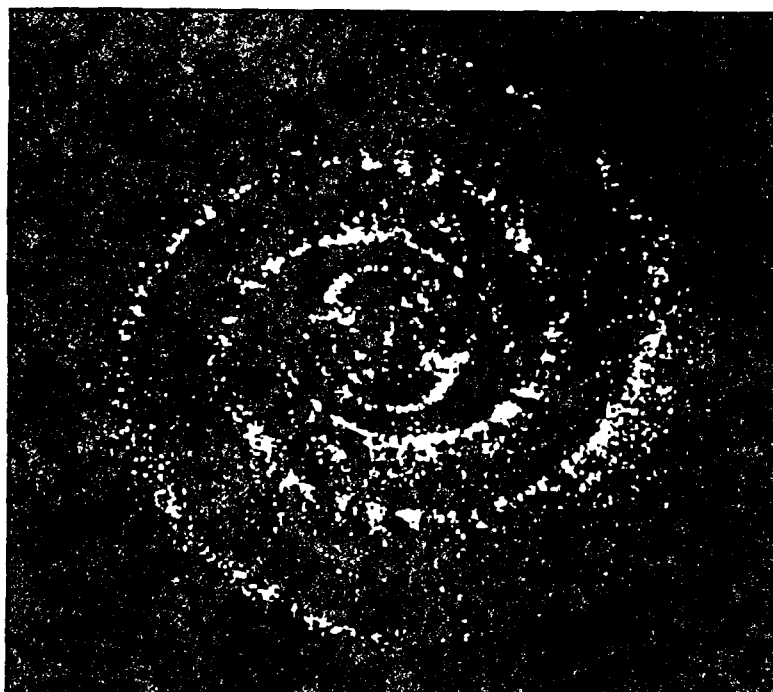


Figure 7.

An intriguing challenge is already emerging within the current theoretical and computational studies. This bears on the important multifold role played by the gas in its self gravitation. As already evident in Figure 7 when self-gravitational effects of the gas are present, the global distribution of the gas becomes quite ragged, with massive aggregations and large complexes of clouds appearing throughout the global spiral structures. For higher gas content, the situation becomes even more interesting. For cases in which the gas mass fraction exceeds a moderate value (25%), what is most striking is the strength with which gas cloud aggregations and complexes interact on local scales and strongly perturb the global two-armed gaseous spiral structure. These perturbations take the form of multitudes of spurs, feathers, and secondary features. The most urgent questions requiring immediate attention in view of these new results are the fundamental questions of stability and persistence. To what extent do these continually-evolving, transient manifestations naturally perturb and rip apart the global spiral structure? To what extent do they enhance the global structure? In the present studies, local spurs, feathers, and secondary features continually break apart and reform as the loosely-associated aggregations and giant complexes of clouds continually disassemble and reassemble over time. Can the global spiral structure persist, in particular for higher gas mass fractions, where there are significant perturbations on local scales? If so, under what conditions?

#### Acknowledgements

This work was supported in part by the National Science Foundation under grants AST-82-04256 and MCS-83-04459 and the National Aeronautics and Space Administration under grant NAGW-929.

#### References

1. Roberts, W. W. and Hausman, M. A. 1984, Ap. J., 277, 744.
2. Hausman, M. A. and Roberts, W. W. 1984, Ap. J., 282, 106.
3. Roberts, W.W., and Stewart, G.R. 1987, Ap. J., 314, 10.
4. Adler, D.S., 1987, Ph.D. Dissertation, University of Virginia, in preparation.
5. Miller, R.H. 1976, J. Comput. Phys., 21, 400.
6. Miller, R.H. and Smith, B.F. 1979a, Ap. J., 227, 407.
7. Miller, R.H. and Smith, B.F. 1979b, Ap. J., 227, 785.

# THE CLOUDY INTERSTELLAR MEDIUM: AGGREGATION OF GIANT MOLECULAR CLOUDS IN SPIRAL STRUCTURES

William W. Roberts, Jr. and David S. Adler  
University of Virginia  
Charlottesville, Virginia

Physical mechanisms and dynamical processes underlying the clumpy, cloudy ISMs of spiral galaxies are investigated. Through computational studies, we focus on the important roles played by the orbital dynamics of ISM clouds, dissipative cloud-cloud collisions, and self gravitational effects in the aggregation of giant molecular clouds in the global spiral structures of such galactic systems.

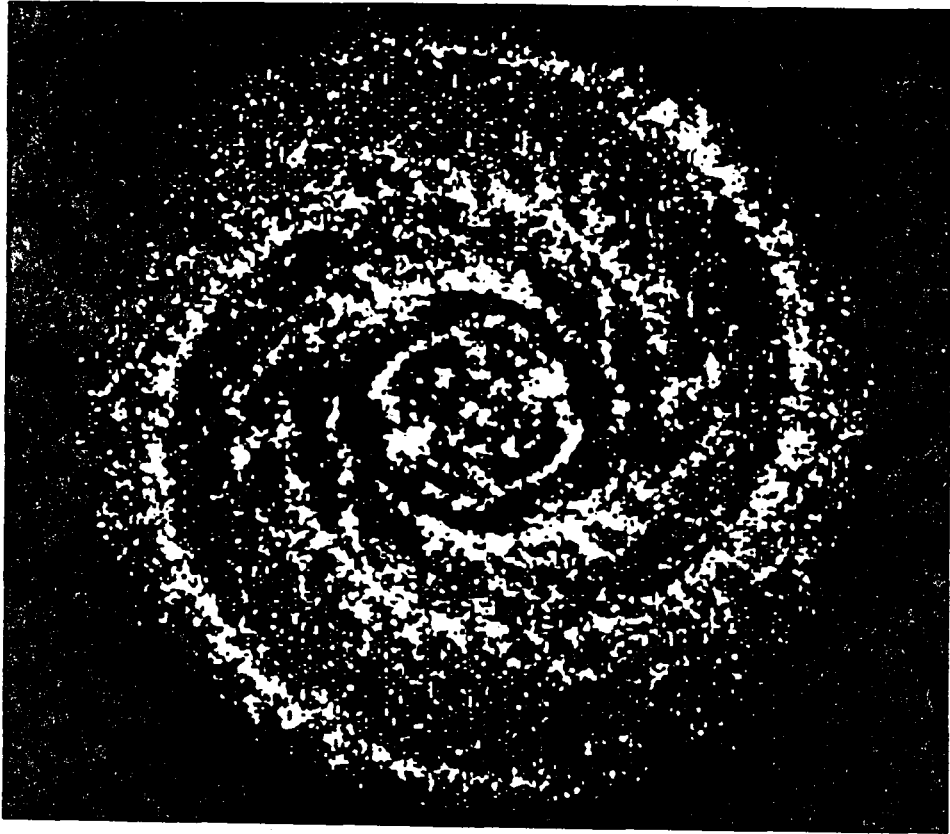


Figure 1. Photographic intensity map of the gas (patches) and young to middle-aged stellar association (white dots) distributions in a representative simulation at a sample epoch [ $t = 800$  Myr] during the computations.



Figure 4.

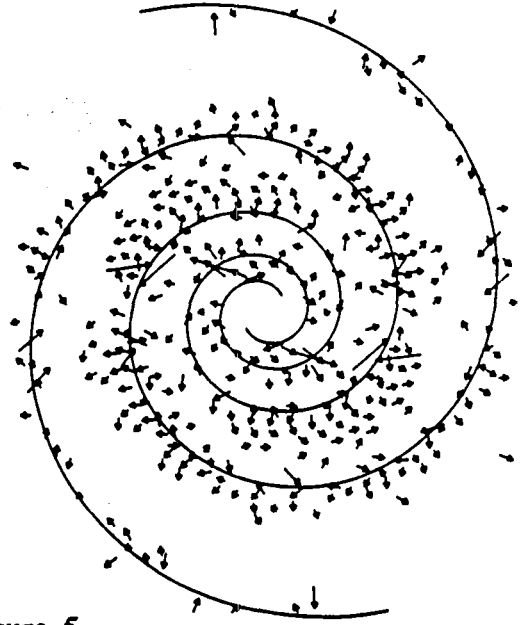


Figure 5.

Figure 4. Instantaneous velocity vectors of 1000 gas clouds (per half disk) randomly selected. Dots are at current positions of clouds; line segments point along velocity directions. Note that all velocities are shown with respect to the frame corotating with the spiral perturbation.

Figure 5. Local velocity differences between post-supernova associations and clouds. Only differences significant at better than the  $1\sigma$  level are shown.

The intriguing nature of the cloud system's orbit crowding leads us to inquire whether there are any significant differences between the stellar and cloud velocity fields. Figure 5 examines this by displaying the differences between the average stellar and cloud velocities. Each arrow is at the center of one of the 576 bins and points in the direction of the (stellar association - cloud) velocity difference. The stellar associations considered here are those young to middle aged stellar associations which have undergone their supernova events up to 60 Myr in the past. Only those bins in which the velocity difference is statistically significant to the one-sigma level are represented, assuming an intracell velocity dispersion of  $6 \text{ km s}^{-1}$  (one dimension).

We can see that across much of the disk, especially the interarm regions, the difference between the average stellar and cloud velocities is indeed small. However near the arms the differences are significant and of order of  $10\text{-}20 \text{ km s}^{-1}$ . In particular, stellar associations just outside (i.e. downstream) of the spiral arm region tend to have a positive radial component relative to the clouds. It is natural that the differences should be greatest in the arms, since this is where the higher frequency of cloud collisions and SNR impulses will have the greatest influence on the clouds' otherwise unperturbed trajectories. The positive radial velocity difference of the stellar associations in the arms apparently reflects the loss of kinetic energy which collisions inflict upon the cloud orbits. Note that because the stellar associations considered here were all formed within clouds no more than 80 Myr (and active no more than 60 Myr) in the past, about two-thirds the time required for a single passage between spiral arms, the stellar associations are still rather strongly correlated with their parent clouds and the velocity differences shown in Figure 5 are lower than is typical for older, more common stars.

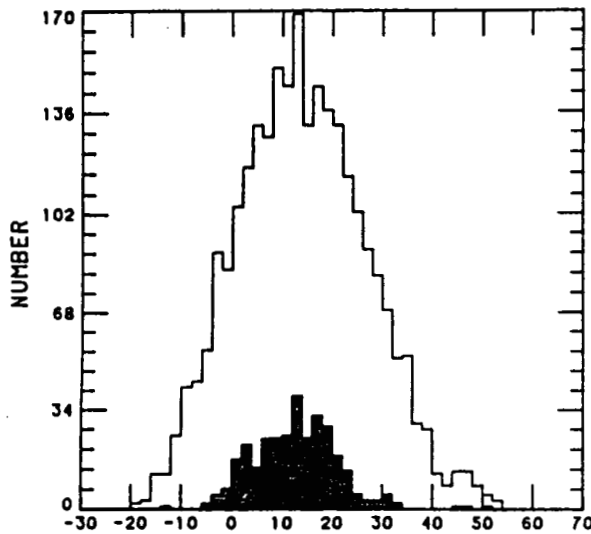


Figure 6a.  $U_{\perp}$  KM/S

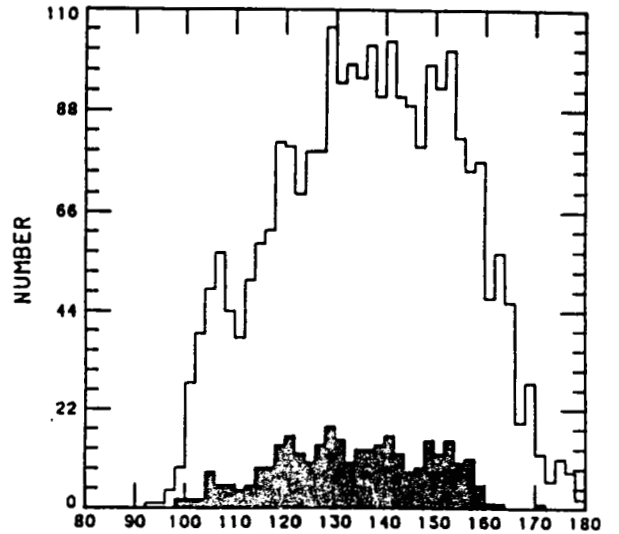


Figure 6b.  $U_{\parallel}$  KM/S

Figure 6. Histograms of the components of the stellar association velocities perpendicular and parallel to loci of constant spiral phase. The blackened sample is presupernova associations; the white sample is postsupernova associations. Both samples are restricted to galactocentric radius 4 - 10 kpc and spiral phase  $150^{\circ}$  -  $240^{\circ}$ .

In our model the velocities of clouds and newborn stellar associations are determined self-consistently by their physical interactions, so we need make no restrictive assumptions about initial velocities of the newborn associations. Figure 6 shows histograms for the velocity components of stellar associations perpendicular [Fig. 6a] and parallel [Fig. 6b] to lines of constant spiral phase. The black-shaded sample denotes the presupernova (not yet active) associations; the white sample denotes the postsupernova associations active during the past 60 Myr. Both samples are restricted to galactocentric radius 4 - 10 kpc and spiral phase  $150^{\circ}$  -  $240^{\circ}$ . Because the velocity changes in our cloud-particle models' arms are not discontinuous, we find initial velocities spanning the full range between pre-arm and post-arm values. In Figure 6a, we see that both presupernova and postsupernova associations are peaked strongly in the range 10 - 20  $\text{km s}^{-1}$  with only small tails in the negative region. Very few associations recross the potential minimum inwards; most associations penetrate the downstream interarm region to varying distances.

#### Acknowledgements

This work was supported in part by the National Science Foundation under grants AST-82-04256 and MCS-83-04459 and the National Aeronautics and Space Administration under grant NAGW-929.

#### References

- Adler, D.S., 1987, Ph.D. Dissertation, University of Virginia, in preparation.
- Hausman, M. A. and Roberts, W. W. 1984, Ap. J., 282, 106.
- Miller, R.H. 1976, J. Comput. Phys., 21, 400.
- Miller, R.H. and Smith, B.F. 1979a, Ap. J., 227, 407.
- Miller, R.H. and Smith, B.F. 1979b, Ap. J., 227, 785.
- Roberts, W. W. and Hausman, M. A. 1984, Ap. J., 277, 744.
- Roberts, W.W., and Stewart, G.R. 1987, Ap. J., 314, 10.

Gaseous Self Gravitational Effects in the  
Aggregation of Giant Molecular Clouds and  
the Stability of Global Spiral Structures

William W. Roberts, Jr. and David S. Adler  
University of Virginia

Self-gravitational effects of the clumpy, cloudy ISM in model spiral galaxies are shown to play an important multifold role in the global distribution of gas in the disks. For cases in which the gas to stellar disk mass fraction is low, e.g. 5% - 20%, the global distribution of the gas becomes quite ragged under the influence of gaseous self gravitational effects, with massive aggregations and large complexes of clouds appearing throughout the global spiral structures. For higher gas content, the situation is even more interesting. For cases in which the gas mass fraction exceeds a moderate value (25%), what is most striking is the strength with which gas cloud aggregations and complexes interact on local scales and strongly perturb the global two-armed gaseous spiral structure. These perturbations take the form of multitudes of spurs, feathers, and secondary features.

The most urgent questions that need investigation in view of these results are the fundamental questions of stability and persistence. To what extent do these continually-evolving, transient manifestations naturally perturb and rip apart the global spiral structure? To what extent do they enhance the global structure? In our present studies, local spurs, feathers, and secondary features continually break apart and reform as the loosely-associated aggregations and giant complexes of clouds continually disassemble and reassemble over time. Can the global spiral structure persist, in particular for higher gas mass fractions, where there are significant perturbations on local scales? If so, under what conditions? These important issues are under current investigation within the framework of the computational studies.

This work was supported in part by the National Science Foundation under Grant AST-82-04256 and the National Aeronautics and Space Administration under Grant NASA-NAGW-929.

The Mass Spectrum of Molecular Clouds  
in Computational Studies of Spiral Galaxies

David S. Adler and William W. Roberts, Jr.  
University of Virginia

Physical mechanisms and dynamical processes underlying the mass spectrum of molecular clouds in the cloudy ISMs of spiral galaxies are investigated. Through computational studies, we focus on the important roles played by the orbital dynamics of ISM clouds, dissipative cloud-cloud collisions, self gravitational effects, and star formation processes. The assembly of giant cloud complexes from smaller clouds is found to be remarkably efficient in view of the fact that collisional coalescence of individual clouds into larger entities is not a requirement of the model. Gravitationally driven crowding and temporary trapping of cloud orbits in spiral arms, along with dissipative cloud-cloud collisions, underlie the aggregation of the clouds into the giant cloud complexes as well as the organization of the complexes along the ragged global spiral structures. Likewise, the dispersal of giant cloud complexes is not restricted in dependence on rapid and highly disruptive star formation episodes. The loosely-associated aggregations and giant complexes of clouds in the computational studies are followed in their evolution and found to continually disassemble and reassemble rather naturally over time under the influence of the various physical mechanisms and dynamical processes underlying the cloudy ISMs in these model spiral galaxies. Indeed, it may be that substantially fewer GMCs than heretofore thought are gravitationally bound entities.

This work was supported in part by the National Science Foundation under Grant AST-82-04256 and the National Aeronautics and Space Administration under Grant NASA-NAGW-929.



CHAPTER 4  
PLANETARY INTERIORS, PETROLOGY, AND  
GEOCHEMISTRY



## PROPERTIES OF PLANETARY MATERIALS AT HIGH PRESSURES AND TEMPERATURES

W. J. Nellis, D. C. Hamilton, N. C. Holmes, H. B. Radousky, and F. H. Ree  
Physics Department and Institute of Geophysics and Planetary Physics  
Lawrence Livermore National Laboratory, University of California  
Livermore, CA 94550

M. Nicol  
Department of Chemistry and Biochemistry  
University of California, Los Angeles, CA 90024

Voyager II showed that Uranus has a strong planetary magnetic field, which can be described by a dipole of moment  $0.23 \text{ gauss } R_U^3$ , where  $R_U$  is the planetary radius (25,600 km). The dipole is offset from the center of the planet by  $0.3 R_U$  and its axis is tilted  $60^\circ$  from the axis of rotation. The maximum field at the surface is 1.1 gauss (1), twice the value for the Earth. This unexpected and unusual data emphasizes the need for measurements for planetary materials at interior conditions in order to derive planetary models. We report new shock-wave electrical conductivity and equation-of-state (EOS) data for planetary "ices" and for a liquid with a composition representative of a mixture of the "ices." Our conductivity data provide density and temperature dependences up to 75 GPa (0.75 Mbar) and 5000 K and provide an upper bound on the value which can be used in dynamo models to explain the magnetic field.

The composition of Uranus is estimated from the mass, radius, rotational rate, and gravitational field (2,3). The magnetic field data of Ness *et al.*, yielded an improved measurement of the rotation rate of the interior of 17.3 hours (1). This result led to improved values of the density moments which provide a constraint on the equations of state of candidate materials. Prior to Voyager II Hubbard and MacFarlane proposed that Uranus consists of three layers: an outer gas layer of  $H_2$ -He, a middle "ice" layer composed mostly of  $H_2O$ ,  $CH_4$ , and  $NH_3$ , and an inner rocky core (2).

After Voyager II Kirk and Stevenson proposed that the magnetic field and the density moments are consistent with a greater degree of material mixing (4), than in the pre-Voyager models. One model consists of an outer gas-ice-rock region, which is mostly  $H_2O$ - $H_2$ , and an inner rocky core. The boundary is at  $0.3 R_U$  and 300 GPa and 6000 K. The magnetic field is produced primarily in a  $H_2O$ -rich region near  $0.7 R_U$  at 50-100 GPa, based on a dynamo model which uses the electrical conductivity of water extrapolated from data up to 10 GPa and 1300 K. A unique model for Uranus is not yet possible. The fact that the magnetic field is centered at  $0.3 R_U$  indicates that the relevant conductivity data is in the range 10-100 GPa and several 1000 K, the regime in which we have made our measurements.

We have measured conductivity and shock temperature data for  $NH_3$  to 61 GPa, for  $CH_4$  to 37 GPa, and for the mixture we call "synthetic Uranus" to 75 GPa, for which EOS data were also measured. This mixture is H-rich with an H:O composition ratio of 3.5:1 and cosmological abundance ratios of O:C (7:4) and O:N (7:1). It is a solution of water, ammonia, and isopropanol ( $C_3H_8O$ ). High densities and temperatures achieved in shock experiments quickly induce chemical and thermal equilibrium, so that our results are expected to be weakly sensitive to the initial structure of the specimens.

Strong shock waves were generated by the impact of metal plates onto liquid-specimen holders. Plates were accelerated up to 7 km/s by a two-stage light-gas gun. Techniques to measure electrical conductivity (5), shock temperature (6), and equation-of-state data (5) have been described previously.

The conductivities of shock-compressed liquid ammonia, methane, and synthetic Uranus are plotted vs shock pressure in Fig. 1. Previous data for ammonia and water (5) are shown for comparison. Temperature measurements show that our conductivities are in the range 1500–5000 K. Figure 1 shows that the conductivities of synthetic Uranus, water, and ammonia all approach  $20 \text{ (ohm-cm)}^{-1}$  above 40 GPa, thus providing an upper limit on the value of electrical conductivity that can be used in dynamo calculations. Below 40 GPa the conductivity of synthetic Uranus is a factor of 2–3 less than that of water.

Kirk and Stevenson showed that the magnetic field of Uranus can be calculated using the conductivity of water suppressed a factor of 10. They assumed this factor to take account of dissolved insulating  $\text{H}_2\text{-He}$  (4). The conductivity of synthetic Uranus is a factor of 3–5 larger than they used and allows for the presence of insulating phases. Thus, the shock-wave conductivity data for synthetic Uranus is consistent with the dynamo calculations of the magnetic field.

EOS points were measured and chemical equilibrium calculations (7) of the shock-compression curve of synthetic Uranus were performed. The calculations suggest that at lowest pressures methane forms and separates from the water and ammonia. As pressure and temperature increase diamond starts to form and methane has an increasing tendency to stay in solution.

A picture of the nature of materials inside Uranus can now be developed. For example, at depths where the pressure exceeds 100 GPa and temperatures are several 1000 K, molecules and ions are expected to dissociate and form dense, stiff monatomic and/or H–O–C–N species. This statement is based on observations of molecular dissociation at high shock pressures and temperatures. For example,  $\text{N}_2$  dissociates at only 30 GPa at 6000 K (8) but remains molecular to 130 GPa at 300 K (9), illustrating that the high temperatures inside Uranus are expected to drive dissociation. Shock-compression curves for diamond, nitrogen, and oxygen and theoretical curves for monatomic simple-cubic N and O at 0 K (10) are plotted in Fig. 2. The curves for the monatomic phases are all steep. The shock-compression curves of liquid nitrogen and oxygen have steep slopes above 60 GPa and 10,000 K, similar to those of the monatomic phases at 0 K. When dissociation occurs, relatively soft van der Waals molecular repulsion is replaced by stiff interatomic repulsion. This transition is expected to proceed continuously along the planetary isentrope. Rock also has a stiff equation of state at high pressures. Thus, at depths below  $\sim 0.5 R_U$  and pressures above 100 GPa, the planetary materials are close to their limiting compression, which contributes strongly to the large volume of Uranus. In this sense, one can consider all materials in the deep interior to be similar in nature to the high-bulk-modulus diamond phase of carbon, which has been suggested to form inside Uranus (11).

This work was performed under the auspices of the U. S. DoE by LLNL under contract number W-7405-ENG-48, with support from NASA Grants W-16-180 and NAGW-104. Work at UCLA was supported by the LLNL Branch of the UC IGPP.

#### REFERENCES

1. N. F. Ness et al., Science 233, 85 (1986).

2. W. B. Hubbard and J. M. MacFarlane, *J. Geophys. Res.* **85**, 225 (1980).
3. D. J. Stevenson, *Annu. Rev. Earth Planet. Sci.* **10**, 257 (1982).
4. R. L. Kirk and D. J. Stevenson, *Astrophys. J.* **316**, 836 (1987); D. J. Stevenson, *Bull. Am. Astron. Soc.* **19**, 851 (1987) and private communication.
5. A. C. Mitchell and W. J. Nellis, *J. Chem. Phys.* **76**, 6273 (1982).
6. H. B. Radousky *et al.*, in *Shock Waves in Condensed Matter*, edited by Y. M. Gupta (Plenum, New York, 1986), p. 467.
7. F. H. Ree, *J. Chem. Phys.* **81**, 1251 (1984).
8. W. J. Nellis *et al.*, *Phys. Rev. Lett.* **53**, 1661 (1984); H. B. Radousky *et al.*, *Phys. Rev. Lett.* **57**, 2419 (1986).
9. R. Reichlin *et al.*, *Phys. Rev. Lett.* **55**, 1464 (1985).
10. A. K. McMahan and R. LeSar, *Phys. Rev. Lett.* **54**, 1929 (1985); A. K. McMahan, private communication (1987).
11. M. Ross, *Nature* **292**, 435 (1981).

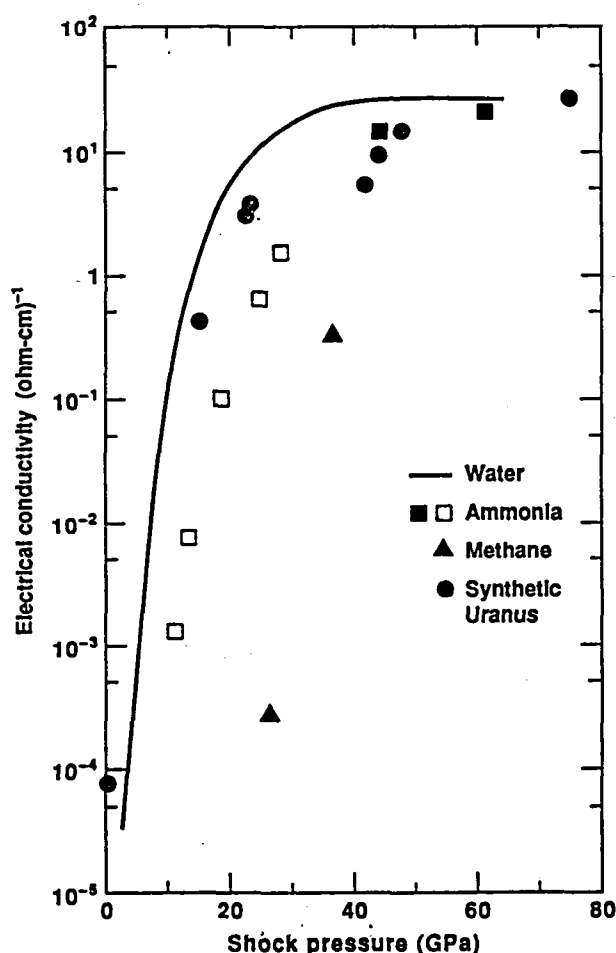


Fig. 1 Electrical conductivity vs. shock pressure for planetary fluids. Solid symbols are this work: Solid curve is smooth curve through earlier water data.

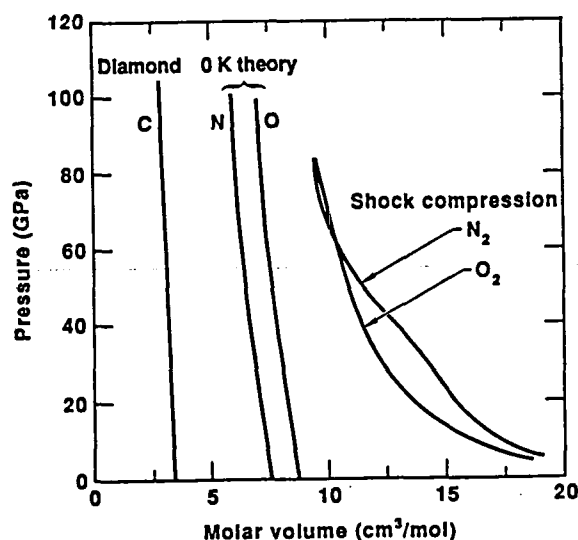


Fig. 2 Shock-compression equations of state for C (diamond) and liquid N<sub>2</sub> and O<sub>2</sub> and calculated O-K isotherms for monatomic N and O. The O-K curve for diamond is nearly same as shock-compression curve shown.

## MELTING STUDIES AT HIGH PRESSURE

William A. Bassett, Maura S. Weathers, and Eugene Huang  
Department of Geological Sciences, Cornell University,  
Ithaca, NY 14853

Focused infrared light from a YAG laser is used to heat samples at high pressure in a diamond anvil cell. Spectra of the incandescent light from the hot sample are obtained by means of a grating spectrometer, photodiode array, and optical multichannel analyzer. These spectra are then fit to blackbody curves to determine the temperature.

The carbon phase diagram is being mapped. We are measuring the temperature of melting of graphite up to the triple point graphite-diamond-melt at ~110 kbar and ~4800 K. At pressures above the triple point we are measuring the temperature of the conversion of graphite to diamond as a function of pressure and the temperature of melting of the diamond as a function of pressure. Our samples consist of fibers of graphite 0.8 micron in diameter imbedded in NaCl. The focused laser beam is used to heat a portion of a fiber at a time. At 120 kbar and temperatures between approximately 3000 K and 5000 K the the portion of fiber heated by the laser becomes transparent but holds its shape indicating a solid-state conversion of graphite to diamond. At temperatures above 5000 K the fibers not only become transparent but are severed at the hottest point. The transparent ends of the fiber at the severed point are rounded indicating the melting of diamond. Ultimately we hope to determine the sign, slope, and pressure dependence of the melt curve of diamond up to several hundred kilobars.

Initially our temperature measurements were too low. This problem probably resulted because we mixed the incandescent light from the highest temperature as well as the lower temperature portions of the sample. We have solved that problem by placing a pinhole where it allows only the light from the highest temperature part of the sample to enter the spectrometer for analysis. Our temperature measurements now agree much more closely with known melting temperatures.

Our criteria for determining if melting took place can also be applied to metals. Fine fibers of metal can be imbedded in NaCl and heated. Melting causes severing of the fiber, a phenomenon that is easily recognized under a microscope even while the sample is still loaded in the diamond cell. Our plan is to apply this method to the study of iron and its alloys and compounds to provide information that can be used to interpret the nature of the cores of the Earth and other planets.

## MELTING STUDIES AT HIGH PRESSURE

William A. Bassett, Maura S. Weathers, and Eugene Huang  
Department of Geological Sciences, Cornell University,  
Ithaca, NY 14853

Focused infrared light from a YAG laser is used to heat samples at high pressure in a diamond anvil cell. Spectra of the incandescent light from the hot sample are obtained by means of a grating spectrometer, photodiode array, and optical multichannel analyzer. These spectra are then fit to blackbody curves to determine the temperature.

The carbon phase diagram is being mapped. We are measuring the temperature of melting of graphite up to the triple point graphite-diamond-melt at ~110 kbar and ~4800 K. At pressures above the triple point we are measuring the temperature of the conversion of graphite to diamond as a function of pressure and the temperature of melting of the diamond as a function of pressure. Our samples consist of fibers of graphite 0.8 micron in diameter imbedded in NaCl. The focused laser beam is used to heat a portion of a fiber at a time. At 120 kbar and temperatures between approximately 3000 K and 5000 K the the portion of fiber heated by the laser becomes transparent but holds its shape indicating a solid-state conversion of graphite to diamond. At temperatures above 5000 K the fibers not only become transparent but are severed at the hottest point. The transparent ends of the fiber at the severed point are rounded indicating the melting of diamond. Ultimately we hope to determine the sign, slope, and pressure dependence of the melt curve of diamond up to several hundred kilobars.

Initially our temperature measurements were too low. This problem probably resulted because we mixed the incandescent light from the highest temperature as well as the lower temperature portions of the sample. We have solved that problem by placing a pinhole where it allows only the light from the highest temperature part of the sample to enter the spectrometer for analysis. Our temperature measurements now agree much more closely with known melting temperatures.

Our criteria for determining if melting took place can also be applied to metals. Fine fibers of metal can be imbedded in NaCl and heated. Melting causes severing of the fiber, a phenomenon that is easily recognized under a microscope even while the sample is still loaded in the diamond cell. Our plan is to apply this method to the study of iron and its alloys and compounds to provide information that can be used to interpret the nature of the cores of the Earth and other planets.

HIGH PRESSURE COSMOCHEMISTRY OF MAJOR PLANETARY INTERIORS: LABORATORY STUDIES OF THE WATER-RICH REGION OF THE SYSTEM AMMONIA-WATER

Malcolm Nicol, Steven Boone, Hyunchee Cynn, and Andrea Koumvakalis  
Department of Chemistry and Biochemistry  
University of California, Los Angeles, CA 90024-1569

Models of the major planets and their satellites make simple, rather arbitrary assumptions concerning deep interiors. "Rock" cores or "ice" (water-ammonia-methane) layers are often invoked without considering thermodynamic consistency. Properties of "gas-ice" mixtures at very high pressures are poorly understood, even under laboratory conditions. When this project began, few measurements existed on binary or multicomponent gas-ice systems at 1 GPa and higher pressures. We set out, therefore, to determine the pressure-temperature-composition (P-T-X) diagram of ammonia ( $\text{NH}_3$ ) and water ( $\text{H}_2\text{O}$ ), with plans eventually to extend the work to include methane ( $\text{CH}_4$ ), hydrogen ( $\text{H}_2$ ), and helium ( $\text{He}$ ).

Our first goal was to show that a multi-phase binary system can be characterized at high pressures with reasonable precision. We began with ammonia-water because these mixtures are relevant to planetary interiors and are relatively easy to prepare. Some of the P-T-X space had been determined, including: P-T surfaces of pure water [see, for example, Mishima and Endo, 1980] and pure ammonia [Mills et al., 1982] and the T-X surface of ammonia-water at atmospheric pressure [Rollet and Vuillard, 1956]. The latter surface includes two water-rich compounds ammonia dihydrate ( $\text{NH}_3 \cdot 2\text{H}_2\text{O}$ ) and ammonia hydrate ( $\text{NH}_3 \cdot \text{H}_2\text{O}$ ). Recent models [Lunine and Stevenson, Icarus, 1987] suggest that dihydrate and hydrate are important in the evolution of the interior and surfaces of the icy satellites. The study was initiated by Ms. Andrea Koumvakalis and Dr. Mary Johnson [Johnson et al., 1985; Johnson and Nicol, 1987] and is being continued by Mr. Steven Boone, Mr. Hyunchee Cynn and Ms. Koumvakalis.

Even ammonia-water, however, presents experimental problems. All of the ammonia-water phases are colorless. When the work began, some phases could be identified at high pressures only unambiguously, by shapes and birefringence. Little also was known about how materials used in pressure cells behave toward ammonia-water mixtures. Thus, we began to map the phase diagram by using visual clues to identify how authentic samples of ammonia dihydrate and ammonia monohydrate might be prepared and characterized by vibrational spectra, x-ray diffraction patterns, and other properties which would unambiguously identify these phases in mixtures. As the following discussion demonstrates, the spectroscopy and diffraction work have shown that some mis-identifications have resulted from unexpected reactivity of the ammonia-water with cell components at high pressures. At such times, the reactive component has to be identified, a substitute material had to be found and tested, and the mapping repeated.

In a recent publication, Dr. Johnson [Johnson and Nicol, 1987] described a visual mapping of the  $(\text{NH}_3)_x(\text{H}_2\text{O})_{1-x}$  phases to  $P = 5$  GPa,  $T$  from 240 to 370 K, and  $x$  from 0.00 to 0.30. This work was done with samples



confined by gaskets of 316 stainless steel. (Dr. Johnson had shown that this steel was not attacked when exposed to 30% ammonia for several weeks at ambient pressure and temperature.) Dr. Johnson observed that, at high pressures, melting at 20%  $\text{NH}_3$  and higher compositions is complex. Although she expressed concern about ambiguous visual identifications, she suggested that the phase diagram could be reasonably well constrained by her observations, including the conclusion that ammonia dihydrate has an important role between 2 and 3.5 GPa at X from 0.15 to 0.30.

During the past year, Mr. Boone and Cynn attempted to prepare authentic samples of the solid which Dr. Johnson called ammonia dihydrate in order to determine its structure and spectra. Mr. Cynn grew large crystals from 33% liquid confined by 316 stainless steel gaskets and showed by x-ray diffraction that the crystals were not ammonia dihydrate. Further studies demonstrated that this and many of the solids, which Dr. Johnson had thought to be dihydrate, were ices and other compounds formed by reactions between the stainless steel and aqueous ammonia at high pressures and temperatures. About the same time, Mr. Boone reached similar conclusions from visual observations of samples of 33% ammonia. Mr. Boone then developed techniques for electroplating steel gaskets with a gold barrier which inhibits reactions between the steel and ammonia-water mixture to at least 50%  $\text{NH}_3$ , 450 K, and 10 GPa.

When Mr. Boone and Mr. Cynn repeated the visual studies of  $(\text{NH}_3)_x(\text{H}_2\text{O})_{1-x}$ , they could not detect crystals similar to those which Dr. Johnson called ammonia dihydrate. With the gold-plated gaskets, Mr. Cynn also obtained good Raman spectra ammonia-water samples; with Raman spectra, he found that the Ice VII-fluid boundary continues from  $X = 0.2$  to the Ice VII-fluid-monohydrate eutectic at 3.4 GPa for X between 0.4 and 0.5. Monohydrate was shown to be in the eutectic by comparing the Raman spectra with spectra of monohydrate which Ms. Koumvakalis and Mr. Cynn prepared from liquid at  $X = 0.50$ . These results will be presented at the December AGU meeting. For her thesis, Ms. Koumvakalis also will collect complete Raman spectrum of ammonia monohydrate and map the  $X = 0.50$  isopleth from 150 to 450 K to above 15 GPa. Mr. Cynn also has grown a large crystal

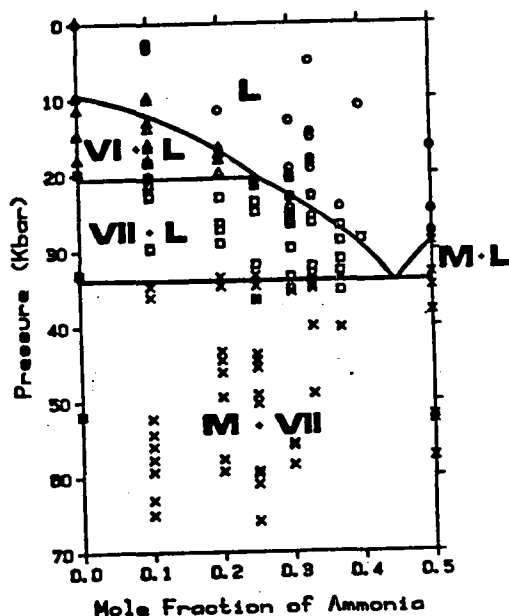
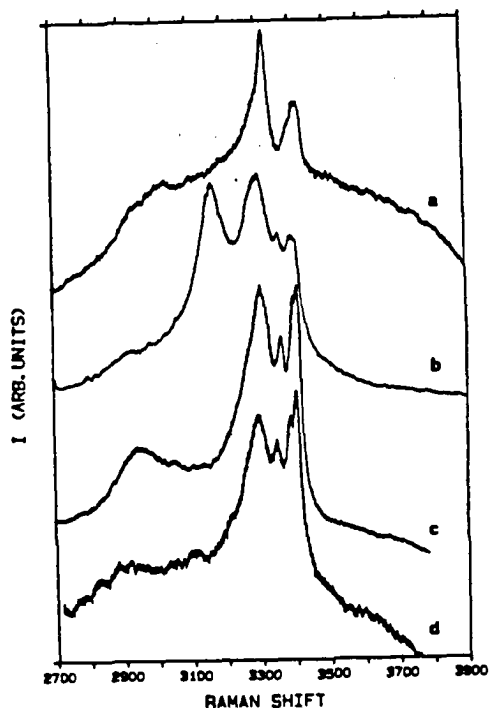


Fig. 1. 295-K isotherm to 7 GPa and 50%  $\text{NH}_3$  determined with samples in gold plated gaskets. Key: X, monohydrate + Ice VII; triangle, Ice VI + liquid; O, liquid; square, Ice + liquid. The eutectic composition is approximate.

of monohydrate at room temperature and is collecting diffraction data in order to determine its structure and density.

Fig. 2. Raman spectra used to distinguish phases of 33%  $\text{NH}_3$ . a: Ammonia dihydrate made by cooling 33% aqueous  $\text{NH}_3$  at 1.6 GPa to 125 K and compressing to 4.1 GPa. b: Ice VII and ammonia monohydrate at 5.9 GPa and 295 K made by compressing 20%  $\text{NH}_3$ . c and d: Ammonia monohydrate made by freezing 50%  $\text{NH}_3$  at (c) at 8.2 GPa and 160 K and (d) 5.2 GPa and 295 K.



With the gold-plated gaskets, Mr. Boone and Mr. Cynn also examined the  $X = 0.33$  isopleth to more than 5 GPa between 100 and 400 K both visually and by Raman spectroscopy. They detected four phases by visual methods and identified three of these phases by Raman spectra as: fluid, Ice VII, and ammonia monohydrate. Although the fourth phase melts incongruently to ammonia monohydrate and Ice VII at high pressures, it can be crystallized from the liquid at pressures less than 1.8 GPa and temperatures below 240 K. Work on the phase diagram, spectra, and growth of a crystal for x-ray diffraction analysis are in progress. Mr. Boone also is preparing for studies of the binary methane-water and methane-ammonia systems.

#### REFERENCES

- Johnson, M. L., A. Schwake, and M. Nicol, 1985, in Klinger J. et al., eds., *Ices in the Solar System* (D. Reidel, Dordrecht) 39-47.  
 Johnson, M.L., and M. Nicol, 1987, *J. Geophys. Res.* 92, 6339-6349.  
 Lunine, J.I., and D.J. Stevenson, 1987, *Icarus* 7, 61-77.  
 Mills, R.L., D.H. Liebenberg, and Ph. Pruzan, (1982), *J. Phys. Chem.* 86, 5219.  
 Mishima, O., and S.J. Endo, 1980, *J. Chem. Phys.* 73, 2454.  
 Rollet, A.-P., and G. Vuillard, 1956, *C. R. Acad. Sci. Paris* 243, 383.

Implications of Convection in the Moon and the Terrestrial Planets  
Donald L. Turcotte, Department of Geological Sciences, Cornell University,  
Ithaca, NY 14853-1504

During the past year we have worked on two principle lines of research:

- 1) The early thermal and chemical evolution of the moon and the terrestrial planets. During the past year we have studied the implications of a variety of models of global geochemical cycles on isotope systematics. We were particularly interested in the role of the recycling of crustal material on the evolution of planetary bodies. The earth's oceanic crust is regularly recycled by plate tectonics and significant quantities of recycling of continental crust may also occur. The mixing of recycled material by mantle convection produces a fertile region for contemporary basaltic volcanism. On the moon and Mars there is essentially no evidence for plate tectonics. However, an important question is whether crustal material can be recycled by crustal delamination? Are the heat producing elements transported to a stable, cool lithosphere thus resulting in a "dead" plate? For Venus similar questions must be considered.

During this period our major effort was to study the tectonic implications of radiogenic  $^4\text{He}$  and  $^{40}\text{Ar}$  in planetary atmosphere. In addition to the PI and Ms. Louise Kellogg this work was carried out in collaboration with Professor Gerald Schubert. From January 1 to May 30, 1987 both the PI and the research assistant Ms. Louise Kellogg were visiting the Institut de Physique du Globe de Paris, University of Paris VI. During this period we actively collaborated on this problem with Professor Claude J. Allegre and his associates in the radiogenic isotope group.

For the earth constraints on the total  $^{40}\text{Ar}$  content in the atmosphere and the  $^4\text{He}$  flux from the oceans to the atmosphere were utilized. Balances for total  $^{40}\text{Ar}$  content were also applied to Venus and Mars. Implications of the rate of loss of  $^4\text{He}$  from the atmosphere of Venus were considered. Also, implications of the  $^{40}\text{Ar}$  flux from the interior of the moon were considered. This work was presented at the 18th Lunar and Planetary Sciences Conference (1) and has been accepted for publication (2).

- 2) Fractals. The concept of fractals and the renormalization group approach are having a major impact on a variety of scientific disciplines. We have applied the fractal concept to fragmentation with applications to the frequency-size distribution of meteorites and asteroids and most recently to the fractal interpretation of topography and geoid spectra on the moon and the terrestrial planets. This work has now been published (3). We are continuing to apply fractal statistics to a variety of planetary problems. We are examining available data on topography, gravity, and magnetism.

- (1) D.L. Turcotte and G. Schubert, Tectonic implications of radiogenic noble gases in planetary atmospheres, Lunar Planet. Sci. XVIII, 1028-1029, 1987.
- (2) D.L. Turcotte and G. Schubert, Tectonic implications of radiogenic noble gases in planetary atmospheres, Icarus (in press), 1987.
- (3) D.L. Turcotte, A fractal interpretation of topography and geoid spectra on the earth, moon, Venus, and Mars, J. Geophys. Res. 92, E597-E601, 1987.

## ATMOSPHERIC-LITHOSPHERIC INTERACTIONS ON VENUS: EXPERIMENTAL INVESTIGATIONS

*D.W. Tucker, J.R. Marshall, R. Greeley\*, C Moore\*, Department of Geology and \*Center for Meteorite Studies, Arizona State University, Tempe, AZ 85287, and J. Pollack, NASA-Ames Research Center, Moffett Field, CA 94035*

Gas-mineral equilibria occurring at the atmospheric-lithospheric interface have long been postulated to play an important role in buffering the concentrations of a variety of atmospheric species on Venus. Thermodynamic treatments have predicted the reactions involved, the stable mineral fractions present, and the consequences these equilibria impart to chemical and physical weathering. However, the lack of kinetic and thermodynamic data concerning heterogeneous gas-solid reactions greatly restricts their predictive power. In addition, the absence of data concerning the mineral species at the surface and the gaseous concentrations immediately above the surface severely limits our understanding of this interface. These factors and the virtual absence of confirmatory investigations are the primary driving forces for our experimental investigations.

We report here the distinctive features of a chemical reactor (Figure 1), an apparatus to study the kinetics and mechanisms of pertinent gas-mineral equilibria suspected of playing a major role in the dynamics of the venusian atmosphere. The specifically designed equipment, located at NASA-Ames Research Center, consists of a high-pressure, high-temperature reactor interfaced to a Hewlett Packard 5880A gas chromatograph. The chromatograph is specifically configured for multi-component gas analysis of species known and presumed present in the atmosphere of Venus. It is a highly dynamic system with three detectors (TCD, FID, FPD) and is capable of automated multi-column operation. Chromatographic techniques and associated support equipment will serve to monitor gas composition over time. Calibration is accomplished with the exponential dilution method and checked against certified standards.

The reaction vessel is an Autoclave Engineers Model AE 0100, designed and manufactured for high-pressure, high-temperature operation in the presence of sulfur-containing gases. The reactor has an internal volume of one liter, a diameter of 7.5 cm, and a length of ~22.5 cm. The vessel rests horizontally and is surrounded by a circular resistance heater. It is designed to operate over a wide T,P range, *i.e.*, pressures from 920 atmospheres at 298 K to ~240 atmospheres at 925 K. The vessel and all internal wetted surfaces are constructed of Hastelloy C-276 to limit reactions between container walls and reactive gases. An internal cooling coil allows the reactor contents to be cooled from maximum operating temperature to less than 398 K in less than 5 minutes. Pressure measurement is accomplished with a Setra Systems Model 204 pressure transducer and Model 300D digital pressure readout. Pressure measurement is accurate to  $\pm 0.11\%$  full scale. The temperature measurement and control system is an Autoclave Engineers Model MPK-CP1. It is a dual purpose instrument--the vessel controller is a microprocessor-based three mode (PID) type with proportional output that includes set-point programming, and the furnace controller is an ON/OFF type utilized as an over-temperature device for the heating elements. Temperature measurement is accurate to  $\pm 0.2\%$  full scale.

Preliminary experiments will investigate the degree to which postulated gas-mineral equilibria are occurring on Venus. Representative rocks and minerals will be subjected to atmospheric conditions characteristic of Venus. However, temperatures will be enhanced to promote reaction progress. Concentrations of atmospheric constituents will be varied over large ranges because of our present lack of knowledge concerning concentration gradients in the lower atmosphere. Gas composition will be quantified by the gas chromatograph, and solid samples will be examined by SEM, x-ray diffraction, and electron microprobe techniques. These preliminary tests will provide important information for choosing candidate equilibria for further study of the kinetics and mechanisms involved in gas-mineral reactions.

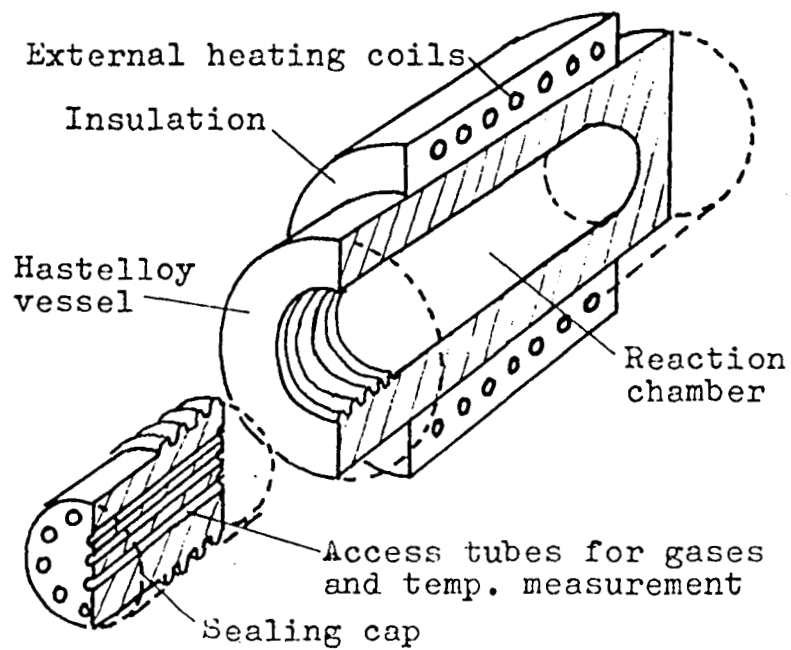


FIGURE 1. Simplified diagram of the reaction vessel used for investigation of mineral/gas reactions on Venus.

## IRON OXIDATION STATE IN ANTARCTIC SHERGOTTITE EETA 79001

Roger G. Burns and Teresa C. Solberg, Department of Earth, Atmospheric and Planetary Sciences, Massachusetts Institute of Technology, Cambridge, MA 02139.

**Abstract.** Mossbauer spectral measurements of basaltic lithology A and impact melt glass lithology C have revealed that less than 2 percent of the iron is in the ferric state in shergottite EETA 79001 from the Antarctic Meteorite Collection. Although the glass lithology C appears to contain trapped Martian atmospheric gases and relict products of pre-terrestrial chemical weathering, the low ferric iron content of this SNC meteorite indicate that it did not originate from the outermost oxidized surface of Mars.

**Introduction.** The consortium study of Shergotty and other SNC meteorites (1) again highlighted the important discovery that glass in the Antarctic shergottite EETA 79001, designated as glass lithology C, contains trapped gases resembling the composition of the Martian atmosphere (2). Subsequent pyrolysis and SEM/EDS measurements of this lithology C (3,4) identified oxidized sulfur (assumed to be sulfate) in the glass, in addition to calcite, gypsum, and sulfur-rich aluminosilicate phases, which were suggested to be relict grains of chemical weathering products on Mars. The Viking Lander XRF experiment (5,6) had earlier measured high sulfur and iron concentrations in the martian regolith, leading to the widely held belief [supported by visible region remote-sensing spectroscopy (7)] that oxidized iron (as ferric), as well as oxidized sulfur (as sulfate), may predominate on the surface of Mars (8). These conclusions led us to search for evidence of ferric-bearing phases, which might have originated from extraterrestrial chemical weathering, in two distinctive lithologies of shergottite EETA 79001, using the technique of Mossbauer spectroscopy. We report here evidence demonstrating that only low concentrations of ferric iron are present in this martian-derived meteorite.

**Specimens Studied** Samples of the shergottite EETA 79001 acquired from the Antarctic meteorite collection included 100 mg of homogenized powder of lithology A and two chips totalling 50 mg of lithology C extracted from a glass-rich pocket in the meteorite which had been the source of samples used in previous trapped noble gases (2) and SEM/pyrolysis (3,4) measurements. Lithology A is a basaltic rock containing clusters of coarse-grained and compositionally zoned olivine, orthopyroxene rimmed with pigeonite and euhedral chromite, which are dispersed in a fine-grained matrix of chemically-zoned pigeonite + augite, maskelynite, opaques (titanomagnetite, ilmenite, pyrrhotite, chromite), phosphates and mesostasis (9-11). Analytical and mineralogical data indicate that the iron is partitioned among pigeonite (~73.4%), olivine (~10.6%), augite (~4.2%), orthopyroxene (~3.5%), opaques (~7.8%), and maskelynite (~0.5%). The chemically determined ferric content was determined to be 3.4 wt.% (9), and was assumed to be in distributed in ulvospinel and Cr-spinel phases to satisfy stoichiometry (9,11). Bulk compositions of glass lithology C in EETA 79001 resemble basaltic lithology A, but the glasses are slightly enriched in the maskelynite component, suggesting that they were derived from shock-induced, nearly bulk melting of lithology A (9). This correlates with the relict olivine, pyroxene, and spinel observed in these impact glasses (9). SEM examination of glass lithology C (3) revealed it to be heterogeneous and to contain nearly equal proportions of smooth vitreous material ("smooth glass") and sub-vitreous to dull aphanitic material ("ribbed glass") interpreted as quench-textured crystals with pyroxene-like compositions. Traces of aluminosilicate phases, together with gypsum, calcite, and jarosite, are disseminated throughout both "smooth" and "ribbed" glasses (3,4) and were suggested to be relict grains of Martian weathering or alteration products. The majority of iron in lithology C is expected to be partitioned between silicate glass

and relict or quenched pyroxene, olivine and spinel phases. Determining how much of the iron is in the ferric state was the objective of our Mossbauer spectral measurements.

**Results.** Mossbauer spectral measurements and spectrum-fitting procedures of rock samples are described elsewhere (12). The spectra of lithologies A and C (figure 1) are dominated by two approximately equal-area envelopes centered near zero and 2.5 mm/sec, indicating that ferrous ions predominate in both lithologies A and C. Contributions from ferric ions, which usually produce peaks in the region 0.6-1.0 mm/sec in Mossbauer spectra of silicates, are inconspicuous, particularly in the glass lithology C spectrum.

The lithology A spectrum (fig.1a) was successfully fitted to four ferrous doublets and one ferric doublet. The outermost ferrous doublet (peaks A & A') has parameters (table 1) consistent with  $\text{Fe}^{2+}$  ions in the (unresolved) olivine (M1 + M2) sites, and the innermost ferrous doublet (peaks C & C') is attributed to  $\text{Fe}^{2+}$  ions in pyroxene M2 sites. The central ferrous doublet (peaks B & B') originates from  $\text{Fe}^{2+}$  in pyroxene M1 sites. Peaks D & D' may be assigned to  $\text{Fe}^{2+}$  in opaque oxide phases, and peaks E & E' represent octahedrally coordinated  $\text{Fe}^{3+}$  ions. The peak areas of the ferric doublet E-E' amount to 1.9% (+/- 0.1%), which is in reasonable agreement with the chemically determined percentage of  $\text{Fe}^{3+}$  ions in lithology A (9). The spectrum of glass lithology C (fig.1b) was best-fitted to five ferrous doublets. Relict and quenched olivine, pyroxene and opaque oxide phases (9) are again represented by doublets A-A', C-C', and D-D', respectively. Peaks F & F' and G & G' having parameters comparable to those measured for lunar basaltic glasses (13), are assigned to  $\text{Fe}^{2+}$  ions in the glass phase of lithology C. A ferric doublet comparable to peaks E & E' for lithology A could not be resolved, indicating that there is less than one percent ferric iron in glass lithology C.

**Discussion.** The Mossbauer spectra of shergottite EETA 79001 clearly show that only a small proportion of ferric ions, at most 2% of the iron in the basaltic lithology A, is present in this meteorite. Some of the ferric iron might be derived from terrestrial oxidation in the Earth's polar environment; Mossbauer spectral measurements of other achondrites and chondrites from the Antarctic meteorite collection revealed ferric iron concentrations derived from chemical weathering of the meteorite in the icecap to be in the range 2-30 wt. % ferric iron (14). The low contents of ferric iron in the two distinctive lithologies A and C in shergottite EETA 79001 are in marked contrast to the ferric-rich materials believed to constitute the bright regions of Mars' surface (7), on which Viking Lander experiments strongly indicated the presence of ferric-bearing oxides, clay silicates and sulfate phases in the regolith (5,6,8). It appears, therefore, that this SNC meteorite did not originate from the *outermost* oxidized surface of Mars. Even low albedo, dark regions of Mars' surface appear to be unlikely sources; oxidized ferric phases believed to coat relatively unoxidized mafic rocks there (7) would contribute significantly to, and be detectable in, a Mossbauer spectrum.

The significant discovery of trapped gases resembling martian atmosphere in glass lithology C of EETA 79001 (2) indicated a near-surface crustal origin of this meteorite. The presence of oxidized sulfur in the glass was attributed (3) to rock-atmosphere reactions on Mars prior to or during the melting event that produced lithology C and trapped atmospheric gases. If such processes did occur on Mars, the negligible ferric iron content of glass lithology C components demonstrated by Mossbauer spectroscopy suggests that the conditions leading to glass formation, entrapment of calcite, etc., and development of sulfate-rich phyllosilicates (3) were insufficiently oxidizing to generate ferric iron in the basaltic horizon from which the shergottite was ejected (15).



## References

- (1) Laul, J.C. *Geochim. Cosmochim. Acta*, **50**, 875 (1986). (2) Bogard, D.D. & Johnson, P. *Science*, **221**, 651 (1983). (3) Gooding, J.L. & Muenow, D.W. *Geochim. Cosmochim. Acta*, **50**, 1049 (1986). (4) Gooding, J.L., Wentworth, S.J., & Zolensky, M.E. *Geochim. Cosmochim. Acta* (in press). (5) Toulmin III P., Baird A.K., Clark B.C., Keil K., Rose H.J.Jr, Christian R.P., Evans P.H., & Kelliher W.C. *J Geophys. Res.*, **82**, 4625 (1977). (6) Clark, B.C., Baird, A.K., Weldon, R.J., Tsusaki, D.M., Schnabel, L. & Candelaria M.P. (1982) *Journ. Geophys. Res.*, **87**, 10059 (1982). (7) Singer, R.B. *Adv. Space Res.*, **5**, 59-68 (1985). (8) Burns, R.G. *Nature*, **320**, 55 (1986). (9) McSween Jr, H.Y. & Jarosewich, E. *Geochim. Cosmochim. Acta*, **47**, 1501 (1983). (10) McSween Jr, H.Y. *Geology*, **12**, 3 (1984). (11) Steele, I.M. & Smith, J.V. *J. Geophys. Res.*, **87**, A375 (1982). (12) Dyar, M.D. & Burns, R.G. *Amer. Mineral.*, **71**, 955 (1986). (13) Burns, R.G. & Dyar, M.D. *J. Geophys. Res.*, **88**, B221 (1983). (14) Solberg, T.C. & Burns, R.G. *Lunar Planet. Sci.*, **XVIII**, 936 (1987). (15) Research supported by NASA grants NSG-7604 and NAGW-1078.

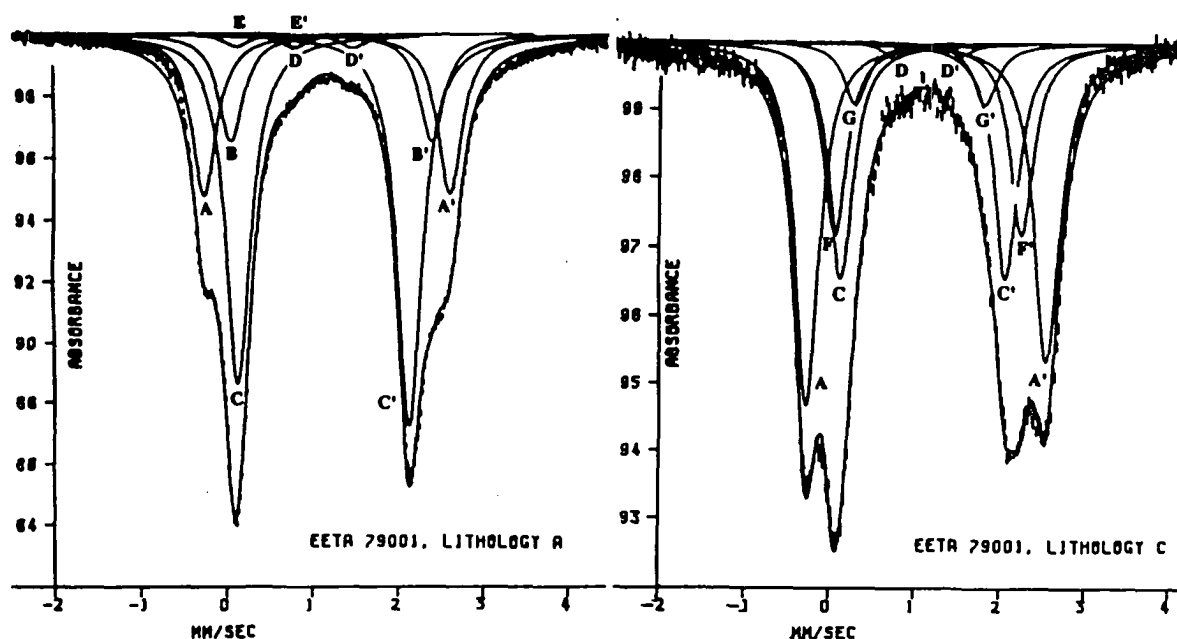


TABLE 1. Parameters from the Mossbauer Spectra of Shergottite EETA 79001.  
Lithology Peaks I.S. Q.S. H.W. % Area Assignment

basalt A	A & A'	1.17	2.88	0.35	23.9	Fe <sup>2+</sup> /olivine (M1+M2)
	B & B'	1.22	2.35	0.35	16.2	Fe <sup>2+</sup> /pyroxene M1
	C & C'	1.13	2.00	0.35	58.9	Fe <sup>2+</sup> /pyroxene M2
	D & D'	1.10	0.70	0.35	2.1	Fe <sup>2+</sup> /opaque oxides
	E & E'	0.43	0.69	0.35	1.9	octahedral Fe <sup>3+</sup>
glass C	A & A'	1.15	2.82	0.34	41.2	Fe <sup>2+</sup> /olivine (M1+M2)
	C & C'	1.10	1.94	0.34	27.3	Fe <sup>2+</sup> /pyroxene M2
	D & D'	1.10	0.70	0.34	1.9	Fe <sup>2+</sup> /opaque oxides
	F & F'	1.15	2.19	0.34	22.3	Fe <sup>2+</sup> /glass
	G & G'	1.05	1.53	0.34	7.3	Fe <sup>2+</sup> /glass

## MARTIAN (?) VOLATILE COMPOUNDS IN SNC METEORITES

J. L. Gooding<sup>1</sup>, K. Aggrey<sup>2</sup>, and D. W. Muenow<sup>2</sup>. <sup>1</sup>Planetary Materials Branch, NASA/Johnson Space Center, Houston, TX 77058. <sup>2</sup>Dept. of Chemistry and Hawaii Institute of Geophysics, University of Hawaii, Honolulu, HI 96822 USA.

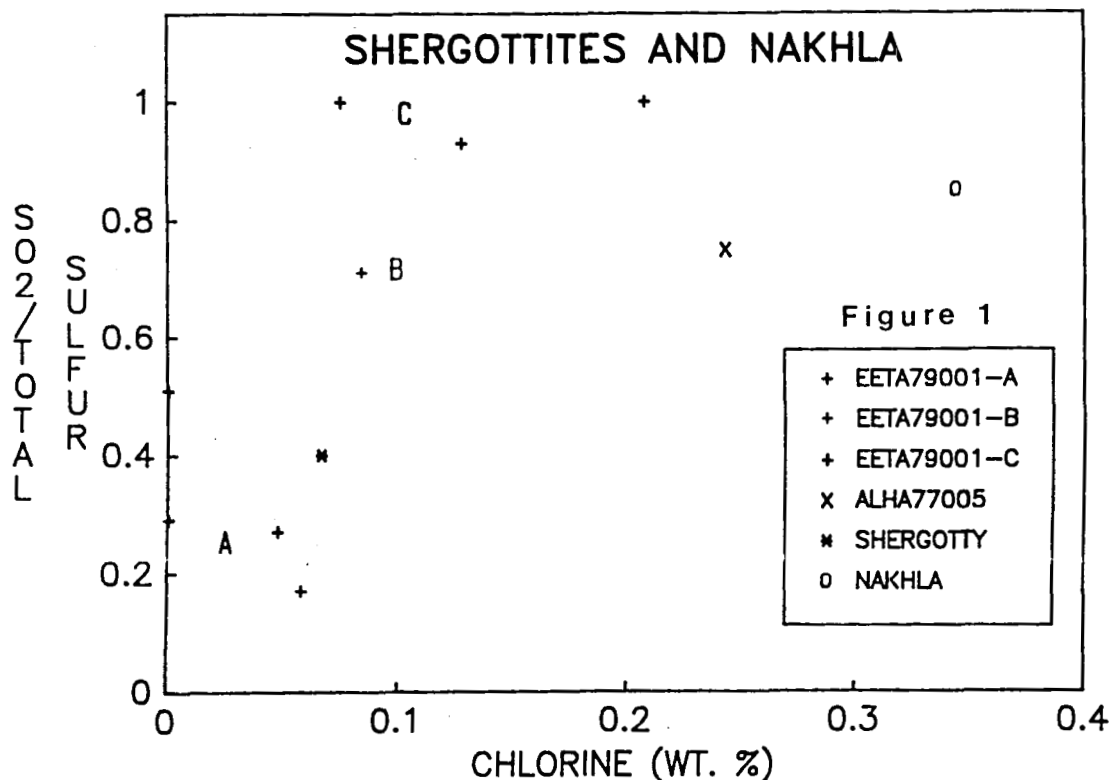
**Introduction.** Shergottite, nakhlite, and chassignite (SNC) meteorites are mafic and ultramafic igneous rocks that formed on a geologically active, Earth-like planet. If the SNC parent body is Mars, as is widely believed, then contents of potential atmosphere- and ocean-forming elements in SNCs should be important data in establishing the abundance of Martian volatiles and their role in Martian geologic evolution. Toward that end, bulk concentrations of water, hydrocarbons, carbon dioxide, chlorine, and sulfur (including oxidized and reduced species) in meteorites were measured by evolved gas analysis (Knudsen-cell vacuum pyrolysis at 25-1250° C with quadrupole mass spectrometry). Both interior (> 1-cm depth) and exterior (with fusion crust) samples of 20-60 mg were analyzed from shergottites (ALHA77005, EETA79001, Shergotty), Nakhla, and eucrites (ALHA81001, EETA79004, Pasamonte). Interior samples of eucrites (non-SNC basaltic achondrites) and exterior samples of both eucrites and SNCs served as controls for distinguishing terrestrial from pre-terrestrial volatiles.

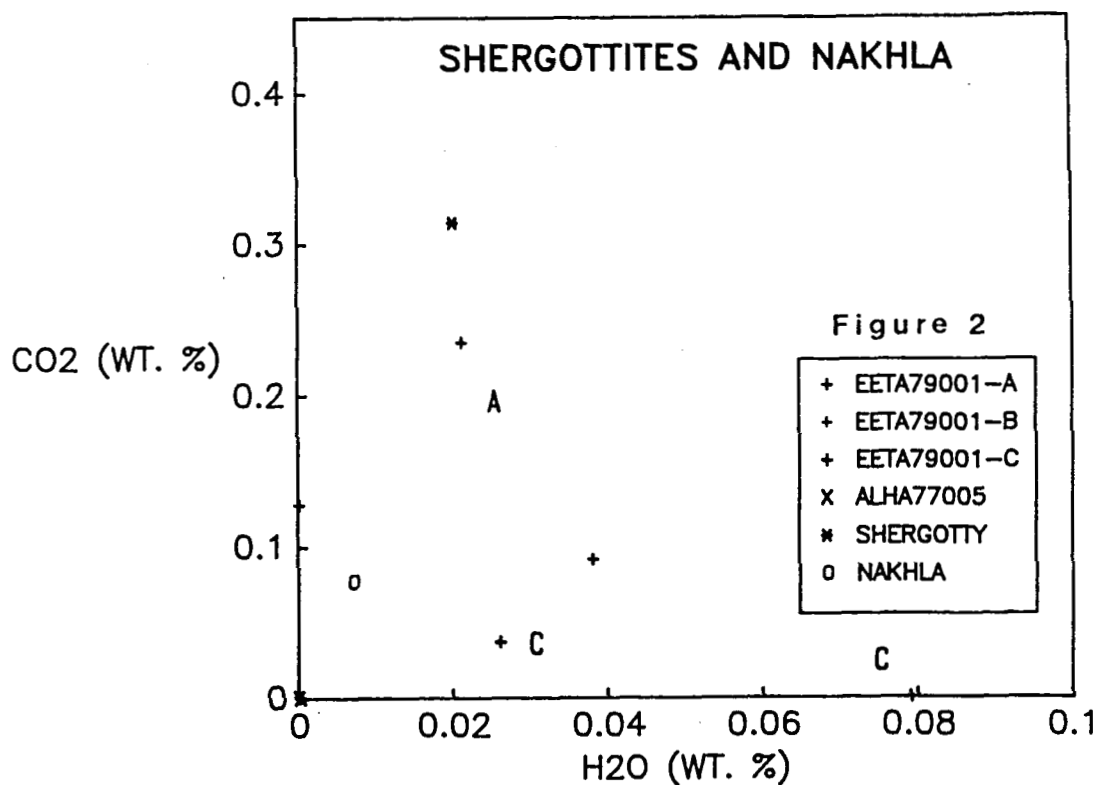
**Terrestrial Weathering/Contamination Signatures.** Eucrite exterior samples evolved 0.4-5 wt. % total volatiles, including hydrocarbons (mostly saturated C<sub>1-4</sub>; 50-500° C), CO<sub>2</sub> (100-600° C), H<sub>2</sub>O (50-500° C), Cl (300-800° C), and SO<sub>2</sub> (100-1250° C). Hydrocarbons crudely covaried with CO<sub>2</sub> but not with H<sub>2</sub>O, Cl, or SO<sub>2</sub>. At least for the Antarctic eucrites, which displayed the most volatile-rich exteriors, the volatile-bearing phases were clay-mineraloid and sulfate weathering products of terrestrial origin [2]. Hydrocarbons undoubtedly accumulated on Earth through natural exposure and sample handling. Interior samples evolved 0.3-0.9 % total volatiles (with fewer hydrocarbons) but with sulfur dominantly as S<sub>2</sub>, as expected for a reduced carrier such as pyrrhotite or troilite. The net effects of terrestrial weathering were to strongly enrich surface zones of the eucrites in total sulfur and oxidized (sulfate) sulfur. Exterior enrichments of H<sub>2</sub>O and CO<sub>2</sub> were significant but less pronounced than for sulfur. Chlorine also tended toward surface enrichment but in a less systematic way.

Contrasts between respective exterior and interior samples of shergottites and Nakhla were similar to those for eucrites, with important exceptions noted below. For a given depth within a particular meteorite, though, the SNC samples were consistently more oxidized and volatile-rich than were the eucrite samples, as would be expected if the SNCs originated on Mars.

**Martian (?) Volatiles.** The dominant sulfur species evolved from shergottite and nakhlite interior samples was  $\text{SO}_2$ , as previously observed for Lithology C from EETA79001 [1]. Only bulk Shergotty and bulk Lith-A from EETA79001 contained significant amounts of reduced sulfur. Bulk Nakhla and bulk Lith-B from EETA79001 rivaled Lith-C in terms of degree of sulfur oxidation. Chlorine and  $\text{SO}_2$  abundances generally covaried and were greatest in Nakhla (Fig. 1).  $\text{CO}_2$ , associated with minor  $\text{SO}_2$ , evolved from Nakhla as two distinct peaks (450, 650°C) although total  $\text{CO}_2$  and  $\text{SO}_2$  concentrations were not strongly correlated in other samples. The  $\text{CO}_2$  release from Nakhla corroborates previous evidence for carbonates in that meteorite [3]. The high ratio of  $\text{SO}_2$  to  $\text{CO}_2$  in EETA79001 Lith-C suggests that gypsum predominated over calcite among the relict salt grains previously identified [4]. Concentrations of  $\text{H}_2\text{O}$  and  $\text{CO}_2$  varied significantly among the samples but were mostly inversely correlated (Fig. 2).

In general, these data indicate pre-terrestrial oxidation and volatile enrichments in shergottites and nakhlites and support interpretation of those meteorites as Martian rocks. Considering that the SNCs are all igneous rocks, their  $\text{H}_2\text{O}$  and  $\text{CO}_2$  contents are surprisingly high and are probably attributable to disseminated traces of aqueous alteration products. If Mars is, indeed, the SNC parent body then there exists clear evidence that at least some of the global inventories of H, C, O, and S have reacted with the lithosphere to form irreversible volatile sinks as sulfates and carbonates.





**References:** [1] Gooding J. L. and Muenow D. W. (1986) *Geochim. Cosmochim. Acta*, 50, 1049-1059. [2] Gooding J. L. (1986) *Geochim. Cosmochim. Acta*, 50, 2215-2223. [3] Carr R. H. et al. (1985) *Nature*, 314, 248-250. [4] Gooding J. L. et al. (1987) *Lunar Planet. Sci. XVIII*, Lunar and Planetary Institute, Houston, 345-346.

## SULFIDE MINERALIZATION: ITS ROLE IN CHEMICAL WEATHERING OF MARS

Roger G. Burns, Department of Earth, Atmospheric and Planetary Sciences, Massachusetts Institute of Technology, Cambridge, MA 02139.

**Summary.** Pyrrhotite-pentlandite assemblages in mafic and ultramafic igneous rocks may have contributed significantly to the chemical weathering reactions that produced degradation products in the martian regolith. By analogy with terrestrial processes, a model is proposed whereby supergene alteration of these primary Fe-Ni sulfides on Mars has generated secondary sulfides (e.g. pyrite) below the water table and produced acidic groundwater containing high concentrations of dissolved Fe, Ni and sulfate ions. The low pH solutions also initiated weathering reactions of igneous feldspars and ferromagnesian silicates to form clay silicate and ferric oxyhydroxide phases. Near-surface oxidation and hydrolysis of ferric sulfato- and hydroxo-complex ions and sols formed gossans above the water table consisting of poorly crystalline hydrated ferric sulfates (e.g. jarosite), oxides (ferrihydrite, goethite) and silica (opal). Underlying groundwater, now permafrost, contains hydroxo sulfato complexes of Fe, Al, Mg, Ni, etc., which may be stabilized in frozen acidic solutions beneath the surface of Mars. Sublimation of permafrost may replenish colloidal ferric oxides, sulfates and phyllosilicates during dust storms on Mars.

**Background.** The presence of massive volcanoes in the Tharsis and Elysium regions, the distinctive petrology of SNC meteorites, and a compendium of results from the Viking Lander experiments all point to extrusive and plutonic mafic and ultramafic igneous rocks on Mars having analogies to terrestrial komatiites [1]. On Earth, the latter are associated with massive and disseminated sulfides containing pyrrhotite, pentlandite, and accessory pyrite and chalcopyrite [2]. Near-surface oxidation of these sulfides have produced conspicuous rust-colored gossans, which often betray the occurrence of unexposed ore deposits (Figure 1). Studies of gossans and sub-surface minerals [3-5] suggest pathways of oxidative weathering reactions that may be applicable to Mars.

Pyrite is pivotal to chemical weathering reactions of sulfides. It may occur as a minor constituent of primary igneous sulfides, or be formed by supergene reactions involving deep weathering of pyrrhotite (see equation {1} in Table 1.). At or near the water table, oxidation of pyrite by aerated groundwater occurs {6},{7}. Ferric iron liberated in this reaction, not only promotes the initial alteration of pyrrhotite {1} and of pentlandite {2} to secondary sulfides in the absence of dissolved oxygen, but also aids the dissolution of pyrite {5} below the water table. Supergene enrichment reactions also occur there {3},{4}, leading to high concentrations of Ni, etc. in secondary sulfides. Strongly acidic and sulfate-rich groundwater is produced which stabilizes dissolved ferrous iron and a variety of complex ferric ions [6] including those listed in {8} and {9}. At elevated temperatures, these complexes produce a variety of hydroxo-ferric sulfate sols [7] (e.g. carphosiderite {8},{9}), which may be the precursors to a number of ferric sulfate minerals [8] often found in gossans in arid regions. In less acidic environments above the water table, dissolved ferric ions and monodispersed sols are hydrolysed to poorly crystalline FeOOH phases (e.g. ferrihydrite, goethite {10},{11},{12}), which coexist with silica (opal, jasper) and the hydrated ferric sulfate minerals in gossans. The fields of relative stabilities of gossaniferous phases are depicted in the oxidation-acidity diagram shown in Figure 2.

Reactions {4} to {11} formulated in Table 1 demonstrate that groundwater in the vicinity of oxidizing sulfides is highly acidic. Such low pH solutions promote the chemical weathering of feldspars, pyroxenes and olivine in host igneous rocks [9], liberating dissolved silica, Al, Ca, Mg, Na and additional Fe ions, and producing secondary clay silicates (e.g. smectite) and iron oxyhydroxides. On Earth, seafloor basalts and gabbros erupting along submarine spreading centers have undergone extensive hydrothermal alteration by seawater circulating through underlying tectonically-fractured oceanic crust. As a result, the acidity of aqueous solutions is buffered by seawater-basalt interactions, leading to the slight alkalinity (pH 8.2) of present-day terrestrial oceans.

The oxidative power of atmospheric oxygen is the driving force in the weathering of sulfides (in the absence of bacterial activity). The dissolution of oxygen in groundwater and its migration to sulfide reaction centers involve diffusion processes and are probably rate-controlling. When the concentration of dissolved oxygen is very low and the supply of water is limited, oxidative reactions become sluggish and involve hydrogen peroxide. Furthermore, ferric-bearing solutions may liberate elemental sulfur [13],[14],[15]. Thus, metastable sulfur is observed in pyrite-jarosite-sulfur assemblages associated with some ultramafic pyrrhotite-pentlandite deposits [10].

**Martian Weathering.** On Mars, where plate tectonic activity appears to have been insignificant, vast volumes of iron-rich basaltic magma has reached the surface of the planet via immense shield volcanoes. Fracturing associated with this volcanism, as well as impact cratering, facilitated deep-weathering reactions by permeating groundwater early in the history of Mars. However, the apparent absence of spreading centers and subduction zones, which cause recycling of the Earth's crust, has minimized acid-buffering of aqueous solutions by wall-rock alteration on Mars. Therefore, the acidity of groundwater, now permafrost, may have been maintained during the chemical evolution of the martian surface, thereby aiding the solubility and transport of Fe, Al, Mg, Ni, silica, etc. Geomorphological evidence attesting to the flow of water on Mars suggests that gossan-forming reactions may have occurred in the past. However, the present-day cold surface of Mars has impeded deep-weathering of sulfides in host basaltic rocks due to slow reaction rates and restricted access of dissolved oxygen or ferric iron to reaction centers. Nevertheless, some oxidative weathering may still be occurring in the frozen environment on Mars, as indicated by the oxidation of Fe and FeS phases observed in Antarctic meteorites [11]. When sublimation of martian permafrost occurs, species held in solution could be hydrolysed, precipitated as colloidal material and transported in dust storms..

**Discussion.** Evidence for gossan formation on Mars stems from several sources. First, remote-sensed reflectance spectral profiles are matched closely by ferrihydrite-silica gels and jarosite-bearing clay assemblages [12]. Second, jarosite which is so characteristically an oxidative weathering product of iron sulfides, may be present in SNC meteorites [13,14] believed to have originated from Mars. Third, the magnetic phase detected in the Viking magnetic experiment [15] may be remnant pyrrhotite which has been incompletely oxidized, particularly if the level of the water table has dropped on Mars. Finally, a limited supply of water and a low concentration of dissolved water, which favor the formation of hydrogen peroxide and promote the production of peroxide and superoxide phases, may account for results obtained in the Viking biology experiments [16].

## References.

- [1] Baird, A.K. & Clark, B.C. (1981) *Icarus*, 45, 113-123.
- [2] Guilbert, J.M. & Park, Jr, C.F. (1986) *The Geology of Ore Deposits* (W.H.Freeman).
- [3] Thornber, M.R. (1975) *Chem. Geol.*, 15, 1-14 & 117-144.
- [4] Blain, C.F. & Andrew, R.L. (1977) *Minerals Sci. Engng*, 9, 119-150.
- [5] Burns, R.G. (1987) *Lunar Planet. Sci.*, XVIII, 141-142; *Proc. 18th LPSC*, in press.
- [6] Sapiesszko, R.S. *et al.* (1977) *J. Phys. Chem.*, 81, 1061-1068.
- [7] Matijevic, E. *et al.* (1975) *J. Colloid. Interfac. Sci.*, 50, 567-581.
- [8] Burns, R.G. (1987) *JGR*, 92 (B4) E570-574.
- [9] Siever, R. & Woodford, N. (1979) *Geochim. Cosmochim. Acta*, 43, 717-724.
- [10] Nickel, E. (1984) *Mineral. Mag.*, 48, 139-142.
- [11] Gooding, J.L. (1981) *Proc. 12th LPSC*, 1105-1122.
- [12] Sherman, D.A. *et al.* (1982) *JGR*, 87 (B12), 10169-10180.
- [13] Smith, J.V. & Steele, I.M. (1984) *Meteoritics*, 19, 121-133.
- [14] Gooding, J.L. (1986) *Geochim. Cosmochim. Acta*, 50, 2215-2223.
- [15] Hargraves, R.B. *et al.* (1979) *JGR*, 84, 8379-8384.
- [16] Huguenin, R.L. (1982) *JGR*, 87 (B12), 10069-10082.

Table 1. CHEMICAL WEATHERING REACTIONS INVOLVING SULFIDES

- {1}  $\text{Fe}_7\text{S}_8$  (pyrrhotite) +  $6\text{Fe}^{3+} = 4\text{FeS}_2$  (pyrite) +  $9\text{Fe}^{2+}$
- {2}  $(\text{Fe,Ni})_9\text{S}_8$  (pentlandite) +  $2\text{Fe}^{3+} \Rightarrow 3\text{Fe}^{2+} + 2(\text{Fe,Ni})\text{Ni}_2\text{S}_4$  (violarite)
- {3}  $(\text{Fe,Ni})\text{Ni}_2\text{S}_4$  (violarite) +  $\text{Ni}^{2+} \Rightarrow \text{Fe}^{2+} + (\text{Ni,Fe})\text{Ni}_2\text{S}_4$  (polydymite)
- {4}  $\text{Ni}_3\text{S}_4$  (polydymite) +  $\text{H}_2\text{O} + 15/2 \text{O}_2 = 3\text{Ni}^{2+} + 4\text{SO}_4^{2-} + 2\text{H}^+$
- {5}  $\text{FeS}_2 + 14\text{Fe}^{3+} + 16\text{H}^+ = 15\text{Fe}^{2+} + 2\text{SO}_4^{2-} + 16\text{H}^+$
- {6}  $2\text{FeS}_2 + 2\text{H}_2\text{O} + 7 \text{O}_2 = 2\text{Fe}^{2+} + 4\text{SO}_4^{2-} + 4\text{H}^+$
- {7}  $4\text{FeS}_2 + 2\text{H}_2\text{O} + 15 \text{O}_2 = 4\text{Fe}^{3+} + 8\text{SO}_4^{2-} + 4\text{H}^+$
- {8}  $2\text{FeSO}_4^+ + \text{FeOH}^{2+} + 6\text{H}_2\text{O} = \text{Fe}_3(\text{SO}_4)_2(\text{OH})_5 \cdot 2\text{H}_2\text{O}$  (carphosiderite) +  $4\text{H}^+$
- {9}  $\text{Fe}(\text{SO}_4)_2^- + 2\text{FeOH}^+ + 4\text{H}_2\text{O} = \text{Fe}_3(\text{SO}_4)_2(\text{OH})_5 \cdot 2\text{H}_2\text{O} + \text{H}^+$
- {10}  $\text{Fe}^{3+} + 2\text{H}_2\text{O} = \text{FeOOH}$  (ferrihydrite, goethite) +  $3\text{H}^+$
- {11}  $\text{FeSO}_4^+ + 2\text{H}_2\text{O} = \text{FeOOH} + 3\text{H}^+$
- {12}  $\text{Fe}_3(\text{SO}_4)_2(\text{OH})_5 \cdot 2\text{H}_2\text{O} = 3\text{FeOOH} + 2\text{SO}_4^{2-} + 4\text{H}^+ + \text{H}_2\text{O}$
- {13}  $\text{FeS}_2 + 2\text{Fe}^{3+} = 3\text{Fe}^{2+} + 2\text{S}$
- {14}  $\text{Fe}_7\text{S}_8 + 14\text{Fe}^{3+} = 21\text{Fe}^{2+} + 8\text{S}$
- {15}  $(\text{Fe,Ni})_9\text{S}_8 + x\text{Fe}^{3+} \Rightarrow y\text{Fe}^{2+} + z\text{Ni}^{2+} + 8\text{S}$

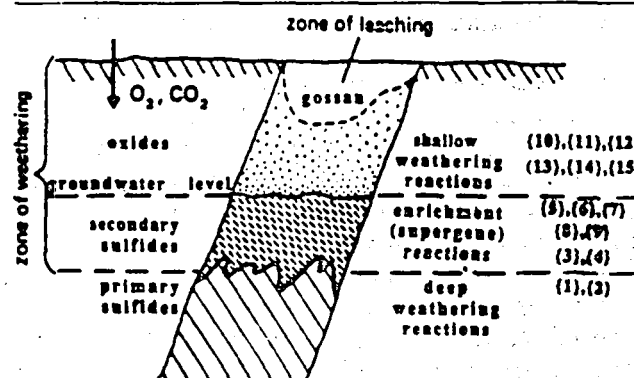
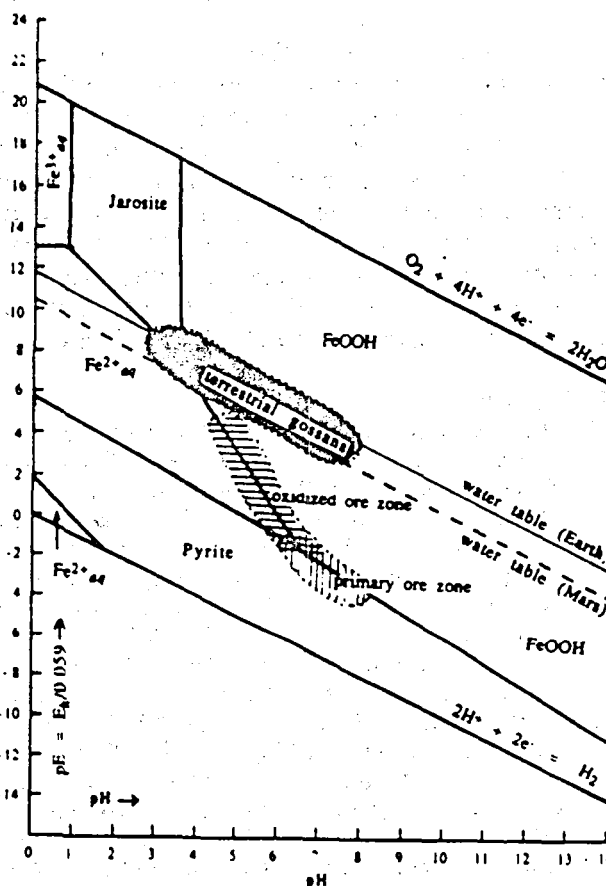


Figure 1 (above). Zones of weathering associated with gossan formation above sulfide mineralization. The scale of the sulfide vein may be a few microns to several meters in diameter. Reactions {1} to {15} correspond to those in Table 1.

Figure 2 (right). Equilibrium diagram for pyrite and its oxidative products, including jarosite and FeOOH, occurring in gossans at 25°C (modified from [5]). Ranges of pE and pH measured in oxidized pyrrhotite-pentlandite assemblages are shown [3-4], as well as values for dissolved oxygen in groundwater on Earth and Mars. (At 298.16°K,  $E_h = 0.05916 \times \text{pE}$ .)



CLIMATE, ATMOSPHERE, AND VOLATILE INVENTORY EVOLUTION: POLAR  
PROCESSES, CLIMATE RECORDS, VOLATILE INVENTORIES; J.B. Pollack,  
NASA Ames Research Center

Climate change on Mars has been driven by long term changes in the solar luminosity, variations in the partitioning of volatiles between the atmosphere and near-surface reservoirs, and astronomical variations in axial and orbital properties. There are important parallels between these drives for Mars and comparable ones for the Earth.

In the early history of the solar system, the Sun's luminosity was 25 to 30% lower than its current value. Yet, the Earth is known to have had water oceans and life over almost its entire history. It has been suggested that an early benign climate on Earth was due to the presence of much more carbon dioxide in its atmosphere at these early times than currently resides there. Such a partitioning of carbon dioxide, at the expense of the carbonate rock reservoir, may have resulted from a more vigorous tectonic and volcanic style at early times, which implies a faster recycling rate for carbonate rocks formed by surface weathering reactions.

Such a line of reasoning may imply that much more carbon dioxide was present in the Martian atmosphere during the planet's early history than resides there today. If atmospheric partial pressures of 1 to 5 bars were achieved, surface temperatures in excess of the freezing point of water could have been achieved. Furthermore, carbonate rocks formed by weathering reactions could have been rapidly recycled by burial and thermal decomposition at these early times. Thus, Mars could have had a wet, warm climate in its early history. If so, large quantities of carbonate rocks, formed near the end of this epoch, could be key indicators of such an early environment.

It is now widely recognized that astronomical variations of the Earth's axial and orbital characteristics have played a dominant role in causing the succession of glacial and interglacial periods characterizing the last several million years. The magnitude of the axial and eccentricity variations are much larger for Mars than Earth. Such changes on Mars could result in sizeable variations in atmospheric pressure, dust storm activity, and the stability of perennial carbon dioxide and water ice polar caps. These quasi-periodic climate changes occur on periods of 100,000 to 1,000,000 years and may be recorded in the sedimentary layers of the polar layered terrain.



## The Effects of Insolation Penetration into Icy Regoliths: Application to Europa.

Fraser P. Fanale and James R. Salvail, Planetary Geosciences Division,  
Hawaii Institute of Geophysics, 2525 Correa Rd., Honolulu, Hawaii 96822

Conventional thermal models of planetary surfaces and regoliths have been formulated under the assumption that solar radiation is absorbed entirely at the surface and that the physical properties of the regolith are not altered by the heat flow. Matson and Brown (1987) and Brown and Matson (1987) have studied the effects of insolation penetration into regoliths composed of particulate materials translucent in the visual and UV and opaque in the infrared. Their model predicts that near surface temperatures in a regolith composed of pure water ice, such as may exist on Europa, may be hundreds of degrees higher than previously thought, based on models in which insolation is absorbed only at the surface. These high temperatures result from the fact that translucent water ice readily admits visual and UV radiation but cannot reradiate in the infrared from the subsurface. Therefore, radiation initially deposited below the surface can escape only by conduction. If the thermal conductivity of the regolith is very low, as it is on Europa, the heat input during a diurnal cycle will exceed the heat loss, causing the temperature of the regolith to rise significantly above that of conventional models. The maximum temperature will be somewhere below the surface, and the temperature gradient above the temperature maximum will continue to rise until the heat loss due to conduction is equal to the heat input from radiation. Brown and Matson's results are not realistic for ices because their model does not take into account phase changes, heat convection, mass redistribution within the regolith and changes in the physical properties of the regolith.

We have formulated a one dimensional analytical model that builds on the work of Brown and Matson and explicitly includes the effects of sublimation and condensation throughout a volume, heat convection, mass transfer within the regolith and changes in the density, the porosity and the thermal conductivity of the regolith as functions of depth and time. The icy regolith is modeled as a porous medium in which tortuous capillaries extend in three dimensions. The pores/capillaries of the regolith contain water vapor which, when at equilibrium with the solid ice, is maintained at the vapor pressure governed by the local temperature. Therefore, a temperature variation with depth results in a predictable pressure variation and gradient. The pressure gradient induces a flow which momentarily perturbs the vapor pressures away from the equilibrium values. When this occurs, ice is sublimed or vapor is condensed, depending on the direction of the pressure perturbation, at a rate such that the local vapor pressure is maintained. The governing energy equation includes latent heat effects, heat convection and the conservation of mass principle, and it also accounts for the possibility of free molecular flow and continuum flow. The energy equation is solved using an implicit numerical method at various levels in a regolith column and for various times in a diurnal cycle until a quasi steady state is reached after several hundred rotations. The physical properties of the regolith are considered using two conceptual models. In one model the regolith is assumed to be a rigid matrix in which the properties change with

depth and time due to local sublimation and condensation. After quasi steady temperatures are reached, the density, the porosity and the thermal conductivity are calculated through the regolith column over a time scale of hundreds to thousands of years. Temperatures are then recomputed using the new properties, and the cycle is repeated. The second model assumes the regolith to be unstructured with the ice having the consistency of fine snow. When a particular site within the regolith undergoes a solid to gas phase change resulting in a vacancy in the ice, the vacancy is immediately filled by a solid particle. In this model the temperature continues to be influenced by latent heat and convection, as in the first model, but the solid ice is mobile and maintains the density and porosity constant throughout.

The most important physical parameters for this problem are the thermal conductivity and the insolation extinction coefficient. The surface thermal conductivity for Europa has been estimated from eclipse data, and that value is used as a baseline value for the model. The insolation extinction coefficient is more or less unknown, but Brown and Matson have deduced a plausible range of values. Their baseline value for the reciprocal of the extinction coefficient is 5.0. We have obtained preliminary results using this value and find that the maximum temperature in Europa's near surface regolith is  $\sim 250^\circ\text{K}$ . This is much lower than Brown and Matson's corresponding result, which is  $\sim 420^\circ\text{K}$ . We conclude that the vapor phase within the porous icy regolith functions as a significant reservoir of latent heat, permitting the regolith temperatures to remain much lower than reported by Matson and Brown. In addition, preliminary results indicate that physical property changes in the rigid matrix model are unstable. At a position of maximum temperature the density and the thermal conductivity would decrease. This would tend to increase the temperature and pressure gradients and further decrease the density and the thermal conductivity. The model is sufficiently general and can be applied to other planetary bodies with icy regoliths.

#### References:

- Brown, Robert H. and Matson, Dennis L. Thermal effects of insolation propagation into the regoliths of airless bodies. *Icarus*, in press.  
Matson, Dennis L. and Brown, Robert H. Solid state greenhouses and their implications for icy satellites. Submitted to *Icarus*.

## **Experimental Studies of Sublimation in Ice and Ice/Particulate Mixtures: Applications to Mars**

Jeffrey M. Moore, and Michael C. Malin, Department of Geology, Arizona State University, Tempe, AZ 85287-1404

Recent studies of the heavily cratered terrain on Mars have lead to the need for more detailed information about landforms created when a cemented sediment disintegrates. In particular, the suggestions that volatile cements within heavily cratered materials could sublime, leading to morphological decay, need to be assessed. Sublimation of particulate-contaminated ices ( $H_2O$  and others) has similarly been proposed to be significant in the evolution of the surfaces of a variety of other solar system objects. Theoretical models of such processes rely on simplified, idealized solutions amenable to mathematical analysis, and terrestrial field examples where ice sublimation occurs as a singular geologic process are rare but thought provoking. Experimental investigation is potentially the best approach to examining the effects of non-volatile particulates on the sublimation of ice.

The design of an experimental apparatus to investigate ice/non-volatile particulate interactions during sublimation under martian conditions was completed in May 1987. The apparatus provides a Mars-like environment for a 1 m diameter by 50 cm thick sample of  $H_2O$  ice and ice mixed and/or covered with non-volatile particles. The apparatus consists of two parts: a sample container that holds the ice/non-volatile particulate mixtures, and the sample chamber, to which the surface of the sample is exposed. Associated with these two parts is an environmental control and analysis system.

The sample container is cooled from its base to establish a constant, lower value for the sample's thermal gradient. The base temperature is selected to establish subfreezing (but close to  $0^\circ C$ ) temperatures throughout the icy component of the sample. To maintain this temperature, the aluminum base plate is cooled by freon circulating in coils. The walls of the sample container are fabricated from plexiglas both to allow visual inspection and to provide thermal insulation from the external environment. Additional insulation is placed outside the chamber and around the sample container walls. Temperature sensors are placed at various depths within the sample, and their outputs recorded by the environmental control and analysis system.

Above the sample container is an experiment chamber that provides a volume 1 m in diameter by 85 cm high for sample examination. This volume is occupied by a pure  $CO_2$  atmosphere at approximately 3 mb pressure (chosen to be representative of Mars but below the water triple-point) and maintained a few degrees above  $0^\circ C$ . Although this temperature and that within the sample will be  $\sim 75^\circ K$  warmer than the martian frostpoint temperature ( $\sim 198^\circ K$ ), the temperature-dependence relationships of the relevant phenomena (i.e., equilibrium vapor pressure and gaseous diffusion) are well known. The expressions for temperature dependence are used to scale the experimental results to martian temperatures. Other major conditions within the apparatus (e.g., atmospheric pressure and composition, ice and non-volatile particle size, etc.) more closely simulate those at the martian surface.

Environmental maintenance is an important aspect of the apparatus. High-intensity lamps, mounted on the top of the chamber, provide uniform irradiance to the surface of the sample. A piston-and-cylinder pump completely cycle the gas in the chamber every  $\sim 200$  s through a condenser that removes all  $H_2O$  from the  $CO_2$  atmosphere. The environment within the apparatus is normally a closed system, but excess pressure may be pumped out through the condenser or  $CO_2$  may be bled into the chamber if necessary. Pressure is automatically maintained with sensors and trip-switches. The  $H_2O$  collector in the condenser can be changed quickly, while isolated from the chamber. The collector is changed at regular intervals and its

H<sub>2</sub>O content measured to determine the rate of sublimation. Windows in the chamber allow viewing of the sample at both vertical and oblique angles.

The apparatus is operated within a large refrigerated room in which the temperature can be maintained at constant values both above and below 0° C. Room temperature control is used to establish the thermal background sensible to the sample surface.

Design trade-off studies were used to determine the dimensions of and materials to be used in the manufacture of the apparatus. The overall dimensions of the apparatus were selected on the basis of the scale of the phenomena to be studied and the thermophysical properties of the most likely materials from which the apparatus could be made. The diameter of the sample container was selected on the basis of the centimeter to decimeter scale of terrestrial ablation textures, on the assumption that they might be analogous to martian sublimation-induced textures. The depth of the sample container was chosen on the basis of a design goal of studying the evolution of the upper 10-20 cm of the sample and on the basis of conservative calculation of the additional thickness needed to assure uniform temperature and compositional conditions beyond the depth where sample alteration would occur. The sample container materials, plexiglas and aluminum, were selected after consideration of the relative acceptable contribution of the external environment compared to the sample environment maintenance requirements, and of the ease and cost of manufacture. The thermal conductivities of the sample materials ( $\sim 0.02\text{--}0.05 \text{ W cm}^{-1} \text{ K}^{-1}$ ) are typically two orders of magnitude greater than the plexiglas sample container walls ( $2 \times 10^{-4} \text{ W cm}^{-1} \text{ K}^{-1}$ ), thus insuring a dominant vertical thermal flux with little edge effects from the walls. Conversely, the thermal conductivity of aluminum ( $2.36 \text{ W cm}^{-1} \text{ K}^{-1}$ ) is two orders of magnitude higher than that of the sample materials, promoting the quick establishment of equilibrium boundary conditions for the sample.

Delivery of the apparatus occurred in December, 1987. The first series of experiments was designed to investigate samples of pure ice of various particle sizes: 1) non-porous massive or "block" ice, 2) 1 cm and 1 mm diameter granular ice, and 3) fine ice ("snow" < 1 mm diameter). Calculations of ice grain growth rates and sintering suggest that ice grains in martian polar deposits probably range in size between 1 mm and 1  $\mu\text{m}$ . Ice grains of this size range will be utilized in subsequent experiments involving the interaction of ice and non-volatile particulates. The initial runs, only involving ice, are intended to verify the selection of ice-grain size and to calibrate the actual requirements for experiment durations.

The next series of experiments will investigate the sublimation rate and mantle evolution from samples that are intimate mixtures of ice and non-volatile material. Three non-volatile particle sizes ( $\sim 10 \mu\text{m}$ ,  $250 \mu\text{m}$ , and 1 mm) will be used to evaluate the effect that factor has on sublimation rate and mantle formation. These sizes were selected from inferred abundances of particles with these sizes on Mars. An additional set of runs during this series will examine the effect of particle albedo while keeping other factors constant.

The third series of runs will examine the ice sublimation rate of clean ice under a pre-existing, non-accreting mantle. One set of runs will vary mantle thickness holding all other factors constant. A second set will vary particle size holding all other factors constant.

The final set of experiments will address the effects of separated, cm-sized particles, both on a pre-existing mantle surface and embedded along with fine material within ice, on sublimation rate, mantle formation, and mantle surface texture.

## References

Mercer, J.H., *J. Glaciol.*, 10, 319-320, 1971.

## Clathrate and Ammonia Hydrates : Physical Chemistry and Applications to the Solar System.

J.I. Lunine, S.K. Croft and J. Kargel (Lunar & Planetary Laboratory, University of Arizona, Tucson, AZ)

Interpretation of spacecraft data on the icy satellites of the outer solar system and on Halley's comet requires application of the physical chemical properties of low-temperature compounds of water ice and more volatile substances. Work this year has focussed on applying clathrate hydrate thermodynamics to the compositional measurements performed by the ESA Giotto spacecraft near the nucleus of Halley's comet, and on determination of the equation of state of ammonia-water liquids (in collaboration with S.K. Croft and J. Kargel) for application to the satellites of Saturn and Uranus.

1. Trapping of Gases in Water Ice and the Volatile Inventory of Halley's Comet: The trapping of gases in water ice by clathrate hydrate formation is accompanied by substantial chemical fractionation effects, as some molecules are incorporated preferentially compared to others. Lunine used the Giotto Ion Mass Spectrometer results (1,2) and a quantitative thermodynamic model to calculate the relative abundances of major carbon- and nitrogen- bearing species in the environment in which Halley's comet formed, under the assumption that the water ice in the nucleus is largely clathrate hydrate. The thermodynamic model is described in (3). Application to comets is timely for the following reasons: (a) Very recent experimental work (4) identified the clathrate hydrate of CO as the structure I cubic type, with dissociation pressure intermediate between the structure II N<sub>2</sub> and O<sub>2</sub> clathrates, validating the predictions of the thermodynamic model. Recent Raman spectroscopy (5) indicates that CO<sub>2</sub> fits in the large cages of the clathrate structure but not the small ones, also in agreement with the model (and contrary to some earlier work). (b) Interpretations of the Giotto results in terms of the formation environment of Halley's comet have not hitherto quantitatively considered fractionation effects in water ice.

The following results were obtained : CO to CH<sub>4</sub> ratio: The measured ratio of CO to CH<sub>4</sub> (~1 - 10) in the region near Halley's nucleus implies a CO to CH<sub>4</sub> ratio in the primordial gas of 10 to 10<sup>5</sup>, depending upon the amount of water available to form clathrate (i.e., the degree of exposure of the ice to gas in the grain-forming region). This nebular CO to CH<sub>4</sub> ratio is consistent with that obtained in models of the solar nebula constructed by Lewis and Prinn(6). Incorporation of CO<sub>2</sub> in clathrate: Despite carbon dioxide's stability as a condensate at low temperatures, a significant fraction of CO<sub>2</sub> in comets may also be incorporated in

clathrate hydrate. Hence while comet activity at large distances from the sun may be driven by CO<sub>2</sub> ice, at least some of the CO<sub>2</sub> measured by Giotto may have been trapped primordially in clathrate hydrate.

Since we do not actually know how volatiles are trapped in Halley, we cannot adequately constrain the comet's formation from Giotto data; in-situ identification of volatiles and trapping mechanisms in a comet's nucleus (as planned on CRAF) is crucial.

2. Equation of State of Ammonia-Water Liquid: In collaboration with S.K. Croft and graduate student J. Kargel, an equation of state for ammonia-water liquid was determined by performing laboratory measurements and combining these with data extracted from the literature. The ammonia hydrates, chemical compounds of ammonia and water, could comprise as much as 10% of the total mass of some of the satellites of Saturn and Uranus. The presence of ammonia in water ice reduces the melting point to as low as 175K. As pointed out by a number of workers, this melting temperature is low enough to be reached by radioactive heating in the interiors of satellites >500 km in radius, possibly accounting for some of resurfacing seen in Voyager images. However, the chemical and physical properties of the ammonia hydrates and their associated liquids are poorly determined; hence the present study was conducted. The work is in press in Icarus.

Liquid equation of state: By combining density data in the literature with laboratory measurements on the liquid performed at Arizona an equation of state was derived for use at pressures, temperatures and compositions appropriate to the interiors of icy satellites. The one bar slice of this diagram is displayed as figure 1. We also derived density-temperature-pressure relationships for the solid hydrates. Several interesting results were obtained:

1. The bulk modulus and density data for the liquid at intermediate (~50% ammonia composition) show substantial deviation (about 10% in the density) from values obtained by simple averaging techniques. Accurate characterization of the behavior of the ammonia-water liquids should not therefore rely on simple mixing models for the endmembers.
2. The density of the ammonia-water peritectic liquid at melting (~175K) is about 0.946 g/cm<sup>3</sup>. This is greater than the density of ice I at this temperature but much less than the density of a mixture of rock and ice obtained in an undifferentiated satellite. Comparison of the "first melt" density with other ammonia hydrate solids shows that the melt is nearly neutrally buoyant.

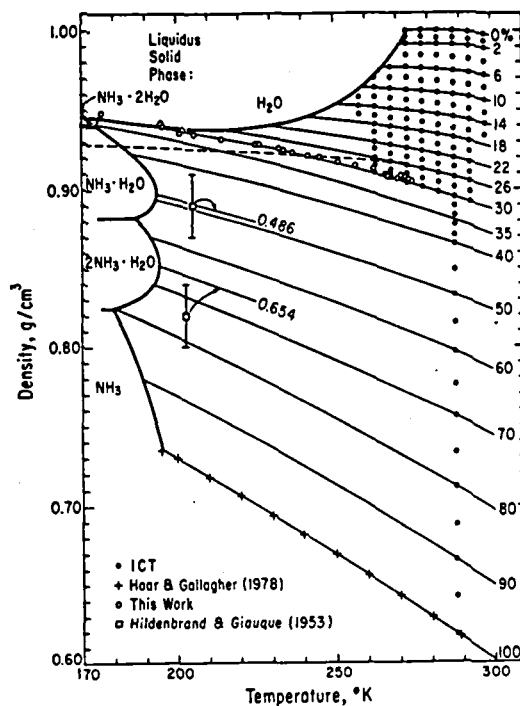
Styles of ammonia-water volcanism: The density information derived in this study is of critical importance in understanding the types of ammonia-water volcanism expected on icy satellites. This is discussed in the abstract by Croft in this volume.

Ammonia-water system at high pressure: Using the equation of state information for ammonia-water solid and liquid phases derived in this study, we explored the phase diagram of ammonia-dihydrate at high pressure. We confirmed an earlier conclusion (7) that existing data on the dihydrate at high pressure (8) are compatible with low pressure results only if a structural change in the dihydrate occurs at roughly one kilobar.

# References

1. Allen, M.A. et al., Astron. and Astrophys., in press, 1987.
2. Eberhardt, P. et al., Astron. and Astrophys., in press, 1987.
3. Lunine, J.I. and D.J. Stevenson Astrophys. J. Suppl. **58**, 493, 1985.
4. Davidson, D.W., et al., Nature **328**, 418, 1987.
5. Seitz, J.C., et al., Geochim. Cosmochim. Acta **51**, 1651, 1987.
6. Lewis, J.S. and Prinn R.G. Astrophys. J. **238**, 357, 1980.
7. Lunine, J.I. and D.J. Stevenson, Icarus **70**, 61, 1987.
8. Johnson, M.L. and M. Nicol, J. Geophys. Res. **92**, 6339, 1987.
9. Harr, L. et al. NBS/NRC Steam Tables, Hemisphere Publ., 1984.
10. Hildenbrand, D. L. and W.F. Giaque, J. Am. Chem. Soc. **75**, 2811, 1953.

Figure 1: Density-temperature-composition relations for liquid ammonia-water at 1 bar derived in this study. The dashed lines indicate the density of Ice Ih. (Croft, Lunine and Kargel, Icarus **73**, in press).



## Low Temperature Mineral Phases on Phobos?

Kathryn K. Pierce and Bruce Murray  
Division of Geological and Planetary Sciences  
California Institute of Technology

Phobos, like the Moon, appears to be covered by a fine surface material with a low thermal inertia between  $0.9-1.6 \times 10^{-3} \text{ cal cm}^{-2} \text{ s}^{-1/2} \text{ K}^{-1}$  (Lunine et al., JGR 87, 10297-10305, 1982) in a vacuum environment. Yet, its low density of 2.0 g/cm<sup>3</sup>, very low bond albedo of 0.02 and spectral reflectance curve point to a non-lunar composition - namely, a volatile-rich, carbon-aceous chondritic composition.

In April of 1989, the Russian Phobos '88 spacecraft will skim past Phobos near local noontime at an altitude of 50 m. The surface temperature distribution and morphology will be recorded by the radiometer TERMOSKAN (spatial resolution of 1.5 cm and bandwidth of 8-13  $\mu\text{m}$ ) and the TV cameras FREGAT. This study examines whether a high spatial resolution radiometer can detect the presence of low temperature mineral phases on Phobos' surface.

Two extreme materials are considered as possible surface compositions in this study. A devolatilized material of high temperature mineral phases serves as the lunar-like extreme with a thermal conductivity of  $7.0 \times 10^{-6}$  and a thermal inertia of  $1.0 \times 10^{-3}$  (cgs units as above). A volatile material of low temperature mineral phases serves as the contrasting extreme with a higher thermal conductivity of  $1.0 \times 10^{-4}$  and a thermal inertia of  $3.2 \times 10^{-3}$ .

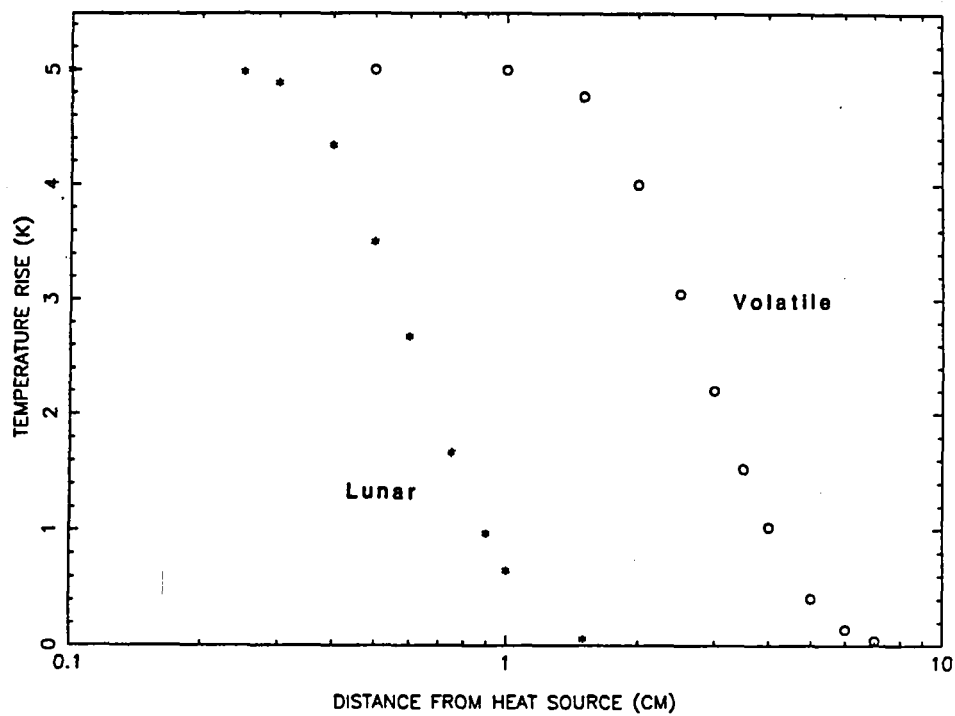
Surface thermal wave profiles were calculated by numerically solving the heat diffusion equation with homogeneous thermal parameters. The surface boundary condition consisted of an energy balance between annual solar insolation, thermal conductance and thermal emission. The bottom boundary condition consisted of zero thermal flux. The resulting thermal wave profiles (Figure 1) show a detectable difference of 15 K in local noontime surface temperature between the two material cases.

Across Phobos' surface, however, topography will establish pockets of heat. Such topography was schematically modelled as isolated heat sources on a flat surface. The heat equation was then solved analytically to give the rise in temperature above ambient temperature at a certain distance from a 10 K heat source over 50 minutes (Figure 2). These curves show the wider spread of horizontal heat flow for the volatile material in comparison to the lunar-like material.

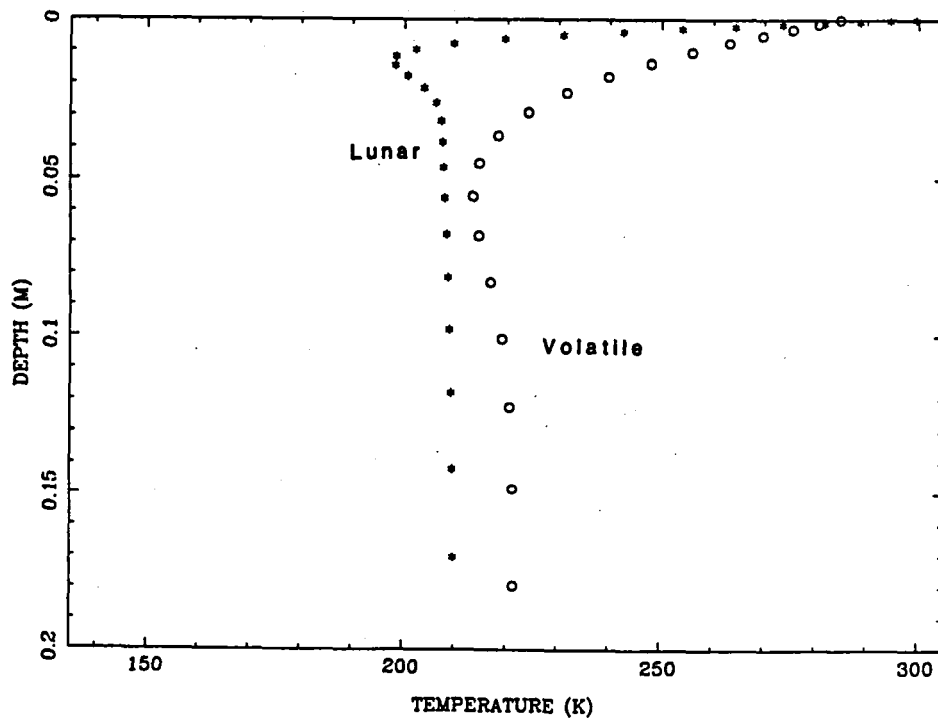
Thus, TERMOSKAN should be able to detect the presence of low temperature mineral phases from their lower noontime temperatures and lower thermal gradients across topography.



TEMPERATURE RISE DUE TO HORIZONTAL HEAT FLOW



PHOBOS' SURFACE THERMAL WAVE AT NOONTIME





## CHAPTER 5

### SPECTROSCOPY AND REMOTE SENSING



## Automated Analysis of Reflectance Spectra

Roger N. Clark, U.S. Geological Survey, Mail Stop 964, Box 25046 Federal Center, Denver, CO 80225

### Introduction

The analysis of reflectance spectra has traditionally been a task requiring days of work by a scientist trained in spectroscopy. The new mapping spectrometers to be flown on Mars Observer and CRAF as well as terrestrial instruments such as AVIRIS will return millions of spectra to analyze. Traditional analysis methods are too slow to use on such data.

The goal of this study is to develop new and fast analysis tools that can be used on the forthcoming flood of data. The requirements imposed by the data and the desire to extract all the information present are ambitious:

- 1) complete automation of spectral analysis,
- 2) the analysis must be fast enough to keep up with projected data rates,
- 3) the tools should be usable by a scientist not trained in spectroscopy and
- 4) the results should be interpretable by scientists trained in geology.

### Analysis Method

The key to analysis of reflectance spectra lies in continuum definition. Some continuum can be so strongly sloping that there are no local minima (e.g. as in some lunar spectra). Traditional minima-finding routines and derivative analysis ones may not even find an absorption band. Continuum analysis solves this problem by removing the local slope (see Clark and Roush, 1984 for a theoretical basis for continua).

### Continuum Analysis

The analysis of a reflectance spectrum typically involves removing a continuum, analyzing band positions, comparing band positions to the positions observed in known materials and estimating the abundances. A first generation automatic continuum analysis routine has been developed earlier this year (Clark et al., 1987).

The continuum-analysis method was developed by analyzing how a spectroscopist chooses a continuum. The method was modified to be both fast and consistent so that it will not fail under any conditions. The algorithm derives an "upper hull" over segments of the spectrum and then removes it by division. The remaining spectrum is then analyzed again where the hull is effectively allowed to curve more on each iteration. Locations where the continuum "touches" the spectrum are called continuum-tie points and the iterations are continued until there are no local minima

(within the noise level) between them. The product of all continua exactly matches the original spectrum.

The interesting result of the method is that the continuum analysis extracts absorption features. On complex absorptions, the continuum will first describe the overall band shape and then on additional iterations the continuum will follow the fine detail.

### Feature Analysis

The features in each continuum are found by looking for minima between continuum-tie points. In order to maintain speed, complicated analyses such as a nonlinear least squares Gaussian fit are not feasible. However, an absorption can be modeled by short line segments and the computation is very fast. In order to describe the "peakiness" as well as asymmetry, width and depth in a feature, several parameters were found necessary to fully describe it:

- 1) band center:  $C$ ,
- 2) band width (Full Width at Half Maximum, FWHM):  $W$ ,
- 3) band depth:  $D$ ,
- 4) continuum reflectance at band center:  $R_c$ ,
- 5) band quarter width (Full Width at  $\frac{1}{4}$  Maximum, FWQM):  $Q$ ,
- 6) band asymmetry:  $A$ ,
- 7) error bar in depth:  $E$ ,
- 8) continuum iteration level:  $I$ , and
- 9) fraction of continuum data points that fall on the spectrum:  $F$ .

The last three parameters are used with the band depth to derive the significance of the band. Some features in the continua are describing gross shape and have few data points that follow the actual spectrum. Others describe the fine detail. The  $F$  parameter is a description of this case: the greater the  $F$  value, the more the continuum follows the fine details of the spectrum.

### Spectral Feature Identification

Given a spectral library that is sampled at the same wavelengths and resolution as the flight (or laboratory) instrument, one can apply the continuum plus feature analysis and derive a spectral features library for that instrument. This has been done at the USGS in Denver and a test spectral features library now has about 8000 entries. Analysis of a spectrum of an unknown with uses the same algorithms as used to generate the library. A cross-correlation of all independently identified features is done to identify the species present.

The final step examines the identified features compared to the strength of features in the library and derives the "spectral abundance." The spectral abundance is simply the depths of the absorptions in the unknown divided by the depths from the library. It is not necessarily true abundance. However, it does give an idea of whether a little or a lot of the material is present.

The spectral abundance will be used in the next step as a first indicator of abundance to the radiative-transfer analysis. The radiative transfer analysis was described at last year's DPS meeting in Paris (Clark, 1986). That method solved for true mineral abundance and grain size but requires knowledge of the minerals present. When combined with the methods presented here a complete analysis package from unknown spectrum to mineral abundance is in hand!

## Discussion

The analysis method described here is quite fast. All times below are for a Sun 3/160 computer projected for a typical VIMS spectrum having 320 spectral channels covering 0.4 to 5  $\mu\text{m}$ . A Sun 3/160 computer has a speed for this application of about 2.5 to 3 times the speed of a VAX 780. Continuum + feature analysis will take about 1.2 seconds per spectrum. Feature identification will take less than about 1 second. Total analysis times including input plus output is < 3 seconds to identify the minerals present and derive the spectral abundance with no human interaction!

## Conclusions

The analysis methods described here provide full automation of reflectance spectra such that data can be analyzed from future planetary spacecraft on a routine basis as the data are received. The results could be used to produce images of mineral location and their spectral abundance. Such images would be of tremendous value to geologists. Future routines might use this information to derive rock type.

The present algorithm is still under development. While a working version is complete, it must include additional analysis when absorption bands overlap to the degree that no inflection points occur (strongly overlapping bands). The difficult parts of the problem have been solved and there should be no problem producing a production version by the time data are received from planetary spacecraft such as Mars Observer or CRAF. This first-generation system will be tested on AVIRIS data in the near future.

The success of the final version will be dependent on a complete spectral library. If materials are encountered that are not in the library then the method will fail. Current funding levels for library development are extremely small.

## References

- Clark, R.N., The derivation of Mineral Abundance from Reflectance Spectra: *Bull. of the Am. Astron. Soc.* 18, 760-760, 1986.
- Clark, R.N., T.V.V. King, and N.S. Gorelick, Automatic Continuum Analysis of Reflectance Spectra: *Proceedings of the Third Airborne Imaging Spectrometer Data Analysis Workshop*, JPL Publication 87-\_\_\_, in press, 1987.
- Clark, R.N. and T.L. Roush, Reflectance Spectroscopy: Quantitative Analysis Techniques for Remote Sensing Applications, *J. Geophys. Res.*, 89, 6329-6340, 1984.

### Mid-Infrared (2.1-25.0 $\mu$ m) Spectroscopic Studies

John W. Salisbury, U.S. Geological Survey, Reston, VA 22092  
and Louis S. Walter, NASA Goddard Space Flight Center, Laboratory for  
Terrestrial Physics, Greenbelt, MD 20771

**Mineral Spectra:** The first edition of a spectral library for minerals has been completed (Salisbury et al. 1987), and measurements for a second edition are underway. This digital spectral library is unique in that each mineral sample is carefully characterized and the nature and extent of characterization procedures is documented. Also, data are presented in transmittance, as well as in biconical reflectance for different particle size ranges, and are available in digital form from the Principal Investigator.

Of particular interest for remote sensing of planetary surfaces are the spectra of fine particulate materials. These data document the occurrence of two spectral features, transparency peaks and Christiansen frequency minima, that promise to be very important in interpretation of emittance spectra of fine particulate regoliths.

Transparency peaks occur in a region of relatively low absorption between the fundamental Si-O stretching and bending modes. In this wavelength region, fine particles are optically thin and photons undergo volume scattering that results in a reflectance maximum. This spectral feature often is more prominent than the fundamental vibration bands for fine particle size materials.

Another spectral feature that is prominent in spectra of fine particulates occurs at the principal Christiansen frequency. This is a reflectance minimum that occurs because the real part of the refractive index undergoes rapid changes (anomalous dispersion) at a slightly shorter wavelength than the most intense molecular vibration band. Consequently, the refractive index approaches 1, resulting in a minimum of scattering, at a wavelength where absorption is still relatively low. With little scattering and low absorption, infrared radiation can penetrate a sample relatively easily, resulting in a minimum in reflectance or a maximum in emittance.

Both of these spectral features shift wavelength position in conjunction with the fundamental molecular vibration bands. Thus, they may be used as indirect indicators of composition. When the wavelengths of transparency peaks of representative rock-forming minerals are plotted against their Christiansen frequencies, very good separation of different mineral groups is obtained, leading us to believe that different rock types might also be distinguished on the same basis.

In contrast with fine particulate materials, spectra of solid mineral samples display strong fundamental molecular vibration (reststrahlen) bands. As has been known for a long time, these reststrahlen bands shift systematically in wavelength as silicate minerals undergo structural changes due to "depolymerization" (i.e., changing from a framework, to a



sheet, chain, double tetrahedron, and finally to an isolated tetrahedron structure).

Substitution of the divalent cations, calcium, iron, and magnesium accompanies this depolymerization, and we have proposed a chemical index based on this phenomenon that was found to correlate extremely well with the spectral changes that result (Walter & Salisbury, 1988). This SCFM index, the ratio of silica to silica plus the oxides of calcium, iron and magnesium, also correlates very well with the spectral changes due to the changing mineral content of different rock types (see below).

Rock Spectra: Unlike mineral spectra, which were obtained in biconical reflectance, rock spectra were recorded in directional hemispherical reflectance using a gold-coated integrating sphere. This resulted in more quantitative data for rocks from which can be calculated directional emittance (Nicodemus, 1965).

A complete suite of 38 igneous rocks has been measured, including coarse-grained, fine-grained, and glassy varieties. All have been well-characterized chemically and, where possible, mineralogically. Analysis of the solid sample spectra is complete and an excellent correlation with the SCFM chemical index has been found. In addition, we have shown that most of the compositional information in the 8-12  $\mu\text{m}$  region is in the broad band envelope of the Si-O stretching fundamental vibration band, rather than in the fine structure. Thus, there is relatively little advantage gained from high spectral resolution for multispectral remote sensing of solid igneous rocks (Walter & Salisbury, 1988).

Spectral data for particulate samples of the same rocks are still being acquired. They will be analyzed for variations of Christiansen frequency and transparency peak with each other and with the SCFM Index, and then published with the solid sample data as another digital spectral library.

Meteorite Spectra: Biconical reflectance spectra of 25 particulate meteorite samples have been measured (sample size is not large enough for the directional hemispherical measurement). The initial results are interesting for two reasons. First, these particulate samples display well-defined Christiansen frequencies and transparency peaks, which show that ordinary chondrites, achondrites, and carbonaceous chondrites (and presumably their parent bodies) can be distinguished using these spectral features.

A second interesting result from initial meteorite spectra concerns weathering and hydrocarbon contamination. Earlier work showed a correspondence between a "redness index" and the depth of the water band near 3  $\mu\text{m}$  in chondrites (Salisbury and Hunt, 1974) which suggested that even carefully preserved meteorite "falls" could be affected by limonitic weathering. In the case of the meteorites measured here, chemical analyses by Dr. Eugene Jarosewich of the Smithsonian National Museum of Natural History provided data on total water content of each meteorite. We have found excellent agreement between water content, 3  $\mu\text{m}$  band depth,

and redness index, suggesting limonitic weathering as the source of the H<sub>2</sub>O in these analyses. In addition, however, unexpected hydrocarbon bands have been found in spectra of the chondrites and achondrites. Their band depths are in excellent agreement with chemical analyses of total carbon, and there is also a good correlation between hydrocarbon and water content. Thus, it appears that meteorites in museum storage may absorb and be contaminated by both water vapor and hydrocarbons from the air, which is also our experience with terrestrial rocks in the laboratory. One outcome of the spectral measurements reported here is the potential for development of a non-destructive technique for determining the degree of contamination/weathering of meteorite samples, which would be important for both spectroscopic studies in support of remote sensing measurements and for geochemical research on meteorites. This work is being done in cooperation with Dr. Jarosewich.

Field Spectrometer: A field instrument capable of direct measurements of spectral emittance from 2.5 to 14  $\mu$ m is under construction and due for completion in January 1988. It is an interferometer (FTIR) design that uses a rotating refraction plate, instead of the traditional moving mirror of FTIR spectrometers, to achieve path length differences. This rugged design is insensitive to temperature changes and instrument orientation, so that measurements can be made under a wide variety of observational conditions. For example, we intend to investigate the effects of different illumination and observation geometry, as well as the effects of micrometeorological parameters such as air temperature and wind speed, on spectral emittance.

Cooperation With Other Investigators: Mid-infrared measurements were made for Dale Cruikshank of the University of Hawaii, Tom Jones of the Lunar and Planetary Laboratory at the University of Arizona, and Jim Garvin of Goddard Space Flight Center. Samples characterized and measured in the mid-infrared were shipped to Roger Clark in Denver for measurement in the visible/near-infrared under a separate project.

References: Nicodemus, F.E., 1965, Directional reflectance and emissivity of an opaque surface: *Applied Optics*, v. 4, p. 767-773.

Salisbury, J.W., and Hunt, G.R., 1974, Meteorite spectra and weathering: *Journal of Geophysical Research*, v. 79, p. 4439-4441.

Salisbury, J.W., Walter, L.S., and Vergo, Norma, 1987, Mid-Infrared (2.1-25  $\mu$ m) Spectra of Minerals: USGS Open-File Report 87-263, 357 pp.

Walter, L.S., and Salisbury, J.W., 1988, Thermal-infrared (8-12  $\mu$ m) spectral characterization of igneous rocks: (in preparation).

### Abundance Estimates Derived From Reflectance Spectra of Tricomponent Mixtures

MUSTARD, J. F. and C. M. PIETERS (Dept. of Geol. Sci. Brown University, Providence RI, 02912)

Quantitative abundance estimates recently calculated from bidirectional reflectance spectra of binary mixtures containing igneous rock-forming minerals, and of mixtures containing complex terrestrial desert soils, have been shown to be accurate to within 5% for mixtures not containing strongly absorbing components (Mustard and Pieters, *Proc. LPSC 17th.*, 1987). This approach has been expanded to tricomponent mixtures of igneous rock-forming minerals to explore the accuracy of prediction for higher dimension mixtures.

Eight mixtures containing varying amounts of anorthite, enstatite, and olivine, were constructed with controlled mass fractions and particle diameters (wet sieved to the 45 to 75  $\mu\text{m}$  particle size). Bidirectional reflectance spectra of the mineral mixtures as well as each mineral component were measured in the laboratory from 0.4 to 2.5  $\mu\text{m}$ . The reflectances were converted to single scattering albedo (SSA) using Hapke's (*JGR*, 86, 1981) equations for bidirectional reflectance simplified by assuming that particulate surfaces scatter light isotropically at intermediate phase angles ( $B(g)=0$ ,  $P(g)=1.0$ ). The endmember SSA spectra were mixed and fit to the mixture SSA spectra in a least squares sense. The proportion of each endmember required to minimize the variance between the measured and computed spectra determine the relative geometric cross sections (RGCS) for each component (proportional to mass fraction/ density  $\times$  particle diameter). Since the densities and particle diameters of the components are known, mass fractions were calculated from the computed RGCS. The mass fractions calculated from this spectral inversion agree with the actual mass fractions used in the prepared mixtures to better than 7%. Quantitative abundance estimates of multicomponent surfaces can thus be derived from high spatial and spectral resolution reflectance data soon to be obtained by imaging spectrometers (e.g. AVIRIS, NIMS, VIMS). The accuracy of this approach will allow mineralogic variations on the surface to be identified and studied on a regional scale.

**EFFECTS OF SMALL-SCALE SURFACE ROUGHNESS ON THE BIDIRECTIONAL REFLECTANCE SPECTRA OF NICKEL-IRON METEORITES.** Daniel T. Britt and Carle M. Pieters, Department of Geological Sciences, Brown University, Providence, RI 02912.

Spectral reflectance studies have suggested that elemental iron is a major component of the surface mineralogy of M and S-type asteroids [1,2]. Both asteroid types exhibit a spectral red-slope (increasing reflectance with increasing wavelength) that has been interpreted as characteristic of the presence of large amounts of elemental iron. As asteroids become more frequent targets of remote sensing observations, both from ground-based telescopes and spacecraft, it is important to understand the bidirectional reflectance properties of metallic surfaces and how these surfaces relate to processes on metal-rich bodies.

The effect of small-scale (<1 mm) surface roughness and viewing geometry on the bidirectional reflectance of iron meteorites has been investigated using NASA's RELAB facility located at Brown University [3]. Samples of the Canyon Diablo and Gibeon [4] meteorites were polished with aluminum oxide and diamond abrasive grits to controlled surface roughnesses and checked with a reflected light microscope. After polishing, each sample was immediately washed in ethyl-alcohol and dried to prevent corrosion. At each roughness a series of spectra were taken at specular ( $i=e$ ) and non-specular geometries. Spectra were also taken of several other complex metallic surfaces that are potential analogs for metallic regoliths resulting from asteroid processes such as cratering and particle size commutation. These included fresh filings of the Canyon Diablo meteorite (particle size range 30 microns to 1 mm) and two small craters in the Gibeon meteorite produced by experimental hyper-velocity impacts [5]. One crater was formed by a metal projectile, the other by a basalt projectile. Surface relief on both craters is in the range of 0.1 to 1 mm.

These measurements suggest that the spectra of metallic surfaces can be divided into three general groups that correspond to degree of surface roughness. Group I consists of surfaces rougher than 10 microns and smoother than 1 mm. Group II covers the roughness range from 10 microns to 0.3 microns. Finally, Group III consists of surfaces smoother than 0.3 microns.

**Group I (10 microns–1 mm):** A surface on the Canyon Diablo meteorite was polished with 400 grit aluminum oxide, producing relief in the range of 10–40 microns. The spectra of this sample is shown in figure 1 and is characterized by a classic iron red-slope exhibiting a featureless but steadily increasing reflectance. The albedo and spectral shape of this sample at both specular ( $i=e=10$ ) and non-specular ( $i=0$ ,  $e=30$ ) geometries are similar, indicating that the surface is effectively a diffuse reflector. The spectra of the three complex metallic surfaces (filings, metal on metal crater, and basalt on metal crater) are also included in figure 1. Although the albedos of the three surfaces vary by a factor of 7, their spectral shapes (figure 2) are similar to the 400 grit surface. This suggests that for the roughness range of 10 microns to 1 mm the spectral properties of metallic surfaces are very similar, although albedos may differ substantially.

**Group II (0.3–10 microns):** Spectra of a sample of the Gibeon meteorite polished with 1200 grit aluminum oxide, producing a relief in the range of 1–5 microns, are shown in figures 3 and 4. Spectra of this group are characterized by complex scattering processes. The specular component (figure 3) shows a maximum reflectance in the near infrared that decreases in wavelength position with increasing phase angle. The non-specular component (figure 4) flattens with increasing phase angle, progressively losing its characteristic red-slope. Samples of the Canyon Diablo meteorite polished to this roughness show similar results.

**Group III (< 0.3 microns):** A sample of the Canyon Diablo meteorite was polished with diamond grit, producing surface relief less than 0.3 microns. At this roughness the surface is smoother than the wavelength of visible light and effectively a featureless mirror to light in the 0.5 to 1.8 micron range. Most of the incident light is reflected into the specular component with a minor contribution from the non-specular component. The spectra show a very bright and red-sloped specular reflection (figure 5) that flattens with increasing wavelength. The non-specular component, on the other hand, is dark and flat, showing none of iron's characteristic red-slope (figure 6).

**Conclusions:** Surfaces in the 10 micron to 1 mm roughness range are effectively diffuse reflectors, producing bidirectional reflectance spectra that are similar to each other and to published M-type asteroid [1] and directional-hemispherical (diffuse) iron meteorite [6] spectra. Smoother surfaces produce complex scattering behavior and the separation of the specular and non-specular components into distinctly different spectral types. Natural metallic asteroidal surfaces are probably best modeled by surfaces rougher than 10 microns.

**REFERENCES:** [1] Gaffey, M.J. and McCord, T.B. (1976) *Space Sci. Rev.* 21, pp. 555–628. [2] Zellner, B. (1979) In *Asteroids*, pp. 783–806, Gehrels, T. ed., Univ. of Ariz. Press, Tucson. [3] Pieters, C.M. (1983) *JGR* 88, pp. 9534–9544. [4] Buchwald, V.F. (1975) *Handbook of Iron Meteorites*, Univ. of Calif. Press, Berkeley. [5] Matsui, T. and Schultz, P.H. (1984) *PLPSC 15*, in *JGR* 89, pp. C323–C328. [6] Gaffey, M.J. (1976) *JGR* 81, pp. 905–920.

# SPECTRA OF IRON METEORITES

Britt, D.T. and Pieters, C.M.

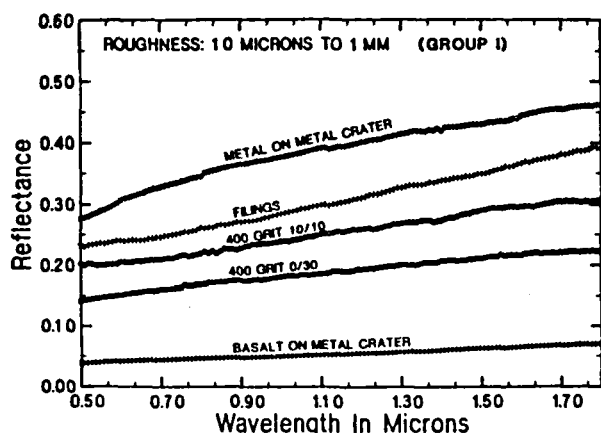


Figure 1: Bidirectional spectra of Group I "rough" metallic surfaces. Viewing geometry is expressed i/e. (Halon Standard)

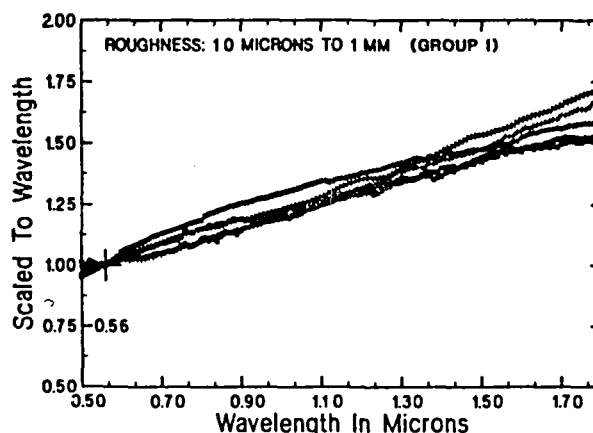


Figure 2: Bidirectional spectra of Group I surfaces scaled to 1.0 at 0.56 microns. (Halon Standard)

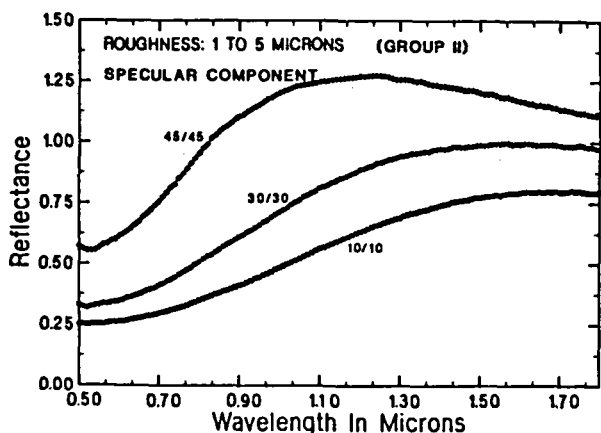


Figure 3: Bidirectional spectra of Group II moderately smooth surface. Specular reflectance ( $i=e$ ) of Gibeon meteorite. Angle of incidence is indicated for each spectra. (Halon Standard)

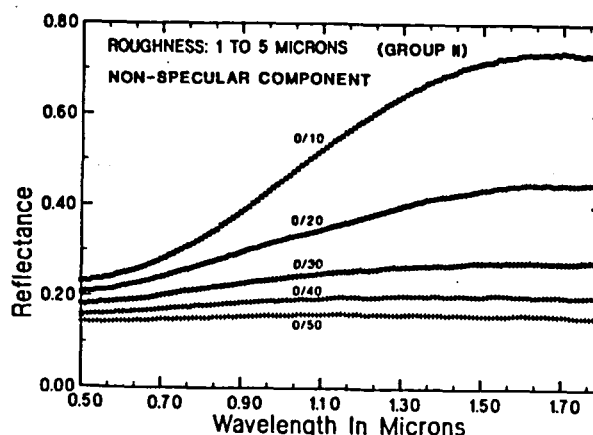


Figure 4: Bidirectional spectra of Group II surface. Non-specular reflectance ( $i \neq e$ ) of Gibeon meteorite. The spectral shape becomes flatter with increasing phase angle. (Halon Standard)

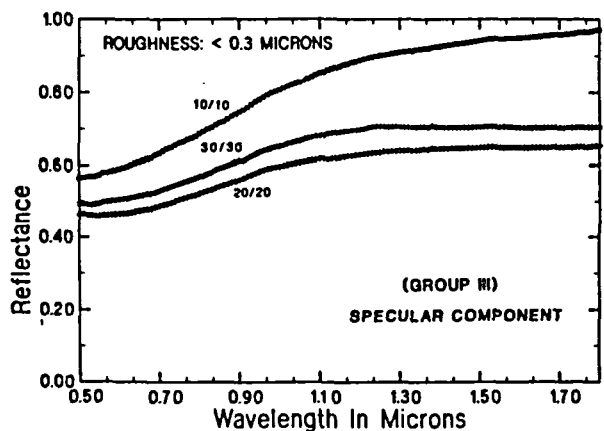


Figure 5: Bidirectional spectra of Group III smooth surface. Specular reflectance ( $i=e$ ) of Canyon Diablo meteorite. (Calibrated Aluminum Mirror Standard)

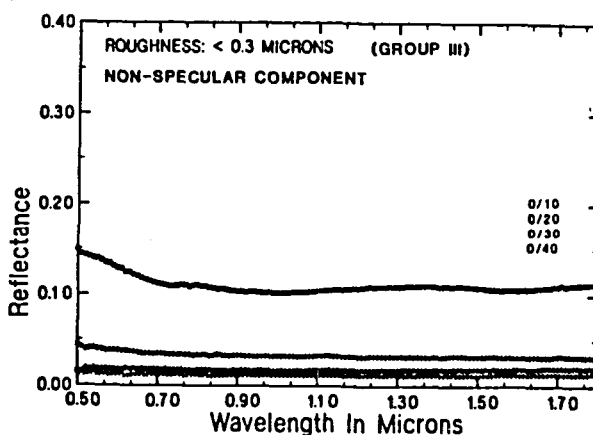


Figure 6: Bidirectional spectra of Group III smooth surface. Non-specular reflectance ( $i \neq e$ ) of Canyon Diablo meteorite. (Halon Standard)

# SPECULAR REFLECTIONS AND THE NATURE OF PARTICLE SURFACE INTERACTIONS

S.A. Yon and C.M. Pieters, Dept. of Geological Sciences, Brown University, Providence, R.I. 02912

**Introduction** Light reflected from a particulate surface has undergone multiple transmissions and reflections between particles (1,2). Scattering by a particulate sample is a function of both bulk sample properties (compaction, particle size, etc.) and the scattering efficiency of the individual particles (1). The complexity of the solution to the equation of radiative transfer for real particulate samples has prompted the simplifying assumption that all particle surface interactions are specular reflections, which are approximated mathematically by Fresnel's equations (1). This approach contains an implicit assumption that particle surfaces are optically smooth for all wavelengths considered.

In natural surfaces, single particles may scatter light by single or multiple specular (Fresnel) reflections, or by resonant (Rayleigh) scattering, which occurs from particles or surface features close in size to the incident wavelength (2). Light which interacts with a surface by one of these two mechanisms is polarized in a manner diagnostic of the mechanism. The angular distribution of scattered light can also be used to differentiate between Fresnel and Rayleigh interactions. Specular (Fresnel) reflections are confined to directions for which the incident angle,  $i$ , equals the emergent angle,  $e$ , although rough surfaces may geometrically disperse light through specular interactions from randomly oriented surface facets. Rayleigh scattered rays, on the other hand, are dispersed nearly isotropically (3).

**Data Acquisition** To investigate light interactions with particle surfaces, obsidian slabs were prepared with controlled surface roughness to approximate natural particle surfaces. The visible near IR spectra of three obsidian samples are shown in figure 1. Slab surfaces may be thought of as one end member of a series of particulate samples of increasing mean particle size. Obsidian was chosen to minimize internal crystal boundary reflections. The lack of significant absorption features in such slab spectra indicate that internally transmitted light is unimportant compared to surface interactions of radiation.

Two obsidian slabs were prepared by grinding with a) 400 grit (40 $\mu$ m) and b) 400 then 1200 grit (5 $\mu$ m) Al oxide powder. These will be called the rough and smooth slabs, respectively. Using the RELAB bidirectional reflectance spectrometer the reflectivity relative to halon between 0.35 and 1.8 $\mu$ m, and the polarization state of reflected light between 0.6 and 1.8 $\mu$ m, were measured for each of the slabs for phase angles between 15 and 90 degrees. Polarization determinations require 6 measurements: 4 sample measurements with polarizing optics in both incident and reflected beams, and 2 measurements to determine the light source polarization bias. This arrangement allows the depolarizing properties of the sample to also be measured in the crossed-polars configuration.

**Results** Shown in figure 2 are reflectivity measurements of the smooth slab at 3 specular geometries. For all of these geometries, reflectivity is seen to undergo a transition from short (<0.8 $\mu$ m) to long (>1.2 $\mu$ m) wavelengths. Short wavelengths exhibit low reflectance which increases with phase angle,  $g$ , while long wavelengths exhibit high reflectance which also increases with  $g$ . The transition zone between short and long wavelength behavior is seen to move toward shorter wavelengths with increasing  $g$ . Reflectivity measurements at a constant  $i$ , for several values of  $e$ , were also obtained. These show that at the longer wavelengths, the flux is strongly concentrated along the specular direction. As  $g$  increases, all wavelengths show a preferential brightening along the specular direction.

The reflectivity of the rough slab for  $i=45^\circ$  and five  $e$  positions, including the specular direction, are shown in figure 3. The long wavelength specular surge is absent and all curves are remarkably similar, varying only in relative brightness. No preferred direction of reflectivity is observed at any geometry.

Polarization of light reflected from the slabs for two selected wavelengths is shown in figures 4,5. Specular ( $i=e$ ) geometries are labeled S for the smooth slab and R for the rough slab. Points labeled M and N are the smooth and rough slabs, respectively, for which  $i \neq 0$  but the effective incident angle plotted is half  $g$ . The predicted polarizations for Rayleigh scattering and Fresnel reflections, which depend on the complex index of refraction, are also shown. The refractive indices used to generate these Fresnel curves are in general accord with those found in other volcanic glasses (4). For all measurements, the cross polarized terms were insignificant. (<5% as bright as the two non-cross polarized terms.)

**Discussion** The dramatic reflectivity variation with wavelength of the smooth slab suggests that two modes of reflection are in operation between 0.35 and 1.8 $\mu$ m. Long wavelengths are reflected specularly from the smooth slab surface. This is confirmed by the polarization of these wavelengths at specular geometries (S). Short wavelengths, however, are more geometrically dispersed, apparently from randomly oriented facets. The polarization state of this dispersed light (M) indicates that short wavelengths have also undergone a single Fresnel reflection. The migration of the transition zone and the increase in brightness with  $g$  of the short wavelengths suggest that these two modes are mixed in different proportions. This slab surface is thus optically smooth at longer wavelengths but optically rough at the shorter wavelengths.

For any given wavelength, all polarization measurements for both slabs (figures 4,5) fall on the same Fresnel polarization curve, regardless of slab roughness or instrument geometry. The structure of the surface determines the degree of dispersion of reflected radiation.

These results indicate that single Fresnel reflection dominates the first surface interaction of light with particle surfaces in the wavelength range 0.35–1.8 $\mu$ m. Rayleigh scattering is apparently unimportant even when surface features comparable in size to the incident wavelength are known to exist.

**References** 1) Hapke, B. 1981 *J. Geophys. Res.* **86**, 3039–3054 2) Wolff, M. 1975 *Appl. Optics* **14**, 1395 3) Bohren, C. and Huffman, D., 1983 "Absorption and Scattering of Light by Small Particles" J. Wiley & Sons 4) Pollack, J.B. et. al., 1973 *Icarus* **19**, 372–389

# PARTICLE SURFACE INTERACTIONS

Yon, S.A. and Pieters, C.M.

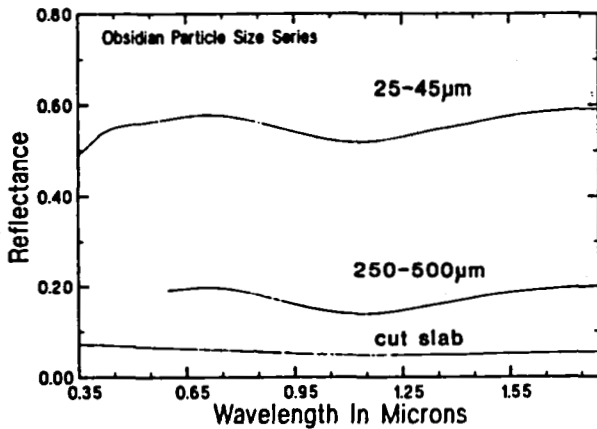


Fig. 1 Bidirectional reflectance spectra of two particulate and one cut slab (rough) sample of obsidian.  $i=0$ ,  $e=30$ deg (Halon Standard)

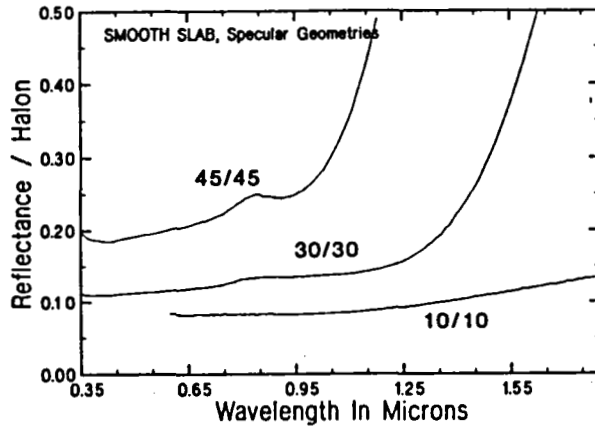


Fig. 2 Bidirectional reflectance spectra of smooth slab at 3 specular geometries. Angles in deg. (Halon Standard)

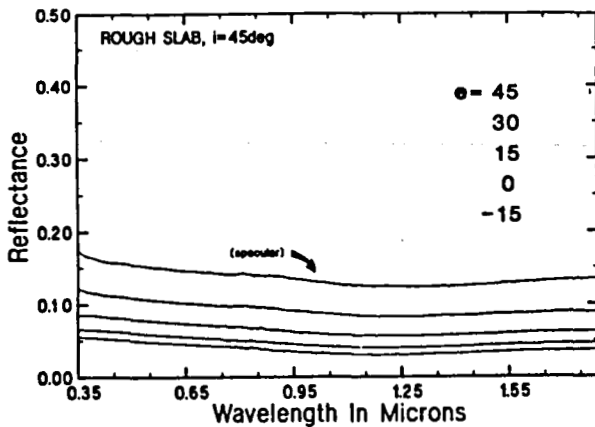


Fig. 3 Bidirectional reflectance spectra of rough slab at 5 geometries including the specular direction. Emergent angles in deg. (Halon Standard)

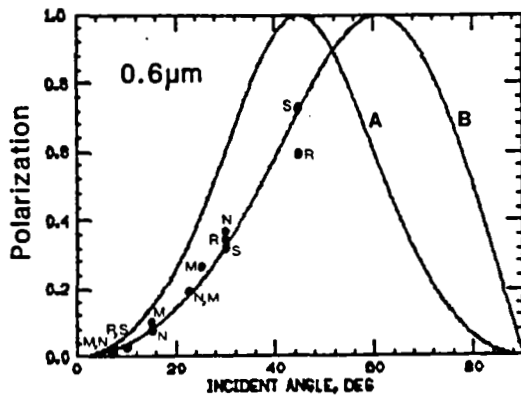


Fig. 4 Predicted Rayleigh (A) and Fresnel (B,  $n=1.8$ ,  $k=0.001$ ) polarizations for  $i=e$ , and experimentally derived polarizations for smooth and rough slabs at  $0.6\mu\text{m}$ .

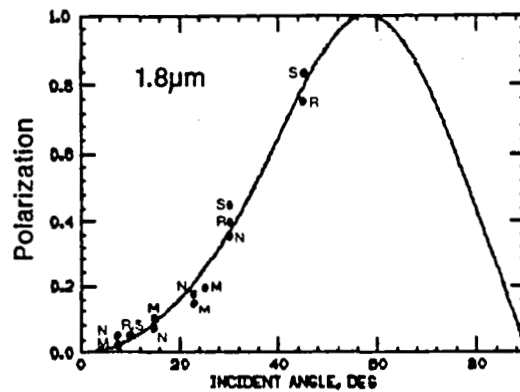


Fig. 5 Predicted Fresnel polarization ( $n=1.6$ ,  $k=0.001$ ) for  $i=e$ , and experimentally derived polarizations for smooth and rough slabs at  $1.8\mu\text{m}$ .

## Reflectance Properties of Planetary Surface Materials

William D. Smythe, Bonnie J. Buratti, Robert M. Nelson,  
Linda Horn, V. Gharakhani (JPL), Bruce W. Hapke (U. Pittsburgh)

The purpose of this activity is to obtain laboratory measurements of the bi-directional reflectance properties of planetary surface materials at a range of viewing geometries, especially small solar phase angles. The laboratory measurements are compared to theoretical models and to remote sensing observations (from both telescopes and spacecraft) to determine the surficial texture and composition of the regoliths of airless bodies - important physical characteristics for understanding surface processes and evolution.

Materials of interest include both volatile and non-volatile species covering the range suggested for planetary surfaces and suitable for testing results from models. We have investigated a suite of materials with controllable albedo and porosity, including several clays, basalts, sulfur, carbonaceous materials and photometric standards (MgO, BaSO<sub>4</sub>, Halon). In addition, we have continued on a program to measure the reflectance properties of condensible species (which porosities and grain sizes are not so easily controlled).

The controlled porosity experiments are particularly useful for developing an approach to solving the problem of enhanced reflectance near zero phase angle (opposition effect) - a major difficulty for the correct interpretation of ground-based studies of the outer planets and satellites. Our measurements show that bright materials have a significant opposition effect, similar to that predicted for dark materials (Smythe et. al. 1986)(figure 1). The first results of the porosity experiments have been reported (Buratti, et. al., 1987a), and utilized to achieve better understanding of the surface properties of the Galilean satellites (Buratti, et. al., 1987b). By combining our laboratory measurements and theoretical models with spacecraft measurements, we have shown that the regoliths of Io and Callisto are extremely porous (about 90% void space), whereas those of Ganymede and Europa are compacted.

Measurements of condensed species in our laboratory include greatly improved reflectance spectra of methane and nitrogen. Previously reported measurements of methane frost are difficult to obtain and uneven in quality - presumably due to the difficulties of sample preparation. Our new spectra demonstrate that the observed spectrum of Triton may be explained entirely by a very thin pathlength of methane frost (Smythe, et. al., 1987), (figure 2), and that it is difficult to attribute the 2.16 feature in that spectrum to nitrogen (see Cruikshank, et. al. 1987).

Technical improvements over the past year include construction of an additional goniometer which can achieve phase angles as small as 0.5 degrees without use of a beam-splitter (beam splitters have undesirable polarization and parasitic reflection characteristics), acquisition and installation of PTI light sources, new detectors for extending detectivity and spectral range, and inclusion of a quadrupole mass spectrometer in the goniometric environmental chamber.



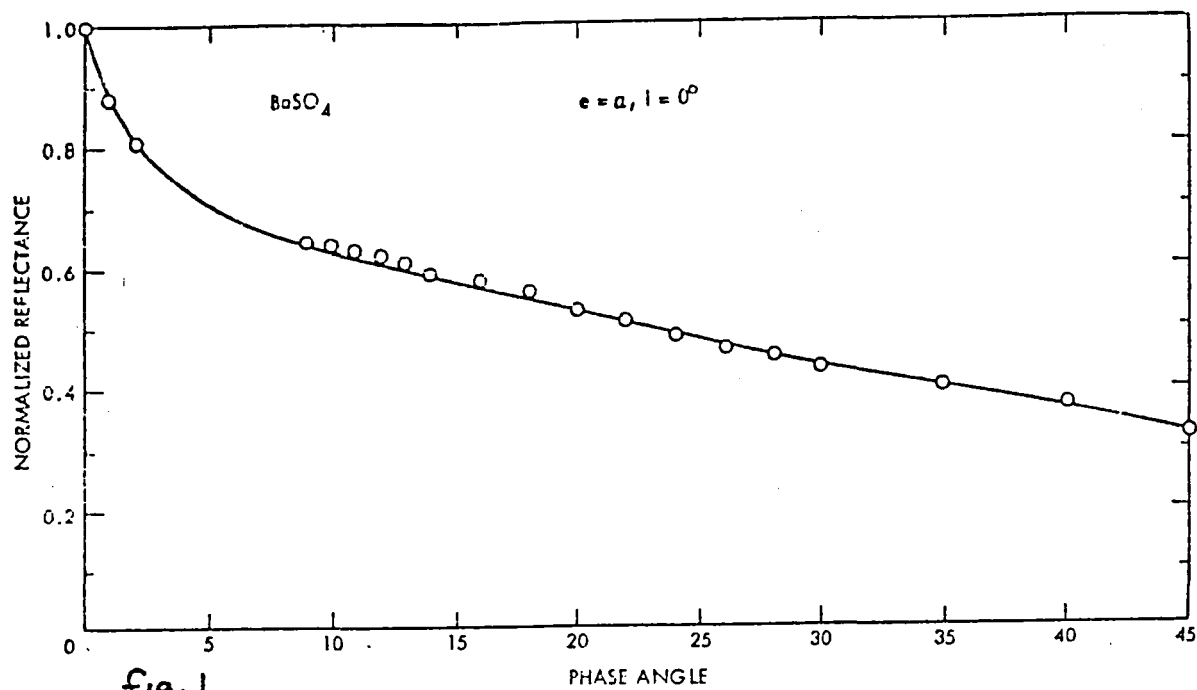


fig. 1

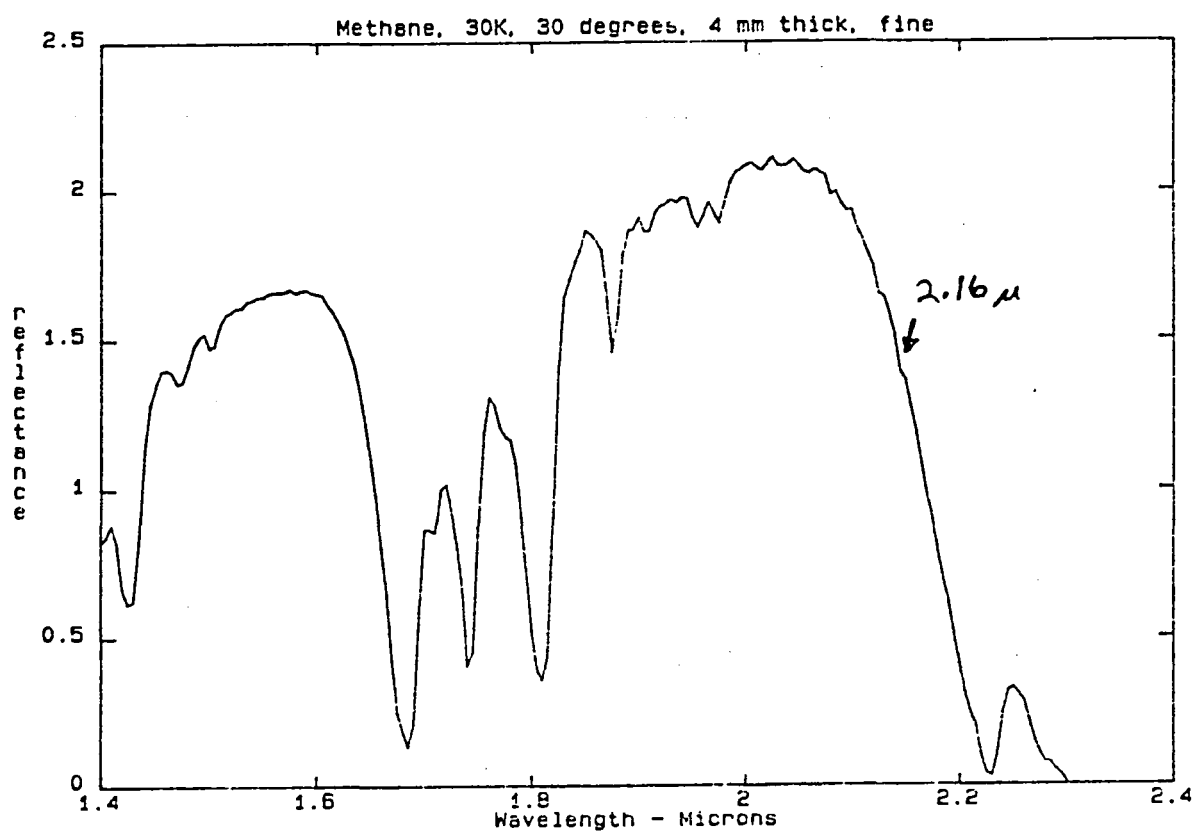


fig. 2.

## REFERENCES

- Smythe, W. D., Buratti, B., Nelson, R., Hapke, B., and Gharakhani, V. (1986) Measurements of the opposition effect BAAS, 18, p761
- Buratti, B., Smythe, W. D., Nelson, R., Gharakhani, V. (1987a) A spectrogoniometer for measuring planetary surface materials at small phase angles", Applied Optics, in press
- Buratti, B., Nelson, R., Lane, A. (1987b) Surficial textures of the Galilean Satellites, Nature, in press
- Smythe, W. D., Horn, L., Gharakhani, V, Arakelian, T. (1987) Solid nitrogen and methan spectra - Triton data revisited, BAAS 19, p844
- Cruikshank, D. P., Brown, R. H, Tokunaga, A. T., Smith, R. G., Piscitelli, J. R. (1987) Volatiles on Triton: The infrared spectral evidence, 2.0-2.5 micrometers, ICARUS, in press

### Figure 1

The opposition effect for Barium Sulfate. The steep increase at zero phase is predicted for dark (Irvine model) materials, but is remarkable for bright materials.

### Figure 2

The reflectance spectrum of methane frost at 30K. The particle size is small (<100 microns), sample thickness is about 4 millimeters, phase angle is 30 degrees. Note the developing absorption ca. 2.16, on the wing of the 2.35 band. If it is possible to decrease the strength of the 2.35 band, and if the observed 2.16 feature becomes more evident as the 2.3 band shrinks, the lab spectra will match that seen in the ground-based spectra of Triton and methane will adequately describe all observed features. Experiments are presently underway to test if it is possible to decrease the absorption strengths sufficiently to match the spectrum of Triton.

## THE OPTICAL EFFECTS OF SURFACE PROCESSES ON SMALL BODIES.

D.T. Britt and C.M. Pieters, Brown University, Providence, RI 02912.

**Introduction:** One of the puzzling questions in meteoritics is the source of ordinary chondrite meteorites. Ordinary chondrites account for 78.3% of meteorite falls [1], but spectral studies have not found main belt parent bodies that would account for this large flux of meteorites. The two asteroids with ordinary chondritic spectral signatures [2] are both small and in eccentric earth-crossing orbits, suggesting they are collisional fragments of larger parents. Carbonaceous chondrites are relatively rare in meteorite falls (4.5%), while their asteroidal spectral analogs, referred to as C-types (Tholen's B, C, F, and G-types [2]), are the most common types of asteroids [3,4]. Several explanations have been suggested for this disparity. (a) Orbital and collisional dynamics in the asteroid belt preferentially deliver ordinary chondrites from a relatively few very productive parent bodies [5]. (b) Ordinary chondrite parent bodies are too small at this stage of asteroid collisional evolution to be detected by current technology in astronomy [3]. (c) There is some combination of surface processes that alter the spectral signature of regolith material on the ordinary chondrite parent body surface. Such alteration processes would imply that the parent bodies of ordinary chondrites could be undetected in the populations of asteroids that are thought to be possible parent bodies for other meteorite types. Indications that optical alteration of asteroidal regoliths does occur are briefly examined below.

**Processes:** What are the possible processes that could cause spectral alteration on asteroidal surfaces? Preliminary research results suggest three broad areas. First are processes associated with impacts: shock, heating, compression, ejecta blanketing, particle size comminution. Impacts probably provide most of the energy for alteration and movement of material. Second are effects associated with direct exposure to the space environment such as low oxygen fugacity, implantation of solar wind gases, and radiation darkening. These processes can change the chemistry or mineral phases of regolith materials. Finally, there are the effects associated with the low-velocity accretion of additional material to the regolith. The optical alteration of asteroidal regolith is probably a combination of all of these processes, with each supplying a particular thermal, chemical, or physical component.

**Meteorite Collections:** Evidence from meteorite collections suggests that significant optical alteration has occurred in some ordinary chondrites. About 19% of ordinary chondrites are classified as regolith material from the upper layers of their parent bodies. These regolith meteorites consist of solar gas-rich ordinary chondrites (5% of collections) and fragmental breccias (14% of collections) [8]. Solar gas-rich meteorites are composed of light clasts in a dark, shock-lithified matrix. The dark matrix material is rich in solar wind implanted gases and is thought to represent samples of the regolith "soil" of asteroids [6]. The spectrum of the dark matrix is altered by the presence of micron-sized metal grains and shows much lower albedo and subdued absorption bands compared to the light clasts [7]. The fragmental breccias are thought to be samples of the asteroidal mega-regolith [8] and are characterized by brecciated textures and the presence of impact-melt rocks and exotic clasts. About 35% of these fragmental breccias appear dark in hand sample [9] and have been called "black chondrites". Black chondrites are characterized optically by lower albedo and more subdued or absent absorption features compared to most ordinary chondrites [10]. The causes of these abnormal optical features in gas-rich and black chondrites are not well understood, but some workers [11] suggest that opaque material such as elemental iron and troilite have been mobilized and dispersed in glassy grain boundary melt as a result of shock.

**Statistics:** Direct comparisons of meteorite and asteroid spectral data sets can be performed using statistical techniques. Principal components analysis, for example, determines how similar each spectrum is to all other spectra and quantifies the relative similarity. When the data are examined in a coordinate system of orthogonal principal components

the distance between two objects is the measure of their relative similarity [12]. Shown in figure 1 are the first two principal components for scaled spectra (wavelength range 0.35  $\mu\text{m}$  to 0.8  $\mu\text{m}$ ) of low albedo objects including 38 C-type asteroids [13], 4 carbonaceous chondrites, and 3 low albedo ordinary chondrite fragmental breccias (black chondrites) [10]. The carbonaceous chondrites uniformly plot in a tight group substantially away from the field of C-type asteroids. The black chondrites show more variance, but some plot closer to or inside the C-type asteroid field. Black chondrites may, in some cases, be better analogs for the field of C-type asteroids. Note that asteroid 1 Ceres, which has been suggested as a spectral analog for the Martian moon Phobos [14], plots very much away from the group of carbonaceous chondrites and the black chondrites. Another statistical measure useful for the comparison of spectra is the Red/Blue ratio and the BEND value {Red/Blue = Reflectance at 0.7  $\mu\text{m}$  / Reflectance at 0.4  $\mu\text{m}$ ; BEND = (R at 0.56  $\mu\text{m}$  - R at 0.4  $\mu\text{m}$ ) - (R at 0.73  $\mu\text{m}$  - R at 0.56  $\mu\text{m}$ )} [13]. These are measures of the spectral slope and turndown in the visible region. Shown in figure 2 is a plot of R/B against BEND for the same meteorite and asteroid spectra analyzed with principal components. Once again the field of C-type asteroids plots away from the carbonaceous chondrites and closer to the black chondrites. These statistical measures suggest: (a) Carbonaceous chondrites are not complete spectral analogs for the C-type asteroids. (b) Black chondrites are possible spectral analogs, but do not fully represent the spectral character of the C-type asteroids. (c) There may be materials or alteration products on the surface of C-type asteroids that control the spectral character of their regoliths but that are not represented in the meteorite collection.

**Conclusions:** Carbonaceous chondrites may not be the only possible spectral analog for C-type asteroids since the effects of alteration processes on silicates in an asteroidal regolith must also be considered. These alteration processes may widen the field of possible compositions of the C-type asteroids to include ordinary chondritic material.

[1] Wasson, J.T. (1974), *Meteorites*, Springer-Verlag, New York. [2] Tholen, D.J. (1984) *Ph.D. Thesis*, Univ. of Arizona. [3] Bell, J.F. (1986) *LPSC XVII*, pp. 985-986. [4] Zellner, B. (1979) in *Asteroids*, T. Gehrels, ed., Univ. of Arizona Press, pp. 783-806. [5] Wetherill, G.W. (1985) *Meteoritics* 20, 1-22 [6] Suess, H.E., Wanke, H., and Wlotzka, F. (1964) *GCA* 28, pp. 595-607. [7] Bell, J.F. and Keil, K. (1987) *LPSC XVIII*, pp. 58-59. [8] Rubin, A.E. et. al. (1983) *Meteoritics* 18, pp. 179-196. [9] Britt, D.T. (1986) personal observation of meteorite collection in the National Museum of Natural History, Smithsonian Institution. [10] Gaffey, M.J. (1976) *JGR* 81, pp. 905-920. [11] Fredriksson, K., et. al. (1962) *Space Research III*, pp. 974-983. [12] Davis, J.C. (1986) *Statistics and Data Analysis in Geology*, Wiley, New York. [13] Chapman, C.R. and Gaffey, M.J. (1979) in *Asteroids*, T. Gehrels, ed., Univ. of Arizona Press pp. 1064-1089. [14] Pang, K.D., et. al. (1978) *Science* 199, pp. 64-66.

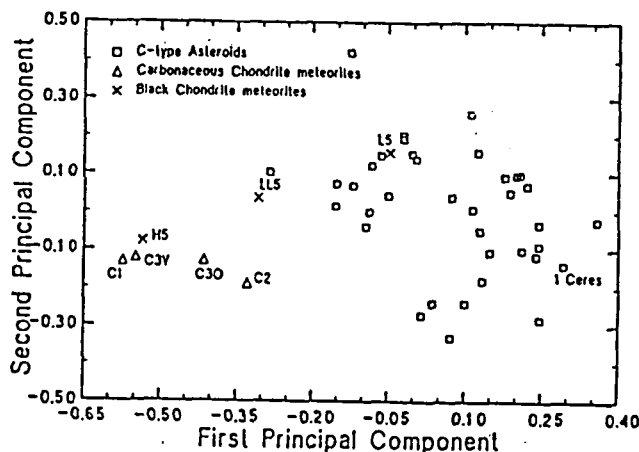


Figure 1: Principal components of spectra of asteroids and meteorites.

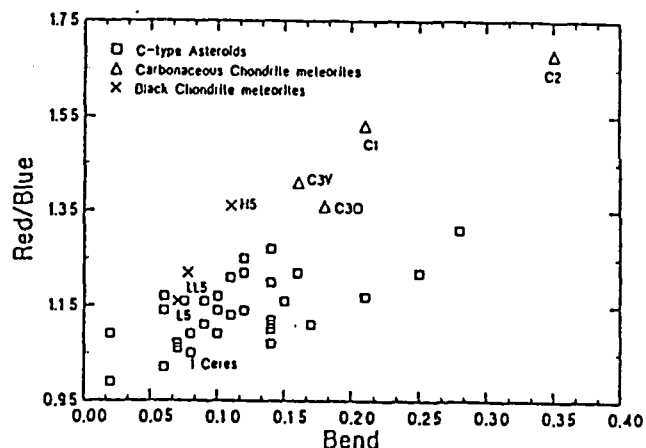


Figure 2: R/B ratio and BEND for asteroid and meteorite spectra.

## THE GLOBAL DISTRIBUTION, ABUNDANCE, AND STABILITY OF SO<sub>2</sub> ON IO

Alfred S. McEwen<sup>1</sup>, Torrence V. Johnson<sup>2</sup>, Dennis L. Matson<sup>2</sup>, and Laurence A. Soderblom<sup>1</sup>, 1. U. S. Geological Survey, Flagstaff, AZ 86001; 2. Jet Propulsion Laboratory, Pasadena, CA 91109.

Sulfur dioxide distribution and abundances, bolometric hemispheric albedos, and passive surface temperatures on Io are modeled and mapped globally from Voyager multispectral mosaics, Earth-based spectra, and photometric descriptions. Photometric models indicate global average values for regolith porosity of 75-95% and macroscopic roughness with a mean slope angle of ~ 30°. Abundances of SO<sub>2</sub> suggested by observations at uv-visible wavelengths and at 4.08 µm are partially reconciled by intimate-mixing models; 30-50% SO<sub>2</sub> coverage of the integral disk is indicated. Three major spectral end members, with continuous mixing, are recognized from the Voyager multispectral mosaics; one of these end members is identified as SO<sub>2</sub>. Intimate-mixing models with the three spectral end members are used to produce abundance maps for the optical surface; ~ 30% of Io's total optical surface consists of SO<sub>2</sub>. The SO<sub>2</sub> is concentrated in the bright equatorial band and is relatively deficient in the region of Pele-type volcanic eruptions (long 240°-360°) and the polar regions. Temperatures are computed to vary over a 40 K range, at the same illumination angle, according to variations in surface bolometric hemispheric albedo. The brightest (and locally coldest) areas correspond to areas rich in SO<sub>2</sub> and are concentrated in an equatorial band (± 30° latitude), but many small cold patches occur elsewhere. These cold patches have radiative equilibrium temperatures < 120 K at the subsolar point, resulting in SO<sub>2</sub> saturation vapor pressures < 10<sup>-8</sup> bars. Midlatitude areas and the region of Pele-type plume eruptions are generally warmer (due to lower albedos). These results for surface temperatures and SO<sub>2</sub> abundances and distribution support the regional coldtrapping model for the surface and atmospheric SO<sub>2</sub> presented by Fanale et al. (1982, Satellites of Jupiter, D. Morrison, Ed., pp. 756-781, Univ. of Arizona Press, Tucson), although the region of Pele-type volcanic eruptions may be better characterized by the regolith coldtrapping/volcanic-venting model of Matson and Nash (1983, J. Geophys. Res. 88, 4771-4783). The bright equatorial band is especially effective at slowing the formation of polar caps of SO<sub>2</sub>, both by reducing the sublimation rate near the subsolar point and by coldtrapping the SO<sub>2</sub> in the equatorial region, so that competing processes of sputtering and volcanic resurfacing may prevent the formation of polar SO<sub>2</sub> caps.

## IO SULFUR PROCESSES

Robert M. Nelson and William D. Smythe (Jet Propulsion Laboratory/California Institute of Technology, Pasadena, CA 91109)

For more than two decades, elemental sulfur has been suggested as a major surface constituent of Jupiter's satellite, Io. Pre-Voyager research efforts in this area suggested that cyclo-octal sulfur ( $S_8$ ), the most common sulfur allotrope, might explain the strong ultraviolet absorption observed in Io's spectral geometric albedo, if the sulfur was mixed with a spectrally flat material. It was also suggested that because sulfur exists in many allotropic forms other than  $S_8$ , it may be possible for some of these other allotropes to be present on Io's surface. These other allotropes include ring structures with  $n \neq 8$  and long- and short-chain polymers. Surveys of the chemistry literature indicate that these allotropes may be produced (and altered) by a variety of processes including: a) melting and quenching, b) particle bombardment, and c) exposure to various types of electromagnetic radiation (Nelson and Hapke, 1978).

We have measured the spectral reflectance of  $S_8$  powders at low temperature ( $77^\circ\text{K}$ ) after exposure to x-rays and light from a He-Xe lamp. We have used USP grade and ultrapure sulfur for these experiments. We observe that after exposure to a modest flux ( $< 0.04 \text{ w/cm}^2$ ) of x-rays from a tungsten source, the color of the sulfur changes from white to pink-yellow. After warming to room temperature and cooling to  $77^\circ\text{K}$  again, the powder is observed to be white again. Spectral reflectance measurements indicate that the color change is due to the formation of absorption features at  $0.42$  and  $0.49 \mu\text{m}$ .

Fig. A-1 shows the laboratory spectral reflectance of ultrapure sulfur at  $77^\circ\text{K}$ . After exposure to x-rays, the spectral reflectance is shown in Fig. A-2. The features at  $0.42$  and  $0.49 \mu\text{m}$  are quite apparent in the spectrum. Exposure to the ultraviolet light source bleaches the feature at  $0.49 \mu\text{m}$ , but not the one at  $0.42 \mu\text{m}$  (Fig. A-3). Subsequent exposure to x-rays caused the feature at  $0.49 \mu\text{m}$  to be formed again (Fig. A-4). We interpret these features as being due to the formation of sulfur polymers (allotropes) (Nelson et al., 1987).

The laboratory spectral reflectance of sulfur after exposure to x-rays and UV light is in closer agreement with Io's disk integrated spectrophotometry (Fig. B) and disk resolved photometry from the Voyager imaging system (Fig. C).

Future research into questions regarding the presence of elemental sulfur on Io's surface should consider the combined effect of thermal processes, exposure to particle bombardment, and electromagnetic radiation of the type expected in the Jovian environment.

## REFERENCES

Nelson, R. M. and B. W. Hapke (1978). *Icarus*, **36**, 304-329.

Nelson, R. M., W. D. Smythe, B. W. Hapke and A. J. Cohen (1987). *Bull. Amer. Astron. Soc.*, **19**, 855.

### S<sub>8</sub> ULTRAPURE

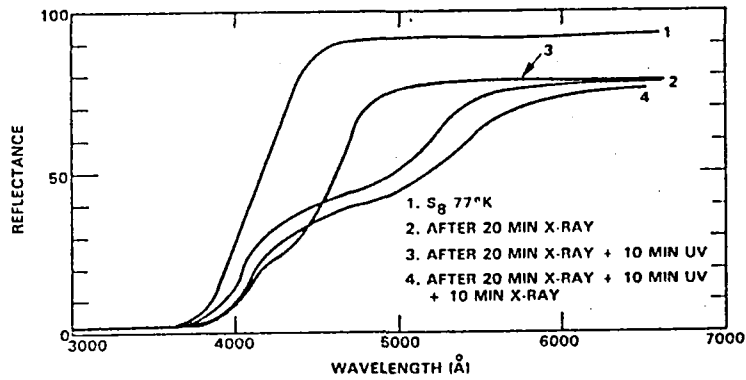


Figure A

### IO $\theta = 32^\circ$ SPECTRAL GEOMETRIC ALBEDO NELSON & HAPKE

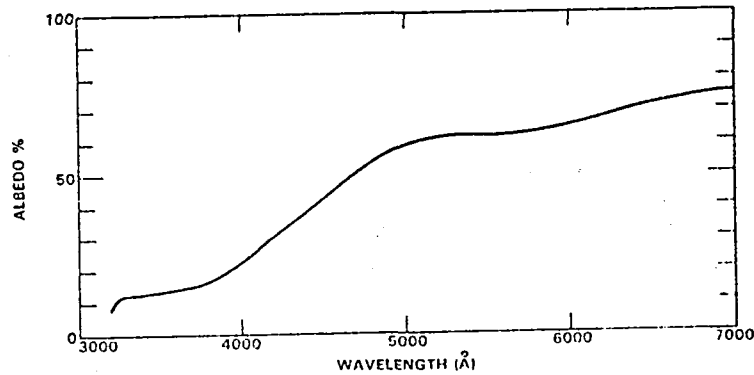


Figure B

### IO DISK RESOLVED PHOTOMETRY (SIMONELLI, THESIS)

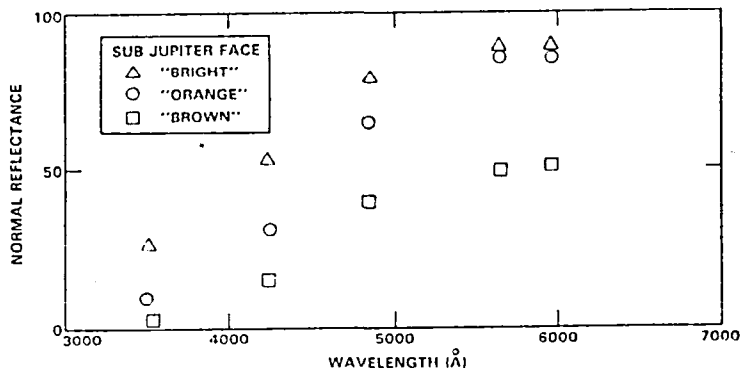


Figure C

EXPERIMENTS ON VACUUM WEATHERING OF SULFUR & APPLICATIONS TO IO  
Doug Nash and Julie Moses, JPL/Caltech, Pasadena, Calif. 91109

Further lab experiments were conducted on the newly discovered vacuum weathering phenomenon of frozen sulfur (Nash, 1987). Here we report results of examining the effects of surface temperature on temporal behavior of sublimation rate and spectral reflectance change. We found that surface temperature is a dominant parameter controlling the rate of vacuum weathering. Because of high sublimation rates, and thus rapid weathering that would occur at Io hotspot temperatures, major changes in color and microtexture of freshly frozen sulfur on Io's surface may occur in a matter of hours to days. These changes should be readily detectable by spacecraft optical instruments such as those on Galileo, and in certain instances by Earthbased telescopes. High time-resolution synoptic observations of Io from Earth in the UV/VIS may be useful in determining frequency of Io volcanic activity.

Important new results were obtained on the effect of sample temperature on the rate of vacuum weathering. In the examples shown in Fig. 1, we found the vacuum sublimation rate of frozen sulfur to be an order of magnitude higher at an increase in surface temperature of 22 °C. This behavior is consistent with the characteristic steepness of the equilibrium vapor pressure curve (P vs T) for sulfur (e.g., as shown in Fig. 12 of Nash, 1987). From our new data we define two sublimation rate curves (shown here in Fig. 2) for a limited range of temperatures typical of most hotspots on Io (~300-350 °K) (Pearl and Sinton, 1982; McEwen et al, 1985): one represents temperature-dependency of sublimation for fresh-frozen (unweathered) sulfur, and one for vacuum-mature (weathered) sulfur. This tells us that the sublimation rate of sulfur frozen on Io's surface is between the limits set by these two curves. An important conclusion here is that if sulfur deposits are present at the surface in Io hotspot locations, the sublimation rate there is enormous (on the order of  $>10^{14} \text{ cm}^{-2} \text{ sec}^{-1}$ ) and the corresponding erosion rate ( $>1 \text{ mm yr}^{-1}$ ) greatly exceeds any sputter induced erosion by impact of magnetospheric or torus ions ( $<10^{10} \text{ cm}^{-2} \text{ sec}^{-1}$ ).

The dramatic change in color and UV/VIS spectral reflectance of frozen sulfur is shown in Fig. 3: spectrum #1 is fresh solid immediately after freezing in vacuum and cooling to 28 °C from a melt temperature of 120 °C. The spectral change progresses with time as shown by spectra #1 through #7; the material brightens from a translucent butterscotch yellow color (spectrum #1) to bright opaque white (spectrum #7). In the UV (below ~0.41  $\mu\text{m}$ ) the reflectance initially rises slightly (spectrum #1 to #2) and then quickly drops (spectrum #2 to #3) to a steady-state level ~1/3 its starting level. Thus, we confirm the earlier result (Nash, 1987) that vacuum weathering causes frozen sulfur to greatly brighten and whiten in the visible, and greatly darken in the UV. The final curve



in the sequence in Fig. 3 (spectrum #7) represents vacuum weathering carried to complete spectral maturity; this is indicated by a rounding off of the notched shoulder (blending of two adjacent absorption edges) between 0.45 and 0.50  $\mu\text{m}$ ; this is physically caused by the polymeric-rich fluff layer becoming optically thick ( $\sim 1$  mm), preventing photons from the  $\text{S}_8$ -rich substrate from contributing to the spectrum. The time rate of change of these spectral properties is shown in Fig. 4 which traces temporal behavior at two key wavelengths (0.45 and 0.35  $\mu\text{m}$ ) for three samples vacuum weathered at sublimation temperatures of 28, 39, and 50  $^{\circ}\text{C}$ . Note that the rate of spectral weathering is greatly accelerated by an increase in surface temperature from 28  $^{\circ}\text{C}$  to 50  $^{\circ}\text{C}$ .

These results suggest that vacuum-like conditions on Io will cause fresh frozen sulfur (e.g., crusts of flows, ponds, lakes) to display rapid change in color, spectral reflectance, and micro-texture on a time scale of hours to days; with the rate of change indicative of relative surface temperature, and the instantaneous spectral condition indicative of relative age of the surface. These results support an earlier postulate (Nash, 1987) that for frozen sulfur surfaces in active volcanic areas on Io, a relatively dark visible reflectivity (or bright UV) may mean a relatively young (or cold) nonporous surface; whereas bright white reflectivity (or dark UV) means a relatively old (or hot) porous surface.

We summarize the vacuum weathering model for sulfur on Io's surface in Fig. 5, starting with step #1 when liquid sulfur first forms a frozen solid crust, allowing differential sublimation of the two dominant molecular species in frozen sulfur ( $\text{S}_8$  &  $\text{S}_u$ ) to begin forming a porous  $\text{S}_u$  surface layer; and ending at step #5 with cooling of the weathered surface to ambient (solar equilibrium) temperature, and condensation of atmospheric  $\text{SO}_2$  in the porous fluff layer. This final weathered condition is then subject to subsequent modification by other resurfacing agents such as plume fallout, condensation of thick  $\text{SO}_2$  or  $\text{S}_8$ , sputter erosion (in areas where volcanism is inactive), remelting of the surface, or burial by fresh sulfur lava; the latter two processes causing repetition of the vacuum weathering process at that locale.

McEwen, A.S., D.L. Matson, T.V. Johnson, and L.A. Soderblom (1985). Volcanic hot spots on Io: Correlation with low-albedo calderas. J. Geophys. Res. 90, 12345-12379.

Nash, D.B. (1987). Sulfur in vacuum: sublimation effects on frozen melts, and applications to Io's surface and torus. Icarus 72, 1-35.

Pearl, J.C. and W. M. Sinton (1982). Hot spots on Io. In Satellites of Jupiter (D. Morrison, Ed.), Univ. Ariz. Press, Tucson, 724-755.

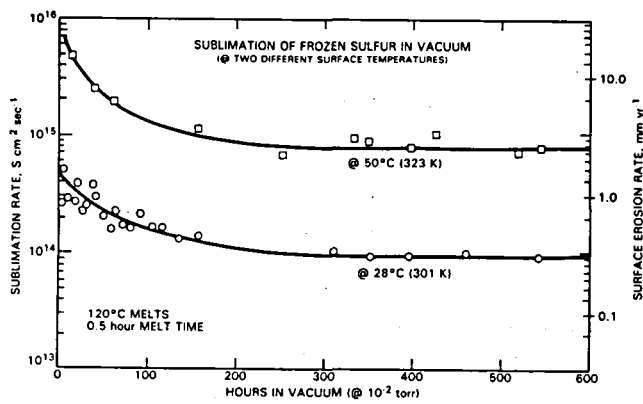


FIG. 1

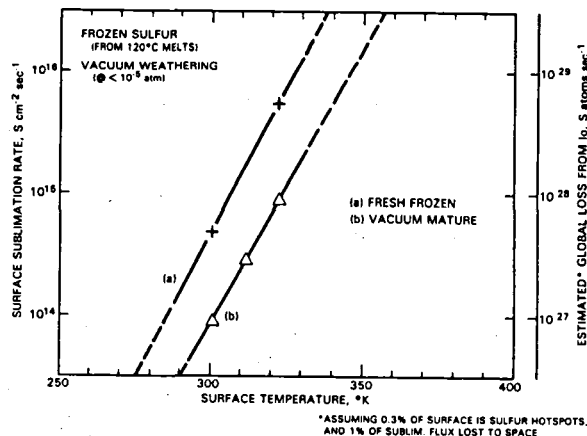


FIG. 2

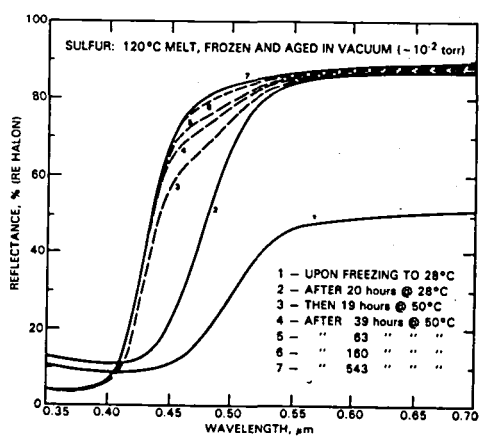


FIG. 3

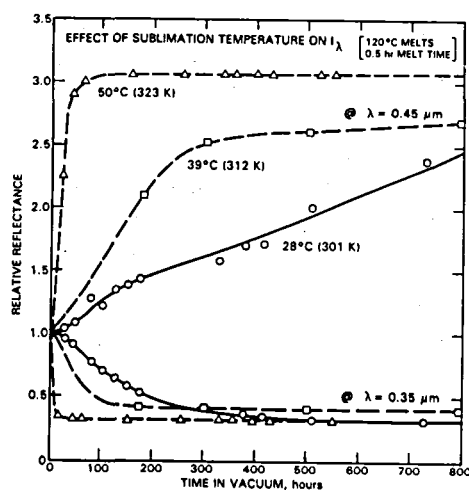


FIG. 4

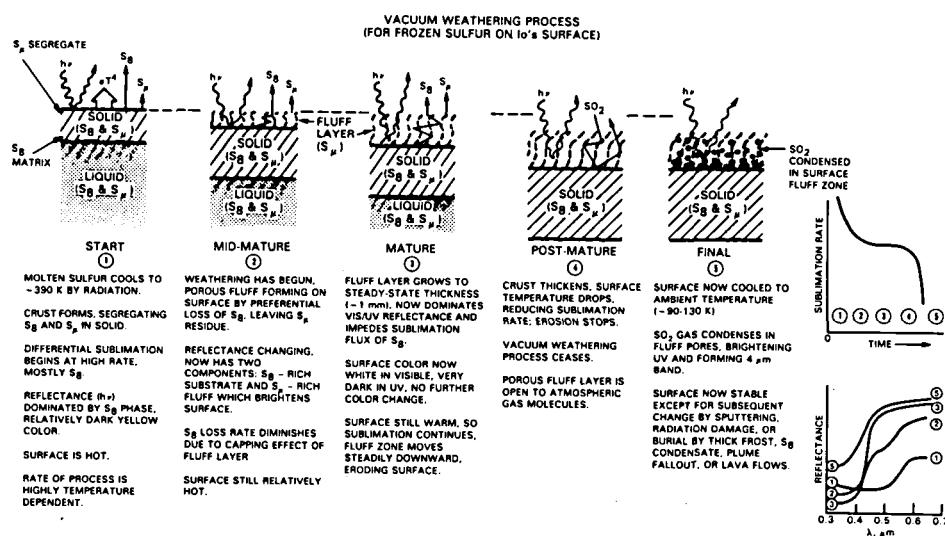


FIG. 5

### The Surface of Io: a New Model

Bruce Hapke, Dept. of Geology & Planetary Science,  
University of Pittsburgh, Pittsburgh, PA 15260

The evidence for elemental sulfur on the surface of Io is examined. There are a number of arguments against it, particularly the poor fit to the spectrum of Io below 400 nm. It is concluded that elemental sulfur is not present in spectrally significant amounts. A new model is presented in which the exposed surface consists of silicate extrusives, probably basaltic in composition, partially covered with condensates of sulfur dioxide and its dissociation products, disulfur monoxide and polysulfur oxide. In any model of Io these materials must be present on the surface, and various combinations of them can account in detail for the spectrum of Io and the spectral variations across the surface without any need to hypothesize elemental sulfur. The hot spots are silicate volcanoes that emit small quantities of sulfur dioxide, similar to terrestrial volcanoes. Several different models for the distribution of sulfur dioxide on the surface are considered quantitatively. It is concluded that some of the frost occurs in optically-thick, semi-permanent, scattered patches covering about 10% of the surface; in the equator the frost occurs in optically-thin, ephemeral, partial coatings on the topmost regolith particles. Several spectral features of Io are also displayed by Europa, although weakly, and may have the same cause: endogenic volcanic sulfur dioxide, rather than imbedded sulfur from Io.

# Spectral Properties of Disulfur Monoxide, Polysulfur Oxide and Irradiated Sulfur

Bruce Hapke & Francis Graham, Dept. of Geology & Planetary Science, University of Pittsburgh, Pittsburgh, PA 15260

The spectral reflectances of several compounds of interest for the interpretation of planetary observations have been measured over the range 200-1700 nm. These materials include disulfur monoxide and polysulfur oxide, which are condensates of dissociation products of sulfur dioxide, and elemental sulfur irradiated with UV and X-rays. Solid disulfur monoxide is dark red in color because of two strong absorption bands at 420 and 530 nm. Polysulfur oxide is a non-volatile, pale-yellow solid whose spectrum at low temperature resembles that of sulfur at room temperature. Elemental sulfur has several strong bands in the UV. It is normally white at low temperature, but UV irradiation turns it yellow by broadening the UV bands. Irradiation of elemental sulfur by X-rays produces a light orange color by creation of a band at 460 nm.

IO: A COMPARISON OF OLD AND NEW HAPKE PARAMETERS FROM  
VOYAGER DISK-INTEGRATED PHOTOMETRY

Paul Helfenstein and J. Veverka, Center for Radiophysics and Space  
Research, Cornell University, Ithaca, NY, and Damon P. Simonelli,  
NASA Ames Research Center, Moffett Field, CA

Over the past quarter-century, Hapke's photometric equation<sup>1,2,3,4,5</sup> has appeared in various increasingly refined forms. The most recent version<sup>5</sup> is of the form

$$\frac{I}{F} = \frac{\tilde{\omega}_0}{4} \frac{\mu_0}{\mu_0 + \mu} \left[ [1 + B(\alpha, h, S_0)] P(\alpha, g \text{ or } b, c) + H(\mu_0, \tilde{\omega}_0) H(\mu, \tilde{\omega}_0) - 1 \right] S(\mu_0, \mu, \alpha, \tilde{\theta}) \quad [1]$$

where  $I$  is the intensity of light scattered from a surface element toward the observer and  $\pi F$  is incident flux. Photometric geometry is specified by phase angle ( $\alpha$ ) and the angle cosines of incidence and emission ( $\mu_0$  and  $\mu$ , respectively). The primary functional components of this equation are  $S(\mu_0, \mu, \alpha, \tilde{\theta})$  which describes the photometric effects of macroscopic surface roughness, the Chandrasekhar  $H$ -functions, which describe the contribution of multiply scattered light between particles, the particle phase function,  $P(\alpha, g \text{ or } b, c)$ , and backscatter function,  $B(\alpha, h, S_0)$  which describes the shape of the opposition surge. The independent parameters are the single scattering albedo ( $\tilde{\omega}_0$ ), a parameter which relates the angular width of the opposition surge to the state of compaction of the surface ( $h$ ), a parameter describing the amplitude of the opposition surge ( $S_0$ ), arguments of the particle phase function ( $g$  for the Henyey-Greenstein function or coefficients  $b, c$  if a second-order Legendre polynomial is used), and the mean slope angle of subresolution scale macroscopic roughness ( $\tilde{\theta}$ ).

Equation [1] is identical to a slightly earlier version<sup>3,4</sup> except that a more rigorous backscattering function (with a new definition of  $h$ ) has replaced the previous empirical formulation. Unlike the new equation, in which the opposition amplitude is controlled by a new term,  $S_0$ , in the former equation the opposition amplitude was entirely controlled by single-scattering albedo,  $\tilde{\omega}_0$ . Values of Hapke's parameters for his earlier equation have been reported for a variety of planetary surfaces<sup>4,6,7,8</sup>. While parameters of Hapke's new equation are rapidly becoming available for many solar system objects<sup>7,9,10,11,12,13,14</sup>, it is important to understand how earlier results and their interpretations may be changed by the introduction of Hapke's new backscatter function. It is already clear that parameters of Hapke's equation are strongly and non-linearly coupled and that, when performing fitting of Hapke's equation to photometric data, uncertainty in a single parameter can influence the "best-fit" values of the remaining terms<sup>7</sup>.

In the present study, we fit Hapke's new equation to Voyager broadband narrow angle camera observations of Io's disk-integrated phase curves reported by Simonelli and Veverka<sup>9</sup> who used them to fit Hapke's 1984 equation. We compare our new results to those of Simonelli and Veverka and to recently derived Hapke parameters for Titania<sup>11,12,13</sup> and the Moon<sup>9</sup>. Since the difficulty in finding unique solutions for Hapke's equation for disk-integrated data is a subject of continued

concern<sup>6,7,8,9,12,13,15</sup> we pay special attention to optimal approaches for parameter determination.

Simonelli and Veverka provided separate phase curves for Voyager broadband violet, blue, clear, green and orange filters (effective wavelengths = 0.41, 0.48, 0.50, 0.55 and 0.58  $\mu\text{m}$ , respectively). Phase angle coverage for the violet filter data ( $\alpha = 2\text{--}159^\circ$ ) is adequate to constrain all of Hapke's parameters. Phase angle coverage from the other filters, while comparable, does not generally constrain the opposition surge parameters as well. For each phase curve, the non-linear least-squares algorithm of Marquardt<sup>16</sup> was used to find values of parameters which minimized the rms residual between observed disk-integrated brightnesses and those computed from equation [1] integrated over the disk at appropriate phase angles with an eight-point Gaussian quadrature<sup>8</sup>. Since it is possible for different combinations of macroscopic roughness and particle phase function to predict nearly identical phase curves, we performed a series of fits in which  $\bar{\theta}$  was held constant and the remaining parameters were allowed to adjust to optimal values. Plots of rms residual vs.  $\bar{\theta}$  were used to identify possible multiple solutions. A separate set of trials was performed in which residuals were computed on a magnitude scale and a brightness (I/F) scale, respectively. Results from fits on the brightness scale were found to fit the high-phase angle data poorly in comparison to results obtained on a magnitude scale and were subsequently discarded. The comparatively poor fit at high phase angles of the linearly (I/F) scaled data is clearly due to the fact that high phase angle brightnesses are much smaller than those at small phase angles and contribute negligibly to the rms residual on this scale.

Plots of rms residuals vs.  $\bar{\theta}$  suggest two possible solutions for the violet filter phase curve; one with  $\bar{\theta} = 16^\circ$  and the other with  $\bar{\theta} = 53^\circ$ . In order to identify the "correct" solution, we examined the consistency of each solution with the disk-resolved limb-darkening photometric behavior of Io's surface characterized by the  $k$  parameter of the empirical Minnaert photometric equation. The  $\bar{\theta} = 53^\circ$  solution predicts a physically unrealistic  $k = 0.32$  at  $\alpha = 5^\circ$ , while the  $\bar{\theta} = 16^\circ$  solution predicts  $k = 0.52$  in good agreement with  $k = 0.50$  reported for Simonelli and Veverka's<sup>8</sup> "average" materials on Io from disk-resolved observations at  $\alpha = 5^\circ$ . Thus, we conclude that the  $\bar{\theta} = 16^\circ$  fit is the correct solution.

The Hapke parameters found for Io are summarized in Table 1. Also shown are the solutions for Hapke's former equation given by Simonelli and Veverka. Comparison of the old and new Hapke parameters for Io generally show qualitatively similar systematic variations with wavelength. Old values of  $\bar{\omega}_0$  increase with wavelength from 0.68 (violet) to 0.94 (orange). New values of  $\bar{\omega}_0$  increase with wavelength in the same fashion from 0.48 (violet) to 0.85 (orange) but are systematically lower in absolute value than their earlier counterparts and they extend over a broader range of albedoes as well. Old values of particle phase function parameter ( $g$ ) show a tendency for increasingly more backscattering particles (more negative  $g$ 's) with increasing wavelength from  $g = -0.14$  (violet) to  $g = -0.28$  (orange). New values of  $g$  similarly become more negative with increasing wavelength from  $g = -0.33$  (violet) to  $g = -0.40$  (orange),

Table I: Optimal Hapke Parameters for  
Disk-integrated Phase Curves of Io\*

	Filter	w	h	S0	g	$\bar{\theta}$
New Equation	violet	0.48	0.018	0.895	-0.33	16
	blue	0.75	(0.018)	1.143	-0.38	18
	clear	0.66	(0.018)	1.878	-0.36	(16)
	green	0.84	0.018	0.885	-0.41	16
	orange	0.85	0.017	1.237	-0.40	15
Old Equation	violet	0.68	0.24		-0.14	30
	blue	0.93	(0.24)		-0.2	30
	clear	0.87	(0.24)		-0.2	30
	green	0.92	(0.24)		-0.30	20
	orange	0.94	(0.24)		-0.28	20

\*Figures in parentheses are violet filter values. Old equation values from Simonelli and Veverka<sup>8</sup>.

however, all new values of  $g$  are systematically more negative than their old counterparts.  $h$  and  $\bar{\theta}$  represent mechanical properties of the surface and should not change with wavelength. The old and new  $h$  parameters have different physical definitions and can only be compared in a relative sense. Old values of  $h = 0.24$  were significantly smaller than the value of old  $h = 0.40$  derived for the Moon<sup>2,6</sup> suggesting that Io's regolith structure is more porous. Likewise, the new value of  $h = 0.018$  is lower than the new lunar  $= 0.07^9$  and compares well to the value of new  $h = 0.018$  derived for Titania<sup>11,12,13</sup>, whose regolith is apparently more porous than typical lunar regolith. Both old and new values of  $\bar{\theta}$  are accurate only to about  $\pm 10\%$ . Average values of  $\bar{\theta}$  for the Moon are  $\bar{\theta} = 20-25^\circ$  regardless of the backscatter function used in the fitting<sup>4,6,9</sup>. Previous values of  $\bar{\theta} = 20-30^\circ$  for Io suggested that Io's photometric roughness was lunarlike; new values of  $\bar{\theta} = 15-18^\circ$  suggest that on average Io may be somewhat less rough than the lunar highlands, but is considerably rougher than the lunar maria<sup>9</sup>.

Acknowledgement: This research was supported by NASA grant NSG-7606.

REFERENCES: <sup>1</sup>Hapke, B. (1963), *JGR* 68, 4571-4586. <sup>2</sup>Hapke, B. (1966), *Ast. J.* 71, 333-339. <sup>3</sup>Hapke, B. (1981), *JGR* 86, 3039-3054. <sup>4</sup>Hapke, B. (1984), *Icarus* 59, 41-59. <sup>5</sup>Hapke, B. (1986), *Icarus* 67, 264-280. <sup>6</sup>Buratti, B. (1985), *Icarus* 61, 208-217. <sup>7</sup>Helfenstein, P. (1986), Ph.D. thesis, Brown Univ. <sup>8</sup>Simonelli, D. and J. Veverka (1986), *Icarus* 68, 503-521. <sup>9</sup>Helfenstein, P. and J. Veverka (1987), *Icarus*, in press. <sup>10</sup>Smith, B.A. et al. (1986), *Science* 233, 43-64. <sup>11</sup>Thomas, P. et al. (1987), *JGR*, in press. <sup>12</sup>Veverka, J. et al. (1987), *JGR*, in press. <sup>13</sup>Helfenstein, P. et al. (1987), *Icarus*, in press. <sup>14</sup>Verbiscer, A. and J. Veverka (1987), *Bull. AAS* 19, 822. <sup>15</sup>McEwen, A.S. (1987) submitted to *Icarus*. <sup>16</sup>Marquardt, D.W. (1963), *J. Soc. Ind. Appl. Math.* 11, 431-441.

Reassessment of the Reflectance Spectra of Callisto and Ganymede  
T.L. Roush, J.B. Pollack, and F.C. Witteborn  
NASA Ames Research Center, Moffett Field, CA 94035

The presence of water ice on Ganymede (J3) and Callisto (J4) has been known for a number of years (Pilcher et al., 1972); Lebofsky, 1977; Pollack et al., 1978; Clark and McCord, 1980; Lebofsky and Feierberg, 1985). However interpretation of its abundance and distribution varies (Pilcher et al., 1972; Pollack et al., 1978; Clark, 1980; Spencer, 1987).

Our current interpretations are based on comparison of the albedoes of J3 and J4 with laboratory spectra of mineral-water ice mixtures (Clark, 1980; Clark and McCord, 1980; Clark et al., 1986; Spenser, 1987).

However, previous laboratory studies did not include the wavelength region where fundamental absorptions of water ice occur (Clark, 1981; Clark and Lucey, 1984).

The current study covered the 0.6-4.3  $\mu\text{m}$  wavelength region which included the  $\nu_1$  and  $\nu_3$  vibrational fundamentals of ice. End members used in this study were two crystalline clays, one X-ray amorphous weathering product of basaltic glass, and liquid water. These minerals were mixed with water and then flash frozen to liquid nitrogen temperature. The frozen mixture was maintained at these temperatures, ground, sieved, and placed in an evacuated chamber for data collection.

Comparisons are made with a previously unpublished, high quality, aircraft obtained spectra of J4 and with groundbased and aircraft spectra of J3.

The geometric albedos of Ganymede and Callisto, at and beyond  $3\mu\text{m}$ , are consistent with the reflectance characteristics of those particulate water ice-mineral mixtures of this study which contain,  $\geq 75$  weight percent contaminants. Based on this study, the absolute abundance of contaminants present on Ganymede and Callisto is greater than previously considered for a homogeneous surface. The presence of crystalline, aluminous, hydroxyl-bearing phyllosilicates as a major surface material, while consistent with the parameters presented here, is inconsistent with the measured geometric albedos of the icy Galilean satellites.

#### REFERENCES:

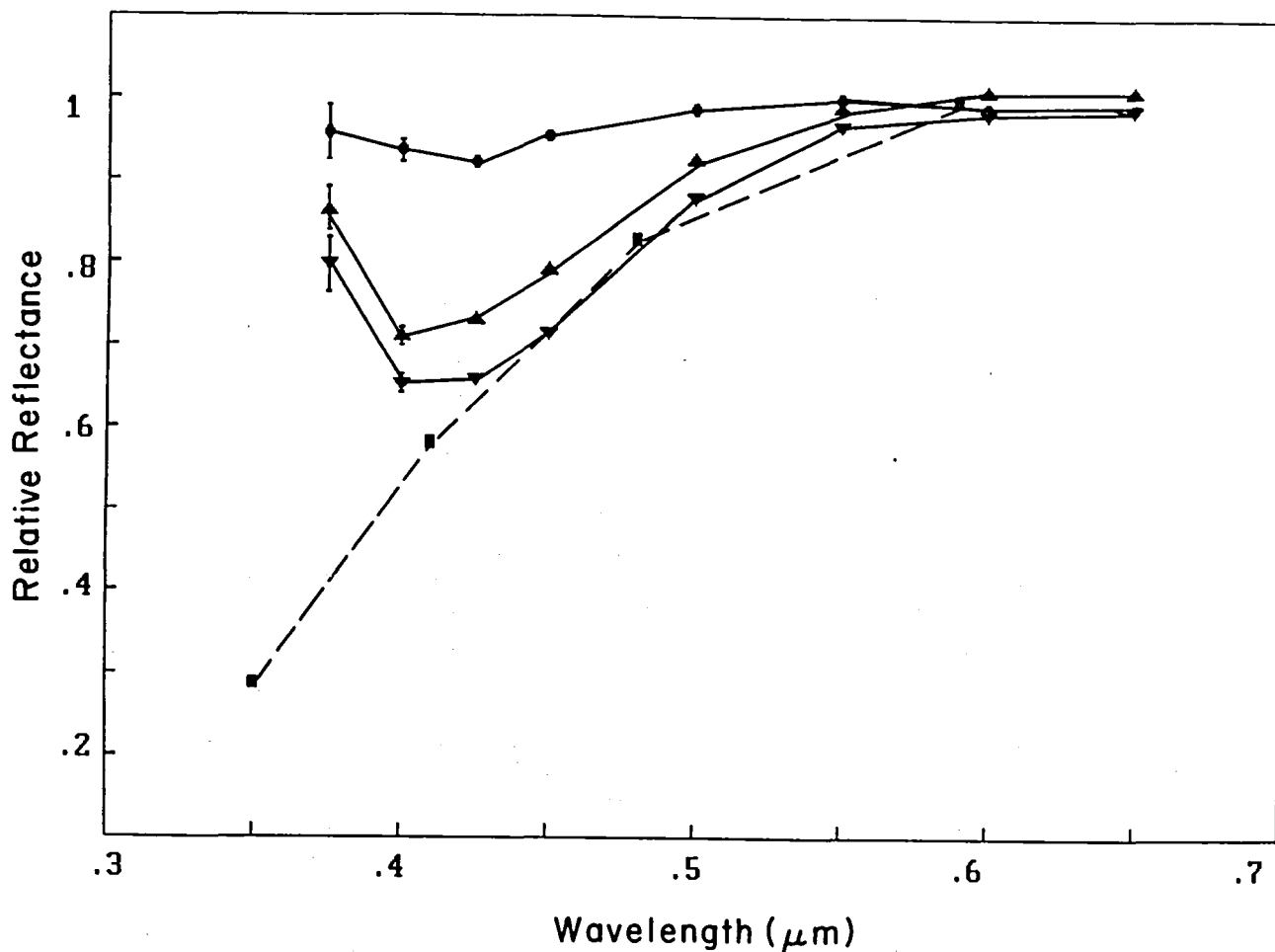
- Clark, R.N. (1980), *Icarus*, 44, 308-409.  
Clark, R.N. and T.B. McCord (1980), *Icarus*, 41, 323-339.  
Clark, R.N., F.P. Fanale, and M.J. Gaffey (1986), in *Satellites*, J. Burns and M. Matthews, Eds., Univ. Arizona Press, Tucson, Arizona, pp. 437-491.  
Lebofsky, L.A. (1977), *Nature*, 269, 785-785.  
Pilcher, C.B., S.T. Ridgeway, and T.B. McCord (1972), *Science*, 178, 1087-1089.  
Pollack, J.B. and F.P. Fanale (1982) Origin and Evolution of the Jupiter Satellite System, in *Satellites of Jupiter*, D. Morrison, Editor, University of Arizona Press, Tucson, Arizona, pp. 872-910.  
Pollack, J.B., F.C. Witteborn, E.F. Erickson, D.W. Strecker, B.J. Baldwin, and R.T. Reynolds (1978), *Icarus*, 36, 271-303.  
Spencer, J.R. (1987), *Icarus*, 70, 99-110.



## Charged Particle Modification of Surfaces In the Outer Solar System

R.E. Johnson, University of Virginia

The coupling between the properties of the surfaces of the icy moons of the outer planets and their magnetospheric plasmas is a topic of considerable current interest for both describing the plasma composition and for understanding the evolution of the surfaces of these bodies. The plasma bombardment erodes the icy surfaces thereby altering their reflectance spectra as well as supplying fresh plasma. Therefore, well-known surface characteristics of the visible reflectance spectra have been attributed to this bombardment. This is the case in spite of the dearth of laboratory data on the nature of the changes induced by a plasma. In this work we are analyzing the Voyager data using our laboratory measurements of the wavelength dependence of the alteration of the visible reflectance spectra of H<sub>2</sub>O ice irradiated by keV ions. It is found (attached figure) that when the implanted species is chemically neutral ice reddens slightly, showing enhanced absorption below 0.55  $\mu\text{m}$ . For an incident ion species containing sulfur an absorption feature is also found at  $\sim 0.4 \mu\text{m}$  corresponding, probably, to S<sub>2</sub>. These results bear on the recent interpretations of the Voyager reflectance data of Europa and other icy satellites. We have also calculated the spatial dependence of the sulfur ion bombardment and have shown a strong correlation with the absorption coefficient in the UV (0.35  $\mu\text{m}$ ) which we extracted earlier. This feature is not yet seen in our measurements.



Relative reflectance vs wavelength: solid lines connect the data points for reflectance of irradiated ice sample relative to unirradiated ice (●, 33 keV Ar<sup>+</sup>,  $3.2 \times 10^{17}$ ; ▲ 40 keV SO<sub>2</sub><sup>+</sup>,  $1.6 \times 10^{17}$  ions/cm<sup>2</sup>, ▼ 40 keV SO<sub>2</sub><sup>+</sup>,  $3.2 \times 10^{17}$  ions/cm<sup>2</sup>). Error bars represent root-mean-squared deviation of repeated ratios on each sample. Uncertainties due to reproducibility on different samples are larger, but trends are always the same. Dashed line connects reflectance of trailing hemisphere of Europa, relative to point at 0.59 μm set equal to one, as seen through the filters of Voyager.

## ALBEDO PATTERNS OF THE SATURNIAN SATELLITES

Bonnie J. Buratti, Joel A. Mosher, Richard J. Terrile  
(JPL/Caltech)

Albedo and color patterns on planetary surfaces have traditionally been used as a basis for understanding both geologic history and endogenic alteration. A detailed spectrophotometric analysis of 6 mapped geologic units, 3 types of lineaments, and brown spots on Europa has shown that only two fundamental terrain types exist on the satellite: pristine, high albedo plains, and redder, silicate rich units (Buratti and Golombek, 1987). Table 1 summarizes the colors and albedos of the three plains units (plains, bright plains, dark plains, and fractured plains), the lineaments, the two mottled terrain units (brown and gray), and the brown spots. The plains material has undergone progressive darkening by the infilling of fractures with silicate-rich material to form the lineaments, mottled terrain, and the spots.

For the five inner medium sized Saturnian satellites (Mimas, Enceladus, Tethys, Dione, and Rhea), we have not found such a clear correlation between mapped geologic units and spectrophotometric properties (Buratti, 1987). Table 2 summarizes the results for Enceladus: the four mapped geologic terrains of this satellite, which range in age (according to crater counts) from less than one billion years (ridged plains) to four billion years (cratered terrain), show no measurable difference in albedo or color. We have attributed this observation to the fact that there is an optically thick coating of fresh ice, probably from the E-ring of Saturn, on the satellite's surface.

Over the past year, we have investigated the albedo variations on the Saturnian satellites in a global manner, and have compared the results to geologic maps (Buratti et al., 1987). Figure 1 shows a map of normal reflectances for Tethys. The most pronounced feature is a dark spot centered on the trailing side of the satellite: the spot is 15% lower in albedo than the surrounding areas. There is in addition a significant color change associated with this feature: the Voyager orange to violet ratio changes from 1.0 at the edge of the feature to 1.15 at the center. The other major albedo feature on Tethys appears on the leading side, and is about 5% darker than the ambient albedo. A comparison with the geologic map prepared by Moore and Ahern (1983) shows that neither of these features are correlated with geologic features or terrains. We also note that the south pole of the satellite is brighter than the north pole.

The only clear relationship between albedo or color and geologic structure is that of the bright, wispy streaks on the trailing sides of Dione and Rhea, where the normal reflectance at 0.47 microns changes from 0.35 (Dione) or 0.45 (Rhea) for the plains material to 0.60 for the wispy streaks. Enceladus may have similar features (see Buratti, 1987).

Our conclusion is that the inner Saturnian satellites are coated with an exogenically created deposit. The high visual geometric albedos of the satellites (0.5 to 1.0) suggests that the deposit is relatively fresh ice. The origin of the coating may be the E-ring, which is a tenuous, diffuse structure reaching from the orbit of Mimas past the orbit of Dione, or possibly transient structures similar to the E-ring which have appeared in the past and disappeared due to the effects of plasma drag.

#### REFERENCES

1. Buratti, B.J. (1987). Enceladus: implications of its unusual photometric properties, Icarus, in press.
2. Buratti, B.J., and M. Golombek (1987). Geologic implications of spectrophotometric measurements of Europa, Icarus, in press.
3. Buratti, B.J., Terrile, R.J., Mosher, J.A., and A.B. Rossiter (1987). Albedo and color variations on icy satellites, B.A.A.S. 19, p. 822.
4. Moore, J. and J. Ahern (1983). The Geology of Tethys, J.G.R. 18 Supplement, p. A577-584.

Table 1 - Colors and Albedos of Europa

<u>Terrain</u>	<u>Normal reflectance</u> (0.46 microns, +/- 0.08)	<u>Orange/violet ratio</u> (+/- 0.1)
Plains	0.80	1.2
Lineaments	0.65	1.6
Brown spots	0.48	1.6
Mottled terrain	0.74	1.3

Table 2 - Colors and Albedos of Enceladus

<u>Terrain</u>	<u>Normal reflectance</u> (+/- 0.05)	<u>Orange/violet ratio</u> (+/- 0.03)
Smooth plains	1.0	1.06
Cratered terrain	1.02	1.05
Ridged plains	1.02	1.05
Cratered plains	1.02	1.10

## TETHYS

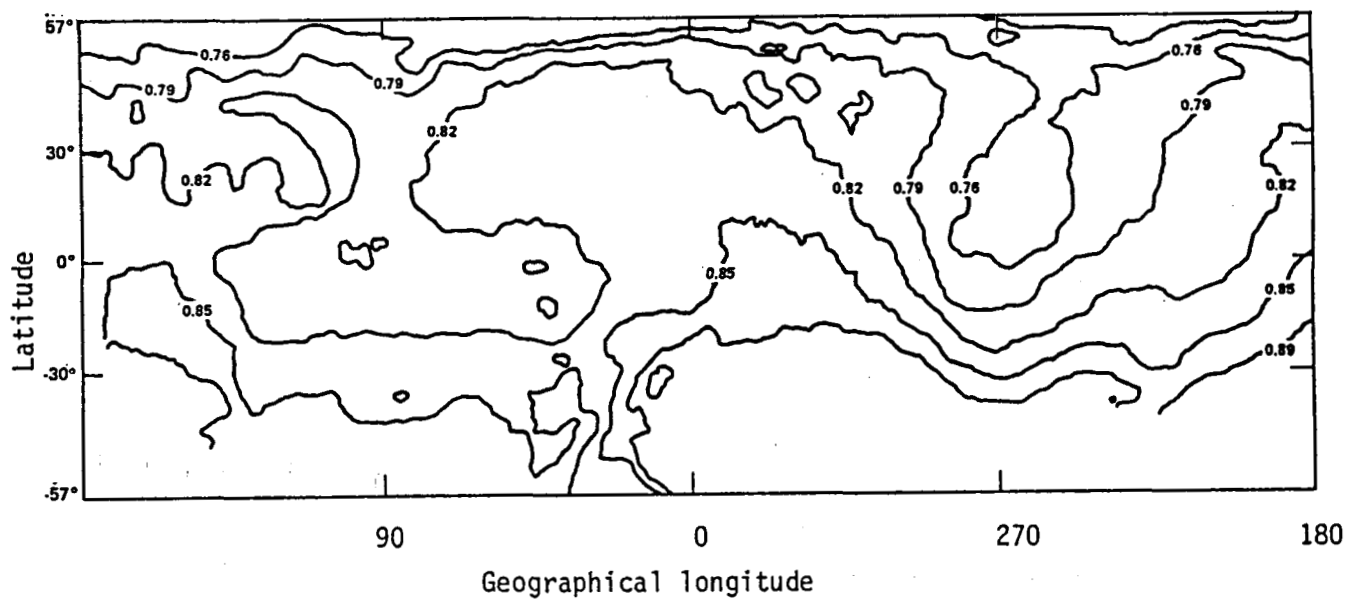


Figure 1. A map of normal reflectances of the surface of Tethys in the Voyager clear filter (0.46 microns).

Color and Albedo Maps of Miranda  
J. Hillier, P. Helfenstein, and J. Veverka, Cornell University

We have constructed color/albedo maps of Miranda based on Minnaert parameters ( $B_0$ ,  $k$ ) determined globally and for Miranda's principle terrains (Cratered, Bright Chevron, Dark Inverness Corona, Bright and Dark Arden Corona, and Elsinore Corona materials), using Voyager Clear Filter ( $0.48 \mu\text{m}$ ) images covering phase angles of  $13^\circ$  to  $43^\circ$ , and Violet ( $0.41 \mu\text{m}$ ) and Green ( $0.56 \mu\text{m}$ ) images at  $16^\circ$  phase. Global Minnaert  $k$ 's range from about 0.6 at  $13^\circ$  to about 0.8 at  $43^\circ$ , and are essentially independent of wavelength.  $B_0$ 's at  $16^\circ$  range from 0.17 for the darkest materials to about 0.35 for the brightest. To convert these values to normal reflectances requires an extrapolation to zero phase which cannot be accomplished with certainty since there are no Voyager data below  $13^\circ$  phase. If the phase coefficient determined by Veverka et al. (1987) is used (thus ignoring the possibility of a strong opposition effect)  $B_0$  at  $16^\circ$  can be converted to approximate normal reflectances by multiplying by a factor of 1.3. On the other hand, if Miranda's opposition surge is as pronounced as that of Titania, the appropriate factor is closer to 1.5 (Helfenstein et al., 1987). The albedo results are summarized in Figure 1 and Table 1, in which a factor of 1.3 is suggested as appropriate for a conservative conversion to normal reflectances.

Table 1: Albedos on Miranda

Terrain	Mean $B_0$ ( $\alpha = 16^\circ$ )	Estimated Normal Reflectance*
Global	0.250	0.325
Cratered	0.255	0.332
Chevron	0.30	0.39
Dark Inverness	0.21	0.273
Dark Arden	0.20	0.26
Elsinore Corona	0.25 <sup>+</sup>	0.325

\*The  $B_0$ 's were converted to the normal reflectances by multiplying by 1.3 (see text).

<sup>+</sup>Elsinore data at  $\alpha = 30^\circ$  converted to  $\alpha = 16^\circ$ .

Color ratios ( $V/G$ ,  $V/Cl$ ,  $G/Cl$ ) are essentially constant over all terrain types and albedo ranges on the satellite. Miranda is spectrally grey and bland. As noted by Smith et al. (1986), colors on Miranda are similar to those of C-asteroids, and distinctly less red than those observed for D-objects. Color ratios for the brightest areas do not differ significantly from those for the darkest regions. No localized spots that differ in color from the global mean have been identified.

The color data are consistent with a model in which varying amounts of a material, spectrally similar to, or slightly greyer than asteroidal C-material are mixed in with an icy component.

This research was supported by NASA Grant NSG 7156.

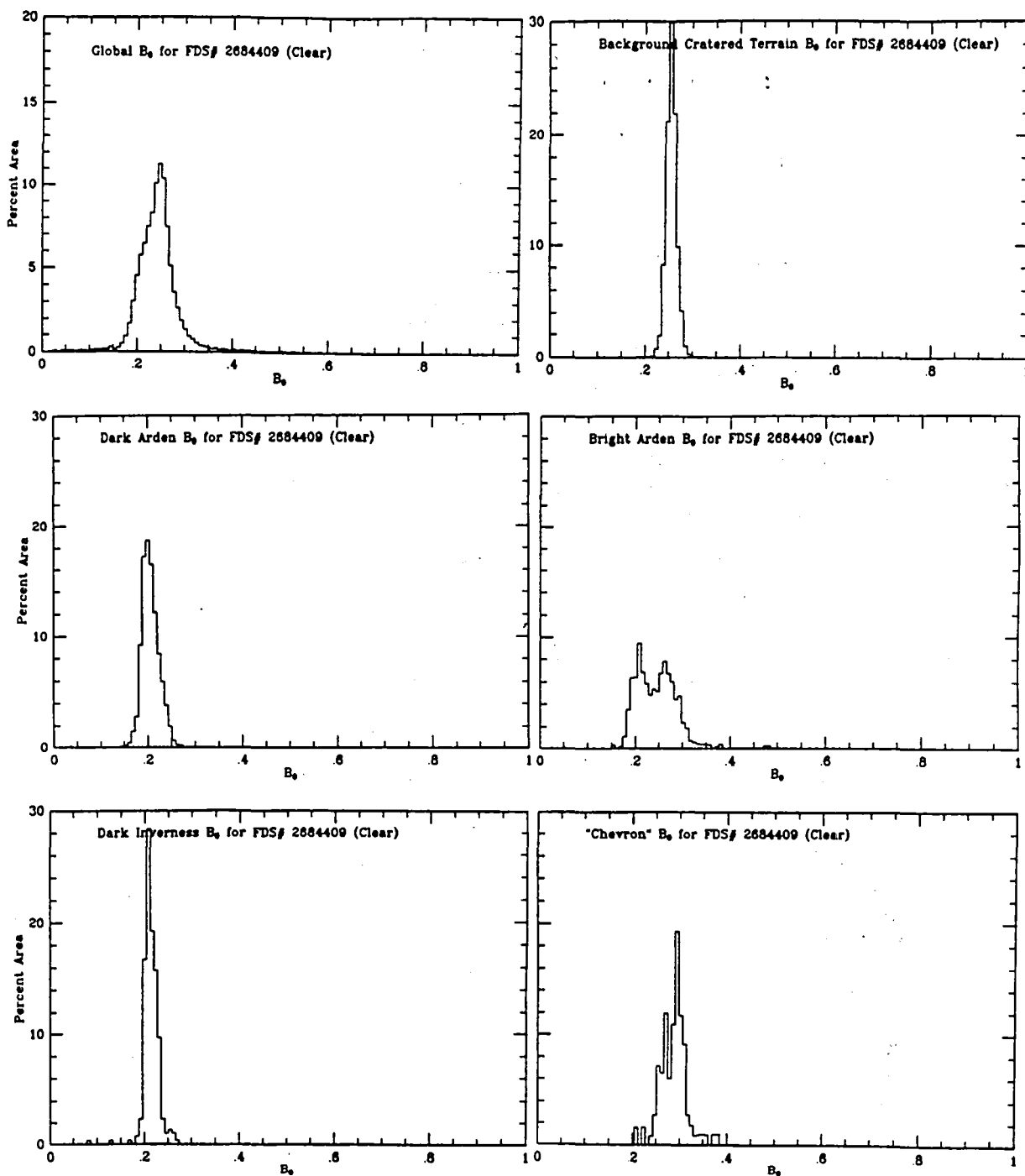


Figure 1: Histograms of  $B_0$  (at  $\alpha = 16^\circ$ ) for Miranda. To convert to normal reflectances, multiply by 1.3.

## References:

- Veverka, J., Thomas, P., Helfenstein, P., Brown, R. H., and Johnson, T. V. (1987). Satellites of Uranus: Disk-integrated Photometry from Voyager Imaging Results. J. Geophys. Res., in press.
- Helfenstein, P., Veverka, J., and Thomas, P. (1987). Uranus Satellites: Hapke Parameters from Voyager Disk-Integrated Photometry. Icarus, in press.
- Smith, B. A., L. A. Soderblom, R. Beebe, D. Bliss, J. M. Boyce, A. Brahic, G. A. Briggs, R. H. Brown, S. A. Collins, A. F. Cook II, S. K. Croft, J. N. Cuzzi, G. E. Danielson, M. E. Davies, T. E. Dowling, D. Godfrey, C. J. Hansen, C. Harris, G. E. Hunt, A. P. Ingersoll, T. V. Johnson, R. J. Krauss, H. Masursky, D. Morrison, T. Owen, J. B. Plescia, J. B. Pollack, C. C. Porco, K. Rages, C. Sagan, E. M. Shoemaker, L. A. Sromovsky, C. Stoker, R. G. Strom, V. E. Suomi, S. P. Synnott, R. J. Terrile, P. Thomas, W. R. Thompson, J. Veverka (1986). Voyager 2 in the Uranian System: Imaging Science Results. Science 233, 43-64.



# RHEA: ANALYSIS OF PHOTOMETRY USING HAPKE'S EQUATION

A. Verbiscer and J. Veverka, Cornell University

The recent success in fitting Hapke's new photometric function (Hapke, 1986) to Voyager 2 observations of the icy satellites of Uranus enables a comparison of the derived regolith parameters for other objects, such as the satellites of Saturn. Until now, this could not be done because the extensive work of Buratti (e.g., Buratti, 1984) on Saturn's satellites was completed prior to the availability of Hapke's 1986 equation.

Voyager phase angle coverage for Rhea is the most complete for any satellite of Saturn ( $\alpha = 1.8^\circ - 135^\circ$ ) and includes many images with high spatial resolution. Low phase angle data allow the evaluation of the opposition surge parameters ( $h$  and  $S_0$ ) and make it possible to search for terrain-related texture differences. The high phase angle data are essential to good determinations of  $\bar{\theta}$ , the macroscopic roughness parameter.

Separating phase and rotation effects by means of an iterative process yields mutually consistent Voyager phase and rotation curves for the clear filter. Assuming Buratti's phase coefficient  $\beta = 0.021 \text{ mag/deg}$  (Buratti and Veverka, 1984) and extrapolating to zero phase produces the Voyager rotation curve (Fig. 1). The Voyager 1 data are fit to a sine curve with amplitude 0.3 mag. Correcting for orbital phase results in the extended Voyager clear filter phase curve (Fig. 2) normalized to Rhea's geometric albedo,  $p_V = 0.65$  (Buratti and Veverka, 1984). The curve is fit using Hapke's 1986 equation, characterized by the following parameters: single scattering albedo  $\bar{\omega}_o = 0.91$ ; average macroscopic roughness  $\bar{\theta} = 21^\circ$ ; regolith compaction parameter  $h = 0.05$ ; opposition surge amplitude parameter  $S_0 = 2.00$ ; Henyey-Greenstein phase function  $g = -0.27$ .

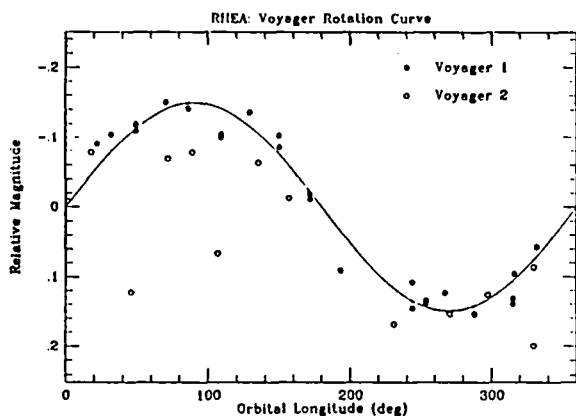


FIG. 1. Voyager clear filter orbital light-curve. Solid line represents a sinusoidal fit to Voyager 1 data.

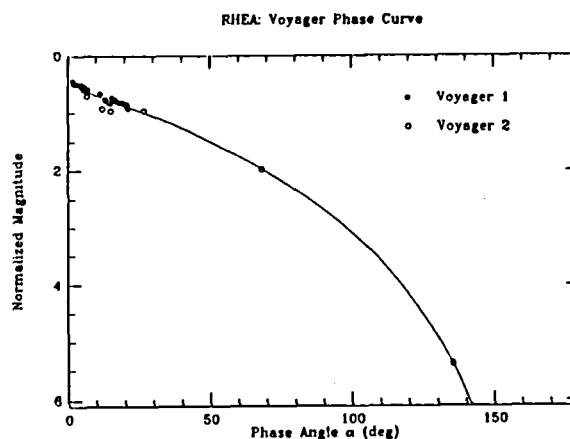


FIG. 2. Extended Voyager clear filter phase curve ( $\alpha = 1.8^\circ - 135^\circ$ ) normalized to mag  $p_V$  and fit to Hapke's 1986 equation. See text for regolith parameter values.

This fit models an opposition effect which is most easily observed when the phase curve is examined from  $\alpha = 0^\circ - 40^\circ$  (Fig. 3). Dashed line fits for different values of  $h$  the regolith compaction parameter (with the opposition amplitude  $S_0$  held constant) demonstrate the sensitivity of the fit to this parameter.

The inclusion of high phase angle data at  $\alpha = 135^\circ$ , not used in the initial analysis of Buratti and Veverka (1984), also allows a better determination of the phase integral  $q$ . Recall that a discrepancy has existed between  $q$  derived from photometry (0.7) and that inferred from Voyager IRIS data ( $\sim 1.0$ ). The new extended phase curve gives a more accurate phase integral  $q = 0.79$ .

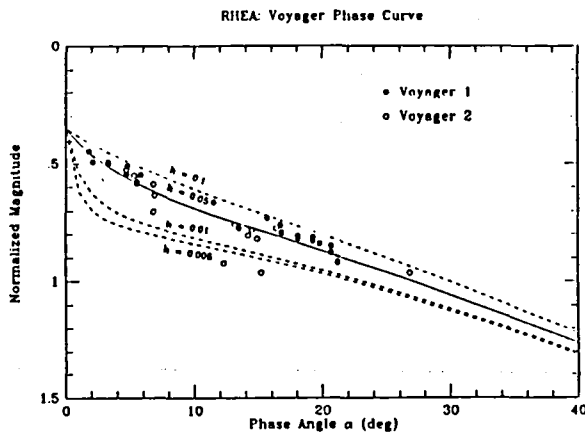


FIG. 3. Voyager clear filter phase curve  $\alpha = 0^\circ - 40^\circ$  demonstrating opposition effect. Dashed lines are alternate Hapke fits using different values for  $h$ , the regolith compaction parameter, with constant opposition amplitude  $S_0 = 2.00$ .

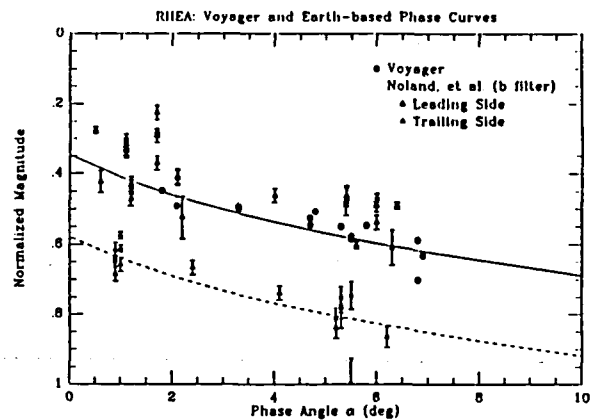


FIG. 4. Phase curves from the Voyager clear filter and Earth-based (Noland *et al.*, 1974) Strömgren b filter. Solid line is the Hapke fit to the Voyager data, while the dashed line is the Hapke fit plus 0.23 mag.

We have processed the Earth-based data of Noland *et al.*, (1974) from the Strömgren b filter in the same manner. These data, shown in Fig. 4 with the Voyager points, are too scattered to attempt fitting to Hapke's equation, although the same shape curve appears to fit both hemispheres. This also demonstrates that good agreement exists between both Earth-based and Voyager data.

Hapke's 1986 equation has been applied to a number of solar system objects, including the Uranian satellites and the Moon, allowing us to compare Rhea, an icy Saturnian satellite, to other icy bodies in the Uranian system and to the Moon, a silicate body in the inner solar system. In the Uranian system, the most complete phase coverage exists for Titania; therefore, we restrict our comparison to this Uranian object alone. Table 1 lists the Hapke parameters for Rhea, Titania, and the Moon. Rhea and Titania have similar macroscopic roughness parameters,  $\bar{\theta}$ , but distinct regolith compaction parameters  $h$ . Titania's  $h = 0.018$  implies that its surface is more porous than that of Rhea. Rhea and the Moon have very similar roughness and regolith

compaction parameters. It is interesting to note that Rhea, an icy outer Solar System satellite exhibits photometric properties very similar to those of the Moon, a silicate terrestrial satellite.

TABLE 1  
HAPKE PARAMETERS COMPARED

	Single-Scattering Albedo $\tilde{\omega}_0$	Regolith Compaction $h$	Opposition Amplitude SO	Macroscopic Roughness $\bar{\theta}$	Asymmetry Factor $g$
Rhea	0.91	0.05	2.00	21°	-0.27
Moon <sup>a</sup>	0.21	0.07	0.71	20°	-0.1
Titania <sup>b</sup>	0.48	0.018	0.77	23°	-0.28

<sup>a</sup> Helfenstein and Veverka, 1987

<sup>b</sup> Veverka et al., 1987

This research was supported by NASA Grant NSG 7156.

## REFERENCES

- BURATTI, B. J. (1984). Voyager disk resolved photometry of the Saturnian satellites. *Icarus* **59**, 392-405.
- BURATTI, B. J., AND J. VEVERKA (1984). Voyager photometry of Rhea, Dione, Tethys, Enceladus, and Mimas. *Icarus* **58**, 254-264.
- HAPKE, B. (1986). Bidirectional reflectance spectroscopy. 4. The extinction coefficient and the opposition effect. *Icarus* **67**, 264-280.
- HELFENSTEIN, P. AND J. VEVERKA (1987). Photometric properties of lunar terrains derived from Hapke's function. *Icarus*, in press.
- NOLAND, M., J. VEVERKA, D. MORRISON, D. P. CRUIKSHANK, A. R. LAZAREWICZ, N. D. MORRISON, J. L. ELLIOT, J. GOGUEN, AND J. A. BURNS (1974) Six-color photometry of Iapetus, Titan, Rhea, Dione, and Tethys. *Icarus* **23**, 334-354.
- VEVERKA, J., P. THOMAS, P. HELFENSTEIN, R. H. BROWN, AND T. V. JOHNSON (1987). Satellites of Uranus: Disk integrated photometry from Voyager imaging observations. *J. Geophys. Res.*, in press.

## ABSOLUTE PHOTOMETRY OF THE MARTIAN SURFACE AND ATMOSPHERE

K. E. Herkenhoff and B. C. Murray  
Division of Geological and Planetary Sciences  
California Institute of Technology  
Pasadena, CA 91125

We have re-evaluated the photometric accuracy of the Mariner 9 cameras and developed a new processing procedure that removes instrumental signature to within 10% (Herkenhoff et al., 1987). The software and data files required to process Mariner 9 images will soon be available to the entire scientific community as part of the Planetary Image Cartography System through the U. S. Geological Survey, Flagstaff. Corrected Mariner 9 data may be used for a variety of scientific investigations. We have used Mariner 9 Infrared Interferometer Spectrometer data and simultaneously acquired images of the south polar residual cap to study its thermodynamic state. This work indicates that the residual cap was held at sublimating CO<sub>2</sub> temperatures throughout the summer despite the observed breakup of the polar frost (Paige et al., 1987).

Investigation of the albedo and photometric properties of the surface of Mars is complicated by the presence of dust in the Martian atmosphere, especially during the Mariner 9 mission. Atmospheric scattering must be removed in order to analyze the surface, and absolute photometric measurements of the surface and atmosphere are required to model the atmospheric scattering. While the Viking Orbiter television data have been calibrated to 9% absolute accuracy (Klaasen et al., 1977), previous studies have been unable to reconcile the more accurate earth-based spectrophotometric measurements of Martian color with the Viking observations (McCord et al., 1982). We have found that the disk-integrated brightness of Phobos seen by Viking is consistent with earth-based Phobos observations (Veverka and Burns, 1980), indicating that Viking absolute calibration is indeed accurate to 9%. We have modeled Viking Orbiter observations of a dense dust storm over Arabia using scattering parameters given by Pollack et al. (1979), with the exception that larger values of the single-scattering albedo are needed to reproduce the red and violet brightnesses. Larger values for the single-scattering albedo would be expected if the dust particles in the upper atmosphere (the source region of most of the scattered light in an optically thick dust storm) are coated with some type of condensate. Jaquin et al. (1986) also found that larger values for the single-scattering albedo are required in their modeling of Viking Orbiter limb observations. Our model predicts that the same scattering parameters will produce a significantly "redder" dust storm when observed from earth at small phase angles (McCord et al., 1977). We conclude that the discrepancy in color between earth-based and spacecraft measurements may be due to phase-dependent color changes. In contrast, decreasing spectral slope at visible wavelengths with increasing phase angle has been noted by O'Leary and Rea (1968) and McCord and Westphal (1969). Earth-based measurements of the color of Mars are extrapolated to large phase angles and compared to Viking dust storm observations in Figure 1. More detailed analysis of the Viking data is clearly needed to reconcile these data, and will be reported in a manuscript in preparation.

The case of optically thin dust scattering has been investigated in the south polar region using Viking images of the terminator taken through three different color filters. The brightnesses observed at the terminator have been successfully modeled using the scattering parameters given by Pollack et al. (1979) and reasonable surface albedo values. For this study we have modified a radiative transfer program provided by Yuk Yung's group at Caltech to include the effects of spherical geometry on the incoming solar flux. This model may be used to predict the atmospheric scattering at any point in these

images using the parameters derived from terminator data. Subtraction of the component of brightness due to atmospheric scattering from these images is then straightforward, resulting in an image containing only surface brightness information.

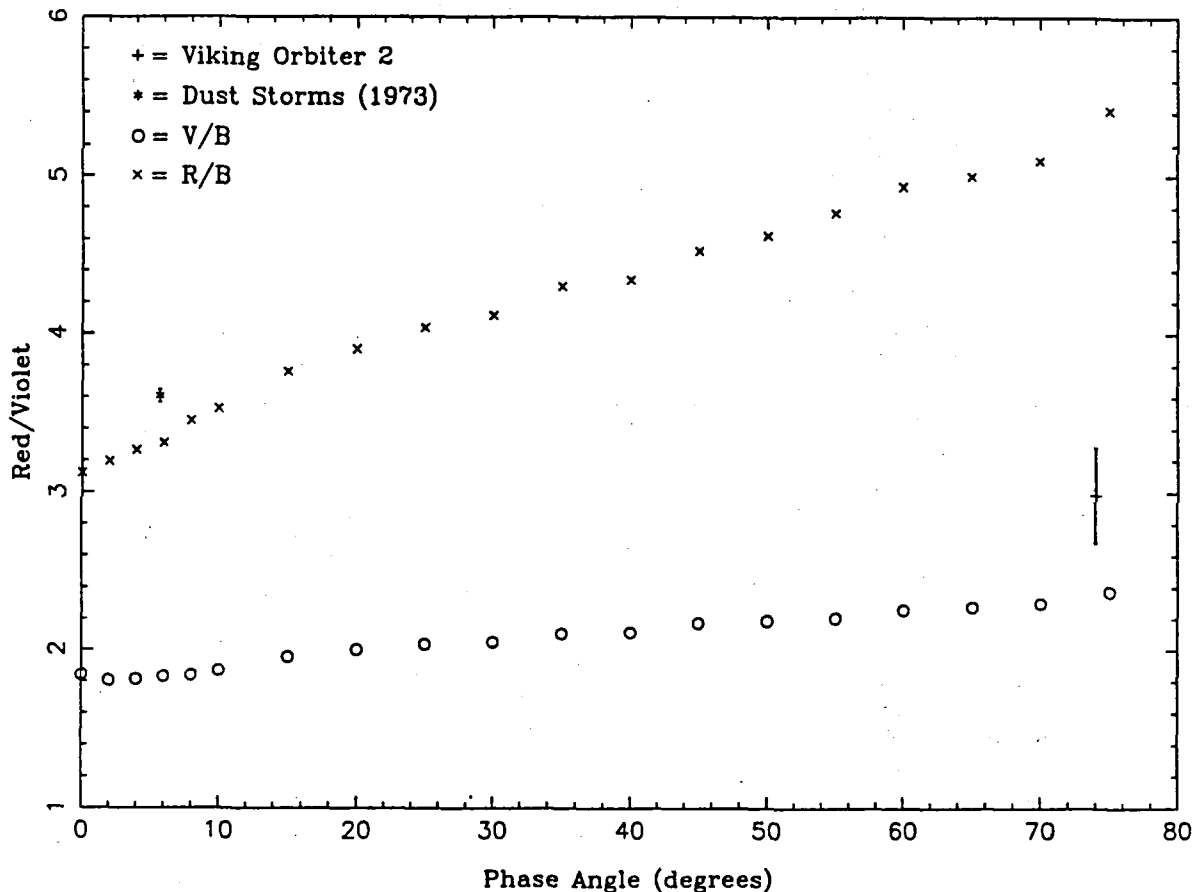


Figure 1: Mars integrated disk color vs. phase angle (O'Leary and Rea, 1968) and Viking Orbiter red/violet ratio for dust storm observations. V-band (0.55 micron) and R-band (0.67 micron) data are divided by B-band (0.43) data. Viking violet filter has effective wavelength similar to B-band. Earth-based dust storm observations (McCord et al., 1977) were used to find the red/violet ratio for the Viking bandpasses.

## REFERENCES

- Cutts, J. A. and Lewis, B. H. (1982). Models of Climate Cycles Recorded in Martian Polar Layered Deposits. *Icarus* 50, 216-244.
- Herkenhoff, K. E., Soderblom, L. A., Murray, B. C., and Danielson, G. E. (1987). Mariner 9 Television Calibration--Revisited (submitted to *Icarus*).
- Jaquin, F., Gierasch, P., and Kahn, R. (1986). The Vertical Structure of Limb Hazes in the Martian Atmosphere. *Icarus* 68, 442-461.
- Klaasen, K. P., Thorpe, T. E., and Morabito, L. A. (1977). Inflight Performance of the Viking Visual Imaging Subsystem. *Applied Optics* 16, 3158-3170.
- McCord, T. B., Huguenin, R. L., Mink, D., and Pieters, C. (1977). Spectral Reflectance of Martian Areas during the 1973 Opposition: Photoelectric Filter Photometry 0.33-1.10  $\mu\text{m}$ . *Icarus* 31, 25-39.
- McCord, T. B., Singer, R. B., Hawke, B. R., Adams, J. B., Evans, D. L., Head, J. W., Mouginis-Mark, P. J., Pieters, C. M., Huguenin, R. L., and Zisk, S. H. (1982). Mars: Definition and Characterization of Global Surface Units With Emphasis on Composition. *J. Geophys. Res.* 87, 10,129-10,148.
- McCord, T. B. and Westphal, J. A. (1971). Mars: Narrow-band Photometry, From 0.3 to 2.5 Microns, of Surface Regions During the 1969 Apparition. *Ap. J.* 168, 141-153.
- O'Leary, B. T. and Rea, D. G. (1968). The Opposition Effect of Mars and Its Implications. *Icarus* 9, 405-428.
- Paige, D. A., Herkenhoff, K. E., and Murray, B. C. (1987). Mariner 9 Observations of the South Residual Polar Cap of Mars: Evidence for Residual CO<sub>2</sub> Frost (in preparation).
- Pollack, J. B., Colburn, D. S., Flasar, F. M., Kahn, R., Carlston, C. E. and Pidek, D. (1979). Properties and Effects of Dust Particles Suspended in the Martian Atmosphere. *J. Geophys. Res.* 84, 2929-2945.
- Veverka, J. and Burns, J. A. (1980). The Moons of Mars. *Ann. Rev. Earth Planet. Sci.* 8, 527-558.

REMOTE SENSING OF MARS. Bruce M. Jakosky, Laboratory for Atmospheric and Space Physics, University of Colorado, Boulder, CO 80309-0392

The martian surface shows abundant evidence of a diverse set of geologic processes. Observations from the Viking landers reveal the presence of widespread fine material which is presumably of aeolian origin (at least in part), rocks on top of and embedded within the surface, a duricrust of bonded fine material, localized drifts of fine material, and complications arising from the mixing together of these materials both horizontally and vertically. Observations from orbit show evidence of a wide variety of processes which are capable of affecting the surface at the scales visible from the landers, including aeolian deposition and erosion due in part to the global dust storms, fluvial episodes in the past, volcanism, and ejection of impact debris, among others; of course, imaging is available only at the 10- to 100-meter scale and is incapable of directly revealing the results of those processes which directly affect the surface at the centimeter-to-meter scale. In our ongoing investigations of the nature of the martian surface using remote-sensing data, our aim is to determine the nature of the surface at the micron-to-meter scale and to describe those physical processes which are responsible for the evolution of the surface. The use of remote-sensing observations allows us to measure properties of the surface at a scale of, typically, between a few microns and a meter in the vertical, depending on technique; this scale differs from the horizontal resolution, which can be up to a few hundred kilometers across.

During the past year of effort, we have: synthesized thermal and radar properties at a global level in terms of surface rock abundance, near-surface duricrust, and deposits of unbonded fine material; compared thermal-infrared and radar estimates of surface rock abundance and roughness in order to better understand the physical constraints imposed by each data set; and constructed a model for the thermal radio emission from the martian surface in order to use Earth-based radio measurements to derive the electrical properties of the surface.

In the global analyses, we have done a first-order comparison of those remote-sensing observations which are related to the surface physical properties of the surface. These include global thermal inertia values derived from the Viking Infrared Thermal Mapping experiment (IRTM), radar cross-section measurements made with Earth-based telescopes, global albedo measurements made from the IRTM experiment, and thermal-emission observations made at millimeter and centimeter wavelengths. Values obtained from each of these data sets place constraints on the physical nature of the near-surface layer. The thermal inertia, for example, is most closely related to the thermal conductivity which is itself a function of both the average particle size of the particles within the topmost ten or so centimeters of the surface and the degree of bonding which occurs between the particles. The radar cross section depends most strongly on the bulk density or porosity of the surface, and so describes either the packing together of grains or the filling of pore spaces by solid material. The fact that there is a correlation between these values, as spatially resolved over the planet, suggests the presence of systematic spatial variations of the surface which are related to the processes involved in the evolution of the near-surface layer. Based on the global nature of the observed correlations, we have suggested that spatial variations are dominated by the degree of formation of a bonded duricrust,

with regions of low thermal inertia consisting of unbonded fines and regions of high thermal inertia consisting of fines which have been bonded together. The two Viking lander sites are located in regions which appear to contain physical properties which are not representative of the majority of the surface. These results were reported in Jakosky and Christensen (1986a, b).

In order to interpret the thermal properties, we have also modeled the role of particle size in determining the thermal inertia of the surface. While a high thermal inertia can result from many different surface configurations, including the presence of particles larger than about 500  $\mu\text{m}$ , an admixture of rocks on the surface, or bonding together of fine grains, a low thermal inertia can only occur if the surface consists of small particles (less than 3-30  $\mu\text{m}$  in size) or in the unlikely case of an unmodified porous volcanic product such as reticulite. Thus, the regions of low thermal inertia on Mars consist of aeolian deposits of fine dust. Additionally, the thermal inertia of intracrater deposits, about  $10 \times 10^{-3} \text{ cal/cm}^2 \text{ s}^{1/2} \text{ K}$ , is consistent with particles which are 1-10 mm in size, and is consistent with modes of formation which have been described based on photogeological methods. These results have been reported in Jakosky (1986).

We have also modeled the diffuse component of radar reflection based on a surface distribution of rock coverage derived from thermal-infrared observations. The diffuse component arises from scattering of radar energy by surface elements which have size or radius of curvature which are comparable to or smaller than the radar wavelength, here about 12 cm, or from multiple reflections off of surface elements with larger size. The latter mechanism is unlikely to provide the bulk of the diffuse return in this case. Consistency between the infrared and radar data is required, as they are both sensitive to the same surface. Two physically plausible models for the orientation of surface rocks were used in the model, and plots of scattering cross section as a function of the doppler shift were derived, in similar format to the actual measurements. The modeled plots showed some similarities to the measured curves, but had lower magnitudes, particularly in the Tharsis region. In order to bring the modeled curves into agreement with the measured ones, surface rock abundances which are inconsistent with the infrared measurements were required; this leads us to conclude that subsurface scattering elements play an important role in producing the observed scattering cross sections. Results of this research were discussed in detail by Calvin et al. (1987).

Finally, we have produced models of the thermal emission from the martian surface at centimeter wavelengths in order to aid in the interpretation of radio measurements made at 2 and 6 cm. The radio emission arises from blackbody energy generated in the subsurface and transmitted through the surface boundary and to the observer on Earth. The radio absorption length at these wavelengths is about 30 and 90 cm, respectively, so that the variation of temperature with depth in the regolith and the absorption of energy between each depth and the surface must both be taken into account. The emissivity at radio wavelengths is given by the Fresnel relation for transmission of energy through a dielectric boundary, possibly modified by surface roughness effects. By varying the model dielectric constant and radio absorption length, which determine the emissivity of the surface and the relative weighting of the subsurface temperatures, respectively, models of the emission could be compared with observations made at the Very Large Array and values of these parameters could be estimated. Although the values are not at high



spatial resolution, they do provide information on the nature of the surface which is not readily available by other means. Results of these analyses have been presented by Rudy et al. (1987).

#### References

- Calvin, W.M., B.M. Jakosky, and P.R. Christensen, A model of diffuse radar scattering from martian surface rocks, submitted to Icarus, 1987.
- Jakosky, B. M., On the thermal properties of martian fines, Icarus, 66, 117-124, 1986.
- Jakosky, B.M. and P.R. Christensen, Global duricrust on Mars: Analysis of remote sensing data, J. Geophys. Res., 91, 3547-3559, 1986a.
- Jakosky, B.M. and P.R. Christensen, Are the Viking lander sites representative of the surface of Mars? Icarus, 66, 125-133, 1986b.
- Rudy, D.J., D.O. Muhleman, G.L. Berge, B.M. Jakosky, and P.R. Christensen, Mars: VLA observations of the northern hemisphere and north polar region at wavelengths of 2 and 6 cm, Icarus, 71, 159-177, 1987.

VIKING LANDERS AND REMOTE SENSING -- H.J. Moore, U.S. Geol. Survey, Menlo Park, CA, 94025; Jakosky, B.M., LASP, Univ. of Colorado, Boulder, CO, 80309; P.R. Christensen, Dept. of Geology, Arizona State Univ. Tempe, AZ, 85287.

Thermal and radar remote sensing signatures of the materials in the lander sample fields can be crudely estimated from evaluations of their physical-mechanical properties, laboratory data on thermal conductivities and dielectric constants, and theory. The estimated thermal inertias and dielectric constants of some of the materials in the sample fields are close to modal values estimated from orbital and Earth-based observations. This suggests that the mechanical properties of the surface materials of much of Mars will not be significantly different than those of the landing sites.

Three soillike materials, and rocks, occur in the sample fields: (1) drift, (2) crusty to cloddy, and (3) blocky [1]. Bulk densities near  $1100 \text{ kg/m}^3$  were inferred for disturbed drift material [2]; those of porous clods of blocky material ranged between  $1100$  and  $1900 \text{ kg/m}^3$  [3]. Angles of internal friction of crusty to cloddy and blocky materials ( $28$ – $39^\circ$ ) are compatible with moderately dense soils ( $\sim 1400 \text{ kg/m}^3$ ), while the angle of internal friction of drift material ( $20^\circ$ ) is compatible with a loose soil ( $\sim 1000 \text{ kg/m}^3$ ). Mineral grains in drift and crusty to cloddy materials are small ( $0.2$  to  $2 \mu\text{m}$ ) [4,5]. All materials have cohesions and form fragments, clods, crusts, and weak lumps. Cohesions of crusty to cloddy and drift materials are several kPa and less, while those of blocky material are a few to as much as  $10 \text{ kPa}$  [1,3]. Cohesions of the rocks are probably of the order of MPas. Best estimates of bulk densities, cohesions, angles of internal friction, and the fractions of samplefield areas covered are listed in Table 1.

Thermal inertias,  $I_s$  ( $10^{-3}$  cgs units), of materials in the sample fields can be estimated by assuming that the  $I_s$  of the sample fields are the same as those determined from orbit [6] and two or three component models [7]. From orbit,  $I$  is  $8 \pm 1.5$  for Lander 2 [6]. A two-component model of rocks ( $I=40$ ) and crusty to cloddy material ( $I=6.3$ ) will yield an  $I$  of  $8$  for the entire sample field. From orbit,  $I$  is  $9 \pm 0.5$  for Lander 1 [6]. Lander 1 data requires, at least, a three-component model. Drift material is a loose porous powder with a fine grain size. The  $I_s$  of loose porous powders in  $7$ – $9 \text{ mbar}$  atmospheres should be near  $2$ – $4$  [8,9,10] or lower [11]. Tentatively,  $I=3$  is assigned to drift material. A three component model for Lander 1 would have drift material ( $I=3$ ), rocks ( $I=40$ ), and blocky material ( $I=9$ ).  $I_s$  for crusty to cloddy and blocky materials are larger than those expected for their bulk densities [10] so that cementation may contribute to their large  $I_s$  [12].

Radar reflectivities may be interpreted as a dielectric constants [13],  $E_s$ , which may, in turn, be interpreted as a bulk densities [14]. Two reflectivities reported for the area of the Lander 1 site from Earth-based radio echoes at  $12.6\text{-cm}$  wavelength are  $0.07$  [13] and  $0.13$  [15], which imply  $E_s$  of  $2.9$  and  $4.5$ , respectively. An  $E$  of  $3.3 \pm 0.7$  was estimated for the Lander 1 site at  $78.7\text{-cm}$  wavelength using the Lander-Orbiter relay links [16]. If the surface materials at the Lander 1 site behave like dry powders made from rocks with zero porosity, a bulk density of  $2600 \text{ kg/m}^3$  and an  $E$  of  $8$  [14], the Rayleigh mixing formula gives bulk densities of  $1400$ ,  $2000$ ,  $1600 \pm 300 \text{ kg/m}^3$  for the above values of  $E_s$ . The predicted  $E_s$  for the soillike materials are:  $2.4$  (drift),  $3.3$  (blocky), and  $2.8$  (crusty to cloddy). There are, of course,

other models. For examples,  $E_s$  are near 2-2.5 for sandy to clayey soils with unspecified bulk densities at 3, 10, and 100-cm wavelengths [17]. Similar dry soils with bulk densities near 1300 kg/m<sup>3</sup> have  $E_s$  of 2.5 at 1.15 and 3.8-cm wavelengths and 3.0 at 7.5 and 60-cm wavelengths [18].

Although the bulk  $I_s$  and  $E_s$  of the sites do not appear to be representative of Mars as viewed remotely [19], material components in the sample fields may be good analogs for the materials of much of Mars. As inferred here, the mechanical properties of drift (with  $I=3, E=2.4$ ) and crusty to cloddy (with  $I=6.3, E=2.8$ ) materials are probably not significantly different from those of the materials represented by the remote sensing modes of  $I=2, E=2$  and  $I=5.5, E=2.9$ , respectively [19,20]. The  $I=9$  of blocky material is large, but the  $E=3.3$  is quite plausible.

There are uncertainties because the interpretations are model dependent. For example, moderately dense cohesionless sand ( $\sim 300 \mu\text{m}$ ) cannot be distinguished from moderately dense compacted fine soil on the basis of  $I$  and  $E$  alone.  $I_s$  and  $E_s$  depend not only on bulk densities (porosities), but also the chemical-mineralogical properties of the materials. Sensible interpretations require as much additional evidence as possible such as albedos, colors [21], and, especially, high resolution images.

Table 1. Estimated mechanical properties and remote sensing signatures of the surface materials in the sample fields of the Viking landers.

	Bulk density (kg/m <sup>3</sup> )	Cohesion (kPa)	Angle of internal friction (degrees)	Fraction of area covered	Thermal inertia (10 <sup>-3</sup> cgs units)	Dielectric Constant
Lander 1						
Drift Material	1,200±100	$\frac{1}{2}$ - 2	14-21	0.14	3	2.4
Blocky Material	1,600±400	2 - 9	27-32	0.78	9	3.3
Rocks > 3.5 cm	2,600 ±	1,500-50,000	40-60	0.08	40	8.0
Sample Field	1,620 ±	—	—	1.00	9	3.4
Remote Sensing	1,600 (1,290-1,845) 1,400 2,000	—	—	—	9±0.5	3.3±0.7 2.9 4.5
Lander 2						
Crusty to Cloddy Material	1,400±200	$\frac{1}{2}$ - 5	28-39	0.85	6.3	2.8
Rocks	2,600 ±	1,000-50,000	40-60	0.15	40	8
Sample Field	1,580 ±	—	—	1.0	8	3.3
Remote Sensing	?	—	—	—	8±1.5	2.8-12.5

# Reference List

- [1] Moore, H. J. and others, 1982, A summary of Viking sample-trench analyses for angles of internal friction and cohesions: J. Geophys. Res., v. 87, p. 10,043-10,050.
- [2] Clark, B. C. and others, 1977, The Viking X-ray Fluorescence Experiment: Analytical methods and early results: J. Geophys. Res., v. 82, p. 4577-4594.
- [3] Moore, H. J. and others, 1987, Physical properties of the surface materials of the Viking landing sites on Mars: U.S. Geol. Survey Prof. Paper 1389, in press.
- [4] Ballou, E. V. and others, 1978, Chemical interpretation of Viking Lander 1 life detection experiment: Nature, v. 271, p. 644-645.
- [5] Oyama, V. I. and Berdahl, B. J., 1977, The Viking Gas Exchange Experiment results from Chryse and Utopia surface samples: J. Geophys. Res., v. 82, p. 4669-4676.
- [6] Kieffer, H. H., 1976, Soil and surface temperatures at the Viking landing sites: Science, v. 194, p. 1344-1346.
- [7] Kieffer, H. H. and others, 1977, Thermal and albedo mapping of Mars during the Viking primary mission: J. Geophys. Res., v. 82, no. 28, p. 4249-4291.
- [8] Wechsler, A. E., and Glaser, P. E., 1965, Pressure effects on postulated lunar materials: Icarus, v. 4, p. 335-352.
- [9] Fountain, J. A. and West, E. A., 1970, Thermal conductivity of particulate basalt as a function of density in simulated lunar and martian environments: Jour. Geophys. Res., v. 75, p. 4063-4069.
- [10] Horai, Ki-iti, 1979, Loose and compacted soils: Two basic units composing the martian surface?: Lunar and Planet. Science X, p. 564-566.
- [11] Jakosky, B. M., 1986, On the thermal properties of martian fines, Icarus, v. 66, p. 117-124.
- [12] Jakosky, B. M., and Christensen, P. R., 1986, Global duricrust on Mars: Analysis of remote-sensing data: J. Geophys. Res., v. 91, p. 3547-3559.
- [13] Tyler, G. L. and others, 1976, Radar characteristics of Viking 1 landing sites: Science, v. 193, p. 812-815.
- [14] Campbell, M. J., and Ulrichs, Juris, 1969, Electrical properties of rocks and their significance for lunar radar observations: J. Geophys. Res., v. 74, p. 5867-5881.
- [15] Harmon, J. K., and Ostro, S. J., 1985, Mars: Dual-polarization radar observations with extended coverage: Icarus, v. 62, p. 110-128.
- [16] Tang, C. H. and others, 1977, Bistatic radar measurements of electrical properties of the martian surface: Jour. Geophys. Res., v. 82, p. 4305-4315.
- [17] Von Hippel, A. R., 1954, V. tables of dielectric materials, in/ Von Hippel, A. R., ed., Dielectric materials and applications, New York, John Wiley and Sons, Inc., 430 p.
- [18] Hoekstra, P., and Delaney, A. 1974, Dielectric properties of soils at UHF and microwave frequencies: J. Geophys. Res., v. 79, p. 1699-1708.
- [19] Jakosky, B. M., and Christensen, P. R., 1986, Are the Viking landing sites representative of the surface of Mars?: Icarus, v. 66, p. 125-133.
- [20] Christensen, P. R., 1986, The spatial distribution of rocks on Mars: Icarus, v. 68, p. 217-238.
- [21] Smith, M. O. and others, 1987, Viking Orbiter multispectral images linked to lander images and laboratory analogs: Lunar and Planet. Sci. XVIII, p. 934-935.

## SURFACE COMPOSITION OF MARS: A VIKING MULTISPECTRAL VIEW

<sup>1</sup>John B. Adams, <sup>1</sup>Milton O. Smith, <sup>2</sup>Raymond E. Arvidson, <sup>2</sup>Mary Dale-Bannister,  
<sup>2</sup>Edward A. Guinness and <sup>3</sup>Robert Singer

<sup>1</sup>University of Washington, Seattle, WA 98195

<sup>2</sup>Washington University, St. Louis, MO 63130

<sup>3</sup>University of Arizona, Tucson, AZ 85721

A new method of analysing multispectral images [1] takes advantage of the spectral variation from pixel to pixel that is typical for natural planetary surfaces, and treats all pixels as potential mixtures of spectrally distinct materials. For Viking Lander images, mixtures of only three spectral endmembers - rock, soil and shade - are sufficient to explain the observed spectral variation to the level of instrumental noise.

Inferences about the composition of martian rocks and soil can be constrained by using mixtures of reference spectra; however, interpretations comparing image pseudospectra in terms of single reference spectra may be ambiguous. For example, spectra of a single rock viewed at different illuminations or orientations can be different. These spectra may be fit by different reference spectra. Also, if the rock is smaller than a pixel, then the spectrum may be influenced by adjacent materials such as soil. The possible modifications of a pure rock spectrum can be specified by mixtures with other spectral endmembers.

The endmember rock at the Viking 1 site is consistent with a broad class of andesites/basalts (H190), and the endmember soil fits the spectrum of weathered palagonitic basalt tephra (H34)[1]. Further work shows that these results with minor modifications also hold for the Lander 2 site, corroborating the remarkable similarity of the two sites on the basis of surface chemistry and other properties. The spectral mixing volume defined by these endmembers and shade includes some other rocks and minerals that have been proposed for Mars. For example, nontronite cannot be distinguished from mixtures of the above endmembers using the six Lander bandpasses.

In the Viking Lander images it is possible to use the image context to select pixels that are relatively pure compositionally. Many scenes show smooth, clean rock, areas of pure soil, and shadows cast by the rocks. This type of image facilitates selection and evaluation of endmember spectra.

Viking Orbiter images, however, present a more challenging problem. The Lander 1 site in Chryse Planitia imaged by Orbiter includes within each pixel the spectral contributions of rock, soil and shade. From the context of the Lander images, we know that these endmembers must be present; however, none has sufficient areal extent to be spatially resolved by Orbiter. Even if compositionally pure areas occur elsewhere in Orbiter images at the pixel scale, there probably will be topographic and textural effects of shade and shadow. To compare spectra taken at the scale of Orbiter (or telescopic spectra) with pure reference spectra, it is necessary at the minimum to allow for the presence of spatially unresolved shade. It probably is necessary to treat pixels as mixtures of rock, soil and other potential

endmembers, also.

Image endmembers were determined for a 1978 Orbiter mosaic that includes the Lander 1 site. After initial calibration of the image, the image endmembers were calibrated to reflectance using a method that simultaneously solves for endmember fractions and for gains and offsets. The image-derived endmembers - ideal shade, blue unit, white unit, and Lunae Planum - are contained within the volume defined by pure reference spectra - ideal shade, H34-63 (<63 nm) and H190 (Fig.1). These results are consistent with the view that the mixing volume for any Orbiter image cannot lie outside the mixing volume defined by the pure endmembers that would correspond to reference samples. The reference endmembers also encompass the mixing volume of the Viking Lander images, therefore, they meet the constraints imposed by the six Lander bandpasses, as well as the three Orbiter bandpasses.

We conclude from Fig. 1 that the Lander materials and the laboratory reference spectra fit the spectral variation in the Orbiter image that includes parts of Chryse Planitia, Acidalia Planitia, Kasei Valles, and Lunae Planum. The major compositional differences among the Orbiter spectral units are consistent with mixtures of rock and soil, and shade/shadow. Different fractions of shade imply topographic and/or textural variations. There is no way of knowing from the spectral data what the scale is of the shade component. It could be caused by spatially unresolved topographic elements, large boulders, rocks similar to those seen at the Lander sites, or opaque sand grains.

We interpret the Orbiter "blue" unit (prominent in Kasei Valles) as a mixture of a class of rock represented by H190 (Hawaii basalt) and shade, with little or no soil component. The scale of the shade, and therefore, the texture of the surface is unspecified. Photogeologic evidence, however, shows that some portions of the blue unit are located against topographic barriers and in crater floors, implying that the material is wind-deposited, possibly tephra sand. The "white" unit (prominent at the margin of Lunae Planum) is interpreted as a mixture of soil similar to H34 (palagonite) and H190 (basalt), with little or no shade component. This suggests a mixture of weathered and unweathered fine soil or tephra. The Lunae Planum unit is interpreted as a mixture of soil, rock, and shade. It is somewhat darker than the Chryse Plains unit, which includes the Viking Lander 1 site. Chryse also is consistent with a mixture of soil, rock, and shade, but appears to be smoother and to have less rock. This interpretation of the Orbiter data is consistent with what is observed spectrally and contextually in the Lander images.

We conclude that a large portion of the martian surface consists of only two spectrally distinct materials, basalt and palagonitic soil. We emphasize, however, that as viewed through the three broad bandpasses of Viking Orbiter, other materials cannot be distinguished from the mixtures discussed. It remains possible that the surface composition, as manifested spectrally, is indeed simple. Images of Mars with additional bandpasses coupled with telescopic, thermal and photogeologic evidence, should clarify interpretations.

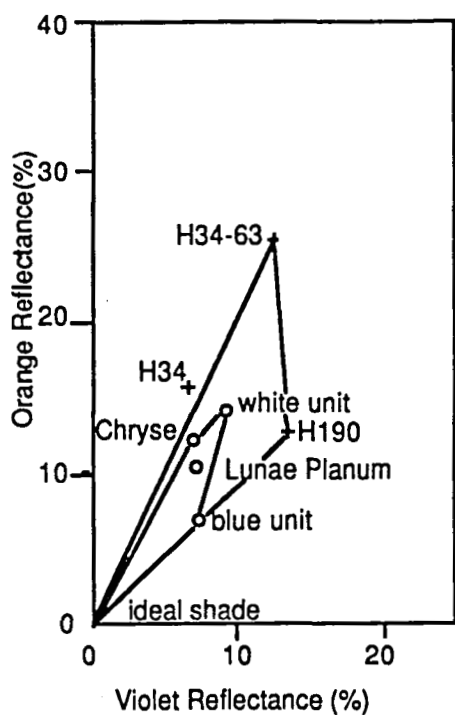


Figure 1. Viking Orbiter image endmembers (open circles) and laboratory reference spectra (crosses) in two dimensional projection (orange/violet) of the Orbiter three bandpasses. Image endmembers lie within the mixing volume defined by the pure reference endmembers.

#### Reference

1. Adams, J. B., M. O. Smith, and P. E. Johnson (1986), *J. Geophys. Res.* 91, 8098-9112.

## NATURE AND DISTRIBUTION OF SURFICIAL DEPOSITS IN CHRYSE PLANITIA AND VICINITY, MARS

R. Arvidson, E. Guinness, M. Dale-Bannister, McDonnell Center for the Space Sciences, Department of Earth and Planetary Sciences, Washington University, St. Louis, MO 63130, J. Adams, M. Smith, Department of Geological Sciences, University of Washington, Seattle, WA 98195, P. Christensen, Department of Geology, Arizona State University, Tempe, AZ 85287, R. Singer, Lunar and Planetary Laboratory, University of Arizona, Tucson, AZ 85721.

An important objective of the Mars Observer mission is the production of maps showing the global distribution of surface mineralogy and chemistry. These data will be of fundamental importance in evaluating the extent of differentiation of the planet and the nature and history of weathering. Atmosphere-surface interactions on Mars have involved a number of processes, including transportation of dust,  $\text{CO}_2$ , and  $\text{H}_2\text{O}$ , together with oxidation, hydration, and perhaps carbonation of exposed materials. Thermal inertias of martian surface materials, as determined from Viking IRTM data, do not exceed about  $12 \text{ cal}/(\text{cm}^2\text{s}^{1/2}\text{K})$  [1]. Since rock outcrops should have thermal inertias three times higher, exposure of loose debris is the rule rather than the exception when averaged over the 30 km field of view of the IRTM instrument. Furthermore, the efficacy of lateral transport of material by winds is well-known from Earth-based, orbital, and Viking Lander observations. Thus, interpretation of maps depicting mineralogy and chemistry will have to include models for lateral and vertical mixing of fresh and weathered materials over a variety of length scales. We have characterized and mapped the distribution of surficial units for a broad region surrounding the Viking Lander 1 site to evaluate the extent to which local materials are exposed. The region includes Chryse Planitia, Acidalia Planitia to the north, Kasei Vallis to the northwest, Lunae Planum to the west, and Xanthe Terra to the south.

Lander blue, green, red images acquired on Sol 611 were used to extract photometric properties of typical soils. The Lander data were compared to data from violet, green, red images acquired by the Orbiter on Sol 609 as a first-order check on the Orbiter radiometric calibrations, assuming reasonable atmospheric properties. The single scattering albedo and single particle phase function of typical Lander soil were estimated from color images acquired at variable lighting following the methods described in Arvidson et al. [2] and Guinness et al. [3]. The atmospheric multiplicative term was removed using a solar optical depth value determined by the Lander camera. The additive term was removed by using the brightness of shadows cast by rocks onto the soil. The derived single scattering albedos are 0.34, 0.50, and 0.82 for the blue, green, and red data, respectively, with estimated errors of  $\pm 0.02$ . In addition, the soil at Lander 1 has an asymmetric phase function and is a backscattering material. The estimated asymmetry factors for the Henyey-Greenstein function are -0.06, -0.08, and -0.12 (blue, green, and red) with an uncertainty of  $\pm 0.03$ . Furthermore, the anisotropic scattering precludes use of a single radiance factor (i.e., acquired at one lighting and viewing geometry) to extract the single scattering albedo.

A sequence of four violet ( $0.45 \pm 0.03 \mu\text{m}$ ), green ( $0.55 \pm 0.03 \mu\text{m}$ ), and red ( $0.59 \pm 0.05 \mu\text{m}$ ) Viking Orbiter images were used to determine the characteristics and distribution of surficial units in the study area. The images were processed using the PICS image processing software and calibration files developed at the U.S.G.S. Astrogeology Branch, Flagstaff, Arizona [4]. First, the image data were converted to



values in proportion to radiance factor. Radiance factor is defined as the ratio of radiance from a target to the radiance from a Lambertian surface of unit reflectance that is normally illuminated and at the same heliocentric distance [5]. The Orbiter images were then registered to the U.S.G.S. Mars control network [6], mapped to a sinusoidal equal area projection, and mosaicked. The mosaic data were also converted to intensity, hue, and saturation (IHS) images [7] to better understand the optical characteristics of surficial units. The two dominant surficial units that were identified by examining the Orbiter color and IHS images of the study region contain red material and dark gray (i.e., less red) material. The red material was subdivided into bright red and dark red units, with the bright red unit including the region of the Lander 1 site.

Radiance factor values were determined from the Orbiter images for each of the mapped units. The values were corrected for atmospheric and photometric effects. The difference between Orbiter radiance factors over the landing site and radiance factors computed from Lander data at the Orbiter lighting and viewing geometry can be accounted for by scattering and attenuation by atmospheric aerosols. Thus, bright red soil exposures must dominate the Orbiter image data for Chryse Planitia and surrounding areas, a result that is consistent with the extensive soil exposures seen in Lander images. Radiance factors for the bright red soil obtained from Lander data are 0.08, 0.14, and 0.35 (blue, green, and red) at a 20° incidence angle and 0° emission angle. These three-point spectra are most like laboratory spectra for fine-grained palagonite. The data are also similar to Earth-based spectra for classical bright areas. The bright red material is interpreted as dust (i.e., aeolian suspension load) accumulating in the area just south of Acidalia Planitia, which includes the younger volcanic terrains that dominate Chryse, and against topographic barriers such as craters and cliffs in adjacent regions. Dark gray material is exposed on the floor and against north-facing cliffs within Kasei Vallis, and as dark streaks downwind of craters in Xanthe Terra. This dark gray material is probably an outlier of wind-blown sands (i.e., aeolian saltation and traction loads) from the classical dark area, Acidalia Planitia. Dark gray material has three-point spectra that are indicative of lithic fragments with a mafic composition, mixed with a minor amount of palagonite-like material. Dark red material occurs in Lunae Planum to the west, Xanthe Terra to the south, and Oxia Palus to the east of the Lander. Dark red material has a noticeable lack of aeolian features. It is interpreted to be a substrate (e.g., deflated, duricrusted material) over which bright red and dark gray materials migrate. The three-point spectra of dark red material are most like palagonite mixed with or coating dark material such as basalt or basaltic glass.

The general outcrop pattern of red, dark red, and dark gray materials in the region of 0° to 90° west longitude and 0° to 60° north latitude follows topography and is locally modulated by surface roughness. The lowest areas (Acidalia and Chryse) have highest thermal inertias as derived from IRTM data [8]. These areas are also the darkest, except for red dust in Chryse and a bright red border on the southern edge of Acidalia Planitia. The bright red material in these areas must be, on average, optically thick (100's  $\mu\text{m}$ ), but thin as compared to the diurnal skin depth (centimeters). Areas with intermediate elevation (Lunae Planum, Xanthe, and Oxia) have intermediate inertias and dark red material. Highest areas (Tharsis and Arabia) have lowest inertias and are covered by bright red material. The broad correlation with topography and the lack of correlation with geology implies regional-scale meteorological controls on the outcrop patterns of surficial materials. Low threshold friction velocities in lowlands may be able to keep surfaces swept clean of bright red, low inertia dust, except where

local roughness elements (e.g., younger volcanic plains in Chryse, cliffs, craters, etc.) cause dust to accumulate [9-10]. Intermediate elevations have been stripped to a lesser extent, leaving dark red, immobile material, perhaps as duricrusted mixtures of dust and lithic fragments. Duricrust formation may be precluded in lowest areas because of frequent wind erosion and transport of debris. Highest areas are sites of accumulation of dust because of high threshold friction velocities associated with low atmospheric densities [9-10].

Interpretation of chemical and mineralogical maps to be produced from Earth-based telescopic observations and by Mars Observer will need to include models for the mixing of bright red materials with both dark red and dark gray units [11-12]. Further, mixing of dark gray with dark red material will need to be explicitly dealt with. Both dark gray and dark red units may expose igneous lithic fragments. In some cases the lithic material may be derived from local bedrock, although deciphering which materials are local as opposed to aeolian sediment will be a challenge. Finally, both Earth-based and Mars Observer data should be used to test the hypothesis that the dark red areas are exposures of deflated, duricrusted materials.

### References

- 1) Kieffer, H., and others, 1977, *J. Geophys. Res.*, 82, 4249-4291.
- 2) Arvidson, R., and others, 1987, submitted to *J. Geophys. Res.*.
- 3) Guinness, E., and others, 1987, *J. Geophys. Res.*, 92, E575-E587.
- 4) Batson, R., 1987, *Photogram. Eng. and Remote Sens.*, 53, 1211-1218.
- 5) Hapke, B., 1981, *J. Geophys. Res.*, 86, 3039-3054.
- 6) Wu, S., and F. Schafer, 1984, *Proc. Amer. Soc. Photogrammetry*, 2, 456-463.
- 7) Gillespie, A., and others, 1986, *Remote Sens. Environ.*, 20, 209-235.
- 8) Christensen, P., 1986, *Icarus*, 68, 217-238.
- 9) Bagnold, R., 1941, *The Physics of Blown Sand and Desert Dunes*, 265 pp.
- 10) Greeley, R., and J. Iversen, 1985, *Wind as a geological process*, 333 pp.
- 11) Adams, J., and others, 1986, *J. Geophys. Res.*, 91, 8098-8112.
- 12) Singer, R., and T. McCord, 1979, *Proc. Lunar Planet. Sci. Conf. 10th*, 1825-1848.

## NATURE AND ORIGIN OF MATERIALS EXPOSED IN THE OXIA PALUS-WESTERN ARABIA-SINUS MERIDIANI REGION, MARS

M. Presley and R. Arvidson, McDonnell Center for the Space Sciences, Department of Earth and Planetary Sciences, Washington University, St. Louis, MO 63130.

A key objective of the Mars Observer Mission will be to map the physical, elemental and mineralogical properties of the martian surface. Surficial deposits may be either: a) the result of the mechanical or chemical breakdown of local bedrock, or b) accumulations of weathered material brought in from other areas of the planet. The ability to utilize the Mars Observer data to characterize the martian crustal materials will depend on whether in situ debris, which can supply direct evidence of the composition and alteration of the local bedrock, can be distinguished from debris that has been laterally transported, and is therefore decoupled from the underlying geology. To assess whether local materials related to bedrock can be identified with Viking data, the southwestern boundary of Arabia, an area that includes Sinus Sabaeus, Sinus Meridiani and the region to the east of Oxia Palus, is examined in detail. This region is located within the ancient, heavily cratered terrain of the Noachian System [1]. The area was selected because the variation in color and albedo across the region indicates that there is a wide range of material properties over a relatively small area of the planet. Previous studies of this region [2-4] have concentrated on the determination of possible stratigraphic relationships between units defined from Viking multispectral images. Kieffer et al. [4] also used thermal inertia values derived from the Viking Orbiter Infrared Thermal Mapper (IRTM) to evaluate the thermal properties of the color/albedo units. In each of these studies the same color/albedo units were identified, but different conclusions were made about the stratigraphy of those units. Thomas [5] examined the color properties of dark streaks and splotches in the area, and concluded that stratigraphic relations are unclear, if even existent, because the units are of eolian origin and can vary laterally without layering.

In this abstract, we discuss additional data and analyses to search for evidence connecting the surficial units to bedrock geology. Crater statistics from the Mariner 9 data set compiled by Mutch et al. [6] and crater counts from high resolution Viking Orbiter images were used to provide broad constraints on the timing and extent of local debris production. Regional variations in the nature and extent of erosional and depositional features identified in Viking Orbiter medium resolution frames, which may be indications of lateral transport of debris, were mapped. Six overlapping sets of calibrated Viking Orbiter images taken through red, green, and violet filters were used to characterize and map surficial materials and to evaluate evidence for mixing between the various units. Block abundance and fine component thermal inertia, as derived from the Viking Orbiter IRTM data [7], were used to assess the amount of rock exposed at the surface and to characterize the thermal properties of the surficial deposits.

In the central equatorial heavily cratered terrain, crater obliteration models imply that kilometers of debris have been locally produced over the lifetime of the surface, although the average obliteration rate for the past few billion years has been less than  $8 \times 10^{-3} \mu\text{m/yr}$ . This study has investigated whether the materials currently exposed at the surface can be identified as part of these locally derived materials or as laterally transported debris unrelated to the underlying geology. Three color/thermal units were identified on the basis of distinct differences in reflectance, as derived from the

calibrated Viking Orbiter violet, red and green images, and on the basis of fine component thermal inertia, as derived from the Viking IRTM data. These units are referred to as the bright red unit, the dark violet unit, and the brown unit. Since the crater retention age does not vary significantly over the study area, since the distribution of morphologic features is not correlated with unit locations, and since topographic relief is not discernible at unit boundaries, it is likely that these units are relatively thin eolian deposits, decoupled from the underlying geology. Fluvial and eolian landforms give further support to the idea that extensive lateral transport and mixing of debris has played an important role in the formation of these units.

A global view of the color data shows that both the bright red material (i.e., classical bright areas) occupies large regions of the planet, regardless of morphology or inferred geology. It has the highest reflectances in both the red (0.20) and the violet (0.065) and the lowest fine component thermal inertia (2.4). Color data further indicate that the brightest, reddest material is mixing spatially with the darker materials. The bright red unit, therefore, is most likely a mantle of globally homogenized dust, with the contiguous portion of the unit possibly increasing in thickness through a positive feedback mechanism [8-10]. The current depth of this deposit must be greater than 10 cm in order to produce the observed thermal inertia, yet be less than 30 m in order to fit the limits of the crater data.

Global exposures or deposits of dark violet material are much less extensive than those of the bright red unit. Small scale features, however, such as dark streaks, splotches and dunes, which are associated with the large craters in Oxia, indicate that the dark material is also mobile. The dark violet material has the lowest reflectances in both the red (0.095) and the violet (0.045), and the highest fine component thermal inertia (6.4). These observations imply that the dark violet unit is probably composed of sand-sized lithic fragments. No evidence was found to indicate that the dark violet material is directly related to underlying bedrock units.

The brown unit is intermediate in both reflectance values (0.15 - 0.17 for the red, 0.05 - 0.06 for the violet) and fine-component thermal inertia (4.6). The sharpness of the boundaries between the brown unit and both the dark violet and the bright red units indicate that the brown unit is relatively immobile. One way this observation can be reconciled with the thermal data is if the brown unit is assumed to be indurated dust deposits.

Future missions, in particular, Mars Observer, will provide extensive information on the composition and mineralogy of surficial units. This study has shown that the optical and thermal signatures of bedrock are likely to be extensively contaminated or obscured by those of overlying eolian deposits, which have been laterally transported and are unrelated to local bedrock materials. In the  $6 \times 10^6$  km<sup>2</sup> of the study area in situ debris, derived from the breakdown of local bedrock, cannot be unequivocally identified with the available data. Unraveling the mixtures and assignment of components to local bedrock origins will indeed be a major challenge for the Mars Observer mission.

## References

- 1) Scott, D., and M. Carr, 1978, *U.S. Geol. Survey Misc. Geol. Inv. Map I-1083*.

- 2) Soderblom, L., and others, 1978, *Icarus*, 34, 446-464.
- 3) Strickland, E., 1980, *Lunar and Planetary Science XI*, 1106-1108.
- 4) Kieffer, H., and others, 1981, *Proc. Lunar Planet. Sci. Conf. 12*, 1395-1417.
- 5) Thomas, P., 1984, *Icarus*, 57, 205-227.
- 6) Mutch, T., and others, 1976, *The Geology of Mars*, 400 pp.
- 7) Christensen, P., 1986a, *Icarus*, 68, 217-238.
- 8) Zimbelman, J., and H. Kieffer, 1979, *J. Geophys. Res.*, 84, 8239-8251.
- 9) Christensen, P., 1982, *J. Geophys. Res.*, 87, 9985-9998.
- 10) Christensen, P., 1986b, *J. Geophys. Res.*, 91, 3533-3546.

Thermal Emission from Planetary Regoliths  
Bruce Hapke, Dept. of Geology & Planetary Science,  
University of Pittsburgh, Pittsburgh, PA 15260

The reflectance spectroscopy theory developed earlier under the present NASA grant has been extended to include the effects of thermally emitted radiation. These effects are of considerable importance to the interpretation of data from spacecraft instruments that measure the radiation from planetary regoliths in the mid and thermal IR, such as NIMS and VIMS. Although the theory is still under active development, preliminary results are as follows. The directional emissivity of a particulate medium is given by  $\gamma(1+2\mu)/(1+2\gamma\mu)$ , where  $\gamma = \sqrt{1-w}$ ,  $\mu = \cosine$  of the angle of observation, and  $w$  = the average single particle scattering albedo at the wavelength of interest. The hemispherically-integrated emissivity is given by  $2\gamma\pi/(1+\gamma)$ . The effects of thermal gradients in the regolith can be neglected only if  $2\gamma l \gg 1$ , where  $l$  is the ratio of the thermal scale height to the extinction length in the medium. In the mid-IR, thermal radiation will decrease the spectral contrast of diagnostic absorption bands, but such bands should be observable at wavelengths shorter than 5  $\mu m$ .

## THERMAL EMISSION SPECTROSCOPY OF MINERALS AND MIXTURES

*Philip R. Christensen* Arizona State University, Tempe AZ 85287

The general purpose of this work is to study the thermal emission properties of natural materials in emission, in order to develop an understanding of future spacecraft observations of planetary surfaces using thermal-infrared spectroscopy. Pioneering studies of the thermal-infrared absorption characteristics of minerals have been performed (Lyon, 1962, 1964; Farmer, 1974; Hunt and Salisbury, 1974, 1975, 1976; Salisbury et al., 1987) which illustrate the usefulness of this spectral region for compositional determinations. The particular aspect of the activity described here is an initial study of mineral mixtures. In this regard, emission spectra are particularly important for studying mixtures and coatings, where the interaction of the emitted energy with the sample, and therefore the observed spectrum, is different in emission and reflection.

### Instrument Setup

Much of the effort to date has focused on the development of an emission spectroscopy laboratory at ASU to collect spectra of rock and mineral materials. At the present time, virtually all thermal-IR spectral work has been done in reflection rather than in emission. Spectra of planetary surfaces are acquired in emission, however, necessitating the acquisition of emission spectra of the type the ASU lab was specifically designed to collect. The current laboratory is based on a prototype spacecraft instrument developed during the instrument development phase of the Thermal Emission Spectrometer (TES) investigation. The present instrument operates from 6.5 to 18  $\mu\text{m}$ , with a spectral resolution of 3.5  $\text{cm}^{-1}$ . The instrument is controlled, and data collected, analyzed, and stored, on an IBM PC-XT microcomputer. The initial set of software to acquire, process, analyze, and store spectra has been fully developed. The instrument is fully calibrated, using a commercial blackbody with an emissivity of  $>0.99$  and a temperature controllable to  $<0.1$  K. This calibration standard, together with the use of a liquid nitrogen cold blackbody, allow radiometrically calibrated spectra with absolute calibration of better than 1% to be collected.

### Data Acquisition

Acquisition of emission spectra require either heating samples to greater than room temperature, or developing a sample chamber with cold ( $<100$  K) walls in order to maximize the energy received from the sample relative to the surroundings. At present, samples processed at ASU are heated in a temperature controlled oven to approximately 100 C for 6 hours to achieve uniform temperatures within the sample and minimize temperature gradients. The thermal emissivity was determined by calibrating the observed flux using the high-temperature and liquid nitrogen blackbodies, and by fitting the resultant radiance curve to blackbody curves to determine the sample temperature. This determination of temperature agrees to within 1-2 K with the oven temperature and with the temperature of the sample measured using an attached thermocouple, and is considered to provide the most accurate estimate of sample temperature.

### Thermal-IR Spectra of Single Minerals

An initial suite of materials has been studied using the current laboratory setup at ASU. This study has focused on a limited number of candidate planetary materials in order to study the performance of the ASU instrumentation and to develop operational techniques. Examples of these spectra (shown as thermal emissivity, computed as discussed above) are given in Figure 1 for different composition feldspar minerals, illustrating the significant differences of

minerals as measured in the thermal-IR. Although feldspar minerals have essentially the same crystal structure, the observed differences in feldspar spectral features are produced by differences in the vibration frequencies due to subtle differences in composition (Farmer, 1974).

### Mineral Mixtures

Initial progress has been made studying mixtures of materials, which will undoubtedly be encountered on real planetary surfaces. One of the most difficult situations to analyze quantitatively is the mixture of two or materials of very different grain sizes. Unfortunately, this complex case is precisely the case most likely encountered on Mars, as with the intimate mixing of sand and clay.

There are two important results that have been obtained to date from the study of mixtures. The first is the verification that multiple components can be identified in mixtures, and the second is demonstrating that there are consistent trends in the spectra of mixtures (Figure 2). Given a quartz sand-montmorillonite clay mixture, it is possible to identify the spectral signature of quartz when it occurs at the ~25% level by volume (Figure 2). Thus, it is possible to identify components, even when one component has a relatively low abundance and is mixed with complex, coating materials such as a very fine-grained clay. Secondly, as can be seen in Figure 2, there are systematic trends in the spectral signature of mixtures, proceeding from 100% quartz sand to 100% montmorillonite. Although there is not a simple, linear trend of absolute abundances in the mix, the relative depth of the spectral features is directly related to the component abundances. Future work will be focus on quantifying the observed trends, and on studying additional types of mixtures, including multiple components.

### References

- Farmer, V.C. (ed.), 1974, The Infrared Spectra of Minerals, Mineralogical Society, London, 539 pp.
- Hunt, G.R., and J.W. Salisbury, 1974, Mid-infrared spectral behavior of igneous rocks, Environ. Res. Paper 496-AFCRL-TR-74-0625, 142 pp.
- Hunt, G.R., and J.W. Salisbury, 1975, Mid-infrared spectral behavior of sedimentary rocks, Environ. Res. Paper 510-AFCRL-TR-75-0256, 49 pp.
- Hunt, G.R., and J.W. Salisbury, 1976, Mid-infrared spectral behavior of metamorphic rocks, Environ. Res. Paper 543-AFCRL-TR-76-0003, 67 pp.
- Lyon, R.J.P., 1962, Evaluation of infrared spectroscopy for compositional analysis of lunar and planetary soils, Stanford Research Inst. Final Report Contract NASA 49(04).
- Lyon, R.J.P., 1964, Evaluation of infrared spectrophotometry for compositional analysis of lunar and planetary soils: Part II: Rough and powdered surfaces, NASA Contractor Report CR-100, 172 pp.
- Salisbury, J.W., L.S. Walter, and N. Vergo, 1987, Mid-infrared (2.1-25  $\mu$ m) Spectra of Minerals: First Edition, U.S. Geological Survey Open File Report 87-263.



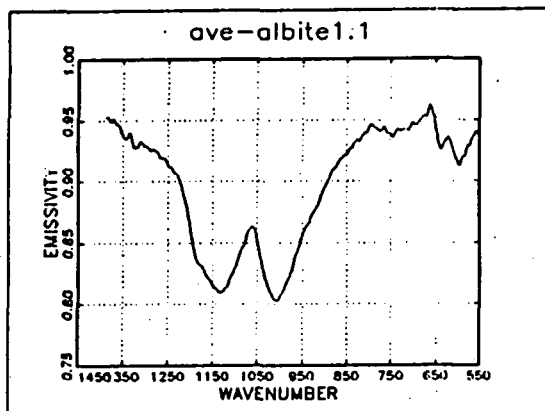


Figure 1a

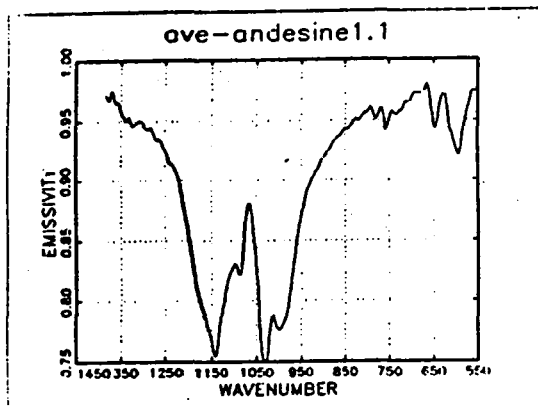


Figure 1b

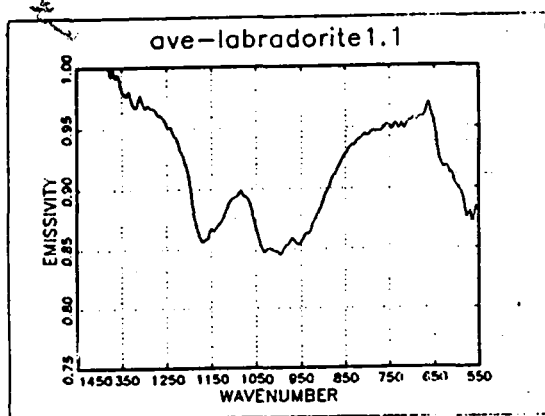


Figure 1c

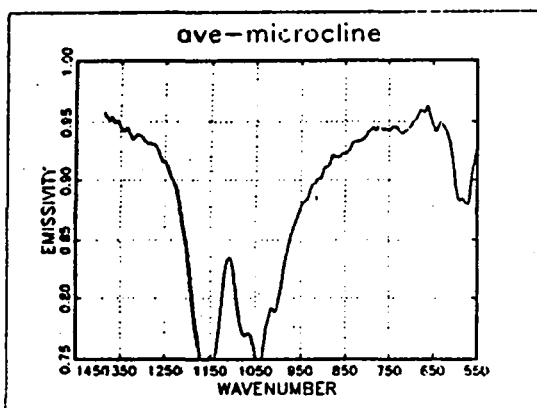


Figure 1d

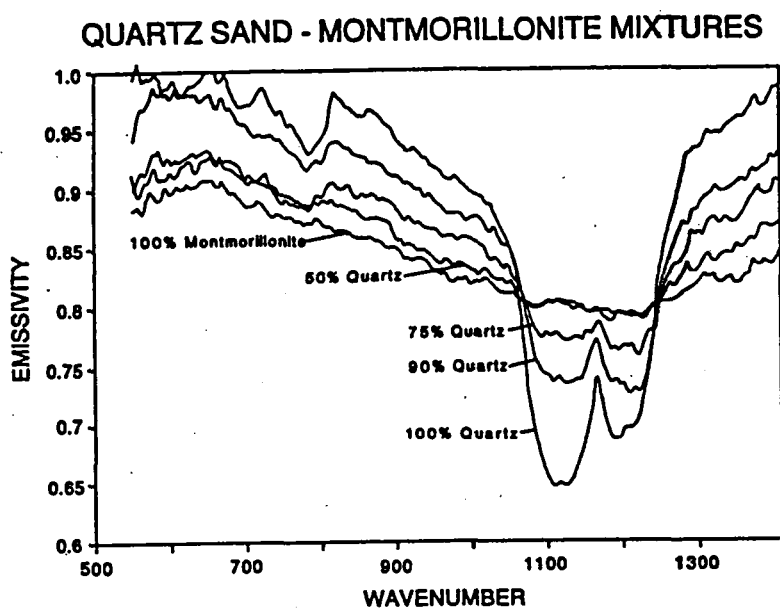


Figure 2

## HIGH RESOLUTION THERMAL IMAGING OF VOLCANIC TERRAINS ON MARS

*Philip R. Christensen and Michael C. Malin* Arizona State University, Tempe AZ 85287

The determination of thermal inertia was one of the primary goals of the Viking Infrared Thermal Mapper (IRTM) experiments (Kieffer et al., 1977). Thermal inertia is important because it provides a measure of the mean surface particle size and the spatial variations in effective particle sizes across the planet. As pointed out by numerous authors, a wide range of surface properties, including the abundance of rocks and bonding of surface materials, can contribute to differences in thermal inertia (Kieffer et al., 1977; Palluconi and Kieffer, 1981; Christensen, 1986; Zimbelman and Leshin, 1987). Nonetheless, the thermal inertia does provide a relative means for assessing the state and origin of the current martian surface.

In the pioneering effort, global thermal inertia determinations were made by fitting diurnal measurements of the surface to modeled curves of diurnal temperature variations to retrieve the thermal inertia (Palluconi and Kieffer, 1981). These determinations provide the most accurate measure of the inertia, together with the magnitude of the deviations of the surface from a simple model (see Dittéon, 1982). However, to obtain diurnal coverage from the Viking spacecraft over a relatively small range of seasons it was necessary to bin observations into  $2^\circ \times 2^\circ$  latitude, longitude bins. Thus, the highest spatial resolution available from this method is  $120 \text{ km} \times 120 \text{ km}$  at the equator (Palluconi and Kieffer, 1981).

Using the map of Palluconi and Kieffer as a base, we have compared the thermal inertia obtained in this manner to that obtained by fitting the thermal inertia model to a single, pre-dawn observation. Histograms of this difference, computed for every Viking pre-dawn measurement, show very good agreement between the two methods. This consistency is reasonable, given that the thermal inertia determination is very strongly sensitive to the pre-dawn temperature values. During clear periods, when atmospheric dust does not affect the pre-dawn temperatures,  $\sim 80\%$  of the single point values fall within an inertia of  $\pm 1$  (in units of  $10^{-3} \text{ cal cm}^{-2} \text{ K}^{-1} \text{ sec}^{-1/2}$ ). This agreement indicates that pre-dawn measurements alone provide a reasonable estimate of inertia, and can be used to generate a map of thermal inertia at a substantially higher spatial resolution than by using the full diurnal fits.

### Data

A series of Viking 1 and 2 pre-dawn observations were used to construct a global thermal inertia map from  $\sim 60^\circ \text{ S}$  to  $60^\circ \text{ N}$ . The spatial resolution of these observations vary, but is  $\sim 30 \text{ km}$ , with somewhat higher resolution in the southern hemisphere. They were collected into  $1/2^\circ \times 1/2^\circ$  latitude, longitude bins, consistent with the binning strategy of the Mars Consortium. The data used were obtained during 6 "walks" around the planet by the Viking 1 Orbiter, and 3 "walks" by Orbiter 2. Single-point thermal inertias were obtained using the Viking Standard Thermal Model described by Kieffer et al. (1977). A subset of these data were discussed by Zimbelman and Kieffer (1979). The data from each walk were binned together to create 9 images, each covering a range of latitudes at nearly all longitudes. Care was taken to analyze the resulting thermal inertia images and to remove all observations that had problems. These 9 images were then mosaicked together. In many areas overlapping coverage was acquired; in these cases the highest resolution observations were used. The final result is shown in Figure 1. Although observations at higher spatial resolution are available for specific regions (Kieffer et al., 1977) the data set described here provides the highest resolution, consistent data obtained pre-dawn during clear periods. As such it represents the

best global thermal image available for Mars until observations can be obtained by the Mars Observer Thermal Emission Spectrometer experiment.

### Discussion

The most striking feature of the thermal image presented in Figure 1 is the presence of small-scale structure in the surface properties not previously recognized on a global scale. Of particular interest are an intriguing series of relatively high thermal inertia materials that occur within the volcanic province of Tharsis. These high inertia materials occur at the base of the scarp around Olympus Mons and its aureole, as well as other topographic features in the area. Detailed comparison of the location of these features indicates that they are located on the downslope side of these escarpments. Several possible explanations exist for the origin of these features. Two basic mechanisms can be envisioned. They may represent local, in-place changes to the surface character, such as bonding, or they represent localized accumulations of relatively coarse materials. The first mechanism appears less likely due to the small scale and high degree of correlation with local topography and morphology. A mechanism is required to locally bond or alter material only in specific regions, while leaving material 50 km away unaffected. The second possibility appears more likely, either through local entrapment of a coarse, mobile surface fraction, or through the accumulation of coarse talus at the base of these escarpments.

These data also indicate other regions with subtle thermal inertia differences that can be associated with surface morphology. Of interest for volcanic terrain analysis are the apparent discrete changes in thermal inertia in the Lunae Planum region. This non-continuous change in surface properties suggests that a non-continuous process has acted to produce the present surface. Aeolian mixing of material is not a good candidate in this particular case; differing degrees of bonding of material of possibly different ages is a possible explanation. Some additional features of interest include the high-inertia zones associated with crater streaks in Oxia Palus, high-inertia materials in the rim and walls of large craters in Arabia, and high-inertia, intra-crater deposits in the summer hemisphere (Christensen, 1983).

These data provide a new view of the martian surface and surface processes that suggests a much more varied and heterogeneous surface than suggested by a lower resolution global view previously available. They suggest that Mars will display increased variability in surface characteristics as the resolution of the observations increases. Thus, localized processes appear to operate in addition to global-scale processes that have been proposed to produce the "continental-scale" inertia variations (Christensen, 1986). Additional analysis of these variations will provide more information on local surface processes and surface evolution in volcanic terrains, and may help to separate surface properties produced by initial surface emplacement from those produced by subsequent modification.

### **References**

- Christensen, P.R., 1983, Eolian intracrater deposits on Mars: Physical properties and global distribution, *Icarus*, 56, 496-518.
- Christensen, P.R., 1986, Regional dust deposits on Mars: Physical properties, age, and history, *J. Geophys. Res.*, 91, 3533-3545.
- Ditteon, R., Daily temperature variations on Mars, *J. Geophys. Res.*, 87, 10,197-10,214, 1982
- Kieffer, H.H., T.Z. Martin, A.R. Peterfreund, E.D. Miner, and F.D. Palluconi, Thermal and albedo mapping during the Viking primary mission, *J. Geophys. Res.*, 82, 4249-4292, 1977.
- Palluconi, F.D. and H.H. Kieffer, Thermal inertia mapping of Mars from -60° to +60°, *Icarus*, 45, 415-426, 1981
- Zimbelman, J.R. and L.A. Leshin, A geologic evaluation of the thermal properties for the Elysium and Aeolis quadrangles of Mars, *J. Geophys. Res.*, 92, E588-E596, 1987.

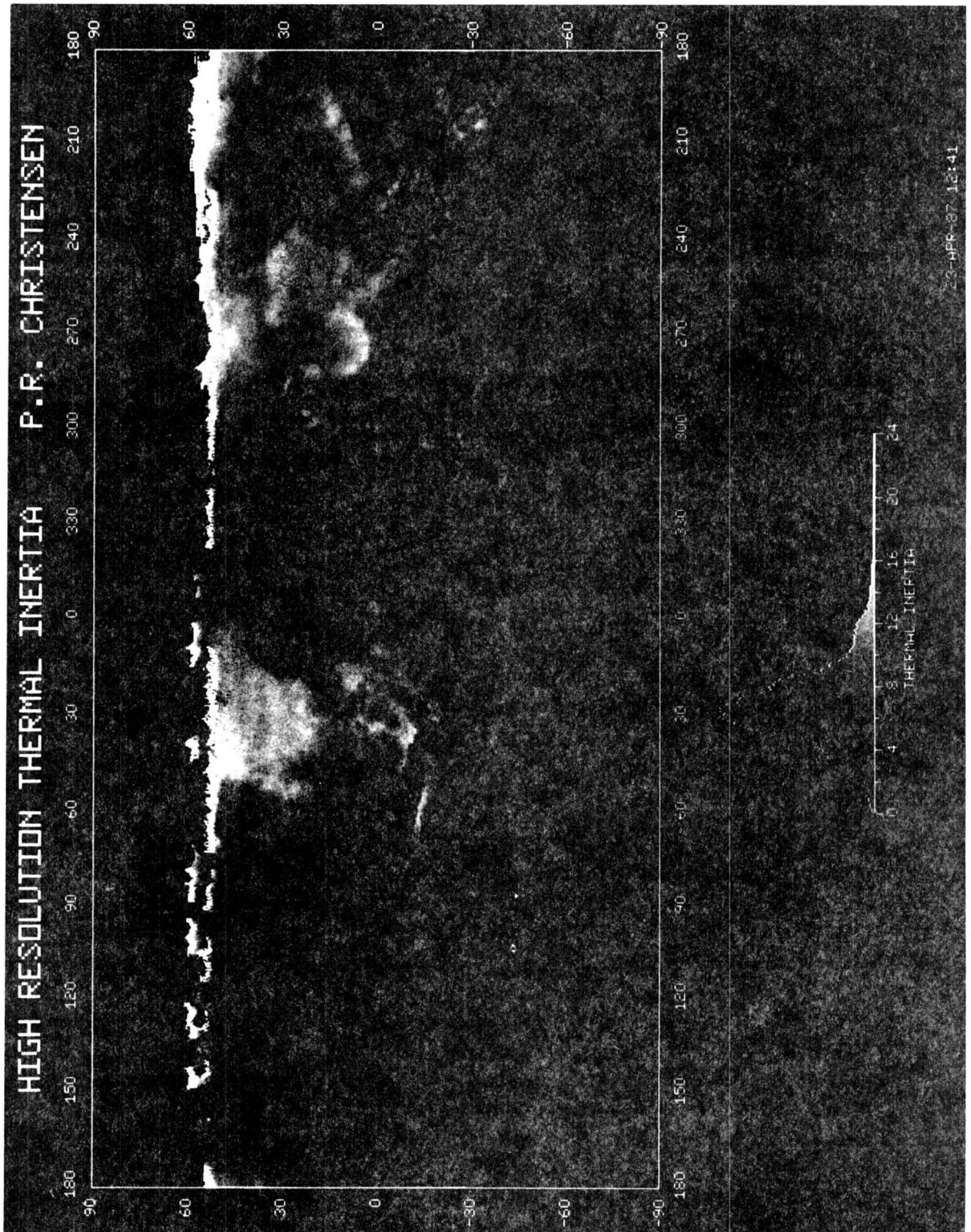


Figure 1

## A SEARCH FOR SUBSURFACE ICE ON MARS USING VIKING THERMAL MAPPER OBSERVATIONS

David. A. Paige, UCLA, Los Angeles, CA 90024

Thermal models for the distribution of martian permafrost indicate that subsurface water ice could presently be stable throughout the year at depths ranging from 10 to 100 cm at latitudes poleward of  $\pm 40^\circ$  (1). Proof for the existence of such deposits would have important implications for our understanding of the initial volatile inventory, atmospheric evolution, geology, and climate of Mars. The goal of this study is to map the distribution of surface and subsurface permafrost at high latitudes by using Viking IRTM surface temperature observations in conjunction with diurnal and seasonal thermal model calculations.

Solid water ice or hard-frozen ground can be distinguished from fine, unconsolidated surface materials on the basis of thermal inertia. Solid water ice has a thermal inertia of  $I = 50 \times 10^{-3} \text{ cal cm}^{-2} \text{ sec}^{-1/2}$ , whereas mid-latitude martian surface materials have thermal inertias ranging from  $1 \times 10^{-3}$  to  $15 \times 10^{-3} \text{ cal cm}^{-2} \text{ sec}^{-1/2}$  (2). Thermal inertia can be inferred from remote sensing observations because it has a major influence on the amplitudes of diurnal and seasonal surface temperature variations. Since martian diurnal temperature waves penetrate a few centimeters into the surface, and seasonal temperature waves penetrate to at least a meter, surface temperature observations can be used to infer the presence of permafrost.

To assess the feasibility of this project, we have conducted a pilot study of three small regions in the north polar area (3). The results have shown that the bulk thermal properties of martian surface materials at high latitudes can be reliably inferred from IRTM observations. The north polar water ice cap has a thermal inertia of  $40 \times 10^{-3} \text{ cal cm}^{-2} \text{ sec}^{-1/2}$ . The dune fields surrounding the north polar cap have a thermal inertia of  $6.5 \times 10^{-3} \text{ cal cm}^{-2} \text{ sec}^{-1/2}$ . The pilot study also gave evidence for high thermal inertia material below the surface at  $+75^\circ$  north latitude (3).

Our plan for completing this project can be divided into eight separate tasks:

1. Extract and time-sequence IRTM polar observations from complete data set.
2. Explore the sensitivity of thermal model results to solar forcing and subsurface structure.
3. Explore the sensitivity of thermal model results to atmospheric effects such as water ice and dust clouds.
4. Determine optimal bin sizes for time-sequenced IRTM observations.
5. Identify key high latitude regions for intensive study.
6. Use observations and models to test for the presence of subsurface high-inertia material at selected high latitude locations.
7. Interpret results using all available information.
8. Publish results.

During the first six months of this project, we have made significant progress on tasks one and two.

## REFERENCES

1. Farmer, C. B. and P. E. Doms, *J. Geophys. Res.* 84, 2881 (1979).
2. Palluconi, F. D. and H. H. Kieffer, *Icarus* 45, 415 (1981).
3. Paige, D. A. and H. H. Kieffer "The Thermal Properties of Martian Surface Materials at High Latitudes: Possible Evidence for Permafrost", Symposium on Mars: Evolution of its Climate and Atmosphere, July 17-19, Washington D. C., (1986)

## A SEARCH FOR SUBSURFACE ICE ON MARS USING VIKING THERMAL MAPPER OBSERVATIONS

David. A. Paige, UCLA, Los Angeles, CA 90024

Thermal models for the distribution of martian permafrost indicate that subsurface water ice could presently be stable throughout the year at depths ranging from 10 to 100 cm at latitudes poleward of  $\pm 40^\circ$  (1). Proof for the existence of such deposits would have important implications for our understanding of the initial volatile inventory, atmospheric evolution, geology, and climate of Mars. The goal of this study is to map the distribution of surface and subsurface permafrost at high latitudes by using Viking IRTM surface temperature observations in conjunction with diurnal and seasonal thermal model calculations.

Solid water ice or hard-frozen ground can be distinguished from fine, unconsolidated surface materials on the basis of thermal inertia. Solid water ice has a thermal inertia of  $I = 50 \times 10^{-3} \text{ cal cm}^{-2} \text{ sec}^{-1/2}$ , whereas mid-latitude martian surface materials have thermal inertias ranging from  $1 \times 10^{-3}$  to  $15 \times 10^{-3} \text{ cal cm}^{-2} \text{ sec}^{-1/2}$  (2). Thermal inertia can be inferred from remote sensing observations because it has a major influence on the amplitudes of diurnal and seasonal surface temperature variations. Since martian diurnal temperature waves penetrate a few centimeters into the surface, and seasonal temperature waves penetrate to at least a meter, surface temperature observations can be used to infer the presence of permafrost.

To assess the feasibility of this project, we have conducted a pilot study of three small regions in the north polar area (3). The results have shown that the bulk thermal properties of martian surface materials at high latitudes can be reliably inferred from IRTM observations. The north polar water ice cap has a thermal inertia of  $40 \times 10^{-3} \text{ cal cm}^{-2} \text{ sec}^{-1/2}$ . The dune fields surrounding the north polar cap have a thermal inertia of  $6.5 \times 10^{-3} \text{ cal cm}^{-2} \text{ sec}^{-1/2}$ . The pilot study also gave evidence for high thermal inertia material below the surface at  $+75^\circ$  north latitude (3).

Our plan for completing this project can be divided into eight separate tasks:

1. Extract and time-sequence IRTM polar observations from complete data set.
2. Explore the sensitivity of thermal model results to solar forcing and subsurface structure.
3. Explore the sensitivity of thermal model results to atmospheric effects such as water ice and dust clouds.
4. Determine optimal bin sizes for time-sequenced IRTM observations.
5. Identify key high latitude regions for intensive study.
6. Use observations and models to test for the presence of subsurface high-inertia material at selected high latitude locations.
7. Interpret results using all available information.
8. Publish results.

During the first six months of this project, we have made significant progress on tasks one and two.

## REFERENCES

1. Farmer, C. B. and P. E. Doms, *J. Geophys. Res.* **84**, 2881 (1979).
2. Palluconi, F. D. and H. H. Kieffer, *Icarus* **45**, 415 (1981).
3. Paige, D. A. and H. H. Kieffer "The Thermal Properties of Martian Surface Materials at High Latitudes: Possible Evidence for Permafrost", Symposium on Mars: Evolution of its Climate and Atmosphere, July 17-19, Washington D. C., (1986)

## A SEARCH FOR SUBSURFACE ICE ON MARS USING VIKING THERMAL MAPPER OBSERVATIONS

David. A. Paige, UCLA, Los Angeles, CA 90024

Thermal models for the distribution of martian permafrost indicate that subsurface water ice could presently be stable throughout the year at depths ranging from 10 to 100 cm at latitudes poleward of  $\pm 40^\circ$  (1). Proof for the existence of such deposits would have important implications for our understanding of the initial volatile inventory, atmospheric evolution, geology, and climate of Mars. The goal of this study is to map the distribution of surface and subsurface permafrost at high latitudes by using Viking IRTM surface temperature observations in conjunction with diurnal and seasonal thermal model calculations.

Solid water ice or hard-frozen ground can be distinguished from fine, unconsolidated surface materials on the basis of thermal inertia. Solid water ice has a thermal inertia of  $I=50 \times 10^{-3} \text{ cal cm}^{-2} \text{ sec}^{-1/2}$ , whereas mid-latitude martian surface materials have thermal inertias ranging from  $1 \times 10^{-3}$  to  $15 \times 10^{-3} \text{ cal cm}^{-2} \text{ sec}^{-1/2}$  (2). Thermal inertia can be inferred from remote sensing observations because it has a major influence on the amplitudes of diurnal and seasonal surface temperature variations. Since martian diurnal temperature waves penetrate a few centimeters into the surface, and seasonal temperature waves penetrate to at least a meter, surface temperature observations can be used to infer the presence of permafrost.

To assess the feasibility of this project, we have conducted a pilot study of three small regions in the north polar area (3). The results have shown that the bulk thermal properties of martian surface materials at high latitudes can be reliably inferred from IRTM observations. The north polar water ice cap has a thermal inertia of  $40 \times 10^{-3} \text{ cal cm}^{-2} \text{ sec}^{-1/2}$ . The dune fields surrounding the north polar cap have a thermal inertia of  $6.5 \times 10^{-3} \text{ cal cm}^{-2} \text{ sec}^{-1/2}$ . The pilot study also gave evidence for high thermal inertia material below the surface at  $+75^\circ$  north latitude (3).

Our plan for completing this project can be divided into eight separate tasks:

1. Extract and time-sequence IRTM polar observations from complete data set.
2. Explore the sensitivity of thermal model results to solar forcing and subsurface structure.
3. Explore the sensitivity of thermal model results to atmospheric effects such as water ice and dust clouds.
4. Determine optimal bin sizes for time-sequenced IRTM observations.
5. Identify key high latitude regions for intensive study.
6. Use observations and models to test for the presence of subsurface high-inertia material at selected high latitude locations.
7. Interpret results using all available information.
8. Publish results.

During the first six months of this project, we have made significant progress on tasks one and two.

## REFERENCES

1. Farmer, C. B. and P. E. Doms, *J. Geophys. Res.* **84**, 2881 (1979).
2. Palluconi, F. D. and H. H. Kieffer, *Icarus* **45**, 415 (1981).
3. Paige, D. A. and H. H. Kieffer "The Thermal Properties of Martian Surface Materials at High Latitudes: Possible Evidence for Permafrost", Symposium on Mars: Evolution of its Climate and Atmosphere, July 17-19, Washington D. C., (1986)

## **Martian Polar Frost and Atmosphere/Soil Water Exchange**

**Tomas Svitek and Bruce C. Murray**  
Division of Geological and Planetary Sciences  
California Institute of Technology

Observations of the martian polar frost yields clues about the actual volatile transport processes operating on Mars (Leighton and Murray 1966), and about interactions between the atmosphere and soil (Zent et al 1986).

In this study we are focusing on two specific lines of investigation to better delineate the properties of Martian surface frost and the related effects of the atmosphere/soil water exchange:

1) Viking Lander 2 (VL-2) observations of the winter frost (Guinness et al 1979, Jones et al 1979) are particularly important as our only in-situ observations of the seasonal polar cap. The question of composition is apparently not yet resolved (Hart and Jakosky 1986). On the one hand, CO<sub>2</sub> ice is assumed not to be stable under the estimated thermodynamical regime. On the other hand, more H<sub>2</sub>O ice would be required, based on the Lambertian phase function measured from the Lander images by Wall 1981, than is consistent with the Orbiter MAWD measurements. Most of frost disappears significantly before there is a rise in water vapor column in the atmosphere. We propose to resolve this problem by invoking cold trapping in the soil during the latter phase of frost presence because of the bimodal character of the aerial coverage of the frost as a function of the season - see Figure 1. During this second phase, the frost accumulates at thermodynamically favorable locations because its removal by the atmospheric circulation is limited. This effect leads to a much thicker layer of frost than otherwise expected, and thus satisfies the phase function observations.

We are currently in the process of acquiring better observational support for the above proposed mechanism by A) performing detailed measurements of the variation of frost color and phase function as a function of  $L_s$ ; B) calibrating the calculated surface temperature data by measurements from the Lander and from the IRTM on the Viking Orbiter (Figure 2); and C) better estimating the atmospheric water vapor holding capacity and transport rate at the given season using the Lander meteorology dataset (Hess 1977) plus MAWD measurements (Figure 3). These preliminary data analysis shows to be in support of the above mentioned hypothesis.

2) In addition, we are studying atmosphere/soil exchange by correlating the observations from different orbiter instruments over the edges of both polar caps. This should better constrain the structure of the seasonal and residual polar caps, and also help delineate the seasonal reservoir of water (Christensen and Zurek, 1984). The relevant unbinned data from IRTM and MAWD, and imaging as well, are being correlated in order to identify the process of disappearance of the CO<sub>2</sub> and H<sub>2</sub>O frost cover. This procedure should indicate if the water ice forms a substrate for the seasonal dry ice cap, or if it is incorporated into the seasonal cap, or if it is being exchanged between the atmosphere and surface.



## REFERENCES CITED

- Christensen, P. R., and R. W. Zurek, 1984. Martian North Polar Hazes and Surface Ice, *JGR*, 89, 4587-4596.
- Guinness, E. A., et al, 1979. Color Changes at the Viking Landing Sites Over the Course of a Mars Year, *JGR*, 84, 8355-8364.
- Hart, H. M., and B. M. Jakosky, 1986. Composition and Stability of the Condensate Observed at the Viking Lander 2 Site on Mars, *Icarus*, 66, 134-142.
- Hess, S. L., et al, 1977. Meteorological Results From the Surface of Mars: Viking 1 and 2, *JGR*, 82, 4559-4574.
- Jones, K. L., et al, 1979. One Mars Year: Viking Lander Imaging Observations, *Science*, 204, 799-806.
- Leighton, R. B., and B. C. Murray, 1966. Behavior of Carbon Dioxide and Other Volatiles on Mars, *Science*, 153, 136-144.
- Wall, S. D., 1981. Analysis of condensates formed at the Viking 2 Lander site - the first winter, *Icarus*, 47, 173-183.
- Zent, A. P., et al, 1986. Distribution and state of  $H_2O$  in the high-latitude shallow subsurface of Mars, *Icarus*, 66.

## Fractional Ground Coverage by Frost (as observed by Viking Lander 2)

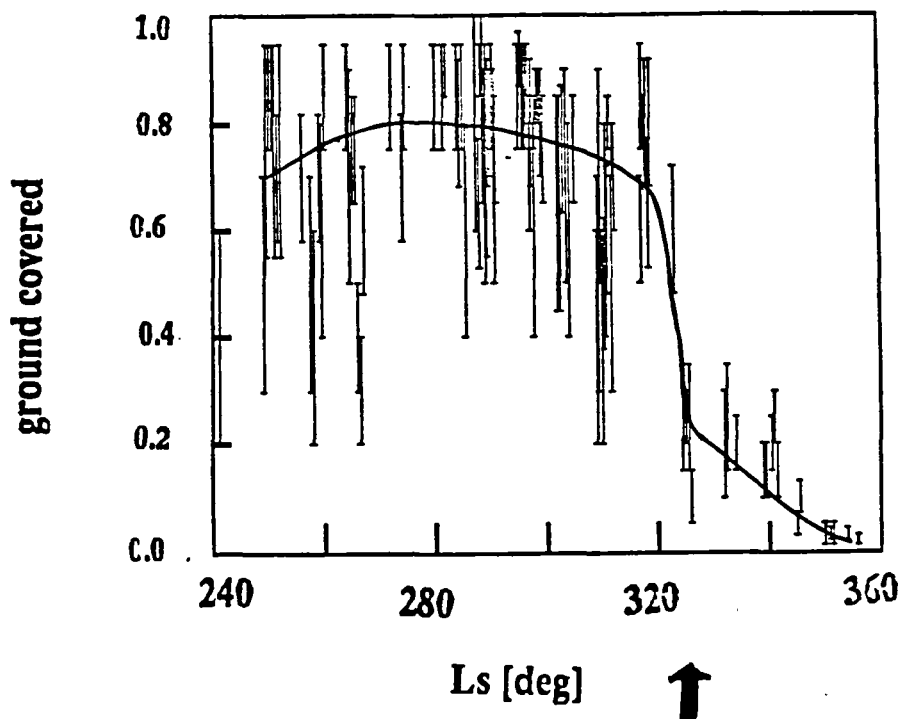


Figure 1 The frost surface coverage as a function of  $L_s$ . Notice that the frost existed in two different forms: first, as an almost complete ground cover for most of the winter, and later, in a much smaller but probably much thicker surface coverage (about 10%; mostly shadows and other cold traps). This is in spite of the relatively high soil temperatures reached during the day. The removal of the frost may be limited by the atmospheric transport rate.

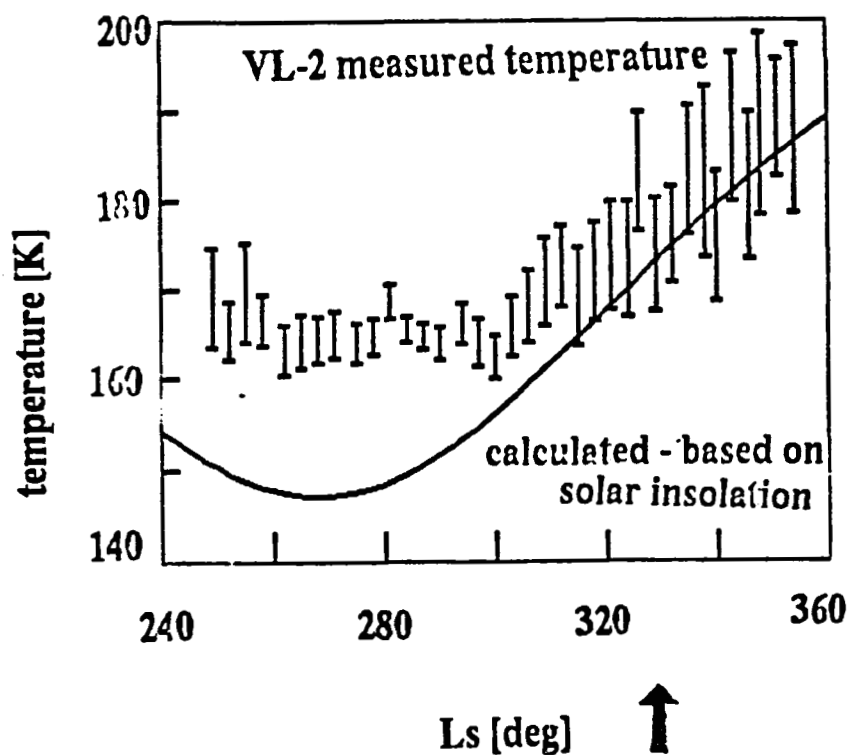


Figure 2 Water frost stability derived from the VL-2 meteorology experiment and from a calculation of solar insolation. Note that the complete-coverage frost disappears when the surface temperature approaches the air temperature, as expected.

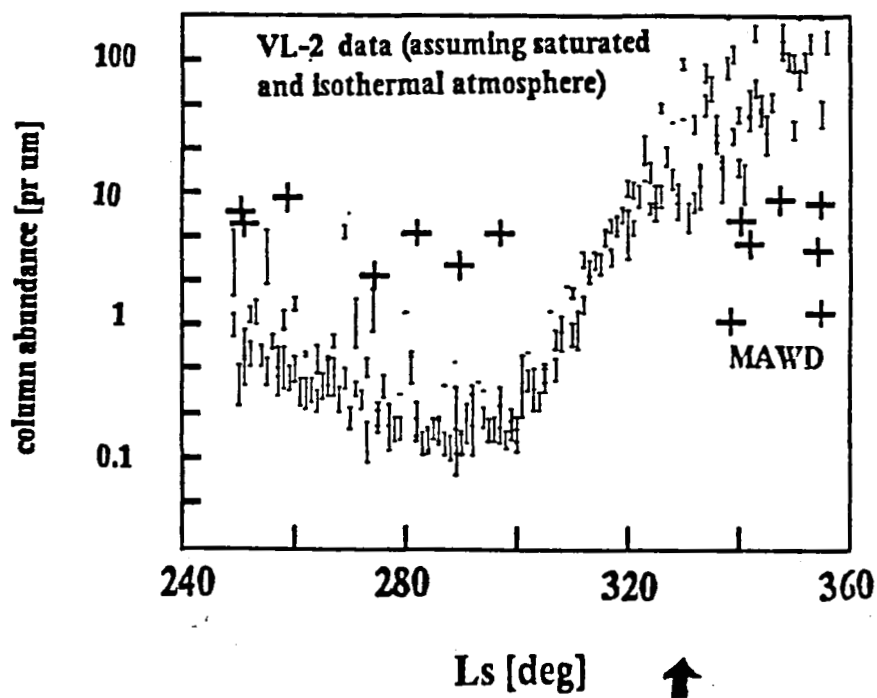


Figure 3 Water vapor column abundance derived from the MAWD and VL-2 measurements. The frost disappears when the calculated holding capacity of the lower atmosphere exceeds the measured value.

DETECTING THE POSSIBLE PRESENCE OF LUNAR ICE  
BY MEANS OF COUPLED NEUTRON-GAMMA RAY SPECTROSCOPY  
A. E. Metzger, Jet Propulsion Laboratory, Pasadena, CA 91109  
E. L. Haines, Sunrise Research Inc., Eugene, OR 97404

The possible presence of water ice at high lunar altitudes has been postulated (1). Several sources of water have been identified (1,2), namely, solar wind hydrogen which can be oxidized by ferrous iron oxide in the lunar surface, impacting comets and meteorites, and primitive water which could have been outgassed during the early cataclysmic period of lunar history. Whether measurable quantities of water have been ballistically transported to polar regions and trapped in permanently shadowed areas has been the subject of several studies (2-5). The question is of obvious importance scientifically, as well as in determining the resource inventory of the moon. We have been studying the applicability of gamma-ray spectroscopy with an added neutron mode for this purpose and find that the simultaneous detection of gamma rays and neutrons from the lunar surface can provide a sensitive test for water.

Gamma rays emanating from a planetary surface are produced by prompt or delayed gamma-ray emission following neutron capture in surface elements, by inelastic collisions between fast neutrons and surface elements, and by natural radioactivity. A large number of the lines observable by remote gamma-ray sensing are neutron capture lines. A gamma-ray spectrometer (GRS) is capable of determining hydrogen from lunar orbit by means of a neutron capture reaction which produces an excited state of deuterium with emission of a 2.223 MeV gamma ray (6). One hundred hours of gamma-ray data accumulation with a high resolution instrument will permit the detection of about 0.2% H<sub>2</sub>O by weight. The neutrons which cause the reaction are produced at high energies in the cosmic-ray cascade interaction and undergo sequential inelastic collisions, in the course of which their energy is reduced to epithermal and thermal levels. Hydrogen is the most sensitive element in modulating the slowing down process, so that a direct measurement of the thermal neutron flux, or better still, of both the thermal and epithermal neutron fluxes, will be indicative of the quantity of water present. Moreover, this will be true at depths up to about one meter, even if the water is buried beneath a dry layer sufficient to obscure the hydrogen gamma-ray line.

The passive neutron technique described below is particularly well suited for the type of small spacecraft mission which has recently been receiving attention. A more sensitive and elaborate system is under development for the Mars Observer GRS (7). The passive neutron detection technique employs one or two layers of neutron absorber material (8). In the latter case, an outer layer of Sm-149 absorbs virtually all of the thermal neutrons but is largely transparent to higher energy epithermal neutrons. The inner layer, containing B-10, absorbs about 40 percent of the epithermal neutrons. On capturing a neutron, Sm-149 emits a family of monoenergetic gamma rays, the most abundant of which has an energy of 334 keV. Boron-10, on capturing a neutron, briefly forms the unstable nucleus B-11\* which quickly breaks into He-4 and Li-7. The Li-7 emits a gamma ray at 477 keV. These gamma rays are partially absorbed by the germanium

detector, where their count rates may be interpreted in terms of the incident neutron fluxes. In this manner the GRS has also become a passive, two-channel neutron spectrometer.

A neutron detector simulation code has been created to account for the perturbations to the incident neutron flux caused by the detector itself. The neutron detector is assumed to consist of concentric cylinders, closed at one end for the absorbing layers, and the anticoincidence shield surrounding the Ge detector. The code follows incident neutrons through scattering, absorption, and escape processes. It tells the effects of each event at each energy level and follows those neutrons which lose energy through scattering. "Crosstalk", the absorption of epithermal neutrons by Sm-149 and of thermal neutrons by B-10, is also calculated. Gamma rays emitted by Sm-149, B-10, and H are adjusted for geometry, attenuation, and detector efficiency.

The end result of the simulation is a matrix which shows the gamma-ray count rate of 334 and 477 keV photons recorded by the Ge detector, including "crosstalk", for unit fluxes of incident thermal and epithermal neutrons. If the matrix is inverted, the inverse matrix can be used to interpret count rates in the 334 and 477 keV photopeaks in terms of thermal and epithermal neutron fluxes incident on the neutron detector. Figure 1 simulates the interaction of unit incident fluxes with the neutron detector when the anticoincidence shield is in place, figure 2 when the shield is removed. The plots are  $\log(\text{flux})$  vs  $\log(\text{energy})$ . Shown in the figures are the incident flux, thermal and epithermal absorption by Sm-149, thermal and epithermal absorption by B-10, the down-scattered flux, the total absorption by H in the detector system, and the escaping flux.

When the anticoincidence shield is in place, the simulation shows greater capture of neutrons by H as expected. However, the plot also shows a greater escape of neutrons in the energy interval  $10^{-3}$  to  $10^3$  ev, contrary to expectation. At energies greater than  $10^3$  ev, scattering due to more H appears to reduce the chance of escape, and the integrated escape rate is smaller. Thus the simulation serves to sharpen an understanding of the many interactive processes imposed by the neutron detector which perturb the signal expected from the incident flux. More importantly, the simulations provide the means by which gamma-ray signals of Sm and B can be used as measures of the incident thermal and epithermal fluxes under a variety of detector configurations.

Joint detection of neutrons and gamma rays turns out to be mutually complimentary. A knowledge of the neutron fluxes which give rise to gamma-ray emission from the lunar surface is needed to derive absolute concentrations from gamma-ray data. Conversely, without the knowledge provided by gamma-ray spectroscopy, small variations in the observed neutron flux due to hydrogen will not be distinguishable from those caused by other elements such as Fe and Ti. In the absence of a joint gamma-ray mode, the calculated sensitivity to  $\text{H}_2\text{O}$  using the neutron absorption technique described here is about eight times greater than by gamma-ray detection. With a joint gamma-ray mode which employs a high resolution Ge detector, the ratio rises to about 50. Such a system should allow the detection of  $\text{H}_2\text{O}$  at a concentration level of one percent with five hours of data accumulation,

given that this concentration exists in as little as three percent of the area above 75° latitude.

- 1) Watson, K., B.C. Murray, and H. Brown, 1961, *J. Geophys. Res.*, 66, 3033-3046.
- 2) Arnold, J.R., 1979, *J. Geophys. Res.*, 84, 5659-5668.
- 3) Hodges, R.R., Jr., 1980, *Proc. Lunar Planet. Sci. Conf.*, 11th, 2463-2477.
- 4) Lanzerotti, L.A., W.L. Brown, and R.E. Johnson, 1981, *J. Geophys. Res.*, 3949-3950.
- 5) Arnold, J.R., 1987, *Lunar and Planet. Sci. XVIII*, Lunar and Planetary Institute, Houston, Texas, 29-30.
- 6) Haines, E.L., and A.E. Metzger, 1984, *Nuc. Instr. Meth.*, 226, 509-16.
- 7) Feldman, W.C., and D.M. Drake, 1986, *Nucl. Instr. & Meth.*, A245, 182-190.
- 8) Haines, E.L., and A.E. Metzger, 1984, *Nuc. Instr. Meth.*; 226, 517-523.

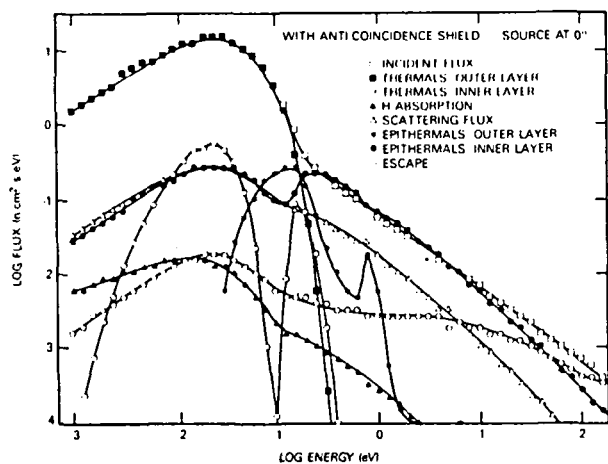


Figure 1

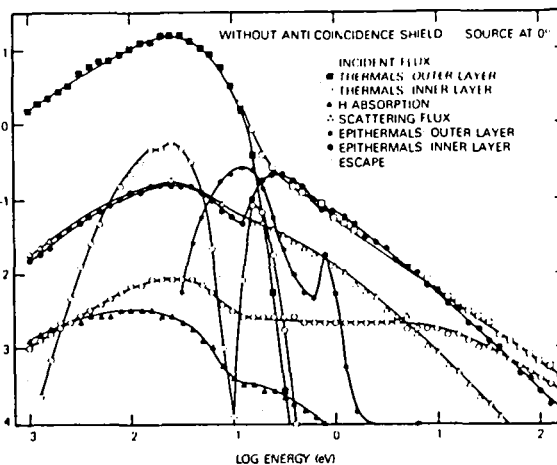


Figure 2

## RIMA HYGINUS AND VICINITY: PRELIMINARY REMOTE SENSING STUDIES

B.R. Hawke and C.R. Coombs, Planetary Geosciences Division, Hawaii Institute of Geophysics, University of Hawaii, Honolulu, HI 96822.

**INTRODUCTION:** The Rima Hyginus region contains numerous enigmatic deposits and features. The nature and origin of these are of high interest in lunar science. The Rima Hyginus region occupies a broad structural trough concentric to the Imbrium basin, which has played an important role in controlling the geology of the area. Hyginus crater (9 km in diameter) is located just south of Mare Vaporum at the juncture of the two branches of the Hyginus linear rille (Figure 1). The crater is characterized by the absence of a raised rim and numerous domical hills on the crater floor and is surrounded by a smooth, low-albedo unit of uncertain origin. The two linear rille branches trend northwest and east, respectively. These linear grabens are characterized by associated chains of low-rimmed craters of endogenic origin. Light plains deposits of the Cayley Formation dominate the surficial geology of the Rima Hyginus region. Portions of the Fra Mauro Formation and of a regional dark mantle deposit occur in the northern part of the region (see Pike, 1976<sup>1</sup>).

Several excellent geologic studies of the Rima Hyginus region have been conducted. The area was included in the geologic map of the Mare Vaporum Quadrangle made by Wilhelms (1968).<sup>3</sup> Schultz<sup>4</sup> conducted an intensive photogeologic analysis of Rima Hyginus using the Lunar Orbiter photography. Pike<sup>1</sup> produced a very detailed geologic map (scale = 1:250,000) for the Rima Hyginus region using Apollo, Lunar Orbiter, and Earth-based photography. The results of these studies provided answers to many important geologic questions. Still, many major problems remain unresolved. These include the following: 1) the nature and composition of the dark material around Hyginus crater, 2) the processes responsible for the formation of Hyginus crater, 3) the composition and origin of the Cayley plains in the region; and 4) the composition of the regional dark mantling material exposed in the northeastern portion of the Rima Hyginus region.

We addressed several of these questions using a variety of existing and new remote sensing data. The results of this effort are presented here.

**RESULTS AND DISCUSSION:** Both multispectral imagery<sup>5</sup> and color difference photography<sup>6</sup> exist for the Rima Hyginus region. Both the dark unit around Hyginus crater and the regional dark mantling deposit northeast of Hyginus exhibit high values on the 0.95/0.56  $\mu\text{m}$  multispectral ratio image. High 0.95/0.56  $\mu\text{m}$  values are generally attributed to shallow  $1\mu\text{m}$  bands and/or steep continuum slopes. These spectral characteristics have been found to be associated with regional pyroclastic deposits

elsewhere on the Moon.<sup>7,8,9</sup> Unfortunately, no 0.40/0.56  $\mu\text{m}$  images exist for this region. However, it is included in the color difference photograph presented by Whitaker.<sup>6</sup> Both the regional dark mantling deposit and dark unit surrounding Hyginus appear dark (high UV/VIS ratio values or "blue") in this image. While this spectral characteristic is consistent with a pyroclastic composition for the dark unit around Hyginus crater, it does not rule out a high- or medium-Ti mare basalt deposit. In fact, several apparent mare basalt ponds in the region also exhibit high UV/VIS values ("blue").

High-resolution 3.8-cm radar backscatter data has been presented for this region by Zisk and co-workers.<sup>2,9,10,11</sup> It was pointed out that the proposed Apollo landing site (just north of Hyginus crater) was located on a small area of low radar backscatter and hence apparently has a smooth, rock-free surface.<sup>2,10</sup> The area with low radar values correlates with the dark unit around Hyginus crater. The "blue" mare basalt ponds in the region do not exhibit low radar values. A pyroclastic origin for the dark unit surrounding Hyginus crater is suggested. It seems unlikely that this dark unit is a mare basalt deposit which was emplaced in a broad topographic low prior to the formation of the crater or rille as has been suggested.<sup>1</sup>

Zisk *et al.*<sup>2,10</sup> noted that the Rima Hyginus region exhibited numerous radar anomalies. Chief among these are the rille walls and their associated chains of endogenic craters. Shorthill<sup>2,12</sup> reported high thermal values associated with the rille and crater chains. These observations suggest the presence of immature surfaces with a relatively high abundance of rocks. The 3.8-cm radar images do not show low radar returns from the deposits around the endogenic crater chains. This observation, plus the absence of albedo and spectral anomalies associated the units around these crater chains, indicate that these endogenic features are not volcanic vents. The subsidence or collapse model proposed by Pike<sup>1</sup> for the origin of these craters is supported.

Radar and spectral data for the regional dark mantling deposit north and northeast of Rima Hyginus were presented by Pieters *et al.*<sup>9</sup> The received depolarized radar signal level for most of this unit was nearly zero. An unusually rock-free surface was indicated. The spectrum (0.3 - 1.1  $\mu\text{m}$ ) obtained for the deposits exhibited the same distinctive spectral characteristics as other dark mantling deposits for which spectra were available; i.e., they are very "blue" in the visible region and relatively bright in the near-infrared. These workers<sup>9</sup> and others<sup>e.g., 7,13</sup> have interpreted this unit to be a rock-free pyroclastic deposit composed of glass-rich basaltic debris. We have recently obtained new near-infrared spectra (0.6-2.5  $\mu\text{m}$ ) for several areas within this unit. Preliminary analyses of this data have yielded spectral parameters consistent with the above interpretation.

McCord *et al.*<sup>14</sup> presented five spectra (0.3-1.1 $\mu\text{m}$ ) for the Rima Hyginus region. The spectra obtained for the dark unit around Hyginus crater exhibit relatively high reflectivity in the ultraviolet and the near-infrared. These are the same spectral

characteristics that are exhibited by lunar dark mantle deposits of probable pyroclastic origin. A similar origin is implied for the dark unit surrounding Hyginus crater. This pyroclastic interpretation is supported by a near-infrared spectrum that we obtained in October, 1984 for this dark unit. Additional near-infrared spectra were recently collected for geologic units in the region. Analysis and interpretation of these new spectral should provide further insight concerning the composition and origin of these units.

**REFERENCES:** 1) Pike, R.J., *USGS Map I-945*, 1976; 2) Lunar Landing Site Summary Book, Manned Spacecraft Center, Houston, VIII 1-18, 1970; 3) Wilhelms, D.E., *USGS Map I-548*, 1968; 4) Schultz, P.H., *Moon Morphology*, Univ. of Texas Press, 1976; 5) McCord, T.B. et al., *Icarus*, 29, 1-34, 1976; 6) Whitaker, E., Personal Comm., 1976; 7) Gaddis, L.R. et al., *Icarus*, 61, 461-489, 1985; 8) Hawke, B.R. et al., *PLPSC 10th*, 2995-3015, 1979; 9) Pieters, C.M., et al., *J. Geophys. Res.*, 78, 5867-5875, 1973; 10) Zisk, S.H. and Hagfors, T., *Radar Atlas of the Moon*, Lincoln Lab., MIT, Lexington, 1970; 11) Zisk, S.H., et al., *Moon*, 10, 17-50, 1974; 12) Shorthill, R.W., *Brief Description of Apollo Landing Sites in Terms of Earth-Based Infrared Observations*, Boeing, Technical Note 016, 1970; 13) Head, J.W., *PLSC 5th*, 207-222, 1974; 14) McCord, T.B. et al., *Moon*, 5, 52-89, 1972.

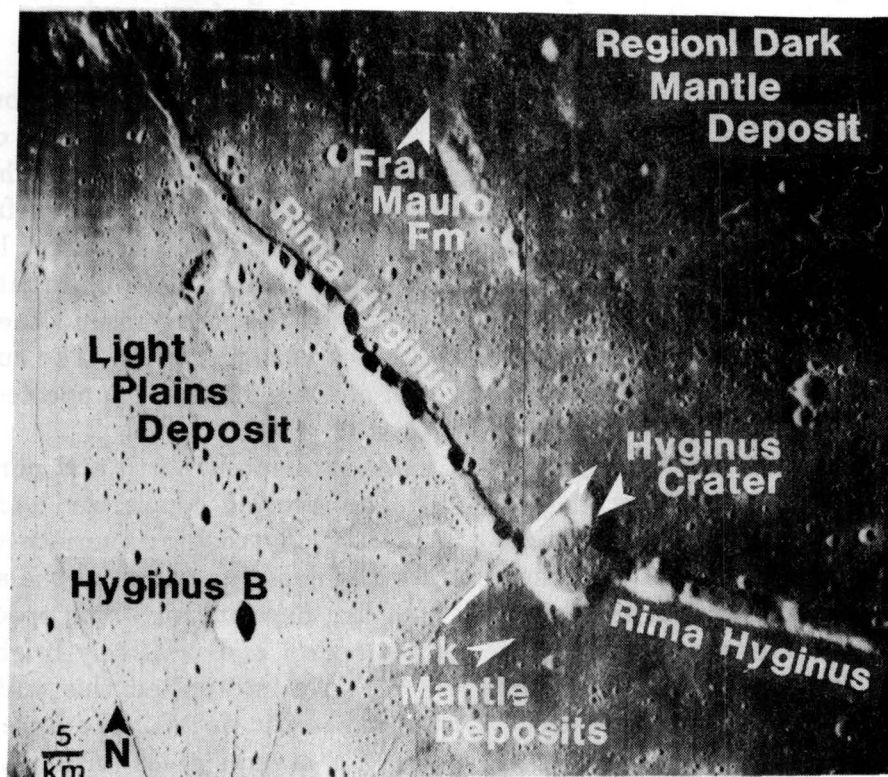


Figure 1: Oblique view of Rima Hyginus showing Hyginus Crater and both segments of Hyginus rille. (Orbiter III-073-M).



STRATIGRAPHY AND EVOLUTION OF THE LUNAR HIGHLAND CRUST: A  
SAMPLING OF VERTICAL AND REGIONAL HETEROGENEITIES C. M. Pieters,  
Geological Sciences, Brown University, Providence, RI 02912

The Apollo and Luna programs have gradually provided lunar scientists, after extended and meticulous analysis, with a sufficient variety of samples to suspect the evolution of the lunar crust is considerably more complex than the simple differentiation of a magma ocean proposed during the first blush of Apollo exploration (1). The chemistry and mineralogy of the select small group of pristine rocks (2), which escaped much of the transformations incurred during the high impact flux of early lunar history, indicate that the evolution of the lunar crust is likely to have involved several differentiation events separated either spatially or temporally. Discussed below are remotely acquired new mineralogical data for unsampled lunar regions, that begin to document the heterogenities of the lunar crust and provide tantalizing evidence for a very varied lunar crustal evolution. The full lunar coverage and high spatial resolution of the LGO mapping spectrometer (VIMS) will provide a more complete assessment of lunar mineralogy and distribution of crustal rock types required for crustal evolution models.

Near-infrared reflectance spectroscopy is particularly sensitive to the mafic mineral composition and content of surface material. Spectra of pyroxenes exhibit paired absorption bands (3): the first band for low-Ca orthopyroxenes occurs at 0.90 - 0.93  $\mu\text{m}$  and for high-Ca clinopyroxenes at 0.96-0.99  $\mu\text{m}$ . Olivines exhibit a distinct broad multiple band centered beyond 1.0  $\mu\text{m}$ . Assessment of mineral abundance from reflectance spectra requires modeling of known or suspected components in a multicomponent system (e.g. 4). For lunar highland materials, noritic compositions are easily distinguished from gabbroic by identification of the dominant type of pyroxene composition present and its abundance, troctolites and dunites are distinguished by identification of abundant olivine, and anorthosites by the absence of significant amounts of mafic minerals. Each of these compositions has been detected at different lunar locations using telescopic near-infrared reflectance spectra (see review in 5). Although current data are limited and only include nearside regions, the composition of the megaregolith has been shown to be dominated by a variety of anorthositic norites, while deeper crustal material (from 5-10 km depth and exposed in the central peaks of large craters) exhibit a much wider range of rock types including gabbros, norites, troctolites and anorthosites (5).

With spectroscopic measurements of sufficient spatial resolution on the surface (earth-based telescopes currently obtain spectra for areas 3-5 km in diameter), the stratigraphy of the crust can be studied at individual regions using an understanding of the systematic excavation and deposition of material from depth during a major impact event. By analyzing the composition of surface material in a spatial context around a crater, the local stratigraphy can thus be reconstructed. Briefly, the deepest material forms the central peaks; material from higher stratigraphic zones is deposited on the rim or forms the walls.

Presented in Figures 1a - 1h are residual reflectance spectra (after removal of a continuum estimated as a straight line) for a few small areas associated with several large impact craters on the nearside. Based on the nature and positions of observed absorption features, the following inferences can be made about the general composition of the upper and lower stratigraphic zones for the first ~10 km at each site (upper/lower): Copernicus -- noritic/troctolitic; Eratosthenes -- noritic/gabbroic; Lansberg -- noritic/noritic; Bullialdus -- gabbroic/noritic; Tycho -- gabbroic/gabbroic; Arzachel -- noritic/noritic; Theophilus -- noritic/anorthositic; Aristarchus (6) -- (gabbroic + troctolitic)/gabbroic.

*Discussion:* Unlike the megaregolith composition, only three of these craters exhibit noritic compositions at depth, emphasizing the heterogeneity of crustal materials below the megaregolith. In addition, more than half exhibit varying compositions with depth. Although subsurface cumulates of a given composition must be several tens of kilometers in extent (in order to form the large central peak mountains of distinct mineralogy), compositional stratigraphy or zoning is clearly not uniform across the nearside. For example, Copernicus, Eratosthenes and Lansberg, separated by only a few hundred kilometers, each exhibit a noritic upper crustal composition but have distinctly different lower stratigraphic compositions (troctolitic, gabbroic, and noritic, respectively). Each of these eight craters display a different compositional

LUNAR CRUST  
Pieters, C.M.

stratigraphy and rich geologic history. Major advances in our understanding of the lunar crust and its evolution are anticipated as more detailed information on surface composition becomes available from remote measurements and is analyzed in terms of regional geology and crater history. Lunar evolution, often considered an end-member in planetary science studies, is not likely to remain as simple as originally envisioned from the first phase of lunar exploration.

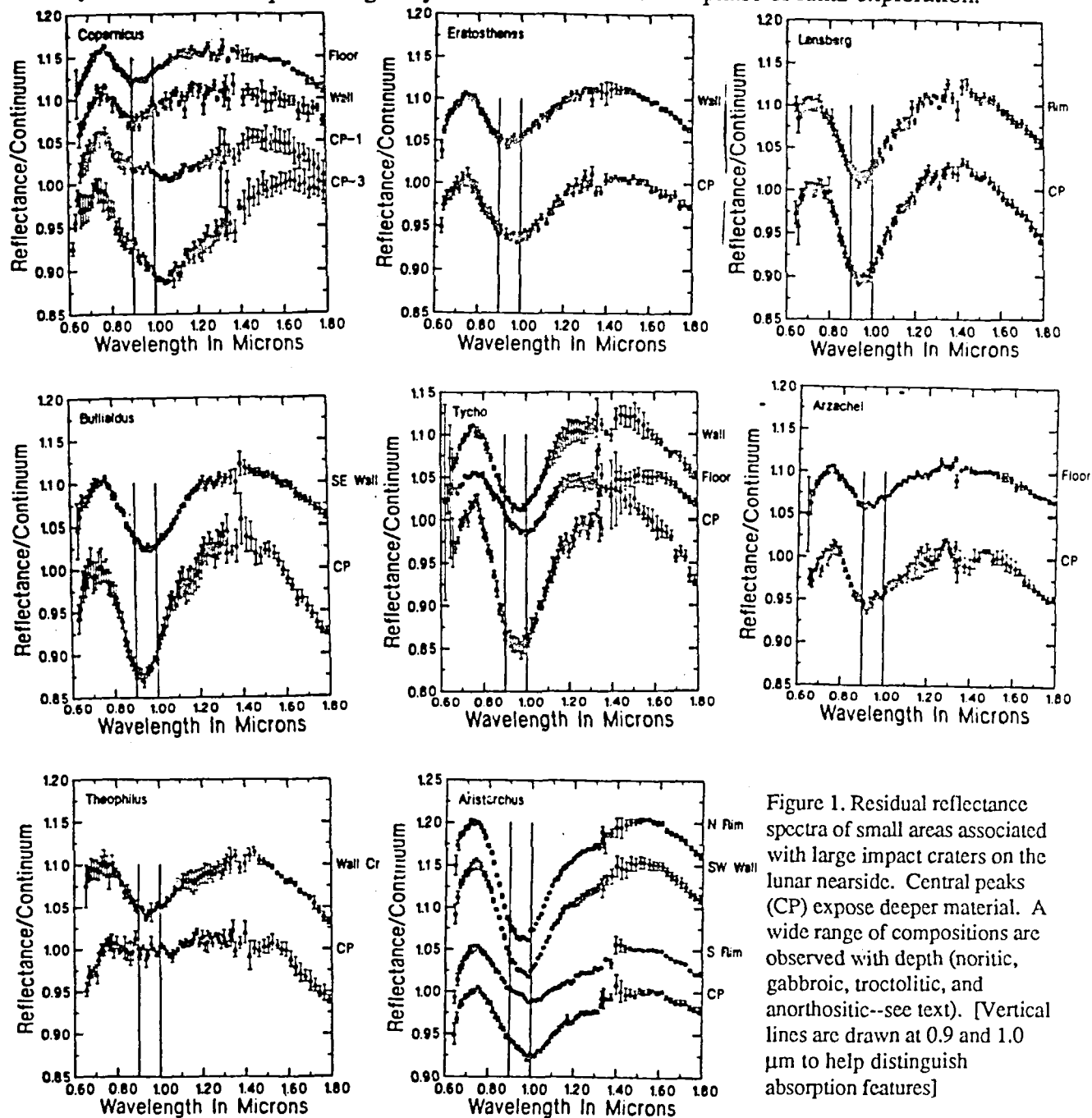


Figure 1. Residual reflectance spectra of small areas associated with large impact craters on the lunar nearside. Central peaks (CP) expose deeper material. A wide range of compositions are observed with depth (noritic, gabbroic, troctolitic, and anorthositic--see text). [Vertical lines are drawn at 0.9 and 1.0  $\mu\text{m}$  to help distinguish absorption features]

References: (1) Walker, 1983 *Proc. LPSC 14*, B17-B25; Warren, 1985, *An Rev. Earth & Plan. Sci.* 13, 201-240. (2) Warren and Wasson, 1977, *Proc. LPSC 8th*, 2215-2235; Warren and Wasson, 1980, *Proc. Conf. Lunar High. Crust*, 81-99; James, 1980 *Proc. LPSC 11th*, 365-393. (3) Adams, 1974 *JGR*, 79, 4829-4836. (4) Mustard and Pieters, 1987, *Proc. LPSC 17*. (5) Pieters, 1986, *Rev. Geophys.*, 24, No2, 557-578. (6) Lucey et al., 1986, *Proc. LPSC 16th*, *JGR*, 91, D344-354.

CHAPTER 6  
RADAR APPLICATIONS



## GOLDSTONE RADAR OBSERVATIONS OF MARS: 1986 RESULTS

T. W. Thompson, Jet Propulsion Laboratory  
California Institute of Technology  
Pasadena, CA 91109

Radar echoes from the planet Mars were obtained on 22 S-band (wavelength = 12.5 cm) and 2 X-band (wavelength = 3.5 cm) tracks using the Goldstone Solar System Radar. These observations took advantage of the favorable 1986 opposition since the earth-Mars distance was 0.40 AU at opposition (the smallest earth-Mars distance since the 1971 and 1973 oppositions) and radar echo strength is proportional to inverse-fourth-power to the distance to the target. Another equally favorable opposition occurs in 1988; these favorable geometries do not reoccur until the next century.

The observations were conducted via the cw-spectra techniques described by Harmon et al. (1982 and 1985). A continuous tone was transmitted at Mars and the radar echo was sampled to obtain a Doppler-spread spectrum. Each received event was separated into polarized (opposite sense circular, OC) and depolarized (same sense circular, SC) periods. Also, a minute or two of noise was recorded in each transmit-receiver cycle. The total echo time was the round-trip travel-time which was varied from about seven minutes near opposition to over twelve minutes for last runs in October. Coverage on Mars started at 8° S, travelled toward the equator to 3° S during August, and then migrated south to 14° S for the last run in October.

The results of these observations in terms of total echo powers are shown in Figure 1. Echo strengths are shown as radar cross-sections normalized to the geometric cross-section of the disk. These are plotted versus longitude where the left hand panels of Figure 1 shows the 240 S-band (12.5 cm wavelength) observations from 1986 while the right panels shows arecibo S-band (12.6 cm) results for 20°-25° north reported by Harmon et al. (1982 and 1985) as well as the results from the Goldstone X-band (3.5 cm wavelength) observations in 1986. The bottom panels show  $\mu$ , the ratio of depolarized (SC) to polarized (OC) cross-sections plotted versus longitude.

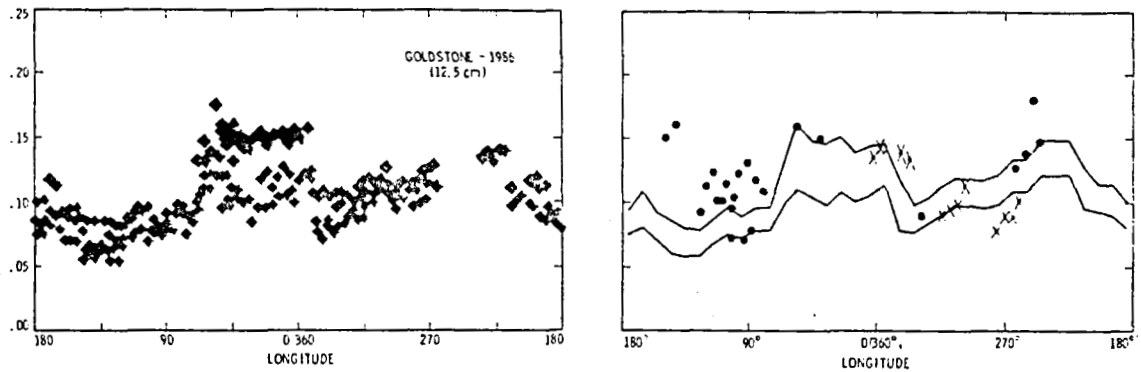
The data in Figure 1 shows that the three types of data agree with each other. Furthermore, the depolarized (OC) echoes are relatively strong when the subradar longitude is between 90° and 180° and the Tharsis region is in view (as shown by Harmon et al., 1985). Also, there are relatively strong polarized and depolarized echoes for longitudes of 0° to 90° when the subradar point was near the Vallis Marineris.

### References

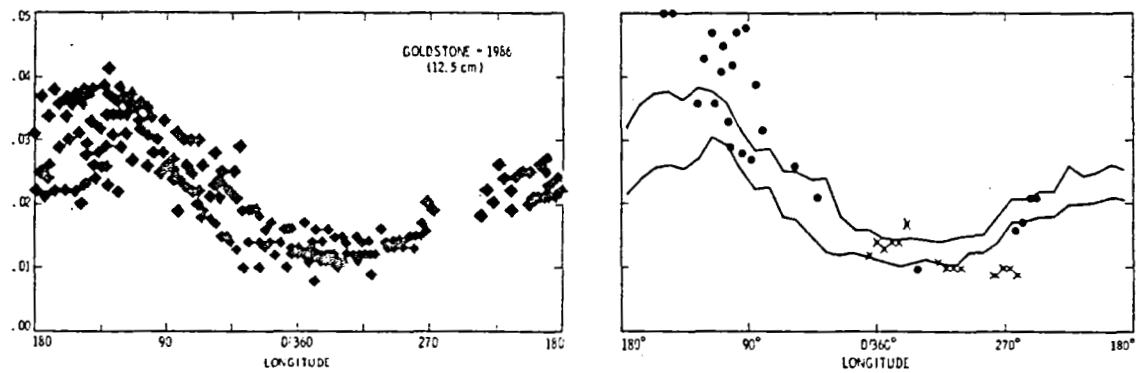
- J. K. Harmon, D. B. Campbell, and S. J. Ostro (1982), Dual-Polarization Radar Observations of Mars: Tharsis and Environs, Icarus, 52, 171-187.  
J. K. Harmon and S. J. Ostro (1985), Mars: Dual-Polarization Radar Observations with Extended Coverage, Icarus, 62, 110-128.

GOLDSTONE RADAR OBSERVATIONS OF MARS  
T. W. Thompson

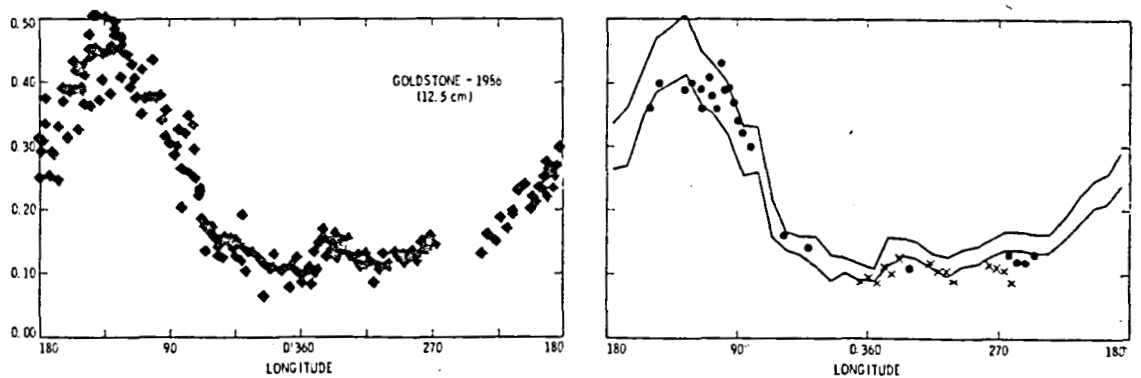
POLARIZED (OC) RADAR CROSS-SECTIONS vs. LONGITUDE



DEPOLARIZED (SC) RADAR CROSS-SECTIONS vs. LONGITUDE



$$\mu = \left( \frac{\text{DEPOLARIZED (SC) RADAR CROSS-SECTIONS}}{\text{POLARIZED (OC) RADAR CROSS-SECTIONS}} \right) \text{ vs. LONGITUDE}$$



◆ = GOLDSTONE - 1986 (12.5 cm)      X = GOLDSTONE - 1986 (3.5 cm)      ● = ARECIBO - 1980-1982 (12.6 cm)

Figure 1: 1986 Goldstone Radar Observations of Mars: Plots of Radar Cross-sections Versus Longitude

ULTRA-HIGH RESOLUTION RADAR MAPPING OF THE MOON AT 70 CM WAVELENGTH  
Thomas W. Thompson, Jet Propulsion Laboratory  
California Institute of Technology  
Pasadena, CA 91109

There have been three recent successful attempts to acquire radar images of the Moon with the best possible resolution. Don Campbell and his colleagues at the Arecibo Observatory have produced a radar images of several areas with about 125 m radar cell-size at 12.5 cm wavelength. Stan Zisk and his colleagues at the Haystack Observatory have produced radar images of the Apollo landing sites with about 100 m radar cell-size at 3 cm wavelength. This abstract describes observations at 70 cm wavelength using the high-power pulse 430 Mhz radar at the Arecibo Observatory. These have the potential of about 500 m radar cell-size.

There were three observations in July 1986 followed by six observations in May 1987. The first four observations were conducted by transmitting from and receiving echoes with the main 330 m diameter antenna. This yielded polarized (opposite sense circular, OC) data with high signal-to-noise ratios. The last five observations were conducted by transmitting from the main antenna and receiving echoes at a smaller, 100-meter antenna. This yielded both polarized and depolarized (same sense circular, SC) data with lower signal-to-noise ratios. Radar parameters for these observations are given in the tables. These observations have been analyzed yielding delay Doppler spectra. The conversion of the spectra to maps of normalized powers versus latitude and longitude will be done in the next few months.

To obtain the best possible range resolution, the transmitter pulse was shortened to 2, 4, or 6 microseconds yielding edge-on resolutions of 0.3, 0.6 and 0.9 km. Surface resolutions in the tables are at beam center, accounting for projection effects. To obtain the equivalent resolution in the spectra analysis, some 4096 consecutive pulses were integrated. The total integration time was 409.6 seconds (6.83 minutes) yielding a bandwidth of only 0.0024 hz which was about 0.0001 times the total limb-to-limb Doppler spread across the moon. The equivalent edge-on resolution was 0.6 km. Some sites were close to the "apparent Doppler meridian" so the resolution on the surface was near 0.1 km. (The other lunar radar mapping attempts at 3.0 and 12.5 cm wavelengths have a distinct advantage since their limb-to-limb Doppler spreads were large and better surface resolution can be obtained with less integration).

In summary, these preliminary, exploratory observations have shown that the high power 430 MHz (70 cm wavelength) radar at the Arecibo Observatory can produce lunar radar maps with 0.5 km cell sizes. The next observations may yield even better resolution using new equipment being installed at Arecibo and longer integration times. It should be possible to integrate 8192 consecutive pulses yielding Doppler resolutions one half those mentioned here.

ULTRA-HIGH RESOLUTION RADAR MAPPING OF THE MOON  
T. W. Thompson

Table 1. Lunar Radar Observations\* - July 1986

Date	01 Jul 86	02 Jul 86	03 Jul 86
Beam Center	Copernicus	Apollo-15	Delisle
Beam Center Latitude	9-30 N	26-06 N	29-50 N
Beam Center Longitude	20-00 W	3-39 E	35-30 W
Delay Resolution	2 micros.	2 micros.	4 micros.
Beam Center Resolution	0.7 km	0.6 km	0.8 km
Frequency Resolution	0.0024 hz	0.0024 hz	0.0024 hz
Limb-Limb Doppler Spread	13.8 hz	14.6 hz	13.4 hz
Beam Center Resolution	0.6 km	0.6 km	0.8 km

Table 2. Lunar Radar Observations\* - May 1987 - 1

Date	23 May 87	29 May 87	29 May 87
Beam Center	Copernicus	Apollo-15	Plato
Beam Center Latitude	12-00N	24-00N	51-00N
Beam Center Longitude	21-00W	00-00	9-00W
Delay Resolution	2 micros.	4 micros.	4 micros.
Beam Center Resolution	0.6 km	1.2 km	0.7 km
Frequency Resolution	0.0024 hz	0.0024 hz	0.0024 hz
Limb-Limb Doppler Spread	12.9 hz	12.9 hz	12.9 hz
Beam Center Resolution	0.6 km	0.6 km	0.6 km

Table 3. Lunar Radar Observations\* - May 1987 - 2

Date	30 May 87	30 May 87	30 May 87
Beam Center	Aristarchus	Apollo-17	Tycho
Beam Center Latitude	24-00N	20-00N	43-00S
Beam Center Longitude	48-00W	31-00E	11-00W
Delay Resolution	4 micros.	4 micros.	4 micros.
Beam Center Resolution	0.7 km	0.9 km	1.0 km
Frequency Resolution	0.0024 hz	0.0024 hz	0.0024 hz
Limb-Limb Doppler Spread	13.0 hz	13.1 hz	12.8 hz
Beam Center Resolution	1.0 km	0.8 km	0.6 km

\*Transmitter Frequency = 430 Mhz;  
Radar Wavelength = 70 cm  
Antenna Beamwidth = 9 arc-min



# RADAR ALTIMETRY OF THE MARTIAN CRATERED HIGHLANDS

L. E. Roth, Jet Propulsion Laboratory, California Institute of Technology, Pasadena, California 91109.

A detailed, point-by-point examination of radar altimetric data collected by the Goldstone Solar System Radar during the Martian oppositions of 1971, 1973, 1975, 1978, and 1980 (1) (Table 1) has been completed. The data provide a solid evidence of detection of topographic features on Mars by observers on Earth. Echoes from over 150 craters ranging from 25 km to 475 km in diameter can be recognized in the data. Limited morphometry was performed on 102 craters. Of those, 87 were scanned during the 1971/1973 oppositions, the remaining 15 during the 1975-1980 oppositions. Range-doppler data taken during the 1982 and 1986 oppositions have not been processed, and due to funding limitations are not likely to be processed in the near future. Thus, the presently available radar morphometry of Martian craters is not expected soon to be augmented by new data.

Opposition	Lat (deg)	Dist (AU)	Ls (deg)	# scans
1971	-14.107 to -18.310	0.376 to 0.580	200.94 to 271.53	36
1973	-14.807 to -22.169	0.436 to 0.834	241.78 to 324.12	32
1975	~0.29 to ~4.34		324.68 to 48.97	7
1978	9.438 to 12.195	0.655 to 0.934	37.35 to 59.97	14
1980	20.981 to 23.157	0.677 to 0.925	48.97 to 72.64	13
1982	~20 to ~23		~70 to ~110	<10
1984		No Observations		
1986	~5			1

Table 1. Goldstone altimetry of Mars. Latitudes on and distances to the planet: JPL Ephemeris SE-118. A full program of range-doppler observations of Mars (one observation every 3 to 6 days, for a period of about four months) was last carried out during the perihelic oppositions 1971/1973.

The results of our analysis suggest that, at the 100-m range resolution, the rims of large craters are barely distinguishable against the surrounding terrain. While on the moon topographic expression of a crater may extend to distances of at least one crater radius from the rimcrest (2), the topographic expression of craters in the Goldstone sample rarely extends beyond the immediate vicinity of the crater cavity. Thus the low or non-existent exterior relief appears to constitute the general characteristic of large martian craters. The often-noted shallowness (3,4) of these craters is perhaps not so pervasive since even some rimless structures (e.g., basin Ladon) have preserved relatively deep depressions. Low rims in small Martian craters may be genetically related to an impact into a volatile-rich upper crust (5).

Excavation of large craters into a volatile-poor lower crust should not result in anomalously low rims. An advanced stage of structural adjustment of large craters would presumably be accompanied by the simultaneous loss of much or all of both the interior and the exterior relief (6,7). Because it is mostly the exterior relief that has been lost, while the interior relief, although reduced, has been largely retained, neither the rapid post-impact rebound nor the protracted relaxation are the likely principal contributors to the present rimless appearance of the large martian craters. Eolian-erosion induced disappearance of the competent exterior relief appears to be improbable (8,9). Likewise, fluvial erosion is an unlikely agent of the exterior relief suppression (10). Thus, while Martian craters were certainly subjected to the action of all the commonly considered modification processes, the emergence of a rimless, flat-floored crater is probably related to a specific class of events, associated with the intermittent plains-resurfacing episode/episodes (11,12). A scenario in which pre-plains, late heavy bombardment-related large crater degradation is followed by post-plains degradation quiescence (13) apparently has to include an intermediate, co-plains, degradation-intense stage (12), nonuniform with respect to space and perhaps also time, and involving extensive volcanic resurfacing. If the relatively well-preserved exterior relief of basin Huygens is viewed as a marker, then intercrater-plains deposits to an average depth of perhaps as much as 1 km can be inferred. These conclusions, considered tentative, underscore the need for a reliable topographic information when attempting to reconstruct the geologic history of terrestrial planets.

Apart from its intrinsic geologic interest, the detailed analysis of the Goldstone Mars altimetry served also another purpose, viz. to determine the reproducibility of radar altimetry. It was found that the Goldstone data are reproducible for targets that are at least 10 resolution cells wide. This sets a lower limit of about 80 km on the diameters of scanned craters, if the data are to be used for quantitative studies. It remains to be seen whether this result is valid also for radar altimeters with a circular footprint.

References: (1) Downs, G. S. et al. (1975) *Icarus* 26, 273; (1978) *Icarus* 33, 441. (2) Settle, M. and Head, J. W. (1977) *Icarus* 31, 123. (3) Murray, B. C., Soderblom, L. A., Sharp, R. P. and Cutts, J. A. (1971) *J. Geophys. Res.* 76, 313. (4) Pike, R. J. (1971) *Icarus* 15, 384. (5) Cintala, M. J. and Mouginiis-Mark, P. J. (1980) *Geophys. Res. Lett.* 7, 329. (6) Ramberg, H. (1963) *Bull. Geol. Inst. Uppsala* 42, 1. (7) Danes, Z. (1965) *Astrogeol. Stud. Ann. Prog. Rep.* (8) Arvidson, R. E. (1986) *Lunar Planet. Sci.* XVII, 17. (9) Aubele, J. C. and Crumpler, L. S. (1987) *Lunar Planet. Sci.* XVIII, 36. (10) Baker, V. R. and Milton, D. J. (1974) *Icarus* 23, 27. (11) Chapman, C. R. (1974) *Icarus* 22, 272. (12) Chapman, C. R. and Jones, K. L. (1977) *Ann. Rev. Earth Planet. Sci.* 5, 515. (13) Malin, M. C. and Dzurisin, D. (1977) *J. Geophys. Res.* 82, 376.

## DEVELOPMENT OF A TECHNIQUE TO SIMULATE THE ABILITY OF MAGELLAN'S SAR TO DISCRIMINATE VOLCANIC UNITS

S.D. Wall, E.Theilig\*, and R.S. Saunders, Jet Propulsion Laboratory, California Institute of Technology, Pasadena, CA.  
\*National Research Council (at JPL)

Morphological and geochemical evidence indicate that basaltic volcanism has been an important process on Venus [1-5]. Understanding the distribution of volcanic features, their eruptive styles, and emplacement mechanisms will provide information on the thermal evolution of the planet. The Magellan Mission to Venus will use a synthetic aperture radar (SAR,  $\lambda = 12.6\text{cm}$ ) to map at least 80% of the planet. To maximize the quality of SAR data returned by Magellan, look angle (and thus the incidence angle at the surface) will be varied ( $14$  to  $50^\circ$ ) in a controlled way with latitude. Because radar backscatter is dependent partly on incidence angle, this variation could influence the ability to discriminate volcanic units at different latitudes. A technique is being developed to investigate the ability of radar to discriminate lava flows at look angles to be used by Magellan and to determine the optimum angles for identifying different flow textures.

Pisgah lava field, California, was selected for initial study because calibrated radar data at a range of incidence angles are available and three flow units with different textures are present [6,7]. The lava field consists of flows from three eruptive phases. Phases 1 and 3 produced lava flows with a predominantly pahoehoe surface texture; whereas, Phase 2 lavas developed more of an aa texture. However, surface texture across the field is actually a mixture of aa and pahoehoe with the relative percentage of each varying. A meso-scale texture is also present in the form of tumuli and pressure ridges within all three units. Flow margins, particularly on the west, have been modified by aeolian and alluvial deposits and form an additional texture unit.

Calibrated radar backscatter coefficients were acquired in a linear track across the flow by the NASA/Johnson Space Center scatterometer. For the preliminary study we used the L-band ( $\lambda = 19\text{ cm}$ ), horizontal transmit and receive polarization data to approximate the Magellan SAR and remain comparable to existing spaceborne SAR systems. Data were acquired at incidence angles of  $5$  to  $50^\circ$  and time-sorted into five degree bins. Pahoehoe, aa, and mantled pahoehoe units were identified on the scatterometer data using geologic maps and aerial photographs. Representative backscatter coefficients were obtained by averaging the return values across one area of each unit. Backscatter curves produced from the average backscatter coefficients versus incidence angle indicate that the separation between backscatter from the flow units is not statistically significant although the return from the mantled surface tends to be lower. The lack of separation in the backscatter curves may result from the mixture of surface textures across the flow.

Although the Phase 2 lavas are predominantly aa, they contain large areas of pahoehoe.

A linear discriminant analysis program [8,9] is used to statistically determine the best incidence angle for discriminating the units on the Pisgah lava field. The texture units identified on the scatterometer data provide training data sets for the program. The ability to separate the data sets are analyzed by a sequential addition of variables which, in this case, are the different incidence angles. Classification functions are developed in steps by adding the most useful angle for discriminating among the training areas. Additional angles are added until none remain or there is not statistical basis for adding more. At each step the initial data are compared to the computed group classification functions and the accuracy of the classification assessed.

Plots of the percent correctly classified versus incidence angle can be used to evaluate the optimum angles for separating the flow units. For Pisgah the best discrimination of the surface texture units was obtained at 25, 35, 40, and 45° incidence angle. The difficulty in separating the units below 35° may be a function of the similarity in meso-scale surface texture. Tumuli and pressure ridges form local slopes commonly equal to or less than 30° which may result in the addition of quasispecular reflection to the returned signal. In this case, the amount of backscatter may be dependent partly on the size, distribution, and orientation of the ridges.

Because of the absence of definitive surface textures and the influence of the meso-scale texture at Pisgah, this study needs to be extended to an area with a greater variety of basaltic surface textures. Future application of this technique will be made on a part of the Craters of the Moon lava field, Idaho. This area is crossed by four scatterometer tracks and includes several flows of different surface textures and ages. C-band ( $\lambda = 6.3$  cm) scatterometer data will be used in conjunction with the L-band to bracket the wavelength to be used by Magellan.

#### REFERENCES

- [1] Saunders, R.S., and M.C. Malin, 1977, Geophys. Res. Lett. 4: 547-550.
- [2] Barsukov, V.L., A.T. Basilevsky, R.O. Kuzmin, et al., 1984, Geokhimiya 12: 1811-1820.
- [3] Barsukov, V.L., A.T. Basilevsky, B.A. Burba, et al., 1986, Proc. Lunar Planet. Sci. Conf., 16th, J. Geophys. Res. 91: D378-D398.
- [4] Surkov, Yu.A., L.P. Moskalyeva, O.P. Shcheglov, et al., 1983, Proc. Lunar Planet. Sci. Conf. 13th, Part 2, J. Geophys. Res. 89: B393-B402.
- [5] Surkov, Yu.A., F.F. Kirnozov, V.N. Glozov, et al., 1987, Proc. Lunar Planet. Sci. Conf. 17th, Part 2, J. Geophys. Res. 92: E537-E540.
- [6] Wise, W.S., 1966. Technical Letter NASA - 11. 8 pp.
- [7] Farr, T.G., and N.E. Engheta, 1983, Proc. Intl. Geosci. and

- Remote Sensing Symp. pp. 2.1-2.6.
- [8] Dixon, W.J., (Ed.), 1970, BMD Biomedical Computer Programs.  
Berkeley, CA: Univ. Calif. Press.
- [9] Blom, R.G., L.R. Schenck, and R.E. Alley, 1987, IEEE Trans.  
Geosci. and Remote Sensing GE-25: 208-213.

# INVESTIGATIONS OF THE RELATIONSHIP BETWEEN RADAR BACKSCATTER AND AEOLIAN ROUGHNESS CHARACTERISTICS OF DESERT SURFACES - A PRELIMINARY REPORT

*R. Greeley, N. Lancaster, R. Sullivan, Department of Geology, Arizona State University, Tempe, Arizona 85287; R.S. Saunders, E. Theilig, S. Wall, Jet Propulsion Laboratory, 4800 Oak Grove Drive, Pasadena, California 91109; A. Dobrovolskis, NASA Ames Research Center, Moffett Field, California 94035; B.R. White, Department of Mechanical Engineering, University of California at Davis, Davis, California 95616; J.D. Iversen, Department of Aerospace Engineering, Iowa State University, Ames, Iowa 50010*

The ability of the wind to initiate particle movement and the flux of windblown particles as a function of average wind velocity at a given height are strongly dependent on the roughness of the surface [1,2], as measured by the aeolian roughness ( $z_0$ ). This is a function of the size and spacing of roughness elements on the surface [3,4]. For a given radar system, the radar backscatter of a surface is dependent on: (i) the roughness of the surface at the scale of the radar wavelength, (ii) the local incidence angle between the surface normal and the incoming microwave radiation, and (iii) the complex dielectric constant of the surface. For surfaces without major relief features, and with similar electro-magnetic properties, the first effect dominates, and the radar backscatter can be regarded as a measure of the surface roughness at or near the wavelength scale [5,6]. Radar backscatter data may therefore be useful in obtaining an aeolian roughness parameter which can be used to assess aeolian sediment transport on a regional scale. The objective of the research documented here is to establish an empirical relationship between aeolian roughness and radar roughness, which will permit the analysis of aeolian sediment transport potential on Venus using radar data from the Magellan mission.

Calibrated LHH, CHH and KuVv data acquired by the NASA/Johnson Space Center scatterometer experiment in 1979 were used to derive characteristic backscattering coefficients ( $\sigma_0$ ) for three lava flow units (aa, pahoehoe, and pahoehoe mantled with aeolian sand and silt), together with adjacent alluvial fan and playa surfaces at Pisgah Lava Field, California. L- and C-band data bracket the radar wavelengths to be used on the Magellan mission. The units were identified on a plot of against time along track using the geological map of Wise [7] and the aerial photographs acquired simultaneously with the radar data. Backscattering coefficients were then averaged across an area of each geomorphic unit to obtain a representative backscatter coefficient for each incidence angle. Backscattering coefficients increase with an increase in surface roughness from the playa surface to the aa lava flow. Differences between the lava flow surfaces are not statistically significant, but the mantled pahoehoe tends to have a lower radar return. Backscatter coefficients for all the lava flow units are higher in the L- and Ku-bands compared to C-band. On the basis of Bragg scattering theory, this suggests an overall surface composed dominantly of blocks larger than 15 cm, with a small-scale roughness of less than 2 cm. This is confirmed by our field observations. Alluvial fans are intermediate in roughness and radar backscatter coefficients, whereas the playa exhibits the lowest backscatter coefficients.

The objective of the wind measurements undertaken was to derive characteristic values of wind friction speed ( $u_*$ ), aeolian roughness ( $z_0$ ), and zero plane displacement ( $D$ ) for each surface. Wind data were reduced following the methods employed by Greeley and Iversen [7], using an iterative procedure to calculate  $u_*$ ,  $z_0$  and  $D$  from the wind profile data. Profiles were measured on the three lava flow surfaces at Pisgah using 8 or 15 m towers, instrumented with 8 or 10 cup-anemometers respectively. Data for an alluvial fan surface were taken from experiments conducted at Amboy lava flow [8] and playa data from an experiment conducted by Sullivan [9]. Mean values of  $z_0$ ,  $D$ , and  $u_*$  for each site are given in Table 1.

There is an increase in  $z_0$  values from the playa at Lucerne Dry Lake, through the alluvial fan surface at Amboy, to the lava flows at Pisgah. The friction speed ratio,  $u^*/U$  (6.9 m) shows a parallel increase from the playa to the roughest lava flow surface. There is a strong correlation between the friction speed ratio and  $z_0$  which indicates that, for a constant wind velocity, friction speed increases with  $z_0$  and therefore with surface roughness.

Figure 1 shows the relationship between aeolian roughness ( $z_0$ ) and average radar backscatter coefficients ( $\sigma_0$ ) (incidence angle  $35^\circ$ ) for the playa, alluvial fan, and the three lava flow surfaces. Because of the variation in surface roughness over alluvial fans, the wind data from Amboy was compared to two distal alluvial fan surfaces at Pisgah. Plots for incidence angles of  $30^\circ$ ,  $40^\circ$ , and  $45^\circ$  were also produced and although the values are shifted slightly, the general trend remained the same for each wavelength. Backscatter values from the lava flow at small incidence angles ( $<30^\circ$ ) may be a function of the number, orientation, and distribution of pressure ridge slopes, rather than variations in small-scale surface roughness.

These preliminary results indicate that both aeolian roughness and backscatter coefficients increase with increasing surface roughness from smooth playa to rough lava flow. They show great promise and suggest that it will be possible to derive an empirical aeolian roughness parameter from radar data. However, the uncertainties associated with comparison of wind and radar data from different localities mean that the exact relationship cannot be defined. Aeolian and radar data from more sites are needed to better define this relationship. Further theoretical studies of the factors which determine aeolian roughness and radar roughness are also needed to establish and model the physical basis of these observations.

## REFERENCES

- [1] Chapil, W.S. *Soil Science*, 60, 397-411 (1945).
- [2] Lyles, L., Schrandt, R.L. and Schneider, N.F., *Transactions, American Society of Agricultural Engineering*, 17, 134-139 (1974).
- [3] H. Lettau, *Journal of Applied Meteorology*, 8, 828-832 (1969).
- [4] Greeley, R. and Iversen, J.D. *Wind as a Geological Processes on Earth, Mars, Venus and Titan..* Cambridge: Cambridge Univ.Press. (1985).
- [5] Farr, T.G. and Engheta, N., *Proceedings International Geoscience Remote Sensing Symposium (San Francisco)*, 2.1-2.6 (1983).
- [6] Blom, R.G., Schenk, L.R. and Alley, R.E., *IEEE Transactions, Geoscience and Remote Sensing*, GE-25, 208-213 (1987).
- [7] Wise, W.S., *NASA Technical Letter*, 11, 8pp. (1966)
- [8] Greeley, R. and Iversen, J.D. *Geophysical Research Letters*, 14, 925-928 (1987).
- [9] Sullivan, R., *unpublished MS thesis, Arizona State University* (1987).

Table 1. Mean values of wind profile parameters

Site	$z_0$ (m)	D (m)	$u^*/U(6.9m)$
Pisgah			
aa	0.0173	-0.091	0.1132
pahoehoe	0.0060	0.007	0.0474
mantled pahoehoe	0.0141	-0.021	0.0686
Amboy			
alluvial fan	0.00173	-0.113	0.0441
Lucerne Dry Lake	0.000186	-0.0067	0.0382

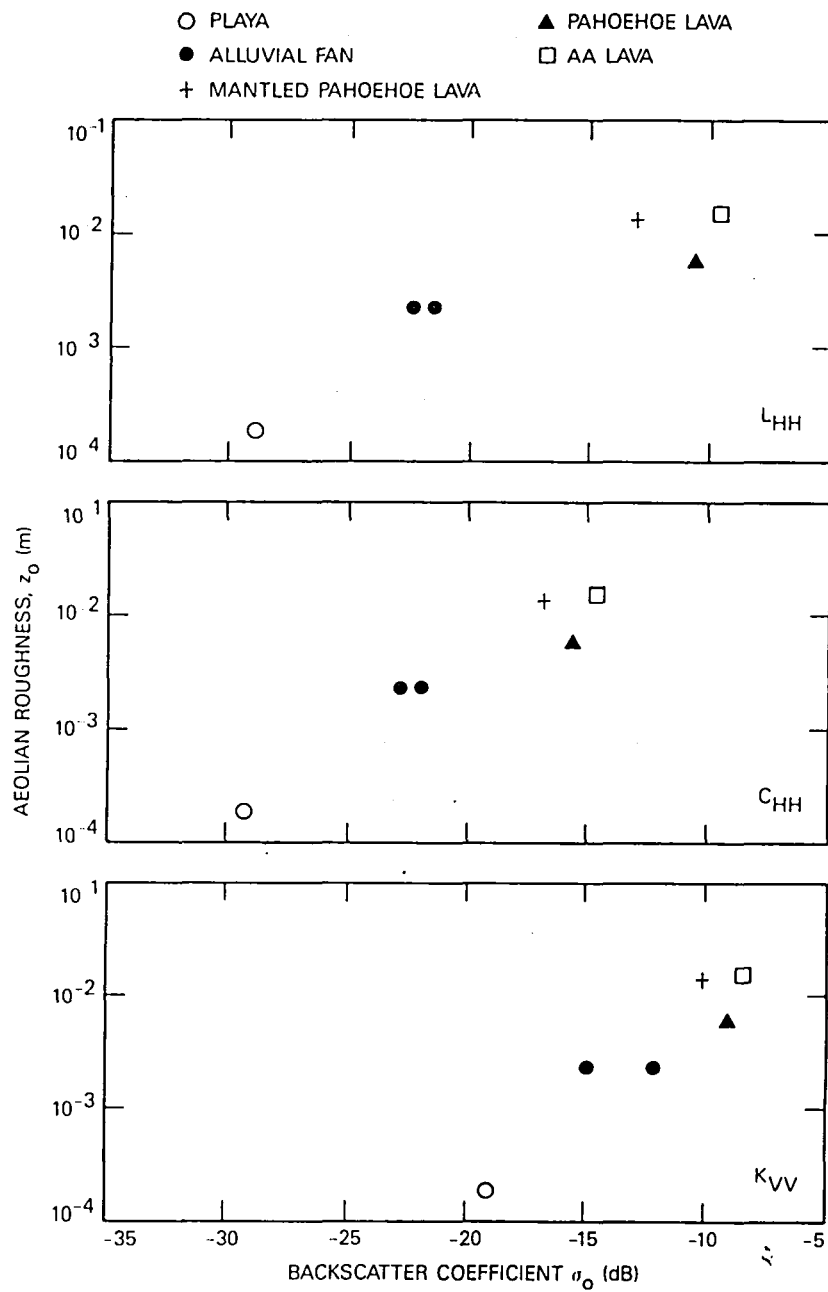


Fig. 1. Relationships between aeolian roughness ( $z_0$ ) and radar backscatter coefficient ( $\sigma_0$ ) for  $35^\circ$  incidence angle.



## **ANALYSIS OF SIMULATED VENERA AND MAGELLAN IMAGES OVER TERRESTRIAL REGIONS AND IMPLICATIONS FOR CHARACTERIZING SURFICIAL PROCESSES ON VENUS**

R. Arvidson, M. Schulte, McDonnell Center for the Space Sciences, Department of Earth and Planetary Sciences, Washington University, St. Louis, MO 63130, R. Kwok, J. Curlander, C. Elachi, J. Ford, and R. Saunders, Jet Propulsion Laboratory, California Institute of Technology, Pasadena, CA 91109.

The geology of Venus is a topic of growing interest to the earth and planetary sciences community, since Earth-based radar images [1-3], combined with the Soviet Venera 15, 16 orbital images show a relatively young surface with extensive faulting, folding, and volcanism [4-6]. In fact, it has been suggested that the surface of Venus is dominated by volcanic and tectonic processes and that surficial processes (e.g., mass wasting, corrosion of surface materials due to reactions with the atmosphere, aeolian erosion and deposition) have played minor roles in the evolution of the landforms now present on the planet [5]. For example, Bindschadler and Head [7] call upon tectonic disruption and mass wasting of surfaces to create debris, since they consider interactions with the atmosphere to be ineffective, even at centimeter to meter length scales.

In this abstract, we discuss an independent evaluation of the importance of surficial processes on Venus. Appropriately degraded radar images of Earth are used to determine the extent to which morphological analyses allow delineation and characterization of surficial processes using a controlled setting (i.e., Earth), where the processes can be independently characterized from field studies. The terrestrial images are degraded both to Venera image characteristics and to the characteristics expected for data from the upcoming Magellan mission. Magellan is an Orbiter scheduled for launch in 1989 that includes a radar system that will acquire imaging data over 90 percent of the surface, with an order of magnitude better resolution than Venera and more radar looks. The intent in generating and analyzing both Venera and Magellan simulations is to provide indications of the increase in geological information content with increasing resolution, using well-characterized targets.

One look Seasat radar images covering the Gran Desierto dune complex, Sonora, Mexico; the Appalachian Valley and Ridge Province; and accreted terranes in the central interior of Alaska were digitally processed to simulate both Venera 15, 16 images of Venus and image data expected from the upcoming Magellan mission. Since filters were used to simulate the appropriate range and azimuth resolutions, speckle was introduced as multiplicative noise, and additive Gaussian noise was included to simulate expected signal to thermal noise ratios. The Sonora and Appalachian images each cover about 100 by 100 km. The Alaska scene is a digital mosaic of 32 Seasat frames and covers about 330 by 400 km.

The Gran Desierto dunes, the largest complex in North America, are not discernable in the Venera simulation, whereas the higher resolution Magellan simulation shows the dominant dune patterns and specular reflections from dune faces oriented perpendicular to the incident radar. Anticlinal and synclinal structures are evident in both simulations over the Appalachians, mainly because differential weathering and erosion left resistant units (quartzites, sandstones, and conglomerates) as topographic highs that delineate the folds. The Magellan simulation also shows that fluvial

processes have dominated erosion and exposure of the folded structures. Mountainous terrains and their degree of erosion are discernable in both simulations over Alaska, although only the Magellan simulation shows that fluvial, glacial, and aeolian processes have all been active in shaping the landscape.

Neither the Venera nor the Magellan simulation provides evidence that the Alaskan lithotectonic terranes were juxtaposed (i.e., accreted) by plate tectonic processes, since the primary evidence needed is lithological, whereas radar returns are dominated by topography and surface roughness, parameters only weakly indicative of lithology.

Comparison of the simulations and Venera images suggests that at least some landforms on Venus (e.g., grooved terrain) have been significantly altered by weathering and erosion. Such an interpretation is fully consistent with the presence of a hot, dense, corrosive atmosphere, the likelihood of wind erosion, and the high probability that tectonic and volcanic processes will expose surfaces that will weather and erode at variable rates. The lack of direct evidence for the Venusian processes involved (e.g., corrosion and wind erosion) and the resultant products (e.g., dune complexes or even extensive soil exposures) may simply be a consequence of the resolution available with Venera and the particular sedimentary cycle relevant to the planet. Magellan data, with an order of magnitude increase in spatial resolution, should allow surficial processes and their importance in Venusian geology to be characterized in detail.

## References

- 1) Campbell, D., and others, 1983, *Science*, 221, 664-647.
- 2) Campbell, D., and others, 1984, *Science*, 226, 167-170.
- 3) Jurgens, R., and others, 1980, *J. Geophys. Res.*, 85, 8282-8294.
- 4) Basilevsky, A., and others, 1986, *J. Geophys. Res.*, 91, D399-D411.
- 5) Barsukov, V., and others, 1986, *J. Geophys. Res.*, 91, D378-D398.
- 6) Crumpler, L., and others, 1986, *Geology*, 14, 1031-1034.
- 7) Bindshadler, D., and J. Head, 1987, *Icarus*, in press.

## Venus Gravity

W. L. Sjogren, Jet Propulsion Laboratory

During the past year we have concentrated our efforts on four tasks which include 1.) the correlation of PVO gravity data with the Soviet SAR imagery, 2.) the sensitivity of the original navigation trajectories used in the reduction of PVO altimetry, 3.) the analysis of significant systematic Doppler residuals in long arc fits to PVO data, and 4.) the search through lunar gravity data for an optimal data set to perform a detailed analysis of Mare Imbrium.

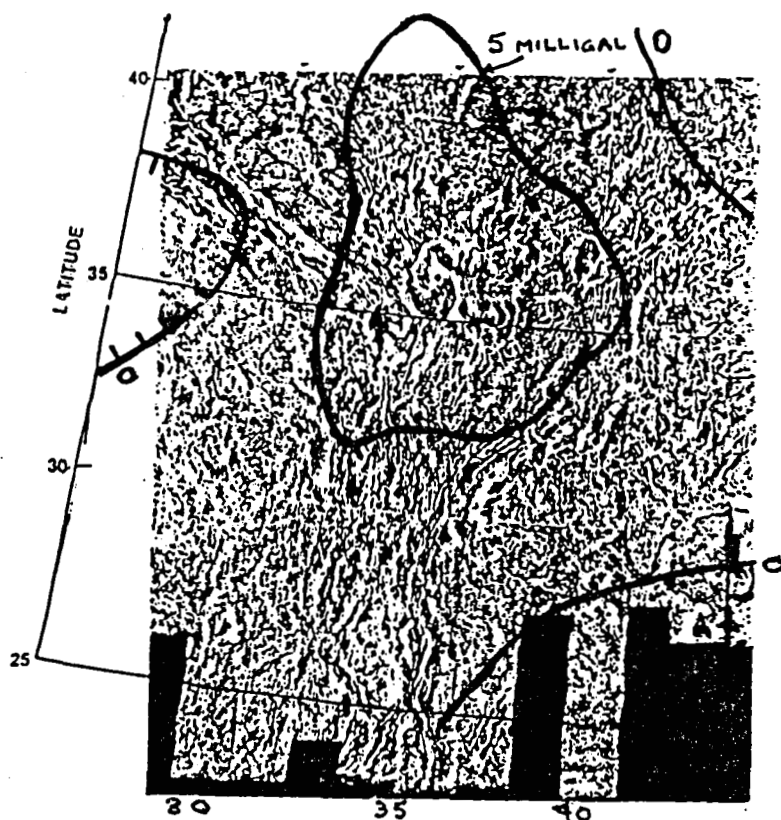
We have received approximately 25% of the total Soviet SAR imaging coverage, plotted on a Lambert Conformal grid. The PVO gravity data have been plotted to this same projection with contoured overlays, so correlations with SAR features can be easily discerned. These results were presented at the Brown University Symposium attended by our Soviet colleagues and copies of the overlays were given to the Soviets. There was one especially interesting correlation that may have some significant geophysical implications. An Arachnoid nest located at 35°N latitude and 35°E longitude correlated with a gravity high in a topographic low (a rather rare gravity-topography relationship for Venus) (see figure 1). We have also set up a stereographic overlay for a USGS SAR map, however it is also far from complete coverage. It is anticipated that by early 1988 a complete Soviet SAR map from 30°N latitude to the north pole will be complete for gravity contour overlays and correlation studies.

Last year we produced an article for publication showing a remarkable correlation of the gravity-topography ratio with feature longitude. Peer review brought to light some concerns about the altimetry data set used in our analysis. We indeed had used an old set, in fact the same one that the MGN project was using to set its SAR parameters. Discussions with Peter Ford at MIT revealed that he had refined his results and had made changes to the original trajectories supplied by the navigation team. To verify that there was a need to correct the trajectories and to know the sensitivities to the gravity and atmospheric parameters, we made independent reductions of 20 trajectories. This was accomplished by using only the two hours of Doppler data near periapsis rather than the 22 hours of data away from periapsis that was used by the navigation team. Not only were the data different, but the gravity and atmospheric parameters were grossly changed to determine sensitivities on all trajectories. The net result was that the new trajectories were very close to the original navigation team results (i.e. at least within the error of the altimeter measurement of 150-200m). Therefore it was concluded that the corrections, Peter Ford had made, were to correct for erroneous time tags associated with the raw measurements (i.e. the on board spacecraft clock had problems). We will be re-evaluating the gravity-topography ratio work using the latest topography data set to determine if there is a significant change in our conclusions.

The third task involved analysis of long arcs of Doppler data. Very sizeable systematic signatures resulted in the Doppler residuals when

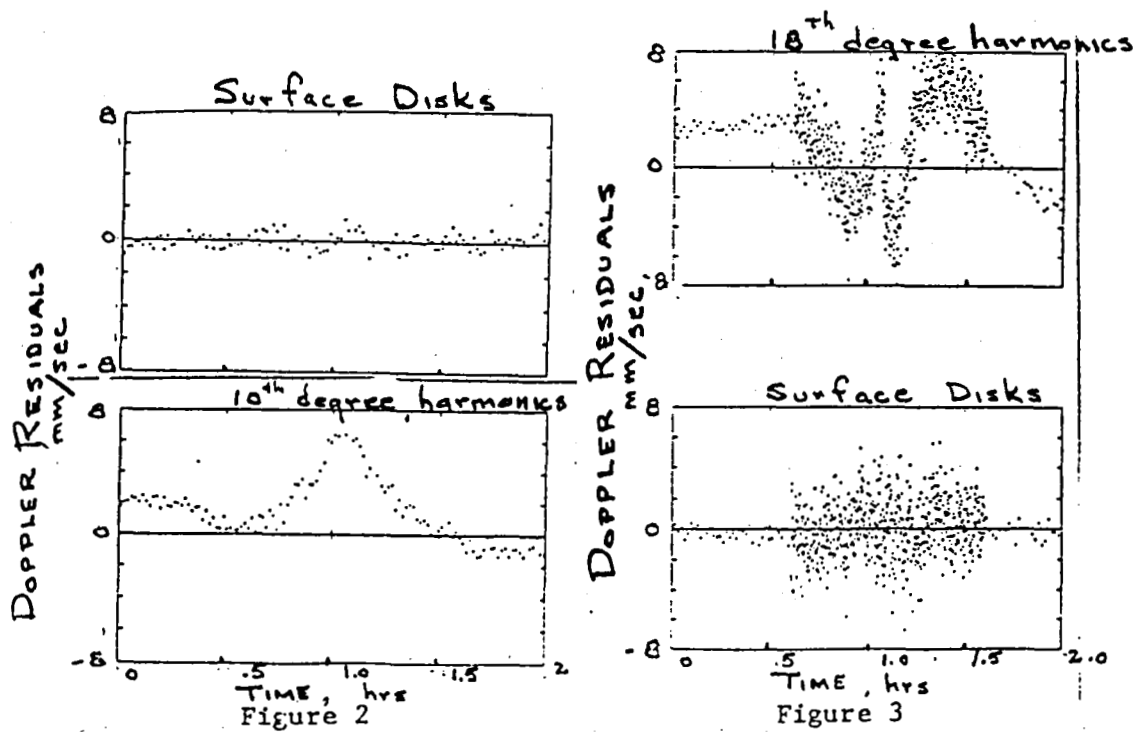
continuous multiple orbits of data were reduced using what was considered as the "best" gravity field models (i.e. 10th and 18th degree and order spherical harmonics) (see figures 2 and 3). These results were typical for reductions as short as 3 orbits. Instead of any harmonic functions, the gravity field was modeled using a small set of surface disks which are located at significant surface topography. The residuals in figures 2 and 3 labeled mascons show the dramatic improvement in removing the systematic signatures. The results in figure 2 are typical for a continuous 20 orbit fit where periapsis altitudes were 1000+km. The results in figure 3 are typical for a 4 orbit fit where periapsis altitudes were 150 km. The larger high frequency noise is due to the 5 second sample rate versus 60 seconds elsewhere. Next year we plan to reduce a complete circulation of these data and produce a global gravity field based solely on a surface disk model. This model should be of interest to the Magellan mission navigators for it is dynamically consistent and fast to compute. It will also provide the geophysicist with a relatively simple model to analyse regional internal structures.

The fourth effort was directed toward a detailed lunar gravity analysis of the Mare Imbrium basin. The gravity data from all Lunar Orbiters and Apollo spacecraft including their subsatellites were reviewed. Out of some several hundred profiles over Imbrium, fifteen were selected that had the best sensitivity and geometric coverage (i.e. lowest altitudes and E-W versus N-S profiling). It was anticipated that T. Thompson at JPL would obtain some very detailed topographic relief data from earth-based radar. However, due to acquisition problems at the tracking station these data were never obtained. Since the topography data are critical for quantitative modeling of internal structure, this effort has stopped until these data are hopefully acquired in the future. We did publish a User's Guide (JPL 86-16) for the new block of several thousand gravity observations reduced from raw data last year.



SOVIET SAR IMAGE WITH PVO GRAVITY CONTOURS

Figure 1



# IMPROVEMENT IN PRECISION OF MEASUREMENTS MADE BY THE SYNTHETIC APERTURE RADAR COMPILATION SYSTEM FOR THE MAGELLAN MISSION

Sherman S.C. Wu, Francis J. Schafer, and Annie Howington-Kraus,  
U.S. Geological Survey, Flagstaff, Arizona 86001

A compilation system has been developed for the extraction of topographic information from synthetic aperture radar (SAR) images of Venus to be obtained from the Magellan mission. The system's software has been installed on an AS-11AM analytical stereoplotter. The software has been extensively tested and implemented by using stereoradar images from various radar systems, both spacecraft and airborne, including SeaSat, SIR-B, NASA 102A, and ERIM X-C-L (Wu et al., 1986, 1987). Measuring precision depends on image resolution and the geometry of the stereomodel, i.e., the base-to-height ratio or the intersection angle between the two look angles of the pair of radar images. Repeatability of elevation measurements of about 1 m and 5 m were obtained respectively from SeaSat and airborne radar images.

To improve precision, the system's software has been enhanced by incorporating to higher order the mathematical terms in the software's underlying analysis. This enhanced software was tested with a stereomodel of Spitsbergen, Norway, from the ERIM X-C-L radar system. Eight control points were used for the test. Results before and after enhancement are shown in Table 1; standard errors of measurement of the control points are 61.5 m and 18.2 m, respectively. Coordinates of control points were determined by the Defense Mapping Agency using geodetic methods.

By using the SAR compilation system's software, a topographic map was compiled from the stereomodel, on an AS-11AM analytical stereoplotter, at a scale of 1:25,000 with a contour interval of 20 m (Fig. 1).

Table 1. SAR elevation measurements before and after software enhancement.

Point ID	Elevation (m)	Before Enhancement		After Enhancement	
		Measurement (m)	Error (m)	Measurement (m)	Error (m)
10	175	242	-67	193	-18
11	155	185	-30	190	-35
15	177	190	-13	178	-1
16	148	161	-13	165	-17
18	131	98	33	131	0
19	109	49	60	92	17
22	111	50	61	92	19
31	174	50	124	175	-1
Absolute Mean		50.1		13.5	

## References Cited

- Wu, S.S.C., Schafer, F.J., and Howington, A.E., 1986, Radargrammetry for the Venus Radar Mission: Reports of Planetary Geology and Geophysics Program-1985, National Aeronautics and Space Administration Technical Memorandum 88383, p. 570-573.
- Wu, S.S.C., Schafer, F.J., and Howington, A.E., 1987, A compilation system for Venus Radar Mission (Magellan): Reports of Planetary Geology and Geophysics Program-1986, National Aeronautics and Space Administration Technical Memorandum 89810, p. 233-236.

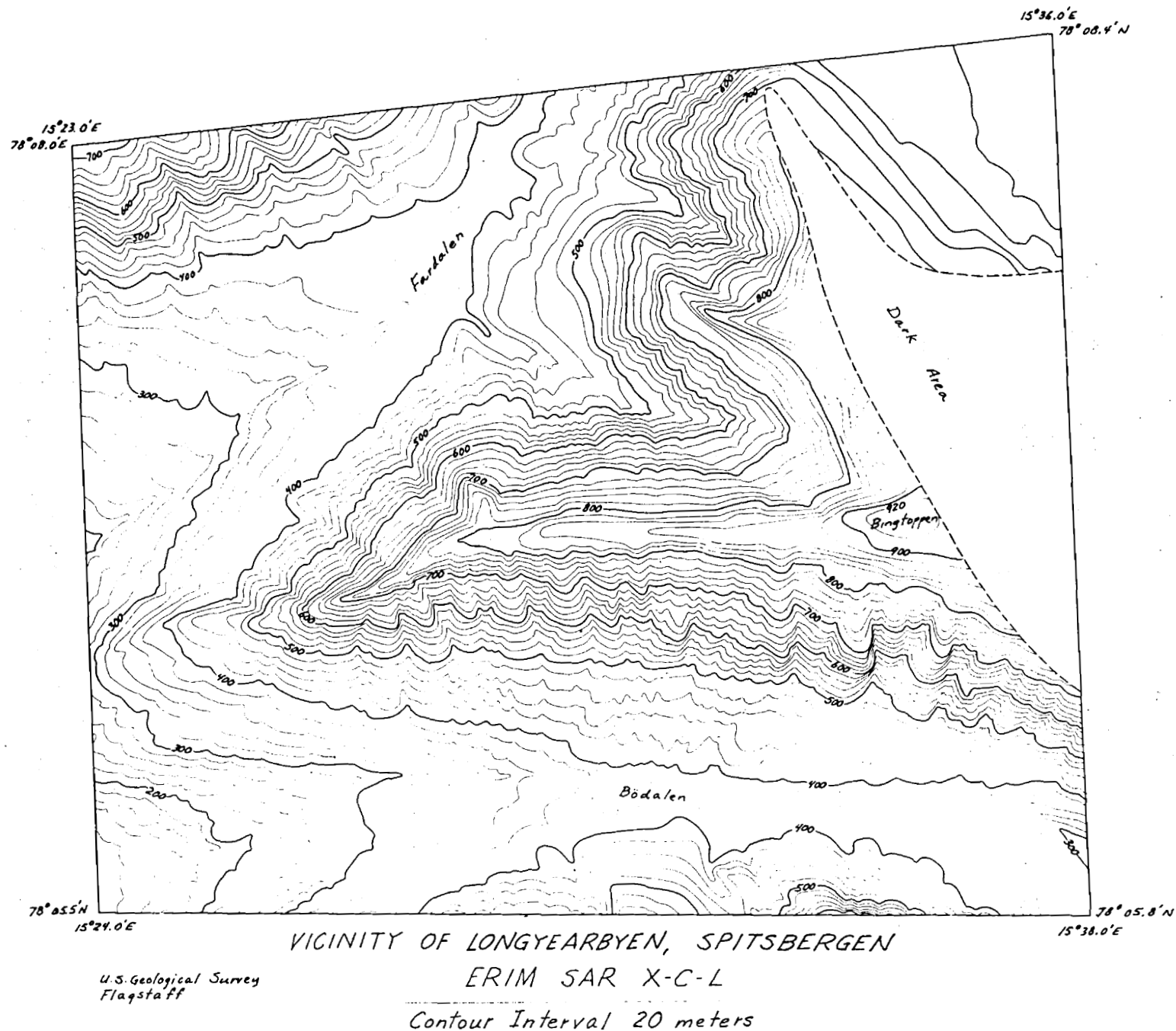


Figure 1. Topographic contour map of vicinity of Longyearbyen, Spitsbergen, produced by using the SAR compilation system with ERIM X-C-L radar images on an AS-11AM analytical stereoplotter.

## LUNAR RADAR INVESTIGATIONS

Peter J. Mougini-Mark and Bruce C. Campbell, Planetary Geosciences Division, Hawaii Institute of Geophysics, University of Hawaii, Honolulu, HI 96822

**BACKGROUND:** Lunar radar observations have been used in a number of studies to investigate mare geologic units (Thompson *et al.*, 1974; Schaber *et al.*, 1975), the variation in dielectric constant (Hagfors, 1970), and general surface morphology (Zisk *et al.*, 1971, 1974). In the past, such radar studies have been limited by the spatial resolution of the data, which precluded their direct correlation with high resolution Lunar Orbiter V or Apollo images. Radar data were used primarily as images of surface roughness, without taking advantage of their calibrated nature or the phase information contained within the like- and cross-polarized radar data. Here we describe our preliminary analyses of newly acquired (1986/7) high resolution 3.0-cm and 70-cm radar backscatter data to study volcanic processes on the moon by evaluating the thickness and areal extent of lunar pyroclastic ("dark mantle") deposits. In addition, we are exploring the potential of applying recently developed techniques for the analysis of quad-pol radar data (Thompson *et al.*, 1986; Zebker *et al.*, 1987), which demonstrate that significant new information about the volume scattering properties of geologic materials (especially volcanic ash and impact ejecta) can be derived from a study of the phase information of lunar like- and cross-pol radar images.

**DATA SETS:** New 15-30 meter resolution 3.0 cm radar images have been recently obtained at Haystack Observatory (S. Zisk, pers. comm., 1987), and 1-2 km resolution 70 cm radar images at Arecibo Observatory (T. Thompson, 1987). In a collaborative effort with Drs. Zisk and Thompson, we have initiated several geologic studies using radar data collected in 1986 (cf., Zisk *et al.*, 1987; Campbell *et al.*, 1987). Radar images of southern Mare Imbrium, Hadley Rille/Rima Mozart, Copernicus crater and Alphonsus crater were obtained in June - August 1987 at 3.0 cm wavelength. New ~1 km-resolution 70 cm radar images cover the same areas on the moon as the 3-cm data. For both data sets, a circular polarized signal was transmitted, and both senses of polarization were received. Power returned in the same sense (handedness) as the transmitted signal is termed depolarized, while that returning in the opposite sense is termed polarized. The polarized return consists of quasi-specular and diffuse components (Evans and Pettengill, 1963; Hagfors and Evans, 1968).

Both the distribution and the depth of the pyroclastic deposits and ejecta blankets, as well as the volume scattering (degradational) properties of ejecta blankets, can be determined from the new lunar radar data. This depth determination can be accomplished by modeling the behavior of the 70 cm radar signals in a comparable manner to the analysis of Shuttle Imaging Radar-B for the Earth (Farr *et al.*, 1986). We are using the 3.0 cm radar data to further define the spatial distribution of the dark mantle deposits, map the vent areas, and study the spatial distribution of impact ejecta, with the objective to further understand volcanic and impact cratering processes on the moon.

**VOLCANIC STUDIES:** Our first study using these new high resolution data has focused on lunar pyroclastic deposits, in part because these deposits have recognizable radar signatures, and also because a better understanding of their distribution and thickness will enable us to further constrain models of lunar explosive volcanism (cf., Wilson and Head, 1981). Lunar pyroclastic deposits are characteristically dark in radar images at both wavelengths used in our analysis (Zisk *et al.*, 1977). Pyroclastic deposits are fine-grained, agglutinate ash and glass layers produced by explosive volcanism more than three billion years ago, and are thought to have occurred contemporaneously with the early stages of mare infilling (Head, 1974). Subsequent lava flows buried many deposits, so that in most cases we are constrained to study only those pyroclastic deposits which remain on the exposed terrae surfaces.

The eruptive styles and settings of lunar pyroclastics have been studied numerically by Head and Wilson (1979), and by Wilson and Head (1981). These numerical models relied primarily on photogeologically-determined dimensions for the distribution of mantle materials, and contained only very approximate estimates for the thickness of the deposits. A major objective of our work has been to provide additional constraints for these numerical models, in terms of the spatial distribution of the vents that experienced explosive activity (as opposed to effusive eruptions of lava) and the distribution and depth of the mantle deposits. The high concentrations of metallic oxides (Schaber *et al.*, 1975; Gaddis *et al.*, 1985) and the very smooth surface texture (Zisk *et al.*, 1977) make the pyroclastic deposits ideal for long-wavelength radar penetration, with minimal surface and volume scattering. As is described below, the



new Earth-based radar data provide us with the capability to not only better define the physical extent of these explosive volcanic materials on the Aristarchus Plateau, but also to determine the spatial variation of deposit thickness at this locality.

The Aristarchus Plateau: We have recently completed a study (Campbell *et al.*, 1987) focused on the determination of pyroclastic deposits on the Aristarchus Plateau, using 70 cm wavelength radar data collected by Thompson (1987). The distribution and depth of pyroclastic deposits were estimated from the analysis of radar attenuation. Our analysis technique was based on recent studies of Space Shuttle Imaging Radar (SIR-A and SIR-B) signal penetration in arid terrestrial environments (Schaber *et al.*, 1986; Farr *et al.*, 1986). Pyroclastic deposit depth was estimated for a range of dielectric constants and loss tangents ( $\epsilon' = 1.5$  to 2.5,  $\tan \delta = 0.003$  to 0.007) that are consistent with the measured properties of returned lunar samples.

The maximum depth of the pyroclastic materials around the Cobra Head of Schroter's Valley is inferred from their radar attenuation to be as great as ~18 m, while the mean depth of the deposit on the Plateau may be as much as ~13 m. Analysis of Lunar Orbiter and Apollo photographs of the region supports such depth estimates; a minimum mantle depth of 2 to 12 m is indicated by partially buried impact craters in the size range 150 to 300 m in diameter, while bright-halo impact craters indicate a maximum depth of 18 to 20 meters for the mantle thickness at a distance of 35 to 40 km from the Cobra Head. Assuming a radially symmetric eruption, and using the radar data to approximate a maximum radial range of ~200 km, the original pyroclastic deposit volume (prior to mare embayment) may have been as large as  $\sim 1 \times 10^3 \text{ km}^3$ . By applying the numerical models of lunar volcanic eruptions developed by Wilson and Head (1981), this volume is <1% that of the lavas believed to have erupted contemporaneously from the same vent, but nevertheless implies (for an eruption lasting ~530 days; Head and Wilson, 1981) a mass eruption rate of  $\sim 2 \times 10^8 \text{ kg s}^{-1}$  from a vent ~40 meters in diameter.

**FUTURE DIRECTIONS:** Over the next year, our collaborative efforts with Drs. Zisk and Thompson are expected to include the investigation of other high resolution lunar radar data in order to address the following geologic problems:

- 1) We intend to conduct a more complete (compared to the study of Campbell *et al.*, 1987) delineation of the pyroclastic material covering the Aristarchus Plateau, and in particular the area around the Cobra Head. We believe that the Cobra Head may have been the source vent for most (if not all) of the pyroclastic material that mantles the Aristarchus Plateau, but the 1 - 2 km resolution 3.8 and 70 cm radar data that we employed in Campbell *et al.* (1987) were of insufficient resolution to study the source regions (<2 km dia.) of the smaller sinuous rilles on the Plateau, or to unambiguously exclude radar-bright surface materials that are caused by secondary cratering by Aristarchus ejecta. In both cases, the new 15 m radar data to be used will enable us to avoid these problems.

- 2) What is the distribution of radar-dark materials around Hadley Rille and Rima Mozart? Models for the eruption of basaltic magma on the moon (Wilson and Head, 1981) depend critically on distinguishing between fire-fountaining (producing a halo of scoria a few hundred meters around the vent) and quiet effusive activity of turbulent lava. Using the high resolution 3.0 cm radar images, we should be able to see if pyroclastic volcanism (strombolian or continuous fire-fountaining) was associated with the formation of these rilles;

- 3) We intend to map the distribution of dark mantle deposits around the volcanic craters within Alphonsus. A major question concerning the style of activity associated with these dark-halo craters (Head and Wilson, 1979) is the relative amount of juvenile material that was erupted compared to vent material. One way to resolve this issue is to determine whether there are any large clasts within the dark halo deposits (large clasts probably being vent material ejected by vulcanian activity); this can probably be achieved using the new radar images to provide both a higher spatial resolution image of these deposits and identify subsurface scatterers (if present).

In addition to these studies of lunar volcanic phenomena, we also intend to initiate studies of impact craters and their ejecta blankets. Copernicus crater has already been imaged at both X - and P-band, and our intent is to further pursue the analysis of Oberbeck (1975) and Pieters *et al.* (1985) concerning the role of secondary cratering in the formation of a large crater ejecta blanket.

**REFERENCES:**

- Campbell, B.C., S.H. Zisk, P. J. Mouginis-Mark, L.R. Gaddis, and T.W. Thompson (1987). Lunar pyroclastic deposits: Distribution and depths on the Aristarchus Plateau from Earth-based radar. Submitted to J. Geophysical Research, 1987.
- Evans, J.V. and Pettengill, G.H. (1963). The scattering behaviour of the moon at 3.6, 68, and 784 cm. J. Geophys. Res., **68**, 423-447.
- Farr, T.G., Elachi, C., Hartl, P., and Chowdrey, K. (1986). Microwave penetration and attenuation in desert soil: A field experiment with the Shuttle Imaging Radar. IEEE Trans Geosci. Rem. Sen., **GE-24**, 590-594.
- Gaddis, L.R., Pieters, C.M., and Hawke, B.R. (1985). Remote sensing of lunar pyroclastic mantling deposits. Icarus, **61**, 461-489.
- Hagfors, T. (1970). Remote probing of the moon by infrared and microwave emissions and by radar. Radio Sci., **5**, 189-227.
- Hagfors, T. and Evans, J.V. (1968). Radar studies of the moon. In: Radar Astronomy, McGraw-Hill, pp. 243-244.
- Head, J.W. (1974). Lunar dark-mantle deposits: Possible clues to the distribution of early mare deposits. Proc. 5th Lunar Sci. Conf., 207-222.
- Head, J.W. and Wilson L. (1979). Alphonsus-type dark-halo craters: Morphology, morphometry and eruption conditions. Proc. Lunar Planet. Sci. Conf. 10th, 2861-2897.
- Head, J.W. and L. Wilson. (1981). Lunar sinuous rille formation by thermal erosion: Eruption conditions, rates and durations (Abs.). Lunar Planet. Sci. XII, 427-429.
- Oberbeck, V.R. (1975). The role of ballistic erosion and sedimentation in lunar stratigraphy. Revs. Geophys. Space Phys., **13**, 337-362.
- Pieters, C.M., Adams, J.B., Mouginis-Mark, P.J., Zisk, S.H., Smith, M.O., Head, J.W., and McCord, T.B. (1985). The nature of crater rays: The Copernicus example. J. Geophys. Res., **90**, 12393-12413.
- Schaber, G.G., Thompson T.W., and Zisk, S.H. (1975). Lava flows in Mare Imbrium: An evaluation of anomalously low Earth-based radar reflectivity. The Moon, **13**, 395-423.
- Schaber, G.G., McCauley, J.F., Breed, C.S., and Olhoeft, G.R. (1986). Shuttle imaging radar: Physical controls on signal penetration and subsurface scattering in the Eastern Sahara. IEEE Trans. Geosci. Rem. Se., **GE-24**, p. 603-623.
- Thompson, T.W. (1987). High-resolution lunar radar map at 70-cm wavelength. The Earth, Moon and Planets, **37**, 59-70.
- Thompson, T.W., Shorthill, R.W., Whitaker, E.A. and Zisk, S.H. (1974). Mare Serenitatis: A preliminary definition of surface units by remote observations. The Moon, **9**, 89-96.
- Thompson, T.W., Zebker, H.A., and Van Zyl, J.J. (1986). Lunar radar polarimetry. Eos, **67**, # 44, 1075.
- Wilson, L. and Head, J.W. (1981). Ascent and eruption of basaltic magma on the Earth and Moon. J. Geophys. Res., **86**, 2971-3001.
- Zebker, H.A., van Zyl, J.J. and Held, D.N. (1987). Imaging radar polarimetry from wave synthesis. J. Geophys. Res., **92**, 683-701.
- Zisk, S.H., Carr, M.H., Masursky, H., Shorthill, R.W. and Thompson, T.W. (1971). Lunar Apennine-Hadley region: Geological implications of Earth-based radar and infrared measurements. Science, **173**, 808-812.
- Zisk, S.H., Hodges, C.A., Moore, H.J., Shorthill, R.W., Thompson, T.W., Whitaker, E.A. and Wilhelms, D.E. (1977). The Aristarchus-Harbinger region of the moon: Surface geology and history from recent remote-sensing observations. The Moon, **17**, 59-99.
- Zisk, S.H., Mouginis-Mark, P.J., Pettengill, G.H., and Thompson, T.W. (1987). New very-high-resolution radar measurements at 3.0 cm wavelength: Initial maps of the Hadley/Apollo 15 area (Abs.). Lunar Plan. Sci. XVIII, 1130-1131.
- Zisk, S.H., Pettengill, G.H., and Catuna, G.W. (1974). High-resolution radar maps of the lunar surface at 3.8-cm wavelength. The Moon, **10**, 17-50.

## Numerical Modeling of Radiowave Scattering

R.A. Simpson and G.L. Tyler

Center for Radar Astronomy

Stanford University

Stanford, CA 94305-4055

Radio wave scattering is an effective and important method for remotely studying planetary surfaces. It is particularly appropriate when information about surface texture on scales of tens of centimeters to tens of meters is needed. On cloud-covered bodies such as Venus and Titan, radio methods provide the only means by which surface mapping on a global scale can be carried out.

Despite the long-term use of radio scattering in planetary studies, theoretical work has lagged experimental discoveries. Numerical techniques, and especially advances in computer technology, now provide one possible alternative for interpretation. Relatively simple and robust algorithms, but ones which demand considerable computation power, allow us to simulate some electromagnetic scattering problems. Although there are only a very limited number of analytical solutions which can be used for checking, the clarity with which the problems may be stated plus an understanding of the computer's numerical limitations provide assurance that the results are correct.

A large body of computer software has been developed nationally for calculating electric and magnetic fields near objects that can be described in relatively simple terms -- wires and plates (antennas, for example) and cylinders and cones (aircraft, missiles, ships, etc.). The calculations usually incorporate, either as initial conditions or as an intermediate result, information about the currents on the conducting surfaces involved. The radiated fields (including scattering as a special case) then represent the response to these currents. As in many electromagnetics problems, a particular solution may be derived more easily by concentrating on either the electric or the magnetic equations. Dielectric materials (as opposed to perfect conductors) and statistically rough surfaces (as opposed to those with well-defined curvature) increase the complexity of these problems considerably. Both variations, of course, must be accommodated in any application to real planetary surfaces.

We have acquired the massive Numerical Electromagnetic Code (NEC) from Lawrence Livermore Laboratory. NEC-2 (the version obtained) may be used to analyze the electromagnetic response of an arbitrary structure consisting of wires *and* surfaces in free space or over a ground plane. During 1986-87 we converted and tested NEC-2 on our Data General MV/10000. The program can now be used to calculate currents, charges, and radiation patterns associated with wire structures and/or rather general surfaces. The program is presently limited to analysis of structures having 300 or fewer elements; since assumptions within the code require that elements be no larger than 1/10 wavelength, this effectively restricts two dimensional structures to being a few wavelengths on a side.

NEC-2 may be used to determine scattering from a structure assembled using small linear elements or surface patches. With patches the structure must be closed; that is, there can be no cavity or hole in the patch pattern. Approximating a sphere by patches is allowed, for example, as the sphere is a closed figure. A spheroidal object may also be modeled; thus one could study the scattering expected from a rock of general shape, subject to the understanding that real rocks are not made of perfectly conducting material. The

approximation of a planetary surface by a plane of randomly oriented patches could not be analyzed readily by NEC-2 (though we intend to look into possible code modifications). Experienced users of NEC have recommended that we work with wire grids rather than patches in order to model rough surfaces. Although the wire grid is "porous," a grid with wire spacings on the order of 1/10 wavelength behaves very nearly the same as a continuous sheet with the same shape.

It is the detail with which NEC-type problems can be described that makes the NEC approach most attractive; that is, the one-tenth wavelength or smaller surface structure can be handled. At the same time it is the detail that rapidly consumes computational resources in obtaining solutions. Finding reasonable trade-offs between descriptive complexity and overall accuracy is a major issue in using NEC-2 for surface scattering problems. One solution to this is to resort to one-dimensional surface descriptions. If (rather than insisting on two dimensions) we simplify a surface problem to one-dimension, we can allocate the 300 elements available in NEC-2 to specify a "structure" with a dimension of thirty wavelengths. A second key to employing numerical techniques in planetary surface studies is that the surfaces of interest are generally random. It is then not so important that a single scattering solution be precise if an ensemble of solutions gives the correct "average" answer.

Since NEC-2's highest potential for immediate application to surface scattering appears to be in its one-dimensional "mode," we decided to test it on a one-dimensional *sinusoidal* surface  $z=f(x)$ . We approximated the surface by a wire described by

$$z = z_{\max} \sin \pi x$$

over the range  $0 \leq x \leq 20$  meters; the difference between the wire and a one-dimensional surface is negligible if consideration is restricted to the x-z plane. We illuminated the surface/wire with a 300 MHz (wavelength  $\lambda = 1$  meter) wave with its electric vector in the plane of incidence (the x-z plane). The E-field induces currents in the surface/wire; we used NEC-2 to calculate the scattered field. We set  $z_{\max}=0$  and calculated the scattered field for normal incidence ( $\theta_i=0^\circ$  in Figure 1). We then changed the incidence angle to  $\theta_i=40^\circ$  and calculated scattering for several values of  $z_{\max}$  in the range 0.0-0.5 meters.

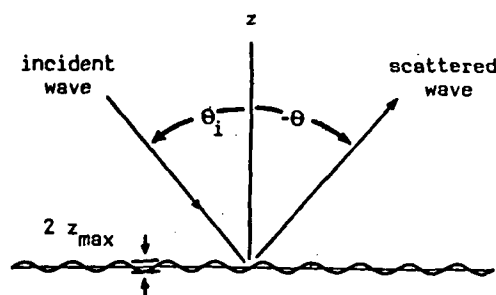


Figure 1 - Scattering geometry.

Figure 2 shows the scattering pattern for the case of normal incidence and no roughness. The solid curve shows the scattering pattern determined by NEC-2; the dots show the radiation pattern of a uniformly illuminated rectangular aperture antenna with the same linear dimension as the wire (Stutzman and Thiele, *Antenna Theory and Design*, 1981). Over the main lobe and first five side lobes the agreement is excellent (easily within 1 dB). For large scattering angles NEC-2 and theory agree well on positions of nulls and peaks, but NEC-2 predicts increasing amplitude with angle while theory predicts decreasing amplitude. Measurement would be needed to determine which was the better match to the real case. The approximations made in deriving the theoretical curve -- principally that the aperture is uniformly illuminated -- suggest that the NEC-2 solution may, in fact, provide the better answer. The wire has finite length,

so currents induced on the wire will *not* be uniform, as assumed for the theoretical solution. Phenomena associated with wire ends will distort the ideal radiation pattern, while the fact that we have a wire rather than an aperture will tend to increase radiation toward its ends. None of these effects is included in the theoretical model.

Figure 3 shows the NEC-2 scattering pattern when incidence angle is shifted to  $40^\circ$  and a small amount of roughness is added. Note the slight broadening of the main lobe (a projection effect) as well as the offset to the specular angle of  $-40^\circ$  in comparison with the NEC2 curve in Figure 2. Small amounts of roughness do not change the gross properties of the scattering pattern, as here; but, by the time roughness has increased to  $z_{\max}=0.4$ , maximum power is in the *backscatter* direction ( $\theta=60^\circ$ ) while the specular lobe ( $\theta=-40^\circ$ ) has been reduced to third largest.

In the next year further work with one-dimensional calculations is planned, to determine the extent to which rough "surfaces" can be defined and their scattering patterns calculated. We will also consider to what extent separately calculated solutions may be combined by taking advantage of the fact that randomness is expected. Continued study of random surface descriptors will also be required, though we note that a closed form description is not necessary for setting up NEC problems. The numerical approach offers new opportunities for greatly improving the interpretation of scattering from geophysical surfaces; we hope to apply these techniques to planetary remote sensing for practical inference of surface properties.

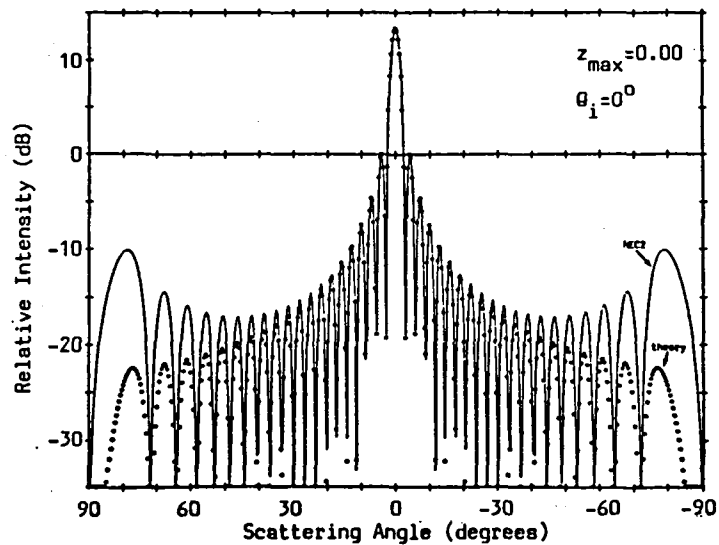


Figure 2 - Numerical result (NEC2) and closed form (theory) from flat "surface" at normal incidence.

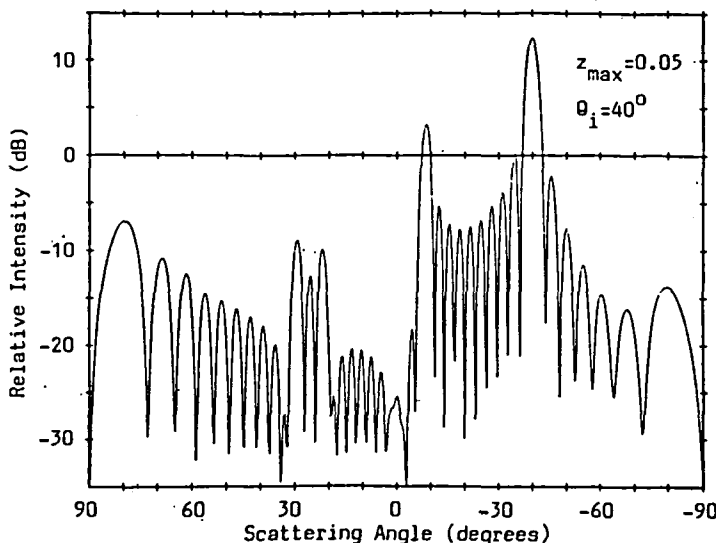


Figure 3 - Oblique incidence on slightly rough surface shows scattering at angles different from specular.

## PROGRESS IN TWO-DIMENSIONAL RADARCLINOMETRY

Robert L. Wildey, U.S. Geological Survey, Flagstaff, AZ 86001

Although my exploration of the mathematical foundations of radarclinometry has recently lead me to a new formulation that is more genuinely two-dimensional, I have continued to exploit the line integral approach because it is easier to implement, it is especially adaptable to the peculiarities of radar images, and it has not until now been brought to its full potential. Along the characteristic curves of the partial differential equations of radarclinometry, the line integral development of elevation is deterministic without auxiliary assumptions. The inherent nature of radarclinometry is that one must find, either explicitly or implicitly, a minimum-error compensation for missing boundary profiles that tie together the zero points of elevation at the terminus of the characteristic curves. In the pure line integral approach, the amount of image information that can be brought to bear in constraining the topography compared with the missing information is much than in a less direct but full-frame approach.

The line integral approach takes the form that, from a starting strike (angular horizon azimuth of unchanging elevation), one can evolve both elevation and strike along a line of range by (1) relating the slopes directly and unambiguously to the value of the image pixel at the given strike, and (2) relating the step in strike to the local surface curvature as it, in turn, relates to the gradient in the image of the value of the image pixel. Because a range-line does not exactly correspond to a characteristic curve of the partial differential equations governing the evolution of strike, an auxiliary curvature assumption is required as an additional constraint. In radar images, the characteristic curves meander only slightly about the straight lines of increasing range, thus ameliorating the effects of naiveté in whichever of the several curvature hypotheses is employed. However, this precludes affecting two-dimensional topography by simple branching of the line integral at the range threshold of the image. Along the resulting path in the direction of radar azimuth, the influence of the curvature hypothesis too strongly outweighs that of the radiometric constraint.

The following procedure is currently the most effective of many that I have tried. Of all the possible starting strikes for each line integration of topography over range, the one affecting solution is the one resulting in the minimization of the gravitational potential energy of the underlying, vertically oriented plane slab. Consistent with this minimization, the collection of range profiles is adjusted to agree in mean elevation. Criteria exist for the selection of a curvature hypothesis at each range integration step. If the local characteristic strip makes a sufficiently small angle with the ground-range direction, radiometric determinacy is selected (no curvature hypothesis is needed). A consequence is that the azimuth-azimuth component of the curvature tensor is indeterminate, but that component does not influence an integration in the range direction. If the aforementioned angle is too large, local sphericity is selected, primarily because it is an over-constraint, so that the pixel gradient components are observables that are least-square fitted to the prediction of the radius and the location of the center of the sphere. If neither of the foregoing choices is affected, and if the radius of curvature of the local image isophote is sufficiently large, local cylindricity is selected. Finally, the default curvature hypothesis is implicit in the Euler/Lagrange equation associated with the minimization of surface area, from the calculus of variations.

I have now completed a parallel effort to alleviate a persistent problem facing radarclinometry: that due to the uncertainties in the applicable radar-reflectance function and the radiometric calibration of the radar system employed. A new algorithm solves the integral equation relating a one-dimensional frequency distribution over slope-component, extractable from an altimetry profile, to the histogram of DN values in the radar image being processed. If the hypsometric gradient analysis is a priori isotropic, the reflectance function/radiometric calibration is determinate (if a priori monotonic). The isotropy assumption is judged a posteriori valid for terrain having no visually obvious directional trends.

I have tested the bootstrap algorithm and the radarclinometry algorithm in the Lake Champlain West quadrangle, in a portion of which the digitized standard topography is shown in Figure 1 (left). On the right is shown the corresponding artificial radar image based on a reflectance function approximately characteristic of broken desert. Bootstrapping the reflectance function, expressed in terms of equivalent error in incidence angle, is precise to within  $0.1^\circ$  over the central 99% of pixel values in the image histogram. The precision drops to  $1^\circ$  at both 99.9% data boundaries, and it diminishes to  $6^\circ$  at both absolute signal extremes, where the effects of low-number statistics are obviously severe.

In Figure 2 (left) the retrieval of topography from Figure 1 (right) is shown as performed by radarclinometry. The characteristic low spatial frequency errors of radarclinometry over range have aliases at high spatial frequency in azimuth, an unsurprising result of the line integral approach. In Figure 2 (right) are shown the results of interactive box-car filtering. A narrow notch filter in the two-dimensional Fourier domain could be expected to produce virtually perfect directional noise removal, but insufficient time was available to carry out the more elaborate filtering procedure.

The use of artificial radar images has been essential in the cause of decipherable diagnostics. On the basis of these successes, I have begun to apply these techniques to Venera imaging in the region of Cleopatra Patera.

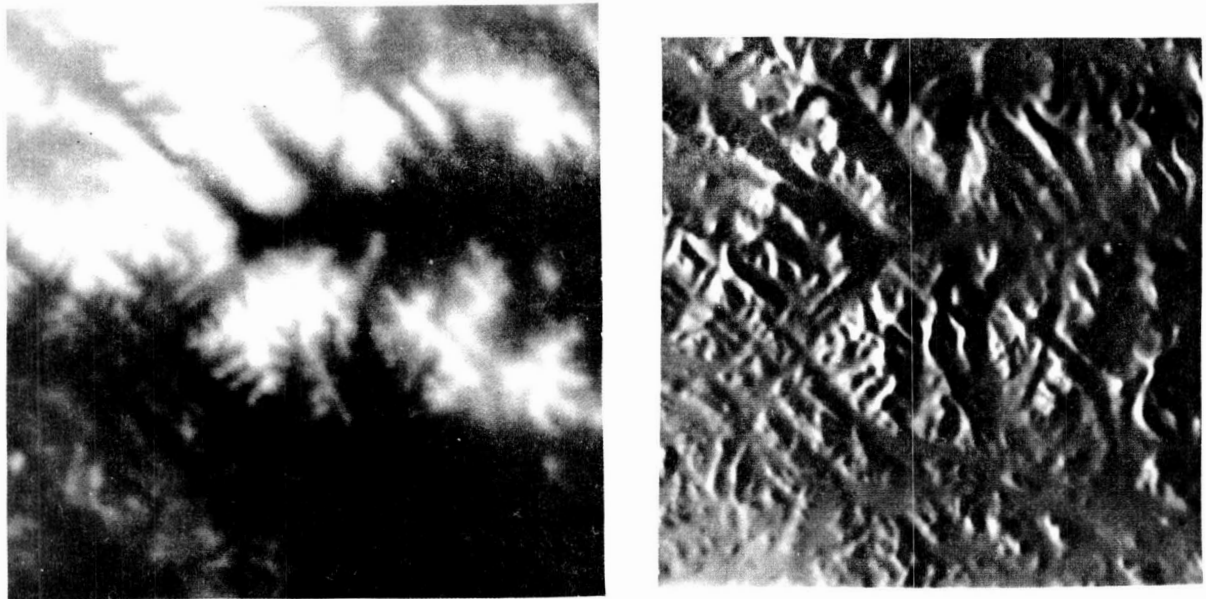


Fig. 1. (Left) Topography in Lake Champlain West. Bright is high. Relief range void of regional trend is 2.5% of the 35-km-format width. (Right) Corresponding artificial radar image.

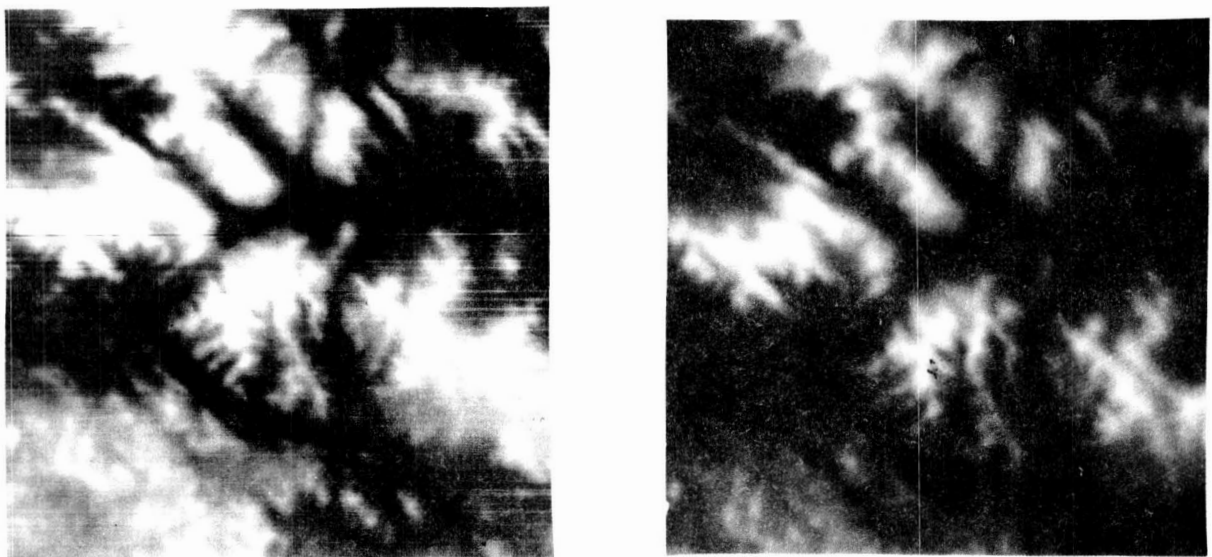


Fig. 2. (Left) Radarclinometric topography from Figure 1 (right). (Right) Radarclinometric topography after low-pass and high-pass box-car filtering by P.S. Chavez, U.S. Geological Survey.



COMPLEX DIELECTRIC CONSTANTS OF CRYOGENIC LIQUID ALKANES AT 1.2GHz  
Vincent G. Anicich and Taguhi Arakelian, Jet Propulsion Laboratory,  
Pasadena, CA 91109

We have measured both the real and imaginary parts of the complex dielectric constants for candidate Titan ocean materials at 1.2 GHz. This frequency is close to what is expected for radar sounding of the surface and ocean of Titan. A particularly important parameter is the loss tangent, which is the ratio of the imaginary part to the real part of the complex dielectric constant. The loss tangent is a measure of the ability of the radio wave to penetrate the material. Chemical models of the atmosphere and surface<sup>1,2</sup> based on Voyager results lead to the prediction of ethane-methane oceans on the surface and exotic hydrocarbon aerosols in the atmosphere<sup>3</sup>.

A literature survey reveals very little work that has been done to measure the dielectric constant of hydrocarbon liquids at the frequencies and temperatures of interest. The solid lines in Figure 1 show a summary of the information available on the dielectric constants of saturated hydrocarbons<sup>4-8</sup>. The measurements were all done at a frequency of 1 kHz using capacitance devices. Gelsthorpe and Bennett<sup>5</sup> have measured the loss tangent for n-hexane and n-heptane at several temperatures and frequencies in the microwave range, and have found values on the order of a few times  $10^{-4}$ . The loss tangent increased with temperature over the temperature range 0 to 50°C and decreased with decreasing frequency over the range 8 to 1000 GHz. At very much higher frequencies, the refractive indices of hydrocarbons have been measured at room temperature with the sodium D line (589 nm or  $5.1 \times 10^6$  GHz). The dielectric constant for a material is equal to the square of the refractive index at the same frequency. Comparison of the dielectric constants of heptane, hexane, and pentane measured at 1 kHz, 1.2 GHz, and  $5.1 \times 10^6$  GHz show that the dielectric constants of these hydrocarbons are constant over this large range of frequencies. This is expected for these particular hydrocarbons since they have neither dipole moments nor any ionic component to their chemical structure. Electronic effects in the ultraviolet region will effect the dielectric constant at much higher frequencies.

A Rohde and Schwarz slotted line was used to measure dielectric constants in this work. This device is typically used at frequencies between 0.3 and 3.0 GHz. A sliding diode probe samples the electric field in the coaxial line through the longitudinal slot. The diode detector and a standing wave ratio (SWR) meter were used to measure the power along the length of the line. The line was mounted vertically and a shorted sample holder was used to contain the liquid sample. Typically the sample holder was filled to 10 cm with the liquid. Analysis of the data for the real and imaginary parts of the dielectric constants was made using the procedures outlined by von Hippel<sup>10,11</sup>. The standard deviation of the measurements gives  $\pm 0.006$  as an error for the real part of the dielectric constant measurement. Slush baths were used to insure constant sample temperature at 0°C, -78°C, -90°C, -130°C and -158°C. The lowest temperatures used are below the dew point of water and it was necessary to have a dry nitrogen

environment in order to eliminate the condensation of water into the sample or the slotted line.

We have measured the complex dielectric constants of ethane, propane, n-butane, n-pentane, n-hexane, and n-heptane at 1.2 GHz (Table 1). Our measurements agree well with the measurements made at 1 kHz. This is illustrated in Figure 1 in which our data points are plotted over the lines representing the literature values. Our measurements were made at atmospheric pressure; the difference between the vapor pressure of the liquid and 760 Torr being made up with nitrogen gas.

The imaginary part of the dielectric constants, represented as the loss tangents, are found to vary from  $1.3 \times 10^{-3}$  to  $1.0 \times 10^{-4}$ . The uncertainty in the loss tangent measurements, obtained from statistics on each individual measurement, is  $\pm 2.5 \times 10^{-4}$ . While most of the loss tangents are larger than this uncertainty it is not clear that the loss tangents are really represented by these values. Precautions were taken to eliminate the meniscus and to avoid evaporation by using a Teflon plug, but the effectiveness of these procedures is not known. This could be caused by the inability to adequately remove the meniscus above the Teflon plug. There are enough uncertainties that we claim only that the loss tangents of all the hydrocarbon that we have measured are  $\leq 1 \times 10^{-3}$ .

The Kramers-Kronig relationship<sup>12,13</sup> states that if the real part of the dielectric constant is known for all frequencies, the loss tangent at any particular frequency can be determined. The real parts of the dielectric constants of octane, heptane, hexane, and pentane are known to be the same within experimental error at 1 kHz, 1.2 GHz, and  $5.1 \times 10^6$  GHz. Using the Kramers-Kronig relationship and a function which has a perturbation to the ultraviolet side of the sodium D line, it is found that the expected loss tangents for these molecules at 1.2 GHz will be of the order of  $2 \times 10^{-6}$ . The expected loss tangent for frequencies between 8 and 1000 GHz will correspond to a smooth increase, similar to that found by Gelstrophe and Bennett<sup>9</sup>, except without the oscillations.

#### REFERENCES

1. Y. L. Yung, M. Allen, and J. P. Pinto, *Astrophys. J. Supp. Series*, **55**, 465 (1984).
2. J. I. Lunine, D. J. Stevenson, and Y. L. Yung, *Science*, **222**, 1229 (1983).
3. M. Allen, J. P. Pinto, and Y. L. Yung, *Astrophys. J.*, **242**, L125 (1980).
4. G. C. Straty and R. D. Goodwin, *Cryogenics*, Dec., 712 (1973).
5. W. P. Pan, M. H. Mady, and R. C. Miller, *AIChE Journal*, **21**, 283 (1975).
6. R. T. Thompson, Jr. and R. C. Miller, *Adv. Cryog. Eng.*, **25**, 698 (1980).
7. W. G. S. Soaife and C. G. R. Lyons, *Proc. R. Soc. Lond.*, **A370**, 193 (1980).
8. M. G. Gaikwad, R. Chandrasekar, S. K. David, and V. G. Alwani, *Phys. Lett.*, **80A**, 201 (1980).

9. R. V. Gelsthorpe and R. G. Bennett, J. Phys. D, 11, 717 (1978).
10. A. R. von Hippel, Dielectrics and Waves, Wiley, New York (1954) pp 73-77.
11. A. R. von Hippel, ed., Dielectric Materials and Applications, The Technology Press of M.I.T. and Wiley, New York (1954) pp 3-18, 63-73.
12. J. D. Jackson, Classical Electrodynamics, 2nd Ed., Wiley, New York (1975).
13. C. Kittel, Introduction to Solid State Physics, 5th Ed., Wiley, New York (1976.)

**Table 1**

**Dielectric Constants vs. Temperature @ 1.2 GHz**

<u>Temp</u>	<u>Heptane</u>	<u>Hexane</u>	<u>Pentane</u>	<u>Butane</u>	<u>Propane</u>	<u>Ethane</u>
-157					2.006	1.886
-130			2.065	2.011	1.953	1.828
-94			2.020	1.960	1.897	
-75	2.047	2.014	1.976	1.920		
0	1.951	1.916	1.876			
21	1.928	1.889	1.834			

Error Bars  $\pm 0.006$

**Dielectric Constants vs Temperature  
This Work @ 1.2 GHz**

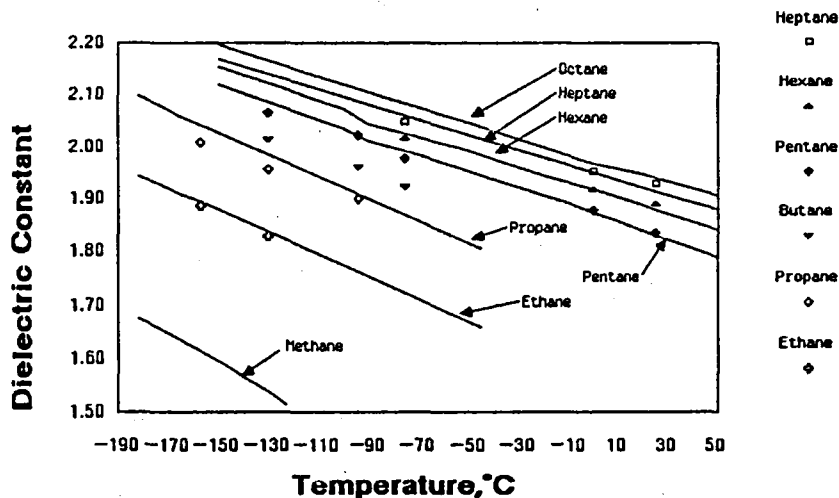


**Figure 1**



## **CHAPTER 7**

### **AEOLIAN PROCESSES**



# THE EFFECT OF PARTICLE SPEED AND CONCENTRATION ON AEOLIAN GRADATION: EARTH, MARS, AND VENUS.

*S. H. Williams and R. Greeley, Department of Geology, Arizona State University, Tempe, Arizona 85287*

Aeolian gradation, the erosion, deposition, and transport of surface materials, is an important part of the geologic cycles on the Earth, Mars and Venus. The mode of aeolian transport that is most capable of causing gradation is *saltation*, in which sand-sized particles are bounced along the surface by the wind. The rate at which gradation occurs and the types of erosional features or bedforms produced are strongly affected by the speed and concentration of particles undergoing saltation.

Three wind tunnels were used in this study: an open-circuit, fan-powered tunnel at ASU that operates under terrestrial conditions (Greeley et al., 1983), an open-circuit wind tunnel powered by gas injection, housed in a very large vacuum chamber at the NASA Ames Research Center allowing operation at martian atmospheric density (Greeley et al., 1981), and a closed-circuit, fan-powered tunnel that operates at venusian atmospheric density, also at NASA Ames (Greeley et al., 1984a). Particle speeds were measured using a particle velocimeter adapted from a USDA Forest Service design (Schmidt, 1977) or by the analysis of high-speed motion pictures. Mean particle speeds and the distribution of particle speeds were determined for several particle sizes and densities, as was saltation flux. Particle concentration at a specific height was calculated from saltation flux and particle speed at that height (Williams and Greeley, 1987).

Some models of saltation hold that there are two populations of particles in the saltation cloud: "successive saltators" that skip continuously along the surface, and lower speed "reptators" that are splashed from the surface by saltation impact and then cease moving (Mitha et al., 1986; and others). Anderson (1987) has developed a model of ripple formation based on the saltator-reptator view in which ripple growth is favored at a wavelength in which the reptation gain to reptation loss ratio is a maximum, typically about six times the average reptation pathlength. It was found in this study that the distribution of particle speeds is more complex than a bimodal model, except for small, light particles (Figure 1). Ripples are observed to form under conditions when there is a poorly-developed bimodal particle speed distribution; therefore, the Anderson (1987) model may be correct, but it is simplistic.

While many environmental factors impede movement of surficial material by the wind (Chepil and Woodruff, 1963), saltation can be considered self-limiting in two cases. The first is when the wind speed is just sufficient to initiate and maintain saltation (saltation threshold). There are too few saltation impacts per unit surface area for saltation to be considered fully developed, if there are many particles on the surface that would saltate if a slight additional amount of energy from a nearby saltation impact were available. The second case is when wind speeds are so high that too much material is moving for there to be uninterrupted saltation trajectories, a condition termed "choking." The geological significance of each self-limiting case depends on surface and environmental conditions. The onset of choking conditions are characterized by a reduction in the rate of increase of saltation flux with increasing wind speed because momentum that would have been transferred directly from the wind to the surface via the saltating particle is scattered by mid-air collisions in the saltation cloud. The odds of mid-air collisions become good when the particle concentration, represented as a mean-free-path distance, becomes similar in length to the portion of the saltation trajectory at that concentration, essentially the saltation pathlength (Williams and Greeley, 1987).

When choking conditions prevail, particle trajectories are randomized by mid-air collisions resulting in there being no average reptation pathlength. The ripple formation models of Bagnold (1941) and Anderson (1987) indicate that no ripples could form under such conditions; a prediction substantiated by field and wind tunnel observations (Williams, 1987). Thus, the onset of choking conditions represents a change in flow regime, analogous to that which in water is represented by the change from ripples to plane beds.

Saltation trajectories are large on Mars and particle speeds are high, a condition that retards full saltation development because of the low number of saltation impacts on the surface at wind speeds near saltation threshold. Wind speeds at least 10% above saltation threshold are required for full development of saltation (Williams and Greeley, 1986). The amount of abrasion per saltation impact is large because of high particle kinetic energies; however, the large saltation trajectories spread the zone of abrasion through a much greater vertical extent than on the Earth. Erosional notches of the type formed on the Earth where the effects of saltation flux and particle speed are maximized (Sharp, 1964) are not expected on Mars because of the increased martian saltation trajectory height. Choking is not expected to occur under martian conditions. Rocky surfaces have saltation clouds even more diffuse due to increased saltation rebound from impact on the rocks.

The situation on Venus is reversed; both particle trajectories and speeds are small. Saltation readily becomes fully developed, yet it chokes at wind speeds only ~2 times saltation threshold, as opposed to ~5 times threshold under terrestrial conditions (Williams, 1987). Aeolian abrasion is restricted to a zone within a few centimeters of the surface. Ripples are not expected because of short particle trajectories and commonplace choking conditions; none are observed in wind tunnel experiments under venusian atmospheric density (Greeley et al., 1984b).

## REFERENCES

- Anderson, R. S., 1987, A theoretical model for eolian impact ripples, California Institute of Technology, Basic and Applied Physics Brown Bag Preprint Series, BB-56, 36 pp.
- Bagnold, R. A., 1941, *The Physics of Blown Sand and Desert Dunes*, Methuen, London, 265 pp.
- Chepil, W. S., and N. P. Woodruff, 1963, The physics of wind erosion and its control, *Advances in Agronomy*, 15, p. 211-302.
- Greeley, R., B. R. White, J. B. Pollack, J. D. Iversen, and R. N. Leach, 1981, Dust storms on Mars: Considerations and simulations, in *Desert Dust: Origin, Characteristics, and Effect on Man*, edited by T. Pewe, *Special Papers of the Geological Society of America*, 186, p. 101-121.
- Greeley, R., S. H. Williams, and J. R. Marshall, 1983, Velocities of windblown particles in saltation: Preliminary laboratory and field measurements, in *Eolian Sediments and Processes*, edited by M. E. Brookfield and T. S. Ahlbrandt, Elsevier, Amsterdam, p. 133-148.
- Greeley, R., J. Iversen, R. Leach, J. Marshall, B. White, and S. Williams, 1984a, Windblown sand on Venus: Preliminary results of laboratory simulations, *Icarus*, 57, p. 112-124.
- Greeley, R., J. R. Marshall, and R. N. Leach, 1984b, Microdunes and other aeolian bedforms on Venus: Wind tunnel simulations, *Icarus*, 60, p. 152-160.



- Mitha, S., M. Q. Tran, B. T. Werner, and P. K. Haff, 1986, The grain-bed impact process in aeolian saltation, *Acta Mechanica*, 63, p. 267-278.
- Schmidt, R. A., 1977, *A System That Measures Blowing Snow*, USDA Forest Service Research Paper RM-194, 80 pp.
- Sharp, R. P., 1964, Wind-driven sand in Coachella Valley, California, *Bulletin of the Geological Society of America*, 75, p. 785-804.
- Williams, S. H., 1987, A comparative planetological study of particle speed and concentration during aeolian saltation, unpublished Ph.D. dissertation, Arizona State University.
- Williams, S. H., and R. Greeley, 1986, Wind erosion on Mars: Impairment by poor saltation cloud development (abs.), *Lunar and Planetary Science Conference*, 17th, p. 952-953.
- Williams, S. H., and R. Greeley, 1987, Particle speed and concentration in the saltation cloud: Full saltation development and choking (abs.), *Lunar and Planetary Science Conference*, 18th, p. 1088-1089.

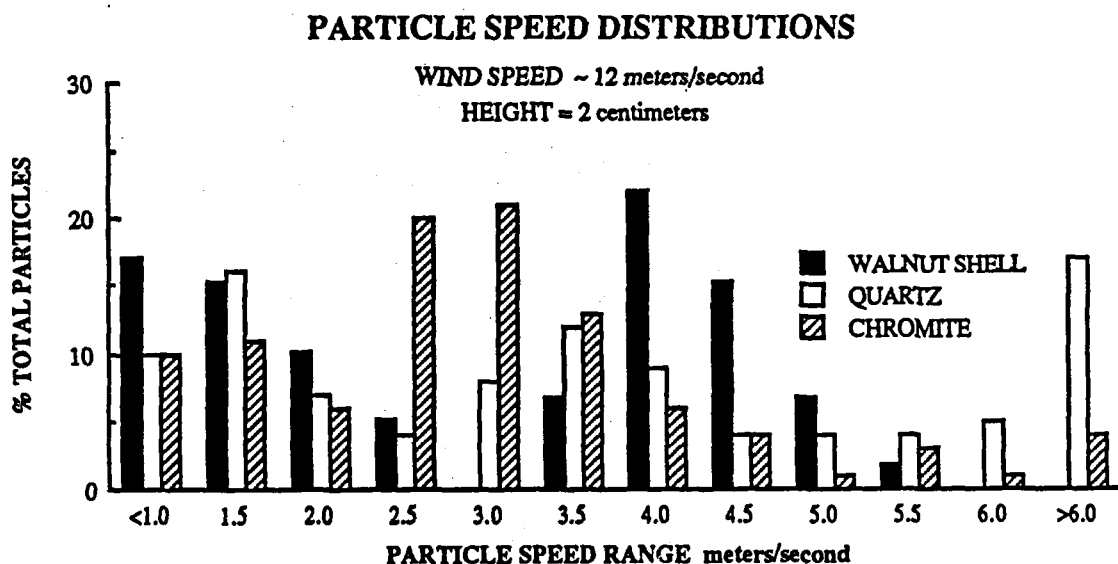


Figure 1. Particle speed distributions for particles of three different densities: walnut shell, ~1.1; quartz, ~2.7; and chromite, ~4.5 grams/(centimeter)<sup>3</sup>. Particle size range is 170-211 microns. The values on the abscissa are particle speed ranges between the value shown and the next slowest speed, except for the endpoints. Only the walnut shells have a bimodal particle speed distribution.

## AEOLIAN SORTING OF HEAVY MINERALS ON VENUS

R. Greeley, J.R. Marshall, Department of Geology, Arizona State University, Tempe, AZ 85287, D. Clemens, A. Dobrovolskis, and J. Pollack, NASA-Ames Research Center, Moffett Field, CA 94035

Previous investigations with the Venus Wind Tunnel (VWT) have shown that windblown sand in an atmosphere of equivalent density to that of Venus will produce small-scale aeolian structures referred to as microdunes (Greeley *et al.*, 1984; Marshall *et al.*, 1984). These have some of the characteristics of full-scale terrestrial dunes, and some characteristics typical of current ripples in water. Microdunes are highly asymmetrical structures with gentle stoss slopes and steep lee faces (slip faces), and they occur as transverse trains of structures with a fairly consistent wavelength of ~20 cm. The structures are very efficient at sorting material according to size: fine sand is concentrated in the crest and on the stoss slope, while coarse sand concentrates on the slip face and within a basal layer (Fig. 1A).

Present investigations with the VWT reveal that microdunes are also efficient in sorting according to mineral density. Relatively heavy particles of sand are concentrated in the same way as fine particles--on the stoss slope and in the crest of the microdune (Fig. 1B). Evidently, the weight of a particle (a function of both size and density) has a complex role in the sorting process.

The VWT is a closed-circuit boundary-layer wind tunnel that can be pressurized with carbon dioxide to produce an atmosphere of equivalent density to that on Venus (0.065 g/cm<sup>3</sup>). It is operated at 30 bar/20°C to achieve the same atmospheric density as that produced by 95 bar/464°C on Venus. The test section allows for a bed of sand ~1.2 m long, 0.2 m wide, and ~0.01 m thick.

In one series of tests, grains of pyrite sand (90-125  $\mu$ m) were mixed with basalt sand (180-250  $\mu$ m) in concentrations of 0.1, 0.25, 1.0, and 10.0 percent. Microdunes developed in these mixtures at a (freestream) wind speed of ~1 m/s, and the pyrite became concentrated on the stoss slopes and in the crests of the structures. Concentrations of pyrite as a function of depth in the microdunes were quantified by weighing samples taken at ~5 mm depth intervals. In all cases, the crests had concentrations in excess of those in the initial beds, and in the case of the 10% pyrite experiment, the concentration in the crest approached 100% after a test duration of only 700 seconds, and a downstream dune migration distance of 0.3 m. Figure 2 shows the concentration of pyrite in microdunes from three initial 10% mixtures with various particle size combinations. It is noteworthy that the basal layers of the microdunes are actually depleted of pyrite with respect to the initial concentrations.

An experiment was also conducted with a mixture of quartz and chromite. An initial concentration of 10% 125-180  $\mu$ m chromite in 125-180  $\mu$ m quartz produced a crest concentration of chromite in excess of 75%. Again, the basal layers of the microdunes showed a depletion of the heavy mineral component. Quartz and chromite mixtures were used to determine the roles played by both particle size and particle density in the sorting process. Two mixtures were tested; in the first, a 50% mixture of 90-125  $\mu$ m chromite with 50% 180-250  $\mu$ m quartz was used to enhance sorting because the heavier mineral was also of the smallest size. Microdune crests did indeed show a concentration of chromite, and the basal layers were depleted with respect to the original mixture. In the second 50%/50% mixture, the sizes of the grains were reversed for the respective minerals. This should have caused some conflict between the attraction of the chromite to the crests because of its greater density, and the attraction to the basal layers because of its larger size. However, the chromite again became concentrated in the crests, but there was no depletion of the basal layers. It appears that particle density takes precedence over particle size in the sorting of materials in microdunes.

The results of the pyrite and chromite experiments suggest that windblown material on Venus will become rapidly sorted according to mineral density. As microdunes migrate over an area of loose sediment, the amount of material "processed" by the structures increases, and a situation can be envisaged in which the surface becomes a 100% enrichment of the heavier minerals in transport. The VWT data suggest that even initial concentrations of <1% may lead

to high surface enrichments with sufficient transport fetch. Such concentrations could lead to changes in the radar reflectivity of a region, although present data are insufficient to permit any speculation on the possible magnitude of this effect.

## References

Greeley, R., J.R. Marshall, and R.N. Leach (1984). *Icarus* 60, 152-160.  
Marshall, J.R., S. Bougan, and R. Greeley (1984). *EOS* 65, 982.

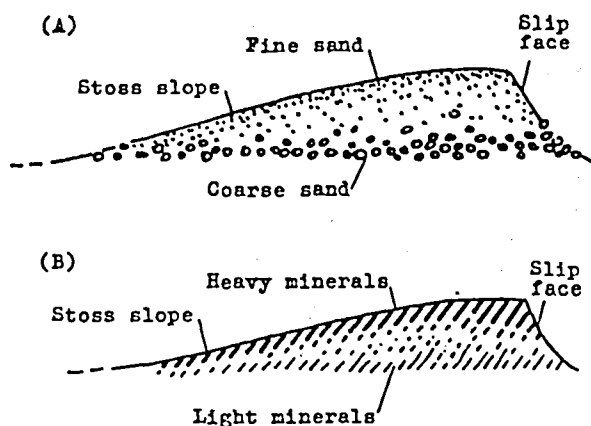


FIGURE 1. Sectional view of microdunes.  
(A) Sorting by particle size.  
(B) Sorting by particle density.

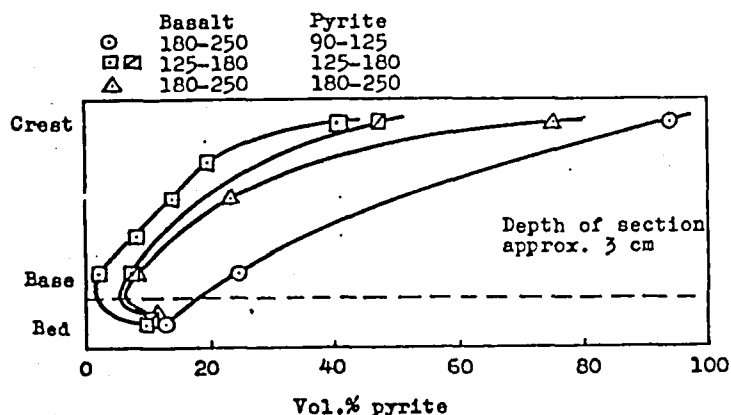


FIGURE 2. Sorting of pyrite in microdunes from an initial 10% concentration.

## MECHANICAL AEOLIAN WEATHERING OF VENUSIAN SURFACE MATERIALS

J.R. Marshall, D.W. Tucker, and R. Greeley

Department of Geology, Arizona State University, Tempe, Az 85287

Laboratory simulations of aeolian action on Venus have shown that rock surfaces acquire an accretionary layer in response to low-velocity impact of particles. The accretionary material is derived from the comminution products of the particles. Tests conducted over wide temperature and pressure ranges show that the accretion is a temperature-dependent phenomenon, but it is independent of atmospheric pressure.

The response of rocks and particles to aeolian action on Venus is investigated with the Venus Simulator, a specially constructed device that impacts single particles against rock targets in a high-temperature, high-pressure carbon dioxide atmosphere. The Simulator is essentially a pressure vessel containing a tube furnace (Fig.1) with access through a small flange at one end. The flange incorporates a quartz window that enables viewing of the impact process. The rock target to be impacted is mounted in a 3 cm-long low-velocity gas gun that is inserted into the furnace through the access port. The impacting particle rests on a mesh at the bottom of the gun (Fig.2) and is projected upward at the target by a momentary gas pulse. After impact, the particle falls to rest on the mesh, and the process is repeated. The impact cycle is 0.5-1.0 seconds. The particle-impelling gas pulse is controlled outside the pressure vessel by a pneumatic system that sets particle velocity and automatically counts the number of impact cycles.

Figure 3 shows the points where data have been acquired within the T,P test field. Experiments were conducted along a high-temperature (737 K) isotherm at atmospheric pressures between 12 and 95 bar to determine if pressure has any effect upon impact phenomena. In addition, experiments were conducted at conditions representative of the highest and lowest elevations of Venus. A low-temperature control test is also shown in Figure 3. All experiments subjected flat, polished tholeiitic basalt targets to 100,000 impacts. The impacting particles were 3 mm diameter angular clasts derived from crushing the same basaltic material. Impact velocity was in all cases between 0.5 and 1.0 m/s as determined by high-speed video filming (a velocity range to be expected for particles of this size on Venus).

With the exception of the low-temperature control sample, all basalt targets exhibited a lack of abrasion as a result of impact, and instead, they developed a layer of accretionary material that was derived from the damaged corners and edges of the impacting particles. Typically, the accretionary material was a few microns thick at most (as determined by SEM), and consisted of slab-like lumps of material of an apparently coherent nature with friable and fragmentary material at their rims (Fig.4). At present, the mechanism of adhesion is unknown, but it appears to prevail only at elevated temperatures. Neither the mode nor the extent of adhesion appeared to be influenced by atmospheric pressure. The slab-like configuration of much of the accretionary material suggests that plastic deformation may be

involved in the process of transfer from particle to target.

The basalt target from the low-temperature, low-pressure control test was abraded by the impacting particle, and did not have an accretionary layer.

The initially angular particles were very slightly rounded by impact, and SEM analysis revealed that the abraded areas (that had contributed material to the targets) consisted of relatively deep depressions produced by chipping, with smoothed intervening asperities that appeared to have an altered surface layer produced by repeated microfracturing, plastic deformation, and some reincorporation of comminution fragments. The surface textures showed no variation with atmospheric pressure, and surprisingly, did not appear to be influenced by temperature either.

The results from these experiments involving 100,000 impacts on each target are presently being confirmed by a test sequence involving only 20,000 impacts. The latter is being conducted to determine, with many more data points, where the boundary lies between accretion and abrasion within the T,P field in Figure 3.

For Venus, the experimental results suggest the following: 1) Aeolian particles on Venus are abraded by impact even at very low velocities ( $<1$  m/s), 2) Rocks that are impacted by aeolian material may develop very thin veneers of material derived from the impacting particles. This may change the surface physical properties of the rocks (e.g., specular reflectance) as well as surface chemistry, 3) Liberation of aeolian comminution products (e.g., micron-size material) into the venusian atmosphere may be limited because some of the material tends to remain at the site of an impact where it forms an accretionary layer.

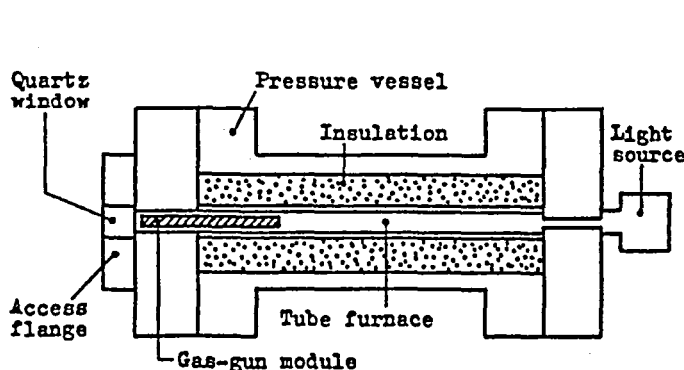


FIGURE 1. Venus Simulator

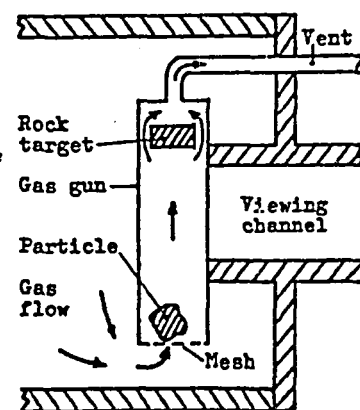


FIGURE 2. Gas gun

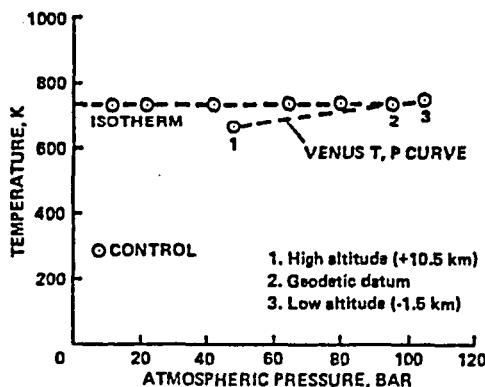


FIGURE 3. T,P test field

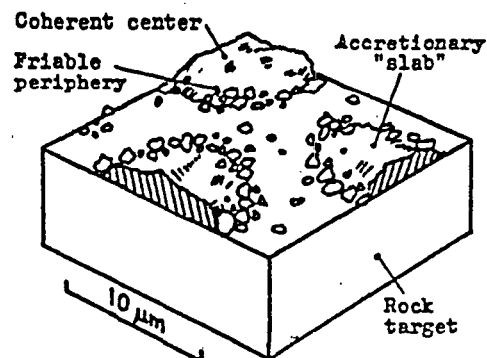


FIGURE 4. Accretionary material

**COMPARISON OF AEOLIAN SURFACE ROUGHNESS MEASURED IN A FIELD EXPERIMENT AND A WIND TUNNEL SIMULATION; Robert Sullivan and Ronald Greeley, Department of Geology, Arizona State University, Tempe, AZ, 85287.**

The objective of this study is to determine how aeolian roughness measured over scale models in wind tunnels correlates with actual values of aeolian roughness measured in the field. Motivation for this study derives from the desire to determine aeolian roughness,  $z_0$ , at the Viking Lander sites on the surface of Mars. Spacecraft imagery of the martian surface returned by Mariner 9 and Vikings 1 and 2 reveals the widespread occurrence of surface features associated with aeolian activity: albedo wind streaks associated with craters and other topographical features [1,2,3]; dunes within craters, and surrounding the north polar ice cap [4,5,6]; and yardangs [7]. Temporal variation of wind streak patterns and recurring dust storm activity indicate to many workers that aeolian processes currently dominate surface activity on Mars [e.g., 8]. Much investigation into martian aeolian processes has necessarily been conducted in regional frameworks imposed by orbital spacecraft data sets, although local wind velocity data have been returned from two surface locations by Viking Lander spacecraft [9,10,11]. The difficulty in integrating the Lander meteorological data sets into investigations of martian aeolian processes stems from wind velocity being measured at only the single ~1.6 m elevation of each Lander's meteorology boom. Without velocities measured simultaneously at a second elevation, or knowledge of  $z_0$  for the surface surrounding each Lander, an infinite number of wind profiles can be fit through each wind velocity data point. This wind profile ambiguity is unfortunate, because the Viking Lander sites are the only locations capable of providing "ground-truth" for regional investigations of martian aeolian processes carried out with orbital data sets. Determination of  $z_0$  for the Viking Lander sites might eventually be accomplished by a sufficiently sophisticated scale model simulation in a wind tunnel. As a first step toward this goal, the current study was undertaken to determine how well scale models in wind tunnels can predict full-scale field values of  $z_0$ . This study consists of: (1) a field experiment measuring  $z_0$  over a variety of surfaces of known, controlled geometry; (2) a wind tunnel scale model simulation of the field study, measuring scaled values of  $z_0$ ; (3) a comparison between the results of the field and wind tunnel studies, with an evaluation of the ability of the wind tunnel to predict full-scale field results.

The main requirement of the field experiment for this study is that its surface geometry should be sufficiently controlled to be accurately modelled in the wind tunnel. All surface roughnesses sampled in this study consist of arrays of overturned 12-qt. buckets placed on a dry lake bed. For the purposes of this study, requirements of a good field site include: (1) a smooth, stable surface; (2) frequent windy conditions; (3) a consistent prevailing wind direction; and (4) sufficient upwind fetch of the surface into the prevailing wind direction. The field site chosen for this study was the eastern section of Lucerne Dry Lake, CA. The field experiment was conducted from 12 March - 13 May, 1987. Wind profiles were measured over bare playa and three roughness arrays of overturned 12-qt. buckets. Array 1 had a roughness element spacing of 3.2 m and a roughness fetch of 89.6 m; array 2 had a roughness element spacing of 1.6 m and a roughness fetch of 40.0 m; array 3 had a roughness element spacing of 0.8 m and a roughness fetch of 16.0 m. Wind velocity was measured at ten heights (0.24-15.0 m) by 3-cup anemometers. Temperature was monitored by shrouded iron-constantan thermocouples at heights of 1 m and 15 m. Fourteen hours of valid data were recorded over array 1 from 1-4 April. Twelve-and-one-half hours of valid data were obtained over array 2 from 10-11 April. Eight-and-three-quarters hours of valid data were recorded over the bare playa from 2-13 May. Richardson numbers for each velocity interval were calculated with the temperature data, and thermally neutral intervals were identified (required for validity of the wind profile log-law). The wind profile was plotted for each thermally neutral period and internal boundary layers characteristic of each roughness array were identified. Only those anemometers immersed within the internal boundary layers were used in the final determinations of  $z_0$  and  $U_*$ . Values of  $z_0$  for each array, obtained by applying a least-squares

fit to the internal boundary layer profiles, are found to increase with increasing roughness element density.

Wind profiles were measured in the wind tunnel with a 60 cm 30-port pitot-tube "rake." The bare playa was simulated in the wind tunnel with smooth masonite flooring. The overturned buckets of arrays 1, 2, and 3 were simulated at 1/10 and 1/20 scales by dowel cylinders cut to appropriate lengths. The matrix of experimental runs was as follows: 2 scales (1/10 and 1/20) x 3 arrays x 5 freestream velocities x 3 trials each = 120 runs. The data was reduced in as similar a manner as possible to the field data reduction. Since the lowest anemometer in the field study was located at the height of the top of the roughness elements (~0.24 m), the base of the usable profile for the wind tunnel data was taken to be port 20 for 1/10 scale runs (.0255 m), and port 24 for 1/20 scale runs (.0135 m). From these base points the profiles were extended upward through the adjacent points until the data began to deviate from these lines (extending into the complex freestream transition zone). These points of deviation defined the tops of the usable profile sections. For each profile the value of  $z_0$  was determined by performing a least-squares fit of the appropriate points.

A comparison between the wind tunnel values for  $z_0$  over each array (multiplied by the inverses of their scales) and the measured field values is presented in figure 1. Wind tunnel  $z_0$  values for each array at each scale are averages of five freestream runs. The results lie in a straight line but do not suggest a 1:1 correspondence. A least-squares regression results in

$$z_{0 \text{ field}} = 0.0966 \cdot (z_{0 \text{ model}} \cdot \text{scale}^{-1})^{0.6464} \quad (1)$$

Although equation (1) fits the results closely, a simpler 1:1 correspondence between  $z_{0 \text{ model}} \cdot \text{scale}^{-1}$  and  $z_{0 \text{ field}}$  remains an appealing idea. Deviation of the array 1 and array 2 results from the 1:1 correspondence relation might be considered acceptable, but the discrepancy of the array 3 results would require explanation. A possible source for this discrepancy is differing amounts of flow compression in the field and in the wind tunnel among the densely spaced roughness elements of array 3. In the field, much of the air flow below the height of the roughness elements of array 3 possibly would be forced to "leak" out the sides of the array. This is not possible in the wind tunnel, since the tunnel walls contain the flow. This effect might result in greater flow compression among the roughness elements in the field than in the wind tunnel, effectively increasing wind tunnel values of  $z_0$ .

At the Viking Lander sites on Mars calculations of  $U_*$  must rely on only a single velocity measurement at a height of 1.6 m, and a knowledge of  $z_0$ . The ability of equation (1) to predict accurate values of  $U_*$  in these circumstances is evaluated in Table 1. Rows 1,2 represent values of  $z_0$  and  $U_*$  calculated using all heights and velocities occurring within the internal boundary layers for each array. Row 3 represents values of  $U_*$  calculated with the same  $z_0$  values, but with only the single velocity measured at a height of 1.45 m. Agreement is good between  $U_*$  values measured at this single height and the average  $U_*$  values for the internal boundary layers. Row 4 represents  $z_0$  values predicted for each array by the wind tunnel scale models and equation (1). The agreement between the wind tunnel predictions and the actual field values of  $z_0$  is very consistent, indicating that equation (1) is a good description of the wind tunnel vs. field correspondence. Row 5 represents  $U_*$  values for each array calculated with the wind tunnel results, equation (1), and the single velocity measured at 1.45 m. Agreement between  $U_*$  calculated with all internal boundary layer anemometers per profile (with  $z_0$  equally well-defined), and  $U_*$  values calculated with  $z_0$  predicted by wind tunnel scale models, equation (1) and the single velocity at  $z = 1.45$  m is excellent. Average error is 0.9%. If similar comparisons are made assuming a simple 1:1 correspondence (table 1, rows 6-7), errors for predicted  $U_*$  values are larger, averaging 17.9%.

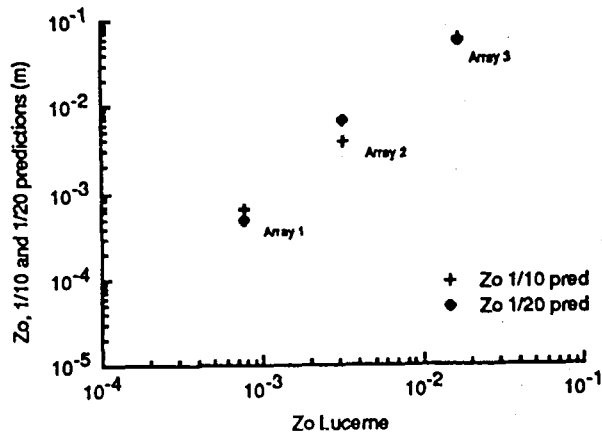


Figure 1. Correlations of  $z_0$ . Full-scale field values of  $z_0$  plotted against wind tunnel scale model predictions of  $z_0$ . Scale model predictions of  $z_0$  are obtained by multiplying wind tunnel values of  $z_0$  for each array by the inverse of its scale (10 or 20).

TABLE 1. Predictions of  $z_0$  and  $U_*$  values.

		<u>Array 1</u>	<u>Array 2</u>	<u>Array 3</u>
1	$z_0$ (m) field values	.000775	.00313	.0168
2	$U_*$ (m/sec)	.402	.648	1.011
3	$U_*$ (m/sec) calculated with anem. 7 height, speed, and row 1 $z_0$	.400	.646	1.021
4	$z_0$ (m) predicted by: equation (1) applied to wind tunnel results	.000776	.00323	.0155
5	$U_*$ (m/sec) calculated with predicted $z_0$ (row 4), anem. 7 height, speed	.400	.649	1.003
5E	$U_*$ Error	0.5%	0.5%	1.8%
			(average error = 0.9%)	
6	$z_0$ (m) predicted by: a 1:1 correspondence applied to wind tunnel results	.000574	.00521	.059
7	$U_*$ calculated with predicted $z_0$ (row 6), anem. 7 height, speed	.384	.704	1.422
7E	$U_*$ Error	4.5%	8.6%	40.7%
			(average error = 17.9%)	

References. [1] Sagan, C., Veverka, J., Fox, P., Dubisch, R., French, R., Gierasch, P., Quam, L., Lederberg, J., Levinthal, E., Tucker, R., Eross, B., and Pollack, J. B., *J. Geophys. Res.*, 78, 4163-96, 1973. [2] Sagan C., Veverka, J., Fox, P., Dubisch, R., Lederberg, J., Levinthal, E., Quam, L., Tucker, R., Pollack J. B., and Smith, B. A., *Icarus*, 17, 346-372, 1972. [3] McCauley, J. F., *J. Geophys. Res.*, 78, 4123-37, 1973. [4] Cutts, J. A., Blasius, K. R., Briggs, G. A., Carr, M. H., Greeley, R., and Masursky, H., *Science*, 194, 1329-37, 1976. [5] Breed, C. S., Grolier, M. J., and McCauley, J. F., *J. Geophys. Res.*, 84, 8183-204, 1979. [6] Tsoar, H., Greeley, R., and Peterfreund, A. R., *J. Geophys. Res.*, 84, 8167-80, 1979. [7] Ward, A. W., *J. Geophys. Res.*, 84, 8147-66, 1979. [8] Greeley and Iversen, *Wind as a Geological Process*, Cambridge Univ. Press, 1985. [9] Hess, S. L., Henry, R. M., Leovy, C. B., Ryan, J. A., and Tillman, J. E., *J. Geophys. Res.*, 82, 4559-74, 1977. [10] Ryan, J. A., Henry, R. M., Hess, S. L., Leovy, C. B., Tillman, J. E., and Walcek, C., *Geophys. Res. Lett.* 5, 715-18, 1978. [11] Ryan, J. A., and Henry, R. M., *J. Geophys. Res.*, 84, 2821-29, 1979.



WIND TUNNEL  
SIMULATION OF PLANETARY EOLIAN PHENOMENA

James D. Iversen

The boundary layer wind tunnel has proved to be a useful instrument for unraveling the mysteries of the physics of saltation. No wind tunnel experiment, however, is ever equal to "the real thing", i.e., the natural or full-scale phenomenon which is to be simulated. There are, however, some analyses which can be performed to determine how well the simulation approximates nature.

For the situation in which a small-scale model is employed in a wind tunnel to simulate the larger scale natural saltation, for example, of the drifting of snow or sand around a topographic obstruction, it is necessary to run a complex series of experiments in order to determine the effects of the various scaling parameters (see, for example, Iversen 1982).

On the other hand, for studying the physics of the saltation process, the wind tunnel is used, not to model the natural phenomenon in miniature, but to study a two-dimensional "slice" of the natural three-dimensional saltation field. The constricting presence of the wind tunnel walls and ceiling act to limit the realism of the modeling. The side-walls restrict the lateral motion of the wind so that major time-dependent fluctuations in the wind direction are not possible to the same scale they are in the field. The streamwise turbulence characteristics of the wind are also different in the wind tunnel from the natural atmosphere. The differences in turbulence characteristics, however, are not as serious if the particles are sufficiently large ( $>200\ \mu\text{m}$ ) so that their trajectories are not significantly affected by turbulence. It is important to try to simulate the atmospheric boundary layer wind profile and turbulence structure in the wind tunnel as closely as possible (see, for example Tieleman 1982, Cermak 1982, Cook 1982). We have attempted to do that in our wind tunnels with combinations of sufficient test section length and

turbulence generators (Iversen, 1982; Greeley et al, 1980, 1984).

Additional simulation parameters of importance in studying saltation physics are:

1. Density ratio  $\rho_p/\rho$
  2. Suspension - saltation ratio parameter  $U_f/u_{*t}$
  3. Threshold speed ratio  $u_*/u_{*t}$
  4. Reynolds number  $u_*^3/gv$
  5. Wind tunnel Froude number  $u_*^2/gH$  or  $U_\infty^2/gH$
1. The density ratio  $\rho_p/\rho$

We have shown as a result of the Venus wind tunnel threshold experiments that the dimensionless saltation threshold friction speed seems to be a continuous function of density ratio (Iversen et al 1987). For large particles ( $D_p > 200 \mu m$ ) and large grain friction Reynolds numbers ( $u_{*t} D_p/v > 10$ ) the Bagnold threshold coefficient  $A = (\rho u_{*t}^2 / (\rho_p - \rho) g D_p)$  varies from close to 0.1 at large values of particle to fluid density ratio ( $\rho_p/\rho > 1000$ ) to about 0.2 for particles in liquids ( $\rho_p/\rho$  approaching 1). The reason for the variation of the threshold parameter with density ratio is apparently due to relative variation of the force with which airborne particles impact with stationary particles. That variation of impact force probably also affects the characteristics of the saltation layer at speeds higher than threshold. Since the mass transport rate near threshold is a strong function of the ratio  $u_*/u_{*t}$ , the transport rate would also be at least indirectly a function of  $\rho_p/\rho$ .

2. Suspension - saltation parameter  $U_f/u_*$

This parameter is extremely important. The root-mean-square of the vertical component of the time-dependent turbulent fluctuation in the boundary layer is close to the value of the friction speed  $u_*$ . If the terminal speed  $U_f$  is much less than  $u_*$ , then the turbulent fluctuations will greatly affect the particle trajectory and the particle is said to be in suspension. If,

on the other hand, the terminal speed - friction speed ratio  $U_f/u_{*}$  is much larger than one, the particle trajectory is little affected by turbulence and the particles are in saltation. The surface bed-form features are thus expected to be strong functions of this ratio as well as the friction speed ratio  $u_{*}/u_{*t}$  and the particle size distribution.

### 3. Threshold speed ratio $u_{*}/u_{*t}$

This ratio is important for determination of the mass transport rate and the portion of the particles which may be in saltation as opposed to suspension. It is easily adjusted by changing the wind tunnel speed.

### 4. Roughness Reynolds number $u_{*}^3/gv$

The aerodynamic roughness in saltation is generally considered to be proportional to  $u_{*}^2/g$  (Owen, 1964). Thus a roughness Reynolds number can be defined as  $u_{*}^3/gv$ . The boundary layer wind speed profile is a function of the roughness height  $u_{*}^2/g$  but the role of viscosity  $v$  in controlling the profile in the presence of saltation is not known with certainty. Kind (1976, 1986) considers the profile to be independent of Reynolds number for values of  $u_{*t}^3/2gv \geq 30$ .

### 5. Wind tunnel Froude number $u_{*}^2/gH$ or $U_{\infty}^2/gH$

It would seem to be important, if the natural process of saltation is to be simulated in an ideal fashion in the wind tunnel, that the mass transport  $q$  should be independent of the streamwise distance  $x$  over a significant streamwise portion of the saltation bed. Owen and Gillette (1985) have performed an interactive analysis of boundary layer development over a saltating bed in a wind tunnel. They derive a constraint on tunnel size based on tunnel Froude number. Their conclusion is that for values of Froude number  $F = U_{\infty}^2/gH \leq 20$ , the friction speed variation with downwind distance  $x$  should be very small ( $u_{*}$  nearly uniform) except very near the windward edge of the bed ( $U$  is the wind tunnel free stream speed, and  $H$  the test section height). In regions

where the streamwise variation of friction speed is negligible, the mass transport variation should be also, provided the lag distance between mass transport  $q$  and friction speed  $u_*$  is correspondingly small.

Owen and Gillette (1985) performed saltation experiments in a small wind tunnel to determine friction speed as a function of distance along the bed. As Froude number  $F$  increases (by increasing wind speed or reducing tunnel size), the portion of the saltation bed for which the friction speed and thus the mass transport is uniform decreases.

We have measured saltation transport as a function of streamwise distance in the Mars wind tunnel (Leach, 1984). At a pressure of one atmosphere ( $F=6.1$ ), the rate of mass transport is quite constant with streamwise direction. For very low pressures corresponding to the surface of Mars, however, the mass transport rate increases with downstream distance for large Froude numbers as predicted by Owen and Gillette. Our results for threshold at low atmospheric pressure are not invalidated even at large Froude numbers, however, because these experiments do not involve the measurement of general saltation characteristics. Those experiments which do involve a saltation layer, such as particle trajectory measurements, may be representative only of the upwind edge of a saltating field if the tunnel free stream speed exceeds about 14.4 m/s (corresponding to minimum threshold at pressures  $> 100$  mb).

The operation of the Venus wind tunnel is closer to ideal, because of the much higher pressures, even though the physical size of the tunnel is much smaller. The threshold wind speed for all operating pressures above 5 bars is far below the uniform saltation boundary. The marginal wind speed of 5.4 m/s is higher than the wind speed for the usual experiment and thus the saltation layer is always expected to be macroscopically uniform in the streamwise direction (discounting the local effects of ripples and dunes).

## References

- Cermak, J. E. (1982) Physical modeling of the atmospheric boundary layer in long boundary layer wind tunnels. T. A. Reinhold, ed. Wind Tunnel Modeling for Civil Engineering Applications, Cambridge University Press, 97-125.
- Cook, N. J. (1982) Simulation techniques for short test-section wind tunnels: Roughness, barrier and mixing device methods. T. A. Reinhold, ed. Wind Tunnel Modeling for Civil Engineering Applications, Cambridge University Press, 126-136.
- Greeley, R., J. D. Iversen, R. N. Leach, J. Marshall, B. White, S. Williams. Windblown sand on Venus: Preliminary results of laboratory simulations. Icarus, Vol. 57, 1984, pp. 112-124.
- Greeley, R., R. Leach, B. White, J. D. Iversen, J. Pollack. Threshold wind-speeds for sand on Mars: Wind tunnel simulations. Geophysical Research Letters, Vol. 7, 1980, pp. 121-124.
- Iversen, J. D. (1982) Small-scale modeling of snow-drift phenomena. T. A. Reinhold, ed. Wind Tunnel Modeling for Civil Engineering Applications, Cambridge University Press, 522-545.
- Iversen, J. D., R. Greeley, J. R. Marshall, J. B. Pollack. (1987) Aeolian salutation threshold: The effect of density ratio. Sedimentology, Vol. 34, 699-706.
- Kind, R. J. (1976) A critical examination of the requirements for model simulation of wind-induced erosion deposition phenomena such as snow drifting. Atmospheric Environment, 10, 219-227.
- Kind, R. J. (1986) Snowdrifting: A review of modelling methods. Cole Regions Science and Technology, 12, 217-228.
- Leach, R. (1984) Private communication.

- Owen, P. R. (1964) Saltation of uniform grains in air. Journal of Fluid Mechanics, 20, 225-242.
- Owen, P. R. and D. Gillette. (1985) Wind tunnel constraint on saltation. O. E. Barndorff-Nielsen, J. T. Moller, K. R. Rasmussen, B. B. Willetts, eds. Proceedings of International Workshop on the Physics of Blown Sand, Memoirs No. 8, Vol. 2, Aarhus University, Denmark, 253-269.
- Tieleman, H. W. (1982) Simulation criteria based on meteorological or theoretical considerations. T. A. Reinhold, ed. Wind Tunnel Modeling for Civil Engineering Applications, Cambridge University Press, 73-96.

## SEMI-QUANTITATIVE REMOTE SENSING OF AEOLIAN TERRAINS USING A LINEAR MIXING MODEL

G. BLOUNT, R. GREELEY, P.R. CHRISTENSEN AND N. LANCASTER,  
*Dept. of Geology, Arizona State University, Tempe, Arizona, 85287*

Techniques are being examined which will allow for the remote identification of aeolian sand source areas, transportation paths and deposition sites and to discriminate between active and inactive windblown sediments. The ability to assess the history of aeolian deposits and to determine their degree of current surface activity is critical to the forthcoming Mars Observer Mission, not only for addressing the general "climate" goals of the mission, but also for the interpretation of surface landforms and compositions. In order to develop an understanding of the martian surface, it is desirable to be able to use remote sensing data to determine surface aeolian activity, source areas, transport paths and depositional history. These goals are being approached by computer simulations of aeolian mixing trends at a terrestrial test site, the Gran Desierto of Sonora, Mexico. Field studies of this area have been used to provide an empirical check on the derived results.

Three major research tasks are being pursued; 1) field studies of the Gran Desierto to determine the current dynamic state of the area, 2) laboratory analysis of samples from provenance sites and their resulting aeolian products and 3) computer modeling of aeolian mixing trends using LANDSAT Thematic Mapper (TM) data of the test area in conjunction with a linear mixing model (Adams, Smith and Johnson, 1986).

The 5,700 km<sup>2</sup> study area is bounded by the Colorado River delta on the west; granitic mountain ranges to the north, the Cenozoic Pinacate volcanic shield to the east and the northern shore of the Gulf of California on the south (Lancaster et al., 1987). Sediment source areas, transportation paths and deposition sites have been identified at regional control points.

Representative samples have been gathered at more than 200 ground-controlled locations. Surface aeolian activity has been assessed at more than 150 locations. Major geologic and stratigraphic relationships have been identified for most of the study area. Estimates of vegetative cover which may affect the spectral signatures of ground locations have been performed. Field observations indicate that at least three discrete sand populations exist within the Gran Desierto: 1) coarse fluvial sands derived from the adjacent Colorado River delta, 2) coarse alluvial sands derived locally from granitic inselbergs within and along the margins of the sand sea and 3) fine-grained quartz sands with substantial carbonate fractions derived from the Gulf of California. Substantial mixing has occurred between these units in many areas. These sand populations and their unique source areas are compositional end-members which undergo various degrees of mixing during the erosion, transportation and deposition processes they undergo.

Sediment variables which may affect the TM spectra have been quantified by laboratory work on samples including grain-size analysis, compositional point-counts as a function of grain-size, optical microscope examination of all samples and scanning electron microscopy for selected samples. These analysis support the field impression of discrete sand populations superposed in one geographic location. Furthermore, examinations of grain coatings and frostings indicates that the sand populations were emplaced at different times in the geologic past. An examination of the Gran Desierto therefore, does not simply provide an understanding of a single geologic episode, but rather of a series of geologic processes whose products converge and mix at a single geographic location.

The linear mixing model of Adams, Smith and Johnson (1986) has been used to generate "concentration images" of individual spectral end-members. These processed image products have been correlated with the empirical data gathered by field and laboratory studies. Preliminary results have been described by Blount et al. (1987a). By utilizing the linear mixing model approach it is possible to define the  $n$ -dimensional mixing space (within the TM spectral data) for each compositional end-member ( $n$ ) and its daughter aeolian products. Deviations from these pure, that is 100% saturated, spectral signatures can be interpreted as mixing

vectors along which sediments will travel as they are transported farther away from a source area. The mixing model thus describes a series of mixing lines within the spectral data, along which aeolian materials will move. The position of a TM pixel within the spectral mixing space determines the relative proportion of each end-member component present. Computer modeling of aeolian mixing trends shows that the discrete sand populations discussed previously can be separated spectrally and their dynamic history (provenance, transport and deposition sites) determined from remote sensing data. Fourteen end-member groups have been tested based on combinations of plagioclase granite, microcline granite, basalt, diorite, carbonate sand, active quartz sand, inactive quartz sand, mesquite vegetation, creosote vegetation and macroscopic shade. Predicted concentration values are currently being correlated with field data. Initial results show that the linear mixing model is capable of discriminating all major spectral classes in the field area including variations arising from different sand populations.

The macroscopic shade end-member has proved useful for identifying small-scale superposed aeolian bedforms which were previously unresolvable at TM spatial resolution (Blount and Greeley, 1987b). The bedforms of interest are not sub-pixel (30 meters) in size, but have been unresolvable as individual morphologic units because the shade they produce (on low-angle,  $<34^\circ$ , slopes) is at the noise level of the TM instrument. The intensity of the macroscopic shade component is largely due to variations in local illumination geometry on the ground. Small bedforms which are spectrally identical to the surrounding sands will nevertheless induce variations in lighting geometry. Since the mixing model approach requires the simultaneous solution of  $n$  equations (where  $n$  = the number of end-members present) for each pixel, the bedform-induced shade variations are effectively correlated on all six of the VNIR bands and can be displayed in the shade concentration image. The existence and orientation of these newly resolved features has been confirmed by groundtruth.

It has been found that several of the compositional end-members are not spectrally unique within the thematic mapper bandpasses. High-resolution laboratory spectra have therefore been obtained from 25 representative samples to assess the level of spectral resolution required for mixing discrimination. Ambiguous units include plagioclase/microcline granites, carbonate sand/granite sand and basalt/diorite.

Approaches and techniques are being identified which can be successfully employed to use remote sensing data for the determination of the dynamic state and recent geologic history of surface aeolian deposits. Results from this study are being assessed in terms of the potential data to be obtained from the Mars Observer mission, particularly from the VIMS and TES instruments. Composition and grain-size variations within the sample set are being correlated with the concentration values predicted by the mixing model images. The empirical variables responsible for differences in predicted concentration level will be quantified. Spectral and spatial limitations of the technique are also being identified. Recommendations can then be made regarding strategies for the interpretation of remote sensing data from the widespread aeolian terrains of Mars.

#### References Cited:

- Adams, J.B., Smith, M.O. and Johnson, P.E., 1986, *J. Geophys. Res.*, v. 91, 8098-8400
- Blount, H.G., Greeley, R. and Christensen, P.R., 1986, *G.S.A. Abs. with Prog.*, v. 18, n. 6, 544
- Blount, G., Greeley, R., Lancaster, N., Christensen, P.R. and Arvidson, R., 1987a, *LPSC* 18, pt. 1, 95-96
- Blount, G. and Greeley, R., 1987b, *Bull. Amer. Astronomical Soc.*, v. 19, n. 3, 847
- Lancaster, N., Greeley, R. and Christensen, P.R., 1987, *Earth Surf. Processes and Landforms*, v. 12, 277-288



## VARIATIONS IN SURFACE SHEAR STRESS OVER A SMALL AEOLIAN DUNE

*N. Lancaster, Department of Geology, Arizona State University, Tempe, Arizona 85287*

The shear stress imparted by the wind on the surface of aeolian sand dunes is an important quantity, which ultimately determines their size, shape and rate of movement, through its influence on sand transport rates [1-3]. Information on surface shear stress patterns is an important input to numerical models of dune size and shape in different planetary environments. Such models are necessary for validation of dune shapes and dimensions derived from photoclinometric studies and to determine whether martian dunes are currently active.

The study reported here was conducted on a transect extending for 200 m across a isolated barchan dune with a height (H) of 4 m, located west of the Salton Sea, California on a sparsely vegetated gravel surface. Wind velocities were measured at heights of 0.4, 1.4 and 4.7 m above the surface. A reference anemometer array was maintained at a distance of 9H upwind of the dune, whilst a second tower was sited successively at points 2H or 4H m apart on the stoss slope and crest of the dune, together with two locations on its lee side. Wind velocities at a height of 4.7m averaged  $10.25 \text{ m}\cdot\text{sec}^{-1}$ , giving rise to active sand transport on all parts of the dune. Atmospheric conditions were assumed to be thermally neutral during the course of the experiment. Wind directions during this period varied by less than  $10^\circ$ .

Mean wind velocities at a height of 4.7 m increased by a factor of 1.23-1.30 as the wind passed over the dune (Fig. 1) and were found to vary directly with elevation on the dune ( $r=0.95$ ). Similar speed-up or amplification factors have been observed on dunes elsewhere [1-4] and result from compression of streamlines in the atmospheric boundary layer [5]. The shape of the curve of the increase in wind velocity with distance closely follows the profile shape of the dune, and with the slight decrease in wind velocity just upwind of the dune, confirms predictions made by Tsoar [3]. In the lee of the dune, wind velocities decreased to 0.53 of those at an equivalent height upwind, and remained below those recorded upwind of the dune for a distance exceeding 10 times the dune height.

Wind profiles upwind of the dune and at the base of the stoss slope of the dune are logarithmic, but become concave upward towards the dune crest as airflow in a zone 1 - 2 m above the surface is accelerated as it passes over the dune. The profile observed between the dune crest and the brink of the slip faces is a composite consisting of low velocities in a zone of expanded flow close to the surface, but accelerated flow at higher elevations. Profiles in the lee of the dune consist of a zone of stagnant air below 3 m with flow which has separated from the surface above that.

Values of friction speed ( $U_*$ ) were derived from the wind profiles using the methods outlined in Bagnold [5]. Some doubt exists as to the reliability of the values of  $U_*$  which are derived from profiles which are not truly logarithmic, and this problem requires further investigation. Values of friction speed increased by a factor of 3.17 times from  $0.28 \text{ m}\cdot\text{sec}^{-1}$  upwind of the dune to a maximum of  $0.73 \text{ m}\cdot\text{sec}^{-1}$  just upwind of the dune crest (Fig. 2). The friction speed ratio ( $U_*/V_{1.4 \text{ m}}$ ) increased directly with local elevation on the dune ( $r=0.85$ ).

Potential sand transport rates, calculated using the formula of Bagnold [5], increase exponentially up the windward slopes of the dune. Sand transport rates at the dune crest are 35 times those at the upwind base of the dune. For a given overall wind velocity, potential sand transport rates are directly proportional to local bed elevation ( $r=0.98$ ) (Fig.3).

The observations reported above provide further evidence to support the view that the morphology (size, shape) of small desert dunes is controlled by spatial variations in sand transport rates. This is determined by the requirements of sediment conservation [7]  $\partial h/\partial t = -\partial Q/\partial x$ , where  $h$  is the elevation of the local sand surface and  $Q$  is the spatially averaged volumetric sand transport rate. The stoss slopes of transverse dunes are erosional because

sand transport rates are increasing upslope. A dune may be considered to be in an equilibrium state when it migrates without changing shape. The forward migration rate ( $c$ ) of each part of the stoss slope is given by  $\partial Q / \partial x (1 / \tan \alpha)$ , where  $\alpha$  is the local slope angle, and the dune migration rate ( $C$ ) is given by  $Q_{\text{crest}} / H$ . Combining the equations for sediment continuity and dune migration rates, it follows that the local elevation of the sand surface ( $h$ ) is governed by  $h/H = k \cdot Q_{\text{(local)}} / Q_{\text{(crest)}}$ . The relationship  $Q_{\text{(local)}} / Q_{\text{(crest)}}$  may also be expressed in terms of the shear stress imparted by the wind as  $U_{* \text{(local)}} / U_{* \text{(crest)}}$ . On the dune studied, there is an excellent correlation ( $r=0.94$ ) between local bed elevation ( $h/H$ ) and the ratio between local and dune crest friction speeds ( $Q_{\text{(local)}} / Q_{\text{(crest)}}$ ) and between local bed elevation and calculated potential sand transport rates ( $r=0.98$ ) (Fig. 3). The shape of the stoss slope of the dune is therefore adjusted so that friction speed and sand transport rates increase at a rate which maintains an equal rate of migration at all points and accommodates an increasing volume of sediment eroded from the slope. Wind velocities, however, also vary with time, so the equilibrium is never perfect and dunes may be considered to be in a state of dynamic equilibrium with respect to time averaged sediment transport rates.

## REFERENCES

- [1] Howard, A.D. et al. *Sedimentology*, 25, 307-338 (1978).
- [2] Lancaster, N. *Sedimentology*, 32, 581-593 (1985).
- [3] Tsoar, H. *Geogr. Ann.*, 67A, 47-59 (1985).
- [4] Wippermann, F.K. & Gross, G. *Boundary-Layer Met.*, 36, 319-334 (1986).
- [5] Jackson, P.S. & Hunt, J.C.R. *Quart. J.R. Met.Soc.*, 101, 929-955 (1975).
- [6] Bagnold, R.A. *The Physics of Blown Sand and Desert Dunes* (Chapman & Hall, London, 1941)
- [7] Rubin, D. & Hunter, R.E. *Sedimentology*, 29, 129-138 (1982).

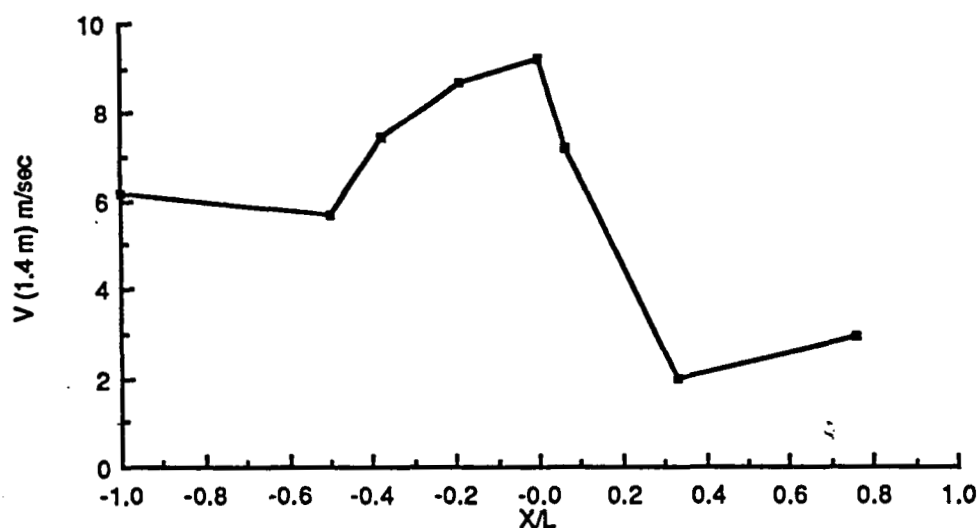


Fig. 1. Variation of wind velocity at a height of 1.4 m across the study dune.  $x/L$  = horizontal distance / length of stoss slope of dune.

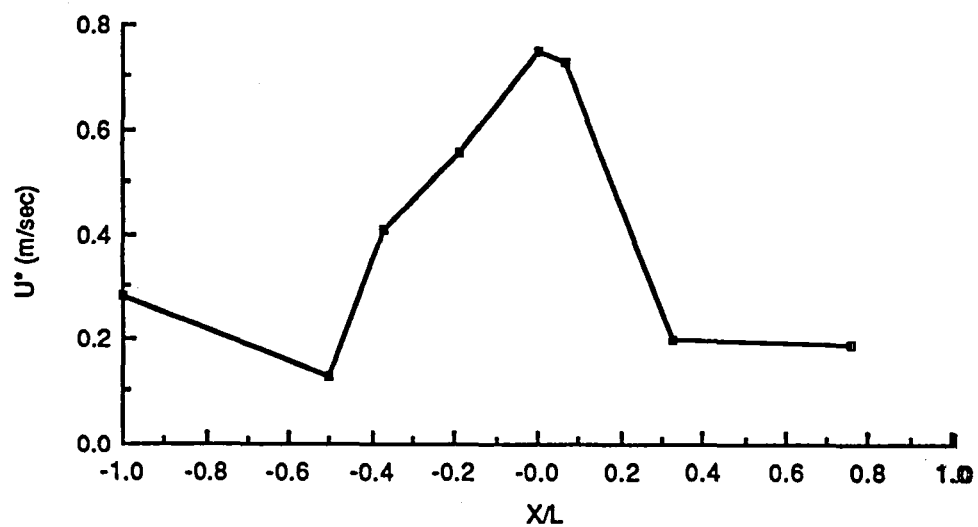


Fig. 2. Variation of wind friction speed ( $U_*$ ) across the study dune;  $x/L$  = horizontal distance/length of stoss slope of dune.

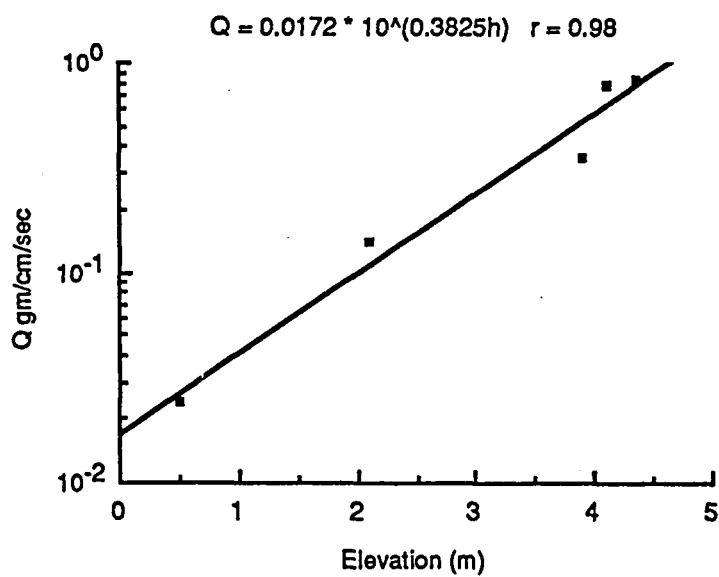


Fig. 4. Relationship between local bed elevation and local potential sand transport rate.

A POSSIBLE VOLATILE-RICH AIR-FALL DEPOSIT IN THE ELECTRIS REGION OF MARS; J.A. Grant and P.H. Schultz, Geological Sciences, Brown University, Providence, RI 02912

**INTRODUCTION:** A regional, unconformable, mantled and etched deposit occurs in the Electris region at the western end of Sirenum Fossae. This deposit has been interpreted as lava filling volcano-tectonic depressions (1) and as fluvial deposits filling large degraded craters (2); however, both studies considered only the thickest deposits. Examination of all occurrences indicates it is more likely the result of air-fall deposition. Evidence favoring rapid emplacement and short duration suggests that it resulted from a sudden, short-lived, climate change.

**OBSERVATIONS:** The deposit is unconformable and occurs as an irregular unit on both highlands and plains where it partially to completely buries surfaces and landforms. The deposit attains a thickness of over 700 m, with the thickest occurring in degraded 50 to 200 km impact craters. Deposits in craters range in thickness from  $450 \pm$  m in eastern areas to  $700 \pm$  m to the west. Both the deposit and exhumed surfaces display similar, low, crater densities. Although displaying no regular, thin layering, the deposit does appear to consist of several thick layers (10s to 100s of m) in some craters.

The deposit covers approximately  $1.8 \times 10^6$  km<sup>2</sup> (from about 160°W to 200°W and 30°S to 47°S). It appears to be undergoing active removal which has progressed farthest on low relief plains. Although the original extent is not known, partially filled craters to the immediate south suggests this area was also covered. The surface of the deposit is partially dissected by valley networks which head within the unit, but seldom incise underlying surfaces. A heavily eroded dome is located at 179°W, 36.5°S (Fig. 1) in the northeast portion of the deposit.

The deposit occurs in four distinct classes of differing thicknesses. In some locations (A in Figs. 1, 2), it thins gradually, thereby resulting in an obscure contact between mantled and unmantled areas. Slightly thicker deposits adjacent to these areas resemble gullied cuestas (B in Figs. 1, 2) commonly forming partial rings around degraded craters at constant elevation. These deposits are bounded by low, serrated scarps, usually facing away from the impact center on one side and thinning on the other. A third class of deposits form irregular promontories and mesas about 300 to 400 m thick that are bounded by scarps without basal talus (C in Figs. 1, 2). Such deposits isolated by adjacent valley networks thin in the down-valley direction, whereas other examples are completely ringed by a scarp of near constant relief. The fourth class represents the thickest deposits and occurs in large degraded craters (2) as irregular, angular, flat topped and rounded blocks resembling chaotic terrain (D in Figs. 1, 2). These blocks are from 400 to over 700 m thick and grade into uncovered or thinly buried plains.

**DISCUSSION:** The fourth class of deposits has been interpreted as lava filled volcano-tectonic depressions (1) and as collapsed fluvial deposits, resulting in the present chaotic appearance (2). We feel the deposit is likely a volatile-rich (ice?) air-fall deposit based on: A) consideration of all four classes of deposits; B) its occurrence over both uplands and lower plains; and C) patterns of removal.

Evidence favoring air-fall accumulation comes from the observation that the deposit covers both high relief uplands and low relief plains. Emplacement over this range of terrain by flood basalts, fluvial processes, or other processes, is unlikely. The deposit appears more easily eroded on plains than in the highlands, probably due to differences in surface roughness. The low density of valley networks/area exhumed and an absence of flow-related features indicates that fluvial erosion is secondary. Efficient eolian erosion of large areas across the deposit argues for the presence of fairly uniform fine-grained material, consistent with an air-fall deposit.

Relatively young valley networks incising the deposit indicate at least local volatile concentrations. This is consistent with observed atmospheric water concentrations over the deposit even in winter (3). The daily winter occurrence of Electris clouds over the most dissected portion of the deposit also suggests a locally high volatile content. These clouds are presumed to be composed of CO<sub>2</sub> (4), but may be water ice.

It is not known if current disparities in thickness reflect original depths and/or variations in rate of removal. Deposits that gradually thin may denote relatively low strength volatile poor zones and/or zones not thick enough for overburden welding, that are undergoing direct eolian deflation. Deposits occurring as scarp-bounded promontories, mesas, and irregular flat-topped and angular blocks may be higher strength volatile-rich areas thick enough to have undergone overburden welding and are dominated by mass-wasting and scarp retreat. The eroded cuesta-like appearance of some intermediate thickness deposits and the chaotic appearance of the thickest may require additional processes.

If the eroded dome to the northeast (Fig. 1) is a volcanic edifice (1, 5) it may have provided a source for the deposit. The major structural fabrics of the area are large ridges/scarps (compression) oriented NNW-SSE (6) and fractures (extension) oriented ENE-WSW (7). If the dome is volcano-tectonic in origin, it is oriented obliquely to both, perhaps due to redirection of the principal local stress field. However, several characteristics of the dome suggest it was not a source of the deposit: A) its isolated nature; B) large deposit volume (about 900,000 km<sup>3</sup>) compared to the dome size; C) apparent singular history; D) eroded style compared to adjacent deposits; and E) morphological similarity with other types of terrestrial domes. Other modes of formation (diapirism or sub-deposit basaltic eruptions?) may be required.

Origin by long-term seasonal accumulation during periods of high obliquity (8) is unlikely because of: A) low crater densities on both the deposit and exhumed surfaces favoring rapid emplacement and a short lifetime; B) an absence of thin layering; and C) limited regional extent. Based on gross estimates of the crater density on the deposit, accumulation occurred near the time of formation of Hesperia Planum. This suggests emplacement of the deposit may have been due to a sudden, but significant, short-lived change in climate and erosion rates occurring at that time (9). Similarity of this deposit in age and appearance to other transient deposits in the Isidis, Hellas, and Argyre Basins (10) implies they may be related. The thick layered appearance of the deposit in some large craters may indicate several earlier episodes of burial.

REFERENCES: (1) Scott, D. H. (1982), *J. Geophys. Res.*, 87, 9839-9851. (2) Lucchitta, B. K. (1982), *NASA Tech. Memo.* 85127, 235-236. (3) Huguenin, R. L. and Clifford, S. M. (1982), *J. Geophys. Res.*, 87, 10227-10251. (4) Briggs, G. et al. (1977), *J. Geophys. Res.*, 82, 4121-4149. (5) Scott, D. H. and Tanaka, K. L. (1981), *Proc. Lunar and Planet. Sci. Conf. XII*, 1449-1458. (6) Chicarro, A. F. et al. (1985), *Icarus*, 63, 153-174. (7) Wichman, R. and Schultz, P. H. (1986), *Lunar and Planet. Sci. XVII*, 942-943, LPI, Houston. (8) Jakosky, B. M. and Carr, M. H. (1985), *Nature*, 315, 559-561. (9) Schultz, P. H. (1987), Impact cratering and the martian climate, submitted for publication. (10) Grizaffi, P. and Schultz, P. H. (1987), *Lunar and Planet. Sci. XVIII*, this volume.

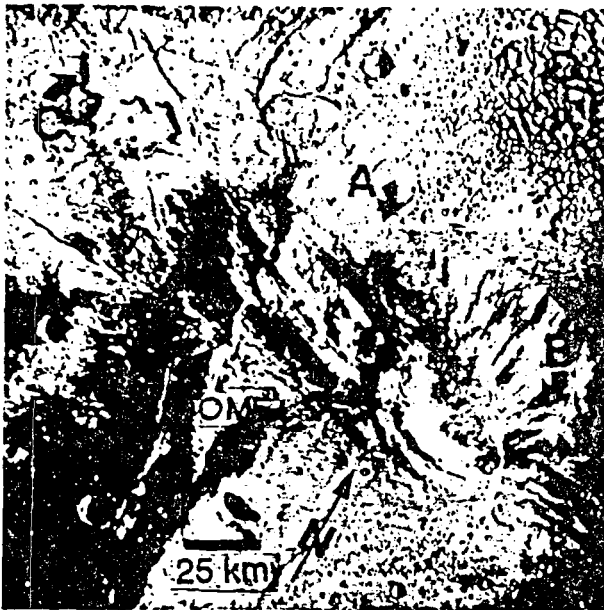


Figure 1. Eroded dome at 179°W, 36.5°S. All four classes of unconformable deposit are shown (A,B,C,D). See text for discussion. Image 597A85.



Figure 2. Exhumed (E) and buried topography at 164°W, 37°S, just west of Figure 1. All four classes of unconformable deposits are shown (A,B,C,D). See text for discussion. Image 372S09.

DISTRIBUTION AND TIMING OF THICK TRANSIENT AIR-FALL DEPOSITS IN ELECTRIS: IMPLICATIONS FOR THE NATURE OF THE UPLAND PLAINS; J.A. Grant and P.H. Schultz, Geological Sciences, Brown University, Providence, RI 02912

**INTRODUCTION:** A large area in the Electris region of Mars is (or once was) covered by an unconformable and etched deposit. Although interpreted as lava filling volcano-tectonic depressions (1) or fluvial deposits filling large degraded craters (2), more recent work has shown the deposit is more likely the result of air-fall deposition (3,4). Crater densities on both the surface of the deposit and on exhumed, underlying ridged plains indicate that the deposit was emplaced and eroded over a relatively short time. These crater statistics also demonstrate that the relative age of the Electris deposit is similar to those obtained for other unconformable deposits, thereby suggesting they may be related.

**OBSERVATIONS:** The Electris deposit is unconformable and occurs irregularly over both ridged plains and cratered upland surfaces. Remnants of the deposit extend over an area of approximately  $1.8 \times 10^6$  km<sup>2</sup> (from 160°W to 200°W and 30°S to 47°S), but the presence of partially filled craters to the immediate south of this region suggests initially broader coverage. The deposit has an estimated volume of 900,000 km<sup>3</sup> with average thickness ranging from 300+ m in the east up to 700+ m in the west (based on shadow measurements). The thickest deposits occur as chaotic unconformable material (2) filling degraded 50 to 200 km craters. Deposits in some craters display thick, poorly defined layering (10's - 100's of m), there is an absence of regular, thin layering.

Valley networks head within the Electris deposit and partially dissect its surface; however, they do not appear to incise the underlying ridged plains unit. Other characteristics of the deposit include a heavily eroded dome located at 79°W, 36.5°S in the northeast portion of the deposit and several examples of inverted topography (e.g. 190.5°W, 40°S).

Four classes of the Electris deposit have been identified. In some locations the deposit grades from mantled to unmantled areas. A second, slightly thicker class resembles gullied cuestas that form partial rings around the inside of degraded impact craters at constant elevation. The third class of deposit forms irregular promontories and mesas that are 300 m to 400 m thick and bounded by scarps lacking basal talus accumulations. The thickest class of the deposit resembles chaotic terrain and is found in large degraded craters (2). The irregular blocks comprising this class of the deposit are 400 m to over 700 m thick and typically grade into exhumed or only thinly mantled ridged plains. In contrast to some other areas having thick unconformable deposits (4,5), pedestal craters in the Electris region are uncommon.

**DISCUSSION:** Consideration of the characteristics of all four classes of the Electris deposit suggests that it is: A) the result of air-fall deposition; and B) volatile rich (3). The occurrence of the deposit over both high-relief cratered uplands and low-relief ridged plains strongly favors air-fall accumulation. It seems unlikely that extrusion of flood basalts, fluvial processes, or other processes could account for emplacement over such a range in relief. In addition, the low density of valley networks/area exhumed, an absence of flow-related features, and a deficiency of talus at the base of most scarps, demonstrate that eolian processes dominate erosion of the deposit. Efficient eolian erosion indicates the presence of fairly uniform fine grained material, consistent with an air-fall deposit. A locally high volatile content within the deposit is indicated by: A) relatively young valley networks that head within the deposit; B) observed atmospheric

water concentrations over the deposit even in the winter (6); and C) the daily winter occurrence of *Electris* clouds over the most dissected portion of the deposit (thought to be composed of CO<sub>2</sub> (7), but may be H<sub>2</sub>O ice).

It is unclear whether current disparities in thickness of the deposit reflect original depths and/or variations in the rate of removal. Thin deposits may reflect low strength volatile poor zones and/or zones not thick enough to have undergone overburden welding and that underwent direct colian deflation. Thicker deposits may be higher strength volatile rich zones that have undergone overburden welding and were dominated by scarp retreat and mass-wasting. Deposits inside craters resembling gullied cuestas and chaotic material are perhaps remnants of higher strength layers deposited on lower strength material that have undergone differing amounts of erosion and/or collapse. The thick layered appearance in some large craters suggests that several periods of burial may have occurred. A paucity of pedestal craters and the similarity between crater densities on both the deposit and exhumed ridged plains surfaces (Fig. 1) indicates rapid deposition and subsequent erosion of the *Electris* deposit.

The eroded dome in the northeast portion of the deposit has been described as a volcanic edifice (1,8). If this assessment is correct, it may have provided a source for the deposit. However, several characteristics of the dome suggest it was not a source: A) its isolated nature; B) large deposit volume compared to the dome size; C) large deposit volume compared to terrestrial deposits associated with volcanoes (9); D) apparent singular history; E) eroded style compared to adjacent deposits; and F) similarity with other types of non-volcanic terrestrial domes (e.g. diapiric).

Crater statistics indicate that emplacement of the ridged plains took place soon after formation of Sinai, Syrtis Major, and Hesperia Planum (Fig. 1). This was rapidly followed by formation of the *Electris* deposit and its subsequent modification by erosion (Fig. 1). Emplacement of the *Electris* deposit nearly coincided with the formation of similar unconformable deposits in Sinus Meridiani and Isidis basin (10), the thicker unconformable sequences of Arabia and Mesogaea (4), and the end of a peak in geomorphic activity identified in the Margaritifer Sinus quadrangle (11). The major outflow channels formed soon after these events (Fig. 1).

**IMPLICATIONS:** The *Electris* deposits appear to be representative of a period when unconformable deposits were widespread and geomorphic processes were high (11). While the *Electris* and other debris mantles in Sinus Meridiani and Isidis were emplaced and removed in a relatively short time, thicker accumulations occurred over a longer time in Arabia and Mesogaea. All deposits are believed to reflect an epoch when atmospheric volatiles were in abundant supply, whether from primary exogenic (12) or endogenic sources (13). Sources for volatile release and global deposition of these volatiles include the finite thermal history associated with impact basins (14,15) perhaps amplified by processes such as polar wandering (4) and high obliquity prior to the development of Tharsis (16). Outflow channels forming soon afterwards may reflect a re-release of these trapped volatiles.

The nature of the *Electris* and other similar deposits document periods of gradation on Mars that affected widely separated regions of the surface. Their eroded expression and locally thick layering demonstrates that such deposits were originally more widespread and that several periods of deposition and erosion may have taken place. Volcanic plains in some areas of the cratered uplands may be deeply buried by or wholly due to such deposits, thereby increasing ambiguities in interpreting the nature of some upland plains.

References: (1) Scott, D.H. (1982), J. Geophys. Res., 87, 9836-9851. (2) Lucchitta, B.K. (1982), NASA Tech. Memo. 85127, 235-236. (3) Grant, J.A. and Schultz, P.H. (1987), Lunar and Planet. Sci. XVIII, 355-356. (4) Schultz, P.H. and Iaitz, A.B. (1987), Icarus, in press. (5) Scott, D.H. and Tanaka, K.L. (1982), J. Geophys. Res., 87, 1179-1190. (6) Huguenin, R.L. and Clifford, S.M. (1982), J. Geophys. Res., 87, 10227-10251. (7) Briggs, G. et al. (1977), J. Geophys. Res., 82, 4121-4149. (8) Scott, D.H. and Tanaka, K.L. (1981), Proc. Lunar and Planet. Sci. Conf. XII, 1449-1458. (9) Francis, P.W. and Wood, C.A. (1982), J. Geophys. Res., 87, 9881-9889. (10) Grizzaffi, P. and Schultz, P.H. (1987), Lunar and Planet. Sci. XVIII, 370-371. (11) Grant, J.A. (1987), NASA Tech. Memo. 89971, 1-268. (12) Schultz, P.H. (1987), Kagaku, 57, 486-495. (13) Greeley, R. (1987), Science, 236, 1653-1654. (14) Wichman, R. and Schultz, P.H. (1987), Lunar and Planet. Sci. XVIII, 1078-1079. (15) Schultz, P.H. (1987), This volume. (16) Jakosky, B.M. and Carr, M.H. (1985), Nature, 315, 559-561. (17) Marinsky, H.J. et al. (1977), J. Geophys. Res., 82, 4016-4038. (18) Baker, V.R. (1982), The Channels of Mars, Univ. Texas Press, 198p. (19) Neukum, G. and Wise, D.U. (1976), Science, 194, 1381-1387.

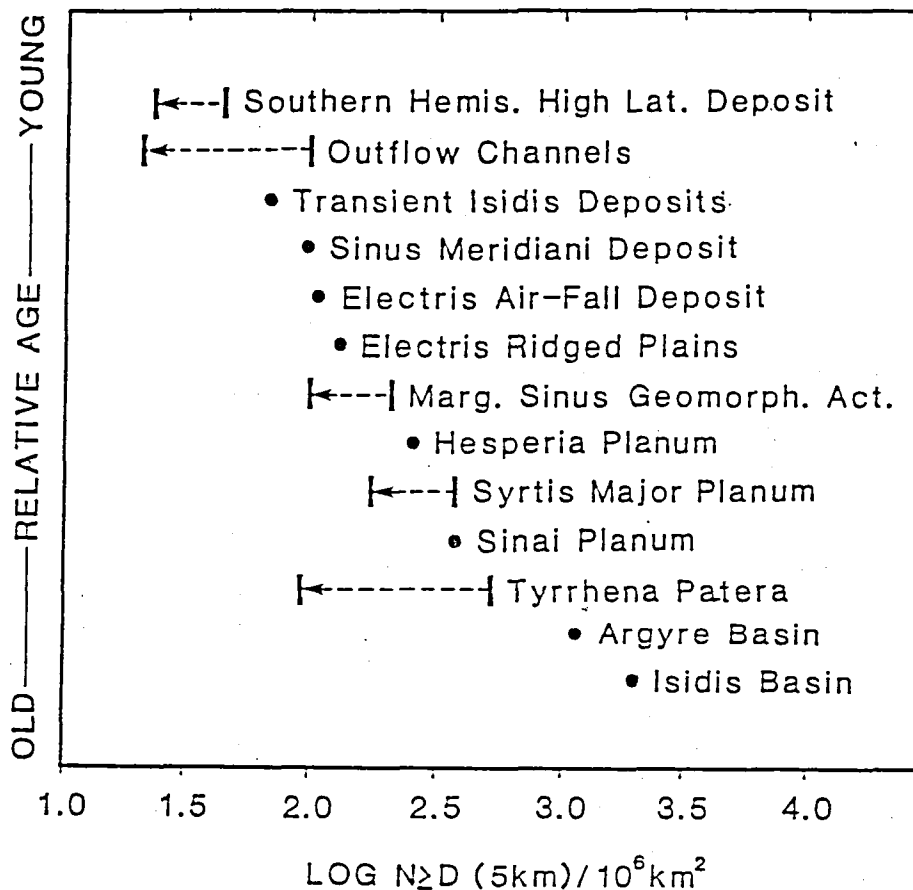


Figure 1. Relative ages of the Electris air-fall deposit, underlying ridged plains, and other selected surfaces and features, arranged by increasing age from top to bottom. Data for the outflow channels are from 17,18. Ages are given as the log of the number of craters  $> 5$  km, normalized using the Neukum and Wise standard crater curve for Mars (19).



## Erosional and Depositional Processes in the Martian Heavily-Cratered Terrain

Jeffrey M. Moore and Michael C. Malin, Department of Geology, Arizona State University, Tempe, AZ 85287-1404

Mosaics of high-resolution (20 to 80 m/pixel) contiguous images and other data (i.e. IRTM and radar) are being used to examine the erosional and depositional processes responsible for various surface features within large tracts of martian heavily-cratered terrain. Regional chronologies and stratigraphies are being developed in order to determine the succession of climatological and environmental factors which influenced the shaping of the surface of the heavily-cratered terrain.

The first region of heavily-cratered terrain studied was northeastern Arabia (~20-35°N, ~285-325°W). Within this area are two subdivisions of the Plateau Sequence as mapped in the recent USGS effort (Greeley and Guest, 1987). The upper unit is classified as *etched material*, interpreted to be a mixture of lava flows, pyroclastic material, and impact ejecta degraded by wind erosion, decay and collapse of ground ice, and minor fluvial processes. The lower unit is termed *ridged material* and is thought to be an uneroded deposit of materials similar to those composing etched material but subjected to normal faulting, volcanic construction, and/or compressional tectonics.

An initial conclusion of this study is that the ridged material mapped in Greeley and Guest (1987) has been eroded to produce the surface mapped as etched material. The ridged material of this region has a characteristically distinctive topography wherein changes in slope are gradual (i.e., slope crests appear "rounded"). Some researchers refer to this phenomenon as "terrain softening" (Squyres and Carr, 1986). Smaller craters on this unit are less distinct than larger craters, and most  $\leq 10$  km craters appear only as rimless circular undulations on the surface. There are a number of fresh craters (mostly  $< 10$  km in diameter) superimposed on the muted craters. As has been previously noted, there are parallel ridges on this unit spaced ~50-200 km. Malin (1976) felt that these ridges resembled those of the mercurian intercrater plains, which are interpreted there to be the result of compressive stress (Murray et al., 1974). Malin suggests a similar origin for the martian ridges.

The smooth, undulating surface of the ridged material becomes progressively pitted and incised in the eastern part of the study area (Figure 1). North of Antoniadi and between Augakuk Vallis and Huo Hsing Vallis the surface consists of elongated, steep-sided mesas, whose long dimension appears co-aligned with the dominant wind direction (Figure 2). The top surfaces of the mesas are in some cases smooth at the resolution (~50 m/pixel) of the images. Other mesas and much of the surface in the transition zone between the ridged unit and etched unit are capped by a thin, steep-slope-forming (probably indurated or competent) layer of material that, when eroded, reveals the smooth and rounded top of the dominant mesa-forming material below. Two forms suggesting relief inversion are seen: several mesas are circular in plan view and are interpreted to have formed within craters, and some mesas are curvilinear and appear to have formed from inversion of channel relief. These forms suggest that the mesa-forming material infilled pre-existing topography and, once emplaced, was more resistant to erosion than surrounding materials. Areas where erosion has removed all but faint trace of previously higher standing materials contain roughly circular deposits of resistant material with a distinctly lower albedo than the surrounding terrain (Figure 3). Areas where the ridged material appears to have been completely removed are covered with low, equidimensional hills, most  $< 500$  m across (Figure 3).







The etched unit is coincident with an area identified by Pollack et al. (1981) as potentially subjected to intense, unidirectional winds which decrease to the west. Wind clearly played a significant role in the erosion of the etched materials. They appear relatively unconsolidated near the top of undisturbed sections but become increasingly competent with depth. This mechanical property, and the undulatory character of the uneroded unit's surface, are reminiscent of a differentially compacted, zonally indurated sedimentary deposit. Welded pyroclastic deposits have this character, as described in Sheridan and Ragan (1976). However, this resemblance is insufficient in itself to permit that origin of the deposit to be inferred. The nature of the deposit and the processes which have controlled its erosional habit are the subject of ongoing investigation.

## References

- Christensen, P.R. (1986) *Icarus* 68, 217-238.  
Christensen, P.R. (1986) *J. Geophys. Res.* 91, 3533-2545.  
Greeley, R., and J.E. Guest (1987) U.S. Geol. Surv. Misc. Inv. Map I-1802-B.  
Malin, M.C. (1976) Ph.D. Diss., Calif. Ins. Tech.  
Murray, B.C., et. al. (1974) *Science* 185, 169-179.  
Pollack, J.B. et al. (1981) *J. Atmos. Sci.* 38, 3-29.  
Sheridan, M.F. and D.M. Regan (1976) *Developments in Sedimentology* 18B, 677-713.  
Squyres, S.W. and M.H. Carr (1986) *Science* 231, 249-252.



# KEY

-  UNERODED RIDGED-PLAINS MATERIAL
-  PITTED AND INCIPIENTLY-ERODED RIDGED-PLAINS MATERIAL
-  UPPER EROSION-RESISTANT COMPONENT OF RIDGED-PLAINS MATERIAL
-  LOWER, LOW-ALBEDO, EROSION-RESISTANT COMPONENT OF RIDGED-PLAINS MATERIAL
-  DEBRIS-COVERED BASAL SURFACE
-  SUBDUED RIMS OF CRATERS BLANKETED WITH RIDGED-PLAINS MATERIAL

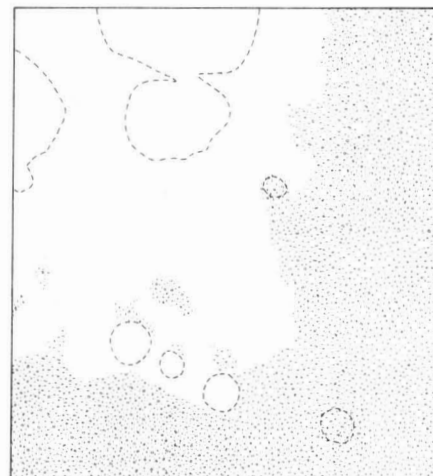


**Fig. 1** Image of Ridged unit - Etched unit transition zone at 33°N, 296° W. The topography of large craters is muted or undulatory. Superimposed over the large crater are small fresh craters. The pits in the right and bottom of the image represent the onset of erosion of this material. (Viking Orbiter image 187S16)



N  
↑

All figures

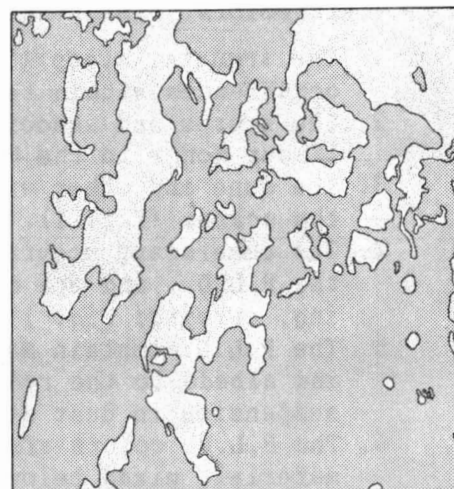


**Fig. 2** Mesas formed by erosion of ridged unit at 28°N, 295°W. An unconsolidated layer has been removed to reveal the smooth tops of the mesas. The long dimension of the mesas is oriented in the direction of the wind. (Viking Orbiter image 181S13)



10 km

All figures

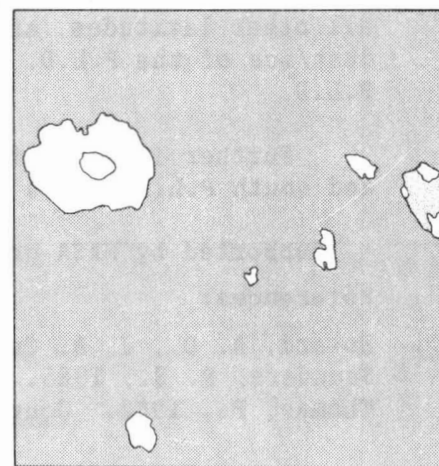


**Fig. 3** Area where most of the mesa-forming material has been removed at 25°N, 298°W. There are a few, usually circular deposits of relatively erosion-resistant material with a distinctly lower albedo than the surrounding terrain. The remaining surface is covered with low, equidimensional hills, all < 500 m in any dimension. (Viking Orbiter image 181S01)

**MARS: DUNE SAND SOURCES IN NORTH POLAR LAYERED DEPOSITS**  
P. C. Thomas, Cornell University

The study of the sources of dune sands on Mars has recently focussed on the relationship of dunes to polar layered deposits (P.L.D.). This study of the morphologic and color relationships of the polar dunes to other materials extends the initial observations of several studies (Howard et al., 1981; Thomas, 1981; Saunders, 1986).

Our investigation starts from the apparent association of dunes and the P.L.D. Previous workers (refs. above) noted that dunes appeared to be forming in association with steep scarps in the layered deposits, and therefore might be material eroded from the layers. Traditional views of the polar layered deposits as dust/ice carried to the poles in suspension have caused considerable reluctance to accept the P.L.D. as sources of sand-sized material moved by saltation. For this study we have mapped the occurrence of dunes in the P.L.D., their morphologic associations, and their colors. Important relations found include:

1. The arcuate, steep (5-20°) scarps are associated with most dune occurrences within the area of P.L.D. (Figs. 1, 2).
2. The scarps and associated dunes have restricted occurrences in two linear zones in the P.L.D.
3. The dune and other wind-directed features indicate movement away from the scarps (Fig. 1).
4. The dune/scarp occurrences are near the edges or in large reentrants of the P.L.D., and are often in areas of complex trough patterns (crossing, curving; Fig. 1).
5. The P.L.D. contain material that is similar in color (red/ violet = 3) and albedo to the red dust seen elsewhere on Mars and carried in suspension in dust storms (Fig. 3).
6. The P.L.D. colors also indicate some areas have darker, less red material, mixed below the resolution limit of 50 m/pixel.
7. The polar dunes are basically the same colors as dark dunes elsewhere on Mars (Fig. 3).

From these observations it can be concluded that the material making up the polar dunes is essentially the same as materials forming dunes at all other latitudes, and that they are in some manner interbedded with the dust/ice of the P.L.D. This material is currently being eroded from the P.L.D.

Further investigation aims at morphologic differences between north and south P.L.D. and a more complete analysis of sand sources on Mars.

Supported by NASA grant NAGW-111.

**References:**

- Howard, A. D., J. A. Cutts, and K. R. Blasius, 1982. Icarus 50, 161-215.  
Saunders, R. S., 1986. NASA TM 88383, 260-261.  
Thomas, P., 1982. Jour. Geophys. Res. 87, 9999-10008.

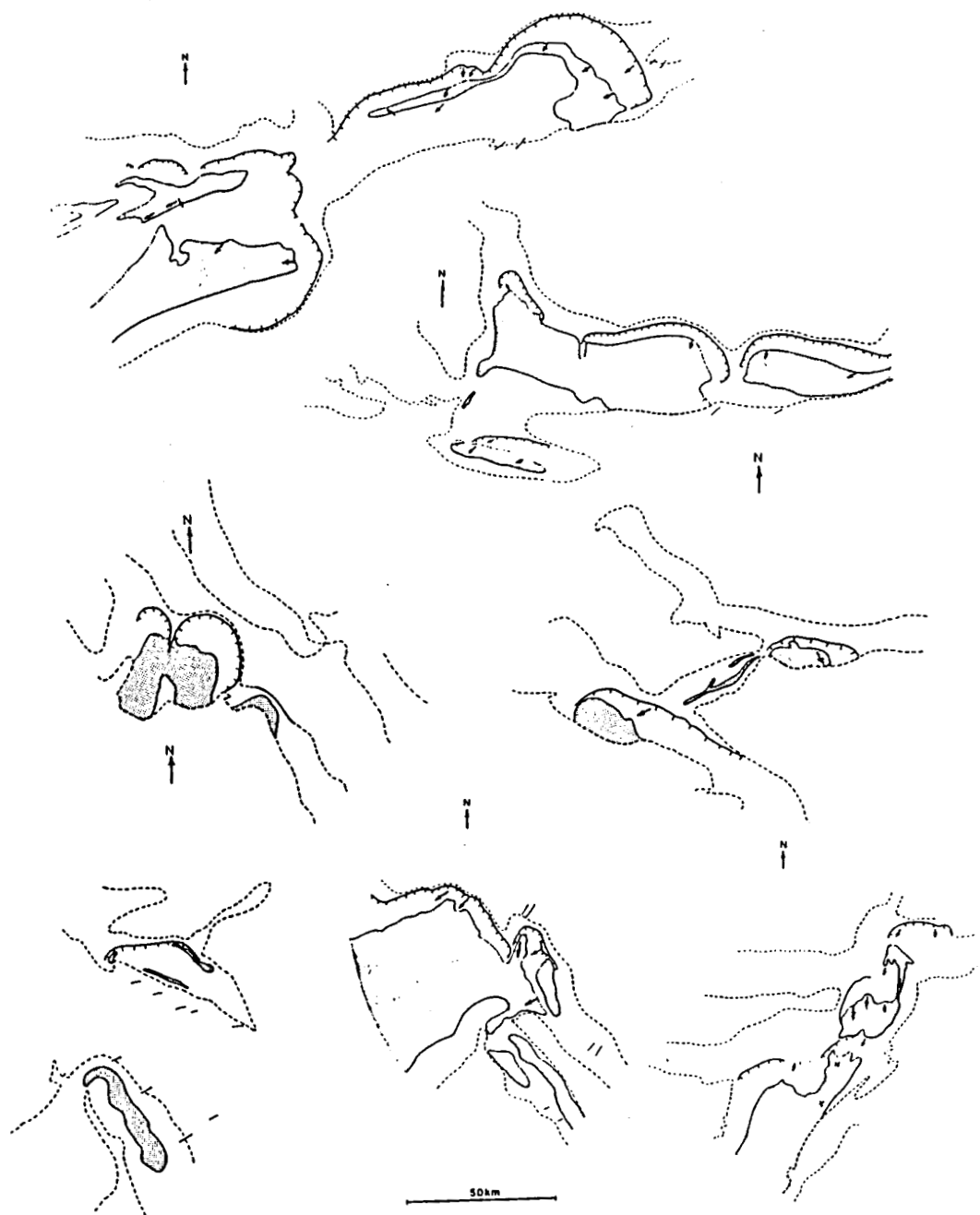


Fig. 1. Examples of the association of polar dunes and steep, arcuate scarps in P.L.D. Stippled areas are dunes, dashed lines mark trough margins, and scarps are hachured lines. Wind directions from barchan orientations, framing dunes, and wind streaks indicate flow out from the scarps.

Fig. 2. Location of dune sources in P.L.D. Dark areas mark dunes near scarps. The restricted occurrence suggests structural control, as do trough outlines. The dune occurrence in the outer and lower parts of the P.L.D. suggest sands are in older parts of the P.L.D.

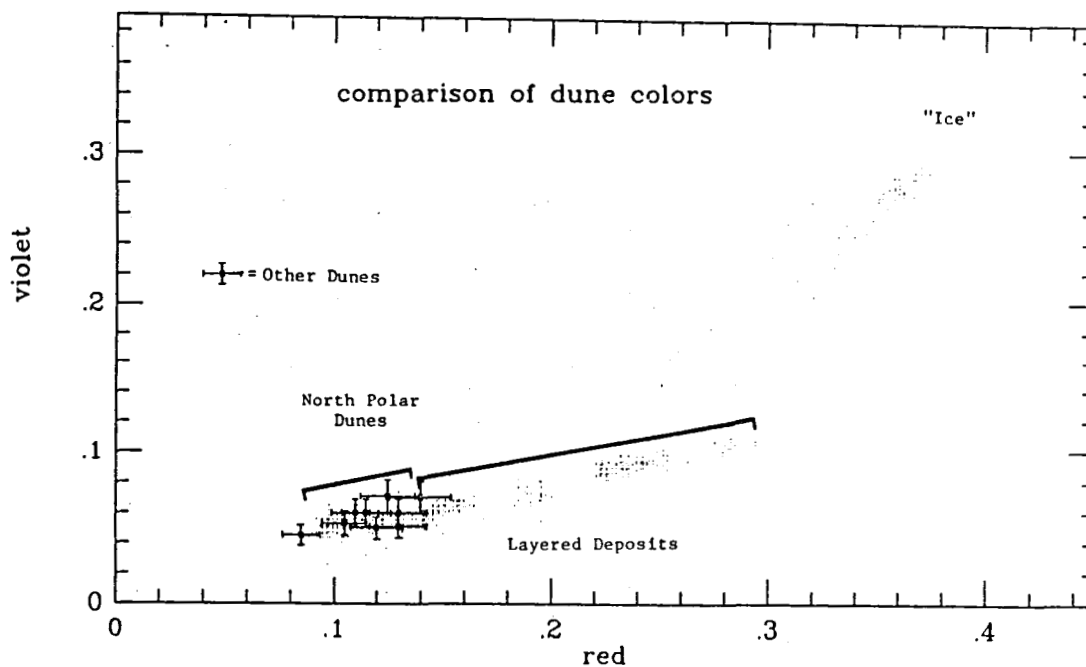
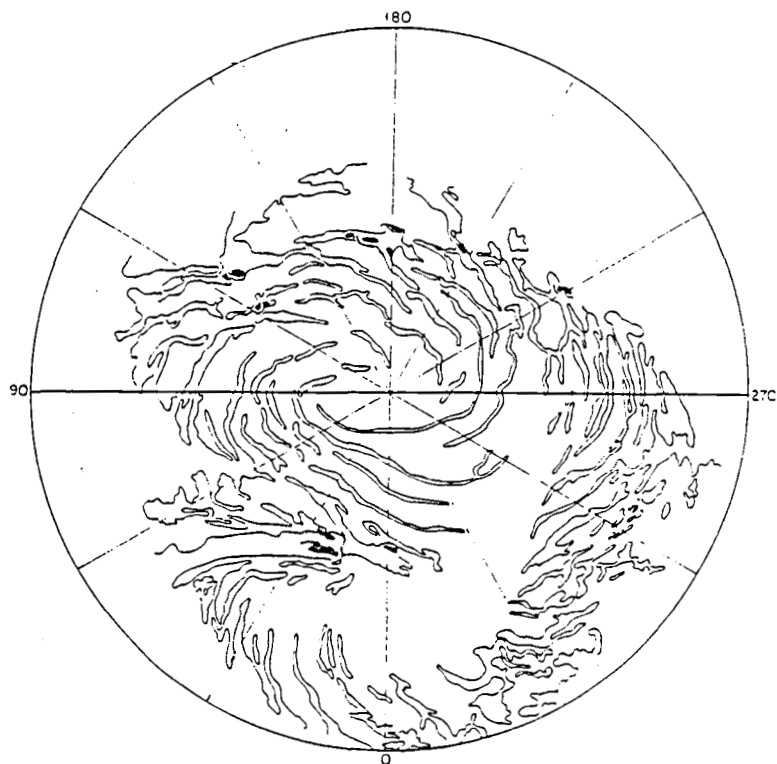


Fig. 3. Colors of polar layered deposits dunes and "ice" at  $\sim 83^\circ\text{N}$ ,  $240^\circ\text{W}$ . Data from VO images with scattering function used to compare data from different areas. P.L.D. contain bright, red "dust," and some darker material. Dune colors from several locations at lower latitudes are compared, and are similar to polar dunes ( $R/V \sim 2.0$ ).

## ACCUMULATION OF SEDIMENTARY DEBRIS IN THE SOUTH POLAR REGION OF MARS AND IMPLICATIONS FOR CLIMATE HISTORY

J. Plaut, R. Kahn, E. Guinness, and R. Arvidson, McDonnell Center for the Space Sciences, Department of Earth and Planetary Sciences, Washington University, St. Louis, MO 63130.

The martian polar regions provide first-order information on martian climate history because they are sites of several kilometer thick deposits of ice and sedimentary debris. The nature and rate of accumulation is thought to be strongly modulated by climatic conditions and by the ability of the atmosphere to transport volatiles and suspended particles to higher latitudes [1]. The south polar area was particularly well imaged by the Viking spacecraft because of high spatial resolution (100 to 200 m/pixel) and clear atmospheric conditions [2]. However, except for studies of the layered terrains [3-4], most published work on the south polar region has relied upon Mariner 9 images, with typical A-frame resolution of 1 km/pixel and limited high resolution coverage [5-9]. This abstract summarizes our work [10] where Viking Orbiter images were used to conduct photogeological analyses of probable sedimentary units and to characterize crater size frequency distributions. The crater data were used to model the timing and rate of accumulation of polar debris. These estimates were then used to provide quantitative estimates of depositional history and to constrain models of martian climatic evolution.

Detailed modeling of crater size frequency distributions [11] suggests that equatorial and polar cratered terrains of Mars experienced an enhanced episode of obliteration as the period of early heavy bombardment ended at about 3.7 Ga. This conclusion depends on the assumed log-log linear production function, which is based on analogy to the standard interpretation of lunar crater data. Modeling results imply that cratered terrains poleward of 65° south latitude have since experienced steady state accumulation of material at a rate of about 0.1 km/Ga, while equatorial cratered terrains have been retained in relatively pristine form. Plains of Noachian and Hesperian ages embay the polar cratered terrain in a number of regions. These plains have craters in production at least in some areas, with crater retention ages similar to the extensive older equatorial plains, including intercrater plains and ridged plains. A debris mantle of upper Hesperian age overlies the polar plains and underlies the polar layered deposits. The mantle is pitted, exposing cratered terrain in some areas, with pit depths typically  $\leq 1$  km. Mantle plateaus are in crater production at least in some areas, with crater retention ages only a few hundred million years younger than underlying plains. Thus, about 1 km of debris accumulated in a short interval to form the debris mantle, with an average rate of about 5 km/Ga. Fifteen craters with impact features were identified on the south polar layered terrain, suggesting the surface is at least  $0.12 \pm 0.04$  Ga in age. The layered terrain craters have a size frequency distribution consistent with a steady state deposition rate less than or equal to  $8 \pm 2$  km/Ga. Values significantly lower than the upper bound are probable, given that local erosion and obliteration, combined with viscous relaxation, will also remove craters.

Results imply significant secular variations in the accumulation of south polar debris. After formation of cratered terrain and older plains, an extensive debris deposit accumulated rapidly. The deposit was pitted by subsequent activity. Polar layered deposits began accumulating later at a comparable rate. Surrounding cratered terrains continued to accumulate debris but at a substantially lower rate. Even the upper limit

of a 10 km/Ga deposition rate for the layered deposits is too small by more than an order of magnitude to produce the characteristic 10-40 m thick layers over  $4 \times 10^4$  year intervals associated with orbital obliquity oscillations. The 1 Ma intervals associated with eccentricity variations in climatic conditions are more likely candidates for producing the observed layering.

### References

- 1) Pollack, J. and O. Toon, 1982, *Icarus*, 50, 259-287.
- 2) Kahn, R., and others, 1986, *Icarus*, 66, 22-38.
- 3) Blasius, K., and others, 1982, *Icarus*, 50, 140-160.
- 4) Howard, A., and others, 1982, *Icarus*, 50, 161-215.
- 5) Murray, B., and others, 1972, *Icarus*, 17, 328-345.
- 6) Cutts, J., 1973a, *J. Geophys. Res.*, 78, 4231-4249.
- 7) Cutts, J., 1973b, *J. Geophys. Res.*, 78, 4211-4221.
- 8) Sharp, R., 1973, *J. Geophys. Res.*, 78, 4222-4230.
- 9) Condit, C., and L. Soderblom, 1978, *USGS Misc. Inves. Series Map 1076*.
- 10) Plaut, J., and others, 1987, submitted to *Icarus*.
- 11) Phillips, R., and M. Malin, 1980, *Science*, 210, 185-188.



## **CHAPTER 8**

### **FLUVIAL PROCESSES**



## POWER OF MARTIAN FLOODS

Victor R. Baker, Department of Geosciences and Department of Planetary Sciences, University of Arizona, Tucson, AZ 85721.

The Martian outflow channels are a class of trough-like landforms that display evidence of large-scale fluid flow on their floors (Mars Channel Working Group, 1983). The outflow channels are immense, as much as 100 km wide and 2000 km in length. It was recognized shortly after their discovery that they possessed a similar suite of bedforms and morphological relationships to what was exhibited in the Channeled Scabland (Baker and Milton, 1974). Included are streamlined uplands, longitudinal grooves and inner-channel cataracts, depositional fan complexes, anastomosis, scour marks, and others (Baker, 1982, 1985). Particularly important are the scour marks and the necessity for the responsible fluid to possess a free, upper surface. The entire assemblage of landforms can only be explained by the action of a fluid with physical properties similar to turbulent water. The present consensus is that water in concert with entrained debris and ice was the primary agent of outflow channel genesis (Mars Channel Working Group, 1983).

The ability of river flows to erode and transport sediment has long been known to be related to channel boundary shear stress,  $\tau$ , expressed in  $\text{N/m}^2$ , according to the formula

$$\tau_r = \gamma R S, \quad (1)$$

where  $\gamma$  is the specific weight of the fluid ( $9807 \text{ M/m}^3$  for clear water),  $R$  is the hydraulic radius (m), and  $S$  is the energy slope. In two dimensions it may be possible to substitute flow depth  $D$ (m) for  $R$ , yielding the following expression for local bed shear stress:

$$\tau_d = \gamma D S. \quad (2)$$

Another important concept for sediment transport is the energy developed per unit time, or power (Bagnold, 1966). Total power per unit length of stream,  $\Omega$ , expressed in watts/m, is given by the formula

$$\Omega = \gamma Q S, \quad (3)$$

where  $Q$  is discharge ( $\text{m}^3/\text{s}$ ).

Total stream power varies with the discharge (size) of a river. Therefore, another useful measure of power is its value per unit area of bed, expressed in  $\text{watts/m}^2$  ( $\text{w/m}^2$ ), given by the formula

$$\omega = \frac{\gamma Q S}{W}, \quad (4)$$

where  $W$  is the water-surface width (m), and other parameters are defined as above.

For many rivers  $Q$  may be expressed as a simple function of width  $W(m)$ , mean flow velocity  $\bar{V}$  (m/s) and depth  $D$  (m):

$$Q = W D \bar{V} . \quad (5)$$

Substituting equation 5 into 4 yields

$$\omega = \tau_d \bar{V} , \quad (6)$$

The largest terrestrial fluvial values of boundary shear stress and stream power per unit area were achieved in the great cataclysmic floods of the Pleistocene (Baker and Costa, 1987). The Missoula Floods at the Soap Lake constriction (Baker, 1973) achieved a bed shear stress  $\tau$  of  $1 \times 10^4$  N/m<sup>2</sup> ( $10^5$  dynes/cm<sup>2</sup>) and a power per unit area of bed  $\omega$  of  $3 \times 10^5$  w/m<sup>2</sup> ( $3 \times 10^8$  ergs/cm<sup>2</sup>-sec) (Baker and Komar, 1987).

Parameters for maximum flood flows on Mars are discussed by Komar (1979), Carr (1979), and Baker (1982). In calculating power per unit area,  $\gamma$  is 3720 N/m<sup>3</sup> because of the lower Martian gravity. For a Martian flood a critical cavitation velocity  $V_m$  (m/s) can be defined (Baker, 1979, 1982), which reduces in the lower Martian atmospheric pressure to

$$V_m = 1.6 (D)^{1/2} . \quad (7)$$

For a hypothetical Martian flood flowing 100 m deep at a gradient of 0.01, equations 7 and 6 yield a maximum  $\omega$  of  $6 \times 10^4$  watts/m<sup>2</sup>. For a flood 500 m deep at a 0.01 gradient, the maximum  $\omega$  is  $1 \times 10^5$  watts/m<sup>2</sup>. Thus, maximum flood power per unit area on Mars is comparable to that on Earth.

In comparison to other processes which operate to shape the surfaces of planets, cataclysmic floods seem to be second only to high-velocity bolide impacts in terms of power generation per unit surface area.

Stream powers of the magnitudes reported here can accomplish a variety of unusual and rare sedimentologic and hydraulic phenomena, including (a) suspension of gravels, (b) erosion of bedrock, (c) movement of boulders several meters in diameter, and (d) the transport of enormous quantities of sediment. The effects of dynamic flood conditions are especially noteworthy as to the sizes of sediment carried in the various modes of transport; that is, as bedload, suspension, and washload. As discussed by Komar (1980), it is theoretically possible to extend the domains of these transport modes to evaluate intense floods. Komar finds that typical river floods generating  $\tau = 10$  N/m<sup>2</sup> can entrain and transport sediment grains of about 1 cm diameter, while sediment finer than 1 mm moves in suspension, and the washload consists of sediments finer than 0.1 mm. Exceptionally powerful floods with  $\tau = 10^3$  N/m<sup>2</sup> can transport gravel as coarse as 10 to 30 cm in suspension and sand-size diameters of 0.4 to 0.8 mm and finer in the washload. The increase in  $\tau$  to  $10^4$  to  $10^5$  N/m<sup>2</sup> for the Missoula and the Martian floods implies that even boulders can be transported in suspension with the sand-size grains in the washload. Estimates based on this analysis of sediment transport in clear water actually are likely to be conservative, especially for cases involving

high concentrations of washload. These high concentrations reduce the settling velocities of the coarser sediments so that they could be transported more readily in suspension. Such analyses of the modes of sediment transport confirm that the Missoula and the Martian floods had phenomenal capacity for eroding and transporting sediments.

#### References

- Bagnold, R.A., 1966, An approach to the sediment transport problem from general physics: U.S. Geological Survey Professional Paper 422-I, 37 p.
- Baker, V.R., 1973, Paleohydrology and sedimentology of Lake Missoula flooding in eastern Washington: Geological Society of America Special Paper 144, 79 p.
- Baker, V.R., 1979, Erosional processes in channelized water flows on Mars: Journal of Geophysical Research, v. 84, p. 7985-7993.
- Baker, V.R., 1982, The channels of Mars: Austin, Texas, University of Texas Press, 198 p.
- Baker, V.R., 1985, Models of fluvial activity on Mars, in Woldenberg, M., ed., Models in geomorphology: Allen and Unwin, London, p. 287-312.
- Baker, V.R., and Costa, J.E., 1987, Flood power, in Mayer, L., and Nash, D., eds., Catastrophic flooding: Allen and Unwin, London, p. 1-24.
- Baker, V.R., and Komar, P.D., 1987, Cataclysmic flood processes and landforms, in Graf, W.L., ed., Geomorphic systems of North America: Geological Society of America Centennial Special Volume 2, p. 423-443.
- Baker, V.R., and Milton, D.J., 1974, Erosion by catastrophic floods on Mars and Earth: Icarus, v. 23, p. 27-41.
- Carr, M.H., 1979, Formation of Martian flood features by release of water from confined aquifers: Journal of Geophysical Research, v. 84, p. 2955-3007.
- Komar, P.D., 1979, Comparison of the hydraulics of water flows in Martian outflow channels with flows of similar scale on Earth: Icarus, v. 37, p. 156-181.
- Komar, P.D., 1980, Modes of sediment transport in channelized water flows with ramifications to the erosion of Martian outflow channels: Icarus, v. 43, p. 317-329.
- Mars Channel Working Group, 1983, Channels and valleys on Mars: Geological Society of America Bulletin, v. 95, p. 1035-1054.

## POWER OF MARTIAN FLOODS

Victor R. Baker, Department of Geosciences and Department of Planetary Sciences, University of Arizona, Tucson, AZ 85721.

The Martian outflow channels are a class of trough-like landforms that display evidence of large-scale fluid flow on their floors (Mars Channel Working Group, 1983). The outflow channels are immense, as much as 100 km wide and 2000 km in length. It was recognized shortly after their discovery that they possessed a similar suite of bedforms and morphological relationships to what was exhibited in the Channeled Scabland (Baker and Milton, 1974). Included are streamlined uplands, longitudinal grooves and inner-channel cataracts, depositional fan complexes, anastomosis, scour marks, and others (Baker, 1982, 1985). Particularly important are the scour marks and the necessity for the responsible fluid to possess a free, upper surface. The entire assemblage of landforms can only be explained by the action of a fluid with physical properties similar to turbulent water. The present consensus is that water in concert with entrained debris and ice was the primary agent of outflow channel genesis (Mars Channel Working Group, 1983).

The ability of river flows to erode and transport sediment has long been known to be related to channel boundary shear stress,  $\tau$ , expressed in  $N/m^2$ , according to the formula

$$\tau_r = \gamma R S, \quad (1)$$

where  $\gamma$  is the specific weight of the fluid ( $9807 \text{ N/m}^3$  for clear water),  $R$  is the hydraulic radius (m), and  $S$  is the energy slope. In two dimensions it may be possible to substitute flow depth  $D$ (m) for  $R$ , yielding the following expression for local bed shear stress:

$$\tau_d = \gamma D S. \quad (2)$$

Another important concept for sediment transport is the energy developed per unit time, or power (Bagnold, 1966). Total power per unit length of stream,  $\Omega$ , expressed in watts/m, is given by the formula

$$\Omega = \gamma Q S, \quad (3)$$

where  $Q$  is discharge ( $m^3/s$ ).

Total stream power varies with the discharge (size) of a river. Therefore, another useful measure of power is its value per unit area of bed, expressed in watts/ $m^2$  ( $w/m^2$ ), given by the formula

$$\omega = \frac{\gamma Q S}{W}, \quad (4)$$

where  $W$  is the water-surface width (m), and other parameters are defined as above.

For many rivers  $Q$  may be expressed as a simple function of width  $W(m)$ , mean flow velocity  $\bar{V}$  (m/s) and depth  $D$  (m):

$$Q = W D \bar{V} . \quad (5)$$

Substituting equation 5 into 4 yields

$$\omega = \tau_d \bar{V} , \quad (6)$$

The largest terrestrial fluvial values of boundary shear stress and stream power per unit area were achieved in the great cataclysmic floods of the Pleistocene (Baker and Costa, 1987). The Missoula Floods at the Soap Lake constriction (Baker, 1973) achieved a bed shear stress  $\tau$  of  $1 \times 10^4$  N/m<sup>2</sup> ( $10^5$  dynes/cm<sup>2</sup>) and a power per unit area of bed  $\omega$  of  $3 \times 10^5$  w/m<sup>2</sup> ( $3 \times 10^8$  ergs/cm<sup>2</sup>-sec) (Baker and Komar, 1987).

Parameters for maximum flood flows on Mars are discussed by Komar (1979), Carr (1979), and Baker (1982). In calculating power per unit area,  $\gamma$  is  $3720$  N/m<sup>3</sup> because of the lower Martian gravity. For a Martian flood a critical cavitation velocity  $V_m$  (m/s) can be defined (Baker, 1979, 1982), which reduces in the lower Martian atmospheric pressure to

$$V_m = 1.6 (D)^{1/2} . \quad (7)$$

For a hypothetical Martian flood flowing 100 m deep at a gradient of 0.01, equations 7 and 6 yield a maximum  $\omega$  of  $6 \times 10^4$  watts/m<sup>2</sup>. For a flood 500 m deep at a 0.01 gradient, the maximum  $\omega$  is  $1 \times 10^5$  watts/m<sup>2</sup>. Thus, maximum flood power per unit area on Mars is comparable to that on Earth.

In comparison to other processes which operate to shape the surfaces of planets, cataclysmic floods seem to be second only to high-velocity bolide impacts in terms of power generation per unit surface area.

Stream powers of the magnitudes reported here can accomplish a variety of unusual and rare sedimentologic and hydraulic phenomena, including (a) suspension of gravels, (b) erosion of bedrock, (c) movement of boulders several meters in diameter, and (d) the transport of enormous quantities of sediment. The effects of dynamic flood conditions are especially noteworthy as to the sizes of sediment carried in the various modes of transport; that is, as bedload, suspension, and washload. As discussed by Komar (1980), it is theoretically possible to extend the domains of these transport modes to evaluate intense floods. Komar finds that typical river floods generating  $\tau = 10$  N/m<sup>2</sup> can entrain and transport sediment grains of about 1 cm diameter, while sediment finer than 1 mm moves in suspension, and the washload consists of sediments finer than 0.1 mm. Exceptionally powerful floods with  $\tau = 10^3$  N/m<sup>2</sup> can transport gravel as coarse as 10 to 30 cm in suspension and sand-size diameters of 0.4 to 0.8 mm and finer in the washload. The increase in  $\tau$  to  $10^4$  to  $10^5$  N/m<sup>2</sup> for the Missoula and the Martian floods implies that even boulders can be transported in suspension with the sand-size grains in the washload. Estimates based on this analysis of sediment transport in clear water actually are likely to be conservative, especially for cases involving

high concentrations of washload. These high concentrations reduce the settling velocities of the coarser sediments so that they could be transported more readily in suspension. Such analyses of the modes of sediment transport confirm that the Missoula and the Martian floods had phenomenal capacity for eroding and transporting sediments.

#### References

- Bagnold, R.A., 1966, An approach to the sediment transport problem from general physics: U.S. Geological Survey Professional Paper 422-I, 37 p.
- Baker, V.R., 1973, Paleohydrology and sedimentology of Lake Missoula flooding in eastern Washington: Geological Society of America Special Paper 144, 79 p.
- Baker, V.R., 1979, Erosional processes in channelized water flows on Mars: Journal of Geophysical Research, v. 84, p. 7985-7993.
- Baker, V.R., 1982, The channels of Mars: Austin, Texas, University of Texas Press, 198 p.
- Baker, V.R., 1985, Models of fluvial activity on Mars, in Woldenberg, M., ed., Models in geomorphology: Allen and Unwin, London, p. 287-312.
- Baker, V.R., and Costa, J.E., 1987, Flood power, in Mayer, L., and Nash, D., eds., Catastrophic flooding: Allen and Unwin, London, p. 1-24.
- Baker, V.R., and Komar, P.D., 1987, Cataclysmic flood processes and landforms, in Graf, W.L., ed., Geomorphic systems of North America: Geological Society of America Centennial Special Volume 2, p. 423-443.
- Baker, V.R., and Milton, D.J., 1974, Erosion by catastrophic floods on Mars and Earth: Icarus, v. 23, p. 27-41.
- Carr, M.H., 1979, Formation of Martian flood features by release of water from confined aquifers: Journal of Geophysical Research, v. 84, p. 2955-3007.
- Komar, P.D., 1979, Comparison of the hydraulics of water flows in Martian outflow channels with flows of similar scale on Earth: Icarus, v. 37, p. 156-181.
- Komar, P.D., 1980, Modes of sediment transport in channelized water flows with ramifications to the erosion of Martian outflow channels: Icarus, v. 43, p. 317-329.
- Mars Channel Working Group, 1983, Channels and valleys on Mars: Geological Society of America Bulletin, v. 95, p. 1035-1054.



## PEAK FLOWS FOR CATAclySMIC FLOODS

Victor R. Baker, Department of Geosciences and Department of Planetary Sciences, University of Arizona, Tucson, AZ 85721; and Jim E. O'Connor, Department of Geosciences, University of Arizona, Tucson, AZ 85721.

New field evidence at key locations in the Channeled Scabland region of Washington provides the input data to flow modeling of cataclysmic flood discharges generated from late Pleistocene glacial Lake Missoula. The flow modeling procedures were developed in studies of exceptionally large Holocene floods in the southwestern U.S. (1,2,3) and central Australia (4). They are being refined for application to Mars (5).

At Wallula Gap and downstream, peak discharges were confined to the Columbia River valley. Because of the reservoir effect associated with hydraulic damming behind the constriction at Wallula Gap, flows were probably steady. Preliminary field studies have identified abundant evidence of peak flow stages in the vicinity of Wallula Gap that correspond to a modeled maximum discharge of  $10,000,000 \text{ m}^3 \text{ s}^{-1}$  (Fig. 1). This discharge estimate is approximately two-thirds of that estimated near the breakout point, but still more than an order of magnitude greater than that of the Bonneville Flood (6), the second largest known terrestrial cataclysmic flood.

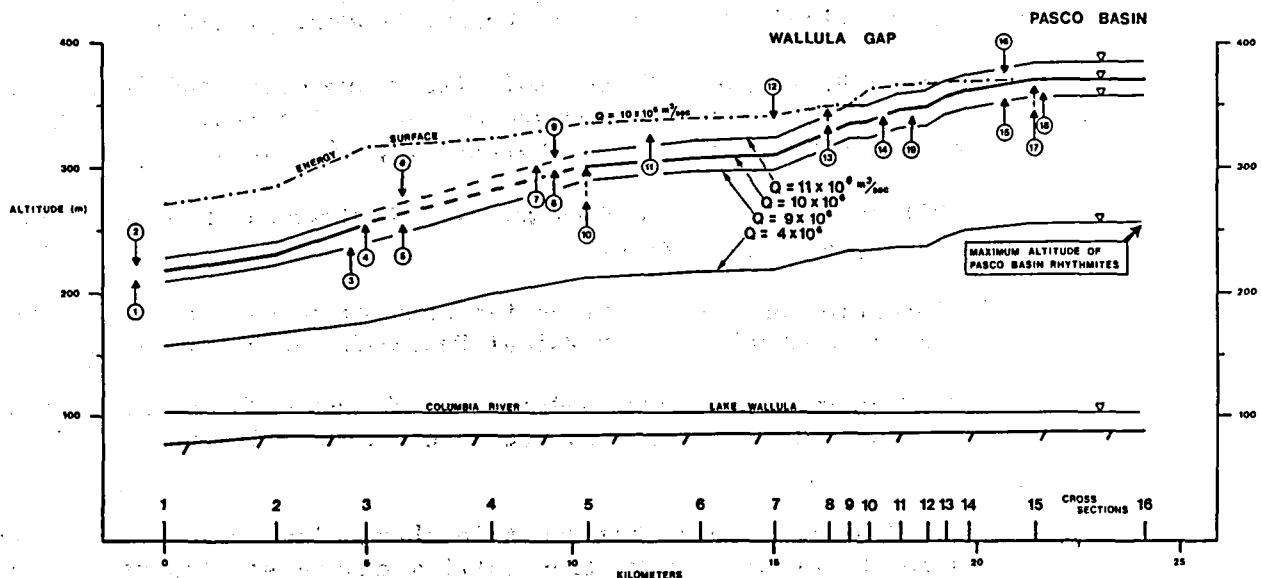


Figure 1. Computer-generated water-surface profiles for various flood discharges in Wallula Gap, east-central Washington. The circled numbers refer to various peak stage indicators.

The peak stage indicators used for comparison to the modeled water-surface profiles include divide crossings, scabland topography, loess scarps,

ice-rafted erratics, and flood deposits. The interpretation of these high-water marks is described by Baker (7,8). The modeling assumes that the existing topography closely approximates the topography extant at the peak flood stages and that flow-resistance formulae are appropriate for floods of this scale. Step-backwater computer procedures are applied to flow that is steady, gradually varied, and two-dimensional. It was found that hydraulic control for flood waters leaving the Pasco Basin and entering the Columbia River gorge was imposed by the contraction at the "gap" (between cross sections 10 and 14) in conjunction with channel constrictions downstream in the vicinity of cross sections 3 and 4 (Fig. 1). The maximum velocities through the modeled reach ranged from  $3.6 \text{ ms}^{-1}$  at cross section 16 to  $36 \text{ ms}^{-1}$  at cross section 4.

We also modeled flows at Rathdrum Prairie, a site close to the Lake Missoula breakout location (7). The assumption of steady flow may not be as tenable here as at Wallula Gap. The proximity of this site to the breakout point allows for the possibility that some of the highwater indicators may have been emplaced by transient waves or flood surges. However, significant sediment accumulations (eddy bars, longitudinal bars) with elevations approaching peak-stage indicators suggest that these effects may be minor. In addition, uncertainties in channel bottom elevation probably result in underestimation of peak discharges. A significant amount of the existing valley fill was probably not present during peak floods, resulting in larger-than-modeled cross-section areas. The valley margins were probably fairly stable.

As shown in Fig. 2, a discharge of  $15,000,000 \text{ m}^3 \text{ s}^{-1}$  results in a computed water-surface profile for Rathdrum Prairie that surpasses or approaches the field evidence for minimum peak flood stages. This discharge is probably a

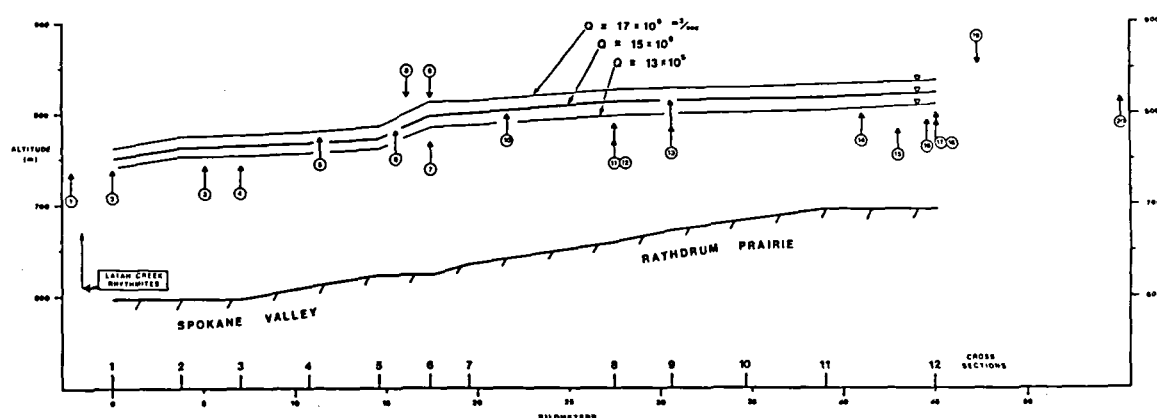


Figure 2. Computer-generated water-surface profiles for various flood discharges at Rathdrum Prairie, northeastern Washington and northern Idaho.

minimum estimate for maximum Missoula outburst discharges because of the probabilities that other flow paths were operating and that the channel bottom was significantly lower than at present.

Discharges obtained in this study are somewhat lower than those calculated for the Missoula Flood peak using simpler procedures (7), but they are much higher than predicted by models assuming dam failure by ice-tunneling (9) and by regression analysis of historic jökulhlaups (10). The new estimates seem consistent with a more catastrophic mode of ice dam failure for Lake Missoula than envisioned in several recent studies (9,10,11). However, our new estimates are constrained directly by the field evidence, and do not rely on a chain of assumptions about dam-failure modes. Moreover, the estimates at Rathdrum and Wallula are mutually consistent because downstream attenuation of peak flow rates is to be expected. Moreover, the stages associated with these discharges are significantly higher than the highest extent of rhythmically-bedded flood deposits in the Pasco Basin and Spokane Valley (11,12). This may indicate that the floods that emplaced the rhythmites were of significantly lower magnitude than those associated with field evidence of maximum flows.

These results do not preclude the occurrences of scores of relatively small late Pleistocene jökulhlaups capable of emplacing low-energy flood deposits, as described in recent studies by R.B. Waitt (11,12,13) and B.F. Atwater (14,15,16). However, these studies of low-energy depositional facies provide no constraint on the truly cataclysmic, largest Missoula flood flows (17). It is the latter that are most important in relation to the similarly-scaled flows thought responsible for the origin of the Martian outflow channels (18).

#### References

- (1) L.L. Ely and V.R. Baker, Phys. Geogr. **6**, 103-126 (1985). (2) J.E. O'Connor, R.H. Webb, and V.R. Baker, Geol. Soc. America Bull. **97**, 410-420 (1986). (3) J.B. Partridge and V.R. Baker, Earth Surf. Proc. and Landforms **12**, 109-125 (1987). (4) V.R. Baker and G. Pickup, Geol. Soc. America Bull. **98**, 635-646 (1987). (5) V.R. Baker and J.E. O'Connor, NASA Tech. Memo. **88383**, 274-276 (1986). (6) R.D. Jarrett and H.E. Malde, Geol. Soc. America Bull. **99**, 127-134 (1987). (7) V.R. Baker, Geol. Soc. America Spec. Paper **144**, 1-79 (1973). (8) V.R. Baker, in The Channeled Scabland (NASA, Washington, D.C., 1978), pp. 59-79. (9) G.K.C. Clarke, W.H. Mathews, and R.T. Pack, Quat. Res. **22**, 289-299 (1984). (10) J.E. Beget, Quat. Res. **25**, 136-138 (1986). (11) R.B. Waitt, Geol. Soc. America Bull. **95**, 1271-1286 (1985). (12) R.B. Waitt, Quat. Res. **22**, 46-58 (1984). (13) R.B. Waitt, J. Geol. **88**, 653-679 (1980). (14) B.F. Atwater, Geology **12**, 464-467 (1984). (15) B.F. Atwater, U.S. Geol. Survey Bull. **1611** (1986). (16) B.F. Atwater, Quat. Res. **27**, 182-201 (1987). (17) V.R. Baker and R.C. Bunker, Quat. Sci. Rev. **4**, 1-41 (1985). (18) V.R. Baker and P.D. Komar, in Geomorphic Systems of North America (Geol. Soc. America, Boulder, 1987), pp. 287-312.

THE INVENTORY OF WATER ON MARS. Michael H. Carr, U. S.  
Geological Survey, Menlo Park, CA 94025

Water plays a crucial role in the evolution of a planet, affecting not only deep-seated magmatic processes but also processes such as weathering, erosion, and sedimentation that alter and redistribute materials near the surface. The amount of water also has climatologic and biologic implications. For Mars, if the higher estimates of some workers are correct, a warm, wet period likely occurred early in its history. Current estimates of the amount of water outgassed by Mars and still present near the surface differ by two orders of magnitude. If we are to understand Mars' geologic and climatologic history, therefore, we must better evaluate the current near-surface inventory of water and better understand how the conflicting estimates may be reconciled.

The lower estimates are based mainly on geochemical arguments. After Viking determined the low  $^{36}\text{Ar}$  and  $^{40}\text{Ar}$  content of the Martian atmosphere, Anders and Owen (1977) and Rasool and Le Sergeant (1977) concluded that Mars has outgassed only 6-10 m of water, as compared with 3 km for Earth; they based this value on the assumption that Mars has the same noble gas to nonnoble gas ratios as do meteorites. However, lack of isotopic fractionation of oxygen in the atmosphere indicates that such oxygen must interchange with oxygen in a surface reservoir. McElroy and Yung (1977) showed that if this surface reservoir is mostly water, it must contain at least 13 m of  $\text{H}_2\text{O}$ . After discovery in the Venusian atmosphere of the relatively high content of  $^{36}\text{Ar}$  with respect to other volatiles, the assumption of meteoritic ratios was questioned by Pollack and Black (1979), who argued, on the basis of a model of differential incorporation of volatiles in the terrestrial planets, that Mars could have outgassed 80-160 m of water. More recently, the water inventory has been estimated from SNC meteorites: Dreibus and Wanke (1987) showed that if these meteorites come from Mars, Mars is richer in most volatiles than is Earth. They concluded, however, that the water inventory is much less than on Earth. They suggested that the total planetary inventory was only 130 m at the end of accretion and that only a fraction of this amount is likely to have subsequently outgassed to the surface. Their conclusion was based on the low concentration of chalcophile elements in the Martian mantle, which indicates that the mantle is in equilibrium with the core and implies that most of the water originally present would have reacted with Fe to form  $\text{FeO}$  and  $\text{H}_2$ , which was subsequently lost. Thus the geochemical estimates of Martian outgassing of water range from 6 to 160 m.

Geologic estimates of the near-surface inventory of water, based on its observed erosive effects, are significantly larger than the geochemical estimates. The water present as ground ice at depths shallower than 1 km is estimated from mobilization of the near-surface materials at high latitudes observed as debris flows and terrain softening (Squyres and Carr, 1986). The features diagnostic of surface flow are found almost ubiquitously in heavily cratered terrain at latitudes higher than  $30^\circ$  and are almost absent at lower latitudes. The assumptions that

no ice is present at depths shallower than 1 km at low latitudes and that ice must be present at high latitudes in amounts in excess of the rock porosity leads to the estimate that the equivalent of 50 m of water is present planetwide at depths shallower than 1 km (Carr, 1986). Most of the outgassed water appears, however, to be at greater depths, and the amount of ground water at these depths can be estimated from the degree of erosion that it caused by catastrophic breakout (Carr, 1986). Around the Chryse basin, the canyons, chaos, and channels have a total volume of  $5.9 \times 10^6 \text{ km}^3$ . Part of this volume is created tectonically, as evidenced by fault scarps in the canyons; the rest appears to result from water erosion. If we conservatively assume that the main east-west Ius, Melas, and Coprates Chasmata were formed entirely by faulting,  $4.4 \times 10^6 \text{ km}^3$  was removed by water. Assuming that all this water carried its maximum sediment load,  $6.6 \times 10^6 \text{ km}^3$  of water passed through the Chryse channels, the equivalent of 46 m planetwide. The Chryse artesian basin covers one-tenth to one-sixth of the planet's surface. It is improbable that all the outgassed water on the planet accumulated in this one local area. More probably, ground water was present over the entire planet, as indicated by the distribution of valley networks, and outflow channels formed around Chryse because there the conditions necessary for catastrophic release were achieved (Carr, 1979). The Chryse volumes can then be extrapolated to the whole planet to give a total deep-water inventory of 270-460 m, depending on the area of the Chryse artesian basin. If we add to this value that of the shallow water, we get a planetwide inventory of 320-510 m. This estimate is conservative in assuming that all the water passing through the circum-Chryse channels carried its maximum sediment load, but it is optimistic if there was significant recycling of the water that passed through the channels.

The geologic estimates can be reconciled with the geochemical estimates based on noble gases if significant amounts of the noble gases were lost from the planet, e.g., by large impacts (Watkins and Lewis, 1986) or by hydrodynamic escape (Hunten et al., 1987), both of which appear likely. Loss by large impacts would tend to be more effective on a small planet like Mars than on Earth or Venus. The Dreibus and Wanke (1987) estimates based on SNC meteorites may be in error because of the assumption of completely homogeneous accretion. If a small fraction of the volatile-rich component accreted late, after core formation, as apparently occurred on Earth, Mars could have retained a larger amount of water than the Dreibus and Wanke estimates. Thus there are no decisive geochemical arguments against the large geologic estimates. If, nominally, 0.5 km of water outgassed, approximately 10 bars of  $\text{CO}_2$  and 0.1 bars of  $\text{N}_2$  probably outgassed also. It is likely that these gases are now mostly fixed in the ground as carbonates (roughly 200 m) and nitrates.

The outgassed water has been redistributed since the geologic record emerged at the end of heavy bombardment. At that time, liquid water was present close to the surface over the whole planet, as indicated by the wide distribution of valley networks. The lack of terrain softening at low latitudes suggests, however, that even then insufficient water or ice was present to alter the rheological properties of the near-surface

rocks. Subsequently, the low latitudes lost much of their near-surface water to the cold trap at higher latitudes. At the end of heavy bombardment, the climate may have been warmer and wetter than at present. Conditions, however, became more like the present as the CO<sub>2</sub> became fixed as carbonates in the ground. A thick permafrost developed, trapping ground water at greater depths. The sequence envisioned is that ground water catastrophically broke through the permafrost periodically, causing large floods. Most of these floodwaters pooled and froze in low areas, particularly at high northern latitudes. The ice deposits so formed are probably still present in these areas, as indicated by the presence of a wide variety of features attributed to ice action. Meanwhile, the volatile-rich, ancient surface became progressively overplated with volatile-poor, mantle-derived volcanic materials.

#### REFERENCES.

- Anders, E., and Owen, T., 1977, Mars and Earth: Origin and abundance of volatiles: *Science*, v. 198, p. 453-465.
- Carr, M. H., 1979, Formation of Martian flood features by release of water from confined aquifers: *J. Geophys. Res.*, v. 84, p. 2995-3007.
- Carr, M. H., 1986, Mars: A water-rich planet?: *Icarus*, v. 68, p. 187-216.
- Dreibus, G., and Wanke, H., 1987, Volatiles on Earth and Mars: A comparison: *Icarus*, v. 71, p. 225-240.
- Hunten, D. M., Pepin, R. O., and Walker, J. C. G., 1987, Mass fractionation in hydrodynamic escape: *Icarus*, v. 69, p. 532-549.
- McElroy, M. B., and Yung, Y. L., 1977, Photochemistry and evolution of Mars' atmosphere: Viking perspective: *Icarus*, v. 82, p. 4379-4388.
- Pollack, J. B., and Black, D. C., 1979, Implications of the gas compositional measurements of Pioneer Venus for the origin of planetary atmospheres: *Science*, v. 205, p. 56-59.
- Rasool, S. I., and LeSergeant, L., 1977, Volatile outgassing from Earth and Mars: Implications of the Viking results: *Nature*, v. 266, p. 822-823.
- Squyres, S. W., and Carr, M. H., 1986, Geomorphic evidence for the distribution of ground ice on Mars: *Science*, v. 231, p. 249-252.
- Watkins, G. H., and Lewis, J. S., 1986, Evolution of the atmosphere of Mars as the result of asteroidal and cometary impacts: *Lunar and Planet. Inst. Tech. Report 86-06*, p. 46-47.

## CHARACTERISTICS OF MARTIAN CHANNEL MATERIALS

Robert A. Craddock<sup>1</sup>, Ronald Greeley<sup>1</sup>, Philip R. Christensen<sup>1</sup>, and Frank T. Aldrich<sup>2</sup>, <sup>1</sup>Department of Geology, <sup>2</sup>Department of Geography, Arizona State University, Tempe, Arizona 85287

High resolution (~3 km) thermal infrared mapping using the Viking IRTM has been completed for several of the larger martian outflow and fretted channels including Dao (-40.0°, 267.0°), Harmakis (-45.0°, 268.0°), Ma'adim (-20.0°, 182.0°), Mangala (-17.0°, 147.0°), and Shalbatana (0.0°, 45.0°) Valles [1]. Typically at least two high resolution sequences were used to calculate the distribution of thermal inertia ( $I$ , expressed in units of  $10^{-3} \text{ cal cm}^{-2} \text{ sec}^{-1/2} \text{ K}^{-1}$ ) and relative rock abundances [2] within each of these channels. Previous results [3,4] have been based on thermal inertia data only. Calculation of the rock abundances in association with the thermal inertia measurements allow several observations and interpretations to be made:

(1) Wider portions of Ma'adim, Dao, and Harmakhis Valles and portions of Shalbatana Vallis exhibit higher overall thermal inertias than the surrounding terrains or the narrower portions of the channels. Typically these values are between 7.0 and 9.0 (effective grain-size of between 0.25 to 0.5 mm; [5]) and correspond to dark materials within the channels. Low rock abundances (<5%) were observed in Ma'adim and Shalbatana Valles, suggesting that these dark materials are composed primarily of a fine-grained component close to the diameter of their effective grain-sizes. These observations help to confirm previous interpretations of dark materials being aeolian in origin [6,7]. Because they are not unique to the channel themselves but are contained in local broad low-lying areas (e.g., craters), they probably represent regional or local modification processes and are not materials left over from the channels formation as might be suggested by [8].

(2) Although 10 to over 100 km across in places, Mangala Valles does not exhibit any concentration of dark materials as observed in the other channels. The low thermal inertia (4.0) corresponds to material that can be related to the large dust sink in Amazonis Planitia identified by [9,10]. Perhaps due to a lack of relief or the low settling rates for fine-grained particles after the martian dust storms, this material seems to "drape" the area and local features--including Mangala Valles. However, lower thermal inertia materials ( $I = 2.5$  to  $3.5$ ; effective grain-sizes =  $0.03$  to  $0.05$  mm) seem to be concentrated in the graben/source area. Rock abundances (10 to 17%) indicate that these materials are possibly masking large diameter particulates ( $\geq 10$  cm) which may be related to the formation of the channel and/or the graben.

(3) Narrow portions of the channels exhibit thermal inertias and rock abundances identical to the values observed outside of the channels. This suggests that the processes that formed the channels and the processes that formed the surrounding terrains may have both resulted in deposits that have the same effective grain-sizes and rock abundances. More likely, however, processes that have occurred after the formation of these features have worked to modify and homogenize the upper surface, or the thermal skin depth, of the regions studied. Aeolian activity is well known to be one of most active geologic process occurring on Mars at the present time, and it probably acts as the homogenizing agent by depositing similar size materials uniformly over broad areas.

(4) A notable exception to an area with high thermal inertias ( $I = 9.0$  to  $12.0$ ; effective grain-sizes =  $0.55$  to  $1.5$  mm) that does not correspond to any dark materials is within Shalbatana Vallis. [11] have made similar observations in Ares Vallis, which is also located in the Oxia Palus quadrangle ~2,000 km to the east. Rock abundances within Shalbatana Vallis are as high as 14% (11–20  $\mu\text{m}$  bands with emissivity correction); observations made by [12] show that rock abundances within Ares Vallis are  $\geq 14\%$  (7–20  $\mu\text{m}$  bands). These areas may represent channel deposits that have not been substantially modified since their emplacement; this seems unlikely however, considering that Shalbatana Vallis has obvious aeolian materials deposited within it at other locations (e.g.,

the large dark streak originating from the chaotic terrain/source area). A mechanism is needed whereby certain areas within the channels are kept free from debris brought in from outside aeolian processes.

(5) A large drop-off in thermal inertias  $\sim 25$  to  $\sim 50$  km inside of Chryse Planitia corresponding to  $I = 13.0$  to  $I = 7.0$  indicates that the effective particle sizes decrease from  $\sim 2.0$  to  $\sim 0.5$  mm. Although not a large decrease in particle sizes, it may be weakly indicative of emplacement by liquefaction processes [13]. Other debouching areas are not as clear: Harmakhis Vallis has thermal inertia values that seem too widespread to be directly associated with channel formation. Dao Vallis has local deposits of moderate and high thermal inertia materials ( $I = 7.0$  to  $11.0$ ), but these values correspond to regional values obtained by [9,10] and may also represent dark aeolian material contained in local areas. The thermal inertia values ( $I \geq 7.0$ ) observed in the distal portion of Ma'adim Vallis and the crater Gusev correspond to dark material with a low rock abundance ( $< 5\%$ ); this is highly indicative of aeolian material. Amazonis Planitia, the debouching area for Mangala Valles was not observed in this study.

(6) Limited thermal emissivity observations suggest that "bedrock" outcrops, or materials with different compositions  $\sim 3$  km in diameter, are not present along the channel walls, the channel floor, or on the surrounding terrains. This suggests that materials are compositionally homogeneous at the depth of a few 10's of centimeters (i.e., thermal skin depth).

These results indicate a dominance of aeolian activity in and around the channels that produces a geologic cover possibly 10's of centimeters deep. This cover does not permit an evaluation of deposits related to the channel forming events [e.g., 14] to be made by currently available thermal infrared (IRTM) data. Observations made by the IRTM do, however, allow ongoing aeolian processes within the channels to be assessed, and it is probable that the channels behave as topographic sources of local winds that have produced the observations made in this study. These channel winds are probably created and driven through a process of differential heating which would occur throughout a martian day. Differential heating would be enhanced by the morphology of the channel, namely depth, orientation, and slope. These variables are difficult to apply directly to the channels because the topography of the channels is extremely complex [e.g., 15,16] and because the topographic information for these features is generally poor [17]. Assuming that the channels are simple valleys, then diurnal variations in wind speed and direction as a function of differential heating are probably similar to those established by [18,19,20] for terrestrial valleys.

IRTM data confirm that the channels do receive different amounts of insolation due to their morphology. Sequences taken over Shalbatana Vallis during the northern hemisphere spring indicate that the sunlit channel wall can be  $\sim 42.0^\circ\text{K}$  warmer in the late evening than the channel floor contained in the shadows 2.5 km below. Temperature differences of only  $5.0^\circ\text{K}$  in the 1 km deep Dischma Valley, West Germany created winds of  $\sim 5.0$  m/sec [21]. Based on wind tunnel simulations [22], winds speeds of more than 35 m/sec need to be generated in the martian channels in order to remove dark materials with effective grain-sizes of between 0.5 to 1.5 mm ( $I = 8.0$  to  $12.0$ ). Whether or not wind speeds this great could be produced in the channels is subject to future work. However, the assumption is that they are produced and that they can explain some of the IRTM observations made in this study:

(1) Channel winds may decrease when the channel widens or reduces slope, perhaps explaining the occurrence of dark materials ( $I = 8.0$  to  $12.0$ ) within the wider portions of the channels. These dark materials may thus be eroded channel deposits, materials that were deposited in the narrower portions of the channels after the martian dust storms, or materials that have fallen into the channels from above; all of which were subsequently removed and re-deposited by the channel winds.



(2) Portions of Shalbatana and Ares Valles that have high thermal inertia values ( $I \approx 11.0$ ) not corresponding to any dark materials may have lag deposits created by very strong channel winds induced by locally high topographic relief.

(3) Channel portions that have thermal inertia comparable to the surrounding terrain may have data that was gathered after the martian dust storms. This suggests that the climatic conditions necessary to produce the channel winds take time to adjust, and newly deposited materials are left on the surface. It may also be that the channel winds in those particular portions are not strong enough to remove materials.

(4) Channel winds do not seem to be produced in Mangala Valles, possibly because it is a broad low-relief channel that undergoes very little differential heating. Materials deposited on the surface after the dust storms and other processes are never removed.

(5) As suggested above, the dark streaks originating from and extending beyond Ma'adim and Shalbatana Valles are probably materials eroded from the channel. Future simulations of the Ma'adim channel streak may help quantify some of the physical variables of the channel winds.

Further qualitative and quantitative studies of the channel winds and future data from the Mars Observer thermal emission spectrometer (TES) may help verify the possibilities of some of the above arguments.

#### References

- [1] Craddock, R.A., 1987, *High Resolution Thermal Infrared Mapping of Martian Outflow and Fretted Channels*, Unpublished M.S. Thesis, Department of Geology, Arizona State University.
- [2] Christensen, P.R., 1982, *Jour. Geophys. Res.*, **87**, 9985-9998.
- [3] Craddock, R.A., R. Greeley, and P.R. Christensen, 1987, *NASA TM 89810*, 261-263.
- [4] Craddock, R.A., R. Greeley, and P.R. Christensen, 1987, *Lunar Planet. Sci. XVIII*, 203-204.
- [5] Kieffer, H.H., T.Z. Martin, A.R. Peterfreund, B.M. Jakosky, E.D. Miner, and F.D. Palluconi, 1977, *Jour. Geophys. Res.*, **82**, 4249-4292.
- [6] Christensen, P.R., 1983, *Icarus*, **56**, 496-518.
- [7] Zimbelman, J.R., 1986, in *Papers Presented to the Symposium on Mars: Evolution of Its Climate and Atmosphere*, 112-114.
- [8] Cutts, J.A., and K.R. Blasius, 1981, *Jour. Geophys. Res.*, **86**, 5075-5102.
- [9] Palluconi, F.D., and H.H. Kieffer, 1981, *Icarus*, **45**, 415-426.
- [10] Christensen, P.R., 1986, *Jour. Geophys. Res.*, **91**, 3533-3545.
- [11] Henry, L.Y., and J.R. Zimbelman, 1987, in *Papers Presented at the Third Annual Summer Intern Conference*, 13-14.
- [12] Christensen, P.R., 1986, *Icarus*, **68**, 217-238.
- [13] Nummedal, D., and D.B. Prior, 1981, *Icarus*, **45**, 77-86.
- [14] Baker, V.R., and D.J. Milton, 1974, *Icarus*, **23**, 27-41.
- [15] Masursky, H., J.M. Boyce, A.L. Dial, G.G. Schaber, and M.E. Strobell, 1977, *Jour. Geophys. Res.*, **82**, 4016-4038.
- [16] Lucchitta, B.K., and H.M. Ferguson, 1983, *Jour. Geophys. Res.*, **88**, A553-A568.
- [17] U.S. Geological Survey, 1987, *Topographic Map of Mars*, in press.
- [18] Prandtl, L., 1942, *Fuhre durch die Stromungslehre*, F. Vieweg and Sohn, Braunschweig, 124 pp.
- [19] Prandtl, L., 1952, *Essentials of Fluid Dynamics*, Blackie and Son Ltd., London, 242 pp.
- [20] DeFant, F., 1951, in *American Meteorological Society--Compendium of Meteorology*, 655-672.
- [21] Urfer-Henneberger, C., 1970, *Archiv fur Meteorologie, Geophysik und Bioklimatologie Series B*, **18**, 21-42.
- [22] Greeley, R., R. Leach, B. White, J. Iversen, and J. Pollack, 1980, *Geophys. Res. Lett.*, Vol. 7, No. 2, 121-124.

## MORPHOLOGIC CONTRASTS BETWEEN NIRGAL AND AUQAKUH VALLES, MARS: EVIDENCE OF DIFFERENT CRUSTAL PROPERTIES.

David J. MacKinnon, Kenneth L. Tanaka, *U.S. Geological Survey, Flagstaff, AZ 86001*,  
Philip J. Winchell, *Wittenberg University, Springfield, OH 45501*

We have made photoclinometric measurements of sidewall slopes in Nirgal and Auqakuh Valles and have interpreted these results in terms of the geologic setting and a simple geomorphic model to provide new insights into the physical properties of crustal materials in these areas. Nirgal has been interpreted to be a runoff channel and Auqakuh to be a fretted channel by [1]. Geomorphologic arguments for the sapping origin of Nirgal and Auqakuh Valles have been presented by [1] and [2]. The morphologies of the channels, however, differ greatly: the tributaries of Nirgal end abruptly in theater-headed canyons, whereas the heads of tributaries of Auqakuh shallow gradually. The plateau surface surrounding both channels appears to be covered by smooth materials, presumably lava flows; they are continuous and uneroded in the Nirgal area, but at Auqakuh they are largely eroded and several layers are exposed that total about 200 m in thickness. For Nirgal Vallis, our measurements show that sidewalls in the relatively shallow upper reaches of the channel (200-m to 400-m depth) have average slopes near 30 degrees and, in the lower reaches (500-m to 1000-m depth), sidewall slopes exceed 50 degrees. Auqakuh, on the other hand, has maximum sidewall slopes of 14 degrees and an approximate maximum depth of 1000 m. Faint, horizontal layering in portions of the lower reaches of Nirgal may indicate inhomogeneity in either composition or topography.

A key relation is whether these slopes are above, near, or below the angle of repose for loosely consolidated and noncohesive materials. (Such an angle of repose is about 30 degrees and is independent of gravity [3, 4, 5].) Slopes above the angle of repose may indicate competent rock, cemented fines, or compaction of poorly sorted materials [6]; slopes near the angle of repose may be composed of dry talus, soil, and other granular materials, and slopes below the angle of repose may suggest modification by volatiles. Selby [4, p. 200] and Moon [3] showed that equilibrium (stabilized) slope values are highly correlated with the strength of intact rock and spacing of joints; they tested models on scarps in Antarctica, New Zealand, and South Africa. Where soil formation is limited in "dry" climates and in mountains, slope angles reflect rock strength. We have extrapolated this correlation and its implied geomorphologic relation on Mars, along with our sidewall profiles and interpretation of the geologic settings of Nirgal and Auqakuh Valles in order to understand the physical and hydraulic properties of their materials.

## Nirgal Vallis:

Low slope angles (less than 30 degrees) in the upper 200 m of crust below the surface lava flows indicate a fairly well brecciated or fine grained material. This material is probably highly cratered: some low-rimmed craters are seen protruding through the caprock. The slope increases with depth, suggesting that the material becomes either less brecciated or more cemented with depth. In either case, the permeability and pore space would decrease with depth as well. This reduction in hydraulic capabilities indicates that, under present circumstances, only high discharges from a necessarily large volume of water-saturated material would be capable of removing materials to form the channel. Other possibilities include past climatic conditions that caused recharge of the ground water or surface flows sufficient to remove the materials.

## Auqakuh Vallis:

The relatively gentle sidewall slopes for Auqakuh are not consistent with the "fretted" classification suggested by [1,2,5]. The sidewall slopes are, in fact, significantly below the angle of repose for unconsolidated material. Based on our model, this relation strongly suggests that the sidewall slopes were modified by periglacial mass-wasting, involving ground ice, as previously suggested by [1]. The surface lava flows are largely eroded, possibly by mass-wasting and wind, indicating that earlier processes had weathered the flows into relatively fine material. Alternatively, some of the fine material may be eolian deposits. Below the flows, a lower layer of undetermined thickness (at least 600 m) appears to have a rough surface and is heavily cratered where exposed on the plateau. Because downslope processes have shed debris from the upper layers into the channel, it is uncertain whether this lower layer is actually exposed. The same downslope processes in the channel may have removed or subdued crucial indicators of Auqakuh's early formation. What is clear, though, is that an enormous volume of crustal material has been removed from the channel. If the material was fine grained and loosely consolidated, it was more readily removed by sapping and eolian processes than materials in Nirgal Vallis.

## Future Considerations:

We have explored only one geomorphologic model that interprets crustal properties in Nirgal and Auqakuh Valles. Other aspects that need to be considered carefully include apparently large differences in time of formation of the channels and variations in associated climate. Auqakuh, which is older than several heavily degraded craters, 10km diameter or greater, may have been initiated during the end of the heavy bombardment

(it is about the same age as with other ancient valley systems) and later modified by surface volatiles and a colder climate. Nirgal, on the other hand, is only sparsely cratered and probably formed much later from subsurface aquifers (if such can be justified in terms of our earlier argument) after water from the surface layers was depleted. Its formation was possibly contemporaneous with the Tharsis tectonism that appears implicated in the formation of the large outflow channels east and north of Valles Marineris. Both may have even formed at nearly the same time if surface volatiles were never present at Nirgal Valles: each channel lies in a region roughly 30 degrees from the equator that is assumed to be transitional between an ice-poor and ice-rich regolith [8].

Clearly our interpretation of slopes needs to be more sharply qualified. For example, those slopes below the angle of repose for loosely consolidated materials may have been formed by landslides, eolian deposits, volatiles, earthquakes, or all of the above. We plan to produce more photoclinometric and stereophotogrammetric sidewall slope measurements of other channels and develop qualified geomorphologic models to obtain a broader understanding of the influence of crustal materials and climate on the formation of aquifer and channel systems on Mars.

#### References Cited:

- [1] Baker, V. R., 1982, The channels of Mars: Univ. of Texas Press, Austin, 198 p.;
- [2] Sharp, R. P., and M. C. Malin, 1975, Channels on Mars: Geol. Soc. Amer. Bull., v. 86, p. 593-609;
- [3] Moon, B. P., 1984, Controls on the form and development of rock slopes in fold terrane, in Hillslope processes (edited by A. D. Abrahams): Boston, Allen & Unwin Ltd., p. 225-243;
- [4] Selby, M. J. 1982, Hillslope materials and processes: London, Oxford Univ. Press, 246 p.;
- [5] Terzaghi, K., and R. Peck, 1967, Soil mechanics in engineering practice, 2nd ed.: New York, John Wiley & Sons, 729 p.;
- [6] van Burkalow, A., 1945, Angle of repose and angle of sliding friction: An experimental study: Geol. Soc. Amer. Bull., v. 56, p. 669-708;
- [7] Carr, M. H., 1981, The surface of Mars: Yale Univ. Press, New Haven, 349 p.;
- [8] Fanale, F. P., J. R. Salvail, A. P. Zent, and S. E. Postawko, 1986, Global distribution and migration of subsurface ice on Mars: Icarus, 67, p. 1-18

**EASTERN LUNAE PLANUM OUTFLOW COMPLEX: ANALOGY TO OVERBANK FLOODING;**  
R. A. De Hon, Department of Geosciences, Northeast Louisiana University, Monroe LA 71209.

**Introduction.** Lunae Planum stands as a broad, volcanic capped plateau on the eastern flank of the Tharsis bulge. The surface is lightly cratered and relatively unmarked by erosion except along its western and northern periphery where steep escarpments face Kasei Vallis. Along the eastern margin, the plateau merges with older cratered terrain on the western rim of the Chryse basin. The eastern edge of Lunae Planum is marked by a broad scour and channel system that originates from Juventae Chasma and is traced northward along the boundary between plains and cratered terrain (1,2,3). Eleven hundred kilometers north of the source, three canyon systems cut eastward across the cratered terrain to empty onto the lower Chryse plains surface (1,2,3). Sixteen hundred kilometers north of Juventae Chasma, the Lunae Planum surface is cut by the eastward draining Kasei Vallis. This entire system of drainage will be referred to as the Eastern Lunae Planum Outflow Complex. The complex is made up of three distinct systems: the Upper Maja Vallis system (2) on Lunae Planum; the canyon system which consist of the Maja Valles, Vedra Valles, Maumee Valles, and Bahram Vallis; and the unconfined flow from these canyons onto and across Chryse Planitia. The complex has characteristics in common with terrestrial overbank flooding.

**Descriptive Overview.** The outflow originates from Juventae Chasma (1,3); a box canyon that separates Lunae Planum from Ophir Planum north of the Coprates Chasma. Juventae Chasma grades northward through chaotic terrain into the outflow region of the Upper Maja Vallis (1,2). The broad flow northward across the plains surface is marked by streamlined islands, scour markings, and inner channels which are best developed nearest the source and become less distinct northward. This zone varies from 100 to 200 km wide along its southern coarse and has a gradient of approximately 0.002. The eastern edge is marked by the contact between plains material of Lunae Planum and older cratered plateau material. The western edge of the flow is an ill-defined zone between flow-modified and unmodified plains materials of Lunae Planum. The western boundary of the upper system becomes indistinct along its northern reaches. Vestiges of surface flow are traced 1100 km to the vicinity of the three eastward running valles (canyons). Unfortunately, superposition of young craters masks surficial features in this region. It is possible that the flow responsible for the Upper Maja Vallis reached the northern escarpment and discharged into Kasei Vallis.

Three canyon systems reach from the Upper Maja Vallis surface 130 km to the lower Chryse Planum surface to the east. The canyon systems head at the Lunae Planum/cratered terrain boundary and discharge onto the lower Chryse Planum surface. The gradient averages 0.008, four times that of the upper system. Verda and Maumee valles form complex networks of low angle, converging channels of low sinuosity incised into cratered plateau material. The major channel of both systems truncates several of their tributaries producing "hanging valleys" (1). Maja Vallis is characterized by a straight, deeply incised channel with scoured walls, streamlined islands, longitudinal grooves and cataracts (1,2). The lower ends of Maja and Maumee valles are marked by faint depositional aprons (alluvial fans) which are cut by numerous, small, divergent channels (distributaries). The Bahram Vallis, north of the canyon system, is different (1). It heads on the Lunae Planum surface and extends 170 km across the plains as a steep walled, sinuous channel with few tributaries. Bahram then cuts across the cratered terrain to the Chryse surface.

Unconfined outflow from Maja and Maumee valles onto the Chryse plain is traced for 300 km northeast across Chryse Planum by a series of streamlined islands, scour marks,

and breached dorsa (1,2,3). The gradient on Chryse Planum averages 0.01 approximately equal to the canyon gradient. Evidence of the flow is lost less than 100 km from the Viking 1 landing site.

Analogy. The Upper Maja Vallis system is the result of catastrophic flooding similar to glacial outburst of the Channeled Scablands (4,5,6). The entire Eastern Lunae Planum Outflow Complex is analogous to a flooded, leveed river system on a low gradient plain. During periods of peak discharge, flood waters may rise above natural levees and flow unhindered down slopes away from the main channel. Overbank discharge cuts crevasses in the levee and forms splays on the flood plain.

By analogy, the main channel of the system is represented by the upper Maja Vallis stretching from Juventae Chasma to Kasei Vallis. The initial outflow was a quasi-sheetflood confined between the eastward sloping Lunae Planum surface and the slightly higher cratered plateau materials (2) which form a levee to the east. As the flood surged northward, overbank flooding on the east side of the broad channel spilled flood waters eastward onto the steeper slope down to the Chryse plain. Beginning as sheetflow, the overbank flood rapidly cut channels (crevasses) in the steeper, irregular slope. From a multitude of early channels (lower Bahram, Vedra, Maumee, and Maja valles and their tributaries) flow became channelized into a few, main channels (lower Bahram, Vedra, Maumee and Maja valles) which continued to downcut as tributaries were abandoned. Gradually, one of the channels (Maja Vallis) captured most of the overbank flow to become the main relief for the flood waters.

During the early stages of overbank flooding, channels were rapidly cut into the cratered plateau material. Debris carved from the channels was deposited as thin alluvial aprons at the mouths of the canyons. Later flow from the canyons cut channels in the alluvial aprons. As the flow debouched from the canyons onto the Chryse surface, unconfined flood waters spread across the surface similar to crevasse splays on a flood plain.

Small, temporary lakes were formed as the initial overbank flooding inundated craters and other topographic lows in the cratered plateau. A large lake formed on the upper Lunae Planum surface by incomplete drainage of the flood waters. Another lake formed on the Chryse surface at the mouth of Maja Vallis by flood waters ponded behind ridges (2).

The length of time required for the development of the entire complex is unknown, but it was certainly a short time, measured in days or weeks. A greatly reduced flow may have continued in the main channels for some period afterward. Whether the Upper Maja Vallis established a short-lived continuous flow into Kasei Vallis or was briefly ponded on the northern Lunae Planum, establishment of drainage from the plateau onto the lower Chryse surface was probably a single event and does not require multiple outburst from the source area. The portion of the Bahram Vallis developed on the Lunae Planum surface must be postdiluvian. The upper channel developed through headward erosion either by groundwater sapping and caving or by slow drainage of the remnant lake at the northern end of Upper Maja Vallis.

#### REFERENCES

- (1) Theilig, E. and R. Greeley (1979) J. Geophys. Res. 84 , 7994-8010.
- (2) Baker, V. R. and R. C. Kochel (1979) J. Geophys. Res. 84 , 7961-7983.
- (3) Carr, M. H. (1984) NASA SP-469, 251-256.
- (4) Bretz, J. H. (1969) J. Geol. 31, 617-649.
- (5) Baker, V. R. (1973) Geol. Soc. Amer. Sp. Paper 144, 79p.
- (6) Baker, V. R. and D. J. Milton (1974) Icarus 23, 27-41.

## FLOW-COMPETENCE EVALUATIONS OF THE HYDRAULIC PARAMETERS OF FLOODS: AN ASSESSMENT OF THE TECHNIQUE

Paul D. Komar, College of Oceanography, Oregon State University, Corvallis, OR 97331.

Flow competence is a technique that has been employed to evaluate the hydraulics of river floods from the sizes of the largest sediment particles transported (Baker and Ritter, 1975; Costa, 1983). The evaluated parameters include flood discharges, mean velocities and bed stresses. Flow competence has become an important tool for assessing the hydraulics of exceptional floods on Earth, including those which eroded the Channeled Scabland of eastern Washington (Baker, 1973). The objective of my research has been to examine the techniques involved in competence evaluations, and to examine their potential for assessing the hydraulics of floods which carved the outflow channels on Mars. This work has been completed, and the results written up in two journal publications and in two chapters for special volumes (see "in press" references).

Flow-competence evaluations have been empirical, based on data compiled from a variety of sources including major terrestrial floods. The data summary by Costa (1983) supports the relationship

$$\tau_c = 26.6 D^{1.21} \quad (1)$$

for the mean bed stress ( $\tau_c$ ) as a function of the diameter  $D$  of the maximum-size gravel or boulders transported (units are in the cgs system, respectively dynes/cm<sup>2</sup> and cm). However, further tests of this relationship with recently-obtained data on gravel transport in rivers, measurements collected under more controlled conditions, indicate that this empirical equation can lead to significant over-evaluations of flood-flow parameters. Furthermore, it was demonstrated that this equation is inconsistent with expected patterns of selective entrainment by currents of grains from deposits of mixed sizes. For these reasons, I concluded that equation (1) should not be used in flow-competence evaluations, either on Earth or Mars.

An alternative relationship was sought, one that does agree with the measurements of selective entrainment and transport of gravel. Based on several data sets, I derived

$$\tau_c = 0.045(\rho_s - \rho)gD_{50}^{0.6}D_i^{0.4} \quad (2)$$

where  $\rho_s$  and  $\rho$  are respectively the grain and water densities,  $D_{50}$  is the median diameter of the deposit as a whole, and  $D_i$  is the diameter of the individual grain that is transported. In flow-competence evaluations  $D_i$  becomes the size of the largest boulder moved by the flood. The inclusion of  $D_{50}$  results from the dependence of selective entrainment on the ratio  $D_i/D_{50}$ . This relationship provides a much better prediction of flow competence than did equation (1), one that is consistent with the processes of selective entrainment. Furthermore, equation (2) is dimensionally homogeneous and includes gravity ( $g$ ), so that it can be used to evaluate Martian floods as well as those on Earth.

Similar relationships can be derived for the critical discharge per channel width,  $q_{ci}$ , and take the form

$$q_{ci} = q_t(D_i/D_{50})^n \quad (3)$$

where  $q_t$  is the threshold discharge for deposits of uniform grains, and  $n$  is an empirical coefficient that appears to depend on the degree of sorting of the bed sediments. Analyses using equations for turbulent boundary layers indicate that equations (2) and (3) are compatible, and therefore they can be used simultaneously in competence evaluations.

There are two approaches to the application of flow-competence evaluations to the floods on Mars. Equations (2) and (3) can be employed to make approximate estimates of the maximum sizes of boulders that could have been transported during the floods. Using my previous analyses of flow stresses of those floods (Komar, 1979), the maximum-size boulders transported would have been on the order of 5 meters diameter. This provides an illustration of the extreme magnitudes of the Martian floods and their erodability. Unfortunately,



these sizes are still too small to be resolved in orbital photographs. However, it is anticipated that future missions will provide the basic measurements for such an application. Should the landing site be within an outflow channel, the flow-competence equations could also be used to predict the potential sizes of boulders in the area.

#### REFERENCES:

- Baker, V.R. (1973) Paleohydrology and sedimentology of Lake Missoula flooding in eastern Washington: *Geol. Society of America Special Paper* 14, 79 p.
- Baker, V.R., and D.F. Ritter (1975) Competence of rivers to transport coarse bedload material: *Geol. Society of America Bull.* , v. 86, p. 975-978.
- Costa, J.E. (1983) Paleohydraulic reconstruction of flash-flood peaks from boulder deposits in the Colorado Front Range: *Geol. Society of America Bull.* , v. 94, p. 986-1004.
- Komar, P.D. (1979) Comparisons of the hydraulics of water flows in Martian outflow channels with flows of similar scale on Earth: *Icarus* , v. 37, p. 156-181.
- Komar, P.D. (in press) Selective gravel entrainment and the empirical evaluation of flow competence: *Sedimentology* .
- Komar, P.D. (in press) Applications of grain-pivoting and sliding analyses to selective entrainment and flow-competence evaluations: *Sedimentology* .
- Komar, P.D. (in press) Sediment transport by floods: In *Flood Geomorphology* , edited by V.R. Baker and R.C. Kochel, John Wiley & Sons, New York.
- Komar, P.D. (in press) Flow competence evaluations of the hydraulic parameters of floods: An assessment of the technique: Proceedings of Flood Workshop (May 1987), Lancaster, England, British Geomorphological Res. Group [to be published by John Wiley & Sons].

### **Three-Dimensional Digital Simulation of Drainage Basin Development: Modeling the Martian Valley Networks**

Alex D. Kelley, Department of Computer Science and Michael C. Malin, Department of Geology, Arizona State University, Tempe, AZ 85287

Considerable controversy remains concerning the nature and origin of martian valley networks. While most investigators agree that these networks appear to have originated through fluid flow processes, consensus has not developed concerning whether the primary control of the valley systems was established through overland flow, seepage runoff, or sapping processes. In order to determine whether these processes produce diagnostically different networks, a three-dimensional computer graphic simulation program which models the development of drainage basins has been developed. This model permits planimetric properties of channel networks to be interactively selected and integrated with existing empirical and physically-based models of hydrological relationships. The program is extremely modular, so that a physical model may be exchanged with an alternate one easily. This permits tests of several different models for each planimetric property.

The program incorporates models for tributary arrangements along main streams, interior and exterior link lengths, link density, stream junction angles, drainage divide development, longitudinal profile, and valley side-wall slope. Networks may be grown headward or initiated "full-born" using the above properties to control the branching relationships and three dimensional properties of the network. Variations in all properties can be obtained through a separate, stochastic parameter generator that may be applied to one or more of the controls both dependently and independently.

The resulting networks are tested against existing systems using empirical measures common in hydrology. Networks generated by the model can, using properly selected or derived parameter values, exhibit a realistic physical appearance, both visually and empirically indistinguishable from real networks. In particular, mainstream migration during computation and unrealistically irregular basin geometries, both problems often encountered in simulations (Leopold and Langbein, 1962; Dunkerly, 1977), are not seen in networks produced by this model.

Tributary arrangement along mainstreams is modeled according to observations made by Flint (1980). Exterior and interior link lengths are presently determined using a stochastic equation. Headward growth is controlled using an additional dimensionless parameter when the equation is applied to an exterior link. When an exterior link's length reaches a stochastically determined maximum, the "source" becomes fixed. Distributions of link length other than purely random, in particular gamma and exponential distributions, are presently under study.

Dunkerly's (1977) simulation model is used to determine link density by incorporating a relationship between link length and drainage area (Smart, 1972). Junction angles are determined using two quantitative models. For conjoining tributaries whose magnitude differences are less than five, Howard's (1971) geometric model is used. For differences greater than five, the junction angles are estimated using Horton's model (1945). This scheme provides good agreement with Abraham's (1980) Perth Amboy results. The model adjusts junction angles to the gradients of the respective tributaries by allowing the junction points to migrate.

Drainage divides are computed geometrically, using as a basis planes that represent valley side-walls. The planes are inclined at the average angle of the valley sides. Thus the orientations of the divides depend on the slope of the links and the slope of the valley sides. Side-wall evolution is modeled to provide realistic side-wall intersections. The resulting semi-divide angles are equivalent to those calculated from the expressions in Abraham's (1980) geometric model.

The longitudinal profile of each stream is constructed by computing the depth of the valleys at each point of junction. A power function relating link magnitude to link mean depth is used, combined with a stochastic parameter to provide variation. The model is patterned after that of Richards (1980) for channel width. The model produces the characteristic concave upward profile (Morisawa, 1968).

Valley-sides are modelled using polygons inclined at an average angle. As the depth of link increases, the width of the valley increases in order to maintain its slope. This model essentially reproduces the valley width analysis of Richards (1980).

The preceding models provide a coarse framework for a surface network pattern. Surface fitting is accomplished by triangulation and interpolation using splines under tension (Nielson and Franke, 1984). The tension parameters enable valley slope profiles to be modeled as a potential energy transport system.

The model was completed in December 1987. It is presently being used to evaluate a number of terrestrial drainage systems for which the relevant, detailed field observable data are available (e.g., networks on the pumice plains and blast deposit at Mount St. Helens, Janke and Malin, 1986). Map analysis and application of the model to valley systems in Margaritifer Sinus are just beginning.

## References

- Abrahams, A. D., *Geogr. Anal.*, 12, 157-171, 1980.  
Dunkerly, D. L., *J. Geology*, 85, 459-470, 1977.  
Flint, J. J., *Am. J. Sci.*, 280, 26-45, 1980.  
Horton, R. E., *Geol. Soc. Am. Bull.*, 56, 275-370, 1945.  
Howard, A. D., *Water Resour. Res.*, 7, 863-873, 1971.  
Janke, D. R. and Malin, M. C., Reports of Planetary Geology and Geophysics Program—1985, NASA Tech Mem. 88383, 449, 1986.  
Leopold, L. B., and Langbein, W. B., *U.S. Geol. Surv. Prof. Pap. 500-A*, 1962.  
Morisawa, M. E., *Streams: Their Dynamics and Morphology*, McGraw-Hill Inc. 1968.  
Nielson, G. M., and Franke, R., *The Rocky Mountain Journal of Mathematics*, 14, 203-221, 1984.  
Richards, K. S., *Water, Resour. Res.*, 16, 241-244, 1980.  
Smart, J. S., *Water Resour. Res.*, 8, 1487 - 1496, 1972.

## LABORATORY SIMULATION OF OUTFLOW CHANNEL FORMATION ON MARS

Kimberly A. McGeehan and S.A. Schumm  
Department of Earth Resources, Colorado State University  
Fort Collins, CO 80523

Sharp and Malin (1975) have identified two general groups of channels on Mars: runoff channels and outflow channels. The runoff channels are similar to channels on Earth and could have been formed when the Martian climate was denser and more conducive to precipitation than it is now. Outflow channels emerge fully formed from discrete source areas (Squyres, 1984), usually chaotic terrain. Masursky, et al. (1977) suggested that chaotic terrain could be the result of subsurface emplacement of molten rock, which melted ground ice and caused subsidence of the surface and runoff of the meltwater. Evidence for ground ice has been suggested by Rossbacher and Judson (1981) by the water inventory method and by geomorphic evidence.

Our experiment was designed to test the hypotheses that 1) chaotic terrain is the source of water for outflow-type channels on Mars; 2) chaotic terrain was formed by the melting of ground ice by molten rock emplacement in the subsurface; and 3) the processes of formation of chaotic terrain is similar to thermokarst formation on Earth.

Equipment used in the experiments includes: a 22.2 cubic meter vacuum chamber; two large pumps used for pumping the chamber from atmospheric pressure to 6.3 torr (8.5 mbar); a small pump to stabilize the pressure at 6.3 torr; two 15 cubic foot freezers; two 50cm x 80cm x 30cm sample boxes made of aluminum frame and bottom, 1-inch styrofoam insulation sides, and 4-mil plastic liner; and a heat source. The samples were prepared in several layers, similar in construction to the samples prepared by Manker and Johnson (1982). The bottom 10cm is a 40:60 clay/fine sand mixture. This impermeable layer is overlain by a 7.5cm layer of saturated coarse-grained sand. Next is 2.5cm of pure water ice, frozen before the next layer is added to insure that all water is in solid form. During sample preparation, it is important that the layers beneath the ice layer are frozen solid to avoid liquefaction caused by vibration of the pumps and that all voids below the ice layer be water-filled and not air-filled to avoid explosions due to greater air pressure in the soil pores than at the sample surface.

As the sample is prepared, the heat source is placed at the coarse sand/ice interface. Three Cu-Ni thermocouples are located within the sample: 1) at the heat source; 2) at the coarse sand/ice interface distant from the heat source; 3) 2-4cm above the sample surface.

The frozen sample is loaded into the vacuum chamber at a slope between  $8^{\circ}$  and  $16^{\circ}$ , the pressure in the tank is reduced, and the heat source is activated. During the run, pressure is maintained as close as possible to 6.3 torr (8.5 mbar), the three thermocouple temperatures are monitored, and observations of surface changes are noted. A camera mounted above the sample surface also records changes on the sample surface.

When the heat source is generated, a rapid increase in temperature occurs at thermocouple 1. The temperature in the subsurface continues to rise without change at the surface until the subsurface temperature is between  $-1.0^{\circ}\text{C}$  and  $0.5^{\circ}\text{C}$  when water appears at the surface, either through tiny holes which grow in size and eventually coalesce, or by an explosion which forces water and sand to the surface. Pressure will remain constant for the former condition, and will rise for the latter. The pressure rise is contingent on the violence of the explosion. As the hole expands, liquid water begins to flow downslope. Because the heat capacity of liquid water (1.0 cal/g) is greater than that of ice (0.5 cal/g), a channel is eroded into the underlying ice layer. The experiment continues until the water supply is depleted.

The heat source simulates the effect of subsurface emplacement of molten rock by melting the ice layer from the subsurface upward, causing collapse of the surface. Water stored in the resulting depression spills out of the depression and flows downslope. Squyres (1984) described the outflow channels on Mars as narrow and deep proximal to the heat source and broad and shallow downslope. The experimental channels have a similar appearance. A narrow, deep channel forms at the edge of the "thermokarst" depression, and it gradually becomes broader and shallower downslope.

Preliminary results indicate that water can exist at Martian pressure conditions if liquid water is produced at a rate greater than the rate of evaporation. Water flowing on the frozen surface will cut channels into it.

Manker, J.P. and A.P. Johnson, 1982, Simulation of Martian chaotic terrain and outflow channels: *Icarus* 51:121-132.

Masursky, Harold, J.M. Boyce, A.L. Dial, G.G. Scaber, and M.E. Strobell, 1977, Classification and time of formation of Martian channels based on Viking data: *J. Geophys. Res.* 82:4016-4038.

Rossbacher, Lisa A. and Sheldon Judson, 1981, Ground ice on Mars: inventory, distribution, and resulting landforms: *Icarus* 45:34-54.

Sharp, R.P. and M.C. Malin, 1975, Channels on Mars: *GSA Bull.* 86:543-609.

Squyres, Steven W, 1984, The history of water on Mars: *Ann. Rev. Earth Planet. Sci.* 12:83-106.

## Preliminary Investigation of Geological Controls on Valleys Influenced By Groundwater Sapping, Southern Colorado Plateau, Arizona and Utah

R. Craig Kochel and Michael A. Phillips, Department of Geology, Southern Illinois University, Carbondale, Illinois 62901

Studies of the Viking images of Mars have resulted in the identification of at least four major classes of channels: 1) large outflow channels formed by cataclysmic flooding; 2) dry valley networks with dendritic patterns formed on ancient hilly and cratered terrain; 3) longitudinal valleys networks with short, stubby tributaries having amphitheater heads; and 4) slope valley networks with short, amphitheater-headed networks formed along major Martian escarpments such as Valles Marineris. The origins of the valley networks are less certain than the outflow channels. Peculiarities in their morphologic expression compared to terrestrial runoff valleys, such as the amphitheater heads and low drainage density, have led numerous investigators to invoke groundwater sapping processes for their genesis (Baker, 1982; Higgins, 1982; Kochel and others, 1985; Laity and Malin, 1985; Howard and others, 1988).

Recently, we began to study potential analog valleys in a variety of terrestrial settings where valleys formed dominantly by runoff processes could be compared with neighboring valleys strongly influenced by groundwater sapping processes (Kochel and Piper, 1986). This study focuses on the valleys incised into the southern Colorado Plateau (*Fig. 1*), an area predominantly underlain by the porous and permeable Navajo sandstone. The Navajo has ideal characteristics for the interception and efficient transmission of groundwater. Rainfall and snow collect in surface depressions caused by uneven weathering of large-scale trough cross-bedding and potholes, then slowly percolates down through the sandstone until less permeable boundaries are encountered, such as the Navajo - Kayenta formational contacts, where it begins to move laterally (*Fig. 2*). Concentration of the groundwater flow produces zonal seeps and results in the erosion of the poorly-cemented sandstone along canyon walls, eventually undermining and collapsing material above by this sapping-generated erosion process.

In order to better interpret the genesis of valleys on Mars from their morphologic characteristics observable in Viking imagery, we collected morphometric data from Colorado Plateau valley analysis of aerial photographs at approximately 1:80,000 scale. Basins selected represent a subset of sapping-dominated and runoff-dominated examples from an area near Shonto in northern Arizona (*Fig. 3*). The dominance of sapping vs. runoff processes was determined from field reconnaissance which observed large numbers of active seeps and associated alcoves in the headward regions and along tributaries to the valleys mapped as sapping-dominated systems. These basins represent areas underlain by differing lithologies and comprised a set of 11 sapping-influenced valleys and 8 runoff-dominated systems. Table 1 shows an abbreviated list of parameters compared in this study. Sapping-dominated valleys have higher junction angles, are more elongate, have lower drainage densities, have higher relief, and have greater basin area in canyon than their neighboring runoff-dominated counterparts, even between runoff and sapping-dominated valleys, formed in the Navajo.

Many factors influence groundwater sapping processes in sedimentary rocks. These can be organized into a hierarchy based upon their scale of influence on valley geometry (*Fig. 4*). Major canyons and intermediate-sized tributary systems appear to be dominantly influenced by dip. Sapping-dominated valleys are typically asymmetrical, with their long tributaries along their up-dip sides (i.e. *Fig. 3*, Tsegi Canyon). In contrast, short valleys on the down-dip sides of the mainstream will probably remain small because they receive only localized groundwater recharge. Therefore, in areas of uniform regional dip like the Tsegi-Shonto area, most of the active seeps and associated alcoves are oriented down-dip. In areas of more variable dip, like the central Lake Powell area in Utah, the orientation of active seeps and alcoves is also variable and can be used on a limited basis to infer major underlying structure.

Joints provide local zones of increased permeability, helping to localize groundwater flow and accelerate sapping processes. These effects are particularly pronounced in Colorado Plateau valleys underlain by the Navajo in their smaller tributaries and headward regions of the basins. The prominence of joints helps explain the high junction angles characteristic of networks strongly influenced by sapping processes.

Variations in the internal sedimentological characteristics of rocks such as the Navajo Sandstone also affect the morphology of sapping-dominated valleys, but on more localized scales. Aeolianites such as the Navajo have numerous internal bounding surfaces across which there are major permeability contrasts that strongly influence the pattern of valley development by groundwater sapping. Interdune facies are one example of these variations. Interdune deposits are typically formed of impermeable carbonate which forms major ledges along canyon walls cut into the Navajo. Major seeps and alcoves are localized above these interdune deposits, resulting in the formation of multi-level or tiered alcoves (Fig. 2). Limited lateral extent of many interdune deposits acts as a major control on alcove dimensions and distribution. Another locally important permeability contrast is the boundary of major aeolian cross-bed sets. Fine-grained sediments often occur at these boundaries and localize seepage along their margins. Finally, dip direction of the cross-beds influences groundwater flow. Lateral permeabilities are much higher than vertical permeabilities across the cross-bed laminations. This directional permeability can be important as a major control where there is regional consistency of cross-bed dip direction as occurs in the Navajo outcrop area of northern Arizona and southeastern Utah (Marzolf, 1983).

The coincidence of structural and sedimentologic factors promulgating accelerated groundwater flow in the same direction in the Shonto-Tsegi area (Fig. 3) results in a strong alignment of sapping-influenced canyons toward the southwest. Here, groundwater flow is dominantly toward the southwest because dip is to the southwest, prominent joints trend northeast-southwest and northwest-southeast, and cross-bed dip is toward the southeast.

More studies are in progress to increase the data base from diverse terrains for comparing runoff-dominated valleys with those having strong influence by sapping. The result of this work, in combination with our flume experiments also in progress, may lead to criteria useful in inferring process genesis based upon morphometric observations detectable in studies of aerial imagery of Mars. Ground-truth field observations of terrestrial analogs are important to calibrate interpretations of Viking images and promises to permit inferences about gross geologic structure in areas characterized by sapping-dominated valley networks.

#### References:

*Table 1. Comparison of Sapping-Dominated and Runoff-Dominated Basins*

#### DRAINAGE BASIN COMPARISONS

	AREA (km <sup>2</sup> )	ICT <sup>2</sup> (o)	SHAPE (k)	CAN.% (%)	DD (km) km <sup>2</sup>	EL (/km <sup>2</sup> )	RELIEF (m)
<b>SAPPING BASINS</b> (n = 11)							
mean	27.7	73.2	24.9	45.8	9.9	4.2	297
std dev	17.8	3.4	12.8	12.4	1.4	0.7	79
<b>RUNOFF BASINS</b> (n = 8)							
mean	48.5	52.1	17.4	17.0	12.2	5.7	150
std dev	38.1	6.9	8.1	12.6	5.3	4.4	38.6

- Baker, V.R., 1982, *The Channels of Mars*. Univ. of Texas Press, Austin, 198pp.
- Higgins, C.G., 1982, *Geology*, v.10, p. 147-152.
- Howard, A.D., Kochel, R.C., and Holt, H., 1988 in press, *Proceedings and Field Guide for the NASA Groundwater Sapping Conference*. NASA, Wash., DC, 208p.
- Kochel, R.C., Howard, A.D., and McLane, C., 1985, in *Models in Geomorphology*, Allen & Unwin, Boston, p. 313-341.
- Kochel, R.C., and Piper, J.F., 1986, *J. Geophys. Res.*, v. 91, p. E175-E192.
- Laity, J. E., and Malin, M.C., 1985, *Geol. Soc. Amer. Bull.*, v. 96, p. 203-217.
- Marzolf, J.E., 1983, in *Eolian Sediments and Processes*, Amsterdam, Elsevier, p. 635-660.

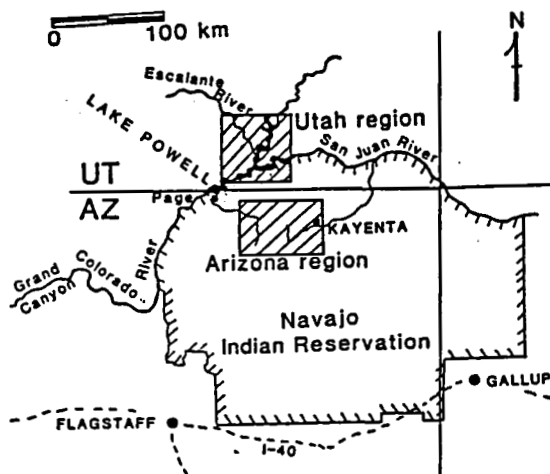


Figure 1. Location map of southern Colorado Plateau study areas.

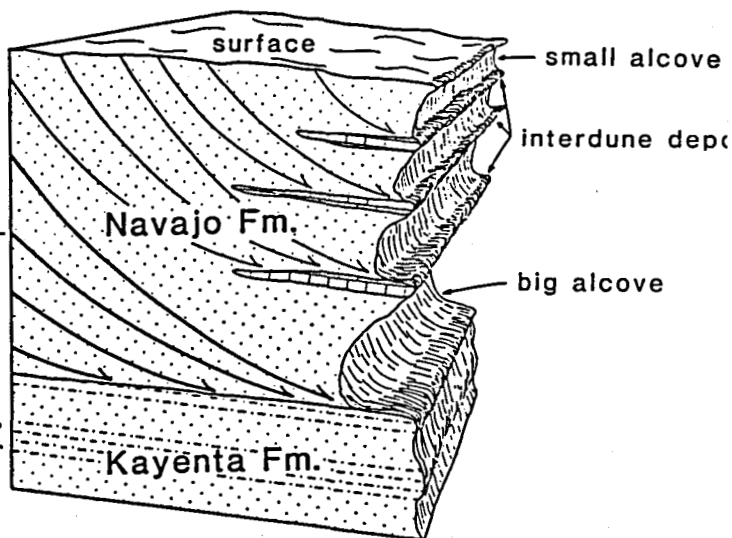


Figure 2. Schematic of Navajo sandstone showing infiltration and concentration of groundwater flow creating sapping alcoves.

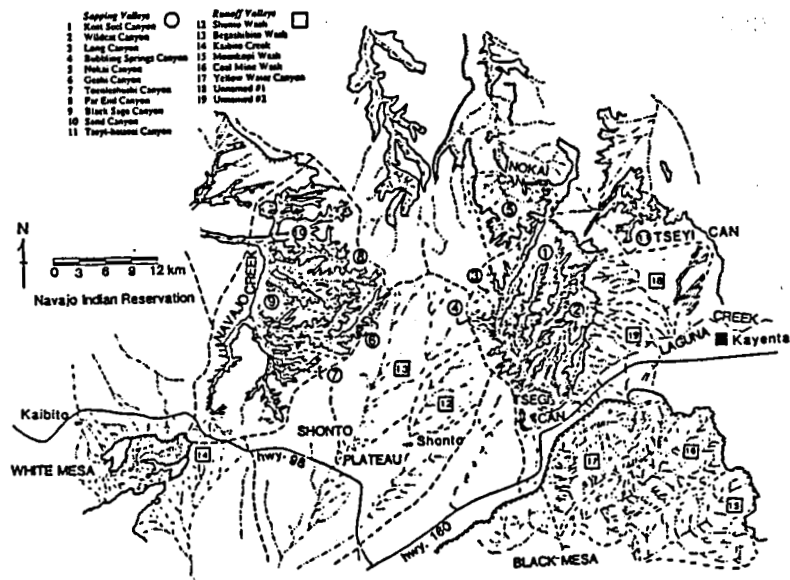


Figure 3. Location of 19 basins used in morphometric comparisons.

Controls on Sapping Valley Morphology

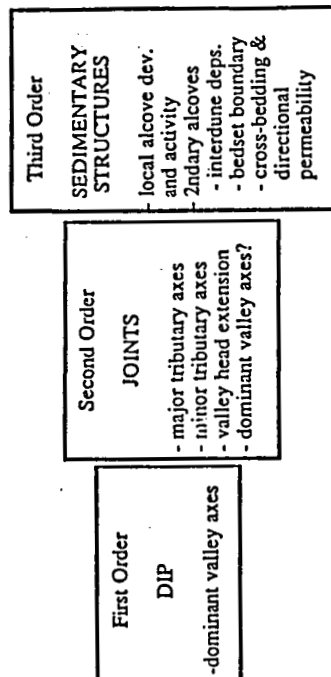


Figure 4. Hierarchy of controls on the sapping-influenced valleys.



## **CHAPTER 9**

### **VOLCANIC PROCESSES AND LANDFORMS**



## VOLCANO STUDIES ON MARS

Pete Mouginis-Mark, Lionel Wilson and Alan Mathews\*; Planetary Geosciences Division, Hawaii Institute of Geophysics, Univ. Hawaii, Honolulu, HI 96822. \*NASA Summer Intern 1987.

**INTRODUCTION:** We are in the process of study a variety of aspects of the volcanic history of Mars, using the morphology of the volcanic constructs to constrain models of volcano evolution and eruptive style. The traditional view of martian volcanism is one in which effusive activity has dominated the entire preserved geologic history of the planet, with the minor exception of phreatomagmatic activity and associated volcano ground-ice interactions (cf., refs 1-3). However, two lines of evidence have made us reconsider this view, and have led us to study the possible role of explosive volcanism on Mars. First, detailed analysis of high resolution Viking Orbiter images has provided good evidence for explosive activity on Hecates Tholus (4) and Alba Patera (5, 6). Secondly, the problems believed to exist in associating explosive volcanism with silicic magmas on Mars, and the consequent unusual magmatic evolutionary trend for martian volcanoes from silica-rich to silica-poor (7), may now be circumvented by the consideration of basaltic plinian activity similar in kind to terrestrial eruptions such as the 1886 Tarawera eruption (6, 8). Here we briefly review the morphologic evidence for an early phase of explosive activity on Mars and present a model that we have developed for the emplacement of ash-flow deposits on martian volcanoes. The volcanoes Alba Patera and Olympus Mons are considered in this context, along with some of the older martian tholi and paterae. Additional studies of the summit area of Olympus Mons are also underway.

**PREVIOUS OBSERVATIONS:** Pyroclastic (explosive) volcanism was first proposed for Mars from the analysis of low resolution (~1 km) Mariner 9 images (9, 10). These studies identified small cone-like hills that were believed to be cinder cones. A more detailed analysis of the volcanoes Hecates, Ceranius, and Uranus Tholi and Uranus Patera (11) suggested that the channelized flanks of these volcanoes were created by volcanic density flows similar to terrestrial nuee ardentes (the melting of permafrost supplying the water required in base surge generation). Following detailed mapping using Viking Orbiter images (4) an alternative explanation was proposed for some of these channels, wherein the unconsolidated flanks of Hecates Tholus, formed from numerous air-fall deposits, had been carved by surface water released by sapping from the volcano's flanks. Recently, we have also used this argument to explain the distribution of digitate channel networks on the flanks of Alba Patera (5, 6). Other, more enigmatic deposits in Amazonis have also been proposed to be ignimbrites (12). The key aspect of most of these recent investigations has been the attempt to associate volcanoes with channelized flanks to explosive activity; this attempt has of necessity been subjective, since it is difficult to recognize pyroclastic materials from orbit even for the Earth (7). For Hecates Tholus and Alba Patera, the connection between channelized flanks and pyroclastic materials depends on the assumption that the surface materials are more easily eroded than lava flows (since volcanoes such as Arsia and Ascraeus Montes display ample evidence for the eruption of lava flows, but lack the same kind of channelized flanks; refs. 4, 13), and that the most plausible alternative form of volcanic deposit would be pyroclastic materials created by explosive eruptions (either phreatomagmatic or initiated by juvenile volatiles).

**VOLCANO TOPOGRAPHY:** Hecates Tholus, Tyrrhena Patera and Alba Patera are all low-relief shields when compared to Tharsis Montes (5, 14, 15). Maximum elevations for the summits of these volcanoes are ~6 km for Hecates, 750 - 1,000 m for Tyrrhena, and ~ 2 km for Alba, while the Tharsis Montes may each possess 25 km of relief (cf. 16). These low elevations may not be coincidental, nor may the fact that they are all ~500 to 600 km in diameter (and so is the volcano Hadriaca Patera). For the case of Alba Patera, the constraint on maximum width of the volcano may be the run-out distance of pyroclastic flows (5), and such a model may also hold for these other low-relief martian volcanoes. Previous explanations for the low topography of these shields were that they were made of very fluid lavas (10) but a volatile-rich martian mantle

could also produce abundant pyroclastic volcanic materials capable of forming wide-spread ash-flow sheets (17). We have recently proposed a new five-stage model for the evolution of Alba Patera (5), which would account for the low-relief of the volcano by the emplacement of pyroclastic flows as the basement materials, their subsequent partial burial by younger lava flows, and the formation of the channels by melt water. It is not clear if this evolutionary trend is unique to Alba Patera, or whether it is simply easier to recognize at this location due to preservation of both explosive and effusive eruptive materials on the surface.

**OLYMPUS MONS:** The basal escarpment that surrounds Olympus Mons has as much as 9 - 13 km of relief (18, 19). Several origins for this feature have been proposed, including erosion of ash flow tuffs (20), which if correct would suggest that explosive volcanism characterized the early eruptive history of Olympus Mons. We are reconsidering this idea because if correct it would imply a diverse eruptive history for the volcano. If the materials underlying the Olympus Mons edifice are indeed pyroclastic units, then the subsidence associated with terracing on the upper flanks (21, 22) may have been associated with compaction of the ash layers due to the overlying denser lava flows. Alternatively, the erosion may have taken place within the pre-existing volcano substrate, rather than within materials erupted from the Olympus Mons vent (23). Gravity sliding and spreading of materials containing ground ice at low strain rates has also been proposed to account for the general morphology of the aureoles and the Olympus Mons basal escarpment (18, 24). Olympus Mons is unique in the extent of large-scale gravity spreading and basal scarps: perhaps such features, if they ever existed, have been buried by lava flows on other volcanoes, or perhaps their eruptive histories did not permit the development of such features.

We are also conducting a detailed study of the summit caldera of Olympus Mons, in order to better constrain the diversity of summit activity that occurred on a martian shield volcano. The summit caldera of the martian volcano Olympus Mons has been studied using ~10 m/pixel Viking Orbiter images and the 200 m contour map of the volcano produced by the U.S. Geological Survey (19). Six sub-calderas comprise the summit, and range in size from ~20-60 km dia. and 0.8-3.0 km deep. From stratigraphic relationships, the largest sub-calderas are also the oldest. The rim of the caldera possesses considerable relief, possibly due to progressive dike emplacement within the summit area, being at an altitude of 24.4 km around the oldest sub-caldera and 26.2 km around the most recent areas of collapse. The floors of the sub-caldera are essentially flat, indicating little post-flow emplacement tilting of the summit area. A total of 369 graben are located on the caldera floor and occur within 15 km of the caldera walls. 350 wrinkle ridges (that resemble lunar mare ridges) have also been identified. Average graben length is 3.1 km, average graben width is 0.23 km, and average ridge length is 2.0 km. From the topographic map, the graben are seen to lie on the steepest portions of the caldera floor, while the ridges are on relatively flat terrain in the middle of the caldera floor. By analogy with the width and spacing of circumferential graben around the lunar maria, we estimate a thickness of 200-250 meters for individual stratigraphic units (solidified lava lakes?) within the caldera. Such values for Olympus Mons imply lava thicknesses comparable to those of terrestrial lava lakes and are consistent with the observation that none of the sub-caldera walls (typically 1-2 km high) were overflowed by younger intra-caldera lava flows. These values also imply a volume of ~60-700 km<sup>3</sup> for each eruptive episode at the summit of Olympus Mons.

**CONCLUSIONS:** Volcano morphology suggests that an evolution took place in the type of flank deposits that were produced at different times in martian history. Early in the preserved geologic record, explosive eruptions dominated, with the production of ash cones such as Hadriaca and Tyrrhena Paterae. These volcanoes probably experienced ignimbrite-forming eruptions of relatively volatile-rich magmas that produced low-aspect shields that were subsequently easily eroded by sapping of ground water. Ignimbrites do not necessarily imply silicic magmas, and an objective of our research is to search for evidence of possible compositional variations between the flank deposits of these volcanoes and the lava-producing shields. Later in martian history, the more commonly cited effusive activity predominated,

producing the lava flows observed on the Tharsis Montes, the Syrtis Major volcanoes, and Elysium Mons. Certain volcanoes, particularly Alba Patera, but also possibly Olympus Mons, display morphologic evidence for the transition from an early explosive phase to later effusive eruptions. The implications of this evolutionary trend are two-fold: first magmatic evolution took place, from volatile-rich to volatile-poor, at a time when parts of the martian geologic record could be preserved until the present; and second this magmatic evolution would have dramatically affected climatic evolution on Mars, due to the decrease in magmatic gases which were liberated late in the planet's history (6).

**FUTURE STUDIES:** We believe that continued analysis of the Viking image data set will continue to provide new information on several of the unresolved problems pertaining to magmatic diversity and the morphologic interpretation of martian volcanoes. In particular, our studies over the next year will be directed towards the following topics:

1) Is there any evidence for multiple episodes of explosive eruptions and channel formation on volcanoes such as Hadriaca and Tyrrhena Paterae, or was there only one period of explosive activity at each volcano?

2) What role (if any) should we ascribe to volcano/ground ice interactions in controlling the large-scale morphology of martian volcanoes?

3) Is the summit activity observed on Olympus Mons typical for all of the shields where lava flow fields dominate the preserved geologic record, or did the summit areas of the Tharsis shields evolve in different manners?

4) How well can we determine the relative ages of these martian volcanoes? There is a need to refine the current age estimates based on crater frequencies (25) in order to see if some martian volcanoes experienced a transition in eruptive style before other volcanoes.

5) Is there any latitudinal or elevation dependence to the ash cones that could be used to infer variations in near-surface volatiles (or juvenile volatiles) within the erupted materials?

6) It is possible that the base of Olympus Mons is made of pyroclastic material. Of interest is the question of whether we would see similar deposits on other martian shields had they not been buried by many large lava flows. It may not, for instance, be coincidental that Olympus Mons and volcanoes with channelized flanks are all ~500 - 600 km in diameter. Perhaps this size marks the maximum radial distance that early (basement-forming) pyroclastic flows could travel on Mars?

**REFERENCES:** 1) Greeley, R. and Spudis, P. (1981). Revs. Geophys. Space Phys., 19, p. 13-41. 2) Mouginis-Mark, P.J. (1985). Icarus, 64, p. 265-284. 3) Squyres *et al.* (1987) Icarus, 70, p. 385-408. 4) Mouginis-Mark, P.J. *et al.* (1982). J. Geophys. Res., 87, p. 9890-9904. 5) Mouginis-Mark, P.J., Wilson, L. and Zimbelman, J.R. (1987). Polygenic eruptions on Alba Patera, Mars: Evidence of channel erosion on pyroclastic flows. Submitted to Bull. Volcanol. 6) Wilson, L. and Mouginis-Mark, P.J. (1987). Volcanic input to the atmosphere from Alba Patera, Mars. Nature, in press. 7) Francis, P. and Wood, C.A. (1982). J. Geophys. Res., 87, p. 9881-9889. 8) Walker, G.P.L. *et al.* (1984). J. Volcanol. Geotherm. Res., 21, p. 61-78. 9) West, M. (1974). Icarus, 21, p. 1-11. 10) Peterson, J.E. (1978). Proc. Lunar Planet. Sci. Conf. 9th, p. 3411-3432. 11) Reimers, C.E. and Komar, P.D. (1979). Icarus, 39, p. 88-110. 12) Scott, D.H. and Tanaka, K.L. (1982). J. Geophys. Res., 87, p. 1179-1190. 13) Mouginis-Mark, P.J. (1981). Proc. Lunar Planet. Sci. Conf., 12B, p. 1431-1447. 14) Hord, C.W. *et al.* (1974). Pressure-altitude measurements on Mars - An atlas of Mars local topography. Lab. for Atmos. and Space Phys., Univ. Colorado, Boulder. 15) Wu, S.S.C. *et al.* (1986). Rpts. Plan. Geol. Geophys. Prog. 1985, NASA TM-88383, p. 614-617. 16) Carr, M.H. (1981). The surface of Mars. Yale University Press, 232 pp. 17) McGetchin, T.R. and Smyth, J.R. (1978). Icarus, 34, p. 512-536. 18) Tanaka, K.L. (1985). Icarus, 62, p. 191-206. 19) Wu, S.S.C. *et al.* (1984). Nature, 309, p. 432-435. 20) King, J.S., and Riehle, J.R. (1974). Icarus, 23, p. 300-317. 21) Hodges, C.A. and Moore, H.J. (1979). J. Geophys. Res., 84, p. 8061-8074. 22) Lopes, R.M.C. *et al.* (1980). The Moon and Planets, 22, p. 221-234. 23) Head, J.W. *et al.* (1976). Nature, 263, p. 667-668. 24) Francis, P. and Wadge, G. (1983). J. Geophys. Res., 88, p. 8333-8344. 25) Neukum, G. and Hiller, K. (1981). J. Geophys. Res., 86, 3097-3121.

## POSSIBLE EFFECTS OF EPOCHAL/EPISODIC RELEASE OF $\text{SO}_2$ ON EARLY MARTIAN CLIMATE

S.E. Postawko, F.P. Fanale, and A.P. Zent, Planetary Geosciences Div., HIG, Univ. of Hawaii, Honolulu, HI 96822

Erosion of the martian surface by the flow of liquid water has apparently taken place at different times and locations on the planet. Valley networks and outflow channels are the most readily identifiable evidence that liquid water erosion has occurred. The valley networks are mostly confined to ancient, cratered terrain, and are interpreted to be old themselves [with a few exceptions] (1). Their morphology implies formation by sapping (2). The larger outflow channels have a greater range of location and age, and appear to have formed episodically throughout much of martian history (1). The favored explanation for formation of the outflow channels is catastrophic release of water from confined aquifers, perhaps due to impact or faulting (3). It is possible that outflow channels could form under present-day martian conditions (3,4).

Many attempts have been made to explain the valley networks seen on the martian surface by invoking a strong atmospheric  $\text{CO}_2/\text{H}_2\text{O}$  greenhouse early in the history of the planet (5,6,7). Recent calculations have shown that when reduced solar radiation is taken into account, it is necessary to have at least 5 bars of  $\text{CO}_2$  in the atmosphere in order for the mean global temperature to be above freezing (8). [Lesser amounts of  $\text{CO}_2$  are required if only equatorial temperatures are to be above freezing. However, the valley networks are not confined to the equatorial regions (1).] It has been assumed that these large amounts of  $\text{CO}_2$  would have disappeared mostly due to carbonate formation. However, carbonates have yet to be positively identified in martian spectra.

It is clear that volcanism has occurred throughout much of the history of Mars. Presumably gases such as  $\text{SO}_2$  would have been released along with  $\text{CO}_2$  and  $\text{H}_2\text{O}$ . Several studies have touched on the effects of  $\text{SO}_2$  on martian climate (9,10). In our study, however, we have made estimates of amounts and rates with which  $\text{SO}_2$  may have been released into the martian atmosphere; how this may have affected global climate; and the implications this may have for episodic and/or epochal erosion of the martian surface by liquid water.

The amount of  $\text{SO}_2$  released from terrestrial volcanoes varies greatly (cf., 11,12). For this study we have chosen 0.1 to 1 weight percent of  $\text{SO}_2$  as reasonable bounds. The steady-state concentration of  $\text{SO}_2$  is also dependent on its atmospheric lifetime. The lifetime of  $\text{SO}_2$  in a volcanically perturbed martian atmosphere is somewhat difficult to assess. Settle (13) has estimated that the lifetime of  $\text{SO}_2$  in a present-day martian atmosphere would be on the order of 6 [Earth] years. Terrestrial volcanoes, however, also release substantial amounts of water vapor, along with other gases. Since the concentration of odd hydrogen species in the martian atmosphere appears to be directly proportional to the water vapor abundance, and the oxidation rate of  $\text{SO}_2$  is directly proportional to the concentration of odd hydrogen species, increased atmospheric water vapor would decrease the lifetime of  $\text{SO}_2$ . Settle estimates the lifetime of  $\text{SO}_2$  in a volcanically perturbed martian atmosphere would be comparable to, or somewhat greater than, the lifetime of  $\text{SO}_2$  in the Earth's stratosphere. For our study we have chosen lifetimes of 1/4 year [approximate lifetime of  $\text{SO}_2$  in the Earth's stratosphere (13)], and 1 year [a compromise

between the lifetime in the present martian atmosphere and the lifetime in earth's stratosphere].

First let us consider an epochal time scale. Total magma erupted during each of 7 martian epochs was taken from Greeley (14). If volcanism had taken place uniformly through each epoch, then magma flux rates would have been between  $\sim 0.1 \text{ m}^3/\text{s}$  and  $\sim 10 \text{ m}^3/\text{s}$ , depending on the epoch. If the lifetime of  $\text{SO}_2$  were on the order of 1 year, then for even 1 wt.% of  $\text{SO}_2$  the steady-state concentration of  $\text{SO}_2$  in the atmosphere would have been too low during each epoch to have significantly affected surface warming on a global basis.

Rather than continuous volcanism through each epoch, it is more likely that volcanism occurred episodically. We have chosen 2 magma flux rates for our study:  $5 \times 10^4 \text{ m}^3/\text{s}$ , corresponding to a mid-range eruption rate for Alba Patera, Mars (15); and  $10^6 \text{ m}^3/\text{s}$ , corresponding to some estimates for eruption rates of the Yakima Basalts of the Columbia Plateau (16), and for some flows on Alba Patera (17). For a 1 year lifetime and 1 wt.% of  $\text{SO}_2$ , these magma flux rates produce steady-state atmospheric  $\text{SO}_2$  abundances which increase mean annual global surface temperature by about  $5^\circ\text{K}$  and  $10^\circ\text{K}$ , respectively.

Work is continuing to study the possibility that under certain circumstances  $\text{SO}_2$  could have contributed even more to surface warming. Although the above magma flux rates are probably as high as possible, the steady-state atmospheric abundance of  $\text{SO}_2$  could be significantly increased if the  $\text{SO}_2$  lifetime were greater than 1 year. This may occur, for example, during periods of low obliquity when polar cold trapping acts to keep the atmosphere very dry. Since the valley networks are believed to be primarily formed by sapping, a dry atmosphere does not necessarily preclude flowing water in the near subsurface.

## References

- (1) Carr, M.H. and G.D. Clow (1981), *Icarus*, 48, 91-117.
- (2) Pieri, D.C. (1980), *Science*, 210, 895-897.
- (3) Carr, M.H. (1979), *J. Geophys. Res.*, 84, 2995-3007.
- (4) Wallace, D. and C. Sagan (1979), *Icarus*, 39, 385-400.
- (5) Pollack, J.B. (1979), *Icarus*, 37, 479-553.
- (6) Cess, R.D., V. Ramanathan, and T. Owen (1980), *Icarus*, 41, 159-165.
- (7) Toon, O.B., J.B. Pollack, W. Ward, J.A. Burns, and K. Bilski (1980), *Icarus*, 44, 552-607.
- (8) Kasting, J.F. (1986), In *Mars: Evolution of Its Climate and Atmosphere*, LPI Tech. Rpt. 87-01, Lunar and Planetary Inst., Houston, TX.
- (9) Postawko, S.E. and W.R. Kuhn (1986), *J. Geophys. Res.*, 91, D431-D438.
- (10) Kondratyev, K.Y., N.I. Moskalenko, and S.N. Parzhin (1986), *Earth, Moon, and Planets*, 35, 13-18.
- (11) Anderson, A.T. (1975), *Rev. Geophys. Space Phys.*, 13, 37-54.
- (12) Meszaros, E. (1981), In *Atmospheric Chemistry: Fundamental Aspects*, Elsevier Scientific Pub. Co., New York, pp 72-90.
- (13) Settle, M. (1979), *J. Geophys. Res.*, 84, 8343-8354.
- (14) Greeley, R. (1987), *Science*, 236, 1653-1654.
- (15) Baloga, S.M., D.C. Pieri, J. Plescia, and P. Davis (1987), *Proc. Lunar and Planet. Sci. Conf. XVIII*, Lunar and Planetary Institute, Houston, TX, pp 42-43.
- (16) Swanson, D.A., T.L. Wright, and R.T. Helz (1975), *Am. J. Sci.*, 275, 877-905.
- (17) Cattermole, P. (1986), *Proc. Lunar and Planet. Sci. Conf. XVII*, Lunar and Planetary Inst., Houston, TX, pp105-106.

## RHEOLOGIC MODELING OF THE OLYMPUS MONS AUREOLE

Jonathan Fink, Geology Dept., Arizona State University, Tempe, AZ 85287

Among the most controversial deposits on the martian surface is the multi-lobed aureole that surrounds Olympus Mons. Published emplacement models include the erosion of an originally larger volcanic construct, ice-lubricated, slow gravitational spreading with thrust faulting, catastrophic landsliding, sub-aerial or sub-glacial lava flows, and pyroclastic flows. Prominent surface features of the deposit include symmetrical transverse ridges in distal areas with wavelengths of 2-10 km and amplitudes of 0.2-1.0 km, radial and oblique strike slip faults with variable amounts of both normal and lateral displacement, and proximal transverse graben with spacings similar to those of the distal ridges. These structures, although up to two orders of magnitude larger, resemble those found on debris avalanche deposits such as the 300-year-old Chaos Jumbles at Mount Lassen (CA), suggesting that during its emplacement the aureole may have had physical properties and behavior comparable to those of the Jumbles.

The Chaos Jumbles avalanche has been successfully modeled as a pseudo-plastic material with high finite strength emplaced over a nearly frictionless base (Eppler et al., 1987). Under sufficient compression in distal areas, a surface folding instability develops, with the ratio of fold wavelength to total flow thickness ranging from 2.0 (for relatively weak debris) to 2.8 (for strong debris). Low basal friction is indicated by the long runout of the deposit. The tendency to develop surface folds scales as the inverse of gravity, so compressional ridges on debris avalanches are three times as likely to form on Mars as on Earth. Strike slip faults develop readily in pseudo-plastic materials when shear stresses exceed yield values, which occurs simultaneously with folding as an avalanche comes to rest. An extensional instability in the proximal area may produce regularly spaced, transverse grabens if the deposit has a relatively brittle zone overlying a more plastic substrate.

Structural similarities between the Chaos Jumbles and Olympus Mons aureole support models for emplacement by catastrophic landsliding (e.g. Lopes et al., 1982). Both have regularly spaced transverse ridges, strike slip faults, finite marginal scarps, and relatively long runout distances. The extremely long runout of the aureole suggests some sort of fluidization during emplacement. The acoustic fluidization model (Melosh, 1979; Melosh and Gaffney, 1983) predicts a strongly non-linear, power-law rheology for mobilized debris, with shear stresses concentrated in a fluid zone near the base, and with a finite yield strength developing as the debris comes to rest. These properties can account for the structural features described from the Olympus Mons aureole (Tanaka, 1985). By comparing ridge spacings with estimated deposit thicknesses, it is possible to test the relevance of surface folding to the Olympus Mons aureole. In order for the rheological model to be strictly applicable, the ratio of wavelength to thickness must be within the range of 2 to 2.8. We measured spacings along 10 profiles across the aureole deposits and found mean spacings ranging from 2.7 to 4.3 km. Combining these ridge spacings with published thickness estimates for the same locations (Tanaka, 1985) gave wavelength to thickness ratios of 1.5 to 3.0. The close correspondence between predicted and observed ridge geometries lends further support to a model for catastrophic emplacement of the Olympus Mons aureole through a process of acoustic fluidization.



## REFERENCES

- Eppler, D.E., Fink, J.H., and Fletcher, R.C., 1987, Rheologic modeling and kinematics of emplacement of the Chaos Jumbles debris avalanche deposit, Lassen Volcanic National Park, California, Jour. Geophys. Res. 92, 3623.
- Lopes, R.M.C., Guest, J.E., Hiller, K.H., and Neukem, G.P.O., 1982, Further evidence for a mass movement origin of the Olympus Mons aureole. Jour. Geophys. Res., 87, 9917-9928.
- Melosh, H.J., 1979, Acoustic Fluidization: A new geologic process? Jour. Geophys. Research, 84, 7513-7520.
- Melosh, H.J. and Gaffney, E.S., 1983, Acoustic fluidization and the scale dependence of impact crater morphology. Jour. Geophys. Research, 88 suppl. A, 830-834.
- Tanaka, K.L., 1985, Ice-lubricated gravity spreading of the Olympus Mons Aureole deposits, Icarus, 62, 191-206.

## PHYSICAL AND CHEMICAL CONDITIONS IMPLIED BY VOLCANIC CALDERAS

by

Diane F. Sailer

California State University, Los Angeles, CA, 90032

and

David Pieri

Jet Propulsion Laboratory, Pasadena, CA, 91109

The morphologies of volcanoes and the corollary morphologies of the features that comprise them are a direct consequence of a number of physical and chemical variables related to their initial emplacement processes and evolution. In an attempt to address the relationship between formation process, composition, and resulting morphologies, we have compiled physical, chemical, and morphological data for 236 terrestrial and 15 martian volcanoes. These data have been broken down into 15 classes using the scheme of Pike and Clow (1981). Published observations of volcano height, basal diameter, caldera diameter, maximum eruption volumes and flow lengths, percent silica range, eruption style, tectonic regime, eruption rates, and energies and durations of eruptions were compared. We are currently examining this data base for correlations between morphometric, chemical and physical aspects for these volcanoes. This data base will then be used for comparisons with martian examples.

Initial results using caldera diameters and volcano basal diameters from Pike and Clow (1981), show a maximum caldera diameter for a given basal diameter. This maximum size is a ratio which ranges from 2:1 to 8:1 (basal diameter : caldera diameter), depending on the class of volcano. In addition, there is a distinct range of ratios for most classes, which is indicative of the range of caldera diameter. Using this ratio range, the martian classes of paterae (MP) and tholi (MT) appear similar to terrestrial volcanoes of the AA, AP, and KCS types (ash flow plains: alkalic and calc-alkalic, and silicic stratocones with calc-alkalic affinities.). The martian montes (MM) fit the alkalic stratocones (KA) and the grouping of shield volcanoes, KTG, KTU, and KTH (e.g., Galapagos, Hawaii).

Table 1 is a quantification of the intuitive notion that silicic volcanoes generally have larger calderas. Specifically, volcanoes grouped by Pike and Clow (1981) into silicic classes have ratios in the range of 2:1 to 6:1, calc-alkalic and alkalic from 2:1 to 21:1, and tholeiitic from 8:1 to 40:1. Mixed alkalic - tholeiitic compositions produced ratios in the range of 2:1 to 14:1, overlapping all others. The martian paterae and tholi fall within the ranges of silicic, calc-alkalic and alkalic compositions, while the montes are between or overlapped by the alkalic and tholeiitic compositions.

Clearly, the empirical results presented here are of limited utility alone, and beg fundamental questions of how chemical and environmental (e.g., water abundance, gravity) fold into a series of formation processes that appear to operate in highly non-linear and possibly chaotic fashions. Nevertheless, these observations must be accommodated in any models that attempt to explain dimensions and histories of martian volcanoes, and additionally suggest a richer range of volcanic compositions than have been traditionally asserted for Mars. Such results, however, may be consistent with recent assertions of high ( $>10^5$  poise near vent) viscosities for some martian lava flows (Baloga and Crisp -- personal communication).

### REFERENCE:

Pike, R.J. and Clow, G.D., 1981, Revised classification of terrestrial volcanoes and catalog of topographic dimensions, with new results on edifice volume: U.S.G.S. Open-file report 81-1038, 40p.

TABLE 1

PIKE & CLOW CLASS AND CHEMICAL AFFINITY			# IN CLASS	APPROX. RATIO RANGE(BASE:CALD)
SCA	AA	silicic - alkalic	9	2:1 - 4:1
I AL	AP	silicic - calc-alkalic	24	2:1 - 4:1
LLK	MP	?	5	2:1 - 4:1
I CA	MT	?	4	2:1 - 5:1
C - L	KCS	silicic - calc-alkalic	33	2:1 - 5:1
I AI	KMA	alkalic - mixed alk/thol	10	2:1 - 40:1
CLC				
* K *	KAS	silicic - alkalic	19	3:1 - 6:1
**	KO	mixed alk/thol	11	3:1 - 6:1
**	KC	calc-alkalic	44	3:1 - 21:1
*				
*	KMM	alkalic - mixed alk/thol	4	4:1 - 14:1
*	KA	alkalic	57	4:1 - 21:1
	MM	?	6	5:1 - 25:1
T	KTG	tholeiitic	8	8:1 - 20:1
H	KTU	tholeiitic	9	8:1 - 30:1
O	KTH	tholeiitic	8	8:1 - 40:1

## GEOMORPHOLOGY OF VALLEYS, ALCOVES, AND ETCHED TERRANES AT ALBA PATERA

David Pieri and Dale Schneeberger, Jet Propulsion Laboratory,  
Pasadena, CA 91109

Alba valleys have been the object of speculation and discussion since their discovery by Mariner 9 in 1971. Early descriptive accounts likened these systems to terrestrial dendritic rainfall-formed networks and asserted that their presence was prima-facie evidence of a past more earthlike martian climate, while other workers suggested a variety of alternative formative processes. As a result of detailed mapping of these complex valley networks, interspersed among and across various tabular and crested flows in the northwest quadrant of Alba, certain characteristics and relationships, which constrain models for valley formation and evolution, are emerging.

It appears that the overall group of features commonly called "valley networks" or "dendritic channels" represent several different types of valley and alcove networks, as well solitary individual features, acting within and on several contrasting terrane units. Taken together, particularly as seen in moderate to low resolution images, they present a filigreed texture yielding a misleading impression of uniform areal degradation. Rather, it appears that various morphological types are restricted to discrete units, discrete relationships with regard to tabular flows, and perhaps discrete time horizons, as well. No unambiguous channels (either fluvial or volcanic) have been identified, although several lunar-rille-like features may represent lava channels or collapsed lava tubes.

There appear to be several types of ramified networks present. Branching valleys appear throughout the region. Generally they possess both U- and V-shaped links. Exterior links appear to be mostly theater-headed, however, often with shallow troughs extending uphill above source links. No systematic width versus interior link magnitude relationships can be discerned. These networks tend to be quite parallel with junction angle "alpha" values (related to rate of decrease in slope with respect to increasing link magnitude) (Pieri, 1980, 1984) of the order of  $-0.01$  to  $-0.05$ , suggesting very flat longitudinal profiles. Often, interior valley links appear quite long and exterior links quite short, giving a sparse, somewhat pinnate, appearance to the network pattern. Valley walls are relatively steep and uniform throughout their length, with crisp upper-surface/valley-wall junctures. The depth distribution of these valley networks appears to be bimodal, with both deeply incised ( $<500\text{m}$  deep) and shallow ( $<100\text{m}$ ) groupings. This bimodal distribution may be related to the characteristic depth of the layer into which these valleys are cut, as is seen in sapping situations (Laity and Malin, 1985).

Filamental valleys appear more as traces of valleys in contrast to the more well-expressed deep valleys. They commonly are expressed as shallow headward extensions of theater-head terminations of deep valleys. The filamental valleys are characterized as being very slender or thread-like and are typically about 50 meters or less in depth and have no tributaries.

Alcoves appear on the sides of many slopes throughout this region. Often they are theater-headed, but in plan pattern, teardrop alcoves taper

downslope. Equant alcoves tend to be circular to ovoid in plan pattern. All have steep sidewalls and headwalls. Sometimes they occur in rudimentary networks and sometimes as groupings of individual unconnected alcoves.

Several observed relationships are worth mentioning in regard to these features:

(1) All valley elements throughout this region occur both independently and in an intermingled fashion. Sometimes they exploit each other and sometimes various elements are totally absent.

(2) Where branching valleys are juxtaposed with tabular flows, interior link paths meticulously conform to flow margins. This is true (even particularly true) in high resolution images.

(3) Filamental valleys often extend (a) down the middle of tabular flows, (b) alongside tabular flows, but most importantly, (c) often continuously across flow and intra-flow units. In a few cases, they also cut across crested flows.

It appears from preliminary mapping and classification that the Alba valleys are very likely polygenetic in origin. As for many valley networks elsewhere on Mars, (1) the parallel network patterns, (2) the generally low junction angles and lack of systematic downstream increase, (3) the relative rarity and short length of exterior links versus long interior links, and the (4) theater-headed terminations, generally point to a restricted surface or subsurface source of eroding fluid, probably liquid water. The close planimetric association with flow margins suggests a causal relationship between flows and branching valleys, perhaps due to melting of groundice by hot lava flows, although the heat transport balance is not necessarily obvious. We see no clear evidence of rainfall-induced erosion. Filamental valleys are somewhat more problematic in that they occur both within and across the tabular flows, not conforming to expectations about lava channels. Some filamental valleys may be lava channels, while others may be related to seepage runoff of water. Branching valley networks may exploit pre-existing filamental valleys. Alcoves appear to be independent of the other valley types, and could to be the result of mass wasting of a incompetent layer by either liquid flow, sublimation, or aeolian deflation. Overall, all Alba valleys suggest the presence of a permeable, erodable aquifer subjacent to large well-expressed lava flows. A 100-500m blanket of pyroclastic material would be an ideal candidate. Such a conclusion is broadly consistent with those of other workers (Gulick and Baker, 1987; Mouginiis-Mark et al., 1987).

As mentioned above, there appears to be a layer of material conducive to erosive transport processes, throughout the NW area of Alba. Inspection of the entire Alba photomosaic shows the characteristic subdued nature of terrain subjacent to large flows on Alba flanks to be common elsewhere, particularly across Alba's northern tier where numerous valleys also occur. Additionally, displayed prominently within the NW quadrangle are swarms of alcoves which we collectively term etched terrane. Such etching appears to be most prominent on hillslopes, appearing as a transitional state between a smooth un-etched blanket in swale bottoms or on flat surfaces versus hilltops which appear to have the blanketing material completely removed. The characteristic teardrop alcove morphology suggests removal of material

from exposed prominences along ridges, as if a blanket were being preferentially stripped. The etching process appears to have been caught in various stages of completion from total denudation to minimal pitting, and the degree of etching appears to characterize individual units. This would suggest either variable susceptibility based on material competence or a constant process attacking successively emplaced units. Again, the presence of these features may indicate a strippable pyroclastic blanket.

#### REFERENCES

- Gulick, J. and V.R. Baker, 1987, Origin and evolution of valleys on martian volcanoes: the Hawaiian analog, Proc. LPSC XVIII, p. 376-377.
- Laity, J.E. and M.C. Malin, 1985, Sapping processes and the development of theater-headed valley networks on the Colorado Plateau, Geol. Soc. Am. Bull. 96, p. 203-217.
- Mouginis-Mark, P.J., L. Wilson, and J.R. Zimbelman, 1987, Polygenetic eruptions on Alba Patera, Mars: evidence of channel erosion on pyroclastic flows, submitted to Bulletin of Volcanology.
- Pieri, D.C., 1980, Martian valleys: morphology, distribution, age, and origin, Science, 210, p. 895-897.
- Pieri, D.C., 1984, Junction angles in drainage networks, Jour. Geophys. Res., 89, 6878-6884.

## SOME NEW DESIGNATIONS FOR LAVA FLOWS AT ALBA PATERA

David Pieri and Dale Schneeberger, Jet Propulsion Laboratory,  
Pasadena, CA 91109

Although there is surprisingly little systematic Alba-specific work in the literature, previous researchers have described and classified a number of flow-like morphologies (Carr et al., 1977; Greeley and Spudis, 1981; Cattermole, 1987; Mouginis-Mark et al., 1987). Descriptions have focused on two major flow types, one being the extremely large (100-500km long) flat-topped flows that typically occur on Alba flanks, and the other being a class of somewhat shorter, more diffuse features which appear to be a series of gentle ridges, consequent upon pre-existing topography, often arrayed in a distributary pattern. Other flows, within what appears to be a central caldera complex, appear to be somewhat smaller versions of the first type.

As we proceeded into our more detailed investigations of the Alba Patera flow complexes, we were, frankly, somewhat unsatisfied with existing flow nomenclature, which we felt was not descriptive enough and a little too genetically biased. Such nomenclature basically originated during the heat of the Viking mission, and since little subsequent systematic geomorphology has been carried out for Alba anyway, we devised our own scheme based on detailed analyses of medium (20-30 m/pixel) and high resolution (9 m/pixel) Viking Orbiter data.

We see generally two classes of lava flow-like morphologies expressed on Alba Patera. The first we term tabular flows. These are equivalent in most cases to the "sheet flows" and "flat-topped", described by other workers (e.g., Carr et al., 1977; Greeley and Spudis, 1981). Such flows, indeed, appear flat topped with little surface relief, even in high resolution images. In general, they appear to exhibit no obvious intra-flow morphological units (e.g., levees, lava channels, spillovers, abandoned flow-fronts). They are radially arrayed relative to the central caldera complex, tend to be of relatively uniform width over most of their reaches, however, widening by an order of magnitude at their distal terminations. They are characteristically not only "flat-topped", but appear to be truly "flat" topographically and of fairly uniform thickness over most of their length, hence the choice of the term "tabular". Photo-clinometric thickness measurements (Baloga et al., 1987) taken along flow margins appear to confirm this. Proximal to the central caldera, these flows tend to disperse and thin into generally undifferentiable lava flow terranes, and no unambiguous source vents have yet been identified. Distally, tabular flows tend to thicken appreciably only at their immediate terminal margins. Local thickening appears to reach an estimated 150 meters or more.

The composition and rheological regimes of the tabular flows are somewhat problematical. The longitudinal profiles of these flows are much flatter than, for instance, typical Hawaiian flows. Their overall thicknesses tend to argue against low viscosity (e.g., ultra-mafic or mafic) lavas. Best fit viscosities assignable to the first discernable upstream manifestation of a discrete flow tend to hover around 100,000 poise, suggesting basaltic-andesite or andesite compositions (Baloga et al., 1987) for reasonable effective radiation temperatures. Such compositions are more silicic than have been suggested previously for Alba (Carr et al.,

1977), however, they may be more consistent with current suggestions of evidence of pyroclastic activity (Mouginis-Mark et al., 1987).

The other major recognized flow type we term crested flows. These are generally equivalent to the "ridge flows", "tube-fed flows", and "tube-channel" flows described by other workers (Carr et al., 1977; Greeley and Spudis, 1981). We use the term "crested" to describe the major morphological attribute of these features, namely that they typically are features of positive relief with an axial, often medial, apex. Such axial apices often (but may not necessarily) coincide with axial longitudinal valleys or longitudinally-aligned pits. We feel that the evidence as to whether these longitudinal valleys represent true lava channels or whether the aligned pit chains represent true collapsed lava tube/channel systems, while adequate to support such a working hypothesis, is not generally unequivocal. Data with spatial resolution adequate to resolve their interior morphologies is not available for more than one example. Flow margins appear to smoothly grade into the surrounding terrain, although in a few cases marginal ramparts can be discerned. Overall, crested flows are remarkably uniform in plan width, as are axial troughs, where they exist. In many cases, it is clear that crested flows conform to pre-existing topography and are centered between marginal pre-existing ridges. Upstream source vents for these features are not discernable, and often individual flow digits merge upstream into generally smooth deposits.

The genesis of crested flows is problematical. A logical terrestrial analog would appear to be flows with collapsed lava tube-lava channels (e.g., Snake River Plain, Hawaii) (Greeley, 1987; Greeley, 1977; Green and Short, 1971). There are several disparities, however. Such terrestrial flows typically have tube-channels that are  $\sim 1/10$  the width of the flow width. On Alba, such channels are of the order of  $\sim 1/100$  of the flow width. On the earth, type examples of such flows are of the order of 5-10 km long. On Mars, Alba crested flows are several hundred kilometers in discerned length (source vents are invisible; distal terminations often appear buried by subsequent superjacent plains materials). Additionally, while overall similar features of comparable terrestrial scale on Olympus Mons show clear evidence of flanking margin buildups by repeated overflows, no such evidence is discernable on the Alba flows. Finally, typical crested flows are very uniform in width (as are associated axial troughs), with little of the downstream-accumulated planimetric "noise" (i.e., variability in plan width) common in most lava flows (Baloga-personal communication). Thus, the emplacement mechanisms, rheological and compositional regimes of these crested flows remain unclear and should continue to be a topic of study.

#### REFERENCES

- Baloga, S.M., D.C. Pieri, J. Plescia, and P. Davis, 1987, Profiles of lava flows at Alba Patera, Mars, Proc. LPSC XVII, p. 42-43.
- Carr, M.H., R. Greeley, K.R. Blausius, J.E. Guest, and J.B. Murray, 1977, Some martian volcanic features as viewed from Viking Orbiters, Jour. Geophys. Res., 82, p. 3985-4015.
- Cattermole, P., 1987, Sequence, rheological properties, and effusion rates of volcanic flows at Alba Patera, Mars, Jour. Geophys. Res., 92, B4, E553-E560.



- Greeley, R. 1977, Aerial guide to the geology of the central and eastern Snake River Plain, pgs. 59-112, in Volcanism of the Eastern Snake River Plain, Idaho, Greeley and Kings, eds., NASA CR-154621 (Langley), 308 pp.
- Greeley, R., 1987, The role of lava tubes in Hawaiian volcanoes, pgs. 1589-1602, in USGS Prof. Paper 1350, Decker et al., eds., 1667 pp.
- Greeley, R. and P. Spudis, 1981, Volcanism on Mars, Rev. Geophys. Space Phys., 19, 13-41.
- Green, J. and N.M. Short, 1971, Volcanic landforms and surface features, Springer-Verlag, New York, 519 pp.
- Mouginis-Mark, P.J., L. Wilson, and J.R. Zimbelman, 1987, Polygenetic eruptions on Alba Patera, Mars: evidence of channel erosion on pyroclastic flows, submitted to Bulletin of Volcanology.

# A NEW MODEL FOR LEVEED FLOWS ON MARS

Stephen M. Baloga and Joy A. Crisp (Jet Propulsion Laboratory/Caltech, Pasadena, CA)

Lava flows with prominent central channels and lateral, embanking levees are evident in many Viking images of Mars. Numerous quantitative studies [4,5,8,9,11] have used dimensional data on such flows to develop compositional, rheological and volcanological inferences about Mars volcanism. The models that have been used in these studies have two features in common. First, all the models implicitly assume steady-state emplacement conditions. That is, time-dependent changes in vent conditions, flow depths, flow rates and so-forth are ignored. Second, a Bingham rheology is conjectured to explain the limited lateral expansion of the flows. We will show that the assumptions of steady-state conditions and a Bingham rheology produce a kinematic effect [1] that makes these assumptions incompatible unless levees are constructed at or near the flowfront at a certain rate. Requiring compatibility of these assumptions produces a simple new model for the emplacement of leveed lava flows.

A variety of different levee-building processes have been identified for terrestrial flows [6,7,10]. Some recent studies of basaltic and basaltic andesites [3,6] suggest that much of the levee emplacement occurs at the flowfront or in the distal reach of the advancing flow. We will assume that the leveed flows on Mars also behave this way. By applying the new model to previously published dimensional data, new estimates of yield strengths are obtained below. Table 1 provides the symbols and definitions used here.

The flow of a Bingham fluid in a channel on an inclined plane is usually described by the following equations:

$$\begin{array}{ll} \text{Momentum Conservation in} & \frac{\partial \tau}{\partial y} + \rho g \sin \theta = 0 \\ \text{the Viscous Zone:} & \end{array} \quad (1)$$

$$\begin{array}{ll} \text{Constitutive Relation:} & \tau = \tau_o + \mu \frac{\partial u_v}{\partial y} \end{array} \quad (2)$$

$$\begin{array}{ll} \text{Interface Condition:} & \tau_o = \rho g \sin \theta (h - h_v) \end{array} \quad (3)$$

$$\begin{array}{ll} \text{Boundary Conditions:} & u_v(0) = 0 \quad \text{and} \quad \tau(0) = \rho g \sin \theta h \end{array} \quad (4)$$

The interface condition divides the flow into two vertical regions, an inner core undergoing viscous shear according to eqs. (1) and (2), and an upper zone of strain-free plug flow. These relations give the textbook solution for the velocity profile and various algebraically related forms

$$u_v(y) = \frac{g \sin \theta}{\nu} y(h - y/2) - \frac{\tau_o y}{\mu} = \frac{g \sin \theta}{\nu} y [h_v - y/2] \quad (5)$$

$$u_p = \frac{g \sin \theta}{2\nu} h_v^2 = \frac{(\tau_w - \tau_o)^2}{2\mu \rho g \sin \theta}$$

The most important consequence of the velocity profiles, however, is that we can calculate the volumetric flowrates in each of the two regions:

$$Q_v = W \int_0^{h_v} u_v dy = \frac{g \sin \theta}{3\nu} h_v^3 W \quad (6)$$

$$Q_p = W \int_{h_v}^h u_p dy = u_p W(h-h_v) = \frac{g \sin \theta}{2\nu} h_v^2 W (h-h_v) .$$

Algebraically equivalent results have been discussed numerous times in the literature. If steady-state conditions truly prevail in the flow, then these flowrates are valid at every point along the path of the flow and at every time after the passage of the flowfront. Consequently, we must have volume conservation in each of the two regions separately. Thus,

$$W h_v L_v = Q_v t , \quad \text{and} \quad W(h-h_v) L_p = Q_p t \quad (7)$$

in the shear and plug zone, respectively. With eq. (6), one can show that  $L_p$  is always greater than  $L_v$ . Similar kinematic effects also follow for a Newtonian rheology [1,2]. Because the actual length of the flow must be governed by the inner viscous nucleus, we are left with two alternatives. One alternative is that steady-state conditions and Bingham rheology are incompatible because volume cannot be conserved. The other alternative is that *the excess volume of the plug region is transferred from the active part of the flow and deposited in stationary margins*. To maintain a steady-state in the active channel, the volume in the levees must grow according to

$$V_L = W (h-h_v) (L_p - L_v) = W (h-h_v) g \sin \theta h_v^2 t / 6\nu \quad (8)$$

$$= Q_p t / 3 = u_p (h-h_v) W t / 3$$

These relationships are purely a function of the dynamics in the channel. To confine the flow, the levee must be as thick as the viscous core ( $h_v$ ), but it may be as thick as the flow itself ( $h$ ). If the levee have a simple wedge shape with width  $W_L$  on each side, then the lava volume in the levees is also given by

$$V_L = L_v h_v W_L \quad \text{or} \quad V_L = L_v h W_L \quad (9)$$

By equating these two independent expressions (eqs. 8 and 9) for the levee volume and using eqs. (3, 6 and 7), we obtain minimum and maximum values for the yield stress,

$$\tau_o \text{ min} = \frac{\rho g \sin \theta h}{1 + W / 2 W_L} \quad \text{and} \quad \tau_o \text{ max} = \frac{2 W_L \rho g \sin \theta h}{W} . \quad (10)$$

These forms are ideal for planetary applications because we can usually obtain estimates of all quantities on the right hand sides from the Viking data. It is important to note that these formulas require depth as well as width information, unlike the methods used by previous investigators. Table 2 shows the resulting yield strength from eq. (10) and data adapted from previous analyses by other authors. These new results tend to be comparable to those of previous investigators, but some are significantly lower. This may be due to the fact that these new estimates are more closely related to the yield strength in the channel while the flow was active. Further consequence of this approach to leveed flows on Mars will appear elsewhere.

TABLE 1: Symbols and Definitions

$y$	distance above the flowbed	$Q_v$	flowrate in viscous core
$t$	time	$Q_p$	flowrate in plug zone
$h$	thickness of the flow	$W_p$	width of channel
$h_v$	thickness of the viscous core	$W_L$	width of levees
$\tau_o$	yield stress	$g$	gravity
$\tau_b$	basal stress	$u_p$	velocity of plug
$\nu$	plastic viscosity (kinematic)	$u_v$	velocity in shear zone
$\mu$	plastic viscosity (dynamic)	$L_v$	extent of the shear zone
$\rho$	density		and length of flow
$\theta$	slope of the flowbed	$L_p$	extent of the plug zone

TABLE 2: Computed Yield Strengths for Lava Flows on Mars

Flow	$\sin \theta$	$h(m)$	$W + 2 W_L(m)$	$W_L$	$\frac{\tau_{min} \tau_{max}}{(N/m^2)}$		Source
Ascraeus Mons	A1	0.1045	30	1175	388	19339 56808	Zimbleman 1985
	C1	0.0872	20	625	163	8475 17656	
	D1	0.0872	20	500	88	5704 8776	
	E2	0.0872	35	625	100	9127 13422	
Alba Patera	L13	0.01	14	1750	300	467 710	Cattermole 1987
	L14	0.01	16	1600	250	486 707	
	L15	0.01	20	3000	750	972 1945	
	L16	0.01	20	3000	900	1167 2917	
	L17	0.01	15	1750	450	750 1544	
Arsia Mons	#3	0.0038	11	2087	435	169 291	Moore et. al., 1978
	#4	0.0047	27	2609	695	657 1407	
	#7	0.007	22	2980	890	894 2221	

## REFERENCES

- [1] Baloga, S. (1987). *J. Geophys. Res.*, 92, 9271-9279. [2] Baloga, S. and D. C. Pieri (1986). *J. Geophys. Res.*, 91, 9543-9552. [3] Borgia, A. et al. (1983). *J. Volcan. Geotherm. Res.*, 19, 303-329. [4] Carr, M. H. et al. (1977). *J. Geophys. Res.*, 82, 3985-4015. [5] Cattermole, P. (1987). *J. Geophys. Res.*, 92, E553-E560. [6] Decker, R. W. et al. (1987). *USGS Prof. Paper 1350*. [7] Greeley, R. (1970). *Mod. Geol.*, 2, 207-223. [8] Hulme, G. (1976). *Icarus*, 27, 207-213. [9] Moore, H. J. et al. (1978). *Proc. Lunar Planet. Sci. Conf.*, 9th, 3351-3378. [10] Sparks, R. S. J. et al. (1976). *Geology*, 4, 269-270. [11] Zimbleman, J. R. (1985). *J. Geophys. Res.*, 90, D157-D162.

**CONSTRAINTS ON MARS SAMPLING BASED ON MODELS OF BASALTIC FLOW SURFACES AND INTERIORS; J. C. Aubele and L. S. Crumpler, Dept. of Geological Sciences, Brown University, Providence, RI 02912**

We assume that basaltic plains units on Mars are a dominant terrain type and, for future missions, will be a landing site of choice due to engineering or sampling constraints. Proposed rover/sample return missions will traverse, or at least photograph and sample, small-scale surface blocks and outcrops within large flow units. Actual contacts between rock types may be difficult to find or recognize for an in situ lander or even for a rover of limited range. However, the surface characteristics of the plains units, (blocks, cobbles, outcrops, dunes, and other surficial materials) will be visible, and may even act as limiting parameters to rover trafficability or lander sampling strategies. These surface characteristics can be interpreted in a geologic context if we understand the nature of degraded basaltic flow surfaces.

Recent field observation and numerical modeling of the pattern and origin of vesicle zones and joints in terrestrial basaltic flows [1] has resulted in increased understanding of the processes which affect flow surface morphology. This work has documented the ubiquitous occurrence of three vertical zones in basalt flows: (1) an upper vesicular zone; (2) a middle vesicle-free zone and (3) a lower vesicular zone. The upper vesicular zone is generally about one-half of the total flow thickness. Computer modeling of the development of these zones confirms that vesicle zonation is a result of the nucleation, growth and rise of bubbles in solidifying lava and can be expected to occur in all basaltic flows. Degradation of basaltic flows, therefore, will produce vesicular blocks until the erosional level reaches the central vesicle-free zone. In addition, observation of terrestrial basaltic flows [2] has shown that most thin (less than 10m thick) flows have a regular pattern of orthogonal joints in vertical section in which the spacing of joints increases with depth beneath the flow surface. Therefore, as a flow erodes vertically the degradational surface of that flow will be characterized by blocks of a size similar to the spacing of joints at that level in the flow. Generally, as a crude approximation, the joint spacing at a specific level in the flow will be roughly equivalent to the depth from the primary flow surface to that level. As a basaltic flow degrades, the erosional surface will be characterized by a bimodal distribution of fines and blocks. The mode of the block size population is an indication of the depth to which that flow has been eroded.

Using these studies we have performed a preliminary analysis of the Viking lander sites [3]. If the rocks at the Viking lander sites are basaltic, and if the pits visible in lander imagery are vesicles, then certain basic assumptions can be stated regarding the geology of the sites. The natural degradation of a basaltic flow can result in a blocky surface. Impact disturbance of the surface may add some large blocks but is not required as a mechanism for generating the observed blocks on the surface. The general size of the block populations at both sites [4] indicate a flow disturbed by erosion to a depth of tens of centimeters. Blocks containing abundant vesicles could be from the upper vesicular zone. A few large blocks (greater than 1m), without vesicles, visible at both lander sites probably represent excavation by impact from some greater depth in the flow than has been reached by erosion.

## SAMPLING AND MODELS OF BASALTIC FLOWS

AUBELE, J.C. and CRUMPLER, L.S.

These studies, and the new understanding of basaltic flow surfaces that they provide, also have implications for future Mars sample return missions. For example, trafficability is related to the abundance and size of blocks at the surface, which in turn is related to the depth of erosion of a basalt flow. Flows which have experienced disturbance of the surface to a deep level may be more difficult to traverse because modal block size will be larger. In terms of an *in situ* sample mission, a sample from near the surface of a basaltic flow will contain less mass per unit volume than will a sample from the vesicle-free interior. In other words, a sample collected from the top of the upper vesicular zone would be predominantly voids. Maximum mass per unit volume will occur in samples from the vesicle-free zone. In addition, basalt from the upper vesicular zone is frequently more microcrystalline than is basalt from the vesicle-free zone and consequently more difficult to characterize petrographically. For these and other reasons, optimal sampling of a basalt flow would require a sample from the vesicle-free zone. If basaltic flow structure on Mars is comparable to that on Earth, then this means a flow which has been eroded down to one-half its total flow thickness. But this type of surface cannot be easily traversed, in the event of a rover mission, because of its large blocks. One solution may be a landing site on a basalt flow of intermediate age with a surface disturbed by a few small impact craters which have excavated blocks from the interior of the flow.

In future work, we anticipate formulating a detailed model of the mechanics of formation of the interior structure (vesicle formation, vesicle zones, joint patterns) of basaltic flows, and the way in which this structure constrains the surface morphology of degraded flows. This model will then be used to (a) predict the surface properties of basaltic plains units which will act as limiting parameters to future Mars lander/sample return/rover missions, and (b) to construct models of basaltic surfaces by which the imagery and samples from future lander missions can be evaluated and interpreted.

**References.** [1] Aubele, J.C., et al., 1987, *J. Volc. Geoth. Res.*, in press; [2] Aubele, J.C., et al, 1980, *NASA TM-82385*, 231; [3] Aubele, J.C. and Crumpler, L.S., 1987, *Lunar Planet. Sci. Conf. XVIII*, (abst.), 36; [4] Garvin, J.B., et al., 1981, *Moon Planets*, 24, 355.

SMALL MARTIAN VOLCANOES; Philip A. Davis and Kenneth L. Tanaka, U.S. Geological Survey, Flagstaff, AZ 86001

Various types of volcanoes have been identified on Mars, mainly on the basis of qualitative morphologic criteria such as relief, circularity, summit craters, and alignment with structural trends [e.g., 1-11]. Some of the volcano types thus far identified include shields, stratovolcanoes, silicic domes, table mountains, and cinder cones. We are currently conducting a survey of Viking Orbiter images to identify possible candidates for Martian volcanoes. Our selection is based on two criteria: the features have relief and a summit crater, and they are shown on images that have sufficient spatial resolution to allow acquisition of photoclinometric profiles across the features. The upper size limit for this survey is represented by tholi and paterae; the lower limit is dictated by Viking Orbiter image resolution. These two selection factors may allow features to be included in the database that appear similar to volcanoes because of fortuitous circumstances (e.g., an erosional mound that has a centrally located impact crater). However, we think that such circumstances will be rare and their effect on the database will be minimal. This survey and subsequent analyses will not include maars because they can be distinguished from impact craters only by their circularity [12], whose measurement for all such features would be very time consuming if not impossible, considering the spatial resolution of Viking Orbiter images.

The topographic profiles of the selected Martian volcanoes that are currently being acquired will be compared with tabulated data for terrestrial and lunar volcanoes [12-17] in an attempt to determine the types of volcanism that have occurred on Mars. Variation in volcanic style with age will also be examined. We hope that these analyses will also indicate clearly whether water or water-ice was involved in some periods of Martian volcanic history (such as in the production of tuff cones or table mountains).

An example of what may come from this study is the topographic data (Table 1) of a small volcano in northern Noctis Fossae (see Viking Orbiter frame 931A03), which we have already profiled. The topographic characteristics of this volcano (i.e., ratios involving volcano height and width and crater depth and diameter) are more similar to the average topographic characteristics of Icelandic lava shields than to those of all other types of terrestrial and lunar volcanoes reported in [12-14]. Of the 17 Icelandic-type lava shields reported in [13,14], the topographic data for the Baldheidi (Iceland) shield (Table 1) are most similar to those of this Martian volcano. Kilometer-sized volcanoes that occur elsewhere on Mars have been compared with terrestrial cinder cones [18,19]. However, the topographic characteristics of the Noctis Fossae volcano are very different from the topographic data reported for terrestrial cinder cones and tuff cones [13,14]. This observation may not hold true for the majority of the kilometer-sized volcanoes when more data are acquired. Also, we cannot exclude as yet the possibility that the Martian volcano is a pyroclastic deposit that differs from those on Earth because of degradation, incomplete evolution, or gravity scaling effects between the planets.

## REFERENCES.

1. West, M. (1974) Icarus 21, p. 1-11.
2. Ward, C.A. (1979) Proc. Lunar Planet. Sci. Conf. 10, p. 2815-2840.
3. Scott, D.H., and Tanaka, K.L. (1981) Lunar Planet. Sci. XII, p. 952-953.
4. Greeley, R., and Theilig, E. (1978) Rept. Planet. Geol. Prog. 1979-1980, NASA TM 79729, p. 202.
5. Plescia, J.B. (1981) Icarus 45, p. 586-601.
6. Scott, D.H. (1979) Proc. Lunar Planet. Sci. Conf. 10, p. 3039-3054.
7. Plescia, J.B., and Saunders, R.S. (1979) Proc. Lunar Planet. Sci. Conf. 10, p. 2841-2859.
8. Pike, R.J., and Clow, G.D. (1981) Third Intern. Coll. on Mars, LPI Contrib. 441, p. 199-201.
9. Hodges, C.A., and Moore, H.J. (1979) J. Geophys. Res. 84, p. 8061-8074.
10. Scott, D.H. (1982) J. Geophys. Res. 87, p. 9839-9851.
11. Scott, D.H., and Tanaka, K.L. (1981) Proc. Lunar Planet. Sci. Conf. 12, p. 1449-1458.
12. Pike, D.J. (1980) U.S. Geological Survey Prof. Paper 1046-C, 77p.
13. Pike, D.J. (1978) Proc. Lunar Planet. Sci. Conf. 9, p. 3239-3273.
14. Pike, D.J., and Clow, G.D. (1981) U.S. Geological Survey Open-File 81-1038, 40 p.
15. Wood, C.A. (1980) J. Volcano. Geotherm. Res. 7, p. 387-413.
16. Wood, C.A. (1980) J. Volcano. Geotherm. Res. 8, p. 137-160.
17. Dohrenwend, J.C., Wells, S.G., and Turrin, B.D. (1986) Geol. Soc. Amer. Bull. 97, p. 421-427.
18. Scott, D.H. (1979) Proc. Lunar Planet. Sci. Conf. 10, p. 3039-3054.
19. Frey, H., and Jarosewich, M. (1982) J. Geophys. Res. 87, p. 9867-9879.

Table 1. Topographic characteristics of a Noctis Fossae volcano and an Icelandic shield volcano.

	Crater Diameter (m)	Crater Depth (m)	Cone Height (m)	Flank Width (m)
Noctis Fossae	640±60	9±5	212±25	1107±60
Baldheidi <sup>1</sup>	600	10	240	2600

<sup>1</sup> Data from [13].



**PROGRESS IN DETERMINING THE THICKNESS AND DISTRIBUTION OF VOLCANIC MATERIALS ON MARS: R. A. De Hon, Department of Geosciences, Northeast Louisiana University, Monroe LA, 71209.**

Volcanic plains and constructs comprise over half the surface of Mars (1). Volcanism has ranged from the earliest period to the youngest rocks visible on the planet (2,3). The volume of volcanic materials provides important constraints to the history and structure of the planet. Volume estimates require sensible estimates of the surface area covered by volcanic materials and reasonable estimates of the thickness of volcanic materials. Estimates of the area of extent are provided by geologic mapping (2,4,5). Thickness estimates are provided by geophysical or photogeologic methods. One method of photogeologic estimation of lava thickness based on partial burial of craters (6) has been adapted for use on the moon (7) and Mars (8). Lacking sufficient topographic data, early martian estimates (8,9) employed crater geometric relationships based on lunar and Mercury observations (10,11), but improved observations based on Viking data allow a uniquely martian relationship (12) to be employed (13, 14).

Data for Mars based on partially buried craters must be used with caution. To construct reasonable isopachous maps, the surface on which the craters rest must be sufficiently cratered to provide an acceptable geographic distribution and point density. In addition, the craters must not be greatly degraded by erosional processes prior to burial. Further, the geologic contacts of the unit being mapped must be known. The contacts provide zero thickness-limits that are necessary for construction of isopachous maps.

Buried craters do not provide information 1) for regions in which volcanic flooding followed plains formation too rapidly to allow a sufficient number of craters to collect on the surface; 2) for regions in which flooding is sufficient to totally bury the pre-existing crater population; or 3) for regions of densely cratered volcanic terrain for which the initial character has been destroyed. Hence, the volume of materials within the large volcanic centers associated with Tharsis, Olympus Mons, and Elysium Mons cannot be estimated in this manner. Minimum estimates may be provided for these regions by simple geometric estimates of the positive topography of these regions, but subsurface volcanic materials can only be estimated by geophysical techniques. Even more difficult are estimates of presumed thick lenses of volcanics within basins such as Isidis.

The completion of 1:2M Viking photomosaics and a refined geologic map based on Viking photography (4,5) set the stage for improved thickness studies and volume estimates. Currently, a revised (but incomplete) data base of approximately 725 partially buried craters has been compiled (Table I) using Mars photomosaics at 1:2M for initial identification and measurement. The revised crater-diameter to rim-height relationship (12) reduces thickness estimates reported earlier (9) by more than one-half. Most plains-forming materials have thicknesses ranging from 0.25 to 0.60 km. Because martian craters are probably degraded by various processes, thickness estimates are probably maxima, and true thickness may be less than those recorded.

**REFERENCES:** 1) Greeley R. and Spudis P.D. (1981) Rev. Geophys. Space Phys. 19, 13-41.; 2) Scott D.H. and Carr M.H. (1978) USGS Misc. Inves. Map. I-1083.; 3) Greeley R. (1987) Sci. 236, 1653-1654.; 4) Scott D.H. and Tanaka K.L. (1985) USGS Misc. Inves. Map I-1302A.; 5) Greeley R. and Guest J.E. (1985) USGS Misc. Inves. Map (in press).; 6) Marshall C.H. (1963) Astrogeol. Stud. Ann. Prog. Rep., 1962, 19-31.; 7) De Hon R.A. and Waskom J.D. (1976) Proc. LSC 7th, 2729-2746.; 8) De Hon R.A. (1982) J.G.R. 87, 9821-9828.; 9) De Hon R.A. (1982) NASA Tech. Mem. 85127, 129-131.; 10) Pike R.J. (1977) in Impact and Explosion Cratering, 489-510.; 11) Cintala M.J. (1979) Proc. LPSC 11, 2423-2436.; 12) Pike R.J. and Davis P.A. (1984) LPSC 15, 645-646.; 13) De Hon R.A. (1985) LPSC 16, 171-172.; 14) De Hon R.A. (1985) LPSC 16, 173-174.

TABLE I  
CURRENT STATUS OF THICKNESS ESTIMATES BY QUADRANGLE

QUAD	NO. OF POINTS	MAXIMUM VALUE	MINIMUM VALUE	QUAD	NO. OF POINTS	MAXIMUM VALUE	MINIMUM VALUE
2NW	2	0.34	0.34	14SE	4	0.28	0.18
2NE	1	0.24	0.24	15NE	8	0.36	0.19
2SW	9	0.96	0.23	15SW	5	0.34	0.19
2S-C	6	0.36	0.20	15SE	9	0.67	0.24
3NW	7	0.53	0.25	16NW	3	0.46	0.40
3NE	2	0.30	0.29	16NE	2	0.32	0.22
3SW	2	0.31	0.27	16SW	11	0.40	0.24
3SE	1	0.19	0.19	16SE	12	0.56	0.22
4NW	2	0.44	0.39	17NW	5	0.34	0.16
4SW	10	0.49	0.24	17NE	4	0.41	0.16
4S-C	8	0.71	0.25	17SW	9	0.55	0.16
4SE	2	0.57	0.36	17SE	4	0.60	0.20
5NE	4	0.43	0.33	18NW	7	0.63	0.15
5SW	3	0.51	0.34	18NE	12	0.57	0.27
5SE	2	0.34	0.34	18SW	6	0.56	0.21
6NW	2	0.39	0.31	18SE	10	0.49	0.19
6SW	7	0.38	0.18	19NW	8	0.50	0.26
7SE	22	0.61	0.22	19NE	8	0.42	0.23
7S-C	3	0.29	0.22	19SW	9	0.53	0.30
7NE	5	0.42	0.34	20NW	31	0.64	0.19
8NW	23	0.96	0.18	20NE	16	0.55	0.27
8SW	17	0.80	0.19	20SW	8	0.47	0.20
8SE	3	0.37	0.34	20SE	13	0.45	0.24
9NW	2	0.27	0.21	21NE	6	0.40	0.28
9NE	5	0.24	0.15	22NW	2	0.31	0.25
9SW	1	0.27	0.27	22SE	24	0.49	0.23
9SE	2	0.27	0.24	22SW	21	0.46	0.23
10NW	4	0.43	0.20	23NE	6	0.38	0.18
10NE	11	0.51	0.18	23NW	7	0.46	0.20
10SW	11	0.66	0.18	23SW	9	0.40	0.19
10SE	12	0.62	0.31	23SE	12	0.55	0.31
11NW	12	0.51	0.29	24N-C	37	0.59	0.20
11NE	6	0.55	0.30	24NE	26	0.40	0.19
11SW	6	0.52	0.38	25NW	7	0.65	0.20
11SE	8	0.54	0.33	25NE	6	0.58	0.27
12NW	7	0.40	0.25	26NW	10	0.58	0.28
12NE	4	0.44	0.25	27NW	4	0.45	0.33
12SW	25	0.53	0.20	27N-C	8	0.43	0.31
12SE	4	0.46	0.30	27NE	5	0.44	0.24
13NW	5	0.47	0.19	27SE	12	0.53	0.28
13NE	4	0.30	0.22	28NE	9	0.64	0.23
13SW	3	0.53	0.23	29NW	12	0.28	0.27
13SE	9	0.43	0.16	29N-C	2	0.44	0.22
14NW	11	0.46	0.20	29NE	3	0.31	0.25
14NE	2	0.35	0.30	29SW	4	0.53	0.30
14SW	3	0.44	0.34				

--Thickness values in km--

## IRTM ANALYSIS OF POSSIBLE EXPLOSIVE VOLCANIC DEPOSITS ON MARS

*D.A. Crown, L.A. Leshin, and R. Greeley, Department of Geology, Arizona State University, Tempe, Arizona, 85287*

Analysis of Viking Infrared Thermal Mapper (IRTM) data covering proposed ash (ignimbrite) deposits on Mars has been initiated to complement photogeologic studies using Viking imagery and to develop criteria for the identification of explosive volcanic deposits. The focus of this study is the martian highland paterae, large, low relief volcanoes proposed to be the consequence of phreatomagmatic eruptions in ancient martian history [1]. The objective of this component of the project is to determine whether the martian highland paterae possess a distinct thermal signature (thermal inertia, rock abundance) and how the thermal properties indicated in the IRTM data correlate with the observed surface geology. To this end, several areas of postulated explosive deposits have been examined for comparison with the highland paterae. Earlier results of IRTM studies and a brief review of previous studies considering the existence of explosive volcanism on Mars are presented in [2].

### *Ignimbrites of the Amazonis, Memnonia, and Aeolis Quadrangles*

Scott and Tanaka [3] proposed the existence of a series of welded and nonwelded ash flow units covering approximately  $2.2 \times 10^6 \text{ km}^2$  in the Amazonis Planitia Region of Mars. These postulated ash flow units extend in a broad belt along the highland-lowland boundary from the western and southern margins of Olympus Mons to the Apollinaris Patera region. The mapped materials are thought to be ignimbrites on the basis of morphologic similarities to ignimbrites in the Pancake Range of central Nevada. These similarities include the existence of thick ( $\geq 100 \text{ m}$ ), areally extensive sheets which subdue the underlying topography, joint sets (presumably in welded materials), and the superposition of patches of smooth, high albedo (presumably nonwelded) materials onto jointed, low albedo (presumably welded) materials. Grooved surfaces which are apparently yardangs are present throughout Amazonis Planitia.

Five high resolution IRTM data tracks cross the proposed ash flow units. These tracks exist in the eastern region of the ignimbrite province and cross units described as both welded and nonwelded tuffs. No distinct, consistent thermal inertia signature is exhibited by the ignimbrite units as a whole and no systematic differences are apparent between the postulated welded and nonwelded materials. In one track (537A01) the thermal inertia of the ignimbrites is no different than that of the surrounding terrain, whereas a region of yardangs has thermal inertia values  $6-7 (x 10^{-3} \text{ cal cm}^{-2} \text{ sec}^{-1/2}/\text{K}^{-1})$  units higher. This is in agreement with Zimbelman [4] who in a study of the aeolian features of the Elysium-Amazonis region noted high thermal inertias and high block abundances over this group of yardangs. In two other tracks (498A06, 498A10) the ignimbrites show slightly higher values of thermal inertia than the surrounding terrain, but the changes in inertia values are gradual and do not correlate with the mapped boundaries of the ignimbrite units. Another track (460A02) shows no difference in thermal inertia values between the ignimbrites and the surrounding materials. While no consistent distinct thermal signature exists over these deposits, the existence of ignimbrites is not necessarily discounted by the data, as local features and apparent mantling by a fine layer of dust can dominate thermal inertias [5].

### *Fracture System Radial to Arsia Mons*

Carr et al. [6] describe a set of fractures which is radial to Arsia Mons and contained within the flow field to the south of Arsia Mons. This fracture system extends from approximately  $22^\circ \text{ S}$ ,  $123^\circ \text{ W}$  to  $30^\circ \text{ S}$ ,  $129^\circ \text{ W}$  and both cuts and is covered by flows. These fractures are suggested to be the sources of the lava which composes the surrounding flow

field. On Earth, such zones are frequently chemically altered to clay deposits as a consequence of heat and fumarolic activity. If similar alteration occurred on Mars, the resulting deposits may be identifiable using IRTM data.

Two high resolution IRTM data tracks cross the fracture system at roughly right angles. However, the quality of the data and the coverage of the fracture system is poor. The northernmost track (574A10) shows no correlation between the location of the fractures and the value of the thermal inertia. Near the rift thermal inertia values range from 4.7 - 6.4, and along the rift thermal inertia values vary from 4.7 - 6.2. These values are consistent with those of the surrounding terrain. Other features along the data track have thermal signatures. A small cluster of craters (~20 km long) possesses slightly lower thermal inertia values, and higher values are concentrated along a topographic high to the southeast. If changes in surface properties at a scale similar to these examples occur across the fractures, it is probable that they would be detected in the IRTM data. The southernmost data track (650A02) again shows no correlation between the rift and thermal inertia, although thermal inertia values do increase significantly along the track from southeast to northwest (from ~5.0 - ~7.0).

### *Apollinaris Patera*

Apollinaris Patera, which is located adjacent to the highland-lowland scarp (9° S, 186° W), is elliptical in plan view and possesses a central caldera which is multiple in form with channels radiating from its outer rim. Aeolian activity is evident in the region; yardangs are present and the northern flank of the patera appears to be mantled by dust.

Two high resolution nighttime tracks trending NW-SE cross Apollinaris Patera. In both the northern and southern regions of Apollinaris Patera thermal inertias are significantly greater than those observed in the surrounding areas. The thermal signature of Apollinaris Patera is more prominent on its southern flanks; within the southernmost of the two tracks thermal inertias increase from ~3.0 - 3.5 in the region surrounding Apollinaris Patera to a high of greater than 6.0 on the volcano and within the northern track from ~1.9 to a high of 3.4. Lower thermal inertias on the northern flanks of Apollinaris Patera are consistent with the regional trend reflecting the transition from the cratered uplands to the smooth plains [5] and also with observations of less morphologic detail on the northern flanks suggesting more thoroughly mantled surfaces.

### *Hadriaca Patera*

Hadriaca Patera is located northeast of the rim of Hellas Basin (267° W, 30° S) and is asymmetric in plan view due to the regional slope created by the basin. Broad, radial channels extend from a large summit caldera which contains smooth plains displaying wrinkle ridges [7]. Several outflow channels originate in large depressions to the south of Hadriaca Patera. These channels cut the southern flanks of the patera and extend to the southwest.

Three high resolution (633A14, 635A04, and 636A02) and one moderate resolution (704A07) data tracks cross Hadriaca Patera and the region to the northeast. Thermal inertia values vary from ~3.5 to 14.0 in the three high resolution tracks, with most values between 5.0 and 9.0. The values of the thermal inertia in the region to the northeast of Hellas Basin are generally higher than the values in the Apollinaris Patera and Amazonis Plantita regions. This reflects the differences between the ancient cratered highlands and the more heavily mantled lowland regions. Although anomalous areas are evident, the thermal inertia values over Hadriaca Patera are consistent with the region as a whole. Preliminary analysis suggests that the several areas of high thermal inertia present correlate with inter-crater deposits. However further investigation is required, as one area which correlates with the position of a crater on the eastern flanks of Hadriaca Patera is larger than the crater itself and may be indicative of the materials forming the patera. The high thermal inertia values of the anomalous regions correspond to coarse sand to gravel sized particles [8].

While the thermal inertia values over Hadriaca Patera are consistent with the region as a whole, the surface of Hadriaca Patera is more coarse-grained than the surrounding terrains. Using the rock abundance model of Christensen [9], rock abundances have been calculated for the region from Hadriaca Patera extending to the south over Dao and Harmakhis Valles [10]. For the 7-20  $\mu\text{m}$ , 11-20  $\mu\text{m}$ , and 11-20  $\mu\text{m}$  (with an emissivity correction) spectral differences both the caldera and flanks of Hadriaca Patera are shown to have high rock abundances. The 11-20  $\mu\text{m}$  spectral difference (with an emissivity correction) indicates that the caldera floor is composed of 14 - 25% rocks. The 18% rock abundance contour for the 7-20  $\mu\text{m}$  spectral difference corresponds directly to the caldera wall. The flanks of the patera have rock abundance values between 0 - 18% for the 11-20  $\mu\text{m}$  spectral difference (with an emissivity correction). While the moderate thermal inertias indicate a non-primary surface, the high rock abundances over Hadriaca Patera and especially in the caldera are apparently indicative of the volcanic materials forming this low-relief shield volcano.

## References

- [1] Greeley, R., and Spudis, P.D., 1981, *Rev. Geophys. Space Phys.*, 19, 13-41.
- [2] Crown, D.A., Leshin, L.A., and Greeley, R., 1987, *NASA TM-89810*, 327-329.
- [3] Scott, D.H., and Tanaka, K.L., 1982, *J. Geophys. Res.*, 87, 1179-1190.
- [4] Zimbelman, J.R., 1986, *LPI Tech. Report*, 86-09, 73-75.
- [5] Zimbelman, J.R., and Leshin, L.A., 1987, *Proc. Lunar Planet. Sci. Conf.*, 17th, *J. Geophys. Res.*, 92, E588-E596.
- [6] Carr, M.H., Greeley, R., Blasius, K.R., Guest, J.E., Murray, J.B., 1977, *J. Geophys. Res.*, 82, 3985-4015.
- [7] Albin, E.F., 1986, *Mars: Volcanic Features in the Cratered Uplands and Possible Tectonic Associations*, Master's Thesis (unpublished), Arizona State University, 84 pp.
- [8] Zimbelman, J.R., 1984, *Geologic Interpretation of Remote Sensing Data for the Martian Volcano Ascraeus Mons*, Ph.D. Dissertation, Arizona State University, 286 pp.
- [9] Christensen, P.R., 1982, *J. Geophys. Res.*, 87, 9985-9998.
- [10] Craddock, R.A., 1987, *High Resolution Thermal Infrared Mapping of Martian Outflow and Fretted Channels*, Master's Thesis, Arizona State University, in preparation.

## OCEAN-FLOOR VOLCANISM AS A VENUS ANALOG

Peter J. Mouginis-Mark, Patricia Fryer and Lionel Wilson, Planetary Geosciences Division, Hawaii Institute of Geophysics, University of Hawaii Honolulu, HI 96822

**BACKGROUND:** In recent years, the investigation of ocean-floor volcanic processes by deep-sea submersible (e.g., 1-4) and imaging sonar (e.g. 5-7) has revealed a wide range of volcanic landforms. Many of these landforms have direct subaerial terrestrial equivalents, and include volcanic craters and calderas, lava flows and, possibly, lava tubes (8). Because of the high ambient water pressure under which such submarine activity takes place, we believe that there is good relevance to study the diversity of submarine activity in order to better predict volcanism on Venus (cf., 9, 10).

Most of the submarine volcanic landforms can be explained by effusive activity, comparable to the eruption of basaltic magma in the subaerial environment (11). However, because of the confining pressure of the over-lying water column, the occurrence and distribution of explosively derived submarine volcanic products and fragmental debris are more enigmatic. Despite the recognition of abundant hyaloclastite on the flanks of certain seamounts (4, 6), the style of the eruption that produced these deposits is unknown due to the fragmental nature of the hyaloclastite and their frequent occurrence (in the form of talus streams) far from the vent. Imaging sonar data (12, 13) have also revealed a number of larger volcanic features which may have been produced by explosive submarine activity. In order to further our understanding of volcanic processes operating under high ambient pressure, we have initiated an examination of a wide variety of fresh volcanic surfaces using a number of techniques (described below) at water depths of 1,200 to 3,500 meters.

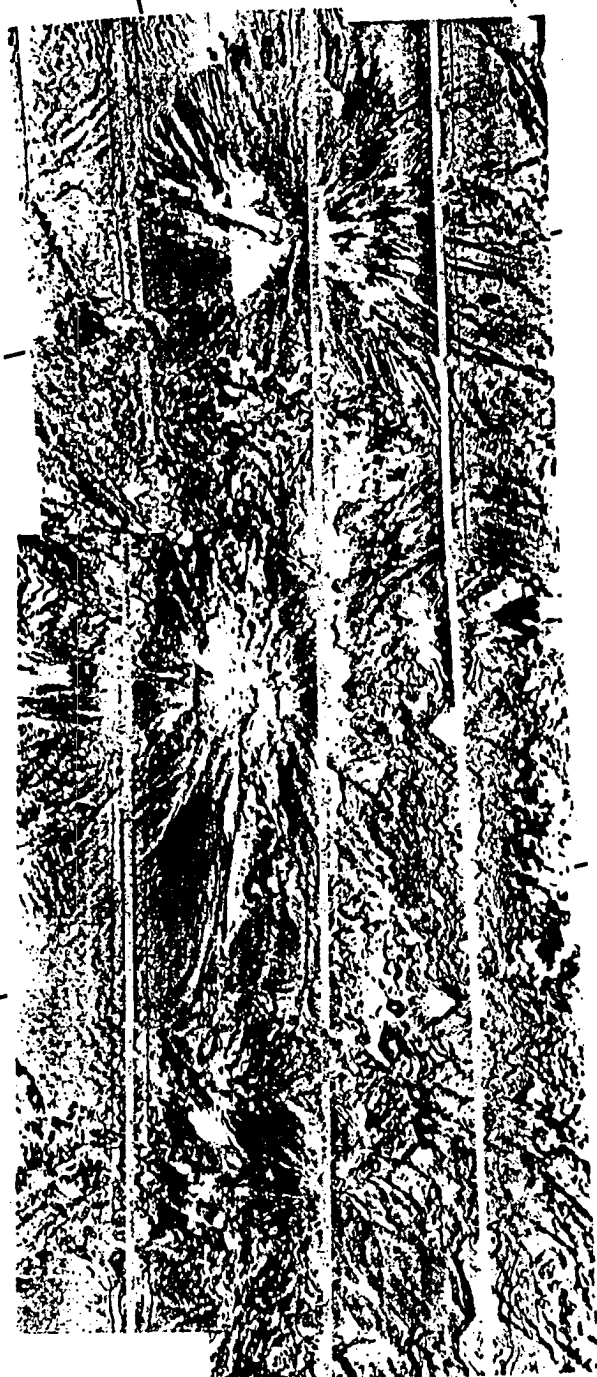
**DATA SETS:** In early July 1987, a two-week cruise to the Western Pacific collected several data sets that are of value to the interpretation of volcanism under high ambient pressures (comparable, or greater than, atmospheric pressure on Venus; ref. 10) and in the analysis of imaging data comparable to the different Venus radar systems. This cruise utilized the deep-sea submarine *Alvin* and the support ship R/V *Atlantis II* (14). In 1983, SeaMARC II imaging sonar and bathymetric data had been acquired for three seamounts in the Northern Mariana Arc (13, 15). These seamounts have basal diameters in excess of 20 km and rise from abyssal depths of ~4 km to within 400 meters of the surface. The following data sets were obtained:

- 1) A set of eight *Alvin* dives were completed on the three cross-chain seamounts (Figure 1). During each dive, a video camera was recording the outside geology (to a distance of ~10 meters from the submarine). A total of 3 - 5 hours of video per dive was obtained. In addition, approximately 500 - 1200 35-mm photographs (some in stereo) were obtained by the external cameras on *Alvin*. Rock samples from representative exposures were collected on each dive.

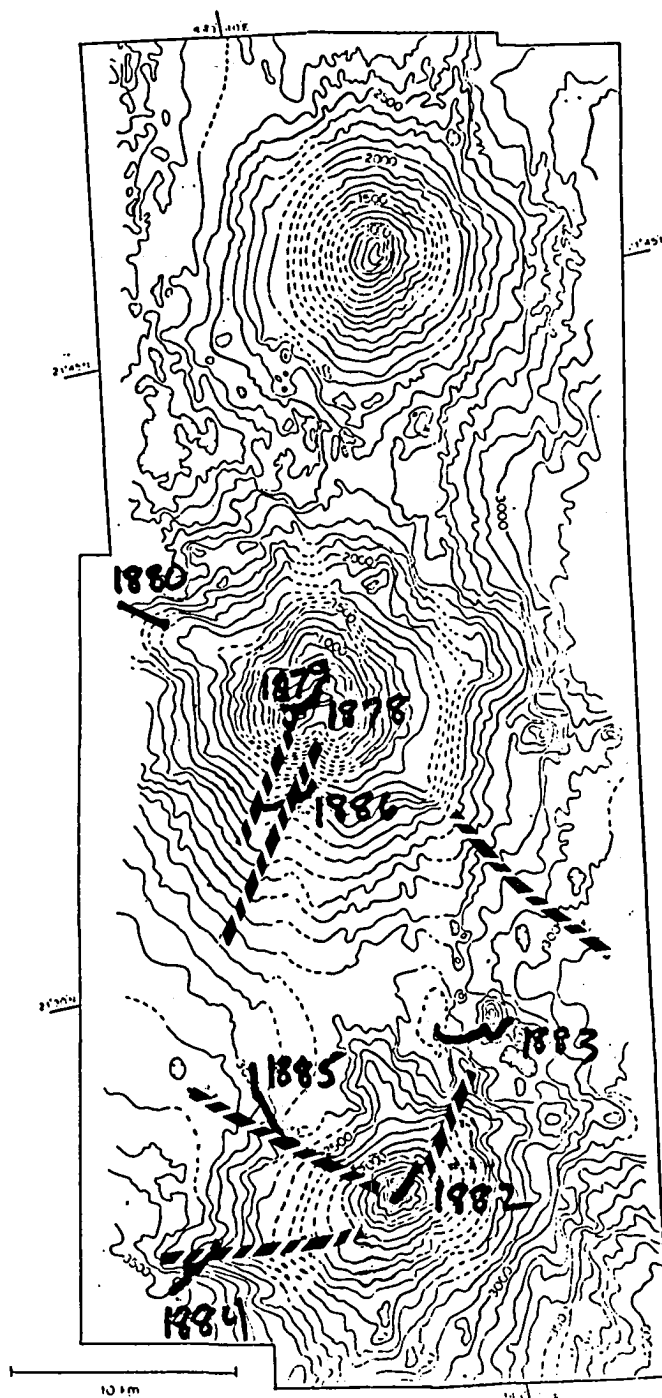
- 2) One of the objectives of the *Alvin* dives was to specifically study pillow basalts and talus slopes at water depths of 2,800 - 3,050 meters. During one of the dives, a custom-made tripod was deployed on representative surface units with the objective of determining the size-frequency distribution of boulders and exposed surfaces for areas of known sonar backscatter properties (i.e., to attempt a quantification of surface geology as imaged by a sonar system with a wavelength comparable to the Magellan radar: 10 - 12 cm). Stereo images from multiple look-directions were obtained for four different terrains (massive pillows, talus, sediment and pillows, sediment).

- 3) A deep-towed camera system was used on the cruise. This automatic camera system was lowered from the ship until it was 4 - 8 meters above the ocean floor, at which time the system imaged the bottom every 15 seconds. As a result of the ship's movement relative to the ocean floor, five hours of data acquisition on each of six camera runs produced over 7,200 photographs of the flanks of the seamounts. Each one of these photographs was accurately located to within ~200 meters by ship's navigation (LORAN and GPS), and 3.5 and 12.5 kHz echo soundings of the topography beneath the *Atlantis II*. We thus have a very large image data set of approximately 25 km x 10 m of ocean floor, at a resolution of ~3-5 cm, for which we also have SeaMARC II imaging sonar data.

- 4) In addition to the photography, the camera sled also carried a sonar altimeter, which operated when the sled was within 50 meters of the ocean bottom. These altimetric measurements can be considered to be the equivalent of a radar altimeter with a foot-print size of 2-5 meters. Data were obtained every 5 seconds along-track, with a resultant spatial separation of approximately 1.4 meters.



SeaMARC II Side-Scan Mosaic



SeaMARC II Bathymetry

Figure 1: SeaMARC II imaging sonar data for the three seamounts in the Northern Marianas where the field data were collected. (Left): Sonar backscatter image of the three volcanoes (from Hussong and Fryer, 1983); (Right): SeaMARC II derived bathymetric map, showing the locations of the Alvin dive sites (solid lines, with Alvin dive numbers) and camera sled ground-tracks (dashed lines). The PI participated in dive #1885 to collect bottom roughness data to be studied here.

**MODELLING OF UNDERWATER ERUPTIONS:** The factors known or suspected to be of importance in triggering and driving subaerial eruptions are also believed to play the same role for submarine eruptions. These factors include: the opening of fissure systems extending vertically for tens of kilometers through the crust as a result of large scale tectonic adjustments (16); the over-pressurizing of magma reservoirs at various depths in the lithosphere as a result of magma crystallization, gas exsolution, or injection of new magma at the base of the reservoir (17); and the vertical or lateral propagation of dikes from magma sources at depth as a result of the buoyancy of the magma or the excess pressures in the reservoirs (18, 19). Reviews of many of these processes are given by Shaw (20) and Spera (21).

There are, however, very important differences between the effects of the absolute pressure on the exsolution of volatiles from magmas erupting in subaerial and submarine environments (22), which we are modelling since they may also be critical in the case of Venus (10). The ambient pressures at water depths of 1 to 3 km (the range over which many of our observed submarine eruptions occurred) are the same as those at depths of about 0.3 to 1 km in the subaerial lithosphere, and it is over just this range of pressures that the bulk densities of most magmas decrease and their ascent velocities increase significantly as a result of the nucleation, growth and decompression of bubbles containing the volatiles which exsolve as the pressure decreases (11, 23, 24). The fact that magmas erupting on the sea floor emerge at these higher pressure levels ensures that they must do so at systematically lower velocities (25, 26) and with lower gas vesicle contents (both in terms of the sizes and volume fractions of vesicles) than magmas of similar bulk composition and volatile content emerging on land. Although underwater eruptions have rarely been seen taking place except as an extension of activity on land (27), the vesicularities of samples taken from sea-floor lava flow deposits strongly support this latter conclusion (28-30).

Another contrast between submarine and subaerial conditions which we are considering concerns the cooling of erupted materials - both pyroclastics and coherent lava flows. The thermal capacity of water (and the atmosphere of Venus) is much greater than that of air and convective cooling rates should be much greater for bodies surrounded by water. However, any body immersed in water and having a temperature greater than the boiling point of the water under the ambient pressure conditions will be surrounded by a film of steam (31). The insulating effect of this film can, in some circumstances, be the dominant factor controlling the cooling rate (32), though this effect must cease to operate at water depths greater than about 2 km since the distinction between steam and liquid water vanishes at pressures greater than 21.8 MPa, the critical pressure.

Steam film thicknesses and lava cooling rates as a function of depth below the sea surface are therefore expected by us to be important, and we intend to explore the consequences of this phenomenon for the likely lengths and surface textures of submarine flows. Such results will also most likely enable us to better interpret the morphology and mode of emplacement of venusian lava flows. A lava flow erupted in air loses heat by radiation from all of its surfaces, by conduction into the substrate on which it moves, and by natural or forced convection (whichever is more efficient) from its top, front and sides. The same general pattern must hold for submarine flows (with water replacing air as the convective medium) and for flows on Venus (with the thick carbon dioxide atmosphere being a more effective heat sink than the Earth's atmosphere). However, at water pressure less than the critical point pressure of 21.8 MPa (i.e., at water depths shallower than about 2.2 km), a thin film of steam will form over the lava surface as long as the surface temperature is greater than the boiling temperature of water at the ambient pressure. If the steam film is thin enough, convection within it will probably be inhibited, and heat (other than the radiated component) will be transmitted across it by conduction alone. Since conduction is an inefficient process, we are attempting to model numerically the efficiency of the subsequent convective loss into the water.

**OBJECTIVES AND GOALS FOR THE NEXT YEAR:** It should be emphasized that our studies of the Mariana data set are at an early stage. However, we intend to pursue three aspects of our submarine data sets as potential Venus analogs: 1) Study the observational evidence for the presence of different styles of volcanic eruptions (particularly possible explosive eruptions) at water depths as great as 3.5 km; 2) Investigate numerically the relevant controls on submarine volcanic activity in order to determine for Venus what additional constraints can be placed on the mass eruption rate and volatile content of the magmas involved in the activity. 3) Perform a terrain analysis of bottom photographs and altimetry obtained by during the July 1987 *Alvin* cruise of terrains also imaged by the SeaMARC II sonar. Such techniques have already been applied by us in a comparison between Space Shuttle Imaging Radar-B (SIR-B) and field measurements for the Kilauea Volcano area of Hawaii (33, 34), and enable the local data on the size and number of surface boulders and fine particles to be extrapolated to a more regional scale.



**REFERENCES:** 1) Lonsdale, P. (1977) Geology, 5, 147 - 152. 2) Ballard, R.D., Holcomb, R.T. and van Andel, T. H. (1979) J. Geophys. Res., 84, 5407-5422. 3) Fornari, D.J., Peterson, D.W., Lockwood, J.P., Malahoff, A. and Heezen, B.C. (1979) Geol. Soc. Amer. Bull., 90, 435-443. 4) Lonsdale, P. and Batiza, R. (1980) Geol. Soc. Amer. Bull., 91, p. 545 - 554. 5) Fornari, D.J., Ryan, W.B.F., and Fox, P.J. (1985). Geology, 13, 413-416. 6) Batiza, R. D.J. Fornari, D.A. Vanko and P. Lonsdale (1984). J. Geophys. Res., 89, 8371-8390. 7) Breen, N.A., Silver, E.A., and Hussong, D.M. (1986). Geol. Soc. Amer. Bull., 97, 1250-1261. 8) Fornari, D.J. (1986) Bull. Volcanol., 48, 291-298. 9) Mougini-Mark, P.J., Fryer, P., Hussong, D., and Zisk, S.H. (1984) (Abs). Lunar Planet. Sci. XV, 577-578. 10) Head, J.W. and Wilson L. (1986) J. Geophys. Res., 91, 9407-9446. 11) Wilson, L. and Head, J.W. (1981) J. Geophys. Res., 86, 2971-3001. 12) Searle, R.C. (1983). Marine Geology, 53, 77 - 102. 13) Hussong, D.M. and Fryer P. (1983) EOS, 64, 627-632. 14) Fryer, P., Gill, J., Jackson, M., Fiske, R., Hochstaedter, McMurtry, G., Sedwick, P., Malahoff, A., Mougini-Mark, P. and Horikoshi, E. (1987). Eos, 68, p. 1531. 15) Fryer, P., Ambos, E.L., and Hussong, D.M. (1985) Geology, 13, 774-777. 16) Fedotov, S.A. (1978) Intl. Gl. Rev., 20, 33-48. 17) Blake, S. (1981) Nature, 289, 783-785. 18) Johnson A.M. and Pollard, D.D. (1973) Tectonophysics, 18, 261-309. 19) Johnson, D.J. (1987). In: Volcanism in Hawaii. U.S. Geological Survey Prof. Paper 1350, p. 1297-1306. 20) Shaw, H.R. (1980). In: Physics of Magmatic Processes (ed. R. Hargraves), Princeton Univ. Press. 21) Spera, F.J. (1980). In: Physics of Magmatic Processes (ed. R. Hargraves), Princeton Univ. Press. 22) McGetchin, T.R. and Ullrich, W.G. (1973) J. Geophys. Res., 78, 1833-1853. 23) Wilson, L., Sparks, R.S.J. and Walker, G.P.L. (1980) Geophys. J. Ry. astron. Soc., 63, 117-148. 24) McBirney, A.R. (1963) Bull. Volcanol., 26, 455-469. 25) Wilson, L. (1980) J. Volcanol. Geotherm. Res., 8, 297-313. 26) Wilson, L. and Head, J.W. (1983) Nature, 302, 663-669. 27) Moore, J.G., Phillips, R.L., Grigg, R.W. and Swanson, D.A. (1973) Geol. Soc. Amer. Bull., 84, 537-546. 28) Moore, J.G. (1965) Am. J. Sci., 263, 40-52. 29) Moore, J.G. (1970). Contrib. Mineral. Petrol., 28, 272-279. 30) Moore, J.G. (1979) Nature, 282, 250-253. 31) Reid, C. and Dewey, H. (1908). Q. J. geol. Soc. London., 64, 264-272. 32) Mills, A.A. (1984). J. geol. Soc. Lond, 141, 183-186. 33) Kaupp, V.H., Gaddis, L.R., Mougini-Mark, P.J., Derryberry, B.A., MacDonald, H.C. and Waite, W.P. (1986) Rem. Sen. Environ., 20, 283-290. 34) Gaddis, L.R., Mougini-Mark, P.J., Singer, R., and Kaupp, V. (1987). Geologic analyses of Shuttle Imaging Radar (SIR-B) data of Kilauea Volcano, Hawaii. Submitted to Geol. Soc. Amer. Bull.

**Classification and Distribution of Possible Volcanic Structures in the Equatorial Region of Venus.** D. A. Senske and J. W. Head, Department of Geological Sciences, Brown University, Providence, RI 02912.

Radar images at a resolution of 1 to 3 km obtained by Veneras 15 and 16 have revealed numerous tectonic and volcanic structures in the northern latitudes (1) and suggest that a variety of styles of volcanism exist. In addition to the Venera radar imaging, the Pioneer Venus spacecraft has imaged the equatorial region of the planet between 15° S to 45° N at a resolution of 10 km. Incidence angles for the Pioneer Venus radar system varies from 30° to 58° (2). At this range of incidence angles, images show variations in surface roughness. In contrast, the radar systems on Veneras 15 and 16 have incidence angles of 10°, and are primarily sensitive to variations in topographic slope. We have carried out a regional study of features in the equatorial region of Venus, using both sets of radar image data, Arecibo radar images, Pioneer Venus altimetric data, and gravity data--expressed as line-of-sight (LOS) accelerations of the Pioneer Venus spacecraft. These features have been divided into 4 classes based on morphologic character, surface distribution, and radar properties. The dominant characteristics of each class are shown schematically in Figures 1 and 2.

The four classes of constructional features include the following: 1) Upland rises, broad, radar-dark, topographic highs with individual peaks. These peaks are typically radar-bright, suggesting that they are rough at the wavelength of the Pioneer Venus radar system (17 cm). The detailed radar signatures of the peaks varies from a complex integrated texture, containing material that is both intermediate and radar-bright, to one characterized by topographically high central regions of radar-dark material surrounded by flanking bright material (3,4). 2) Rifted highlands, radar-bright highland regions, which lie along an equatorial belt, and are characterized by radar-bright individual peaks and a central rift valley, showing varying degrees of complexity. 3) Dark halo plains, broad, radar-dark sub-circular regions possessing very little topographic relief and are observed exclusively in plains (3,4). The radar-dark material often appears to embay surrounding radar-bright features. A central radar-bright ring, which itself has a radar-dark center, is frequently found at the center of the dark material. 4) Cone/dome fields, observed exclusively in the Venera data are found in association with a variety of tectonic structures.

The first class of features, Upland rises (Figure 1A), are concentrated in a zone south of Maxwell Montes and north of Tinatin Planitia, extending from 5° N to 40° N in latitude and 25° W to 60° E in longitude. Specific features in this category include Western Eüsila Regio with its associated peaks, Gula Mons and Sif Mons, Bell Regio with its 4.5 km high peak Tepev Mons, and Sappho Patera. The width of the broad topographic high corresponding to each feature is 2400 km, 1000 km, and 1500 km respectively. All three features possess positive gravity anomalies and thus have a positive correlation with regional topography (5). Respective maximum anomalies are +35 mgal for Western Eüsila Regio, +33 mgal for Bell Regio, and +26 mgal for Sappho Patera.

Rifted highlands (Figure 1B) include Beta Regio, Atla Regio, and Aphrodite Terra. High-resolution Arecibo images of Beta Regio show two peaks, Theia Mons and Rhea Mons, which are also observed in Pioneer Venus altimetry data and flank the rift valley Devana Chasma (6). Both Theia Mons and Rhea Mons are characterized by having a radar-dark summit with radar-bright flanks and are similar to several of the features observed in the first class of structures.

Large positive gravity anomalies (+73 and +64 mgal respectively) are associated with Beta Regio and Atla Regio. Although Aphrodite Terra exhibits radar properties similar to both Beta Regio and Atla Regio, its gravity signature is substantially less with highs centered over Ovda Regio and Thetis Regio (+28 and +25 mgal respectively).

Dark halo plains (Figure 1C) are characterized by radar-dark material which extends over distances of 100's of km, and appears to embay surrounding radar-bright material. Specific occurrences are located west of Eüsila Regio, at 22° N, 330°, and west of Atla Regio, at 23° N, 140°. Both features possess a central radar-bright ring structure whose interior is radar-dark (3,4).

Venera 15/16 imaging of the northern 1/3 of the planet revealed a variety of tectonic and volcanic features. Among these are cone/dome fields (Figure 2), in which individual domes have diameters on the order of 10's of km. These domes are associated with tectonic features such as coronae (7) and are also scattered throughout the rolling plains province (8). These structures are below the resolution of the Pioneer Venus data and are therefore not observed in this data set.

The four classes are interpreted to be volcanic for the following reasons: 1) Areas of high topography correlate with flow like features whose radar properties and shape suggest that they are lava flows. 2) Embayment relations expressed by dark-halo plains units suggest flooding by low viscosity material. 3) Large positive gravity anomalies

associated with highland structures and their associated peaks have been interpreted to be related to thermal anomalies (9). They suggest a variety of styles of volcanism, which may be related to the formation and evolution of the equatorial highlands region. The structure and radar character of the peaks associated with Western Eüsila Regio are similar to peaks in Bell Regio. Tepev Mons which has been interpreted to be a shield volcano (10,11) possesses a radar-bright signature similar to that of Sif Mons. Many of the flow features associated with Tepev Mons exhibit a radar-bright signature at the 17 cm Pioneer Venus wavelength, suggesting a dominance of blocky lava flows such as aa. On the basis of the overall similarity in radar properties between Western Eüsila Regio and Bell Regio, and the specific similarity between Tepev Mons and Sif Mons, we suggest that Western Eüsila Regio and Bell Regio may have formed in a similar manner.

Although the radar-bright highland regions all have similar radar properties, they exhibit variable morphologies and gravity signatures. Both Beta Regio and Atla Regio are characterized by a domal rise and large gravity anomalies. The rift system of Beta Regio, however, appears to have developed as a central rift structure while Atla Regio is located at the intersection of three different rifts. Analysis of Arecibo radar images reveals that large-scale volcanism is associated with Beta Regio and its rift valley (6, 12). Due to the lack of high resolution images of Atla Regio, it is difficult to infer the degree of volcanic activity of this region. Pioneer Venus altimetric data reveal two peaks associated with Atla Regio, Maat Mons and Ozza Mons. Like the peaks at Beta Regio, these features are in close proximity to the rift structures, suggesting that large scale volcanism may, also be significant in this area. Rifts in Aphrodite Terra exhibit varying degrees of complexity. The rift system in eastern Aphrodite is well developed, with a characteristic central rift valley, while rifts in western Aphrodite are less developed. Western Aphrodite is also a plateau rather than a domal structure, and exhibits a gravity anomaly on the order of 40 mgal less than those at Beta Regio or Atla Regio, suggesting a possible difference in subsurface structure. Crumpler and Head (13) have identified a number of topographic discontinuities across the strike of Aphrodite, and have suggested that these cross-strike discontinuities may be analogous to terrestrial oceanic fracture zones. Similar features have not been observed in association with Beta Regio or Atla Regio. This diversity of tectonic and volcanic features may represent different stages in the evolution of the highlands; corresponding in a progression from the Atla style of rifting and volcanism to late stage structures at Aphrodite Terra.

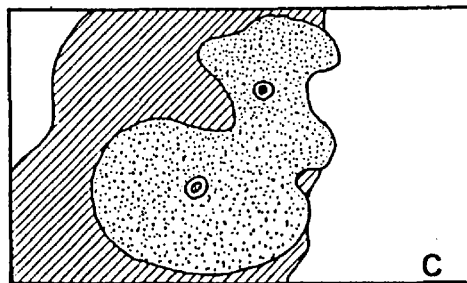
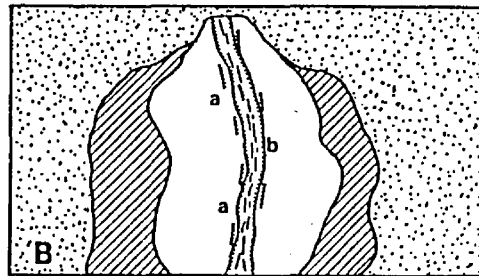
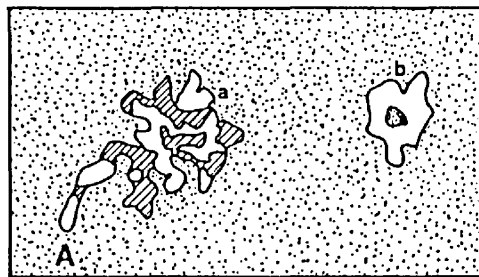
The radar-dark plains unit may have been emplaced by a style of volcanism different from that inferred in the highlands. The embayment relations exhibited by the radar-dark material suggests lava flooding and the radar-dark character of the unit suggests that it is relatively smooth. Head and Wilson (14) show that pyroclastic deposits should not be dominant on Venus, supporting the interpretation of lava flooding. The radar-bright central structure may be a source region for the dark material, but evidence to support such an interpretation is not conclusive. However, the bright structure associated with the unit west of Atla Regio exhibits positive topographic relief, suggesting that it may be a small rise or construct.

The small domes do not appear to be associated with any single class of tectonic feature. They are often found in plains units, and are often associated with regions of ridge belts and coronae. This diverse distribution suggests a correlation with volcanism on a regional scale related to regional tectonic activity but not necessarily with formation of highland structures.

Volcanism in the equatorial region of Venus covers an extensive area and occurs on a large scale. It has been estimated that units of volcanic origin cover approximately 75% of the surface at northern latitudes (15) imaged by Veneras 15 and 16 (1). We suggest that a similar percentage of volcanic units covers the equatorial region. On the basis of morphologic character and radar properties, two different styles of volcanism are inferred to be represented in the equatorial region. Large constructs which possess a variety of radar properties are interpreted to represent episodes of shield type volcanism while radar-dark features in the plains are believed to be associated with lava flooding.

#### References:

- 1) Barsukov V. L., *et al.*, *J. Geophys. Res.*, 91, D378-D398, 1986.
- 2) Pettengill G. H., *et al.*, *J. Geophys. Res.*, 85, 8261-8270, 1980.
- 3) Stofan E. R., *et al.*, *Lunar and Planet. Sci.* XV, 824-825, 1985.
- 4) Stofan, E. R., M. S. Thesis, 1-64, 1985.
- 5) Sjogren W. L., *et al.*, *J. Geophys. Res.*, 88, 1119-1128, 1983.
- 6) Campbell D. B. *et al.*, *Science*, 226, 167-170, 1984.
- 7) Stofan, E. R., and J. W. Head, *Lunar and Planet. Sci.* XVII, 1033-1034, 1986.
- 8) Masursky H., *et al.*, *J. Geophys. Res.*, 85, 8232-8260, 1980.
- 9) Campbell B. A. and R. C. Kozak, manuscript in preparation, 1987.
- 10) Janle, P. *et al.*, submitted to *Earth, Moon, and Planets*, 1987.
- 11) Basilevsky, A. T., and P. Janle, *Astron. Vestnik.*, 21, 109-121, 1987.
- 12) Stofan E. R. *et al.*, submitted to *Geology*, 1987.
- 13) Crumpler L. S. and J. W. Head, submitted to *J. Geophys. Res.*, 1987.
- 14) Head J. W. and L. Wilson, *J. Geophys. Res.*, 91, 9407-9446, 1986.
- 15) Bindschadler D., M. S. Thesis, 1-94, 1986.



500 km

Figure 1. Idealized sketch maps of features interpreted to be associated with volcanic activity. A) Upland rises with individual peaks (a and b). B) Rifted highlands with radar-bright peaks (a) and rift valleys (b). C) Dark halo plains with central bright ring structure.



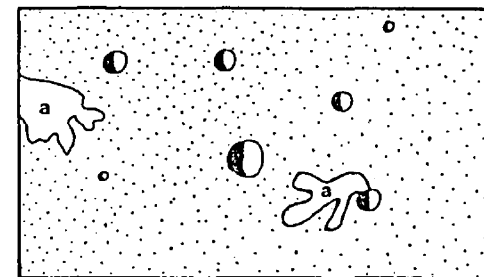
Radar-dark material-- This unit usually forms a transitional boundary with material of intermediate brightness. Sharp boundaries with radar-bright material also occur.



Intermediate radar-bright material-- This unit contains both radar-dark material along with a component of diffuse radar-bright material.



Radar-bright material-- This unit forms either a sharp contact with radar-dark material or is transitional with material of intermediate brightness.



50 km

Figure 2. Generalized sketch map of a cone/dome field. The map is based on Venera 15/16 radar images. Flow units (a) show a variety of textures ranging from radar-bright to radar-dark. The dark region on each dome is the radar shadow.

## RHEOLOGIC PROPERTIES OF INDUSTRIAL SULFUR FLOWS

David A. Crown, Department of Geology, Arizona State University, Tempe, Arizona 85287

Several investigators have considered the possibility of sulfur flows on Io based upon flow morphologies and color progressions in channelized flows [1-5]. However, the spatial and spectral resolution of Voyager data is insufficient for unique compositional determinations of ionian surface features, and the precise role of sulfur in ionian volcanism remains controversial. Interpretations of existing data are hindered by an inadequate knowledge of the thermal properties and rheologic behavior of sulfur flows, due to the rarity of such flows on the Earth. Industrial sulfur flows, which are being studied as analogs to possible ionian flows [6-8], occur at a scale comparable to that of the few naturally occurring terrestrial sulfur flows [9-14]. The well-constrained conditions under which industrial sulfur flows are produced allow a quantitative analysis of their rheologic properties to be made.

Liquid sulfur (99.6% pure) is poured into flat-floored, ~100 m<sup>2</sup> vats at 130° C for 30-35 minutes. The vat floors and walls are composed of solidified sulfur ( $\rho = 2.06 \text{ g/cm}^3$ ) from previous pours. The flow rate from the source is ~15 metric tons/min (~7.5 m<sup>3</sup>/min), and each pour totals ~500 metric tons (~250 m<sup>3</sup>). For comparison, the estimated effusion rate of the Siretoko-Iosan flow [13], one of the largest natural sulfur flows, was approximately twice that of the industrial sulfur flows. Each pour has a total thickness of ~6-10 cm and is composed of a series of extremely complex, thin (1-4 cm) flow units. Channelized flows exhibiting marginal levees of cooled sulfur are observed. Channels are typically 10-40 cm wide and 3-4 cm deep with 5-20 cm wide levees. Measured channel flow velocities range from 0.10 - 1.05 m/sec with a mean value of 0.46 m/sec.

Hulme's [15-16] technique for obtaining rheologic information from lava flows can be used to examine the rheology of industrial sulfur flows. Hulme derived a relationship between two dimensionless parameters which allows an analysis of the laminar flow of an isothermal Bingham liquid based upon its geometry and flow behavior:

$$\Gamma = 2/15 (W)^{5/2} - 1/4 (W)^2 + 1/6 (W) - 1/20$$

where  $\Gamma = F \eta (g \rho)^3 (\sin \alpha)^4 (1/S_y)$  and  $W = w/2w_b$

and where  $F$  = (channel) flow rate (cm<sup>3</sup>/sec),  $\eta$  = viscosity (poise = g/cm sec),  $g$  = gravitational acceleration (980 cm/sec<sup>2</sup>),  $\rho$  = density (g/cm<sup>3</sup>),  $\alpha$  = slope in degrees,  $S_y$  = yield strength (g/cm sec<sup>2</sup>),  $w$  = flow width (cm), and  $w_b$  = levee width (cm) (see Figure 1).

The range of channel dimensions observed yields values of the width variable,  $W$ , between 1.5 and 3.5 from which the right-hand side of Hulme's equation can be evaluated. Table 1 lists channel widths, flow velocities, and flow depths of industrial sulfur flows and calculated values of the flow rate in various channels. The values listed in the first three columns are not actual measurements but cover the range of measurements taken. The 10 cm flow depth reflects a typical pour thickness. The three flow rates in each section correspond to the three given flow depths and are calculated at velocity values reflecting the minimum, mean, and maximum values measured. The five channel widths cover the range generally observed. The yield strength can be calculated based upon measurement of the levee width,

$S_y = 2 w_b \rho g (\sin \alpha)^2$  [15-16]. The levee width values used (1-25 cm) cover the range of measured levee widths. The density of liquid sulfur is assumed to be 1.8 g/cm<sup>3</sup> [17]. The slope used in the calculations is 0.5°. This is considered to be a reasonable value for the local slope on a sulfur vat and represents a change in relief of 1 cm in 1 m. The overall slope of the vat is thought to be much less (~0.06°), as a change in relief of ~10 cm (one pour thickness) is the maximum typically seen over the extent of a vat (~100 m).

The viscosity of the industrial sulfur flows can be calculated using Hulme's equation. Flow rates of 100, 1000, 10000, and 100000 cm<sup>3</sup>/sec and yield strengths of 0.27, 1.34, 2.69, 4.30, 5.38, and 6.72 g/cm sec<sup>2</sup> are used in all possible combinations with values of the width variable, W, equal to 1.5, 2.0, 2.5, 3.0, and 3.5. Extremely low viscosity values are obtained (see Figure 2). Only with high values of W (3.0, 3.5), high yield strengths (~5-7, which represent large levees), and low flow rates (100 cm<sup>3</sup>/sec) are viscosity values similar to published values obtained. Using viscosity values from [14] (0.110 poise @ 121.1° C, 0.149 poise @ 104.4° C, and 0.193 poise @ 93.3° C), Hulme's equation can be used to calculate the flow rate. The calculated flow rates are much lower than those observed. Flow rates comparable to the lowest measured are predicted only for high values of W and high yield strengths. Interestingly, the changes in viscosity occurring during cooling (as predicted from the published values) do not have as prominent an effect on the magnitude of the calculated flow rate as do changes in W or the yield strength. Using published values of the viscosity of sulfur and the "measured" values of the flow rate, Hulme's equation generally predicts higher yield strengths than are calculated from the measured levee widths. Only with high values of W and low flow rates are values consistent with observations obtained.

It is clear from this analysis that the problem is not well enough constrained to use Hulme's method to precisely determine the viscosity or yield strength of the industrial sulfur flows. The measured flow rates are observationally well documented. If the published values of the viscosity of sulfur are assumed to be correct for the industrial sulfur flows, the values of the yield strength must be greater than those calculated in the manner Hulme does from the levee width. With the yield strength values calculated from the levee widths, significantly lower values of the viscosity are predicted. Alternatively, the Bingham model suggested by Hulme may only be applicable to a small number of the sulfur flows observed. A categorization of sulfur flows within the presently existing sample is not possible. The data suggest that the Bingham model applies only in the latter stages of a flow as the viscosity and yield strength increase in magnitude and the flow rate is low. This is consistent with observations of the flows, which appear to be laminar and quite viscous as they solidify, but can be turbulent in early stages, and in agreement with calculations of the Reynolds number,  $Re = \rho h v / \eta$  (where h=flow depth (cm) and v=flow velocity (cm/sec)), which indicate both laminar and turbulent behavior from measured flow depths and velocities and viscosities from [14].

## References

- [1] Sagan, C., 1979, *Nature* 280, 750-753. [2] Pieri, D.C., et al., 1984, *Icarus* 60, 685-700. [3] Greeley, R., and Fink, J., 1981, *NASA TM-84211*, 38-40. [4] Greeley, R., and Fink, J.H., 1984, *Astronomy Express* 1, 25-31. [5] Fink, J.H., et al., 1983, *Icarus* 56, 38-50. [6] Greeley, R., and Lee, S.W., 1986, *Lunar Planet. Sci. Conf.*, XVII, 285-286. [7]

Lee, S.W., et al., 1987, *NASA TM-89810*, 514-516. [8] Lee, S.W., et al., 1987, *Lunar Planet. Sci. Conf.*, XVIII, 545-546. [9] Colony, W.E., and Nordlie, B.E., 1973, *Econ. Geol.* 68, 371-380. [10] Greeley, R., et al., 1984, *Icarus* 60, 189-199. [11] Naranjo, J.A., 1985, *Nature* 313, 778-780. [12] Skinner, B.J., 1970, *Pacific Sci.* 24, 144-145. [13] Watanabe, T., 1940, *Jap. J. Geol. Geogr.* 17, 289-310. [14] Theilig, E., 1982, *NASA CR-3594*, 34 pp. [15] Hulme, G., 1974, *Geophys. J. Roy. Astron. Soc.* 39, 361-383. [16] Hulme, G., 1976, *Icarus* 27, 207-213. [17] Nash, D.B., et al., 1986, in *Satellites* (J.A. Burns and M.S. Mathews, eds.), University of Arizona Press, 629-688.

Table 1. Calculation of the Flow Rate in Channelized Industrial Sulfur Flows

Width (cm)	Velocity 1 (cm/sec)	Depth a (cm)	Depth b (cm)	Depth c (cm)	Rate 1a (cm <sup>3</sup> /sec)	Rate 1b (cm <sup>3</sup> /sec)	Rate 1c (cm <sup>3</sup> /sec)
5	10	1	5	10	50	250	500
10	10	1	5	10	100	500	1000
25	10	1	5	10	250	1250	2500
50	10	1	5	10	500	2500	5000
100	10	1	5	10	1000	5000	10000

Width	Velocity 2	Depth a	Depth b	Depth c	Rate 2a	Rate 2b	Rate 2c
5	50	1	5	10	250	1250	2500
10	50	1	5	10	500	2500	5000
25	50	1	5	10	1250	6250	12500
50	50	1	5	10	2500	12500	25000
100	50	1	5	10	5000	25000	50000

Width	Velocity 3	Depth a	Depth b	Depth c	Rate 3a	Rate 3b	Rate 3c
5	100	1	5	10	500	2500	5000
10	100	1	5	10	1000	5000	10000
25	100	1	5	10	2500	12500	25000
50	100	1	5	10	5000	25000	50000
100	100	1	5	10	10000	50000	100000

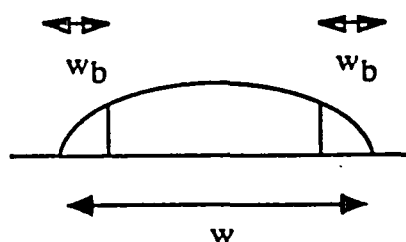
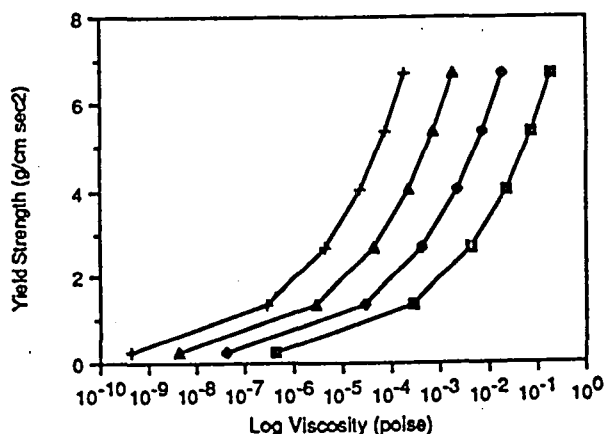


Figure 1. Cross-section of a channelized flow indicating flow width (w) and levee widths ( $w_b$ ).

Figure 2. Plot showing the relationship between the yield strength and viscosity calculated from Hulme's equation for four different flow rates (squares = 100 cm<sup>3</sup>/sec, diamonds = 1000 cm<sup>3</sup>/sec, triangles = 10000 cm<sup>3</sup>/sec, and pluses = 100000 cm<sup>3</sup>/sec). Data are for W = 3.0.



## RELATIONSHIPS BETWEEN MORPHOLOGY AND RHEOLOGY OF LAVA FLOWS

Jonathan Fink, Geology Dept., Arizona State University, Tempe, AZ 85287

Jim Zimbelman, Lunar and Planetary Institute, Houston, Texas 77058

The purpose of this project is to develop methods for remotely estimating the rheology and composition of lava flows based on their morphology. Field, photogeologic, and theoretical studies of flow morphology for terrestrial lavas of three different compositions were carried out during the past year. Emphasis was placed on longitudinal variations in calculated yield strengths and viscosities, with the aim of discovering relationships that allow remote identification of flow composition.

Our previous study at Kilauea (Fink and Zimbelman, 1986) showed that the heights of flow margins provide more consistent estimates of yield strength and viscosity than levee or central channel dimensions. We also found that viscosity could not be reliably calculated without information about flow velocities, making it a more problematic rheologic parameter than yield strength to use in extra-terrestrial studies. We have thus focussed our attention on variations in yield strength calculated along the lengths of flows of different compositions.

Our earlier data for yield strength of the Phase 5 Royal Gardens flow showed a clear linear increase with distance from the vent (Figure 1a). This year we analyzed a second flow (Phase 2) by the same detailed method, constructing 12 cross sections of the most distal 1.8 km. Again the profiles showed sharp distal increases in both yield strength and viscosity, with the variation rates being very similar to those found in the Phase 5 flow (Figure 1b). Because flow margin heights provide the most reliable indicators of yield strength variations, and surveying methods are not practical for martian flows, a third set of calculations was made relying solely on measurements of margin heights collected by the USGS as part of their monitoring program of the East Rift basalt flows (Wolfe et al., 1987). These data extend from near the vent to the toes of many of the flows. Calculated yield strengths from the entire length of the Phase 5 flow based on this USGS data set were compared with the earlier distal values computed from detailed cross sections. Distal strength values were similar to those obtained from cross sections, whereas proximal values indicated a much more gradual downstream increase in strength (Figure 1c).

A fourth set of calculations involved a flow (Phase 30) for which cross sections had not been made previously. Again we found a gentle downstream increase in strength that became more pronounced in the most distal 2 km. (Figure 1d). The rates of increase for the distal and proximal regions were similar to those obtained for the Phase 2 and 5 flows. These bi-modal patterns of strength increase may be explained by gradual cooling in the advancing flow while effusion rates at the vent remain constant, followed by more rapid cooling near the flow front as the eruption rate at the vent wanes. These patterns suggest that systematic variations in rheology might constitute a useful tool for interpreting remotely observed lava flows. Quantification of this approach requires collection of data from many more flows, along with measurements of comparable resolution for flows of different composition.



We are currently analyzing three additional data sets to help quantify longitudinal variations in yield strength. The USGS has provided us with flow margin heights along the lengths of 36 different phases of Kilauea's currently active East Rift lava flows. We have also contracted with the USGS to make a detailed (2-m-contour interval) topographic map of the "Worm Complex" silicic andesite flows on the south side of Mount St. Helens. The "Worm" flows all have identical chemical composition, but were emplaced on different slopes and show a wide range of morphologic features. At the silicic end of the spectrum, digital manipulation of a unique set of 18 high resolution topographic maps of the Mount St. Helens dacite dome allowed volumes, extrusion rates, relative amounts of endogenous and exogenous growth, flow thicknesses, and yield strengths to be calculated to greater accuracy than has been possible before.

The techniques being developed and the correlations between observed and predicted morphologic indicators of flow rheology and composition are being applied to lava flows on Olympus Mons (Zimbelman, 1985) and Ascræus Mons volcanoes. We next plan to analyze several flows along the southern scarp of Olympus Mons for which terminations, leveed channels, and flow margins can be observed, and where 200 meter contour interval topographic data are available. Photo-clinometric techniques should allow marginal heights to be estimated to within 10 m. Comparison of observed longitudinal yield strength trends with those for various terrestrial flows should allow composition to be estimated.

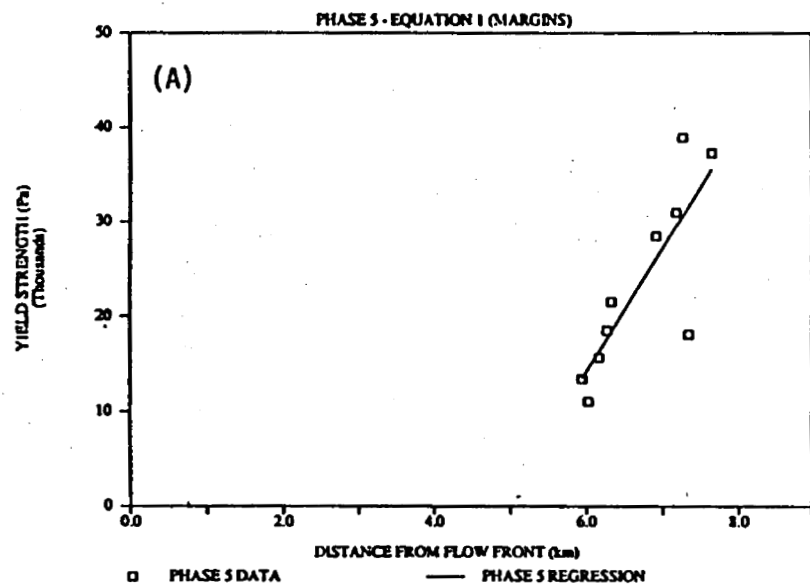
#### REFERENCES

- Fink, J.H. and Zimbelman, J.R., 1986, Rheology of the 1983 Royal Gardens basalt flows, Kilauea Volcano, Hawaii. Bulletin of Volcanology, 48, 87-96.
- Zimbelman, J.R., 1985, Estimates of rheologic properties for flows on the martian volcano Ascræus Mons. Proc. Lunar Planet. Sci. Conf., 16th, D157-D162.

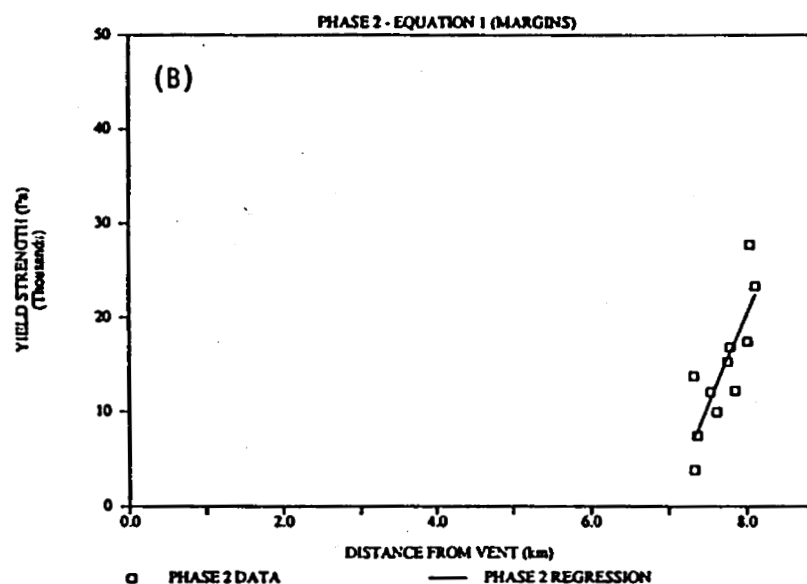
#### FIGURE CAPTIONS

1. Plots of yield strength versus distance for three Royal Gardens basalt flows. All strengths calculated as product of density, gravity, flow margin thickness and sine of underlying slope angle.
  - a) Distal portion of Phase 5 flow. Flow thickness derived from flow margin heights measured on carefully surveyed profiles; slope surveyed along base of flow margin. Note linear strength increase of 12.6 kPa/km.
  - b) Distal portion of Phase 2 flow. Strengths calculated by same method as in (a). Note similar strength increase of 13.5 kPa/km.
  - c) Calculated strength values for entire length of Phase 5 flow, using USGS flow margin height data obtained by hand-leveling, and slopes from 1:24000 topographic quadrangle maps. Note bi-modal pattern of strength increase: 1.1 kPa/km for proximal portion of flow; approximately 12.5 kPa/km for distal part. Latter rate is similar to that derived from carefully surveyed data in (a).
  - d) Calculated strengths for Phase 30 flow, using USGS margin heights and topographic map data. Bi-modal pattern again apparent. Break in slope of strength/distance plot possibly corresponds to point at which vent effusion rate began to decrease.

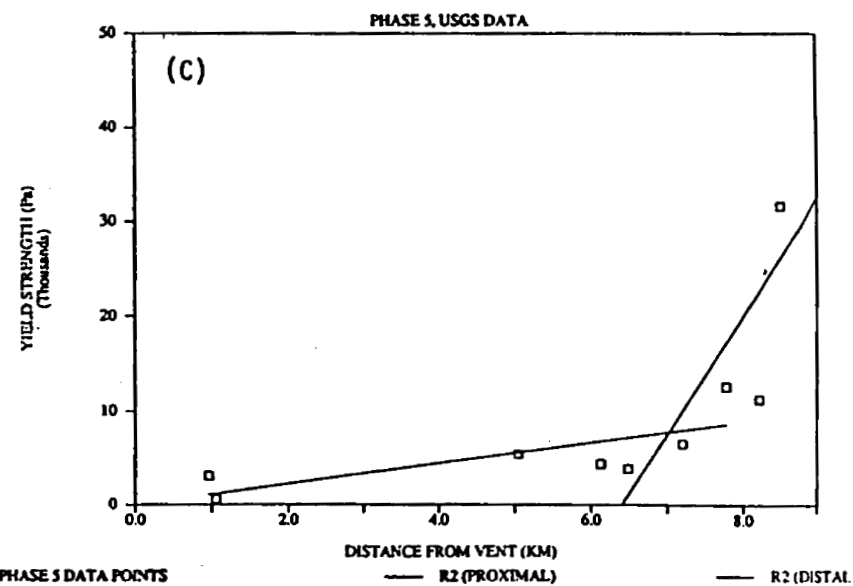
# YIELD STRENGTH VS DISTANCE



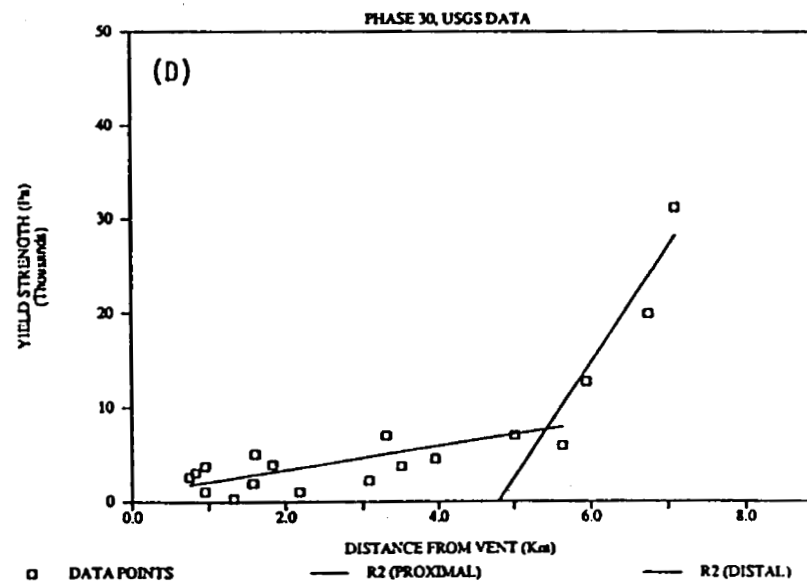
# YIELD STRENGTH VS DISTANCE



# YIELD STRENGTH VS DISTANCE



# YIELD STRENGTH VS. DISTANCE



## Morphology of the Bishop Tuff

Michael F. Sheridan, Department of Geology, Arizona State University, Tempe, AZ 85287

The morphology and spectral reflectance of the Bishop Tuff was examined to establish characteristics could serve as criteria for identification of ignimbrites on other planets. Digital terrain models (DTM) were used to model the first-order emplacement of the ignimbrite sheet as a gravity-driven density currents affected by topography using algorithms that evolved from Malin and Sheridan (1982; 1983). Numerical models were used to determine the cooling history and to model its vertical density profiles (Riehle, 1973; Horn and Sheridan, 1983). This data is useful in assessing the toughness of the sheets to erosion and the development of a qualitative geomorphic model.

The Bishop Tuff is a large Pleistocene ash-flow sheet that originally covered about 7000 km<sup>2</sup> in eastern California. The original margins of the sheet are preserved in many places so that the effect of topography on emplacement and deposition can be interpreted. The tuff has a strongly-welded central part but grades to a nonwelded top and base (Ragan and Sheridan, 1972). Except for a few deep canyons, erosion has barely begun to form a marginal escarpment. Only one canyon has cut entirely through the sheet and the tuff has a nearly continuous outcrop around the caldera rim. At most only the upper 20 m of non-welded ash has been removed by a combination of slope wash and aeolian processes. Aeolian erosion is locally a major sculptor of the surface. The high desert climate has preserved many surface features that are missing from other large ash-flow sheets such as fumarolic mounds, ridges, and joints which are locally prominent on the surface (Sheridan, 1970).

Although much smaller in volume than some of the supposed martian ignimbrites, the Bishop Tuff could serve as an archetype for many of their features. Facies of welding and crystallization exert the principal controls on the subsequent surface morphology due to erosion. A geologic map of the Bishop Tuff shows welding and crystallization facies for part of the sheet (Crowder and Sheridan, 1972). The surface distribution of 5 units have been mapped: 1) densely-welded devitrified zone, 2) partially-welded vitric zone, 3) nonwelded vitric zone, 4) zone of vapor-phase crystallization, and 5) zone of fumarolic mounds and ridges.

A digital terrain model used to simulate the emplacement distribution of the Bishop Tuff using an algorithm for a gravity-driven density current. A simple model that fit the known distribution well could be applied to supposed ignimbrites on mars with little modification.

The major morphologic features of the Bishop Tuff visible at moderate resolution have been identified and catalogued. Some of these features are also visible on the digital terrain model. The surficial expression of fault scarps, joint sets, and erosional features are directly related to welding facies and erosional processes. Especially interesting is the juxtaposition of nonwelded zones with those that are indurated due to welding and secondary crystallization. Density profiles from 65 measured sections show how the development of landforms relates to the density profiles (and hence toughness) of the Bishop Tuff. Calculated density profiles were compared with the measured data using a program for cooling and welding of ignimbrites (Horn and Sheridan, 1983).

Spectral reflectance data for the Bishop Tuff were obtained from controlled field measurements made in 1968. About 50 targets of Bishop Tuff were examined on sites that represent a variety of the mapped facies. The data was recorded at 25 nm bands from 350 nm to 1250 nm. This unpublished data has been compiled for analysis by correlation with facies of welding and crystallization. Preliminary results suggest that material with a vitric matrix can be distinguished from material with a devitrified matrix. The detection and mapping of facies characterized by hydrated glass is significant because it can be related to models of emplacement, cooling, welding, and crystallization which are confirmed by field mapping and morphology of the unit that displays various zones of welding and crystallization.

#### References:

- Crowder, D.F. and Sheridan, M.F., 1972, Geologic map of the White Mountain Peak Quadrangle, Mono County, California, U.S. Geological Survey Map GQ-1012.
- Malin, M.C., and Sheridan, M.F., 1982, Computer-assisted mapping of pyroclastic surges: *Science*, v. 217, p. 637-640.
- Ragan, D.M. and Sheridan, M.F., 1972, Compaction of the Bishop Tuff, California. *Geological Society of America Bulletin*, v. 83, p. 95-106.
- Riehle, J.R., 1973, Calculated compaction profiles in rhyolitic ash-flow tuffs: *Geological Society of America Bulletin*, v. 84, p. 2193-2216.
- Sheridan, M.F., 1970, Fumarolic mounds and ridges of the Bishop Tuff, California: *Geological Society of America Bulletin*, v. 81, p. 851-868.

## **LATERAL MIGRATION AND ERUPTION OF MAGMA IN VOLCANIC EDIFICE RIFT ZONES: THE PU'U 'O'O ERUPTIONS OF THE EAST RIFT ZONE OF KILAUEA VOLCANO, HAWAII**

J. W. Head, Dept. Geological Sciences, Brown Univ., Providence, RI 02912. and L. Wilson, Dept. Environmental Science, Univ. of Lancaster, U.K.

Using basic principles of magma ascent and eruption derived from previous planetary studies (1,2) we have been examining several aspects of the nature and deposits of recent eruptions of the Kilauea East Rift Zone. Below we summarize the areas of study and some preliminary results:

### **1. PYROCLASTIC FOUNTAIN HEIGHTS AND EXSOLVED MAGMA VOLATILE CONTENT:**

We have reviewed the factors determining lava fountain heights in Hawaiian-style basaltic eruptions such as those occurring during the recent series of eruptive episodes at the Pu'u 'O'o vent, east rift zone of Kilauea Volcano, Hawaii. Numerical solutions to the equations describing the fluid dynamics of such eruptions predict that lava fountain heights, which are indicators of the velocity of magmas in vents, should be controlled much more strongly by amounts of exsolved volatiles than by any other factors. The next most important factor is the width of the conduit system, which determines frictional losses and can be characterized by the volume flux of magma. The diameter of the surface vent required to accommodate a given discharge (i.e., instantaneous volume rate of eruption) is also a function of exsolved magma volatile content, but is less dependent on this factor than is the fountain height. We simulate fountain heights for typical discharges at Pu'u 'O'o and find implied exsolved gas contents very close to those determined by other methods. The corresponding predicted vent diameters are comparable with (and somewhat smaller than) the observed diameter of the Pu'u 'O'o vent. The discrepancy is probably a consequence of processes occurring in the lava pond which is present over the vent during eruptions. The variation of fountain height with time during eruptive episodes can be used as a measure of changing exsolved magma volatile content, which can be related to processes occurring in the subsurface dike system.

(3)

### **2. LATERAL MAGMA MOVEMENT IN DIKES IN RIFT ZONES:**

Flank eruptions, especially those on the rift zones of volcanoes, are fed by lateral magma movement in dikes. The sizes and shapes of such dikes must be consistent with the dynamics of magma movement through them and with the static stress field generated in the surrounding rocks. We use data from the recent series of eruptions at the Pu'u 'O'o vent on Kilauea's East Rift zone to calculate the geometry of the dike system permitting steady magma flow, finding a dike thickness of about 1.8 m and a dike height close to 3 km. The typical magma speed (a little less than  $0.1 \text{ m s}^{-1}$ ) is such that a given batch of magma moves only about one-fifth of the way through the rift system in a single eruptive episode, and thus undergoes several cooling events before being erupted. We use arguments related to the consequent modification of the rheological properties of the magma to discuss the factors controlling the onset and cessation of eruptive episodes. We also model the extent and

consequences of the probable non-uniformity of the dike geometry resulting from the interaction of a new dike with the partly-cooled residues of earlier dikes. (4)

### 3. NATURE OF CONDUIT SYSTEMS AT SHALLOW DEPTHS BENEATH BASALTIC VENTS:

We investigate quantitatively the sizes and shapes of conduit systems at shallow depths beneath basaltic vents. The fluid dynamics of eruptive episodes are used to determine the geometries of conduits, taking the well-documented eruptions at Pu'u 'O'o, Kilauea as illustrations. Cooling calculations are employed to study the long-term survival of conduits and the consequences of multiple dike injection events. We find that sub-vent conduits must have planar geometries at depths greater than a few tens to at most a few hundreds of meters, with thicknesses typically less than one meter, and lengths and heights of order one km. These structures are clearly the residues of the pre-eruption dikes. Although such features can be thickened somewhat by repeated dike emplacement events, there is no reason to suppose that much more equant magma reservoirs develop at shallow depth, even when considerable degassing occurs after single eruptions or between repeated eruptions. (5)

### 4. FACTORS DETERMINING THE NATURE OF FOUNTAIN DYNAMIC MORPHOLOGY AND NEAR-VENT PYROCLASTIC DEPOSITS:

Two variables (magma gas content and volume flux) determine the detailed structure (dynamic morphology) of the gas-pyroclast dispersions (commonly called fire fountains) produced by explosive basaltic eruptions and the nature of near-vent pyroclastic deposits. The two main manifestations of variations in gas content and volume flux are clast size and fountain structure. Although the detailed relationships between gas content and clast size are not fully understood from a physical point of view, suitable empirical data are available for basaltic magmas. Fountain structure (dynamic morphology) is determined by the velocity profile at any given pressure level and the maximum spread angle of the fountain from the vertical. These two parameters completely determine the paths of pyroclasts in the fountain and their ultimate resting places. The combination of the pyroclast size and the spatial distribution determines the clast number density and thus the opacity of the fountain and the ability of the pyroclasts to cool in their local fountain environment. For a given set of conditions, two factors thus become important in determining the structure and morphology of pyroclastic deposits: local temperature and accumulation rate. For example, in typical basaltic pyroclastic eruptions, the majority of pyroclasts remain inside the optically thick central part of the fountain, undergo minimal cooling, and return to the surface to coalesce and contribute to a lava pond or lava flow. In the optically thinner outer parts of the fountain, clasts undergo relatively more cooling and return to the surface to contribute to the building of the pyroclastic cone (if the accumulation rate is low) or to form rootless flows (if the accumulation rate is high and minimal further cooling occurs). The relationships between these various parameters are investigated for hawaiian-style eruptions in general and applied to the interpretation of post-eruption deposits (residual morphology). (6)

The results of these analyses are being applied to the study of the nature and evolution of shield volcanoes on Mars and Venus.

#### References:

- (1) Wilson, L. and Head, J.W. (1981) Ascent and eruption of basaltic magma on the Earth and Moon: *Journal of Geophysical Research*, 86, No. B4, 2971–3001.
- (2) Wilson, L. and Head, J.W. (1983) A comparison of volcanic eruption processes on Earth, Moon, Mars, Io and Venus: *Nature*, 302, No. 5910, 663–669.
- (3) Head, J.W. and Wilson, L. (1987) Lava fountain heights at Pu'u 'O'o, Kilauea, Hawaii: Indicators of amount and variations of exsolved magma volatiles: *Journal of Geophysical Research*, in press.
- (4) Wilson, L. and Head, J.W. (1987) Geometry of volcano rift dike systems and the dynamics of magma supply to flank eruptions: Pu'u 'O'o and the Kilauea East Rift zone: submitted to *Journal of Geophysical Research*.
- (5) Wilson, L. and Head, J.W. (1987) The nature of local magma storage zones and the geometry of conduit systems below basaltic eruption sites: the Pu'u 'O'o, Kilauea East Rift, Hawaii example: submitted to *Journal of Geophysical Research*.
- (6) Head, J.W. and Wilson, L. (1987) Basaltic explosive eruptions: Influence of gas-release patterns and volume fluxes on near-vent dynamic morphology, and the formation of subsequent pyroclastic deposits (cinder cones, spatter cones, rootless flows, lava ponds, and lava flows): submitted to *Journal of Volcanology and Geothermal Research*.

## EXPLOSIVE VOLCANISM IN THE MOHON MOUNTAIN VOLCANIC FIELD, ARIZONA AND POSSIBLE MARTIAN ANALOGS

Ardyth M. Simmons and John S. King, Department of Geology, State University of New York at Buffalo, 4240 Ridge Lea, Amherst, NY 14226

The Mohon Mountains form the center of a volcanic field which covers a 500 km<sup>2</sup> area of west-central Arizona. Eruptive activity spanned a period from 20 m.y. to 8 m.y. ago and followed an overall eastward trend of migration. The field consists of scattered domes, plugs, and flows that surround the central vent of Mohon Mountain, a deeply dissected composite volcano which records the earliest period of activity in the field. The Mohon volcano was highly explosive and produced at least 112 km<sup>3</sup> of pyroclastic breccias alternating with flows. Two distinct compositions of pyroclastic and flow material were produced during at least four eruptive episodes. The earliest activity produced vitric eruptives with a hornblende-rich trachyandesitic composition. These continued to erupt during later episodes in smaller volumes. The trachyandesites fractionated to produce a phenocryst-rich dacite containing andesine, hornblende, biotite, orthopyroxene, and clinopyroxene. The dacite comprises the major volume of the later eruptive materials.

The Mohon composite volcano is subcircular with a diameter of 17.4 km. Its western and southern boundaries grade imperceptibly into volcanic units from other provinces. Mohon Mountain rises to an elevation of 2273 m with 909 m of local relief above the surrounding basalt and volcanoclastic covered plains. Its southern flanks are breached by two explosively produced basins which together are believed to comprise erosional remnants of the vent area. The basins are bridged by low ridges which preserve resistant plugs that were part of the internal portion of the vent. Mohon Mountain is rimmed on the north, west, and south by younger parasitic cones and endogenous domes which produced smaller volumes of eruptives.

One purpose of this study was to search for landforms on Mars which might have been formed by processes similar to those which produced the morphological expression of Mohon Mountain. Martian imagery was used along with published descriptions of features to provide comparisons between Mohon Mountain and landforms found on Mars. Characteristics that were examined and compared to those on martian volcanoes include the overall shape of the Mohon vent complex with its breached southern flank and satellite vents, steepness of slope, projected uneroded height, circularity, and ratios comparing topographic parameters of height, depth, crater diameter, and flank width.

Several classes of constructs on Mars have been proposed to exhibit pyroclastic activity. 1) One hypothesis of origin for the enigmatic Olympus Mons aureole is that it is an ash flow tuff (King and Riehle, 1974; Morris, 1980). 2) Scott and Tanaka (1982) proposed the occurrence of a widespread ignimbrite deposit in the Amazonis Planitia region, based on photogeologic methods. 3) Hundreds of subkilometer cratered volcanoes in Elysium, Isidis, and Utopia Planitia were proposed to be analogs of terrestrial cinder cones (Frey and Jarosewich, 1982). 4) Wood (1981) identified twenty martian calderas, but stressed their low occurrence compared to numbers of



terrestrial calderas. 5) Plescia (1981) distinguished between shield volcanoes and composite cones in the Tempe province based on morphological characteristics. Except for the composite cones found in the Tempe province, none of these constructs provides a suitable analog for Mohon Mountain. However, three promising structures with some similarities to the Mohon composite volcano may be found in Tyrrhena Patera, Elysium Mons, and Hecates Tholus.

Tyrrhena Patera is one of the older martian central vent volcanoes. It is located in the Hesperia Planum in the southern cratered terrain hemisphere. Structurally Tyrrhena Patera belongs in the category of highland patera. Tyrrhena Patera displays three stratigraphic units: 1) an oldest eroded unit north and west of the center which shows structures concentric to the main edifice, 2) radially furrowed material which makes up the bulk of the volcano and is interpreted as ash deposits erupted during the main shield building stage (Spudis and Greeley, 1981), and 3) lava exhibiting channels and wrinkle ridges that erupted during waning stages of activity.

Elysium Mons is most likely a composite volcano. It has flank slopes of 10-12 degrees, which are significantly steeper than those of Olympus Mons and the Tharsis shields (Basaltic Volcanism Study Project, 1981). As at Mohon Mountain, the outer boundary of the volcanics is indistinct and merges with the surrounding plains. Long, shallow linear depressions with distinct radial patterns trend from the caldera-like summit. Malin (1977) proposed that steeper slopes and sparse evidence for individual flow features is an indication of more silicic volcanism than that found at the Tharsis shields. However, Viking data revealed numerous flows on Elysium Mons (Basaltic Volcanism Study Project, 1981), so its slope may be due to a different eruptive rate rather than to a different lava composition. The highly subdued appearance of its flanks suggests the presence of a blanketing material such as ash, which conforms to underlying irregular mounds that perhaps are more viscous lava flows. In addition, the presence of numerous endogenic flank craters suggests explosive ejection of magmatic material.

Hecates Tholus is the northernmost of three volcanoes in the martian Elysium province. It has relatively steep, dome-like, convex slopes, a height of 6 km and a diameter of 180 km. An embayment into the dome in the northwest is flooded by plains material and may have originated through erosion of the slope of the volcano or through modification of a preexisting depression interior to the dome boundary (Mouginis-Mark and others, 1982) as is the case with embayment of the southern slope of Mohon Mountain. The northern boundary of Hecates Tholus is indistinct. Numerous channels are seen on its slopes (Malin, 1977). Wilson and others (1981) and Mouginis-Mark and others (1982) cite evidence for explosive activity at the summit of Hecates Tholus based on the observed dearth of small craters and channel source areas to the west of the caldera and faint radial striations on the southwestern flanks of the volcano. They interpret these to be caused by a thick, relatively recent airfall deposit which subsequently scoured the surface.

Central vent volcanism has not been widespread on Mars (Spudis and Greeley, 1981). It is interpreted to be remnants of a style of volcanism that occurred early in the volcanic history of the planet

and decreased with time (Greeley and Spudis, 1981). Evidence for liquid water, both at the surface and in the regolith (Basaltic Volcanism Study Project, 1981), is widespread for the past. Water could have reacted with the magma to produce phreatomagmatic eruptions. Pike and Clow (1981) compared gross morphologies of montes, tholi, and paterae and concluded that these are distinct morphological divisions of genetic significance. This is in agreement with Plescia's (1981) comparison of conical features with summit craters in the Tempe province. When compared with the dimensional data of terrestrial volcanoes, the crater diameter/basal diameter ratio of the martian features is more compatible with terrestrial composite volcanoes than with basaltic shields or cinder cones. The tholi and paterae resemble stratovolcanoes more than do the shield-like montes. Pike and Clow (1981) concluded that at least a different combination of processes, if not a different chemistry, must have given rise to the tholi and paterae which do not correspond morphologically to shield volcanoes on earth.

Disruption of erupting magma into scoriaceous or pumiceous clasts and released gas can be expected on Mars for wide ranges in magma composition, volatile type, and content (Wilson and Head, 1981). Pyroclastic eruptions should be more common on Mars than on Earth because of its lower atmospheric pressure. For both silicic and basaltic magmas, if an eruptive episode involving magma disruption continues for more than several minutes, a plinian airfall deposit may be formed (Wilson and Head, 1981).

Therefore, taking into consideration factors which differ on Mars and Earth, such as lithospheric thickness, eruptive rates, erosional processes, density of atmosphere, and possibly chemical composition of eruptives, it seems possible that central vent pyroclastic volcanism occurred during early stages of martian volcanic history and that Elysium Mons, Hecates Tholus, and Tyrrhena Patera provide examples which can be compared morphologically to composite cones on Earth such as Mohon Mountain.

#### REFERENCES

- 1) Basaltic Volcanism Study Project, 1981, Basaltic Volcanism on the Terrestrial Planets, Pergamon Press, New York, 1286 p.
- 2) Frey, H. and Jarosewich, M., 1982, J. Geophys. Res. 87, p.9867-9879.
- 3) Greeley, R., and Spudis, P.D., 1981, Rev. Geophys. Space Phys. 19, p. 13-41.
- 4) Malin, M.C., 1977, Geol. Soc. Am. Bull. 88, p. 908-919.
- 5) Mouginis-Mark, P.J., Wilson, L., and Head, J.W., 1982, J. Geophys. Res. 87, p. 9890-9904.
- 6) Pike, R.J., and Clow, G.D., 1981, LPI Contrib. 441, p. 199-201.
- 7) Plescia, J.B., 1981, Icarus 45, p. 586-601.
- 8) Scott, D.H., and Tanaka, K.L., 1982, J. Geophys. Res. 87, p. 1179-1190.
- 9) Wilson, L., and Head, J.W., LPI Contribution 441, p. 278-280.
- 10) Wood, C.A., 1981, LPI Contrib. 441, p. 284-286.

**Picacho Butte Volcanics**  
**Cenozoic volcanism in the southern Mount Floyd Volcanic Field**

Andrew P. Kisiel and John S. King, Department of Geology, University at Buffalo, 4240 Ridge Lea Road, Amherst, N.Y. 14226

Picacho Butte is the southernmost silicic center in the Mount Floyd volcanic field, located in north central Arizona on the southern Colorado Plateau. Detailed mapping revealed Picacho Butte to be an extensively eroded cumulo-dome composed of pale pink to dark pink and light gray to lavender hornblende rhyodacite. Flow folding and flow banding are common as with other silicic centers in the Mount Floyd field (Nealey, 1980). The rhyodacites are trachytic, containing variable amounts of plagioclase, hornblende, and biotite phenocrysts in a cryptocrystalline to glassy groundmass with plagioclase and opaques. Chemically the rocks are classified as subalkaline with calc-alkaline affinities (68-71% SiO<sub>2</sub>)(normalized). K-Ar dates by Goff et al (1983) indicate the dome is 9.8 +/- 0.7 m.y. old.

The dominant volcanism in the area is basaltic. The mafic rocks are olivine basalts with some quartz-bearing basaltic andesites. Chemically they are alkaline to subalkaline, with silica values ranging from 45.5-51.4% SiO<sub>2</sub> (normalized). The quartz-bearing basaltic andesite (58.3-59.3% SiO<sub>2</sub>) underlies basalts south of Picacho Butte. The mafic lavas contain variable amounts of xenocrysts, some quartz grains which are fractured, embayed, and lined with clinopyroxene crystals.

The Picacho Butte vicinity contains many basaltic vent areas, some which exhibit characteristic Strombolian-like volcanic activity. Strombolian eruptions typically involve moderately fluid magma. Explosive eruptions range from weak to violent with ejection of bombs, cinder, and small to large amounts of ash (Williams and McBirney 1979, Macdonald 1972). Effusive activity commonly is in the form of thicker and less extensive flows than occurs in Hawaiian or flood basalts (McDonald, 1972).

A few basaltic vents around Picacho Butte produced cinder cones generally with two stages of activity. An early pyroclastic stage consists of a basal basaltic tuff, altered to a yellow to buff colored palagonitic tuff. Palagonitization may be a result of ordinary weathering processes, occurring after cone erosion (Macdonald, 1972, Haer and Illins, 1968). Following deposition of the initial tuff the basaltic eruptive activity continued with the formation of agglutinates, and pyroclastics in the form of spherical and tear shaped cinders, lapilli, and small ribbon to large spherical and fusiform shaped bombs. The Picacho Butte basaltic vent sequence usually culminated with extrusive activity dominated by moderately thick massive to vesicular basalt flows. The Picacho Butte basaltic vent sequence is similar to the Mt. Floyd basaltic activity documented by Nealey (1980). Subsequent erosion of many basaltic vents in the Picacho Butte vicinity (up to 4km distance) has exposed internal dikes and central basalt plugs. Erosion has exposed three radiating dikes along with a central plug 1 km northwest of Picacho Butte. Picacho Butte cinder cones are small, less than a 1 km in radius.

Styles of volcanic activity and eruptive products are subject to magma composition, volatiles, and magma chamber vent conditions. Pyroclast formation

entails two processes, fragmentation and cooling (Fisher, 1984). Expansion of volatiles at shallow confining pressures during magma ascent through the conduit induces magma vesiculation, resulting in pyroclastic material formed by fragmentation and cooling above the vent (Fisher 1984). Disruption of magma occurs when the gas volume fraction reaches 0.75 (Fisher 1984). In contradistinction, interaction of magma with exoteric water (ie. groundwater) results in rapid cooling followed by fragmentation (Fisher, 1984).

Frequently, the initial activity of the Picacho Butte basaltic vents was explosive. Interaction with ground water may have been a major factor in the eruptive style of the basaltic volcanism early in the evolution of the vent. However, with the presence of some highly vesicular flows in the study area, pyroclastic activity may have been the result of both magma volatile content as well as the interaction with external water.

Interpretations of volcanic landforms on other planetary bodies through comparative studies of terrestrial morphologic products of basaltic volcanism may provide insight into the physical processes at work on other planetary bodies.

Terrestrial volcanoes exhibit a diverse range of volcanic landforms due to a wide variety of styles of volcanic activity. The Picacho Butte vicinity Strombolean-like explosive eruptive activity lead to the formation of cinder cones. Identification of similar morphologic features on Mars implies explosive style eruptions on that planet have occurred in the past.

Although large scale explosive eruptions on Mars is controversial (Francis and Wood, 1982) small scale explosive volcanism has been postulated by some workers (Wood, 1979, Plescia, 1980; Frey, 1982). Numerous small conical features with simple summit craters have been interpreted as cinder cones (Plescia, 1981, Frey, 1982). Whether these were the result of phreato-magmatic or magmatic eruptions is unclear (Francis and Wood, 1982). The constructs have steep slopes with a distinct contact with surrounding plains, explained as an abrupt change in slope (Plescia, 1981).

Frey et al (1981) propose that a possible analog for the small cones are Icelandic pseudocraters, based on studies of crater/cone ratios, morphology, and distribution of the small cones. Icelandic pseudocraters form by steam explosions under lava flows. The cones are however, 2-3 times the size of their terrestrial counterparts (Frey, 1982).

Small conical summit crater cones are abundant in many regions on Mars, including the Northern Plains from Arcadia through Utopia. If these are volcanic in origin, the small scale explosive activity on Mars may be similar in eruptive style to the basaltic volcanism in the Picacho Butte vicinity.

## References

- Fisher, R.V., and Schmincke, H.U., 1984, *Pyroclastic Rocks*: Springer- Verlag, New York, 472 p.
- Frances, P.W., and Wood, C.A., 1982, Absence of silicic volcanism on mars: implications for crustal composition and volatile abundance: *Journal of Geophysical Res.*, v.87, no.B12, p.9881-9889.
- Frey, H., and Jarosewich, M., 1982, Subkilometer martian volcanoes: properties and possible terrestrial analogs: *Journal of Geophysical Res.*, v.87, no.B12, p.9867-9879.
- Goff, F.E., Eddy, A.C. and Arny, B., 1983, Reconnaissance geologic strip map from Kingman to south of Bill Williams Mountain, Arizona: LA 9202-MAP, Los Alamos, New Mexico.
- Hay, R.L., and Iijima, A., 1968, Nature and origin of palagonite tuffs of the Honolulu group on Oahu, Hawaii: *Geol. Soc. Amer. Mem.* v.116, p.331-376.
- Macdonald, G.A., 1972, *Volcanoes*: Prentice Hall, London, 510 p.
- Plescia, J.B., 1981, Tempe volcanic province, mars: *Icarus*, v.45, p.594-597.
- Plescia, J.B., 1980, Cinder cones of Isidis and Elysium: NASA Tech. Memo., 82385, p.263-265.
- Williams, H., and McBirney, A.R., 1979, *Volcanology*: Freeman, Cooper and Co., San Francisco, 397 p.
- Wood, C.A., 1979, Monogenetic volcanoes of the terrestrial planets: *Proc. Lunar Planet. Sci. Conf.*, 10th, 2815-2840.

BASALTIC PLAINS VOLCANISM ON THE EASTERN SNAKE RIVER PLAIN,  
IDAHO: A GEOLOGIC AND PETROLOGIC STUDY OF PINE AND CRATER BUTTES

Paul F. Mazierski and John S. King, Department of Geological Sciences, State University of New York at Buffalo, 4240 Ridge Lea Road, Amherst, NY 14226

Pine and Crater Buttes are two basaltic volcanic centers located 35 km north of St. Anthony, Idaho and 9 km west of the Island Park caldera complex on the far Eastern Snake River Plain (ESRP). Relatively voluminous tube and channel-fed olivine tholeiitic basalt flows, derived from a variety of vents in the Pine/Crater Butte area, represent some of the youngest activity within the northeastern corner of the Mud Lake volcanic area [1] along the Spenser Rift Zone [2], a discontinuous set of fractures which extends eastward over 58 km from Spencer, Idaho to the edge of the Island Park caldera. The Mud Lake volcanic area displays a wide variety of vents which vary both in structure and composition including 1) low relief basaltic shields, often with summit pit craters, 2) spatter and dribble cones, 3) lava rings, 4) cinder cones and 5) more silicic tuff cones [3].

The Pine/Crater Butte study area displays features characteristic of basaltic plains type volcanism [4] in which numerous flows have been erupted from a number of local vents associated with a N 18° W trending rift zone. The area around Pine and Crater Buttes contains a marked variety of the types of vents present, almost completely representing the classification groups of Stearns [3] and typifies the various basaltic landforms found throughout the Mud Lake region. Six major vents and a number of smaller local vents were identified within the area of study. All of the large constructs are coalescing low shields produced by the accumulation of tube and channel-fed compound flows from a single feeding vent. Cumulative thicknesses of flow units erupted during a single episode of activity range from 6 to 12 m. Spatter cones and spatter ramparts constitute the majority of the smaller vents where local concentration of activity along the rift zone has occurred.

Pine Butte is a large, elongate low shield with two large, flat floored collapse pits, Pine Butte East and West, at its summit. Pine Butte East is a subcircular collapse crater .28 km wide and Pine Butte West is an elongate collapse pit .27 km wide and .43 km long. A distance of only 259 m separates the two craters implying that these vents are genetically related although the majority of the activity at Pine Butte East appears to be slightly older than that at Pine Butte West. Pine Butte West apparently initially developed as a large rift related eruption along the western flank of the low shield of Pine Butte East. Subsequent to this, activity shifted to the new Pine Butte West eruptive center with the accumulation of flows toward the south and southwest, away from the topographically higher Pine Butte East, producing the westward elongation of the Pine Butte construct.

Crater Butte consists of two coalescing shields identified by Little and Big Craters. Little Crater is an irregular shaped,

shallow depression from which the majority of the eruptive products in the area have been derived. Big Crater is a small, deep collapse/explosion pit crater located 1 km east of Little Crater along the rift zone. Geochemical data suggests that a genetic relationship exists between Little and Big Craters although, physically, this relationship is not as clear as in the case of Pine Buttes East and West. Other large low shield constructs investigated in this study include Rocky Butte, a circular shield with a smaller steep summit cone located 2.3 km southwest of Pine Butte West and S.P. Butte, a large elongate shield located 5 km due west of Rocky Butte.

In the eastern portion of the study area the rift zone is a tensional crack while closer to the main vent area it is marked by abundant elongate spatter ramparts and spatter cones. Spatter ramparts are typically less than a meter in height while the spatter cones often attain heights greater than 4 m where local concentration of activity around small vents coincident with the rift zone has occurred. An unnamed hourglass shaped lava ring, produced by repeated overbank flow of an active lava lake, was observed just to the northeast of Big Crater.

The suite of basalts obtained within the Pine/Crater Butte area defines a transitional series from relatively primitive, low K lavas to the slightly evolved olivine tholeiites which dominate the ESRP. Major and trace element variations within this suite suggest that low pressure ( $<8$  kb) olivine and plagioclase fractionation, consistent with the work of Leeman [5] and Thompson [6], have controlled the evolution of successive flows from a given vent and that lavas from the entire area, regardless of how many feeding magma chambers exist, have evolved along a common liquidus line of descent. Major and trace element petrogenetic modelling suggests that a fractionating assemblage of olivine, plagioclase and clinopyroxene accounts for the chemical evolution of the area. The addition of clinopyroxene to the fractionating assemblage, although it appears rarely as a phenocryst phase, constituted the only plausible explanation for a substantial Cr depletion toward the more evolved flows.

The importance of basaltic volcanism in the formation and modification of extraterrestrial surfaces throughout the history of the solar system has long been recognized. Geologic interpretation of surface features observed through fly-by, orbiter and manned missions has demonstrated a variety of basaltic morphologies ranging from the extensive flood sheets of the Moon to the massive shield constructs of Mars. More detailed investigation of these volcanic landforms, in order to evaluate the styles in which these different morphologies were emplaced, is crucial to the development of models for the evolution of such volcanic areas. Basaltic plains type volcanic terrains have been identified in various mare regions of the Moon and the volcanic provinces of Mars [7]. Important features of the Pine and Crater Butte area which typify plains type activity and are the criteria by which morphologic comparisons to these lunar and martian regions are to be made include 1) an association between source areas and extensional features (i.e. rifts, grabens), 2) the importance of lava tube and channel systems in flow emplacement

and. 3) shifts of activity with time producing coalescing low shield constructs.

Portions of the Orientale Basin including Lacus Veris and Lacus Autumni, the upper parts of Mare Imbrium, Oceanus Procellarum and many of the smaller lunar mare have been proposed as areas of plains type activity [4] by the presence of small, low relief constructs, commonly aligned along linear trends, and a marked abundance of sinuous rilles relative to other mare regions. Other lunar basaltic plains analog areas include the Marius Hills [8] and the Aristarchus Plateau. Regions of Mars which display features indicative of basaltic plains type activity include the Mareotis/Tempe Fossae region [9], Isidia Planitia [10], the Cydonia Mensae region in southeast Acidalia Planitia [11], the southeastern part of Chryse Planitia [12] and an area southeast of Uranus Patera.

The majority of these extraterrestrial basaltic plains terrains occur within the younger mare units of impact basins or, in the case of the Martian analogs, along the periphery of the Tharsis province. This relationship implies that the development of these terrains, relative to the more prevalent flood basalts, is a product of an overall decrease in volcanic activity late in an impact basin's history or as one moves radially away from the center of the Tharsis province in the case of the Martian areas. In this case individual constructs are built through the accumulation of thin sheet flows, as opposed to the emplacement of vast featureless flood plains, associated with zones of weakness produced either through impact or extensional tectonics.

#### REFERENCES

- [1] Stearns, H.T., 1939, U.S. Geol. Surv. Water Supply Paper 818, 124 p.
- [2] LaPoint, P.J.I., 1977, U.S. Geol. Surv. Map MF-850.
- [3] Stearns, H.T., 1926, Amer. Jour. Sci. 11, #64, 353-363.
- [4] Greeley, R.C., 1976, Lunar Plan. Sci. VII Proc., 2747-2759.
- [5] Leeman, W.P., 1982, Olivine tholeiitic basalts of the Eastern Snake River Plain, Idaho: in Cenozoic Geology of Idaho, Idaho Bureau of Mines and Geology Bull. 26, 181-191.
- [6] Thompson, R.N., 1975, Contrib. Mineral. Petrol. 52, 213-232.
- [7] Greeley, R.C. and P.H. Schultz, 1977, Possible Planetary Analogs to Snake River Plain Features, NASA CR-154621, 233-251.
- [8] Greeley, R.C., 1971, The Moon 3, 289-314.
- [9] Hodges, C.A., 1980, NASA Tech. Mem. 81776, 181-183.
- [10] Carr, M.H., 1984, NASA SP-469, 241-243.
- [11] Hodges, C.A., 1979, NASA Tech. Mem. 80339, 247-249.
- [12] Greeley, R.C. et al., 1977, Jour. Geophys. Res. 82, 4893-4109.



## CHAPTER 10

### CRATERING PROCESSES AND CHRONOLOGIES



## IMPACT AND COLLISIONAL PROCESSES IN THE SOLAR SYSTEM

*Thomas J. Ahrens, Seismological Laboratory 252-21, California Institute of Technology, Pasadena, CA 91125.*

Volatile-bearing minerals, especially phyllosilicates, carry much of the water in carbonaceous chondrites [1], and probably control the oxidation state of accretion planets [2], and contribute to the atmosphere of planets and satellites (Earth, Venus, Mars, and Titan) during accretion [3,4,5].

Recovery experiments on porous and solid phyllosilicates (serpentine) are in progress. As discussed by Lange and Ahrens [5] much of the impact-induced water production takes place in the porous regolith of the accreting planet. The results of such experiments have been used to calculate the evolution of an early water-rich atmosphere on the earth. Recently Abe and Matsui [6,7,8] have used our experimental data to calculate the thermal history of an accreting planet taking into account the evolution of water upon impact devolatilization and its solution in a water-bearing magma ocean.

In order to study impact devolatilization of porous minerals as these would exist on an accreting planetary regolith, we have started capturing gases (for manometric and isotopic analysis) as these are driven off from impacted mineral samples enclosed in an initially evacuated chamber.

Fig. 1 shows the results of solid recovery experiments performed for comparison to the gas recovery experiments. The good agreement between the two techniques (although based on sparse data) suggests that the two techniques do represent independent measures of the same phenomenon. If so, the gas recovery technique should allow investigations of chemical reactions between evolved gaseous species from complicated mixtures (i.e., carbonaceous chondrites) and comparison with results of solid recovery experiments may allow definitive study of shock-induced isotopic fractionation (or lack thereof) of volatile materials. Furthermore, investigations of the effects of ambient gas pressure appear possible.

In order to tie shock recovery experiments to infall velocity and construct thermodynamic models for various porosity regoliths, knowledge of the Hugoniot and release isentrope equation of state is required. We have in the last year investigated the Hugoniot (Fig. 2) and release isentrope paths of the nearly pure end-member serpentine polymorphs, antigorite (Thurman, N.Y.) and lizardite (Globe, Arizona).

It has been suggested by Lange et al. [9] that in addition to causing the immediate loss of some of the structurally bound water in serpentine, impact causes 'loosening' of the water remaining in the solid material required for dehydration and reduces the activation energy associated with the dehydration reaction (the shock wave also lowers the dehydration temperature). We recently obtained results of a thermogravimetric study of shocked serpentine performed to determine the activation energy for water loss of the shocked material. The study has been performed using the differential thermal analytical technique outlined by Kissinger [10].

Our results show that the activation energy derived from a plot for unshocked serpentine is about 81 kcal/mol, which is consistent with the result of Brindley et al. [11] who obtained a value of 68 kcal/mol under vacuum and a value of 89 kcal/mol under 1.2 mm vapor pressure of H<sub>2</sub>O.

Our new data shows the results of the activation energy calculation; the activation energy for the water loss reaction for the shocked serpentine lies in the range 52-56 kcal/mol. Thus, we can quantitatively determine the increased ease of devolatilization in the shocked material over the unshocked material.

Recently, we completed a series of shock recovery experiments on Murchison carbonaceous chondrite (C2M) performed to determine the conditions for loss of H<sub>2</sub>O and other volatiles upon impact from material more representative of an accreting planetesimal than single minerals.

The new data show that incipient devolatilization occurs at an initial shock pressure of about 11 GPa, and complete devolatilization occurs at an initial shock pressure of about 30 GPa.

We conclude that impact-induced H<sub>2</sub>O loss for crystal-density serpentine and for 20% porous serpentine, approximate the range of densities of many carbonaceous chondrites. These results bracket the data for Murchison, consistent with the observation that septechnolites are the major H<sub>2</sub>O-bearing phase in Murchison. This also indicates that the results of devolatilization experiments on Mg end-member serpentine may be extrapolated to carbonaceous chondrites.

In the process of carrying out the shock devolatilization experiments on samples of Murchison meteorite, we recognized that reactions were taking place between minerals in the meteorite which were in gross disequilibrium at the high post-shock temperatures produced in our experiments. The especially reactive mineral phases were the water-bearing phyllosilicates, metal and sulfide grains, and silicate grains. Clearly post-shock reactions between mineral species such as occurred in our laboratory experiments must also take place on the surface of accreting planets. In order to place some experimental constraints on the process of shock-induced melting of say, iron sulfide, we conducted recovery experiments using 33% porous pyrrhotite. Two types of melting were apparent. The first occurred even at relatively low shock pressures and was present also in the higher pressure experiments. Scanning electron microscopy and electron microprobe analysis indicate that the recovered materials from this first type of melting occurred in highly localized bands. It is distinguished by the presence of a large number of voids and strong depletion of sulfur, apparently due to incongruent vaporization during isentropic release. Where this type of melting was in contact with the sample container (made of copper), the container material tended to alloy with the iron in the sample, while the sulfur was lost, presumably by vaporization. Quantitative knowledge of shock and post-shock temperatures provide the physical basis for describing the melting and partial vaporization and phase transitions associated with planetary accretion and impact.

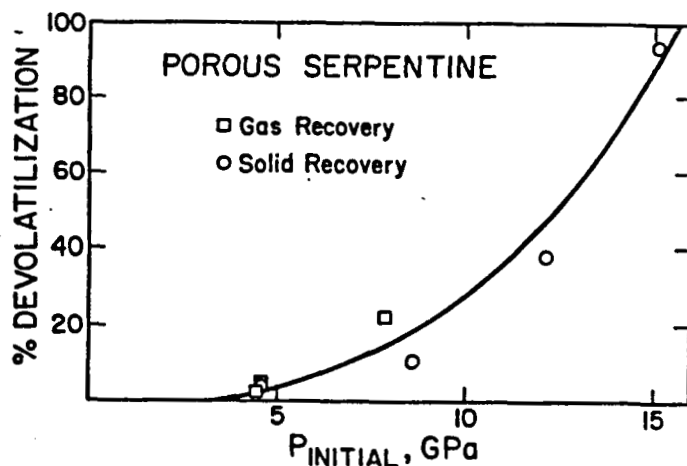
Our work has led us to recognition of three regimes of shock induced radiation (Schmitt and Ahrens, 1983, 1984) for minerals. With *decreasing* pressure, these are:

(1) The nearly blackbody radiation regime demonstrated, for example, by  $\alpha$ -quartz shocked into the stishovite range. Other materials shocked to temperatures above  $\approx 4000$  K for which we have observed continuum temperatures corresponding to the equilibrium shock state include MgCaSi<sub>2</sub>O<sub>6</sub>, CaAl<sub>2</sub>Si<sub>2</sub>O<sub>8</sub>, NaCl, H<sub>2</sub>O, Mg<sub>2</sub>SiO<sub>4</sub>, CaO, MgO, Mg<sub>3</sub>Si<sub>3</sub>Al<sub>2</sub>O<sub>12</sub>, Ag, and very recently, Fe.

(2) The heterogeneous low emissivity hot spot regime [12]. We have for the first time demonstrated the existence of heterogeneous temperature distributions in shocked minerals

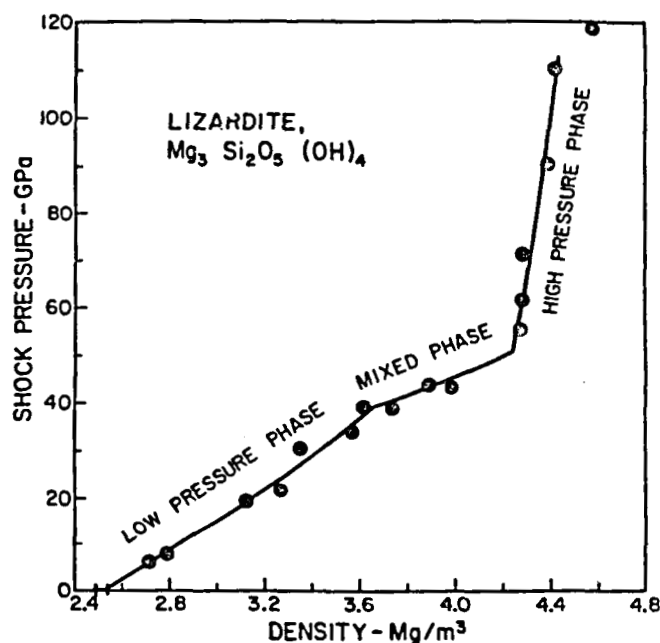
and obtained data for  $\text{NaCl}$ ,  $\text{CaCO}_3$ ,  $\text{CaSO}_4 \cdot 2\text{H}_2\text{O}$  [13], for  $\text{CaAl}_2\text{Si}_2\text{O}_8$  [14,15],  $\text{SiO}_2$ , and recently  $\text{Mg}_3\text{Si}_2\text{O}_5(\text{OH})_4$ ,  $\text{Al}_2\text{O}_3$ ,  $\text{KCl}$  and  $\text{LiF}$  [16]. We conclude that the radiation detected in this regime demonstrates the existence of a population of small hot shear bands or zones behind the shock front. We believe these shear bands have long been recognized as "planar features" by petrologists who have studied shocked silicates from impact craters on the earth, the moon, and in meteorites [17].

Fig. 1. Percent devolatilization, versus, initial impact pressure for porous serpentine (35% porosity). Results for gas recovery and solid recovery shots (Tyburczy, Epstein, and Ahrens, unpublished).



TJA86076SFD

Fig. 2. Shock pressure-density Hugoniot data for crystal-density lizardite (serpentine) (Tyburczy and Ahrens, unpublished).



TJA86071LFD

## References

- [1] Robert, F. and Epstein, S., 1982, *Geochim. Cosmochim. Acta*, **46**, 81-95.
- [2] Ringwood, A.E., 1979, *Origin of the Earth and the Moon*, Springer-Verlag, 295 pp.
- [3] Benlow, A. and Meadows, A. J., 1977, *Astrophys. Space Sci.*, **46**, 293-300.
- [4] Arrhenius, G., De, B.R., and Alvéén, 1974, in *The Sea*, ed. by E. D. Goldberg, pp. 839-861, Wiley, New York.
- [5] Lange, M. A. and Ahrens, T. J., 1982, *Icarus*, **51**, 96-120.
- [6] Abe, Y. and Matsui, Y., 1985, *Proc. 15th Lunar & Planet. Sci. Conf., Part 2, J. Geophys. Res.*, **90**, C545-C559.
- [7] Matsui, T. and Abe, Y., 1986, *The Earth, Moon, and Planets*, **34**, 223.
- [8] Matsui, T. and Abe, Y., 1986, *Nature*, **319**, 303.
- [9] Lange, M. A., Lambert, P., and Ahrens, T. J., 1985, *Geochim. Cosmochim. Acta*, **49**, 1715-1726.
- [10] Kissinger, H. E., 1957, *Anal. Chem.*, **11**, 1702-1706.
- [11] Brindley, G. W., Nahira, B. N., and Sharp, J. H., 1967, *Amer. Miner.*, **52**, 1697-1705.
- [12] Grady, D. E., 1980, *J. Geophys. Res.*, **85**, 913-924.
- [13] Kondo, K. and Ahrens, T. J., 1983, *Phys. Chem. Minerals*, **9**, 173-181.
- [14] Schmitt, D. R. and Ahrens, T. J., 1983, *Geophys. Res. Lett.*, **10**, 1077-1080.
- [15] Schmitt, D. R. and Ahrens, T. J., 1984, in *Shock Waves in Condensed Matter*, ed. by J. R. Asay, R. A. Graham, and G. K. Straub, Elsevier Science Publishers, 313-316.
- [16] Schmitt, D., Svendsen, B., and Ahrens, T. J., 1986, *Proc. Amer. Phys. Soc. Topical Conf. on Shock Waves in Condensed Matter*.
- [17] Stöffler, D., 1972, *Fortschr. Miner.*, **49**, 50-113.

## IMPACT CRATERING CALCULATIONS

*Thomas J. Ahrens and John D. O'Keefe, Seismological Laboratory 252-21, California Institute of Technology, Pasadena, CA 91125.*

The issue as to what is the essential origin of large flat-floored and ringed craters on the surface of the planets has been a long-standing problem of planetary geology. At issue is the question of whether the process forming the large impact structures on the moon, e.g., Imbrium, or Mercury e.g. Caloris, has brought material from deep in the planetary mantle to the surface as ejecta at depths comparable to the diameter of the apparent crater, or, whether the impact process at large scales has inherently different flow which limits the sampling of the planetary interior to shallow depths. Croft (1) pointed out that there were at least six different hypotheses as to the origin of concentric ring structures. These included:

- 1) "frozen" gravity waves in a fluidized medium
- 2) terraced gravity slumping of a transient crater rim
- 3) slumping of a transient crater into a plastic planetary interior
- 4) fracture and slumping of a transient crater plus associated volcanic activity
- 5) nested craters in a layered crust
- 6) fluidized motion and an oscillation of a central peak

As discussed below, our recent results indicate that **none of the above** are required to explain large flat-floored ring craters. Flat-floored craters are formed as a result of elastic and gravity driven rebound. No other physics such as fluidization, faulting, volcanism is required.

In order to examine planetary impact on a very large scale we used a computer model which employed a two-dimensional mixed Lagrangian-Eulerian numerical code. This was used to calculate the flow fields due to a spherical  $2.6g/cm^3$  silicate projectile having an impact velocity of 12 km/s. We address the following issues: 1) What is the maximum depth that the impactor penetrates the planetary surface? and 2) what is the maximum depth that is excavated by the cratering flow? We address these issues over a broad range of gravities, material strengths, and impactor sizes (from meters to those that formed the multiringed basins). We examine the deformational histories of planetary material both beneath the crater and in the region forming the ejecta plumes. These results, when taken with observed deformations of exposed and deeply eroded terrestrial, and perhaps in the future, craters on other planets, will constrain the impact history of a given structure.

In the hydrodynamic or gravity controlled regime, the crater depth of penetration and excavation scale as  $gD/U^2$ , where  $g$  is the planetary gravity,  $D$  is the projectile diameter and  $U$  is the impactor velocity (2). For earth gravity, we studied the cratering resulting from scaled impactor diameters which varied from 10 m to  $10^4$  km.

We find that in the regime of small planetary strengths (gravity dominated), the maximum relative depth of penetration is independent of impactor diameter up to diameters in the range of  $10^2$  km.

The region or depth of excavation can be determined by examining the tracer particles (Fig. 1). For angles greater than around  $10^\circ$  relative to centerline and point of impact, the cratering flow is nearly radial and outward into the planet. In the region less than  $10^\circ$ , the

flow is upward and it is from this region that material is excavated to produce the ejecta plume and blanket. Note that this region is less than a projectile diameter in depth. The deformations of the planetary material under the point of impact is complex and depends upon scale and strength of the planet. For low planetary strengths and large impactors, the region below the point of impact flows upward during the cratering flow evolution and is part of a toroidal flow field that also reverses the direction of the velocity field near the surface. This reversal of the surface velocity fields arrests the radial growth of the ejecta plume (see Fig. 1).

Two new areas which have just started to obtain results is the comparison of crater growth curves for different strengths silicate planetary crusts with the coupling parameter formulation of Holsapple & Schmidt (3).

The second area is study of the amount of material in the ejecta which comes from different depths.

The general idea that large body impacts are capable of transferring enough thermal energy into an atmosphere such that upon isentropic expansion a substantial amount of the atmosphere is lost from the planet has recently been revived in a very provocative paper by Cameron (4).

He suggested that the atmospheric  $^{36}\text{Ar}$  budget of the terrestrial planets (on a gram per gram of planet basis) which is  $2.5 \times 10^{-9}$  for Venus,  $3.5 \times 10^{-11}$  for Earth, and  $2.1 \times 10^{-13}$  for Mars, may provide a constraint on the amount of total atmosphere these planets have lost during accretion of the solid portion of the planets.

During the last year we have begun to carry out a calculation of the interaction of a large (10 km diameter) impactor with a self-gravitating exponential adiabatic planetary atmosphere. Previously we studied to a very limited extent the impact into a constant density atmosphere (5). To study gas loss to space via air impact we have begun a calculation of the impact of a large bolide with a polytropic,  $\gamma = 1.4$ , atmosphere extending from a surface density of  $10^{-3} \text{ g/cm}^3$  upward to  $10^{-5} \text{ g/cm}^3$ . A second approach we have taken to studying impact onto the atmosphere involves the approximation that the flow looks like an explosion in the atmosphere.

Using the approximation that the energy of the impactor is totally delivered to the atmosphere at the surface we examined the shock-induced flow from such impacts on the earth for an exponential atmosphere. This interesting problem has been studied by Zeldovich and Raizer (6) and is often called the Zeldovich flow. Its application to present planetary atmospheric cratering we believe is novel with our work. In an exponential atmosphere the downward propagating shock (from a finite height explosion) slows down and the upward propagating shock accelerates both in shock velocity and particle velocity behind the shock front (Fig. 2).

We show (7) within the framework of the Zeldovich theory of atmospheric escape for an atmosphere lying above a halfspace (no earth curvature) the maximum mass of gas which can escape from a single explosion or impact will be the mass of gas above a plane tangent to the spherical earth. For the earth's atmospheric parameters, this mass of gas is  $2.6 \times 10^{18} \text{ g}$  and compares to a mass of  $1.6 \times 10^{16} \text{ g}$  which is the largest mass which we calculate can escape from a single impact (Fig. 3). Thus we conclude that within the framework of the Zeldovich flow problem, only some  $5 \times 10^{-6}$  of the total atmosphere of the earth can be lost



by a single impact. The minimum impact energy for this maximal atmospheric loss event is in the range of  $0.5$  to  $1 \times 10^{30}$  ergs. This corresponds to a  $2g/cm^3$  density, 3-6 km diameter, projectile infalling at 11 km/sec into the present atmosphere. This maximal atmospheric loss projectile is only a factor of  $\sim 10$  lower in energy than that inferred by Alvarez et al. (1980), O'Keefe and Ahrens (5) for the Cretaceous-Tertiary extinction bolide.

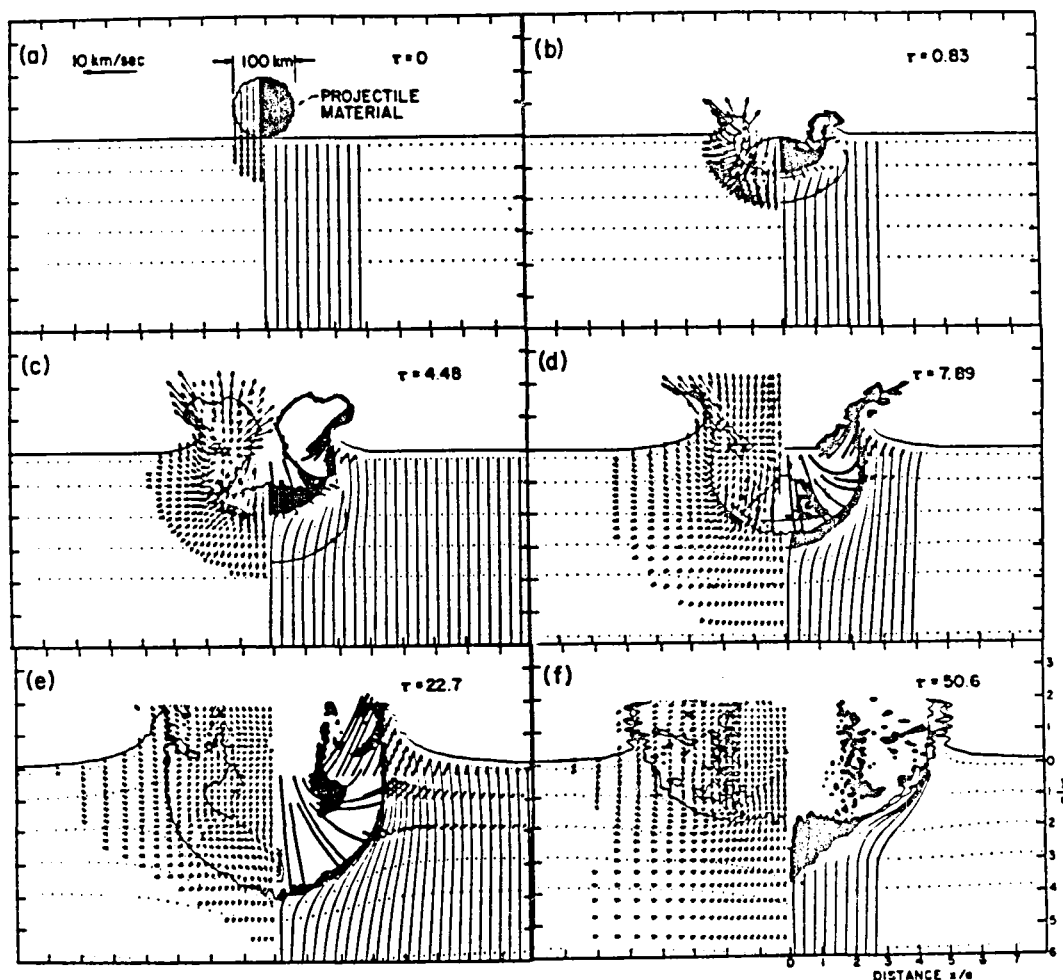
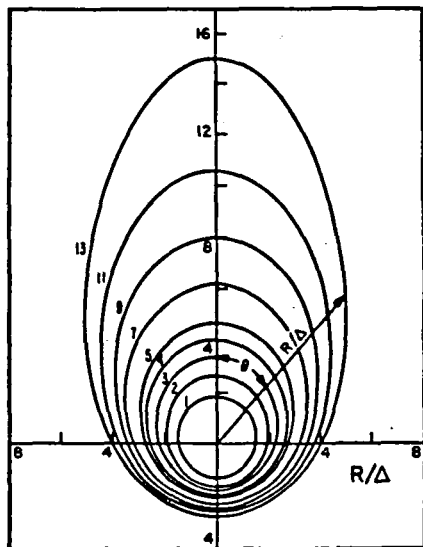
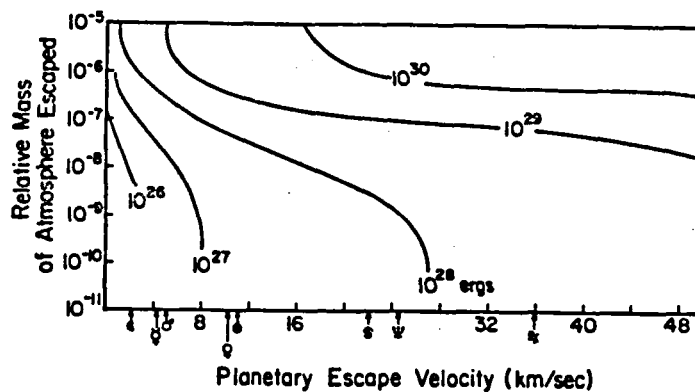


Fig. 1. Flow field upon impact of 100 km diameter silicate impactor onto silicate halfspace with earth gravity at 12 km/sec. Panels (a), (b), (c), (d), (e), and (f) show flow at  $\tau = 0, 8.3, 4.48, 7.89, 22.7,$  and  $50.6$ . Particle velocity arrows in left panels indicate particle velocity motion scaled to 10 km/sec vector of (a). Heavy curve in right hand panels of (b), (c), (d), and (e) indicate trajectories of particle motion in transient cavity. Light vertical lines in right hand panel, and horizontal aligned dots in both right and left hand panels are fixed to material in target and demonstrate total displacement. Note gravity driven rebound motion of floor of transient cavity between (e) and (f) resulting in flat floored crater and reduction in displacement of vertical lines and horizontal dots (after Ahrens and O'Keefe, [7]).



TJA86064SFD



TJA86067MFD

Fig. 2. Shock envelopes for an explosion in an exponential atmosphere for various values of the non-dimensional time ( $\tau = 1.4$ ) (After Ahrens and O'Keefe [7]).

Fig. 3. Relative mass of a hemisphere of atmosphere, which will escape for an exponential atmosphere with  $\tau = 1.4$ ,  $\rho = 10^{-3}$  g/cm<sup>3</sup>, and  $\Delta = 7$  km, versus, planetary escape velocity. For comparison escape velocity for moon, Mercury, Mars, Venus, Earth, Uranus, Neptune, and Saturn is indicated [7]).

#### References

- (1) Croft, S. K., 1981, *Multi-ring Basins, Proc. Lunar Planet. Sci. Conf.*, 12A, 227-275.
- (2) Holsapple, K. A. and Schmidt, R. M., 1987, *J. Geophys. Res.*, 87, 1849-1870.
- (3) Holsapple, K. A., and Schmidt, R. M., 1987, *J. Geophys. Res.*, 92, 6350-6376.
- (4) Cameron, A. G. W., 1983, *Icarus*, 56, 195-201.
- (5) O'Keefe, J. D. and Ahrens, T. J., 1982, *Proc. Conf. on Large Body Impacts and Terrestrial Evolution, Sp. Paper #190, Geol. Soc. Am.*, 103-120.
- (6) Zel'dovich, Ya., B. and Raizer, Y. P., 1967, *Physics of Shock Waves and High-Temperature Hydrodynamic Phenomena, II*, Academic Press, New York.
- (7) Ahrens, T. J. and O'Keefe, J. D., 1987, *Proc. 1986 Hypervelocity Impact Symp.*, San Antonio, TX, October 21-24, *Int. J. Impact Engineering*, 5, 13-32.

## Experimental Impact Cratering Mechanics

Robert M. Schmidt, Boeing Aerospace Co., M/S 3H-47, P.O. Box 3999, Seattle WA 98124

This abstract is a summary of recent progress in an experimental cratering program whose objective is to understand the formation of large impact craters. The main tool used in this program is a geotechnical centrifuge, which provides simulations of cratering events at a scale otherwise unattainable in the lab. For a given target material and impact velocity, the simulated kinetic energy in a centrifuge cratering event is  $G^3E$ , where  $E$  is the kinetic energy of the actual impactor used in an experiment. Thus at a gravity level of 600 G, we can effectively attain an increase in kinetic energy of more than eight orders of magnitude, when compared to a 1G test using the same impactor. For the lunar case, gravity can be increased by a factor of 3600, so we can effectively increase the energy by more than ten orders of magnitude. Even so, we cannot directly simulate events at the size scale of lunar basins. Hence one of the objectives of this program is to use the centrifuge results, in conjunction with impact experiments performed by others, in order to develop scaling relations which allow the experiments to be properly extrapolated to larger sizes.

In previous reports we have summarized scaling relations for apparent crater size, rate of crater growth, time of formation, ejecta velocities and debris profiles. This abstract summarizes two areas of recent study: scaling relations for rim diameters and crater ejecta blocks.

### Scaling of Rim-Crest Diameter

In many scaling applications, the rim-crest diameter is of more interest than the apparent diameter, because it can be determined directly from photographs without needing to determine the height of the pre-impact surface. Housen *et al.* (1) have shown that the rim-crest diameter is geometrically similar in the gravity regime and is approximately 25% greater than the apparent diameter for dry sand targets. Figure 1 gives a fit to the nondimensional rim diameter versus the gravity-scaled size  $\pi_2$ . The slope is in agreement with a value of the gravity exponent  $\alpha = 0.51$ . There is still some uncertainty in the proportionality coefficient, but it is in the range of 1.94 to 2.18.

Figure 2 compares rim-crest geometry from centrifuge experiments with lunar data give by Pike (2). The centrifuge data are plotted in lunar prototype dimensions, that is, multiplied by the ratio of gravity between the test environment and that of the Moon. A current best estimate for the proportionality coefficient is 2.06, although it should be considered as a preliminary value.

Figure 1: Centrifuge Data

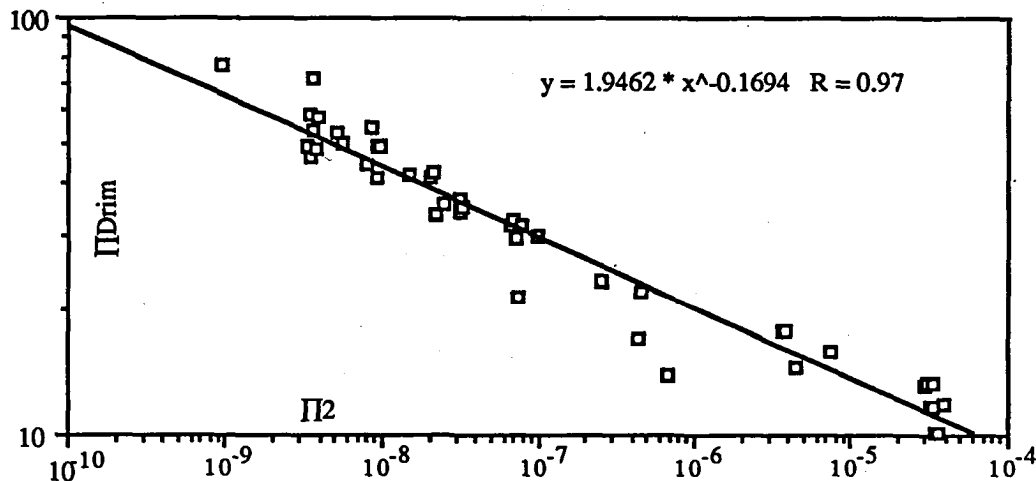
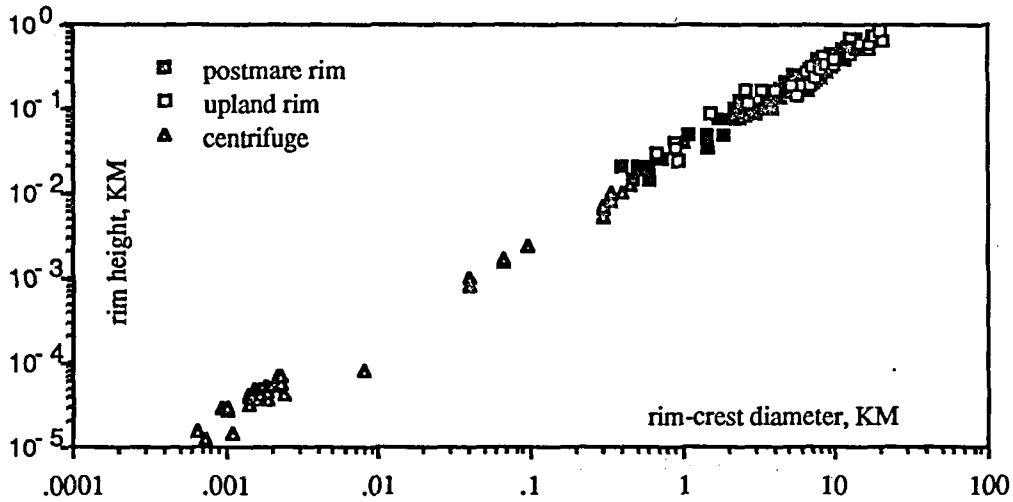


Figure 2: Lunar Crater Rim Data from Pike (1977)



### Scaling of Crater Ejecta Blocks.

Crater formation in rocky materials is thought to be governed by two basic mechanisms, depending on the size scale of the event. At small scales, crater size is determined primarily by the strength properties of the rock, whereas at much larger scales gravity plays a more dominant role than strength. The transition between these strength and gravity regimes is often suggested to occur at a critical value of  $Y/\rho g D$  where  $Y$  is an appropriate measure of the material strength,  $\rho$  is the density,  $g$  is the gravity field strength and  $D$  is the crater diameter (e.g. 1,3,4,5). Because of the difficulty in estimating  $Y$  for planetary or satellite surfaces, it is hard to decide to which regime a given set of craters belongs based solely on the  $Y/\rho g D$  criterion. It is useful therefore to search for other criteria. For example, one can show that the ejecta blankets of gravity-dominated craters should be *geometrically similar* (1). Hence a strength-gravity transition can be identified if observations of ejecta deposits indicate geometric similarity only above a critical diameter. This can provide useful information regarding the competence of the surface material.

The purpose of this study is to investigate block-size distributions as another possible indicator of a strength-gravity transition. Observations of block fields have been reported for a wide range of craters formed on the Earth, the Moon, Phobos and Deimos (6-10). Proper interpretation of these results can only be done if one knows the appropriate scaling laws for the strength and gravity regimes.

Consider a projectile of radius  $a$ , velocity  $U$ , and density  $\delta$  which impacts a rocky "target", described by its density  $\rho$ , and an arbitrary number,  $n$ , of mechanical properties,  $Y_1, \dots, Y_n$ . For the moment, assume that the  $Y_i$  all have units which can be derived from combinations of the units of stress and density (e.g. a wave speed has units of  $(\text{stress}/\text{density})^{1/2}$ ). Hence this excludes the case of rate-dependence. We further introduce a point-source coupling parameter,  $C$ , for the impactor (1,11). As such, the impactor properties  $a$ ,  $U$  and  $\delta$  are represented completely by  $C$ . The number of fragments of size  $s$  or larger which are ejected at range  $r$  from the impact can be written as

$$N(s) = F [ C, \rho, r, s, Y_1, \dots, Y_n ] \quad (1)$$

The crater diameter  $D$  produced in the impact can be expressed as

$$D = F [ C, \rho, Y_1, \dots, Y_n ] \quad (2)$$

Combining eqs. (1) and (2) in a nondimensional form gives

$$N(s) = F [ r/D, s/D, Y_2/Y_1, \dots, Y_n/Y_1 ] \quad (3)$$

The maximum block size at range  $r$  is obtained by setting  $N(s)=1$  and solving for  $s$ . Furthermore, one can infer that the smallest blocks are ejected close to the impact because they are observed to occur at the largest distances from the crater. The largest blocks generally are launched (and land) near the crater rim. Hence, the maximum block size  $s_{\max}$  around the crater is found by setting  $r/D=1/2$  in eq. (3). The result is

$$s_{\max}/D = F [ Y_2/Y_1, \dots, Y_n/Y_1 ] \quad (4)$$

Thus, for a given target material, the ratio of the size of the largest block to the size of the crater should be constant.

In the gravity regime, the final crater size is determined by gravity, i.e.

$$D = F [ C, \rho, g ] \quad (5)$$

The underlying fragment distribution should be independent of gravity, at least for surface spalls which are small enough that lithostatic stress is not important. For example, assuming a spall strength of say  $10^8$ - $10^9$  c.g.s. for lunar ejecta, lithostatic stress should not be significant for fragments less than a kilometer or so in size. Hence, even in the gravity regime, the fragment distribution should be given by eq. (3). Combining eq. (3) and (5) gives

$$s_{\max}/D = F [ Y_1/\rho g D, Y_2/Y_1, \dots, Y_n/Y_1 ] \quad (6)$$

or, for a given material,

$$s_{\max}/D = F [ gD ] \quad (7)$$

Therefore, in the gravity regime, the ratio of maximum block size to crater diameter should be a function of  $gD$ , with different curves for different materials.

Figure 3 shows the ratio of block diameter to crater diameter as a function of  $gD$ . The data were collected from refs. 6 and 7. There is significant scatter in the results. However, one might interpret the small-crater results as following the horizontal line shown in the figure. For craters with  $gD$  larger than roughly  $10^5$ , the ratio of block size to crater size decreases monotonically with crater size. This is interpreted as an indication of a gravity regime.

The diameter dependence in the gravity regime can be estimated by using a result from the spallation model of Melosh (12). That model suggests that spall thickness is proportional to  $r^{2.87}$ , for fixed impactor velocity. In particular,

$$s_{\max}/a \propto (r/a)^{2.87} \quad (8)$$

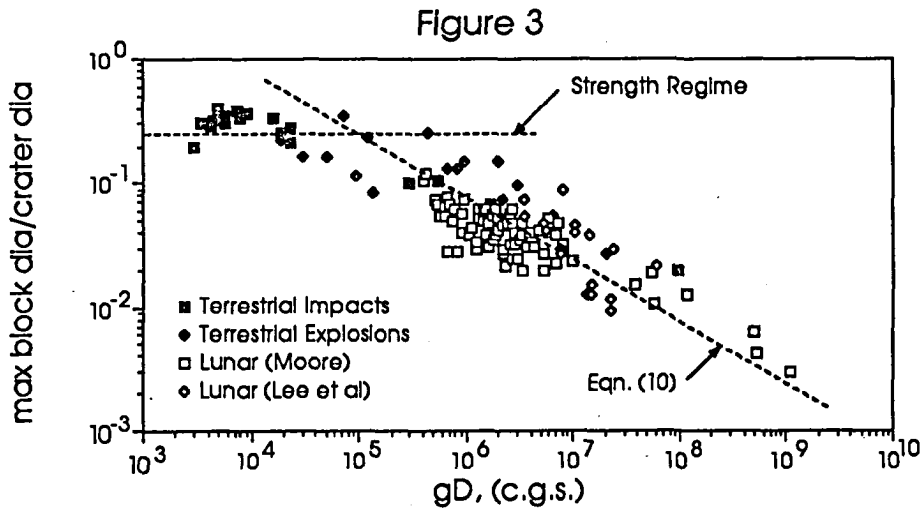
For gravity regime cratering in rock, the crater diameter should scale as (1,11)

$$D \propto a^{0.78} g^{-0.22} \quad (9)$$

for fixed impactor velocity. By setting  $r=D/2$  in eq. (8) and using eq. (9) to replace the impactor radius by  $D$  and  $g$ , the maximum block size at the crater rim becomes

$$s_{\max}/D \propto (gD)^{-0.53} \quad (10)$$

Hence for constant impactor velocity, the ratio  $s_{\max}/D$  should decrease as crater size increases. As shown in Figure 3, this agrees quite well with the data, suggesting that the downward-sloping trend is indicative of a gravity regime. The apparent strength-gravity transition at  $gD=10^5$  seems too low based on other estimates of the transition for crater size (e.g. 1,5), which suggest a value on the order of  $10^6$ - $10^7$ . We are currently investigating the possibility that this may be due in part to the effects of a strain-rate dependent material strength.



**References:** (1) Housen K.R., Schmidt R.M. and K.A. Holsapple (1983), *JGR*, 2485-2499. (2) Pike, R.J. In *Impact and Explosion Cratering*, 489-509. Pergamon. (3) Gault, D.E. and J.A. Wedekind (1977). In *Impact and Explosion Cratering*, 1231-1244. Pergamon. (4) Gaffney E.S. (1978) *Proc. LPSC 9th*, 3831-3842. (5) McKinnon W.B. (1983) *EOS*, 747. (6) Moore H.J. (1972), *Apollo Prelim Sci. Rept*, NASA SP-315. (7) Lee S.W., Thomas, P. and J. Veverka, *Icarus*, 77-86. (8) Cintala J.J., Garvin J.B. and S.J. Wetzell (1982), *Proc. LPSC 13th*, 100-101. (9) Garvin J.B. (1985) *Proc. LPSC 16th*, 260-261. (10) Vickery A.M. (1986) *Icarus*, 224-236. (11) Holsapple K.A. and R.M Schmidt (1987) *JGR*, 6350-6376 (12) Melosh H.J. (1984), *Icarus*, 234-260.

# IMPACT VELOCITY AND CHANGES IN CRATER SHAPE, MORPHOLOGY, AND STATISTICS P.H. Schultz, Geological Sciences, Brown University, Providence, RI 02912

The effects of impact velocity on crater size, shape and morphology have not received widespread study largely due to the belief that the combined effects of projectile mass and velocity are inseparable. Laboratory experiments and reanalysis of planetary crater data, however, indicate that velocity effects may be preserved.

**Crater Shape:** Laboratory experiments (1, 2) reveal a systematic increase in the crater diameter ( $D$ ) to depth ( $d$ ) ratio (the aspect ratio) with an increase in projectile penetration time expressed as the projectile radius ( $2r$ ) divided by velocity ( $v$ ). For a constant impact velocity is assumed, then derived scaling relations predict different domains for  $D/d$  depending on a transition crater diameter ( $D_t$ ): (1)  $D < D_t$ :  $D/d = k$ , (2)  $D > D_t$ :  $D/d \propto D_t^{-1/2}$ , (3) where  $D_t \propto v^{1.1}/g$ ,  $\omega = .24$ . Table I compares the observed and calculated transition diameters for different planets. The exponent  $\omega$  from experiments is smaller than observed values for planetary craters where  $\omega = 0.5$  (Mercury) to 0.7 (Moon). This disparity may reflect: modification (floor uplift and enlargement); impactor type (comet, asteroid); and/or too low a value from experiments.

**Pit Craters/Basins:** Craters on Mars (Fig. 1) and Ganymede are characterized by large central pits or central peaks with pits (3, 4). Although most studies interpret such pits as expressions of impactor-volatile interactions (e.g., 5), both bodies also have relatively low rms impact velocities ( $< 20$  km/s). Moreover, craters on the Moon (6) and Mercury exhibit similar central peak morphologies although in fewer relative numbers (Fig. 2). These structures may reflect impactor rather than substrate characteristics.

Figure 3 compares central pits with the gravity-corrected diameters on Mercury, Moon, and Mars. Five observations from this study can be made: (a) the martian pit-crater data exhibit no dependence on latitude or general terrain/unit type in agreement with previous studies (3); data for each planet exhibit very similar slopes, slightly larger than unity; d) data for planets with higher rms impact velocities are shifted to larger diameters; and e) data for 2-ring impact basins on Mars and Mercury are coincident. The first and second observations lessen the direct role of volatiles in the formation of such craters. The third through fifth observations can be explained by the effects of average impactor velocities.

Incorporation of impact velocity into the observations requires several assumptions: a) the central pit reflects the impactor diameter; b) the pits largely represent the lower velocity impactor population; and c) post-impact modification is only weakly dependent on crater size for complex craters. The initial assumption is an intuitive leap based on the observations that: central pits are found on very different planets; and double pit craters can be found on Mars; and peak impact pressures at any velocity eventually follow the same decay curve dependent on the distance scaled to the impactor size (9). If the central pit reflects a common peak-pressure limit, then its size will directly depend on impactor size. The second assumption is based on the observation that the relative number of central pit craters is highest for planets with low average rms impact velocities. Pit craters comprise 60% of the total crater population on the ridged plains of Mars. The third assumption is based on crater models plastically deformed on a centrifuge (10) and measurements of crater wall widths (11, 12). This assumption results in each crater at a given gravity-adjusted diameter to be modified equally, thereby allowing use of laboratory-derived scaling relations. Table II shows the calculated impact velocities where the experimentally derived scaling relations have been applied to the observed pit and crater diameters. If correct, then 2-ring basins on Mars and Mercury appear to represent impacts by low-velocity objects with a narrow range in dispersion, i.e., prograde heliocentric objects (see Table II). Such a hypothesis has been proposed for late impacting objects on Mercury (15). Croft (4) interprets the anomalous pit craters as representatives of the high-velocity end. Although in conflict with the conclusions here, his mechanism seems necessary for the other class of pit craters.

**Conclusions:** Impactor size and velocity may be reflected in the transition in crater aspect ratios for gravity-controlled impacts, the relation between  $D$  and  $D/d$ , and in crater morphology. A direct consequence is that crater production slopes will change at different diameters on different planets, and perhaps with time. Such inflections are observed (16) for the post-mare cratering

populations (Table I). The changes in production slopes do not necessarily reflect changes in impactor size distributions or sources but the ratio of impactor size to velocities at a given time on a given planet.

The above views may seem heretical since dynamic modifications processes are widely believed to destroy most information about crater excavation. These contrasting views may not be contradictory but only reflect some of the unique results of impacting large objects (1 km) at relatively low velocities <20 km/s).

**References:** (1) Schultz, P.H. and Gault, D.E. (1986) *Lunar and Planet. Sci. XVII*, 777-776, LP1, Houston. (2) Schultz, P.H. and Gault, D.E. (1987) *Lunar and Planet. Sci. XVIII*, (this volume) LP1, Houston. (3) Hodges, C.A. (1978) *Lunar Planet. Sci. IX*, 521-522, LP1, Houston. (4) Croft, S.K. (1983) *J. Geophys. Res.*, 88, B71-B89. (5) Carr, M.H. (1986) *Icarus*, 68, 187-216. (6) Schultz, P.H. (1976) *The Moon*, 15, 241-273. (7) Gault, D.E. and Wedekind, J. (1977) In: *Impact and Explosion Cratering* (D. Roddy et al., eds), 1231-1244, Pergamon, N.Y. (8) Schmidt, R. and Holsapple, K. (1982) *Geol. Soc. Am. Sp. Paper 190* (L. Silver and P. Schultz, eds), 93-102. (9) Ahrens, T.J. and O'Keefe, J.D. (1977) In: *Impact and Explosion Cratering* (D. Roddy et al., eds), 639-656, Pergamon, N.Y. (10) Gault, D.E. and Baldwin, B.S. (1970) *Trans. Am. Geophys. Union (EOS)*, 51, 342. (11) Pike, R.J. (1977) In: *Impact and Explosion Cratering* (D. Roddy et al., eds), 489-509, Pergamon, N.Y. (12) Pearce, S.J. and Melosh, H.J. (1986) *Lunar and Planet. Sci. XVII*, 652-653, LP1, Houston. (13) Hartmann, W.K. (1977) *Icarus*, 31, 260-276. (14) Hartmann, W.K. et al. (1981) In: *Basaltic Volcanism Study Project*, 1049-1127, Pergamon, N.Y. (15) Leake, M.A. et al. (1981) *NASA TM-84211*, 405-410. (16) Strom, R. et al. (1981) *J. Geophys. Res.*, 86, 8659-8674. (17) Pike, R.J. (1986) In: *Mercury* (preprint), U. Ariz. Press.

TABLE I. TRANSITION DIAMETERS (km)

	CRATER SHAPE*		MORPH**		STATS†
	Observed D <sub>i</sub>	Calculated ΔD <sub>i</sub>	D <sub>i</sub>	ΔD <sub>i</sub>	
Mercury	5.6	5-15	6.7	7-18	10 (14)
Venus	-	-	2.2	2-5	-
Earth	2	2-4	1.9	2-4	3 (4)
Moon	10	10-15	(10)	10-17	19 (21)
Mars	4	4-10	3.8	3-5	5 (10)
Ganymede	-	-	8	8-14	-

\* Diameter/depth transitions for mean value  $\bar{D}_i$  and range in values  $\Delta D_i$  from (17). Calculated values are based on the mean impact velocities for asteroidal impacts with the range ( $\Delta \bar{D}_i$ ) from the range in velocities for different types of impactors. Calculations are based on impact velocities given in (4,14) and were normalized to 22 km/s for the Moon.  
\*\* Mean diameter and largest simple crater (parentheses) from (11)  
† Inflection in crater statistics from -3 to -2 slope for larger post-mare craters.

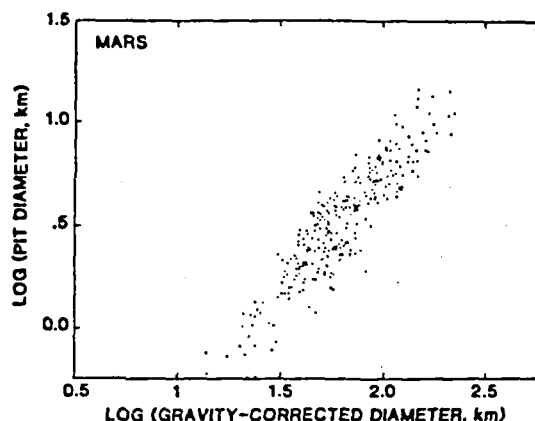


Figure 1. Diameter of central pit on Mars as a function of crater diameter adjusted for gravity.

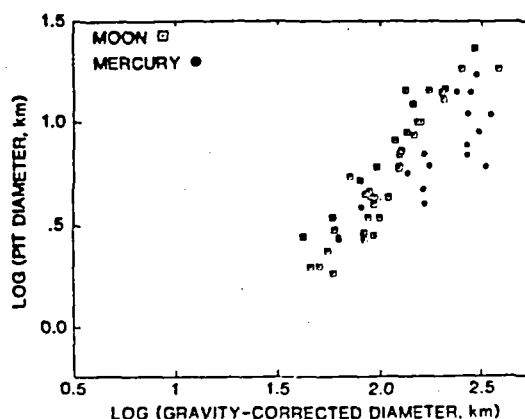


Figure 2. Diameter of central pits on the Moon and Mercury versus gravity-adjusted crater diameter.

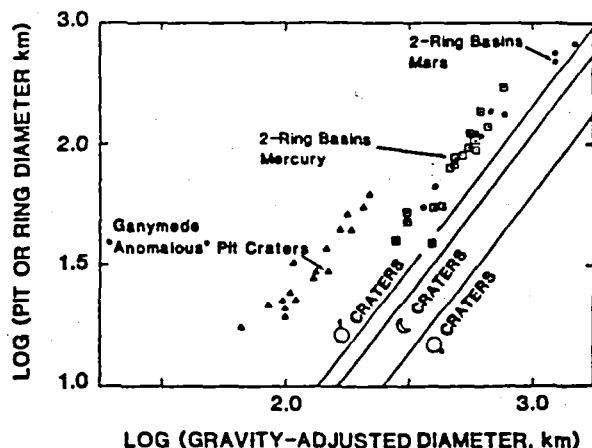


Figure 3. Diameter of inner ring as a function of basin diameter, adjusted for gravity. Also shown are the anomalous pit craters on Ganymede from (4).

TABLE II. PREDICTED RELATIVE VELOCITY\*

	PREDICTED RELATIVE VELOCITY*			DERIVED VELOCITY**	
	PARABOLIC COMETS	PERIODIC COMETS	ASTEROIDS	RELATIVE	ABSOLUTE (km/s)
Mercury	4.0	2.0	1.5	1.5 (0.67)	33 (15)
Venus	2.8	2.0	1.2	-	-
Earth	2.4	1.9	1.1	-	-
Moon	2.4	1.8	1.0	1.0	22
Mars	1.9	1.1	0.86	0.83 (0.67)	18 (15)
Ganymede	1.2	0.74	0.68	0.37	8.1

\* Relative to Earth-crossing asteroids impacting the Moon ( $v = 22$  km/s) from (14).

\*\* From pit diameters and scaling relations.

Values in parentheses are for 2-ring impact basins.

Ganymede estimates are for "anomalous" pit craters only (4).

**TRANSITION DIAMETERS FOR CRATER SHAPE IN LABORATORY EXPERIMENTS  
AND ON PLANETS** P.H. Schultz, Geological Sciences, Brown University, Providence, RI 02912  
and D.E. Gault, Murphys Center of Planetology, Box 833, Murphys, CA 95247

Laboratory experiments indicate that impact craters in granular targets become shallower as projectile penetration time increase (1, 2, 3). Further analysis has characterized specific domains and transitions for crater aspect ratios ( $D/d$  for diameter,  $D$ , and depth,  $d$ ) as functions of a wide range of projectile/target parameters: impactor velocity ( $v$ ), size (mass,  $m$ , radius,  $r$ , or length,  $l$ ), density ( $\delta_p$ ), strength ( $Y_p$ ), shape ( $2r/l$ ), sound speed ( $c_p$ ); and target density ( $\delta_t$ ), sound speed ( $c_t$ ), porosity ( $P$ ), grain size ( $a$ ), and strength ( $Y_t$ ). Impacts into non-porous ductile targets reveal similar systematic changes in the aspect ratio for impact velocities from 6 to 11 km/s. These results have potentially important implications for crater excavation depths, dimensional scaling relations, crater morphology, and flux rates derived from observed crater diameters on the planets.

**Granular Targets:** Crater aspect ratio and impactor parameters follow three distinct relations. For a *given* projectile impacting a *given* target,  $D/d$  increases with increasing impact velocity until exceeding the target sound velocity. Thereafter  $D/d$  varies inversely with  $v$ . Above a critical velocity, however,  $D/d$  varies directly as  $v^2$ . This systematic change in the aspect ratio occurs over a wide range in projectile sizes and compositions and can be shown to be related to projectile size divided by the impact velocity, which is related to the time for projectile penetration (2, 3). Figure 1 illustrates the different relations between crater aspect ratio and  $2r_e/v$  where  $r_e = (m/\delta_p)^{1/3}$ . The crater aspect ratio in the low velocity regime (Regime A, Figure 1a) reflects the effect of compression in porous targets and depends on the momentum/area or  $\delta_p l v$ . After maximum pore compaction is achieved,  $D/d$  varies inversely as  $\delta_p (2r_e/v)$ . The quantity  $\delta_p (2r_e/v)$  can be viewed as the penetration time or as the ratio between momentum/area divided by the specific kinetic energy ( $KE/m$ ). In this domain (Region B) projectile deformation and comminution are observed. Undeformed projectiles will follow this relation provided that  $v > c$ ; conversely, deformed projectiles will still vary as in A if  $v < c$ . Data in Region C generally exhibit less scatter if  $D/d$  depends on the  $\pi_2$  parameter (4), but the specific power-law relation depends on the style of failure of the projectile in a given target: brittle impactors typically exhibiting little change in the aspect ratio with increasing impact velocity. For fine-grained (No. 24) targets, the dependence in Region B can be more generally expressed as  $\eta = (2r_e/v)(c_p/c_t)(\delta_p/\delta_t)(2r/l)$  which includes a shape factor and ratios of projectile/target sound speed and density (Figure 2). The transition from B to C is labeled  $\eta_c$ .

Coarse targets (No. 6-8 mesh sand) exhibit considerable scatter and little dependence between  $2r_e/v$  and  $D/d$  for large values of  $2r_e/v$ . This can be interpreted as the result of individual grain disruption as sand grain size exceeds projectile size. Such an interpretation is supported by comparisons of data with similar ratios between projectile and average grain size. The increase in  $D/d$  with decreasing  $\pi_2$  more generally may reflect internal energy losses by comminution since it has been documented that impact-induced failure of brittle spheres increases with increasing specific energy,  $KE/m_g$  where  $m_g$  is the mass of the sphere (5, 6). Moreover, data reveal that the increase in aspect ratio primarily reflects a constant scaled depth ( $d/r$ ) with increasing impact velocity while the scaled diameter increases as  $\pi_2$ .

**Ductile Targets:** Data for various non-porous, ductile targets have been re-examined in order to determine if similar changes in crater aspect ratio occur. Impacts by polyethylene and aluminum projectiles over a wide range of sizes (0.159 cm - 1.27 cm) into hard and soft aluminum targets from 2-11 km/s (7, 8) have been compared with polyethylene into polyethylene impacts (7). For a Al-Al impacts, the crater aspect ratio rapidly decreases with increasing velocities until about 3 km/s. Between this velocity and the target sound speed, the aspect ratio increases or plateaus. This "knee" has been attributed to a change in cratering physics from compression to hydrodynamic flow (8). At higher velocities (6-11 km/s),  $D/d$  increases as  $2r_e/v$  provided that  $\delta_p r v$  is below a critical value; however, aluminum targets (1100-0) exhibit an inverse relation. Data for different combination of projectiles and impactors coincide if the same dimensionless ratios used to describe  $\eta_c$  for granular targets are multiplied by the target yield strength for 6-11 km/s



# CRATER SHAPES

P. Schultz and D. Gault

impacts. Moreover, the three regimes described for granular targets apply for ductile targets except for velocities well below  $c$  (Figure 1b).

**Discussion:** The similarity in crater shape dependences for non-porous and porous targets indicates that the observed late-stage aspect ratio is controlled by the early-time transfer of energy and momentum. Since the cratering flow field is controlled by shock rarefaction at the free-surface, the observed change in the aspect ratio may reflect a transition from an extended shock wave profile (including perhaps elastic precursors) controlled by projectile-penetration time to the "instantaneous" point-source analogy implicitly incorporated in the  $\pi_2$  analogy (4).

The critical value  $\eta_c$  for gravity-controlled granular targets can be more generally expressed as  $\eta_c(Y_g/\delta_t u^2)$  where  $Y_g/\delta_t u^2$  is a dimensionless strength ratio, including both the lithostatic overburden ( $Y_g = \delta_t g y$ ) for gravitational acceleration ( $g$ ) and depth ( $y$ ) and the limiting cratering flow field velocity ( $u$ ). Because  $y$  is proportional to  $D$  and  $u$  depends on  $D^{1/2}$ , the dimensionless strength parameter simplifies to  $k g$ . If this result is combined with scaling relations  $D/r$  using the  $\pi_2$  parameter (4), then it can be shown that the transition diameter between a near constant  $D/d$  and  $D/d$  increasing with  $2r_e/v$  is simply expressed as:  $D_t = k v^{1.12}/g$ . This expression can be used to accurately compare the  $D/d$  transitions for different planets (9) and provides a new perspective for interpreting changes in crater shape, morphology, and statistics (10).

- 1) Schultz, P.H. and Gault, D.E. (1985) *J. Geophys. Res.* 90, 3701 - 3732. 2) Schultz, P.H. and Gault, D.E. (1985) *Lunar Planet. Sci.* XV, 742 - 743, LPI, Houston. 3) Schultz, P.H. and Gault, D.E. (1986) *Lunar Planet. Sci.* XVI, 777 - 778, LPI, Houston. 4) Schmidt, R. and Holsapple, K. (1980) *J. Geophys. Res.* 85, 235 - 252. 5) Gault, D.E. and Wedekind, J. (1969), *J. Geophys. Res.* 74, 6780. 6) Cintala, M.J. and Horz, F. (1984) *Lunar and Planet Sci.* XV, 158 - 159. 7) Le Comte, C.L. and Schaaf, R. (1966) in *Fluid Dynamic Aspects of Space Flight*, 315 - 330, Gordon & Breach, NY. 8) Debardo, B.P. and Nysmith, C.R. (1966) in *Fluid Dynamic Aspects of Space Flight*, 389 - 402, Gordon & Breach, NY. 9) Pike, R.J. (1987) *Mercury* (preprint) U. Arizona Press. 10) Schultz, P.H. (1987) *Lunar Planet. Sci.* XVIII, (this volume).

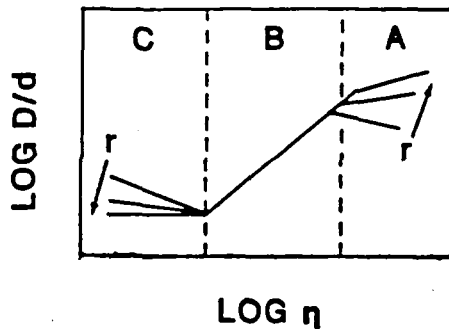


Figure 1a. Different relations between diameter ( $D$ )/depth ( $d$ ) and projectile-diameter ( $2r$ )/impact-velocity ( $v$ ) for sand targets. Region A reflects drag-controlled penetration; B, rate-dependent energy-momentum transfer; C, point-source energy-momentum release and internal energy losses by comminution.

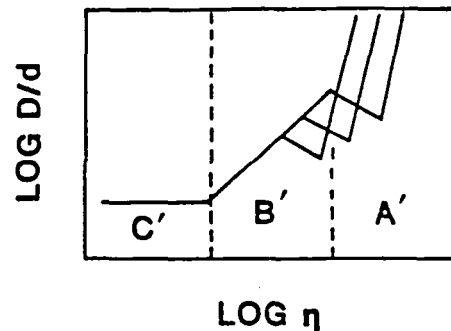


Figure 1b. Different relations between  $D/d$  and  $2r/v$  for non-porous ductile targets. Region A includes non-hydrodynamic compression cratering with a transition zone as impact pressure exceeds target strength; B, hydrodynamic cratering and rate-dependent energy-momentum transfer; C, hydrodynamic cratering and point-source transfer.

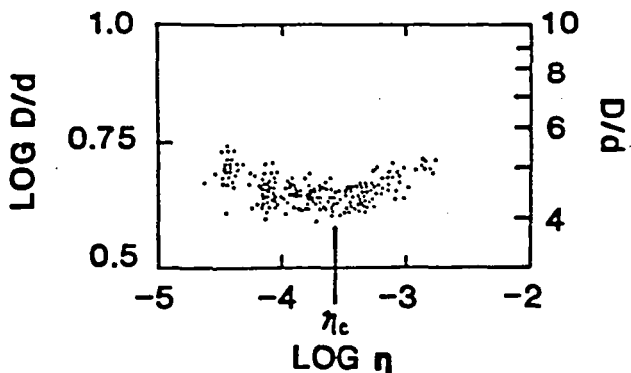


Figure 2. Diameter ( $D$ ) to depth ( $d$ ) ratio as a function of penetration time multiplied by projectile/target ratios of sound velocity and density for impacts by Al, Fe, Pb, and pyrex spheres into No. 24 sand.

**Introduction:** Exploratory experiments previously revealed that oblique impacts into dry-ice enhance the production of a self-luminous cloud recorded in high-frame rate cameras (1, 2). Continued experiments and analysis have quantified the nature and efficiency of this process through a variety of complementary approaches. First, expansion of the vapor cloud permits deriving an estimate of the internal energy and amount of vaporization. Second, direct pressure measurements during and after passage of the cloud provides an independent estimate of vaporization. Third, spectra reveal the composition and state of the luminous vapor. And fourth, measurements of electromagnetic emissions provide new information about the ionized state and perhaps structure in the cloud. Results from the last approach are reported elsewhere (3).

**Experimental Conditions:** All experiments were performed at the NASA-Ames Vertical Gun Range using the two-stage hypervelocity launch facility. Aluminum spheres (0.635 cm diameter) were launched from 2-8 km/s into both dry-ice blocks (20 x 20 x 4 cm) and sand under different atmospheric pressures and compositions with impact angles from  $7.5^\circ$  to  $90^\circ$ . Beckman-Whitley (35,000 fps) and Nova (8000 fps) cameras were used to record the events.

**Impact Vaporization:** Under low atmospheric pressures, two different self-luminous clouds are observed for low-angle ( $15^\circ$ ) impacts. The first component travels downrange at about the velocity of impact while expanding at about half the impact velocity. Small (1-2 cm) spikes generally lead the cloud and may represent ricocheted fractions of the projectile. The second component forms a less brilliant hemispherical cloud rapidly expanding above the point of impact. Taylor (4) derived a simple expression relating the time history of a fireball to the source energy as shown in Figure 1. The constant K depends on the atmospheric density, ratio of specific heats ( $\gamma$ ) pressure, and temperature. From approximations (4), the value of K can be given as a function of  $\gamma$  which depends on the composition of the fireball. In the impact experiments both air ( $\gamma = 1.4$ ) and argon ( $\gamma = 1.7$ ) were used. Although  $\gamma$  will change throughout expansion, it was shown to be reasonably constant (or behaved as though constant) at late times when  $5/2 \log R$  increases as  $\log t$  for the radius (R) of the cloud at time, t. Consequently, solution to the equation in Figure 1 was possible only after about 0.2 ms.

Figure 2 reveals that the fraction of energy in the self-luminous cloud increased with increasing velocity and approached 30% at 6 km/s which corresponds to about 20 projectile masses. Preliminary results indicate the vaporized mass fraction increases as  $v^{5.4}$ . Figure 2 shows that without dry ice, the fraction of energy in the observed self-luminous cloud was 100 times lower; the nature of this cloud is uncertain. Vertical impacts were 10 times less efficient with or without an atmosphere in contrast with previous impressions based just on the cloud intensity (1). Preliminary results indicate that lower impact angles are also less efficient (Fig. 2).

Independent estimates of the vapor fraction were made by direct monitoring of pressure in the chamber during and after impact. Pressure measurements used an ultrasonic (40kHz) emitter/detector. Sound amplitudes, which varied nearly linearly with pressure over the experimental range (1 mm to 20 mm, Hg) yielded measurements with a time resolution of 25  $\mu$ s. During passage of the downrange cloud, pressure increased to about 20-30 mm but quickly reduced to a steady value of 1 mm (200 ms). The record is believed to indicate a measure of the total vaporized dry-ice fraction prior to the effects from the launch tube since impacts without dry-ice produced no measurable change over the same time. If the 1 mm is assumed to occupy the entire impact chamber, then the amount of released  $\text{CO}_2$  exceeds 70 projectile masses. The difference in results is believed to reflect effects of additional  $\text{CO}_2$  released by spalled fragments.

Spectra showed that the brilliant downrange vapor cloud contained strong emission lines of aluminum oxide, AlO. In order to avoid possible contamination by air, the impact chamber was evacuated to 5 mm (Hg) of air, refilled to 100 mm of argon, and re-evacuated to 5 mm. Consequently, it is believed that the AlO resulted from impact-vaporized dry ice reacting with Al melt (or vapor?). Impacts into dry-ice at low velocities ( $<3$  km/s) and into sand only at high velocities (6 km/s) produced no identifiable spectra. Further experiments are planned in order to characterize further the interaction between projectile and target.

**References:** (1) Schultz, P. and Gault, D. (1985) *Lunar and Planet. Sci. XVI*, 740-741, LPI, Houston. (2) Schultz, P. and Gault, D. (1986) *Lunar and Planet. Sci. XVII*, LPI, Houston. (3) Crawford, D. and Schultz, P.H. (1987) *Lunar and Planet. Sci. XVIII* (this volume), LPI, Houston. (4) Taylor, G. (1951) *Proc. Royal Soc. Ac. 201A*, 175-186.

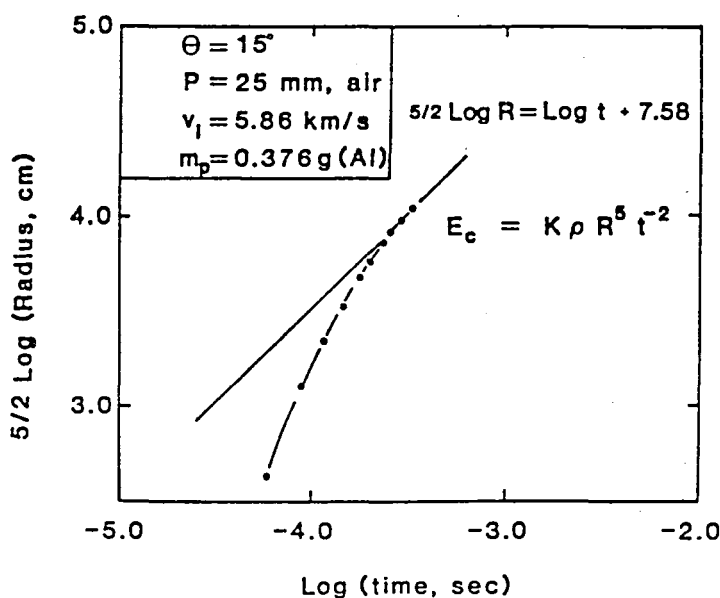


Figure 1. Radius of self-luminous vapor cloud above impact point as a function of time. Vapor cloud produced by the impact of an aluminum sphere (see insert) into a dry-ice block at  $15^\circ$  from the horizontal. When the cloud grows as  $0.4 \log t$ , it can be used to estimate the equivalent source energy following the blast-wave solution of Taylor (4).

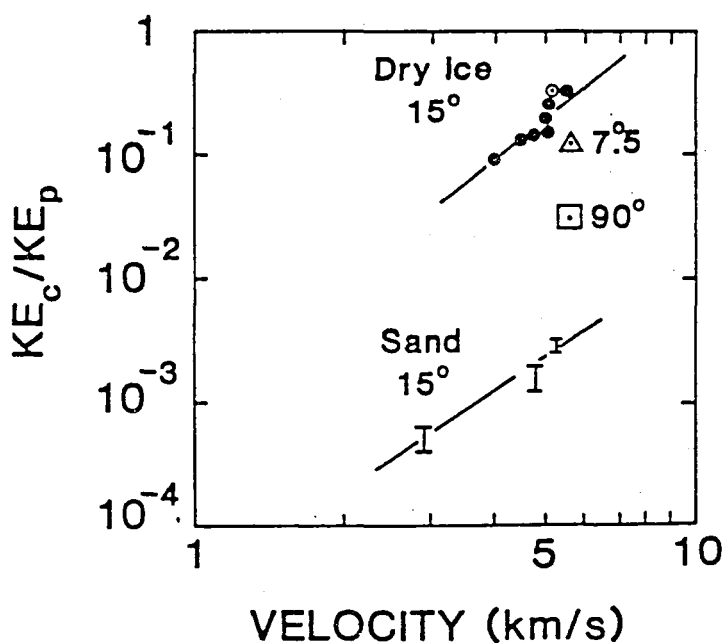


Figure 2. Energy partitioned to the self-luminous cloud relative to impactor kinetic energy as a function of impact velocity for  $7.5^\circ$ ,  $15^\circ$ , and  $90^\circ$  from the horizontal. Atmospheric pressure in impact chamber was typically  $< 25$  mm (Hg) with one exception indicated by circle ( $700$  mm, Hg, of argon).

### Experimental Studies on the Impact Properties of Water Ice

Frank G. Bridges, D.N.C. Lin, Artie P. Hatzes and John S.B. McDonald  
Boards of Studies in Physics and Astronomy and Astrophysics, UCSC

#### **I. Coefficient of Restitution Measurements**

For the past several years we have been undertaking an experiment to study the impact properties of water ice. Our experimental apparatus consists of an ice sphere mounted on a disk pendulum and contained in a stainless steel cryostat. The position of the ice sphere before, during, and after a collision with an ice brick is measured with a capacitive displacement device. With this setup we have been able to achieve measurable impact velocities as low as  $0.015 \text{ cm s}^{-1}$  and temperatures as low as  $85^\circ\text{K}$ . We have completed the first phase of experimental studies which consists of measurements of the coefficient of restitution as a function of velocity, surface geometry, and surface conditions. We have been able to obtain accurate measurements of the coefficient of restitution for ice spheres impacting with velocities in the range  $0.015$  to  $2. \text{ cm s}^{-1}$ . The coefficient of restitution as a function of velocity,  $\epsilon(v)$ , for ice spheres with four different radii of curvature ( $R = 2.5, 5, 10, 20 \text{ cm}$ ) and with a variety of surface conditions has been obtained. Our coefficient of restitution data can be well fit by an exponential law of the form  $\epsilon(v) = Ce^{-\gamma v}$ , where  $\gamma = 0.41 - 0.01R$ . We find, however, that the surface conditions of the ice can drastically alter the resulting value of  $\epsilon$ . In particular the presence of frost or a roughened contact surface (via sublimation) can lower  $\epsilon$  at a given velocity by 10-30% from that of a smooth sphere. We also found that the presence of frost can change the velocity dependence of  $\epsilon$  from an exponential to a power law form. The full detail of these results are presented in a forthcoming article in the *Monthly Notices of the Royal Astronomical Society*.

#### **II. Sticking Measurements**

Measurements of the sticking force between the ice sphere and ice brick have been made utilizing an electromagnetic "kicker" which consists of a magnet attached to the pendulum and a solenoid mounted to the base of our cryostat. When the pendulum is in its stationary position the magnet rests in the center of the solenoid. When current is allowed to flow through the coil a force is exerted against the pendulum. After a sticking collision the current in the coil is slowly increased until the bond between the ball and brick is broken. Using a calibrated current versus force curve, the resulting sticking force is obtained.

The experiment has thus far been performed at temperatures of  $150^\circ\text{K}$  and pressures of  $10^{-5}$  torr. It was found that there is no measurable sticking force when the surfaces of the ice ball and ice brick are smooth and clean. However, the sticking force increases appreciably when a layer of frost is present on the contact surface of the iceball. A gas handling system is employed to deposit a layer of frost by blowing water saturated nitrogen gas across the contact surface of the iceball. All of the results to date have been obtained with frosted ice particles. It is suspected that all of the frost that has been applied to the ice particles is of the ice I cubic phase and that at no time during an experiment did the frost go through a phase change.

Our preliminary results indicate that typical sticking forces are between 20 and 50 dynes but that sticking forces as high as several hundred dynes has been observed. We find that the magnitude of

the sticking force is dependent on the collision history of the particle. The largest sticking forces have been measured for collisions occurring after a fresh layer of frost has been deposited on the sphere and the smallest forces after the ice sphere has undergone several high velocity impacts. Figure 1 shows typical data collected for a sticking run. It gives the sticking force as a function of collision number. Also indicated is the impact velocity of the ice sphere prior to sticking. There are several interesting features to note about this figure. First the sticking force is a factor of 3-5 greater for intermediate velocity collisions ( $v \sim 0.1$  cm/sec) than for low velocity collisions. Also, after a high velocity impact ( $v \sim 1$  cm/sec) no further sticking was observed. Evidently the magnitude of the sticking force is highly dependent on the surface structure of the layer of frost. Intermediate velocities seem to maximize the area between the two surface areas responsible for the cohesive bonds. The high velocity collisions serve to effectively destroy this structure resulting in a greatly reduced cohesive force.

It also appears that the sticking force can be approximated by a linear spring attached to the surface of the ice sphere and acting over a limited distance. Figure 2 shows the displacement versus time for an ice sphere impacting at a velocity of  $0.09 \text{ cm s}^{-1}$  and which remains bonded to the brick after the collision. The ice sphere undergoes damped harmonic motion before coming to a rest 13 microns (approximate thickness of frost layer) above the surface of the ice brick. From the period of oscillation we derive an effective spring constant of  $3 \times 10^5 \text{ dynes cm}^{-1}$ . Current work centers on obtaining an independent measure of this spring constant by using a computer to slowly ramp up the current applied to the solenoid. At the same time the computer will be measuring the displacement of the pendulum. This current (force) displacement relationship should be a linear one while the ice sphere is in the range of the force.

### III. Mass Transfer Measurements

Dynamics of planetary ring environments also depend on the erosion processes between the individual constituent particles. Experimental determination of the mass transfer in collisions is important to the development of accurate ring dynamics theories. We also have carried out measurements of the mass transferred between water ice particles during low velocity collisions that are relevant to icy particle disk systems. The experiment was conducted at about  $160^\circ\text{K}$ . Ice particles of 2.5 cm radius were collided with a massive ice brick at velocities near  $0.5 \text{ cm s}^{-1}$ . Fluorescent dyes were used to measure the miniscule transferred mass between the ice particles. Preliminary results indicate that the mass accreted per collision is about  $5.0 \times 10^{-8}$  grams of water for smooth ice surfaces and  $1.0 \times 10^{-7}$  for ice with a roughened surface. The amount of fluorescent dye transferred reached a rough equilibrium after many collisions for the two initial ice surface conditions studied. For smooth ice surfaces, total dye transfer reached an equilibrium corresponding to  $\sim 1.0 \times 10^{-6}$  grams after 40 collisions. The amount of dye transferred by the rough ice surfaces also saturated after 40 collisions but at a much higher value corresponding to  $\sim 1.4 \times 10^{-5}$  grams. Figure 3 shows the results of our data for roughened ice spheres. Attempts will be made to apply interpretations of the data to icy particle disk systems such as Saturn's rings and the solar nebula. The results described here may extend overall evolutionary time scales for ring systems and icy nebulae in general.

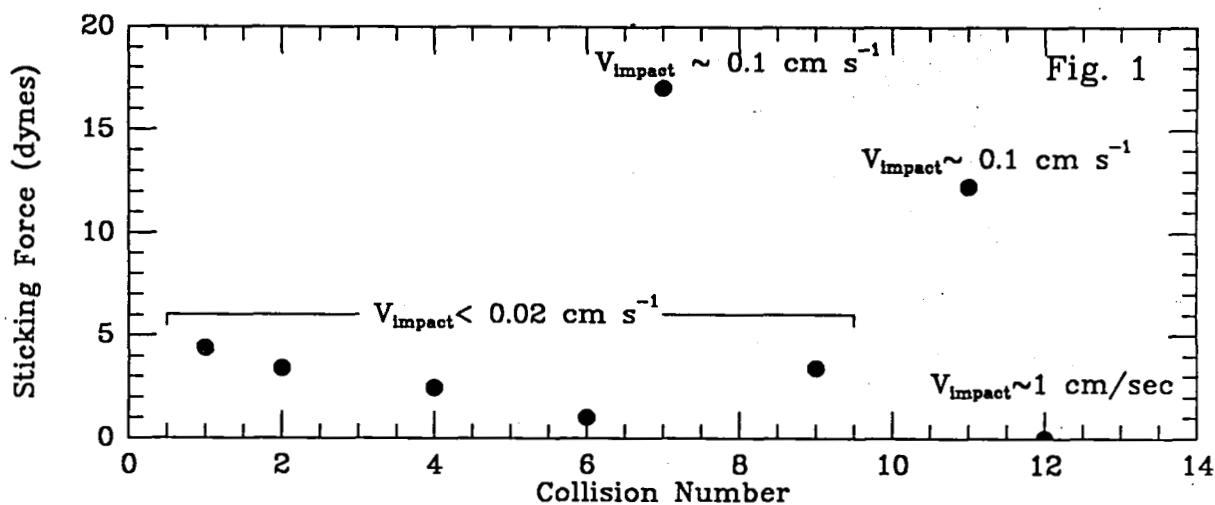


Fig. 1: The sticking force for a frost covered ice sphere as a function of collision number. The approximate velocity of the impact is also shown.

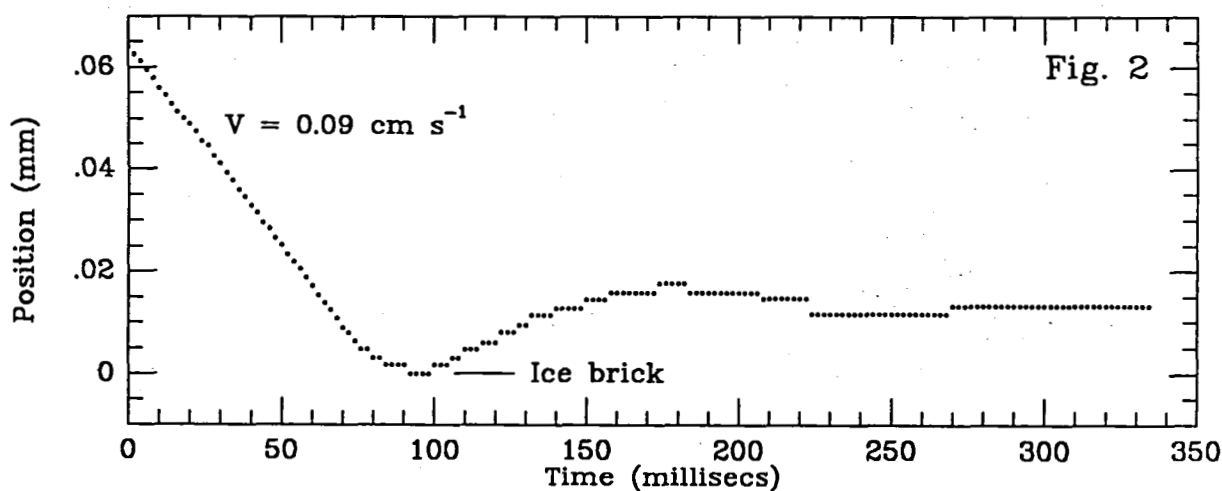


Fig. 2: The position of an ice sphere as a function of time for a sticking collision.

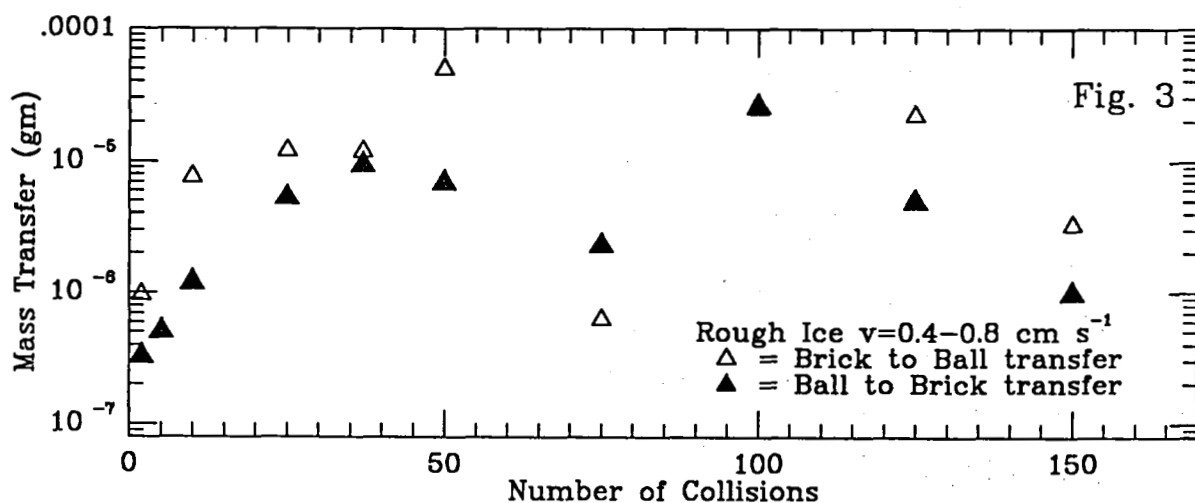


Fig. 3: Mass transfer from ice ball to brick and brick to ball as a function of the number of collisions.

## CRATER STUDIES ON THE ICY SATELLITES AND MERCURY

Paul M. Schenk, Andrew C. Leith, and William B. McKinnon, Department of Earth and Planetary Sciences and McDonnell Center for the Space Sciences, Washington University, Saint Louis, MO 63130.

### *Depth/diameter measurements of craters on Uranian and Saturnian satellites: Preliminary results*

Crater depth/diameter values for the intermediate-sized Uranian and Saturnian satellites Ariel, Umbriel, Titania, Oberon, Mimas, Tethys, Dione and Rhea have been measured using both photoclinometry and shadow measurements. Photoclinometric depths of simple craters on Ariel, Mimas, Dione and Rhea are 25 to 50% shallower (at 9 km diameter) than simple lunar craters (Fig. 1). Shadow measurements of simple craters on Mimas and Rhea indicate that much of this difference may be real and not due to the photoclinometric technique. Least-squares fits to the depth/diameter data for complex craters on the six satellites examined to date have slopes ranging from 0.5 to 0.8 (Fig. 1; except Ariel and Umbriel where the data is particularly noisy), substantially higher than for any of the terrestrial planets [1]. Simple-to-complex transition diameters for Titania, Oberon and Umbriel, for which only complex craters are distinguishable, were calculated assuming the least-squares fit to simple craters on Ariel. Within the approximate margin of error due to scatter in the data, transition diameters for Dione, Umbriel, Ariel, Titania and Rhea follow an inverse gravity trend (Fig. 2).

	Mimas	Tethys	Dione	Umbriel	Ariel	Rhea	Oberon	Titania
Transition diam. (km)	14.2	12.1	17.5	15.5	16.4	9.0	2.4	3.4
Surface gravity (cgs)	6.5	18.5	22.4	22.9	28.7	28.5	33.0	36.2
Number of craters	25	16	39	26	35	65	13	34

Mimas, and perhaps Oberon and Titania, may be somewhat below this trend (Fig. 2). Crater collapse on the icy satellites begins at smaller diameters than would be expected from simple extrapolation of the terrestrial transition diameter trend [1], supporting conclusions based on central peak studies [2].

Collapse, as a function of crater diameter, does not appear to take place to the same degree as in terrestrial craters, however, consistent with the poor development of terraces on these satellites. This suggests there may be a fundamental difference in the crater modification process relative to the terrestrial planets, a question that requires further investigation. Measurements of craters on Miranda and Ganymede are in progress.

### *The post-impact strength of the Mercurian crust as estimated from slump terrace widths*

The strength of the Mercurian crust immediately after impact is estimated from the widths of the outermost slump terraces of craters, using the equation  $w = c / \rho g ((1 + 16\lambda^2)/16\lambda^2)$  where  $c$  = yield strength,  $w$  = terrace width and  $\lambda$  is the crater depth/diameter ratio [3]. This approach is similar to that used by Pearce and Melosh [4] for the Moon. The width of the outermost terrace is used, because reconstruction of crater geometry prior to slumping is easier for the outer terrace than for those closer to the centre of the crater; also the outer terrace has been subject to lower shock pressures than the others and could yield more consistent values from one crater to another. The assumed density is  $3.0 \text{ g/cm}^3$  and  $g$  is  $3.7 \text{ m/s}^2$ . Crater depths were taken from [5]. In cases where our estimate for the diameter of a crater differed from that of [5], the depth was scaled to our diameter using relations in [1]. Fig. 3 diagrams the method used to construct crater depth prior to slumping of the outer terrace. A val-

ue of  $30^\circ$  was assumed for  $\phi$  from previous measurements of lunar craters [4, 6];  $10^\circ$  was used for  $\theta$  [7]. Fig. 4 shows that there is a fairly wide distribution of strengths with the majority falling in the 1-2 Mpa range. This implies that the crust of Mercury post-impact is not any stronger than that of the Moon. If anything Mercury's crust appears to be the weaker of the two. A different approach for evaluating rim flank slopes was used in [4], however. If our slope values are used on lunar craters the yield strength values for the Moon and Mercury turn out to be similar. Crater 80 (Brahms) in Fig. 4 may be anomalous as its outer terrace is not its widest. Thus while the estimated post-impact strength of Mercury is subject to a large degree of uncertainty (Fig. 4 is based on 14 craters), and will vary with the size distribution of craters measured, comparison with the lunar study (4) suggests that there may not be much strength difference between the immediate post-impact surfaces of Mercury and the Moon. Assuming  $\rho g H/c = 7$  to be a criteria for the start of wall collapse, this study implies that the change in slope of a depth-diameter plot for Mercurian craters should occur near a diameter of 5 km, consistent with the newer depth-diameter estimates in [8].

REFERENCES: [1] Pike, R.J. (1980) *Proc. Lunar Planet. Sci. 10th*, 2159-2189; [2] Chapman, C.R., and W.B. McKinnon (1986) In *Satellites* (Univ. of Ariz.), 492-580; [3] Melosh, H.J. (1977) In *Impact and Explosion Cratering* (Pergamon Press), 1245-1260; [4] Pearce, S.J., and H.J. Melosh (1986) *Geophys. Res. Lett.* 13, 1419-1422; [5] Malin, M.C., and D. Dzurisin (1977) *J. Geophys. Res.* 82, 376-388; [20] Settle, M., and J.W. Head (1979) *J. Geophys. Res.* 84, 3081-3096; [7] Grieve, R.A.F., and J.B. Garvin (1984) *J. Geophys. Res.* 89, 11561-11572; [8] Pike, R.J., and G.D. Clow (1983) NASA Tech. Mem. 86246, 104-106.

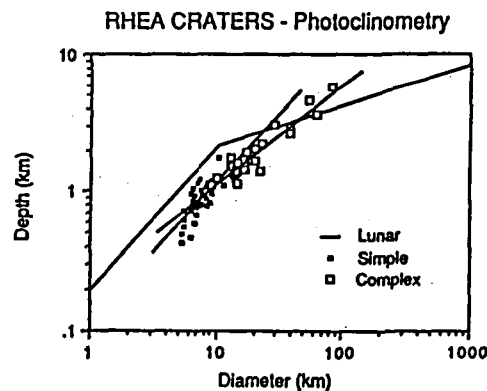


Figure 1. Depth/diameter plot of craters on Rhea. Bent line is fresh lunar crater data from [1]. Least-squares fits are drawn through simple and complex data.

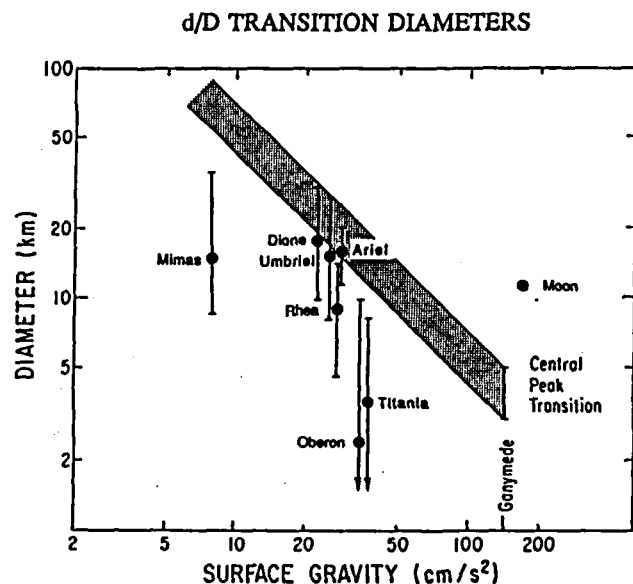
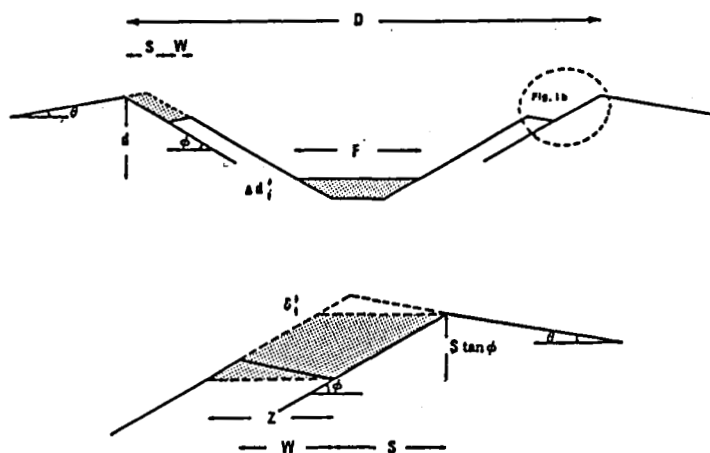
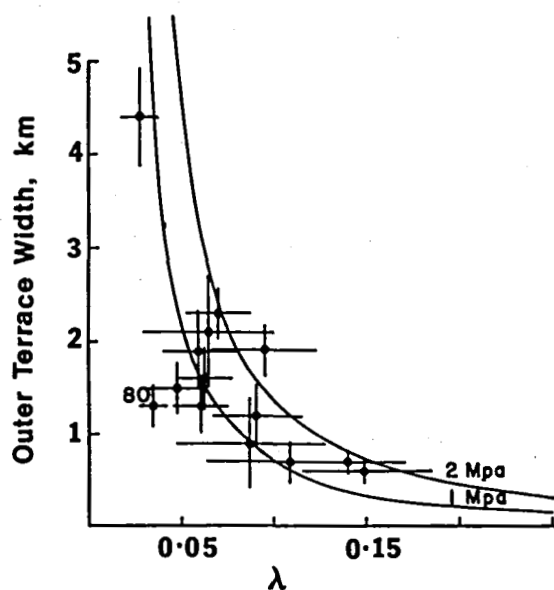


Figure 2. Simple-to-complex transition diameters vs. gravity for icy satellites, from depth/diameter inflection points. Stipled area is extrapolation of central peak transition diameter for Ganymede [2]. Titania, Oberon and Umbriel points from intersection with Ariel simple crater fit.





**Figure 3.** (a) Diagram of the measurements and parameters used in the calculation of crater depth prior to the collapse of the outer terrace. The shaded material lost from the rim is equated with the shaded material gained by the crater floor. (b) Detail at the crater rim.



**Figure 4.** Outer terrace width versus a reconstruction of crater depth/diameter immediately prior to collapse of the outer terrace. The theoretical curves are derived using  $\rho = 3.0 \text{ g/cm}^3$  and  $g = 3.7 \text{ m/s}^2$ . Crater 80 (Brahms) is discussed in the text.

## **Icy Satellites: Cratering and Volcanism**

Steven K. Croft, Lunar and Planetary Laboratory, University of Arizona, Tucson, Arizona 85721

*I. Crater Populations:* Extensive new crater counts have been carried out on Ganymede and Callisto, including global compilations of all craters  $\geq 30$  km on Ganymede and  $\geq 40$  km on Callisto, to obtain the following objectives: 1) to establish the most accurate crater size distribution curves possible with Voyager imagery, particularly at large diameters, 2) to investigate the origin(s) of the cratering populations in the Jovian system, and 3) to investigate the chronology and extent of volcanic activity on Ganymede (section III below). The new size distribution curves are similar to those of (1) and (2) between  $\sim 15$  and 70 km on Ganymede, and confirm the extension of the  $\sim -2$  log slope to smaller diameters suggested by (2). Likewise the distribution for Callisto below  $\sim 70$  km is similar to that of (1) and about  $2 \frac{1}{2}$  higher in density than Ganymede's dark terrain. At diameters above  $\sim 70$ , however, the curves are more complete and with somewhat higher densities than found by (1), and virtually identical in shape and overall density on both satellites.

A leading-trailing asymmetry of  $\sim 4:1$  has been established for craters  $> 30$  km in diameter on Ganymede. The asymmetry disappears for craters  $< 20$  km (3). There is no pole-equator asymmetry. Also, as between Ganymede and Callisto, the crater density for craters  $> 60$  km is nearly identical between the light and cratered dark terrains on Ganymede. The density difference of  $\sim 2$  between the light and dark terrains noted previously (1,4) develops for craters  $< 60$  km (which comprise the vast majority). Detailed crater counts on Callisto along the Voyager 1 and Voyager 2 terminators and craters  $> 25$  km in the Voyager 1 hemisphere show neither pole-equator variations nor any non-random regional variations except around Valhalla. These observations are interpreted to indicate the existence of two separate crater populations in the Jovian system: 1) a population external to the system responsible for the large craters on both satellites which has dominated the cratering record since about the time of light terrain emplacement on Ganymede, nominally 3-4 billion years ago. The presence of pits in these craters presumably related to impact melting and vaporization is consistent (5) with the high impact velocities ( $> 10$  km/sec) characteristic of external populations compared to the low impact velocities of internal populations ( $\sim 2-3$  km/sec). 2) A population internal to the system which dominated cratering early in the system's history and is the source of most of the small craters on both satellites.

*II. Depth-Diameter Measurements:* Shadow depth measurements have been made for fresh craters on Ganymede, Callisto, Mimas, Enceladus, Tethys, Dione, Rhea, Miranda, Umbriel, and Titania, and correlated with morphologic variations and diameter. Depth/diameter/morphology relations comparable to those on the terrestrial planets are found: simple craters are geometrically similar with depth/diameter ratios of  $\sim 0.1$  to  $0.12$  (somewhat shallower than the  $\sim 0.2$  for terrestrial craters), complex craters are non-symmetrical with log slopes between  $0.3$  and  $0.5$  (similar to terrestrial craters), and the simple/complex transition corresponds with the change in the depth/diameter ratios. The transition diameters follow the trends previously noted (6,7): a rough inverse correlation with gravity but with smaller transitions at a given gravity than occur on the terrestrial planets. These observations confirm a suggestion made by (8) that the shallow depths

of fresh craters on Ganymede and Callisto in particular are due to impact processes and not to viscous relaxation as suggested by (4). The depth/diameter relations on Ganymede and Callisto do show an inflection near 70 km in diameter characteristic of relaxation, but this is at a substantially larger diameter than allowed by any current theory. Monte-Carlo calculations indicate that theoretical relaxation times must be increased  $10^2$  to  $10^3$  times to be consistent with observations. This increase must be accounted for by some combination of increased effective viscosity over laboratory measurements, decreased radioactivity below chondritic levels, and/or an enormous compression in the cratering time scales, all of which have significant repercussions for other icy satellite studies.

Except at the largest sizes (e.g. Odysseus on Tethys), none of the other satellites show any evidence of viscous relaxation of craters except Enceladus, which shows local collapse indicative of locally high fluxes of tidally generated heat (as on Io).

*III. Resurfacing on Ganymede.* The differences in crater densities between the light and dark terrain on Ganymede indicate different episodes of resurfacing. The range of crater densities on the dark terrain is smaller than on the light, indicating a shorter period of emplacement, usually interpreted as a single global event. Yet variations in density by factors of 2 in adjoining counting areas were reported (9). Further, geologic mapping on Ganymede indicated several areas within the dark terrain differing in albedo and texture. New crater counts (10) were carried out in Galileo, Marius, and Nicholson Regiones specific to the different geologic areas to investigate crater density variations. Significant depletions of smaller craters were found in the dark smooth terrain of Galileo Regio bordering Uruk Sulcus (< 15 km) and in central NE Marius Regio between Thebes Facula and Erech Sulcus (< 25 km). The pattern of the depletions are characteristic of eradication of smaller craters by flooding. The edges of the depleted areas are poorly defined and exhibit no flow fronts at Voyager resolutions, indicating a low viscosity for the flooding material (probably "muddy" water). Thus the dark terrain also had an extensive series of flooding episodes and is not a single, simple geologic unit. New crater counts were also done on light terrain in the polar regions. The north polar area has a substantially lower crater density than the south pole indicating that the polar deposits formed at different geologic times. Thus, there was apparently no "wave of freezing" beginning at the poles and working toward the equator as suggested by (9), but rather episodic flooding unrelated to latitude.

*IV. Volcanic Processes.* The chemical and physical nature of volcanism on the icy satellites is still poorly constrained, thus studies of potential "magmas" and flow morphology and structure have been initiated.

Ammonia-water liquid is a frequently invoked composition for flows on the icy satellites. A new equation of state of ammonia-water liquid has been derived using data from the literature and some new experimental data (11). The equation applies to liquids of 0-100%  $\text{NH}_3$ , between atmospheric and 10 kb pressure, and at temperatures below  $\sim 300^\circ\text{K}$ . Expressions for the density of the three ammonia hydrate solids between  $0^\circ\text{K}$  and their respective melting points have also been derived. The important volcanological result is that the peritectic liquid and solid are very nearly the same density. Thus ammonia-water "magmas" will easily reach the surface at the beginning of differentiation in an ice-rock satellite, but if melting continues and a thick rind of frozen ammonia-water materials forms, later melts will be nearly neutrally buoyant with respect to the rind, resulting in stagnation of melts at shallow depths. Thus later volcanic activity may be largely plutonic, producing

limited surface flooding but possibly extensive tectonics such as groove-like structures due to dike swarms or the formation of large magma chambers.

Experiments on the viscosity of ammonia-water liquids and slushes have also been carried out (12,13). Peritectic ammonia-water liquids are  $\sim 2X$  more viscous than pure liquid  $H_2O$  and  $\sim 10X$  more viscous than pure liquid  $NH_3$  at similar temperatures, implying that ammonia and water molecules interact more strongly with each other than they do with themselves. Ammonia-water slushes show increases of viscosity of several orders of magnitude with only 10-20% crystallization, comparable to the increases in partially congealed silicate lavas. The relatively higher viscosity of the peritectic liquids and pattern of viscosity increase with partial freezing suggest that ammonia-water magmas polymerize in a manner analogous to silicate magmas, allowing the production of a wide range of magmatic viscosities with a concomitantly wide range of morphologies for flows reaching the surface. The possible stagnation conditions due to the neutral buoyancy noted above could allow magma pockets to partially congeal at depth before becoming large enough to extrude onto the surface.

Finally, a fairly extensive analysis of volcanic landforms on Miranda has been carried out (14). Individual flow deposits exhibit raised edges and surface corda comparable to similar features on viscous flows on Earth. Estimates of effective viscosities and Bingham yield stresses on these features indicate properties comparable to terrestrial extrusive flows. In particular, the implied viscosities are  $10^8$  to  $10^9$  poise, about 6-7 orders of magnitude above molecular-liquid viscosities and the same below solid ice viscosities, implying emplacement as partially congealed flows. The source vents are linear fissures rather than circular vents. Terrestrial eruptions begin as fissure flows that rapidly change to circular vents due to both enhanced wall rock erosion at locally wide sectors of the fissure and rapid freezing in narrow sectors. It is suggested that eruptions on icy satellites remain fissure eruptions due to the generally wider and larger cracks expected on small satellites (15), and, if the magmas are ammonia-water liquids, to the lower effective erosion of the presumably largely water-ice fissure walls. Modeling of these processes is in progress.

1. Strom, R.G. *et al.* (1981) *J.G.R.* 86, 8659—8674.
2. Nuekum, G. and S. Pozio (1984) *Lunar Planet. Sci.* XV, p. 601—602.
3. Duxbury, E.D. and S.K. Croft (1987) *Adv. Planet. Geol.*, submitted.
4. Passey, Q.R. and E.M. Shoemaker (1982) in *Satellites of Jupiter*, p. 379—434.
5. Croft, S.K. (1983) *J.G.R. (Supp.)* 88, B71—B89.
6. Pike, R.J. (1982) *Lunar Planet. Sci.* XIII, 627—628.
7. Croft, S.K. (1982) *Saturn, Prog. and Abstracts*, p. 77.
8. Croft, S.K. (1981) *Lunar Planet. Sci.* XII, p. 187—189.
9. Shoemaker, E.M. *et al.* (1982) in *Satellites of Jupiter*, p. 435—520.
10. Croft, S.K. (1987) *Lunar Planet. Sci.* XVIII, p. 209—210.
11. Croft, S.K., J.I. Lunine, and J. Kargel (1988) *Icarus*, in press.
12. Kargel, J.S. (1987) *Lunar Planet. Sci.* XVIII, p. 475—476.
13. Kargel, J.S. and S.K. Croft (1988) *Icarus*, submitted.
14. Croft, S.K. (1987) *Lunar Planet. Sci.* XVIII, p. 207—208, and *Icarus*, submitted.
15. Stevenson, D.J. (1982) *Nature* 298, 142—144.

## DARK RAY AND DARK FLOOR CRATERS ON GANYMEDE

Paul M. Schenk and William B. McKinnon, Department of Earth and Planetary Sciences and McDonnell Center for the Space Sciences, Washington University, Saint Louis MO 63130.

Dark ray and dark floor craters are rare and intriguing classes of craters on Ganymede. Poscolieri [1] originally identified eight dark ray craters, seven occurring on dark terrain and none larger than 40 km in diameter. He thus concluded that these craters reflect target composition, and that dark terrain in particular consists of a rock-ice mixture to a depth of ~4-5 km. This latter conclusion was made despite that the size distribution of bright ray craters on dark terrain was not demonstrably different from that of the dark ray craters. The interspersed bright and dark ray craters also indicated that any subsurface horizontal stratigraphy was discontinuous. No crater locations were given [1]. Hartmann [2] quoted earlier results of [1] of a much more restricted range of dark-ray crater sizes, and argued for a distinct subsurface layer. This interpretation is no longer valid.

Conca identified forty-three "dark-ray" craters [3]. Selection effects were judged negligible for those twenty-one greater than 5 km in diameter, and these were equally divided among the bright and dark terrains that are roughly equally abundant on Ganymede. Conca's spatial distribution is strongly skewed towards the antapex of orbital motion, and increasing areal coverage of low albedo deposits around dark ray craters and decreasing geometric albedo were said to correlate with decreasing distance from the antapex. These observations argued for a magnetospheric role in the creation and maintenance of dark ray deposits; their scarcity and lack of terrain correlation argued for a dominant role for projectile characteristics [3]. Correspondingly, Conca modeled the creation of dark rays as being due to differential sputtering of dirty-ice ejecta by Jovian magnetospheric ions. The contaminant was assumed to be in the form of small particles with volume percentages ranging between  $10^{-5}$ - $10^{-2}$ , and the rays were assumed to be initially bright (albedo = 0.35), decreasing to an albedo of 0.12. A plausible range in contaminant size and volume fraction was found to work, leading to the hypothesis that a rare velocity component of the projectile population could suffice as well as one of rare composition. Shoemaker et al. [4] further argue that insolation-driven sublimation as well as sputtering play a role in dark ray formation.

We have reexamined dark ray craters on Ganymede, and find that there are at least two distinct classes: dark ray craters and dark floor craters. The 25 identified dark ray craters, (the largest of which typically have brighter floors), range in size from 40 km in diameter down to the limit of resolution, and are all found on the trailing hemisphere, equally divided between dark and bright terrain. Most are found in the Tiamat Sulcus quadrangle between  $\pm 25^\circ$  latitude. Three very large (up to 500 km long), overlapping, ancient (by virtue of their irregular appearance), dark ray systems are seen in this quadrangle. One source crater to the south is obscured by younger bright ejecta, one occurs in an unimaged area to the west, and one is probably associated with a dark circular region partially obscured by the young bright crater Tammuz. It would appear that close to the antapex, dark ray craters are not at all rare. Assuming a lunar like scattering law for dark rays gives photometric phase function values intermediate to those of Ganymede dark terrain and Callisto dark terrain [5]. Scaling the slope of the phase function to these values, and using the opposition surge for Ganymede dark terrain [5], we estimate minimum Voyager clear filter reflectances for dark rays of ~0.20. Dark floor craters, on the other hand, are characterized by extremely dark floors (~0.15 clear-filter reflectance, similar to that of Callisto dark terrain); some of these are surrounded by a narrow bright halo and occasionally have dark streamer-like deposits. The 33 dark floor craters are approximately equally divided between bright and dark terrain, and are not concentrated toward the antapex. These craters are probably not of the same origin as dark ray craters. Helfenstein [6] has hypothesized that they are due to the formation of "devolatilized impact melt," presumably meaning a contaminant-enriched surface layer. More than

eleven other dark "something" craters have been identified so far, but they have not been classified due to their small size. Most of these are less than 5 km across and occur on bright terrain, but their small size would make detection difficult on dark terrain. The dark terrain, though, has innumerable small dark regions of uncertain origin.

Voyager orange/violet ratios, incorporating the calibration corrections of Buratti (in[7]), for the three largest dark ray craters Antum, Mir and Kittu, and adjacent terrains are:

	<u>Dark rays</u>	<u>Dark terrains</u>	<u>Bright terrains</u>	<u>Phase angle</u>
Antum	1.38 $\pm$ 0.03	1.34 $\pm$ 0.02	1.32 $\pm$ 0.03	22°
Mir	1.43 $\pm$ 0.03	1.32 $\pm$ 0.03	1.32 $\pm$ 0.03	22°
Kittu	1.29 $\pm$ 0.07	1.49 $\pm$ 0.05	1.44 $\pm$ 0.06	52°

Both Mir and Antum rays are "red" with respect to surrounding terrains (Fig. 1). We note that the brighter floors of these craters are comparatively less "red", as are bright rim and ray deposits on Ganymede [8]. Kittu dark rays are relatively less "red" relative to local terrains, and are less "red" than any other dark ray or dark floor crater (Fig. 1). Of the smaller craters for which we have color measured to date, five are "red", three are "neutral", and two are less "red" relative to surrounding terrains (Fig. 1). There does not appear to be any correlation of color with terrain type or apparent age. Although Voyager wavelengths extend only from 0.35 to 0.65  $\mu$ m, different Voyager colors for various dark rays and dark floors indicate there may be different impacting projectile compositions, if this latter hypothesis is correct. Color differences of this type are not obviously expected if dark rays excavate from a uniform; dark subsurface horizon.

Earth-based spectra of Ganymede [9] and of abundant low-albedo outer solar system bodies [10-13], including C- and D-type asteroids, some "inactive" comets and outer Jovian satellites were convolved with the Voyager band passes for comparison (Fig. 2). D-type asteroids, primarily the Trojan asteroids, and some comets are the reddest of these. None of these, including the D-types, are as "red" as the ground-based Ganymede spectra (Fig. 2), and probably cannot account for the "red" dark-ray colors unless spectrally modified by the Jovian magnetosphere, probably due to magnetospheric sulfur implantation and Fe <sup>+3</sup> absorption [14]. The relatively "bluer" color of Kittu and several of the smaller craters argues against significant alteration of the dark component, however, at least to the extent of turning a Kittu-like ray into an Antum-like ray. The "flat" spectra of C-type asteroids and outer Jovian satellites are compatible with "neutral" or slightly "red" rays and spectrally-modified D-type material may be compatible with the more "red" rays.

If dark-rays are due to projectile contamination, such craters might be expected on Callisto, the other heavily cratered Galilean satellite. The lowest estimated reflectances of Ganymede dark rays and floors are equal to or greater than that of Callisto dark terrain, however, so dark rays should be almost impossible to detect on Callisto. Numerous small dark splotches can be seen on Callisto, but their origin is unclear. We note that ray craters of any type are virtually absent in the Saturn system.

Although it is not possible with Voyager data to uniquely identify source bodies for the formation of dark ray and dark floor craters, their distribution, size range and limited Voyager color measurements suggest that these craters may record the influx of projectiles of differing compositions, and this material may be incorporated into the ray deposits. These craters are prime candidates for higher spatial and spectral resolution observation planned for Galileo. Identification of projectile types would help in isolating projectile source regions and estimating bombardment rates in the Jovian system, and may also provide clues to the source and composition of darkening agents on these predominantly icy worlds.

REFERENCES: [1] Poscolieri, M. (1982) In *Comparative Study of the Planets* (Reidel), 485-494;

[2] Hartmann, W.K. (1980) *Icarus* 44, 441-453; [3] Conca, J. (1981) *Proc. Lunar Planet. Sci. Conf.* 12B, 1599-1073; [4] Shoemaker, E.M., et al. (1982) In *Satellites of Jupiter* (Univ. of Ariz.), 435-520; [5] Squyres, S.W. and J. Veverka (1981) *Icarus* 46, 137-155; [6] Helfenstein, P. (1986) *Lunar Planet. Sci. XVII*, 331-332; [7] Schenk, P.M., and W.B. McKinnon (1985) *J. Geophys. Res.* 90, C775-C783; [8] Johnson, T.V., et al. (1983) *J. Geophys. Res.* 88, 5789-5805; [9] McFadden, L.A., et al. (1980) *Icarus* 44, 410-430; [10] Zellner, B., et al. (1985) *Icarus* 61, 355-416; [11] Chapman, C.R., and M.J. Gaffey (1979) In *Asteroids* (Univ. of Ariz.), 655-687; [12] Tholen, D.J., and B. Zellner (1984) *Icarus* 58, 246-253; [13] Tholen, D.J., et al. (1986) *Proc. 20th ESLAB Symp.*; [14] Clark, R.N., et al. (1986) In *Satellites* (Univ. of Ariz.), 437-490.

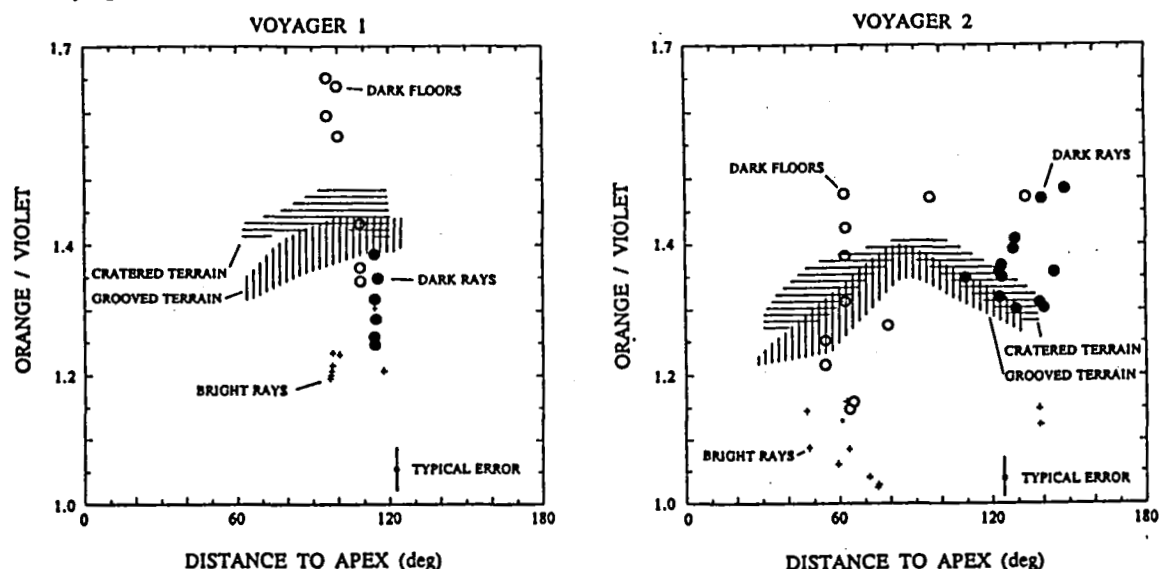


Figure 1. Voyager 1 and 2 orange/violet ratios for Ganymede terrains and crater deposits. Data are not corrected for the differing phase angles of the observations. Dark ray data in top portion are from "Kittu".

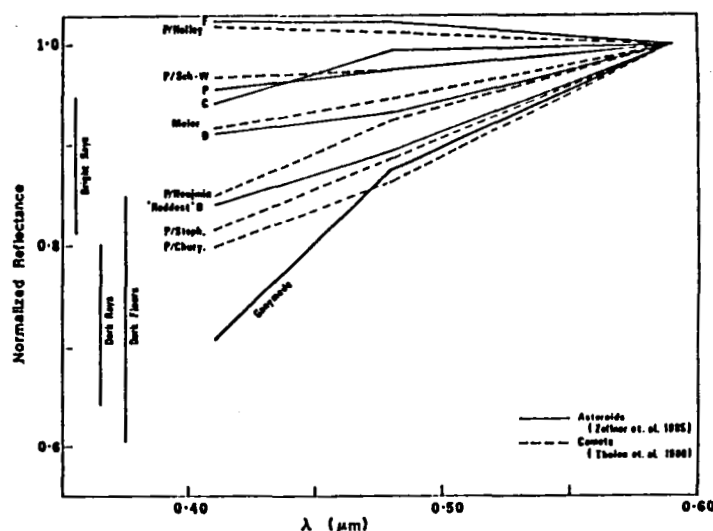


Figure 2. Normalized Earth-based spectra of asteroids, comets, and Ganymede, convolved to Voyager bandpasses. Vertical bars are the range of normalized Voyager violet reflectances (at 0.41  $\mu\text{m}$ , from Figure 2) for bright and dark crater deposits on Ganymede.

## SPATIAL DISTRIBUTION OF IMPACT CRATERS ON VENUS

Jeffrey J. Plaut, Raymond E. Arvidson, McDonnell Center for the Space Sciences, Department of Earth and Planetary Sciences, Washington University, St. Louis, MO 63130.

Impact crater populations provide fundamental information about the evolution of planetary surfaces, including relative and absolute ages, the nature of resurfacing processes, and lateral variations in resurfacing history. Since impact events occur randomly across a planet's surface, departures from a randomly dispersed crater population imply lateral variations in the nature and rate of crater obliteration. Radar backscatter images returned during the Venera 15 and 16 missions show some 146 impact craters located north of approximately 25° N latitude according to [1] and [2]. In this study the hypothesis that this sample is drawn from a randomly dispersed population is evaluated, and implications concerning the observed variations in crater abundance are discussed.

The data used in this analysis consist of the 146 craters catalogued by [2] which show "some morphological features of an impact." The list is confined to craters with diameters greater than 8 km, to avoid uncertainties associated with the resolution limit of the radar imaging system. The current lack of understanding of crater formation and obliteration under Venusian conditions implies that considerable uncertainty still exists in positive identification of impact features. However, for the purposes of this analysis, the classification of [2] is accepted. A review of available Venera images by us reinforces our belief that the catalogue at least includes pristine impact structures. The existence of numerous circular features which lack obvious impact characteristics, however, suggests that some severely degraded craters have not been included in the compilation. Thus, the impact crater abundances discussed in this paper should be considered as lower bounds on the actual Venusian values.

In order to detect lateral variations in crater abundance across a planetary surface, it is necessary to subdivide the observed crater sample as a function of location. The subarea size used should be small enough to detect regional variations, yet large enough to include a sufficient number of craters to have reliable statistics. Thus, the total number of craters critically affects the minimum size of the subarea to be used. The method of [3] for determining this subarea size is adopted here. The number of craters expected to lie within a given subarea,  $E$ , for a randomly dispersed population is simply:

$$E = NA$$

where  $N$  is the total number of craters, and  $A$  is the size of the subarea expressed as a fraction of the total area. The size of the subarea is so chosen that if the craters are indeed randomly dispersed, the number expected to fall within a given subarea (based on the average areal density) is three times the standard deviation predicted by a binomial distribution. The standard deviation of a binomial distribution is,

$$\sigma = \sqrt{NA(1-A)}.$$

Letting  $\sigma = E/3$ , we obtain  $A = 9/(N+9)$ . With the subarea size thus selected, it can be shown that any area in which the crater abundance exceeds the expected value by 3



or more times the predicted standard deviation ( $E+3\sigma$ ) should be considered inconsistent with the random hypothesis.

The subarea size appropriate for the population of 146 Venusian impact craters is approximately 6% of the total area. Venera 15 and 16 coverage consists of approximately  $115 \times 10^6 \text{ km}^2$  [4], so the resulting subarea occupies about  $6.7 \times 10^6 \text{ km}^2$ . An algorithm was utilized that tallied local crater abundance (number/subarea), within a  $14^\circ$  radius (1458 km) of  $1^\circ$  intersections of latitude and longitude. The resultant gridded data set was then converted into a Lambert azimuthal equal area map (see figure). Results show a region of high crater abundance is found when the subarea is centered within  $280^\circ\text{E}$ - $340^\circ\text{E}$  longitude, and  $57^\circ\text{N}$ - $78^\circ\text{N}$  latitude. Since all points within this area exceed the expected value by three times the standard deviation predicted for a randomly dispersed population, the hypothesis of random dispersion can be safely rejected.

The analysis described above reveals a broad region of the northern hemisphere with a significantly higher crater abundance than the average. This area, encompassing  $2.28 \times 10^7 \text{ km}^2$ , or about 20% of the imaged surface, contains 48 (33%) of the 146 impact craters. The abundance of craters with diameters  $> 10 \text{ km}$  within the area is  $2.11 \times 10^{-6} \text{ km}^{-2}$ , compared to  $1.04 \times 10^{-6} \text{ km}^{-2}$  outside of it. The high crater abundance area includes western Ishtar Terra (Lakshmi Planum, Maxwell Montes), surrounding foothills and plains to the south and west, and the north pole.

Results presented here are not in agreement with the recent finding of [2] that there is "no reason to reject the hypothesis of a random crater distribution." We suggest that their result is spurious due to the use of a subarea ( $700 \text{ km} \times 700 \text{ km}$ ) too small to reliably sub-sample the observed crater population. Because of the small total number of craters, sampling at this scale leads to the extreme case of having a single crater in the subarea or not having any craters within the subarea. It will not be sensitive to the broad variations in crater abundance described here. In addition, there appears to be an improper application of the chi-square test by [2] in their analysis of the areal distribution of other circular features on Venus. The small number of features produces expected frequencies well below the minimum that most investigators allow for a meaningful chi-square calculation [5].

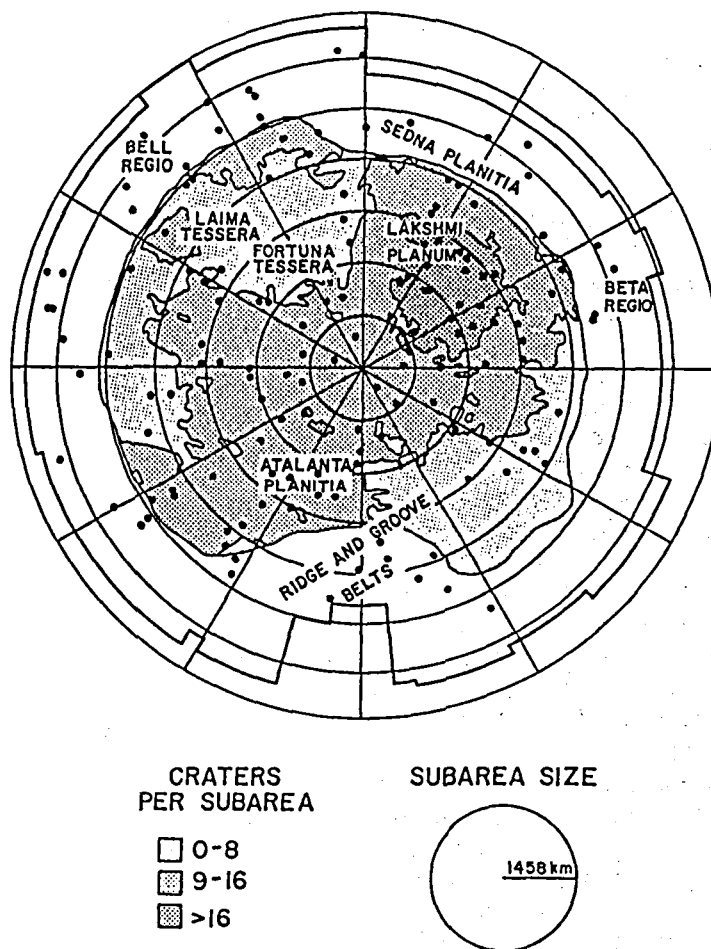
The region of high abundance of craters with "impact features" includes a number of geologic units and features as mapped by [6], including the Lakshmi Plateau and associated linear mountain systems, which contain the highest elevations on the planet. However, crater abundance does not correlate with elevation. The high abundance area extends west and south well into the low-lying plains regions.

Major uncertainties exist concerning cratering rates at the surface of Venus [1,7], making absolute crater age determinations difficult. As noted, problems in positive identification of impact craters provide additional uncertainties, and imply that current estimates are only lower bounds on impact crater abundances and therefore ages. Regardless of absolute values, however, our analysis requires that distinctions be made when estimating crater retention ages, since the abundance of likely "impact features" varies laterally across Venus' surface. Resurfacing processes have apparently been acting at a lower rate and/or have stopped in the region with high crater abundance. A possible interpretation is that the two populations represent areas in which resurfacing

events occurred in two distinct time frames. Further analysis of the abundance of both fresh and degraded impact craters from Venera images is needed to clarify the situation.

### References

- 1) Ivanov, B.A., and others, 1986, *Proc. Lunar and Planet. Sci. Conf. 16th*, in *J. Geophys. Res.*, 91, D413-D430.
- 2) Basilevsky, A.T., and others, 1987, *J. Geophys. Res.*, in press.
- 3) Kamb, W.B., 1959, *J. Geophys. Res.*, 64, 1891-1909.
- 4) Barsukov, V.L., and others, 1986, *Proc. Lunar and Planet. Sci. Conf. 16th*, in *J. Geophys. Res.*, 91, D378-D398.
- 5) Cochran, W.G., 1954, *Biometrics*, 10, 417-451.
- 6) Armand, N.A., and others, *The Planetary Report*, 6, 8-9, 1986.
- 7) Schaber, G.G., and others, 1987, *Lunar and Planetary Science XVIII*, 874-875, Lunar and Planetary Institute, Houston.



Impact crater density in the northern hemisphere of Venus. Map covers 20° N to pole, prime meridian at top. Values correspond to the number of craters within 1458 km (about 14°) of 1° latitude-longitude grid intersections. The occurrence of values in excess of the quantity  $E+3\sigma$  predicted by the binomial distribution (16.9), indicates crater abundances are not randomly controlled. Heavy line indicates limits of Venera 15/16 coverage. Data from grid intersections that lie within 14° of the coverage boundary are not included.

## VISCOUS RELAXATION OF IMPACT CRATER RELIEF ON VENUS: CONSTRAINTS ON CRUSTAL THICKNESS AND THERMAL GRADIENT.

Robert E. Grimm and Sean C. Solomon, Department of Earth, Atmospheric, and Planetary Sciences, Massachusetts Institute of Technology, Cambridge, MA 02139.

**Introduction.** Substantial viscous relaxation of topography has been anticipated for Venus [1-3] because of the high surface temperature and the strong temperature dependence of strain rate. Venera 15-16 radar altimetric profiles across impact craters 25-140 km in diameter, however, indicate crater depths of several hundred meters, suggesting that little relaxation has occurred for these features [4]. We seek to test the internal consistency among current estimates of the mean crater retention age of the surface, the internal thermal structure of Venus, and the inferred rheology of crustal and upper mantle material. Our approach is to apply a general numerical formulation of gravity-driven flow in a viscous fluid to an initial topographic model of an impact crater on Venus. We compare the predicted results with Venera observations, and we develop formal statistical confidence limits on key parameters of each model.

**Diameter-depth relationships.** Regression analysis on the depth  $d_v$  (in km) of 8 Venus impact craters with diameter  $D > 30$  km [4] gives  $\log d_v = -0.66 \pm 0.04 + (0.27 \pm 0.22) \log D$  (Fig. 1), with correlation coefficient  $r = 0.49$ . Observations of crater dimensions on the Earth, Moon, and Mars [5-7] have been invoked to suggest alternatively that the depth of complex craters and the transition diameter  $D_t$  from simple to complex crater morphology may vary inversely with surface gravity. While these two relations are mutually exclusive, the difference in predicted outcome for our problem is minor. We therefore use the latter relation to predict the initial depth of fresh craters on Venus. The regression curve for 52 fresh lunar craters scaled to Venus under the assumption that  $gD_t = \text{constant}$  is  $\log d_i = -0.52 \pm 0.01 + (0.31 \pm 0.04) \log D$ , with  $r = 0.77$ ; this expression along with 95% confidence limits on  $\log d_i$  [8] are shown in Fig. 1.

**Statistical approach to viscous relaxation.** Given the regression curves and confidence intervals for both predicted and observed depths of Venus craters, we may estimate from Fig. 1 how much viscous relaxation can be tolerated at each diameter before the depth of a partially relaxed crater is no longer consistent with the observations. We do this formally by means of the following statistical approach: For fixed  $D$ , we assume that all craters have the same age, given by half the mean crater retention age. We further assume that depths are log-normally distributed with mean  $\log d_i$  and variance  $\sigma_i^2$ . Viscous relaxation will reduce the mean depth to  $\delta(D)$ . We test the null hypothesis  $H_0: d_v = \delta$  by forming the Smith-Satterthwaite T-statistic [8] using  $\delta$ ,  $\sigma_i^2$ , and the mean  $\log$  depth and variance  $\sigma_v^2$  of observed craters. By integrating the upper-tailed t-distribution, we solve for the significance level  $\alpha$  at which the null hypothesis may be rejected in favor of  $H_1: d_v > \delta$ . The parameter  $\alpha$  provides a measure of the likelihood of a particular viscous relaxation model given predicted and observed crater depths.

**Viscous relaxation model.** By direct numerical integration of the equations of motion of a linearly viscous fluid [9], relaxation of crater topography can be evaluated for a medium with an arbitrary depth dependence of viscosity. We use the temperature-dependent effective viscosities of diabase [10] and olivine [11] to represent the crust and mantle, respectively. Because the dependence of laboratory-derived flow laws on stress is nonlinear, the effective viscosity must be evaluated at some characteristic stress difference  $\tau$ , which we take to be the average of the initial maximum stress difference within a cylindrical volume of radius  $D$  and depth  $D/2$ . Since near-surface rock strength is limited by frictional sliding rather than creep [12], we assume that effective viscosity above the brittle-ductile transition (BDT) is limited by frictional strength. An arbitrary lower bound of  $10^{20}$  Pa-s is also imposed on the

viscosity at all depths. Different densities in the crust and mantle are accommodated by solving the equations of motion in the two regions and matching appropriate boundary conditions [13]. The initial state of local isostatic compensation of crater relief must then be specified.

**Application to Venus.** We illustrate this formalism with the following example for  $D = 140$  km. We assume that initial topography is given by an azimuthally averaged, gravity-scaled profile [14] of the lunar Copernican-age crater Langrenus ( $D = 132$  km). We take 170 m.y. as a minimum estimate for the mean crater retention age of the portion of Venus imaged by Venera 15-16 [15]. By specifying all other parameters (Table 1) except the thermal gradient  $dT/dz$  and crustal thickness  $H$ , maps of the fractional change in crater depth (Fig. 2) and associated confidence levels (Fig. 3) can be constructed for this two-parameter space.

**Discussion.** The model illustrated requires a thin ( $<10$  km) crust in order that crater topography be preserved over the past  $\sim 90$  m.y., if the mean thermal gradient is appropriate ( $\sim 20^\circ \text{ K/km}$ ) to a planet in which lithospheric heat transport is dominated by conduction [16]. Of course, the results can differ for other combinations of adopted parameters. For instance, a younger mean age would permit a thicker crust and a higher thermal gradient. The alternative gravity-scaling relation (depth  $\sim g^{-1}$ ) yields shallower initial depths; the lesser topographic load leads to lower strain rates and less topographic relaxation for a specified time interval. Less relaxation is allowed at each confidence level, however, so that the distribution of confidence levels is not very different from that in Fig. 3.

With a larger sample of impact craters and improved estimates of crater depths, data likely to be provided by the Magellan mission, the formalism described here should lead to tighter constraints on permissible values of crustal thickness and mean thermal gradient on Venus.

**References.** [1] J. Weertman, *PEPI*, 19, 197, 1979; [2] S. C. Solomon et al., *JGR*, 87, 7763, 1982; [3] S. K. Stephens et al., *LPSC*, XIV, 747, 1983; [4] B. A. Ivanov et al., *PLPSC 16th*, *JGR*, 91, D413, 1986; [5] R. A. F. Grieve and P. B. Robertson, *Icarus*, 38, 212, 1979; [6] R. J. Pike, in *Impact and Explosion Cratering*, Pergamon, 489, 1977; [7] R. J. Pike, *Icarus*, 43, 1, 1980; [8] J. L. Devore, *Probability and Statistics for Engineering and the Sciences*, Brooks/Cole, 1982; [9] L. M. Cathles, *The Viscosity of the Earth's Mantle*, Princeton, 1975; [10] Y. Caristan, *JGR*, 87, 6781, 1982; [11] C. Goetze, *Phil. Trans. R. Soc. Lond.*, A288, 99, 1978; [12] W. F. Brace and D. H. Kohlstedt, *JGR*, 85, 6248, 1980; [13] S. C. Solomon et al., *JGR*, 87, 3975, 1982; [14] S. H. Zisk, pers. comm., 1986; [15] G. G. Schaber et al., *Solar Sys. Res.*, in press, 1987; [16] S. C. Solomon and J. W. Head, *JGR*, 87, 9236, 1982.

---

Table 1. Adopted Parameters

Crustal density:	2.9 g/cm <sup>3</sup>
Mantle density:	3.4 g/cm <sup>3</sup>
Initial compensation:	none
Average stress $\tau$ :	60 bar
Depth of BDT, crust:	1 km
Depth of BDT, mantle:	11 km
Surface temperature:	738 K

---

Fig. 1. Venera 15-16 observations of depths and diameters of impact craters on Venus [4], excluding Cleopatra Patera. Solid lines show the linear regression and 95% confidence intervals for craters with diameter  $D > 30$  km. Dashed lines show predicted depth-diameter relation and 95% confidence intervals predicted from gravity-scaled lunar craters.

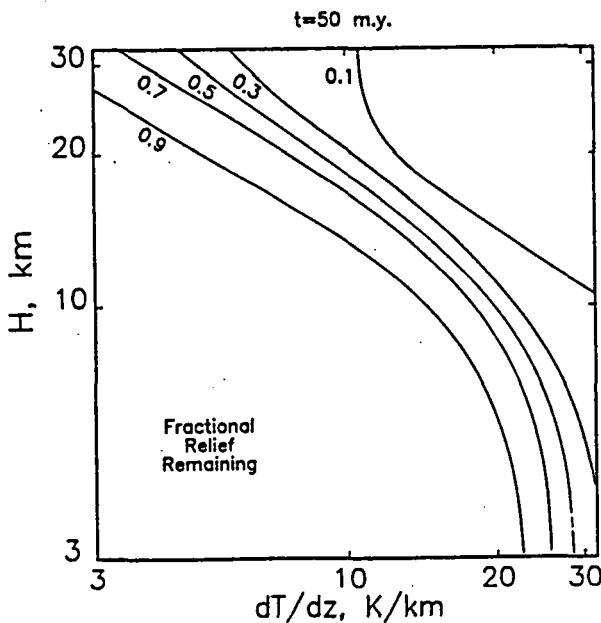
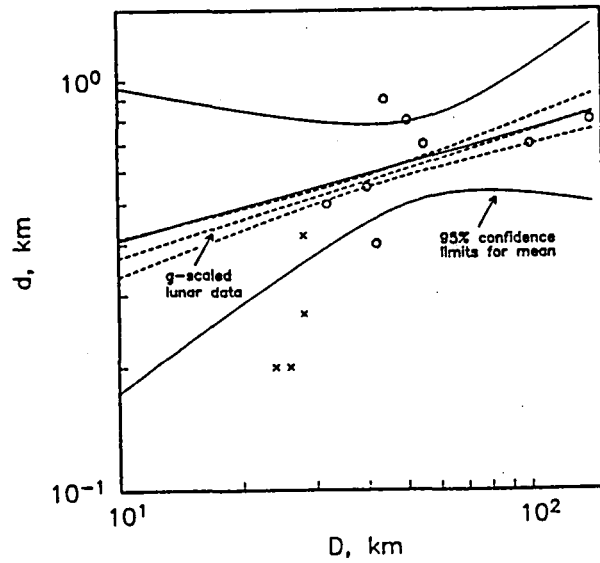


Fig. 2. Fractional relief remaining after 90 m.y. for a 140-km diameter crater as a function of mean crustal thickness  $H$  and temperature gradient  $dT/dz$ .

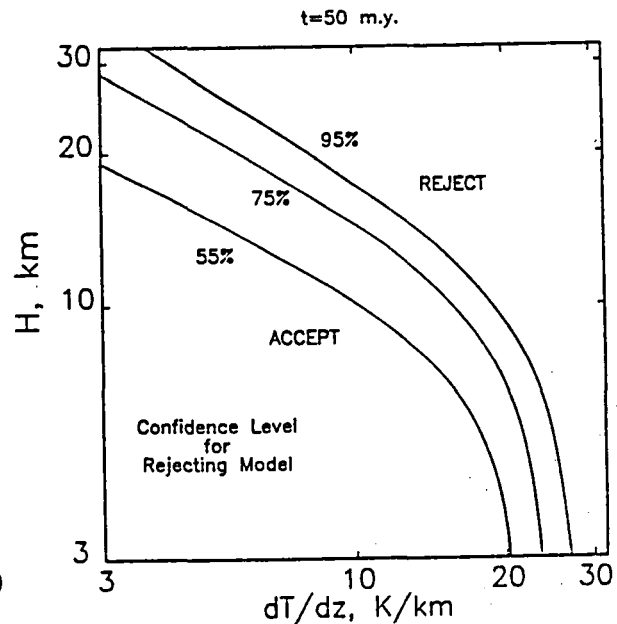


Fig. 3. Significance levels for Fig. 2. At the indicated significance level  $\alpha$ , combinations of  $H$  and  $dT/dz$  to the right of each curve may be rejected.

## LIMITS ON MODES OF LITHOSPHERIC HEAT TRANSPORT ON VENUS FROM IMPACT CRATER DENSITY.

Robert E. Grimm and Sean C. Solomon, Department of Earth, Atmospheric, and Planetary Sciences, Massachusetts Institute of Technology, Cambridge, MA 02139.

**Introduction.** Characterization of the dominant mode of lithospheric heat transport on Venus remains an important step in understanding the internal evolution of the planet [1]. Images of the Venus surface from Earth-based radar [2,3] and Venera 15-16 [4,5] have revealed evidence for widespread volcanism and tectonism but also a significant density of impact craters [6,7]. On the basis of simple models of impact crater production and obliteration, we present a formalism to place bounds on the contributions to lithospheric heat transport by volcanism and lithospheric recycling.

**Cratering.** Estimates of the mean crater retention age of the Venus surface vary considerably, principally because of different assumptions about the surface features interpreted as impact craters [4,6-8]. Calculation of an age also requires a scaling factor to convert the rates of crater production on the Moon or Earth to that on Venus [9]. To obtain upper bounds on the rates of volcanic resurfacing or lithospheric recycling, we should use the largest reasonable scaling factor. We therefore adopt a crater production rate a factor of 4 [10] that of the lunar maria [9]. From this assumption and the crater density-diameter data of Venera 15-16 [7], the number of craters per  $\text{km}^2$  produced per billion years in the diameter interval  $D$  to  $\sqrt{2}D$  is given by  $F(D) = 1.5 \times 10^{-3} D^{-1.8}$ .

**Volcanic resurfacing.** Impact craters, of course, can be obliterated by many processes, including erosion, sedimentation, viscous relaxation, and tectonic disruption, as well as volcanic resurfacing and lithospheric recycling. Several studies [11,12] suggest that the effects of erosion and sedimentation on Venus are unimportant at this scale. As a working hypothesis, we first assume that volcanism is the major resurfacing process and is equally likely anywhere on the Venus surface. This hypothesis is at least partly supported by the widespread occurrence of smooth plains, flow features, and volcanic cones, domes, and calderas [3,4]. The combined effects of other obliteration processes serve only to decrease the contribution of volcanism required, which ensures that our estimate of volcanic flux will be an upper bound.

To maintain a conservative approach, we assume that a crater must be buried by volcanic flows to the top of its rim in order that it not be observable in a Venera radar image. We estimate the rim height  $h$  of fresh craters on Venus by applying a gravity scaling factor to the power-law relation between  $h$  and diameter  $D$  for lunar craters [13]. Two different scaling rules are possible, based on suggestions that either the depth (and by inference, the rim height) of complex craters or the transition diameter between simple and complex crater morphology varies inversely with gravity [14,15]. We choose the latter scaling rule here because it predicts higher rims and hence requires more volcanic resurfacing to achieve crater obliteration. The prediction for Venus rim heights is then  $h = 0.085 D^{0.4}$ .

For a specified time  $t$  since initiation of resurfacing at a constant rate of volcanic burial  $ds/dt$ , there exists a critical crater diameter  $D_c$  at which the rim height is equal to the total thickness of volcanic flows:  $h(D_c) = t(ds/dt)$ . Craters with  $D > D_c$  are unaffected by the resurfacing process and reflect the crater density prior to resurfacing; craters with  $D < D_c$  are continually obliterated and replaced. The crater density in the latter state is in equilibrium and depends on the ratio of the rate of cratering to that of obliteration [16]:

$$N(D) = F(D) h(D) / (ds/dt) \quad (1)$$

where  $N$  is the number of preserved craters per  $\text{km}^2$  in the diameter interval  $D$  to  $\sqrt{2}D$ . Figure 1 shows equilibrium crater densities for steady volcanic fluxes of 1, 2, and 4  $\text{km}^3/\text{yr}$ . If we take the size of the largest reported crater in the Venera images (140 km) as the critical

diameter, the minimum periods of surfacing so that eq. (1) is valid over the diameter range spanned by the Venera data are 280, 140, and 70 m.y., respectively. On the basis of Fig. 1, an upper limit to the volcanic flux consistent with the observations is  $2 \text{ km}^3/\text{yr}$ . Of course, volcanic extrusion has not been steady but has likely fluctuated about a gradually decreasing function of time. The inferred upper bound on the rate of resurfacing on Venus remains valid, however, as such a volcanic history would have eliminated more craters than assumed by a constant-flux model. The rate of heat  $Q$  delivered to the surface by a volcanic flux  $dV/dt$  is  $Q = \rho(C_p \Delta T + H_f) (dV/dt)$ , where  $\rho$  is the density,  $C_p$  is the heat capacity,  $H_f$  is the heat of fusion, and  $\Delta T$  is the temperature drop across the lithosphere. Using  $\Delta T = 1015 \text{ K}$  [17],  $\rho = 2.8 \text{ g/cm}^3$ ,  $C_p = 1.2 \text{ J/g K}$ , and  $H_f = 400 \text{ J/g}$ , the rate of heat loss due to a volcanic flux of  $2 \text{ km}^3/\text{yr}$  is  $2.9 \times 10^{11} \text{ W}$ , or less than 1% of the rate of global heat loss of  $3.4 \times 10^{13} \text{ W}$  [1]. Although this rate of heat transport is negligible on a planetary scale, this result does not preclude the possibility of a significant component of heat transport by shallow conduction above igneous intrusions [18].

**Lithospheric Recycling.** We next consider as an alternative working hypothesis that the principal mechanism of impact crater obliteration is lithospheric recycling. Such recycling may be considered to occur either by foundering or by subduction, though we recognize that evidence for neither process has yet been observed in images of the Venus surface [4]. The smallest reported estimate of the mean crater retention age for Venus, 170 m.y. [10], then yields an upper bound on the rate of lithosphere recycling. If we assume that there are no preferentially preserved "islands" of more ancient terrain, the rate of plate recycling is inversely proportional to the mean age of the surface. The mean age of oceanic lithosphere on Earth is approximately 60 m.y. [19], which would imply under the above assumptions that any lithospheric recycling on Venus is at least a factor of 3 slower than on Earth. The terrestrial rate of creation of new lithosphere is  $3 \text{ km}^2/\text{yr}$  [20]; the maximum rate on Venus would thus be  $1 \text{ km}^2/\text{yr}$ . We note, however, that the presence of ancient terrain uninvolved in the recycling process would seriously bias this estimate; for instance, the mean age of the Earth's surface including the continents is about 400 m.y. [19]. The rate of heat loss due to lithospheric recycling is approximately  $Q_r = 0.5 \rho C_p L \Delta T (dA/dt)$ , where  $L$  is the thickness of the thermal lithosphere and  $dA/dt$  is the areal rate of plate creation. With  $dA/dt = 1 \text{ km}^2/\text{yr}$ ,  $C_p$  and  $\Delta T$  as above,  $\rho = 3.3 \text{ g/cm}^3$  and  $L = 94 \text{ km}$  [17],  $Q = 6 \times 10^{12} \text{ W}$ , or 18% of the nominal Venus heat loss [1], in strong contrast to the Earth, where plate recycling accounts for approximately 65% of the global heat loss [19]. Kaula and Phillips [17] derived a similar upper bound using different arguments.

**Conclusions.** The surface density of impact craters in Venera 15-16 images limit the rate of volcanic resurfacing on Venus to be less than  $2 \text{ km}^3/\text{yr}$  and the rate of lithospheric recycling to be less than  $1 \text{ km}^2/\text{yr}$ . These figures correspond to 1% and 18% of the rate of global lithospheric heat loss, respectively. We conclude that the dominant mode of heat loss at least in the upper lithosphere of Venus is conduction. Substantial lateral variation in vertical thermal gradients may be associated with lithospheric thinning [21] or magmatic intrusions [18]. Detailed characterization of volcanic, tectonic, and impact processes on Venus will be facilitated by the Magellan mission and will provide tests of the simple models and arguments presented here.

**References.** [1] S. C. Solomon and J. W. Head, *JGR*, 87, 9236, 1982; [2] D. B. Campbell et al., *Science* 221, 644, 1983; [3] D. B. Campbell et al., *Science* 226, 167, 1984; [4] V. L. Barsukov et al., *PLPSC 16th*, *JGR*, 91, D378, 1986; [5] A. T. Basilevsky et al., *PLPSC 16th*, *JGR*, 91, D399, 1986; [6] D. B. Campbell and B. A. Burns, *JGR*, 85, 8271, 1980; [7] B. A. Ivanov et al., *PLPSC 16th*, *JGR*, 91, D413, 1986; [8] H. Masursky et al., *JGR*, 85, 8232, 1980; [9] BVSP, *Basaltic Volcanism on the Terrestrial Planets*, Pergamon, 1981; [10] G. G. Schaber et al., *Solar Sys. Res.*, in press, 1987; [11] J. B. Garvin et al.,

*JGR*, 89, 3381, 1984; [12] J. W. Head et al., *JGR*, 90, 6873, 1985; [13] R. J. Pike, in *Impact and Explosion Cratering*, Pergamon, 489, 1977; [14] R. J. Pike, *Icarus*, 43, 1, 1980; [15] R. A. F. Grieve and P. B. Robertson, *Icarus*, 38, 212, 1979; [16] C. R. Chapman and K. L. Jones, *Ann Rev. Earth Planet. Sci.*, 5, 515, 1977; [17] W. M. Kaula and R. J. Phillips, *GRL*, 8, 187, 1981; [18] J. W. Head and L. Wilson, *JGR*, 91, 9407, 1986; [19] J. G. Sclater et al., *RGSP*, 18, 269, 1980; [20] B. Parsons, *GJRS*, 67, 437, 1981; [21] P. Morgan and R. J. Phillips, *JGR*, 88, 8305, 1983.

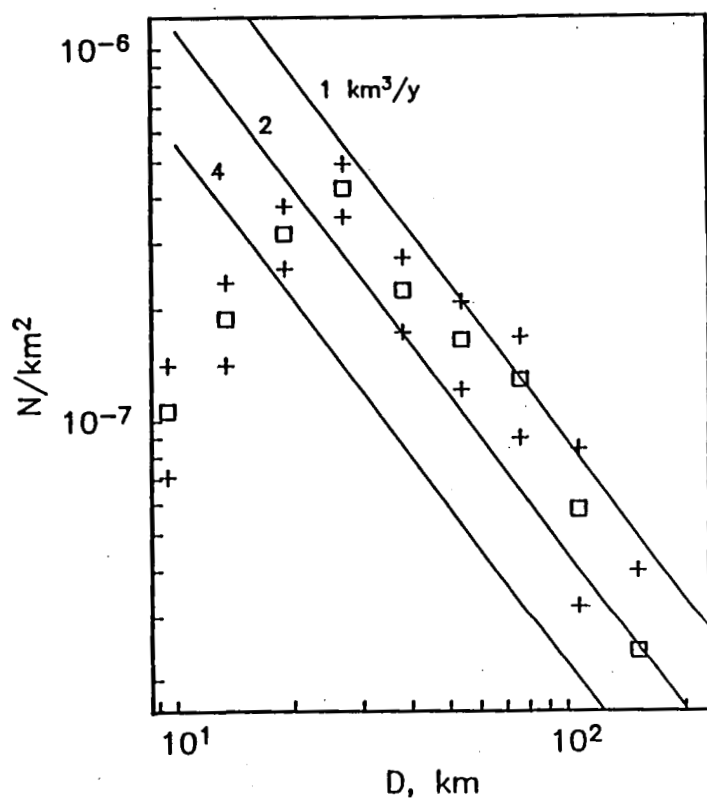


Fig. 1. Incremental crater density versus diameter from Venera 15-16 observations [7]; one- standard-deviation limits are denoted by crosses. Equilibrium crater densities for constant assumed volcanic fluxes of 1, 2, and 4 km<sup>3</sup>/yr are shown as solid lines.



## The Terrestrial Planet Cratering Record: Implications for the Origin of the Objects Responsible for the Period of Late Heavy Bombardment

Robert G. Strom, Department of Planetary Sciences, University of Arizona, Tucson, Arizona 85721

In the inner Solar System, the heavily cratered terrain on the Moon, Mercury, and Mars all have similar crater size/frequency distributions representing the period of late heavy bombardment (Figure 1). The size distributions are characterized by highly structured curves with multiple population indices. On Mercury and Mars, there is a paucity of craters less than about 40 km diameter relative to the Moon. This paucity of craters is probably the result of crater obliteration by intercrater plains formation on Mercury (the most extensive terrain type) and both intercrater plains and atmospheric erosion and deposition on Mars.

The crater population superposed on the lunar maria and younger martian plains is different from that in the heavily cratered terrains. It is characterized by a differential single-slope population index of -3 compared to -2.3 over the same diameter range for the lunar highlands. This crater population almost surely represents the accumulation of comet and asteroid impacts from the end of late heavy bombardment up to the present time.

A comparison of the cratering curves representing the period of late heavy bombardment on the Moon, Mercury, and Mars shows that they are laterally displaced with respect to each other at diameters between about 40 km and 150 km, where the curves are probably unaffected by erosion and the statistics are good. They are displaced in such a manner that higher impact velocities are required at planets with smaller heliocentric distances, i.e., larger craters on Mercury and smaller craters on Mars compared to a given size crater on the Moon. This is consistent with a single family of objects in heliocentric orbits. Relative to a 100 km diameter crater on the Moon, the limits for the displacement are from 0 to 20 km larger on Mercury and 20 to 30 km smaller on Mars. Figure 2 shows the best fit where for a 100 km crater on the Moon, the crater size on Mercury is 120 km and on Mars 80 km.

Impact velocities required to form a given size crater for a constant size projectile on the Moon, Mercury, and Mars can be calculated from the following modified Holsapple-Schmidt (1982) crater scaling law (Strom, 1987):

$$V = \left( \frac{D_q^{0.15} D_r^{0.85} g^{1/6}}{d^{1/1.2} K c^{1/3} [1 - 0.095(1 - \sin A)]^{1/3}} \right)^3$$

where  $D_q$  is the transition diameter from simple to complex craters,  $g$  is the surface gravity,  $K$  is a coupling factor,  $c$  is the ratio of projectile to target density,  $A$  is the impact angle from the horizontal,  $D_r$  is the observed rim diameter, and  $d$  is the projectile diameter.

From these velocities the impact velocity ratios, Mercury/Moon and Mars/Moon can be determined for a given size projectile. They range from 1.37 to 2.18 for the Mercury/Moon ratio and from 0.48 to 0.68 for the Mars/Moon ratio. The best fit in Figure 2 gives a Mercury/Moon impact velocity ratio of 2.18 and a Mars/Moon impact velocity ratio of 0.68.

The orbital elements (semimajor axes and eccentricities) and impact velocity ratios of impacting objects in heliocentric orbits can be derived from the equation for impact velocity where, in simplified form,

$$V_p = (U^2 + V_e^2)^{1/2}$$

$$V_s = (U^2 + V_{eo}^2 + V_{es}^2)^{1/2}$$

where  $V_p$  is the planetary impact velocity,  $V_s$  is the satellite impact velocity,  $U$  is the encounter velocity at infinity,  $V_e$  is the escape velocity of the planet,  $V_{eo}$  is the escape velocity of the planet at the orbit of the satellite and  $V_{es}$  is the escape velocity of the satellite.

Figure 3 is a plot of the comparison of the impact velocity ratios for Mercury/Moon (a) and Mars/Moon (b) verses impactor semimajor axes from 0.5 to 6.5 AU for eccentricities from 0.6 to 0.95. Only those parts of the eccentricity curves that lie within the hachured areas have impact velocity ratios compatible with the observed shifts in the crater size/frequency distributions. The results indicate that only planetesimals with semimajor axes between about 0.8 and 1.2 AU simultaneously satisfy the observed impact velocity ratios. The best fit of the curves is given by objects with semimajor axes of about 0.85 AU and eccentricities of about 0.95. This strongly indicates that the objects responsible for the period of late heavy bombardment on the terrestrial planets were in orbits confined to the inner Solar System and are most likely to have been accretional remnants as proposed by Wetherill (1977).

Holsapple, K.A., and R.M. Schmidt, 1982. On the scaling of crater dimensions. 2. Impact Processes. *J. Geophys. Res.* **87**, 1849-1870.

Strom, R.G., 1987. The Solar System cratering record: Voyager 2 results at Uranus and implications for the origin of impacting objects. *Icarus* **70**, 517- 535.

Wetherill, G.W., 1977. Evolution of the Earth's planetesimal swarm subsequent to the formation of the Earth and Moon. *Proc. Lunar Sci. Conf.* 8th, **1**, 1-16.

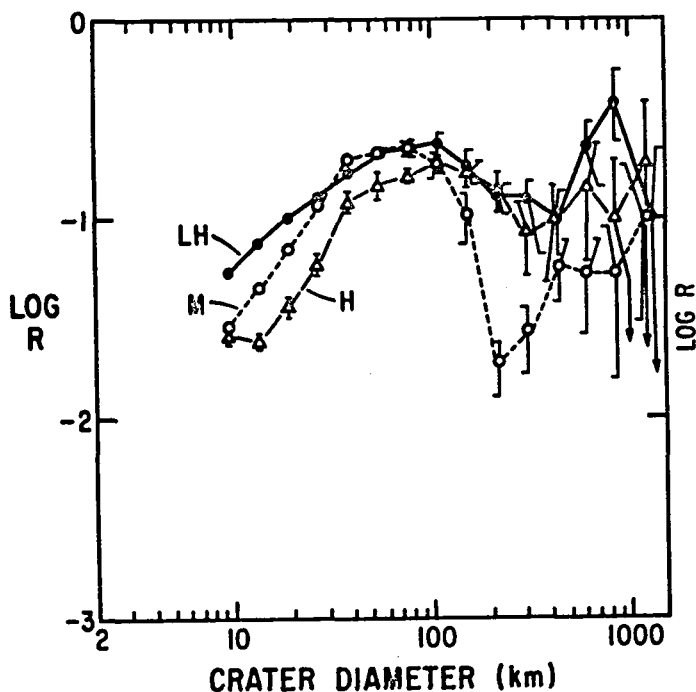


Figure 1. R plot of the size/frequency distributions of the lunar highlands (LH), martian highlands (M), and mercurian highlands (H).

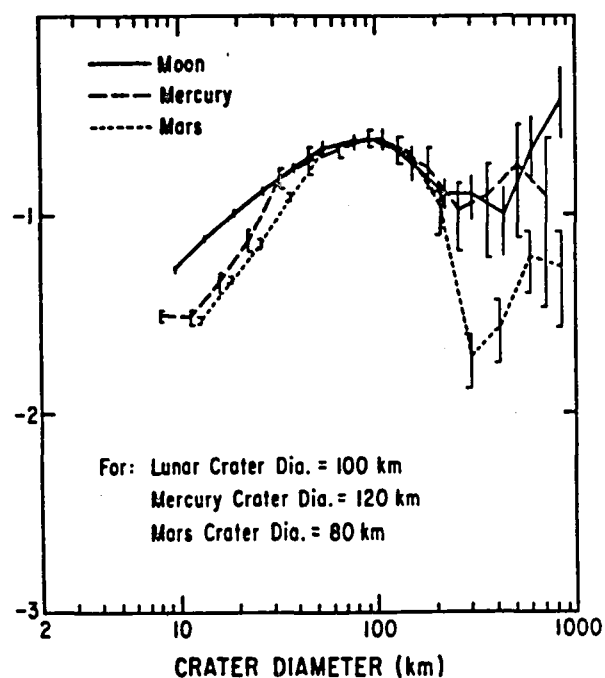


Figure 2. Best fit between about 40 and 150 km diameter of the highlands crater curves for the Moon, Mercury, and Mars.

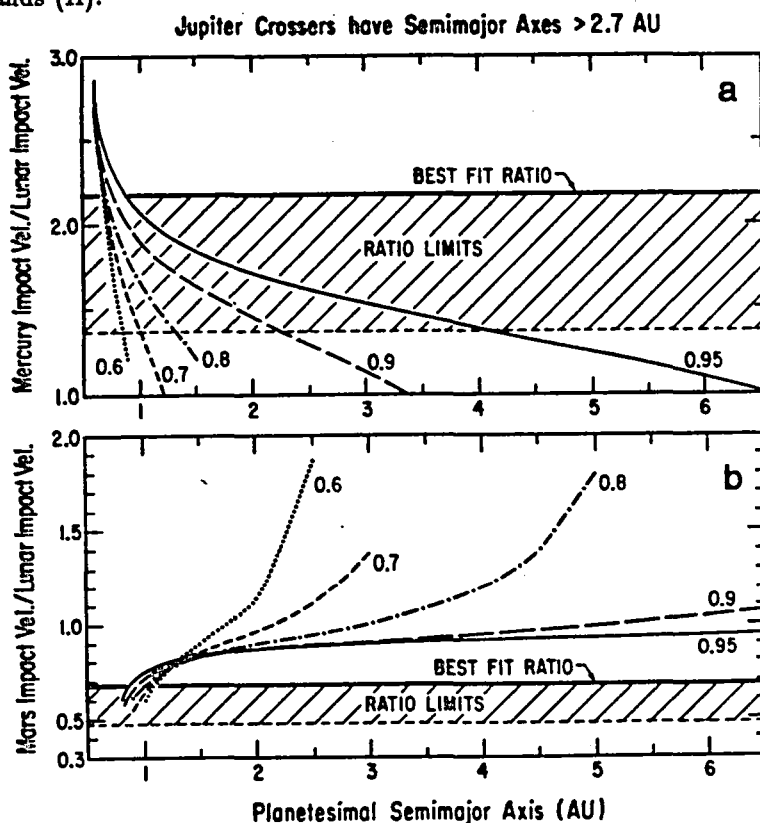


Figure 3. See text for explanation.

EARLY INTENSE CRATERING: EFFECTS ON GROWTH OF EARTH'S CRUST  
William K. Hartmann, Planetary Science Institute, Tucson, AZ 85719

Observations of crater densities in lunar regions of various ages show that the cratering rate during the first 500 my of lunar history was  $\geq 10^3$  x the present rate (1). Because of O isotope ratios and other evidence, we believe the moon formed close to Earth, and the same early intense cratering affected Earth, too. Probably it was a solar-system-wide phenomenon, resulting from sweep-up of the planetesimals at the end of planet formation.

In all probability, the cratering rate in the first 10-100 my averaged vastly higher. The mass flux needed to accumulate Earth and the moon within the permitted formation interval of 10-100 my is of the order  $2(10^9)$  x the present rate (2). This is entirely understandable from accretion models, which indicate a very rapid accretion of planetesimals (3) and a longer, declining rate of sweep-up of the remaining planetesimals after the planets gained nearly their present mass (4).

This situation has two related effects on formation of crusts of Earth and other planets. First, as pointed out by Safronov (5) and Hartmann and Davis (6), the 2nd, 3rd, .... largest bodies accompanying the planets may have been large enough, relative to the planets themselves, to have dramatic effects, including disruption of large volumes of the planet, including mantle and crust if they had formed. Hartmann and Davis (6) attributed the moon's origin to such a giant, disruptive impact. Recent modelling (7,8) shows that large regions of any pre-existing crust and upper mantle could be vaporized and/or ejected as finely disseminated and heated dust, with consequent geochemical effects. Giant impacts would be stochastic events, dotted through the first  $10^8$  years or so, until the required large bodies collided with planets or were ejected from the solar system.

The second effect involves the more continual rain of impactors that were smaller (but large by present day standards). These would form a continuum with the "giant impacts." (The nature of the impactor size distribution was such that the smaller the body, the more of them.) Ringwood (9) discussed the possible production of a silicate atmospheres devolatilized from the crust. Frey (10) proposed that large impacts punched holes in the early crust, piling up "continental" crustal ejected debris in other areas and exposing hot mantle areas where convection was enhanced; this could have abetted proto-continent formation. Hartmann noted that magma ocean evolution must be modelled in the presence of this process, which competes with crust formation by continually breaking up and redistributing the early, solid, anorthositic surface (11). Also, the impact rate at the close of planet forming period was high enough that impacts comparable to the proposed K-T boundary event happened on roughly a monthly-to-yearly basis (12).

Figure 1 (adapted from Fig. 12) illustrates some of these points. Curve "t=0" shows the approximate impact rate shortly after the close of

planet formation; curve "t=500 m.y." shows the rate 500 m.y. after planet formation. The curves are based on the above results. The actual impact rate declined approximately exponentially with time from the first to the second curve. As can be seen, during this interval there was opportunity for a few giant impacts, many impacts large enough to create basins comparable to the moon's Orientale and Imbrium basins ( $10^3$ -km-scale in diameter of disrupted zone), and thousands of smaller-scale craters.

Depending on the time-scale of crustal formation and evolution on Earth and other planets, models of proto-crustal evolution should take into account the possible competitive influence of repeated impact cratering, which would disrupt any hypothetically homogeneous proto-crustal layer, creating thick and thin spots, and affecting cooling timescales and global- or continental-scale topographic/structural/tectonic features.

While the geographic expression of these effects may be long vanished on Earth because of tectonic and erosive effects, they may be still visible on Mars, where large impact basins may be detected, and where relatively young volcanics dominant one hemisphere, while a much older crustal surface dominates the other hemisphere. (13)

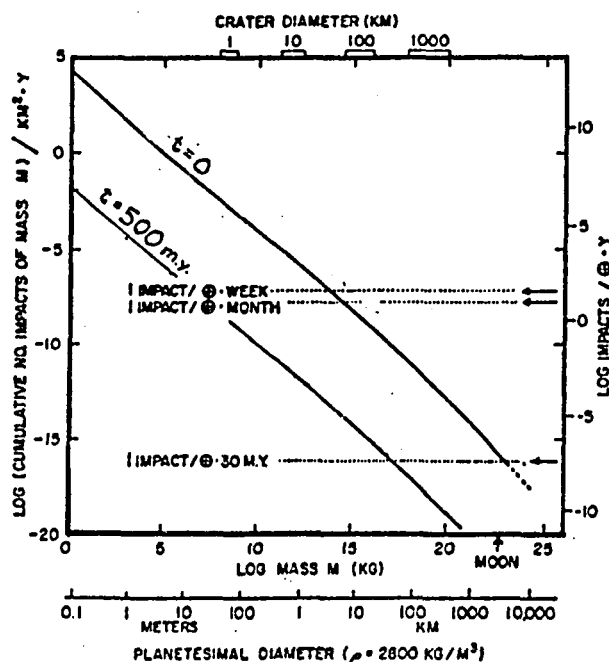


FIG. 1. Estimated impact cratering rate on early Earth at close of planet formation and 500 m.y. later. These rates are on the order of  $10^9$  and  $10^3$  times the present rate, respectively. (Adapted from ref. 12).

# REFERENCES

1. Hartmann, W.K. (1972). Astrophys. Space Sci. 12, 48-64.
2. Hartmann, W.K. (1980). Icarus 44, 441-453
3. Greenberg, R., Wacker, J., Hartmann, W.K., and Chapman, C. (1978). Icarus 35, 1-26.
4. Wetherill, G.W. (1977). Proc. Lunar Sci. Conf. 8th, 1-16.
5. Safronov, V. (1966). Sov. Astron. AJ 9, 987.
6. Hartmann, W.K. and Davis, D.R. (1975). Icarus 24, 504-515.
7. Benz, W., Slattery, W., Cameron, A. (1986). In Origin of the Moon (Houston: Lunar & Planetary Inst.).
8. Melosh, H. and Sonett, C.P. (1986). In Origin of the Moon (Houston: Lunar & Planetary Inst.).
9. Ringwood, A.E. (1979). Origin of the Earth and Moon. (Springer-Verlag, New York), p. 295.
10. Frey, H. (1977). Icarus 32, 235.
11. Hartmann, W.K. (1980). In Proc. Conf. Lunar Highlands Crust (Houston: Lunar & Planetary Institute).
12. Hartmann, W.K. (1986). In Origin of the Moon (Houston: Lunar & Planetary Inst.).
13. Wilhelms, D.E. and Squyres, S.W. (1984). Nature 309, 138-140.

A total of 19 sites of known or probable impact structures have been identified in Australia (Table 1). By the close of our fourth field season in 1987, we had studied all of these sites in the field except the Liverpool Crater, Northern Territory, and the Darwin Crater, Tasmania; the Liverpool Crater, however, was examined by means of low-level aerial reconnaissance in 1987 by EMS and D.J. Roddy.

The recognized impact structures range in age from Holocene to Early Proterozoic and in size from tens of meters to about 35 km. Five sites are the localities of one or more young and relatively small craters with associated meteorites. The remaining sites are of larger individual eroded or exhumed craters or of deeply eroded impact structures.

A distinctive feature of the Australian impact record is that 7 of the 13 structures larger than one km diameter probably are Proterozoic in age, including the 4 largest. Three of these structures, whose ages are not yet well determined, are formed in Proterozoic rocks and are overlapped with strong unconformity by Cambrian beds.

More impact structures of probable Proterozoic age have now been identified in Australia than in the rest of the world. Preservation and recognition of these structures are due chiefly to the remarkable tectonic history of the Australian craton. Continental basins of Early to Late Proterozoic age, which contain gently to moderately deformed, relatively unmetamorphosed sedimentary rocks, are extensively exposed in Australia. Impact deformation is fairly readily recognized in these basins, and the large impact structures, once formed, have been neither too deeply eroded nor too deeply buried to render them undetectable.

Of seven structures of Phanerozoic age (exclusive of the very young meteorite craters), only Gosses Bluff exceeds 10 km in diameter. On the basis of estimates of the collision rate of Earth-crossing asteroids and comets (Shoemaker, 1983; Shoemaker and Wolfe, 1987) and the impact record of North America and the Eo-European craton (Grieve, 1984), we calculate that about  $35 \pm 15$  Phanerozoic impact structures larger than 10 km in diameter should be exposed on the Australian continent. Our present knowledge of the Phanerozoic impact history of Australia probably is extremely incomplete.

Factors that impede detection of impact structures in Australia include low relief and extensive deep weathering of much of the land surface and blanketing by extensive sheets of eolian sand and other surficial deposits. Another factor is structural complexity of certain terrains, such as the large Yilgarn block of Archean age in Western Australia, where the only impact structure found thus far is the tiny Dalgarranga meteorite crater. Despite these impediments, many further discoveries of Australian impact structures should be anticipated. Vigorous, ongoing programs of geologic mapping and research in Australia, exploration for minerals and fossil fuels, heightened awareness of impact structures among Australian geologists, and systematic search for impact structures, such as our present survey, should continue to lead to significant extension of our knowledge of the impact record.

#### References Cited in Text:

- Grieve, R.A.F., 1984, The impact cratering rate in recent time: *Journal of Geophysical Research*, v. 89, supplement, p. B403-B408.
- Shoemaker, E.M., 1983, Asteroid and comet bombardment of the Earth: *Annual Review of Earth and Planetary Sciences*, v. 11, p. 461-494.
- Shoemaker, E.M., and Wolfe, R.F., 1987, Crater production on Venus and Earth by asteroid and comet impact (extended abs.): *Lunar and Planetary Science XVIII*, p. 918-919.

Table 1. Impact Structures of Australia (1987)

	<u>Latitude</u>	<u>Longitude</u>	<u>Diameter (km)</u>	<u>Trace of impactor</u> <u>1/</u>	<u>Impact melt</u> <u>2/</u>	<u>Shatter cones</u>	<u>Age (m.y.)</u>
Dalgaranga, W.A.	27° 38'S	117° 17'E	0.024	m			<0.003(?)
Veevers, W.A.	22° 58'S	125° 22'E	0.070	m			<0.004(?)
Henbury Craters, N.T.	24° 34'S	133° 08'E	0.18	m	e		0.0042±0.0019
Boxhole, N.T.	22° 38'S	135° 12'E	0.17	m			0.0054±0.0015
Wolfe Creek, W.A.	19° 10'S	127° 48'E	0.88	m	e		~0.5
Darwin Crater, Tas.	42° 18'S	145° 40'E	1		e		0.74±0.04
Goat Paddock, W.A.	18° 20'S	126° 40'E	5		c	x	~55
Connolly Basin, W.A.	23° 32'S	124° 45'E	9				60±40
Mt. Toondina, S.A.	27° 57'S	135° 22'E	3				<100
Liverpool, N.T.	12° 24'S	134° 03'E	~3(?)				>140(?)
Gosses Bluff, N.T.	23° 49'S	132° 19'E	22		c	x	133±3
Piccanniny, W.A.	17° 26'S	128° 26'E	7				<360
Lawn Hill, Qld.	18° 40'S	138° 39'E	~20		c	x	>540
Kelly West, N.T.	19° 56'S	133° 57'E	10-20			x	>540
Strangways, N.T.	15° 12'S	133° 35'E	26	s	c	x	>570
Lake Acraman, S.A.	32° 01'S	135° 27'E	~35	f	c	x	~630
Spider, W.A.	16° 44'S	126° 05'E	13			x	>700
Teague Ring, W.A.	25° 52'S	120° 53'E	30			x	~1600(?)
Fiery Creek Dome, Qld.	19° 13'S	139° 13'E	30			(?)	~1700

1/ m = associated meteorites; s = siderophile elements in impact melt; f = siderophile elements in fallout layer.

2/ e = ejected impact melt (impactite); c = impact melt rocks preserved in crater.



# Notes on Sources of Data Listed in Table 1

- Dalgaranga: Plane-table topographic and geologic map (unpubl.) by EMS & CSS, 1986; age estimated from degree of infilling of crater and preservation of rays.
- Veevers: Plane-table topographic and geologic map (unpubl.) by EMS & CSS, 1986; meteorites discovered by CSS and EMS, 1984; age estimated from degree of infilling of crater.
- Henbury: Strawn field of at least 13 craters; diameter shown is of long axis of largest crater; five craters mapped by D.J. Milton (1968); completion of mapping of remaining craters by EMS and D.J. Roddy in progress; fission-track age from impactite (Storzer and Wagner, 1977).
- Boxhole: Geologic map (unpubl.) by EMS and D.J. Roddy, 1987; terrestrial age of meteorite from Kohman and Goel (1963).
- Wolfe Creek: Geologic map (unpubl.) by EMS, 1985; impactites discovered by CSS, 1985; preliminary terrestrial age of meteorite by K. Nishizumi (personal communication, 1987).
- Darwin Crater: Drilling and gravity investigation reported by Fudall and Ford (1979); fission track age from impactite (Darwin glass) by Gentner et al. (1973).
- Goat Paddock: Geologic map (unpubl.) by D.J. Milton; age based on early Eocene palynomorphs from sediments resting directly on breccia in crater floor (Harms et al., 1980).
- Connolly Basin: Geologic map and gravity survey (unpubl.) by EMS and CSS, 1986; youngest rocks deformed are Early Cretaceous in age and sediments filling crater are tentatively correlated with beds of Late Cretaceous or early Tertiary age.
- Mt. Toondina: Impact origin confirmed from style of deformation in central uplift (studied by EMS and D.J. Roddy, 1987) and from subsurface structure revealed by seismic reflection profiles. Youngest beds deformed are Lower Cretaceous. Structure may possibly be source of high-Na tektites (Chapman and Schieber, 1969) found relatively nearby in South Australia.
- Liverpool: Size of structure estimated from aureole of low relief surrounding outcrops of impact breccia. Tentative upper bound for age based on lithologic correlation of sediments filling crater by Guppy et al. (1971).
- Gosses Bluff: Comprehensive geologic and geophysical investigations summarized by Milton et al. (1972). Geologic maps by Glickson et al. (1978) and Milton et al. (1978).
- Piccaniny: Geologic map (unpubl.) by EMS, G.M. Beere and A. Wilson, 1985; youngest beds deformed are of Late Devonian age.
- Lawn Hill: Geologic map by Sweet and Hutton (1982); description of shock features by Stewart and Mitchell (1987); youngest rocks deformed are Early Proterozoic in age; impact structure is overlapped by beds of Middle Cambrian age.
- Kelly West: Field investigation by EMS and CSS in 1986 showed that feature mapped by P. Tonkin (1973) is part of central uplift; diameter of impact structure is very roughly estimated from size of central uplift and sparse outcrops along one radius. Youngest rocks deformed are of Proterozoic age; central uplift is overlapped by beds of Middle Cambrian age.
- Strangways: Geologic map (unpubl.) by D.J. Milton; siderophile elements in impact melt reported by Morgan et al. (1981). Youngest rocks deformed are Late Proterozoic in age; impact structure is overlapped by beds of Middle Cambrian age and apparently by volcanic rocks of Early Cambrian age.
- Lake Acraman: Estimated diameter is based on field observations of shock effects rather than on distant structural arcs reported by Williams (1986). Age estimated from stratigraphic position of distant fallout layer described by Gostin et al. (1986); anomaly in siderophile elements noted by V. Gostin (personal communication, 1987).
- Spider: Geologic map (unpubl.) by EMS completed in 1985. From estimated depth of erosion, impact structure is interpreted to predate nearby Late Proterozoic glacial deposits.
- Teague Ring: Geology mapped at a scale of 1:250,000 by Bunting et al. (1982). Apparent whole-rock isochron reported for syenite in central uplift by Bunting et al. (1980) is interpreted here as approximate age of shock event and formation of structure.
- Flery Creek Dome: This well-mapped dome and surrounding structural depression (Hutton and Wilson, 1984) is interpreted as a probable impact structure on the basis of reconnaissance by EMS and CSS in 1987. Rocks deformed are of Early Proterozoic age; structure is overlapped by younger strata of Early Proterozoic age.

# PROGRESS ON THE IMPACT ORIGIN OF THE MOON AND OTHER TOPICS.

H. J. Melosh and A. M. Vickery, Lunar and Planetary Laboratory, University of Arizona, Tucson, AZ. 85721

## 1. Impact Origin of the Moon

I have completed roughly a dozen more 2-D computer simulations of the impact of a Mars-size impactor with the proto-earth in collaboration with M.E. Kipp at Sandia using the numerical hydrocode CSQ II. In addition to these numerical studies, a highly successful analytic model for vapor expansion subsequent to the impact was constructed. Ann Vickery adapted her 1-D hydrocode to the case of an expanding spherical cloud in the presence of a vapor-solid transition. We used the ANEOS equation of state package to construct a phase diagram for dunite, and checked that it agrees well with data on condensation of silicate vapor at low pressure. The CSQ II results from the main computation were used to determine input parameters for the expanding sphere computation. Once the vapor is largely condensed we use Keplerian orbital mechanics to determine the ultimate fate of the condensates. The results are summarized in Table 1. It is clear that the higher velocity impacts inject more material into orbit outside the Roche limit. We are able to get about one lunar mass into orbit with an appropriate choice of parameters. In all cases the condensate enters a highly elliptical orbit around the earth. Under these circumstances only slight perturbations would be necessary to inject much of the "crashed" material into orbit also. We are currently evaluating the effect of solar perturbations to see if three-body effects might result in more material attaining orbit.

A 3-D version of CSQ is currently in the test phase and when it is running we have reserved time to perform a number of 3-D runs in which self gravity will be included. More on this in the work statement.

See the LPSC XVIII abstracts by Kipp and Melosh (1987) and Vickery and Melosh (1987a) for more information on these efforts.

Table 1

Fate of ejected material for various impact condtions

Encounter Velocity km/sec	Impact Parameter Earth Radii	Angular Momentum Present angular momentum	mass mass of moon		
			Crash	Orbit	
Escape					
0	0.5	0.57	8.2	0	0
0	1.0	1.13	2.0	0.03	0.62
7.8	0.5	0.85	1.5	0	1.8
7.8	1.0	1.70	0.10	1.4	0

## **2. *Sinker Tectonics on Miranda***

D. Janes, a graduate student, has made a great deal of progress on this topic. He has found that a sinking mass near the surface of a planet induces inward flow the mantle that, when coupled to an elastic lithosphere, results in a concentric pattern of thrust faults or folds. This pattern closely resembles the tectonic interpretations of the Ovoids on Miranda and also the Ovoids on Venus. We have integrated the sinker model with the chaotic tumbling model of Greenberg and Marcialis (1987) to produce a consistent tectonic and thermal history of that satellite. A full paper is in press at JGR. See the LPSC XVIII abstract Janes and Melosh (1987).

## **3. *Mechanics of Graben Formation***

Using a finite element model I was able to show that the formation of a normal fault in a sequence of crustal (that is, not viscoelastic) rocks almost immediately induces a second fault parallel to the first, separated by a distance of the order of the first fault's width. By examining changes in total strain energy graduate student C. Williams demonstrated that this fault is always antithetic to the first in the absence of applied shear stress. These relations are not significantly affected by the presence of layers with different elastic moduli. We have used stiff over weak and weak over stiff layer configurations and obtained nearly the same results. This suggests that the width of extraterrestrial grabens might not be a good indicator of the thickness of postulated crustal layers, except insofar as these layers control the depth of faulting. A full paper on this topic is currently in preparation.

The full computations performed here required the modification of my finite element code and the introduction of internal nodes where free slip is permitted. These "slippery nodes" permit the imposition of a specified resolved shear stress across any line within the model and are able to accurately simulate the effect of faulting. We have also developed the capability of 3-D modeling which a number of students in the department are now using to model more complex tectonic situations on the surfaces of the satellites in the outer solar system.

See the Fall AGU abstract Melosh (1986).

## **6. *Other Topics***

A number of other problems have come up as "targets of opportunity" and have been solved or have been published in this past few months.

Mr. Kevin Horstman, a graduate student, has completed an experimental investigation of the landforms produced by drainage of a loose regolith into underlying fissures. This work is aimed at explaining the grooves and pits on Phobos. He has found that as drainage begins, pits first form over the fissures which then connect up to form grooves. The pit spacing is nearly exactly equal to the regolith thickness. Using pit spacing data from Phobos, it appears that the regolith is nearly 300m thick, a figure in excellent agreement with an independent estimate based on crater morphology (Duxbury et al. 1984). A full paper is submitted to JGR, but see LPSC XVIII abstract Horstman and Melosh (1987).

Ms. Valerie Hillgren has undertaken a finite element study of the collapse of craters that are large enough to penetrate the lithosphere of the planet on which they form. She has shown that large radial extensional stresses that may produce one or more multiple rings around the crater develop as a result of the inward flow of the asthenosphere, but only if the viscosity *increases* with depth below the asthenosphere. Otherwise the upward flow of a deep

asthenosphere results in simple updoming beneath the crater and radial, not circumferential, extension. This may explain why multiring basins are so well developed on Ganymede and Callisto (eg. Valhalla), and not on Mercury or Mars (Ganymede and Callisto are widely speculated to possess a thin zone of especially fluid ice II below their surfaces). Multiring basins may be common on the moon because of a viscosity increase at the base of the once-molten magma ocean. Work on this topic continues and we expect to be able to begin preparation of a paper on the major results this fall. See also the LPSC XVIII abstract Melosh and Hillgren (1987).

Ann Vickery has completed an intensive investigation of the sizes of fragments as a function of velocity ejected from craters on the Moon, Mars and Mercury in an attempt to verify or invalidate the predictions of my spall model. This work was based on observations of secondary craters around different size primaries on these bodies. She has concluded that the data supports the spall model. In particular, the secondary crater fields are distinct from the general mass of ejecta thrown out of a crater. The diameter of the secondary crater pattern scales differently than the ejecta blanket thickness and extent as gravity is changed, and the total mass represented by secondary fragments is only a few percent of the total mass ejected. Both these features are consistent with secondary craters being made almost exclusively by spalls. See Vickery (1986a), and Vickery (1987a).

Ann has also completed her work on the gas acceleration of ejecta from impact craters as a possible explanation of the SNC meteorite's ejection from Mars. She has concluded that, although small fragments in the range of 10 cm to perhaps 1 m can be ejected from 30 km craters on Mars by this mechanism, it is incapable of lofting larger rocks to Martian orbit. Ann and I have proposed that the SNC meteorites must have been ejected from a much larger crater to explain both their exposure ages and abundance on earth. See Vickery (1986b), Vickery (1987b), and Vickery and Melosh (1987b).

## REFERENCES

- Duxbury, T.C., J.D. Callahan, and A.C. Ocampo, Phobos: Close encounter imaging from the Viking orbiters, NASA Ref. Pub. 1109, 51pp (1984). Horstman, K.C. and H.J. Melosh, Experimental drainage pits as possible analogs to structures on Phobos, LPSC XVIII, 439-440 (1987). Janes, D.M., and H.J. Melosh, Surface tectonics from sinker induced mantle convection: Application to Miranda, LPSC XVIII, 458-459 (1987). Kipp, M.E. and H.J. Melosh, A numerical study of the giant impact origin of the moon: The first half hour, LPSC XVIII, 491-492 (1987). Marcialis, R. and R. Greenberg, Warming of Miranda during chaotic rotation, *Nature*, in press (1987). Melosh, H. J., The mechanics of graben formation in crustal rocks, *EOS*, 67, 1212 (1986). Melosh, H.J. and V. Hillgren, A finite-element study of multiring basin tectonics, LPSC XVIII, 639-640 (1987). Vickery, A.M. and H.J. Melosh, Orbital evolution of the vapor jet from a giant impact, LPSC XVIII, 1042-1043 (1987). Vickery, A.M. and H.J. Melosh, The large crater origin of the SNC meteorites, *Science*, 237, 738-743 (1987b). Vickery, A.M. Size-velocity distribution of large ejecta fragments, *Icarus* 67, 224-236 (1986a). Vickery, A.M. Effect of an impact-generated gas cloud on the acceleration of solid ejecta, *J. Geophys. Res.* 91, 14,139-14,160 (1986b). Vickery, A.M. Variation in ejecta size with ejection velocity, *Geophys. Res. Lett.* 14, 726-729 (1987a). Vickery, A.M. Effect of an impact-generated gas cloud on entrained surface boulders and spall ejecta, *Int. J. Impact Engng.*, 5, 655-661 (1987b).

THE USE OF BASIN EJECTA TO DETERMINE LUNAR CRUSTAL STRUCTURE AND COMPOSITION: CURRENT MODELS AND LGO CONTRIBUTIONS. Paul D. Spudis, USGS, Flagstaff, AZ 86001 and B. Ray Hawke, HIG, Univ. Hawaii, Honolulu, HI 96822.

Our knowledge of the composition and structure of the lunar crust has important ramifications for understanding the origin, crustal formation, and geologic evolution of the Moon. Although the Apollo samples provided us with a wealth of information on lunar compositions, we still do not understand completely how those samples relate to global rock types and when and where they were distributed in the crust. Fortunately, the Moon has obliged us in one respect towards this end by providing for our inspection over 40 large impact craters, i.e., multi-ring basins [1]. Through the use of basins as natural drill holes into the crust, we are able, in principle, to determine the chemical and petrological composition of the crustal target.

Although this technique is applicable in theory, numerous difficulties and uncertainties attend its application in practice. The purpose of this paper is to review some of these difficulties and to assess the probable uncertainties of using basins as probes of the lunar crust. Also, we will examine current understanding in this field derived from Apollo sample data, orbital chemical data, and Earth-based spectroscopy, and we will estimate the contributions and improvements to our understanding that are likely to be provided by data from the Lunar Geoscience Observer (LGO) mission [2].

Problems in using basins as drill holes. A long-standing controversy in the field of basin research involves the shape and dimensions of the original cavity of excavation [e.g., 1, 3-5]. This problem is critical to the use of basins as crustal probes; some estimates of the original size and shape of the excavated cavity must be made prior to any inference of crustal composition and/or layering. Most excavation models fall into two broad categories: proportional-growth models [e.g., 3, 5, 6], in which basins are simply larger versions of smaller craters, and nonproportional-growth models [e.g., 1, 4, 7], in which the size and shape of the excavated cavity are fundamentally different from those of smaller craters. Quantitative proportional-growth models are now available [6], but no quantitative model of nonproportional-growth excavation has yet been developed. This controversy is not likely to be resolved in the near future; investigators using basins to probe the crust must choose at the outset some type of semi-quantitative excavation model to estimate ejecta volumes and probable depths of ejecta derivation.

.. An equally important controversy in basin studies is related to the nature of the ejecta blanket itself. During Apollo planning, it was widely believed that deposits extending continuously from the basin rim were primary ejecta from the basin cavity, hence the name "ejecta blanket" and selection of the Fra Mauro (Apollo 14) landing site [1]. Later experimental and theoretical study [8-10] suggested that the impact of basin ejecta on the lunar surface excavated the preexisting local terrain and that this local material is mixed with primary ejecta in basin deposits. These results suggested that near Fra Mauro (the edge of Imbrium continuous deposits), primary Imbrium ejecta constitute only 15%-20% of the total mass of the deposit; near the rim of the apparent crater (Apennines at Imbrium), the Oberbeck et al. model predicts that roughly half of the material is primary ejecta [9]. Recently Schultz and Gault [11] have investigated the effects of deposition of clouds of comminuted debris during ejecta emplacement, instead of the single-body impactors assumed by Oberbeck et al. [8, 10]; they found that primary ejecta constitute greater than 90% of the deposit near basin rims and up to 80% at Fra Mauro ranges [11]. Thus, near-rim basin deposits consist of at least 50% to greater than 90% primary ejecta.

A final problem in using basins to probe the crust is the nature of the ejecta stratigraphy (if they are indeed stratified). Studies of ejecta from simple craters indicate that materials from the deepest horizons of a crater target tend to concentrate nearest the crater rim (the "overturned flap") [12]. On the basis of this analogy, near-rim basin ejecta would be dominated by ejecta from the deepest parts of the crustal target, possibly leading to an incorrect assessment of the target's composition. However, detailed study of the deposits of the Ries crater [13] suggests that for large-scale impact events, ejecta tend to be well-mixed averages of all stratigraphic horizons in the crustal target and that they include (unfortunately) the local material incorporated into basin continuous deposits, as noted.

Current use of basins as crustal probes. In the past several years, we have attempted to use basin ejecta to understand lunar crustal structure and composition [3, 14-17]. We have been well aware of the problems discussed above that are associated with this usage but we have felt that the potential insights into crustal structure given us by basins greatly outweigh the model uncertainties. For basin excavation, we have relied on the proportional-growth model for two main reasons: (1) evidence from terrestrial impact craters [5, 13] and lunar photogeology [15, 18] suggest that this model is valid for basins, and (2) this model permits some quantitative modeling of ejecta volumes and derivation depths [6, 15, 17]. To put it another way, nothing in the lunar data suggests that proportional growth for basins is not valid. For determining the local vs. primary ejecta content of basin deposits, we have used only the clearly mappable deposits that are one-half to one apparent basin radius from the basin rim, and we have assumed that these deposits are mostly primary basin ejecta. The observation that near-rim basin deposits tend to be compositionally different from the average interbasin deposits on the Moon [16, 17] suggests that this assumption is reasonable to a first order. Of course, this means that we have inevitably included some local material [cf. 9, 11] in our estimate of basin ejecta composition, and in this sense our results are model dependent. We have assumed that basin ejecta are well mixed, in accordance with the Ries data [13], and also that a given sector of basin deposits is representative of the basin deposits as a whole. (No lunar basin has complete orbital chemical coverage of all of its deposits.)

Based on these assumptions, studies of lunar basin deposits indicate the following: (1) the lunar crust is both laterally and vertically heterogeneous [14, 16, 17]; (2) roughly the upper half of the crust consists of "anorthositic gabbro" ( $\text{Al}_2\text{O}_3$  26%-28%), while the lower half is grossly "noritic" ( $\text{Al}_2\text{O}_3$  20%) [17]; (3) rocks of the Mg-suite [19] make up a minor fraction of upper crustal rock types [16, 17]; (4) the polymict lunar rock types "LKFM basalt" and "VHA basalt" may represent impact melts formed during basin impacts [17, 20]; and (5) the average alumina content of the bulk crust ( $\text{Al}_2\text{O}_3$  25%) suggests that most of the crust formed during a global "magma ocean" stage [e.g., 19], rather than by "serial magmatism" [e.g., 21]. Such tentative results address basic problems, but, based on so many uncertainties, but how valid are they? More importantly, how much better will we be able to do with LGO data?

LGO data and lunar crustal problems. Because the Apollo 15 and 16 missions flew in near-equatorial orbits, only about 19% of the lunar surface and only 11 lunar basins are covered by at least some chemical data [14, 17]. Spectroscopic measurements are limited to the lunar nearside. Data from the LGO mission will greatly augment this meager information. First, of the 40 basins randomly distributed over the Moon, at least half display recognizable

(preserved) deposits [1]. Thus, we will at least double our statistical sample of basins. Second, global coverage will allow petrologic and chemical measurement of all the deposits of a given basin; moreover, the chemical data will be nearly complete for major and trace elements, as opposed to the minimal data we currently have for some basins (e.g., for Orientale, we know only the Th, Fe, and Ti contents of the northern one-quarter of basin deposits). Third, nonchemical data from LGO (gravimetric, topographic, imaging) will permit better assessment of lunar crustal-thickness variations and models of basin formation [2].

Some of the basic problems of basin formation can also be addressed with LGO data. By examining certain large craters in detail at high resolution, we may find evidence to resolve both the proportional-growth controversy and the local mixing ratio problem. That such an approach is potentially useful is well demonstrated by a recent study of the crater Copernicus that used Earth-based spectroscopy; results indicate both adherence to and divergence from the Oberbeck et al. local mixing model [22]. High-resolution gravimetric and topographic data from LGO will permit refined estimates of the excavated volume of large craters and basins, an important referent in the proportional-growth controversy. Images from LGO will permit examination of basins currently poorly covered by Lunar Orbiter pictures, and such images could lead to recognition of additional prebasin topography [15, 18].

The larger quantity and better quality of LGO data as compared with the current dataset will probably allow a definitive resolution of one of the most important lunar problems, i.e., the origin of the crust. Current estimates of the total plagioclase inventory in the crust (equivalent thickness of plagioclase 20 km; [17, 23]) is at the high end of the permissible range of values for some "serial magmatism" models (10-20 km; [24]). The greater quantity and precision of data available from LGO should permit the resolution of this question [2]. The mechanism of lunar crustal formation has important ramifications for general models of terrestrial planet evolution [19].

We believe that the LGO mission will provide not only good science for its own sake, but also results of great significance for planetary exploration in general. The sooner this mission flies, the better.

References: [1] Wilhelms, D.E. (in press) USGS PP 1348. [2] LGO Workshop (1986) Contributions of LGO Mission to Lunar Science, SMU, 86 p. [3] Spudis, P.D. (1986) LPI Tech. Rpt. 86-03, 100. [4] Hodges, C.A. and Wilhelms, D.E. (1978) Icarus 34, 294. [5] Grieve R.A.F. et al. [1981] PLPSC 12A, 37. [6] Croft, S.K. (1981) PLPSC 12A, 207; (1985) PLPSC 15, JGR 90, C828. [7] Schultz, P.H. and Gault D.E. (1986) LPS XVII, 777. [8] Oberbeck, V.R., et al. (1975) Moon 12, 19. [9] Morrison, R.H. and Oberbeck, V.R. (1975) PLSC 6, 2503; (1978) PLPSC 9, 3763. [10] Oberbeck, V.R. (1975) RGSP 13, 337. [11] Schultz, P.H. and Gault D.E. (1985) JGR 90, 3701. [12] Gault, D.E., et al. (1968) Shock Metamorphism, 87. [13] Hörz F., et al. (1983) RGSP 21, 1667. [14] Spudis, P.D. et al. (1984) LPS XV, 812. [15] Spudis, P.D. et al. (1984) PLPSC 15, JGR 89, C197. [16] Davis, P.A. and Spudis, P.D. (1985) PLPSC 16, JGR 90, D61. [17] Spudis, P.D. and Davis, P.A. (1986) PLPSC 17, JGR 91, E84. [18] Schultz, P.H. and Spudis, P.D. (1978) LPS IX, 1033. [19] Warren, P.H. (1985) Ann. Rev. Earth Planet. Sci. 13, 201. [20] Spudis, P.D. (1984) PLPSC 15, JGR 89, C95. [21] Walker, D. (1983) PLPSC 14, JGR 88, B17. [22] Pieters, C., et al. (1985) JGR 90, 12393. [23] Wood, J.A. (1986) Origin of Moon, 17. [24] Longhi, J. and Ashwal, L. (1985) PLPSC 15, JGR 90, C571.

**A MODEL FOR THE FORMATION OF MAGNETIC ANOMALIES ANTIPODAL TO LUNAR IMPACT BASINS; L. L. Hood, Lunar and Planetary Laboratory, University of Arizona, Tucson, Arizona 85721.**

**Introduction:** Maps of the distribution of lunar magnetic anomalies produced by the electron reflection method have shown that the largest concentrations of lunar crustal magnetization occur antipodal (diametrically opposite) to 4 relatively young large impact basins: Imbrium, Orientale, Serenitatis, and Crisium (1). Each of these regions is also marked geologically by the occurrence of (a) unusual grooved or pitted terrain that is believed to be the result of modification by converging seismic waves generated by the associated basin impact (2); and (b) swirl-like albedo markings of the Reiner Gamma class (e.g. ref. 3). By analogy with the mascons, which are directly correlated with young large lunar basins, these magnetization concentrations antipodal to young large lunar basins have been referred to as 'magcons'.

**Model Description:** In this paper, we develop a model for the formation of the magcons that considers the basin formation process, antipodal seismic modification effects, and the interaction of a thermally expanding impact-produced plasma cloud with an ambient magnetic field. As initial conditions, we assume the presence of a weak ambient field that has had time to diffuse into the highly electrically conducting lunar interior (Fig. 1A). The ambient field could in principle be produced by a weak former core dynamo but, for simplicity, only a spatially uniform interplanetary field oriented along the impact symmetry axis is considered here. Typical present-day interplanetary field amplitudes are in the range of 6–12 nT but may have been as large as 60–80 nT during the time of formation of Imbrian-aged basins. For the case of a basin-forming impact occurring at an incident velocity greater than about  $10 \text{ km s}^{-1}$ , partial vaporization and subsequent ionization of projectile and target material occurs leading to the formation of a thermally expanding vapor and plasma cloud (Fig. 1B,C). Previous detailed calculations of ionization rates and approximate electrical conductivities show that the magnetic Reynolds number of the expanding gas is  $\gg 1$  so, to first order, it is admissible to neglect diffusion of the field through the plasma cloud in comparison to advection. The internal energy density of the cloud is much greater than that of the ambient field; the field will therefore be excluded from the volume occupied by the highly conducting gas. As the gas expands around the Moon, field lines are tied to the highly conducting solid lunar interior but are forced away from the impact point external to the surface leading to a strong concentration of flux at the antipode (Fig. 1D,E). From conservation of flux alone, the field intensity within a circular zone of radius  $\sim 100 \text{ km}$  near the basin antipode (comparable in size to the magcons) would be amplified by a factor of about 300. Field intensities as large as 0.1–0.2 G ( $1 \text{ G} = 1 \text{ Oe} = 10^{-4} \text{ T}$ ) are therefore expected for assumed ambient field amplitudes of 40–80 nT. If a former core dynamo provided significantly larger surface fields, then these estimates would be increased in proportion. As the compression approaches the antipode, plasma physical processes including reconnection of the compressed field and diffusion of the field into the dissipating plasma cloud must be considered and will eventually act to limit the maximum field amplitude.

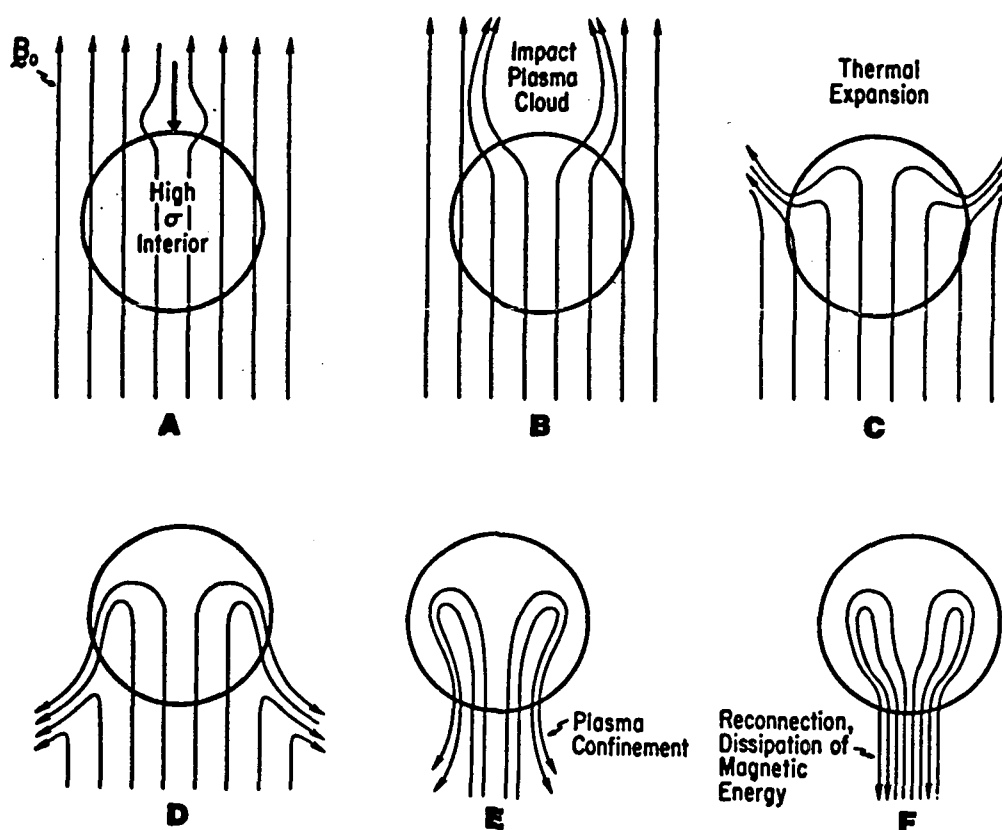
**Remanence Acquisition:** Acquisition of magnetic remanence in the antipodal zone during the period of compressed field amplification may occur by one of several mechanisms: (a) Acquisition of shock remanence during the seismic modification process; (b) acquisition of shock remanence by impact of solid ejecta from the basin forming event; and (c) thermoremanence of subsurface magma intrusions released by antipodal crustal fracturing. To investigate the plausibility of each, the time scales characterizing these processes may be compared to the rate of expansion of a basin-forming impact plasma cloud and the time scale for decay of thermal energy within the cloud. The expansion velocity determines the approximate time for arrival of compressed ambient magnetic fields at the antipode while the internal energy decay determines the maximum length of time during which field amplification can persist. For the purpose of calculating the latter two quantities, we use a one-dimensional numerical model for the expansion of impact-produced vapor clouds which includes a geometrical spreading factor to translate the modeled linear expansion into an approximate spherical expansion (4). Results show that a nominal 100-km radius silicate (gabbroic anorthosite) impactor with an incident velocity of 15 km/sec produces a plasma cloud that expands to a distance comparable to half the lunar circumference in a time of  $\sim 200 \text{ sec}$  and has an internal energy density that exceeds that needed to confine a compressed 1 G field for of the order of  $10^5 \text{ sec}$ . For comparison, arrival times of seismic body waves with velocities of 8 km/sec would be about 8 minutes while those of surface waves with velocities of  $\sim 1.2 \text{ km/sec}$  would be about 80 minutes. In the case of basin ejecta, ballistic calculations on a spherical



moon for ejection angles of  $30^\circ$  to  $60^\circ$  yield antipodal arrival times of 28–50 minutes (e.g. ref. 2). In the case of magmatic intrusions, the time scale for conductive heat loss and acquisition of thermal remanence is at least years and probably tens of years. Consequently, mechanisms (a) and (b) are viable while mechanism (c) requires considerably more time than appears realistic for plasma confinement of an ambient field.

If shock remanent magnetization (SRM) produced by seismic waves or by secondary basin ejecta impacts in antipodal zones is the primary remanence mechanism, then it is of interest to consider expected magnetization intensities for reasonable shock ranges and compressed ambient field amplitudes. In the case of antipodal seismic effects, theoretical calculations indicate that a basin-forming impact with energy  $\sim 10^{34}$  ergs would produce an antipodal seismic wave with a compressive stress of several hundred bars (2). These shock pressures are considerably below those at which stable SRM has been found to occur in shocked lunar soils (50–250 kbar; ref. 5). However, even weak shock ranges ( $< 5$  kbar) have been shown to produce magnetically soft SRM in several experiments (6). In the case of antipodal secondary ejecta deposition, peak shock pressures from secondary impacts produced by basin-forming events have previously been estimated as a function of ejecta range (e.g. Table 3 of ref. 4). The resulting shock pressures exceed 100 kbar and are therefore sufficiently strong that efficient acquisition of magnetically hard SRM is expected. By comparison with the experimental results of refs. 5, remanent magnetization intensities of the order of  $10^{-4}$ – $10^{-3}$  G cm<sup>3</sup> g<sup>-1</sup> may be estimated. These levels are comparable to or larger than the largest magnetization intensities measured for returned samples and would be sufficient to account for the observed anomalies if a sufficiently large volume of material acquired SRM.

**References:** (1) Lin, R.P., K.A. Anderson, and L.L. Hood, *Icarus*, submitted, 1987; Lin et al., *Lunar Planet. Sci. XVII*, p. 480, 1986; Lin et al., *Lunar Planet. Sci. XI*, p. 626, 1980. (2) Schultz, P. and D. Gault (1975) *Moon*, 12, 159. (3) Hood, L.L., *Proc. Lunar Planet. Sci. Conf. 12th*, 817, 1981. (4) Hood, L.L. and A. Vickery (1984) *J. Geophys. Res.*, 89, C211; see also Srnka, L. (1977) *Proc. Lunar Sci. Conf. 8th*, 795. (5) Fuller, M., Rose, F., and Wasilewski, P. (1974) *Moon*, 9, 57; Cisowski, S.M., J.R. Dunn, M. Fuller, M.F. Rose, and P. Wasilewski (1974) *Proc. Lunar Sci. Conf. 5th*, 2841; Srnka, L., G. Martelli, G. Newton, S.M. Cisowski, M. Fuller, and R. Schaal (1979) *Earth Planet. Sci. Lett.*, 42, 127. (6) Nagata, T. (1971) *Pure Appl. Geophys.*, 89, 159.



## LARGE IMPACT BASINS AND THE ORIGIN OF THE CRUSTAL DICHOTOMY ON MARS

Herbert Frey, Geophysics Branch, Goddard Space Flight Center, Greenbelt MD 20771 and Richard A. Schultz, Department of Earth and Atmospheric Sciences, Purdue University, West Lafayette IN 47907

The origin of the fundamental crustal dichotomy on Mars remains the outstanding unsolved problem of martian geologic evolution. Wilhelms and Squyres (1984) suggested that a single giant impact early in martian history could account for the separation into heavily cratered terrain and younger, low-lying plains. This hypothesis has numerous difficulties (Frey et al, 1986) but remains attractive because large impacts are capable of rearranging the entire structure of the lithosphere in a relatively short period of time. They may also concentrate long-lived thermal and tectonic processes (Frey, 1980; Solomon et al., 1982; Grieve and Parmentier, 1984; Bratt et al., 1985). In this paper we examine one possible test of the mega-impact origin of the martian crustal dichotomy by examining the total population of large impacts that might be expected to have occurred on Mars if the Wilhelms and Squyres (1984) Borealis Basin was the largest member of that population.

The largest currently recognized impact on the martian surface (beside the Borealis Basin) is the Chryse Basin (Schultz et al., 1982). The maximum proposed diameters for Chryse and for Borealis are 4300 and 7700 km respectively. If each of these represents the largest member of the same type of impacting population, then very different total populations of large impacts on Mars are to be expected. These different populations can be compared with the known population of impacts, which is shown in Figure 1 based on the compilation by Greeley (1985) with additional basins from Stam et al. (1984) and Schultz (1984). The proposed Borealis Basin (Wilhelms and Squyres 1984) is shown as the dashed line.

Figure 2 shows the impact basins from Figure 1 plotted in a cumulative frequency diagram for (a) Chryse the largest basin and for (b) Borealis the largest basin. A  $D^{-2}$  distribution is plotted through the largest basin in each panel to provide a reference for what might be the "expected" original population of large impacts on Mars based on the largest "observed" basin. Note in Figure 2a that the currently recognized martian impact basins (for no Borealis Basin) do tend to follow the  $D^{-2}$  distribution. By differencing the known number of impact basins from the hypothetical "original" ( $D^{-2}$ ) population, it is possible to estimate the number of "missing" basins that have been removed or obscured by geological processes. These are shown in Table 1 for the Chryse-largest and the Borealis-largest cases. Very different numbers of missing basins are implied by the two distributions.

If Borealis is real and the largest member of an original  $D^{-2}$  population, then there are missing from the observed record 1 basin larger than 5000 km, 3-4 basins larger than 3000 km, 10 basins larger than 2000 km and 47 basins larger than 1000 km diameter. By contrast, the number of missing basins for the Chryse-largest case is much more modest: 1 basin larger than 2000 km and 7-8 basins larger than 1000 km. While it is not hard to imagine that subsequent geologic processes could have removed these Chryse-largest missing basins, it is much more difficult to see how the large number of

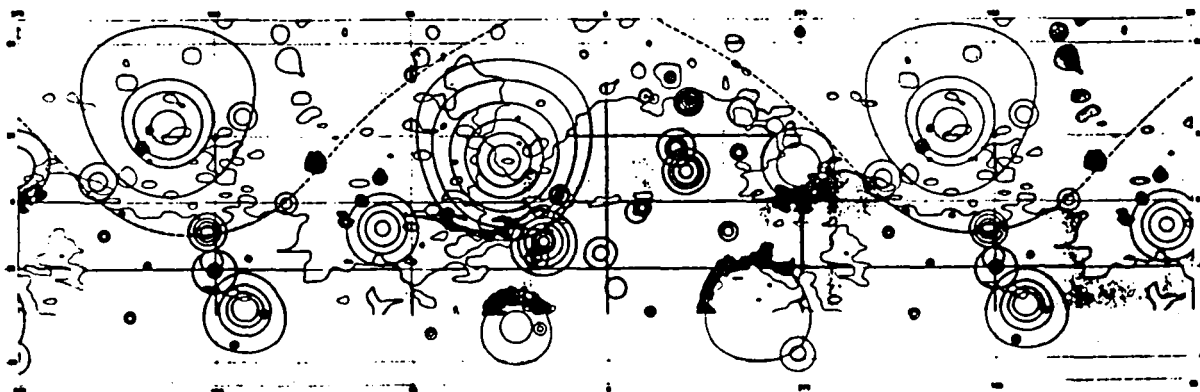
very large basins missing in the Borealis-largest case could have been obscured. The area occupied by these basins totals nearly 80% of the entire surface area of Mars, if allowance is made for overlap of basins. This in turn means they cannot all be hidden under younger geologic units such as the northern lowland plains or the Tharsis volcanic plains. There should be a large number of very large impact basins preserved in the heavily cratered highlands of Mars which to date have not been recognized.

By contrast it is quite possible that the more modest number of "missing" impact basins for the Chryse-largest case could be hidden under the younger geologic units of Mars. These basins require only about 30% of the martian surface area (Table 1) and could in principle all lie beneath the northern plains. This is of course unlikely, but the possibility does offer an alternative for the formation of the martian crustal dichotomy: it could be due to the overlapping effects of large (but not mega-) impacts (Frey et al., 1986).

#### REFERENCES

- Bratt, S.R., S.C. Solomon and J.W. Head (1985) The evolution of impact basins; cooling, subsidence and thermal stress. *J. Geophys. Res.* 90, 12415-12433.
- Frey, H. (1980) Crustal evolution on the early Earth: The role of major impacts. *Precamb. Res.* 10, 195-216.
- Frey, H., R.A. Schultz and T.A. Maxwell (1986) The martian crustal dichotomy: Product of accretion and not a specific event? *Lunar Planet. Sci.* XVI, 241-242.
- Greeley, R. (1985) *Planetary Landscapes*, Allen and Unwin, London.
- Grieve, R.A.F. and E.M. Parmentier (1984) Considerations of large scale impact and the early Earth. *Lunar Planet. Sci.* XV, 326-327.
- Schultz, P.H. (1984) Impact basin control of volcanic and tectonic provinces on Mars, *Lunar Planet. Sci.* XV, 728-729.
- Schultz, P.H., R.A. Schultz and J.L. Rogers (1982) The structure and evolution of ancient impact basins on Mars, *J. Geophys. Res.* 86, 9803-9820.
- Solomon, S.C., R.P. Comer and J.W. Head (1982) The evolution of impact basins: viscous relaxation of topographic relief, *J. Geophys. Res.* 87, 3975-3992.
- Stam, M., P.H. Schultz and G.E. McGill (1984) Martian impact basins: morphology differences and tectonic provinces, *Lunar Planet Sci.* XV, 818-819.
- Wilhelms, D.E. and S.W. Squyres (1984) The martian hemispherical dichotomy may be due to a giant impact, *Nature* 309, 138-140.

#### IMPACT BASINS ON MARS LARGER THAN 200 km DIAMETER



Impact basins from compilation by Greeley (1985) with additional basins from Stam et al. (1984) and Schultz (1984). Proposed Borealis Basin (Wilhelms and Squyres, 1984) dashed.

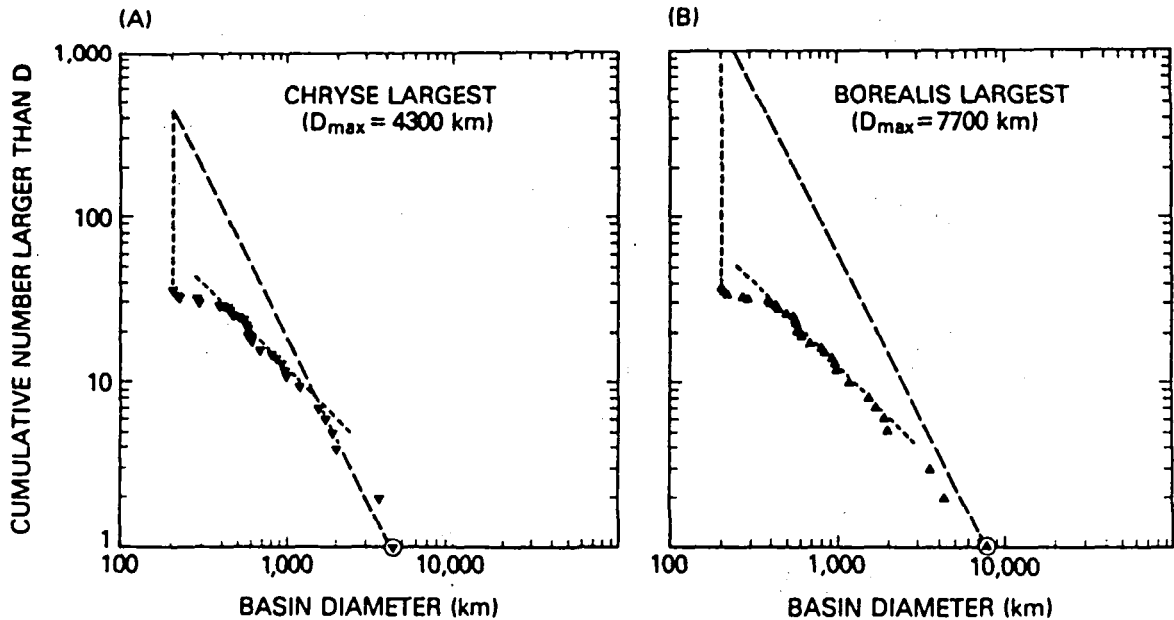
TABLE 1. Size Distribution of "Missing" Basins

DIAMETER	CHRYSE IS LARGEST (4300 km)			BOREALIS IS LARGEST (7700 km)		
	# EXPECTED	# OBSERVED	# "MISSING"	# EXPECTED	# OBSERVED	# "MISSING"
7500				1.05	1*	
7000				1.21	1	
6500				1.40	1	
6000				1.65	1	
5500				1.96	1	1
5000				2.37	1	1
4500				2.93	1	2
4000	1.16	1*		3.71	2	2
3500	1.51	2		4.84	3	2
3000	2.05	2		6.59	3	3-4
2500	2.96	2	1	9.49	3	6-7
2000	4.62	4	1	14.82	5	10
1500	6.22	7	1	26.35	8	18
1000	18.49	11	7-8	59.25	12	47
800	28.89	15	14	92.64	16	77
600	51.36	18	33	164.69	19	146
400	115.56	29	87	370.56	30	341
200	462.25	37	425	1462.25	38	1444

Combined area of "missing" basins	0.32-0.34 $A_J$	1.63-1.75 $A_J$
Area occupied by "missing" basins	0.26-0.29 $A_J$	0.80-0.83 $A_J$

FIGURE 2



Cumulative number of martian impact basins assuming (a) Chryse-largest and (b) Borealis-largest.  $D^{-2}$  distribution through largest basin for reference.

EARLY CRATERING RATES AND THE NATURE OF THE MARTIAN CRATERED UPLANDS; P.H. Schultz, Dept. of Geological Sciences, Brown University, Providence, RI 02912

The cratered uplands of Mars represent a complex sequence of reworked crater ejecta, distant basin ejecta deposits, sedimentary (aeolian and fluvial) deposits, and possible volcanic plains. The heritage of the early period of impact bombardment is documented in the preserved cratering record where the areal density of large craters ( $>20$  km) exceeds that of the Moon and subtle relicts of large impact basins remain. The cratering record provides a means to estimate the early impact flux on Mars, to constrain the direct and indirect effects of the impact process over various scales, and to evaluate the nature of the cratered upland surface materials. Four issues are addressed: the early martian cratering rate; the role of late-stage atmospheric accretion of volatiles; the relative effects of craters and basins on the global redistribution of crustal materials; and the indirect longer term effects of basin formation.

**Early Cratering Rate:** The cratering record of the martian uplands is partly masked by once more active erosional/depositional process and the possible global resurfacing by large impacts. An estimate of the early cratering rate must allow for or avoid such effects. One approach references the cratering record superposed on the youngest major impact basins, Argyre and Isidis, to subsequent martian units, thereby establishing a relative chronology. An absolute chronology requires referencing this history to the lunar time scale and can result in unacceptable surface ages, e.g., an age older than the planet if referenced to the estimates of the present-day flux. Another approach does not require a precise match over the entire martian time scale but only over a more limited time interval since basin formation. The total impact flux and change in impact flux over such time intervals provide explicit implications for the dynamical evolution of martian impactors and permit constraining the possible effects of impact cratering during early martian history.

Figure 1 compares the observed cumulative crater densities on Isidis, Argyre, the Elysium knobby terrains (relicts of dichotomy formation), and the old ridged plains of Hesperia on Mars with the cumulative crater densities on the lunar Imbrium and Orientale basins. The observed difference between crater densities on the youngest lunar and martian impact basins could reflect one or a combination of several processes: (a.) erosional enlargement of craters used in the statistics; (b.) an excessive number of large martian impactors; (c.) secondary impacts from post-Argyre, Isidis-size impacts now removed or buried (e.g., Tharsis region); (d.) martian basin ages much older than the last lunar basins; and/or (e.) a once higher impact flux on Mars. The first process cannot account for the observed difference alone since preserved relief of crater rims is inconsistent with excessive crater widening. Although the second suggestion is possible, it is difficult to prove. The third suggestion is also possible but there is no other evidence for such a feature (e.g., a regional gradient in the areal density of 20–50 km craters). If the lunar and martian impact flux of objects  $< 10^{18}$  g were always the same, then time of formation of Isidis and Argyre would date from an unreasonably early epoch (4.5 by), even after correcting for the difference between lunar and martian gravity. The following discussions, therefore, focus on the consequence of the fifth possibility: the flux of objects  $< 10^{18}$  g following the period of major basin formation on the Moon and Mars was different. Limits on how much they differ can be made by examining the consequences of two assumptions: the assumed age of a selected martian impact basin and the decay rate in the supply of martian impactors. If the Isidis basin on Mars dates to 3.78 by, about the age of Orientale impact on the Moon (1), then the last exposed major basin on Mars (Argyre) dates back to 3.67 by and the martian impact flux was 17 times the lunar flux at the time (after corrections for martian gravity and average impact velocity and an assumed Moon-like decay rate of impactors with a half-life of about 130 my). If the Isidis basin dates to 4.0 by, then Argyre dates to 3.88 by and the impact flux was 5 times the lunar flux. Figure 2 compares the consequences of different decay rates.

An important implication of such an approach is that the rate of surface processes acting to modify primary basin features or the subsequent cratering history can be largely constrained since small features from this epoch (e.g., narrow valley networks) remain preserved. If the observed fall-off in craters smaller than 18 km recorded in the massif/scarp annulus of Isidis reflects an early period of resurfacing, then the crater removal rate on Mars at this time approached the present terrestrial value given by Grieve (2). Although a longer half-life in the decay of post-basin impactors (e.g., 267 my) extends the time interval and decreases the inferred rate of crater removal, unreasonable constraints on the dynamical evolution of impactors and the absolute age of younger

geologic units result: the ridged plains such as Lunae Planum approaching 2.5 by and the impact flux equaling the present rate at 2.0 by.

**Accretion, Erosion, and Release of Volatiles by Impact:** Even the presently tenuous martian atmosphere shields the surface from impacts by small objects. Since the present atmospheric density on Mars at 80 km is comparable to the present terrestrial value at 100 km, atmospheric break-up prevents 50 m diameter craters from forming (3). Smaller mass objects ( $\sim 1$  g) are melted and vaporized during entry and essentially accreted by the atmosphere. On the Moon such impacts result in a net mass loss. If the incoming small mass were volatile-rich cometary material, a maximum equivalent of 15–30 precipitable meters (ppm) of water could have accreted in the 100 million years following Isidis (Figure 3). The post-Argyre accretion rate amounts to 4–11 ppm in the same time period but within 500 my this potential supply dwindled to less than 10 cm every 100 my. The values during and soon after the period of major basin formation approach estimates for water released by internal processes (4). The influx of cosmic volatiles would not result in rainfall but would become incorporated into the atmosphere or scavenged by atmospheric dust, thereby never directly affecting atmospheric pressure.

A competing process of atmospheric blow-off has been proposed (5) but the efficiency of the process remains in debate (6). Recent experimental studies (7) indicate that impact angle is very important in controlling target vaporization even at relatively low impact velocities (5 km/s). Impact vaporization may be more important in recycling (rather than removing) near-surface volatiles. From the derived impact rate, one 100 km-diameter crater would form in a 60,000 year interval (on the average) with less than 1 cm of ejected debris distributed globally. The Argyre impact basin, in contrast, would result in a global deposit 50–400 m with a 0.2–1.4 bar increase in atmospheric pressure if 1% of the excavated debris were released as volatiles. The catastrophic effects of a major basin therefore far outweigh the incremental effects of smaller and more frequent large impact craters. At basin scales, volatiles can be released not only by impact vaporization but also by distant ejecta re-entering the atmosphere, by ejecta impacting the surface, and by rapid devolatilization of an exposed martian mantle. Released volatiles as well as suspended ejecta likely will be drawn back to the basin by strong recovery winds (as seen in the laboratory) and large thermal gradients created above the cooling basin cavity.

Recent comparisons of impact basin ages and associated plains-forming volcanism indicate that tectonism/volcanism persists only for a characteristic time following impact (8). It is proposed that volatiles released by the impact and collected within the basin, whether due to the initial atmospheric response to the impact or due to later orographic control of aeolian (and volatile) deposition, were subsequently recycled during basin-controlled volcanism. As the frequency of major basins decreased, the rate of recycling decreased until the re-trapping or escape rate of volatiles could not be offset by either internal or external sources (9) as illustrated in Figure 4.

**Summary and Implications:** The cratered uplands evolved not only from the local effects of large impact craters (20–200 km) but also from the global consequence of major basin formation. During the very late period of high impact bombardment (4.0 by), the martian crust may have received volatiles not only from internal heating but also from accretion of impactors too small to form impacts. Although impacts producing 100 km diameter craters are significantly more numerous than 1000 km impact basins, basin-scale impacts can be shown to have a much more important effect on the global redistribution of debris and the release of trapped volatiles perhaps expressed by a brief period of widespread unconformable deposits (10, 11) and the decrease in production rate of narrow-valley networks (12) before the development of the Tharsis volcanic constructs. The cratered uplands preserve this complex depositional history in a manner very different from the lunar highlands.

- 
- (1) Wilhelms, D. (1984) In *Geology of the Terrestrial Planets*, NASA SP-469, 107–197.
  - (2) Grieve, R. (1984) *J. Geophys. Res.*, 89, B403. (3) Gault, D. and Baldwin, B. (1970) *Trans. Am. Geophys. Union (EOS)*, 51, 342. (4) Greeley, R. (1987) *Science* 236, 1653–1654. (5) Watkins, H. (1983) *The Consequences of Cometary and Asteroid Impacts on the Volatile Inventory of the Terrestrial Planets*, Ph.D. Dissertation, MIT, Cambridge. (6) Walker, J. (1986) *Icarus*, 68, 87. (7) Schultz, P. and Gault, D. (1986) In *Lunar and Planetary Sci. XVII*, Lunar and Planetary Institute, Houston, 779–780. (8) Wichmann, R. and Schultz, P. (1987) In *Lunar and Planetary Science XVII*, Lunar and Planetary Institute, Houston, 1976–1979. (9) Schultz, P.H. (1987) *Kagaku* 57, 486–496. (10) Grant, J. and Schultz, P. (1987) this volume. (11) Grizzaffi, P. and Schultz, P. (1987) submitted to *Icarus*. (12) Schultz, P. and Britt, D. (1986) In *Lunar and Planet. Sci. XVII*, Lunar and Planetary Institute, Houston, 775–776.
-

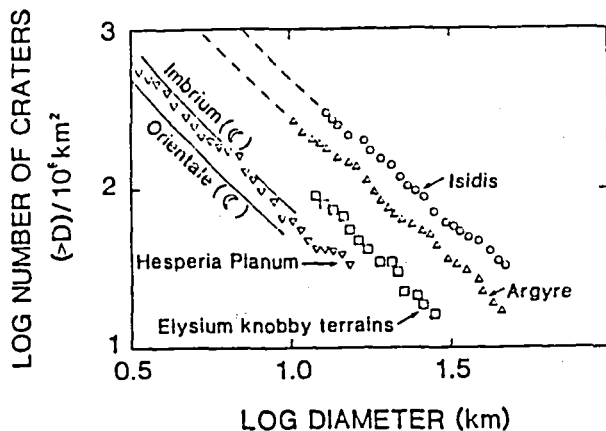


Figure 1. Relative crater densities on the last major martian impact basins (Isidis, Argyre), martian units, and the last major lunar impact basins.

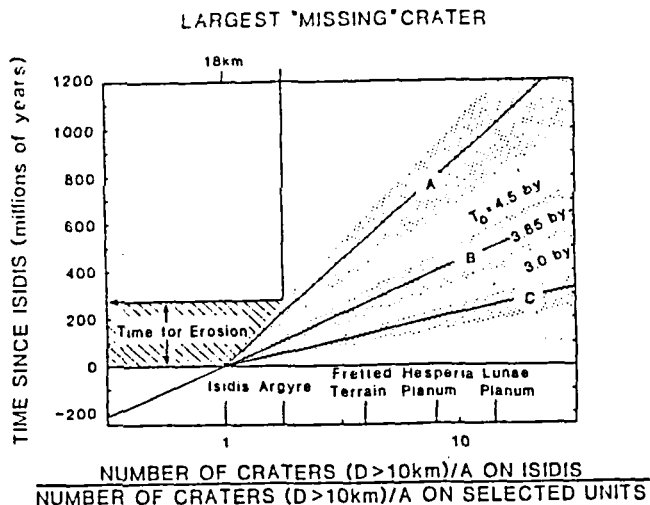


Figure 2. Absolute time intervals based on three different formation times of the Isidis impact basin (4.5, 3.85, 3.0 by) and three different exponential half-lives of impactors (A, B, C). Model A corresponds to a long half-life (267 my); B, to a half-life comparable to post-basin lunar values (133 my); and C, to a very short half-life (67 my). The inferred removal of 18 km diameter craters on Isidis but not on Argyre constrain the time for erosion.

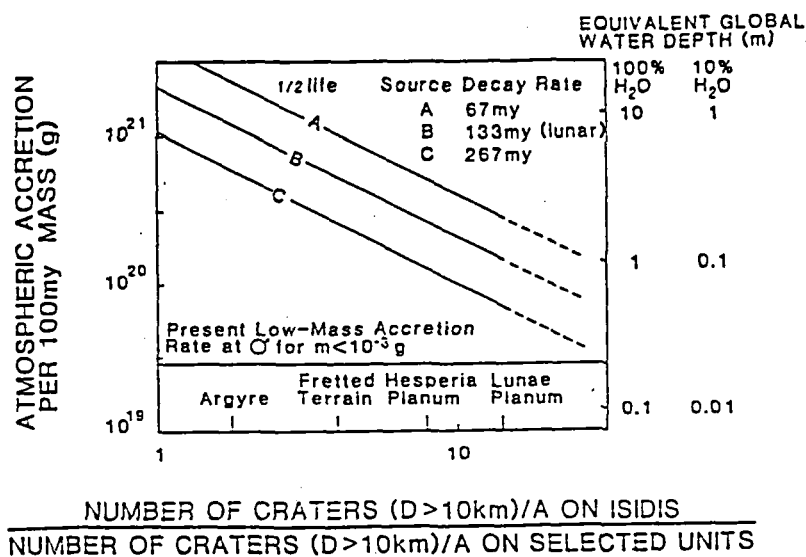
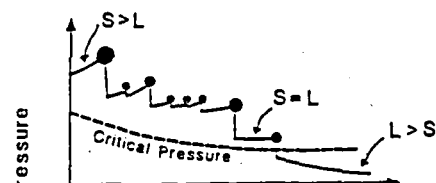


Figure 3. Atmospheric accretion of meteoritic material over 100 my for different assumed source decay rates corresponding to Figure 2 for an assumed age of Isidis equal to the lunar Imbrium basin. The potential depth of added exogenic water is indicated at right for different impactor types (cometary, 100%; C1 chondrites, 10%).

#### CUMULATIVE ATMOSPHERIC EROSION



#### CUMULATIVE RECYCLING

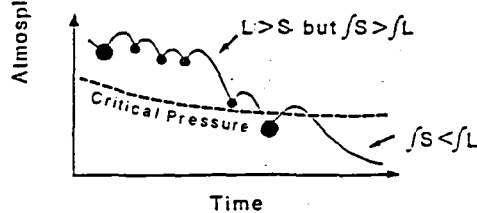


Figure 4. Two contrasting scenarios for episodic supply (S) and loss (L) of volatiles through time in response to formation of different size impact basins (dots of different sizes). In the model at top, the supply of volatiles to the atmosphere at first exceeds the natural loss rate (exospheric, regolith adsorption, etc.) punctuated by sudden impact-triggered losses. Eventually the loss exceeds the supply and the martian atmospheric pressure falls below a level allowing surface run-off of water. A different model (bottom) proposes atmospheric volatile losses generally exceeding the supply at a given time but basin-controlled impact release and hydrothermal recycling replenishes the atmosphere during a finite period of basin-controlled volcanism.

Martian Impact Crater Ejecta and Interior Morphologies: Correlations with Latitude, Diameter, and Terrain.  
Nadine G. Barlow, Lunar and Planetary Institute, 3303 NASA Road One, Houston, TX 77058.

Mariner 9 and Viking images revealed the existence of a variety of ejecta and interior structures associated with martian impact craters. A number of studies have attempted to correlate these morphologies with parameters such as latitude, crater diameter, and geologic unit (Refs. 1, 2, 3). These attempts have met with some success, but the limited data sets used in these analyses result in questionable global implications.

A catalog containing information on 42,286 martian impact craters has recently been submitted to NASA for publication and distribution to the Regional Planetary Image Facilities (Ref. 4). This catalog is complete for craters  $\geq 8$ -km diameter, of which 25,862 craters or 61% of the catalog entries satisfy this criteria. Of these 25,862 craters, 3816 are associated with some type of ejecta and interior structure. This data base consists of craters mapped from the Viking 1:2M photomosaics of the entire martian surface. The craters are situated on 23 different geologic units for which relative crater size-frequency distribution curves were computed resulting in age determination of the units relative to each other and to the end of the heavy bombardment period (Ref. 5).

A new study utilizing this extensive data base is in progress to determine any relationships of ejecta and interior morphologies with latitude, longitude, crater diameter, terrain type, and elevation. Seven ejecta morphologies are considered in this study, primarily following the classification scheme of Mouginis-Mark (Ref. 1): single lobe rampart, double lobe rampart, multiple lobe rampart, radial lineated, diverse, pancake, and unclassifiable. Nine types of interior structures are recognized: symmetric pit, asymmetric pit, summit pit, central peak, peak ring, complex floor, flat floor--pristine, flat floor--deposits, and unclassifiable.

The number of craters displaying a particular ejecta/interior morphology and satisfying a specific latitude range, crater diameter, or terrain type (or combination of these parameters) was computed. These numbers were then compared with (1) the total number of craters across the planet showing the same ejecta/interior morphology; (2) the total number of ejecta/interior craters satisfying the same parameter or set of parameters; (3) the



total number of craters satisfying the same parameter or set of parameters, regardless of whether an ejecta/interior structure is present. The percentages resulting from these comparisons were tabulated and graphically represented by histograms. A chi-square test was performed to determine if the correlations are statistically different from random. Computer generated maps showing the global distribution of craters with a particular ejecta/interior morphology were produced to show any obvious latitudinal and/or longitudinal control.

Some preliminary results of the ejecta morphology portions of the study are as follows: (1) Most ejecta craters  $\leq 30$ -km diameter display either a single- or multiple-lobe morphology. No progression from single lobe through double lobe to multiple lobe is seen with increasing diameter. (2) Rampart ejecta give way to radial, diverse, and unclassifiable ejecta morphologies at crater diameters  $\geq 45$  km. These non-lobate ejecta structures are naturally concentrated in the old, heavily cratered regions of Mars where larger craters are preserved. (3) All pancake craters are  $\leq 15$ -km diameter and 71% display pristine flat floors. (4) Double lobe craters are concentrated between  $35^{\circ}\text{N}$ - $65^{\circ}\text{N}$  in the northern hemisphere. In addition, 51% of all craters containing a flat floor interior structure with deposits are associated with double lobe craters. (5) Single lobe craters show no dependence on terrain and/or latitude. This observation could be interpreted as support for the hypothesis of atmospheric-ejecta interactions as a formation mechanism for this ejecta type (Ref. 6).

Some preliminary results of the interior structure portion of the study are as follows: (1) Central peak craters are found to be distributed fairly evenly across the planet, indicating no specific underlying control in their formation. (2) Flat floored craters with deposits tend to occur on post heavy bombardment aged terrains--65% of these craters exist on plains or mottled plains. (3) Flat floored craters with no deposits primarily occur at higher latitudes and on young terrains. (4) Both type of flat floor craters (with and without deposits) decrease in number with increasing diameter. (5) Among those craters showing central pits, summit pits dominate in craters up to 45-km diameter, symmetric pits up to 65 km, and asymmetric pits dominate at still larger diameters. These results confirm those found by Awwiller and Croft (Ref. 7).

This analysis is continuing by combining more parameters and by including the effects of elevation, longitude, and (where possible) sediment thicknesses. The final results should assist not only in our understanding of

the processes necessary for the formation of particular ejecta and interior morphologies but also may provide information on variations in composition and volatile content of the near-surface layers of Mars.

References: (1) Mouginis-Mark, P.J. (1979). J. Geophys. Res., 84, 8011-8022. (2) Mouginis-Mark, P.J. and E.A. Cloutis (1983). Lunar Planet. Sci. Conf. XIV, 532-533. (3) Wood, C.A., J.W. Head, and M.J. Cintala (1978). Proc. Lunar Planet. Sci. Conf. 9th, 3691-3709. (4) Barlow, N.G. (1987). Catalog of Large Martian Impact Craters. Submitted to NASA. (5) Barlow, N.G. (1987). PhD Dissertation, Univ. Arizona. (6) Schultz, P.H. and D.E. Gault (1984). Lunar Planet. Sci. Conf. XV, 732-733. (7) Awwiller, D. and S.K. Croft (1986). Submitted to Advances in Planetary Geology as a Summer Intern Program Report.

## **EJECTA COVER ON MARTIAN TERRAINS AS A FUNCTION OF INCREASING CRATER DENSITY**

A. Woronow, Geosciences Department, University of Houston, Houston, TX 77004.

Even relatively young surfaces on Mars have superposed craters and must carry a dusting of impact debris. For increasingly more ancient surfaces, deposits of ejecta generally increase in thickness, and the signatures of the geology beneath becomes more obscured. Although we can do nothing about this obscuration, we can describe these newer deposits, temporally and spatially, and thereby avoid falsely interpreting the geology beneath. We begin the task of temporal and spatial characterization by considering the areal variability of ejecta cover with increasing exposure to meteorite bombardment. This study establishes a baseline for evaluating the quality and distribution of exposures of strata lying temporally beneath the ejecta. Of special interest is the distribution of ejecta overlying surfaces that have never sustained a direct impact by a large meteorite, for these retain the volcanic and sedimentary stratigraphy in its most pristine state.

### **Method**

This simulation incorporates the effects of cratering only; as yet it includes no eolian erosion, no fluvial erosion, no tectonic nor volcanic process. But cratering pervades the martian surface as it does the surface of the Moon and accounts for much of the structure and stratigraphy of their ancient terrains. The numerical density of preserved craters on the ancient terrains of Mars approaches that of the lunar highlands, and probably is only a vestige of an equal or greater barrage. Therefore, the ejecta deposits on Mars must have been as extensive as those on the Moon, and their distribution also must be analogous to the Moon's.

An entirely new Monte Carlo simulation is under development along the lines of (1). It currently includes complex crater geometries (flat floor, inner rim, inward-sloping ejecta blanket, and exponentially decaying outward ejecta blanket) according to the parameters given by (2). Crater ejecta blankets extend to five radii from the crater center, conserve excavated volume, and so far mimic ballistic emplacement only. This simulation utilizes a variable-size, gridded target surface with an evolving topography interpolated between the grid points. The grid points serve too as sample points of ejecta thickness.

Crater diameters are selected at random from the production distribution function defined by (3) for craters greater than 8 km in diameter. Crater centers are located uniformly randomly on the surface at the instantaneous local elevation. A zone around this target surface can receive impacts and spray ejecta onto the target surface, but data are not retained on that extended zone.

### **Results**

In applying these results, one must scrutinize the martian surfaces under study for both local and regional resurfacing. Resurfaced terrain will match the ejecta-cover conditions of the simulation of lightly cratered

surfaces. But as the density of superposed craters increases, one might expect an orderly increase in the thickness of the ejecta cover. To some degree this is the case; however, the excavation into, and removal of, preexisting ejecta cover by later cratering complicates this overall trend.

Relatively lightly cratered surfaces, such as 0.5 times the observed lunar highlands density (OLHD), has a distribution of ejecta thicknesses with more symmetry than that for higher crater densities, which are progressively more skewed favoring greater ejecta thicknesses. The range of thicknesses, however, does not change rapidly with increasing crater density, although the upper limit of the ejecta thickness creeps upward slightly and steadily. The uncovered or thinly covered regions of the lightly cratered surfaces are gradually more deeply covered, but craters continually excavate through this cover, and provide fresh exposures so that the percentage of surface showing through the ejecta dusting tends toward a constant with increasing exposure time. But with increasing crater density, the exposures through the ejecta cover become restricted to the crater walls and floors. Of interest are the regions having experienced zero impacts. The 0.5x OLHD case shows little difference between the average conditions across the surface and those for unimpacted sites--particularly in the critical thinly covered tail. But by accumulations of cratering of 3x OLHD, the martian surface is so covered by ejecta that only crater floors and walls provide views to the strata below.

### Conclusions

The surface of Mars must have sustained an impact flux at least as great as that of the lunar highlands. That cumulative flux has been estimated to be between 3x OLHD (4) and 5x OLHD (5). Although some regions will escape direct impacts even at these high cumulative fluxes, only very rare regions may have ejecta cover less than 1/2 km thick unless some other geologic process has stripped it away. The hope of observing very ancient, undisturbed strata on spacecraft images or even at the surface seems slight.

For younger strata (e.g. more recent lava flows), however, the ejecta cover becomes progressively less obscuring, and at even 0.5x OLHD original relief on the order of a few meters may reflect the original surface topography and morphology.

The proportion of surface that remains unimpacted will decrease when smaller craters are also considered, but the large craters dominate the mass of the ejecta cover so that the result given will probably require only slight alterations.

### REFERENCES

1. Cashore, J. and Woronow, A. (1985) Proc. LPSC XV, C811-C815.
2. Pike, R.J. and Davis, P.A. (1984) Abstracts of LPSC XV, 645-646.
3. Woronow, A., Strom, R.G., and Gurnis, M. (1982) Satellites of Jupiter (Morrison, ed.), 237-276.
4. Woronow, A. (1978) Icarus, 76-88.
5. Cashore, J.A. (1987) M.S. Thesis, University of Houston.

## ENSEMBLE HISTORIES OF MARTIAN SAMPLES SUBJECTED TO METEORITE IMPACTS

A. Woronow, Geosciences Department, University of Houston, Houston, TX 77004.

As a portion of the the martian surface becomes more densely cratered, the more the surface and subsurface materials become laterally redistributed and impact metamorphosed. This abstract characterizes specimen redistribution as a function of both impact density and original specimen depth, and also characterizes the impact histories of those specimens.

### Method

An entirely new Monte Carlo simulation is being constructed along the lines of Cashore and Woronow (1985). It currently includes complex crater geometries (flat floor, inner rim, inward-sloping ejecta blanket, and exponentially decaying outward ejecta blanket) according to the parameters given by Pike and Davis (1985). Crater ejecta blankets extend to five radii from the crater center and conserve excavated volume. This simulation utilizes a variable-size, gridded target surface with an evolving topography interpolated between the grid points. For this study, the surface is 1500 km by 1500 km with 256 grid points.

Crater diameters are selected at random from the production distribution function defined by Woronow, et al. (1982) for craters greater than 8 km in diameter. Crater centers are located uniformly randomly on the surface at the instantaneous local elevation. A zone around this target surface can receive impacts and spray ejecta onto the target surface, but data are not retained on that extended zone.

Tracer particles (representing possible "grab samples") may be placed on the surface or embedded in the subsurface. When excavated by an impact, the tracers are "entrained" in both the ejecta and the in-crater fallback. Repeated trials record the number of impacts sustained by each tracer and the tracer's total displacement.

### Results

This abstract reports only on those tracers that, at the termination of the simulation, resided in an ejecta blanket rather than in the crater fallback.

For tracers starting from the same depth, as the cumulative crater flux (measured in multiples of the observed lunar highlands density, OLHD) increases, tracers tend to be spread increasingly farther from their original sites and to experience an increasing number of excavation/redistribution events. However, the displacement distance is only weakly related to the total impact flux, the median displacement for 1x OLHD being about 70 km increasing to only about 90 km for 3x OLHD. The most distantly displaced tracers are not necessarily the ones that experience the greatest number of impacts. This is apparently because large, relatively rare, events at any flux dominate the lateral transport of tracers. Small craters are relatively inefficient dispersers of tracers because 1) they may not excavate to the

tracers buried in an ejecta blanket or subsurface, and 2) in a random walk process like this one, the expected displacement is proportional to  $D\sqrt{n}$  where  $D$  is the average step size and  $n$  is the number of steps. Concentrating on the second of these, the first having a rather obvious effect, we note that  $D$  increases linearly with crater (and ejecta) size whereas  $n$  depends upon the number of craters of size  $D$ . For the assumed production function, if we select  $D_1$  to be 500 km and  $D_2$  to be 10 km then  $n_1/n_2$  is approximately 1000. Therefore, the ratio of  $D_1\sqrt{n_1}/D_2\sqrt{n_2}$  shows that a single 500 km diameter crater, on the average, disperses tracers about 1.5 times farther than the combined efforts of the 1000 corresponding 10 km diameter craters!

Fewer tracers avoid impacts, and the average number of impacts experienced increases from 0.6 to 2.6 for an increase in the flux from 1x to 3x OLHD. As the initial burial depth of the tracers is increased, while maintaining a constant 3x OLHD, the distribution of the number of impacts suffered almost reverts to one like that for a lower flux. However, for shallow burials (e.g. 2 km), although many tracers escape excavation, once excavated they sustain a greater average number of impacts than do samples originating at the surface of a terrain sustaining a lower cumulative flux.

Ignoring those tracers that are never excavated, surprisingly small differences occur in the average number of impacts experienced by tracers originating from 0, 2, and 10 km depth, namely averages of 3.1, 2.6, and 2.3 impacts per tracer. Therefore, samples from a wide range of depths may have quite similar impact-metamorphism histories.

**Conclusions:** 1) Lateral transport of samples found at the surface is not highly correlated with the impact flux, but is dominated by the rare, large impact events. 2) Although specimens collected from higher-flux terrains will have been impacted more frequently (even if they came from depths of 2 km) than would specimens collected from lower-flux terrains, specimens originating at 10 km depth have an impact history more closely corresponding to that of the lower-flux terrain specimens. 3) For a single terrain, samples originating from greater depths will have suffered only a slightly lesser average number of impacts than those originating closer to the surface; therefore, the degree of impact metamorphism is not strongly correlated with the depth of origin of the specimens.

#### REFERENCES

- Cashore, J. and Woronow, A. (1985) Proc. LPSC XV, C811-C815.  
 Pike, R.J. and Davis, P.A. (1984) Abstracts of LPSC XV, 645-646.  
 Woronow, A., Strom, R.G., and Gurnis, M. (1982) Satellites of Jupiter (Morrison, ed.), 237-276.

## CRATER COUNTS IN WEST DEUTERONILUS MENSAE, MARS

Irene Nester

Geology Department, California State University Long Beach, Long Beach, CA

Timothy J. Parker and R. Stephen Saunders

Jet Propulsion Laboratory, California Institute of Technology, Pasadena, CA

Crater counts were obtained for a 300,000 km<sup>2</sup> region in West Deuteronilus Mensae (40-50° latitude, 340-357° longitude) in order to determine relative and absolute age relationships and crater obliteration history. The study area lies across the boundary between the northern lowland plains and southern highlands. Three principal geomorphic zones have been identified in this area (1). The southernmost, zone A, is a mottled heavily cratered upland terrain surface. The next zone to the north, zone B, is a smoother surface with a distinctly lower overall crater density than zone A, and a more uniform, relatively dark surface. Zone B is a transitional surface between the cratered plateau and northern plains surfaces. The northernmost, zone C, consists of "striped" and "mottled" northern plains with a slightly lower crater density than zone B. The boundaries between the zones are roughly parallel and trend approximately east-west in the study area. Much of the eastern part of the area consists of large branching canyons and remnant plateaus termed fretted terrain (2). The fretted terrain is present in all three zones but shows evidence of increasing modification from south to north. The boundary between zones A and B on the plateau is a well defined separation between the relatively bright A surface and the darker B surface. Zones B and C are separated by a moderately well-defined contact separating the relatively dark B surface from the "striped" plains of the C surface. Where this contact crosses the fret canyon floors it is expressed as smooth arcs concave toward zone C. Parker, et al. (1,3) suggested that the zones and zone boundaries could have been produced by successively lower levels of standing water within the northern lowlands during episodes of catastrophic outflow channel development elsewhere along the lowland/upland boundary.

The crater counts were taken from a computer-generated mosaic of the region printed at a scale of 1:410,000. The mosaic is comprised of over 80 Viking orbiter images which vary in resolution from 9m/pixel to 200m/pixel. All visible craters with complete rims and diameters greater than approximately 0.7km were included in the counts. Areas covered by the ejecta blankets of large craters were excluded from the counts due to uncertainties in placement of the zone contacts in these areas. Canyon floors associated with zones A and B were excluded from the counted areas due to the difficulty in delineating the contact between the two zones across the canyon floors.

The results are given in Table 1 and figures 1 and 2. Absolute age relationships between the zones vary with the dating method used. Figure 1 is the combined cumulative crater size-frequency plots for all three zones. Craters with diameters less than 1km have been excluded. Cumulative size-frequency data for craters above 10km in diameter may be unreliable due to overlap between the error bars for the three curves at these crater sizes. The zone A curve plots well above those of zones B and C and displays distinct plateaus at diameters of approximately 3km and 8km. These probably indicate a resurfacing event in which craters with diameters less than about 8km were removed followed by a later event in which craters smaller than about 3km were removed. The 1km intercepts of zones B and C are approximately coincident, but the slope of the curve for zone B is less than that for zone C, probably due a number of large, degraded ghost craters that were identified within zone B but not in zone C.

Table 1 lists absolute ages for the three zones based on the models of Soderblom et al. (4) and Neukum and Hiller (5). The former model relies on the total number of craters with diameters between 4km and 10km per 10<sup>6</sup>km<sup>2</sup>, whereas the latter involves dividing the cumulative size-frequency distribution curve for an area into separate plots at diameters where it deviates from the "Mars standard crater curve" (6). These separated plots approximate the crater populations before and after a resurfacing event. Projection of the Mars standard crater curve through each separate plot to the 1km intercept yields the approximate crater retention age (at D= 1km) for that population (figure 2). This is an indication of the time at which a specific resurfacing event ceased and the "new" surface began accumulating craters. These ages are listed in Table 1

for each surface as the cumulative number of craters with diameters  $\geq 1\text{ km}$  per  $10^6\text{ km}^2$ . The crater number in Table 1 is the actual number of craters counted with diameters  $\geq 1\text{ km}$  normalized to  $10^6\text{ km}^2$  and is an index of absolute age, though it is an "uncalibrated" absolute age.

The crater age of the oldest surface extracted by the method of (5) in zone A is 24,000. This age agrees well with the age of the intermediate, Lunae Planum age surface ( $24,000 \pm 4000$ ) identified by Frey et al. (7) in almost all lowland/upland transitional boundaries in Eastern Mars. Two later resurfacing events can be identified in counts of zone A and at least one can be identified in zone B.

#### References.

- (1) Parker, T. J., Schneeberger, D. M., Pieri, D. C., and Saunders, R. S., 1986, in Symposium on Mars: Evolution of its Climate and Atmosphere, V. Baker et al., eds., LPI Tech. Rpt. 87-01, Lunar Planet. Inst., Houston, p. 96-98.
- (2) Sharp, R. P., 1973, Journ. Geophys. Res., Vol. 78, p. 4073-4083.
- (3) Parker, T. J., Schneeberger, D. M., Pieri, D. C., and Saunders, R. S., 1987, Rept. Planet. Geol. Prog.-1986, NASA Tech. Memo - 89810, p. 319-320.
- (4) Soderblom, L. A., Condit, C. D., West, R. A., Herman, B. M., Kreidler, T. J., 1974, Icarus, Vol. 22, p. 239-263.
- (5) Neukum, G., and Hiller, K., 1981, Journ. Geophys. Res., Vol. 86, p. 3097-3121.
- (6) Neukum, G., and Wise, D. U., 1976, Science, Vol. 194, p. 1381-1387.
- (7) Frey, H., and Semeniuk, J., 1987, Lunar and Planet. Sci. - XVIII. Lunar Planet. Inst., Houston, p. 302-303.

TABLE 1

ZONE [area]	CRATER NUMBER		SODERBLOM et al. age (yrs.)	AGE based on		
	[ $N \geq 1\text{ km}$ $/10^6\text{ km}^2$ ]	[ $4\text{ km} \leq N \leq 10\text{ km}$ $/10^6\text{ km}^2$ ]		NEUKUM zone	& *	HILLER age (yrs.)
A [74,208 $\text{km}^2$ ]	3665	458	$3.7 \times 10^9$	A1	24000	$4.1 \times 10^9$
				A2	8500	$3.9 \times 10^9$
				A3	3000	$3.7 \times 10^9$
B [81,230 $\text{km}^2$ ]	1884	148	$1.8 \times 10^9$	B1	6300	$3.8 \times 10^9$
				B2	1900	$3.6 \times 10^9$
C [109,578 $\text{km}^2$ ]	1834	128	$1.5 \times 10^9$	C	1900	$3.6 \times 10^9$



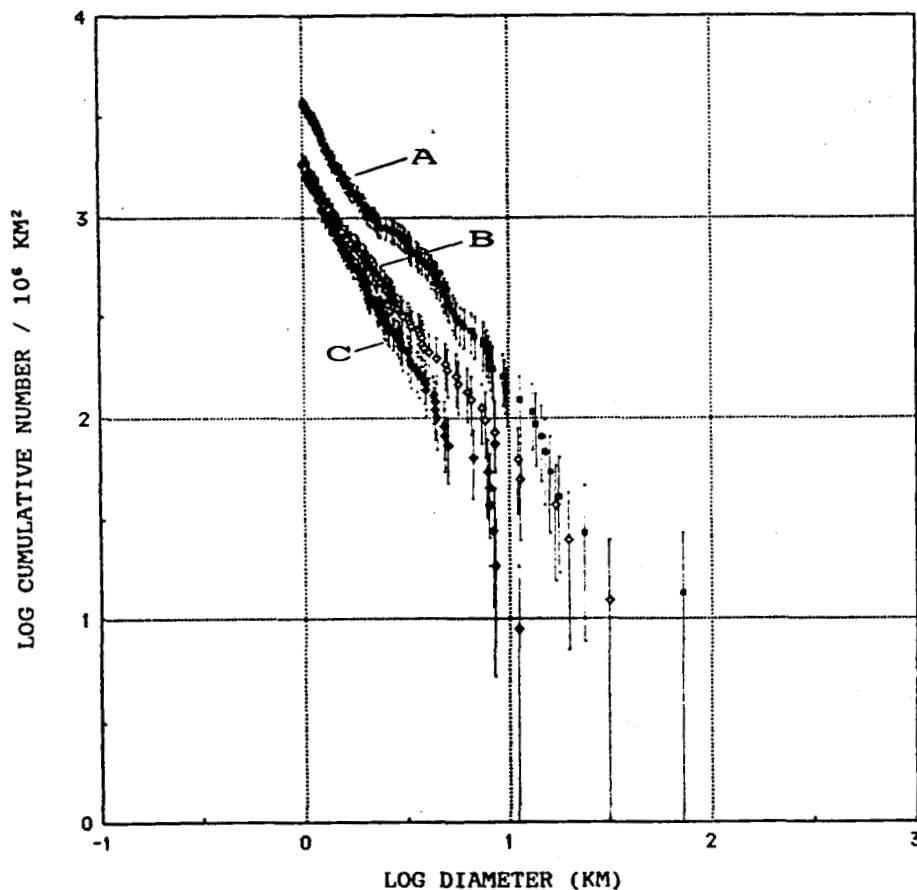
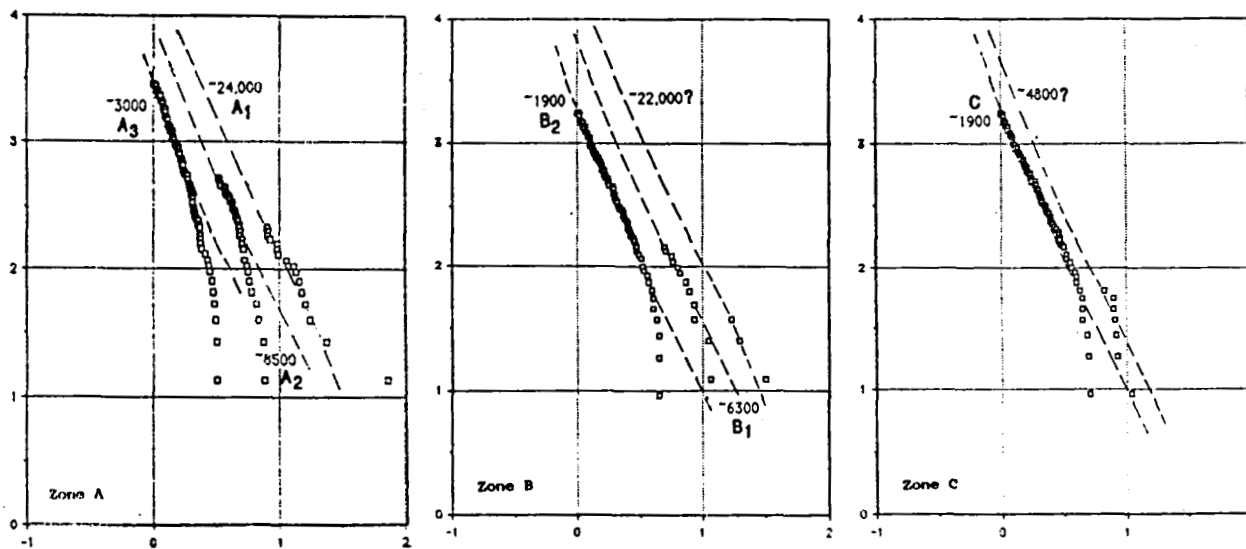


FIGURE 1. Cumulative size-frequency distributions for zones A, B, and C. Number of craters per million  $\text{km}^2$  with a diameter greater than a given diameter versus that diameter. One point is plotted for each of the 628 total craters counted. Error bars represent the standard statistical uncertainty for the actual number of craters counted.

Figure 2. Cumulative size-frequency plots for zones A, B, and C after separation into preresurfacing and postresurfacing crater populations and extraction of relative ages by the method of Neukum and Hiller (1981).

LOG DIAMETER (KM)



LOG CUMULATIVE NUMBER /  $10^6 \text{ km}^2$

## RESURFACING HISTORY OF THE LUNAE PLANUM-XANTHE TERRA REGION ON MARS

Tammie D. Grant and Herbert Frey, Geophysics Branch, Goddard Space Flight Center, Greenbelt MD 20771

Previous study of the cumulative frequency curves for impact craters larger than 5 km diameter in the transition zone, adjacent cratered terrain and smooth plains of the highland/lowland boundary in eastern Mars showed evidence for widespread resurfacing events (Frey et al., 1986; 1987). The most important of these seems to have occurred throughout the region at about the same time, ceasing at a crater retention age [ $N(1)$  = cumulative number of craters with  $D \geq 1$  km diameter per  $10^6$  km<sup>2</sup>] of about 25,000. This is essentially identical to the crater retention age of the ridged plains of Lunae Planum and related surfaces (Wise et al., 1979; Neukum and Hiller, 1981; Frey et al., 1986). These ridged plains serve as the referent for the base of the Hesperian in Tanaka's (1986) stratigraphy, and clearly represent a major event in martian history.

In this paper we examine the details of the resurfacing history of the Lunae Planum and adjacent Xanthe Terra. These two areas are separated by Maja Valles and represent Hesperian age ridged plains to the west and older Noachian age cratered and subdued cratered terrain (Scott and Tanaka, 1986). The Maja Valles channel deposits are of Hesperian age. We subdivided the area into six morphological terrain units; our units coincide closely with those of Scott and Tanaka (1986) except in the detailed location of boundaries in a few areas. Three cratered units are recognized and are designated CPL<sub>1-3</sub>. The oldest of these, CPL<sub>1</sub>, consists of large, densely packed craters with rough intercrater terrain. CPL<sub>2</sub> has more subdued intercrater areas. A lower abundance of craters and smooth, flat intercrater areas are characteristic of CPL<sub>3</sub>. We designate the ridged plains of Lunae Planum as Prg and the channel deposits of Maja Valles as Fch. A small area of smooth plains with a large abundance of large but nearly buried impact craters at 43° W, 10° N we call PL<sub>1</sub>.

For each of these units we counted craters with  $D \geq 5$  km diameter and plotted cumulative frequency curves. All the curves show a tendency to bend over toward smaller diameters, indicating a depopulation which can be described in terms of resurfacing by one or more "events" (Neukum and Hiller, 1981). We broke these curves into several discrete branches by subtracting the last point lying on a "Mars standard production curve" (from Neukum and Wise, 1976) from the remaining smaller diameter points and then replotting these points. The individual branches derived in this way represent separate counting surfaces and mark the time resurfacing events stopped. It is in principle possible to determine the number and "age" (crater retention age, measured as a crater density) of major resurfacing events. The technique developed by Neukum and Hiller (1981) is clearly an oversimplification in its analysis of cumulative frequency curves but has proven useful in our earlier studies (Frey et al., 1986; 1987). Figure 1 illustrates the progressive breaking of the cumulative frequency curves for the plains-forming units Prg, PL<sub>1</sub> and Fch.

The oldest surfaces determined by this technique have a crater reten-

tion age of 300,000 and underly the  $CPL_1$ , Fch and  $PL_1$  units. The oldest buried surface in  $CPL_2$  and  $CPL_3$  have  $N(1) = 200,000$  and 125,000 respectively. Both  $CPL_1$  and  $CPL_3$  were resurfaced by an event which ended at about  $N(1) = 60,000-70,000$ . The first recognizable resurfacing of  $CPL_2$  ended at about  $N(1) = 40,000$ .

The oldest age found for the Prg unit is significantly younger than those described above. We find for the old branch  $N(1) = 25,000$  and no evidence for craters larger than 55 km within the ridged plains. As shown in Figure 1 and summarized in Table 1, there appears to have been only one resurfacing of the ridged plains (for the crater diameters studied here) and that ceased at  $N(1) = 10,000$ . In this respect as well as in the lack of any very large craters the Prg unit appears unique among those in this study.

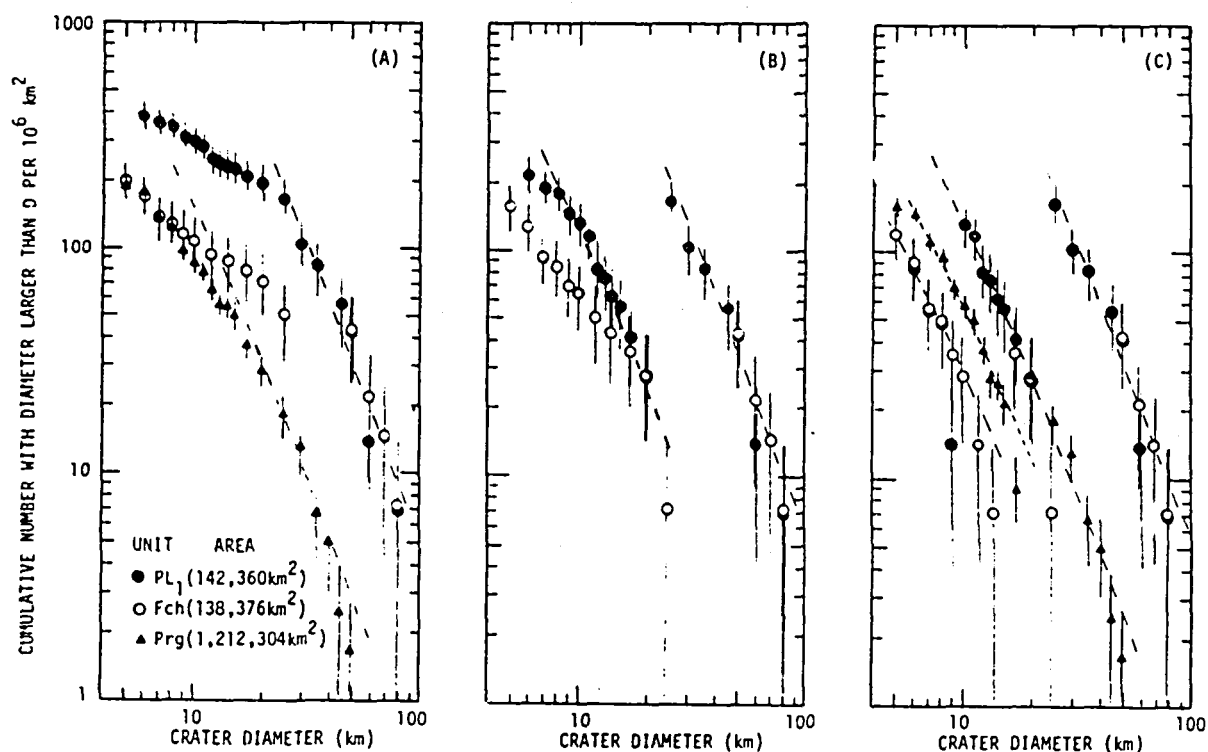
Both  $PL_1$  and Fch have large craters which define an old branch with  $N(1) = 300,000$ , comparable to  $CPL_1$ . Both of these units were resurfaced at about the same time and have an underlying surface whose age is the same as the underlying surface in the Prg unit:  $N(1) = 23,000-26,000$ . It appears that the emplacement of the oldest ridged plains was contemporaneous with the removal of craters in Fch and  $PL_1$  and that these events ceased at nearly the same time. A "Lunae Planum Age" resurfacing of  $CPL_1$  and perhaps of  $CPL_3$  also occurred, as shown in Table 1. Only  $CPL_2$  does not have an event terminating at this time.

The  $PL_1$  and Fch units also show evidence for a subsequent resurfacing which ended at about 5500. The two units have nearly identical histories in terms of the timing of the resurfacing events which modified them, but the efficiency of the resurfacing was always greater in the Fch unit around Maja Valles. This can be seen from the diameter range by which each common age resurfacing event is defined, and the diameter of the smallest craters which survived that resurfacing (as shown by the smallest crater defining the previous branch). In Fch the Lunae Planum Age resurfacing obliterated craters smaller than 50 km, but in  $PL_1$  craters as small as 25 km survive on the underlying surface. Likewise the  $N(1) = 5500$  event left craters larger than 17 km on the Lunae Planum age surface below in Fch but craters as small as 9 km survive in  $PL_1$  on that surface.

#### REFERENCES

- Frey, H., A.M.Semeniuk, J.A.Semeniuk and S.Tokarcik (1986) Crater counts in the transition zone in eastern Mars: Evidence for common resurfacing events. Lunar Planet. Sci. XVII, 243-244.
- Frey, H., A.M.Semeniuk, J.A.Semeniuk and S.Tokarcik (1987) A widespread common age resurfacing event in the highland-lowland transition zone in eastern Mars. Proceed. Lunar Planet. Sci. Conf. 18th (in press).
- Neukum, G. and K. Hiller (1981) Martian ages. J. Geophys. Res. **86**, 3097-3121.
- Scott, D.H. and K.L.Tanaka (1986) Geologic map of the western equatorial region of Mars. USGS Atlas of Mars, 1:15M Series, Western Region, Map 1-1802-A.
- Tanaka, K.L. (1986) The stratigraphy of Mars. Proceed. Lunar Planet Sci. Conf. 17th, J. Geophys. Res. **91**, E139-E158.
- Wise, D.U., M.P.Golombek and G.E.McGill (1979) Tectonic evolution of Mars. J. Geophys. Res. **84**, 7934-7939.

FIGURE 1



DERIVED CRATER AGES FOR RESURFACING EVENTS IN LUNAE PLANUM AREA

UNIT	AREA	CRATER AGE = $\bar{N}(1)$ = CUMULATIVE NUMBER WITH $D \geq 1$ KM PER 10 KM <sup>2</sup>		
CPL <sub>1</sub>	165,063	286,603 (30-50)	69,848 (14-25)	26,615 (5-13)
CPL <sub>2</sub>	298,399	200,910 (30-100)	39,724 (15-25)	11,285 (5-14)
CPL <sub>3</sub>	731,144	125,242 (35-90)	60,237 (15-30)	19,128 (5-14)
PRG	1,212,304			25,688 (20-50) 10,102 (5-17)
PL <sub>1</sub>	142,360	(?)305,003 (25-80)		24,175 (10-20) 5,415 (5-9)
Fch	138,376	330,623 (50-80)		22,562 (17-25) 5,572 (5-14)

COMPARISON OF CRATER AGES DERIVED FOR RESURFACING EVENTS ELSEWHERE ON MARS

CT*	210,000	85,400	31,000	
TZs*		87,000	29,000 - 19,700	11,600 - 5,000
SP*			19,700	6,300 - 5,500
K**	233,00	84,300	26,700	4,900

\* Cratered Terrain, Transition Zone units, Smooth Plains near highland/lowland boundary in Eastern Mars (Frey et al., 1986; 1987)

\*\* Knobby Terrain unit in Elysium-Amazons knobby terrain complex (Frey et al., 1987)

## EVIDENCE FOR MULTIPLE RESURFACING EVENTS IN THE ELYSIUM-AMAZONIS KNOBBY TERRAIN ON MARS

Herbert Frey, JoAnne Semeniuk and Susan Tokarcik, Geophysics Branch, Goddard Space Flight Center, Greenbelt MD 20771

Analysis of cumulative frequency curves for craters larger than 5 km in separate morphological units in the knobby terrain complex of the Elysium-Amazonis region of Mars provide evidence for: (a) an original surface with age comparable to that of the cratered highlands, (b) multiple resurfacing events of varying efficiency throughout the region, (c) common ages for some of these resurfacing events, and (d) temporal commonality with resurfacing events in the highland/lowland boundary zone and adjacent cratered terrain in eastern Mars.

The knobby terrain complex (KTC) in Elysium-Amazonis is particularly important in understanding the large scale evolution of the martian crust. Despite complex and apparently protracted modification over time, the KTC preserves evidence of a surface of great age (Scott and Allingham, 1976; Morris and Dwornik, 1978; Scott and Tanaka, 1986), on which younger units have been superimposed. Its location within the northern lowland plains is difficult to understand in terms of the origin of the martian crustal dichotomy, and its proximity to the Elysium volcanic complex is an important aspect of the relationship of major volcano-tectonic centers to older crust.

We subdivided the Elysium-Amazonis knobby terrain complex into three major units: knobby terrain (K), knobby plains (KP), and smooth plains (PS). Detailed mapping of the knobby plains resulted in further subdivision based on the density of knobs and the relative proportions of knobs and intervening smooth plains. The differences between high (H), moderate (M) and low (L) density knobby plains (KPH, KPM, KPL) as mapped here do not reflect the additional complexity of knob size, which also varies greatly in the region.

The cumulative frequency curves derived from counting craters within the separate morphological units all show complex character, bending over toward smaller diameters. This character is similar to that found previously for cumulative frequency curves from individual morphological units in the highland/lowland transition zone in eastern Mars (Frey et al., 1986; 1987). The bendover can be interpreted as due to resurfacing events. We therefore analyzed these curves using the Neukum and Hiller (1981) technique to break the curves into separate branches where they depart from a "Mars standard production curve" (Neukum and Wise, 1976). The approach, described in more detail elsewhere (Frey et al., 1987), is illustrated in Figure 1 for many of the units studied here. Multiple erosional or resurfacing events can be defined from the cumulative frequency curves. The "ages" of these events are defined in terms of the crater retention of the different surfaces, and are given as the crater density  $N(1)$  = cumulative number of craters with  $D \geq 1$  km per million square kilometers. What is recorded is the "age" at which the resurfacing event stopped and a counting surface was established.

Figure 1 and Table 1 summarize some of our results. Different units can show different numbers of resurfacing events: three events are designated by the four branches for the knobby terrain (K) but the smooth plains unit PS<sub>1</sub>

has only a single branch (no evidence for an underlying, surviving surface). The oldest surface identified has a crater retention age  $N(1)$  230,000 and is found below the knobby terrain (K). This age is comparable to that found by us for the oldest surface below the cratered terrain south of the transition zone (Frey et al., 1987). This result supports the conclusion reached previously that the knobby terrain is partly a relic of ancient crust.

The knobby terrain unit experienced three resurfacing events for the crater diameters studied here. The oldest of these stopped at  $N(1)$  84,000, a resurfacing event also recorded in the cratered terrain to the south. The next resurfacing event at  $N(1)$  26,700 appears to have been coeval with the major resurfacing in the transition zone and elsewhere and which occurred at the time of emplacement of Lunae Planum ridged plains volcanics (Frey et al., 1986; 1987; Grant and Frey, this volume). This resurfacing was widely spread through the Elysium-Amazons area as well, and is recorded in the knobby plains (KPM, KPL<sub>2</sub>) and appears as the oldest surface below the knob-free smooth plains unit PS<sub>2</sub>. Figure 1 shows this common branch for the different units. Note in Table 1 the different diameter ranges over which the event is defined. This implies that the resurfacing, if the same process in the different units, was also variable in its efficiency at removing impact craters from the older, underlying surface.

The strong clustering of points along common production curves in Fig. 1 indicates that many of the resurfacing events were common in their timing of cessation throughout the knobby terrain complex. The youngest recorded events for the knobby terrain and knobby plains all cluster around  $N(1)$  5000, but in the smooth plains resurfacing either extended to more recent times or began and ended after modification of the knobby areas was over. Note the very young age for the most recent event in PS<sub>2</sub> ( $N(1)$  770).

The strong similarity of resurfacing chronologies between the knobby terrain and knobby plains and the units within and adjacent to the transition zone to the south is particularly important. Very old terrain underlies both the knobby units and the cratered terrain south of the transition zone but no surface of this age ( $N(1)$  230,000) is preserved within the transition zone itself. The resurfacing events at  $N(1)$  85,000, 25,000 and 5000 are common to the two regions, despite their apparent physical separation today. This may suggest that resurfacing events were both widespread and perhaps similar in nature, and that their timing may have a global context.

#### REFERENCES

- Frey, H., A.M. Semeniuk, J.A. Semeniuk and S. Tokarcik (1986) Crater counts in the transition zone in eastern Mars: Evidence for common resurfacing events. *Lunar Planet. Sci. XVII*, 243-244.
- Frey, H., A.M. Semeniuk, J.A. Semeniuk and S. Tokarcik (1987) A widespread common age resurfacing event in the highland-lowland transition zone in eastern Mars. *Proceed. Lunar Planet. Sci. Conf. 18th* (in press).
- Morris, E.C. and S.E. Dwornik (1978) Geological map of the Amazonis Quadrangle of Mars, USGS Atlas of Mars, 1:5 M Geologic Series, Map I-1049.
- Neukum, G. and K. Hiller (1981) Martian ages. *J. Geophys. Res.* **86**, 3097-3121.
- Neukum, G. and D.U. Wise (1976) Mars: A standard crater curve and possible new time scale. *Science* **194**, 1381-1387.
- Scott, D.H. and J.W. Allingham (1976) Geologic map of the Elysium Quadrangle of Mars. USGS Atlas of Mars, 1:5 M Geologic Series, Map I-935.
- Scott, D.H. and K.L. Tanaka (1986) Geologic map of the western equatorial region of Mars. USGS Atlas of Mars, 1:15 M Series, Western Region, Map I-1082-A.

TABLE 1. CRATER AGES DERIVED FOR UNITS IN THE ELYSIUM - AMAZONIS KNOBBY TERRAIN COMPLEX

K	(634,000)	233,000 (210,000-264,000) 45-100	84,300 (77,400-87,700) 20-45	26,700 (24,200-30,700) 9-20	4900 (3100-6200) 5-9	
KPM <sub>2</sub>	(788,500)		76,600 (73,800-79,400) 70-80	25,200 (20,400-30,700) 15-70	5800 (5300-6300) 5-15	
KPL <sub>2</sub>	(354,850)		118,700* (117,900-119,400) 60-80	17,900 (16,200-19,300) 17-60	4900 (4100-5900) 5-17	
KPL <sub>3</sub>	(180,825)		92,100 (73,800-115,200) 17-50		4500 (4000-5100) 5-17	
PS <sub>1</sub>	(829,475)				2200 (1890-2520) 5-20	
PS <sub>2</sub>	(544,300)			21,800 (18,000-25,500)	3500 (3200-4800)	770 (690-850)

Shown for each unit is the counting area (in parentheses next to the unit designation), the average crater age determined as described in the text, the range of ages considered possible for this average (in parentheses below the average) and the range of crater diameters for which this age is determined.

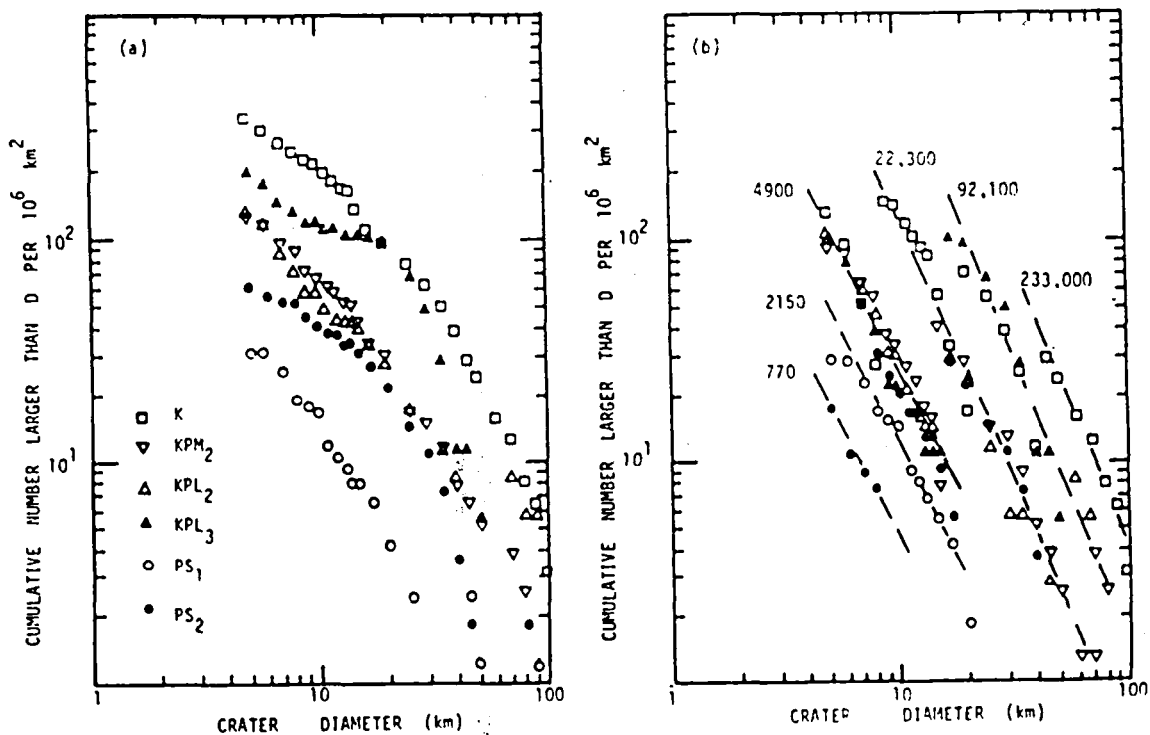


FIGURE 1. Cumulative frequency curves for units in the knobby terrain complex in Elysium-Amazons. (a) Original data binned as in (2). (b) Curves broken and replotted as in (1) and (2).





## CHAPTER 11

### STRUCTURE, TECTONICS, AND STRATIGRAPHY



## INTRODUCTION

New global geologic maps of Mars at 1:15,000,000 scale [1,2,3] have been digitized to obtain accurate measurements of the areal extent of 90 geologic units. These data were used to determine the resurfacing history of Mars by volcanic, eolian, fluvial, periglacial, and impact processes [4]. We presently are extending this work to focus on the extent, magnitude, and duration of volcanism and tectonism (mainly faulting) throughout each of the three time-stratigraphic systems. This work involves detailed mapping to assess volcano-tectonic episodes in terms of their occurrence in eight epochs that represent subdivisions of Martian periods [5].

## MAPPING TECHNIQUES

The global geologic maps of Mars consist of three sheets: (1) western equatorial region, (2) eastern equatorial region, and (3) north and south polar regions. For each of these map sheets, we have prepared three sets of maps (nine in all) showing the areal distribution of materials in the Amazonian, Hesperian, and Noachian systems. Individual faults or fault groups (too numerous to show separately) that originated during each Martian period were then mapped on each sheet. This task could be accomplished because the great majority of faults on Mars can be related to their transection, embayment, or overlap positions with respect to specific time-stratigraphic geologic units.

## RESULTS AND GENERAL OBSERVATIONS

Results of the mapping show that structural deformation throughout Martian geologic history has been almost entirely confined to large elevated volcanic centers--Tharsis Montes, Syria Planum, Olympus Mons, Alba Patera, and the Elysium Mons. Faulting associated with Valles Marineris may be an exception. The Tempe Terra and Acheron Fossae regions are also highly faulted and have prominent, but relatively low relief, volcanic structures. The volcanoes of Tempe Terra lie on the northeast extension of the Tharsis Montes volcanoes. The large known impact basins on Mars, particularly Isidis Planitia, are ringed in places by concentric faults as are basins on the Moon. The Martian basins do not have complex (transverse, radial, and concentric) fault systems that are commonly seen around the large centers of volcanism and uplift on Mars.

The formational sequence of structural landforms in the Syria Planum region of Mars recently has been studied and documented in detail [6,7]. Our work will follow the analytic procedures used in the Syria Planum study for the other volcano-tectonic regions on Mars. In addition, our mapping procedures will allow the magnitude of tectonic deformation as expressed by faulting to be quantitatively measured for each Martian period and epoch. Faults, within fault systems, that have been reactivated during various time periods will be traced in order to estimate the duration and interplay of stress fields associated with the large tectonic centers.

Although our current studies have been restricted to structural dislocations of Mars' surface, other relations among features of probable tectonic origin can be documented further. The pervasive ridge systems, for example, that occur within lava flows of Noachian, Hesperian, and Amazonian age have trends and large-scale spatial distributions that commonly are nearly normal to extensional faults and grabens. It certainly will be important to

determine their relative times and modes of origin.

#### REFERENCES

- [1] Scott, D.H. and Tanaka, K.L. (1986) USGS Map I-1802-A.
- [2] Greeley, R. and Guest, J.E. (in press) USGS Map I-1802-B.
- [3] Tanaka, K.L. and Scott, D.H. (in press) USGS Map I-1802-C.
- [4] Tanaka, K.L. and others (in press) Proc. Lunar Planet. Sci. Conf. 18.
- [5] Tanaka, K.L. (1986) Proc. Lunar Planet. Sci. Conf. 17, E139-158.
- [6] Tanaka, K.L. and Davis, P.A. (1986) PLPSC 18 (abstract), 994-995.
- [7] Tanaka, K.L. and Davis, P.A. (work in preparation).

**VOLCANIC AND TECTONIC EVOLUTION OF MARTIAN IMPACT BASINS** R. Wichman and P.H. Schultz, Dept. of Geological Sciences, Brown University, Providence, RI, 02912.

**INTRODUCTION:** The tectonic and volcanic history of Mars can be separated into an early period of impact basin controlled activity and a late period concentrated in the Tharsis/Elysium region. Previous studies have shown the concentration of early volcanic and tectonic activity along zones of weakness radial and concentric to basin structures (1) and have dated major linear tectonic patterns in the highlands (2). In this study we focus on the timing and sequence of activity about two basins, thereby establishing a progression of basin-controlled modification.

**APPROACH:** Crater counts made on volcanic plains and constructs peripheral to the Isidis and Hellas basins and associated major graben and scarp/ridge systems are used to date volcanic and tectonic activity. Volcanic features and units have sufficient area for standard crater counting techniques. As linear features, however, tectonic structures prevent the application of areal crater counting methods and a technique (2,3) which derives a relative age from the number of craters superposing a linear feature must be used. The mean crater diameter of the superposed crater population is combined with the feature length to provide a value compatible with areal crater ages. The technique has been tested on surfaces of known age and for features with constrained stratigraphic relations. Provided the craters are much larger than the cross-sectional width of the dated feature, the derived ages correlate well with areal counts.

**RESULTS:** Figures 1 and 2 present the developed basin volcanic/tectonic sequences and indicate a similar evolution of tectonic and volcanic activity about the Isidis and Hellas basins. After basin formation (and outer scarp development) radial troughs form: the Amenthes Rupes for Isidis and the Hadriaca Patera/Tyrrhena Patera trough for Hellas. These are radially elongate, downdropped sections of the basin massif ring subsequently inundated by plains. Other partly buried radial troughs about both Isidis and Hellas have been identified on the basis of channel mapping.

Concentric systems of arcuate graben up to 1 basin radius from the basin rim are next to form. The graben about Isidis vary from 2-20 km in width and occur to the northwest and east of the basin near the basin rim. The Hellas graben are from 20-80 km wide and occur to the west and northwest with activity apparently moving away from the basin with time. During the last stages of concentric faulting and immediately thereafter, high-standing plains of considerable thickness are formed on the basin rim near the end of a concentric trough set: Syrtis Major Planum, between 2-3 km thick (4,5) and approximately 900 km diameter; and "Malea" Planum, southwest of Hellas about 700 km in diameter (apparently thick but with no reliable depth determinations). Plains volcanism elsewhere in the basin area occurs coincidentally with planum development. Patera construction succeeds the plains volcanism on the basin rim.

The second cycle of volcanism about Hellas develops the intercrater plains to the southwest and coincides with activity about Isidis. Hesperia Planum and Hadriaca Patera (nearly equidistant from Hellas and Isidis) also form at this time. Later low-relief ridges formed across the dated basin features reflect regional stresses deflected but not controlled by basin structures (6). In contrast with lunar basins, planum-concentric ridges do not develop.

**DISCUSSION:** The derived progression after basin formation is as follows: radial rifting; concentric faulting merging with planum formation on the basin rim; and finally general plains volcanism about the basin region. Volcanic styles apparently evolve over time from widespread plains volcanism to the construction of localized paterae and shields. After the development of Syrtis Major and Hesperia, basin-controlled activity ends.

Radial and concentric faulting about impact basins on the Moon has been modelled in the past. Early radial faulting as a result of stress concentration and isostatic basin uplift (7) is consistent with the observed early radial trough formation. The formation of concentric graben as a result of loading flexure (8) may not be directly applicable. The comparable lunar features are much smaller (< 5 km) and form after initial mare flood basalts which are modelled as the causative load. The martian fractures predate the basin volcanic sequences and their scale would appear unreasonable for a flexural origin. Furthermore, the Moon has no analogue to Syrtis Major and "Malea" Plana, which seem to be associated with the concentric graben. Some process other

than simple basin loading must be invoked to explain these features.

Syrtris Major Planum and "Malea" Planum represent large amounts of magma apparently released by weaknesses due to the concentric fractures and apparently only occur once in basin history. A mechanism allowing this is the rotation of the planetary lithosphere. Calculations indicate that such a process is possible over a relatively short (200 my) time period. If short-termed basin adjustment after impact results in uplifted mantle material, reorientation would expose crustal rock to enhanced heat flows. Thermal expansion over the plume results in large volumes of partial melt accumulating beneath the basin rim. The consistent pattern of patera formation with declining plains volcanism could reflect the evolution of such a partial melt body.

REFERENCES: (1) Schultz, P.H. (1984), *Lunar and Planet. Sci.* XV, p. 728-729; (2) Wichman, R. and Schultz, P.H. (1986), *Lunar and planet. sci.* XVII, p. 942-943; (3) Tanaka, K.L. (1982) *NASA TM 85127*, p. 123-124; (4) Schaber, G.G. (1982) *J. Geoph. Res.*, 87, p. 9852-9886; (5) Downs, G.S. et al. (1982), *J. Geoph. Res.*, 87, p. 9747-9754; (6) Chicarro, A.F. et al. (1985), *Icarus*, 63, p. 153-174; (7) Melosh, H.J. (1978), *Proc. Lunar Sci. Conf.* VII, p. 2967-2982; (8) Solomon, S.C. and Head, J.W. (1979), *J. Geoph. Res.*, 84, p. 1667-1682.

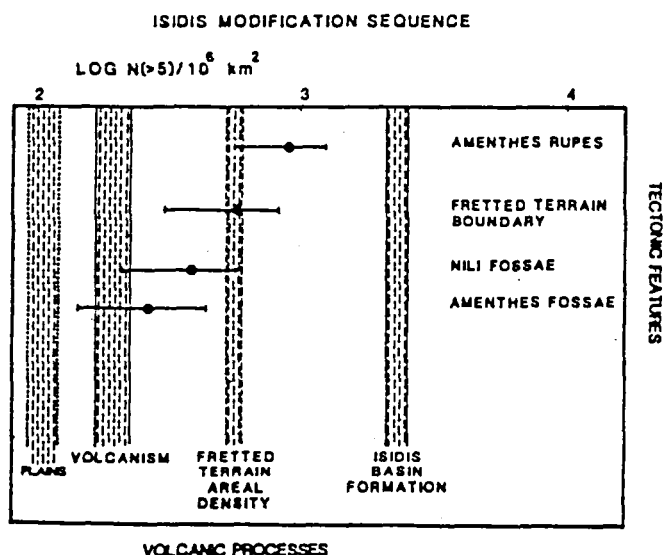


FIGURE 1: A plot of crater-dated tectonic systems and major units around Isidis. Volcanism (vertical hachures) includes Syrtis Major Planum and plains volcanism to the east. The plains unit dates the formation of fractured plains north of the dichotomy. Tectonism (dots with error bars) represents results from linear crater-count approach.

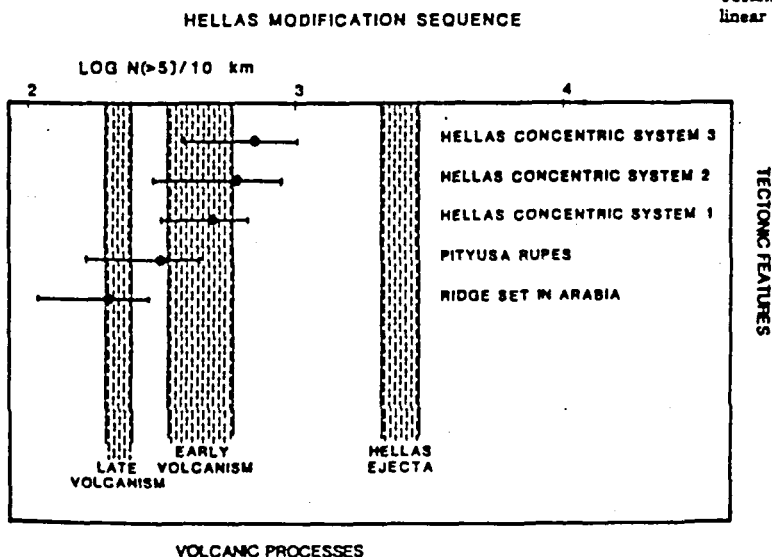


FIGURE 2: Age plot of crater-dated tectonic systems and volcanic episodes around Hellas. Volcanism (vertical hachures) divides into early volcanism in the "Malea" Planum sequence and Tyrrhena Patera construction, and late volcanism in Hesperia Planum, intercrater plains northwest of "Malea" Planum and Hadriaca Patera. Tectonism (dots with error bars) represents results from linear crater-count approach.

## LONGEVITY OF IMPACT-INDUCED FAULTS AS PREFERRED SITES FOR LATER TECTONIC ACTIVITY: AN UPDATE

Sean C. Solomon and Linda Meinke, Department of Earth, Atmospheric, and Planetary Sciences, Massachusetts Institute of Technology, Cambridge, MA 02139.

**Introduction.** The hypothesis that impact-induced faults have been preferred sites for later deformation in response to lithospheric stresses has been suggested for several planets and satellites [e.g., 1-3]. We recently investigated this hypothesis on Earth by examining whether terrestrial impact structures show higher rates of nearby earthquake activity than do surrounding intraplate regions [4]. For 28 of 30 probable impact structures having an original crater 20 km or more in diameter and ages of 3-2000 m.y. [5], we found that rates of nearby seismicity have been no higher than the regional background rates. For two large probable impact structures, Vredefort and Charlevoix, with higher than normal rates of nearby seismicity, factors other than slip on impact-induced faults appear to control the occurrence of earthquakes [6,7]. On the basis of these results, we concluded that impact-induced faults, at least on Earth, do not persist as lithospheric "weak zones" for periods in excess of several million years after the impact event.

One difficulty with generalizing from these findings to other planets and satellites however, is that most of the large terrestrial impact structures are deeply eroded. Because many impact-induced faults are of shallow extent, particularly outside the crater rim [e.g., 8-9], a significant fraction of the faults produced during the formation of older craters on terrestrial continents may no longer be preserved. Such would not be the case, however, for an impact on the continental shelf, where the post-impact environment should have been generally one of subsidence and sediment deposition [e.g., 10]. The recent discovery of the Montagnais impact structure on the continental shelf southeast of Nova Scotia [11] offers an opportunity to search for an association of recent seismicity with an impact structure not significantly affected by post-impact erosion.

**The Montagnais Impact Structure.** The Montagnais structure, located in 100-m-deep water near the outer edge of the continental shelf (Fig. 1), is a complex crater at least 45 km in diameter [11]. The structure has been well elucidated by multichannel seismic reflection profiling and by a drill hole that penetrated the central peak complex to the rocks of the Paleozoic basement; the basal impact melt sheet yields K-Ar ages of 50-55 m.y. [11]. Except for some localized erosion around the crater periphery attributed to back flow of sea water immediately following the impact [11], the crater and its subsurface structure are generally well preserved.

We have searched seismicity catalogues for earthquakes in this century having epicenters in the vicinity of the Montagnais structure. The catalogues of Gutenberg and Richter [12] and Rothé [13] list no earthquakes within about 5° of the center of the impact structure for the periods 1904-1952 and 1953-1965, respectively. The Bulletins of the International Seismological Center (ISC) list no earthquakes within one crater diameter of the center of the impact structure during the 21-year interval 1964-1984; only 4 events occurred within 5 crater diameters during this period (Fig. 1), all of very small magnitude. These rates of earthquake activity per area are not significantly different from that of the regional background.

Despite the low level of seismicity in the region of the Montagnais impact structure, the lithosphere beneath the continental shelves of eastern North America is subject to stress in response to deglaciation of the continent [14], sedimentary loading of the shelf [15], lateral

variations in elevation and crustal thickness [16], and plate tectonic driving forces [17]. The resultant stress field has given rise to a number of large earthquakes along the eastern Canadian continental margin, the largest of which was the  $M = 7.2$  Grand Banks earthquake of 18 November 1929 [12], located about  $6^\circ$  east-northeast of the Montagnais structure. The impact-induced faults of the Montagnais impact structure, therefore, do not appear to be acting as preferred sites of stress release on the Canadian continental shelf.

**Conclusions.** The 45-km diameter Montagnais structure provides another example to support the conclusion that modern intraplate seismicity does not show any general correlation with impact-induced faults associated with the largest terrestrial impact structures [4]. This new example is a particularly important one because of the likelihood that none of the faults formed during the impact have subsequently been removed by erosion. Terrestrial analogs thus continue to offer little support for the hypothesis that impact-induced fractures remain preferred sites for the release of lithospheric stress for periods in excess of several million years after the impact event.

**References.** [1] R. J. Mason, J. E. Guest, and G. N. Cooke, *Proc. Geologists' Assoc.*, 87, 161, 1976; [2] P. G. Thomas, P. Masson, and L. Fleitout, *Earth Planet. Sci. Lett.*, 58, 95, 1982; [3] J. M. Moore and J. L. Ahern, *Proc. Lunar Planet. Sci. Conf. 13th*, *J. Geophys. Res.*, 88, A577, 1983; [4] S. C. Solomon and E. D. Duxbury, *Proc. Lunar Planet. Sci. Conf. 17th*, *J. Geophys. Res.*, 92, E759, 1987; [5] R. A. F. Grieve, *Geol. Soc. Amer. Spec. Pap.* 190, 25, 1982; [6] J. D. Fairhead and R. W. Girdler, *Geophys. J. R. Astron. Soc.*, 24, 271, 1971; [7] F. M. Anglin, *Bull. Seismol. Soc. Amer.*, 74, 595, 1984; [8] D. J. Milton et al., *Science*, 175, 1199, 1972; [9] J. Pohl et al., in *Impact and Explosion Cratering*, Pergamon, 343, 1977; [10] N. H. Sleep, *Geophys. J. R. Astron. Soc.*, 24, 325, 1971; [11] L. F. Jansa and G. Pe-Piper, *Nature*, 327, 612, 1987; [12] B. Gutenberg and C. F. Richter, *Seismicity of the Earth*, 2nd ed., Princeton, 1954; [13] J. P. Rothé, *The Seismicity of the Earth*, UNESCO, 1969; [14] S. Stein et al., *Geophys. Res. Lett.*, 6, 537, 1979; [15] W. F. Haxby and D. L. Turcotte, *Geology*, 4, 181, 1976; [16] E. V. Artyushkov, *J. Geophys. Res.*, 78, 7675, 1973; [17] R. M. Richardson, S. C. Solomon, and N. H. Sleep, *Rev. Geophys. Space Phys.*, 17, 981, 1979.

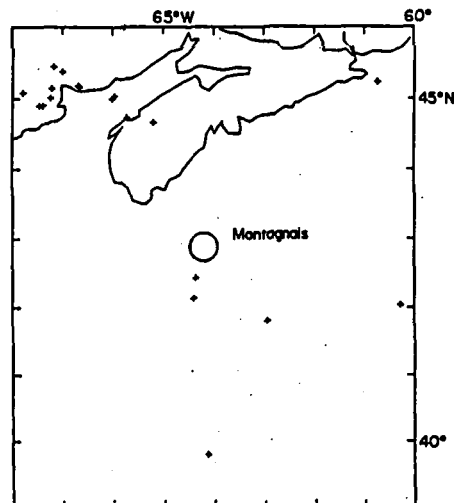


Fig. 1. Recent seismicity in the vicinity of the Montagnais impact structure. Earthquake epicenters (crosses) are from the ISC for the inclusive years 1964-1984. The approximate outline of the impact structure is from [11]. The coastline is also shown. Mercator projection.



## AGES OF FRACTURING AND RESURFACING ALONG THE MARTIAN DICHOTOMY BOUNDARY BETWEEN NEPENTHES AND NILOSYRTIS MNSAE

Ted A. Maxwell and George E. McGill, Center for Earth and Planetary Studies, National Air and Space Museum, Smithsonian Institution, Washington, DC 20560.

The martian crustal dichotomy is generally believed to be a very old feature (e.g., 1), due either to giant impact (2) or mantle convection (1). Later erosion has been proposed to explain the present location of the boundary between northern lowlands and southern highlands in some localities, and to account for the numerous erosion remnants north of the present boundary (3,4). The overall model of crustal history implied by these observations and interpretations involves a single, probably "catastrophic" early structural event that created the crustal dichotomy, followed by episodic or continuous erosion and deposition that have modified the position and appearance of the boundary, and partially filled the northern lowlands with volcanics and/or sediments. Mapping and crater dating of surfaces and materials on both sides of the present dichotomy boundary allows us to place limits on the latter history of erosion and deposition, and suggests that the structural history of the northern plains is complex, and that explaining the dichotomy by a unique early structural "mega-event" may be a significant oversimplification.

The old upland surface immediately south of the dichotomy boundary is commonly very much modified from its more pristine appearance farther south. This modification has been caused by one or more processes, including burial by lavas, planation, pervasive fracturing followed by erosion, and graben faulting. North of the dichotomy boundary, modified upland is buried by younger materials, but remnants of older surfaces are present in many places in the form of knobs and mesas (3,5). These relationships provide opportunities to place the various tectonic, depositional, and erosional events in chronological order.

We have constrained the ages of tectonic events by determining the ages of faults and fractures relative to erosional and depositional surfaces using superposition and cross-cutting relationships, and then measuring the crater ages of the surfaces. In only one case was it necessary for us to extract resurfacing ages from single crater counts using the method outlined by Neukum and Hiller (6); all other resurfacing ages were determined by checking the superposition relationships for every crater used to derive an age. In all these localities, it is possible to determine a lower limit for the age of the old upland by counting all craters present, and to determine the age of resurfacing by counting only those craters superposed on the eroded or partially buried upland surface. In the cratered plateau material of MC-14 SE (the

northernmost unit that is presently in contact with the northern plains), the lower limit for the age of the upland surface is 19,500, as compared with a resurfacing age of 5,800. Consequently, the erosional (?) episode that removed crater rims had ceased by crater number 5,800, about the same time as the emplacement of the adjacent ridged plains to the north.

The age of resurfacing also provides an old limit on the age of faulting in each locality. The young limit on faulting is provided by crater counts on materials that are not affected by faulting or that were deposited on top of tectonically disrupted ancient upland or cratered plateau surfaces. Crater counts on post-faulting surfaces (only those craters that overlie the faults) at the eastern edge of the Isidis basin indicate that the youngest fractures (NNE-trending) had ceased forming by crater number 8,500. However, these younger fractures overlie an older set of faults that are oriented WNW, parallel to the dichotomy boundary in this region. Although it is tempting to relate these old faults to the dichotomy, they are also oriented radial to Isidis, so that a unique interpretation is precluded.

Although crater counting indicates a similar age for the planation of the cratered plateau (see 8) and the emplacement of the ridged plains, superposition relations indicate that the plains material is slightly younger than the cratered plateau. The exact timing of planation does place a constraint on the time of border faulting. If the faulting occurred after planation (as suggested by the smooth-topped character of mesas adjacent to the uplands), then faulting had to occur at about 5,000. In MC-13, faulting occurred after 3,400, but before 2,500 (the age of young, unfaulted plains farther to the north). Similarly, north of Elysium Mons, faulting creating mesas and knobs occurred after 3,800, but before 2,000. Consequently, it appears that these structural events took place in discrete time periods, and occurred in response to local tectonic activity.

Detailed mapping of buried craters in the highland/lowland transition in MC-14 indicates that the surface underlying the ridged plains is not identical to the planated appearing cratered plateau. Assuming that the same sequence of events occurred here as in MC-5, MC-13, and north of Elysium, then age dating indicates a very rapid sequence of border zone formation that involved: 1) Planation (?) of the upland surface, 2) Faulting and downdropping of a 300 km wide transition zone as separate blocks rather than a continuous terrace, 3) Erosion to produce mesas along the northern edge of the transition zone, and 4) Flooding by ridged plains units. Although this sequence of events may be repeated in other areas of the dichotomy boundary, our present data indicate that the individual events (as opposed to resurfacing, 8) were not coeval.

TABLE 1: CRATER COUNTS

<u>SURFACE</u>	<u>N</u>	<u>1A</u>	<u>1B</u>	<u>5</u>	<u>16</u>
Uplands, MC-5SW: all craters	233	130,000	26,000	460	160
:post-resurfacing only	171	30,000	6,000	240	60
Uplands, MC-13NE: all craters	79	100,000	17,500	320	90
:post-resurfacing only	56	8,000	3,400	130	--
Uplands, MC-14SE: all craters	272	60,000	19,500	790	175
:post-resurfacing only	155	11,000	5,800	230	50
"Transition" zone, MC-14SE					
:D>30 km	15	88,000	14,000	570	120
:D<30 km	117	13,000	5,000	195	43
Wrinkle-ridged plains, MC-14	186	12,000	5,100	185	32
Smooth plains, MC-6SE, 7SW, 14-SE,NE	467	4,600	2,100	115	--

(ages as number of craters  $\geq 1, 5$ , or  $16$  km dia./ $10^6$  km<sup>2</sup>;  
 1-km ages derived by projection using curves from 4 (1A) and 7  
 (1B))

REFERENCES CITED: 1) Wise, D.U. et al., Icarus, 38. 456,  
 1979. 2) Wilhelms, D.E., & Squyres, S.W., Nature, 309, 138,  
 1984. 3) Scott, D.H., Icarus, 34, 479, 1978. 4) Hiller, K.,  
 USGS Map I-1110, 1979. 5) McGill, G.E., Geophys. Res. Letts.,  
 13, 705, 1986. 6) Neukum, G. & Hiller, K., J. Geophys. Res.,  
 86, 3097, 1981. 7) Neukum, G., Habilitationsschrift, 1983.  
 8) Frey, H. et al., LPSC XVII, 243, 1986.

## ARCHES, ANTICLINAL RIDGES, CRENULATE AND SUB-CRENULATE RIDGES: THE WRINKLE RIDGE ASSEMBLAGE

Thomas R. Watters, Center for Earth and Planetary Studies,  
National Air and Space Museum, Smithsonian Institution,  
Washington, D.C. 20560

The term "wrinkle ridge" is often used broadly to refer to an association of related features that are morphologically and dimensionally distinct. Many of the same components are shared by analogous ridges on Mercury, Mars and Earth. In order to quantitatively characterize the morphology of the various components, heights and widths for 202 structures were determined based on roughly 900 measurements.

The wrinkle ridge assemblage consists of four primary structures: 1) arches; 2) anticlinal ridges; 3) crenulate ridges; and 4) sub-crenulate ridges. Lunar mare arches are broad, gently sloping topographic rises (figure 1D) ranging in width from 3-18 km and 40-200 m in height. The mare anticlinal ridges (AR) are narrow, relative to arches, sinuous and often strongly asymmetric (figure 1B) ranging in width from 1-5 km and 50-410 m in height. They are usually segmented occurring in en echelon arrangement and many are associated with arches (figure 1D) (see Strom, 1972; Bryan, 1973; Maxwell et al., 1975). Crenulate ridges (CR) are sharp, narrow prominences, similar in morphology to the anticlinal ridges but smaller in dimension (figure 1B), ranging in width from 170-900 m and 10-110 m in height. These features commonly flank or cap the larger anticlinal ridges (figure 1B). Sub-crenulate ridges are similar in morphology but dimensionally smaller still than crenulate ridges ranging in width from 60-90 m and 8-10 m in height. Martian ridge assemblages consist of the same structures as their lunar counterparts. Martian arches range in width from 2-14 km and 90-500 m in height. Martian anticlinal ridges range in width from 1-6 km and 100-570 m in height. As is often the case for mare ridge assemblages, some martian anticlinal ridges are associated with arches. Crenulate ridges range in width from 120-930 m and 50-170 m in height. Like their lunar analogs, martian crenulate ridges often cap or flank anticlinal ridges. Sub-crenulate ridges are also associated with the larger ridge structures ranging in width from 50-80 m and 17-24 m in height. Only arches and anticlinal ridges are observed on Mercury (see Strom et al., 1975). Mercurian arches range in width from 12-30 km and 450-780 m in height. Anticlinal ridges range in width from 1-6 km and 240-700 m in height. Crenulate and sub-crenulate ridges may be present on Mercury, but cannot be resolved in the medium to low (200 to 1,200 m) resolution Mariner 10 images.

Terrestrial analogs for the ridges on the Moon, Mercury and Mars occur in the Miocene flood basalts of the western

Columbia Plateau. The multilayered basalts have been deformed into a series of asymmetric, sinuous, segmented and en echelon anticlinal ridges (figure 1A). Smaller second-order folds with fold axes that trend subparallel to oblique to the larger anticlinal ridges are also observed in the basalts (Reidel, 1984). These structures commonly occur either flanking or adjacent to the anticlinal ridges and are morphologically and dimensionally akin to the crenulate ridges observed on the Moon (figure 1A) and Mars. Broad rises associated with the Horse Heaven Hills Ridge and the Rattlesnake Ridge are morphologically and dimensionally similar to planetary arches (figure 1C) and may serve as analogs. Nothing equivalent to sub-crenulate ridges has been observed, but features of this scale, if they existed, may have been quickly lost to erosion.

The various members of the ridge assemblage can be classified on the basis of dimension as seen in a log-log plot of height versus width for the various structures (figure 2). The size distribution of anticlinal ridges, crenulate and sub-crenulate ridges (ridge data) forms a continuum but with discernible clusterings. The arch data defines a separate field from the other features (figure 2). Regression lines fit to the data are given by a logarithmic expression where the slope  $\log m = 0.72$  and the intercept  $\log c = 0.10$  for the ridge data (correlation coefficient,  $r = 0.85$ ) and  $\log m = 1.2$  and  $\log c = -2.7$  for the arch data ( $r = 0.80$ ) (figure 2). The regression lines can be roughly approximated by a width to height ratio ( $w/h$ ) of 10 for the ridges and 70 for the arches. The observed clustering can be used as a basis for classifying the various members (figure 2). This dimensional criteria may be used to facilitate the description and analysis of the various members of the wrinkle ridge assemblage.

#### References Cited

- Bryan, W.B., Wrinkle-ridges as deformed surface crust on ponded mare lava, Proc. Lunar Sci. Conf. 4th, 93-106, 1973.
- Maxwell, T.A., F. El-Baz, and S.W. Ward, Distribution, morphology, and origin of ridges and arches in Mare Serenitatis, Geol. Soc. Amer. Bull., 86, 1273-1278, 1975.
- Reidel, S.P., The Saddle Mountains: The evolution of an anticline in the Yakima fold belt, Am. Jour. Sci., 284, 942-978, 1984.
- Strom, R.G., Lunar mare ridges, rings and volcanic ring complexes, Modern Geol., 2, 133-157, 1972.
- Strom, R.G., N.J. Trask, and J.E. Guest, Tectonism and volcanism on Mercury, Jour. Geophys. Res., 80, 2478-2507, 1975.

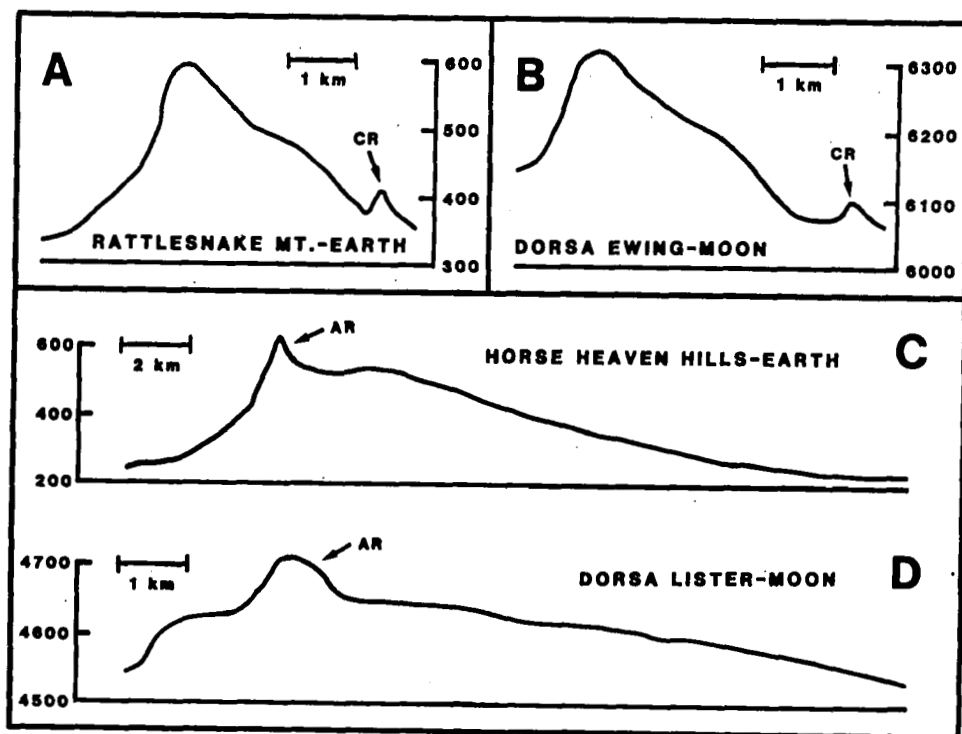


FIGURE 1.

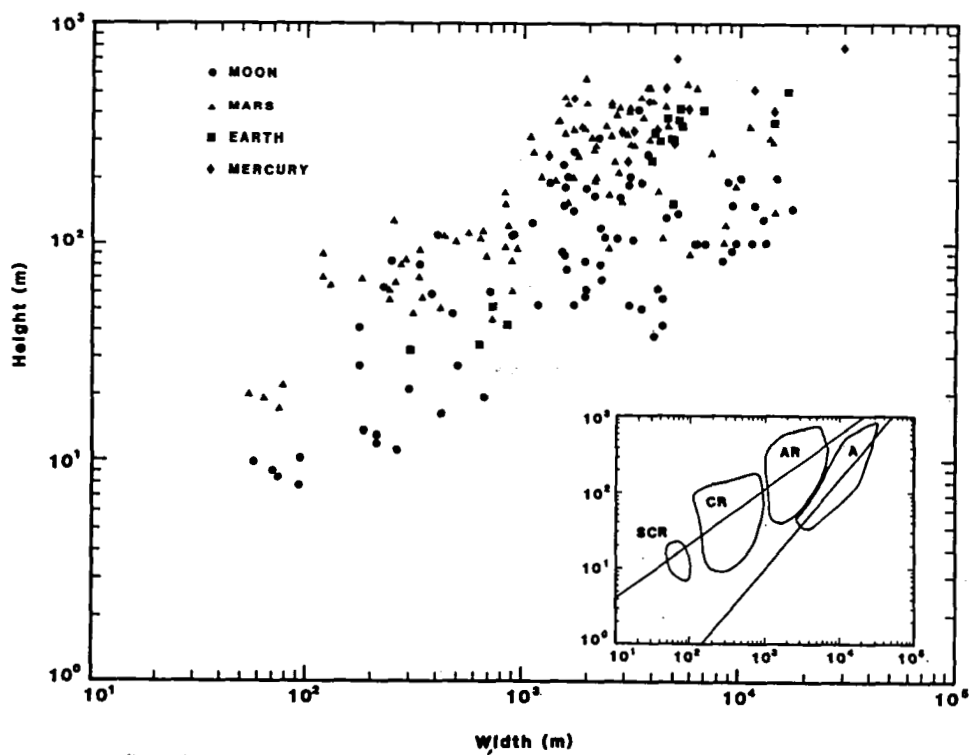


FIGURE 2.

## THE PERIODIC NATURE AND POSSIBLE ORIGIN OF ANTICLINAL RIDGE SPACINGS ON THE THARSIS AND COLUMBIA PLATEAUS.

Thomas R. Watters, Center for Earth and Planetary Studies,  
National Air and Space Museum, Smithsonian Institution,  
Washington, D.C. 20560

An important characteristic shared by the anticlinal ridges of the Tharsis Plateau of Mars and the Columbia Plateau in the northwestern United States is the periodic nature of the ridge spacing. In an effort to characterize the spacing of the ridges on the Tharsis Plateau, measurements were begun in the Coprates region located on the SE margin of the plateau. These measurements are being extended to other regions on the plateau with large expanses of ridged plains (i.e., Lunae Planum, Tempe Terra, Chryse and Amazonis Planitia). The Coprates region south of Valles Marineris was divided into four domains based on apparent spacing and orientation of the anticlinal ridges. The total range in spacing measured in the four domains is from 14-85 km with a mean of 45 km ( $n = 1072$ ) (figure 1A). The anticlines of the Yakima Fold Belt of the Columbia Plateau are generally co-parallel, trending roughly E-W except in the eastern portion of the belt where segments of the Horse Heaven Hills and Rattlesnake Ridge are deflected to the SE along the trend of the Cle Elum-Wallula lineament (CLEW). The Yakima Fold Belt can also be subdivided into three domains on the basis of the spacing and orientation of the anticlinal ridges. The total range in spacing measured in the three domains is 4-36 km with a mean of about 23 km ( $n = 270$ ) (figure 1B). Thus, it is clear that the mean spacing of the anticlines in the Coprates region is larger (by a factor of 2) than in the Yakima Fold Belt.

The periodic spacing observed in the anticlinal ridges of the Columbia and Tharsis Plateaus strongly suggests a dominant wavelength controlled deformational mechanism. It has been suggested that the regular spacing in the Coprates and Lunae Planum regions of Tharsis is the result of viscous buckling of the volcanic plains at a dominant wavelength of folding (Saunders and Gregory, 1980; Saunders et al., 1981; Watters and Maxwell, 1982; 1985). On the Columbia Plateau, the basalts of the Yakima Fold Belt overlie several thousand meters of sediments (Reidel, 1984) that are generally poorly consolidated (N. Campbell, personal communication). The ridged plains units on Tharsis are presumed to be underlain by an extensive, poorly consolidated, regolith layer (Saunders and Gregory, 1980; Watters and Maxwell, 1985). Thus, a significant strength contrast exists between the basalts or volcanic plains and the substrate. If the anticlinal ridges are the results of a flexure-fracture mechanism (i.e., buckling followed by reverse to thrust faulting), the development of regularly spaced folds in a medium can be modeled using plate bending theory. In this analysis it is assumed that: 1) deformation has occurred at

the free surface, 2) the basalts behave as a linearly elastic material, 3) the basalts rest on a mechanically weaker substrate of finite thickness which is in turn resting on a strong rigid boundary; and 4) gravity is not a negligible factor. Given the acceleration due to gravity on Mars ( $g_M = 3.75 \text{ m s}^{-2}$ ) and assuming the regolith substrate has a mean density of  $2,300 \text{ kg m}^{-3}$  and a thickness of 1-2 km for the volcanic plains, the wavelengths obtained range from approximately 32-54 km (figure 2), in good agreement with the observed range of spacing of the anticlinal ridges in the Coprates region. Assuming the thickness of the basalt sequence in the Yakima Fold Belt was between 0.5-1.5 km at the time when the elastic limit was approached and that the density of the underlying sediments is  $2,300 \text{ kg m}^{-3}$ , the expected wavelengths are from approximately 15-34 km (figure 2), also in good agreement with the observed spacing except for the domain which contains the CLEW structures.

In spite of the ability of the model to explain the observed differences in wavelength, the inherent problem in modeling a linearly elastic rheology is the high layer average stress required to achieve buckling. The critical stress predicted by the elastic model is far in excess of the maximum compressive strength of the basalt on the two planets as determined using Byerlee's law. This problem cannot be overcome by modeling of the basalts as either a Newtonian/viscoelastic or power law viscous material.

The anticlinal ridges of the Columbia, however, have developed in part through cataclastic flow. The simplest approximation to cataclastic flow may be plastic yielding. If deformation begins with the development of low amplitude folds, plastic yielding should first occur in the cores of the anticlines where compressive stresses are highest. Yielding confined to the hinge areas of the anticlines would result in folds with narrow crestal hinges and straight limbs. Thus, a combination of elastic buckling and localized plastic yielding may explain the periodic spacing and fold geometry of the anticlinal ridges.

#### References Cited

- Reidel, S.P., The Saddle Mountains: The evolution of an anticline in the Yakima fold belt, Am. Jour. Sci., 284, 943-978, 1984.
- Saunders, R.S. and T.E. Gregory, Tectonic implications of Martian ridges plains, NASA Tech. Memo. TM-82385, 93-94, 1980.
- Saunders, R.S., T.G. Bills, and L. Johansen, The ridged plains of Mars, Lunar Planet. Sci. XII, 924-925, 1981.
- Watters, T.R. and T.A. Maxwell, Fold model for ridges of the Tharsis region of Mars, Lunar Planet. Sci. XVI, 897-898, 1985.



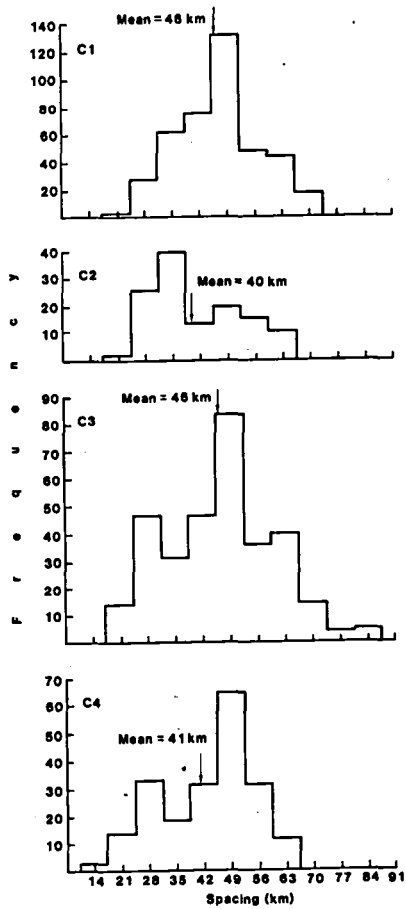


FIGURE 1A.

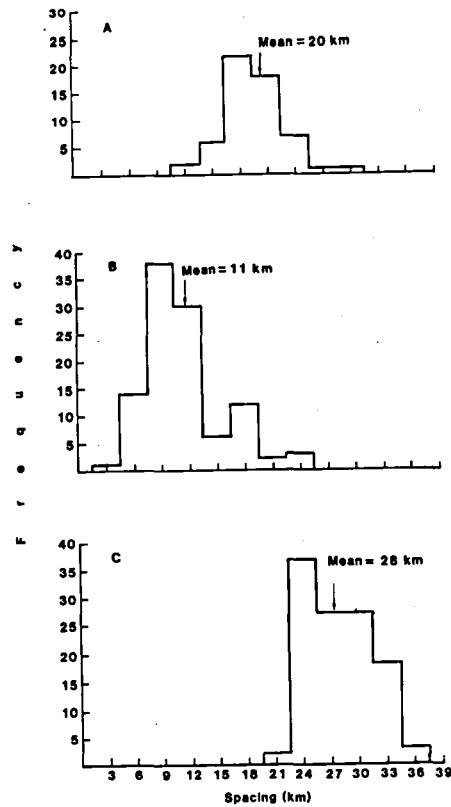


FIGURE 1B.

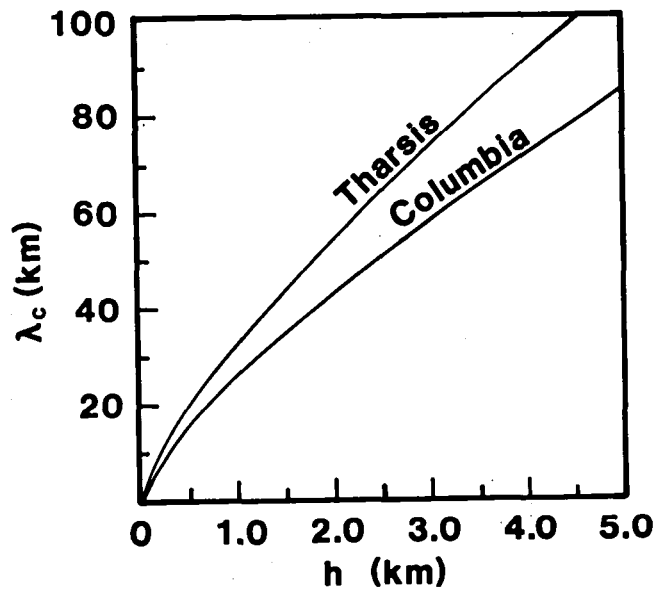


FIGURE 2.

## RELATIVE IMPORTANCE OF FAULTING AND FOLDING IN LUNAR WRINKLE RIDGES

M. Golombek and B. Franklin (Jet Propulsion Laboratory, Caltech, Pasadena, CA 91109)

### Introduction

Wrinkle ridges are linear asymmetric topographic highs with considerable morphologic complexity. They are commonly found on the lunar mare and the smooth plains of Mars and Mercury. Interpretations of their origin have been split between volcanic intrusion and extrusion and tectonic folding and faulting mechanisms (e.g. see references in Plescia and Golombek, 1986). Recent interpretations have focused on the tectonic origin of wrinkle ridges, although the relative role of folding versus faulting is still being discussed. In this abstract, we interpret the results of a detailed physiographic analysis of lunar wrinkle ridges (Golombek and Franklin, 1987) to estimate the relative shortening due to folding and faulting. Our analysis shows that most of the shortening associated with wrinkle ridges is accommodated by motion across one or more thrust faults and that folding is subsidiary, in agreement with the recent interpretation of earth analogs as thrust faults that deform surface rocks (Plescia and Golombek, 1986).

### Physiography and Subsurface Structure

We have constructed a total of 76 detailed topographic profiles from a comprehensive survey of the entire collection of high-resolution Lunar Topographic Orthophoto Maps (10-20 m contour interval) that cover wrinkle ridges. A detailed analysis of this data set (Golombek and Franklin, 1987) has shown that in addition to the three physiographic elements that make up wrinkle ridges (broad rise, superposed hill, and crenulation) all wrinkle ridges show a regional elevation offset. That is, the elevation of the mare surface on one side of the ridge is different from that on the other side, so that wrinkle ridges accommodate a vertical offset between structural units or blocks of the mare that are at different elevations. This regional elevation change requires a fault beneath the ridge to accommodate the change in mare surface elevation. Simple fold structures cannot readily explain this regional elevation change. In addition, the fault beneath wrinkle ridges can not shallow with depth, or the regional elevation change would disappear above the area where the fault becomes horizontal. We believe the broad, low, positive relief structure of wrinkle ridges is most compatible with a low-angle thrust fault origin that involves the compression and folding of surface units. It is not clear how a vertical fault at depth could affect a wide region at the surface producing a broad, low, positive relief structure, particularly when the edges of the structure are characterized by broad rises without apparent structural discontinuity or faulting that breaks the surface. Instead the structures appear very similar to broad folds produced by thrust faults on the earth that typically break the surface (e.g., Plescia and Golombek, 1986). Although we do not know the dip of the thrust faults at depth a number of arguments suggest that the faults dip shallowly. The most convincing argument is that most failure criteria for the brecciated surface material of the moon suggest that deformation under compression will occur on pre-existing faults along which the normal

stress, determined by the frictional resistance to sliding, is a minimum (Brace and Kohlstedt, 1980). Choosing accepted values for low-stress friction (Byerlee, 1978) applicable to the outer layers of the moon suggests that thrust faults should form with dips of about  $25^{\circ}$ , although a variation of about  $10^{\circ}$  is quite possible.

### Shortening

The above constraints for the subsurface structure of lunar wrinkle ridges allow estimates of the compressional strain or shortening that they have accommodated. For example, if a wrinkle ridge is underlain by a  $25^{\circ}$  dipping thrust fault that has resulted in a measurable vertical throw then the shortening due to thrusting is simply the vertical throw divided by the tangent of the fault dip. However, some shortening is likely taken up by folding of the rocks above and perhaps adjacent to the fault and this must be accounted for as well. Three possible models can be used to calculate the shortening across wrinkle ridges: 1) All slip at depth on the fault is reflected in folding at the surface, so that the fault does not break the surface; 2) All slip at depth is taken up by overthrusting (slip) of the fault at the surface plus folding at the surface; 3) All strain at depth is accommodated by slip on the fault and folding adjacent to the fault, so the total shortening is obtained by adding that on the fault (from the regional elevation change) plus that from folding (assuming that the folding at depth is similar to that at the surface). Assuming the strain at depth is solely due to slip on the fault is a possibility, which is represented in models 1 and 2 by making the reasonable assumption that the regional elevation change is a product of slip on the fault at depth. It is also possible that some of the strain at depth is not reflected solely by faulting, in which case folding adjacent to the fault also occurs (model 3). In this case we will assume that the folding at the surface is greater than or equal to that expressed at the surface. Models 1 and 3 are end members; 1 requiring minimum shortening and 3 representing maximum shortening.

Calculations of the shortening due to faulting and folding were made for 31 representative profiles from the total data set. We calculated the shortening due to faulting by dividing the regional elevation change (2-280 m) by the tangent of the fault dip ( $15^{\circ}$ ,  $25^{\circ}$ , and  $35^{\circ}$ ). This assumes that all of the shortening at depth on the fault is reflected as a regional elevation change at the surface. The shortening due to folding was determined by subtracting the line length of the surface profile from the present horizontal width of the wrinkle ridge. Results show that shortening due to folding varied from 2 to 121 m with an average of 40 m. Shortening due to thrusting varied from 7-1044 m, 4-600 m, and 3-400 m for  $15^{\circ}$ ,  $25^{\circ}$ , and  $35^{\circ}$  dipping faults with average values of 311 m, 177 m, and 118 m, respectively. In all but 2 to 8 cases, depending on the fault dip, the shortening due to thrusting exceeded the shortening due to folding, typically by a large margin. On average, the shortening due to thrusting exceeds the shortening due to folding by a factor of 7 for  $25^{\circ}$  dipping faults. These estimates suggest that models 2 or 3 are most appropriate for lunar wrinkle ridges. Model 1 is not reasonable because the shortening due to folding does not equal that due to thrusting as would be expected if the fault did not break the surface and all the shortening due to slip on the

fault at depth was reflected by folding at the surface. Instead the fault must break the surface and a substantial portion of the shortening is likely expressed by slip on the fault at the surface. It is possible that for many lunar wrinkle ridges the strain accommodated by faulting at depth is taken up at the surface by both slip on the fault and folding (model 2). This follows from the shortening due to folding being much smaller than that due to faulting, so that the total surface shortening due to folding and faulting adds up to the slip on the fault at depth. However, if some of the shortening at depth is taken up by folding in addition to the slip on the fault, then the total shortening across the structure is closer to the sum of the shortening due to faulting at depth plus that due to folding, estimated at the surface. Depending on the fault dip, this maximum shortening varies from 15-1101 m, with averages of 158, 217, and 352 m.

#### Discussion and Summary

Our estimates of shortening across wrinkle ridges (hundreds of meters) based on detailed physiographic data and straightforward assumptions are broadly similar to previous estimates (Bryan, 1973; Muehlberger, 1974). These estimates of shortening are also similar to estimates of extension across lunar grabens (hundreds of meters) (Golombek and McGill, 1983), although we leave more detailed comparisons of these data for future work.

The existence of a regional elevation offset across all lunar wrinkle ridges for which detailed topographic information exists requires a planar fault at depth that does not shallow out. This elevation change also allows the calculation of the shortening due to faulting required to produce the vertical throw for reasonable fault dips. Fault dips predicted by the most applicable failure criterion and the low broad structure of wrinkle ridges argue strongly for thrust faults beneath lunar wrinkle ridges with shallow dips of about  $25^{\circ}$ . Calculations of the shortening due to thrusting on average exceed those due to folding by a factor of 7, implying that the dominant deformation occurs by thrust faulting. These data show that the consideration of lunar wrinkle ridges solely as fold structures is unsupportable. Thus our detailed analysis of lunar wrinkle ridges is in agreement with our study of analog structures on earth and indicates that this family of structures is primarily the result of thrust faults that break the surface.

#### References

- Brace, W. F., and D. L. Kohlstedt, 1980, J. Geophys. Res., v. 85, p. 6248-6352.
- Bryan, W. B., 1973, Proc. 4th Lunar Sci. Conf., p. 93-106.
- Byerlee, J., 1978, Pageoph., v. 116, p. 615-626.
- Golombek, M., and B. Franklin, 1987, Lunar Planet. Sci. XVIII, p. 339-340.
- Golombek, M. P., and G. E. McGill, 1983, J. Geophys. Res., v. 88, p. 3563-3578.
- Muehlberger, W. R., 1974, Proc. 5th Lunar Sci. Conf., p. 101-110.
- Plescia, J. B., and M. P. Golombek, 1986, Geol. Soc. Amer. Bull., v. 97, p. 1289-1299.

## RIDGED PLAINS AND GULLIED TERRAIN IN THE MARTIAN UPLANDS

D. E. Wilhelms, R. J. Baldwin, and D. R. Harden, Geology Department, San Jose State University, San Jose, CA 95192 and U.S. Geological Survey, Astrogeology (MS-946), Menlo Park, CA 94025

Two extensive types of geologic unit in the martian uplands are ridged plains [1-3] and gullied ("valley-network") terrain [4-8]. The ridged plains, characterized by "wrinkle ridges" like those of the lunar maria, occupy depressions throughout the uplands. Gullied terrain is also widespread but is absent or rare in uplands dominated by plains or by large crater rims and basin rings [5,8]. The ridged plains are rarely gullied but the gullied terrain and other upland terrains are commonly ridged [9].

The presence of a discrete gullied deposit is shown by its encroachment on crater rims and by the very different appearance of "primitive" crater-and-basin uplands where it is absent or thin [5,8]. This deposit probably consists of fragmental material (mostly impact debris and tuff) that acquired interstitial ice early in martian history when abundant water was being outgassed and could be recharged [7]. The deposit is Noachian and the ridged plains Lower Hesperian in Tanaka's martian stratigraphic scheme [10]. The Noachian-Hesperian boundary is about 3.5 aeons old in the most likely calibration of martian stratigraphy with that of the Moon [10].

A high density of craters in the gullied terrain has led to the assumption that the gullies themselves are old [4-7]. Many may indeed be almost as old as the deposit in which they occur. However, several very fresh-appearing crater rims and ejecta blankets are gullied (Viking Orb. 381S84). Also, our crater counts, in which superposed and buried craters are distinguished, suggest an overlap in age of the gullies and the ridged plains. This finding is somewhat subjective because of uncertain age assignments of many craters. Nevertheless, many gullies are younger than commonly thought and approximate the ridged plains in age.

Three evident but heretofore inadequately explained geologic relations suggest that unexposed lateral extensions of the ridged plains lie topographically (though not stratigraphically) beneath the gullied deposit. (1) Ridges in the gullied deposit, which by itself is probably too weak to deform into discrete narrow ridges, are reasonably explained as ridges that developed within the plains material and that deform the overlying gullied deposit. (2) A generally common level of plains, for example in a crater floor and adjacent canyons, also suggests a lateral continuity of the plains material in the subsurface. (3) Transitional morphologies between the two types of terrain are likely to represent alterations of gullied terrain by the underlying plains. This is particularly evident where thin remnants of a gullied deposit lie on the surfaces of ridged plains, which otherwise have few gullies. Thus, the ridged plains are probably extensive tabular units that happen to be exposed in depressions.

Subsurface flow of water, resulting in sapping of the surface material, is now widely accepted as the origin of the gullies [4-7]. The age similarities and the "underplating" of the gullied deposit by the ridged plains suggest that emplacement of the plains triggered much or most of the gullying. If the plains are volcanic as generally assumed [1-3] (though not actually proven), their heat could have melted some of the interstitial ice in the overlying gullied deposit. The meltwater then seeped out and undermined the surface. Alternatively, if the heat did not actually emanate from the plains material, a generally elevated geothermal gradient might have both warmed the gullied deposit and led simultaneously to the plains' emplacement without further genetic connection between the two units. Still another variant of these schemes is that the ridged plains are not themselves volcanic, but that the heat and the ridging originate in a still more deeply buried set of sills. These sills may be exposed as dark plains in deep upland craters and along the upland-lowland front [11].

The failure of many of the upland magmas to rise to the surface may simply be due to hydrostatic factors. However, the apparent ease with which the plains material was intruded so extensively and so uniformly suggests that a major lithologic discontinuity exists at an approximately common depth beneath the entire study area. The bottom of the fragmental ice-rich gullied deposit may provide this horizon. However, the existence of a more nearly universal horizon is suggested by (1) a common bottom to many other kinds of degradation features such as chaotic and fretted terrains [12] and the fact that ridges cross contacts from plains into "primitive" crater-and-basin terrain (e.g. MC-16 SW) as they do into gullied terrain. The principle localizer of the plains' intrusion may be a global interface 1 to 2 km beneath the surface between an overlying zone in which ice is stable and an underlying zone in which liquid water is stable [12].

Thus, gullying apparently requires (1) the presence of an ancient (Noachian) ice-rich fragmental deposit and (2) later heating of the deposit from below. Most of this heating probably occurred when ridged plains material or underlying sills were extensively intruded along a favorable interface 1 to 2 km beneath the surface starting about 3.5 aeons ago. Plains but not gullies occur where the fragmental deposit was absent. Areal contraction resulting from cooling of the plains material created ridges in the plains and, consequently, in overlying deposits of all types. Gullies cutting young crater rims and young crater-based ages of other gullies suggest that gullying continued long after the main gullying episode. This late gullying was probably the result of late volcanism.

We conclude that the cause of gullying was endogenic and not atmospheric. Furthermore, magmatic activity may have been almost as great in the martian uplands as in the lowlands; the difference is that the igneous rocks are mostly exposed as volcanics in the lowlands but mostly intruded as sills in the uplands.

### References

- [1] Scott D.H. and Carr M.H. (1978) USGS Map I-1083.
- [2] Scott D.H. and Tanaka K.L (1987) USGS Map I-1802A.
- [3] Greeley Ronald and Guest J.E. (in press) USGS Map I-1802B.
- [4] Pieri D.C. (1980) Science 210, p. 895-897.
- [5] Carr M.H. and Clow G.D. (1981) Icarus 48, p. 91-117.
- [6] Mars Channel Working Group (1983) Bull. Geol. Soc. Amer. 94, p. 1035-1054.
- [7] Carr M.H. (1986) Icarus 68, p. 187-216.
- [8] Wilhelms D.E. and Baldwin R.J. (1986) Lunar Planet. Sci. XVII, p. 948-949.
- [9] Raitala J.T. (1987) Lunar and Planet. Sci. XVIII, p. 814-815.
- [10] Tanaka K.L. (1986) J. Geophys. Res. 91, p. E139-E158.
- [11] Squyres S.W., Wilhelms D.E. and Moosman A.C. (1987) Icarus 70, 385-408.
- [12] Soderblom L.A. and Wenner D.A. (1978) Icarus 34, p. 622-637.

**CONSTRAINTS ON THE ORIGIN OF FRACTURED TERRANE, NORTHERN MARTIAN PLAINS; George E. McGill, Department of Geology and Geography, University of Massachusetts, Amherst, MA 01003.**

The terrane characterized by giant fracture systems that commonly define crudely polygonal patterns has received much attention because of its potential importance to such diverse problems as the amount and distribution of interstitial volatiles on Mars, the source of northern plains deposits, and the tectonic evolution of the northern plains. Several hypotheses have been proposed to explain the giant fracture systems, as reviewed by Pechmann (1); but, as originally proposed, most of these are mechanically unsound because of the orders-of-magnitude size differences between the martian features and suggested terrestrial analogues. However, if the nature of the surface upon which the fractured material was deposited is considered, the size problem can be overcome (2).

The crater age of fractured terrane material in Utopia Planitia falls within the range of ages for both major outflow channels and Elysium volcanism (2,3). Furthermore, the fracturing is temporally (and, by inference, causally) related to the deposition process, as indicated by superposition relationships with craters and with adjacent unfractured plains (2,4). These observations suggest that the fractured material was deposited as wet sediment or some type of volcanic. Either wet sediment or hot pyroclastics would possess properties compatible with the differential compaction plus shrinkage model proposed (2) to explain the giant fracture pattern (5). Nevertheless, determining which is most likely is extremely important to considerations of volatile content, and also important for our general understanding of the processes responsible for the deposits blanketing the northern third of Mars.

Lucchitta et al. (6) strongly advocate a sedimentary origin for the fractured material, an opinion that coincides with my own biases and, I suspect, the biases of most martian geologists who have given the matter serious thought. Even so, it is useful to consider the evidence relevant to the source of fractured material, because this evidence is somewhat equivocal.

Associated with the fractured terranes of both Utopia and Acidalia (2,7) are numerous small landforms resembling cinder cones, rows of pit craters aligned with grabens, and patches of material that may be remnants of pyroclastic flows. In the Utopia area, the cones are all external to the fractured terrane, and the other presumably volcanic features appear to be younger than the fracturing event of interest (2). In the Acidalia area, cones occur on fractured terrane (7), and at least some of them are unequivocally younger than the fracturing because they are superposed on the ejecta of craters that are superposed on the giant fractures. These volcanic features also seem pathetically small to be responsible for the areally extensive fractured terranes. Nevertheless, they are the only landforms associated with the fractured terranes of Acidalia and Utopia/Elysium for which an origin can be readily inferred. In the absence of any morphological characteristics of the deposits themselves supporting a sedimentary origin, one might argue that these small volcanic landforms represent the products of late-stage activity in a region with a long volcanic history. In fact, those of us favoring a sedimentary origin for the fractured terranes of Acidalia and Utopia/Elysium need to explain why there should be such an abundance of small volcanic landforms on and near these terranes. My tentative hypothesis is that this abundance is only apparent—an artifact of the great concentration of high-resolution Viking images in the Acidalia and Utopia areas (the small volcanic landforms commonly are not resolvable on typical mapping frames).

A long-standing problem has been the fate of the large volumes of sediment presumably transported by the large runoff and outflow channels on Mars, and the extensive fractured terranes provide a tempting sink because they are conveniently located



—Acidalia near the large channels debouching onto Chryse Planitia, and Utopia/Elysium near the channels draining the Elysium Mons area—and because they occur in topographic lows (6). Ideally, there should be a rough correspondence between the sizes of the channels and the volume of material deposited, and there should be some geomorphic evidence to support transport of sediment from channels to sinks. It is possible to make some headway with these constraints in the Utopia/Elysium area.

The channels draining the Elysium Mons area to the northwest gradually lose their definition in the disordered plains (8) that form an indentation into the fractured terrane (Fig. 3 in 6). But these channels appear to be younger than the fractured terrane (9), a conclusion supported by crater counts (Table 1) showing that disordered plains are the same age as the smooth plains clearly superposed on the fractured terrane of Utopia. On the other hand, fracturing and major erosion of the northern flank of Elysium Mons can be constrained by crater counts (10) to have occurred within a time span that includes the crater age of the fractured terrane. There is an excess of large craters on the disordered plains (Fig. 1) suggesting that beneath the channels and volcanic (?) materials of the disordered plains there is a relict surface at least as old as the fractured terrane of Utopia. This supports speculations (6,10) that the present channels draining northwestward from Elysium Mons have, along with the widespread smooth plains, covered or obliterated evidence for the transport of large volumes of sediment from Elysium Mons to Utopia at an earlier date.

If the boundaries of fractured terrane in Utopia/Elysium are plotted on an orthographic projection centered near Utopia, the distribution appears to be roughly circular with a large indentation where disordered plains occur (Fig. 1 in 11). Assuming that the disordered plains are superposed on fractured terrane, then this roughly circular area contains (or contained) about 3.5 million square km of fractured terrane. The distribution of partially buried craters and ring fractures (Fig. 5 in 2) provides a clue to the thickness of this deposit. The smallest ring fractures are about 8 km in diameter, suggesting that the deposit is thick enough to mask the structural effects of all smaller craters. The complete burial of all craters less than 8 km in diameter implies that the deposit has an intercrater thickness of at least 300 m. Furthermore, there are some well defined, complete ring fractures up to 30 km in diameter, suggesting the burial of even larger craters and thus a deposit thickness greater than 300 m (because the larger craters may have been degraded before burial, it is not possible to be more precise than this). The absence of ring fractures in the northern part of the Utopia fractured terrane is probably due to the lack of complete crater rims of sufficient diameter to affect the surface of the deposit; consequently, there is no longer any control for estimating thickness. Assuming that there is no dramatic change in thickness where the control ceases, an estimate of 500 m for the average deposit thickness seems reasonable, and preliminary analysis suggests that this thickness is adequate to account for the fractures by bending related to differential compaction (5). This thickness leads to an estimate of 1.75 million cubic km of material within the circular area of fractured terrane in Utopia/Elysium. I believe that this is a very conservative estimate, because smooth plains are clearly superposed on fractured terrane peripheral to the circular area of exposure, suggesting a wider distribution of fractured terrane material in the subsurface. This is a lot of material, and it is not at all clear that the Elysium Mons area is large enough to provide it.

TABLE 1

Surface	Total n	n for D>5	N(5)
Smooth plains superposed on fractured terrane	378	24	90
Disordered plains	253	58	90
Fractured terrane of Utopia	118	35	115

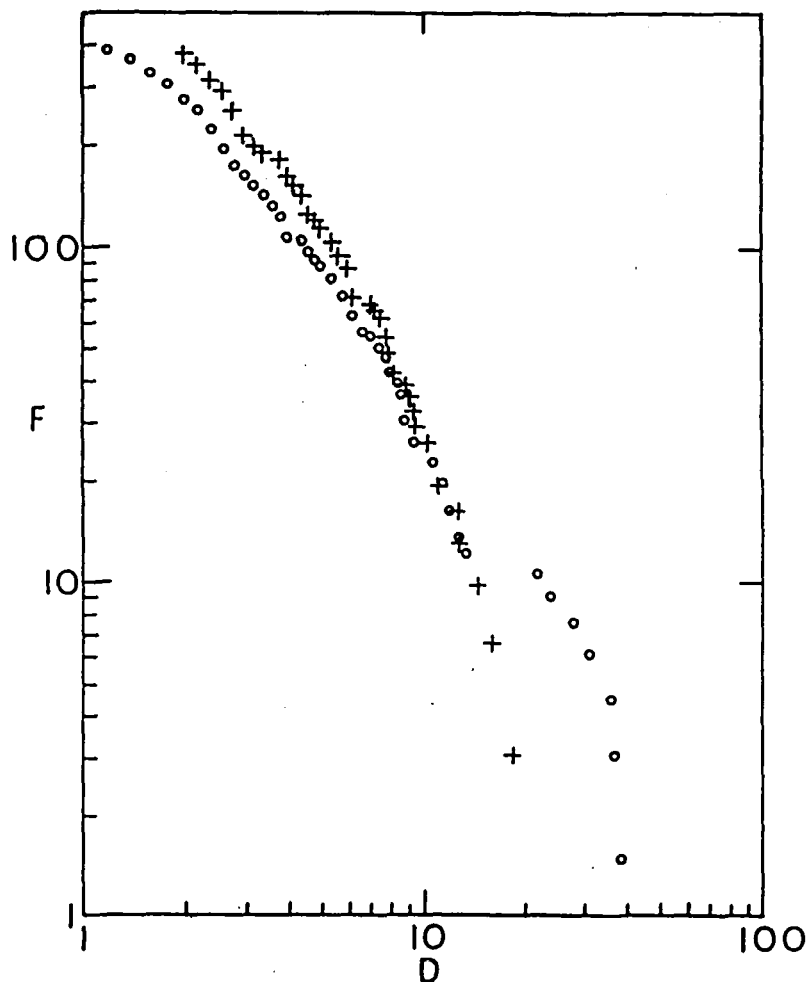


Fig. 1: Cumulative diameter/frequency plot for disordered plains (circles,  $n=253$ ) and Utopia fractured terrane (crosses,  $n=118$ ).  $F$ =cumulative frequency/million square km;  $D$ =crater diameter in km. Note excess large craters on disordered plains and gap between  $D=13$  km and  $D=22$  km.

#### REFERENCES CITED

- (1) Pechmann, J.C., *Icarus*, **42**, 185-210, 1980.
- (2) McGill, G.E., *Geophys. Res. Letts.*, **13**, 705-708, 1986.
- (3) Neukum, G., and Hiller, K., *J. Geophys. Res.*, **86**, 3097-3121, 1981.
- (4) Helfenstein, P., and Mouginis-Mark, P.J., *Lunar Planet. Sci.* **XI**, 429-431, 1980.
- (5) Hills, L.S., *NASA Tech. Mem.* 89810, 495-496, 1987.
- (6) Lucchitta, B.K., Ferguson, H.M., and Summers, C., *J. Geophys. Res.*, **91**, E166-E174, 1986.
- (7) Borrello, M.C., *Lunar Planet. Sci.* **XVIII**, 107-108, 1987.
- (8) Carr, M.H., *The Surface of Mars*, 82-83, 1981.
- (9) Tanaka, K.L., *J. Geophys. Res.*, **91**, E139-E158, 1986.
- (10) McGill, G.E., *Lunar Planet. Sci.* **XVIII**, 620-621, 1987.
- (11) McGill, G.E., *Lunar Planet. Sci.* **XVIII**, 622-623, 1987.

## **Constraining Martian Northern Plains Surface-Forming Processes through Analysis of Boundary Morphology**

by

Timothy J. Parker and R. Stephen Saunders

Jet Propulsion Laboratory, California Institute of Technology, Pasadena, CA

The origin of the surface units of the northern lowland plains of Mars, about one third of the planet's surface, remains unclear after 20 years of analysis of spacecraft data. Hypotheses that have been put forth to explain the morphologies and likely processes include: (I) Volcanic plains emplacement (1,2,3,4); (II) eolian blanketing (5); (III) emplacement of an ice-rich mantle (either eolian or fluvially derived) (1,6,7,8); and (IV) sediment deposition during periods of standing water (9,10,11,12,13).

The chief problem with constraining models of plains formation is that characterizing plains surface-forming processes is dependent upon the identification of distinctive landforms within the plains. Even with specific landforms, the processes inferred by different investigators can differ markedly. The most commonly cited examples of distinctive morphologies found within the northern lowlands include: wrinkle ridges; small domes; giant polygons; and curvilinear ridges and ground undulations.

Wrinkle ridges are common on many northern plains surfaces, particularly those at low latitudes (1). Because wrinkle ridges are common on the lunar mare volcanic plains, they have been taken to indicate volcanic material on Mars as well. Plescia and Golombek (14), however, were able to demonstrate, with convincing terrestrial analogs, that wrinkle ridge formation may be independent of surface composition.

Terrestrial analogs to small domes include volcanic cones and pseudocraters (2,3) and pingos (15). Both hypotheses are based on reasonable morphological comparisons and the possibility, at least, of an association with other features of similar origin.

Giant polygons are common features in the northern lowland plains, being most concentrated in the central Acidalia and Utopia regions (9). They have been interpreted as giant dessication or compaction features in frozen outflow channel sediments (8,9) and as tensional fracture patterns formed by regional up-warping of the surface (16) or cooling of a lava plains surface (1).

Curvilinear ridges and ground undulations, most common within a few tens of kilometers of the lowland/upland boundary, have been interpreted by most investigators as primary or secondary sedimentary structures. Rossbacher (17) compared both types of morphology to terrestrial ground-ice features. Lucchitta et al., (9) compared curvilinear ridges to compressional and flow ridges in Antarctic coastal ice sheets. Parker et al., (10,11) compared the ridges to terrestrial lacustrine or shallow marine coastal spits and barriers. In the model of Lucchitta et al., the northern lowland plains materials would be comprised of outflow channel sediments deposited in a partially or completely frozen northern hemisphere ocean, whereas that of Parker et al. suggests a predominantly liquid water environment in which wave-generated currents are chiefly responsible for the development of the curvilinear ridges.

To further constrain the processes involved in the development of the northern plains, we are conducting a careful analysis of boundary morphology. Superposition relationships, erosional escarpments, crispness of boundary detail, and evidence of flow of plains material over adjacent terrain are characteristics of plains boundary morphology that should prove useful for inferring genesis. Plains units, whether volcanic or sedimentary in origin, are likely to be very thin at the margins, so boundary detail may not be obvious at typical Viking Orbiter image scales. Therefore, we have concentrated our efforts where high resolution (~50m/pixel or better) images are available at or just plainward of the lowland/upland boundary. Two areas that seem to typify plains boundary

morphology are the southwest Cydonia Mensae - Acidalia Planitia region and the west Deuteronilus Mensae region. Several important aspects can be identified in these areas:

(a) In both regions plains units have sharp, crisply defined boundaries with adjacent plains units and elevated terrain (e.g., knobs, massif outliers). They are typically arcuate to sinusoidal with a distinct lack of small-scale irregularities.

(b) Plains boundaries are often parallel to the general trend of the lowland/upland boundary in the regional sense and are locally deflected around clusters of knobby terrain and several kilometers into fret canyon reentrants in what appears to be a topographically conformal fashion (10,12).

(c) Superposition of surrounding terrain by plains units can be described as relatively simple or complex. In the simplest case, the plains material appears to onlap the surrounding elevated terrain or adjacent plains surface without exhibiting any obvious effect on the older surface beyond the contact. In the more complex examples, the boundary may exhibit both negative and positive relief relative to older terrain (11). In the more extreme examples of the former, highland remnants are surrounded by younger, low-lying plains materials, requiring that the uplands be eroded extensively - as much as several hundred kilometers southward - either prior to or contemporaneously with plains emplacement. Examples of boundaries exhibiting both positive and negative relief relative to adjacent terrain in southwest Cydonia Mensae are much lower in topographic relief, probably only a few meters at most.

The four processes for emplacing surface materials outlined in the first paragraph can be considered in light of the boundary morphology:

(1)(a) Volcanic plains emplacement could easily produce a sharp contact with adjacent terrain. Individual flow fronts have very irregular outlines, however. A smooth, sinuous boundary would probably require very low viscosities and a fairly smooth extant terrain surface - still not an impossible condition (18).

(b) Topographically conformal boundaries occur in the lunar mare and would be expected of volcanic plains on Mars.

(c) Erosion of adjacent terrain by lava, producing a smooth, arcuate escarpment, is unlikely. Similar morphology is not found at the margins of the lunar mare. In fretted terrains, the relief between uplands and lowlands is so great that an additional process of erosion is required prior to plains emplacement.

(II) Eolian blankets, most likely loess, would probably be the least likely to produce the observed boundary morphology.

(a&c) Loess blankets would likely thin gradually at the margins, thus making separation from adjacent material dependent mainly on available image resolution (19).

(b) Eolian deposits would not be confined to lower elevations as would low-viscosity lavas or water (either frozen or liquid), so would be unlikely to produce a topographically conformal boundary.

(III&IV) Fluvial emplacement of an ice-rich mantle (7,8) might produce most of the above characteristics if it remained fluid until erosional escarpments had been carved. Very high escarpments in fretted terrains, would require an additional event(s), however. Air-fall deposition of ice-rich sediment (6) might expectedly produce boundary morphology similar to eolian deposits, at least prior to ice removal.

Sediment deposition in a northern plains sea or ocean could produce the observed boundary morphology. Large scale erosional escarpments would be more easily produced in a dominantly liquid than in a frozen ocean environment, however. Freezing-through of a large body of water might expectedly carve drumlin-like forms upon expansion of the ice. Such morphology is decidedly absent along the lowland/upland boundary. Possible periglacial forms become much more common farther plainward of the lowland/upland boundary above 30° latitude, which might indicate later freezing of a

sea or ocean reduced in area by evaporation and loss to groundwater. Such a scenario requires a warm epoch relatively late in the planet's history, however.

#### References:

- (1) Carr, M. H., 1981, *The Surface of Mars*: Yale University Press, New Haven and London, 232 p.
- (2) Frey, H., Lowry, B. L., and Chase, S. A., 1979, Pseudocraters on Mars: *Journ. Geophys. Res.* Vol. 84, p. 8075-8086.
- (3) Frey, H., and Jarosewich, M., 1982, *Journ. Geophys. Res.*, Vol. 87, No. B 12, p. 9867-9879.
- (4) Wise, D. U., Golombek, M. P., and McGill, G. E., *Journ. Geophys. Res.*, Vol. 84, p. 7934-7939.
- (5) Soderblom, L. A., Kriedler, T. J., and Masursky, H., 1973, *Journ. Geophys. Res.*, Vol. 78, p. 4117-4122.
- (6) Grizzaffi, P. and Schultz, P. H., 1987, *Icarus*, In press, 58 p.
- (7) Jons, H.-P., 1985, *Lunar and Planet. Sci. - 16*, Lunar and Planet. Inst., Houston, p. 414-415.
- (8) McGill, G. E., 1985, *Lunar and Planet. Sci. - 16*, Lunar and Planet. Inst., Houston, p. 534-535.
- (9) Lucchitta, B. K., Ferguson, H. M., and Summers, C., 1986, *Journ. Geophys. Res.*, Vol. 91, p. E166-E174.
- (10) Parker, T. J., Schneeberger, D. M., Pieri, D. C., and Saunders, R. S., 1986, in *Symposium on Mars: Evolution of its Climate and Atmosphere*, L.P.I. Tech. Rept. 87-01, Lunar and Planetary Institute, p. 96-98.
- (11) Parker, T. J., Schneeberger, D. M., Pieri, D. C., and Saunders, R. S., 1987, *Rept. Planet. Geol. Prog. - 1986*, NASA Tech. Memo. 89810, p. 502-504.
- (12) Parker, T. J., Schneeberger, D. M., Pieri, D. C., and Saunders, R. S., 1987, *Rept. Planet. Geol. Prog. - 1986*, NASA Tech. Memo. 89810, p. 319-320.
- (13) Parker, T. J., Schneeberger, D. M., Pieri, D. C., and Saunders, R. S., 1987, *Rept. Planet. Geol. Prog. - 1986*, NASA Tech. Memo. 89810, p. 321-323.
- (14) Plescia, J. B., and Golombek, M., 1986, *Geol. Soc. Am. Bull.*, Vol. 97, p. 1289-1299.
- (15) Lucchitta, B. K., 1981, *Icarus*, Vol. 45, p. 264-303.
- (16) Pechmann, J. C., 1980, *Icarus*, Vol. 42, p. 185-210.
- (17) Rossbacher, L. A., 1985, in *Models in Geomorphology*, Michael J. Woldenberg, ed., Allen and Unwin, Boston, p. 343-372.
- (18) Basaltic Volcanism Study Project, 1981, *Basaltic Volcanism On The Terrestrial Planets*: Pergamon Press, Inc., New York, 1286 p.
- (19) Zimbelman, J. R., 1987, *Icarus*, Vol. 71, p. 257-267.

STRIPED PLAINS OF ACIDALIA PLANITA, MARS. R. A. De Hon, Department of Geosciences, Northeast Louisiana University, Monroe La, 71209.

Introduction. Striped plains are one component of the distinctively patterned plains in the martian northern lowlands (1). The major topographic expression of the striped plains is an array of closely spaced, curvilinear ridges. The patterned surface has been interpreted as a remnant terrain left after degradation or removal of a previous surficial layer (2,3). The ridges are thought to be analogous to recessional moraines (4). An apparent transition from unmodified smooth plateau to striped plains is present in Acidalia Planitia west of Deuteronilus Mensae (2). The setting and distribution of these terrains are reviewed in order to access the origin and significance of the striped plains.

Acidalia Planitia. Patterned plains occur throughout the northern hemisphere. Most are located between 30°-50°N, but some are found as far south as 15°N within Isidis Planitia. Generally, striped plains are found between the highlands boundary and polygonally fractured terrain. The striped plains in Acidalia are located near the mouth of the extensive Marners Vallis channel system (45°N; 350°W). The western-most channel of the system runs north-northwest across the cratered terrain of the central highlands to the less cratered terrain of the northern plains (Fig. 1). The channel becomes shallower and gradually fades indistinctly into the plains materials. This smooth surface at the mouth of the channel stands as a low plateau surrounded by even lower-lying patterned plains. The lightly cratered plateau unit is characterized by a smooth to undulating surface with a few isolated hillocks. The edge of the plateau at the top of the scarp is higher than the interior plateau surface. The slope down to the lower patterned plains is undissected and appears to be blanketed with the same materials that comprise the patterned plains. The patterned plains unit is characterized by an undulating surface dimpled with small, closely spaced hillocks and low, parallel, arcuate ridges. The hillocks are several hundred meters across and less than 100 m high. The surface ranges from a disordered array of hillocks to linear trends that resemble the ridges. The ridges are several hundreds of meters across and up to 50 km long. They are spaced one to a few kilometers apart. Both hillocks and ridges are lighter in tone than the surrounding areas, imparting a mottled appearance to the surface. Crater density is about the same on both plateau and patterned plains surfaces, and all craters are rampart craters.

Discussion. Smooth plateau materials were deposited by the outflow from the Marners Vallis channel system. These materials, derived from the cratered highlands, were spread out across the topographically lower surface of the northern plains and presumably contained a high percentage of water or ice at the time of deposition. Rampart craters on the smooth plateau and patterned plains surfaces attest to an ice-rich surficial layer (5). Further from the highland boundary, where the sedimentary column is thicker, desiccation of the once ice-rich sediments formed polygonal fractured plains (6). In areas of thinner sedimentary deposits, dessication led to scarp retreat. Dessication of smooth plateau materials proceeded by ablation from the upper surface, movement of ground water toward the scarp face, and ablation along the scarp. As materials lost both volume and cohesion along the scarp face, they formed a continuous blanket of ablation moraine in front of the retreating scarp. The original depositional unit, smooth plateau materials, degraded by backwasting along the scarp to produce patterned plains as a thick surface mantle of rubble. Ridges parallel to the plateau escarpment seem to indicate an episodic scarp retreat.

Linear and arcuate ridges in the patterned plains have been compared to recessional moraine (1,4). For marginal or recessional moraines to form, the sediment-ice mixture

would have to sustain glacial flow. Surface features indicating glacial flow of smooth plateau materials are absent; hence, the plateau sediment-ice mixture is more like a stagnant ice-sheet. Dead-ice or stagnation moraines are characterized by closely spaced Kame and Kettle topography, and end moraines are faint or entirely lacking (7). Thus, the ridges are not end moraines in the strictest sense. The ridges may be linear ice wedges (pingos) formed during periods when the scarp was not retreating. If episodic retreat of the scarp was seasonal (summer retreat and winter stand still), the rate of retreat was 1-2 Km/yr and bask wasting is measured in hundreds of years. If the retreat is tied to a longer cycle of climate fluctuation, such as the orbital eccentricity, the rate drops to 1-2 Km/10<sup>6</sup> yr and degradation of the ice-rich plateau is measured in millions of years.

#### References.

- (1) Carr M. H. (1984) NASA SP-469, 229-231.
- (2) Guest J. E. et al. (1977) J. Geophys. Res. 82, 4111-4120.
- (3) Arvidson R. E. et al. (1976) Icarus 27, 503-516.
- (4) Carr M. H. and G. G. Schaber (1977) J. Geophys. Res. 82, 4039-4054.
- (5) Gault D. E. and R. Greely (1978) Icarus 34, 486-495.
- (6) McGill G. E. (1985) Lunar Planet. Sci. Conf. 16, 534-535.
- (7) Thornbury W. D. (1969) Principles of Geomorphology, 594p.

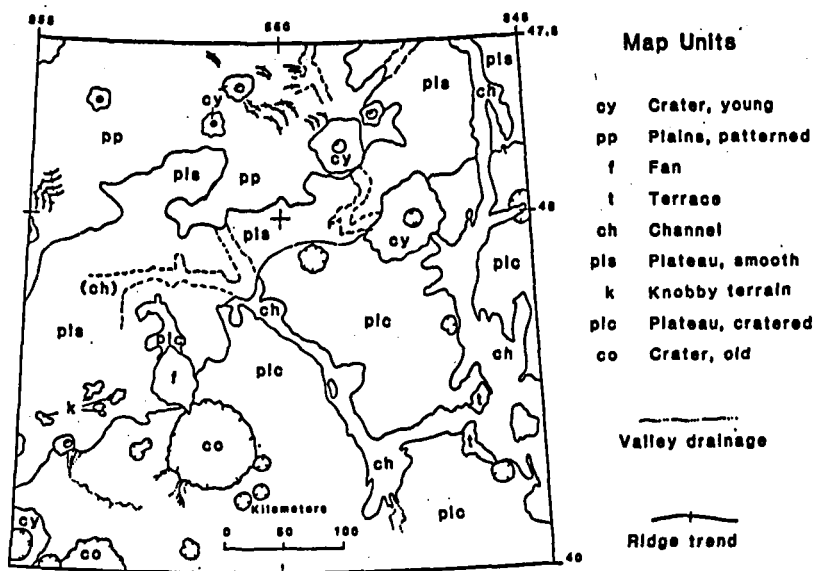


Fig. 1 Physographic sketch map of the north central portion of MC-55W showing distribution of terrains west of Deuteronilus Mensae. The contact between cratered plateau (plc) and smooth plateau (pls) corresponds to the planet-wide boundary between cratered highland and northern plains. Dashed lines mark buried channels.

## INTERCRATER PLAINS DEPOSITS AND THE ORIGIN OF MARTIAN VALLEYS

G. R. Brakenridge, Department of Geography, Dartmouth College, Hanover NH 03755

Detailed geological mapping of portions of the Thaumasia Fossae and Aeolis Quadrangles has documented several interesting relationships between valley development and local geology. At a location 150 km south of Warrego Vallis in Thaumasia, V-shaped branching valleys or sub-parallel slope ravines (figure 1) partially dissect an isolated remnant of intercrater plains deposits (figure 2). Cross-cutting relations and superposition indicate that the valleys developed after: a) plains deposition, b) N-S graben, and c) post-graben, NE oriented faults, one of which exhibits left-lateral displacements of ca. 2.5 km. Although most graben displace the plains material, several do not; this suggests that the (Tharsis-related) graben began forming while plains deposition was still underway. After both styles of faulting, dark flow volcanism covered low-lying areas and partially filled many graben. These extensive, dark, lava-covered plains stretch northward to, and partially cover, the Warrego Vallis tributary channels. Finally, younger, unmodified craters are superimposed on the entire landscape.

When did the valleys form? The stratigraphic relations constrain them as post-graben (many debouch into graben, but they are not cut by graben), and pre-final cratering (some valleys are truncated by ~3 km diameter craters). They might have developed prior to the dark flow volcanics, which are not themselves modified by fluvial activity. However, they could, as well, be coeval to the volcanism. As noted, nearby Warrego Vallis is partially blanketed by similar volcanic rock, indicating that valley development there was terminated by final extrusion of the flow volcanics. Volcanism, or high heat flow from plutonism prior to volcanism, may have first provoked valley development at Warrego, and then culminated in partial valley burial by lavas. Of relevance in this respect is the suggestion of reference 1 that small Martian valleys require ice-rich plains materials as substrata for their development. This emphasizes that the valleys shown in figure 2 could in fact be coeval to the local extrusive volcanism, with their absence on the latter bedrock being due to its lithology rather than to the cessation of a "valley forming" climatic interval.

On the steeper slopes of the plains remnant (and near the resolution limit of the image), light-dark internal stratification is visible. A relatively dark-albedo stratum crops out near the flat surface of the plains, and is both overlain and underlain by higher-albedo strata. The dark unit may be a sill (figure 2) and may represent lava extruded at the same time as the surface flows to the north of the remnant. Supporting this inference is the presence of small (<1 km diameter) dark hills on the remnant surface, which may be cinder cones, and E-trending dark lineaments cropping out on its slopes and to the south, which may be dikes. Nearly all of the valleys visible in this image appear to have heads at the base of the dark stratum. These observations suggest that the dark unit acted as an aquiclude for heated waters which exited as springs along its base: valley development occurred by hot spring activity associated with sill emplacement into ice-rich material (see also reference 2). In contrast, an ancient ground water system due to a past warmer climate is not required,



and suffers from several difficulties, including the need to either percolate water down through the dark unit from the surface or force it up into the remnant from below.

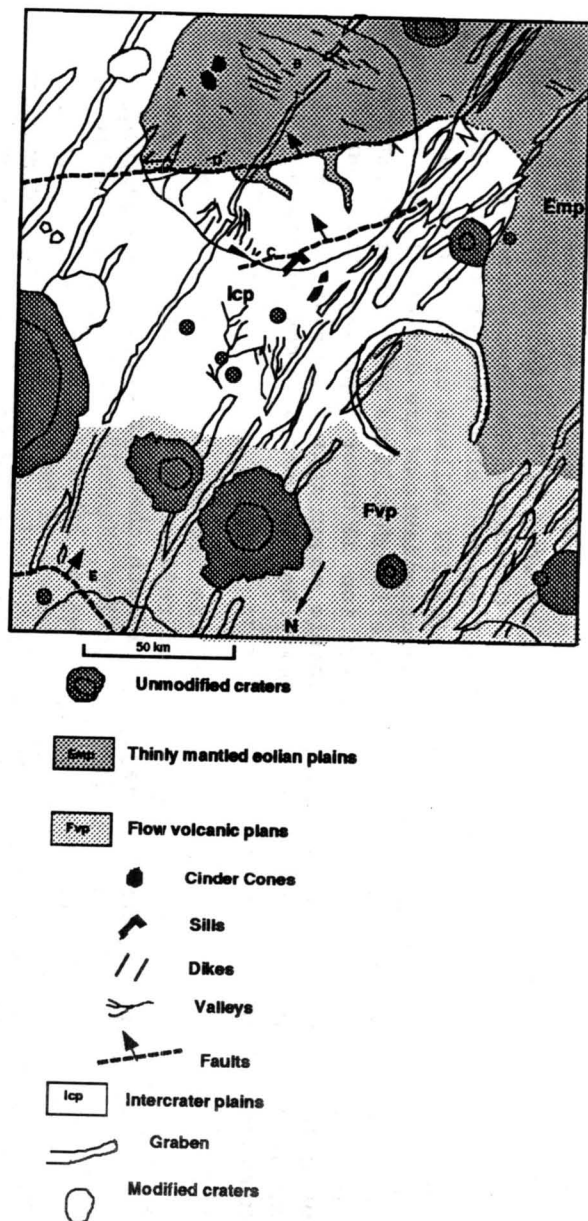
Earlier work in Aeolis suggested that some valleys there are the result of impact melting of icy materials (3). Quadrangle-wide measurements on valley orientations and additional local mapping also indicate: a) strong preferred orientations for the valleys (of 299 valleys or valley segments measured, none were aligned NE, and NW orientations are dominant), b) an association, also described by reference 1, of valleys with intercrater plains deposits, c) internal stratification of these deposits (first noted by Malin, reference 4), and d) a probable major role for mafic plains volcanism near the end of the Late Heavy Bombardment in providing the release mechanism for valley development.

If the upland intercrater plains (the "rough plateau" unit of reference 5, p.67, and the "degraded deposits" of reference 1) do contain ground ice, then the origin of the vast majority of both channels and valleys on Mars (classes 1-3 on figure 1, plus many outflow channels) seems clear: they must have formed by surface flowage of water liberated from frozen groundwater reservoirs by various mechanisms of heating, and especially magmatism and plutonism. A major concern, however, has been how water was added to surficial regions of the Mars crust. In this respect, the inferences of Jakosky and Carr (6) are critical. These workers infer that the calculated pre-Tharsis enhanced obliquity of Mars would have caused ice condensation at low latitudes, where it is now unstable when in contact with the atmosphere. This results in a mechanism for the deposition of ice, perhaps mixed with loess, in the cratered highlands early in Mars history.

The geological principles of uniformitarianism and actualism require that we pay more attention to using the Mars present as a key to its past, rather than searching for terrestrial analogs. Ice-rich, stratified deposits are forming today in the polar regions of Mars. If enhanced obliquity did occur, then a large part of the original Mars endowment of water was probably deposited quite early as ice. It then would have been intermittently released by impact cratering and extensive volcanism as the Heavy Bombardment came to an end. The solar-heating mechanism also outlined by Jakosky and Carr may be less important, but such surface melting could be responsible for the "coarse, disordered texture", including numerous small channels, of the rough plateaus at high resolution (5, p. 67-68), as well as their low crater densities.

1. Wilhelms, D.E. and Baldwin, R.J., 1986: Abstracts, 17th Lunar and Planetary Science Conference, p. 948-949.
2. Squyres, S.W., Wilhelms, D.E., and Mossman, A.C., 1987: Icarus, v. 70, p. 385-408
3. Brakenridge, G. R., Newsom, H.E., and Baker, V.R., 1985: Geology, v. 13, p.859-862
4. Malin, M.C., 1976: Ph.D. dissertation, California Institute of Technology.
5. Carr, M., "The Surface of Mars", Yale University Press, New Haven, 232 p.
6. Jakosky, B.M., and Carr, M.H., 1985: Nature, v. 315, p. 559-561.

Viking 532A15



SURFACE UNITS ON MARS: THE ASSEMBLAGE IN THE VALLES MARINERIS  
B. K. Lucchitta, U.S. Geological Survey, Flagstaff, Ariz. 86001

The Valles Marineris system of troughs offers a unique opportunity to investigate Martian surface units in the third dimension. The troughs are more than 7 km deep in places and thus expose a significant portion of the Martian upper crust.

The geologic units within the Valles Marineris can be subdivided into three broad categories: wall rock, interior deposits, and surficial cover. The wall rock is exposed in the steep scarps bordering the troughs, in spurs projecting into the troughs, and in isolated erosional remnants. Wall rock is also found in the material reworked into landslide deposits. Interior deposits form eroded mesas that locally lap up against or overlap eroded wall rock; they may also underlie parts of the Valles Marineris floor. Surficial cover forms blankets of variable thickness covering the other units.

#### Wall Rock

The wall rock has a layered cap but its lower slopes are massive. The layers are clearly visible on the steep cliffs of the upper walls and are expressed by different albedos or different erosional resistances. Four layers are commonly visible, but as many as eight can be recognized in places. Many of the layers are extensive and some can be traced for hundreds of kilometers. The layers are probably composed of volcanic materials, most likely flood basalts (1), but the possibility that the upper 2 km of the wall is composed of other materials cemented by ice cannot be totally excluded.

In the generally massive lower walls, layers are visible in only a few places, for instance, an extensive bluish layer is seen in the south wall of Coprates Chasma. The lower walls appear to be unstable; they have eroded to form deep gullies, they have generated debris flows, and many have collapsed into gigantic landslides. Thus, the material underlying the walls is apparently poorly consolidated. It is most likely composed of lunar highland-type breccia (2), probably charged with ice and water at some depth behind the surficially desiccated walls (3). The wall material is probably similar to highland material elsewhere on Mars, which appears to be the primary reservoir for ground ice. Because of its ice content, this material gives rise to rock-glacial flow and terrain-softening features in mid-latitudes (4, 5) and to landslides in low latitudes (3).

#### Interior Deposits

The interior deposits reflect two episodes of deposition: an older one responsible for the layered sequence now standing as high eroded mesas that approach the elevation of the plateau surface, and a younger episode in which material was deposited on a deeply eroded surface whose elevation is close to that of the present trough floors. The older layered sequence consists of alternating dark and light layers; the dark layers are generally thin and resistant to wind erosion and the light layers are more massive and highly susceptible to such erosion. Volumetric constraints and observations associated with the younger sequence (see below) suggest that the older beds are largely of volcanic origin (6), even though their

possible deposition within a lake as wind-drifted or fluvial materials (7, 8) may have contributed in a minor way to their buildup.

The younger interior deposits consist of (a) very dark, relatively blue patches with short stubby flows in places, occurring characteristically along faults; (b) light-colored, thick, smooth deposits that are locally associated with apparent volcanic craters; and (c) deposits with lobate fronts, local layering, rough surface textures, and highly irregular albedos. The base of these younger deposits is an unconformity; they embay interior mesas, landslides, and tributary canyons. They are generally thin, but in western Candor Chasma they may reach thicknesses of 3,000 m. These materials are probably volcanic, and the very dark patches may be mafic. Because albedo contrast between the dark and light units is not large, the light units could be palagonitic tuffs (9), a composition that also agrees with the reddish spectral signature of these units.

Some of the younger interior deposits have surface characteristics, such as high-albedo, rolling, smooth surfaces and wind-eroded flutes, that are similar to those of the vast deposits of light materials in southern Amazonis Planitia. If the deposits in the Valles Marineris are indeed of volcanic origin, the similarity would strengthen the hypothesis that those in Amazonis Planitia are also volcanic (10, 11).

#### Surficial Cover

All units in the Valles Marineris are probably covered to some extent by fine dust or wind-drifted sand. Smooth, light-colored materials on trough floors and mesa tops may be composed of thick blankets of light-colored atmospheric dust fallout, but this material cannot be distinguished visually from the underlying rock. Light materials on mesa tops have very low thermal inertia (J. Zimbelman, written commun., 1987), suggesting that the mesa tops are covered by this dust; the reddish spectral signatures of this material suggest a composition of iron-rich clays or palagonitic tuffs.

Dark surficial materials are relatively blue, suggesting mafic compositions. Streaks, dune forms, and entrapment in low areas or crevices suggest that the materials moved by saltation or ground-hugging flow and therefore are probably composed of sand-sized grains. Small patches or thinly covered areas have no characteristic thermal-inertia signature, but more extensive patches (most of which show dune forms) have very high thermal inertia, suggesting abundant grains larger than 1 mm in size. The dark material inside the Valles Marineris troughs appears to be derived from local young volcanic vents (12) or older exposed dikes or sills.

The light-colored, fine material on mesa tops is probably similar in composition and grain size to materials found in many areas on the Martian surface; all these materials most likely originated from atmospheric fallout of very fine material distributed by dust storms. The dark material in the troughs also has characteristics similar to dark materials elsewhere on Mars that occur as streaks or dunes or are trapped inside craters. Observations of the dark materials in the Valles Marineris suggest that some of the dark materials elsewhere may similarly be derived from young volcanic vents or older exposed sills or dikes. This

contention is supported by the apparent preferential occurrence in the western hemisphere of dark material near fractured and faulted terrains that may have facilitated volcanism. (These relations are seen on a color mosaic prepared by A. S. McEwen, U.S. Geological Survey.)

Overall, the exposure of units in the Valles Marineris gives insights into surface units elsewhere on Mars. The observations tend to support hypotheses that the highland material is charged with ice, that some light-colored, rolling, smooth deposits are of volcanic origin, and that dark dunes and streaks are composed of wind-blown mafic materials.

## References

- (1) Scott D.H. and Carr M.H. (1978) Geologic map of Mars: U.S. Geological Survey Miscellaneous Investigations Series Map I-1083, scale 1:25,000,000.
- (2) Carr M.H. (1979) Formation of martian flood features by release of water from confined aquifers: *Journal of Geophysical Research*, v. 84, no. B6, p. 2995-3007.
- (3) Lucchitta B.K. (in press) Valles Marineris, Mars: Wet debris flows and ground ice: *Icarus*.
- (4) Lucchitta B.K. (1984) Ice and debris in the fretted terrain, Mars: Lunar and Planetary Science Conference, 14th, Proceedings, Part 2: *Journal of Geophysical Research*, v. 89, Supplement, p. B409-B418.
- (5) Squyres S.W. and Carr M.H. (1986) Geomorphic evidence for the distribution of ground ice on Mars: *Science*, v. 231, p. 249-252.
- (6) Peterson Christine (1981) A secondary origin for the central plateau of Hebes Chasma: Lunar and Planetary Science Conference, 12th, Proceedings, *Geochimica et Cosmochimica Acta*, p. 1459-1471.
- (7) Lucchitta B.K. (1982) Lakes or playas in Valles Marineris (abs.), in *Reports of Planetary Geology Program--1982: National Aeronautics and Space Administration Technical Memorandum 85127*, p. 233-234.
- (8) Nedell S.S., Squyres S.W., and Andersen D.W. (1987) Origin and evolution of the layered deposits in the Valles Marineris, Mars: *Icarus*, v. 70, p. 409-441.
- (9) Singer R.B. (1982) Spectral evidence for the mineralogy of high-albedo soils and dust on Mars: *Journal of Geophysical Research*, v. 87, no. B12, p. 10159-10168.
- (10) Ward A.W. (1979) Yardangs on Mars: Evidence of recent wind erosion: *Journal of Geophysical Research*, v. 84, no. B14, p. 8147-8166.
- (11) Scott D.H. and Tanaka K.L. (1982) Ignimbrites of Amazonis Planitia region of Mars: *Journal of Geophysical Research*, v. 87, no. B2, p. 1179-1190.
- (12) Lucchitta B.K. (1987) Recent mafic volcanism on Mars: *Science*, v. 235, p. 565-567.

STABILITY OF CHASMA WALLS IN THE VALLES MARINERIS, MARS -- H.J. Moore and G.D. Clow, USGS Survey, Menlo Park, CA, 94025; P.A. Davis, USGS, Flagstaff, AZ, 86001; L.R. Strichartz, Rice Univ., Houston, TX, 77252.

The slopes of the chasma walls in Valles Marineris are not as steep as would be predicted from analyses of slope stability (Baker and Garber, 1978; Clow and Carr, 1980) for homogeneous common geologic materials (Hoek and Bray, 1977). The chasma wall with the greatest relief and steepest slope that we have found to date is in Noctis Labyrinthus. Relief of this wall is about 6 km and the mean slope is near 46 degrees; slopes are locally as steep as about 48 degrees. Stability analyses for this wall, if we assume a homogeneous dry material and logarithmic spiral failure surfaces, constrain the choices of possible geologic materials beneath the slope (fig. 1). Materials similar to tills, clays, sands, and broken rocks must be excluded, but other rocks like those on Earth are possible; those have paired values of cohesions and angles of internal friction above and to the right of the line for stable-unstable conditions in figure 1; some impact and volcanic breccias may have properties near the dashed portion of the line. The mean slopes of the probable logarithmic spiral failure surfaces for the chasma wall in Noctis Labyrinthus are much steeper than those of the chasmata walls where landslides have occurred, even if the angle of internal friction is assumed to be as low as 20 degrees. Positive pore pressures do not alleviate the problem, because they steepen the failure surface.

In the Tithonium-Ius Chasmata region, several wall failures with small displacements are found (Lucchitta, 1979); the mean slopes of their failure surfaces, inferred from topographic data (U.S. Geological Survey, 1980), are between 25° and 35°. Logarithmic spiral failure surfaces for reasonable

values of cohesions and angles of internal friction do not conform with most of these inferred failure surfaces nor are they compatible with slopes elsewhere in the chasmata.

One of these small displacements in Ius Chasma occurs where the slope of the wall is  $25^{\circ}$ . The inferred failure plane for marginal stability can be approximately fit if the cohesion is 400 kPa and the angle of internal friction is  $20^{\circ}$  (see fig. 1). Both the low cohesion and small angle of internal friction suggest that, where landsliding is common, materials in the chasma walls may have been locally altered by some weathering or hydrothermal process related to magmatism (Lucchitta, 1987). Other factors that may have contributed to the weakening of the walls include pre-existing planes of weakness combined with pore water pressures and small cohesions.

#### References

- Baker, R. and Garber, M., 1978, Theoretical analysis of the stability of slopes: *Geotechnique*, v. 28, no. 4, p. 395-411.
- Clow, G. D. and Carr, M. H., 1980, Stability of sulfur slopes on Io: *Icarus*, v. 44, p. 268-279.
- Hoek, E. and Bray, J., 1977, *Rock Slope Engineering*, 2nd Ed., Inst. of Mining and Metall., London, 402 p.
- Lucchitta, B. K., 1979, Landslides in Valles Marineris, Mars: *Jour. Geophys. Res.*, v. 84, no. B14, p. 8097-8113.
- Lucchitta, B. K., 1987, Recent mafic volcanism on Mars: *Science*, v. 235, p. 565-567.
- U.S. Geological Survey 1980, Topographic orthophoto mosaic of the Tithonium Chasma region of Mars: U.S. Geol. Survey Map I-1294, 1:500,000 scale.

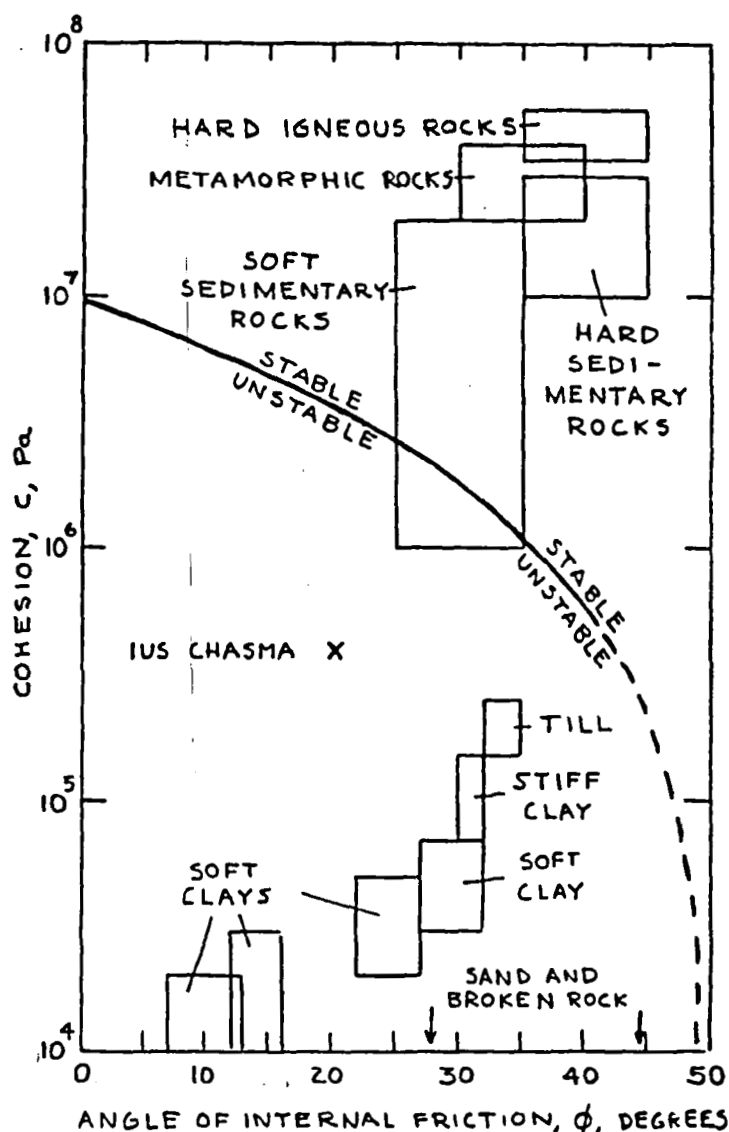


Figure 1. Conditions for stability of a slope in Noctis Labyrinthus, assuming a dry homogeneous material and logarithmic spiral failure surfaces without base failure. Slope is stable for cohesions and angles of internal friction above and to the right of stable-unstable line; below and to the left of the line, the slope is unstable and would fail. Rectangles represent ranges of cohesions and angles of internal friction of the indicated common terrestrial geologic materials. Dashed part of curve is extrapolated and constrained by the maximum local slope ( $48^\circ$ ). X indicates the approximate failure conditions for wall failure with small displacement in Ius Chasma.



A COMPARATIVE PLANETOLOGY STUDY OF LARGE MARTIAN AND TERRESTRIAL LANDSLIDES  
P.J. Shaller and B.C. Murray, California Institute of Technology, Pasadena, CA

Large ( $>10^7 \text{ m}^3$ ) martian and terrestrial landslide deposits share many common characteristics. The study of large terrestrial subaerial deposits has concentrated on the depositional or "long-runout" aspect since the fragmented debris of large slope failures travel great distances from the regions of collapse. Despite several elegant approaches to the subject, a testable mechanical model for long-runout has not been widely accepted. Though of huge scale, the initial slope failures which generated these deposits have been well described. In contrast, neither the mechanics of slope failure nor the subsequent low-friction transport of debris are well understood for martian landslides or terrestrial subaqueous slides. The goal of this research is to illuminate the mechanics of slope failure and long-runout in these deposits by a qualitative and quantitative comparison of common characteristics in light of the dissimilarities in depositional environments. Ultimate goals of this research also include an understanding of the role of water in the martian near-surface environment, and the cause of mega-sliding on Mars and in Earth's oceans, where single slides may involve up to a thousand times the volume of the largest terrestrial subaerial slide. The largest of these, at Saimmarreh, Iran, contains only 1/440 the volume of the largest martian slide and only 1/1000 the volume of the largest undersea landslide on Earth (Harrison and Falcon, 1938; Lucchitta, 1979; Dingle, 1977; see also Table 1).

The study of large-scale landsliding is subdivided into three major categories: headscarp phenomena and the causes of slope failure; deposit morphology and internal depositional structures; and quantitative relationships between deposit physical characteristics. The investigation of these features is being conducted via the study of terrestrial remote sensing data (Landsat TM, SPOT, Seasat and Shuttle LFC, as well as GLORIA and other subsea sonar data), Viking Orbiter images and terrestrial field work.

Headscarp morphologies seem to vary with landslide volume and with the orientations of structures in the slope. Generally, landslides of large volume and those associated with horizontal bedding take on a slump form characteristic of both martian slides and terrestrial undersea slides. Large terrestrial subaerial slides are usually associated with planes of weakness such as bedding- or foliation-planes. Martian headscarps are being studied as a class from stereo Viking Orbiter images to determine other possible characteristic headscarp phenomena, such as regional preferred planes of failure or landsliding related to preferred lithologies or erosional regimes (spur-and-gulley terrain, etc.).

A qualitative comparison of specific martian and terrestrial landslide deposits has been made in the literature; similarities in form between a large landslide in the Gangis Chasma of Mars and the Sherman landslide of Alaska were used to argue for a similar emplacement mechanism (Lucchitta, 1978). A difference of nearly four orders of magnitude (Table 1) in volume, however, strains such conclusions (Shreve, personal communication, 1987). The martian and terrestrial deposits are thus being mapped and studied from the remote sensing data to determine their morphological characteristics as a group. Arguments for a common emplacement mechanism can be supported only when deposits of similar volume on the two planets

are found to display similar characteristics. Emphasis in this area is placed on the study of large, recent terrestrial landslides in the cold, arid environments which most closely approach martian surface conditions. Two such deposits occur in the Pamir mountains of Tadzhikistan, U.S.S.R.; one of these was emplaced during an earthquake in 1911, forming the largest historical landslide (Harrison and Falcon, 1938; see also Table 1). A third lies near the crest of the Argentine Andes (Bloom, personal communication, 1987), and is currently being mapped from Landsat TM images and stereo Shuttle LFC photos.

The interpretation of the remotely-sensed images of the martian and terrestrial landslides is being assisted by field studies of two large landslides in Southern California, the Blackhawk and Martinez Mountain slides (see table 1). In the field research, morphological features mappable at the 30 meter resolution of the Landsat TM images are compared with details visible from aerial photos and with the actual features in the field. Morphological features considered by earlier workers as mechanically significant are of particular interest (Shreve, 1968; Bock, 1977). Field investigation of deposit internal structures and their relationships to overall deposit morphology are also a priority, as an important facet to an understanding of the mechanics of emplacement. Tertiary landslide or "megabreccia" deposits in the southwest are a further source of information on the internal structures of large landslide deposits.

A final component of research is the compilation of a quantitative database of physical parameters of large landslides. These parameters will be used to define any characteristic relationships between such deposit parameters as runout area or maximum length, and volume, elevation loss, degree of confinement of debris, lithology, etc.. An example is given in Figure 1, where a crudely linear relationship is displayed by plotting the logarithm of the volume versus the effective coefficient of friction (height of fall/maximum runout length) of a number of martian and terrestrial deposits. Additional data for martian and terrestrial deposits will be obtained from the study of stereographic remotely-sensed images.

#### References:

- Bock, C.G., 1977. Martinez Mountain rock avalanche: G.S.A. Rev. in Eng. Geol., v. 3, pp. 155-168.
- Dingle, R.V., 1977. The anatomy of a large submarine slump on a sheared continental margin: J. Geol. Soc. Lond., v. 134, pp. 293-310.
- Harrison, J.V. and Falcon, N.L., 1938. An ancient landslip at Saidmarreh in southwestern Iran: J. Geol., v. 46, pp. 296-307.
- Lucchitta, B.K., 1978. A large landslide on Mars: G.S.A. Bull., v. 89, pp. 1601-1609.
- Lucchitta, B.K., 1979. Landslides in Valles Marineris, Mars: J.G.R., v. 84, B 14, pp. 8097-8113.
- Shreve, R.L., 1968. The Blackhawk landslide: G.S.A. Spec. Pap. 108, 47pp.

- ★ = **Unconfined** landslide
- = Landslide **partially** confined by canyon walls, obstacles, etc.
- = Landslide **heavily** confined by opposite canyon wall
- = **Partially** confined landslide that slid across **ice/snow**
- = Confinement unknown

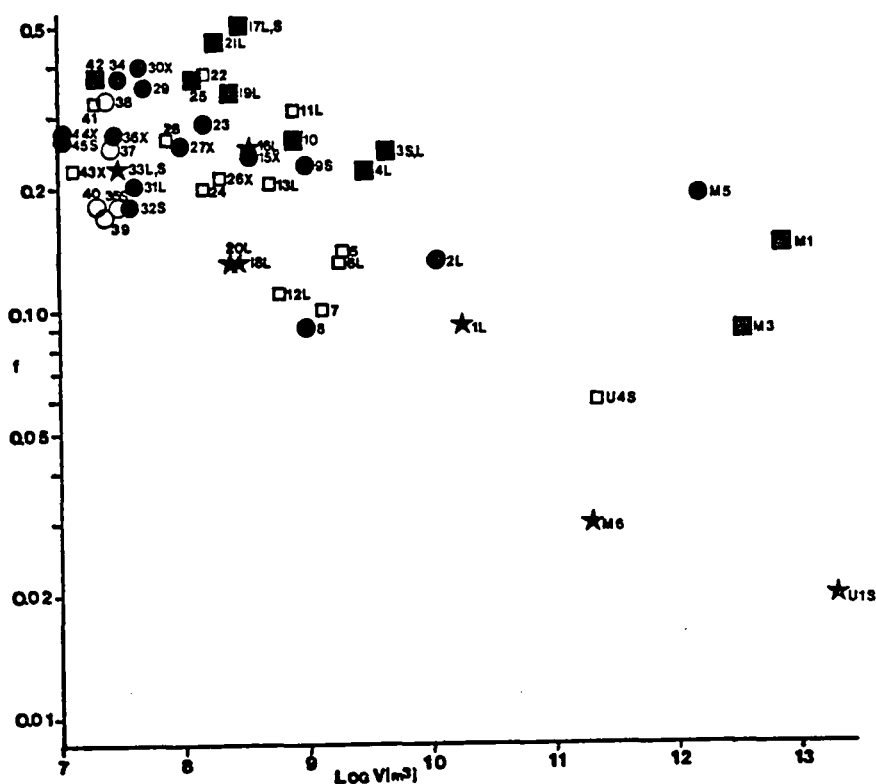


**Table 1. Volume/Friction Data For Martian And Terrestrial Landslides**

Rank	Name/Location	Volume*	Friction						
M1	W. Ius Chasma	8,800,000	0.14	7	Tamins	10.10	32*	Gros Ventre	0.18
M2	E. Ius Chasma	5,800,000	—	8	Fernpass	10.09	33*	Frank	0.22
M3	Ius Chasma	3,500,000	0.09	9*	Mayunmarca	10.24	34	Voralpsee	0.37
M4	W. Tithonium Chasma	2,000,000	—	10	Gl. Gruppen	10.26	35*	Sherman	0.18
M5	Tithonium Chasma	1,400,000	0.19	11	Gl. Gleiter	10.31	36*	Madison	0.27
M6	Gangis Chasma	200,000	0.03	12	Deyen	10.11	37*	Schwan	0.25
U1	Agulhas, SE Africa	20,331,000	0.02	13*	Mt. Granier	10.21	38*	Fairweather	0.33
U2	Bassein, N. Indian	900,000	—	14*	Khait	—	39*	Allen	0.17
U3	Grand Banks	760,000	—	15	Martinez Mtn.	10.24	40*	Steller	0.18
U4	Rockall, N. Atlantic	300,000	0.06	16	Sawtooth	10.25	41*	Cor. de Dosde	0.32
U5	Sagami Wan, W. Pac.	70,000	—	17*	Gohna	10.50	42*	Disentis	0.37
U6	Ranger	20,000	—	18	Blackhawk	10.13	43*	Huascaran 3	0.22
1	Saidmarreh, Iran	20,000	0.09	19*	Valont	10.34	44*	Tahoma Pk.	0.27
2	Flims, Switz.	12,000	0.13	20	Silver Reef	10.13	45*	Elm	0.26
3*	Pamir, U.S.S.R.	4,800	0.24	21	Bormio	10.45			
4	Engelberg, Switz.	3,000	0.22	22	Poschiavo	10.38			
5	Siders, Switz.	2,000	0.14	23	Parpan	10.28			
6	Tin Mtn., CA	1,800	0.13	24	Kandertal	10.20			
				25	Obersee	10.37			
				26	Huascaran 1	10.21			
				27*	Huascaran 2	10.22			
				28	Sci. di Saoseo	10.26			
				29	Diablerets	10.35			
				30*	Hope	10.40			
				31*	Goldau	10.20			

\* = Volume x 10<sup>6</sup> m<sup>3</sup>  
 \* = Historic landslides  
 Bold = Slides for which f is undetermined  
 M = Martian landslides  
 U = Undersea landslides

## **Rock Populations as Indicators of Geologic Processes**

Michael C. Malin, Department of Geology, Arizona State University, Tempe, AZ 85287-1404

Sediments cover most of the surface of the Earth, and are likely to cover most of Mars. Remote sensing observations indicate that only a small fraction of the martian surface is covered by rock-like material (Christensen, 1986a,b), and even casual inspection of terrestrial scenes shows this is also true on Earth.

Most of the focus of studies of both terrestrial and extraterrestrial sediments have concentrated on the easily transported, finer-grained debris. Little effort has been expended in analysis of the coarser debris, generally and collectively termed gravel, but including all materials greater than 2 mm in diameter. On Earth, gravels are chiefly studied as the precursor material incorporated into conglomerates, breccias and other coarse grained, sedimentary rocks. Little work has been done on terrestrial gravel-bearing sedimentary rocks because such rocks are not of economic value (e.g., they are not good oil reservoirs). Studies of gravels not yet forming rocks are even more constrained, being limited primarily to relatively specific or narrow problems of economic (e.g., formation of placers, local derivation of building materials, etc.) or scientific interest (e.g., outwash gravels from Pleistocene continental glaciation in North America). Pettijohn's (1975) comprehensive treatment of gravels, conglomerates, and breccias is characteristically devoted to the rocks and not the sediments.

Terrestrial examples of the applications of analyses of coarse grained sediment include recent work on the processes of selective entrainment (e.g., Komar, 1986a,b), the use of boulder populations in attempts to quantify the hydraulic relationships of large floods (e.g., Baker, 1973; Costa, 1983), and the use of boulders to determine rheological properties of mud- and debris-flows (e.g., Fink, et. al. 1981). In each of these cases, the physical basis for the application has been explored along with the empirical observations that permit the application. Although some of the results have been questioned (e.g., concerns about estimating flood discharge, depth, and velocity solely from the size of the largest particles moved), most applications can be checked against other, independent measures. For example, flood velocities computed from boulder size can be checked against velocities calculated from plunge pool geometry. Under these circumstances, the coarse sediments provide a means of extending observations over larger areas than do the more restricted occurrences of erosional forms.

Recent interest in the surface population of rocks on Mars is based chiefly on the need to address questions of lander safety as advanced Mars surface missions are planned. The answers to questions raised about the martian rock population are necessarily crude because only two locations (Viking Lander 1 and 2 landing sites) have been viewed at resolutions sufficiently high to resolve boulders. From these observations, and following a long-established philosophy of using power laws to represent rock size/abundance relationships (e.g., Shoemaker and Morris, 1969), rough predictions have been made in support of advance mission planning (e.g., Moore, 1987).

The philosophy, based primarily on the shape of crater count curves but including an attempt at physical rationalization on the basis of fragmentation theories, implicitly assumes that the boulders reflect the same population that formed, or formed from, the craters seen on most planetary surfaces. This assumption, however, is not correct on the Earth, and is probably not correct on Mars. On both planets, initial populations, even those following power laws, are likely to experience change selectively with particle size (e.g., the phenomenon of sorting).

Thus, gaussian-like incremental populations, or log-normal cumulative populations are both to be expected, and at least on the Earth, are what are actually observed.

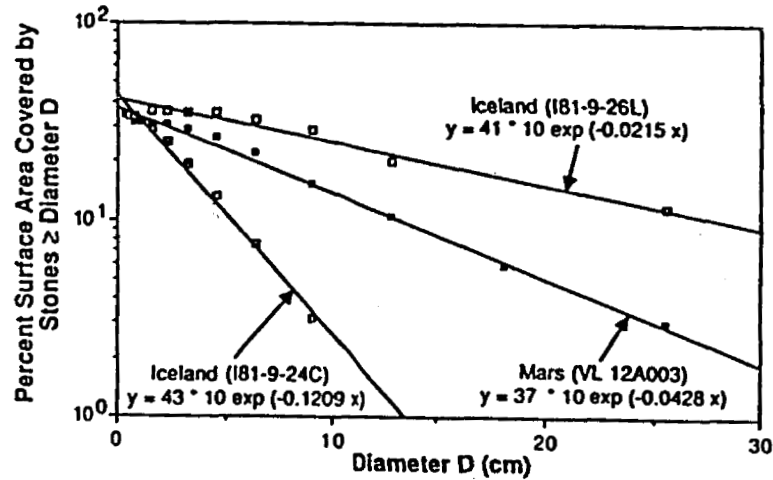
Recent work on terrestrial flood boulder and on wind-modified glacial debris populations show this effectively. The top graph in the accompanying figure shows the percent of surface coverage on stone armored surfaces in Iceland, and compares similar observations from the Viking Lander 1. Note that the total area covered is very similar on Earth and Mars, and that the relationship is clearly exponential/log-normal and not power-like. The lower two graphs in the figure portrays analyses of flood boulders in Iceland, showing size/frequency on the left and calculated areal percentage on the right. The Viking Lander 1 line, used as a predictive tool, is drawn using the reported values and a power law extrapolation (Moore, 1987), not the exponential shown in the top graph. Assuming that a future Mars mission might be targeted to the outwash plain of catastrophic flood, note that the power law underestimates the population at "small" boulder sizes (between 1 and 3 m diameter) and, depending on the location, could also underestimate the number of large boulders. Thus, a landing vehicle could be in severe jeopardy.

## References.

- Baker, V.R., Geol. Soc. Am. Special Paper 14, 79 p., 1973.  
Christensen, P.R., J. Geophys. Res., **91**, 3533-3545, 1986a.  
Christensen, P.R., Icarus, **68**, 217-238, 1986b.  
Costa, J.E., Geol. Soc. Am. Bull., **94**, 986-1004, 1983.  
Fink, J., M.C. Malin, R. Greeley, and R. D'Alli, Geophys. Res. Lett., **8**, 43-46, 1981.  
Komar, P.D., Sedimentology (in press), 1987a.  
Komar, P.D., in Flood Geomorphology, V. Baker, C. Kochel, and P. Patton (eds.), in press, 1987b.  
Moore, H.J., Preliminary Mars Surface Models, Exhibit III of Mars Rover/Sample Return Mission Mobility Study Project Request for Quotation, 1987.  
Pettijohn, F.J., Sedimentary Rocks, (3rd Ed.), (Harper & Row, New York), Chapter 6, 154-194, 1975.  
Shoemaker, E. M. and E. C. Morris, in Surveyor Program Results, NASA SP-184, pg. 82-96, 1969.

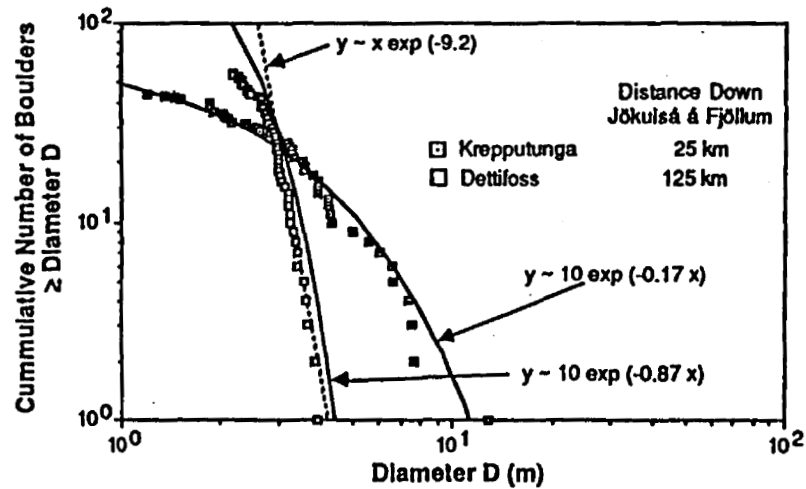
Figure 1: (Top) Comparison of terrestrial and martian stone armors— exponential relationships for percent area covered by stones  $\geq$  diameter D are seen in this graph. Conventional power law representations do not closely approximate actual relationships. Log-normal populations are suggested. Note that, for the small part of the VL-1 site used to produce this graph, about 12-14% is covered by stones 10 cm or larger, and that on both the Earth and Mars, the areal coverage approaches a limit (~30-35%). (Bottom, right) Cumulative size/frequency relationships for two boulder fields associated with a *jökulhlaup* in north central Iceland. Note the falloff with decreasing size is not a "resolution effect" but instead reflects sorting by the fluid flow. Note, too, that the curves are better approximated by exponentials than power laws (actual curves are probably log-normal, i.e., the integral of a gaussian distribution). (Bottom, left) Computed percent area covered by boulders  $\geq$  diameter D, assuming a circular boulder cross-section and integrating the exponential curves. For comparison, the published Viking Lander rock counts and the integral of the presently accepted power law relationship is also portrayed. The power law significantly underestimates the number of boulders between 1 and 3 m in diameter, and is probably unrealistic above 10 m diameter.

## COMPARISON OF TERRESTRIAL AND MARTIAN STONE ARMORS

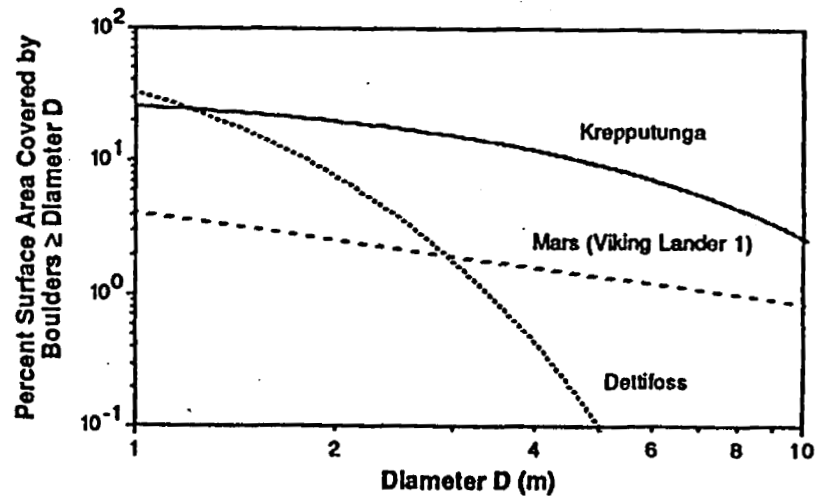


## COMPARISON OF BOULDER POPULATIONS ON EARTH AND MARS

### CUMMULATIVE SIZE/FREQUENCY RELATIONSHIPS FOR BOULDERS TRANSPORTED BY CATASTROPHIC FLOODS



### MODEL CALCULATIONS OF AREA COVERED BY LARGE BOULDERS



## **Studies of Venusian Geology and Tectonics: Status Report**

R.C. Kozak and G.G. Schaber, U.S. Geological Survey, Flagstaff, AZ 86001

Our pre-Magellan geologic and tectonic research of Venus is a four-part undertaking: 1) to produce a tectonic province map of the northern and Earth-facing hemispheres at 1:25 million scale using all data available; 2) to map selected areas of interest at larger scale; 3) to perform topical research on volcanic and tectonic processes and landforms; and 4) to evaluate the nature and age implications of impact-like features.

A map summarizing the tectonic and geologic provinces of the northern hemisphere is about 60% complete. In FY 88 the 1:25 million-scale geologic/tectonic map will be completed and made available. The main results of this effort indicate that horizontal tectonism is indeed an important factor in Venus' appearance. Divergent/convergent plate tectonism is implied by the existence of complementary tensile fracture zones and fold belts. Examples of fracture/fold pairs include Sigrun Fossae/Ausra Dorsa, and "Allat fossae" [1] /Kamari Dorsa. Some fold belts, bordering the northeastern edge of the upland tesserae terrains of Laima Tessera and Tellus Regio, appear to have no extensional zones nearby to complete the pair. However, Sukhanov and Pronin [2] believe the fan-shaped series of ridges centered around the 200° meridian are the expression of a large spreading zone. The orientation of this spreading zone relative to the direction of compression of the mentioned unpaired fold belts is such that the two are probably related. If so, the connection is a start toward solving Sukhanov and Pronin's question: where are the zones that compensate for the spreading they observe?

We will also complete the map of the Earth-facing hemisphere during FY 88. Our previous study of radar properties from PVO data [4] will provide much input to this map, as several of the map units from that study correspond closely with Venera-defined units, allowing mapping of the areas not imaged by Venera to be done in a similar context.

Several local investigations were completed or are nearing completion:

The intriguing question of the origin of Cleopatra Patera on Maxwell was discussed [5]. A preliminary map of the plate-like tectonism of central Ishtar Terra was made and has been very briefly discussed [1, 6]. Details are currently being written up for formal publication.

The geology of Bell Regio was analyzed in light of the Venera altimetry data [7]; gravity modeling over the immense Bell Regio volcanic shield complex indicates anomalously low densities at depth, suggesting that the thermal plume responsible for the shield complex may still be present. Verification of the model results is presently being carried out.

The nature of the craters on Venus has been addressed briefly [6] and will be addressed in the final 1:25M map text. Implications of impact craters to the age of the surface are essentially complete [8, 9, 10].

## References

- [1] Kozak, R.C., and Schaber, G.G., 1987b, A spreading center on Venus?: LPSC 18, 513.
- [2] Sukhanov, A.L., and Pronin, A.A., Signs of spreading on Venus: Doklady AN SSSR, in press.
- [3] Pronin, A.A., Sukhanov, A.L., Tyuflin, Yu.S., et al., 1986, A geologic and morphologic description of Lakshmi Planum: Solar Sys. Res., 20, 53.
- [4] Davis, P.A., Kozak, R.C., and Schaber, G.G., 1986, Global radar units derived from statistical analysis of Pioneer Venus orbiter radar data: JGR, 91, 4979.
- [5] Schaber, G.G., Kozak, R.C., and Masursky, H., 1987, Cleopatra Patera on Venus: Venera 15/16 evidence for a volcanic origin: Geophys. Res. Let., 14, 41.
- [6] Kozak, R.C., and Schaber, G.G., 1987a, Comments on the tectonism of Venus: PGPI-1986, NASA TM 89810, 443.
- [7] Campbell, B.A., and Kozak, R.C., Geology and gravity of Bell Regio, Venus: ms. in final preparation.
- [8] Schaber, G.G., Shoemaker, E.M., and Kozak, R.C., 1987, The surface age of Venus: Applying the terrestrial crater record: PGPI-1986, NASA TM 89810, 405.
- [9] Schaber, G.G., Shoemaker, E.M., Kozak, R.C., 1987, The surface age of Venus: Use of the terrestrial cratering record: Astronomicheskii Vestnik, 21, 144.
- [10] Schaber, G.G., Shoemaker, E.M., Kozak, R.C., 1987 The Venusian surface: Is it really old?: V-Gram (Magellan Quarterly Bulletin), April 1987, 11.



## VENUS: GEOPHYSICAL AND TECTONIC INVESTIGATIONS

R.J. Phillips, Dept. of Geological Sciences, SMU, Dallas, TX 75275

Research in Venus geophysical and tectonic studies has progressed in several areas. These include the topics discussed below.

**Lithospheric Stress by Convective Coupling.** It has been previously asserted that if Venus has a thin elastic (or viscous) lithosphere, as argued by many workers, then the density distributions implied by venusian gravity anomalies are dynamically maintained and the implied flow structure imparts large horizontal normal stresses in the lithosphere [Phillips, 1986]. A difficulty in applying this concept to Venus is the non-uniqueness of models for the density distribution. We have now shown for dynamically maintained topography that the horizontal normal stress in an elastic lid is directly proportional to the observed free-air gravity and the stress magnitude depends only on the assumed thickness,  $h$ , of the elastic layer. This solution is valid for wavelengths much larger than the (greatest) depth of the perturbing density distribution. In this limit, horizontal normal stress is independent of  $z$  and is associated with uniform extension or compression (a stretching mode, as opposed to a bending mode, see Fung, 1965). This result is for constant viscosity but is a lower bound for negative viscosity gradients (temperature increasing with depth). Some specific results for a region west of Aphrodite Terra and south of Ishtar are, for  $h = 10$  km:

Wavelength km	Free-air Gravity Anom. magnitude, mgal	Horiz. Normal Stress, MPa
2234	41	320
1549	52	270
1165	66	260

The gravity values are corrected for line-of-sight effects and are based on power spectral analysis. These stresses should be more than sufficient to induce a tectonic response in the lithosphere. For example, they can be considered as in-plane forces leading to deformation on a scale smaller than the wavelengths listed here.

**Elastic-Plastic Deformation of Lithospheres.** A major effort this year has been to develop the theory and computer code for the elastic-plastic deformation of lithospheres subject to both in-plane (axial or longitudinal) forces and transverse (vertical) loading. The elastic-plastic behavior is governed by a brittle-ductile strength envelope [Brace and Kohlstedt, 1980]. In essence, the lithosphere is described by an elastic core sandwiched between two zones which are perfectly plastic with a depth-dependent yield stress. Our motivation has been to study the initiation of (thrust) faulting and subduction and the general loading of planetary lithospheres.

Various adaptations of the elastic-plastic formulation to geophysical problems have been published over the last decade [e.g., Goetze and Evans, 1979; Bodine et al., 1981; McNutt and Menard, 1982; Owens, 1983; Peters, 1985; McAdoo and Sandwell, 1985; McAdoo et al., 1978, 1985]. In contrast to many of these studies, our formulation is perfectly general in that we can use an arbitrary strength envelope, an arbitrary distribution of surface load, and either tensional or compressional in-plane forces. Further, with only slight modification, the computer code, written in two-dimensional Cartesian coordinates, can accommodate different coordinate systems. For example, elastic-plastic lithospheric loading by large volcanic structures can easily be studied.

The crux of solving the elastic-plastic problem is the development of a relationship between bending moment  $M$  and curvature for a given strength envelope. The combined effect of an in-plane load and a transverse load, which gives rise to a bending moment, is uniquely defined in the elastic range, regardless of the sequence of application of the forces. In the elastic-plastic (or fully plastic) range, the uniqueness of the solution ceases to exist, and the stress distribution depends upon the loading history. We have examined the problem wherein the in-plane load exists first, and subsequently a bending moment is applied (e.g., from vol-

canic or sedimentary loading). The in-plane load,  $N$ , produces yielding in the top and bottom of a lithospheric plate. The elastic core boundaries and the in-plane elastic stress are determined such that the distribution of stress integrates to  $N$ . The addition of a transverse load now creates a bending moment and additional plastic failure of the lithosphere occurs. The neutral axis is determined by the requirement that the net axial force due to bending integrates to zero, and  $M$  follows from simple geometric considerations. The moment-curvature relationship has been used in the equations of equilibrium, which have been solved by finite difference techniques.

As suggested above, the long-wavelength lithospheric stresses resulting from convective coupling provide a regional in-plane force to study lithospheric failure and buckling. The in-plane forces can be calculated directly from free-air gravity anomalies and are independent of plate thickness. The free-air gravity anomaly spectral values listed above produce  $N = \pm 3 \times 10^{12}$  N/m. Here we would assume that the wavelengths are large compared to the tectonic scale of interest and thus that  $N$  is approximately constant in  $x$ . (Alternatively, we can treat this problem mathematically with  $N$  as a function of  $x$ .) Another source of in-plane stress could be that of inhibited lithospheric spreading initiated in the Equatorial Highlands, as has been proposed on the basis of observed extensional features and thermal boundary layer arguments [Phillips and Malin, 1984; see also Head and Crumpler, 1987; Crumpler and Head, 1987].

Moment-curvature plots have been calculated for Venus using for  $N$  the  $\pm 3 \times 10^{12}$  N/m values. As discussed in the next section, it is likely that crustal portions of the venusian lithosphere have ductile strengths no greater than diabase. Maryland diabase [Caristan, 1982], slightly stronger than the diabase of Shelton and Tullis [1981], fails (i.e., the strength envelope is completely saturated) under an in-plane load of  $\pm 3 \times 10^{12}$  N/m, assuming  $T_0 = 725$  K and  $dT/dz = 15$  K/km. Thus if Venus has a crust that obeys a diabase flow law and the viscous flow solution is the correct interpretation of the gravity data, we would tentatively suggest that extensive faulting in response to interior dynamics is common on Venus. In any event, we are not able to generate moment-curvature curves with this rheology. Also, in all of our computer runs, we did not find a case wherein the in-plane load necessary to cause failure exceeded the critical force for buckling. We are able to generate results for websterite [Ave'Lallemant, 1978] and can demonstrate that the same saturation bending moment in compression can be achieved with websterite on Venus with an in-plane force about four times smaller than for the terrestrial oceanic lithosphere.

*Tectonism by Gravity Spreading/Sliding.* Simple, one-dimensional models have been examined [Smrekar and Phillips, 1987] to study the effects of various parameters on ductile deformation, and in particular, on the development of ductile shear zones in the venusian crust. These gravity-driven models represent a viscous slab resting on a slope inclined at an angle  $i$  and are appropriate when the scale of horizontal normal stress variation is large compared to the slab thickness. Boundary conditions consisted of a stress free upper surface and a no-slip (zero velocity) lower surface. Such a basal condition corresponds to a boundary between a more ductile crust overlying a more rigid mantle. Newtonian and non-Newtonian, temperature-dependent (constant temperature gradient) viscosities are considered and plane stress is assumed. Both shear and normal stress increase linearly with depth and depend on the angle of inclination. Because of the positive temperature gradient and the strong temperature-dependence of viscosity, the velocity changes most rapidly (i.e., the strain-rate is highest) in the lowermost, low viscosity regions. This effect, which simulates a region of distributed ductile deformation, is most pronounced for the non-Newtonian rheology.

Beyond the obvious effect of non-Newtonian and Newtonian rheologies, the thickness of the crustal layer is the most important parameter in these models, as both stress and temperature increase with increasing depth. Thermal gradient is perhaps the next most influential parameter, through its effect on temperature and thus viscosity. Given the more constrained range of feasible values of surface inclination and rock type, these parameters have a lesser effect. As these models do not include any deviatoric stress in the downslope direction, the result is that the upper, more rigid portion is carried along by the flow of lower, more ductile regions. Thus the maximum velocity always occurs at the surface.

To evaluate the potential for ductile shear zone development, as well as to simulate realistic rheologies, the temperature-dependent case with an experimentally determined flow law was solved by

numerical integration over a range of parameters. The constants for diabase [Shelton and Tullis, 1981] were selected as most appropriate on the basis of conversion of Venera lander [Surkov, et al., 1984] elemental data to a likely mineral assemblage. A reasonable minimum velocity which could be expected to cause "significant" deformation over limited spans of geologic time might be 0.1 cm/yr. For the 30 km thick crust suggested by Zuber [1987] on the basis of layer instability models for banded terrain, this model predicts a 0.1 cm/yr surface velocity for  $i$  equal to 1 deg and a thermal gradient equal to 21 K/km, or for an  $i$  of 2 deg and a thermal gradient of 16 K/km. This agrees well with estimates of likely thermal gradients [Solomon and Head, 1982] and calculated surface slopes [Sharpton and Head, 1985].

While this approach cannot be used to model deformation within the sliding sheet, the results suggest that gravity provides a sufficient force to cause tectonic deformation on Venus. The models predict both geologically significant velocities and strain-rates over a range of feasible values of thermal gradient, crustal thickness and surface slope. Such models might offer a lower limit to the possible gravity induced stresses and strain-rates as they do not incorporate the effects of normal stresses in the downslope direction, which would contribute to the total deviatoric stress within the sheet. Consequently, these models predict stresses far below those required to produce failure in the rigid part of the crust as determined by Byerlee's law or the Coulomb criterion.

Extensive gravity-driven deformation is known to occur in detached crustal layers on the Earth [Armstrong and Dick, 1974; Elliott, 1976]. The development of ductile deformation zones or detachment surfaces are, in many cases, believed to be greatly assisted by the weakening effect of water [Kirby, 1985]. However, thermally activated processes can also be important. A number of exhumed decollements believed to be associated with the brittle-ductile transition [Armstrong and Dick, 1974; Wiltshko, 1979; Mandl and Shippam, 1981; Price and Johnson, 1982; Miller et al., 1983] are observed on the Earth. While the more commonly observed water-activated processes cannot be expected to be significant on Venus, a number of thermally activated processes, such as feldspar recrystallization [Tullis and Yund, 1985], are likely to be very important in the higher temperature environment. Our model results show that development of such a thermally activated ductile deformation zone is favored by a power law rheology. These simple models provide a minimum crustal thickness necessary for a ductile deformation zone to develop, given an assumed slope inclination and thermal gradient.

*References:* Armstrong, R.L., and H.J.B. Dick, *Geology*, 1, 35-40, 1974. Ave'Lllemant, H.G., *Tectonophysics*, 48, 1-27, 1978. Bodine, J.H., M.S. Steckler, and A.B. Watts, *J. Geophys. Res.*, 86, 3695-3707, 1981. Brace, W.F., and D.L. Kohlstedt, *J. Geophys. Res.*, 85, 6248-6252, 1980. Caristan, Y., *J. Geophys. Res.*, 87, 6781-6790, 1982. Crumpler, L.S., and J.W. Head, *Geophys. Res. Lett.*, 14, 607-610, 1987. Elliott, J. *Geophys. Res.*, 81, 949-963, 1976. Fung, Y.C., *Foundations of Solid Mechanics*, Prentice Hall, Englewood Cliffs, NJ, 525 pp., 1965. Goetze, C., and B. Evans, *Geophys. J. R. astr. Soc.*, 59, 463-478, 1979. Head, J.W., and L.S. Crumpler, *Lunar and Planetary Science XVIII*, Lunar and Planetary Institute, Houston, 409-410, 1987. Kirby, S.H., *Tectonophysics*, 119, 1-27, 1985. Mandl G., and G.K. Shippam, in *Thrust and Nappe Tectonics*, K.R. McClay and N.J. Price, eds., Geol. Soc. London Special Pub. No. 9, Blackwell Scientific Publications, Boston, 1981. McAdoo, D.C., J.G. Caldwell, and D.L. Turcotte, *Geophys. J. R. astr. Soc.*, 54, 11-26, 1978. McAdoo, D.C., and D.T. Sandwell, *J. Geophys. Res.*, 90, 8563-8569, 1985. McAdoo, D.C., C.F. Martin, and S. Poulouse, *Tectonophysics*, 116, 209-222, 1985. McNutt, M.K., and H.W. Menard, *Geophys. J. R. astr. Soc.*, 71, 363-394, 1982. Miller, E.L., P.B. Gans, and J. Garing, *Tectonics*, 2, 239-263, 1983. Owens, T.J., *Tectonophysics*, 93, 129-150, 1983. Peters, R.G., *Tectonophysics*, 111, 3-23, 1985. Phillips, R.J., *Geophys. Res. Lett.*, 13, 1141-1144, 1986. Phillips, R.J., and M.C. Malin, in *Ann. Rev. Earth Planet. Sci.*, 12, 411-443, 1984. Price, N.J., and M.R.W. Johnson, *Tectonophysics*, 84, 131-150, 1982. Sharpton, V.L., and J.W. Head, *J. Geophys. Res.*, 90, 3733-3740, 1985. Shelton G., and J. Tullis, *EOS, Trans. AGU*, 62, 396, 1981. Smrekar, S., and R.J. Phillips, submitted to *Geophys. Res. Lett.*, 1987. Solomon, S.C., and J.W. Head, *J. Geophys. Res.*, 87, 9236-9246, 1982. Surkov, Yu.A., V.L. Barsukov, L.P. Moskalyeva, V.P. Kharyukova, and A.L. Kemurdzhian, *Proc. Lunar Planet. Sci. Conf. XIV*, in *J. Geophys. Res.*, 89, B393-B402, 1984. Tullis, J., and R.A. Yund, *Geology*, 13, 238-241, 1985. Wiltshko, D.V., *J. Geophys. Res.*, 84, 1091-1104, 1979. Zuber, M.T., *Proc. Lunar Planet. Sci. Conf. XVII*, in *J. Geophys. Res.*, 92, E541-E551, 1987.

## DYNAMIC STRESS MODELLING OF VENUS'S LITHOSPHERE

W. B. Banerdt (Jet Propulsion Laboratory, California Institute of Technology, Pasadena, CA 91109)

Patterns of tectonic deformation on planetary surfaces provide direct information on the lithospheric state of stress. This information can be compared with theoretical calculations of the global stress field in order to provide insight into the general structure of the lithosphere and mantle and into the mechanisms of tectonic deformation and topographic support. We have previously published global thin shell stress calculations for Venus's lithosphere which assumed a static model, in which support for long-wavelength topography and gravity anomalies is provided by a combination of Pratt compensation in the mantle and Airy compensation in the crust [Banerdt, 1986]. Those results, while providing a useful first-order approximation to the stress field, indicated that motions in the mantle (presumably caused by solid state thermal convection) must have a major, and perhaps dominant, effect on both long-wavelength topography and gravity and on the stress field.

Preliminary results for the effects of a dynamic mantle have been obtained by Phillips [1986] for the two-dimensional case in which a thick-plate elastic or viscous lithosphere overlies a newtonian half space with an exponential depth dependence of the viscosity, with a specified density distribution driving the flow in the fluid. The solutions are based on the approach of Richards and Hager [1984], in that it is assumed that the deformation of density boundaries reach steady-state in a time short enough such that there is not significant convective displacement in the fluid. These theoretical solutions, combined with information on the depth and strength of density anomalies in the venusian interior inferred by analyses of long wavelength gravity data and topography, suggest that stresses in excess of 100 MPa would be generated in a 10 km thick elastic lid.

In order to address this problem more fully, we have developed a global spherical coordinate formulation of a viscously coupled lithosphere and asthenosphere. The model is extended to spherical coordinates in three dimensions by combining the viscous mantle model of Richards and Hager [1984] with the spherical thin elastic lithosphere model of Banerdt [1986]. The boundary conditions are matched at the lithosphere-asthenosphere boundary, and the resulting system of equations are solved for a piecewise layered rheological structure using propagator matrix techniques [Hager and O'Connell, 1981]. Mathematically, the elastic shell at the surface can be thought of as a boundary condition on the normal stress which is a function of the stresses and displacements at the upper surface of the viscous mantle. Spherical harmonic representations of the topography and the gravity are utilized as external boundary conditions, and two laterally varying density anomalies (one in the mantle, corresponding to chemical or thermal variations, and the other at the crust-mantle boundary, corresponding to variations in the crustal thickness) are included in the formulation. This results in an underdetermined linear system of twelve variables and eleven independent equations. When an additional condition is supplied, one can

simultaneously solve for the state of stress at the surface (which can then be compared to observed tectonic deformational patterns), along with the distribution of crustal thickness and mantle density variation over the planet.

Several strategies will be employed in using this formulation to investigate processes on Venus. One approach is to assume a vertically constant density anomaly within the mantle and specify the flexural state of the lithosphere as the remaining constraint (e.g. assume that the topography is due solely to upwarping of the lithosphere, or that stresses in the lithosphere are minimized). This corresponds to the approach taken by Banerdt [1986], and allows a first order comparison between stress fields due to static and dynamic support of topography and gravity anomalies.

Another approach involves investigating the depth distribution of the density anomaly in the mantle. This appears to be a critical factor in determining the magnitude of the stress in the overlying lithosphere [Phillips, 1986]. (This is contrary to the conclusion of Kiefer et al. [1986] that density-driven viscous flow solutions that match the admittance spectrum are insensitive to the vertical density distribution. However this conclusion has subsequently been withdrawn [see Bills et al., 1987]). Various density distributions can be specified and the resulting stress states can be compared with observations to place limits on acceptable distributions. Guidance on candidate density structures can be derived by assuming that density variations in the mantle are thermally derived and then considering plausible structures associated with convection from both theoretical studies and seismic tomography in the earth. It may not even be necessary to specify the details of the density distribution, as it appears only in integrals over depth in both the external gravitational potential and the driving term for the velocity field in the mantle. Thus our goal will be to find a class of density distributions which will satisfy both the external boundary conditions of gravity and topography, and the observed surface state of stress.

#### REFERENCES

- Banerdt, W. B., Support of long-wavelength loads on Venus and implications for internal structure, *J. Geophys. Res.*, 91, 403-419, 1986.
- Bills, B. G., W. S. Kiefer, and R. L. Jones, Venus gravity: A harmonic analysis, *J. Geophys. Res.*, 92, 10335-10351, 1987.
- Hager, B. H., and R. J. O'Connell, A simple global model of plate dynamics and mantle convection, *J. Geophys. Res.*, 86, 4843-4867, 1981.
- Kiefer, W. S., M. A. Richards, B. H. Hager, and B. G. Bills, A dynamic model of Venus's gravity field, *Geophys. Res. Lett.*, 13, 14-17, 1986.
- Phillips, R. J., A mechanism for tectonic deformation on Venus, *Geophys. Res. Lett.*, 13, 1141-1144, 1986.
- Richards, M. H., and B. H. Hager, Geoid anomalies in a dynamic earth, *J. Geophys. Res.*, 89, 5987-6002, 1984.

## Definition and Characterization of Morphologic Subtypes of the Venus Tesserae

D.L. Bindshadler and J.W. Head, Brown University Dept of Geological Sciences,  
Providence, RI, 02912

The tesserae (or parquet terrain) of Venus were discovered from Venera 15–16 radar images of the surface [1] and described as consisting of orthogonal to obliquely oriented set of ridges and valleys [2]. Tesserae cover more area (~15% of the area north of 30°N) than any of the other tectonic units mapped from Venera data [3,4]. Regions of tessera are strongly concentrated in the region between longitudes 0° E and 150° E and thus lie between a proposed center of crustal extension and divergence in Aphrodite [5,6] and a proposed region of intense deformation [7], crustal convergence and orogenesis in western Ishtar Terra [8,9]. Increased understanding of the tesserae has important implications these as well as for any model of Venus tectonics. As part of an effort to understand this unusual terrain type, we examine the characteristics of the tesserae with the goal of putting forward a range of hypotheses that explain the origin and evolution of the tesserae.

### Observations

#### Pioneer Venus Radar

Pioneer Venus altimeter data show that regions of tessera lie at higher elevations than surrounding plains units and are characterized by relatively higher values of rms slope [4] (a measure of roughness at a scale of ~0.5 m to 10's of m) [10,11]. Tesserae are also characterized by greater cm-scale roughness than the plains due to erosion linked to extensive deformation and possibly to greater relative age [4]. Craters are sufficiently sparse to make determination of the relative age of the tesserae unreliable [12].

#### Gravity Anomalies

For the largest regions of tesserae, line of sight (LOS) gravity data may be used to infer depths of compensation of these high regions. Of the three largest regions of tessera (Tellus Regio, Laima Tessera and Fortuna Tessera) LOS gravity data extend far enough to the north to cover Tellus Regio, to partially cover Laima Tessera, and have not been examined for Fortuna Tessera. These measurements show approximately no anomaly associated with the 2.5 km of topography in Tellus, leading Sjogren et al. [13] to suggest that the region is compensated at relatively shallow depths (i.e. significantly less than the 100 to 300 km depths suggested for regions such as Aphrodite Terra and Beta Regio). Laima Tessera also shows no apparent gravity signature. Large gravity anomalies are associated with the Montes Maxwell and Freyja surrounding Lakshmi Planum [14] but no examination has been made of gravity data over Fortuna Tessera in eastern Ishtar Terra.

#### Morphology

As an aid to understanding the possible modes of origin of the tesserae structures, we extend Basilevsky et al.'s [2] definition for tesserae. In order to be classified as tessera, a region must be characterized by (1) a complex appearance, (2) numerous linear to curvilinear ridges and valleys of wavelengths on the order of 5 to 25 km; (3) at least two distinct intersecting sets of structural features with all trends restricted to the region of tessera. This restriction excludes features such as intersecting ridge belts.

Examination of Venera data of many of the regions of tessera reveals three morphologic subtypes for the terrain. These are the sub-parallel ridged terrain ( $T_{sr}$ ), trough and ridge terrain ( $T_{tr}$ ), and disrupted terrain ( $T_{ds}$ ); each is defined below. Sketch maps of type areas are shown in Figures 1a–1c. In these figures, narrow lines are ridges, broad lines are troughs, and dashed lines are lineaments.

The sub-parallel ridged terrain ( $T_{sr}$ , Fig. 1a) is similar to ridge belts in that it consists of sub-parallel ridges. However,  $T_{sr}$  ridges are less sinuous and do not intertwine. Ridges tend to be disrupted along linear zones of consistent orientation and often form en echelon groups, perhaps indicating strike-slip offset. The two structural orientations consist of the ridges and the lineations along which they are disrupted. Type locale: Fortuna Tessera, east of Maxwell Montes.

Structures in the trough and ridge terrain ( $T_{tr}$ , Fig. 1b) are expressed as troughs in one direction and as ridges and/or valleys in another. The troughs may appear both as broad (~50km) and narrow (< 20 km) structures. Ridges occasionally show en echelon offset. They tend to be spaced approximately 5 to 10 km apart, more closely than the minor troughs (spacing ~10–20 km). Type locale: Eastern Laima Tessera

The disrupted terrain ( $T_{ds}$ , Fig. 1c) is characterized by a general lack of continuous ridges or valleys longer than ~50 km. The terrain is often blocky to chaotic in appearance, depending upon the consistency of ridge orientations. Even in cases where ridge orientations are chaotic, lineaments defined by short troughs, ridges and by discontinuities in ridges preserve consistent orientations over the region of tessera. Disrupted terrain is usually transitional with the  $T_{tr}$  or  $T_{sr}$ . Type locale: Central Tellus Regio.

The contact between tesserae and plains is characterized by two types of boundaries. In the first (Type I), the boundary is highly irregular at the 100 km scale, consisting of numerous ovoidal to polygonal smooth plains regions that may separate small regions of tessera from the main body of a block. Structures within the tessera take on a subdued appearance as the boundary is approached and show little relation to the shape of the tessera-plains boundary. Type I boundaries thus appear to be an expression of embayment of the tessera by plains-forming materials. Type II boundaries are much more regular at the 100 km scale and typically characterized by the presence of the  $T_{sr}$  subtype of tessera as well as steep topography and the presence of small ridges or ridge belts within the adjacent plains. These boundaries appear to be places where the tesserae have formed at the expense of the plains.

### Models

The above observations suggest key characteristics that any successful model of tessera formation must be able to reproduce. We suggest four general types of formational models that will be tested to determine which provides the best explanation for the observed morphology and physical properties of the tesserae.

#### Model I: Horizontal compression

In this model, horizontal motion of crustal material leads to folding, thrusting, and subsequent thickening of the crust. Such a model will rely partly upon analogies with terrestrial orogenic belts such as the Andes or Tibetan plateau. The complex structure of the tesserae could be explained as either (a) superposition of folds due to a change in the principal direction of compression and/or (b) extension due to gravitational relaxation [15,16].

#### Model II: Uplift due to shallow mantle processes

LOS gravity data suggest relatively shallow depths of compensation beneath the tesserae. However, this does not completely rule out mantle processes; a relatively shallow thermal anomaly beneath the crust can produce high topography and extension by thermal and dynamic uplift (perhaps similar to that observed in the Basin and Range). An additional contribution can be caused by emplacement of differentiated (i.e. ~crustal composition) magma bodies within and at the base of the crust. Each of these mechanisms has consequences for deformation at the surface [17,16]

#### Model III: Analogy to terrestrial seafloor

Examination of Pioneer Venus data for Aphrodite Regio has led Head and Crumpler [6] to propose that crustal divergence is occurring there. Model III is thus predicated upon morphologic similarity between terrestrial seafloor and the tesserae. Regions of tessera then represent regions of thick crust (perhaps similar to oceanic plateaus on Earth) that have been deformed but still retain the background structure of near-ridge ocean floor.

#### Model IV: Gravitational relaxation

Models of gravitational relaxation [16] have shown that significant deformation of the surface can occur subsequent to any creations of topography. In Model IV we examine deformation of the tesserae subsequent to any of the constructional processes above. In addition, we are currently examining the possible time-dependent interactions between relaxation and constructional processes that may create uncompensated loads (e.g. large scale thrusting or volcanism) [17].

### References

- [1] Kotelnikov, V.A., A.F. Bogomolov, and O.N. Rzhiga, Radar study of Venus surface by Venera-15 and -16 spacecraft, *Adv. Space Res.*, 5, p. 5-16, 1985; [2] Basilevsky, A.T., A.A. Pronin, L.B. Ronca, V.P. Kryuchkov, A.L. Sukhanov, and M.S. Markov, Styles of tectonic deformation on Venus: Analysis of Veneras 15 and 16 data, *Proc. Lunar Planet. Sci. Conf.* 16th, 91, p. D399-D411, 1986; [3] Sukhanov, A.L., Parquet: Regions of areal plastic deformation, *Geotektonika*, No. 4, p. 60-76, 1986; [4] Bindschadler, D.L. and J.W. Head, Characterization of Venera 15/16 geologic units from Pioneer Venus

reflectivity and roughness data, submitted to *Icarus*, 1987; [5] Schaber, G.G., Venus: Limited extension and volcanism along zones of lithospheric weakness, *Geophys. Res. Lett.*, 9, p. 499-502, 1982; [6] Head, J.W. and L.S. Crumpler, Evidence for divergent plate boundary characteristics and crustal spreading: Aphrodite Terra, Venus, *Science*, in press, 1987; [7] Pronin, A.A., The Lakshmi plateau structure as an indicator of asthenospheric horizontal flow on Venus, NASA TM-880507, transl. from Russian, *Geotektonika*, No. 4, p. 54-59, 1986; [8] Campbell, D.B., J.W. Head, J.H. Harmon, and A.A. Hine, Venus: Identification of banded terrain in the mountains of Ishtar Terra, *Science*, 221, p. 644-647, 1983; [9] Crumpler, L.S., J.W. Head, and D.B. Campbell, Orogenic belts on Venus, *Geology*, 14, p. 1031-1034, 1986; [10] Hagfors, T., Remote probing of the Moon by microwave and infrared emissions and radar, *Radio Sci.*, 5, p. 189-227, 1970; [11] Head, J.W., A.R. Petefreund, J.B. Garvin, and S.H. Zisk, Surface characteristics of Venus derived from Pioneer Venus altimetry, roughness, and reflectivity measurements, *Jour. Geophys. Res.*, 90, p. 6873-6885, 1985; [12] Ivanov, B.A., A.T. Basilevsky, V.P. Kryuchkov, and I.M. Chernaya, Impact craters on Venus: Analysis of Venera 15 and 16 data Proc. Lunar Planet. Sci. Conf. 16th, p. D413-D430, 1986; [13] Sjogren, W.L., B.G. Bills, P.W. Birkeland, P.B. Esposito, A.R. Konopliv, N.A. Mottinger, S.J. Ritke, and R.J. Phillips, Venus gravity anomalies and their correlations with topography, *Jour. Geophys. Res.*, 88, p. 1119-1128, 1983; [14] Sjogren, W.L., B.G. Bills, and N.A. Mottinger, Venus: Ishtar gravity anomaly, *Geophys. Res. Lett.*, 11, p. 489-491, 1984; [15] Froidevaux, C., and Y. Ricard, Tectonic evolution of high plateaus, *Tectonophys.*, 1324, p. 227-238, 1987; [16] Bindshadler, D.L. and E.M. Parmentier, Tectonic features due to gravitational relaxation of topography, *Lunar Planet. Sci. XVIII*, p. 75-76, 1987; [17] Phillips, R.J., A mechanism for tectonic deformation on Venus, *Geophys. Res. Letters*, 13, p. 1141-1144, 1986; [18] Bindshadler, D.L., J.W. Head, and E.M. Parmentier, Preliminary results of mapping and modeling of the parquet terrain, Venus, *EOS*, 68, p. 1340, 1987.

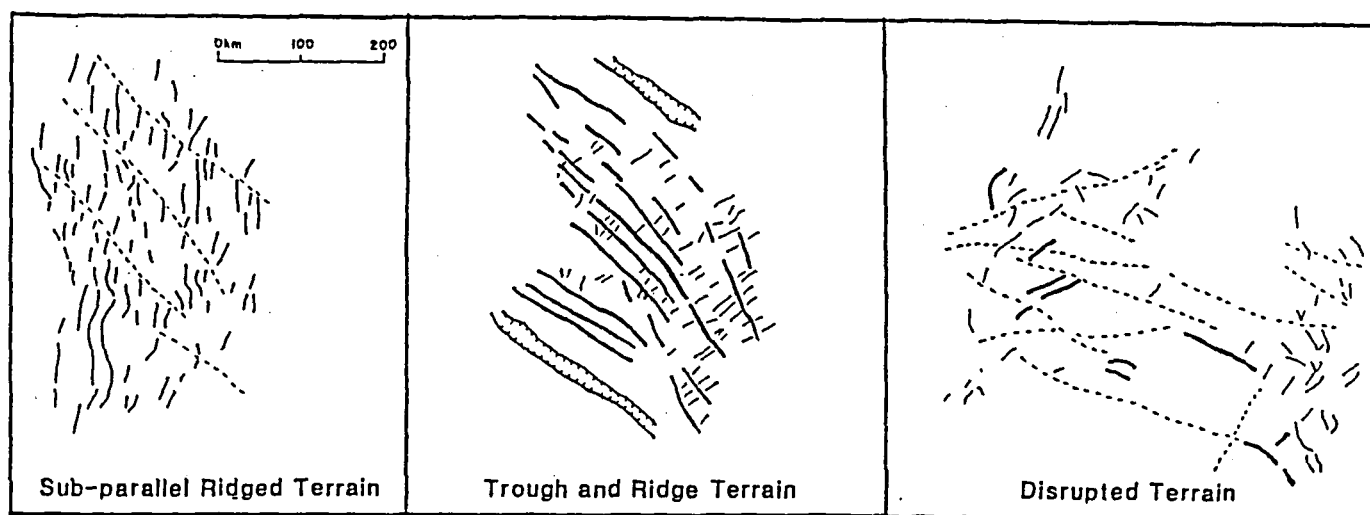


Figure 1a

Figure 1b

Figure 1c



## Evolution of the Lunar Crust: An LGO Perspective

C. M. Pieters (Geological Sci., Brown University, Providence, RI 02912)

During the Apollo program almost two decades ago it was recognized that the lunar crust evolved from a major differentiation event that occurred very early in its evolution. A "Magma Ocean" (an outer zone of molten material perhaps hundreds of kilometers in thickness) that cooled to form the stratigraphy of the outer part of the Moon was widely discussed as a model to explain a feldspathic composition of the highlands crust and a mafic mantle (the source region of the mare basalts). Both the nature of the ancient and brecciated returned samples and the cratering record observed for the Moon (now the standard for planetary studies) suggest extensive disruption and mixing of primordial crustal materials must have occurred during the period of heavy early bombardment. Returned samples indicated the extrusion of mare basalts initially occurred after the crust was well developed and ceased nearly 3 By ago. At the close of the Apollo program the Moon was viewed as a simple, relatively understood system, and was useful for comparisons with more complex planets.

In the post-Apollo years, however, an increasing amount of evidence has been accumulating that indicates our nearest neighbor is far more complex than originally envisioned from that first wave of exploration. Much of this evidence comes from continued analyses of lunar samples as well as ongoing telescopic measurements of the Moon. The magma ocean hypotheses, for example, cannot account for the type and diversity of crustal materials discovered as minor fragments in returned samples and detected as extensive unsampled outcrops with telescopic measurements. The highland crust has recently been found to be not well mixed below 1-2 km and displays extensive unsuspected heterogeneity both laterally and vertically (Pieters, *Rev Geophys.* 1986). This glimpse of the complexity of the lunar crust requires models of crustal evolution to be substantially revised and thus weakens our presumed understanding of early lunar history. Instead of being the most simple example of planetary evolution, the Moon, and more accurately the Earth-Moon system, is emerging as being unique, and its important early history is still shrouded in mystery.

Although many of the fundamental questions to be answered about the Earth-Moon system require a multidimensional exploration approach, one of the missions being investigated for this second phase of lunar exploration is the Lunar Geoscience Observer. Surface composition will be explored at ~1/2 km resolution and will provide the global information necessary to fully evaluate the complex nature of the lunar crust.

## GEOLOGY AND FORMATION OF RIMA MOZART: IMPLICATIONS FOR THE ORIGIN OF LUNAR SINUOUS RILLES

C.R. Coombs, B.R. Hawke and L. Wilson\*, Planetary Geosciences Division, Hawaii Institute of Geophysics, University of Hawaii, 2525 Correa Rd., Honolulu, HI 96822.

\*(also at Department of Environmental Science, University of Lancaster, Lancaster, LA1 4YQ, England)

In order to better understand the processes responsible for the formation of lunar sinuous rilles, we have conducted a study of Rima Mozart (Figure 1) using a variety of geologic, photographic, and remote sensing data. This abstract summarizes the results of our analysis of these data.

The nature and origin of lunar sinuous rilles have long been the subject of major controversy. Lunar sinuous rilles typically occur on mare surfaces, though a few cross into highland terrains. They are generally associated with an endogenic crater or an elongate depression at their highest elevation and they vary in width, depth, length, and degree of sinuosity. Suggested origins for sinuous rilles include: 1) erosion by nuées ardentes,<sup>1</sup> 2) fluvial erosion,<sup>2,3,4,5</sup> 3) tectonic features of tensional origin,<sup>6</sup> 4) formation as lava tubes and channels during lava emplacement,<sup>7,8,9</sup> or, during the draining of a lava lake,<sup>10</sup> 5) incision of channels by thermal erosion and/or turbulent flow through the channels.<sup>11,12</sup>

A number of these possible origins appear to be highly unlikely at this time. For example, it is very unlikely that nuées ardentes would form the smooth sinuous channels on the lunar surface. On the Earth they form hummocky channels and dunes, not smooth curvy channels. Though a morphologic similarity to terrestrial fluvial features has been noted,<sup>2,3,4</sup> a fluvial origin for lunar rilles has long been discounted due to the anhydrous nature of the returned lunar samples (e.g., Taylor, 1975).<sup>13</sup> The similarity of certain lunar rilles to terrestrial channels of fluvial origin merely suggests an origin by fluid flow, though water is not necessarily the erosive agent.<sup>9</sup>

Terrestrial lava tubes and channels commonly originate at vent craters or depressions associated with regional tectonic features such as faults, fissures, or fracture systems that may form concentric to calderas.<sup>8</sup> Similarly, many lunar sinuous rilles are located in areas of structural weakness and often tend to follow pre-existing structural trends. However, the presence of elongate "head" craters, levees, and the fact that lunar sinuous rilles may extend for large distances without offset or mirror images on either side contradicts an origin due to extensional tectonics alone.

Lunar sinuous rilles are also morphologically similar to terrestrial lava channels and collapsed lava tubes in that they commonly originate at irregularly shaped "head" craters, trend down-slope, are discontinuous in areas (tube formation and/or collapse?), taper out at distal ends, and may form distributaries. It has been suggested that they form in several phases, in a manner similar to terrestrial tube-fed lava flows.<sup>14</sup> On Earth, a lava flow may extend for large distances under the insulating layer of its cooled surface. A similar insulation process, in conjunction with the high temperatures and low viscosities typical of lunar lavas, may also provide protection for lunar flows, enabling lava tubes and channels of considerable linear extent to form.

Thermal erosion and turbulent flow may also explain the enormous linear extent as well as the formation of meanders that are commonly associated with lunar rilles.<sup>15</sup>

Rima Mozart is a 40 km-long lunar sinuous rille located near the SE rim of Imbrium basin (25° 21' N, 359° 03' W) and approximately 100 km southwest of the Apollo 15 landing site. It is 250 to 500 m deep and is incised into the volcanically derived KREEP basalts of the Apennine Bench Formation (Figures 2 and 3).<sup>16,17,18</sup> The rille is surrounded by a smooth mare-like, low albedo volcanic unit. While most of this dark unit appears to have been emplaced as voluminous volcanic flows originating at the primary source vent, Kathleen, some of it may represent pyroclastic "dark mantle" material. An analysis of the high-resolution 3.8 cm radar maps of the Rima Mozart region presented by Zisk *et al.*<sup>19</sup> indicates that at least some pyroclastic debris is present around Kathleen. The KREEP basalts of the Apennine Bench Formation are a plains-forming unit of intermediate albedo, with numerous secondary craters and a variety of linear structural features present. Underlying the Apennine Bench Formation is a unit of extremely fractured Imbrium ejecta material. Adjustment and settling of this unit and/or the draining of the once molten Apennine Bench Formation may explain the presence of the linear structural features seen on the surface.<sup>20</sup> Beneath the Imbrium ejecta is a unit of Serenitatis ejecta material.

Photographic data indicate the presence of two major volcanic source vents for Rima Mozart (Figure 1). Now girdled by dark mare-type material, these vents appear to have formed in the underlying Apennine Bench Formation. Kathleen, the primary source vent and the largest of the two, is an elongate crater (5 x 3 km) in the Apennine Bench Formation. From Kathleen, Rima Mozart follows a dominant NW/SE structural trend<sup>18</sup> until its terminus 30 km to the east. About 10 km from the terminus of Rima Mozart the second elongate (2 x 1 km) source vent, Ann, is joined to the main channel by a shallow secondary rille. Evidence of spatter surrounding Ann strongly supports a volcanic origin for this feature. Additional evidence for a volcanic origin for Rima Mozart is the presence of minor pyroclastic vents and associated rilles aligned with Ann along a NW/SE trending fissure zone. At the distal end of Rima Mozart, the rille terminates at Michael, an apparent "sink" crater, and is embayed by "Lacus Mozart", a mare lake. That Michael is a "sink" crater is suggested by the lack of evidence for fire-fountaining around the vent and the fact that it is topographically lower than Kathleen and Ann. The crater Michael may be connected to the NE-trending Rima Bradley, to the southeast, through a conduit marked by a collapse feature, Patricia. This possible extension of Rima Mozart joins Rima Bradley at a 90° angle, reflecting the dominant NW/SE structural trend of the region.

Near-infrared spectra (0.6 - 2.5  $\mu$ m) recently collected at the U.H. 2.2-m telescope on Mauna Kea indicate that both Apennine Bench material and lesser amounts of mare material are exposed in the interior of the source vent, Kathleen. The surface of "Lacus Mozart", the mare deposit southeast of Patricia, is dominated by mature mare basalt with a minor amount of contamination by highland debris. Unfortunately, a more detailed spectral analyses of this area was hindered by adverse weather conditions at the time of data collection which resulted in poor quality spectra.

Based upon our analysis of the available topographic, photographic, geologic and remote sensing data it is clear that the Rima Mozart region is the product of a complex series of geologic processes. For example, Rima Mozart follows a pre-existing,

dominant, NW/SE structural trend suggesting the influence of structural features on the rille orientation, while the volcanic origin of Rima Mozart is strongly supported by the presence of two volcanic source vents and the spatter present around Ann. We suggest that the formation of Rima Mozart began with an explosive eruption at Kathleen. A blanket of pyroclastic material was deposited around the vent while turbulent erupting lava began carving the rille to the southeast. The rapid effusion rate of the magma as well as its high temperature and turbulent nature helped to thermally erode two channels to form the present bifurcated rille. Similar eruptions and flows were also created at Ann and were joined to the main channel by a NE-trending shallow, secondary rille. Although it was once speculated that Rima Mozart formed as a lava tube, our calculations show that it is unlikely that a complete tube once existed along the rille. Such a tube would have had dimensions on the order of 100 m (w) x 500 m (d), implying an eruption rate of  $6 \times 10^5 \text{ m}^3/\text{s}$ . More reasonably, we calculated a total eruptive volume of 6372  $\text{km}^3$  for an open channel, with an eruption rate of about  $8 \times 10^4 \text{ m}^3/\text{s}$  over a period of 947 days. The calculated thermal erosion rate for this time period was  $1.55 \times 10^{-6} \text{ m/s}$ .

REFERENCES: (1) Cameron, W.L. (1964), *JGR*, 69, 2423; (2) Urey, H.C. (1967), *Nature*, 216, 1094; (3) Gilvarry, J.J. (1968), *Nature*, 218, 336; (4) Lingenfelter, R.E., Peale, S.J. and Schubert, G. (1968), *Science*, 161, 266; (5) Schubert, G., Lingenfelter, R.E. and Peale, S.J. (1970), *Rev. of Geophys. and Space Phys.*, 8, 199; (6) Quaide, W. (1965), *Icarus*, 4, 374; (7) Kuiper, G.P., Strom, R.G., LePoole, R.S. (1966), *JPL Lab. Tech. Rept.*, 32-800; (8) Greeley, R. (1971), *Science*, 172, 722; (9) Oberbeck, V.R., Quaide, W.L. and Greeley, R. (1969), *Modern Geology*, 1, 75; (10) Howard, K.A., Head, J.W. and Swann, G.A. (1972), *Proc. 3rd Lunar Science Conf.*, Vol. 2, 1; (11) Carr, M.H. (1974), *Icarus*, 22, 1; (12) Hulme, G. (1973), *Modern Geology*, 4, 107; (13) Taylor, S.R. (1975), *Lunar Science - A Post Apollo View*, 1; (14) Greeley, R. (1977), *NASA CR 154821*, 24-44; (15) Hulme, G. (1982), *Geophys. Surveys*, 5 245-279; (16) Hawke and Head (1978), *Proc. 9th Lunar Planet. Sci. Conf.*, 3285; (17) Spudis (1978), *Proc. 9th Lunar Planet. Sci. Conf.*, 3379; (18) Spudis and Hawke (1986), *Proc. Apollo 15 Conf.*, 105; (19) Zisk, S.H., Pettengill, G.H. and Catuna, G.W. (1974), *The Moon*, 10, 17; (20) Swann, G.A. (1986), *LPSC XVII*, 855

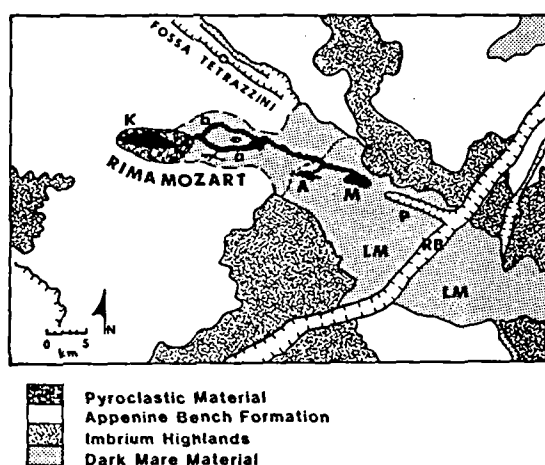


Figure 1: Geologic map of Rima Mozart. Source vents: Kathleen (K), Ann (A). Sink crater: Michael (M).

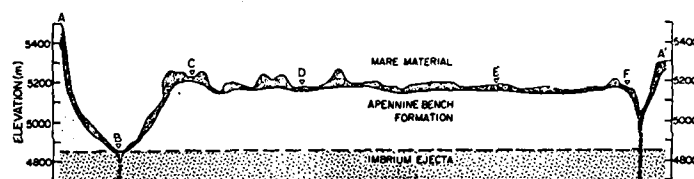


Figure 2: Geologic cross-section of Rima Mozart. (V.E. = 1.69)

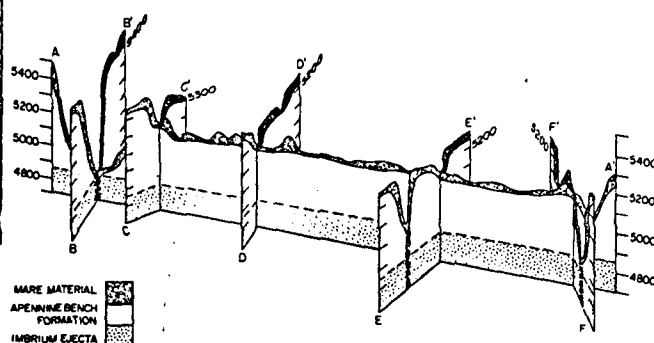


Figure 3: Geologic panel diagram of Rima Mozart and vicinity. (V.E. = 1.69)

THE FORMATION OF HADLEY RILLE AND IMPLICATIONS FOR THE GEOLOGY OF THE APOLLO 15 REGION. Paul D. Spudis, U.S. Geological Survey, Flagstaff, AZ 86001, Gordon A. Swann, Dept. of Geology, Northern Ariz. Univ., Flagstaff, AZ 86011, and Ronald Greeley, Dept. of Geology, Ariz. State Univ., Tempe, AZ 85287

The origin of lunar sinuous rilles via the lava channel/tube mechanism is accepted by most investigators, although the precise mode of formation is a matter of contention. We have combined the results of studies of terrestrial lava tube systems, and the regional and detailed site geology of the Apollo 15 area to develop a model for the formation of Hadley rille. The earliest post-Imbrium basin unit in the region is the pre-mare Apennine Bench Formation; remote-sensing and lunar sample studies have shown that this unit most likely consists of volcanic KREEP basalt flows. Numerous structural depressions in the Apennine Bench Formation were probably produced by regional deformation associated with basin adjustment. These structural and topographic lows provided a network of depressions that were later followed by basalt flows that established two major sinuous rilles in the region, the Mozart and Hadley Rilles. In this model, the rilles are primarily constructional features that developed along preexisting structural depressions. As such, substantial thermal or mechanical erosion by lava during the formation of these rilles did not occur. A consequence of this model for Hadley Rille formation is that the observed outcrop of mare basalt in the rille walls at the Apollo 15 site may represent the total thickness of basalt in that area (less than 50 m). The formation of lunar sinuous rilles by lava erosion, along with associated assimilation of highland debris into mare basalt magmas, may be a much less widespread phenomenon than has been proposed.

## CONSTRAINTS ON THE SUBSURFACE STRUCTURE OF EUROPA

M. Golombek and B. Banerdt (Jet Propulsion Laboratory, Caltech, Pasadena, CA 91109)

### Introduction

Two end member models for the extent of differentiation of Europa have been discussed in the literature. The first suggests that Europa's interior is completely differentiated, with a water crust about 100 km thick [e.g. Squyres et al., 1983]. The second assumes that the satellite is much less differentiated, with most of the water locked up in a thick layer of hydrated silicates and only a thin near-surface layer of water [e.g. Ransford et al., 1981; Finnerty et al., 1981]. Unfortunately, it has not been possible to convincingly distinguish between these two end members based on observational evidence. In this abstract we use observational evidence on the origin of fractures near the anti-Jovian point, along with simple subsurface models for failure of an ice lithosphere, to place constraints on the extent of differentiation, subsurface structure, and near-surface temperature distribution of Europa.

### Origin of Fractures

The geometry of wedge-shaped bands near the anti-Jovian point on Europa argues convincingly that these features are a result of tension cracks that have fractured the ice lithosphere, allowing rotation and translation of intact blocks of ice [Schenk, 1984; Schenk and McKinnon, 1987]. These bands are dark features in lighter plains that have sharp edges (at Voyager resolution) and a triangular or wedge-like shape. The wide ends of the wedge-shaped bands terminate against linear dark bands that are generally perpendicular to the wedge-shaped bands and appear geometrically similar to transform faults. The offsets of pre-existing lineations in the plains material and the shapes of the bands suggest that blocks of lithosphere have rotated apart. The edges of these blocks can be fit back together, indicating that the wedge-shaped bands are vertical tension cracks in the lithosphere that have opened by an amount equal to the width of the bands (10-30 km) and were filled by darker material (presumably dirty ice). Tension cracks are indicated because a single shear (normal) fault results in an elevation difference between the two sides (which is not observed). Note that this elevation change would result even if shear failure occurred at depth, with a tension crack at the surface. In addition, paired faults in a graben do not preserve a close fit between the sides of a band (the downdropped block is covered by dark ice filling the graben). The opening of these bands has allowed systematic rotation of a number of 50-100 km sized intact blocks or plates within a broad zone 1500 by 500 km near the anti-Jovian point. The rotated blocks between the bands show no evidence for internal deformation and thus appear to have acted coherently during the rotation. These observations by Schenk [1984] and Schenk and McKinnon [1987] have led most workers to conclude that the intact ice lithosphere of Europa must have been more than a few km thick to allow rotation of intact ice blocks, but no thicker than a few tens of km [Lucchitta and Soderblom, 1981] or ten km [Schenk and McKinnon, 1987] to have allowed the rotation to occur. In addition, this ice lithosphere must have been decoupled from any silicate or hydrated silicate interior to have allowed the motion to occur. Thus the characteristics of wedge-shaped and dark bands near the anti-Jovian point of Europa argue that they are tension cracks and transform faults in

the ice lithosphere which was at least 3 km thick and decoupled from the silicate interior at the time of rotation.

### Tensile Lithosphere Thickness

The existence of tension cracks on Europa is the first documented case of major tensile (as opposed to shear) failure on the planets and satellites. This suggests that the ice lithosphere on Europa was nearly intact, having few pre-existing cracks or fractures. If pre-existing fractures with favorable orientations existed in the lithosphere, they would have been activated and shear failure would have resulted, because greater stress is required to produce failure of intact ice under tension or shear than is required to initiate sliding on pre-existing steeply dipping fractures [Golombek and Banerdt, 1986]. This situation is different from all other planet and satellite surfaces where extension of the lithosphere has produced normal faulting and grabens.

For tension cracks to form in a lithosphere requires tensile failure to occur as opposed to shear failure. The Griffith failure criteria [e.g. Jaeger and Cook, 1976] limits tensile failure to a maximum depth of  $z = 3S_0/pg$ , where  $S_0$  is the unconfined tensile strength,  $p$  is the mean density, and  $g$  is the gravitational acceleration. For an unconfined tensile strength of ice of 2.5 MPa [Hawkes and Mellor, 1972], this limits the depth at which tension cracks can occur on Europa to less than 6 km with a corresponding maximum stress difference ( $-S_0 + pgz$ ) of less than 10 MPa. At greater depths the overburden stress will increase, resulting in greater stress differences and failure will occur by shear, creating normal faults. These results, along with the observations discussed earlier, place limits on the "tensile lithosphere" thickness of 3 to 6 km at the time of formation of the dark and wedge-shaped bands near the anti-Jovian point.

### Thermal Gradients

Considering these constraints on tensile lithosphere thickness in the context of lithospheric yield strength envelopes allows limits to be placed on Europa's near-surface thermal gradient. The ductile yield stress curve must intersect the brittle failure curve (the brittle-ductile transition) at a depth no greater than 6 km. Otherwise shear failure would occur, which is not observed. Ductile yield stress curves relate stress difference to strain rate, temperature, and a few experimentally determined constants. For an average surface temperature of 100 K and a geologic strain rate of  $10^{-15}$ /sec, a minimum thermal gradient of about  $3^\circ/\text{km}$  is required in order to enable the ductile yield stress curve to intersect the brittle curve at 6 km depth. (See Golombek and Banerdt [1986] for a more complete discussion of ductile yield stress curves and experimental constants used for ice). A 3 km tensile lithosphere thickness requires a 3 km deep brittle-ductile transition and a maximum temperature gradient of about  $10^\circ/\text{km}$ . Thus observational constraints on tensile failure of wedge-shaped bands on Europa with simple failure criteria and lithospheric strength calculations place limits on the thermal gradients on Europa of  $3\text{--}10^\circ/\text{km}$ .

The thermal gradients derived from this analysis are affected by factors such as strain rate and possible fluid pressure within the forming crack. The rotation of blocks on Europa has been used by most workers as evidence of internal geologic activity, so the assumption of geologic strain rates is justified. The events required for rotation to occur are: tensile failure of the lithosphere; opening and rotation of the blocks; and intrusion of the dark material (presumably dirty ice) constituting the dark bands. Each of these events may have occurred more than once, the entire

process repeating itself a number of times. For geologic strain rates of  $10^{-15}$ /sec (3%/m.y.), the 15-20% of strain across the rotated blocks would occur in 5-7 m.y. An order of magnitude faster strain rate would result in the rotation of the blocks in less than one m.y. and would require an increase in the inferred thermal gradients of about  $5^{\circ}$ /km.

The outer layer of water ice on Europa allows the possibility that a fluid pressure could exist within the cracks and that tensile failure could occur to depths greater than 6 km (because fluid pressure counteracts overburden stress). However it must be recognized that even the warmest portion of the brittle lithosphere (at its base) has a temperature that is less than half of the melting temperature, thereby precluding liquid water from existing except as a transient fluid within it. In order for liquid water to extend the depth of tensile failure, a large pressurized reservoir must be available around the crack for each failure episode. We consider this to be unlikely, given that the sharp boundaries of lineations on Europa implies that the ice volcanism is laterally confined within the bands, and thus is secondary to the fracturing.

Our estimates of thermal gradient ( $3-10^{\circ}$ /km) compare favorably with previous workers suggestions for heat flow for Europa. Thermal evolution models by Ransford et al. [1981] give surface temperature gradients of about  $3^{\circ}$ /km. Models by Cassen et al. [1981] suggest similar thermal gradients, whereas estimates by Squyres et al. [1983] imply slightly higher gradients of  $5-15^{\circ}$ /km.

#### Extent of Differentiation

The rotation of the ice blocks on Europa requires that the ice lithosphere be decoupled from the silicate or hydrated silicate interior, because even the weakest hydrated silicates have ductile strengths orders of magnitude higher than ice at these temperatures. This implies a minimum amount of differentiation of water to allow a layer of low yield stress ductile ice between the brittle ice and the silicates. Using thermal gradients derived earlier, we find that at least 15-25 km of differentiated water is necessary for decoupling the ice lithosphere from the silicate substrate. This estimate is a minimum, and greater amounts of differentiated ice are possible. Thus although we are not able to distinguish between the differentiation models completely, minimum thicknesses of water determined here suggest that at least one quarter of the total water on Europa has been differentiated.

#### References

- Cassen, P., S. Peale, and R. Reynolds (1982) Satellites of Jupiter, U. Ariz. Press, 93-128.
- Finnerty, A., G. Ransford, D. Pieri, and K. Collerson (1981) Nature **289**, 24-27.
- Golombek, M., and B. Banerdt (1986) Icarus **68**, 252-265.
- Hawkes, I., and M. Mellor (1972) J. Glaciology **11**, 103-131.
- Jaeger, J., and N. Cook (1976) Fundamentals of Rock Mechanics, Halsted Press.
- Lucchitta, B., and L. Soderblom (1982) Satellites of Jupiter, U. Ariz. Press, 521-555.
- Ransford, G., A. Finnerty, and K. Collerson (1981) Nature **289**, 21-24.
- Schenk, P., (1984) Adv. Plan. Geol., NASA TM-86247, 3-111.
- Schenk, P. and W. McKinnon (1987) Icarus, in review.
- Squyres, S., R. Reynolds, P. Cassen, and S. Peale (1983) Nature **301**, 225-226.



## EARLY THERMAL PROFILES OF GANYMEDE AND CALLISTO

Matthew P. Golombek and W. Bruce Banerdt (Jet Propulsion Laboratory, California Institute of Technology, Mail Stop 183-501, 4800 Oak Grove Drive, Pasadena, California 91109)

On Ganymede, the earliest tectonic features, furrows, have been used to estimate early thermal gradients through a model that relates the thickness of the brittle lithosphere to its temperature profile (Golombek and Banerdt, 1986). One assumption necessary for the model calculation is the strain rate, which has been assumed to have occurred over geologic time scales. However if furrows on Ganymede are rings around an ancient impact, the strain rate must be modified by orders of magnitude to simulate deformation over basin collapse time scales. With this modification, the model can also be used to estimate the early thermal gradient on Callisto from the ring structures around Valhalla. In this abstract we briefly discuss the furrows on Ganymede and similar rings around the Valhalla basin on Callisto, estimate the brittle lithosphere thickness from these structures, calculate the thermal gradients for these times on Ganymede and Callisto, and discuss the results in terms of other estimates of thermal gradient and extant thermal models.

Rimmed furrows on Ganymede are a system of broadly arcuate troughs 6-10 km wide, a few hundred meters deep with slightly raised rims and smooth floors. Their regular spacing, simple geometry, and negative relief have led most workers to conclude they are grabens (McKinnon and Melosh, 1980; Golombek, 1982). Furrows are the oldest geological features preserved on Ganymede and are overprinted by all craters, including the oldest topographically subtle palimpsests (Shoemaker et al., 1982). Features similar to the furrows, but slightly wider (15-20 km), are also found around a portion of the ancient Valhalla basin on Callisto. This led McKinnon and Melosh (1980) to suggest that these structures on both planets are rings formed around large impact basins. A lack of concentricity between some furrows on Ganymede (Zuber and Parmentier, 1984) led other workers to question this origin for furrows and suggest an endogenic origin (Thomas et al., 1986; Cassachia and Strom, 1984). This criticism has been countered by Schenk and McKinnon (1986), who have shown that the same degree of nonalignment and noncircularity occur for the rings around the Valhalla basin. Thus, furrows on Ganymede may, in fact, be ring structures around an ancient impact. If true, then estimates of the thermal gradient can be made from the furrows and rings using our model over basin collapse time scales.

The width of furrows and rings can be used to estimate the thickness of the brittle lithosphere at the time of their formation. The morphology of the furrows and rings suggests they are simple grabens. Simple graben are bounded by two downward converging normal faults that probably initiated near their intersection point at depth

(e.g. Golombek, 1982). For bounding fault dips of about  $60^\circ$ , the thickness of the brittle lithosphere is straightforward to calculate, given that major throughgoing faults initiate near this depth (see discussion in Golombek and Banerdt, 1986). This suggests a 5-10 km thick brittle lithosphere for the 5-10 km wide furrows on Ganymede. The analogous rings around Valhalla are 15-20 km wide, suggesting a 15-20 km thick brittle lithosphere on Callisto.

The thickness of the brittle lithosphere, or the region above the brittle-ductile transition, can be determined from a model using a combination of the frictional resistance to sliding on pre-existing fractures or the brittle yield stress and the ductile flow law. The intersection depth between the curves is the brittle-ductile transition, which is dependent on the thermal gradient and strain rate for a given icy lithosphere. We have assumed standard parameters describing the frictional and ductile behavior (see Golombek and Banerdt, 1986 for a more complete discussion of the model and parameters used). We have completed this calculation for furrows and grooves on Ganymede assuming they formed over geologic strain rates,  $10^{-15}$ /sec or 3%/m.y., and obtained a thermal gradient of  $1.5-6^\circ/\text{km}$  for the furrows on Ganymede (Golombek and Banerdt, 1986). However, if the furrows formed from collapse of a large basin, a strain rate of  $10^{-8}$ /sec is applicable if the roughly 1% strain was accommodated over basin collapse time scales, on the order of a week. Using this strain rate, the 5-10 km thick brittle lithosphere on Ganymede during formation of the furrows suggests thermal gradients of  $10-20^\circ/\text{km}$ , 3-6 times greater than for the slower strain rate. The 15-20 km thick brittle lithosphere for the analogous rings around Valhalla on Callisto yield thermal gradients of  $4-7^\circ/\text{km}$ . These results suggest that there was a factor of three difference between early (around 3.9 b.y. old) thermal gradients on Ganymede and Callisto, in qualitative agreement with the lack of endogenic geologic activity on Callisto and its abundance on Ganymede.

These results are also of interest when placed in the context of other estimates of the thermal gradient and extant thermal models. These estimates of the temperature gradient in the early lithospheres of Ganymede and Callisto are remarkably similar to estimates made by McKinnon and Parmentier (1986) based on a much simpler model relating thermal gradient to lithosphere thickness during basin collapse. However both estimates are about 4 times greater than thermal gradients derived by Passey and Shoemaker (1982) from the effective viscosity of the lithosphere inferred from the profiles of the most relaxed craters on the cratered terrain. In addition, the temperature profiles derived herein for both Ganymede and Callisto are up to 2 times greater than the heat flow for that time from models of fully differentiated satellites based solely on radioactive heating assuming chondritic abundances (McKinnon and Parmentier, 1986). Conversely, if the furrows on Ganymede did form over geologic time scales, then the thermal gradients they indicate are very close to other estimates (Passey and Shoemaker, 1982;

Kirk and Stevenson, 1983) and close to the heat flow for an undifferentiated model of Ganymede from radioactive heating (McKinnon and Parmentier, 1986). Nevertheless, because there is little question about the formation of the Valhalla rings over basin collapse time scales, the geologic strain rate estimates for furrows on Ganymede actually imply a slightly higher early temperature on Callisto ( $4-7^{\circ}/\text{km}$ ) than Ganymede ( $1.5-6^{\circ}/\text{km}$ ), which appears contrary to their divergent geologic histories. Consequently, it seems clear that if these estimates of early heat flow are to be used effectively for constraining the thermal evolution of these icy satellites, determination of the origin (i.e., impact versus endogenic) of the furrows on Ganymede must be made.

#### References

- Cassachia & Strom (1984) Proc. Lunar Plan. Sci. Conf. 14th, J. Geophys. Res. 89, B419.
- Golombek (1982) Proc. Lunar Plan. Sci. Conf. 13th, J. Geophys. Res. 87, A77.
- Golombek & Banerdt (1986) Icarus 68, 252.
- Kirk & Stevenson (1983) Lunar Plan. Sci. XIV, 373.
- McKinnon & Melosh (1980) Icarus 44, 454.
- McKinnon & Parmentier (1986) Satellites, 718.
- Passey & Shoemaker (1982) Satellites of Jupiter, 379.
- Shoemaker, Lucchitta, Wilhelms, Plescia & Squyres (1982) Satellites of Jupiter, 435.
- Schenk & McKinnon (1986) Lunar Plan. Sci. XVII, 764.
- Thomas, Forni & Masson (1986) Earth Moon Plan. 34, 35.
- Zuber & Parmentier (1984) Icarus 69, 200.

**TECTONIC AND VOLCANIC EVOLUTION OF DARK TERRAIN ON GANYMEDE AND ITS IMPLICATIONS FOR INTERNAL STRUCTURE AND EVOLUTION.** Scott L. Murchie and James W. Head, Dept. of Geological Sciences, Brown University, Providence, RI 02912; Jeffrey B. Plescia, U.S. Geological Survey, 2255 N. Gemini Dr., Flagstaff, AZ 86001.

**Introduction.** Half of Ganymede's surface consists of heavily cratered dark terrain which contains sets of parallel to subparallel furrows [1,2]. The commonly accepted model of dark terrain evolution is developed around three central hypotheses [3,4,5,6]: (a) furrows were formed by large impacts on rapid time-scales; (b) dark terrain is the silicate-contaminated, primordial crust of a differentiated ice mantle; and (c) a dense, Callisto-like crater population was removed by viscous relaxation. In this study, we undertake a detailed analysis of dark terrain geology (a) to characterize the formation and evolution of dark terrain and (b) to determine any implications of dark terrain geology for Ganymede's internal structure and evolution. We utilize: (a) maps of both structures and resolvable dark material units; (b) crater-density measurements; (c) calculations of crater-ages of different dark terrain surfaces, based on the impactor flux history and apex-antapex heliocentric flux gradient of [7]; and (d) testing of multiple hypotheses of furrow origin. Our assumption of a heliocentric impactor population is justified by the apex-antapex gradient recognized on Callisto [7], and by our discovery that in some areas calculation of crater-ages of different dark material units requires this assumption for the crater-ages to be consistent with relative ages based on stratigraphy.

**Geology of dark terrain.** The most conspicuous dark-terrain structures are two hemispheric-scale furrow systems, designated systems I and III by [8,9]. System I is located in Marius Regio and Galileo Regio, is dominated by arcuate furrows arranged approximately concentrically to a faint, giant crater palimpsest [3,4,8,9], and contains subradially-arranged furrows having variable lengths and age relations with the arcuate furrows [8,9,10]. System III is located in Perrine Regio, Barnard Regio, and Nicholson Regio, and is dominated by arcuate furrows arranged concentrically to a point in younger light terrain north of Perrine Regio [2,8,9]. No conspicuous ridges or obvious compressional features occur within either system I or III. Furrows in both systems crosscut extremely few older craters, yet occur on material units with significantly different crater-ages ranging between 3.8 and 4.1 Gyr (Figures 1 and 2). Many furrows are partly buried by smooth to hummocky dark materials that appear to have emanated from other furrows, most notably in Galileo Regio [10], central Marius Regio [11], and northwest Nicholson Regio. Younger furrows cut both these resurfacing materials and partially buried craters, yet have morphologies and orientations similar to those of the older furrows. These relations suggest that systems I and III developed over a prolonged period by global extension, possibly in preexisting fracture zones, and that furrow formation was closely related to emplacement of volcanic materials that buried preexisting topography.

The youngest furrow system, system II [8,9,10], is  $\geq 110^\circ$  of arc in radius and contains troughs that are arranged radially to a point about  $40^\circ$  of arc east of the center of system I. System II cuts all dark materials but is buried by younger light terrain, and is therefore about 3.8 Gyr in age. Dark terrain structures and volcanic materials exhibit four additional types of symmetry relative to the center of system II. First, the total thickness of accumulated dark-material deposits, estimated from (a) areal extents of individual deposits and (b) thicknesses of the deposits that are required to bury preexisting topography (1-3 km), decreases from 4-8 km near the center of system II to 1-3 km near the antipode. Second, almost all of the materials which bury system I furrows are circumscribed by a small circle  $70\text{-}80^\circ$  of arc in radius that is centered on the center of system II. Third, surface crater-ages are youngest near the center of system II (3.8-3.9 Gyr) and increase to 4.0-4.1 Gyr toward the antipode. Fourth, the density of system I furrows is greatest within  $50^\circ\text{-}60^\circ$  of arc of the center of system II.

**Origin of the furrow systems.** We tested nine models of furrow origin, by comparing predicted and observed furrow morphology, age relations, spatial organization, and association with impact and volcanic features. These models include: (a) impact-generation of a multiringed structure [12]; (b) fracturing driven by an impact-generated tsunami [13]; (c) fracturing of an isostatic, thermal uplift [14]; (d) fracturing of a dynamic uplift over an upwelling convection current [14]; (e) negative diapirism [15]; (f) reactivation of conjugate tidal fractures [16]; (g) reactivation of parallel tidal fractures; (h) reactivation of fractures produced as in (a); and (i) reactivation of fractures produced as in (b). Of these nine models, observational constraints on the origins of systems I and III are satisfied only by reactivation of impact-generated, multiringed structures by volcanism and global tension. System II is consistent only with fracturing of a circular, isostatic uplift in an environment of global tension. Thus furrows are interpreted to be endogenic features that developed on geologic time-scales, although most of them reused preexisting structures.

**Dark terrain origin and crater removal.** The significant thickness of dark materials ( $\sim 5$  km), their mode of emplacement, their global extent, and evidence that light terrain only shallowly buries downdropped dark blocks [17] together indicate that Ganymede possesses a dark, volcanic "crust." Dark terrain of a wide crater-age range contains undegraded furrows which are commonly associated with smooth to hummocky resurfacing materials [9,10]; such furrows crosscut older craters only very infrequently. A significant number of craters is crosscut only in the second oldest dark terrain area, southeastern Nicholson Regio, and these

craters retain significant relief. In areas possessing more degraded furrows (e.g. central Marius Regio [11], northwest Nicholson Regio), large craters are flattened and commonly embayed by dark materials. These same areas are characterized by depletion of craters <20 km in diameter, indicating that extensive resurfacing has occurred (see [11]). These observations support the hypothesis of [18], that volcanic infilling rather than viscous relaxation was the primary agent of crater degradation and removal in dark terrain.

**State of internal differentiation.** The scale of system II ( $\geq 110^\circ$  of arc in radius) and its radial symmetry require that the isostatic uplift on which it is interpreted to have formed was both circular [19] and hemispheric in scale. The only plausible genetic mechanism for so large and circular an uplift is thermal uplift over the gradually warming, upwelling current of a single, global, axisymmetric convection cell. The concentrations of young, thick volcanic materials and fracturing around the center of system II are consistent with locally thinned lithosphere and high advective heat loss, and thus support this hypothesis.

One-celled convection requires that the radius of any convectively isolated core was  $\leq 0.27$  times the global radius [20]. Such a volume of silicate-enriched material could have been produced by partial accretional melting of a thin outer layer of the satellite, followed by sinking of the silicate-rich fraction through underlying, less dense material. The resulting clean-ice upper mantle would be  $\leq 20$  km thick, and the bulk of the satellite would have remained cold and undifferentiated. Long-term radiogenic warming of such a cool, homogeneous interior would have led initially to 1-celled convection [21], accompanied by thermal uplift over the warming upwelling current as is proposed above. Warming of an undifferentiated interior is also consistent with two further constraints on the geology of Ganymede. First, global tension is interpreted to have occurred throughout furrow formation, and such stress is a predicted consequence of the warming of an undifferentiated interior [22]. Second, the width of endogenic tectonic features decreased with time, implying that the lithospheric thermal gradient [23] and presumably upper-mantle temperature increased with time.

**Implications for dark material composition.** Volcanic and tectonic patterns in dark terrain suggest that 1-celled, whole-mantle convection occurred throughout dark terrain evolution. [24] showed that whole-mantle convection of Ganymede would have broken down into layered convection if the interior became warmer than  $\sim 40^\circ\text{K}$  less than the melting point of pure  $\text{H}_2\text{O}$ -ice. Thus, given that whole-mantle convection did occur, dark material could not have been emplaced by melting and eruption of pure water. Among other cosmochemically abundant volatiles,  $\text{CH}_4$ ,  $\text{CO}$ , and  $\text{CO}_2$  would occur as clathrates, which require even higher temperatures to melt [25]. However, eutectic  $\text{NH}_3$ - $\text{H}_2\text{O}$  solution forms at temperatures and pressures expected to occur in ice-II during whole-mantle convection [26]. If our interpretation of whole-mantle convection is correct, then ascent and eruption of this liquid is the most likely mechanism of dark-material emplacement.

**Conclusions.** The results of this study present a paradigm of dark terrain evolution that is radically different from the commonly accepted model: (a) furrows are endogenic and formed on a geologic time-scale; (b) dark terrain consists of a thick layer of volcanic materials; and (c) a dense, Callisto-like crater population was removed by volcanic infilling. Early radiogenic heating of an undifferentiated,  $\text{NH}_3$ -bearing satellite interior would have been accompanied by the same global processes that are interpreted to have occurred during dark terrain evolution: (a) global expansion and tension; (b) one-celled, whole-mantle convection and hemispheric-scale thermal uplift; (c) long-term lithospheric thinning; and (d) melting and eruption of low-melting-point volcanic material.

**References.** [1] Smith, B. et al., *Science*, 204, 951-972, 1979a. [2] Smith, B. et al., *Science*, 206, 927-950, 1979b. [3] Shoemaker, E. et al., in *The Satellites of Jupiter*, ed. by D. Morrison, pp. 435-520, Univ. of Arizona, Tucson, 1982. [4] Passey, Q. and E. Shoemaker, in *The Satellites of Jupiter*, ed. by D. Morrison, pp. 379-434, Univ. of Arizona, Tucson, 1982. [5] McKinnon, W. and E.M. Parmentier, in *Satellites*, ed. by J. Burns and M. Matthews, pp. 718-763, Univ. of Arizona, Tucson, 1986. [6] Schenk, P. and W. McKinnon, *Lunar Planet. Sci. XVII*, 764-765, 1986. [7] Shoemaker, E. and R. Wolfe, in *The Satellites of Jupiter*, ed. by D. Morrison, pp. 277-339, Univ. of Arizona, Tucson, 1982. [8] Murchie, S. and J. Head, *Lunar Planet. Sci. XVII*, 581-582, 1986. [9] Murchie, S. and J. Head, *Lunar Planet. Sci. XVIII*, 682-683, 1987. [10] Casacchia, R. and R. Strom, *J. Geophys. Res.*, 89, B419-B428, 1984. [11] Croft, S., *Lunar Planet. Sci. XVIII*, 209-210, 1987. [12] McKinnon, W. and H. Melosh, *Icarus*, 44, 454-471, 1980. [13] Van Dorn, W., *Nature*, 220, 1104-1107, 1968. [14] Banerdt, W. et al., *J. Geophys. Res.*, 87, 9723-9733, 1982. [15] Janes, D. and H. Melosh, *Lunar Planet. Sci. XVIII*, 458-459, 1987. [16] Thomas, P. et al., *Earth Moon Plan.*, 34, 35-53, 1986. [17] Schenk, P. and W. McKinnon, *J. Geophys. Res.*, 90, C775-C783, 1985. [18] Woronow, A. et al., in *The Satellites of Jupiter*, ed. by D. Morrison, pp. 237-276, Univ. of Arizona, Tucson, 1982. [19] Withjack, M. and C. Scheiner, *AAPG Bull.*, 66, 302-316, 1982. [20] Zebib, A. et al., *Geophys. Astrophys. Fluid Dynamics*, 23, 1-42, 1983. [21] Hsui, A. et al., *Geophys. Fluid Dynamics*, 3, 35-44, 1972. [22] Zuber, M. and E.M. Parmentier, *J. Geophys. Res.*, 89, B429-B437, 1984. [23] Golombek, M. and W. Banerdt, *Icarus*, 68, 252-265, 1986. [24] Bercovici, D. et al., *Geophys. Res. Lett.*, 13, 448-451, 1986. [25] Davidson, D., in *Water: A Comprehensive Treatise*, ed. by F. Franks, pp. 115-234, Plenum Press, New York, 1973. [26] Johnson, M. et al., *J. Geophys. Res.*, 92, 6339-6349, 1987.

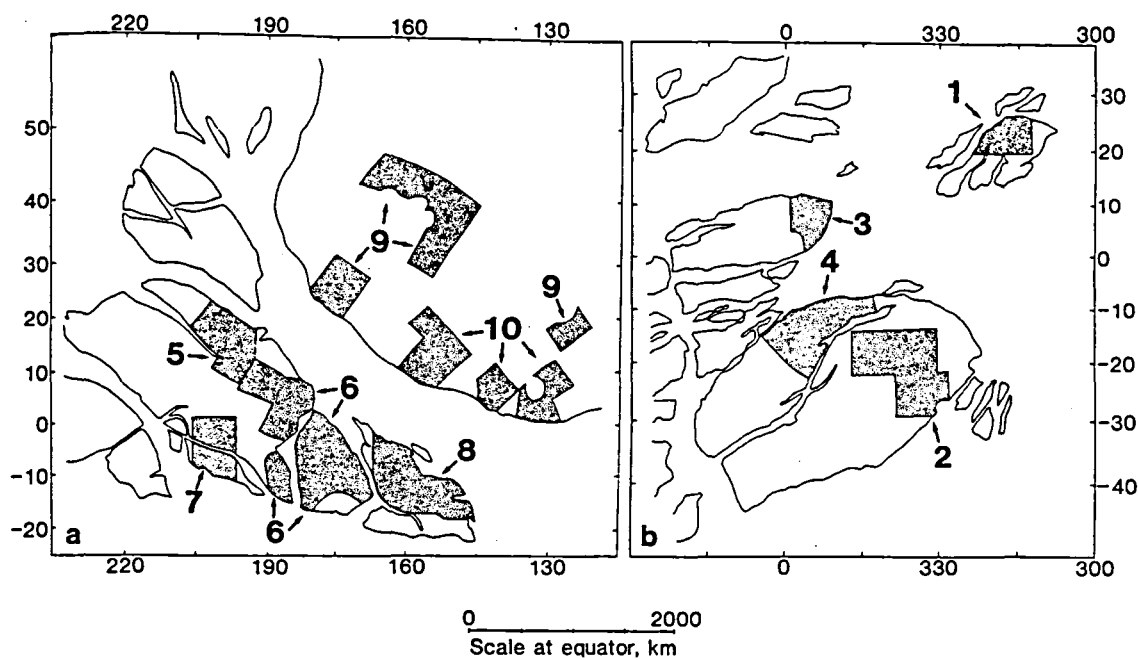


Figure 1. Mercator map of dark terrain areas from which crater-counts were compiled.

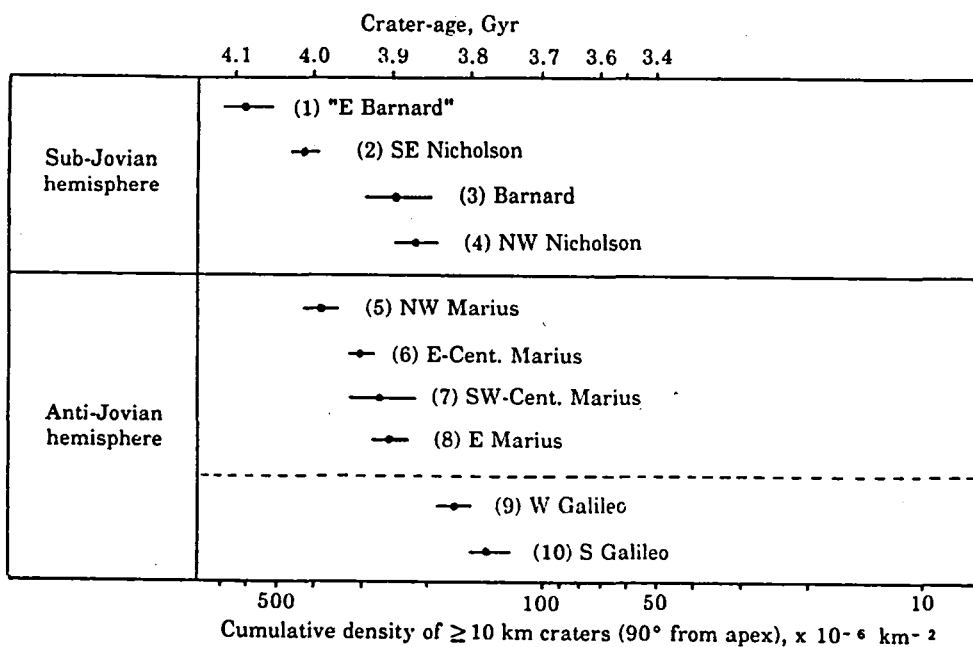


Figure 2. Calculated crater-ages of areas shown in Figure 1.

## CHAPTER 12

### GEOLOGIC MAPPING, CARTOGRAPHY, AND GEODESY





## GEOLOGY OF SIX POSSIBLE MARTIAN LANDING SITES.

Harold Masursky, A.L. Dial, Jr., M.E. Strobell, and D.J. Applebee, U.S. Geological Survey, Flagstaff, Arizona 86001

Thirteen detailed geologic maps of the first six (of ten) possible sites for a future lander/rover/sample-return mission to Mars are either nearing completion or in review. Base mosaics of all sites were available at 1:2 million scale. Mosaics at 1:1/2 million scale have been compiled for the Chasma Boreale (North Pole), Planum Australe (South Pole), Mangala Valles, and Kasei Valles sites; a new base at this scale has been compiled for the Olympus Rupes site and one is being prepared for the Memnonia Sulci site. Study is underway of four additional sites: Candor Chasma, Elysium Montes, Apollinaris Patera, and Nilosyrtris Mensae. In addition to preparing new base maps, we have generated special enhancements of computer mosaics and individual images that delineate the geologic units more clearly, and we have prepared photoclinometric profiles that allow us to measure the thicknesses of geologic units, the depth of channels, and the throw on faults. Topographic profiles and diffuse-scattering data, derived from Earth-based radar data, are being used to evaluate surface slopes and roughness parameters at the equatorial sites; Viking bistatic radar data are being used to determine roughness at the north polar site. Crater counts have been made for each geologic unit.

At the East and West Mangala Valles sites (the West Mangala site is shown in Fig. 1), terrain (unit Nc) is exposed that is thought to be very ancient because it is greatly degraded and does not show layering. Composition of this unit may be similar to lunar norites (ANT suite) or terrestrial granitoid-greenstones, the most ancient material on the Moon and Earth. In the eastern part of the map area, these ancient rocks are mostly covered by intercrater plains material (unit Hpi) that was deposited over a long period of time and is interpreted to be lava flows of possible basaltic or intermediate composition. For the first time, crater-density curves derived from this and other upland units, as we have subdivided them, yield relative ages that are consistent with stratigraphic relations shown by geologic mapping [1,2]. At the East Mangala site, an east-trending fault separates these upland rocks from a series of lava flows that comprise the northern lowland plains. They are thought, from their morphologic characteristics, to be basaltic in origin. These northern flows are overlain, in turn, by young volcanoclastic, probably pyroclastic, flows (unit Apt) that are thought from morphologic characteristics to be rhyolitic in composition. Three generations of fluvial channels (some young) are interspersed within these putative basaltic and volcanoclastic layered rocks; north-trending and east-trending fault zones cut all units except the young volcanoclastic material. These stratigraphic relations are clearly shown in computer-enhanced images.

Rock units in the Memnonia Sulci area are thought to be similar in age and composition to those recognized in the Mangala Valles area (D. H. Scott, written commun., 1987), but the stratigraphic relations are more clearcut at Memnonia. The Memnonia site has one very young channel.

The Olympus Rupes site is situated on smooth plains material (unit Aop) near the southeast flank of Olympus Mons. The gross shape of the volcanic shield and the shapes of individual flows indicate that the shield probably is basaltic but that composition may vary among the four recognizable units (E.C. Morris, written commun., 1987). The construct is bounded by a scarp--Olympus Rupes. At the base of the scarp, lobate flows that may also be basaltic in composition form a smooth plains unit; these flows appear to be younger than the flows that form the volcanic construct and are considered to be among the youngest flows on

Mars [3]. A few young flank flows cascade over the basal fault scarp and may overlie the smooth plains unit.

In the Kasei Valles area, a broad fluvial valley has been carved into layered plateau rocks of Lunae Planum that are of intermediate age. In the southern part of the Kasei site, the broad channel is buried by younger volcanic flows, probably basaltic in composition, that were emitted from sources to the west. Unfortunately, these flows are so widespread that a rover of limited range could not obtain samples of a variety of units. Farther north, where the broad Kasei channel bends and flows eastward, it is cut by a narrow inner channel. Small channels have furrowed the walls of the broad channel and constructed alluvial fans on the floor of the inner channel. Finally, a lava flow, probably basaltic, covered the inner channel and partly buried the fan deposits.

In the north and south polar regions, older rocks are buried by polar layered deposits. These deposits are interpreted by us and by many other investigators (e.g., [4], [5]) to be made up of a multitude of icy layers that contain lesser and greater amounts of dust. At both poles, the layered deposits are overlain by a brighter polar ice cap. In the north (Fig. 2), the cap is water ice; in the south, Viking observations suggest that the cap possibly may be water ice with a surface layer of carbon dioxide ice. Viking bistatic radar data show the north polar area to be one of the smoothest on the planet [6]. The north polar layered deposits are fringed by an enormous erg of dunes that are probably composed of sand grains resedimented as an aggregate of partly cemented silt- and clay-sized particles that move by saltation to form dunes. Similar dunes are common around playa lakes in Nevada. False-color sliced enhancements of polar images show that the ice caps also are layered. It should be possible to construct a complete section of the polar deposits by combining and correlating a series of meter-length cores obtained at many stations (Fig. 2).

We hope to learn as much about near-term climatic changes on Mars by studying the polar deposits as we have learned about the Earth's climatic changes by studying ice cores from Greenland and the Antarctic and deep sea cores. Also, we hope that study of samples from equatorial sites will elucidate the sequence of volcanic, tectonic, and fluvial events in that region and the effect of these events on the climate and geologic history of Mars.

The Mars Observer will image these areas with 10 to 40 times the present resolution and will also obtain geophysical and geochemical data; these data will be used to determine the geologic and engineering suitability of each candidate site.

References: [1] Masursky, Harold, et al., 1986: 18th Lun. and Plan. Sci., 600-601. [2] Masursky, Harold, et al., in A preliminary study of Mars Rover/Sample Return Missions conducted by the Mars Study Team: NASA Headquarters, January, 1987. [3] Scott, D.H. et al., 1982: USGS Misc. Inv. Ser. Map I-1266. [4] Murray, B.C. et al., 1972: Icarus, 17, 328-345. [5] Howard, A.D., Cutts, J.A., and Blasius, K.R., 1982: Icarus, 50, 161-215. [6] Simpson, R.A., Tyler, G.L., Hamon, J.K., and Peterfreund, A.R., 1982: Icarus 49, 258-283.

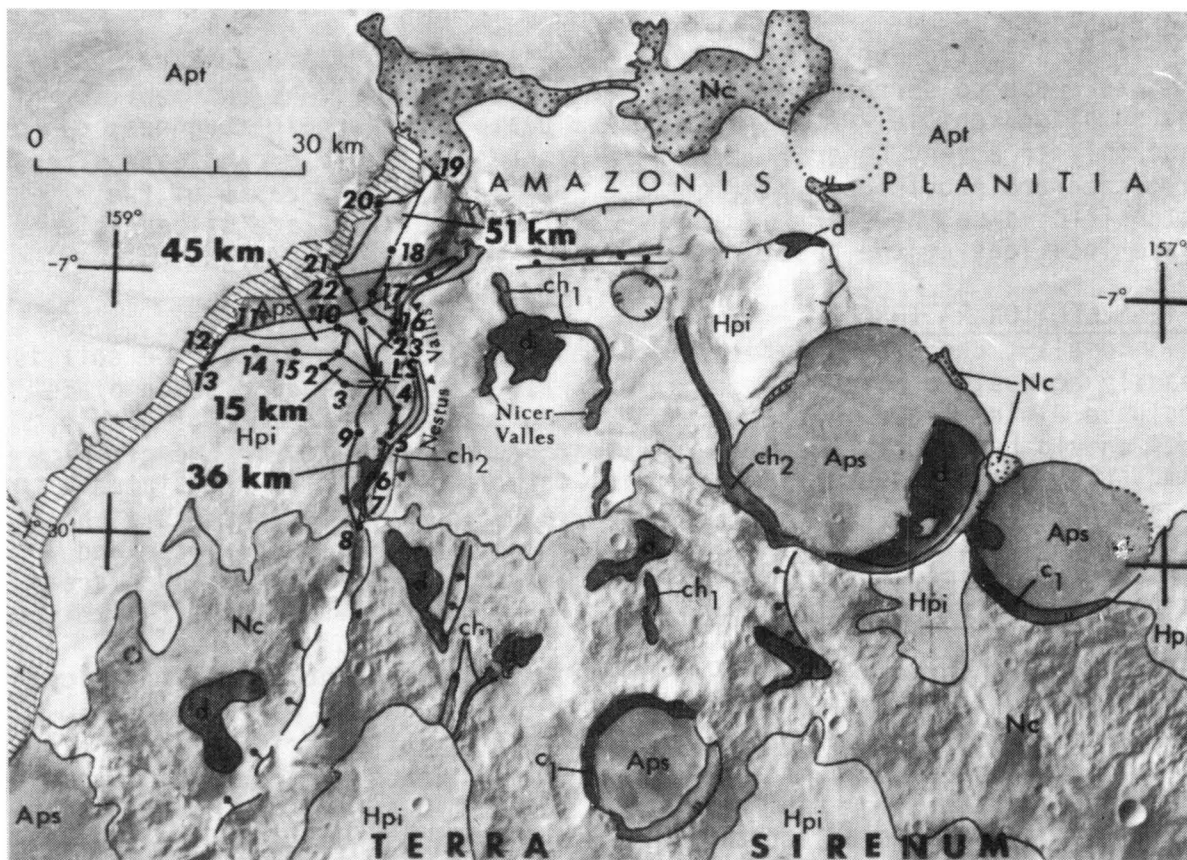


Figure 1. Geologic map and proposed rover traverse of the West Mangala Valles area, Mars.

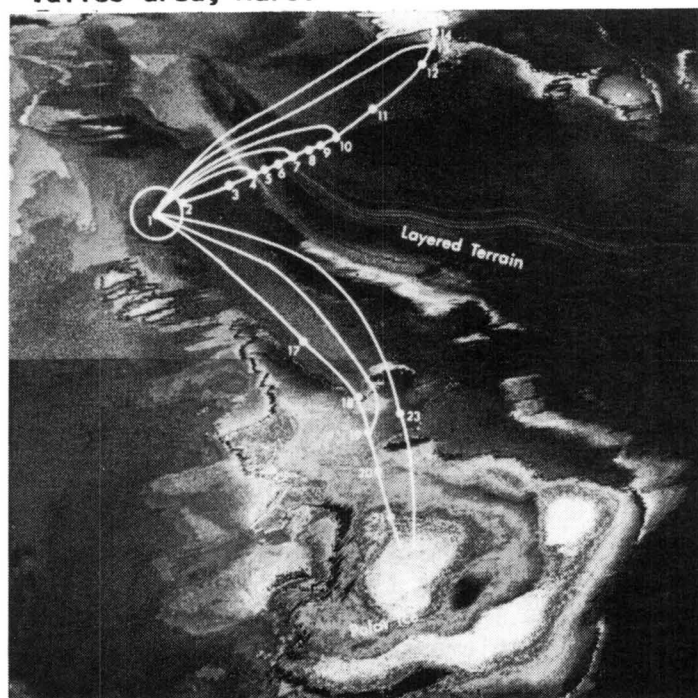
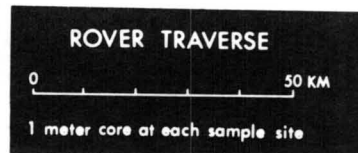


Figure 2. North polar area of Mars: a computer enhanced mosaic showing proposed rover traverse and core drill stations.



## INTRODUCTION

Site-selection priorities for a Mars sample return are constrained by the risks due to terrain that affect the successful descent and mobility of the sampling vehicle. At this time, evaluations of terrain roughness can be made only in a very general way. For this reason, the two candidate sites discussed are provisionally recommended primarily on the basis of their scientific value; however, no adverse surface conditions are discernible at these locations at the resolution of Viking images.

## SITE-SELECTION RATIONALE

Ideally, the site should be located where a suite of rocks and soil is readily accessible to the sampling vehicle. The rocks should be in place and have a wide range in age, lithology, composition, and mode of origin. They should be correlative with other major geologic units in the global time-stratigraphic system. Some of the materials should be associated with important volcano-tectonic episodes and magmatic histories, others with fluvial, eolian, and polar processes that are indicators of climate and atmospheric history. Ultimately, the ideal site would also be in an area where evidence of present or former biological activity would most likely be found.

With our present knowledge of Mars, we have found no single locality where such optimum conditions exist. On the other hand, many areas are known where rock samples would resolve specific problem-oriented questions. Such a narrow focus, however, would leave untouched the broader aspects of Mars geology and history.

The two sample sites considered represent a compromise between broad-based objectives and specific, but highly important, problems that cannot be resolved without material samples. They were selected on the basis of information gained during the global geologic mapping of Mars (1,2,3). Locations are biased toward the western equatorial and polar regions, with which this investigator is most familiar.

SITE 1 (Fig. 1) Tharsis-Olympus Region. The location is about lat 12.5° N., long 125.5°, within the relatively flat, smooth-appearing plains member of the Olympus Mons Formation (unit Aop<sub>1</sub>). This Upper Amazonian member is composed of some of the youngest lava flows on Mars. It extends for more than 2,000 km around the eastern and southern parts of the basal scarp of Olympus Mons. The flows embay a large block of old (Hesperian) fractured crust (unit Hf) as well as the lowermost member (unit Aoa<sub>1</sub>) of the Olympus Mons aureole deposits of Early Amazonian age. The site is within 15 km or less of both of these older units. Sample ages and compositions of these three units would (1) reveal stages in the volcano-tectonic history of one of the largest and most geologically important regions of Mars, (2) provide an upper time limit on the cessation of major faulting in the western hemisphere, (3) closely define the time of occurrence of the last major volcanic episode of both Olympus Mons and Tharsis Montes, (4) answer controversial questions on the composition and origin of aureole deposits around Olympus Mons, (5) provide an upper limit on the time of major flooding in Kasei Valles, and (6) determine indirectly, by enabling correlations of geologic units (possibly supplemented by crater counts), the times of formation of other materials in a large area.

**SITE 2 (FIG. 2) Chasma Boreale (North Polar) Region.** The location is about  $82^{\circ}$  N., long  $57^{\circ}$ , within polar ice and layered terrain materials (units Api, Apl) of probable very late Amazonian age. The dusty ice surface appears smooth and flat to gently sloping; gentle slopes are also suggested by a broad streaked appearance such as would occur where a slightly inclined surface transects nearly horizontal layers of contrasting albedo. Samples could be obtained here from four different types of materials ranging in age from probably very recent to Hesperian: (1) Interbedded ice and dark material (silicate dust?) surrounding the landing site for tens of kilometers. (2) Grooved and polygonally patterned material (unit Hvg) underlying the layered terrain and within 25 km or less from the landing site; this material occurs in patches throughout the northern plains and south of lat  $40^{\circ}$  S. in Mare Acidalium. (3) Ejecta from a sharp-rimmed, 5-km-diameter crater within 20 km of the site; the crater (unit c) lies on grooved material (unit Hvg) and is partly embayed by layered terrain materials. (4) Cliff-forming material, appearing as a thick, massive layer, within 15 km of the site; this material of unknown age, origin, and composition underlies some layered deposits but may be interbedded with others. It appears to overlie the Hesperian grooved unit. The geological interpretation shown in Fig. 2 was made from a photomosaic (1:500,000 scale) compiled from Viking 2 images taken at approximately LS  $53^{\circ}$  (spring). A visit to this site during late northern summer would probably reveal geologic material units covered by less ice and frost.

Geological and geochemical data from these sampled materials would contribute to understanding climatic and atmospheric changes and processes affecting the development of Mars' polar caps. They would also unlock some geologic secrets of the vast northern lowlands that presently elude observation.

Other Mars sample-return sites have been investigated (4, 5, 6) that would also yield valuable data, but the two sites discussed above are believed to be among the best at this stage in our understanding of the geologic history of Mars.

- (1) Scott, D.H., and Tanaka, K.L. (in press), U.S. Geol. Survey Misc. Inv. Map 1802A.
- (2) Tanaka, K.L., and Scott, D.H. (in press), U.S. Geol. Survey Misc. Inv. Map 1802C.
- (3) Greeley, R., and Guest, J.E. (in press), U.S. Geol. Survey Misc. Inv. Map 1802B.
- (4) Masursky, H., and others, 1986, NASA TM 88380, p. 459.
- (5) Masursky, H., and others, 1987, Lunar and Planet. Sci. Conf. 18, p. 600-601.
- (6) Scott, D.H., and Tanaka, K.L. (Abstract, this volume).

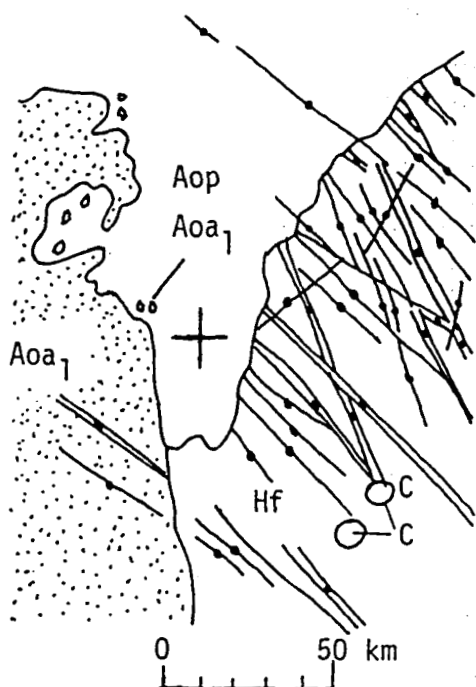


Fig. 1 Site #1 Tharsis-Olympus Region  
Location: lat 12.5°N., long 125.5°

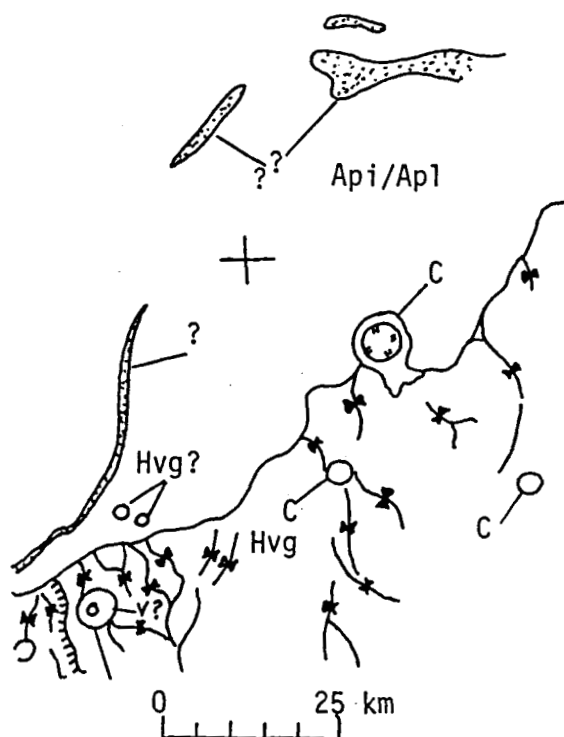


Fig. 2 Site #2 Chasma Boreale  
(North Polar) Region  
Location: lat 82°N., long 57°

**MARTIAN SAMPLE SITES: EXAMPLES BASED ON A GLOBAL GEOLOGIC PERSPECTIVE;** D. H. Scott and K. L. Tanaka, U.S. Geological Survey, 2255 N. Gemini Dr., Flagstaff, AZ 86001

We have selected ten areas that each include several rock units of varying lithology and age (Table 1); these areas were chosen to optimize the geologic and chronologic data return from Mars. Geologic mapping and stratigraphic studies [1-5] identify stratigraphic ages, rock types, and information on Martian geologic history that samples of a given site may yield (Table 2). Volcanic rocks occur over much of the planet and in virtually all stratigraphic positions, and they are amenable to radioisotopic dating. Therefore, a reasonable and essential goal for a sample-return mission is to return datable rocks from widely varying strata.

Generally, about three or four major geologic units can be sampled at any of the sites in Table 1, most of which can probably be dated (Table 2). The Mars Observer mission will aid greatly in interpreting lithology and defining contacts at the high resolution required to actually pinpoint fruitful sample-acquisition sites within these areas.

Table 1. Locations and Rock Units of Proposed Sample Areas

Site No.	Name	Location (lat, long)	Rock Units
1	Tharsis-Olympus	12°, 125°	Aop, flows of Olympus plains Aoa <sub>1</sub> , lowermost aureole of Olympus Mons Hf, fractured flows of Ulysses Fossae
2	Chasma Boreale	82°, 57°	Apl, polar layered material Hvg, grooved plains material c, crater material unmapped, thick deposit
3	Memnonia	-10°, 172°	Amm, middle member of Medusae Fossae Fm Hr, ridged plains material Nplh, hilly unit of plateau sequence
4	Labeatis north	31°, 83°	Ht <sub>2</sub> , member 2 of Tharsis Montes Fm Hr, ridged plains material Nf, highly deformed (faulted) material
5	Labeatis south	24°, 80°	At <sub>4</sub> , member 4 of Tharsis Montes Fm Ht <sub>2</sub> , member 2 of Tharsis Montes Fm Hr, ridged plains material
6	Solis	-27°, 100°	Hsl, lower member of Syria Planum Fm Hf, older fractured flows Nb, basement material
7	Hadriaca	-29°, 269°	Hhp, shield material of Hadriaca Patera Hpl <sub>3</sub> , smooth unit of plateau sequence Hr, ridged plains material Nm, mountains of Hellas rim material
8	Elysium	27°, 185°	Ael <sub>1</sub> , plains flows of Elysium Mons Hr, ridged plains material HNu, knobby remnants of plateau materials

9	Amazonis	22°, 165°	Aa <sub>3</sub> , flows of Amazonis Planitia Hr, ridged plains material HNu, knobby remnants of plateau materials
10	Promethei	-81°, 315°	Apl, polar layered terrain Hdu, upper flows of Dorsa Argentea c, rim material of south polar basin

Note: Sites 1 and 2 described in [6]; geologic units described in [1-3]

Table 2. Stratigraphic Positions, Lithologies, and Ages of Geologic Events at Proposed Sample Sites

Objective	Sites									
	1	2	3	4	5	6	7	8	9	10
a. Stratigraphic position										
Upper Amazonian	L	R*								R*
Middle Amazonian			R*						R	
Lower Amazonian	L				R			R		
Upper Hesperian	R	R*		R	R	R				R
Lower Hesperian			G	G	G	L	L,G	G	G	
Upper Noachian										
Middle Noachian				G				G	G	
Lower Noachian			G			G	R			R
Poorly defined or uncertain		L*								
b. Lithologies										
Lava flows	X		X	X	X	X	X	X	X	X
Polar layered material		X								X
Olympus Mons aureoles	X									
Impact crater material		X								X
Other materials		X	X			X	X	X	X	
c. Ages of geologic events										
Channeling					X					
Tectonism	X			X	X	X				
Impact		X				X				X

Note: Extent of units to be sampled at individual sites indicated by G=global, R=regional, and L=local; asterisk indicates that unit may be undatable. Stratigraphic positions defined by [4, 5].

#### References

- [1] Scott, D.H. and Tanaka, K.L. (1986) USGS Map I-1802-A.
- [2] Greeley, R. and Guest, J.E. (in press) USGS Map I-1802-B.
- [3] Tanaka, K.L. and Scott, D.H. (in press) USGS Map I-1802-C.
- [4] Tanaka, K.L. (1986) Proc. Lunar Planet. Sci. Conf. 17, E139-158.
- [5] Tanaka, K.L. and others (in press) Proc. Lunar Planet. Sci. Conf. 18.
- [6] Scott, D.H. (this volume).



VALLES MARINERIS, MARS: AN OPTIMUM SCIENCE-SAMPLE SITE  
B.K. Lucchitta, U.S. Geological Survey, Flagstaff, Ariz. 86001

The Valles Marineris troughs offer a unique sampling opportunity because they expose a thickness of upper crustal rocks as great as 7 km. Also, because of their long and varied history, the troughs give insights into a number of processes that are critical to deciphering the history of Mars.

Ideal sample sites on Mars would yield information on rocks in close proximity having a range of ages and compositions. The Valles Marineris fulfill these requirements. Very old units of Noachian age (1) are exposed in the lower walls that would give us data on compositions and ages of rocks that are deep below the surface at most other places. The most commonly accepted hypothesis is that these rocks are lunar highlands-type breccia (2). The landslides of the Valles Marineris also furnish excellent sites to sample these ancient rocks, because the slides fell from trough walls and thus incorporated wall rock. Additionally, most landslide materials contain some cap rock of the plateau, thus offering an opportunity to sample material of intermediate age (Early Hesperian) (1). The cap rock is commonly interpreted as flood basalts (3), but other compositions cannot be excluded. Younger intermediate-age rocks (Upper Hesperian) (1) form part of the layered interior deposits. Their origin is uncertain; they have been considered to be volcanic flows, fluvial deposits (4), or wind drifts trapped in ice-covered lakes (5). Samples of these rocks would illuminate an important segment of Martian mid-history and shed light not only on the composition of these materials but also on the processes that operated at that time.

A second suite of interior deposits occurs on the Valles Marineris floors, resting unconformably on all other units and reaching thicknesses of as much as 3,000 m in western Candor Chasma (6). These rocks are young, of Late Amazonian age, and are most likely of volcanic origin. They are locally composed of very dark materials that are easily reworked by the wind and may have come from young volcanic vents (7). Elsewhere these deposits are of varied albedo and rugged, and they may be composed of volcanic rock of unknown composition. Sampling these rocks and obtaining their precise compositions and ages would be an important contribution to unraveling the thermal evolution of Mars.

Samples from the Valles Marineris would also give insights into a number of Martian processes. The effects of tectonism could be assessed by sampling materials on both sides of young faults that cut the trough floors. Mass-wasting processes resulted in talus slopes and landslides. Whether the landslides were wet or dry is not entirely resolved; this question could be addressed by sampling the matrix of landslide deposits. Furthermore, a large channel appears to have emerged from one of the slides and caused a catastrophic flood (8); sampling of the channel-floor material might confirm this origin. The composition of the channel material may also establish whether ice was involved in the flooding. Water or ice in the channel must have come from the trough walls, and the discovery that either was present would confirm the existence of the hypothetical ground-ice reservoir on Mars.

Wind deposits are abundant on the channel floors. Dark barchan dunes consist of reworked dark material that appears to have come from volcanic vents in the troughs; samples of this material would give compositions and ages, and thus they might confirm the existence of such vents. Establishing grain sizes of the dune material would also shed light on the mechanism of emplacement and, by analogy, on the origin of many similar dunes elsewhere on Mars, particularly those trapped inside craters. Light-colored, reddish dust from atmospheric fallout is also abundant in the troughs and might be sampled to obtain its composition, thus resolving the controversy of whether dust-storm material is composed of smectite clay (9) or palagonite (10).

Overall, the Valles Marineris offer an opportunity to sample rocks that reflect various ages and compositions, giving insight into important processes on Mars. Most of the samples would be located within reasonable proximity and could be easily reached by rovers or balloons. Although landing a spacecraft on the floor of the Valles Marineris may be too dangerous for the first sample-return mission to Mars, the scientific rewards would be so great that such a landing should be considered for later flights.

#### References

- (1) Scott D.H. and Tanaka K.L. (1986) Geologic map of the western equatorial region of Mars: U.S. Geological Survey Miscellaneous Investigations Series Map I-1802A, scale 1:15,000,000.
- (2) Carr M.H. (1979) Formation of martian flood features by release of water from confined aquifers: *Journal of Geophysical Research*, v. 84, no. B6, p. 2995-3007.
- (3) Scott D.H. and Carr M.H. (1978) Geologic map of Mars: U.S. Geological Survey Miscellaneous Investigations Series Map I-1083, scale 1:25,000,000.
- (4) Lucchitta B.K. (1982) Lakes or playas in Valles Marineris (abs.), in *Reports of Planetary Geology Program--1982: National Aeronautics and Space Administration Technical Memorandum 85127*, p. 233-234.
- (5) Nedell S.S., Squyres S.W. and Anderson D.W. (1987) Origin and evolution of the layered deposits in the Valles Marineris: *Icarus*, v. 70, p. 409-441.
- (6) Lucchitta B.K. (1985) Young volcanic deposits in the Valles Marineris, Mars (abs.), in *Lunar Science 16: The Lunar and Planetary Institute, Houston, Texas*, p. 503-504.
- (7) Lucchitta B.K. (1987) Recent mafic volcanism on Mars: *Science*, v. 235, p. 565-567.
- (8) Lucchitta B.K. (in press) Valles Marineris, Mars: Wet debris flows and ground ice: *Icarus*.
- (9) Clark B.C. (1978) Implications of abundant hygroscopic minerals in the martian regolith: *Icarus*, v. 34, p. 645-665.
- (10) Singer R.B. (1982) Spectral evidence for the mineralogy of high-albedo soils and dust on Mars: *Journal of Geophysical Research*, v. 87, no. B12, p. 10159-10168.

## PRELIMINARY GEOLOGIC MAPPING IN THE MEMNONIA REGION OF MARS

James R. Zimbelman, Lunar and Planetary Institute, 3303 NASA Road 1, Houston, Texas 77058.

Introduction. Preliminary geologic mapping in the Memnonia region of Mars (7.5°S to 22.5°S, 145°W to 150°W) was carried out as part of the Mars Geologic Mapping project within the Planetary Geology and Geophysics Program. The end product of this project will be new geologic maps of selected areas of Mars at a scale of 1:500,000, using the MTM photomosaics as base maps. The work described here includes MTM sheets -10147, -15147, and -20147 (Fig. 1). The final geologic maps for these three sheets will result from collaboration with researchers at Arizona State University. The new maps should provide the data needed to address the following questions: 1) Is the martian dichotomy boundary at southern midlatitudes comparable in morphology and contact relationships to the boundary in the northern hemisphere? 2) Is there evidence of a local source for surface materials that are responsible for the remote sensing characteristics of the region? 3) What geologic processes have been most important in the formation of the landforms present in the Memnonia region? The preliminary results described here provides information that bears upon these questions but a thorough evaluation of the questions must await completion of the detailed mapping.

Background. Previous geologic maps of global (1,2) and regional (3) extent have delineated the major units present in the Memnonia region. Lightly cratered volcanic plains that originate near the Tharsis Montes cover most of the surface west of 147°W longitude while to the east the terrain consist of moderately to densely cratered plains, in places cut by the channeling events that produced Mangala Vallis (3). The 'dichotomy' of ages represented by the cratering history of the Memnonia plains units is part of a boundary that is global in extent, separating the old highlands of the southern hemisphere from the young lowlands of the northern hemisphere (1). The dichotomy boundary has attracted considerable attention in efforts to date the relative timing and superpositional relationships of units in the Isidis-Amenthes-Aeolis region (4,5,6) and the Nephenthes-Nilosyrtis region (7). The dichotomy boundary in the Memnonia region lacks the vertical relief associated with the boundary at other locations. Numerous grabens with a N70°E orientation cut across all of the plains units in the Memnonia region (3). The largest graben, Memnonia Fossae, is interpreted to be the source of the floods that carved Mangala Vallis (8).

Remote sensing results at thermal infrared and radar wavelengths reveal intriguing variations in surface properties in the Memnonia region. Radar scattering properties around Memnonia Fossae were interpreted in terms of the surface features visible in very high resolution (10 m/pixel) images with the result that both volcanic and aeolian materials contribute to modification of the radar signal (9). Global mapping at thermal infrared wavelengths indicates that the Memnonia region includes a sharp transition from the low thermal inertia that typifies the Tharsis area to the moderate thermal inertia representative of the southern midlatitudes (10). Comparison of thermal and visual characteristics in the Tharsis area (11) and in Sytris Major (12) indicates that thermal inertia variations in the Memnonia region may be related to the presence and relative thickness of an aeolian cover visible in very high resolution images.

**Results.** Eight major units have been identified in the study area (Fig. 2). The youngest units represent three episodes of channel erosion (ch<sub>3</sub>, ch<sub>2</sub>, ch<sub>1</sub>) that contributed to the formation of Mangala Vallis. The youngest channel unit (ch<sub>3</sub>) emanated from a large graben at 18.5°S, 149.4°W but the oldest channel unit (ch<sub>1</sub>) contains erosional features that do not point toward the source area of the youngest channel unit, so that an additional source of water may be the old mountain materials exposed near 16°S, 147°W. The youngest plains unit has a smooth surface texture (ps) at the resolution of the photomosaic images. An aeolian origin for the smooth plains presently is favored. The eastern portion of the map area consists of plains with numerous lobate ridges (pr), here interpreted to be flow fronts of lavas associated with the Tharsis Montes, Arsia Mons in particular. The oldest plains unit contains the highest density of impact craters (pc). The cratered plains are interpreted to be old lava flows that have experienced considerable reworking. The oldest units in the study area form a barrier between the ridged plains to the east and the smooth and cratered plains to the west. Hilly and cratered materials (hc) include numerous sinuous ridges that appear to be tectonic in origin. Isolated mountain areas (m) display a unique, finely grooved surface texture suggestive of a large amount of erosion. Both the hilly and cratered material and the mountain material seem to have undergone extensive modification. Map unit areas (in 10<sup>3</sup> km<sup>2</sup>) are: ch<sub>3</sub> (5), ch<sub>2</sub> (11), ch<sub>1</sub> (19), ps (43), pr (76), pc (24), m (22), hc (70).

Four classes of craters are observed in the study area. Class 4 craters are the youngest of the impact craters and they display distinct ejecta margins and surface texture, have raised rims with a sharp rim crest, and often have complex interior morphology. The class 4 craters are most common on the smooth plains and on the channel materials, where they have been eroded by the channeling process. Class 3 craters lack the ejecta detail evident in class 4 craters but the class 3 craters have raised rims and often have complex interior morphology. The class 3 craters are most common on the ridged plains. Class 2 craters have very subdued rims and flat, featureless floors. The class 2 craters are most common on the cratered plains and the highland materials. Class 1 craters are highly degraded, generally with incomplete rims. Two large class 1 craters are present in the study area, both occurring within the hilly and cratered material.

**Conclusions.** The preliminary mapping in the Memnonia region demonstrates that significant differences exist between the emplacement and modification histories of the ridged plains and the materials not covered by the volcanic flows from Tharsis. The contact relationships between the various map units appear to be dominated by superposition rather than truncation resulting from erosion, with the exception of the channel materials. Preliminary mapping revealed no immediate explanation for the latitudinal variation in remote sensing properties present in this area; examination of high resolution images during the detailed mapping should improve this situation.

This work was supported by NASA contracts NAGW-1223 and NASW-4066.

**REFERENCES:** (1) D.H. Scott and M.H. Carr, U.S.G.S. Map I-1083, 1978. (2) K.L. Tanaka *et al.*, NASA TM 88383, 601-602, 1986. (3) T.A. Mutch and E.C. Morris, U.S.G.S. Map I-1137, 1979. (4) H. Frey *et al.*, Lunar Planet. Sci. XVII, 241-244, 1986. (5) H. Frey *et al.*, Lunar Planet. Sci. XVIII, 302-305, 1987. (6) S. Bougan *et al.*, Lunar Planet. Sci. XVIII, 115-116, 1987. (7) T.A. Maxwell and G. McGill, Lunar Planet. Sci. XVIII, 604-605, 1987. (8) M.H. Carr, The Surface of Mars, pp. 147-148, 1981. (9) P.J. Mouginiis-Mark *et al.*, Proc.

Lunar Planet. Sci. Conf. 11th, 823-838, 1980. (10) H.H. Kieffer et al., J. Geophys. Res. **82**, 4249-4291, 1977. (11) G.G. Schaber, Icarus **42**, 159-184, 1980. (12) J.R. Zimbelman and R. Greeley, Proc. Lunar Planet. Sci. Conf. 12B, 1419-1429, 1981.

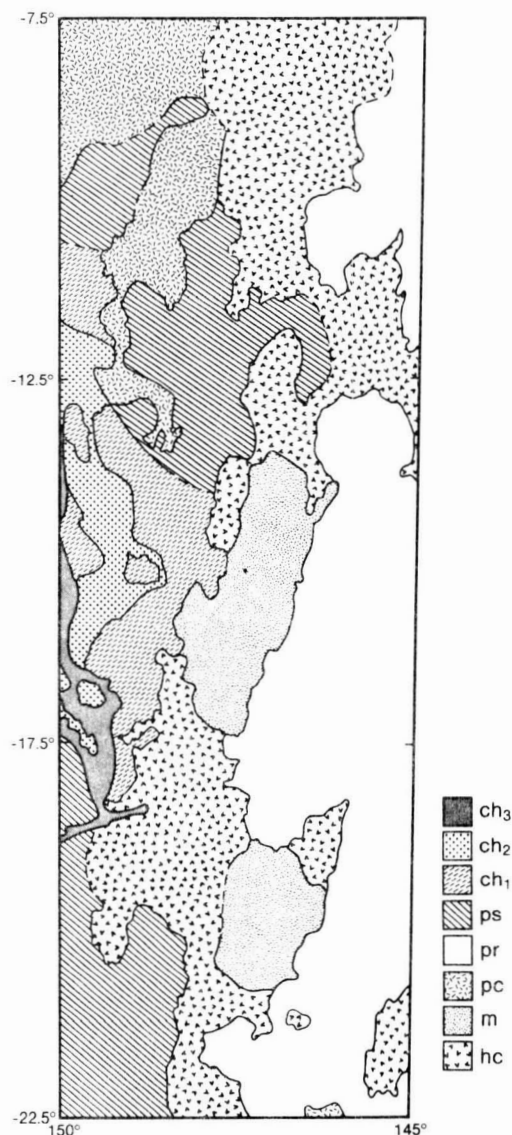


Figure 1. Photomosaic of the Memnonia study area. MTM sheets are -10147, -15147, and -20147.

Figure 2. Simplified geologic map of the Memnonia study area. Contacts are dashed where uncertain or where obscured by crater deposits.

## GEOLOGIC MAPPING OF IO

R. Greeley, R.A. Craddock, D.A. Crown, L.A. Leshin, Department of Geology, Arizona State University, Tempe, Arizona 85287, and G.G. Schaber, U.S. Geological Survey, Flagstaff, Arizona 86001

The presence of numerous active volcanoes and the nearly complete domination of Io's surface by volcanic materials produces an extremely complex surface geology. Detailed photogeologic mapping of Io to determine the geomorphology and stratigraphic relationships of the various geologic units will permit, upon the arrival of the Galileo spacecraft in the 1990s, the temporal variations of the ionian surface to be both qualitatively and quantitatively analyzed. A global geologic map at a scale of 1:15,000,000 has been completed, which synthesizes the previous mapping efforts in the Ruwa Patera Quadrangle (Ji2) [1], the Colchis Region (Ji3) [2], the Lerna Region (Ji4) [3], and the Ra Patera Quadrangle [4]. This geologic map will provide a base from which to identify and describe the volcanic eruptions which have occurred between the Voyager and Galileo encounters.

The surface of Io consists of various volcanic vents and their associated deposits, plains, and mountains [5]. Fifteen geologic units have been defined to describe the types of materials composing these major physiographic terrains. Examination of the flow deposits associated with volcanic vents with regard to albedo, texture, surface morphology, and apparent relief suggests the following categories of flow materials: patera flows, plains-forming flows, lobate flows, breakout flows, tholi, shield materials [6], vent cone materials, and fissure flows. The plains are divided into interpatera plains and layered plains units, and the mountain materials include smooth and grooved units. In the present refinement of Io's geology an attempt has been made to associate volcanic flows with their source vent(s) and to provide a classification of volcanoes from which to analyze the roles of various styles of volcanism in the formation of Io's surface.

## References

- [1] Schaber, G.G., Scott, D.H., and Greeley, R., 1987, *Geologic Map of the Ruwa Patera Quadrangle of Io*, in review.
- [2] Wood, C.A., and King, E., 1987, *Preliminary Geologic Map of the Colchis Region Quadrangle of Io*, in review.
- [3] Whitford-Stark, J.L., and Mouginiis-Mark, P.J., 1985, *Geologic Map of the Lerna Region of Io*, manuscript.
- [4] Greeley, R., Spudis, P.D., and Guest, J.E., 1987, *Geologic Map of the Ra Patera Area of Io*, in press.
- [5] Schaber, G.G., 1982, Geology of Io, in *Satellites of Jupiter*, ed. D. Morrison, University of Arizona Press, Tucson, 556-597.
- [6] Moore, J.M., McEwen, A.S., Albin, A.F., and Greeley, R., 1986, Topographic evidence for shield volcanism on Io, *Icarus*, 67, 181-183.

PALEOGEOLOGIC MAPS OF MERCURY'S SURFACE. Paul D. Spudis, USGS, Flagstaff, AZ 86001 and John E. Guest, Univ. London Observatory, London NW7 4SD, United Kingdom

The three flybys of Mercury by the Mariner 10 spacecraft in 1974 and 1975 provided us with photographic coverage of about 40 percent of the planet's surface with an average resolution of 1 to 2 km [1]. These data were used to prepare a series of nine geologic quadrangle maps at a scale of 1:5 M. Work on a synoptic geologic map of the imaged hemisphere of Mercury at 1:10 M scale (by Spudis) is in progress; this work is summarized in [2]. Through the use of these geologic maps and new geologic analysis [2], we have prepared a series of paleogeologic maps that show the surface geology of the imaged hemisphere of Mercury at six different stages in its history. These new maps facilitate interplanetary comparisons of geologic evolution, particularly with that of the Moon [2].

Mercurian stratigraphic systems. The time-stratigraphic classification developed for the geologic mapping of Mercury [2,3] is patterned after the classification used for lunar mapping [4,5]. Mercurian history is subdivided into five systems; from oldest to youngest, they are (1) pre-Tolstojan, (2) Tolstojan, (3) Calorian, (4) Mansurian, and (5) Kuiperian. The pre-Tolstojan comprises the geologic units emplaced prior to the impact that formed the Tolstoj basin ( $-16^{\circ}$ ,  $164^{\circ}$ ; 510 km dia.). The units include materials of ancient craters and multi-ring basins and intercrater plains [6]. Units emplaced after the Tolstoj impact but before the Caloris impact make up the Tolstojan System. This system encompasses mostly crater deposits, although materials of some basins (e.g., Beethoven) and some plains units were emplaced during Tolstojan time. The Calorian System includes materials of the Caloris basin ( $30^{\circ}$ ,  $195^{\circ}$ ; 1340 km dia.), widespread smooth plains material, and many large craters and double-ring basins (e.g., Bach). Most Mercurian geologic units are of this age or older [2]. The remaining two systems, the Mansurian (whose base is the base of deposits from the crater Mansur,  $48^{\circ}$ ,  $163^{\circ}$ ; 75 km dia.) and Kuiperian (whose base is the base of deposits from the crater Kuiper,  $-11^{\circ}$ ,  $31.5^{\circ}$ ; 60 km dia.), consist only of younger crater deposits; no regional geologic units of these ages are recognized.

Paleogeologic maps and Mercurian geologic evolution. Sometime during the heavy bombardment, the earliest cratering record of Mercury was largely destroyed by the widespread deposition of intercrater plains material [6]. The largest craters of this period (basins), which have been partly preserved [2,7], suggest that Mercury's surface may have resembled the lunar highlands at an earlier stage. The wide, probably global distribution of the intercrater plains suggests that they may be at least partly volcanic in origin [2,8]. The Tolstoj basin impact occurred when the impact flux was beginning to decline but was still high; some plains materials were also emplaced at this time. The Caloris impact formed the largest, best preserved basin on the imaged part of Mercury's surface, and it provides a regionally extensive stratigraphic datum. Some finite but probably short time after this impact, smooth plains material was emplaced over vast regions, probably through eruptions of volcanic flood lavas [2,6,8]. Since this emplacement, a rapidly declining cratering rate has produced minimal changes to Mercury's surface.

Comparisons with lunar stratigraphy. Both on the imaged part of Mercury and on the Moon, almost all geologic activity occurred early in planetary history--during pre-Tolstojan to early Calorian time on Mercury and during pre-Nectarian to early Imbrian time on the Moon [5]. A significant difference between the two bodies is the extended period of mare (smooth plains) deposition on the Moon, which may have extended into Copernican time [9]. Such a wide range in age for Mercurian plains is not evident within the hemisphere imaged by Mariner 10.

To estimate the cratering rates in the early histories of the two bodies, the relative ages of some comparable Mercurian and lunar geologic units can be plotted against crater densities (fig. 1). Although we have absolute ages for only some lunar geologic units (fig. 1b), the general shapes of the two curves are clearly similar. Deposition of the smooth plains material on Mercury was virtually the last global geologic event on that planet; only impact craters have formed since. Crater densities on the Mercurian smooth plains are comparable to the crater density on the lunar Imbrium basin deposits (fig. 1; see also [10]). This suggests that the last major geologic activity occurred on Mercury roughly 3.8 b.y. ago [11], although it is by no means certain that absolute ages may be directly compared between the two bodies [12]. In any event, most Mercurian geologic activity was confined to its early history. Large areas of relatively uncratered units, such as are widespread on Mars [11,13], do not occur on Mercury. It thus appears that in regard to geologic evolution, Mercury has more in common with the Moon than with Mars.

References: [1] Davies, M., et al. (1978) NASA SP-423, 128 pp. [2] Spudis, P.D. and Guest, J.E. (in press), Mercury, U. of Ariz. Press. [3] Spudis, P.D. (1985) NASA TM-87563, 595. [4] Shoemaker, E. and Hackman, R. (1962) in The Moon, Academic Press, N.Y., 289. [5] Wilhelms, D.E. (in press) USGS PP 1348. [6] Trask, N. and Guest, J.E. (1975) JGR 80, 2461. [7] Pike, P.J. and Spudis, P.D. (in press) Earth, Moon, and Planets. [8] Strom, R.G. (1984) NASA SP-469, 12. [9] Schultz, P.H. and Spudis, P.D. (1983) Nature 302, 233. [10] Murray B., et al. (1974) Science 185, 169. [11] Basaltic Volcanism Terrestrial Planets (1981), Pergamon Press, 1286 pp. [12] Chapman, C.R. (1976) Icarus, 28, 523. [13] Scott, D.H., and Carr, M.H. (1978) USGS Map I-1083.



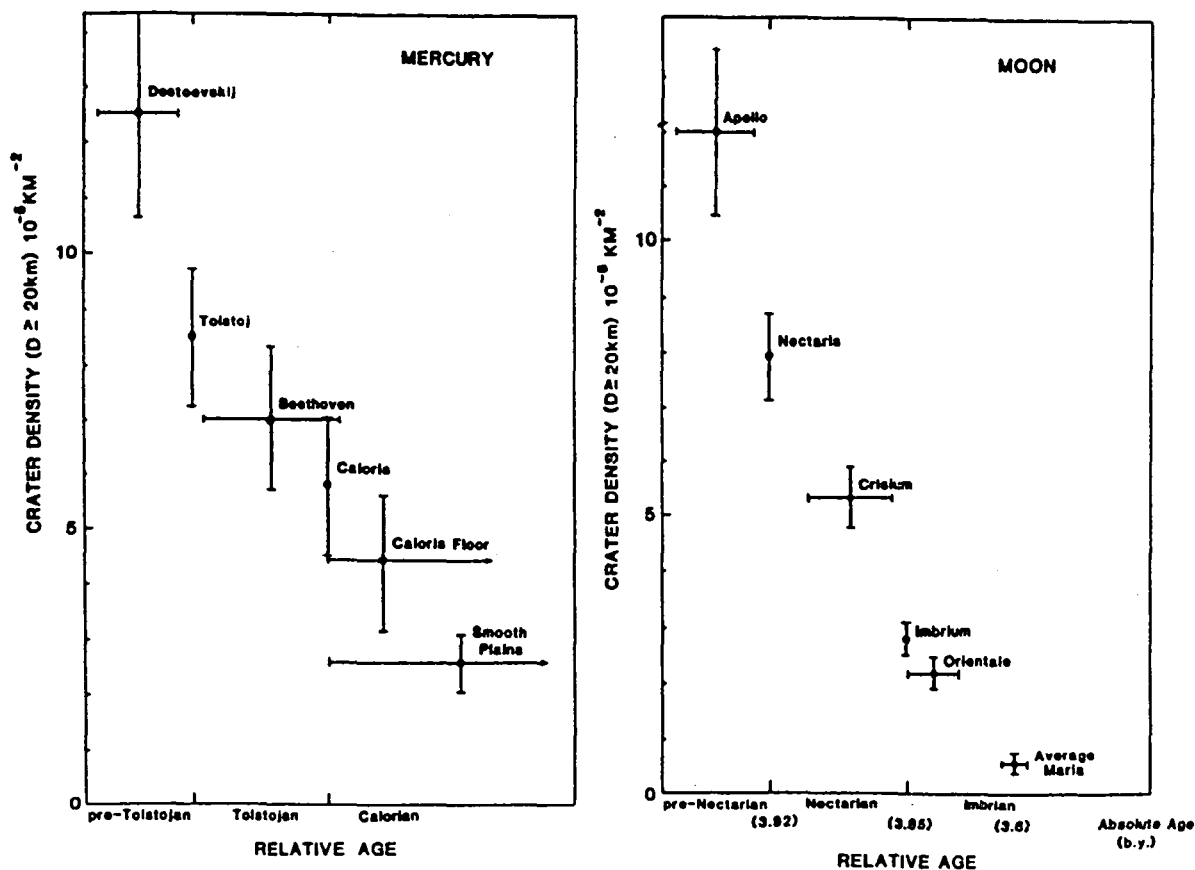


Figure 1. Plots of cumulative density of primary impact craters greater than 20 km in diameter on various geologic units on Mercury and the Moon versus stratigraphically defined relative ages. (a) Mercury. Tolstoj and Caloris basins have no horizontal error bars because they define beginnings of systems. Note that both Caloris basin fill and exterior smooth plains material postdate Caloris basin ejecta. (b) Moon. Nectaris and Imbrium basins have no horizontal error bars because they define beginnings of systems. Crater densities for basins from [5]; data for average maria from [11]. Absolute ages in billion ( $10^9$ ) years. Note that for comparable stratigraphic positions, lunar units display lower absolute crater densities than Mercurian units.

DIGITAL CARTOGRAPHY OF THE PLANETS:  
NEW METHODS, ITS STATUS, AND ITS FUTURE

by

R.M. Batson

U.S. Geological Survey

Flagstaff, Arizona

**ABSTRACT:** A system has been developed that establishes a standardized cartographic database for each of the 19 planets and major satellites that have been explored to date. Compilation of the databases involves both traditional and newly developed digital image processing and mosaicking techniques, including radiometric and geometric corrections of the images. Each database, or digital image model (DIM), is a digital mosaic of spacecraft images that have been radiometrically and geometrically corrected and photometrically modeled. During compilation, ancillary data files, such as radiometric calibrations and refined photometric values for all camera lens and filter combinations and refined camera-orientation matrices for all images used in the mapping, are produced. The system is designed to aid in the following: access to and utilization of spatial data returned by planetary spacecraft; coregistration of cartographic image and topographic elevation models with geological, geophysical, and geochemical databases; and the design and preparation of both standard and custom map products. A major goal of the project is to publish the DIM's on compact computer-compatible media such as digital-optical (CD-ROM) disks.

# GEOMETRIC PROCESSING OF DIGITAL IMAGES OF THE PLANETS

by

Kathleen Edwards

U.S. Geological Survey

Flagstaff, Arizona

ABSTRACT: New procedures and software have been developed for geometric transformation of images to support digital cartography of the planets. The procedures involve the correction of spacecraft camera orientation of each image with the use of ground control and the transformation of each image to a Sinusoidal Equal-Area map projection with an algorithm which allows the number of transformation calculations to vary as the distortion varies within the image. When the distortion is low in an area of an image, few transformation computations are required, and most pixels can be interpolated. When distortion is extreme, the location of each pixel is computed. Mosaics are made of these images and stored as digital databases. Completed Sinusoidal databases may be used for digital analysis and registration with other spatial data. They may also be reproduced as published image maps by digitally transforming them to appropriate map projections.

## DIGITAL MAPPING OF IRREGULAR SATELLITES AND ASTEROIDS\*

R.M. Batson, Chief of Planetary Cartography, U.S. Geological Survey, Flagstaff,

AZ 86001; 602 527 7260

Kathleen Edwards, Cartographer, U.S. Geological Survey, Flagstaff, AZ 86001; 602

527 7118

**ABSTRACT:** A system has been developed for mapping small, irregularly shaped Solar System bodies like Phobos (a satellite of Mars) and Amalthea (a satellite of Jupiter). These are primitive objects, which contain valuable clues regarding the origin of the Solar System. They do not lend themselves to mapping by conventional methods because (1) mathematical projections of their surfaces fail to convey an accurate visual impression of landforms and (2) map scale varies with the shapes of the bodies, making feature measurements difficult. We are producing three-dimensional digital image mosaics by projecting images returned by interplanetary spacecraft onto global topographic models. These models are made from collections of radii derived by a combination of photogrammetry, limb measurement, and photometric analysis that we have labeled "digital sculpturing." Final digital products consist of arrays of geocentric latitudes, longitudes, radii, and photometric brightnesses. No attempt is made to relate radii to any kind of elipsoid. The multidimensional arrays can be projected as images to any conventional or yet-to-be-invented map projections, either for analysis on video display devices or for photographic or lithographic reproduction.

#### DIGITAL ELEVATION MODEL OF MARS

Sherman S.C. Wu and Annie Howington-Kraus, U.S. Geological Survey, Flagstaff, Arizona 86001

For the Mars Observer mission, a Mars Digital Elevation Model (DEM) is being derived as a byproduct of the topographic mapping of Mars (Wu et al., 1985). Digital data are produced by digitizing topographic maps from the series of 1:2,000,000-scale and 1:15,000,000-scale topographic maps of Mars. All 64 quadrangles of the equatorial belt ( $\pm 30^\circ$  lat) have been digitized. The DEM is reformatted into a sinusoidal equal-area projection with 1/64-degree resolution, compatible with the Mars Digital Image Model (DIM) (Batson, 1985) and that of the Martian Consortium (Kieffer et al., 1981).

The interpretive use of the DEM/DIM combination is illustrated by three-dimensional transformations described by Batson et al. (1981) and exemplified in Figure 1. The DEM is used as control to rotate DIM data, which were digitally mosaicked from 102 Viking Orbiter pictures of Mars data by McEwen (1987).

#### References Cited

- Batson, R.M., 1985, A digital image model of Mars: National Aeronautics and Space Administration Technical Memorandum 87563, p. 577-579.
- Batson, R.M., Edwards, Kathleen, and Skiff, B.A., 1981, Orthophoto mosaics and three-dimensional transformations of Viking Orbiter pictures: National Aeronautics and Space Administration Technical Memorandum 84211, p. 493-495.
- Kieffer, H.H., Davis, P.A., and Soderblom, L.A., 1981, Mars' global properties: Maps and applications: Proceedings of the 12th Lunar and Planetary Science Conference, Houston, March 16-20, 1981, p. 1395-1417.
- McEwen, A.S., 1987, Mars as a planet: Proceedings of the 18th Lunar and Planetary Science Conference, Houston, March 16-20, 1987, p. 612-613.
- Wu, S.S.C., Jordan, Raymond, and Schafer, F.J., 1985, Compilation of the Mars 1:2,000,000-scale topographic map series: National Aeronautics and Space Administration Technical Memorandum 87563, p. 612-613.

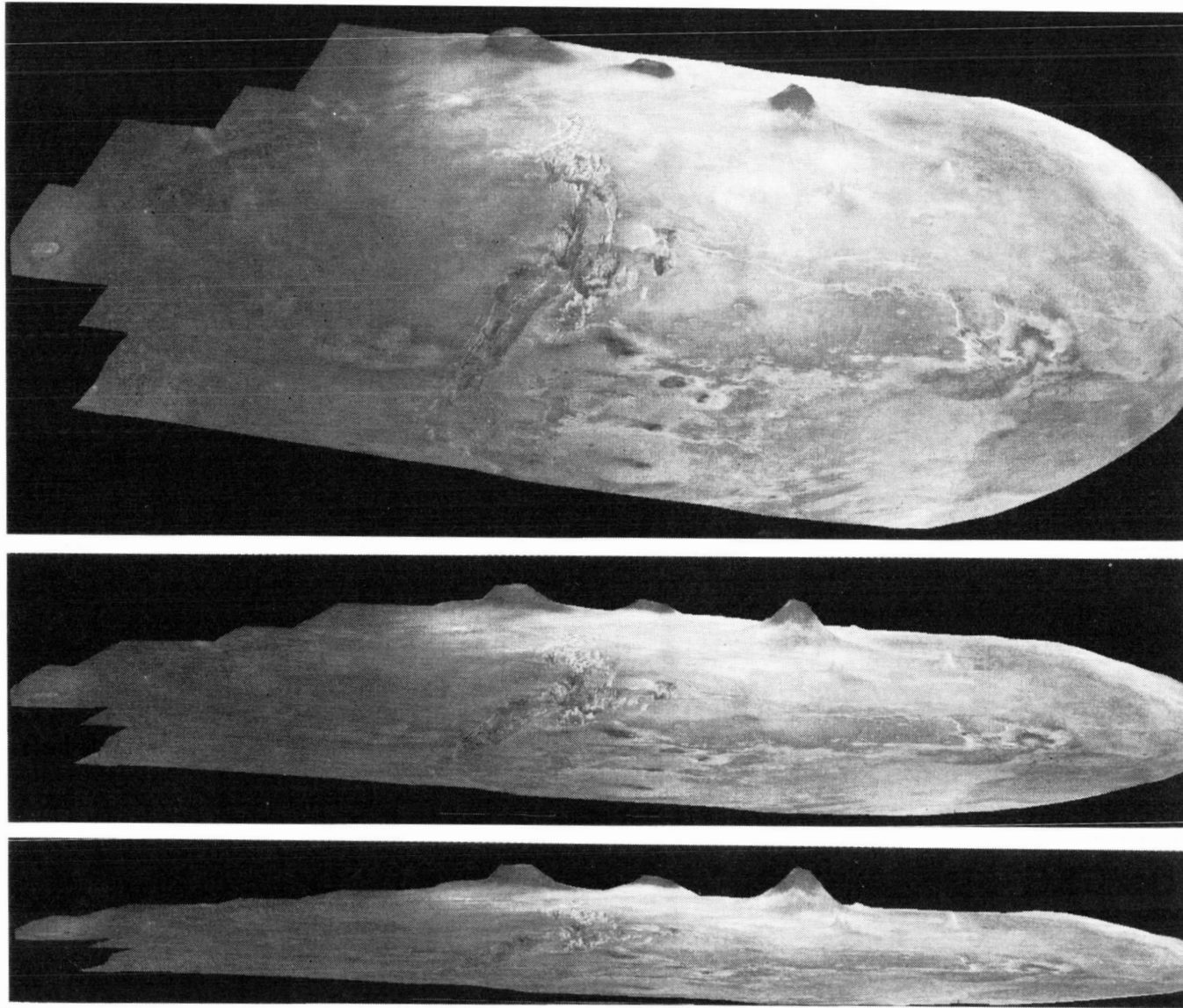


Figure 1. Perspective views covering nearly a hemisphere of Mars, from about lat  $-50^{\circ}$  to  $60^{\circ}$  and from long  $20^{\circ}$  to  $130^{\circ}$ . The entire Valles Marineris system is in the center of the scenes. View is due west. Viewing angles are  $5^{\circ}$ ,  $10^{\circ}$ , and  $25^{\circ}$  from the horizon for the bottom, middle, and top views, respectively. Vertical exaggeration is about 5 times.

## PROGRESS IN COMPILATION OF THE 1:2,000,000-SCALE TOPOGRAPHIC MAP SERIES OF MARS

Sherman S.C. Wu, Raymond Jordan, and Francis J. Schafer, U.S. Geological Survey, Flagstaff, Arizona 86001

The application of special photogrammetric techniques (Wu et al., 1982) is enabling us to systematically map Mars' topography at a scale of 1:2,000,000, using high-altitude Viking Orbiter pictures. In fiscal year 1987, we produced maps of the 16 subquadrangles that make up the quadrangles MC-22, MC-23, MC-3 and MC-6 of the 1:5,000,000-scale series. This work completes compilation of the 64 topographic maps covering the entire equatorial belt ( $\text{lat} \pm 30^\circ$ ). We plan to complete the maps of the remaining subquadrangles of Mars within the next two years.

Elevations on all the topographic maps are relative to the Mars topographic datum (Wu, 1981). The maps have a contour interval of 1 km and a vertical precision of  $\pm 1$  km. The equatorial-belt maps are in Mercator projection and have a true scale at  $\text{lat} \pm 27.476^\circ$ , whereas the medium-latitude maps will be in Lambert Conic Conformal projection and have a true scale at  $\text{lat} \pm 35.83^\circ$  and  $\pm 59.17^\circ$ . These maps provide more precise information than do those previously available, and they will help in understanding the geologic processes that have shaped the Martian surface.

### References

- Wu, S.S.C., 1981, A method of defining topographic datums of planetary bodies: *Annales de Geophysique*, AGEPA 7, Tome 37, fasc. 1, p. 147-160.
- Wu, S.S.C., Elassal, A.A., Jordan, Raymond, and Schafer, F.J., 1982, Photogrammetric application of Viking orbital photography: *Planetary and Space Science*, v. 30, no. 1, p. 45-55.

#### GEODETIC CONTROL NETWORK OF PHOBOS

Sherman S. C. Wu and Francis J. Schafer, U.S. Geological Survey, Flagstaff, Arizona 86001

A control network for Phobos, consisting of more than 300 control points, has been established by using more than 80 high-resolution Viking Orbiter pictures obtained at altitudes ranging from 300 to 620 km. The control network was derived by using analytical photogrammetric methods and the block-adjustment computer program (GIANT) that was employed for the planetwide control network of Mars. Seven primary control points from Duxbury (1974) were used for the adjustment, but more weight was given to Duxbury's orbital parameters (the camera C-matrices). Precision of the preliminary adjustment is better than 30 m.

We plan to use this control network to compile the surface topography of Phobos by photogrammetric methods on an AS-11AM analytical stereoplotter. Contour lines and elevations of points will be determined relative to a triaxial ellipsoid of Phobos (Duxbury, 1974; Turner, 1978). A new map projection developed by Stooke (1986) will be used for the base map grid.

#### References Cited

- Duxbury, T.C., 1974, Phobos: Control network analysis: *Icarus*, v. 23, p. 290-299.
- Stooke, P.J., 1986, Automated cartography of non-spherical worlds: Proceedings of the Second International Symposium on Spatial Data Handling, International Geographic Union and International Cartographic Association, p. 523-536.
- Turner, R., 1978, A model of Phobos: *Icarus*, v. 33, p. 116-140.



THE CONTROL NETWORK OF MARS: NOVEMBER 1987

Merton E. Davies, The RAND Corporation, Santa Monica, CA 90406-2138

The modern control network of Mars was begun in 1970, based on pictures taken by the Mariner 6 and 7 spacecraft. Pictures taken by Mariner 9 permitted the control network to be expanded to encompass almost the entire planet. The small crater Airy-O was selected to define the prime meridian on Mars; thus the longitudes of all points are measured relative to Airy-O. Error associated with the coordinates of points was about 10 km.

The Viking pictures were a dramatic improvement over the Mariner 9 pictures and resulted in important changes to the control network. The Viking lander radio science team was able to accurately measure the direction of the spin axis and the coordinates of the two lander sites. (Michael, 1979). The Viking 1 lander site was identified on a high-resolution picture taken by the orbiting spacecraft (Morris and Jones, 1980). The Viking 2 lander site has never been located on orbiter pictures. Because the Viking 1 lander site coordinates could be transferred to orbiter pictures and because many high-resolution pictures were taken over the entire region, the coordinates of points in this area are known with considerable accuracy. High-resolution pictures of Airy-O were added to the control network, and many strips of pictures were run between Airy-O and the Viking 1 lander site to improve the measurements of longitude throughout the network.

The 1:2,000,000 map series consists of mosaics of pictures with a pixel size of about 250 m. Pictures identified on these maps have been used to form high-resolution strips. Strips were first run from Airy-O to the Viking 1 lander and then from Airy-O north along 0° longitude to 60° latitude. A strip was run from this point to the Viking 1 lander, forming a large triangle. A strip was run from the Viking 1 lander south to the equator and another around the planet at the equator and again at 60° north latitude. These latitude strips were tied by strips at longitudes 90°, 180°, and 270°. At 0° longitude, the strip continues south from Airy-O to 60° south latitude, and a strip at 60° south latitude is now in process. These strips will be continued in the future program.

The accuracy of points near the Viking 1 lander should be about 100 m and in the region between the Viking 1 lander and Airy-O always less than 2 km. Along the strips, the accuracy should always be within 5 km and in the areas not covered by strips, the errors should be less than 7 km.

The status of the control network calculations is summarized as follows:

Number of points.....	8563
Number of pictures.....	2239 (1054 M9, 1185 Viking)
Observation equations.....	57,134
Normal equations.....	23,843
Overdetermination.....	2.40
Standard error ( $\mu\text{m}$ ).....	14.27

All computations are now performed in J2000 coordinates.

#### References

- Michael, William H., Jr., "Viking Lander Tracking Contributions to Mars Mapping," *The Moon and Planets* 20, 149-152, 1979.
- Morris, Elliot C. and Kenneth L. Jones, "Viking 1 Lander on the Surface of Mars: Revised Location," *Icarus*, 44, 217-222, 1980.

# THE CONTROL NETWORKS OF THE SATELLITES OF JUPITER

Merton E. Davies, The RAND Corporation, Santa Monica, CA 90406-2138

An error was found in the transformation of the control networks of the Galilean satellites from B1950 to J2000 coordinates. The networks have been recomputed as follows:

## STATUS OF THE CONTROL NETWORK

	Io	Europa	Ganymede	Callisto
Points	640	179	1,884	818
Pictures	252	120	302	286
Measurements	11,164	3,848	25,780	15,786
Normal equations	2,036	718	4,674	2,494
Overdetermination	5.48	5.36	5.52	6.19
Standard error, $\mu\text{m}$	10.31	10.15	14.78	12.69

The direction of the spin axis of Hyperion at the time of the Voyager flyby was determined while computing the control network. The positions of seven points were measured on 12 pictures, 104 measurements in all. In the control network computation, latitude, longitude, and radius of each point was computed as well as the camera orientation matrix and the right ascension and declination of the spin axis. The overdetermination was 1.76 and the standard error of measurement at the faceplate of the vidicon was 9.74  $\mu\text{m}$ . A 13.1 day period for Hyperion had been previously reported by Thomas et al. (*Nature*, Vol. 307, p. 716, February 23, 1984). The resulting coordinate system, defined in J2000 coordinates, is  $\alpha_0 = 262^\circ.1$ ,  $\delta_0 = -1^\circ.3$ ,  $W = 75^\circ.74 + 27^\circ.4809160d$ .

## Large Scale Topography of Io

R.W. Gaskell and S.P. Synnott (JPL/Caltech)

The use of stereographic images of bodies in order to infer topography is not new. Neither is the idea of setting up a network of control points which can be identified in several images and used as objects for a computerized stereo analysis (Davies et al. 1981, 1983, Davies 1986, Duxbury et al. 1982). Over the past several years, however, we have developed techniques for location of control points to the sub-pixel level, reducing the standard error of the best previous work by at least a factor of three (Gaskell, 1987). For the Voyager 1 images of Io, this reduces the average error in the height determinations from nearly 2 kilometers to less than 600 meters, finally making it possible to obtain useful topographic information.

Previous attempts to locate landmarks have used visual matching, depending primarily on the landmark shape. Our procedure uses the brightness variations within each feature as well. In doing so, we incorporate more information into the description of the landmark and reduce the uncertainty in the image space position. Our software is able to teach itself to recognize a landmark, to update its model of the landmark as new data are added, to determine the displacement of the landmark from its nominal location, and to reject apparitions which are inconsistent with the others in the set.

We define a landmark by its pixel-line location in a single "key" picture. Using the nominal model, including a zero nominal height above the reference surface, we predict its location in the body fixed frame. The vector representing this position is then projected into the image space of the other available pictures to find the nominal pixel-line positions of the landmark in all other pictures.

The nominal landmark location is taken to be the center of a local cartesian coordinate frame whose unit vectors lie in the south, east and vertical directions. From a circular patch of the surface in this frame, we extract all brightness values along with their corresponding positions. We then model these data, solving simultaneously for the model parameters and the amount by which each landmark apparition is shifted relative to the local origin.

Using these shifts we can update our geometric model in the usual way, solving for new camera pointings and landmark locations and heights. For this procedure to succeed, The albedo or topography variations within the landmark should be recognizable and there should be reasonable contrast. At the same time, the variations should be simple enough to allow for modeling with a relatively small number of parameters.

The information which can be obtained at the local scale is ultimately limited by a sort of uncertainty principle. Choosing a large area to define a landmark reduces the formal uncertainty in height but makes it unclear which point in the area should be identified with that height. A small area reduces the amount of data available, increasing the uncertainty. In most cases, the height seems to represent an average over the entire region. It appears that the heights measured for regions including caldera, which show up as dark features in the images, really represent the height of the surrounding surface. Indeed, this must be the case if the surrounding surface is of high albedo, perhaps being covered by  $SO_2$  frost, while the walls and floor of the caldera are darker. In some cases, when there is a really bright feature dominating (Again, probably a local  $SO_2$  deposit), the height more closely represents the feature than the landmark region as a whole.

Our latest results for landmark heights on Io show some softening from those of a few years ago (Synnott et al. 1985, Gaskell et al. 1986). This is primarily due to the elimination of errors which were not recognized then. A more accurate spacecraft trajectory file and corresponding satellite ephemeris file were used, the effect of varying thickness of Voyager wide angle filters was taken into account and better reseau location and interpolation procedures were developed. We found it encouraging that with each improvement, the (independently fit) postfit residuals for the pixel-line landmark locations decreased.

We have used a set of 35 images obtained with the clear and blue filters. The 328 landmarks which appear in three or more frames have an rms height (roughness) of 1.36 km. The rms postfit residual for this study is about 0.2 pixel ( $3 \mu\text{m}$ ). Since our estimated uncertainties in both reseau locations and pixel-line landmark location are about 0.1 pixel, these are both consistent with the theoretical statistics and close to the theoretical limit. The average of the predicted height uncertainties for the landmarks is about 600 meters.

The best-fit triaxial ellipsoid was obtained by minimizing the rms height, weighted by the inverse square of the height uncertainties. The solution is very close to the hydrostatic prediction (Dermott, 1979) with semiaxes  $1830.00 \pm .15$  km,  $1818.65 \pm .13$  km,  $1815.32 \pm .20$  km. This is consistent with the earlier result from limb fitting (Synnott et al. 1985), but the uncertainties have been reduced by a factor of ten.

A global altimetry map of Io (Plate 1) was produced from the elevation points by triangular interpolation between the nearest surrounding landmarks. Higher areas are represented by lighter shades, with a maximum topographic relief of about  $\pm 3$  kilometers. The map suggests a fourfold symmetry of rotation about the polar axis which may be due to asthenospheric tidal dissipation (Segatz et al. 1987, Gaskell et al. 1987)

The centers of the Loki, Pele and Ra regions have heights of about -2, +3 and +2 km respectively. Just south of Loki, however, there are several landmarks with heights around +2.5 km. With the addition of some earlier frames to our data set (FDS 16351-16357) we have been able to study the leading hemisphere in more detail. The most interesting feature seems to be an extensive plateau about 3 km high corresponding closely to Media Regio. Just to the west of this region, starting at about  $110^\circ$ , there is a spectacular drop to an area having landmarks almost four km below the geoid. The resolution of these new pictures is low, about 20 km/pixel, resulting in height uncertainties at the kilometer level. Nevertheless, the deviations from the geoid are well in excess of this uncertainty and form a consistent picture of the surface which is, at the very least, qualitatively accurate.

## References

- M.E. Davies, E.Y. Katayama, *J. Geophys. Res.* **86**, 8635 (1981).  
M.E. Davies, E.Y. Katayama, *Icarus* **53**, 575 (1983).  
M.E. Davies, "Control Networks of the Satellites of Jupiter", NASA Tech. Mem. 89810, 539 (1987).  
T.C. Duxbury and J. Callahan, "Phobos and Deimos Cartography", *Lunar and Planetary Science* **XIII** 190, (1982).  
R.W. Gaskell, S.P. Synnott, "Large scale topography of Io", *BAAS* **18**, No. 3 (1986).

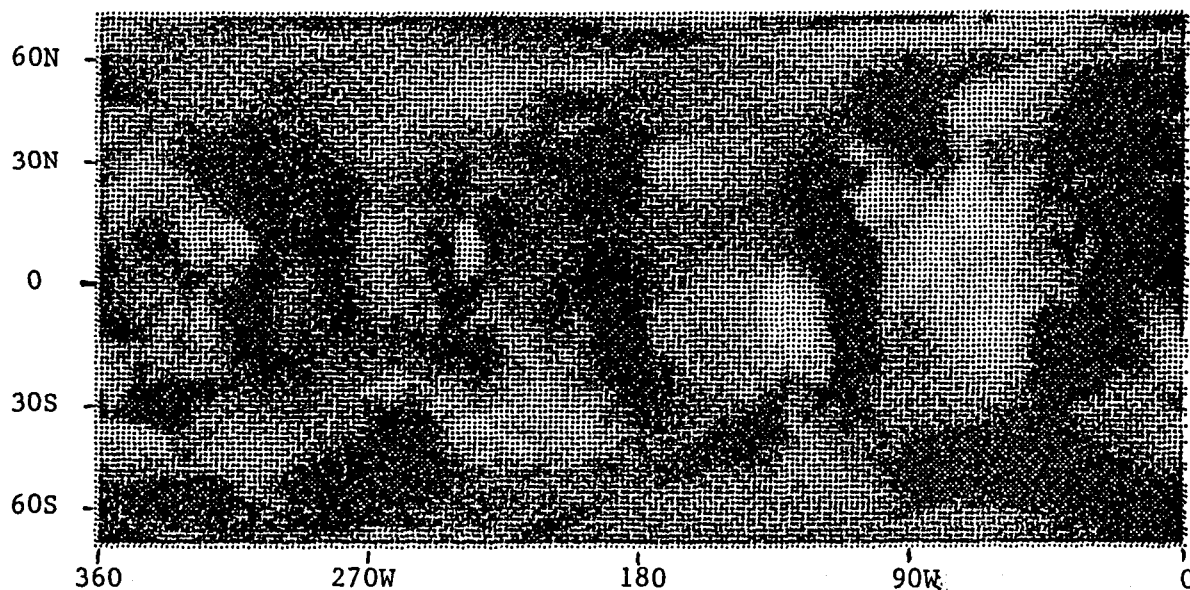
R.W. Gaskell, "Digital identification of cartographic control points" (in preparation).

R.W. Gaskell, S.P. Synnott, A.S. McEwen and G.G. Schaber, "The Large-Scale Topography of Io: Implications for Internal Structure and Heat Transfer" (in preparation).

Segatz, M., T. Spohn, M. N. Ross, and G. Schubert, "Tidal dissipation, surface heat flow, and figure of viscoelastic models of Io", *Icarus*, in press (1987).

S.P. Synnott, J.E. Riedel, R.W. Gaskell, "Shape of Io", AAS DPS October 1985, Baltimore.

Plate I. Altimetry map of Io. Light areas are high, dark areas low.



#### A UNIFIED LUNAR CONTROL NETWORK

Merton E. Davies and Tim R. Colvin, The RAND Corporation, Santa Monica, CA 90406  
Donald L. Meyer. Defense Mapping Agency, Aerospace Center, St. Louis AFS, MO 63118

This program has been designed to combine and transform many control networks of the Moon into a common center-of-mass coordinate system. The first phase, dealing with the near side, has been completed and the report (Davies, et al., 1987) has been accepted for publication in the *Journal of Geophysical Research*. Coordinates of 1166 points on the near side of the Moon are given.

The most accurately defined points on the Moon are locations of the laser ranging retroreflectors (Ferrari et al., 1980) and the VLBI measurements of the locations of the Apollo 15, 16, and 17 ALSEP stations (King et al., 1976). Recent values for the coordinates of the retroreflectors have been received from Williams and Dickey, 1986. The accuracy of these locations is about 30 m and their locations are used to define the center-of-mass and, hence, the origin of the unified lunar coordinate system. The coordinates of the retroreflectors are given in both principal axis and mean Earth/Polar axis systems. Mean Earth/Polar axis coordinates have been recommended by the IAU (Davies et al., 1980) for the moon. The difference in the coordinates is important, more than 600 m in latitude and longitude.

The Apollo 15, 16, and 17 ALSEP stations have been identified on Apollo panoramic photography and their locations transferred to Apollo mapping frames. Thus, their coordinates are available in the control network computations.

Three control networks have been computed based on the Apollo mapping pictures. They are the DMA/A15 system (Schirmerman, 1976), the NOS/USGS system (Doyle et al., 1977), and the DMA/603 system (DMAAC Contract Report, 1981). The DMA/A15 system contained 1287 pictures and 12305 points, the NOS/USGS system contained 1242 pictures and 5318 points, and the DMA/603 system contained 603 pictures and 5346 points. The coordinates of points in one system can be transferred to another system by interpolation between nearby common points. Thus, the coordinates of the three ALSEP stations, which are available in DMA/A15 coordinates, are transferred to NOS/USGS and DMA/603 coordinates. The coordinates are based on picture measurements and the photogrammetric solutions and can then be compared to the coordinates derived by King et al., 1976 and Ferrari et al., 1980.

In order for the control network to have the same origin and mean Earth/Polar axis coordinate system defined by Ferrari et al., 1980, the coordinates of the ALSEP stations should be identical. The RMS of the true distance between corresponding ALSEP points is 333 m for the DMA/A15, 2110 m for NOS/USGS, and 308 m for DMA/603. Transformations permitting translation, rotation, and scale (7 parameters) have been computed for each control system to minimize the

distances between these corresponding points. The RMS of the residuals after the transformations is 73 m for DMA/A15, 76 m for NOS/USGS, and 58 m for DMA/603. After the transformation, the coordinates of points in all three systems are quite similar. The DMA/603 transformed system was selected as the preferred system.

Many control networks have been computed based on pictures of the Moon taken through telescopes; these cover the Earth-facing region. Probably the most carefully prepared network is that published by Meyer, 1980. This is the one incorporated into the present program. 130 points common to Meyer's and the Apollo networks were selected and transformation parameters computed to shift Meyer's coordinates to the transformed Apollo network. The RMS of the residuals of this transformation is 808 m. The mean shift of the coordinates was 1352 m, with a maximum of 2336 m and a minimum of 803 m.

The Mariner 10 control network has been tied to this system through common points and the coordinates of ten points in the north polar region have been computed. Our report contains coordinates of 130 Apollo points, 1026 telescopic points, and ten Mariner 10 points.

At this time, the only control network of the far side of the Moon was published by the DMAAC in April 1975 (*Positional Reference System (PRS)*). It is based on Lunar Orbiter pictures.

We are continuing our work on lunar control. The distribution of points in the PRS is rather good, so we decided to use the same points and numbers in our work to the extent possible and update the coordinates to the mean Earth/polar axes coordinate system. The points have been identified on the Apollo pictures and on the Zond 8 pictures. Our next task is to measure the locations of the points on the Apollo pictures and compute new coordinates. We have given V. V. Shevchenko, Sternberg State Astronomical Institute, and Y. S. Tjuflin, TsNIIGAIK, USSR, Zond 8 pictures with our points identified. In the overlapping areas, we will give them our coordinates of common points, and they can then compute the coordinates of all measured points on the Zond 6 and 8 pictures.

In the areas north and south of the Apollo Zond strip, it will be necessary to transform the PRS coordinates to best fit the new near side, Apollo, and Zond coordinates.



## References

- Davies, M. E., T. R. Colvin, and D. L. Meyer, "A Unified Lunar Control Network: The Near Side," *J. Geophys. Res.*, to be published, 1987.
- Davies, M. E. et al., "Report of the IAU Working Group on Cartographic Coordinates and Rotational Elements of the Planets and Satellites," *Celestial Mechanics*, Vol. 22, January 1980, pp. 205-230.
- Doyle, Frederick J., Atef A. Ellassal, and James R. Lucas, "Selenocentric Geodetic Reference System," National Oceanic and Atmospheric Administration, Technical Report NOS70NGS5, February 1977.
- Ferrari, A. J., W. S. Sinclair, W. L. Sjogren, J. G. Williams, and C. F. Yoder, "Geophysical Parameters of the Earth-Moon System," *J. Geophys. Res.*, Vol. 85, No. B7, July 10, 1980, pp. 3939-3951.
- King, R. W., C. C. Counselman III, I. I. Shapiro, "Lunar Dynamics and Selenodesy: Results from Analysis of VLBI and Laser Data," *J. Geophys. Res.*, Vol. 81, No. 35, December 10, 1976, pp. 6251-6256.
- Meyer, Donald L., "Selenocentric Control System (1979)," Defense Mapping Agency, DMA TR 80-001, April 1980.
- Report on Lunar Control under Contract No. W-14, 453, Defense Mapping Agency Aerospace Center, St. Louis AFS, MO 63118, October 1981.
- Schirmerman, Lawrence A., "The Expanding Apollo Control System," Defense Mapping Agency Aerospace Center, August 1976.
- Williams, J. G. and J. O. Dickey, "Coordinates of the Lunar Laser Retroreflectors," Letter to M. E. Davies, June 18, 1986.



CHAPTER 13  
SPECIAL PROGRAMS



## NASA FIELD WORKSHOP ON IGNIMBRITES AND DOMES, MAMMOTH LAKES, CALIFORNIA.

Michael F. Sheridan and Jonathan H. Fink, Geology Department, Arizona State University, Tempe, Arizona, 85287

A two day NASA-sponsored field workshop was conducted in Long Valley Caldera and vicinity on September 11-12, 1987. The purpose of the workshop was to examine a classic area of large scale silicic volcanism as an analog for similar types of volcanism on other planets. Two themes were emphasized: 1) the textural and geomorphologic characteristics of the Bishop Tuff, a classic ignimbrite deposit; and 2) structural evidence for silicic dike and dome emplacement along the Inyo-Mono Chain, the most recent site of intrusive and extrusive rhyolitic volcanism in the coterminous United States. At each of the 10 stops along the excursion, planetary applications of the observed features were identified and discussed.

During the first part of the workshop we examined the Bishop Tuff as a typical plateau-forming ignimbrite. Ignimbrites are major geologic features on Earth but their presence on other planets in the Solar System remains unproven. The morphology and spectral characteristics of terrestrial ignimbrites is the basis for modeling their properties on other planets. Numerical models of their emplacement and compaction as well as a conceptual model of development of their surface morphology resulting from wind and water erosion are important considerations.

The Bishop Tuff lends support for the emplacement of ignimbrites as gravity-driven density flows constrained by topography. The variations of welding and crystallization in terrestrial ignimbrites depend on their thickness and emplacement temperature. The Bishop Tuff has compacted over previous terrain of high relief and changes in toughness of the unit are due to systematic density variations in vertical profiles. The effects of erosion, density variations, and degree of crystallinity have strongly effected the morphology of the tuff.

The purpose of the second part of the workshop was to observe some very young silicic extrusions which have been studied through careful geologic mapping and scientific drilling. Although not yet positively identified on Viking or Venera images, silicic domes and flows provide opportunities to remotely interpret the tectonic as well as the magmatic history of an area. The stops along this part of the field trip showed evidence for the geometry of the feeder system beneath the Inyo Domes, along with a range of vent and surface structures associated with effusive rhyolitic eruptions. All of the features lie along the 25 km long Inyo-Mono volcanic chain, parts of which erupted within the past 600 years. The sites included Earthquake Fault, a set of fissures and ground cracks that may have formed above a rising dike; Inyo Craters, a series of three co-linear, phreatic craters thought to overlie a dike; and Obsidian Dome, a 550 year old dike-fed rhyolite flow that has been the target of the recent Inyo Scientific Drilling Program sponsored by the Department of Energy, National Science Foundation, and USGS. In addition, a stop at Lookout Mountain provided an overview of the overall structure of Long Valley Caldera, including the elliptical shape, resurgent dome with keystone graben, and multiple extrusions both within the moat and outside the margins of the Caldera.

## **Preliminary analysis of desiccation as a planetary geomorphic process**

Lisa A. Rossbacher, Geological Sciences Department and Office of Academic Affairs, California State Polytechnic University, Pomona, CA 91768

Desiccation is an important process on planetary surfaces, and many studies of comparative planetology have neglected it. The primary landform associated with desiccation is polygonal fracture patterns; because the fractures develop at a scale large enough to be observed from satellite images, polygonal fracture patterns offer a valuable data set for comparative planetology and studies of planetary surfaces.

On Earth, desiccation has been most extensively studied in arid regions, although it is also important in cold regions. The influence of desiccation in cold areas has been noted by many researchers (e.g., Tricart, 1969), and Washburn (1980) has commented on the problems of distinguishing between the effects of frost cracking and desiccation. Drying of near-surface material interacts with the freezing process by creating additional fractures that can fill with water, freeze, and expand; Washburn (1956) also observed that desiccation may be the most important factor in controlling crack patterns in periglacial environments. Desiccation rates, which partially control landform morphology, are in turn controlled by solar insolation, atmospheric temperature and pressure, wind speeds, regolith moisture, clay content of the substrate, and salinity of the water.

On Mars, desiccation seems to have played a significant role, both globally and locally. Evidence for this includes the existence of polygonally fractured landforms that resemble desiccation features on Earth and models for the current and past environmental conditions on Mars. Studies of polygonally fractured ground have identified several areas on Mars that appear to have had substantial amounts of water at some point in the planet's history (Rossbacher and Judson, 1981; Squyres, 1984; Rhodes and Rossbacher, 1985; McGill, 1985; Rossbacher and Rhodes, in press).

Desiccation is also likely to be a significant process elsewhere in the Solar System. It seems to be important in modifying sulfur compounds on Io (Nash, 1986), and it may contribute to the fracture patterns on some of the icy satellites of the outer planets (Pieri, 1981). The high gas production rates of  $1.3 \times 10^{30}$  molecules per second measured for Comet Halley also illustrate the importance of desiccation for comets (Sagdeev et al., 1986).

Most of the clearest examples of desiccation landforms on Earth are associated with climatic drying (Neal and Motts, 1967; Fife, 1980). As regions of the Earth become increasingly arid, an understanding of desiccation processes may provide some predictive capability for the geomorphic activity to be experienced in these regions.

#### References cited

Fife, D.L., 1980, Giant desiccation polygons and playa fissures, in D.L. Fife and A.R. Brown, eds., *Geology and mineral wealth of the California desert: South Coast Geological Society* (Santa Ana, CA), p. 414-429.

McGill, G.E., 1985, Age and origin of large Martian polygons, in *Lunar and Planetary Science XVI: Houston, Lunar and Planetary Institute*, p. 534-535.

Nash, D.B., 1986, Solid sulfur in vacuum: Sublimation effects on surface microtexture, color, and spectral reflectance, and applications to planetary surfaces, in *Lunar and Planetary Science XVII: Houston, Lunar and Planetary Institute*, p. 603-604.

Neal, J.T., and W.S. Motts, 1967, Recent geomorphic changes in playas of western United States: *Journal of Geology*, v. 75, p. 511-525.

Pieri, D.C., 1981, Lineament and polygon patterns on Europa: *Nature*, v. 289, p. 17-21.

Rhodes, D.D., and L.A. Rossbacher, 1985, The surface of Mars, in *Himmel och jord: Ymer* (Yearbook, Swedish Geographical Society), v. 105, p. 7-29.

Rossbacher, L.A., and S. Judson, 1981, Ground ice on Mars: Inventory, distribution, and resulting landforms: *Icarus*, v. 45, p. 39-59.

Rossbacher, L.A., and D.D. Rhodes, in press, Planetary analogs for geomorphic features produced by catastrophic flooding, in *Catastrophic flooding*, L. Mayer and D. Nash, eds.: Allen & Unwin (Boston).

Sagdeev, R.Z., J. Blamont, A.A. Galeev, V.I. Moroz, V.D. Shapiro, V.I. Shevchenko, and K. Szego, 1986, VEGA spacecraft encounters with Comet Halley: *Nature*, v. 231, p. 259-262.

Squyres, S.W., 1984, The history of water on Mars: *Annual Review of Earth and Planetary Science*, v. 12, p. 83-106.

Tricart, J. 1969, *Geomorphology of cold environments*: Macmillan/St. Martin's Press (New York), 320 p.

Washburn, A.L., 1956, Classification of patterned ground and review of suggested origins: *Geological Society of America Bulletin*, v. 67, p. 823-865.

Washburn, A.L., 1980, *Geocryology*: John Wiley & Sons (New York), 406 p.

THE GALILEAN SATELLITE GEOLOGICAL MAPPING PROGRAM, 1987  
B.K. Lucchitta, U.S. Geological Survey, Flagstaff, AZ 86001

The Galilean Satellite Geological Mapping Program was established by the Planetary Geology Programs Office of NASA to illuminate detailed geologic relations on the four large satellites of Jupiter: Io, Ganymede, Europa, and Callisto. The program is administered by the U.S. Geological Survey, and it involves about 40 investigators from various universities, research institutes, and government offices in the United States, England, Germany, and Italy. A total of 24 researchers were assigned to map 15 quadrangles on Ganymede, 15 to map 6 quadrangles on Io, and 3 to map 2 quadrangles on Europa. The maps are at a scale of 1:5 million except for three on Io that cover selected areas where high-resolution pictures permit compilation at scales of 1:2 million and 1:1 million. A 1:15 million-scale map of Callisto has been assigned; it will be the basis for later geologic mapping at a scale of 1:5 million.

During 1987 all final airbrush base materials were sent to the mappers (except Jg2 and Jg14). Three geologic maps (Ji2a, Ji2c, Jg8) have USGS Director's approval and are being drafted by the USGS for publication. Another two have Director's approval (Ji2, Jg4) and submittal to drafting is imminent. One map (Ji4) is undergoing USGS editorial review, another two (Ji3, Jg3) have technical reviews completed and are being revised by the authors, and two others (Jg7, Jg9) are in technical review. Nine geologic maps are still in preparation (Je3, Je4, Ji2b, Jg1, Jg5, Jg10, Jg12, Jg13, and Jg15); six of these are not scheduled to be completed until 1988 or 1989.

As maps are completed, the geologic units are matched along common borders and the map units and symbols are refined and unified. During the last year, the general map layout and information to be placed on the map collar have been selected and colors were assigned to one of the high-resolution maps of Io. Also, a general color scheme was developed for the entire series of Ganymede maps. No general meeting was scheduled during 1987 because major concepts and mapping guidelines have been established in previous meetings; minor concerns will be handled on an individual basis.



## PLANETARY NOMENCLATURE

M.E. Strobell and Harold Masursky, U.S. Geological Survey, 2255 Gemini Drive, Flagstaff, AZ 86001

In FY1987, the nomenclature project concentrated on preparing various materials for future publications as well as supplying nomenclature for new maps. Proof reviews were done of four Martian maps at 1:5 million scale and 12 maps at 1:1/2 million scale. Extensive corrections and additions were made to the computerized master file of nomenclature; in particular, questions concerning nearly 100 names in the lunar section were resolved. (All these changes will be shown in the 1987 version of the Annual Gazetteer, an informal publication; we hope to distribute this version in December 1987.) Adopted nomenclature for Mercury and Rhea was transferred to azimuthal equal-area maps. Nomenclature was transferred to Venera 15/16 maps as we received them from the Soviets. A review of Venus' nomenclature was written for the Magellan quarterly publication "V-Gram"; a revised version of this manuscript will be used for a NASA-sponsored and -approved illustrated Gazetteer that we plan to publish in the next two years.

As one result of the Gazetteer's wide circulation, we have answered an increased number of requests from the public for information regarding names listed in it.

New names were proposed for features on the first two 1:5 million-scale maps of Callisto, the final two maps of Ganymede at that scale, and 14 maps in the Mars MTM series. At the request of investigators, names were added to four Martian features, one basin on Rhea, and 21 craters on Callisto. At this time we are checking a Soviet proposal to add an additional 72 names to small Martian craters. We are also suggesting names for 32 Venusian features.

A list of 186 names, proposed since the last General Assembly of the International Astronomical Union (IAU), was transmitted to and approved by the IAU's Executive Committee.

The IAU's Working Group for Planetary System Nomenclature has approved a system of temporary nomenclature for identifying ring arcs around Neptune that will go into effect in January 1988. Arcs will be identified by the year of discovery; the letter "N" for Neptune; an arabic number to indicate the time sequence in which the entities are reported (first, second, third, etc.); and the capital roman letter A to signify "arc". Thus the first arc discovered will be given the temporary designation 1988 N1A.

Themes have been developed for naming features identified by the future Soviet mission to Phobos and the American Voyager encounter with Neptune, and name banks have been started. Features on Phobos will be named for characters and places in American, Soviet, and French science-fiction books about Mars and Phobos. New satellites of Neptune will be named from Greek mythology in categories related to Neptune, Poseidon, and oceans. Features on Triton will be named from panterrestrial (excluding Greek and Roman) mythologies; fluvial features will be named for water spirits, and all other surface features will be named for mythological rivers, lakes, oceans, swamps, and ponds.

Anticipated nomenclature tasks for FY1988 include (1) proposing nomenclature for new maps of Callisto, Mars, and other bodies as needed; (2) transferring adopted nomenclature to new azimuthal equal-area maps of Saturnian satellites; (3) updating, within the next few months, a chapter that describes Martian nomenclature for the new Mars Atlas; (4) writing a chapter that describes Saturnian nomenclature for a Saturnian satellite atlas that will be completed in FY1988; (5) working on first drafts of chapters for the forthcoming Illustrated Gazetteer of Planetary Nomenclature; (6) completing and distributing the 1987 edition of the Annual Gazetteer of Planetary Nomenclature; (7) completing lists of all names proposed since the last General Assembly of the IAU and transmitting them for consideration at the triennial meeting of the IAU at Baltimore in August 1988.

Nomenclature meetings are planned for Dec. 1, 1987, at the Voyager Imaging Team meeting at Pasadena; for July 1988 at the COSPAR meeting at Helsinki; and for spring 1990 in Europe, either at Rome or in southern France, to work on nomenclature needed as a result of the USA's Voyager-Neptune Encounter and the USSR's Phobos Mission.

## **THE IRPS DATABASE; A COOPERATIVE VENTURE INVOLVING ALL RPIF DATA MANAGERS**

B. Weiss, E. Guinness, S. Slavney, R. Arvidson, McDonnell Center for the Space Sciences, Department of Earth and Planetary Sciences, Washington University, St. Louis, MO 63130.

Washington University's Regional Planetary Image Facility (RPIF) hosted a meeting of RPIF Directors and Data Managers in April, 1987. At that time the MicroVAX-based prototype Image Retrieval and Processing System (IRPS), which had been jointly developed by Washington University and the USGS, Flagstaff, was available for testing and evaluation. The system consists of a MicroVAX with a high capacity disk drive, a compact disk player, an image display buffer, a videodisk player, USGS image processing software, and System 1032, a commercial database management package, and TAE (Transportable Applications Executive) as the user interface. The system is described in "IRPS: A Workstation for Planetary Image Databases and Image Processing" [Slavney et al., this volume].

The IRPS prototype effort concentrated on Viking and Voyager missions data products, since digital image data and documentation from those missions are currently most accessible. These data should also continue to be in demand over the next several years in order to support the upcoming Galileo and Mars Observer missions.

Included in the RPIF-IRPS database are facts about planets and satellites; planetary missions (and the various mission phases for each); spacecraft and spacecraft imaging instruments; and general information on the RPIFs, including address, phone number and names of Director and Data Manager for each. An IRPS user, after searching and displaying this very basic data, may then continue by examining the catalog of standard RPIF holdings; finding out which RPIFs house the datasets he/she would like to use; searching selected SEDR datasets; and viewing chosen images on the videodisk. Digital images can be retrieved from compact disk (CDROM). The more experienced user can also perform image processing procedures on digital image data, including radiometric and geometric calibration.

There are three main goals for the RPIF-IRPS project during this next year: 1) recording in the database where (i.e., in which RPIF) each dataset may be found; 2) expanding the database to include additional planetary missions; and 3) updating and improving the IRPS database management system so as to better serve the planetary geology community. In order to accomplish goals 1 and 2, we have asked for help from the other RPIF Data Managers. Our success in achieving those two goals during this next year is largely dependent upon their help and input.

Goal 1) A copy of a report on the RPIF data products from the Viking and Voyager Missions was sent to all RPIF Data Managers on July 28, 1987. Data Managers were asked to compare their Facility's Viking and Voyager holdings with this list and report to Washington University's RPIF which datasets were housed in their Facility. This task was to be completed by all RPIF Data Managers by October 30, 1987. After that date Washington University RPIF personnel are responsible for recording the reported holdings for each RPIF.

Goal 2) In addition, four RPIF Data Managers volunteered to help Washington University's RPIF by assuming responsibility for particular areas of the database. Margaret Dermott, Cornell University, Mary Ann Hager, Lunar and Planetary Institute, Alenka Remec, University of Hawaii, and Jody Swann, U.S.G.S., Flagstaff, offered to contribute specific mission, mission phase, and spacecraft information for the Ranger, Surveyor, Lunar Orbiter, Apollo, and Mariner missions. This data will be included in the next version of RPIF-IRPS, along with data product and SEDR information for the Mariner missions. SEDR data from the Mariner missions will be gathered and organized by the Washington University RPIF. Even though none of the four volunteers has finished her task as yet, we are hopeful they all will soon.

Goal 3) Personnel at Washington University's RPIF have assumed responsibility for updating and improving the IRPS database management system. Although we expect most of the major system changes to be accomplished during this next year, we understand that it will be an ongoing project over many years. This is, of course, what one would expect with any good DBMS. As a matter of fact, the present system has evolved from one which we first demonstrated to RPIF Directors and Data Managers in March 1985.

The first of two RPIF Data Manager workshops will be hosted by Washington University in spring 1988. Topics to be discussed at that time include relational database concepts and how they apply to System 1032 and the RPIF-IRPS database. A second workshop, dealing with digital image processing and cartography, is tentatively scheduled for fall 1988.

## **IRPS: A WORKSTATION FOR PLANETARY IMAGE DATABASES AND IMAGE PROCESSING**

S. Slavney, E. Guinness, R. Arvidson, and B. Weiss, McDonnell Center for the Space Sciences, Department of Earth and Planetary Sciences, Washington University, St. Louis, MO 63130.

The Regional Planetary Image Facility (RPIF) Image Retrieval and Processing System (IRPS) was developed jointly at Washington University and the Astrogeology Branch, U.S.G.S., Flagstaff, Arizona. Funding for the development of IRPS was directly from the NASA Information Systems Office and from a contract to Washington University from the Planetary Data System. The RPIFs are rapidly moving into an era in which the planetary geology and geophysics community will need efficient access to digital planetary image data. Furthermore, the community will require the capability to radiometrically and geometrically calibrate the raw data and to create and analyze cartographic products. IRPS provides planetary science researchers with access to a large database of information about planetary exploration and the image datasets produced by various missions. Someone using IRPS can find general information about raw and derived planetary data and conduct searches for specific image, mosaic, and map information. Analog versions of images selected during a search can be displayed from a videodisk. In addition, digital image data can be calibrated and processed within the same workstation. The system development was divided into three parts, where system integration and database components were the primary responsibility of Washington University personnel and the image processing components were developed by U.S.G.S. personnel.

The design of IRPS was constrained to meet the following requirements. The system must stand alone and not be dependent on other systems to conduct data fetching or data processing tasks. The system must be relatively inexpensive (approximately \$50K). It must support relational database management software and should include the capability for electronic "picture-book" browsing using an analog videodisk player. It must support radiometric and geometric correction of images, in addition to standard image processing tasks such as contrast enhancements, filters, cosmetic corrections, and algebraic operations. It must be able to access image data stored on compact disk (CDROM). It must be usable as a workstation from a larger multi-user system via a network connection. The system must be compatible with standards and guidelines developed by the Planetary Data System regarding database and software design.

IRPS consists of a combination of computer hardware, commercial software packages, and software developed at Washington University and the U.S.G.S. IRPS is designed in such a way that the hardware and software required to reproduce the system can be chosen based on using all or only part of its capability. Presently, IRPS is implemented on a MicroVAX II computer from Digital Equipment Corporation (DEC). This configuration was chosen because it meets the requirements listed above, and it is compatible with a large number of ongoing VAX/VMS development efforts within the planetary research community. In addition to the MicroVAX, the computer hardware required includes a terminal, a hard disk drive and a cartridge tape drive. These are usually standard components in the MicroVAX configuration. An additional hardware component for IRPS is a CDROM Reader, a device for reading compact disks. The basic software for IRPS includes the VMS operating system and Fortran.

An essential part of the IRPS software is the Transportable Applications Executive (TAE), a user interface software package developed and supported by Goddard Space Flight Center. All IRPS database and image processing programs run under TAE. It stands between the user and the VMS operating system in order to simplify the user's task of entering commands and running programs. TAE is specifically designed to help novice users perform tasks easily, minimizing the need for assistance from manuals or other people.

A software relational database management system is required to use the database capabilities of IRPS. Currently, the database management software is System 1032 by CompuServe of Cambridge, Massachusetts. Additional software was developed at Washington University to provide the user access to the database without knowing how to operate the System 1032 software. If the analog browse capability is needed, then a videodisk player and TV monitor are also required. The System 1032 package was chosen because it met the database and cost constraints of the IRPS. The IRPS database is designed to be as independent as possible of the specific database software used. Thus, it should be possible to implement the database on other systems after some modification of the database and associated software.

The image processing capability of IRPS requires the Planetary Image Cartography Software (PICS) system, which was developed by the U.S.G.S. PICS consists of a collection of programs and related files that provide an integrated system for the display and analysis of planetary image data. A significant feature of PICS is its ability to automatically produce radiometrically and geometrically corrected images from raw planetary images. Digital image mosaicking, interactive TV display features, and image enhancement capabilities are also available. The hardware required to use PICS includes a 24-bit color display controller (currently IRPS uses a device from the Peritek Corp.), color monitor, and an additional hard disk with at least 300 megabytes of storage.

The IRPS database is divided into two parts called the General Information Catalog and the Data Catalog. The General Information Catalog consists of information on planets, missions, spacecraft, and imaging instruments. In addition, it contains a directory of RPIF data products and a list of which RPIFs have a given data product. The Data Catalog contains geometry data (i.e., camera pointing information) and event data (i.e., filter used, exposure time, gain setting) for Viking Orbiter and Voyager images, information on the location of images on magnetic tapes and CDRoms, a catalog of Viking Orbiter mosaic photoproducts, and a catalog of USGS planetary maps.

The database operations available in IRPS allow the user flexibility in searching for data and displaying the results of a search. A search is conducted by specifying constraints for certain data elements. For example, a user could search for images based on such variables as location, time, and filter positions. Data can be displayed on the terminal either one entry at a time or summarized in a table; data can also be written to a file. Images can be displayed from an analog videodisk along with their geometry and event information. Selected data records can be sorted according any specified data element. Selected records from a given dataset can be related to data records in another dataset, if the two datasets have a data element in common. The results of a search can be saved and later restored in another session.

Digital compact disks are rapidly becoming the most desirable media for distribution of image datasets, due to their low production cost and their durability compared to magnetic tape. For example, the entire Voyager-Uranus encounter image dataset is being transferred onto compact disk, with a first test disk already available and in use at several sites. Over the next two to three years most of the existing planetary image data (Mariner, Viking Orbiter, Viking Lander, and Voyager) may be converted to compact disk. In addition, upcoming missions such as Magellan are expected to distribute standard data products on compact disk. IRPS includes the capability to read images from CDROMs onto the MicroVAX for digital image processing. The database software can locate the correct CDROM directory and file for an image (currently implemented only for Voyager-Uranus) and pass this information to the program that reads the CDROM.

The prototype version of IRPS is in place and is now being used on a daily basis at Washington University RPIF and the U.S.G.S. in Flagstaff. During the week of April 13-17, 1987, the IRPS workstation was demonstrated to several visiting groups of NASA-supported scientists and engineers, including the Regional Planetary Image Facilities directors and data managers. The demonstrations involved actual database searches, display of images in analog form on videodisk, retrieval of digital images from compact disk, and processing and display of the digital images. Visitors were encouraged to spend some time using the system on their own. The overall response was very favorable. The RPIF directors and data managers all expressed an interest in having a duplicate workstation at their facilities. It is expected that each facility will eventually have a version of the workstation tailored to its needs, and that all the workstations will be linked via a network. Others in the planetary science community have also inquired about getting a copy of the workstation. Its relatively low cost and flexibility make it attractive to small research groups who do not have the money, time, or personnel to invest in a larger computer system. IRPS will also be demonstrated at the Division of Planetary Sciences (DPS) meeting in Pasadena during the week of November 9-13, 1987.

A revised and expanded version of IRPS is planned for release in April 1988. The new version will include a more complete database with support for more missions, and additional functional capabilities.

## **AUTHOR INDEX**



# AUTHOR INDEX

Adams, J.B., 191, 194  
 Adler, D.S., 99, 102, 105, 106  
 Aggrey, K., 124  
 Ahrens, T.J., 381, 385  
 Aldrich, F.T., 305  
 Anicich, V.G., 251  
 Applebee, D.J., 531  
 Arakelian, T., 251  
 Arvidson, R.E., 191, 194, 197, 235,  
 289, 410, 573, 575  
 Aubele, J.C., 343

Baker, V.R., 293, 296, 299  
 Baldwin, R.J., 479  
 Baloga, S.M., 340  
 Banerdt, W.B., 510, 520, 523  
 Barlow, N.G., 442  
 Bassett, W.A., 112, 112  
 Batson, R.M., 548, 550  
 Bell, J.F., 66  
 Bindschadler, D.L., 512  
 Blount, G., 273  
 Boone, S., 114  
 Brakenridge, G.R., 490  
 Bridges, F.G., 398  
 Britt, D.T., 150, 157  
 Brophy, T.G., 3  
 Buratti, B.J., 154, 173  
 Burns, J.A., 14  
 Burns, R.G., 121, 127

Campbell, B.C., 242  
 Carr, M.H., 302  
 Carusi, A., 95  
 Christensen, P.R., 188, 194, 201,  
 204, 273, 305  
 Clark, R.N., 143  
 Clemens, D., 260  
 Clow, G.D., 496  
 Colvin, T.R., 561  
 Colwell, J.E., 3  
 Craddock, R.A., 305, 544  
 Crawford, D., 396  
 Crisp, J.A., 340  
 Croft, S.K., 135, 404  
 Crown, D.A., 349, 359, 544  
 Grumpler, L.S., 343  
 Curlander, J., 235  
 Cynn, H., 114

Dale-Bannister, M., 191, 194  
 Davies, M.E., 555, 557, 561  
 Davis, P.A., 345  
 De Hon, R.A., 311, 347, 488  
 Dermott, S.F., 18  
 Dial, A.L., Jr., 531  
 Dobrovolskis, A., 232, 260

Edwards, K., 549, 550  
 Elachi, C., 235  
 Esposito, L.W., 3

Fanale, F.P., 131, 328  
 Fink, J., 330, 362, 567  
 Franklin, B., 476  
 French, R.G., 6  
 Frey, H., 436, 452, 455  
 Ford, J., 235  
 Fryer, P., 352

Gaffey, M.J., 63  
 Gaskell, R.W., 558  
 Gault, D.E., 394  
 Gharakhani, V., 154  
 Golombek, M., 476, 520, 523  
 Gooding, J.L., 124  
 Graham, F., 166  
 Grant, J.A., 278, 280  
 Grant, T.D., 452  
 Graps, A.L., 7  
 Greeley, R., 119, 232, 257, 260,  
 262, 264, 273, 305, 349, 519,  
 544

Green, J., 50  
 Greenberg, R., 73, 95  
 Greenzweig, Y., 92, 93, 94  
 Grimm, R.E., 413, 416  
 Guest, J.E., 545  
 Guinness, E.A., 191, 194, 289,  
 573, 575

Haines, E.L., 213  
 Hamilton, D.C., 109  
 Hapke, B.W., 154, 165, 166, 200  
 Harden, D.R., 479  
 Hartmann, W.K., 38, 422  
 Hatzes, A.P., 398  
 Hawke, B.R., 216, 431, 516  
 Head, J.W., 356, 367, 512, 526  
 Helfenstein, P., 167, 176  
 Herkenhoff, K.E., 182  
 Hillier, J., 176  
 Holmes, N.C., 109  
 Hood, L.L., 434  
 Horn, L., 154  
 Howington-Kraus, A., 240, 551  
 Huang, E., 112, 113

Iversen, J.D., 267

Jakosky, B.M., 185, 188  
 Johnson, R.E., 171  
 Johnson, T.V., 159  
 Jordan, R., 553

- Kahn, R., 289  
 Kargel, J., 135  
 Kaula, W.M., 87  
 Kelley, A.D., 316  
 King, J.S., 370, 373, 376  
 Kisiel, A.P., 373  
 Kochel, R.C., 320  
 Komar, P.D., 313  
 Koumvakalis, A., 114  
 Kozak, R.C., 505  
 Kwok, R., 235
- Lancaster, N., 232, 273, 275  
 Leith, A.C., 401  
 Leshin, L.A., 349, 544  
 Lieske, J.H., 76  
 Lin, D.N.C., 398  
 Lissauer, J.J., 7, 38, 39, 46,  
 92, 93, 94  
 Lucchitta, B.K., 493, 539, 570  
 Lunine, J.I., 31, 135
- MacKinnon, D.J., 308  
 McDonald, J.S.B., 398  
 McEwen, A.S., 159  
 McGeehan, K.A., 318  
 McGill, G.E., 467, 482  
 McKay, C.P., 82  
 McKinnon, W.B., 401, 407  
 Malin, M.C., 133, 204, 283, 316,  
 502  
 Marshall, J.R., 119, 260, 262  
 Masursky, H., 531, 571  
 Mathews, A., 325  
 Matson, D.L., 159  
 Maxwell, T.A., 467  
 Mazierski, P.F., 376  
 Meinke, L., 465  
 Melosh, H.J., 428  
 Metzger, A.E., 213  
 Meyer, D.L., 561  
 Moore, C., 119  
 Moore, H.J., 188, 496  
 Moore, J.M., 133, 283  
 Moses, J., 162  
 Mosher, J.A., 173  
 Mougini-Mark, P.J., 242, 325, 352  
 Murchie, S.L., 526  
 Murray, B.C., 138, 182, 210, 499  
 Mustard, J.F., 149  
 Muenow, D.W., 124  
 Myhill, E., 87
- Nelson, R.M., 154, 160  
 Nester, I., 449  
 Newman, W.I., 87  
 Nicholson, P.D., 8  
 Nicol, M., 109, 114
- O'Connor, J.E., 299  
 O'Keefe, J.D., 385  
 Oberst, J., 55  
 Ostro, S.J., 60
- Paige, D.A., 207  
 Parker, T.J., 449, 485  
 Peale, S.J., 17, 46  
 Phillips, M.A., 320  
 Phillips, R.J., 507  
 Pierce, K.K., 138  
 Pieri, D., 332, 334, 337  
 Pieters, C.M., 149, 150, 152,  
 157, 219, 515  
 Plaut, J.J., 289, 410  
 Plescia, J.B., 34, 36, 526  
 Podolak, M., 79  
 Pollack, J.B., 82, 130, 170, 260  
 Porco, C.C., 11  
 Postawko, S.E., 328  
 Presley, M., 197
- Radousky, H.B., 109  
 Ree, F.H., 109  
 Reynolds, R.T., 79  
 Roberts, W.W., Jr., 98, 99, 102,  
 105, 106  
 Rossbacher, L.A., 568  
 Roth, L.E., 227  
 Roush, T.L., 170
- Sailer, D.F., 332  
 Salisbury, J.W., 146  
 Salvail, J.R., 131  
 Saunders, R.S., 229, 232, 235,  
 449, 485  
 Schaber, G.G., 505, 544  
 Schafer, F.J., 240, 553, 554  
 Schenk, P.M., 401, 407  
 Schmidt, R.M., 389  
 Schneeberger, D., 334, 337  
 Schubert, G., 21  
 Schulte, M., 235  
 Schultz, R.A., 436  
 Schultz, P.H., 278, 280, 392,  
 394, 396, 439, 463  
 Schumm, S.A., 318  
 Scott, D.H., 461, 534, 537  
 Semeniuk, J., 455  
 Senske, D.A., 356
- Nakamura, Y., 55  
 Nash, D., 162  
 Nellis, W.J., 109

Shaller, P.J., 499  
 Sheridan, M.F., 365, 567  
 Shoemaker, C.S., 52, 425  
 Shoemaker, E.M., 52, 425  
 Showalter, M.R., 7  
 Simmons, A.M., 370  
 Simonelli, D.P., 82, 167  
 Simpson, R.A., 245  
 Singer, R., 191, 194  
 Sjogren, W.L., 237  
 Slavney, S., 573, 575  
 Smith, M.O., 191, 194  
 Smoluchowski, R., 50  
 Smythe, W.D., 154, 160  
 Soderblom, L.A., 159  
 Solberg, T.C., 121  
 Solomon, S.C., 413, 416, 465  
 Spudis, P.D., 431, 519, 545  
 Squyres, S.W., 38, 39  
 Stewart, G.R., 3, 5, 99  
 Strichartz, L.R., 496  
 Strobell, M.E., 531, 571  
 Strom, R.G., 57, 419  
 Sullivan, R., 232, 264  
 Svitek, T., 210  
 Swann, G.A., 519  
 Synnott, S.P., 558

Tanaka, K.L., 308, 345, 461, 537  
 Terrile, R.J., 173  
 Theilig, E., 229, 232  
 Thomas, P.C., 23, 25, 28, 286  
 Thompson, T.W., 223, 225  
 Tokarcik, S., 455  
 Tucker, D.W., 119, 262  
 Turcotte, D.L., 117  
 Tyler, G.L., 245

Valsecchi, G.B., 95  
 Verbiscer, A., 179  
 Veverka, J., 23, 167, 176, 179  
 Vickery, A.M., 428

Wall, S.D., 229, 232  
 Walter, L.S., 146  
 Watters, T.R., 470, 473  
 Weathers, M.S., 112, 113  
 Weibel, W., 87  
 Weidenschilling, S.J., 84  
 Weiss, B., 573, 575  
 Weissman, P.R., 47  
 Wetherill, G.W., 90  
 Whipple, F.L., 43  
 White, B.R., 232  
 Wichman, R., 463  
 Wildey, R.L., 248

Wilhelms, D.E., 479  
 Williams, S.H., 257  
 Wilson, L., 325, 352, 367, 516  
 Winchell, P.J., 308  
 Wisdom, J., 71  
 Witteborn, F.C., 170  
 Woronow, A., 445, 447  
 Wu, S.S.C., 240, 551, 553, 554

Yanamandra-Fisher, P.A., 3  
 Yon, S.A., 152

Zent, A.P., 328  
 Zimbelman, J., 362, 541

# Report Documentation Page

1. Report No. NASA TM-4041		2. Government Accession No.		3. Recipient's Catalog No.	
4. Title and Subtitle Reports of Planetary Geology and Geophysics Program - 1987				5. Report Date June 1988	
				6. Performing Organization Code EL	
7. Author(s)				8. Performing Organization Report No.	
				10. Work Unit No.	
9. Performing Organization Name and Address Planetary Geosciences Program Solar System Exploration Division Office of Space Science and Applications				11. Contract or Grant No.	
				13. Type of Report and Period Covered Technical Memorandum	
12. Sponsoring Agency Name and Address National Aeronautics and Space Administration Washington, DC 20546				14. Sponsoring Agency Code	
15. Supplementary Notes					
16. Abstract  This is a compilation of abstracts of reports from Principal Investigators of NASA's Planetary Geology and Geophysics Program, Office of Space Science and Applications. The purpose is to document in summary form research work conducted in this program during 1987. Each report reflects significant accomplishments within the area of the author's funded grant or contract.					
17. Key Words (Suggested by Author(s)) planetary geology and geophysics solar system evolution planetary geologic processes formation and evolution of planets				18. Distribution Statement  Unclassified - Unlimited  Subject Category 91	
19. Security Classif. (of this report) Unclassified		20. Security Classif. (of this page) Unclassified		21. No. of pages 604	
				22. Price A99	

**National Aeronautics and  
Space Administration  
Code NTT-4**

**Washington, D.C.  
20546-0001**

**Official Business  
Penalty for Private Use, \$300**

**SPECIAL FOURTH-CLASS RATE  
POSTAGE & FEES PAID  
NASA  
Permit No. G-27**

**NASA**

**POSTMASTER: If Undeliverable (Section 158  
Postal Manual) Do Not Return**

---